PAUL SCHERRER INSTITUT
PSI

ETH
Eidgenössische Technische Hochschule Zürich
Swiss Federal Institute of Technology Zurich

CYC2016

21st International Conference on Cyclotrons and their Applications

September 11 – 16, 2016, Zurich, Switzerland

Hosted by
Swiss Federal Institute of Technology Zurich & Paul Scherrer Institute

International Organizing Committee Chair: Mike Seidel, PSI
Scientific Programme Committee Chair: Marco Schippers, PSI
Local Organizing Committee Chair: Klaus Kirch, ETH/PSI

Themes
Cyclotron Technology
Theory, Models and Simulations
Operation and Upgrades
Cyclotron Applications
Cyclotron Concepts, FFAG and new Projects

www.CYC2016.ch

Proc. 21st International Conference on Cyclotrons and their Applications (Cyclotrons'16)

Foreword

The 21st International Conference on Cyclotrons and their Applications took place from September 11 to 16 in Zürich, Switzerland. It was hosted by the Swiss Institute of Technology ETH and the Paul Scherrer Institute, PSI. The international cyclotron conference series boasts a long tradition, dating back to 1959 when the first edition was held in Sea Island, Georgia, USA.

Over the course of the series, the focus and themes of the conferences have changed considerably. Cyclotron concepts and technologies have been developed and refined in many aspects. After years of research and development, this has resulted in many practical benefits for society, with hundreds of cyclotrons now in use for medical and industrial applications. The broad range of applications was made possible through the industrialization of the concepts, leading to robust and cost effective machines that are in routine operation, e.g., at hospitals. At the same time, the use of cyclotrons is evident in new concepts and applications to drive unique research facilities. The conference program illustrates the wide range of activities being covered by researchers in cyclotrons. They vary from improvements to technical solutions for industrial applications, with the aim of making them more economically effective, to elaborate and new ideas for realizing new research facilities. In particular new developments were presented in the fields of rare isotope beam production and cyclotrons for the acceleration of high intensity beams.

Another worthy aspect of the conference is the strong sense of community that it fosters. Scientists at various stages of their career, gather to exchange information, create networks and form collaborations. With every new idea about cyclotrons and their applications the community reinvents itself continuously. Many young people and students participated at the conference and presented their work. This is a good indication of the vibrancy of the field of cyclotrons and a positive outlook for the future.

Finally, I would like to thank all participants for attending the conference and for their numerous scientific contributions that made the conference such a success.

M. Seidel

Contents

Preface i
Foreword . . . iii
Contents . . . v
Committees . . . ix
Pictures . . . x

Papers 1
MOA01 – Operational Experience and Upgrade Plans of the RIBF Accelerator Complex . . . 1
MOA02 – Upgrade of the LNS Superconducting Cyclotron for Beam Power Higher than 2-5 kW . . . 7
MOBS02 – In Memorium: Mike Craddock . . . 11
MOB01 – Cyclotron Technology and Beam Dynamics for Microbeam Applications . . . 16
MOB02 – Simulation and Detection of the Helical Ion-Paths in a Small Cyclotron . . . 21
MOC01 – Radiation Damage of Components in the Environment of High-Power Proton Accelerators . . . 24
MOD01 – Design of the Energy Selection System for Proton Therapy Based on GEANT4 . . . 30
MODM01 – Design Study of the 250 MeV Isochronous Superconducting Cyclotron Magnet . . . 33
MODM02 – Magnet Optimization and Beam Dynamic Calculation of the 18 MeV Cyclotron by TOSCA and CYCLONE Codes . . . 36
MODM03 – Equivalent Circuit Model of Cyclotron RF System . . . 39
MODM04 – Design of the Fast Scanning Magnets for HUST Proton Therapy Facility . . . 42
MOP02 – Physical Design of External Two-Stage Beam Chopping System on the TR 24 Cyclotron . . . 45
MOP03 – Developed Numerical Code Based on the Effects of Space Charge in Central Region of 10 MeV Cyclotron 49
MOP04 – SPES Cyclotron Beamlines . . . 53
MOP05 – An Air Ionization Chamber Simulation using Monte Carlo Method . . . 57
MOP06 – Physical Design of the Extraction Trim-Rods in a 230 MeV Superconducting Cyclotron . . . 61
MOP08 – Investigation of Minimized Consumption Power about 10 MeV Cyclotron for Acceleration of Negative Hydrogen . . . 64
MOP09 – Simulation Code Development for High-Power Cyclotron . . . 68
MOP10 – Numerical Orbit Tracking in 3D Through the Injector Cyclotron for Heavy Ions at iThemba LABS . . . 71
MOP11 – Injection Line Studies for the SPC2 Cyclotron at iThemba LABS . . . 75
MOP12 – Fast Scanning Beamline Design Applied to Proton Therapy System Based on Superconducting Cyclotrons . . . 79
MOP13 – Production of F-18 and Tc-99m Radionuclides using an 11 MeV Proton Accelerating Cyclotron . . . 83
MOP14 – Study of the Beam Extraction from Superconducting Cyclotron SC200 . . . 87
MOP15 – The ISOLPHARM Project for the Production of High Specific Activity Radionuclides for Medical Applications . . . 91
MOP16 – Beam Optics Considerations for Isotope Production at the PSI Cyclotron Facility . . . 95
MOP18 – Activities for Isotope Sample Production and Radiation Effect Tests at JULIC/COSY Jülich . . . 98
MOP19 – A Diamond Detector Test Bench to Assess the S2C2 Beam Characteristics . . . 102
MOP20 – Study of Geant4 Simulation for Cyclotron Radioisotope Production in Various Target Size . . . 105
MOP21 – Test Production of Ti-44 using RFT-30 Cyclotron . . . 108
MOP22 – Simulation of Optimum Thickness and Configuration of 10 MeV Cyclotron Shield . . . 110
MOE01 – Coupling of Cyclotrons to Linacs for Medical Applications . . . 114
MOE02 – A Multi-leaf Faraday Cup Especially for Proton Therapy of Ocular Tumors . . . 118
TUA01 – Offline Tests with the NSCL Cyclotron Gas Stopper . . . 121
TUA02 – Challenges in Fast Beam Current Control Inside the Cyclotron for Fast Beam Delivery in Proton Therapy 126
TUA03 – New Time Structures Available at the HZB Cyclotron . . . 130
TUA04 – Recent Improvements in Beam Delivery with the TRIUMF's 500 MeV Cyclotron . . . 133
TUB02 – Updated Physics Design of the DAEδALUS and IsoDAR Coupled Cyclotrons for High Intensity H_2^+ Beam Production . . . 137
TUB03 – A Novel Use oF FFAGs in ERLs - in Colliders: eRHIC, LHeC and a Prototype at Cornell University . . . 140
TUB04 – Acceleration of Polarized Deuteron Beams with RIBF Cyclotrons . . . 145
TUC01 – 100 MeV H^- Cyclotron Development and 800 MeV Proton Cyclotron Proposal . . . 149
TUC02 – Charge Stripper Ring for Cyclotron Cascade . . . 155
TUC03 – Extraction by Stripping in the IFNS-LNS Superconducting Cyclotron: Study of the Extraction Trajectories 160
TUP02 – Cold Cathode Ion Source for IBA CYCLONE®230 . . . 164

TUP03 – Extraction System Design for the New IBA Cyclotron for PET Radioisotope Production 167
TUP04 – Magnet Design of the New IBA Cyclotron for PET Radio-isotope Production 170
TUP05 – Installation and Commissioning of the First Cyclone®70p 173
TUP06 – Design of the Cyclone®70p 175
TUP07 – Commissioning and Testing of the First IBA S2C2 178
TUP08 – The Use of Graphene as Stripper Foils in the Siemens Eclipse Cyclotron 181
TUP09 – Diagnostic Tool and Instrumentation for Handling 50 kW Beam Power 184
TUP10 – A New Concept of High Current Power Supply for the Main Cyclotron Magnet at TRIUMF 186
TUP11 – Developments of Ion Sources, LEBT and Injection Systems for Cyclotrons at RCNP 190
TUP12 – High Accuracy Cyclotron Beam Energy Measurement using Cross-correlation Method 193
TUP13 – Magnetic Field Measurement System of CS-30 Cyclotron 196
TUP14 – The Assembly and Adjustment of the Second Stripping Probe System for CYCIAE-100 199
TUP15 – Control System Dedicated for Beam Line of Proton Radiography on 100 MeV Cyclotron CYCIAE-100 202
TUP16 – The High Quality Water Cooling System for a 100 MeV Cyclotron 205
TUP17 – Preliminary Design of RF System for SC200 Superconducting Cyclotron 208
TUP19 – Neural Network Based Generalized Predictive Control for RFT-30 Cyclotron System 212
TUP22 – PLC Control System for Vacuum and 20 Kw RF Amplifier 215
TUP23 – Development of Magnetic Field Measurement Instrumentation for 10 MeV Cyclotron 218
TUP25 – The Methods of Compensation of the Beam Vertical Divergence at the Exit of Spiral Inflector in Cyclotrons 221
TUP26 – Axial Injection Channel of IPHC Cyclotron TR24 and Possibility of Ion Beam Bunching 224
TUP27 – The Design of the Medical Cyclotron RF Cavity 227
TUD01 – Compact Medical Cyclotrons and their use for Radioisotope Production and Multi-disciplinary Research 229
TUD02 – Studies and Upgrades on the C70 Cyclotron Arronax 235
TUD03 – Development of the Cyclone® Kiube: A Compact, High Performance and Self-Shielded Cyclotron for Radioisotope Production 238
TUD04 – BEST 70P Cyclotron Commissioning at INFN LN Legnaro 241
WEA01 – Some Examples of Recent Progress of Beam-Dynamics Studies for Cyclotrons 244
WEA02 – Simulation of the Beam Dynamics in the Axial Injection Beam Line of FLNR JINR DC280 Cyclotron . 251
WEA03 – Space-charge Simulation of TRIUMF 500 MeV Cyclotron 254
WEB01 – A New Digital Low-level RF Control System for Cyclotrons 258
WEB02 – Hybrid Configuration, Solid State-Tube, Revamps an Obsolete Tube Amplifier for the INFB K-800 Superconducting Cyclotron 263
WEB03 – Design and Simulation of Cavity for 18 MeV Cyclotron 267
WEB04 – A Coupled Cyclotron Solution for Carbon Ions Acceleration 270
THA02 – New Developments at iThemba LABS 274
THA03 – Development of FLNR JINR Heavy Ions Accelerator Complex (DRIBs III) 278
THA04 – Status of the Texas A&M University Cyclotron Institute 281
THB01 – The S2C2: From Source to Extraction 285
THB02 – The Ionetix ION-12SC Compact Superconducting Cyclotron for Production of Medical Isotopes 290
THB03 – Development of HTS Magnets for Accelerators 294
THB04 – Status of Hydrogen Ion Sources at PKU 297
THP01 – Development and Validation of a Fast Cryocooler Maintenance System 301
THP02 – Planning Considerations for Radioisotope Production Cyclotron Projects - Regulatory Feedback . . . 303
THP03 – Operation and Maintenance of RF System of 520 MeV TRIUMF Cyclotron 307
THP04 – Status of the COSY/Jülich Injector Cyclotron JULIC 310
THP05 – Beam Intensity Modulation Capabilities for Varian's ProBeam®sochronous Cyclotron 313
THP06 – Recent Ion Source Developments for VARIAN's ProBeam®yclotron 316
THP07 – Development of Control System for 10 MeV Cyclotron 319
THP09 – Mechanical Aspects of the LNS Superconducting Cyclotron Upgrade 322
THP10 – Status and Upgrade of the Cryogenic Plant of the LNS Superconducting Cyclotron After 25 Years of Operation 325
THP11 – Improvement of the NIRS-930 Cyclotron for Targeted Radionuclide Therapy 328
THP13 – Study on Energy Upgrade and Beam Transmission Efficiencies for RIKEN K-70 AVF Cyclotron 332
THP14 – Design of RF Pick-up for the Cyclotron 336
THP15 – Analysis of the Plasma Characteristics for Beam Current Optimization for TR-13 Cyclotron 339
THP16 – Beam Based Calibration Measurements at the PSI Cyclotron Facility 342

THP17 – Automated Documentation of Tunes in the Beam Lines of the COMET Cyclotron 345
THP18 – Suppression of RF Radiation Originating from the Flattop Cavity in the PSI Ring Cyclotron 348
THP19 – Operational Status of the University of Washington Medical Cyclotron Facility 351
THP20 – Magnetic System for SC200 Superconducting Cyclotron for Proton Therapy 353
THP22 – Status of the ISOL Cyclotron System in RISP 356
THP24 – Design of a Beamline from CYRCé for Radiobiological Experiments 359
THP25 – Status of the DC-280 Cyclotron Project 363
THC01 – KURRI FFAG's Future Project as ADSR Proton Driver 366
THC03 – Compact Superconducting Cyclotron SC200 for Proton Therapy 371
THD01 – High Intensity and Other World Wide Developments in FFAG 374
THD02 – Heat Transfer Studies of the IRANCYC-10 Magnet and its Effects on the Isochronous Magnetic Field . 380
THD03 – Recirculating Electron Beam Photo-converter for Rare Isotope Production 383
FRA01 – Single Stage Cyclotron for an ADS Demonstrator 387
FRA03 – Status of the High Intensity Proton Beam Facility at LNL 394
FRB02 – Stable and Exotic Beams Produced at GANIL 398
FRB03 – Proton Radiography Experiment Based on a 100 MeV Proton Cyclotron 401

Appendices **405**
List of Authors 405
Institutes List 411
Participants List 419

Proc. 21st International Conference on Cyclotrons and their Applications (Cyclotrons'16)

.

International Organizing Committee

Seidel, Mike (Chair)	PSI
Bertrand, Patrick	GANIL
Brandenburg, Sytze	KVI
Bylinski, Yuri	TRIUMF
Calabretta, Luciano	INFN-LNS
Conradie, Lowry	Tlabs
Denker, Andrea	Helmholtz-Zentrum Berlin
Gebel, Ralf	FZ-Jüllich
Gikal, Boris	JINR
Goto, Akira	RIKEN
Hatanaka, Kichiji	RCNP
Heikkinen, Pauli	JYU
Jongen, Yves	IBA
Leitner, Daniela	FRIB
Loiselet, Marc	UC Louvain
Lyneis, Claude	LBL
May, Donald	Texas A & M Univeristy
Mori, Yoshiharu	Kyoto University
Okuno, Hiroki	RIKEN
Pandit, Vijay Shanker	VECC
Schweickert, Hermann	ZAG Zyklotron AG
Smith, Susan	Daresbury Laboratory, STFC
Zhan, Wenlong	IMP
Zhang, Tianjue	CIAE
Zhao, Hong Wei	IMP

Scientific Program Committee

Schippers, Marco (Chair)	PSI
Adelmann, Andreas	PSI
Baartmann, Rick	TRIUMF
Brandenburg, Sytze	KVI
Calabretta, Luiano	INFN-LNS
Denker, Andrea	Helmholtz-Zentrum Berlin
Loiselet, Marc	UC Louvain
Machida, Shinji	RAL, STFC
Okuno, Hiroki	RIKEN
Winklehner, Daniel	MIT
Yang, Jianjun	CIAE

Local Organizing Committee

Seidel, Mike	PSI	Chair
Kirch , Klaus	PSI, ETH Zürich	Co-chair
Adelmann, Andreas	PSI	Poster Sessions
Ajmo, Barbara	PSI	Conference Secretariat
Chrin, Jan	PSI	Proceedings
Foiera, Silvio	PSI	IT
Grillenberger, Joachim	PSI	Industrial Exhibition
Schippers, Marco	PSI	Scientific Program

Cyclotrons'16 was hosted by Paul Scherrer Institut and ETH Zürich and held at the Main Building of ETH Zürich, Switzerland, from 11-16 September, 2016

OPERATIONAL EXPERIENCE AND UPGRADE PLANS OF THE RIBF ACCELERATOR COMPLEX

H. Okuno*, T. Dantsuka, M. Fujimaki, N. Fukunishi, H. Hasebe, Y. Higurashi, E. Ikezawa, H. Imao, O. Kamigaito, M. Kidera, M. Komiyama, K. Kumagai, T. Maie, M. Nagase, T. Nagatomo, T. Nakagawa, M. Nakamura, J. Ohnishi, K. Ozeki, N. Sakamoto, K. Suda, A. Uchiyama, S. Watanabe, T. Watanabe, Y. Watanabe, K. Yamada, H. Yamasawa
RIKEN Nishina Center, Wako, Japan

Abstract

The Radioactive Isotope Beam Factory (RIBF) is a cyclotron-based accelerator facility for nuclear science, completed at the end of 2006. RIBF can produce the most intense RI beams using fragmentation or fission of high speed heavy ion beams. Continuous efforts since the first beam have increased the beam intensity and achieved stable operation. 49.8 pnA (3×10^{11} /s) of uranium ion beam was extracted from the final accelerator SRC with energy of 345 MeV/u in 2016, which is currently the world record. For further expansion of the scientific opportunity, an upgrade program has been proposed to increase the intensity of uranium ion beam by a factor greater than twenty. The program includes two components. The first component is increasing space charge limit of the beam intensity in the low-energy ring cyclotron (RRC) by replacing the existing resonators with newer ones to achieve higher accelerating voltage. The second component is skipping the first stripper, which requires an increase in the magnetic rigidity of the ring cyclotron just after the first stripper (FRC). The new ring cyclotron will consist of six-sector magnets with four rf-resonators to maintain approximately 15 mm of turn separation, which is similar to that in the present FRC, the K-value of which is 2200 MeV. A conceptual design of the new cyclotron is ongoing. Certain issues to realize the intensity upgrade are also under discussion.

INTRODUCTION TO RI BEAM FACTORY

The Radioactive Ion Beam Factory (RIBF) is a cyclotron-based accelerator facility that uses fragmentation or fission of heavy ion beams to produce intense RI beams over the whole atomic range [1]. The purposes of the RIBF are to explore the inaccessible region of nuclear chart, to discover the properties of nuclei far from stability, and to advance knowledge in nuclear physics, nuclear astrophysics, and applications of rare isotopes for society. The RIBF facility consists of four cyclotron rings (RRC [2], FRC [3], IRC [4], and SRC [5]) with three injectors, including two linacs (RILAC [6, 7] and RILAC2 [8]) and one AVF cyclotron (AVF) [9]. Cascades of the cyclotrons can provide heavy ion beams from H_2^+ to uranium ion at more than 70% of the speed of light to efficiently produce RI beams. Three acceleration modes are available, as shown in Fig. 1. The first mode is used mainly for mid-heavy ions, such as Ca, Ar, and Zn. The second mode is used for light ions, such as O and N. The third mode is used for very heavy ions such, as Xe and U. Table 1 lists the specifications of the four ring cyclotron of RIBF. RRC has been operating since 1986. FRC and IRC have similar structures to that of RRC. The K-value per weight is listed in the table, which clearly shows that FRC is a very compact machine compared to the other cyclotrons. We can see that SRC is the most challenging machine to obtain an acceleration voltage of 640 MV for uranium acceleration up to energy of 345 MeV/u. The design and construction of the RIBF accelerators started from 1997 and we obtained the first beam at the end of 2006.

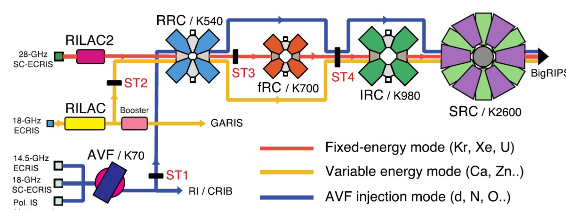

Figure 1: Acceleration modes for RIBF facility.

OPERATION FOR TEN YEARS

Operations for about ten years since the first beam have been very successful. Our continuous efforts have increased beam intensity, especially of very heavy ions, such as Xe and U, as shown in Fig. 2. The maximum beam intensity of uranium ion is 50 pnA, which is the world record. The beam availability has been significantly improved, exceeding 90% since 2014.

A 28 GHz ECR ion source using superconducting solenoids and sextuple magnets was constructed because powerful ion sources are essentially required to increase the uranium beam intensity [10, 11]. The operation of this ion source on the beam line started from 2011 with the new injector linac (RILAC2). Currently, approximately 150 eμA of U^{35+} can be stably extracted with uranium metal sputtering. A high-temperature oven for uranium ions is also under development.

Charge strippers are important devices to increase the intensity of uranium beam because they have a high risk of bottleneck problems owing to fragility against high-power

* okuno@riken.jp

ISBN 978-3-95450-167-0

Table 1: Specification of the RIBF Cyclotrons

	RRC	fRC	IRC	SRC
K-value (MeV)	540	700	980	2600
R_{inj} (cm)	89	156	277	356
R_{ext} (cm)	356	330	415	536
Weight (ton)	2400	1300	2900	8300
K/W	0.23	0.54	0.34	0.31
N_{sec}	4	4	4	6
rf Resonator	2	2+FT	2+F	4+FT
Frequency range (MHz)	18–38	54.75	18–38	18–38
Total Acc. Volt. (MV)	2	2+FT	2+F	640
Acc. Volt. (MV/turn)*	0.28	0.8	1.1	2.0
Δr (cm)*	0.7	1.3	1.3	1.8
I_{sc} (pμA)*	0.7	4.7	6.6	5.1

* in the table indicates that the values are shown for the case of uranium acceleration up to 345 MeV/u.

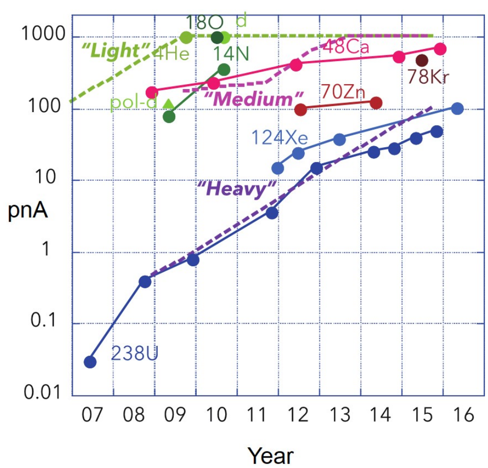

Figure 2: History of the beam intensities at the RIBF accelerator.

beams. After much research and development [12, 13], we developed a helium gas stripper [14] for the first stripper and a rotating disk stripper with a highly-oriented graphene disk for the second stripper [15]. These have been working well so far.

Here we summarize the lessons learned from the first ten years of operation. Firstly, it is a very tough business to operate an accelerator complex where four cyclotrons are connected in series, because we have to inject and extract the accelerated beams four times. Energy matching between the cyclotrons and single turn extraction requires the greatest care and effort. Secondly, multi-step charge stripping should be avoided, because charge stripping decreases beam intensity at every step owing to charge state dispersion. Furthermore, the thickness of the charge strippers at each stage should be as thin as possible because the charge strippers are always sources of emittance growth. Thirdly, the space charge effect in the low-energy cyclotron, RRC, is very severe because of low velocity and low rf voltage. Figure 3 shows the structure of the rf resonator of RRC. This resonator is frequency-tunable by the movable box from 18 to 40 MHz. Because the movable box is very close to the Dee electrode in the case of low frequencies such as 18.25 MHz, high voltage cannot be applied because of discharge between the movable box and the Dee electrode. Of course, we can get higher voltage at the frequency of 36.5 MHz (H = 18); the effective voltage for the beam is zero because the distance between the double gaps is optimized for harmonics of nine. Table 1 lists the space charge limit for the four cyclotrons in the case of uranium beam acceleration according to Baartman's paper [16]. It clearly shows that space charge limit for RRC is small compared to the required current to reach 1 pμA at the exit of SRC. The final point is that approximately 20% of the current from the ion source can reach the exit of SRC, excluding charge stripping efficiency, as shown in Fig. 4. This value is not particularly high but not so small compared to that of other accelerators. In fact, 10 mA from ion source is extracted to obtain 3 mA from the ring cyclotron in the case of the PSI machine. However, it is very important to understand the mechanisms of beam loss to improve and reduce uncontrolled beam loss.

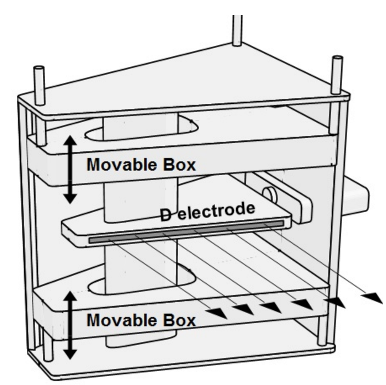

Figure 3: Structure of an rf resonator for RRC.

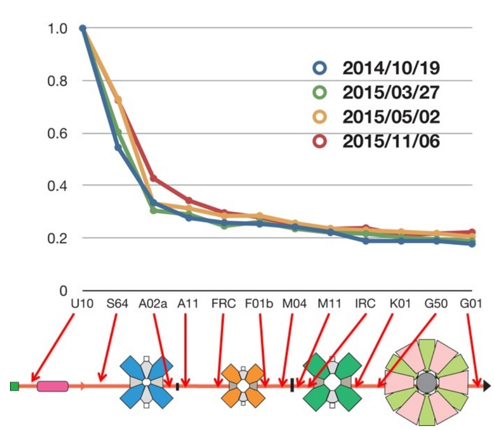

Figure 4: Transmission in the RIBF accelerator complex.

ISBN 978-3-95450-167-0

UPGRADE PLAN

We have just started an upgrade program of the RIBF accelerator complex, mainly to increase uranium ion beam intensity. The goal intensity is approximately 1 pμA of uranium based on the potential of the accelerator complex. The program mainly consists of two components as shown in Fig. 5. Firstly, the first stripper is skipped to avoid the reduction of beam intensity due to the dispersion of the charge state after the stripper. This requires replacement of the existing fRC with a new one that can accept the same charge state, 35+, as that of the ion source. The skipping of the first stripper will improve the beam quality, especially in the longitudinal direction, because charge-exchange energy straggling in the first stripper is significant. This affects the improvement of extraction efficiency at the succeeding cyclotrons. The second component is to resolve the problems with respect to the space charge effect in the low-energy cyclotron, RRC. Our original baseline is the replacement of the RRC with the superconducting linac, as shown in Fig. 5, to eliminate these problems. The current baseline focuses on cost effectiveness. RRC is not abandoned but its resonators are remodeled to increase the space charge limit in the ring cyclotron,

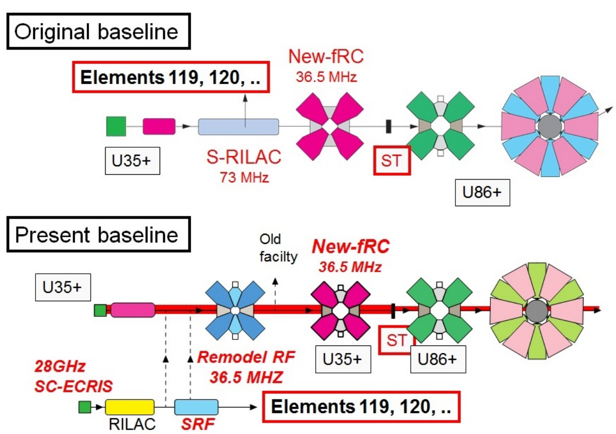

Figure 5: The original and present upgrade plans for the RIBF accelerator complex.

Remodel of RRC Rf Cavities

As mentioned in the previous section, operation of RRC at a frequency of 18.25 MHz limits the Dee voltage, which is approximately one third of that with frequency of 36.5 MHz, owing to its structure. This cavity has double gaps and the distance between the two gaps corresponds to $\beta\lambda/2$ in the case of harmonics of 9 which, which means that effective voltage is zero in the case of harmonics 18, although high voltage can be achieved with 36.5 MHz. The Dee angle was studied to optimize for the harmonics numbers of 18, 9, and 5, which are mainly used for the operation. The study shows that angles between 7.25° and 8.25° can enable sufficiently high voltage in the three studied cases. However, we should take care that operation with such large harmonics number as 18 requires high accuracy of the isochronous field because phase acceptance in the case of harmonics of 18 becomes half of that for harmonics of 9. The power supplies for the trim coils and diagnostics of the isochronous field should be also upgraded for the realization of isochronous field with high accuracy.

Conceptual Design of the New FRC

In Cyclotrons2013, a design of a superconducting ring cyclotron with four sectors and two cavities, the maximum voltage of which is around 500 kV, was presented [17]. We cannot find any problems in this design, but the turn separations are not large enough to extract the uranium beam at more than 1 pμA, which is required to achieve the goal intensity at the exit of SRC. To obtain sufficiently large turn separation, we have just started designing a cyclotron with six-sector normal conducting magnets so as to install four cavities. A preliminary design will be presented in the rest of this subsection.

Figure 6 shows a plan view of the new FRC, with the main specifications listed in Table 2. The number of sector magnets is six and the K-value is 2200. Four accelerating rf cavities and a flattop cavity are used. The acceleration rf frequency is 36.5 MHz, which is the same as that of RILAC2, to achieve wide acceptance in the longitudinal direction. The structure of the rf resonators will be similar to that used in the RIBF accelerator. We can get 15 mm of turn separation using similar rf cavities to those used in the RIBF accelerators. Betatron frequencies were calculated based on the magnetic field simulated by TOSCA [18], as shown in Fig. 7. They indicate that this design can avoid the integral resonance $\nu_z = 1$, which constitutes the most serious imperfection resonance. In the further detailed design process, however, we should take care because ν_z may easily get close to 1 as the sector angle decreases, owing to space problems.

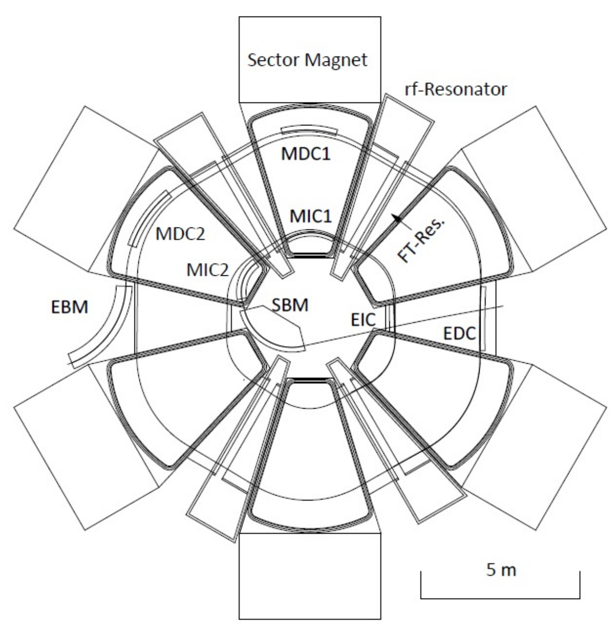

Figure 6: Plan view of new FRC.

ISBN 978-3-95450-167-0

Table 2: Specification of the New FRC

Item	new FRC	exiting FRC
K-value (MeV)	2200	700
Sectors	6	4
rf-Cavities	4+FT	2+T
rf-Frequency (MHz)	36.5	54.75
Injection radius (m)	2.76	1.56
Extraction radius (m)	5.67	3.30
Velocity gain	2.1	2.1
Diameter (m)	19	10.8
Height (m)	6.6	3.34
Weight (ton)	8109 (7563)	1320
Δr (cm)*	1.5	1.3

The number in parentheses of the weight row is the weight estimated by cutting the edge of the yoke, where magnetic field in the iron is low.

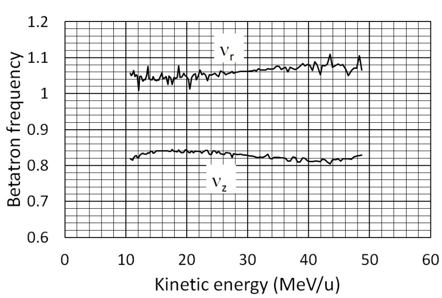

Figure 7: Betatron frequencies in the new FRC as functions of kinetic energy of U^{35+}.

A list of parameters and an illustration of the quarter-cut model of the sector magnet are given in Table 3 and Fig. 8, respectively. The sector magnets use normal-conducting main coils and trim coils, and the weight of the yokes of one sector is approximately 1350 t. The sector angle is 34°. The maximum magnetic field in the beam orbit region is 2.1 T. The excitation curve shown in Fig. 9 shows that the iron pole is almost saturated at the operation point of 180 kAT. The main coil consists of one pair of 60 turns using a conductor, the size of which measures 16×16 mm^2 with a hollow of 9 mm in diameter. The maximum current is approximately 1500 A, requiring a power consumption of 2.42 MW. Isochronous magnetic fields can be generated by optimizing the pole shape with small corrections of the trim coil current, because not only beam energy but also charge-to-mass ratio can be fixed in this cyclotron by selecting the charge from the ion source when other ions than uranium are accelerated.

The injection and extraction orbits for the new FRC are shown in Fig. 6. For beam injection, magnetic channels (SBM, MIC2, and MIC1) and an electrostatic channel (EIC) are used. For beam extraction, an electrostatic channel (EDC), two normal magnetic channels (MDC1, MDC2, and MDC3), and an extraction bending magnet (EBM) are used. Table 4 lists the parameters of these devices for injection and extraction of U^{35+} beams. Similar elements to those for the SRC can be used [5].

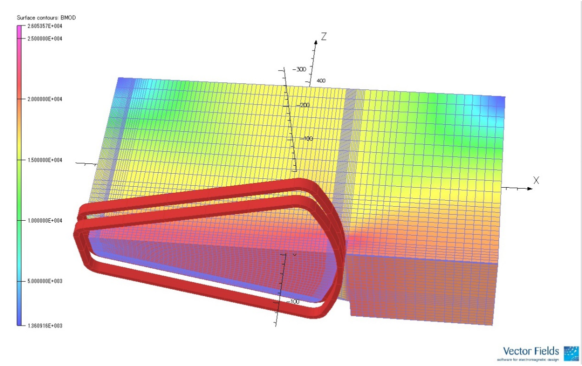

Figure 8: Quarter-cut model of the sector magnet for the new FRC.

Table 3: Specification of the New FRC Sector Magnet

Item	Value
Maximum field	2.1 T
Pole gap	50 mm
Magnetic motif forces	180 kAT
Sector angle	34°
Operational current	1450 A
Power consumption	2.4 MW/total

SOME ISSUES FOR INTENSITY UPGRADE

This section will present a discussion of three issues that should be solved to realize this upgrade program of the RIBF accelerator complex.

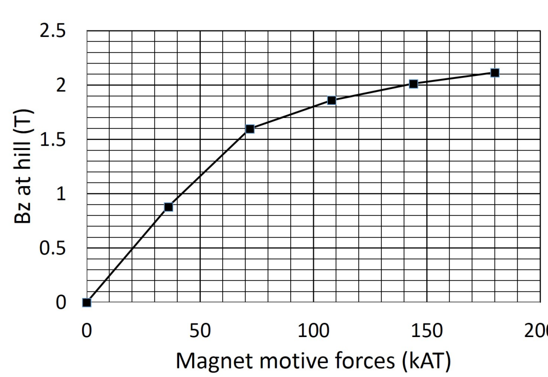

Figure 9: Excitation curve of the sector magnet for the new FRC.

ISBN 978-3-95450-167-0

Table 4: Specifications of Injection and Extraction Elements for the New FRC

	Length (m)	Magnetic/Electric field (T)/(kV/cm)
SBM	2.43	2.1
MIC2	1.28	0.7
MIC1	1.53	0.22
EIC	0.86	90
EDC	2.02	90
MIC1	1.74	0.15
MIC2	2.05	0.25
EBM	3.13	2.5

How to Make the New FRC Smaller

As mentioned in the previous section, the upgrade program does not include a new building for the new FRC. It is supposed to be installed in a room for the secondary beam line RIPS of the existing facility. This requires that the new FRC should be as small as possible.

Increasing the charge state of the accelerated ions will help the down-sizing. We hope to achieve U^{42+} with more than 300 eμA. Some experts of the ECR ion source have already proposed the fourth generation ECR ion source, which is expected to generate such highly charged ions as more than 42+ with high current. On the other hand, they pointed out that much research and development is necessary for the realization of this goal. We hope that the proof-of-principle machine of the fourth generation will appear as soon as possible, because it will save the cost of the new building for the new FRC.

Another way to make the new FRC smaller is by recycling the existing FRC, which is to be replaced with the new FRC. Figure 10 shows an accelerator scheme in which the FRC is reused as the first cyclotron. RILAC will be upgraded for the SHE experiment, by installing SRF linacs. 3.4 MeV/u of U^{35+} from the RILAC can be injected to the reused fRC for acceleration up to 13.58 MeV/u with harmonics of 14. This means that the injection radius for the new fRC can be increased from 2.75 m to 3.14 m. The area of the pole face and the volume of the return yoke can be reduced.

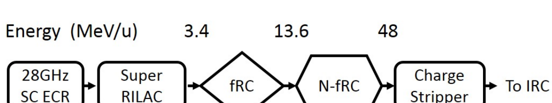

Figure 10: Acceleration scheme reusing the existing fRC.

Usage of Superconducting Wire for the Main Coil

The main coil blocks described in the previous section are made of normal conducting wires. The total power consumption exceeds 2 MW, which sufficiently high that we are studying the option of making the main coil of superconducting wires to save power. The excitation curve in Fig. 9 shows that the contribution of the iron to the magnetic field is large and the required magnet motive force is not large. This is a so-called superferric magnet.

Figure 11 shows a cross-sectional view of the main coil block in the case when a rectangular Al-stabilized superconductor is used. NbTi/Cu monolith round wires with diameter 1.6 mm are embedded in a rectangular pure Al stabilizer, the size of which is 2.9×3.6 mm^2. The ratio of Al, Cu, and NbTi in the wire is 10:2:1. The size of a section is 31×68 mm^2 and its perimeter of the main coils is 14.1 m. The operational current is set to 1000 A, which is less than 10% of the critical current at the maximum magnetic field in the main coil, 1.4 T. The coils are epoxy-impregnated with coil supports and are indirectly cooled by two-phase He flowing through a tube attached to the coil supports.

The electromagnetic forces on the coil in the radial and vertical directions are calculated to be 1.2 ton and 1.4 ton at the operational point. The expansion force on the long straight section is 0.74 ton/m. These are basic data for the design of the support structure of the coil. The solution for the support structures are easily found because they are very small. The rectangle with dotted lines indicates the coil blocks of the normal-conducting wire. It clearly shows that the necessary size for the superconducting coils does not exceed the area of the normal-conducting coil blocks.

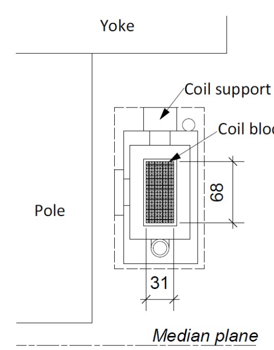

Figure 11: Structure of the main coil block using superconducting wires

Improvement of the Transmission Efficiency

As mentioned in the previous section, approximately 20% of beam from the ECR ion source can survive until the exit of the SRC. Most of the beam loss occurs at low energy until the entrance of fRC. One of the possible reasons for the beam loss comes from the beam buncher located before the RFQ entrance, where DC beam from the ion source is modified to CW beam. Figure 12 shows beam emittance in the longitudinal direction at the entrance and the exit of the RFQ in the RILAC2. Energy modulation generated by the buncher is tuned so as to focus the beam at the entrance of RFQ. The accelerated beams at the RFQ show a characteristic vortex shape, which causes the beam to have a tail. This tail causes beam loss in the succeeding linac and cyclotrons. The scale of the tail is determined by the energy

ISBN 978-3-95450-167-0

modulation of $d\beta/\beta$. Figure 13 shows the dependence of the beam emittance in the longitudinal emittance on the initial velocity modulation. In fact, the emittance grows as the velocity modulation increases, suggesting that mono-energetic beam bunch is important for acceleration without the tail. These simulations were carried out with a zero current limit. Furthermore, space charge force distorts the beam bunch. In any case, we require a more sophisticated bunching system with phase collimation. One idea is a bunching system which consists of two bunchers and in the ring with phase collimations, as shown in Fig. 14. Negative length beam transport helps decrease the energy spread.

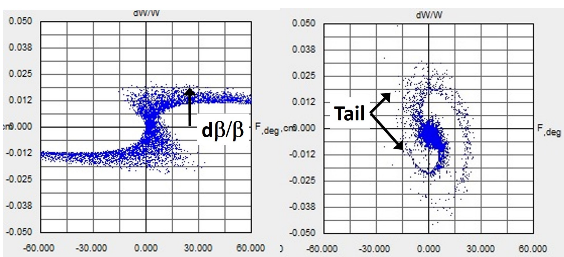

Figure 12: Typical bunch shapes in the longitudinal direction at the entrance and exit of the RFQ.

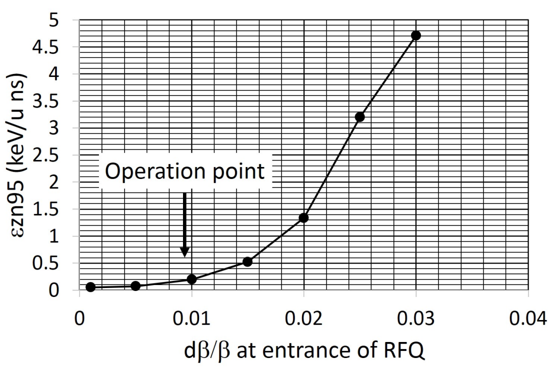

Figure 13: $d\beta/\beta$ dependence of longitudinal emittance after the RFQ.

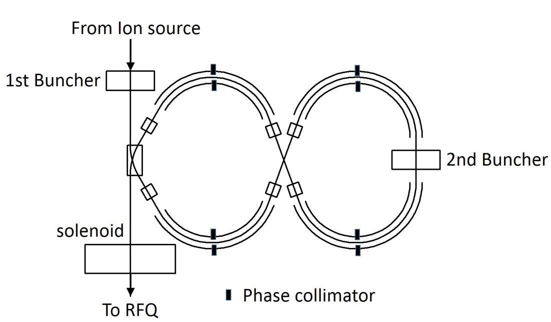

Figure 14: Low-energy ring with two bunchers.

SUMMARY AND OUTLOOK

We have just started an upgrade program to increase beam intensity, mainly of uranium ion beam, based on the successful operational experience of ten years since the first beam at the end of 2006. The program includes two components. Firstly, space charge limit in the low-energy cyclotron of RRC is increased by remodeling the rf resonators. Secondly, the existing fRC is replaced with a new one to skip the first charge stripper. Although we have to address certain issues for the realization of this program, we hope to obtain the first beam from the new, upgraded acceleration complex in 2025.

REFERENCES

[1] Y. Yano, *Nucl. Instrum. Methods Phys. Res.*, Sect. B 261 (2007) 1009.

[2] Y. Yano, in *Proc. Int. Conf. on Cyclotrons and Their Applications (Cyclotrons'92*, p102, (1992).

[3] T. Mitsumoto *et al.*, in *Proc. 17th Int. Conf. on Cyclotrons and Their Applications (Cyclotrons'04)*, p384 (2004).

[4] J. Ohnishi *et al.*, on *Proc. 17th Int. Conf. on Cyclotrons and Their Applications (Cyclotrons'04)*, p197 (2004).

[5] H. Okuno *et al.*, *IEEE Trans. Appl. Supercond.*, 17, p1063 (2007).

[6] M. Odera *et al.*, *Nucl. Instrum. Methods* A227, p187 (1984).

[7] O. Kamigaito *et al.*, *Rev. Sci. Instrum.* 76 (2005) 013306.

[8] K. Yamada *et al.*, in *Proc IPAC'12*, New Orleans, Louisiana, USA, paper TUOBA02 (2012).

[9] A. Goto *et al.*, in *Proc. 12th Int. Conf. on Cyclotrons and Their Applications (Cyclotrons'89)* 51, p439.

[10] T. Nakagawa *et al.*, *Rev. Sci. Instrum.* 81 (2010) 02A320.

[11] Y. Higurashi *et al.*, *Rev. Sci. Instrum.* 83 (2012) 02A308.

[12] H. Kuboki *et al.*, *Phys. Rev. ST Accel. Beams* 13 (2010) 093501.

[13] H. Okuno *et al.*, *Phys. Rev. ST Accel. Beams* 14 (2011) 033503.

[14] H. Imao *et al.*, *Phys. Rev. ST Accel. Beams* 15 (2012) 123501.

[15] H. Hasebe *et al.*, INTDS2016, Cape town (2016).

[16] R. Baartman, in *Proc. 20th Int. Conf. on Cyclotrons and Their Applications (Cyclotrons'13)*, paper WE2PB01.

[17] J. Ohnishi *et al.*, in *Proc. 20th Int. Conf. on Cyclotrons and Their Applications (Cyclotrons'13)*, paper MOPPT022.

[18] Vector Fields Limited, 24 Bankside, Kidlington, Oxford OX5 1JE, England.

ISBN 978-3-95450-167-0

UPGRADE OF THE LNS SUPERCONDUCTING CYCLOTRON FOR BEAM POWER HIGHER THAN 2-5 kW

L. Calabretta†, A. Calanna, G. D'Agostino, D. Rifuggiato, G. Cuttone, A.D. Russo,
INFN-LNS, Catania, Italy

Abstract

The LNS Superconducting Cyclotron has been in operation for more than 20 years. A wide range of ion species from Hydrogen to Lead, with energy in the range 10 to 80 AMeV, have been delivered to users. Up to now the maximum beam power has been limited to 100 W due to the beam dissipation on the electrostatic deflectors.

To fulfil the demand of users aiming to study rare processes in Nuclear Physics, the beam power has to be increased up to 2÷10 kW for ions with mass lower than 40 a.m.u., and extracted by stripping. This development has to maintain the present performances of the machine, i.e. the existing extraction mode for all the ion species allowed by the operating diagram.

To perform the extraction by stripping, a significant refurbishing operation of the Cyclotron is needed, including a new cryostat with new superconducting coils, a new extraction channel with a 60 mm vertical gap, additional penetrations to host new magnetic channels and new compensation bars.

Moreover, the vertical gap of the acceleration chamber is planned to be increased from the present 24 mm up to 30 mm by renewing the existing liners and trim coils.

A general description of the refurbishing project is presented.

INTRODUCTION

The LNS Superconducting Cyclotron (CS), designed by the Milano Group headed by F. Resmini, has been in operation since 1995 [1]. The CS was designed to be operated as a booster of a Tandem accelerator and to deliver beams for nuclear physics experiments mainly. The usual beam power stays around few tens of Watts.

After the year 2000, the CS was equipped with a central region to operate in stand-alone mode. Ion beams are now produced by ECR ion sources and injected into the cyclotron through the axial hole using a spiral inflector. The success of axial injection operation stimulated the development of the EXCYT project to produce radioactive ion beams on a thick target with the ISOL technique [2].

To operate the EXCYT project we pushed the CS to the maximum beam current, but it became clear that despite our efforts, the extraction system and in particular the two electrostatic deflectors (ED) were not able to deliver beam currents more than 150 W. This limit was mainly due to the extraction efficiency of the CS that stays around 50-60% and to the constraints of our ED. Although it is water cooled, can work with a maximum beam loss of 100 W. Recently some nuclear physicists proposed to use the magnetic spectrometer with large solid angle and large momentum acceptance “MAGNEX” to measure the nuclear matrix that is of relevant interest for the double β decay without neutrino emission [3,4]. This experiment, called NUMEN, needs mainly beams of Carbon, Oxygen and Neon with intensity up to 10^{14} pps. The required energies are in the range 15÷70 AMeV, which corresponds to a beam power in the range 1÷10 kW.

According to this relevant scientific interest, the management of LNS-INFN approved a program to upgrade the CS. This upgrade will be relevant also for experiments that use radioactive ion beams produced by in-flight fragmentation. In particular, a new dedicated beam line for the production and selection of the radioactive ion beams is under design. Moreover, the availability of light ion beams with medium power opens the opportunity also to produce radioisotopes of medical interest.

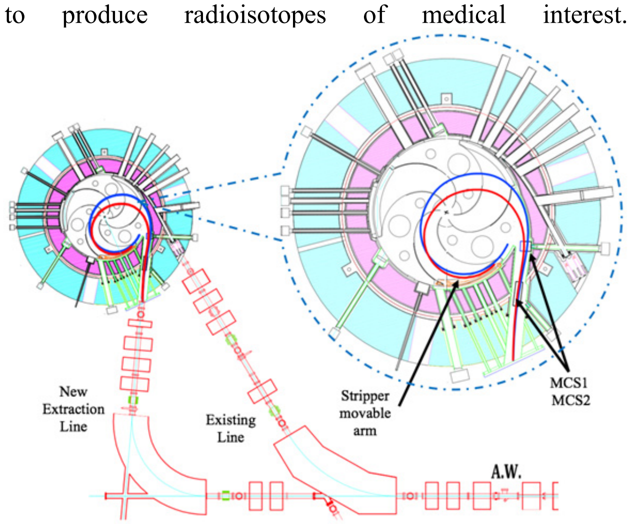

Figure 1: Layout of the Superconducting Cyclotron with the existing and the new extraction beam lines. Two extraction trajectories, in red and blue, are also shown.

MAIN MODIFICATIONS

The extraction of 1÷10 kW beams is not feasible using the ED nor through the existing extraction channel. Indeed, the existing extraction channel allows to extract beams with a transversal size not larger than 8 mm, and this magnetic channel has no thermal shields to dissipate the beam power coming from haloes. So a solution based on extraction by stripping has been investigated [5]. According to Fig. 1, the ion beams are accelerated with a charge state q=Z-1÷Z-3 and after crossing a stripper foil the ions become fully stripped. The use of a stripper foil, placed at a proper position, allows the beam trajectory to escape from the region of the cyclotron pole and to come out through the new extraction channel. This extraction mode is currently used in the cyclotron of FLEROV laboratory [6]. The energies of our beams are enough high,

ISBN 978-3-95450-167-0

so that all the ions of interest, with mass <40 a.m.u., are fully stripped with efficiency higher than 99%. Beam losses well below 100 W are expected due to the stripping process also in the case of an extracted beam power as high as 10 kW.

The Fig. 1 shows the trajectories evaluated just for two ions of interest. More details about the stripping extraction trajectories are presented in another paper presented at this conference [7].

The mechanical study of the new extraction channel and the specifications for the new cryostat are also presented at this conference [8,9].

The main modifications of the new magnet are briefly presented in this paper.

Main Coils

The existing superconducting coils are wound with the so-called technique of the double pancake. This solution is very conservative but it is space consuming because a set of tie rods, beryllium made, are necessary to compress the two pairs of alfa and beta coil to prevent their radial movement.

The tie rods are room consuming both in radial and vertical direction, see Fig. 2. By having a little different coils size and higher current density, it is possible to reduce the vertical coils size and avoid the use of the vertical tie rods compressing, that are replaced by a set of springs placed on the top of the upper beta coil and on the bottom of the lower beta coils [10].

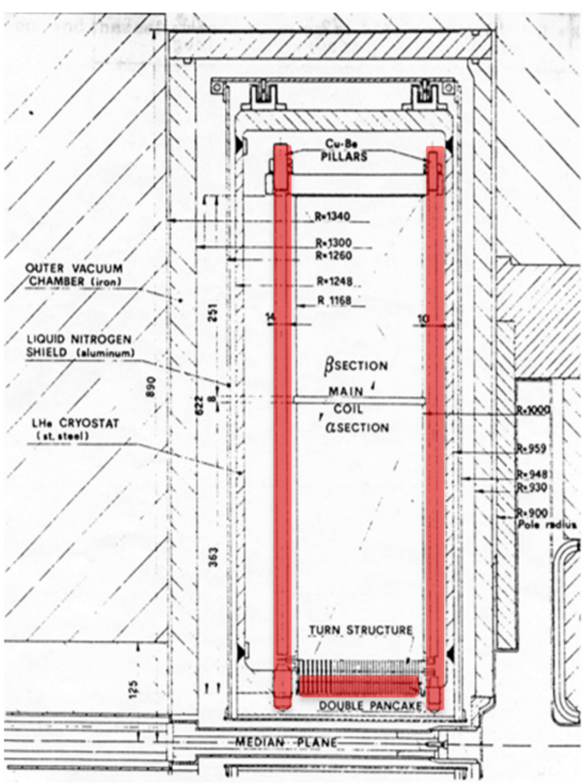

Figure 2: Cross section of the cryostat and of the existing alfa and beta coils. The Cu-Be and the two layers of the alfa coils that have to be removed are highlighted in red.

Liquid Nitrogen Shields

Removing the tie rods, the LHe vessel can be radially smaller. More than 10 mm became available at the inner and outer side of the liquid Helium vessel, which allows the installation of a larger and more reliable Liquid Nitrogen shield. The larger size of the Liquid Nitrogen shield allows to feed it with Liquid Nitrogen flowing with a natural convection mode. This solution should reduce significantly the present liquid nitrogen consumption.

Larger Vertical Gap for the Extraction Channels

The beginning of the alfa coil is planned to stay at around 90 mm from the median plane (the present distance being 62 mm) and allows to increase the vertical gap of the extraction channel up to 60.5 mm vs the present value of 30.5 mm and also to have some extra room of about 10 mm for the liquid nitrogen shield.

PRESENT LIMITS AND PROBLEMS

Some components of the CS are suffering from few problems after 22 years of operations. The liquid nitrogen shield, made by an aluminium made roll bond plate, consists of three main components: the inner wall, the outer wall, the bottom and the top. Unfortunately, the pipeline cooling the inner wall is having serious leaks and has been closed for more than 6 years. The pipeline cooling the outer wall is also having some small leaks towards the cryostat vacuum. These leaks are not critical, but about once per years we are forced to warm up the cryostat up to 100 K to allow the frozen nitrogen to evaporate and to restore the working vacuum pressure in the cryostat. It is evident that this is a serious problem for the future operation of the cryostat, especially if the leaks in the nitrogen shields should increase.

Another problem is related with the vacuum of the acceleration chamber that is slowly worsening. The walls of our vacuum chamber are the internal wall of the cryostat and the two copper made liners, that cover the upper and lower poles, see Fig. 3. The liners separate the vacuum of the acceleration chamber from the vacuum volume trapped among the liners and the poles, the so called "dirty" vacuum. The residual pressure in the acceleration chamber is increasing along the years. The main reason of this worsening are the leaks through the welds of the liners. Indeed, some recent tests in the acceleration chamber showed a strong correlation of the measured residual pressure with the so called dirty vacuum. The worsened vacuum in the acceleration chamber increases the amount of beam losses along the acceleration path and produces additional sparking problems at the RF cavities and in the perspective of higher beam currents the amount of beam losses should became higher. These problems are reducing the reliability of our cyclotron.

FURTHER MODIFICATIONS

The replacement of the cryostat and of the main coil gives us the opportunity to replace also the existing cop

ISBN 978-3-95450-167-0

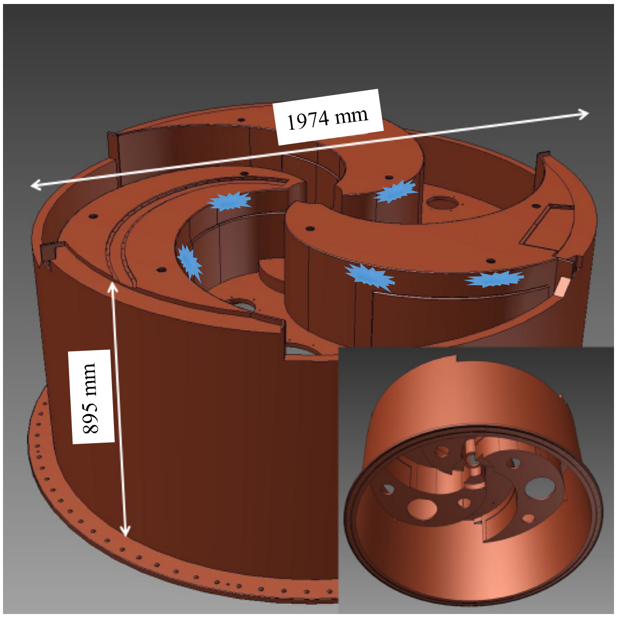

Figure 3: View of one of the two copper made liners. The blue sparking clouds indicate the regions of the possible leaks.

per made liners with new ones. We believe that today it is feasible to realize the new liners with safer welds.

The existing upper and lower liners consist each one of 3 copper plates, 14 mm thick, that cover the hills and 3 thick plates that cover the valleys. These hills and valleys plates are joint by a copper made 3 mm thick wall, that is wrapped around the side of the hills and around the poles, see Fig. 3.

To achieve a better welding between the thin sides of the liners that wrap the hills and the top and bottom plates of liners, we plan to increase the thickness of the copper sides from the present value of 3 mm to 5 mm. This will be quite easily feasible if we replace also the set of 20 trim coils wrapped around each hill of our cyclotron. The cable of the present trim coils has a size of 6.25×6.25 mm and an inner hole of 4.76 mm. The existing trim coil cable has a minimum thickness of about 0.75 mm and this is one additional reason that suggests us to replace the trim coils, to prevent the collapse of some of these 120 trim coils. We plan to replace this cable with a new one with size 6.25×5.00 mm and inner hole with size 4.25×3.00 mm. This new cable has a minimum thickness of 1 mm. Moreover, the reduction of the cable size of 1.25 mm in one direction allows to increase the total gap of the vacuum chamber of 5 mm. Indeed, the trim coils are wound in two turns on each hill and are symmetric vs. the median plane, therefore 2×2×1,25 mm is the full increased gap of the vacuum chamber due to replacement of the trim coils. Reducing the thickness of the copper plates of liners from the present 14 mm down to 13 mm the vertical gap of the vacuum chamber in the region of the hill will increase from the present value of 24 mm up to 31 mm. With the great advantage to minimize the beam loss due to beam halo striking on the liner surfaces and to increase the vacuum conductance.

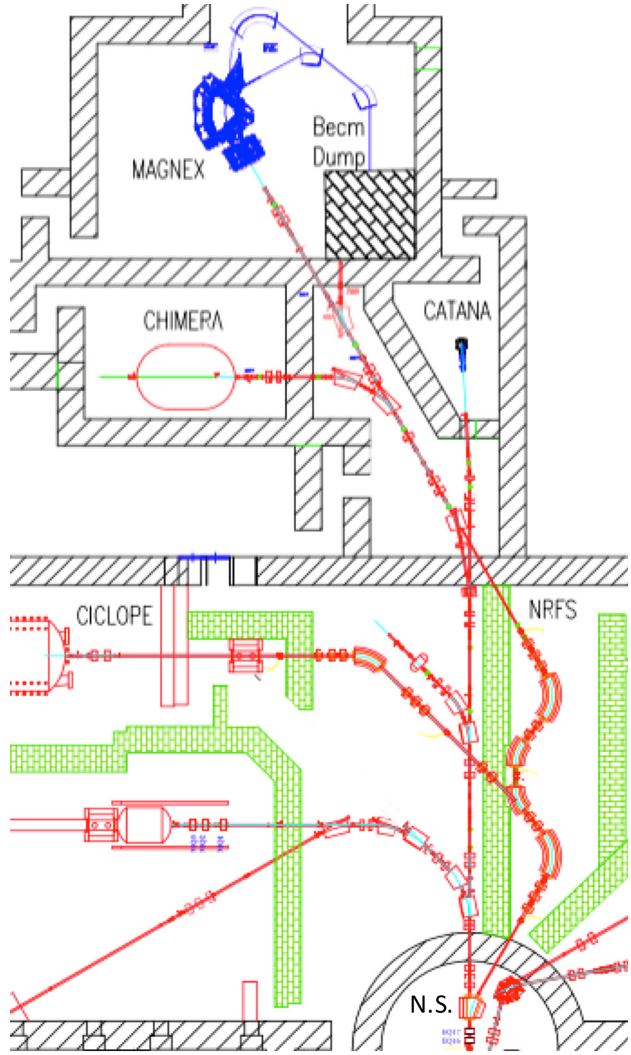

Figure 4: beam transport line of LNS with the proposed New Recoil Fragment Separator (NRFS).

NEW BEAM LINES

As shown in Fig. 1, an additional beam extraction line has to be built to transport the beam extracted through the new extraction channel to the existing beam lines. The main elements of this line are: a steering magnet, three large quadrupoles, a 95° bending dipole and an additional quadrupole doublet. This beam line has to produce an achromatic beam waist at the common point position, labelled “AW” in Fig. 1.

A further mandatory modification is to replace the existing switching magnet with a smaller one with larger gap labelled “NS” in Fig. 4.

Moreover, a New Recoil Fragment Separator (NRFS) able to operate with a primary beam with power up to 2 kW is proposed. The NRFS can be used to deliver radioactive ion beams to three experimental room. The NRFS could be also used to clean the high beam power to be transported to MAGNEX spectrometer to reduce the en-

ISBN 978-3-95450-167-0

ergy spread of the beam extracted by stripping from the intrinsic value of $\pm3\times10^{-3}$ down to $\pm1\times10^{-3}$.

CONCLUSIONS

The call of tender for the construction of the new cryostat including the superconducting coils will be published before the end of this year. The new magnet is expected to be ready not before the middle of 2019. Since the expected time to dismount and to assemble the cyclotron is about 18 months, we expect the restart the cyclotron in the 2021. In the meanwhile, some crucial parts of the existing beam line will be optimised to ensure a beam transmission as high as 99%.

REFERENCES

[1] L. Calabretta et al., "Commissioning of the K800 INFN cyclotron", in *Proc. 14th Int. Conf. on Cyclotrons and their Applications (ICCA'95)*, Cape Town, South Africa, October 1995, pp. 12-19

[2] L. Calabretta et al., "The progress of the EXCYT facility at INFN-LNS", in *Proc. 7th European Particle Accelerator Conf. (EPAC'00),* Vienna, Austria, June 2000, pp. 2597-2599

[3] C. Agodi et al., "Heavy-ion double charge exchange reactions: A tool toward 0νββ nuclear matrix elements", in Proc. Of Neutrino Oscillation Workshop (NOW2014), Conca specchiulla, Otranto, Italy, September 2014, Nuclear and Particle Physics Proceedings 265-266, 2015, pp. 28-30

[4] F. Cappuzzello et al, "Heavy-ion double charge exchange reactions: A tool toward 0νββ nuclear matrix elements" European Phy. Journal, Vol. 51, pp. 145, 2015

[5] A. Calanna et al., "Proposal to increase the extracted beam power from the LNS-INFN Superconducting Cyclotron", in *Proc. 13th Int. Conf. on Heavy Ion Accelerator Technology (HIAT'15)*, Yokohama, Japan, September 2015, pp. 23-26

[6] G.G. Gulbekyan et al., "Extraction by stripping of heavy ion beams from AVF cyclotrons", in *Proc. 18th Int. Conf. on Cyclotrons and their Applications (ICCA'07)*, Giardini-Naxos, Italy, September 2007, pp. 308-313

[7] G. D'Agostino et al., "Extraction by Stripping for Intensity Upgrade of the INFN-LNS Superconducting Cyclotron: Beam Dynamics Studies and Major Modifications", in *Proc. 21st Int. Conf. on Cyclotrons and their Applications (ICCA'16)*, Zurich, Switzerland, September 2016, TUC03, this conference

[8] G. Gallo et al., "Mechanical Aspects of the LNS Superconducting Cyclotron Upgrade", in *Proc. 21st Int. Conf. on Cyclotrons and their Applications (ICCA'16)*, Zurich, Switzerland, September 2016, THP09, this conference

[9] F. Noto et al., "Status and Upgrade of the Cryogenic Plant of the LNS Superconducting Cyclotron After 25 Years of Operation", in *Proc. 21st Int. Conf. on Cyclotrons and their Applications (ICCA'16)*, Zurich, Switzerland, September 2016, THP10, this conference

[10] A. Radovinsky et al. "Design of a Superconducting Magnet for the LNS Cyclotron", IEEE Transactions on Applied Superconductivity, Vol. 26, Issue 4, 2016

ISBN 978-3-95450-167-0

IN MEMORIAM: MICHAEL K. CRADDOCK*

E.W. Blackmore†, TRIUMF, Vancouver, BC, Canada

Abstract

Michael K. Craddock, TRIUMF accelerator physicist and UBC professor, died on 11 November, 2015 after a brief illness. Michael left the UK to join the UBC Nuclear Physics group in 1966, just at the time a new accelerator to replace the aging Van de Graaff was under consideration. He was a leading member of the founding team that decided on a 500 MeV H^- cyclotron and directed the beam dynamics design of the cyclotron to first beam in December 1974. With the cyclotron running at full intensity he moved his interest to higher energies and led the accelerator physics team in the design of the 30 GeV KAON Factory (1982-1994). After retirement from UBC in 2001 he moved his research interest to FFAGs.

INTRODUCTION

Michael Craddock was born on 15 April in Portsmouth, UK and received his early education there. He then attended Oxford University for his Bachelor's and Master's degrees in mathematics and physics in 1957 and 1961 and became a scientific officer at what was then the Rutherford High Energy Physics laboratory (RHEL) working on the 50 MeV proton linear accelerator (PLA) (see Fig. 1).

In parallel he pursued a D. Phil in nuclear physics at Oxford which he obtained in 1964. His thesis topic was "The Nuclear Interactions of High Energy Particles" under the supervision of D. Roaf and R. Hanna. The work involved developing a polarized source, beam polarimeter and cryogenic target for studying proton-He4 elastic scattering at 22 and 29 MeV. As an indication of his future thoroughness in research the thesis contains 14 pages of references. In 1966 Michael joined the Physics Department at the University of British Columbia, later with a joint appointment at TRIUMF, and was TRIUMF's leading beam physicist throughout his career.

Michael with a training in mathematics loved equations and his early note books are filled with formula relating to polarized proton sources, equations of charge at particle motion in magnetic and electric fields etc. He passed this approach on to his many graduate students and beam dynamics team, although eventually embraced computing simulations but usually they were carried out by others. He excelled in writing research papers – the references present only a small subset of his published papers, and was particularly interested in the history of accelerator developments. At the Cyclotron Conference in Lanzhou in 2010 he presented a paper on "Eighty Years of Cyclotrons" [1]. His last scientific article was a history of accelerator science and technology in Canada which was completed by Robert Laxdal and recently published [2].

Michael was a strong supporter of the international accelerator community beginning as the program chair for the 1972 Cyclotron conference in Vancouver, conference chairman for the 1985 and 1997 Particle Accelerator Conferences and also the 1992 Cyclotron conference. He was a valued member of the international organizing committees and scientific advisory boards for these conferences. He gave the after dinner address to the 1992 conference on "Proper and Improper Accelerators – In praise of Cyclotrons and their Builders".

At TRIUMF Michael was the head of the Beam Dynamics group or the Accelerator Research Division for much of his career and was instrumental in training a new generation of beam physicists. Some of these individuals are identified in the references and acknowledgements. (For 29 years he was TRIUMF's correspondent to the *CERN Courier.*)

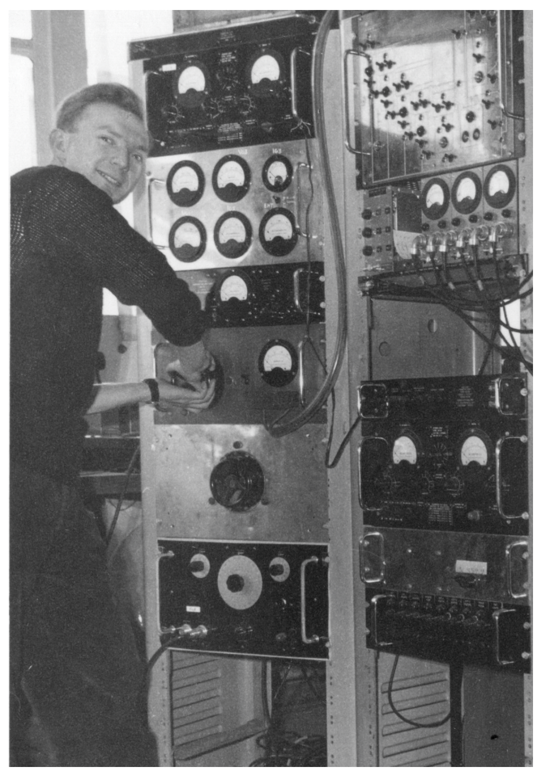

Figure 1: Michael Craddock at the controls of the Rutherford Laboratory PLA in 1964.

* TRIUMF receives federal funding via a contribution agreement through the National Research Council.

† ewb@triumf.ca

ISBN 978-3-95450-167-0

THE TRIUMF CYCLOTRON

Michael Craddock wrote a summary of the 12 June 1965 meeting of representatives from the three British Columbia universities which included the first use of the acronym TRIUMF and the plan to develop a scaled-down version of Reg Richardson's UCLA proposal for an H^- cyclotron (520 MeV, 100 µA). The TRIUMF proposal was to be produced within a year, coordinated by Erich Vogt who was moving from Chalk River National Laboratory to UBC physics. John Warren the head of the nuclear physics group and builder of the 3 MeV Van de Graaff was going on sabbatical to RHEL during that time. Michael Craddock was responsible for the accelerator design and an early step was to bring the scale model of the UCLA magnet to UBC for field mapping. The proposal was completed by November 1966 at the same time Los Alamos was proposing an 800 MeV proton linac and ETH in Zurich was proposing a 590 MeV ring cyclotron for meson physics. All three meson factories were approved by 1968 with the USA choosing the LAMPF proposal over UCLA. John Warren was the first director of TRIUMF (1968-1971) and Reg Richardson was the second director (1972-1976).

The main technical challenges of the cyclotron were the design, engineering and field mapping of the 4000 ton 6-sector magnet which was limited to a maximum magnetic field if 0.576 T due to electromagnetic stripping of the H^- ions and the large radiofrequency structure which had to cover an orbit diameter of 16 m. Mike built up a beam dynamics group consisting of George Mackenzie (1968), Gerardo Dutto (1970) and Corrie Kost (1971) and supervised two early graduate students in the design of the centre region of the cyclotron and the axial injection with a spiral inflector [3]. The large magnet pole gap of 50 cm was a challenge for maintaining vertical focusing. The construction of a full-scale centre region model of the cyclotron led by Ewart Blackmore (1969) tested the ion source and axial injection with the inflector, the centre region design and the resonator structures and successfully accelerated an H^- beam of 100 µA beam to 3 MeV in 1972 [4].

Figure 2 shows the lower half of the TRIUMF cyclotron showing the staff in 1972 and the pole contours for shimming.

Meanwhile initial field measurements of the large magnet revealed that the centre field was too high by 100 g (0.01T) due to differences in permeability between the 0.5" plate used in the model magnets and the 5" plate used in the large magnet. Michael and his group were responsible for determining the position and number of magnet shims to be installed on the pole sides to overcome this problem and produce the required isochronous field to a level that could be corrected further with trim coils. Finally in November of 1974 after 9 months of shimming and with the radiofrequency cavities installed and the ion source ready, beam was injected into the cyclotron. With Reg Richardson at the controls and Michael and the other commissioning team members at his side the beam was worked out in energy (see Fig. 3). After a few technical stops the full energy beam was accelerated and extracted on 14 December 1974. The successful commissioning of the cyclotron was presented first at the June 1975 Particle Accelerator Conference [5] and then in August at the 7th Cyclotron Conference in Zurich [6].

Michael and his group continued to improve the beam performance to reach the design goal of 100 µA in 1977 and today the cyclotron operates routinely at 300 µA into 3 beamlines at different energies. Moreover for special applications it is possible to extract a stable 1 pA of beam on one beamline with more than 100 µA of beam circulating in the cyclotron, a benefit of H^- stripping extraction.

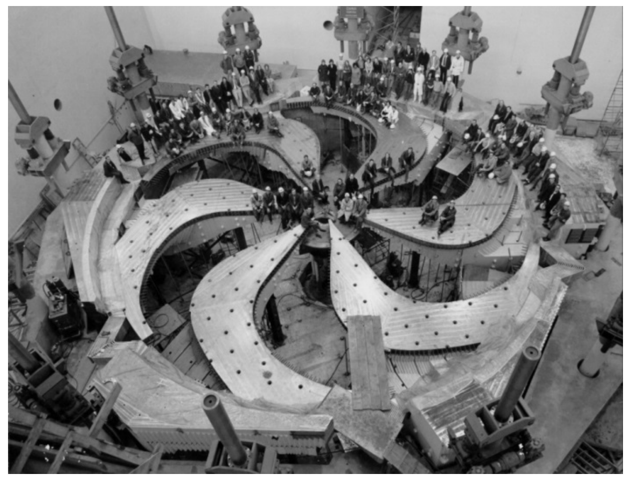

Figure 2: The lower half of the TRIUMF cyclotron showing the staff in 1972 and the pole contours for shimming.

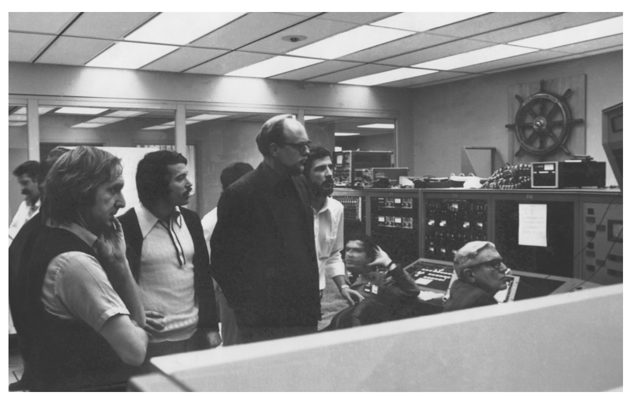

Figure 3: Reg Richardson tuning the TRIUMF cyclotron with Michael Craddock, Ewart Blackmore and George Mackenzie looking on (1974).

THE KAON FACTORY

With the TRIUMF cyclotron beam dynamics in good shape, Michael turned his attention to accelerators with higher energies at higher currents that would be sufficient to produce copious beams of kaons and other particles. The first phase focused on cyclotrons to determine how far this technology could be pushed. Working with Jan Botman and others a magnet design for a 15 GeV superconducting cyclotron was developed with injection

ISBN 978-3-95450-167-0

at 430 MeV from TRIUMF into a 3.5 GeV ring followed by a 3.5 – 15 GeV ring. The magnet sector shapes for the 3.5 GeV are shown in Fig. 4. These sectors have reverse bends, so-called return field gullies which increase the flutter, much like the first FFAG proposals from MURA. Michael enjoyed producing acronyms and this became the CANUCK proposal (Canadian University Cyclotrons for Kaons) in 1983 [7].

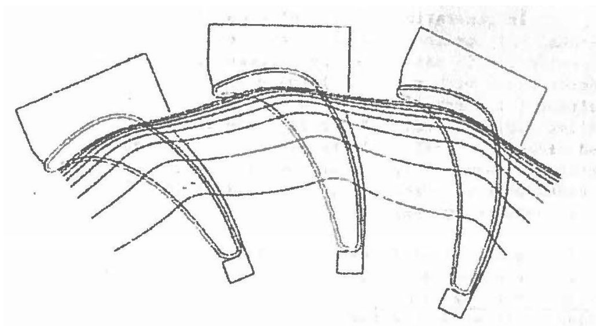

Figure 4: Sector design and orbits for the 3.5 GeV cyclotron using single gullies.

It soon became apparent that 15 GeV was not optimum for a Kaon Factory and that synchrotrons would be necessary. Michael, then head of the Accelerator Research Division and his group starting working on rings of synchrotrons that could be injected at 430 MeV from the TRIUMF cyclotron to produce 100 µA at 30 GeV. This culminated in a Project Definition Study led by Alan Astbury that produced a fully costed accelerator and experimental area design in 1992 [8]. With his love of acronyms Michael called the facility KAON for kaons, antiprotons, other hadrons and neutrinos and the 5 accelerator rings A(accumulator), B(booster), C(collector), D(driver) and E(extender) (see Fig. 5). The funding proposal with costs shared equally between Canada, British Columbia and International contributors was promoted relentlessly by Erich Vogt (Dr. Kaon) and Michael and came close to success. However the project did not get supported by a newly elected federal government in 1994, although TRIUMF did get a new future with 5 year funding for the ISAC radiative beam facility at TRIUMF and accelerator and ATLAS detector contributions to the Large Hadron Collider at CERN.

The design work on the KAON rings was not wasted. In travelling the accelerator world to promote KAON and to collaborate with other beam physicists on the issues of high intensity accelerators (see Fig. 6), Michael was able to attract new students and postdocs to study and work at UBC and TRIUMF. Accelerating high intensities to 30 GeV meant that beam losses had to be kept low, necessitating separated-function magnet lattices with the dispersion kept low to increase the transition energy above the top energy of all rings. Michael and his group published several papers on high γ_T lattices and on instabilities and collective effects [9, 10, 11]. Some of these ideas were later incorporated into the design of the J-PARC accelerators as this facility became the de-facto Kaon factory. In addition to beam dynamics studies, the technical and prototype work during the KAON were instrumental in TRIUMF personnel gaining significant expertise in synchrotron systems and this was applied to the LHC work described in the next section.

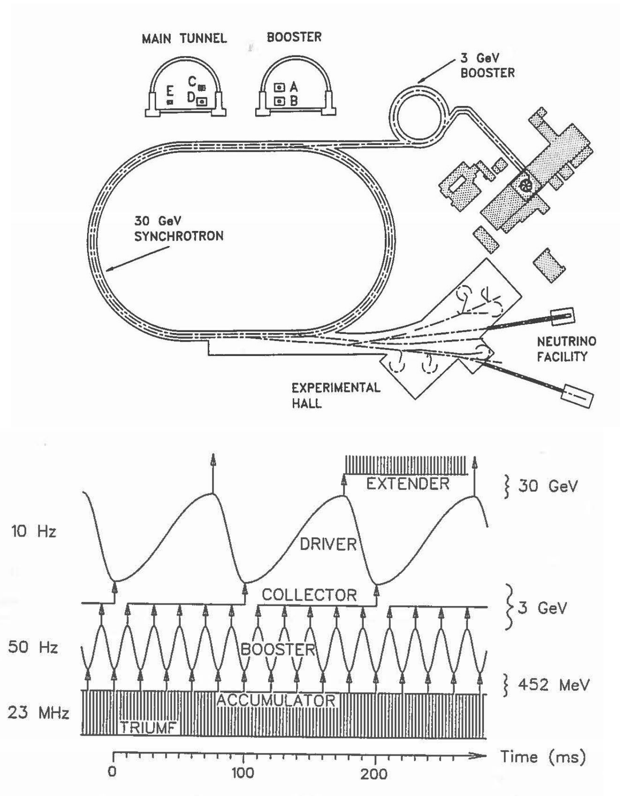

Figure 5: Layout of the KAON rings and the energy-time structure of the beam.

Figure 6: Michael Craddock at Troitsk in 1989 to discuss KAON Factories.

CANADIAN CONTRIBUTIONS TO THE LHC

Over the period 1995-2005, TRIUMF coordinated the $41.5M Canadian contribution to the LHC accelerators. This work involved procurement of magnets, rf systems, kickers, beam diagnostic, power converters and transformers coordinated by Ewart Blackmore [12] but

ISBN 978-3-95450-167-0

also some important beam dynamics contributions coordinated by Michael Craddock. The most significant of these projects was the design of the beam cleaning insertions in the LHC ring to collimate beam halos with large transverse or off-momentum amplitudes [13]. This work was coupled to the fabrication of 52 large twin-aperture quadrupoles with conventional coils to operate in the high radiation environment of the beam cleaning region which was the largest part of the contribution. Other work carried out by Michael and his team involved simulation studies of higher beam currents in the PS complex, space charge and its effect on betatron resonances [14] and beam-beam interactions in the collision regions [15].

FFAGS AND EMMA

About 1999 there was a renewed interest in Fixed (magnetic) Field Alternating Gradient (FFAG) accelerators, initially considered for muon colliders. Groups in Japan and the U.S. came up with independent designs for fixed field (ring style) muon accelerators with very large momentum acceptance, so large an acceptance that other applications became of interest such as compact proton and heavy ion accelerators for hadron therapy. The Japanese designs are descendants of the so-called "scaling FFAGs" pioneered by the MURA group in the 1950s. The early US designs look like separated function synchrotrons, but with the "non-scaling" optics (employing reverse bending) contrived so that the central orbit moves (radially) very little during acceleration [16]. They have, in common with the KAON Factory Booster ring, a very careful manipulation of the dispersion function. Michael became interested in FFAGs about 2003 and having straddled the worlds of cyclotrons and synchrotrons was well placed to make a contribution to this renaissance and emphasized the commonality between the two approaches at the international FFAG workshops from 2004 to 2014.

In a series of calculations and papers from 2003 onward, Michael adapted the Schatz approach (a hard edge matrix method for determining orbits and focusing properties of separated sector cyclotrons) to the non-scaling FFAG lattice designs, and within 3 years was obtaining results that were found to be accurate to within a few percent of tracking codes. By 2007, the centre piece of the FFAG community was the EMMA (Electron Model with Medical Applications) demonstration machine under construction at Daresbury [17] and it was natural that Michael should apply the Schatz method to that machine. In 2009 he returned to the theme of unifying the FFAG efforts, opening a paper [18] with "Nevertheless, cyclotrons and FFAGs have been developed by two different communities, which have sometimes taken different approaches in their work. The studies described here bridge this gap to some extent by applying orbit codes developed for isochronous cyclotrons to FFAGs, and some FFAG ideas to cyclotrons."

That work occupied him for the remainder of this life, concluding in workable designs for a 1 GeV radial sector isochronous cyclotron with reverse bending. For FFAG'11 and onwards, Michael gave historical, overview and educational talks on Cyclotrons and FFAGs both old and modern, continuing to leave his legacy to the accelerator community (Figs. 7 and 8).

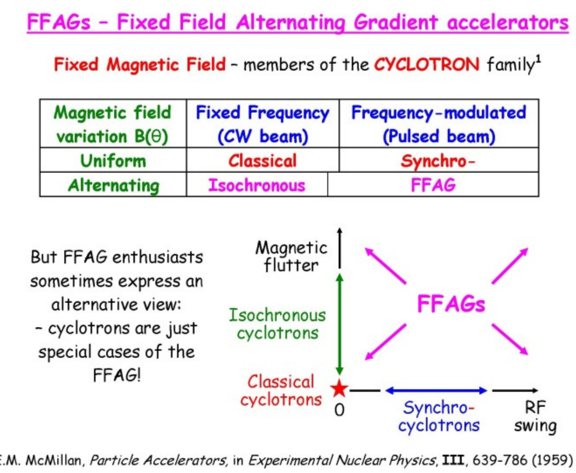

Figure 7: Slide from course at FFAG School in 2011 showing typical Michael Craddock style.

Figure 8: Michael Craddock in 2015.

ACKNOWLEDGMENT

This paper received valuable input from Michael's colleagues in beam dynamics at TRIUMF, Rick Baartman, Fred Jones, Shane Koscielniak and Robert Laxdal. I would also like to thank Prof. Vanessa Auld, Michael's stepdaughter for some of the photographs and information about his early years.

REFERENCES

[1] M.K. Craddock, "Eighty Years of Cyclotron", in *Proc. 19th Int. Cycl. Conf. (PAC'10)*, Lanzhou, 2010, p. 1.

[2] M.K. Craddock and R.E. Laxdal, "Accelerator Science and Technology in Canada from the Microtron to TRIUMF, Superconducting Cyclotrons and the Canadian Light Source", Reviews of Accel. Sci. & Tech.Vol. 8, 2005.

[3] R.J. Louis, G. Dutto, and M.K. Craddock, "Central Region Orbit Dynamics in the TRIUMF Cyclotron", IEEE NS-18, 1971, p. 282.

[4] E.W. Blackmore *et al.*, "Experimental Results from the TRIUMF Central Region Cyclotron", in *Proc. PAC'73*, IEEE NS-20, 248, San Francisco, 1973.

[5] J.R. Richardson, E.W. Blackmore, G. Dutto, C.J. Kost, G.H. Mackenzie, and M.K. Craddock. "Production of Simultaneous, Variable Energy Beams from the TRIUMF Cyclotron", in *Proc. PAC'75*, IEEE Trans. NS-24, 1975, p. 1402.

[6] J.R. Richardson, "The Status of TRIUMF", in *Proc. 7th Int. Cycl. Conf.*, Zurich, 1975.

[7] J.I.M. Botman, M.K. Craddock, C.J. Kost, and J.R. Richardson, "Magnet Sector Design for a 15-GeV Superconducting Cyclotron", IEEE Trans. NS-30, 1983, p. 2007.

[8] M.K. Craddock, "The TRIUMF KAON Factory", in *Proc. IEEE Particle Accelerator Conference*, San Francisco, 1991, p. 57.

[9] R.C. Gupta, J.I.M. Botman, and M.K. Craddock, "High Transition Energy Magnet Lattices", IEEE Trans. NS-32, 1985, p. 2308.

[10] R. Baartman and S. Koscielniak, "Stability of Hollow Beams in Longitudinal Phase Space", in *Proc. Particle Accelerator Conf.*, Vol. 28, 1990, p. 95.

[11] U. Wienands *et al.*, "A Racetrack Lattice for the TRIUMF KAON Factory Booster", in *Proc. HEACC'92*, Hamburg, 1992, p. 1073.

[12] M. Benedikt *et al.*, "The PS Complex as Proton Pre-Injector for the LHC – Design and Implementation Report", CERN 2000-03, Feb. 27, 2000.

[13] D.I. Kaltchev, M.K. Craddock, J.B. Jeanneret, and A. Verdier, "Optics Solutions for the Collimation Insertions of LHC", in *Proc. PAC'99*, New York, 1999; and CERN-LHC-Project-Report-305.

[14] W. Herr, M.P. Zorzano, and F. Jones, "Hybrid fast multipole method applied to beam-beam collisions in the strong-strong regime", *Phys. Rev.* ST Accel. Beams, p. 4, May 2001.

[15] R. Baartman, "Betatron Resonances with Space Charge", *AIP Conference Proceedings,* 448, 1998, p. 56.

[16] C. Johnstone and S. Koscielniak, "New Nonscaling FFAG for Medical Applications", in *Proc. PAC'07*, 2007, p. 2951.

[17] R. Barlow *et al.*, "EMMA – The World's First Non-scaling FFAG", *Nucl. Instr. Meth.*, vol. A624, 2010.

[18] M.K. Craddock and Y.N. Rao, "Cyclotron and FFAG Studies Using Cyclotron Codes", in *Proc. 19th Int. Cycl. Conf.*, Lanzhou, 2010, p. 395.

ISBN 978-3-95450-167-0

CYCLOTRON TECHNOLOGY AND BEAM DYNAMICS FOR MICROBEAM APPLICATIONS

S. Kurashima†, N. Miyawaki, S. Okumura, T. Satoh, H. Kashiwagi, K. Yoshida, T. Yuyama, National Institutes for Quantum and Radiological Science and Technology, Takasaki, Japan
M. Fukuda, Osaka University, Ibaraki, Japan

Abstract

We have been improving a beam quality of the TIARA cyclotron to form a heavy-ion microbeam with a spot size about 1 μm. An energy spread ΔE/E of the beam on the order of 10^{-4} is required for eliminating chromatic aberrations in the focusing magnets. A flat-top acceleration system using the fifth-harmonic frequency was installed in the cyclotron to reduce the energy spread. In addition, a magnetic field stabilization system, an acceleration phase control technique and a new central region were developed to provide the microbeam stably for beam users. A cocktail beam acceleration technique was introduced to quickly change the microbeam to the other one, and a few microbeams can be used in a beam time.

INTRODUCTION

Takasaki Ion accelerators for Advanced Radiation Application (TIARA) facility of the National Institutes for Quantum and Radiological Science and Technology (QST) was constructed to provide high-energy ion beams mainly for research in biotechnology and materials science. QST [1] was newly established in April 2016 by merging the National Institute of Radiological Sciences (NIRS) with a few research institutes of the Japan Atomic Energy Agency (JAEA).

An AVF cyclotron with a *K*-value of 110 [2] and three electrostatic accelerators are installed in TIARA, and ion beams with wide ranges of energy and ion species are available. A microbeam with a spot size about 1 μm is a powerful tool to analyze and/or irradiate a microscopic area. At TIARA, microbeam applications such as in-air Particle Induced X-ray Emission (PIXE) analysis and Proton Beam Writing (PBW) are carried out by focusing ion beams accelerated by the electrostatic accelerators [3]. On the other hand, in a vertical beam line of the cyclotron hundreds MeV heavy-ion microbeam irradiation to living cells is carried out by using micro collimators for elucidation of cellular radiation response [4]. However, spot size of the microbeam is larger than that of the electrostatic accelerator's one due to fabrication limit of the collimator and scattered ions at the edge of the collimator. In addition, targeting speed is too slow since a targeting point is adjusted by moving a mechanical sample stage. To form a microbeam with a spot size about 1 μm, a microbeam formation system using quadrupole magnets with a beam scanner was installed in the other vertical beam line of the cyclotron.

To form such a microbeam using the focusing magnet, an energy spread $\Delta E/E$ of the ion beam must be reduced to the order of 10^{-4} for eliminating chromatic aberrations in the focusing magnet. However, the energy spread of the cyclotron beam is typically on the order of 10^{-3} while that of the electrostatic accelerator on the order of 10^{-4}. A flat-top (FT) acceleration system using a fifth-harmonic frequency was developed to reduce the energy spread. In addition, cyclotron technologies such as magnetic field stabilization system and beam phase control techniques were introduced to ensure the effect of the FT acceleration. In this paper, we briefly describe the above cyclotron development, and also mention a technique to quickly change ion species of the microbeam and recent microbeam development of a 320 MeV $^{12}C^{6+}$.

MICROBEAM FORMATION AND SINGLE-ION HIT CONTROL SYSTEM

Figure 1 shows the system of the focusing microbeam formation and single-ion hit, which means irradiating a targeted point with a high-energy ion one by one. Details of the microbeam formation system [5] are shown in Fig. 2. The system consists of quadruplet quadrupole magnets, a pair of micro slits, a pair of divergence angle defining slits, and so on. The beam shifter upstream the micro slits matches the incident beam trajectory with the microbeam line axis. Magnification factors of the focusing system for *x* and *y* directions are equally 1/5. The 90° bending magnet doesn't have a role as an energy analyser; therefore reduction of the energy spread of the incident beam is indispensable condition. The targeting point is determined by the electrostatic beam scanner. Ions pene-

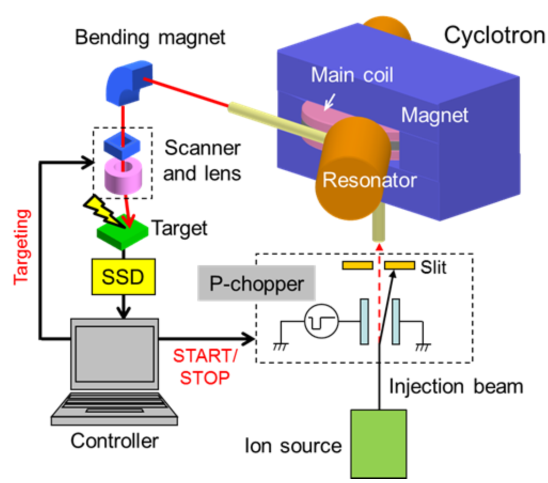

Figure 1: Layout of equipment for microbeam formation and single-ion hit control system at the TIARA cyclotron facility.

† kurashima.satoshi@qst.go.jp

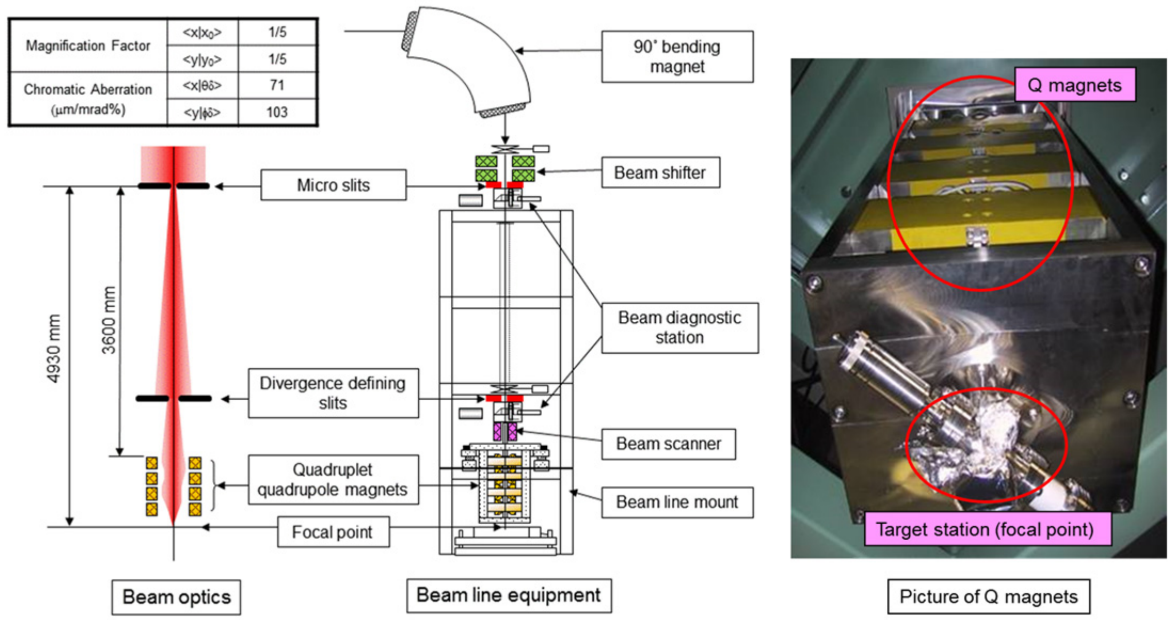

Figure 2: Beam optics, schematic view and picture of the vertical microbeam formation system. The picture was taken peering up at the target station and the Q magnets.

trating a thin target, such as living cells on a plastic film, are detected by a solid-state detector (SSD), and a fast beam kicker (P-chopper) installed in the beam injection line [6] controls a total number of ions to be irradiated as shown in Fig. 1. Fast single-ion hit of 600 samples/min is an achievable objective by using the beam scanner and the P-chopper.

To irradiate living cells, the microbeam is extracted in the atmosphere through a vacuum window made of Si_3N_4 with a thickness of 200 nm. Although the vacuum window is set at the focal point of the Q-magnets the microbeam size is deteriorated because of scattering in the Si_3N_4 and the atmosphere layers. For example, a 260 MeV $^{20}Ne^{7+}$ is enlarged by about 2 µm at a distance of 1 mm from the vacuum window. The target sample must be placed as close to the vacuum window as possible. A microbeam irradiation experiment in vacuum is possible by exchanging the target station to the other one.

FLAT-TOP ACCELERATION SYSTEM

To achieve an energy spread of 10^{-4} an FT acceleration system using the fifth-harmonic frequency was developed for the TIARA cyclotron [7, 8] by reference to the FT system developed at the iThemba LABS for their injector AVF cyclotron with the *K*-value of 8 [9]. Figure 3 (upper) shows the picture of the TIARA cyclotron incorporated with a compact FT resonator. The FT resonator covers a wide range of resonance frequency from 55 to 110 MHz so that the FT acceleration is performed for all ion beams accelerated at the fundamental frequency ranging from 11 to 22 MHz. The fundamental and the fifth-harmonic frequency voltages are generated together on a dee electrode since there is no individual resonator for the harmonic frequency in contrast to a ring cyclotron. Figure 3 (lower) shows an example of the FT voltage waveform observed through a capacitive voltage pick up circuit. The fifth-harmonic voltage, however, has significant variation

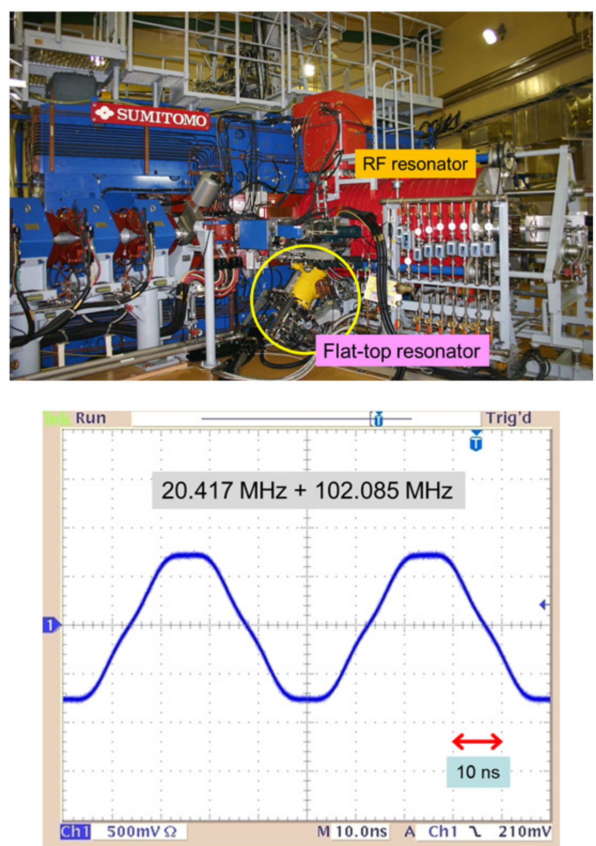

Figure 3: Picture of the TIARA cyclotron incorporated with the FT resonator (upper). Flat-top voltage waveform monitored at the dee voltage pick up (lower). The fundamental frequency (20.417 MHz) voltage was 40 kV.

ISBN 978-3-95450-167-0

along the acceleration gap depending on the resonance frequency [8]. The voltage decreases from the tip of the dee electrode toward the outer radius. On the other hand, in the case of the fundamental frequency, negligible voltage distributions were measured. The optimum fifth-harmonic voltage, therefore, was calculated at each frequency to uniform the overall energy gain of the beam bunch just before extraction from the cyclotron.

CONTROL OF ACCELERATION PHASE AND BEAM PHASE WIDTH

The beam bunch must be kept within the uniform region of the energy gain for successful FT acceleration. In other words, acceleration phase and beam phase width must be carefully controlled. To measure the acceleration phase in a cyclotron, there is a well-known method studied by A.A. Garren and L. Smith [10]. To easily measure and adjust the acceleration phase a new method was developed by us [11] and briefly described below.

Here we assume that no obvious voltage distribution exists along the acceleration gap and an isochronism is quite good. The internal beam current is measured at a fixed radius before extraction by a radial probe for slightly increased or decreased acceleration frequency to find out the current pattern till the beam current decreases to the halves, where we estimate the beam bunch reaches at the energy gain of 0, as shown in Fig. 4. The acceleration phase θ is recognized by analyzing symmetry of the beam current pattern with Eq. (1),

$$\theta = Sin^{-1}\left(1-2\frac{\frac{\Delta f_A}{f}}{\left(\frac{\Delta f_A}{f}-\frac{\Delta f_B}{f}\right)}\right). \tag{1}$$

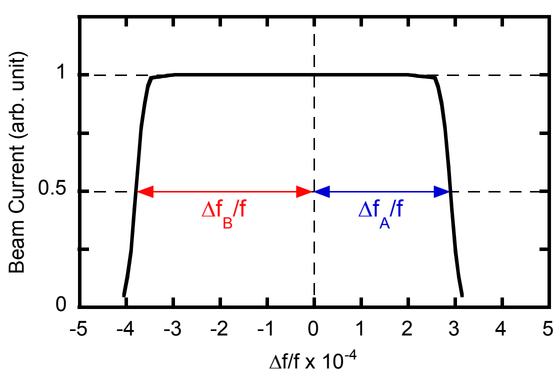

Figure 4: Expected beam current pattern in the cyclotron when the acceleration frequency is scanned. The acceleration phase is lagging in this example.

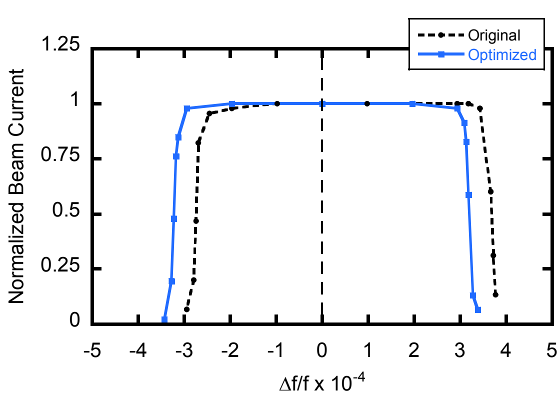

Figure 5: Beam current patterns of the 220 MeV $^{12}C^{5+}$ obtained at a radius of 865 mm before extraction scanning the acceleration frequency. The beam current was normalized at $\Delta f/f = 0$.

Once the acceleration phase has been measured, we can optimize it by changing magnetic field of the central bump as shown in Fig. 5. The acceleration phase was estimated to be 9° advancing for the original condition; therefore the central bump was slightly decreased to optimize the acceleration phase.

In addition to the conventional method using a phase slit for restricting the beam phase width, a new technique to reduce the beam phase width using a phase bunching effect at the first revolution in a central region was developed by our group [12]. Equipment in the central region, such as an rf shielding cover of inflector electrode, a puller electrode and the phase slits were fully renewed. In particular for acceleration harmonics h = 2 the beam phase width can be reduced to about 10° or less by combination of an external beam buncher, without beam cutting by the phase slits [11]. On the other hand, the phase bunching effect has no effect for h = 1 beam of the TIARA cyclotron as described in the last section and the beam phase width should be restricted with the phase slits.

MAGNETIC FIELD STABILIZATION SYSTEM

To regulate the acceleration phase at the optimum point, the magnetic field is needed to be extremely stabilized. The total amount of shift of the acceleration phase reaches tens of degrees in the case of $\Delta B/B = 1 \times 10^{-4}$ for the cyclotron. The magnetic field of the cyclotron, however, gradually changed for long duration over 10 h on the order of 10^{-4} because of heat deformation of the iron yoke caused by heat transfer from a pair of main coils. Variable temperature water-cooled copper plates were installed between the main coil and surface of the magnet yoke to insulate the heat as shown in Fig. 6. The temperature of the cooling water is adjusted between 22 to 25°C by 0.1°C as a function of the main coil current. As a result, the magnetic field instability was remarkably improved to $\Delta B/B = 1 \times 10^{-5}$ for all ion beams [13].

Simultaneously with the stability improvement, a nuclear magnetic resonance (NMR) probe was developed to precisely measure the magnetic field in the cyclotron. An NMR probe is generally used to precisely measure a uniform magnetic field, and it was difficult to obtain sufficient signal intensity in the non-uniform cyclotron magnetic field. To improve a signal-to-noise ratio (S/N) of the NMR probe, a series of actions such as searching proper

ISBN 978-3-95450-167-0

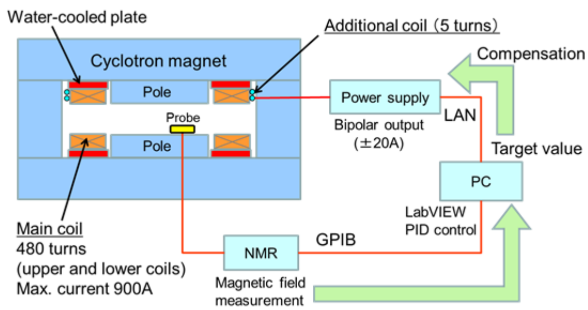

Figure 6: Schematic view of the cyclotron magnetic field stabilization system. The system consists of the water-cooled copper plates, installed between the main coil and the magnet yoke, and the additional coil driven by the PID controller. The NMR probe was placed on a central axis of a sector part of the magnet at a radius of 660 mm.

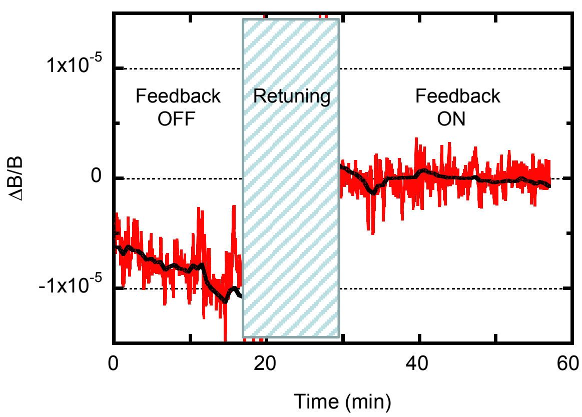

Figure 7: Improvement of the magnetic field stability by using the NMR feedback system. Black solid line was obtained by smoothing. The magnet was excited for acceleration of the 260 MeV $^{20}Ne^{7+}$ beam (B = 2.05 T).

installation position, vibration insulation of the signal pickup cable and addition of a noise filter circuit was carried out.

On the other hand, short duration change of the magnetic field appeared probably due to the stability of the main coil power supply of $\Delta I/I = \pm 1 \times 10^{-5}$. An active control system of the magnetic field using the NMR probe was developed to improve the stability more as shown in Fig. 6. The magnetic field is regulated by using an additional 5 turns coil wound along the upper main coil, a power supply and a PC-based proportional-integral-derivative (PID) controller. Figure 7 shows an example of the change of the magnetic field with or without the feedback control system. The magnetic field was obviously stabilized by using the active control system.

COCKTAIL BEAM ACCELERATION

A 260 MeV $^{20}Ne^{7+}$ (h = 2) microbeam with the spot size and targeting accuracy of less than 1 µm was successful formed in vacuum [5] as a result of the cyclotron development. The energy spread of the beam was reduced to 5×10^{-4} by the FT acceleration. Other ion beams of h = 2 such as a 220 MeV $^{12}C^{5+}$ and a 400 MeV $^{56}Fe^{15+}$ were preliminarily developed and focused to a few µm.

Beam users of the TIARA need several kinds of microbeams providing a wide range of Linear Energy Transfer (LET) in a beam time. However, it takes about 8 h to form the microbeam including tune of an ion source, the cyclotron magnetic field, the FT system and the microbeam formation system. A cocktail beam acceleration technique was applied to the microbeam formation for quick change of the ion species [14]. This technique can change the ion species having almost the same mass-to-charge (M/Q) ratio quickly by slightly adjusting the acceleration frequency or the magnetic field. The M/Q resolution R is defined by Eq. (2) and the value of the cyclotron is estimated to be about 3300,

$$R = \left| \frac{(M/Q)}{\Delta(M/Q)} \right| = \left| \frac{f_{\mathrm{RF}}}{\Delta f_{\mathrm{RF}}} \right|. \tag{2}$$

Table 1 shows an example of the ion species with the $M/Q \approx 2.86$ that the cyclotron is able to completely separate. In the cocktail beam acceleration, magnetic rigidities of the ion species are identical; therefore, lens parameters of the beam transport line need not to be changed. Once a microbeam is formed, another microbeam of different ion species is formed in a short time. After forming the 260 MeV $^{20}Ne^{7+}$ microbeam, the beam was changed to the $^{40}Ar^{14+}$ by changing the acceleration frequency. Corrections of steering magnets in the beam transport line and a shifter magnet of the microbeam formation system were required to match the beam trajectory with the optical axis. As a result, the microbeam was changed in half an hour, and successfully provided for an experiment without deteriorating the beam spot size [15].

Table 1: Ion Species with the $M/Q \approx 2.86$ for the Cocktail Beam Acceleration. For calculation of the M/Q, mass of the stripped electrons and the mass excess of atom were corrected.

Ion	M/Q	$\Delta(M/Q)/(M/Q)$	RF (MHz)	LET in water (keV/µm)
$^{14}N^{5+}$	2.80007	-1.942×10^{-2}	17.8210	186.6
$^{20}Ne^{7+}$	2.85551	0	17.4750	387.2
$^{40}Ar^{14+}$	2.85391	-5.603×10^{-4}	17.4848	1143

MICROBEAM FORMATION OF CARBON BEAM (H = 1)

The spot size of the microbeam is estimated by analyzing a secondary electron (SE) image of a copper grid with 1000 lines/in. as described in Ref. 5. The accuracy of the spot size estimation depends on the S/N of the SE image. In the case of a 320 MeV $^{12}C^{6+}$ (h = 1) microbeam formation, however, the S/N adequate for the estimation could not be obtained because of poor yields of SE since the LET and the beam intensity of this fully-stripped ion was lower than the other microbeam such as the 260 MeV

ISBN 978-3-95450-167-0

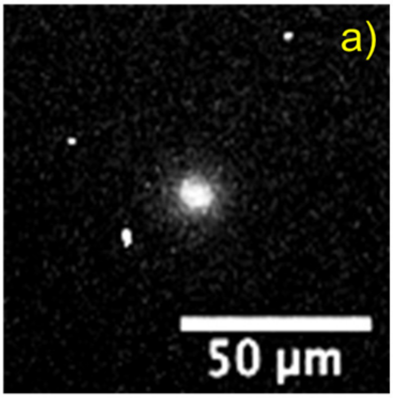

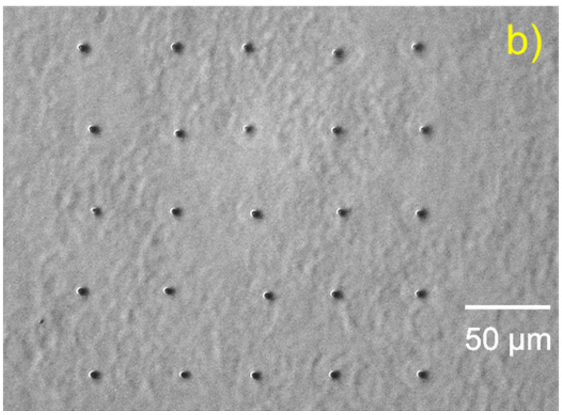

Figure 8: Formation of the 320 MeV $^{12}C^{6+}$ microbeam in the air without the FT acceleration. a) Scintillation image obtained by adding up 100 pictures in which several luminescence points were observed. b) Photomicrograph of the CR-39 detector etched by a solution after 5 × 5 single-ion hits.

$^{20}Ne^{7+}$. Therefore, a new system for estimating the beam size was constructed by using an EMCCD camera with high detection sensitivity and a gadolinium pyrosilicate ($Gd_2Si_2O_7$:Ce, GPS:Ce) scintillator. This system can detect the single-ion hit position and the whole beam image is obtained by adding up individual images in which several ion hits are observed. Figure 8 a) shows the whole beam image of the 320 MeV $^{12}C^{6+}$ microbeam just behind the vacuum window. The beam sizes estimated from the intensity distribution were 8.1 and 6.5 µm (FWHM) for x and y directions, respectively. Since then, the single-ion hit irradiation on a CR-39 solid-state nuclear track detector was done in a pattern of 5 × 5 points with 50 µm pitch as shown in Fig. 8 b). The CR-39 was placed in the air at a distance of 1 mm from the vacuum window. The targeting accuracy was estimated to be 7.6 µm (FWHM) by analyzing etched pit positions shown in Fig. 8 b) and there is no great difference compared with the beam spot size. This microbeam was preliminarily used to irradiate living microscopic worms.

The beam phase width of the $^{12}C^{6+}$ beam was not restricted by the phase slit not to decrease the beam current at the cost of reducing the energy spread. The beam phase width was estimated to be about 20°, and was wider than the h = 2 beam such as the 260 MeV $^{20}Ne^{7+}$ since no phase bunching affects for h =1. The beam intensity produced by the ion source and transmission efficiency from the ion source to the entrance of the microbeam formation system must be increased to adequately restrict the beam phase width by the phase slit. The microbeam size will be reduced down to a few µm by the FT acceleration.

REFERENCES

[1] National Institutes for Quantum and Radiological Science and Technology (QST), http://www.qst.go.jp/ENG/

[2] K. Arakawa *et al.*, “Construction and first year's operation of the JAERI AVF cyclotron” in *Proc. 13th Int. Conf. on Cyclotrons and their Applications*, Vancouver, Canada, 1992, pp. 119-122.

[3] T. Kamiya *et al.*, “Microbeam complex at TIARA: Technologies to meet a wide range of applications”, *Nucl. Instr. Meth. B*, vol. 269, pp. 2184-2188, 2011.

[4] T. Funayama *et al.*, “Heavy-Ion Microbeam System at JAEA-Takasaki for Microbeam Biology”, *J. Radiat. Res.*, Vol. 49, pp. 71-82, 2008.

[5] M. Oikawa *et al.*, “Focusing high-energy heavy ion microbeam system at the JAEA AVF cyclotron”, *Nucl. Instr. Meth. B*, vol. 260, pp. 85-90, 2007.

[6] S. Kurashima et al., “Enhancement of beam pulse controllability for a single-pulse formation system of a cyclotron”, *Rev. Sci. Instrum.*, vol. 86, p. 073311, 2015.

[7] M. Fukuda *et al.*, “Flat-top acceleration system for the variable-energy multiparticle AVF cyclotron”, *Rev. Sci. Instrum.*, vol. 74, pp. 2293-2299, 2003.

[8] S. Kurashima *et al.*, “Single-turn extraction from a K110 AVF cyclotron by flat-top acceleration”, *Rev. Sci. Instrum.*, vol. 80, p. 033302, 2009.

[9] J.L. Conradie, A.H. Botha, J.J. Kritzinger, R.E.F. Fenemore, and M.J. Van Niekerk, “A flat-top acceleration system for the NAC light ion injector cyclotron”, in *Proc. 14th Int. Conf. on Cyclotrons and their Applications*, Cape town, South Africa, 1995, pp. 249-252.

[10] A.A. Garren and L. Smith, “Diagnosis and correction of beam behaviour in an isochronous cyclotron”, in *Proc. Int. Conf. on Sector-focused and Meson Factories*, Geneva, Switzerland, 1963, pp. 18-23.

[11] S. Kurashima *et al.*, “Useful technique for analysis and control of the acceleration beam phase in the azimuthally varying field cyclotron”, *Rev. Sci. Instrum.*, vol. 81, p. 033306, 2010.

[12] N. Miyawaki *et al.*, “Realization of a phase bunching effect for minimization of beam phase width in a central region of an AVF cyclotron”, *Nucl. Instr. Meth. A*, vol. 636, pp. 41-47, 2011.

[13] S. Okumura *et al.*, “Magnetic field stabilization by temperature control of an azimuthally varying field cyclotron magnet”, *Rev. Sci. Instrum.*, vol. 76, p. 033301, 2005.

[14] S. Kurashima et al., “Quick change of ion species of heavy-ion microbeam by cocktail beam acceleration technique with the JAEA AVF cyclotron”, *Nucl. Instr. Meth. B*, vol. 267, pp. 2024-2027, 2009.

[15] G. Vizkelethy, S. Onoda, T. Hirao, T. Ohshima, T. Kamiya, “Time Resolved Ion Beam Induced Current measurements on MOS capacitors using a cyclotron microbeam”, *Nucl. Instr. Meth. B*, vol. 267, pp. 2185-2188, 2009.

ISBN 978-3-95450-167-0

SIMULATION AND DETECTION OF THE HELICAL ION-PATHS IN A SMALL CYCLOTRON

Ch. Wolf, Gymnasium Ernestinum Coburg, Germany
R. Rueß, M. Prechtl, University for Applied Sciences and Arts, Coburg, Germany

Abstract

The small cyclotron COLUMBUS, which was developed in high school Ernestinum Coburg in cooperation with the Institute of Research of Jülich and the University of Applied Sciences of Coburg, is a particle accelerator for education and teaching purposes.

Since its installation, the cyclotron has been continuously upgraded and is now part of the newly created Student Research Centre of the University of Coburg.

In the cyclotron hydrogen ions are accelerated and their positions recorded after a few revolutions by a Faraday cup, which is moved by a linear translator in radial direction across the trajectories of the ions.

This thesis presents a MATLAB simulation of the orbits of the accelerated hydrogen-ions. In contrast to the simpler common school model that approximates the tracks in the acceleration gap by straight tracks, the presented simulation considers the deflection of the ions by the magnetic field in the acceleration gap. So a more realistic picture of the paths can be drawn, which will help to adjust the cyclotron and explore the initial orbits of the ions in detail.

INTRODUCTION

The COLUMBUS project began in 2012 and was first presented at the Cyclotrons 2013 in Vancouver [1]. At this time, however, no jet operation was possible. The first beam was detected in April 2014.

As part of a master's thesis a linear translator was developed in order to move the detector, a Faraday-cup in a radial direction behind the dummy dee. In addition to the registered ions the corresponding x-position of the cup is measured, too [2].

To give students a clear picture of the acceleration processes of the ions in the cyclotron, the ion trajectories are calculated and then visualized in a diagram. This allows qualitative and later quantitative predictions of experiments.

THE STRUCTURE OF THE SIMULATION

As shown in Fig. 1 the simulation consists of three sections, the input-layer, the simulation-layer and the presentation-layer.

The Input-Layer

The input-layer incorporates three groups of parameters which define the ions, the experiment and the geometry of the cyclotron. So the simulation can be easily adapted to different situations.

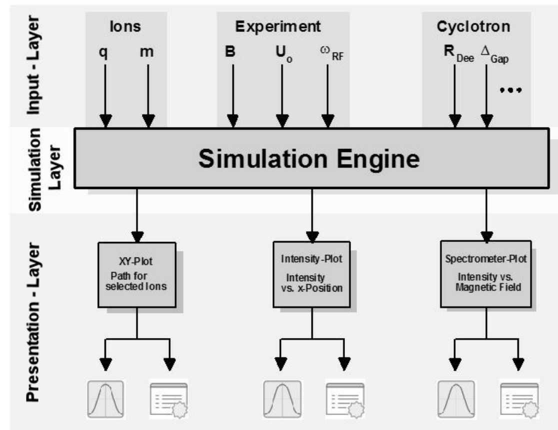

Figure 1: Structure of the Simulation.

The Simulation-Layer

In this layer there is the Simulation Engine, a MATLAB program which calculates all variables such as the positions, the velocity, the radius and the cyclotron-frequency ω_{ZF} of the ions during the acceleration process.

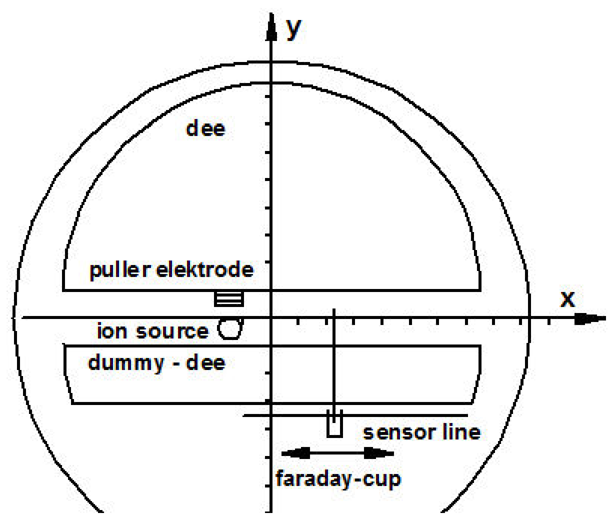

Figure 2: Cartesian coordinate system of the Cyclotron.

For this purpose a coordinate system has been introduced, which has its origin (0, 0, 0) in the center of the vacuum chamber, i.e. Fig. 2. The magnetic field is directed parallel to the z-axis of the coordinate system. The plain z = 0, parallel to the chamber bottom, represents the plain of the path of the accelerated ion beam. The ion source is located at position (-15, 5, 0) (all figures in mm), a Faraday-cup as an ion detector moves along the line y = -31 mm, the so-called sensor-line. This line ex-

ISBN 978-3-95450-167-0

tends parallel to the lower edge of the dummy dee with a distance of about 1 mm.

Each acceleration process consists of two phases:

- Acceleration phase in the gap
- Deflection phase in the dee/dummy dee

During the acceleration phase the energy and therefore the velocity of the ions increases due to the electric field $\vec{E} = \left(0;\, E_y;\, 0\right)$ .Considering the influence of the magnetic field $\vec{B} = \left(0;\, 0;\, B_z\right)$, the following approach in the acceleration gap is made:

$$m \cdot \vec{a} = \sum \vec{F}_i = \vec{F}_C + \vec{F}_L = \\ = q \cdot \vec{E} + q \cdot \left(\vec{v}\, x\, \vec{B}\right) = q \cdot \left(\vec{E} + \vec{v}\, x\, \vec{B}\right) \tag{1}$$

This results in the following system of coupled differential equations:

$$\ddot{x} = \frac{q}{m} \cdot \dot{y} \cdot B_z = \dot{y} \cdot \omega_{ZF} \text{ and} \tag{2.1}$$

$$\ddot{y} = \frac{q}{m} \cdot E_y - \frac{q}{m} \cdot \dot{x} \cdot B_z = \frac{q}{m} \cdot E_y - \omega_{ZF} \cdot \dot{x} \tag{2.2}$$

Here is $\omega_{ZF} = \frac{q}{m} B_z$ the rotational frequency of the ions, which is known to be independent of the radius r of the orbit.

With the approach $E_y = \hat{E} \cdot \cos\left(\omega_{RF} \cdot t - \varphi\right)$ it is possible to solve the DGL in general, but here it is only done numerically [3]. From the solutions of $y\ (t)$, the solutions for

$x\left(t\right) = \int \left[y\left(t\right) \cdot \omega_{ZF} + \dot{x}\left(t_o\right) - y\left(t_o\right) \cdot \omega_{ZF}\right] dt$ are also determined numerically. ω_{RF} is the frequency of the acceleration voltage, which is equal to ω_{ZF} for resonant acceleration and t_o is the time, when an ion enters or leaves the dee/dummy dee.

For a unique solution one needs four other constants, which are calculated from the location $\vec{r}_o = \vec{r}\left(t_o\right)$ and the velocity $\vec{v}_o = \vec{v}\left(t_o\right)$ at the entrance or exit of the dee.

In the dee itself, or, in and behind the dummy dee there is no accelerating electric field so that the ion trajectories can be described by equations of a circle with radius ρ:

$$x\left(t\right) = \rho \cdot \cos\left(\varphi_{in} - \omega_{ZF} \cdot \left[t - t_o\right]\right) + x_M \tag{3.1}$$

$$y\left(t\right) = \rho \cdot \sin\left(\varphi_{in} - \omega_{ZF} \cdot \left[t - t_o\right]\right) + y_M \tag{3.2}$$

$$with\ \ \varphi_{in} = \frac{\pi}{2} + \arctan\left(\frac{v_{yo}}{v_{xo}}\right) \tag{3.3}$$

$$and\ \ \rho = \sqrt{\frac{v_{xo}^2 + v_{yo}^2}{\omega_{ZF}^2}} \tag{3.4}$$

From the known entry position of ions $\vec{r} = (x_o; y_o)$ into the dee, the position of the center $\vec{r}_M = (x_M; y_M)$ can be calculated using Eq. (3.1) and Eq. (3.2) for the time t calculated with Eq. (3.3) and finally the complete circular path until the ions leave the dee is determined.

The change of differential- and circuit-equations is completed as long as the calculated ions meet a virtual obstacle. Such an obstacle can be the ion source, a shield or the vacuum chamber itself. In this case the calculation of the ion trajectory is complete.

The Presentation-Layer

The simulation engine described above has three modules for the evaluation:

- XY-Plot
- Intensity-Plot and
- Spectrometer-Plot

Every module - apart from the graphical output - allows also a data export to a file so that the measured values can be processed by external programs.

The XY-plot allows a selection of different traces at eligible speeds (Fig. 3).

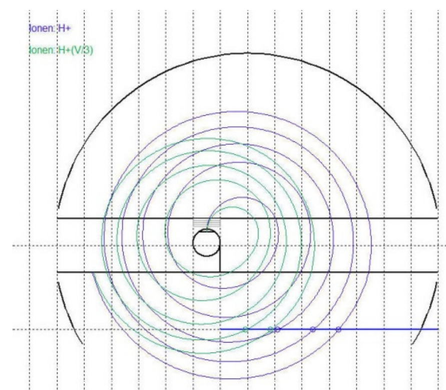

Figure 3: Helical paths of Ions.

So here only the ion paths of protons with $v = v_{max}$ and $v_{max}/3$ are drawn, where v_{max} is the maximal velocity at the given acceleration voltage. It would also be possible to display paths with $v_{max}/5$ and the orbits of H_2^+ - ions at these speeds (Fig. 4).

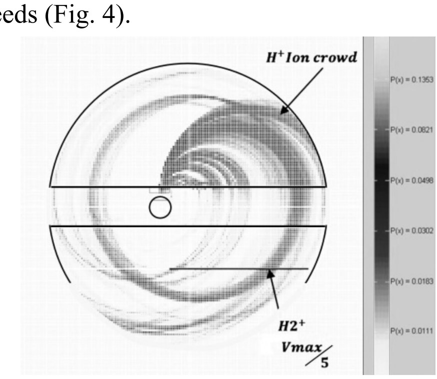

Figure 4: Initial ion-paths.

ISBN 978-3-95450-167-0

Another form of a plot i.e. Fig. 4 examining an initial trajectory of accelerated ions. If B = 66 mT, the simulation predicts a set of closely spaced trajectories of H_2^+ -ions that have $^1/_5$ of the maximum possible speed.

This meets the corresponding measurement (Fig. 5), which shows a remarkable signal in that region:

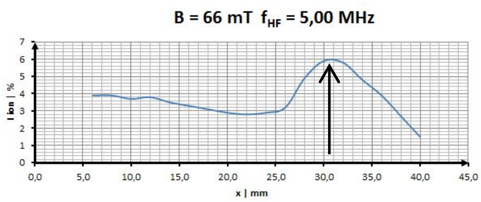

Figure 5: Experimental Diagram.

In the corresponding plot one can see how close the orbits are to each other. So it is obvious that at an Intensity-Plot $I = I\ (x)$ in reality will be an almost continuous chart as shown in Fig. 6. This is qualitatively confirmed by the model, too.

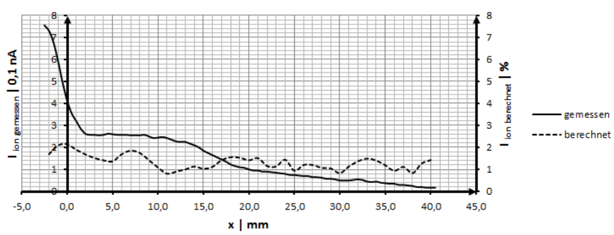

Figure 6: Intensity Plot.

The last module is used for the cyclotron working as a spectrometer. In this experiment the beam is measured in dependence of the magnetic field at a fixed position of the detector. Here one can identify the ions in the beam (Fig. 7).

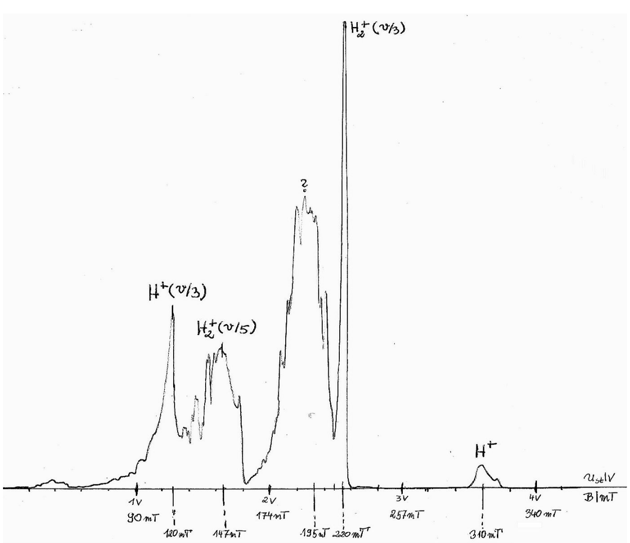

Figure 7: Spectrometer Experiment.

The Spectrometer-Plot (Fig. 8) shows the caluculated probability as a measure for the beam-current vs. the magnetic field and allows to simulate this experiment.

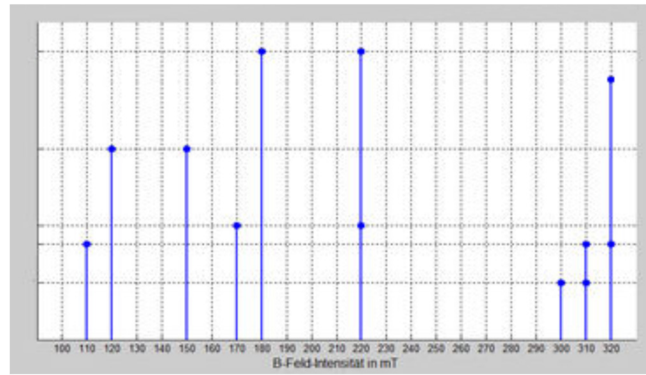

Figure 8: Spectrometer Plot.

CONCLUSION

Of course, the quantitative analysis of the results must be considered very carefully, because there are some assumptions in the simulation that are not met in reality, such as a constant ion beam or the conservation of particles, which is not satisfied, due to the lack of focusing.

Finally, the measurement accuracy in the determination of some parameters was not considered in the simulation.

Nevertheless, the present simulation offers qualitatively a good idea of the acceleration process in the cyclotron and the rest will be a challenge for the future.

ACKNOWLEDGEMENT

The authors thank Prof. Dr. Jirmann for his professional help on every question about RF-problems and also Mr Ehrlicher and Mr Dorn for their assistance.

Our thanks go to the Research Institute of Jülich especially to Prof. Dr. Maier, Dr. Felden and Dr. Gebel from the IKP 4 for their generosity and great support at any time.

We also thank the companies Kaeser Kompressoren, Pfeiffer Vacuum and VACOM Vakuum Komponenten & Messtechnik GmbH for their sponsorship.

REFERENCES

[1] Ch. Wolf, M. Frank, E.Held, *"COLUMBUS- a Small Cyclotron for School and Teaching Purposes*",in *Proc. Cyclotrons2013,* Vancouver, BC, Canada.

[2] D. Görtler, Ch. Wolf, M. Prechtl, R. Bauer, "Detektion der Spiralbahnen in einem Klein-Zyklotron" in *Vakuum in Forschung und Praxis*, Vol. 28 Nr. 3, Juni 2016, pp.26 - 29

[3] Ernst-Abbe-Hochschule Jena, http://www.eah-jena.de/~dathe/MATLAB/WS09_10/Blatt9.pdf

ISBN 978-3-95450-167-0

RADIATION DAMAGE OF COMPONENTS IN THE ENVIRONMENT OF HIGH-POWER PROTON ACCELERATORS

D. Kiselev, R. Bergmann, R. Sobbia, V. Talanov, M. Wohlmuther,
Paul Scherrer Institut, 5232 Villigen, Switzerland

Abstract

At high power accelerators, radiation damage becomes an issue particularly for components which are hit directly by the beam, like targets and collimators. Protons and secondary particles change the microscopic (lattice) structure of the materials, which macroscopically affects physical and mechanical properties. Examples are the decrease of thermal conductivity and ductility as well as dimensional changes. However, the prediction of these damage effects and their evolution in this harsh environment is highly complex as they strongly depend on parameters such as the irradiation temperature of the material, and the energy and type of particle inducing the damage. The so-called term "displacements per atom" (DPA) is an attempt to quantify the amount of radiation induced damage and to compare the micro- and macroscopic effects of radiation damage caused by different particles at different energies.

In this report, the basics for understanding of the mechanisms of radiation damage will be explained. The definition and determination of DPA and its limitations will be discussed. Measurements and examples of the impact of radiation damage on accelerator components will be presented.

INTRODUCTION

The change in material properties due to damage to the lattice structure, which sometimes leads to the failure of components, is called radiation damage. It is a threat particularly to components at loss points in high-power accelerators. These components include targets, beam dumps, and highly exposed collimators. There is renewed interest in the topic of radiation damage owing to new projects and initiatives which require high-power accelerators, and therefore materials which will withstand high power sufficiently long. One such project is the European Spallation Source (ESS), which is being built in Lund, Sweden [1] with a rotating wheel target composed of tantalum cladded tungsten bars irradiated with 5 MW of 2.5 GeV protons. The Facility for Rare Ion Beams (FRIB) is being built at the National Superconducting Cyclotron Laboratory (NSCL) at Michigan State University. This facility will deliver heavy ions with extremely high power densities of 20–60 MW/cm^3 [2]. The Daedalus project is an initiative at MIT with the aim of studying CP violation [3]. For this purpose, a neutrino beam shall be produced by three cyclotrons, each delivering a proton beam with energy of about 800 MeV. The planned beam power on target are foreseen to be 1, 2, and 5 MW for the first, second, and third cyclotron, respectively. At PSI, a 1.3 MW proton beam is routinely available, which constitutes the most intense steady state proton source in the world at present. Higher powers of up to 1.8 MW are envisaged for the future.

For all these projects, it is essential to know how long the heavily irradiated components can be operated safely. In addition, improvement of the lifetime of components needs knowledge about the underlying mechanism of radiation damage and its relation to the changes in material properties. One problem is that components cannot be tested under the same conditions as experienced during operation. Therefore, the correlations between data obtained under different conditions need to be understood.

Prominent macroscopic effects on structural materials caused by radiation damage are the following:

- Hardening, which leads to a loss of ductility;
- Embrittlement, which leads to fast crack propagation;
- Growth and swelling, which lead to dimensional changes of components and can also induce additional mechanical stress;
- increased corrosion rates, in particular in contact with fluids;
- irradiation creep, which leads to deformation of components;
- Phase transformations in the material or segregation of alloying elements, which leads to changes in several mechanical and physical properties.

Besides changes of structural mechanical properties physical properties change as well. Particularly serious is the steep decrease of the thermal conductivity for components, which need to be heavily cooled due to the energy deposition of proton beams. Design studies rely on prediction of the temperature distribution in a component and thus on the knowledge of the thermal conductivity of the material. The consequence is that the component might reach higher temperatures than foreseen, which could lead to the failure of the component.

In pulsed sources, components in addition undergo thermal cycles, causing fatigue. Cracks may occur, which could lead to failure of the component. This phenomenon might be also influenced and accelerated by radiation due to additional hardening and embrittlement. Sometimes, a phenomenon attributed to radiation damage, might in fact be caused by other effects like e.g. rapid heating or pitting.

In the following, some examples of observed radiation damage will be given. In preparation for the above-mentioned FRIB, several objects were studied at NSCL with respect to radiation damage due to heavy ions. For this purpose, a 580 mg/cm^2 tungsten foil, which corresponds to a thickness of 0.03 cm, was irradiated with 76Ge30+ ions at 130 MeV/nucleon. After irradiation of

ISBN 978-3-95450-167-0

the tungsten foil with 5.77×10^{16} Ge ions on a beam spot with diameter of 0.6–0.8 mm, a crack was observed right in the centre of the beam spot. Further investigations [2] revealed that the crack was caused by swelling and embrittlement, which induced additional stress in the foil. Due to the likely decrease of the thermal conductivity by radiation the stress might have been increased by thermal stress.

At the Los Alamos National Laboratory, tungsten was investigated for its suitability as a material for spallation targets. For this, hardness and compression tests were performed at room temperature and at 475°C on irradiated and un-irradiated specimens. Tungsten rods were irradiated for up to 6 months with 800 MeV protons at a current of 1 mA, which corresponds to a dose of 23 Displacements Per Atom (DPA). The temperature during irradiation was kept constant for each sample; it varied between 50 and 270°C for different samples. In the compression tests, the samples were compressed to a strain of about 20%. The irradiated samples suffered from a loss of ductility, which showed up as a longitudinal crack in the compression tests, i.e. in the direction of the force. The compressive yield stress and the hardness increased linearly with the dose except for small doses, where it increased strongly. Optical micrographs of the tungsten compression specimens were also taken [4].

The pyrolytic graphite target at TRIUMF was cooled on the edges with water. After irradiation with 500 MeV protons at a current of 120 µA, the graphite delaminated, i.e. segmented into slices perpendicular to the beam. It is interesting to note that the target stayed intact for currents below 100 µA, however always failed at higher currents. For details and a picture of the target after irradiation, see Ref. 5. After improving the cooling swelling was not observed anymore [6]. This agrees with the assumption that swelling is a high temperature effect. A similar phenomenon was observed at PSI, where a former meson production target made from Beryllium always cracked at 150 µA, but survived at smaller currents. This might be a hint that the damage was influenced also by thermal stress.

At the 1 MW spallation source at SNS examination of the irradiated container of the mercury target revealed an interesting damage pattern, which is not correlated with the beam intensity. Fluid dynamic simulations could show that the damage is correlated with the flow distribution of the mercury. Finally, the damage was attributed to thermal shock caused by the beam in the mercury, which leads to cavitation and pitting on the stainless steel container [7].

UNDERLYING MECHANISM OF RADIATION DAMAGE

When particles penetrate matter they lose energy by several different mechanisms, where some of them will damage the lattice structure of the material. The mechanisms are:

- electronic excitations/ionisation;
- elastic interactions;
- inelastic reactions.

The first of these types of interaction is due to the Coulomb interaction and is therefore possible only for charged particles. Here, energy is used to shift electrons from the atomic core to an outer shell. This is called excitation and can lead to the removal of an electron, i.e. ionization of the atom. The excess energy is dissipated as heat, which might also cause damage to structural materials like a copper beam dump, although this kind of damage has nothing to do with radiation damage. However, in organic materials ionization causes damage by breaking bonds. Therefore, plastics or grease become dark, hard and brittle. The damage due to ionisation is quantified by the ionising dose, which is the absorbed dose in the material (unit Gray). This is a cumulative effect over time. The method to calculate the absorbed dose is well known.

In elastic and inelastic interactions, energy and momentum are transferred from the particle to the nucleus. In case of an elastic interaction, the nucleus is not changed but remains the same isotope. In all cases, the atom gains a recoil momentum. The first atom hit is called the Primary Knocked-on Atom (PKA). Energy and momentum are transferred to the nucleus only and not to its electrons; hence the atom moves in a partly ionized state through the lattice. The recoil energy is mainly lost mainly by Coulomb interactions (ionization and excitation) and is again dissipated as heat. If the energy is large enough, the primary atom can knock on other atoms, which again leave their site. As a result, many atoms can be moved from their original lattice position.

The inelastic reaction usually transfers a larger portion of energy to the atom compared to elastic interactions. Inelastic interactions lead to transmutation of the nucleus, which can be radioactive, but also to the production of many secondary particles. The transmuted nucleus, referred to as an impurity in the following, does not fit ideally into the lattice structure and therefore changes the mechanical properties of the material. Furthermore, in high-conductivity materials such as very pure copper, impurities are known to reduce the conductivity, i.e. they also have an influence on the physical properties. Usually, the damage done to the lattice by the recoils is much larger than that due to the impurities. An exception is when large amounts of helium and hydrogen are produced in highly energetic reactions..

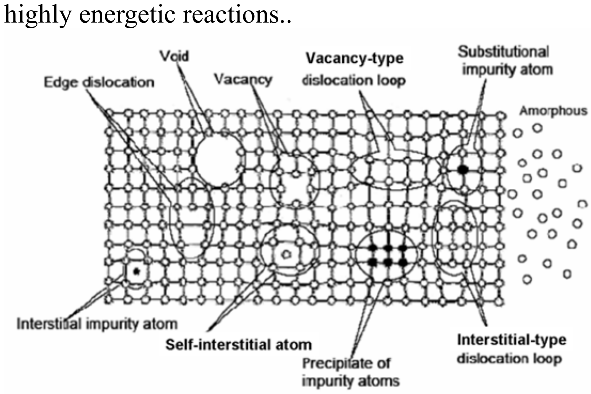

Figure 1: The most important defects in a lattice structure (image from Prof. H. Föll, University of Kiel).

ISBN 978-3-95450-167-0

The most important defects in a lattice are shown in Fig. 1. The open dots belong to the original crystal, and the black dots indicate impurities. The simplest defects are the point defects, also known as zero-dimensional defects. The most prominent representatives of the point defects are self-interstitials and vacancies. Self-interstitials are atoms from the lattice which have left their lattice position for a site not provided in the lattice. The influence of a self-interstitial on its surroundings is a shift of neighbouring atoms away from the self-interstitial to make space for it. A vacancy is just the opposite of a self-interstitial. Here, a lattice atom is missing. These defects also exist in un-irradiated materials. If a defect of this type is caused by irradiation, a vacancy and a self-interstitial appear in a pair. This is called a Frenkel pair. Also, an atom on an interstitial site may have been transmuted by an inelastic reaction to an impurity. It is then called an interstitial impurity atom or extrinsic interstitial.

The dislocation loop belongs to the class of one-dimensional defects. Here, part of a lattice plane is missing or has been added. There are two types of dislocation loop: the vacancy-type dislocation loop and the interstitial-type dislocation loop. In the vacancy type, part of a plane of lattice sites is missing. In the interstitial type, part of a plane of additional atoms has been incorporated into the lattice structure. Dislocations move under the influence of external forces, which cause internal stresses in a crystal. In the ideal case, dislocations move out of the lattice. If more than one plane is involved, a cluster is formed. If several planes are partly missing, one has an agglomeration of vacancies. This is called a void. An agglomeration of impurity atoms replacing neighbouring lattice sites on more than one plane is called a precipitate. Owing to their different sizes and properties, the neighbouring atoms are slightly shifted from their original positions. All of these defects make the lattice less flexible against strain, which manifests in a loss of ductility and an increase in hardness. In addition, the material becomes brittle. Small cracks can develop, which may grow further, and this can lead to the failure of a component.

Usually, the interaction with a particle of more than a few MeV does not cause single defects of the kind described above; instead, a large region containing millions of atoms is affected. For example, a nucleus in gold with a recoil energy of only 10 keV destroys the lattice structure in its surroundings within a radius of about 5 nm. This is called a displacement spike and happens within 1 ps. Since a huge number of atoms is involved in the process, a simulation via a Monte Carlo technique needs considerable effort and a large amount of computer power. Such a simulation has to solve the equation of motion for all atoms at the same time, since each atom can interact with and be influenced by all the other atoms. This is a multibody problem, and the computer time needed grows with the square of the recoil energy of the first knock-on atom. The higher the recoil energy, the greater the number of atoms involved. Therefore such calculations are limited to recoil energies less than 100 keV for practical reasons. In addition, the simulation has to be repeated for each recoil energy. This kind of calculation is called Molecular Dynamics Simulation (MDS). The advantage is that the results are quite realistic, and the various kinds of defects produced can be studied in the simulation. The MDS method is the only way to evaluate how many defects disappear as a result of recombination with other defects. Unfortunately, the MDS method can follow the process for only a few picoseconds, whereas the complete healing process can last for months.

A faster but less accurate method is the Binary Collision Approximation (BCA), where only collisions between two (hence the name 'binary') atoms are considered. The other atoms are considered as spectators. The particles are followed via trajectories as in a Monte Carlo particle transport program. This calculation method is much faster than the MDS method and also works well at higher energies. However, when such approximations are made, much less information about the process and the state of the lattice is available compared with the MDS method.

CALCULATION OF DPA

To estimate and quantify the severity of the damage, a phenomenological approach was developed by Norgett, Robinson, and Torrens, which dates back to the 1970s [8], known as the NRT model after the authors' initials. To quantify the radiation damage, a value is chosen which indicates how often each atom is displaced on average during the irradiation. This quantity is called the Displacement Per Atom (DPA), and is obtained by convolution of the energy-dependent particle fluence $\phi(E)$ (in units of particles/cm^{-2}) with the displacement cross-section $\sigma_{\mathrm{disp}}(E)$:

$$DPA = \int \sigma_{\mathrm{disp}}(E)\ \frac{\mathrm{d}\phi(E)}{\mathrm{d}E}\ \mathrm{dE} \qquad (1)$$

The displacement cross-section gives the number of displacements per particle. It is a function of the energy of the particle responsible for the damage. For charged particles the displacement cross section is determined by the Coulomb interaction at low energy and therefore large, for ions even larger than for protons. Above 10 MeV the displacement cross section is dominated by nuclear reactions and the production of secondary particles and their interactions. Therefore, at higher energies the displacement cross section of protons and neutrons is very similar.

The displacement cross-section is obtained by folding the damage cross section with the damage function $\nu(E_{\mathrm{R}})$ described below:

$$\sigma_{\mathrm{disp}}(E) = \int_{E_{\mathrm{D}}}^{E\,\mathrm{max}} \frac{\mathrm{d}\sigma_{\mathrm{dam}}(E, E_{\mathrm{R}})}{\mathrm{d}E_{\mathrm{R}}}\ \nu(E_{\mathrm{R}})\ \mathrm{d}E_{\mathrm{R}} \quad (2)$$

The integration runs over all recoil energies from the threshold, i.e. E_{D}, to the maximum possible recoil energy. The damage cross-section $\sigma_{\mathrm{dam}}(E, E_{\mathrm{R}})$ is, in addition, a function of the recoil energy of the PKA and is in fact calculated from the recoil spectrum $w(E_R)$. It states how

ISBN 978-3-95450-167-0

many nuclei can be found with recoil energy E_R. It is obtained from

$$\frac{\mathrm{d}\sigma_{\mathrm{dam}}(E,E_{\mathrm{R}})}{\mathrm{d}E_{\mathrm{R}}}=\frac{\mathrm{d}w(E,E_{\mathrm{R}})/\,\mathrm{d}E_{\mathrm{R}}}{xN_V}\ , \qquad (3)$$

where x is the thickness of the sample and N_V is the atom density in atoms/cm^3. To obtain the recoil spectrum, the cross-sections of all reactions occurring in the material have to be known. Since Monte Carlo particle transport programs contain models for all nuclear reaction cross-sections over a wide energy range, a popular application of these programs is to use them to obtain the recoil spectrum. Here, it is important to use a thin target to avoid significant energy loss of the primary particle in the sample. If the object of interest has larger dimensions, the recoil spectrum has to be calculated for different energies of the primary particle to account for the energy loss of that particle. This requires several Monte Carlo runs. Besides this the fluence required in Eq. (1) is calculated in Monte-Carlo particle transport programs. Many such codes like FLUKA, PHITS, and MARS already have a built-in option to obtain the DPA in one run. This is very convenient and avoids a larger effort. Alternatively, one can use Eq. (1) folding the calculated fluence with displacement cross sections provided somewhere else. Eq. (1) has to be applied not only for the primary particle but also for the secondary particles produced.

The energy available to displace other atoms is called the damage energy, T_{dam}, which is equal to the recoil energy minus the energy E_e dissipated in ionization and excitation of the atom. For recoil energies larger than 10 keV, most of the energy is lost by ionization. The fraction of the recoil energy left for the damage energy is called the partition function or, sometimes, the damage efficiency. The amount of energy required for displacing an atom is roughly twice the sublimation energy because, at the surface, only half of the bonding needs to be broken. In Cu, the energy needed ranges from 18 to 43 eV, depending on the crystal orientation [9]. In most calculations, the effective threshold energy E_D for copper is taken equal to 30 eV. When the damage energy T_{dam} is larger than E_D but less than $2E_D$, just one atom can be displaced. The PKA may be captured on the lattice site of the second atom. Since for $E_R = 2E_D$ only one atom is effectively displaced, the damage function $\nu(E_R)$, which gives the number of displaced atoms, is given by

$$\nu(E_{\mathrm{R}})=\frac{\kappa T_{\mathrm{dam}}}{2E_{\mathrm{D}}}$$

The factor κ is set to 0.8, which was obtained by a BCA calculation of the authors of [8]. For $E_R > 2E_D$, a cascade of collisions and displacements will take place.

It has to be emphasized that the NRT approach is a simplified method. It completely neglects the details of the process of the displacement cascade. No interactions of the struck atom with the remaining lattice atoms are taken into account. Parameters of the crystal lattice such as the atomic bonding energy and the properties of the solid are completely absent. Instead, all this is condensed into the displacement threshold energy E_D. In the NRT model, it is implicitly assumed that the defect concentration is equal to the calculated number of displacements. Moreover, the displacements formed are taken to be stable. Molecular dynamics simulations have shown that the defects are not isolated Frenkel pairs as assumed in the NRT model, but are concentrated in a small region influencing each other. A high density of displaced atoms is produced in the first few tenths of a picosecond. This is called the collisional phase. In this phase, the number of displaced atoms is in fact much larger than that predicted by the NRT model. A few picoseconds later, most of the displaced atoms have recombined with vacancies. This is called 'healing'. The interstitial–vacancy annihilation process is completely omitted in the NRT model. This process is especially important at large PKA energies (>5 keV), where cascades of displaced atoms are produced in the initial state and defects are produced close to each other. At higher PKA energies (>20 keV), subcascades are formed and the number of recombination events decreases. Such a high-energy atom shakes the whole lattice and also deposits thermal energy, localized in the defect region. E.g., 10 keV recoil on gold produces a displacement spike with an equivalent temperature of 10000 K. This makes the defects more mobile and facilitates recombination. The assumption of the NRT model that it is sufficient to count the initially produced Frenkel pairs cannot be justified at energies larger than 0.5 keV, where high-energy cascades start to develop.

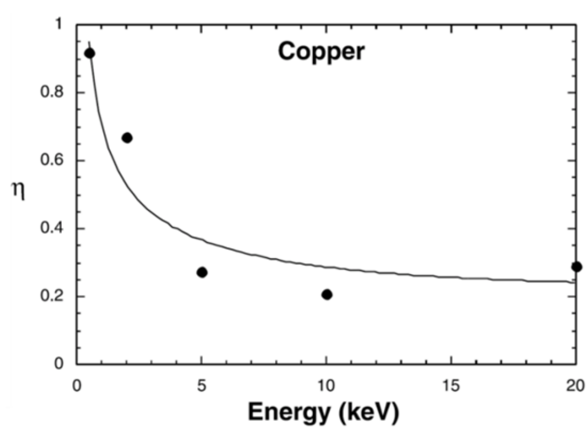

Figure 2: Defect efficiency as a function of the recoil energy in copper [10] at 4 K.

An example of the effect of healing in copper is shown in Fig. 2. The effective healing is just $1-\eta$, where η is the defect or cascade efficiency. It is given as a function of the recoil energy of the PKA. The defect efficiency η is defined as the ratio of the number of Frenkel pairs at the end of phase 1, i.e. at the end of the collision cascade, obtained by an MDS, to the number obtained from the NRT model [10]. The MDS calculation here was performed for a temperature of 4 K. The results confirm that

ISBN 978-3-95450-167-0

the NRT approach is only justified at small recoil energies. Above 5 keV the recombination of defects dominates. The number of Frenkel pairs is five times lower than predicted by the NRT model. This kind of healing is called athermal as it is independent of the temperature and takes place within 50 ps. It is interesting to note that the defect efficiencies in other materials such as W, Fe, and Al show very similar values, even though the final distribution of the defects differ.

Another healing effect is causes by external temperature and therefore also called thermal healing. Already low temperatures (>10 K) make the atoms sufficiently mobile to recombine with vacancies. This effect takes places on a much longer time scale of hours to years – depending on the temperature. It is well known that due to annealing after irradiation the properties of the material are getting closer to the ones of the unirradiated state. In Fig. 3 the surviving defect fraction is shown as a function of temperature for copper.

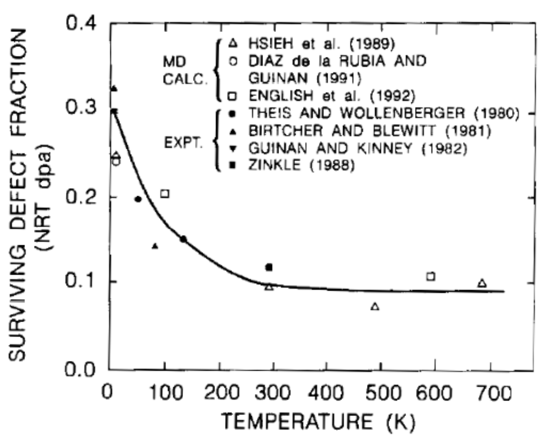

Figure 3: Thermal healing: Surviving defect fraction as a function of temperature for copper [11].

The reduction of the defect efficiency at high PKA energy is important when one is comparing the damage produced by low- and high-energy particles. The materials that suffer radiation damage at today's accelerators are irradiated by high-energy particles, whereas most of the material studies were done in reactors. Figure 2 suggests that one has just to multiply the recoil spectrum of the PKA by the defect efficiency to compare the results and to profit from the large data set that has been taken with reactor neutrons. However, the effect of irradiation can depend on many details, e.g. the production of impurities, specially hydrogen and helium (see below). The good news is that the NRT–DPA method provides a conservative value for DPA.

MEASUREMENT OF DEFECTS

Although the NRT-DPA cannot be measured directly since most of the defects heal out within 50 ps, the number of final defects can be determined by several methods. The increase of the electrical resistivity is directly related to the number of Frenkel pairs created times the contribution to the electric resistivity of one Frenkel pair. The latter quantity is known from X-ray scattering. Comparison of experimental data with MDS revealed satisfying agreement [10]. The defect production efficiency can be obtained by comparing the measured defects with the one predicted by NRT as shown in Fig. 3. However, defects do not consist solely of Frenkel pairs but also of e.g. clusters. It turns out that in most metals clusters contribute with a similar resistivity as Frenkel pairs. In addition, such experiments are usually done at very low DPA, where single defects like Frenkel pairs dominate.

Defects can be also visualized. A common method is using the Transmission Electron Microscope (TEM), which requires very thin samples to detect the transmitted electrons on the backside of the sample. Nowadays resolutions of a few nm are possible. In addition, even in situ TEM just after the irradiation and a few seconds later were performed [12], which revealed the disappearance of nanovoids. However, only defects above the resolution are visible. In addition, the defect distribution measured on materials irradiated at different temperatures and DPA can look very different. Counting the number of defect clusters shows a clear disappearance of defects with temperature, however, the number of single point defects increases. Further, the saturation of the number of defects after a few DPA in stainless steel 316L was measured in a similar way [13] and is valid also for other materials.

TENSION TESTS AND HELIUM

Although different kinds of post irradiation experiments are performed, one common measurement is the tension test, where the material is pulled at both ends until its rupture. Irradiated samples are in general harder, i.e. the tensile strength is higher than in the unirradiated case. In addition, the material becomes more brittle, which can be also seen from the strain-stress diagram. A break of the sample without necking is a clear sign for embrittlement. At high temperatures the embrittlement can be even accelerated by helium produced by inelastic reactions (mostly spallation). Some materials like austenitic steel are really sensitive and a few appm He is sufficient for He induced embrittlement at higher temperature.

Since the hydrogen and helium production can influence the mechanical properties it is important always to note to which H/He content and at which temperature the material was irradiated. The production of He at high energy accelerators can exceed that in fission reactors by about a factor of 100, when high energy particles hit the component directly. Hydrogen production can be increased by a factor 400 to 500 in accelerators compared to fission reactors. Therefore, the large database of measurements in reactors has to be used with care to predict radiation damage at accelerators. Hydrogen leaves e.g. steels at temperatures larger than 250 °C. In metals, which form hydrids, hydrogen leads to embrittlement at lower temperature.

ISBN 978-3-95450-167-0

Helium bubbles can be well visualized with the already mentioned TEM method. They appear as small dots/bubbles equally distributed over the sample. Besides the embrittlement He influences the swelling although both effects, accelerating and reducing swelling, were observed. Another interesting and well visible effect is the blistering or exfoliation of small pieces on the surface. The pressure between larger bubbles just below the surface causes stress, which is not balanced by the tension stress at the surface. Therefore fractures on the surface occur. Such an effect was observed in experiments using He beams. Due to its short range He is implanted just below the surface where it forms bubbles.

INSPECTION OF A COLLIMATOR AT PSI

The collimator KHE2 is located 4.5 m behind the meson production target E, a 4 cm thick graphite wheel, in the 590 MeV proton beam line. Due to multiple scattering the beam is spread in addition to its intrinsic divergence by 6 mrad. To shape the beam the KHE2 absorbs about 10 % of the beam on Target E, i.e. it suffers from a power deposition of about 130 kW. Therefore, it consists of a copper body, 30 cm long (proton stopping range in Cu is 26 cm), and brazed steel tubes around for cooling with water. The KHE2 was in operation from 1990 until 2012. In this period the beam on Target E increased steadily; the integrated charge was 147 Ah. ANSYS calculations using the thermal conductivity of unirradiated copper show a maximum temperature of 380°C inside the collimator at 2 mA. The first 5 cm long section of the inner part of KHE2 experiences an average of 30 DPA, the outer part 4 DPA according to a calculation with MARS [14]. Although MCNPX2.5.0 [15] predicts half of the values obtained with MARS, measurements at similar temperature but performed in reactors, suggested a swelling rate of 0.5 %/DPA. Therefore, the collimator was taken out of the beam line and inspected with a well shielded camera and two laser distance meters for measuring the opening of the collimator. The horizontal dimensions of the apertures of the six “teeth” were measured with the two laser distance meters and a prism mirror. The original values could be reproduced by the measurement with a deviation of less than 0.2 mm, where 0.5 mm corresponds to the accuracy of the method. Another proof of the absence of a dimensional change due to swelling is the slit of 1 mm for thermal expansion, which is completely intact at the entry as well as at the exit side of KHE2.

In Fig. 4, a view of the front of the collimator is shown. In the vertical and horizontal direction, erosion/blistering of the surface can be seen around the slits, which help to release thermal stress. Most astonishing the surface between the horizontal and vertical view is much less affected, although the beam profile is almost circular. A possible explanation might be that around the slits there is more movement of the surfaces due to thermal expansion and shrinking when the beam is on or off. The blistering might be partly due to the helium deposition close to the surface. Between the horizontal and vertical direction, a grey film appears on the surface, which is probably graphite evaporated from Target E. A sample containing Be7 confirms this. On the right of Fig. 4, photos of the vertical surfaces at the beam exit and the horizontal surface at the beam entry are seen. Although the temperature of about 80 to 100 °C does not vary much throughout the collimator at the vertical position, the surface at the beam exit (top picture on Fig. 4) looks much more eroded than at the entry. Pieces of the grey surface are 1-2 mm high and are peeling off. The surfaces at the top and the bottom look essentially the same.

Figure 4: Left: Collimator front view with Ni-aperture. Right: Photo from the exit, vertical position, and entry at horizontal position (picture on the bottom).

At the horizontal surfaces the grey coating cannot be seen, most likely because this is the hottest surface. However, exfoliation also appears here and it seems that some lamella took already off.

REFERENCES

[1] European Spallation Source, `http://ess-scandinavia.eu`

[2] R. Ronningen, in *Proc. HB2010*, Morschach, Switzerland, Sept. 2010, pp. 662-666.

[3] J.M. Conrad *et al.*, arXiv:1012.4853 [hep-ex].

[4] S.A. Maloy *et al.*, *J. Nucl. Mater.,* vol. 34, p. 219, 2005.

[5] E.W. Blackmore *et al.*, in *Proc. PAC 2005*, Knoxville, USA, May 2005, pp. 1919-1921.

[6] E.W. Blackmore, private communication.

[7] B. Riemer *et al.*, *J. Nucl. Mater.*, vol. 450, p. 183, 2014.

[8] M. Norgett, M. Robinson, and I. Torrens, *Nucl. Eng. Des.,* vol. 33, p. 50, 1975.

[9] H.B. Huntington, *Phys. Rev.,* vol. 93, p. 1414, 1954.

[10] M.J. Cartula *et al.*, *J. Nucl. Mater.*, vol. 296, p. 90, 2001.

[11] B.N. Singh, S. Zinkle et al, *J. Nucl. Mater.*, vol. 206, p. 212, 1993.

[12] Y. Chen *et al*, *Nat. Commun.* 6:7036 doi:10.1038/ncomms8036, 2015.

[13] D.J. Edwards, E.P. Simonen, S.M. Bruemmer, *J. Nuc. Matter.*, vol. 317, p. 13, 2003.

[14] N.V. Mokhov, S.I. Striganov, “MARS15 Overview”, Fermilab, USA , Fermilab-Conf-07-008-AD, 2007.

[15] D. Pelowitz, ed., “*MCNPX User's Manual, Version* 2.5.0”, Los Alamos, USA, Rep. LA-CP-05-0369, 2005.

ISBN 978-3-95450-167-0

DESIGN OF THE ENERGY SELECTION SYSTEM FOR PROTON THERAPY BASED ON GEANT4*

Zhikai Liang†, Wei Chen, Bin Qin, Xu Liu, Kaifeng Liu, Jian Zha
Institute of Applied Electromagnetic Engineering
Huazhong University of Science and Technology, Wuhan 430074, Hubei, China

Abstract

Huazhong University of Science and Technology (HUST) has planned to build a proton therapy facility based on an isochronous superconducting cyclotron. The 250 MeV/500 nA proton beam is extracted from a superconducting cyclotron. To modulate beam energy, an energy selection system is essential in the beamline. The simulation based on Geant4 has been performed for the energy selection system and its result will be discussed in this paper. This paper introduces the variation rules of the beam parameters including the beam energy, beam emittance, energy spread and transmission. The degrader's gap and the twiss parameter are proven to be effective ways to reduce the emittance after degrader.

INTRODUCTION

Huazhong University of Science and Technology (HUST) has proposed to construct a proton therapy facility, which includes two rotating gantries and one fixed beam treatment room [1,2]. To modulate the proton beam energy for treatment, an energy selection system (ESS) is located in the beam-line. The beam energy can be modulated by the interactions between the energetic particles and the degrader's material. The ionization process with the electrons, the multiple Coulomb scattering with the nucleus and the nuclear reaction are the mainly components of the interactions, which will contribute to the energy degradation, the emittance growth and the secondary particles' production.

The energy selection system consists of an energy degrader, a set of collimators, and a double bend achromatic (DBA) section with an energy selection slit. An overview of the conceptual layout is shown in Fig. 1, and the main parameters of the beam are listed in Table 1. The energy degrader is aimed at the energy modulation by controlling the thickness of the degrader. The emittance collimators are designed to suppress the beam emittance significantly increased in the degrader. And the energy slit in DBA section is used to limit the energy spread.

This paper mainly describes the variation rules of the beam parameters including the beam energy, beam emittance, energy spread and transmission. And furthermore, the degrader's gap and the twiss parameter are illustrated to be effective ways to reduce the emittance after degrader.

*Work supported by The National Key Research and Development Program of China, with grant No. 2016YFC0105305
† Email address: hust_lzk@163.com

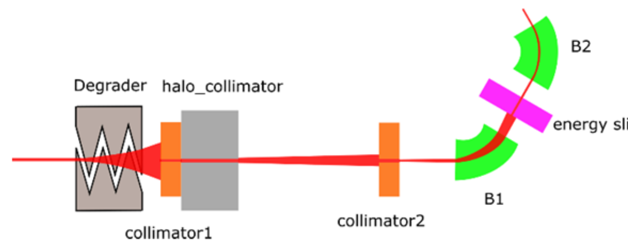

Figure1: Overview of the energy selection system (ESS).

Table 1: Main parameters of the beam

Location	Parameter	Design value
Before ESS	Energy	250MeV
	Current	500nA
	Emittance	5 π mm · mrad
	Energy spread	0.5%
After ESS	Energy range	70~250MeV
	Transmission	0.2%
	Emittance	5 π mm · mrad
	Energy spread	±0.5%

THEORY AND SIMULATION

To simulate the passage of particles through matter, the model of ESS is built in Geant4 [3].Geant4 toolkit consists of many kinds of physical package. For example, the QBBC physical package is effective tool for the simulation of interactions between 250 MeV proton and the material. The detailed model parameters are presented in Table 2 [4]. Therefore, the beam parameters can be obtained from the simulation result.

Table 2: Model parameters of ESS

Object	Material	Central position (mm)	Length (mm)
Degrader	Graphite	0	200
Col1	Copper	167.5	35
Halo_col	Graphite	300	60
Col2	Copper	1187.5	35

Energy Selection

Energy degrading is the main purpose of the energy selection system based on the Bethe-Bloch formula [5] shown in Eq. (1).

$$-\left(\frac{\mathrm{dE}}{\mathrm{dx}}\right)=4\pi \mathrm{N}_a r_e^2 m_e c^2 z^2 \left(\frac{Z}{A}\right)\left(\frac{1}{\beta^2}\right)\left[\ln\left(\frac{2m_e c^2\gamma^2\beta^2}{I}\right)-\beta^2-\frac{\delta}{2}\right]. \quad (1)$$

ISBN 978-3-95450-167-0

Where E is the particle energy, $x = X \cdot \rho$ is the reduced medium thickness, r_e is the classical electron radius, m_e is the static electronic mass, c is the light speed, z is the change of the particle, Z/A is the charge mass ratio of the degrader material, β、γ are the velocity and the mass, I is the ionization potential, $\delta/2$ represents the density effect which can be ignore for 250 MeV protons because of the lower energy. The theoretical and simulated results are shown in Fig. 2

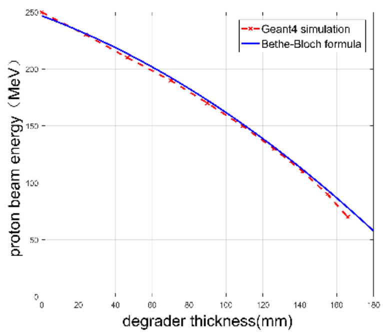

Figure 2: The proton beam energy varies with the degrader thickness.

The result of the Fig. 2 indicates that:

- The degrader thickness ranges from 0 to 166 mm while the beam energy ranges from 250 MeV to 70 MeV.
- The maximum error between the theoretical and simulated result is 3.3% when the energy after degrader is 70 MeV.
- The maximum energy change rate is about 1.46 MeV/mm when the energy is 70 MeV. This means the degrader requires high position accuracy especially when the energy after degrader is low.

Emittance Growth

The emittance growth comes from the multiple Coulomb scattering in the degrader. The multiple Coulomb scattering will lead to the beam divergence angle increase which is the main reason of the emittance growth in the degrader. The multiple scattering angle and the exiting beam emittance can be calculated by Eq. (2) and Eq. (3) [6].

$$\theta_0 = \frac{13.6z}{\beta cp}\sqrt{\frac{L}{L_0}} \times \left(1 + 0.038\ln\left(\frac{L}{L_0}\right)\right). \tag{2}$$

$$\varepsilon_{\mathrm{deg}} = \varepsilon_0 + \beta\theta_0^2 . \tag{3}$$

Where p is the incident momentum, L is the reduced medium thickness, L_0 is the material radiation length, ε_0 is the initial beam emittance before degrader and the β in Eq. (3) is the beam twiss parameter instead of the velocity in Eq. (1). The Eq. (2) and Eq. (3) illustrate that the twiss parameter and the material radiation length are the two main factors that influence the emittance growth.

The proton therapy requires low emittance so that some collimators must be added to reduce the emittance after the degrader. The formula of the emittance after the collimators is as followed [7].

$$\varepsilon_{\mathrm{col}} = \frac{2r_1 \cdot r_2}{L} \tag{4}$$

Where r_1 and r_2 are the incident and exiting aperture of the collimators and L is the whole length from the first collimator to the last.

After the energy slit, the emittance will be further reduced. The simulated result of the emittance for the whole system is shown in Fig. 3.

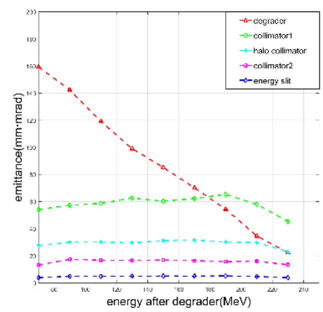

Figure 3: The emittance's variation of the whole system.

Based on the above simulation, some conclusion can be derived.

- The degrader will bring about the emittance growth. The emittance is proportional to the degrader's thickness corresponding to the energy after degrader.
- The collimators can significantly reduce the emittance and maintain a lower value about 5 π mm · mrad.
- The energy slit can further reduce the emittance to a stable value about 5 π mm · mrad while it's aimed to decrease the energy spread to 0.5%.

Energy Spread Increase

The energy spread will increase after the degrader. Besides, the energy spread will be larger when the energy after degrader is higher. The simulation result of the exergy spread after the degrader is shown in Fig. 4.

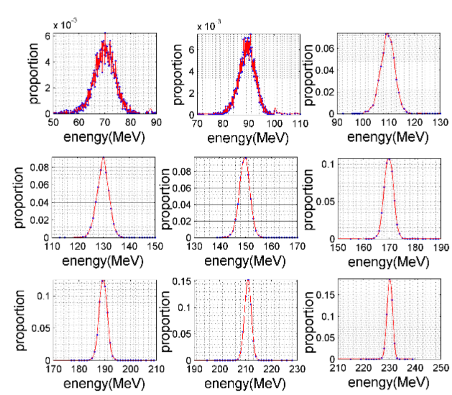

Figure 4: The energy spread after the degrader varies with the energy after degrader.

ISBN 978-3-95450-167-0

The energy spread will maintain a stable value about ±0.5% by using the DBA section and the slit. Proton beam with different energies will deflect in different radius through the bending magnet. Thus, only the protons with proper radius can go through the energy slit.

Transmission

Transmission of the proton beam directly relates to the beam current. The beam losses of the energy selection system are much more significant than other places in the proton therapy equipment. Figure 5 illustrates the transmission of the whole energy selection system.

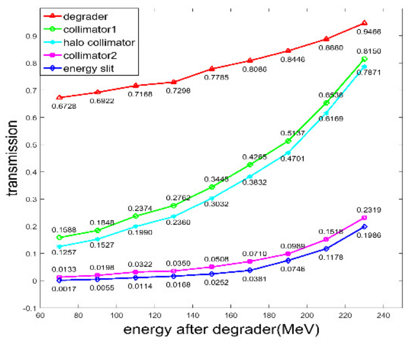

Figure 5: The transmission varies with the energy after degrader.

OPTIMIZATION

To obtain higher transmission efficiency, lower emittance growth after the degrader is essential. According to Eq. (3), the emittance growth is mainly determined by the multiple scattering angle θ_0 and the twiss parameter β. Therefore, on the one hand, material with smaller material radiation length L_0 is chosen such as graphite and beryllium whose atomic number is pretty low. In this paper, due to the virulence of the beryllium, the graphite is used instead. On the other hand, it's effective to locate the center of the degrader at the beam waist or keep the degrader compact so that the twiss parameter β can be smaller. Because the degrader is wedge-shaped, the gap between the dentation structures should be as smaller as possible. Figures 6 and 7 show the simulation result after enlarging the gap so that the degrader length varies from 200 mm to 260 mm.

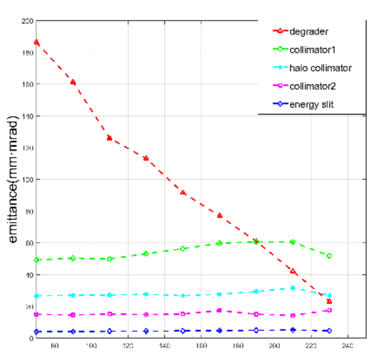

Figure 6: Degrade length becomes 260mm. Showing the emittance.

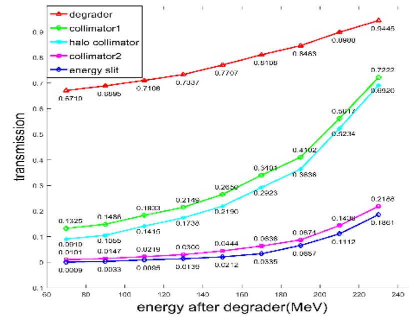

Figure 7: Degrade length becomes 260mm. Showing the transmission.

Compared to Fig. 3 and Fig. 5, some conclusions can be obtained.

- The emittance after degrader will increase when the degrader gap increases.
- The transmission of the whole ESS will decrease when the degrader gap increases.

CONCLUSION

The energy selection system consists of the energy degrader, the emittance collimator, the energy slit and the control component, radiation protection. Owing to the space for the monitor or the cooling, the length of energy degrader is set to 200 mm. The beam parameters can be obtained: 5 π mm · mrad，0.17% as the transmission when the energy spread is ±0.5%.

REFERENCES

[1] Bin Qin, Kuanjun Fan, Mingwu Fan, *et al*, “Fast Scanning Beamline Design Applied to Proton Therapy System Based on Superconducting Cyclotrons”, presented at the 21th International Conference on Cyclotrons and their Applications. (CYC2016), Zurich, Switzerland, Sep 2016, paper MOP12, this conference.

[2] Xu Liu, Bin Qin, Kaifeng Liu, *et al*, “Design of the Fast Scanning magnets for HUST Proton Therapy Facility”, presented at the 21th Inter-national Conference on Cyclotrons and their Applications. (CYC2016), Zurich, Switzerland, Sep 2016, paper MODM04, this conference.

[3] Geant4 Collaboration, “Geant4 User's Guide for Application Developers,” 2011.

[4] M. J. v. Goethem, R. v. d. Meer, H. W. Reist, and J. M. Schippers, “Geant4 simulations of proton beam transport through a carbon or beryllium degrader and following a beam line,” *Physics in Medicine and Biology*, vol. 54, p. 5831, Oct. 2009.

[5] W. R. Leo, “Techniques for Nuclear and Particle Physics Experiments: A How-to Approach.” *Springer Science & Business Media*, Dec. 2012.

[6] V. Anferov, “Energy degrader optimization for medical beam lines,” *Nuclear Instruments and Methods in Physics Research Section A: Accelerators, Spectrometers, Detectors and Associated Equipment*, vol. 496, no. 1, pp. 222–227, 2003.

[7] P. Spädtke, R Hollinger, Beam Transport. Wiley-VCH Verlag GmbH & Co. KGaA, 2005

ISBN 978-3-95450-167-0

DESIGN STUDY OF THE 250 MeV ISOCHRONOUS SUPERCONDUCTING CYCLOTRON MAGNET*

Wei Chen†, Bin Qin, Zhikai Liang, Xu Liu, Kaifeng Liu, Kuanjun Fan
State Key Laboratory of Advanced Electromagnetic Engineering and Technology,
Huazhong University of Science and Technology, Wuhan 430074, China

Abstract

Superconducting cyclotron is an optimum choice to deliver high quality continuous wave (CW) proton beams for proton therapy with its compactness and power saving. Field isochronism and tune optimization are the two crucial factors of cyclotrons during the magnet design. This paper is concentrated on the superconducting magnet design, mainly including the spiral magnet, isochronous field and the tune optimization. The main parameters and some features of the machine will be presented.

INTRODUCTION

Today, cancer is a leading cause of death worldwide especially in industrial countries. Its treatment still presents a real challenge. In China, the survival and cure rate for cancer patients is lower than 15%. It is reported that the number of new cancer cases and deaths will reach 15 million or even more in 2020 [1].

As a method of radiation therapy, proton therapy has attracted widespread attention in recent years. Proton beams have the characteristic Bragg peak in their depth-dose distribution compared to traditional X-ray. Hence, proton therapy is preferable for most types of tumors due to accurate local dose control and minimum damage to the healthy tissues surrounding at the target tumor. Approximately more than 50,000 cancer patients have been treated with proton beams and Proton therapy is recognized as the most effective radiation therapy method for cancers with very high cure rate of 80% [2][3].

There are two main categories of accelerators that are currently used for proton therapy, synchrotrons and cyclotrons, which can accelerate protons up to energies of 230-250 MeV. With the Superconducting technology developed, a superconducting isochronous cyclotron is the best choice for it has great advantages of compactness and economy, saving costs for construction and operation.

For isochronous cyclotrons with fixed RF frequency, the field isochronism is important, which means the azimuthal average magnetic field should be increased to keep the same gyration frequency of the accelerating beam when the beam energy changes. What is more, the axial beam tune due to the field changes is also important and difficult to avoid the axial instabilities, especially the vertical tune is very low. The sectors should be shaped with a suitable geometry which can meet both the two requirements. It is an iterative procedure by matching the sector angle width and the spiral angle to find the shape of the magnet that provides the required magnetic field.

A 250 MeV isochronous superconducting cyclotron (SCC-250) was proposed in HUST for the purpose of proton therapy [4]. This paper mainly focused on the superconducting magnet design ignoring the central region design, including the spiral magnet, isochronous field, and tune optimization. Some special extraction considerations in the demonstrated model are discussed. The main parameters and some features of the machine are presented.

OVERALL DESIGN OF THE MAGNET

A fourfold symmetric compact magnetic structure has been chosen to produce the required azimuthal varying magnetic field. The superconducting coils can product much higher magnetic field and the magnet radius can be much smaller. It is not difficult to reach 4-5 T, but this will make extraction design more challenging due to a smaller accelerated turn separation. Meanwhile, the formation of the isochronous field using a flat pole gap becomes challenging. In our case, the maximum magnetic field flux intensity is about 3.9 T, with the azimuthal average field 3.1 T.

Based on the parameters of extraction energy (250 MeV) and the extraction field *Bext*, the other main parameters, like: the pole diameter, injection field, total ampere turns, hill and valley gap can be determined using simple analytical calculation [5], which define the initial layout of the cyclotron magnet.

In order to ensure the axial stability of the beam during acceleration, it is necessary to shape the edges of the sectors as spirals. The matrix method was applied for approximate description of the dynamic of the beam inside the cyclotron to define the initial spiral angle, and the initial maximum spiral angle in the extraction is about 70 degrees.

The design of the yoke is performed taking account of two parameters: 1) the avoidance of saturation in the yoke; 2) the fringing field shape near the cyclotron. A value of the yoke radius $Ryoke = 2 \cdot Rpole$ should be a conservative choice. Based on the considerations above, the main parameters of the magnet can be determined and are listed in Table 1. Based on the parameters in Table 1, the 1/4 magnet model simulated by TOSCA [6] is shown in Figure 1.

* Work supported by National Natural Science Foundation of China, with grant No.11375068.
† D201377354@hust.edu.cn

ISBN 978-3-95450-167-0

Table 1: Main Parameters of the Magnet

Design parameter	Value
Extraction energy	250 MeV
Injection field	2.4 T
Extraction field	3.1 T
Spiral angle (maximum)	66 degrees
Pole gap at hill	5 cm
Valley gap	64 cm
Pole radius	84 cm

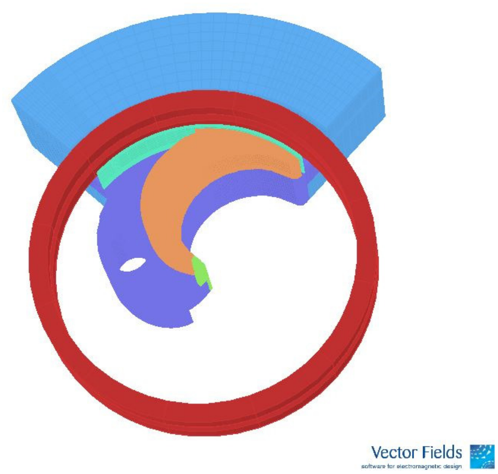

Figure 1: 1/4 model of the magnet in OPERA-3D.

MAGNETIC FIELD DESIGN METHOD

The magnetic field in the acceleration region has to guide the protons on isochronous trajectories and provide the required focusing in order to maintain good internal beam characteristics. These two properties are the result of two effects: 1) The spatial field variations due to the shape of four spiral sectors; 2) the positive radial gradient for the isochronous field is obtained by increasing the angular span of the sectors. The corresponding optimal magnetic field was achieved by shaping the sector geometry according to the two effects.

Magnet Design Process

From the analytical approach we have designed the preliminary model of the machine, assuming the width angle of the sectors to be constant along the radius. Once the dimensions of the structure were fixed, the simulations with 3D code (TOSCA) were carried out, to refine the magnetic field. The sector width and the spiral angle are the two main variables in the model to optimize the magnetic field design and the optimization process is shown in Figure 2. The hill-edge points with the radial step being 2.5 cm are parameterized to modify the sector width and spiral angle in the TOSCA model during the optimization process.

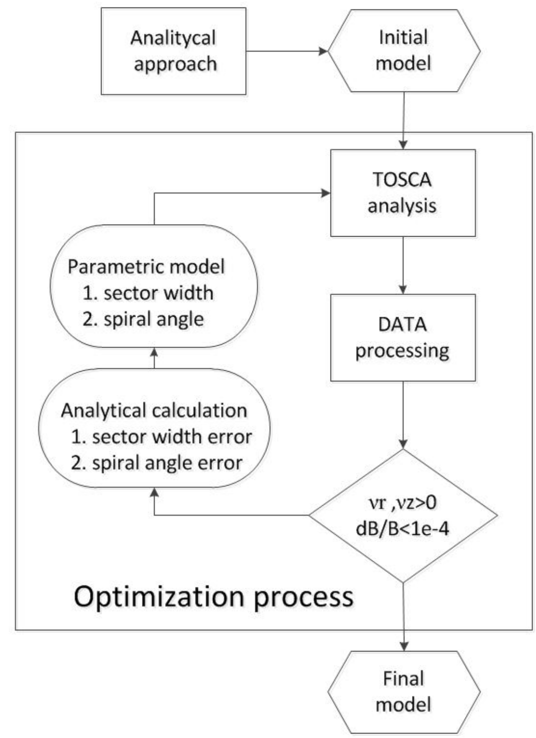

Figure 2: Magnetic field design optimization.

Field Isochronism

For a given magnetic field distribution in the mid-plane, one can compute the gyration frequency $f_p(r)$ of the particles as a function of the pole radius r either from simulated field maps or measured data. $f_p(r)$ can be calculated with equilibrium orbit codes which are based on the numerical integration on particle motion16. Then the isochronous field error $\Delta B(r)$ can be evaluated with Eq. (1) [7].

$$\Delta B(r) = B(r) - B_{iso}(r) = B_{iso}(r)\gamma^2(r)\Delta f(r) = B(r)\frac{\gamma^2(r)\Delta f(r)}{1+\gamma^2(r)\Delta f(r)} \quad (1)$$

Where $B_{iso}(r)$ is the ideal isochronous field at radius r; $B(r)$ is the calculated or measured azimuthal average field at radius r; $\gamma(r) = 1+ E\mathrm{k}(r)/E0$; $\Delta f(r)$ is the gyration frequency error defined by $\Delta f(r) \equiv (fp(r) - f0)/f0$ and $f0$ is the designed ion orbital frequency. For transforming the calculated isochronous field error $\Delta B(r)$ to the sector shape change$\Delta\theta(r)$,the hard edge approximation method[7] was adopt to calculate the sector width error, while maintaining convergence of the field isochronism.

$$\Delta\theta(r) \approx \frac{\Delta B(r)(2\pi/N)}{B_H(r) - B_V(r)} \quad (2)$$

Tune Optimization

Beyond the requirement of isochronism condition, the magnetic field distribution of compact cyclotrons should provide sufficient transversal focusing of the beam, as well as avoid dangerous resonance crossing during beam acceleration, or at least pass through quickly.

ISBN 978-3-95450-167-0

The horizontal tune ν_r and vertical tune ν_z of beam depend on multiple parameters of the magnet, which can be approximately expressed by Eq. (3) and Eq. (4) [7].

$$\nu_r^2 = 1 + k + \frac{3N^2}{\left(N^2-1\right)\left(N^2-4\right)} F\left(1+\tan^2\zeta\right) \tag{3}$$

$$\nu_z^2 = -k + \frac{N^2}{\left(N^2-1\right)} F\left(1+2\tan^2\zeta\right) \tag{4}$$

where $k = \frac{r}{\overline{B}} \cdot \frac{\partial \overline{B}}{\partial r}$ is the radial field index; $B(r)$ is the azimuthal average field at radius r; ξ is the spiral angle; $F = \left(\overline{B^2} - \overline{B}^2\right) / \overline{B}^2$ is the field flutter which represents the azimuthal variation of the magnetic field, is very small with value less than 0.1 due to the highly saturated iron pole. Since $k > 0$ for the condition of field isochronism, the spiral angle of the magnet pole has to be introduced to compensate $-k$. So, the spiral angle should be modulated along the radius and we can calculate the required spiral angle with Eq. (4) during the tune optimization.

THE MAGNET DESIGN RESULT

The main considerations and methods in the superconducting cyclotron magnet design have been introduced. A good agreement between the isochronous field and the average field was achieved without the help of any correction system (trim coils or trim rods). Just with sector shaping and some shims in the extraction, we can get the fine magnetic field.

Figure 3 shows the average magnetic field in the TOSCA model after sectors shaping. The maximum spiral angle is 66◦ and the maximum sector width angle is 45◦ after shaped. Finally, 0.05% local field error and ±20◦ total phase slip during the main acceleration region was achieved as shown in Figure 4. As shown in Figure 5, a well-controlled tune shift was obtained and the $\nu_r = 1$ resonance crossing happened at the energy of 248.4 MeV.

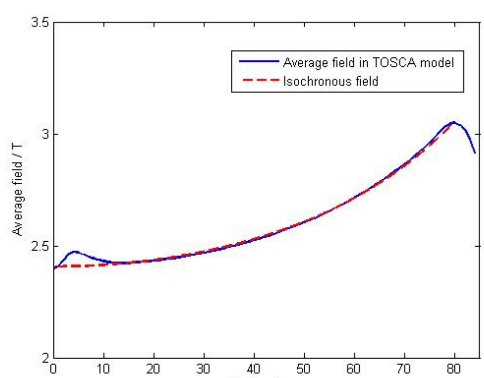

Figure 3: The average magnetic field in TOSCA model after sectors shaping.

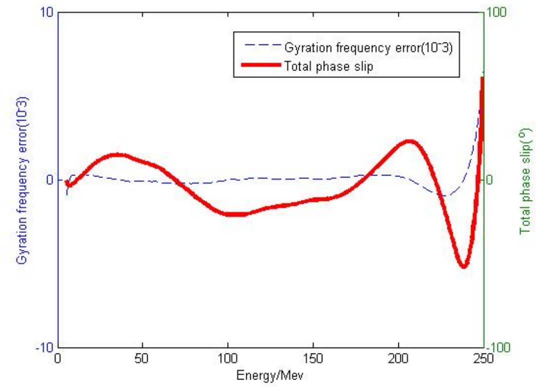

Figure 4: The final gyration frequency and the total phase slip with the change of energy.

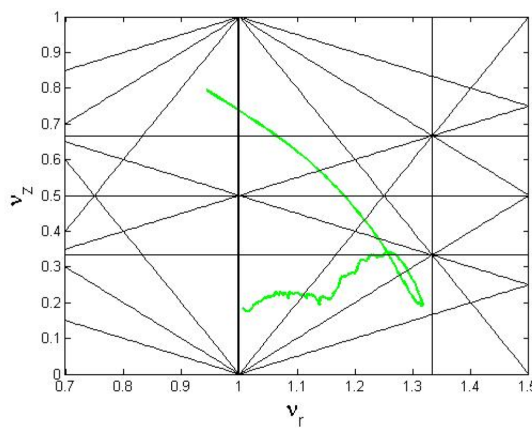

Figure 5: Tune diagram during acceleration.

REFERENCES

[1] Alfred R. Smith, "Present Status and Future Developments in Proton Therapy", *AIP Conf. Proc.* 1153, 426 (2009).

[2] C. Baumgarten, A. Geisler and U. Klein, *et al.*, "Isochronism of the ACCEL 250 MeV Medical Proton Cyclotron", *Nucl. Instr. Meth. A*, vol. 570, no. 1, pp. 10-14, Jan. 2007.

[3] Liu Shiyao, "The Proton and Heavy Ions Therapy and Its Facilities," ISBN, 978-7-03-033532-6, *Science Press*, Beijing, 2012.

[4] B. Qin *et al.*, "Design Study of a 250 Mev Superconducting Isochronous Cyclotron for Proton Therapy", *12th Symposium on Accelerator Physics*, Lanzhou, Aug. 2014.

[5] Y. Jongen and S. Zaremba, "Cyclotron Magnet Calculations, CERN, CERN 96-02, pp. 139-151.

[6] Opera-3D User Guide, Vector Fields Limited, England.

[7] B. Qin *et al.*, "Precise Isochronous Field Shimming Using Correlation Matrix for Compact Cyclotrons", *Nucl. Instr. Meth. A*, vol. 691, no. 1, pp. 129-134, Nov. 2012.

ISBN 978-3-95450-167-0

MAGNET OPTIMIZATION AND BEAM DYNAMIC CALCULATION OF THE 18 MeV CYCLOTRON BY TOSCA AND CYCLONE CODES

N. Rahimpour Kalkhoran, M. Afkhami Karaei, H. Afarideh, S. Sabounchi,
Amirkabir University of Technology, Tehran, Iran
Mitra Ghergherehchi, SKKU University, Suwon, Korea

Abstract

Designing and manufacturing of the 18 MeV cyclotron has been started for producing H^- for applications in Positron Emission Tomography (PET) radioisotopes at Amirkabir University Of Technology. Up to this point, there were 2 steps in magnet design: Initial design and optimization processes. The AVF structure with hill and valley was selected for getting strong axial focusing in magnet design and achieving up to 18 MeV energy for the particle. After finishing the initial design, optimization process in magnet design was started for achieving the best coincidence in magnetic field.

Checking the beam dynamic of the particle is one of the most important and necessary steps after magnet simulation. The phenomenon which confirms simulated magnet validity is obtaining reasonable particle trajectory. This paper focused on the optimization process in magnet design and simulation of the beam dynamic. Some results which ensure a particle can be accelerated up to 18 MeV energy, are presented. All magnetic field calculation in whole magnet was calculated by OPERA-3D (TOSCA) code. Also beam dynamic analysis by applying magnetic field data from the magnet simulation was done in CYCLONE code.

INTRODUCTION

The 18 MeV cyclotron magnet was designed with CST code and the STP file was uploaded in TOSCA code [1]. So all magnet calculations were done in TOSC code. The material of the magnet was considered steel-1010. The magnetic field curve versus radius before applying optimization process is shown in Fig. 1.

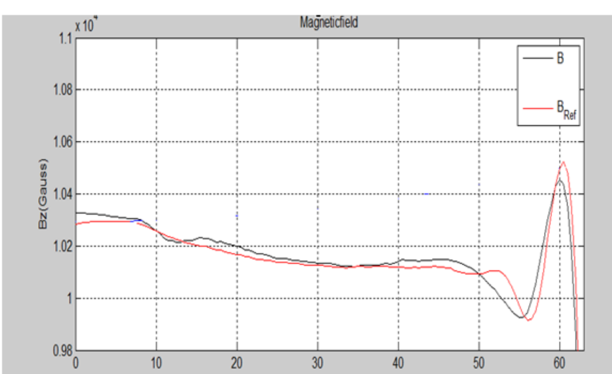

Figure 1: Average magnetic field versus radius before optimization process.

As shown in Fig. 1, B_{ref} (red curve) is the ideal magnetic field and the black one is the simulated magnetic field. Before applying the optimization method, there is not acceptable coincidence between two curves. So optimization process was started.

OPTIMIZATION METHODS

In magnet design, there are some methods which can be used for achieving best results. The methods which were used in optimization process are changing ampere-turn up to 58000, decreasing the gap between poles as a function of radius and shimming of pole edges [2].

Shimming of Pole Edges

At first, in initial design, horizontal shimming was used. In this way achievement to best result in magnetic field was difficult. So in the optimization process shimming of pole edges was changed to vertical form. In vertical shape, some of the pole points were selected and their heights were changed. Also triangle magnet shapes were added the end of the poles for increasing magnetic field at the end of the curve.

Figure 2 shows all used shimming methods in magnet design.

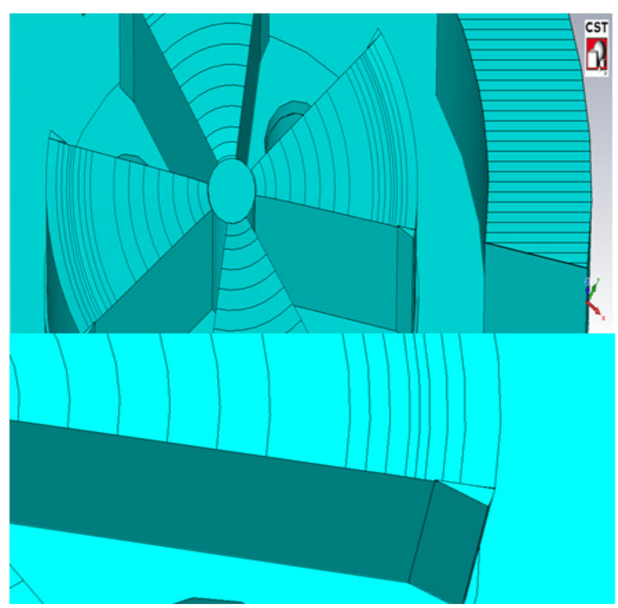

Figure 2: Shimming of pole edges.

ISBN 978-3-95450-167-0

AVERAGE MAGNETIC FIELD

After the using upper methods several times, the curve of magnetic filed versus radius was achieved same as the Fig. 3.

As shown, there is a reasonable coincidence between the ideal magnetic field and simulated value. Also, there is a magnetic filed initial increment at the fist of the curve, because that is necessary for vertical focusing on particle motion [3].

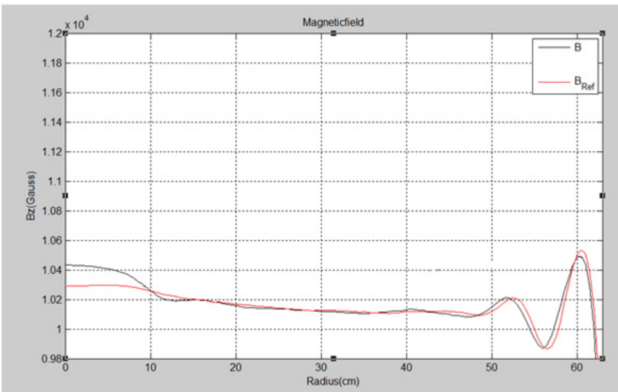

Figure 3: Average magnetic field versus radius after optimization process.

CHECKING THE MAGNETIC FIELD IN MIDDLE PLANE

After magnet simulation, some results should be checked. One of them is the contribution of magnetic field in middle plane. Maximum magnetic field in middle plane, where particle accelerates on it should not be more than saturation point of the magnet material. Figure 4 shows the magnetic field on middle plane.

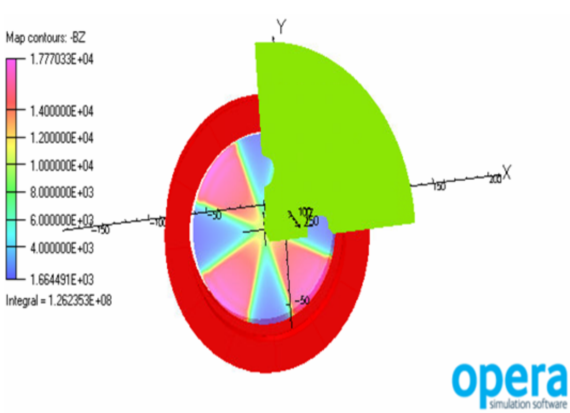

Figure 4: Magnetic field on middle plane.

As shown in Fig. 4, maximum magnetic field on middle plane is 1.77 Tesla is less than the saturation point of the magnet material (1.85 Tesla).

BETATRON OSCILLATIONS

In cyclotron motion (special in final orbits) some oscillations in vertical and horizontal direction occur. These are Betatron oscillations. Because of particle motion sensitivity in final tracks, all these oscillations should be checked. Betatron oscillations factors in tow direction are achieved by following equations:

$$\upsilon_z^{\,2} = 1 - \gamma^2 + \frac{N^2}{N^2 - 1} F \tag{1}$$

$$\upsilon_r^{\,2} = \gamma^2 + \frac{3N^2}{(N^2 - 1)\times(N^2 - 4)} F \tag{2}$$

For increasing particle stability in cyclotron motion, vertical oscillation factor should not be negative and the horizontal (or radial) value should not be less than one.

Figure 5 shows the calculated Betatron oscillation factors, As shown, they are in an acceptable range [4].

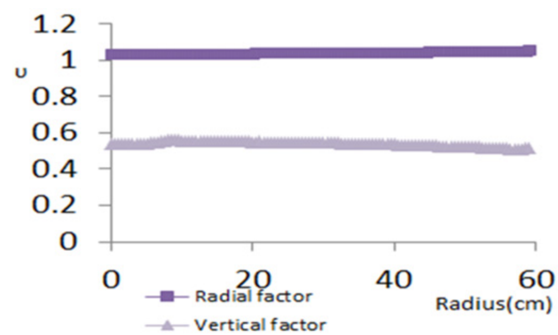

Figure 5: Betatron oscillation factors.

Finally the magnet optimization process was completed and a magnet was designed for 18 MeV energy with properties which are presented in Table 1.

Table 1: Designed Magnet Properties

Parameter	Value
Total radius	122 cm
Total height	129 cm
RF frequency	64.3 MHz
Hill angle	46
Valley angle	44
Pole gap	3.2 -6.68 cm
Coil dimensions	20 *22 cm
Number of amp-Turn	58000

ISBN 978-3-95450-167-0

BEAM DYNAMIC CALCULATION

After magnet simulation, the initial beam dynamic calculation was started until ensures that particle can accelerate up to 18MeV energy by magnetic field of the magnet. So for beam dynamic calculation, all magnetic field data from TOSCA code imported to CYCLONE code [5]. Then by changing the initial condition of particle same as Teta, energy, position, phase, the reasonable results were achieved.

Figure 6 shows the horizontal motion of particle in the middle plane of the cyclotron.

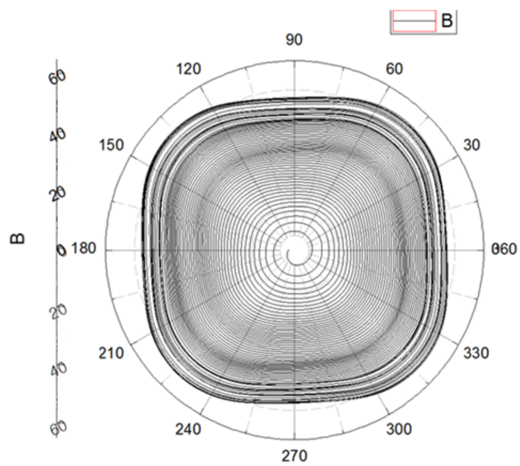

Figure 6: Horizontal motion of particle in middle plane.

As shown, a particle can accelerate in acceptable trajectory in the middle plane of the cyclotron with initial phase 38.027, initial energy 0.020 MeV and initial Teta 92.

Also, kinetic energy curve versus the number of turns are shown in Fig. 7.

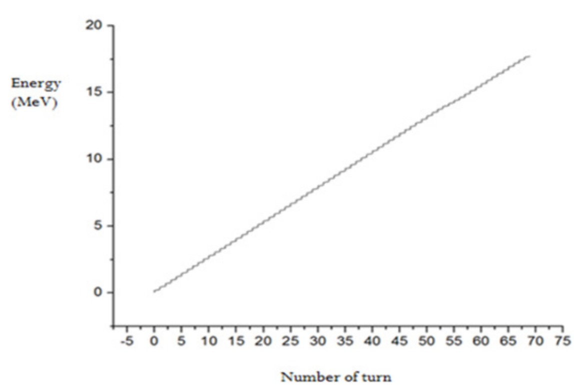

Figure 7: Kinetic energy versus number of turns.

As shown in Fig. 7, a particle can get 18 MeV energy in 70 turns.

CONCLUSION

Magnet optimization process and initial beam dynamic calculation of the 18 MeV cyclotron were presented. About magnet design, detail changes of magnet designing same as shimming was explained. The results of magnet design include magnetic field curve, contribution of magnetic field on middle plane and Betatron oscillations were checked. Then, with importing the magnetic field data from TOSCA code to CYCLONE some beam dynamic calculations were done and particle trajectory and kinetic energy were checked.

In future, by designing central region of 18 MeV cyclotron, beam dynamic calculations and results will be improved.

REFERENCES

[1] OPERA-3D (TOSCA) User Guide, 2012.

[2] R. Solhjou Masouleh, H. Afarideh and B. Mahdian, “Improvement in Design of 10 MeV AVF Cyclotron Magnet”, in *Proc. 20th Int. Conf. on Cyclotrons and their Applications (Cyclotrons’13)*, Vancouver, Canada, 2013, pp. 233-235

[3] S. Zaremba, “Magnet for cyclotrons”, CERN, Geneva, Switzerland, Rep. CERN-2006-012, 2006.

[4] N. Rahimpour Kalkhoran, H. Afarideh and R.Solhju, “Improvement Of 18 MeV Cyclotron Magnet Design By TOSCA Code”, in *Proc. 7th Int. Particle Accelerator Conf. (IPAC’16)*, Busan, Korea, 2016, pp. 1397-1399.

[5] B.F. Milton, “Cyclone 8.4 User Manual”, TRIUMF, Vancouver, Canada, Design Note TTRI-DN-99-4-1999, Jun. 1999.

ISBN 978-3-95450-167-0

EQUIVALENT CIRCUIT MODEL OF CYCLOTRON RF SYSTEM

M. Mohamadian, H. Afarideh, M. Salehi, S. Sabounchi,
Amirkabir University of Technology, Tehran, Iran
Mitra Ghergherehchi, SKKU University, Suwon, Korea

Abstract

Cyclotron cavity modelled via electromagnetic circuits in the desired frequency. The design performed according to resonator basis and also cyclotron acceleration requirements with ADS software and compared to simulations made by the CST microwave studio. The scattering parameters obtained for main resonators of the cyclotron and Dee parts as a diaphragm for each of cavity sections and also for the whole structure. All the characteristics modelled and calculated by the electromagnetic rules and theory of resonators from circuit model. Then it analysed with numerical methods for benchmarking. Finally, it shows that the circuit model able to modelled accurately the cyclotron cavity and especially it can estimate precisely the structure parameters without any time consuming numerical method simulations.

INTRODUCTION

A particle accelerator is a machine that uses electromagnetic fields to propel charged particles to nearly light speed and to contain them in well-defined beams [1]. One kind of accelerators is oscillating field accelerators, which use radio frequency electromagnetic fields to accelerate particles, and circumvent the breakdown problem. Also circular accelerators partition to several types such as; Cyclotrons, Synchrocyclotrons and isochronous cyclotrons, Betatrons and etc. [2].

Cyclotron which is our discussion about, are accelerators in which particles are propelled in spiral paths by the use of a constant magnetic field. This accelerator was invented for the first time by Ernest O. Lawrence in 1932 [3]. The cyclotron was one of the earliest types of particle accelerators, and is still used as the first stage of some large multi-stage particle accelerators. It makes use of the magnetic force on a moving charge to bend moving charges in a semicircular path between accelerations by an applied electric field. The applied electric field accelerates electrons between the "Dees" of the magnetic field region. The field is reversed at the cyclotron frequency to accelerate the electrons back across the gap [4]. One of the main parts of the cyclotron is the RF cavity. In this paper we have proposed the circuit model to consider the cyclotron RF cavity response to analyze its behavior in resonance frequency.

CYCLOTRON ACCELERATORS

The cyclotron principle involves using an electric field to accelerate charged particles across a gap between two "D-shaped" magnetic field regions. The magnetic field accelerates the particles in a semicircle, during which time the electric field is reversed in polarity to accelerate the charge particle again as it moves across the gap in the opposite direction. In this way a moderate electric field can accelerate charges to a higher energy [4]. Cyclotron includes some different sections that is illustrated in block diagram of Fig. 1 which the RF cavity is one of the main parts.

RF CAVITY STRUCTURE

With regard to the overall structure of the cyclotron accelerators been described above, its different parts are illustrated in Fig. 2. The main part of such a device is a resonator which provides resonance at considered frequency. Resonator structures are different. The oscillations in a resonator can be either electromagnetic or mechanical [5]. In the cyclotron accelerator, the cavity resonator is used. Due to the low resistance of their conductive walls, cavity resonators have very high quality factors; that is their bandwidth is very narrow. Thus, they can act as narrow band-pass filters [5]. The different cavity designs are depending on the specifications and geometric layout of a cyclotron [6].

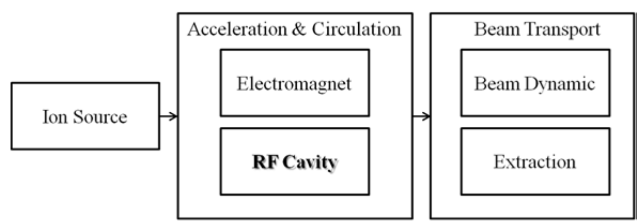

Figure 1: Brief block diagram of the cyclotron accelerator.

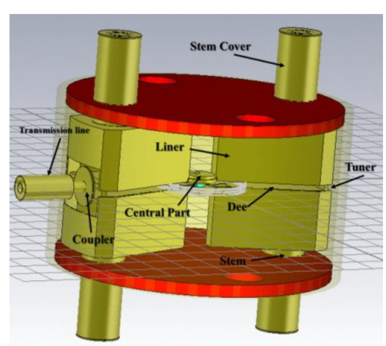

Figure 2: Overall structure of the RF cavity.

Therefore, a coaxial resonator in fixed frequency, double gap and superconducting can be suitable for this application. But as mentioned, the cyclotron, because of the conditions governing the charged particle rotation, requires a region in the center of the resonator to get energy to the particles through an electric field. As a result, in the center, it has to be a horizontal plate, called Dees, with a certain angle that generate the electric field, between the

ISBN 978-3-95450-167-0

coaxial inner core and its outer shell which gives the required energy to the particle in each round of rotation. As it will express in past section, this part is in the form of the D-shape generally, for two accelerating gap design or in the form of triangular plates to have four accelerating gap. So to have the coaxial structure, the outer shell of this part of the transmission line is also triangular shape.

As a result, the appropriate resonator for such a system is composed of a cylindrical coaxial plus a roughly triangular shape coaxial which become short-circuit at the end (Fig. 3). Thus, in such state, in the resonance frequency, the impedance of coaxial TEM waveguide as resonator will be infinity because of creating the open-circuit on the other end, which physically will connected with Dees and so, the wave transmit completely. Also, in the other frequencies, the resonator attenuates the transmitted wave. Generally, it performs like a band-pass filter at the resonance frequency. Therefore, the resonator is modeled with two transmission lines that have different length, characteristic impedance and phase constant.

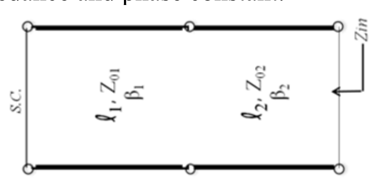

Figure 3: short circuit λ/4 transmission line, Equivalent Transmission Line.

EQUIVALENT CIRCUIT MODEL

The dimension of the resonator including, the quarter wavelength transmission line, calculate in some steps. At first, the phase constant of both cylindrical and triangular transmission line calculated separately. With simple calculation can be shown that the phase constant of both structures are the same as free space phase constant. So the overall structure length of these two parts will be equal to designed coaxial structure length. It means that, in designing the quarter wavelength transmission line, just the sum of the cylindrical and the triangular coaxial length will be important and not each of them alone. Therefore the height of each of these parts related to other considerations of manufacturing, including location of magnets and mechanical implement remarks.

Hence, in overall, resonator is a short circuit transmission line which its input impedance calculate by Zin=j Z0 tan(βl). As it can be shown at circuit model, there is two resonance points which is repeated frequently. These resonances occur in infinity and short circuit impedances which can be modeled with parallel and series LC circuit respectively. Since our resonance point is near the open circuit impedance. So we used parallel LC equivalent circuit. The part called Dees are attached to the inner conductor of coaxial. The Dees are triangular shape as it explained previously. The electric field patterns for a TEM wave are sketched in Fig. 4.

In addition, since we are going to design IranCYC10, our desired structure as discussed in [7] works on fourth harmonic and so the angle of the triangular part obtain approximately via $\theta_{dee} = \frac{180}{h} = \frac{180}{4} = 45$. Where θ_{dee} is the angle of Dee part and h is harmonic number [7].

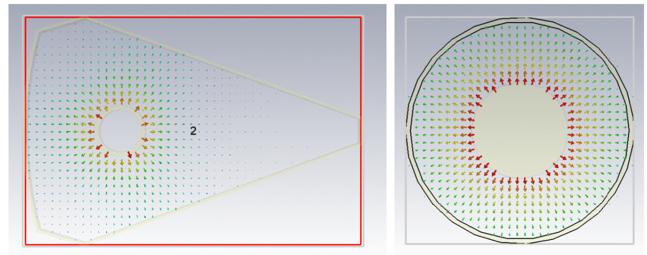

a b

Figure 4: Electric field pattern of between diaphragm and Liner a) Triangular and b) cylindrical section.

For analysing the circuit model of the coaxial resonator, if the region between electrodes is a vacuum, TEM waves propagate with ω/k =c. Therefore, the line has a capacitance C and inductance L per unit length given by $\mathrm{C} = \frac{2\pi\varepsilon}{\mathrm{Ln}\left(\frac{\mathrm{R_0}}{\mathrm{R_i}}\right)}\left(\frac{\mathrm{F}}{\mathrm{m}}\right)$ and $\mathrm{L} = \left(\frac{\mu}{2\pi}\right)\mathrm{Ln}\left(\frac{\mathrm{R_0}}{\mathrm{R_i}}\right)\left(\frac{\mathrm{H}}{\mathrm{m}}\right)$ for cylindrical coaxial lines. But in the overall structure, these relations can't be applied.

Another case that distinguishes this designed resonator from conventional one is the necessity of the Dee part of this structure which discussed about it earlier. This part in resonator works such as a diaphragm in a waveguide. We considered the effects of the diaphragm structures in the triangular transmission line. According to electromagnetic consideration, TEM mode waves propagate inside the coaxial waveguide which at the diaphragm part has a capacitance effect between it and the outer conductor in both sides and inductance effect because of junction of the diaphragm with the inner conductor of coaxial line [8]. The magnetic fields are almost identical to those of the standard transmission line except for field exclusion from the Dees.

$$|S12|^2 = \frac{4}{4+\frac{Z_0^2}{(C\omega-\frac{1}{L\omega})^2}} = \frac{1}{2} \rightarrow \Delta\omega = BW. = \frac{2}{Z_0.C} \tag{1}$$

$$\rightarrow \mathrm{C}=\frac{2}{Z_0 * BW.},\ \mathrm{L}=\frac{1}{4\pi^2 {f_r}^2 C} \rightarrow \text{parallel LC}$$

$$|S12|^2 = \frac{4}{4+\frac{Z_0^2}{(L\omega-\frac{1}{C\omega})^2}} = \frac{1}{2} \rightarrow \Delta\omega = BW. = \frac{Z_0}{2L} \rightarrow \tag{2}$$

$$\mathrm{L}=\frac{Z_0}{2 * BW.},\ \mathrm{C}=\frac{1}{4\pi^2 {f_r}^2 L} \rightarrow \text{Series LC}$$

In contrast, radial electric fields cannot penetrate into the region between Dees. The electric fields are restricted to the region between the outer conductor and the Dees. In fact, in such a model, take the junction between to Dees in half section of overall structure into account.

Furthermore, the diaphragm modeled in CST and its scattering parameters versus frequency has demonstrated in Fig. 5.

ISBN 978-3-95450-167-0

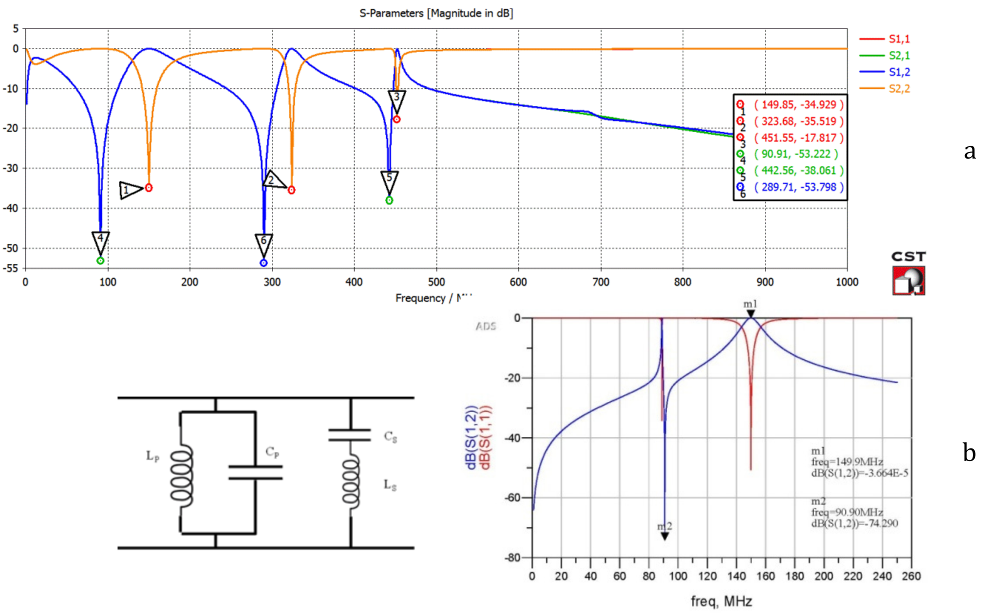

Figure 5: Scattering parameter of diaphragm consideration, a) Scattering parameters b) equivalent microwave circuit model.

It indicates several resonances which some of them are band-pass and another one is band-stop which show diaphragm behavior in this frequency interval as a parallel LC and series LC respectively. So the proper circuit model of this portion as examined with CST simulation will be an LC in the series and another LC in parallel which connected to each other.

RESULTS AND CONCLUSION

According to discussion previously, resonator itself works as a transmission line band pass filter and diaphragm acts as two LC circuit in series and parallel. So as it can be seen, diaphragm causes a notch in transmission power versus frequency in the higher than the resonance frequency of the resonator. So it should keep away from the resonance frequency sufficiently. Therefore, if relation of diaphragm's L and C parameters to be $L\omega<1/C\omega$, because of the inductive effect on the resonator, it decreases the resonance frequency of the total structure, and so if $L\omega>1/C\omega$ because of the capacitive effect on the resonator, it increases the resonance frequency. Ofcource, it also illustrates that the diaphragm makes better quality factor and decreases the resonance frequency. It could be tuned again via changing the resonator dimension. So in the final design includes the four similar resonators with a diaphragm which locate symmetrically in top and down of electron beam revolution path and in the left and right sides. In the equivalent circuit, these parts are parallel with each other. The circuit model demonstrates that the combination of all four sections makes the better quality factor.

According to previous section discussions, resonator, diaphragm and couplers are simulated in CST software. Here should be the structure's scattering matrix to take the effect of the resonator and the diaphragm to consideration. The phase of scattering parameter S11 of this short circuit line and its characteristic impedance in our desired resonance frequency in IranCYC10 which is at 71 MHz, has obtained. As a result of this simulation, the equivalent transmission line length or βl value will be -19.15 and -21.91 at the resonance frequency for cylindrical and triangular coaxial line respectively. So the equivalent capacitance and inductance will be calculated. Consequently, we found an accurate circuit model to design RF cavity which the comparison of the model and CST simulation indicates the acceptable engineering accuracy. So it could lead us to consider such structure with microwave circuit model to calculate its different parameter values to have appropriate cavity with high quality factor without any time consuming simulation.

REFERENCES

[1] C.R. Nave, Cyclotron, Hyperphysics. Dept. of Phy. and Ast., Georgia State University, 2014.

[2] M.S. Livingston, J. Blewett, Particle Accelerators, New York: McGraw-Hill, 1969.

[3] *Handbook of Accelerator Physics and Engineering (2nd Ed.)*, A.W. Chao, K.H. Mess, M. Tigner, and F. Zimmermann, Eds. World Scientific Press, May 2013.

[4] E.O. Lawrence, "Method and apparatus for the acceleration of ions", US patent 1948384, 1934.

[5] D.M. Pozar, *Microwave Engineering*, John Wiley & Sons, 2011.

[6] S.K. Jain, D. Sharma, V.K. Senecha, P.A. Naik and P.R. Hannurkar, "Study of microwave components for an electron cyclotron resonance source: Simulations and performance", Sadhana 39, Part 4, 2014, pp. 901–909.

[7] M. Mohamadian, H. Afarideh, M. Salehi, J.-S. Chai, M. Ghergherehchi, "Development of Optimized RF Cavity in 10 MeV Cyclotron", in *Proc. 7th Int. Particle Accelerator Conf.*, Busan, Korea, May 2016, pp. 1250-1252, doi:10.18429/JACoW-IPAC2016-TUPMR011

[8] T. Dong, L. Zhan, Y. Hong, M. Fan, "Cyclotron cavity analysis based on field circuit model", *Nucl. Inst. and Meth. in Phys. Research*, A 513, 2003, pp. 631–634.

ISBN 978-3-95450-167-0

DESIGN OF THE FAST SCANNING MAGNETS FOR HUST PROTON THERAPY FACILITY*

Xu Liu†, Bin Qin, Kaifeng Liu, Wei Chen, Zhikai Liang, Qushan Chen
Institute of Applied Electromagnetic Engineering
Huazhong University of Science and Technology, Wuhan 430074, Hubei, China

Abstract

For implementation of proton therapy, Huazhong University of Science and Technology has planned to construct a 250 MeV/500 nA superconducting cyclotron for proton therapy. In the beam-line, the scanning system spreads out the proton beam on the target according to the complex tumor shape by two magnets for horizontal and vertical scanning independently. As dipole magnets are excited by alternating currents and the maximum repetition rate is up to 100 Hz, the eddy currents are expected to be large. This paper introduces the design of these two scanning magnets and analyzes the eddy current effect. Slits in the end pole are proven to be an effective way to reduce the eddy current. Different directions, distributions and width sizes of slits are simulated and compared to determine the slits arrangement. At last, the maximum temperature of the optimized scanning magnets reaches the temperature requirements.

INTRODUCTION

Nowadays, particle therapy becomes a more effective method for radiation cancer treatment than traditional X-rays or gamma rays treatment. Huazhong University of Science and Technology(HUST) has proposed to construct a proton therapy facility based on a superconducting cyclotron in 2014 and this project is founded in 2016 [1]. In this project, we plan to build two rotating gantries and one fixed beam treatment room [2]. The energy of the proton beam ranges from 70 MeV to 250 MeV, corresponding to the range in water from 4 cm to 38 cm, and it can be modulated via the energy selection system(ESS) in the beam-line [3]. For active scanning method, a scanning magnet system is located at the end of beam line and precisely controls the beam position to spread out the proton beam on the tumor target. The scanning range at the iso-center is 30 cm×30 cm.

This paper mainly describes the design of two scanning magnets and analyzes the eddy current effect of AC dipole magnets.

SCANNING MAGNETS

The scanning magnet system is a core component of the active scanning system, which consists of two orthogonal H-type dipole magnets (SMX and SMY). The layout of the rotating gantry is shown in Fig. 1 and the main parameters of these two scanning magnets are list in Table 1 . To achieve the fast beam scanning at the iso-center and decrease the radius and cost of the gantry, the length of SAD(Source to Axis Distance) is 2.8 m. The distances from SMX and SMY to the iso-center are chosen as 2.85 m and 2.37 m. The maximum deflection angle is determined by the maximum magnetic rigidity 2.43 T·m, corresponding to 250 MeV proton beam. In the gantry, SMY is located after SMX, indicating that SMY should have a larger gap and pole width than SMX. According to the simulation of beam trajectory, the gap and pole width of SMX and SMY are determined. As for the power supply, these two dipole magnets are excited by alternating currents and the repetition frequencies are 100 Hz and 40 Hz, determined by the target scanning speed 60 m/s in x direction and 24 m/s in y direction. This requires the maximum current ramping speed to be up to 228 kA/s and the maximum magnetic field gradient to be 208 T/s.

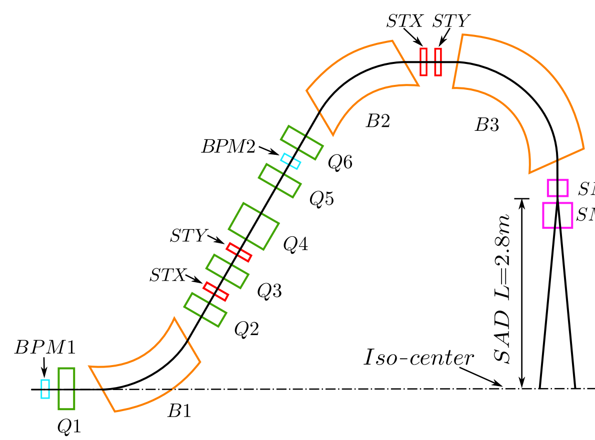

Figure 1: The layout of the rotating gantry and the illustration of the SAD length.

Table 1: Main Parameters of Scanning Magnets

Parameter	Units	SMX	SMY
Max Deflection Angle	mrad	55	65
Magnet Gap	mm	40	90
Magnet Pole Width	mm	90	160
Max Field Strength	T	0.52	0.39
Number of coil turn	Turns/pole	15	18
Coil Inductance	mH/coil	0.3325	0.605
Coil Resistance	mOhm/coil	2.21	2.74
Repetition Frequency	Hz	100	40

* Work supported by Major State Research & Development Program, with grant No. 2016YFC0105305
† lxhustliu@hust.edu.cn

ISBN 978-3-95450-167-0

EDDY CURRENT EFFECT

Origin of Eddy Currents

Eddy current is the major design concern of these AC magnets. Generally, laminated silicon steel sheets for iron core and aluminum stranded wires for the coil conductor are used to reduce the amount of eddy currents and the heat loss. However, the laminated magnets are still not free from the eddy current effect and the temperature rise will destroy the insulation of laminated steel sheets. This requires us do some specific designs for the pole edge.

Simulation Methods and Parameters Setting

To study the eddy current effect in the laminated magnets, we perform the transient electromagnetic simulation in the ELEKTRA Transient program of Opera Vector [4]. By calculating the root mean square value of the loss at different time, the average heat density in a period can be obtained and then imported into the TEMPO Steady State program. The thermal analysis can be carried out and the temperature distribution of the magnet is presented clearly.

In the electromagnetic simulation, the model of dipole magnet consists of the laminated iron core, two stainless steel(SS) end plates and two excitation coils. Coils are excited by sinusoidal alternating current. The laminated iron core is defined as a nonlinear BH curve and the packing factor is 0.98. The SS end plates are set as non-magnetic but conductive.

Simulation Results

The eddy currents are induced in the end laminations of iron core and stainless steel plates, and concentrated in the few centimeters above the magnet gap. Slits in these areas are proven to be an effective method to reduce the eddy current [6]. Due to the higher frequency and magnetic field strength of SMX magnet, the eddy current density will be bigger. That is why the SMX magnet is selected as the research object. To study the effect of slits on the eddy current and temperature rise of the magnet, some different simulations are carried out and compared with each other. To demonstrate the effect of slits, the maximum temperature of the model without sits is 176.8°C and distributed at the corner, as shown in Fig. 2.

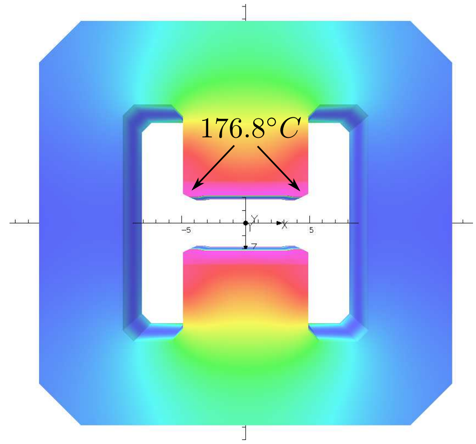

Figure 2: The temperature distribution of the unoptimized SMX magnet. The maximum value concentrates on the pole edge.

Slits direction As we know, the eddy currents in the end plates are formed into circles. The horizontal and vertical slits also can cut the currents into small pieces to reduce the eddy current. Firstly, these two types of slits are simulated individually to determine the optimum direction of slits, as shown in Fig. 3. The solution results show that the vertical slits can reduce the temperature rise of 100°C when compared to the model without slits. However, the horizontal slits cannot reduce the eddy current density, but cause the more concentrated currents at the corner of the magnet. The temperature will be up to 247°C which is higher than the condition without slits. Therefore, the vertical slits are selected.

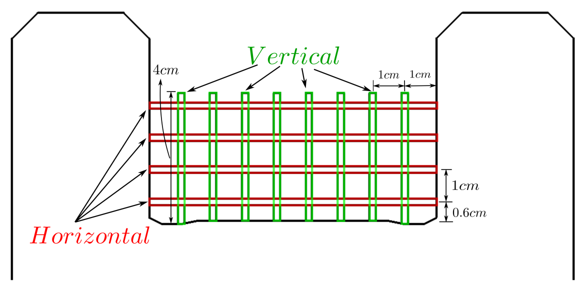

Figure 3: The illustration of slits direction in the pole. The green blocks show the horizontal slits and the red blocks are the vertical slits.

Slits distribution Secondly, three different numbers of vertical slits are compared. All slits are 2 mm wide and symmetrical distributed at intervals of 10 mm. The number of slits is 7, 8, 9, corresponding to the distance between the outermost slit and the pole edge is 15 mm, 10 mm and 5 mm, respectively. The distribution of slits is shown in Fig. 4 and the maximum temperature of the dipole magnet is listed in Table 2. Clearly, the model with eight slits is the better choice than the others. The wide distance can not cut apart the eddy current effectively in the pole edge and the tight distance will concentrate the current and increase the current density.

Table 2: The Relations between Maximum Temperature and Slits Distribution

num_slits	a/mm	b/mm	Max T/°C
7	15	10	72.29
8	10	10	64.16
9	5	10	73.06

Slit width As we know, the slit width determines the processing difficulty of silicon steel sheets. Figure 5 plots the dependence of the magnet's maximum temperature on

ISBN 978-3-95450-167-0

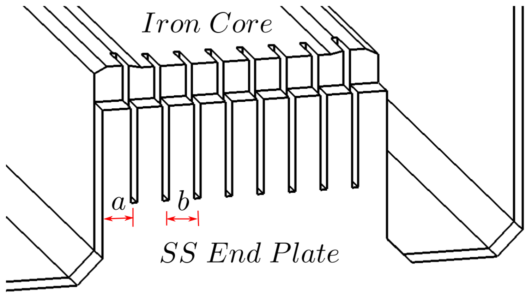

Figure 4: The distribution of slits in the SMX magnet.

the slit width. the temperature rise are not sensitive to the slit width. In order to facilitate the processing, the slit width is designed as 2 mm.

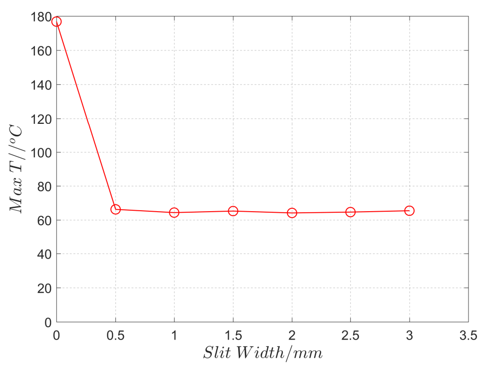

Figure 5: Maximum temperature of the SMX magnet vs. slit width.

From above discussions, the temperature of the SMX model which includes eight slits with 2 mm wide can be reduced to 64.2°C. The temperature distribution of the SMX magnet is shown as Fig. 6.

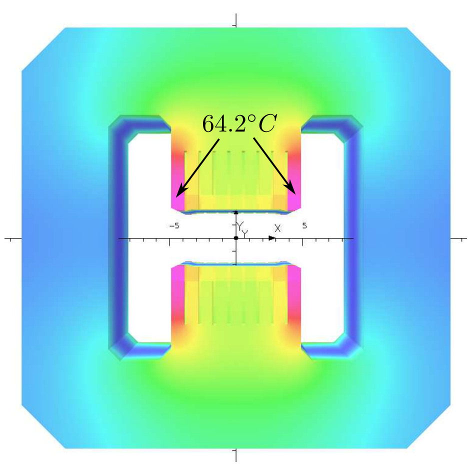

Figure 6: The temperature distribution of the optimized SMX magnet.

SMY Magnet

Eddy currents in the SMY magnet is smaller than the SMX magnet, but the maximum temperature is still up to 123.9°C. This temperature will also destroy the insulation of stainless steel sheet. So eight slits should be added in the end laminations of iron core and SS plates. As a result, the maximum temperature of the optimized SMY magnet is reduced to 43.7°C, lowering the allowance temperature rise.

CONCLUSION

This paper shows the layout of the scanning magnet in the rotating gantry and describes the magnet design of two alternating current dipole magnets. The eddy current effect and the heat loss are serious in the end laminations of iron core and the end stainless steel plates. Slits in these areas are an effective way to reduce the eddy current. Three comparisons are made to determine the arrangement of slits. The temperature of the optimized magnets can reach the allowance temperature rise of the silicon steel sheet. Besides,instead of slits, several water-cooling circuits can also be added in the SS end plates to reduce the temperature rise of the magnet, which requires the thick plates and increases the processing difficulty. The feasibility of this method needs to be validated by later simulations. The proton therapy project is now under design, and more design details will be considered.

REFERENCES

[1] B. Qin, K.F. Liu, D. Li, *et al.*, "Design Study of a 250MeV Superconducting Isochronous Cyclotron for Proton Therapy", in Proc. 12th Symposium on Accelerator Physics (SAP'14), Lanzhou, China, August 2015, paper WEPMH3.

[2] Bin Qin, Kuanjun Fan, Mingwu Fan, *et al.*, "Fast Scanning Beamline Design Applied to Proton Therapy System Based on Superconducting Cyclotrons", presented at the 21th Int. Conf. on Cyclotrons and their Applications (Cyclotrons'16), Zurich, Switzerland, Sep 2016, paper MOP12, this conference.

[3] Zhikai Liang, Wei Chen, Xu Liu, *et al.*, "Fast Energy Selection System Design for Proton Therapy Based on GEANT4 Toolkit", presented at the 21th Int. Conf. on Cyclotrons and their Applications (Cyclotrons'16), Zurich, Switzerland, Sep 2016, paper MOD01, this conference.

[4] Opera-3D reference, `http://www.vectorfields.com`

[5] S. Xian-Jing, D. Chang-Dong, K. Wen, "Transient electromagnetic simulation and thermal analysis of the DC-biased AC quadrupole magnet for CSNS/RCS", *Chinese physics C*, vol. 36, no. 5, p. 443-446, May 2012.

[6] M. Negrazus, D. George, V. Vrankovic, *et al.*, "Eddy current reduction in fast ramped bending magnets", *IEEE Transactions on Applied Superconductivity*, vol. 16, no. 2, p. 228-230, June 2006.

ISBN 978-3-95450-167-0

PHYSICAL DESIGN OF EXTERNAL TWO-STAGE BEAM CHOPPING SYSTEM ON THE TR 24 CYCLOTRON

J. Štursa†, M. Čihák, M. Götz, V. Zach
Nuclear Physics Institute of the CAS, Husinec-Řež 130, CZ 250 68, Czech Republic

Abstract

We briefly introduce a new Cyclotron Laboratory of the Nuclear Physics Institute (NPI) of the Czech Academy of Sciences with the new cyclotron TR 24 which was commissioned in October 2015. One of the planned uses of TR 24 beams is a generation of high-intense fast neutrons fluxes with implementation of a chopping system for spectrometric measurements of neutron energy by the Time-of-Flight (TOF) method. For this purpose, physical design of a new ion-optical beam line was completed as well as comprehensive study of an external fast chopping system on this beam line. A set of home-made programs DtofDeflect has been developed for this system consisting of the first chopper powered by sinusoidal voltage and the second chopper powered by pulse voltage. The programs allow to find the optimum geometric and voltage parameters of the system by the means of mathematical simulations. The chopping system can provide the external 24 MeV proton beam with 2.3 ns pulse length at a repetition period of 236 ns in order to comply with the required pulse length to the repetition period ratio of 1 : 100.

INTRODUCTION

In 2011 it was decided to modernize an experimental basis of the NPI to supplement the original accelerator – isochronous cyclotron U-120M [1] (commissioned in 1977), with a new compact accelerator, which would take over some applications and extend experimental possibilities with its parameters. A good compromise solution between the required new cyclotron parameters (maximum beam energy at maximum beam current) and available funds was the purchase of the cyclotron TR 24 (24 MeV/300 µA) [2] of the Canadian company Advanced Cyclotron Systems, Inc. (ACSI). Research program of the TR 24 will be focused on production of established and novel medical radionuclides (e.g. ^{44}Ti, ^{67}Cu, ^{89}Zr and ^{68}Ga), and to feasibility study of implementing direct production of ^{99m}Tc via (p,2n) reaction as an viable alternative to reactor-produced generator ^{99}Mo/^{99m}Tc. Regarding the long-term experience with generation of fast neutron fields [3] on the cyclotron U-120M, the further important research program will be dedicated to experiments associated with the generation of high fast neutron fluxes. Physical design of the chopping system for spectrometric neutron TOF measurements fulfils one of the potential utilization of the TR 24 beam and defines conditions of its feasibility.

† stursa@ujf.cas.cz

NEW CYCLOTRON LABORATORY

The TR 24 cyclotron forms a core of the new laboratories built instead of a decommissioned (2012) Van de Graaf generator (VdG). The project started in 11/2012 and site acceptance test of the TR 24 was completed in 10/2015.

Figure 1: Old VdG and new cyclotron buildings.

Reconstruction of the VdG building covered design of the cyclotron layout and its shielding within the given ground plan. The cyclotron hall and hall for TOF system are located in the basement, the control room in the first floor above the cyclotron. Due to the space limitations, big care was devoted to minimizing thickness of the ceiling and the walls. Detailed simulations based on the MCNPX code resulted in reducing their thickness to 1.8 and 2.0 m, respectively, including the shapes of cable conduits and ventilation pipes. This solution required precise composition of heavy concrete with the density greater than 3 t/m^3. Effective cyclotron cooling and air-conditioning systems which include also air-conditioning for the radiochemical labs and the 6-floor building were designed so that more than 50% of thermal power produced by the cyclotron can be recuperated and utilized for heating of the building.

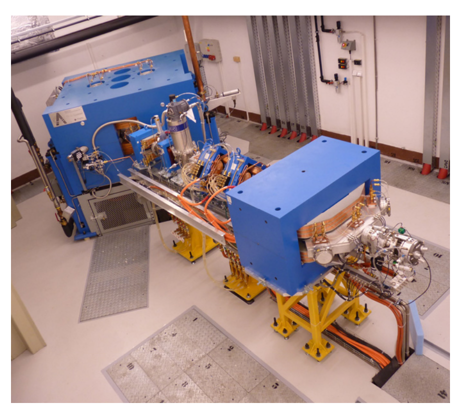

Figure 2: Cyclotron TR 24 with the beam line.

ISBN 978-3-95450-167-0

PHYSICAL DESIGN OF THE EXTERNAL BEAM-CHOPPING SYSTEM

Motivation

Neutron induced reactions play an important role in a wide range of applications including fusion technology – especially in such advanced and safe nuclear-energy concepts like the hybrid fusion-fission nuclear reactor. Due to dependence of technical projects reliability on the correct simulations of neutronic processes, additional measurements of cross-section data are requested (for fast neutrons in particular) for which the neutron source based on TR 24 proton cyclotron will provide neutrons in relevant energy range. Proposed chopping system for neutron facility on TR-24 proton beam is necessary tool for precise measurement of angle/energy-dependent cross-sections by TOF method. Planned facility would be a complementary to other TOF facilities in Europe (GELINA Geel [4], NFS Ganil [5]). Nevertheless, the synergy in research program of all existing facilities is strongly invited due to time and investment consuming character of nuclear data experiments.

Description of Program Utilities

The schematic view of the cyclotron TR-24 with the time structure of beam pulses is shown on Fig. 3.

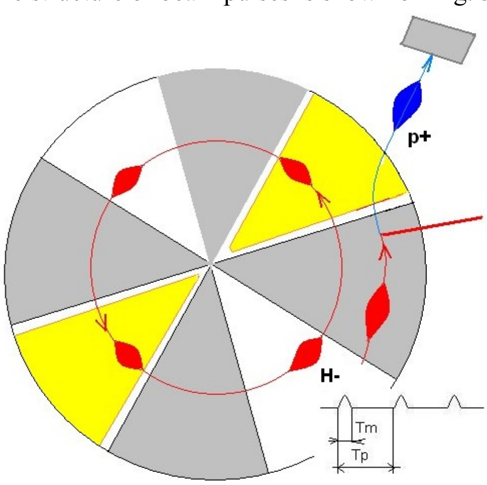

Figure 3: The time structure of the TR 24 beam:

- RF frequency: f_{dees} = 84.75 MHz (4. harmonic),
- width of beam bunches: T_m = 2.3ns,
- period of bunches T_p = 11.8ns,
- the ratio $T_m : T_p = 1 : 5.13$.

For the TOF facility, it is required to reach the ratio $T_m : T_p \sim 1 : 100$. In order to meet these strict requirement and to reach the technical feasibility of the chopping system, two-stage vertical deflection system was chosen as in [6]. The first deflector is powered with sinusoidal voltage and the second one with a pulsed voltage (Fig. 4).

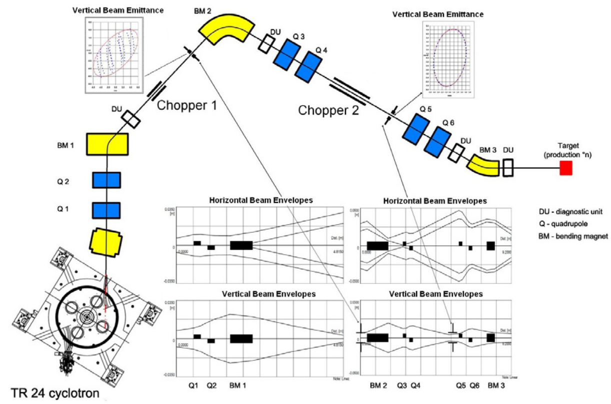

Figure 4: TR-24 external beam shopping system layout.

A mathematical simulation program DtofDeflect was developed for design of the beam chopping system on the TR-24 cyclotron.

This program allows for calculation of extracted beam trajectories when traveling through an electrostatic deflection system. For dynamic calculations, the home-made developed software was used [7]. In interactive mode of the running program, all parameters of the deflection system can be entered (see Fig. 5).

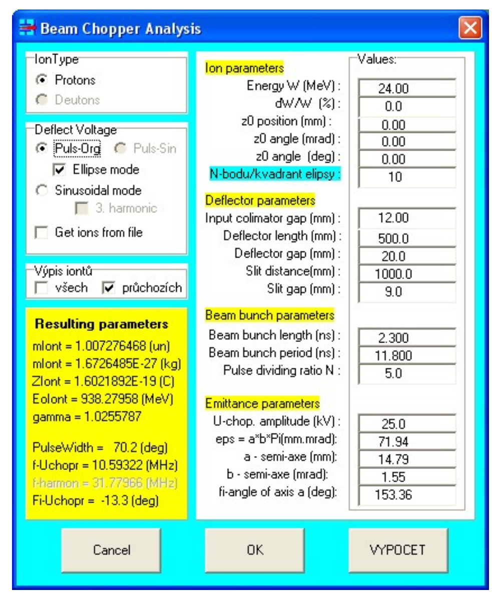

Figure 5: Main dialog window of the DtofDeflect program.

Optimal geometric parameters of the deflection system consisting of two stages are shown in Fig. 6 and Fig. 7.

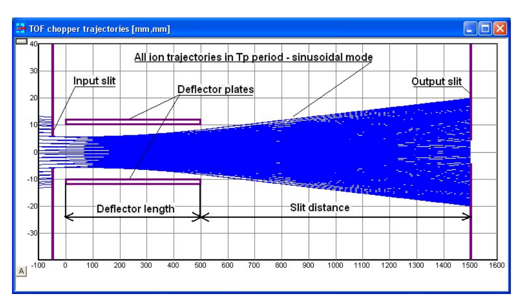

Figure 6: Sinusoidal deflection system arrangement.

ISBN 978-3-95450-167-0

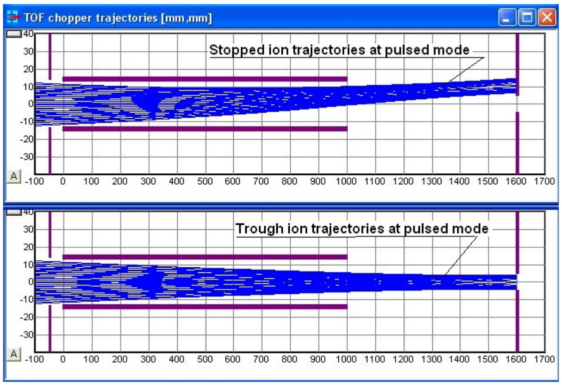

Figure 7: Pulsed deflection system arrangement.

Both deflectors are equipped with input collimators that restrict the undesirable impact of the beam to deflector electrodes and also reduce the output beam emittance. The aim of the thorough calculations was to find an optimal parameters of the ellipse emittance at the deflector entry and further parameters resulting in maximizing beam current through the deflector in selected pulses and minimizing residual beam current going, when beam is deflected to the deflector slit. Time structure of deflection voltage on both choppers is displayed on Fig. 8.

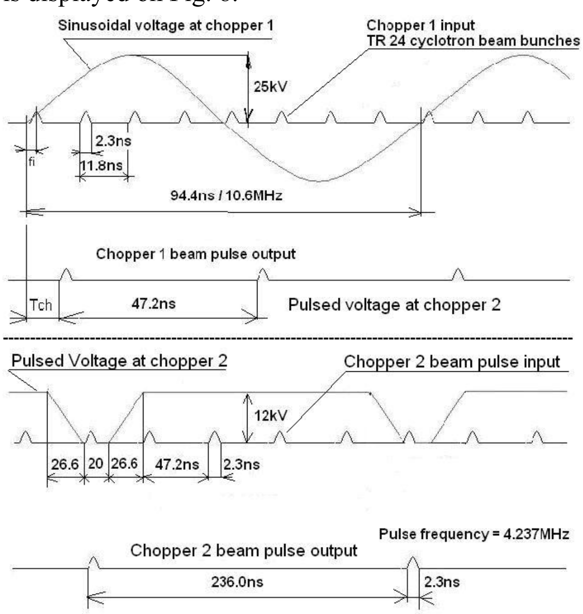

Figure 8: Timing of the deflector voltages on sinusoidal resp. pulsed chopper.

Forming the beam trajectories in the beam line outside the deflectors is carried out by quadrupoles and deflection magnets. Proton beam transport in these parts is solved by means of ion optics. Communication between the dynamic trajectory calculations in the deflection system (Delphi) and beam envelopes in the beam line (AGILE) is provided by conversion of calculated geometric parameters of the beam emittance ellipses to Twiss parameters and vice versa. The influence of a vertical ion velocity component to a horizontal one is negligible in this case. Therefore, the dynamic simulation calculates only the vertical emittance, while ion beam optical calculations provide both vertical and horizontal emittance. For the 24 MeV proton beam extracted from the cyclotron, the vertical emittance 72 mm.mrad resp. horizontal 45 mm.mrad at 95% of the beam intensity were considered [8,9].

Results and Discussion

The three variants (Table 1) that vary in combinations of deflector's voltages and other parameters were analysed. In spite of lower beam transmission, the version III was chosen. Mainly for acceptable parameters of required power supplies and for lower emittance of the selected beam bunches.

Table 1: Comparison of the Three Variants of the Vertical Chopper Arrangement

Sinusoidal chopper 1	I.	II.	III.
Input collimator aperture [mm]	26	26	12
Deflector voltage amplitude [kV]	70.0	40.0	25.0
Deflector plates aperture [mm]	30	26	20
Output slit aperture [mm]	24	12	10
Output slit passing ions [%]	25.0	21.3	15.6
Output slit passing power [W] (for 100μA from cyclotron)	600	510	375
Output beam emittance [mm.rad]	351.86	204.2	90.73
Pulsed chopper 2	**I.**	**II.**	**III.**
Input collimator aperture [mm]	44	40	26
Deflector voltage amplitude [kV]	44.0	22.0	12
Deflector plates aperture [mm]	46	40	26
Output slit aperture [mm]	22	12	10
Output slit passing ions [%]	20.0	20.0	20.0
Output slit passing power [W]	120	102	75
Total system transfer	**I.**	**II.**	**III.**
Through both choppers passes [%]	5.0	4.3	3.1
Total system passing beam power [W]	120.0	102.0	75.0
Output beam emittance [mm.rad]	351.86	207.35	90.48

CONCLUSION

The article briefly introduces the new laboratory of the NPI over the TR 24 cyclotron and planned research program. One of the possible use of the TR 24 beam is a facility for spectrometric neutron measurements with the Time Of Flight (TOF) method that requires defined time structure of the extracted accelerated bunches. The desired width of the bunch period ratio 1 : 100 (2.3 : 236 ns) is feasible by simultaneous employing of the sinusoidal and pulsed choppers. In spite of the reduced beam transmission, the easiest seems to be the alternative with the chopper 1 amplitude of the sinusoidal voltage of 25 kV and 12 kV of the pulsed chopper 2, respectively. The key and demanding task is the precise stable synchronization and phase setting of the deflector's voltage harmonized with the phase of the cyclotron dee voltage.

ISBN 978-3-95450-167-0

ACKNOWLEDGEMENT

We would like to thank ACSI for a kind providing the results of detailed simulations of the properties of the accelerated TR 24 beams. The work was supported by the Czech Academy of Sciences under the NPI research plan AV0Z10480505 and by the CANAM project funded by the Ministry of Education, Youth and Sports of the Czech Republic (project No. LM2011019).

REFERENCES

[1] NPI CAS, http://accs.ujf.cas.cz/

[2] ACSI inc., http://www.advancedcyclotron.com/cyclotronsolutions/tr24

[3] NPI CAS, http://canam.ujf.cas.cz/en/home/item/159

[4] D. Ene *et al.,* "Global characterization of the GELINA facility for high-resolution neutro time-of- flight measurements by Monte Carlo simulation", *Nucl. Instr. and Methods, vol. 618, pp 54-68. 2010.*

[5] X. Ledoux *et al.,* "The Neutrons for Science Facility at SPIRAL-2", *Nuclear Data Sheets, 119, pp 353-356, 2014.*

[6] Y. Yoshida *et al.,* "Beam-pulsing System for the IMS Cyclotron", *Nucl.Instrum. Meth.138(1976)579–588.*

[7] Milan Čihák *et al.,* "Beam Dynamic Simulation in the Isochronous Cyclotron U-120M", *Proc. Cyclotrons'07 Giardini Naxos, Italy, October 2007, pp. 385-387.*

[8] Private ACSI Communication.

[9] R. Apsimon *et al.,* "ProTec – a Normal-Conducting Cyclinac for Proton Therapy Research and Radioisotope Production", *in Proc. of IPAC2015, Richmond, VA, May 2015,* paper THPF084*, pp 3883-3885.*

ISBN 978-3-95450-167-0

DEVELOPED NUMERICAL CODE BASED ON THE EFFECTS OF SPACE CHARGE IN CENTRAL REGION OF 10 MeV CYCLOTRON

M.M. Afkhami Karaei†, H. Afarideh, R. Solhju, S. Azizpourian, M. Mousavinia, F. Taft, Amirkabir University of Technology (AUT), Department of Physics, Tehran, Iran
J.S. Chai, M. Ghergherehchi, Sungkyunkwan University (SKKU) School of Information and Comunication Engineering, Seoul, South Korea

Abstract

To study of space charge effects in 10 MeV cyclotron of Amirkabir University of Technology the C++ code is developed. This cyclotron is designed to accelerate H- up to10 MeV energy. The important components of cyclotron that effect on calculations of space charge include four sector magnets, 2 RF cavities with 71 MHz frequency and internal PIG ion source. Equations of motion and effects of charged particles in electromagnetic field of accelerator are integrated in C++ code. The conventional method, 4-order Runge-Kutta, is used to solve the equations. The results of calculations show space charge effects of beam particles on each other in accelerating process.

INTRODUCTION

The purpose of manufacturing 10 MeV Amirkabir University of Technology produced Fluor-18. The cyclotron contains some component to produce an electric field, magnetic field and injection particle. Component of central region shows in Fig. 1. Beam injection by an internal ion source PIG [1] was carried out. H- Beam with zero kinetic energy produced by the ion source, these particles by the puller that located at a certain distance from the ion source were pulled out due to potential difference between these two points. The primary particles begin to move and primary energy particles from this method will be provided [2]. Voltage of Dummy Dees and pullers are zero and 42 keV respectively, particles that accelerated in a first step and don't have any collection with a body of cyclotron now again accelerated. Continues acceleration of particles performed by a potential difference between the central part of the liner and central part of Dee's. Due to the beam dynamic depended to the early turns, set of electric and magnetic field geometry and initial condition of particle is very important. If the central region was not properly designed, couldn't be expected that particles extracted from cyclotron.

Numerical code was written in C++ program that used the conventional Rung-Kutta method and initial condition of particles and electric and magnetic distribution to calculate the trajectory of space charge effect of particles.

The method that used in this code is of effect of summing up the Coulomb's electric field of particles on one particle. That means effect of electric field of particles on the particle that located near them is considered.

† afkhami1370@yahoo.com

THE METHOD OF CALCULATING OF THE BEAM TRAJECTORY SPACE CHARGE

A code for calculation of particle trajectory in the central region of cyclotron, written by using C ++ language. Electric and magnetic field calculated by OPERA-3D-TOSCA.

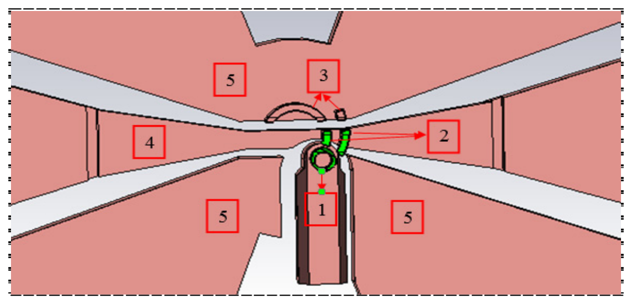

Figure 1: Geometry of electric field in central region 1) head of ion source 2) pullers 3) dummy Dee's 4) central part of Dee 5) central part of liner.

Results of TOSCA extracted and imported in to C++ code. C++ code calculated equation of motion according to the electric and magnetic field data's and initial condition that determined. Equation of motion that used in C++ code followed equation 1, 2, 3 [3].

$$\frac{d\vec{r}}{dt} = \frac{\vec{p}}{m\gamma} \tag{1}$$

$$\frac{d\vec{p}}{dt} = q(\vec{E}\cos\omega t + \frac{d\vec{r}}{dt} \times \vec{B}) \tag{2}$$

$$\frac{dW}{dt} = \vec{F}.\vec{\vartheta} = \frac{d\vec{p}}{dt}.\frac{d\vec{r}}{dt} \tag{3}$$

Above equations are used in Cartesian coordinate(x,y,z), where B(B_x, B_y, B_z), E(E_x, E_y, E_z) are magnetic and electric fields respectively. In this code magnetic field that created from beam current is not considered but electric field of that considered. So the electric field is as follows:

$$E_{(x,y,z)} = \varepsilon^{RF}_{(x,y,z)} + \varepsilon^{SC}_{(x,y,z)} \tag{4}$$

ISBN 978-3-95450-167-0

where $\varepsilon^{RF}_{(x,y,z)}$ is electric field from cavity and $\varepsilon^{SC}_{(x,y,z)}$ is electric field from space charge between particles. Electric field of space charge in Cartesian coordinate are as follow:

$$\varepsilon(i)^{SC}_{x} = \sum_{n=1}^{n=N} \frac{q_n(x_i - x_n)}{4\pi\varepsilon_0[(x_i-x_n)^2+(y_i-y_n)^2+(z_i-z_n)^2]^{3/2}} \quad (5)$$

$$\varepsilon(i)^{SC}_{y} = \sum_{n=1}^{n=N} \frac{q_n(y_i - y_n)}{4\pi\varepsilon_0[(x_i-x_n)^2+(y_i-y_n)^2+(z_i-z_n)^2]^{\frac{3}{2}}} \quad (6)$$

$$\varepsilon(i)^{SC}_{z} = \sum_{n=1}^{n=N} \frac{q_n(z_i - z_n)}{4\pi\varepsilon_0[(x_i-x_n)^2+(y_i-y_n)^2+(z_i-z_n)^2]^{3/2}} \quad (7)$$

where i is characteristic of particle that electric field of other particle calculated on position of it ; n is number of other particle that effect on i particle; q is charge of particle; $\varepsilon_0 = 8.85 * 10^{-12} F/m$ [4]

Initial condition of beam motion in central region of cyclotron 10MeV and specification of cyclotron shown in Table 1.

Table 1: Initial Condition of Particle and Specification of Cyclotron

Parameter	Value
Initial energy of particle	0 keV
Dee width	40^o
Number of sectors	4
RF frequency	71MHz
The magnetic field in the center of the cyclotron	1.18T

Electric and magnetic fields related to the position determined by the C++ code and entered into the calculations when the particle is in any position.

Figure 2 shows the geometry of the magnetic field and poles in the center of the cyclotron. This geometry imported to the TOSCA, after calculation and optimization of the geometry, extracted data's from it. Distribution of magnetic field in center of 10 MeV cyclotron shows in Fig. 3.

In Fig. 1 the geometry of electric field and effective component in electric field is shown. The effective components of the electric field in central region included head of ion source, pullers, dummy Dee's, central part of Dee and central part of liner. Potential of pullers and central part of Dee are 42 kV and potential of other components are zero. This geometry imported to the TOSCA and calculated electric potential with electro static solver of Opra3d.

Electric potential data imported to the C++ code and electric field calculated by it. Electric potential distribution of this geometry is shown in Fig. 4.

Electric and magnetic field and Primary condition of particle including phase, energy and position are determined. With frequent changes in the initial condition of the particle, tested numerical calculation by using C++ code. If we have not received to the appropriate beam dynamic, geometry of electric field and distance of poles were changed. Finally, with optimized geometry and initial condition, horizontal and vertical beam trajectory are achieved.

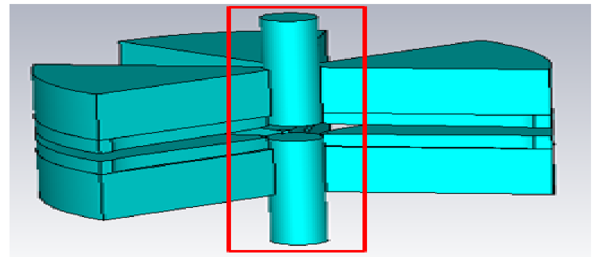

Figure 2: Geometry magnetic field in central region.

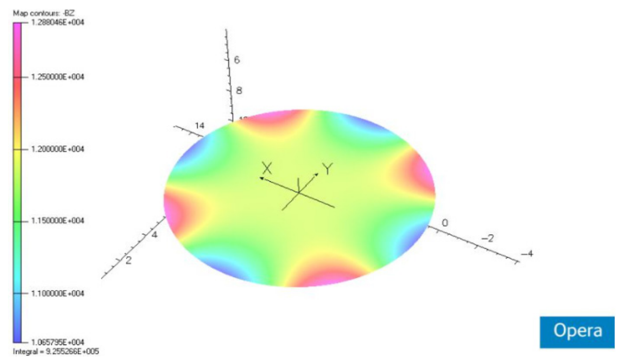

Figure 3: distribution of magnetic field in central region of cyclotron [5].

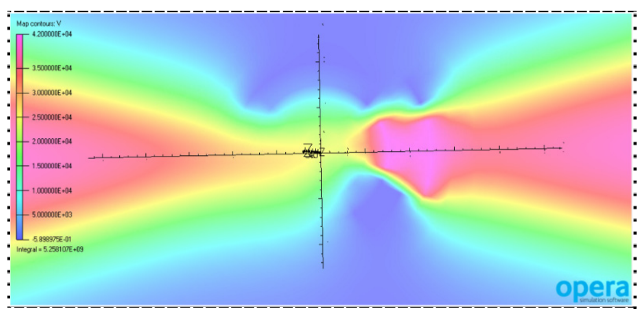

Figure 4: Distribution of electric field in central region.

RESULT OF SPACE CHARGE EFFECT (SCE)

Beam dynamic calculation carried out for 21 particle by ignoring and considering space charge effect. Figure 5 shows the horizontal motion of 21 particles without considering the space charge effect of particles in the central region. Figures 6 and 7 show horizontal motion of 21 particles without considering the space charge effect of particles in the central region. As seen in Figs. 5, 6 and 7 when ignore the space charge effect, particles approximately passes from the same path. But when space charge consider in calculation of equation of motion, seen particle repel each other. If our electric and magnetic field are not correct all of particles will be lost.

ISBN 978-3-95450-167-0

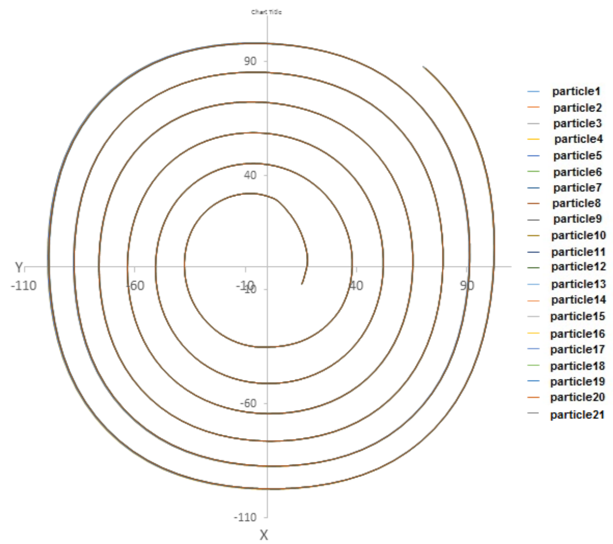

Figure 5: 21 particles Horizontal motion without space.

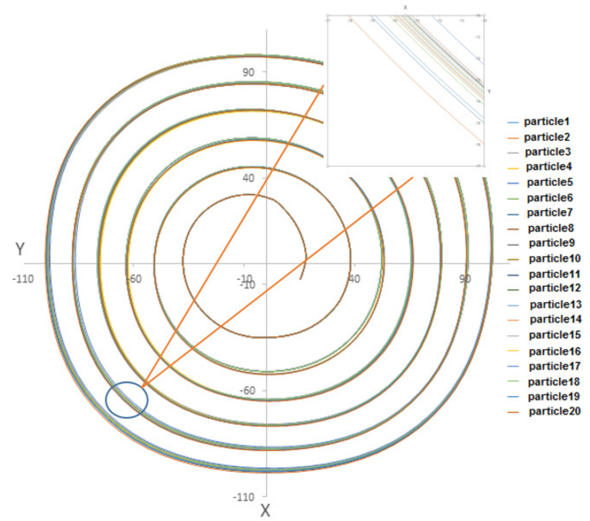

Figure 6: 21 particles Horizontal motion with space charge for the first 6 turns with phase 308^0 without illustrate beam losses.

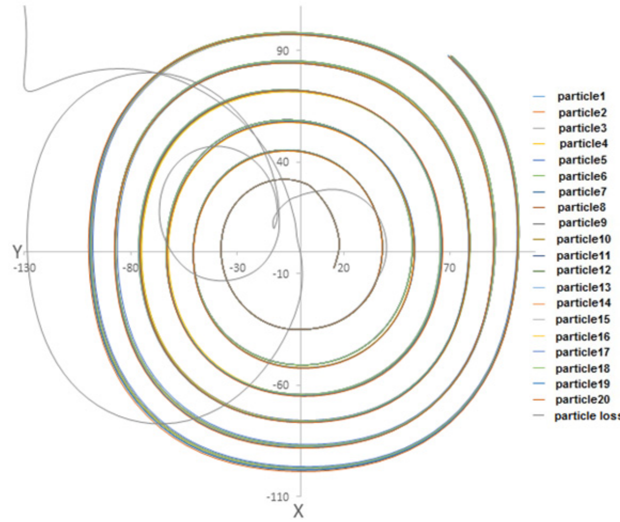

Figure 7: 21 particles Horizontal motion with space charge for the first 6 turns with phase 308^0 and illustrate beam losses.

Figures 8 and 9 show the vertical motion of particles with ignoring and considering space charge respectively

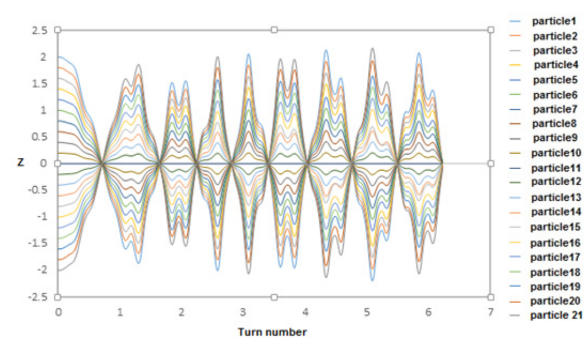

Figure 8: 21 particles vertical motion with space charge for the first 6 turns with phase 308^0 illustrate beam losses.

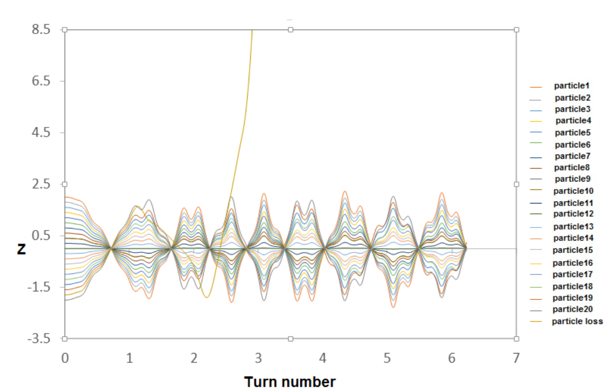

Figure 9: 21 particles vertical motion with space charge for the first 6 turns with phase 308^0 illustrate beam losses.

ISBN 978-3-95450-167-0

CONCLUSION

Previously, beam dynamic calculations carried out to find correct design geometry of central region and location of the tip of ion source [6]. In this paper, the beam dynamic calculation has been done with considering space charge effect of 21 particles by C++ code.

REFERENCES

[1] Jidong, L.O.N.G., *et al.*, “Study on a cold-cathode H-PIG-type ion source”, *Nuclear Science and Techniques*, 24.4: 40201-040201. 2013.

[2] Bin, Q.I.N., *et al.,* “Central region design for a 10 MeV internal ion source cyclotron”, *Chinese Physics* C 33.8: 682. 2009.

[3] Huang, Yunxiang. “A new design of the University of Manitoba cyclotron for D-ion acceleration and a study for the beam extraction from the Princeton University AVF cyclotron”, Ph.D. thesis, University of Manitoba, 1988.

[4] Onischenko, L., *et al.,* “Numerical simulation of space charge effects in the sector cyclotron”, *Nukleonika* 48 (2003): 45-48.

[5] R. Solhju *et al.*, “Magnet design for the 10 MeV AVF cyclotron accelerator”, *Journal of the Korean Physical Society* 63.7, pp. 1347-1350, 2013.

[6] Karaei, Afkhami, *et al,*. “Investigation of central region design of 10 MeV AVF cyclotron”, in *Proc. 7th International Particle Accelerator Conference (IPAC'16),* Busan, Korea, May 8-13, 2016, pp 1253-1255.

ISBN 978-3-95450-167-0

SPES CYCLOTRON BEAMLINES

D. Campo, M. Maggiore, A. Lombardi, P. Antonini, A. Calore, L. Pranovi,
Laboratori Nazionali di Legnaro, Legnaro, Padova, Italy

Abstract

The SPES (Selective Production of Exotic Species) facility purposes are the production of radioactive beams (RIBs) by ISOL technique, the production and the research on innovative radioisotopes and experiments with high intensity neutron beams.

For these reasons, the 70p cyclotron, designed by BEST Cyclotron Systems Inc. (BCSI), has been installed at Laboratori Nazionali di Legnaro (LNL): it is a machine able to produce a beam current up to 700 μA shared into two extraction channels. Beams at the energy values of 35 MeV, 50 MeV and 70 MeV have to be transported to the experimental areas with specific properties and minimizing the beam losses. Here, the main features of the needed beamlines are described.

BEAMLINES OF THE SPES PROJECT

The core of the SPES project is the 70p cyclotron, a 4 sectors machine with room temperature coils, designed to accelerate H^- ions. The extraction by stripping method allows the beam current sharing into two extraction channels: it is possible to carry out simultaneously the production of radioactive ions and other applications [1].

Figure 1 shows the layout of the underground floor of the SPES building. The central vault (A1) houses the 70p cyclotron and it is surrounded by different experimental areas: in particular, there are three bunkers shielded for receiving high power beam (up to 50 kW). Figure 1 reports the beamline for the beam transport to the ISOL target (L1), which was designed by BCSI [2], and the beamlines L3b-L3c and L2, dedicated to the SPES applications. The beamline L1 is actually operational and, with the second extraction channel, it is included in the commissioning of the 70p cyclotron. As concern the other beamlines, the main properties of the achieved solutions are here described: these beamlines have the same initial elements of the beamline L1, from the combo magnet at the cyclotron extraction to the first switching magnet; the new designs have to take into account this fixed part and the preliminary results related to the first machine operations. The main requirement for each configuration is the minimization of the beam losses along the beam path: the allowable limit is 1%.

BEAM TRANSPORT TO ISOL AREA

The beamline to the ISOL area was installed in the vault in May 2015. The beamline design was completed to satisfy all the requirements needed for the ISOL facility, that is, a final RMS spot size around 4 mm. For the cyclotron commissioning by using the beam dumper designed by LNL SPES target team [3], new tunes of the 4 couples of quadrupoles were required, in order to increase the RMS spot size in the range 8 – 12 mm and, then, to optimize the power distribution in the inner surfaces of the device. A summary of the simulation results is reported in Table 1, for the minimum and the maximum values of the RMS spot size: the beam losses are less than the required limit.

Table 1: Simulation Results of the L1 Beamline Tunes

Energy [MeV]	35		50		70	
RMS spot [mm]	8	11	8	11	8	11
Q1 [T/m]	4.99	4.99	6.31	6.31	5.06	4.91
Q2 [T/m]	-5.41	-5.41	-6.69	-6.69	-6.68	-7.66
Q3 [T/m]	-4.35	-4.30	-5.25	-5.15	-5.45	-5.56
Q4 [T/m]	3.05	3.19	3.81	3.81	3.20	3.72
Q5 [T/m]	3.60	3.87	4.51	4.98	5.82	6.84
Q6 [T/m]	-5.06	-5.01	-6.24	-6.52	-7.25	-8.41
Q7 [T/m]	-4.04	-3.81	-4.64	-4.31	-5.90	-4.99
Q8 [T/m]	3.13	2.65	3.34	2.97	4.38	3.35
Losses [%]	0.12	0.22	0	0.19	0.02	0.1

Up to now, the L1 beamline has been fully tested only by using 70 MeV beam and the 4-jaw collimators placed just after the combo magnet have been used to reduce the beam halo. Furthermore, the wobbler system placed just before the A6 bunker entrance has been activated in order to get a uniform beam distribution and to avoid thermal stresses of the beam dumper. These effects have to be included in the complete study of the performance of the L1 beamline and are useful data for the improvement of the design of the new beamlines.

RADIOISOTOPE PRODUCTION

LARAMED (LAboratorio per la Produzione di RAdionuclidi per la MEDicina) is the proposal of LNL for the production of innovative radiopharmaceutical and conventional radionuclides [4]. The beamlines L3b and L3c, which satisfy the requirements described in table 2, share all the elements in A1 hall, then a 45 deg switching magnet is used to bend the beam in the low current experimental area.

Table 2: Main Features of the LARAMED Beamlines

	L3b	**L3c**
Energy range	35 – 70 MeV	35 -70 MeV
Average current	300 μA	< 1 μA
Beam spot size (RMS sigma)	3 mm	3 – 4 mm
Optic layout	3 quad doublets	1 switching magnet, 2 quad doublets

ISBN 978-3-95450-167-0

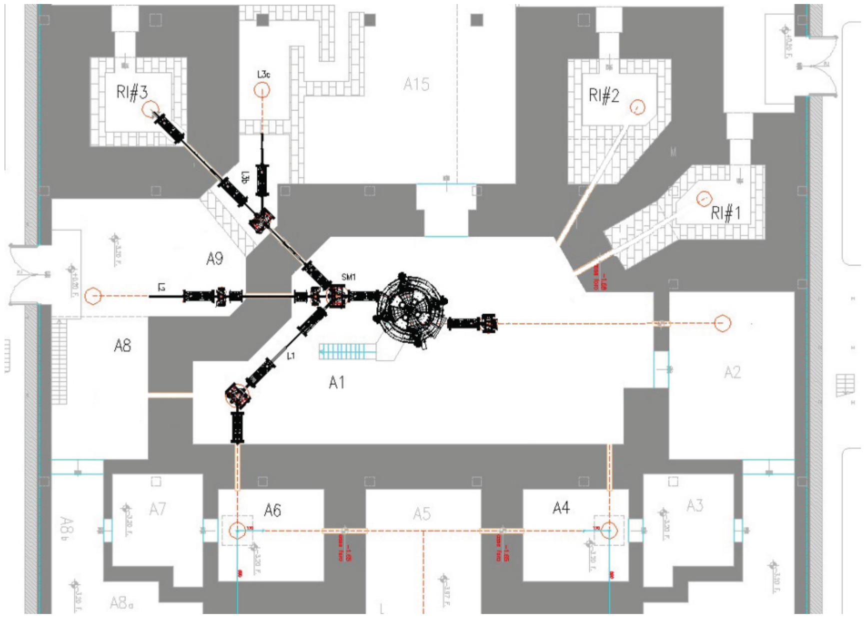

Figure 1: Layout of the SPES facility beamlines. The beamline L1 to transport the beam to the ISOL bunker A6 is under commissioning. The first 45 deg switching magnet along the L1 beamline allows the sharing of the proton beam between the three experimental areas dedicated to experiments with high intensity neutron beams (A9) and the radioisotope production (RI3 bunker and the space aside).

In particular, the L3b beamline follows a straight path from the first 45 deg switching magnet in the A1 vault up to the RI3 bunker: the beam transport is completed by using three couples of quadrupoles; the total line length is 20.8 m. The additional elements needed to complete the L3b beamline have the same properties of the existing L1 beamline elements, which have a maximum gradient value of 10 T/m and an aperture of 102 mm for each quadrupoles. The proposed solutions for the quadrupole tunes and the related envelopes are reported in Table 3 and Fig. 2 respectively: the beam losses for each configuration are less than 0.1%.

Table 3: Quadrupole Tune of the L3b Beamline

Energy [MeV]	35	50	70
Q1 [T/m]	4.682	5.740	8.175
Q2 [T/m]	-5.615	-6.639	-8.680
Q3 [T/m]	-4.422	-4.732	-5.144
Q4 [T/m]	3.831	3.444	3.590
Q5 [T/m]	2.556	2.445	2.562
Q6 [T/m]	-2.113	-2.314	-2.301
Q7 [T/m]	-2.993	-3.112	-3.722
Q8 [T/m]	3.944	4.003	3.968

The L3c beamline has the same elements of L3b beamline in A1 hall, while in A9 hall it needs a 45 deg switching magnet and a quadrupole couple; the total length is about 14.85 m. By using suitable tunes it is possible to produce at the target beam spot with RMS size in the range 3 – 5 mm. In table 4, only the solutions able to obtain a beam spot with a RMS sigma of 3 mm are shown. The beam losses along these configurations are less than 0.1% (see Fig. 3) and occur mainly in the vacuum chamber of the two switching magnets.

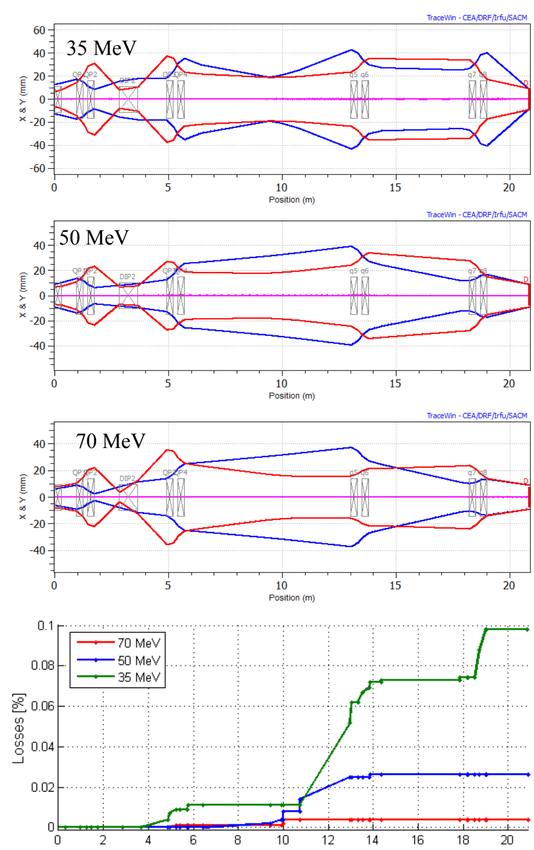

Figure 2: Envelopes (horizontal coordinate in blue, vertical coordinate in red) and beam losses of the beam at the energy values of 35 MeV, 50 MeV and 70 MeV along the L3b beamline.

Table 4: Quadrupole Tune of the L3c Beamline

Energy [MeV]	35	50	70
Q1 [T/m]	4.987	3.555	7.203
Q2 [T/m]	-5.669	-6.589	-7.798
Q3 [T/m]	-4.738	-5.0394	-6.280
Q4 [T/m]	3.982	4.272	5.374
Q5 [T/m]	-3.705	-2.886	-4.235
Q6 [T/m]	3.717	1.225	3.922

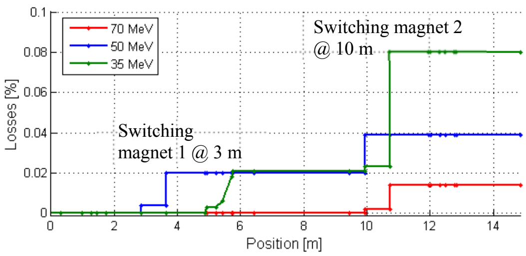

Figure 3: Beam losses along the L3c beamline.

NEUTRON EXPERIMENTAL AREA

The high intensity proton beam is also useful for experiments with intense beams of mono-energetic neutrons and of fast neutrons with the same energy properties of the neutrons observed at sea-level or at flight-altitudes level: these are the purposes of the neutron irradiation facility (NEPIR) of the SPES project [5].

In particular, a complex consisting of two dedicated targets, called the Quasi Mono-energetic Neutrons (QMN) and Atmospheric Neutron Emulator (ANEM), is under study at LNL and it will be placed in A9 hall: the experimental set-up requires a proton beam current of 50 μA in the energy range 20 – 70 MeV. Since the 70p cyclotron is able to produce beams in the energy range 35 – 70 MeV, the use of an energy degrader along the beamline is needed: it means to find out the most suitable position for the device and to evaluate carefully the effects in the A1 vault. The peculiar element of the L2 beamline is a couple of 22 deg vertical dipole magnets: this magnetic chicane minimizes the observation of neutron back-streaming towards the cyclotron hall. In case of the degrader system use, the magnetic chicane allows to achieve the energy selection of the protons and to limit the neutron flux from the degrader to the forward test point.

The design of the L2 beamline requires particular attention because of the limited space available in the A1 hall, between the existing switching magnet and the 3 m wall that separates the cyclotron vault and the A9 hall. In fact, it is necessary to place in few meters, both the first dipole magnet and a couple of quadrupoles in order to achieve a satisfactory focalization of the lower energy-bigger emittance beams (Fig.4). In the actual configuration, L2 beamline consists of the first part of the L1 beamline, from the combo magnet to the first 45 deg switching magnet, plus three quadrupole doublets and the couple of vertical dipole magnets. The beamline length, along the beam path, is about 14.8 m and the vertical jump between the two halls is 2.59 m.

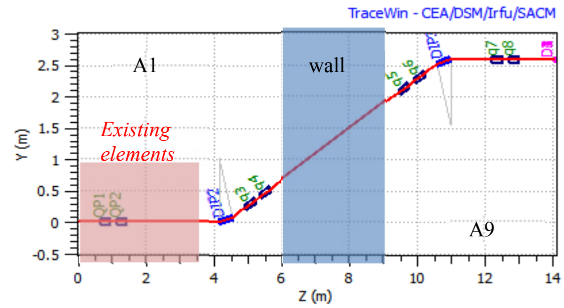

Figure 4: Synoptic (not in scale) of the L2 beamline.

The QMN/ANEM complex requires almost parallel beams with RMS spot size in the range 4 – 7 mm. The simulation results show that this system allows to transport the beam and to achieve several spots in the specified range, with beam losses of 0.2% for the energy value of 35 MeV, while the losses are almost negligible for higher energy values. Also shorter beamline version was completed, to have more space for the targets and the other experimental elements. Moreover, the final configuration will be defined once the degrader position in the A1 hall and the related constrains will be fixed: three different alternatives, in fact, are still under study.

CONCLUSION

All the simulation results here reported were achieved by using TraceWin [6]. While the beamlines for the LARAMED facility are fixed, the beamline for the experiments with intense beams of neutrons needs further study due mainly to reduce the beam energy limits of the 70p cyclotron. Useful data to confirm the effectiveness of these configurations and/or to improve the adopted solutions will be available in the next months, during the 70p cyclotron commissioning. In particular, the transport of beams of different energy along the L1 beamline should outline new critical points and suggest some adjustments in the preliminary configuration.

ACKNOWLEDGEMENT

The authors would like to thank all the colleagues of the BEST Cyclotron Systems Inc. for their valuable work and the helpful discussions.

REFERENCES

[1] M. Maggiore *et al.*, "Status of high intensity proton beam facility at LNL", presented at CYCLOTRONS 2016, Zurich, Switzerland, Sep. 2016, paper FRA03, this conference.

[2] V. Ryjkov, "Cyclotron design note", Best internal report, 2013.

[3] P. Antonini *et al.*, "Diagnostic tool and instrumentation for handling 50 kW beam power", presented at Cyclotrons 2016, Zurich, Switzerland, Sep. 2016, paper TUP09, this conference.

ISBN 978-3-95450-167-0

[4] J. Esposito *et al.*, "Evaluation of 99Mo and 99mTc Production Based on High Performance Cyclotron", *Science and Technology of Nuclear Installations,* vol. 2013, ID972381.

[5] L. Silvestrin *et al.*, "SPES and the neutron facilities at Laboratori Nazionali di Legnaro", *European Physical Journal Plus*, Mar. 2016, 131:72

[6] TraceWin, `http://irfu.cea.fr/Sacm/logiciels/index3.php`

ISBN 978-3-95450-167-0

AN AIR IONIZATION CHAMBER SIMULATION USING MONTE CARLO METHOD*

Shigang Hou†, Guofang Song, Tianjue Zhang, Feng Wang, Lipeng Wen, Shizhong An, ZhenWei Liu, China Institute of Atomic Energy, Beijing, China

Abstract

The CYCIAE-100 cyclotron with proton beam 200uA/100MeV and several beamlines have been developed at China Institute of Atomic Energy (CIAE) [1]. In order to protect the machine from excessive radiation activation, an uncontrolled loss criterion of 1uA is specified. Calculation for radiation shielding shows that high neutron and gamma are produced under this condition. To measure the high energy gamma -ray (about 2 MeV) [2] during machine running and void damage by the prompt radiation, an air ionization chamber is designed to fulfil this goal. A Geant4 program is developed to simulate the energy response of detectors; the EM filed data is also taken into consideration in the program. The simulation results indicate that the energy response linearity satisfies the requirement of the project specification.

INTRODUCTION

The Beijing Radioactive of Ion beam Facility (BRIF) Project has been built at CIAE. BRIF is consist of CYCIAE-100 proton cyclotron, ISOL, existing HI-13 Tandem, and super conducting linac(Tandem's booster). It is used for nuclear physics, proton therapy, materials science and application of nuclear technology etc. [3]. The driving accelerator, a 100MeV H- cyclotron, will provide high intensity stable proton beam from 75MeV to 100MeV up to 200uA. During the commissioning and operation, for the sake of beam loss, high energy neutron and photon will generate, which are harmful to staff's health and the reliability of cyclotron devices. In order to measure the actual radiation dose at real time and evaluate its hazard, a set of radiation dose monitoring system is necessary. We investigate the dose monitoring system of similar accelerators. According to the characteristics of the radiation field brought by the cyclotron, a radiation monitoring system has been constructed.

The monitoring system includes neutron detectors and γ detectors. The Monte-Carlo simulation results for shielding calculation illustrated that the energy of photon distribute from several keV to 10 MeV, the average energy is about 2 MeV yet. The maximum ambient dose equivalent rate is no more than 1Sv/h in the plane of beam transfer during beam delivering at the inner side of the wall of cyclotron vault and experiment hall. It is necessary to development a γ detector with high reliability that can work under above mentioned condition.

In consideration of the wide energy distribution of the photon, the energy response of detectors should have good linearity up to 10 MeV, furthermore working under high flux of neutron and photon, the detectors should have simple structure and less electronics to be maintained. For the reasons mentioned above, Air ionization chambers are very suitable compared with other detectors for the 100 MeV cyclotron radiation monitoring system. In order to study the characteristics of the energy response and determine the optimum size of the components of the chamber, A Geant4 code is programmed to achieve this goal; meanwhile Maxwell 3D is applied to evaluated the electrostatic electric field in the chamber.

SIMULATION TOOLS AND MODEL

Simulation Tools

There are two tools served mainly in this work, Geant4 and Maxwell 3D. The capacitance is important to the design of the preamplifier, moreover the electrostatic field distribution will influence the transit time of electron and ions generated by photon with air significantly. The Maxwell three-dimension (3D) is a set of powerful EM field simulation software; it can precisely solve different EM issue using finite element method. Geant4 is an open source framework, which can be used to simulation the interaction and transport process of particles in materials. Geant4 is widely employed in high energy physics, medical physics, detector studies, etc. [4], which is developed by CERN. It's also a huge Monte Carlo development toolkit. The data of physics models are represented as object oriented in Geant4. All the processes are built in, so the users can accomplish the whole simulation independent of external program.

The Geant4 framework provides toolkits to simulate the EM interactive processes; user can develop programs that emulate electron and photon interaction with different materials, meanwhile Geant4 provide several evaluated data library such as EPDL97, EEDL, EADL, NDL etc.

Detector Structure and Material

The main structure of the air ionization chamber can be sphere or cylinder. The sphere chamber has the most optimum performance of angular response to isometric radiation field. Due to the ionization chambers is installed at the same plane of beam, the cylinder structure is chosen according to our design, and this structure is easy to fabricate also. The sketch of the detector is shown in Figure 1. There are two parts consist in the detector, the air ionization chamber is located at upper cylinder, while the electronics circuit is seated at the bottom of the detector. The outer shell is made of metal to protect the chamber and the electronics circuit.

* Work supported by by NSFC (Grand Nos.11375273 and 1146114103)
† housg@ciae.ac.cn

ISBN 978-3-95450-167-0

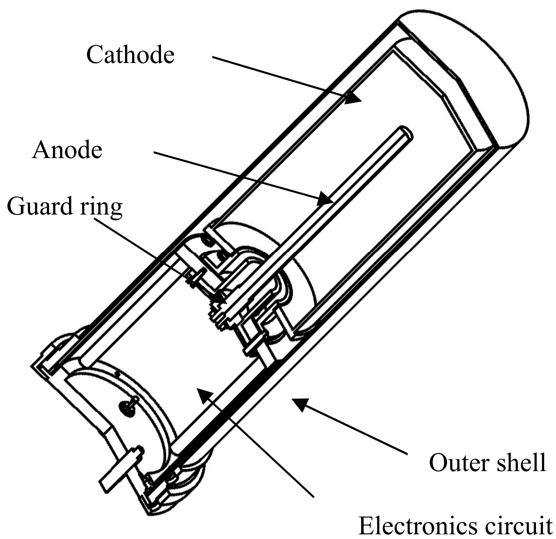

Figure 1: Structure of the detector.

The stainless steel, brass alloy and aluminium alloy are convenient for fabrication, so these materials will be considered for the chamber firstly. Though the stainless steel have the most stop capability to gamma ray among these materials [5], its mechanical strength is better than others. The SS304 is chosen for outer shell. The dimensions and materials of ionization chamber are listed in Table 1.

Table 1: Dimensions and Material of Ionization Chamber

Item	Inner Diameter (mm)	Outer diameter (mm)	Length (mm)	material
anode	-	12	200	brass alloy
cathode	75	77	206	Al alloy
shell	86	88	400	SS304
Guard ring	16	20	25	brass alloy

The material of cathode is aluminium alloy, which has good electric property and low stop capability for gamma ray. The anode will be made of brass alloy; this material is not easy to be corroded, this feature makes it suitable for collecting electron and negative ions long-term. This is because the output current of the air ionization chamber is very small, from tens of fA to several pA. To avoid the current leakage, a guard ring will be installed between the anode and the cathode at the bottom of the ionization chamber. The guard ring is at the same electric potential as the anode.

Electrostatic Field Simulation

The anode of the ionization chamber is connected to the input of preamplifier directly. The anode collects the electron generated by air ionization. The cathode of the chamber is connected to the negative high voltage, this bias voltage produces the electrostatic filed between the anode and the cathode. To avoid sparking in the high gradual area, Maxwell 3D is adopted to simulate the electrostatic filed distribution, furthermore, the data of field will be import into the Geant4 program in energy response analyse. The model for Maxwell 3D is simplified for fast modelling. The material of anode is brass alloy, and cathode is aluminium alloy, between the anode and the cathode is air with 1 atm. The voltage set to anode and cathode is 0 V and negative 500 V respectively. The result of electrostatic filed distribution is shown in Figure 2.

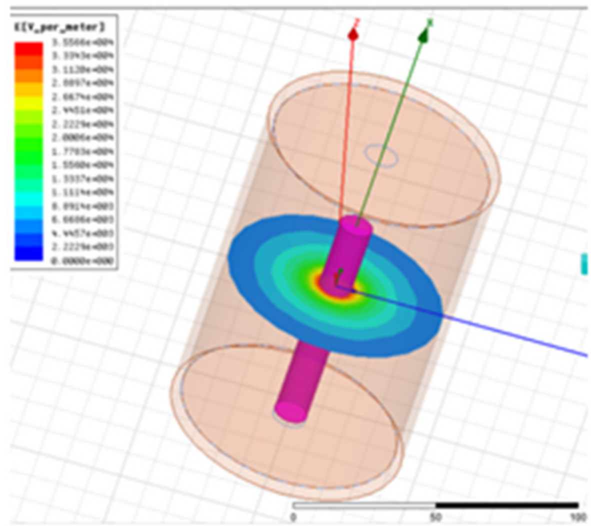

(a) Axial field distribution

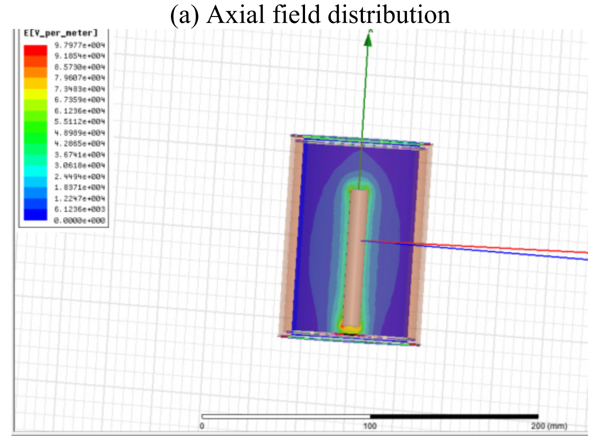

(b) Transverse field distribution

Figure 2: Electrostatic field distribution of the chamber.

The post process result showed that the capacitance of the chamber is 4.324 pF. This parameter will influence the response character of the preamplifier. The gradual of voltage distribution is shown in Figure 2, the purple area is anode and the orange area is cathode. The electrostatic field is smooth at axial direction in the most regions. The maximum value of the electrostatic field occurs around the tail of the anode, about 1.14×10^{4} V/m. The sparking will not generate at this voltage under 1 atm. The voltage distribution data is written to a text file, and then the file will be read by the Monte Carlo program.

ISBN 978-3-95450-167-0

Geant4 Simulation and Analysis

The simulation program which based on the Geant4 version 4.9.2 is worked out. This program used C++ language to realize all the functions, the flow chart of the program is shown in Figure 3.

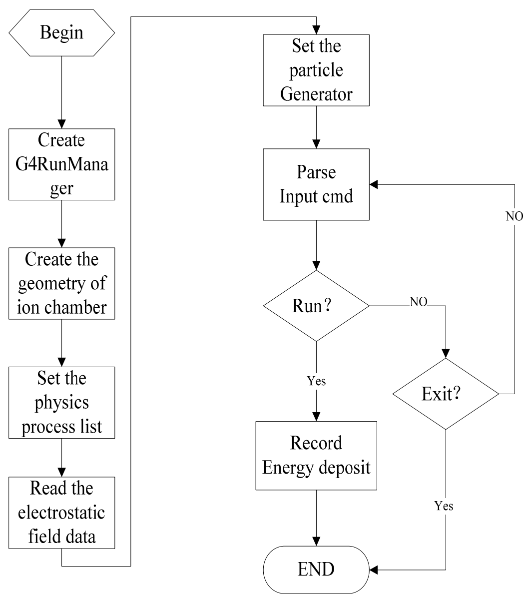

Figure 3: Flowchart of Geant4 simulation program.

There are about dozen of C++ class implement in this program. The detector construction class appoint the dimension of the components of the chamber, and assign the material to the parts. The geometry bodies are associated with the logic volume in the detector construction class also. The ionization chamber and the particle generator are located in a box named "world" in the program. The material of the world is air; the particle generator is a plane, the area of which is same as the transverse size of the chamber. The ionization chamber and the particle generator are illustrated in Figure 4.

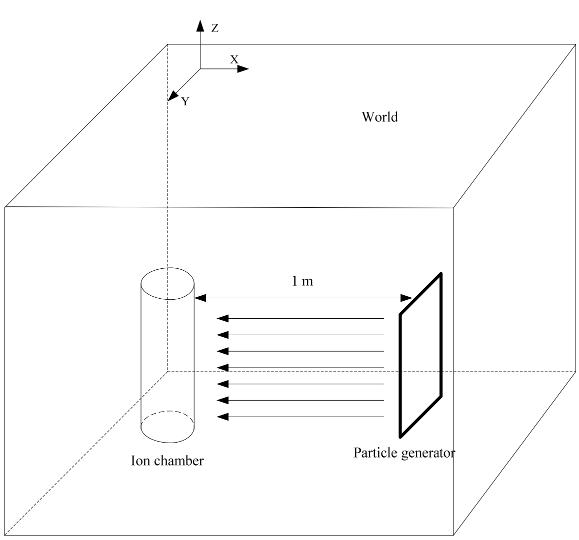

Figure 4: The Geant4 simulation model.

In this simulation program the main physics process include the photon interaction with material and electron interaction with material. The photo-electric effect, Compton scattering and gamma conversion effect are taken into account for photon. The physics processes for electron interaction include multiple scattering, ionisation and Bremsstrahlung effect.

The particle generator locate one meter far from the ionization chamber. The number of the particle can be modified at the beginning of every run. In order to minimize the statistics fluctuation, the particle number is set 10^7 presently.

The air area between the anode and the cathode act as sensitive region, the energy loss by the photon and secondary particles will be recorded in this region. The loss energy is ratio to the output current of the chamber; the normalization energy response curve is shown in Figure 5.

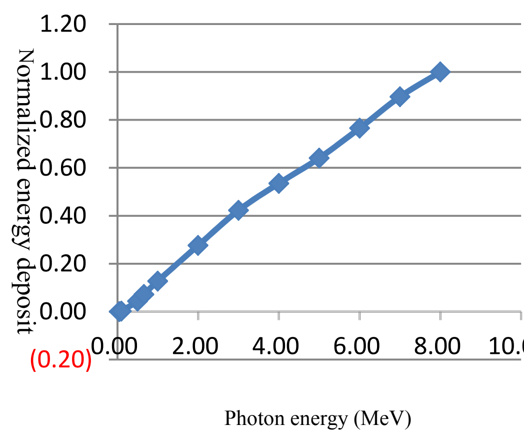

Figure 5: Energy response curve of air ionization chamber.

Figure 5 shows the curve of the energy response from 50 keV to 8 MeV of the air ionization. Though the energy response is somewhat higher at 3 MeV around, the performance of the chamber fulfils the specification of the BRIF project.

CONCLUSION

An air ionization chamber is designed for radiation monitoring system of BRIF project. To achieve the requirement of the project, the Maxwell 3D and Geant4 tools are combined to simulation the performance of the ionization chamber. The simulation result indicates that the chamber has fine linearity of energy from 50keV to 8MeV. According to the simulation, the mechanical structure of the chamber will be optimized so as to improve its performance. This chamber can be used in the BRIF project, also can be used in other similar accelerator facility as radiation monitor or beam loss detectors.

ISBN 978-3-95450-167-0

REFERENCES

[1] Tianjue Zhang, Zhenguo Li, Zhiguo Yin, “Design and construction status of CYCIAE-100, a 100 MeV H cyclotron for RIB production”, *Nuclear Instruments and Methods in Physics Research B, vol.* 266, pp. 4117–4122, 2008 .

[2] Shielding calculation for BRIF, CIAE Internal report, 2006.

[3] Sumin Wei, Shizhong An, Tianjue Zhang, *et al.*, “Transfer beamline design after stripping extraction for CYCIAE-100”, *Nuclear Instruments and Methods in Physics Research B* vol. 266, pp. 4697–4701, 2008.

[4] Geant, `http://www.geant4.org/geant4/`.

[5] Chunyu Liu, Weishi An, Jianping Li, *et al.*, “Study on Design of High Pressure ionization chamber”, *Nuclear Power Engineering*, vol. 27, no. 6, pp. 103-105, 2006 (in Chinese).

ISBN 978-3-95450-167-0

PHYSICAL DESIGN OF THE EXTRACTION TRIM-RODS IN A 230 MeV SUPERCONDUCTING CYCLOTRON*

Dongsheng Zhang†, Ming Li, Chuan Wang, Jianjun Yang, Tianjue Zhang,
China Institute of Atomic Energy, Beijing, China

Abstract

In order to increase turn separation and accordingly extraction efficiency in a superconducting cyclotron CYCIAE-230, a first harmonic bump is required to introduce beam processional motion. Eight trim-rods of variable position are employed at the extraction region to generate the desirable field bump. The amplitude and phase of first harmonics can be adjusted by changing the position of trim-rods to meet the requirements of extraction beam dynamics. However, its side effect on the isochronous field in acceleration region is inevitable. Therefore, the rest positions of trim-rods need to be determined and the re-shimming procedure of main magnet model needs to be implemented interactively. The effects of trim-rods and its influence on the isochronous field in a new model will be presented.

INTRODUCTION

CYCIAE-230, a superconducting cyclotron aims for proton therapy, is under design and construction at China Institute of Atomic Energy [1,2]. Beam dynamics and processional extraction design of CYCIAE-230 are studied for years. First harmonic bump is the source of procession in the extraction region, it could be generated from trim-coils as our former machine [3], but trim-rod field is more predictable and stable in the saturated pole region, and trim-rod method is proved effective in field shimming [4] and field excitation [5]. Extraction efficiency is the key parameter of extraction system, which related to radial oscillation amplitude, turn separation of particle motion and septum width of deflector. Trim-rods which located at the central line of each pole introduce first harmonic bump to provide enough processional motion and turn separation with the help of $\nu_r = 1$ resonance. In former extraction design stage, we adopted ideal Gaussian first harmonic field bump with fixed phase [6]. But real trim-rod field distribution should be employed for a precise result. And real field has effect on main magnet isochronous field which can be analysing by same model.

In this paper, two main magnet models, a 90 degree folded and a 360 degree one, are introduced. Trim-rod field is studied in detail with the 90 degree model, and the procedure of eight trim-rod position design to provide first harmonic bump with certain amplitude and phase is accomplished. Trim-rod field of 90 degree and 360 degree model with the same trim-rod position are compared. And finally, real trim-rod field effect on the isochronous field and the re-shimming results are presented.

* This work was supported by the National Natural Science Foundation of China under Grand Nos.11375273 and 1146114103
† email address: 18810681102@163.com

MAIN MAGNET AND TRIM-ROD MODEL

As the spiral sector pole model of CYCIAE-230 is complicated in trim-rod design, a straight sector pole model is used instead for simplicity. A 90 degree sector model (Fig. 1) is used in preliminary design to analyse the physical properties of trim-rod field and a full 360 degree model is used to determinate final trim rods parameters. The pole angle width and spiral angle had been well designed to get isochronous field and working diagram.

The extraction trim-rods are rod shaped with diameter of 30 mm and length of about 80 cm, located at the central line of each pole with radius 79 cm. Trim-rods are driven by electric motors separately. When a trim-rod is elevated, an air-rod is generated inside the pole, leading to a field bump which decrease main magnet field locally. First harmonic field with amplitude less than 10 Gauss and arbitrary phase can be achieved by positioning eight trim-rods. For simplicity, the trim-rods are replaced by square rods with same cross section area in models.

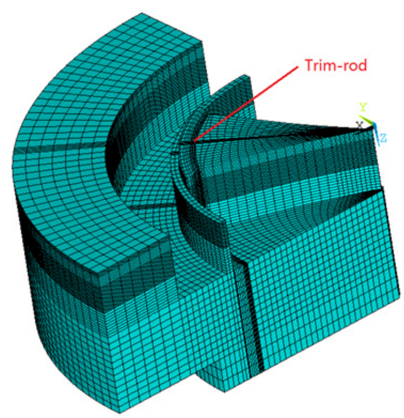

Figure 1: 90 degree straight sector model.

TRIM-ROD POSITION DESIGN

Main task of trim-rods physical design is to determine the height of each air-rod and the rest position of trim-rods. Design process is based on 90 degree sector model and the requirements of extraction beam dynamics. The oscillation amplitude at extraction point is mainly dependent on the amplitude and phase of the first harmonic bump, the FWHM of amplitude radial distribution $B_1(r)$ also has accumulative effect on oscillation amplitude, but the FWHM is hard to adjust.

It had been tested that first harmonic bump with following parameters reaches the highest extraction efficiency: 2.74 Gauss amplitude at 79 cm, 337 degree phase and the Gaussian fit of $B_1(r)$ has $\sigma = 6$ cm, and second harmonic amplitude should be less than 1 Gauss to minimize the effect of second order resonance. About 10% change of

ISBN 978-3-95450-167-0

first harmonic amplitude or 30 degree of first harmonic phase shift would not change extraction efficiency clearly. In design stage, trim-rods are designed to provide 5 Gauss amplitude first harmonic bump with arbitrary phase, and second harmonics vanishes in theory.

The trim-rod position design started with trim-rod field analysis in 90 degree model with one trim-rod. The maximum first harmonic amplitude of different trim-rod position is shown below. The travel length of trim-rod is estimated to be 15 cm. In order to meet the requirements of amplitude and phase, the adjusting range of single trim-rod should cover 5 Gauss range, which means that the travel length of trim-rod could be strict to smaller length to reach better linearity of the curve.

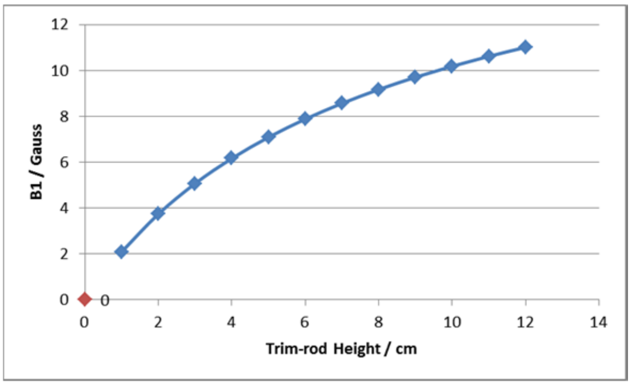

Figure 2: First harmonic amplitude vs trim-rod position.

Three groups of trim-rod travel length cover 5 Gauss range are designed, group 1: 1-5 cm height, group 2: 2-8 cm height, group 3: 3-11 cm height. Group 2 has proper range and margin and it is selected to present design procedure.

The travel length center with height 5cm is determined as the baseline of trim-rods and two steps are used for generate first harmonic bump. 1) Lift or drop eight trim-rod to the baseline, which induce isochronous field change but the first harmonic bump remains zero. 2) Lift or drop opposite four trim-rods to generate first harmonic bump with fixed phase, which would not change isochronous field because of good linearity of curve in Fig. 2.

In the range of 2-8 cm, we assumed that the radial distribution shape of amplitude is independent of trim-rod position, while first harmonic amplitude is linear with trim-rod height, also we supposed that the peak of amplitude distribution lies at 79 cm, and harmonic field phase around 79 cm does not change observably, which have been verified in later simulation result. Then harmonic field at 79 cm can be represented by the equation

$$B(z) = C(z)(0.4961 + 1.0000\cos\theta + 1.0198\cos 2\theta + ..)$$

While the constants are solved from baseline field and $C(z) = az + b$ is linear fitting of curve in Fig. 2 in range 2-8 cm.

In consideration of trim-rod location and first harmonic phase, the total first harmonic field can be written as:

$$\begin{aligned} B_1 =& C(z_1)\cos(\theta-45^\circ) + C(z_2)\cos(\theta-135^\circ) + \\ & C(z_3)\cos(\theta-225^\circ) + C(z_4)\cos(\theta-315^\circ) \\ =& \frac{\sqrt{2}}{2}a[(z_1 - z_2 - z_3 + z_4)\cos\theta \\ & + (z_1 + z_2 - z_3 - z_4)\sin\theta] \end{aligned}$$

and the total second harmonic field is

$$\begin{aligned} B_2 =& 1.0198[C(z_1)\cos(\theta-90^\circ) + C(z_2)\cos(\theta-270^\circ) + \\ & C(z_3)\cos(\theta-450^\circ) + C(z_4)\cos(\theta-630^\circ)] \\ =& 1.0198a(z_1 - z_2 + z_3 - z_4)\sin 2\theta \end{aligned}$$

Synthesize all the constrictions: The phase of first harmonic field need to be $\theta_0 = 337°$, the second harmonic field vanishes in theory, the first harmonic amplitude should be as large as possible, and the position of four trim-rods lies in designed travel length, we get a linear programming dependent on the position of four trim-rod sets :

$$max \quad (z_1 - z_2 - z_3 + z_4)/\cos\theta_0$$
$$\begin{cases} \dfrac{z_1 + z_2 - z_3 - z_4}{z_1 - z_2 - z_3 + z_4} = \tan\theta_0 \\ z_1 - z_2 + z_3 - z_4 = 0 \\ z_1, z_2, z_3, z_4 \in [2cm, 8cm] \end{cases}$$

The result of problem is $z_1 = 3.788$ cm, $z_2 = 8.000$ cm, $z_3 = 6.212$ cm, $z_4 = 2.000$ cm, which could produce 5.78 Gauss first harmonic amplitude in theory. The first harmonic amplitude used in extraction is 2.74 Gauss, and trim-rod position should regression to the baseline according to the amplitude proportion. The theoretical values are $z_1 = 4.425$ cm, $z_2 = 6.422$ cm, $z_3 = 5.575$ cm, $z_4 = 3.578$ cm, respectively.

The solved trim-rod heights are examined by 90 degree model field with rotation and linear interpolation of the field data. The first harmonic has amplitude 2.66 Gauss, and phase 336.78 degree, which lies in the error bound, and the second harmonic amplitude is 0.25 Gauss, isochronous field at 79 cm is dropped by 13.9 Gauss. Error analysis shows that 0.1cm positioning precision would induce 0.24 Gauss first harmonic amplitude error and 4.9 degree first harmonic phase error at the worst case.

TRIM-ROD POSITION VARIFICATION IN 360 DEGREE MODEL

A new 360 degree model is designed to verify trim-rod position, this model contains upper half of the cyclotron, including 4 air-rods of different height. The result in 360 degree model is beyond expectation, while first harmonic amplitude is 2.98 Gauss, first harmonic phase is 339.91 degree. First harmonic amplitude is larger than 90 degree model result, and exceeds 10% limit on error, but the first harmonic phase and second harmonic amplitude is in the bound. The increase of first harmonic amplitude is intelligible, in 360 degree model, trim-rod at quad-

ISBN 978-3-95450-167-0

rant 1 induce minus field in other quads, but in 90 degree model, all the minus field are superposed in quadrant 1, which can reduce the first harmonic amplitude.

The proportional regression method is used again, the positions of four trim-rod sets in 360 degree model are: $z_1 = 4.465$ cm, $z_2 = 6.347$ cm, $z_3 = 5.544$ cm, $z_4 = 3.653$ cm. Calculation executed with new position gives anticipated result, the first harmonic amplitude is 2.74 Gauss, first harmonic phase is 339.94 degree, and the Gaussian fit of first harmonic amplitude radial distribution has $\sigma = 7.40$ cm, the isochronous field drop at 79 cm is 14.02 Gauss, and second harmonic amplitude is 0.21 Gauss. Harmonic amplitude and phase are shown in Fig. 4 and Fig. 5. The results show that after one iteration of trim-rod position, ideal first harmonic amplitude and phase is obtained, the linear assumption and linear programming method is robust.

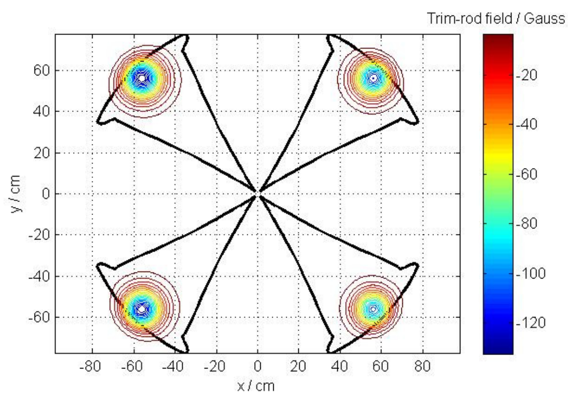

Figure 3: Trim-rod field in straight sector model.

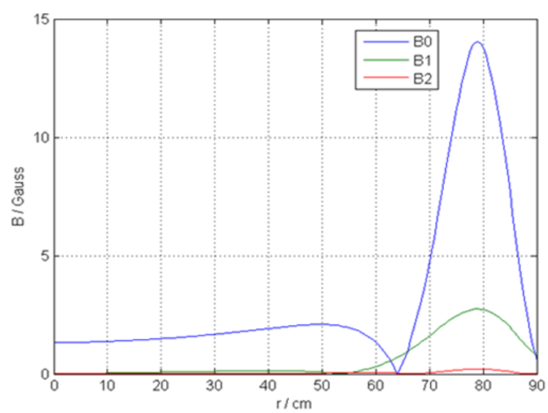

Figure 4: Harmonic amplitude radial distribution.

ISOCHRONOUS FIELD RE-SHIMMING

As shown in Fig. 4, four sets of trim-rod will generate 14 Gauss isochronous field drop at 79 cm, and about 2 Gauss field elevation in whole acceleration region. The frequency error due to trim-rod field is small but keeps negative in acceleration region and positive in extraction region, which can reduce accumulative effect to shift the phase slip curve. The phase slip is shown in Fig. 5. Although the maximal phase slip in acceleration region is about 15 degree, which is in the bound of error limit from acceleration beam dynamics, applying re-shimming process would lead to a smaller phase slip and accordingly a quicker acceleration process.

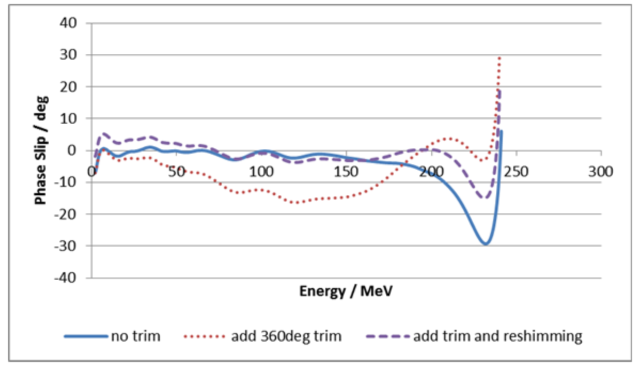

Figure 5: Phase slip and re-shimming effect.

Re-shimming is a negative feedback process of magnet pole angle width to minimize frequency error, and after two times of iteration the re-shimmed phase slip is shown in Fig. 5. And the variation of angle width is less than 0.1 degree.

In view of the trim-rod field effect on isochronous field, we recommend that in preliminary shimming process, the trim-rod effect on the isochronous field could be ignored, and in last time of shimming iteration, trim-rod sets should be placed at baseline.

CONCLUSION

Physical design of trim-rod position aims for providing first harmonic bump with fixed amplitude and phase is introduced in this paper. Linear programming method with linear assumption is used to reach the solution and present high robustness and accuracy. The trim-rod field has a small effect on isochronous field but can not to be reckoned with. And a re-shimming process is adopted to rectify frequency error and phase slip.

REFERENCES

[1] T. J. Zhang *et al.*, "The present situation and the prospect of medical cyclotrons in China", *Science China Physics, Mechanics and Astronomy*, vol. 54, no. 2, pp. 260-265, 2011.

[2] T. J. Zhang *et al.*, "Developments for 230 MeV superconducting cyclotrons for proton therapy and proton irradiation", in *Proc. ECAART'12*, Finland, July 2016, unpublished.

[3] T. J. Zhang *et al.*, "The beam dynamics study for the CYCIAE-100 cyclotron", *Nucl. Instr. Meth. A*, vol. 676, pp. 90-95, 2012.

[4] B. Qin *et al.*, "Design study of a 250 MeV superconducting isochronous cyclotron for proton therapy", in *Proc. SAP2014*, Lanzhou, China, Aug. 2014, paper WEPMH3, pp. 23-25.

[5] T. Stephani *et al.*, "Automated operation and optimization of the VARIAN 250MeV superconducting compact proton cyclotron", in *Proc. Cyclotrons'10*, Lanzhou, China, Sep. 2010, paper MOPCP021, pp. 93-95.

[6] T. Ge, M Li, "Preliminary design of CYCIAE-230 extraction system", internal report, Aug. 2016.

ISBN 978-3-95450-167-0

INVESTIGATION OF MINIMIZED CONSUMPTION POWER ABOUT 10 MeV CYCLOTRON FOR ACCELERATION OF NEGATIVE HYDROGEN

Jongchul Lee†, Khaled M.M. Gad, Huisu Kim,
Department of Energy Science, Sungkyunkwan University, Suwon, Korea

Sangchul Mun, Ho Namgoong, Donghyub Ha, Mitra Ghergherehchi, Jong-Seo Chai[1]
College of Information & Communication Engineering, Sungkyunkwan University, Suwon, Korea

Abstract

SKKUCY-10 cyclotron with 10 MeV particle energy was designed with purpose of production about fluorodeoxyglucose (FDG). Design strategy was maximization of accelerating voltage in order to secure the turn separation. Magnet had deep valley type, RF cavity had four stems and one RF power coupler. There was internal ion source for compact design of cyclotron. Specification of cyclotron was analysed by simulating particle dynamics for central region and whole system. AVF cyclotron had 83.2 MHz of radio frequency, 1.36 T of average magnetic field, 40 kV of main accelerating voltage. Phase slip between RF and beam was less than 15 degrees, minimum turn separation was over 2 mm. Specifications of both single beam analysis of reference particle and multi-beam analysis of bunch of particles were calculated by using Cyclone v8.4 and CST-Particle studio codes.

INTRODUCTION

Cyclotron was one of main device to product medical radio isotopes such as ^{18}F, ^{13}N, ^{11}C, ^{15}O for PET and ^{64}Cu, ^{67}Ga, ^{99m}Tc, ^{123}I for SPECT and so on [1]. Since fluorodeoxyglucose(FDG) was useful for diagnosis of cancer by using positron emission tomography machine, cyclotron was started to developed rapidly for production of ^{18}F isotope. Production yield of ^{18}F was studied with many nuclear reaction, there were optimal condition, acceleration energy, type of particle. Main process was also discovered (p, n) reaction at ^{18}O liquid target with few MeV energy level.

Design strategy of cyclotron was affected by user, medical physicist and researcher of radio isotope, and cyclotron market. Most cyclotron was distinguished by accelerating energy. One of design goal is compact size or high current with low energy for production of medical isotope with 7~20 MeV, another is high efficiency with 30~100 MeV for research field. There also be higher energy 100, 250 MeV cyclotron in order to apply the proton therapy or production of neutron [1- 3].

Cyclotron of ^{18}F production was developed to maximize the beam current with optimal energy 9~11 MeV. Low energy cyclotron usually had sector focus magnet typed pan cake and internal penning ionization gauge ion source. There are two types low energy cyclotron, one is used 4 stems dee and deep valley magnet, other is 2 stems dee and shallow valley magnet [4, 5]. Deep valley design was known that it has advantage of increasing characteristic of vertical focus. It was affected to decrease the beam losses inside cyclotron, to maximize the emission current at the target. One of main limitation of emission current is performance of internal ion source, it is depended on number of particle in the plasma region inside of chimney. So there was high current cyclotron used two internal ion source in order to increase the emission current [6].

DESIGN OF MAIN STRUCTURE

Cyclotron focused production of ^{18}F isotope was designed for acceleration of negative hydrogen ion with 10 MeV peak energy. Main strategy of design was maximization of beam current keeping the small size of cyclotron. Design of cyclotron was performed by progressing four steps. First one is selected radio frequency 83.2 MHz, fourth harmonics considered specification of RF power, size of magnet and coil power.

Design Concept

Cyclotron for 10 MeV was consisted of sector focus magnet, coils, half wavelength resonator, PIG internal ion source and vacuum chamber. Scheme of structure was represented in Fig. 1, it is shown cross section view according to beam plane (z = 0). Magnet has 8 hills and shim bar, four side yokes, RF system was consisted of four dees and four liners, one power coupler and fine tuner. Vacuum chamber was positioned between coil and hill, one PIG ion source connected with chamber.

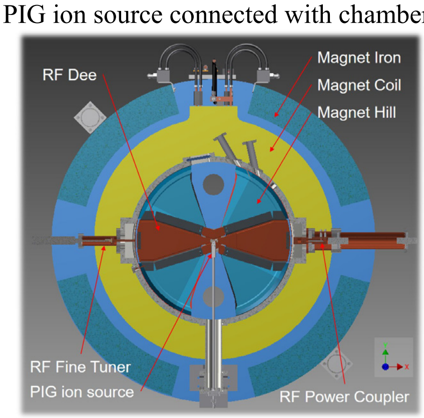

Figure 1: Cross section view of 10 MeV cyclotron.

Main parameter of cyclotron structure was listed up at Table 1. There were four sectors in the magnet iron, pole radius was 750 mm. When radio frequency is 83.2 MHz, isochronous radius for 10 MeV is calculated about 335

[1] jschai@skku.edu Corresponding author
† jcjc@skku.edu First author

mm, average magnetic field is 1.365 T. Hill radius was selected 365 mm, it was considered size and power consumption of coil. Resonator also was designed with consideration about magnet, and power consumption. Since this cyclotron was used internal ion source, electric field and RF was matched and optimized with PIG source structure. Main goal of design was increase of beam current with keeping the emission energy. Beam energy was calculated 9.8 MeV, beam current was analysed 197 µA having 2.15 pC charge in a one bunch at the one turn in central region.

Table 1: Main Specification for 10 MeV Cyclotron

Main parameter	Value
Pole Height [mm]	815
Pole Diameter [mm]	1500
Weigh [t]	9
Number of Sector	4
Coil Consumption Power [kW]	26
RF [MHz]	83.2
Harmonic	4^{th}
Number of Dee	2
RF Consumption Power [kW]	14
Type of Ion Source	Internal PIG
Ion Source Power [kW]	1.5

Magnetic Field Design

Magnet was consisted of return yoke, hills, center poles and coils in the Fig. 2. Design of magnet structure was started firstly for cyclotron, and magnetic field distribution was analysed by using TOCSA in OPERA3D code [7]. Optimization steps were that isochronous magnetic field was calculated, phase error analysis, and correction of magnetic field by using single beam dynamics code, CYCLONE v8.4 [8]. Correction magnetic field was ideal state for accelerating single particle until 10 MeV, so the structure of magnet was changed to satisfy the simulation result compared correction magnetic field with many iterations of simulation.

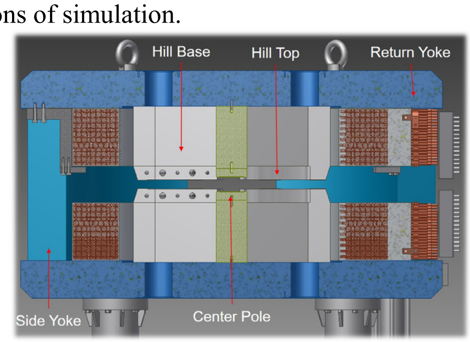

Figure 2: Mechanical scheme of magnet structure in vertical plane direction.

Optimal magnetic field was represented in Fig. 3. In order to get the result rapidly, symmetry of one-eighth was applied. Magnetic field was shown on the centre region of coil, radius was 365 mm. The range of field value was from 0.34 to 2.0 T, and higher field was calculated on the hill.

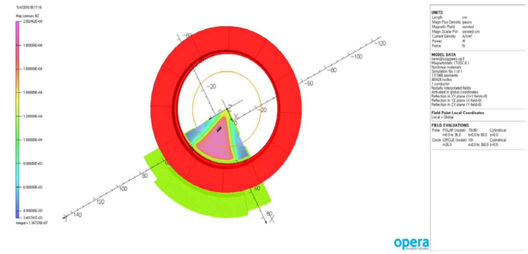

Figure 3: Magnetic field distribution at beam plane by using TOSCA in OPERA3D code. Red color is high magnetic field, almost 2 T, on the hill.

Electric Field Design

Electric field is performed acceleration of particles, resonator was designed by applying the coaxial cable structure. Resonator was consisted of four main dees, four liners and one power coupler and RF tuner in the Fig. 4. Dee and liner were connected with stems, it was played role of inner conductor in coaxial cable. All component is connected vacuum chamber, dees and liners on the left and right side are connected central dee, center liner and puller. Magnet of 10 MeV cyclotron had deep valley structure, so resonator was designed like connected two coaxial cables. Dee angle was selected 35°, stem position and radius was optimized for matching the radio frequency and electric field distribution. Power coupler and RF tuner was designed by applying capacitive coupling.

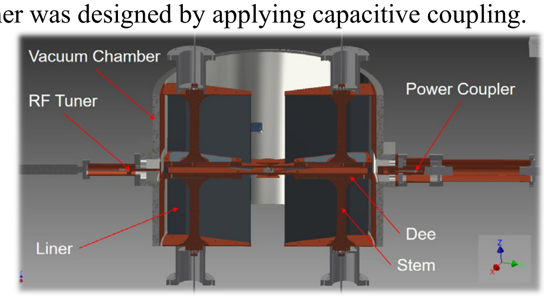

Figure 4: Mechanical drawing of RF resonator on view of vertical cross section, there are four dees and liners, one power coupler and RF tuner.

Resonator was generated accelerating electric field for negative hydrogen particles. Main resonant mode is $TEM_{00}c$ in the coaxial cable. There were many methods to design accelerating voltage, assuming delta function of gap voltage, DC analysis and RF analysis. Cyclotron used PIG internal ion source had puller for extraction particles from chimney in the ion source. So main specification of emitted particle was decided at the central region, and then fine analysis of accelerating voltage should be considered in this position. Figure 5 shows electric field distribution by using eigen mode analysis by using CST-MWS code. The result of electric field fitted absolute value was plotted on the beam plane, and it was normalized to one joule stored energy. Radius 150 mm was selected for standard 40 kV acceleration at an acceleration gap because of unstable voltage distribution at the radius.

ISBN 978-3-95450-167-0

Cavity loss power was calculated 12.7 kW to generate an electric field with 40 kV gap voltage at the gap on the 150 mm radius.

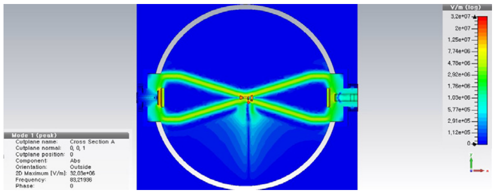

Figure 5: Electric field distribution on the beam plane by using eigen mode simulation in CST-MWS code [9], radio frequency 83.21 MHz and peak electric field was 32 MV/m at stored energy 1 joule.

ANAYLSIS OF BEAM SPECIFICATION

Magnetic and electric field was conformed after beam dynamics was considered by using the calculation code. The design of cyclotron affects two fields, so it is resulted beam specification. Analysis of beam characteristic was separated two parts, one was main accelerating part and other was bunching part. When the magnet structure was designed by correction magnetic field, main feature of acceleration was checked in the Fig. 6 by using CYCLONE v8.4 code. It could be calculated single particle tracking by using magnetic field and acceleration voltage. But it needed assumption about electric field and initial beam characteristics. So phase between beam and isochronous magnetic field was checked carefully, and then other code for more detail analysis was used.

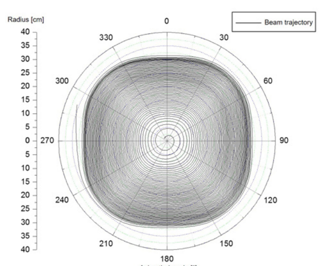

Figure 6: Single particle tracking for 10 MeV cyclotron, magnetic field was used simulation of structure, and electric field was brought assumption the constant voltage value. Initial beam position also was assumed until beam phase was fine result compared isochronous condition.

It was applied to analyse the beam specification by using multi particle calculation, especially central region. Analysis method of single particle tracking was benefit to design magnetic field quickly, but it could not calculate the beam efficiency and bunching effect. So Particle In Cell (PIC) solver was used for checking the particle specification. Electric field as well as magnetic field was imported from each simulation results, and input beam current was selected at an internal ion source. Beam energy and current was checked 190 keV, 197 µA after third accelerating gap because a bunch was formed after 3rd gaps. Figure 7 shows cross section view of particle distribution in the central region. Particles hit to the center dee surface, but they were not high charge density. Charge of a bunch was calculated 2.15 pC with 83.2 MHz frequency.

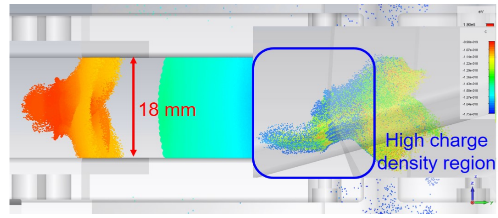

Figure 7: particle distribution, the color of left picture means that red is high energy 190 keV, and right picture shows charge density distribution, blue color means higher charge because of negative signal.

CONCLUSION

10 MeV cyclotron was designed for increase efficiency of beam current in terms of detail structure of magnet, resonator, and so on. Main specification of cyclotron was selected, 1.5 m pole diameter, 0.8 m pole height, 83.2 MHz radio frequency and 4th harmonics. Total consumption power was about 40 kW for beam power 1 kW (peak energy 9.8 MeV, peak current 90 µA). Magnetic and electric field were designed by using TOSCA in OPERA3D, Eigen mode solver in CST-MWS. These fields were possible to accelerate negative particles it was verified by beam dynamics specifications. Main acceleration was checked from analysis of single beam dynamics by CYCLONE v8.4 code, and low energy part, central region, was analysed as a bunch by using PIC solver in CST-PS. Especially initial beam bunch was analysed after cross to 3rd acceleration gap, peak beam energy 190 keV, charge of a bunch 2.15 pC.

ACKNOWLEDGEMENT

This work was supported by the National Research Foundation of Korea(NRF) grant funded by the Korean government (MSIP:Ministry of Science, ICT and Future Planning) (No. NRF-2015M2B2A8A10058096).

REFERENCES

[1] P. W. Schmor, "Review of Cyclotrons Used in the Production of Radio Isotopes for Biomedical Applications", in *Proc. Cyclotrons'10*, Lanzhou, China, September 2010.

[2] A. I. Papash, "Commercial Cyclotrons. Part 1: Commercial Cyclotrons in the Energy Range 10-30 MeV for Isotope Production", *Physics of Particles and Nuclei*, vol. 39, No. 4, 2008, pp. 597-631.

[3] A. Gerbershagen *et al.*, "The Advantages and Challenges of Superconducting Magnets in Particle Therapy", *Superconductor Science and Technology*, vol. **29**, no. 8, 2016, 083001.

[4] E. Forton, "Design of IBA Cyclone 30XP Cyclotron Magnet", in *Proc. Cyclotrons'10*, Lanzhou, China, September 2010.

[5] In Su Jung, "A Design of RF System for KIRAMS-13", *in Proc. of the Korean Nuclear Society Spring Meetings*, Gyeongju, 2004.

[6] IBA, `http://www.iba-radiopharmasolutions.com/`.

[7] OPERA, `http://operafea.com/`.

[8] B. F. Milton, “CYCLONE VERS 8.4”, TRIUMF, Vancouver, BC, Canada, June 1999, TRI-DN-99-4.

[9] CST, `www.cst.com/`.

ISBN 978-3-95450-167-0

SIMULATION CODE DEVELOPMENT FOR HIGH-POWER CYCLOTRON*

Chul Un Choi, Moses Chung†, UNIST, Ulsan, Korea
Seunghwan Shin‡, Jaeyu Lee, Tae-Yeon Lee, PAL, Pohang, Korea
Ga Ram Hahn, KIRAMS, Seoul, Korea

Abstract

A high power cyclotron is a good candidate as a driver of the accelerator driven system for the transmutation of long lived nuclear wastes. In this work, a simulation code has been developed for describing the beam dynamics in the high power cyclotron. By including higher order terms in transverse transfer matrix and space charge effects, we expect to describe the beam motion more accurately. The present code can describe equivalent orbit at each energy, calculate the tunes, and also perform multi-particle tracking. We report the initial results of the code for the simulation of a 13 MeV cyclotron. Lastly, an upgrade plan is discussed to add more features and to increase calculating efficiency.

INTRODUCTION

In Korea, nuclear energy occupies about 40 percent of the electric power production. It can be a solution to the energy problem that we are facing these days before commercializing nuclear fusion energy. But one of the difficulties is that expanding nuclear power plant as the nuclear power is dangerous when natural disaster occurs, thus, high-level radioactive waste that has a half-life of a few hundred thousand years is created. To transmute from high-level radioactive waste to short-lived radioisotope, development of high power cyclotron which is part of ADS (Accelerator Driven System) is very desirable.

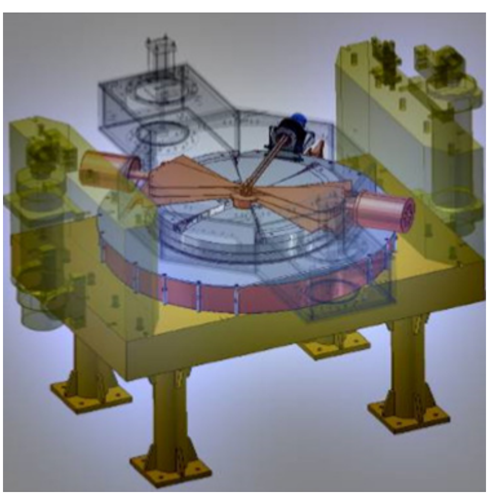

Figure 1: 13 MeV cyclotron.

* This research was supported by the Basic Science Research Program through the National Research Foundation of Korea (NRF-2015R1D1A1A01060049).
† mchung@unist.ac.kr
‡ tlssh@postech.ac.kr

As benchmark study for the simulation code, we simulate beam dynamics in KIRAMS 13 MeV Cyclotron (Fig. 1). The KIRAMS 13 MeV Cyclotron has four sector magnets and a RF cavity where it has its frequency of 77.3 MHz, Ion sources are producing proton beam and the beam current is 80 μA. The EO Code (Equilibrium Orbit Code) including beam tracking function is written by Matlab to demonstrate equilibrium orbit of multi-particle beam. This code uses Runge-Kutta Gill method to solve integration of the canonical equations of motion. This code does not yet include acceleration effect, but the conventional way of adding small energy is adopted. So the present code can describe equilibrium orbit at each energy level, and we can analyze various physical parameters such as equilibrium orbit, phase space, phase error, betatron tune, resonances and Twiss parameters.

In the future, we will add acceleration effect and algorithm of space charge effect in EO Code.

BEAM TRACKING

The magnetic field distribution (Fig. 2) is designed by OPERA-3D.

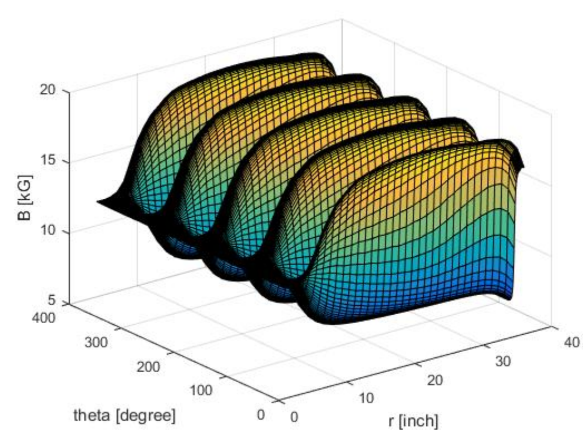

Figure 2: Magnetic field distribution with respect to r and θ.

The characteristic of EO Code is based on the integration of the canonical equations of motion [1]. EO Code uses Runge-Kutta Gill method to calculate differential equations of motion. EO Code consists of several steps. First, this program calculates equations of motion which are r, p_r, x and p_x as a function of θ. Second, this program checks whether closed orbit is made or not. If closed orbit is not made, the program increases r and p_r of particle and iterates to find closed orbit of particle. If a closed orbit is made, the program then calculates the equations of motion in the z and p_z. Third, the program proceeds to the next orbit of the iteration process by increasing energy of particle. This process repeats until our target energy. Finally, we can calculate various physical parameters when this iteration process ends.

$$dr = \frac{rp_r}{p_\theta} d\theta, \tag{1}$$

$$dp_r = (p_\theta - q' rB) d\theta, \tag{2}$$

$$\frac{dx}{d\theta} = \frac{p_r}{p_\theta} x + \frac{rp^2}{{p_\theta}^3} p_x, \tag{3}$$

$$\frac{dp_x}{d\theta} = -\frac{p_r}{p_\theta} p_x - q\left[B + r\frac{\partial B}{\partial r}\right] x, \tag{4}$$

$$dz_z = \frac{rp_{z2}}{p_\theta} d\theta, \tag{5}$$

$$dp_z = \left(\frac{\partial B_r}{\partial r} - \frac{p_r}{p_\theta}\frac{\partial B_\theta}{\partial \theta}\right) d\theta. \tag{6}$$

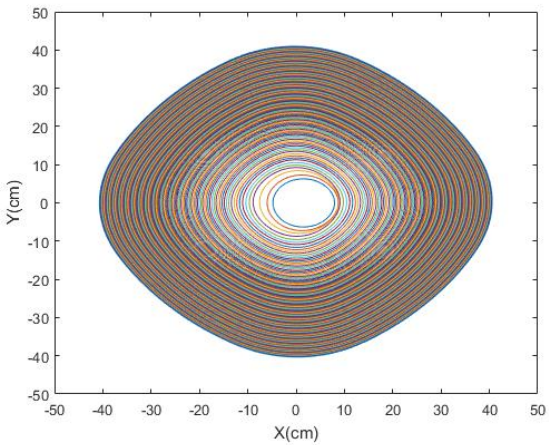

Figure 3: Equilibrium orbit of beam.

DATA ANALYSIS

Using the EO code, we can analyze a variety of physical parameters (i.e., equilibrium orbits, phase space distributions, betatron tunes and resonances, etc.)

Phase Space

We are tracking particle motion in phase space along degree and radial direction by the transfer matrices in Eqs. (7) and (8). The x coordinate represents radial direction, and z coordinate represents vertical direction. The EO Code distributes 2000 particles by Gaussian distribution. We can see how the particle distribution in phase space changes for each angular and radial position of the orbit.

$$\begin{pmatrix} x \\ p_x \end{pmatrix}_\theta = \begin{pmatrix} x_1 & x_2 \\ p_{x_1} & p_{x_2} \end{pmatrix} \begin{pmatrix} x \\ p_x \end{pmatrix}_i , \tag{7}$$

$$\begin{pmatrix} z \\ p_z \end{pmatrix}_\theta = \begin{pmatrix} z_1 & z_2 \\ p_{z_1} & p_{z_2} \end{pmatrix} \begin{pmatrix} z \\ p_z \end{pmatrix}_i . \tag{8}$$

Figure 4 shows the phase space particle motions in vertical plane at two different angles (blue dots at 2 degree and red dots at 300 degree) but same turn number (both in first turn).

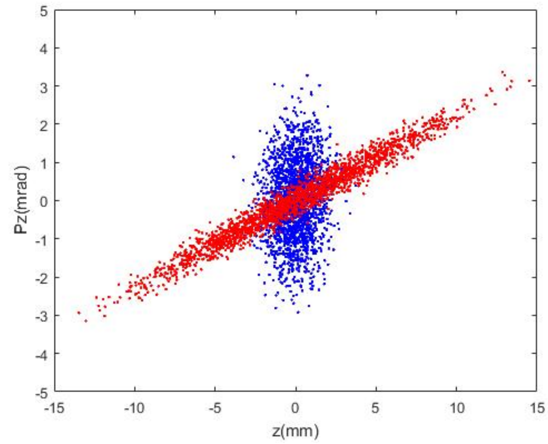

Figure 4: Distributions of particles in phase space for vertical direction.

Betatron Tune and Resonance

Betatron tune is defined as the number of the betatron oscillation during one closed orbit [2]. We can calculate betatron tune by transfer matrices in Eqs. (7) and (8). In Eqs. (9) and (10), ν_x and ν_z are betatron tunes of radial direction and vertical direction.

$$\cos \nu_x = \frac{1}{2}(x_1 + p_{x_2}), \tag{9}$$

$$\cos \nu_z = \frac{1}{2}(z_1 + p_{z_2}). \tag{10}$$

Figures 5 and 6 show turn excursions with respect to beam energy for radial plane and vertical plane, respectively.

Resonance is an important factor in accelerator. Amplitude of betatron oscillation is increased when resonance is occurred and increase of the amplitude causes beam loss. Furthermore, cyclotron has serious damage when beam loss occurs. Therefore, betatron tune must avoid major resonance to decrease such damage. Calculated tunes are compared with the major resonance lines in Fig. 7. Around first few turns, the beam passes through the integer radial tune. This is due to the small field bump applied near the center in order to focus beam vertically. However, it is not so harmful to the beam because the beam passes through this resonance quickly due to the rather large turn separation. Excepting this region, calculated tunes in vertical and radial planes are between integer tune and half integer tune.

ISBN 978-3-95450-167-0

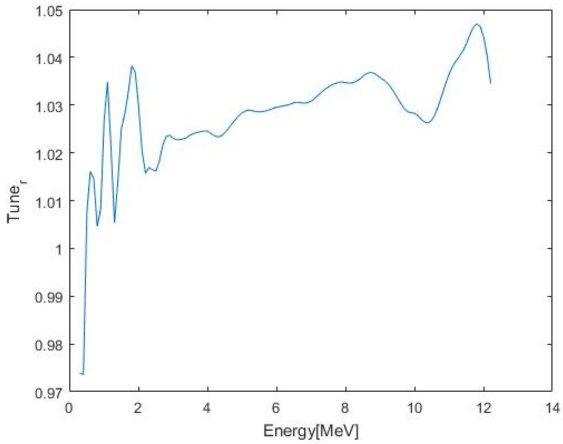

Figure 5: Radial tune variation with respect to beam energy.

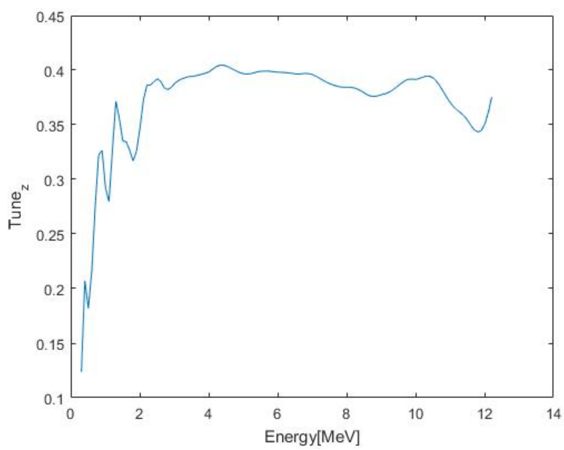

Figure 6: Vertical tune variation with respect to beam energy.

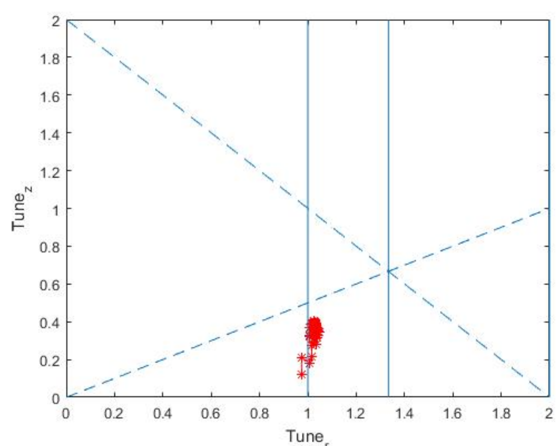

Figure 7: Operating point on tune diagram.

FUTURE PLANS

Now the interest of high power cyclotron is increasing in the world. In Korea, based on the success of 13 MeV and 30 MeV KIRAMS Cyclotrons [3], small project to develop simulation code is carrying out. Main purpose of simulation code is to describe beam dynamics on high power cyclotron.

Currently, we work including acceleration effect in EO Code. And we will add higher order term of beam physics in EO Code by the end of 2016. Space charge effect algorithm which must be considered to simulate high power cyclotron will be inserted in EO Code later. In 2018, we will design high power cyclotron using developed EO Code.

CONCLUSION

EO Code is beam tracking code using Runge-Kutta Gill method. This code doesn't include acceleration effect, but current program adds small energy when one closed orbit is formed. We can analyze various physical parameters by simulating EO Code. In the future, we will add various effect term which are acceleration effect, higher order term and space charge effect for simulating high power cyclotron.

REFERENCES

[1] M. M. Gordon *et al.*, "Computation of closed orbits and basic focusing properties for sector-focused cyclotrons and the design of 'CYCLOPS'", *Particle Accelerators.*, vol. 12, pp. 13-26, Nov. 1983.

[2] Mario Conte, William W Mackay, *An Introduction to the Physics of Particle Accelerators*. Genova, Texas, USA, 2008.

[3] J. Kang, B.H. Hong, D.H. An, H.S Chang, I.S. Jung, J.S. Chai, M.G. Hur, T.K. Yang, and Y.S. Kim, "Design study of the 30 MeV Cyclotron magnet", in *Proc. EPAC'06*, Edinburgh, UK, Jun. 2006, paper WEPLS078, p.2559.

NUMERICAL ORBIT TRACKING IN 3D THROUGH THE INJECTOR CYCLOTRON FOR HEAVY IONS AT iTHEMBA LABS

J. G. de Villiers*, J. I. Broodryk, J. L. Conradie, F. Nemulodi, R. W. Thomae,
iThemba LABS, Somerset West, South Africa
J. J. Yang, T. J. Zhang, CIAE, Beijing, China

Abstract

The electric and magnetic fields of the second injector cyclotron (SPC2) [1] were modelled in 3D with finite element methods, using OPERA-3d [2], in an effort to determine the cause of the relative poor 5% beam transmission through the machine in the 8-turn mode. Simulation of the particle motion was done using machine operational parameters for acceleration of a $^{20}Ne^{3+}$ beam.

Using TOSCA [2], an isochronous magnetic field was calculated from a complete cyclotron magnet model and the electrostatic field distribution from a dee electrode model. The SOPRANO-EV [2] modelling of the RF resonance conditions of the resonators provided radial electric field profiles in the acceleration gaps.

A command line program was developed to combine the information of the three models and implement time-dependent control of the electrostatic fields during the particle tracking.

In addition, based on calculated data from OPERA-3D, the parallel particle-in-cell code OPAL-CYCL [3, 4] was used to calculate a particle orbit for comparison.

SIMULATION MODELS AND CONTROL

General

The SPC2 pre-accelerates heavy ion beams before injection into the separated sector cyclotron. The beam from one of the two external ion sources is axially injected upwards and bent into the median plane of SPC2 through a spiral inflector. It is a solid pole cyclotron with 4 radial magnet sectors and 8 trim coils. The electric fields in the 4 acceleration gaps are provided by two horizontal $\lambda/4$ coaxial resonators with 90° dees that operate in the frequency range 8.6 MHz to 26 MHz [5].

Simulating the 8-turn orbit mode in SPC2 requires cyclotron settings such that a particle crosses 34 acceleration gaps before reaching the electrostatic extraction channel (EEC), followed by another acceleration gap crossing before exiting the machine. The horizontal width of the EEC gap at the entrance is 14 mm and its radial centre position is adjustable between 456 and 470 mm.

The calculations reported here are based on known operational conditions for a $^{20}Ne^{3+}$ beam with an extraction energy of 3.81 MeV, for acceleration at a harmonic number of 6 and peak dee voltage of 37.4 kV at 12.16 MHz. The spiral inflector voltage and ion source extraction voltages are 4.3 kV and 13.37 kV, respectively.

The magnetic flux density in the centre is 0.88 T.

*gdevil@tlabs.ac.za

Cyclotron Magnet Model

The finite element model of the SPC2 magnet includes all geometrical detail of the steel and coils, together with the axial hole in the yoke that, amongst others, contains solenoids and steerer magnets in the lower half of the yoke. The known magnetic material characteristics of the iron are used in the simulation.

The same magnet model was used to build a database that is used to predict the coil currents required for isochronous magnetic fields at different particle energies [6].

The lower pole geometry of the magnet and coils are shown in Fig. 1.

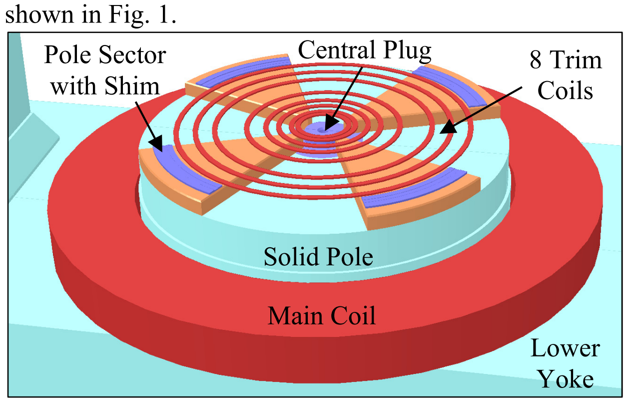

Figure 1: The lower half of the magnet pole geometry, including 4 pole sectors, shims and coils.

Acceleration Electrode Model

In order to obtain the fields in the acceleration gaps under RF conditions, the electric field profile in each acceleration gap was calculated with a model for each of the two RF resonators, using the eigenvalue solver of SOPRANO. The model shown in Fig. 2 includes the dees, dummy dees, puller, capacitors, short-circuit plates and central region, but without the inflector. The calculated normalized field values are shown in Fig. 3.

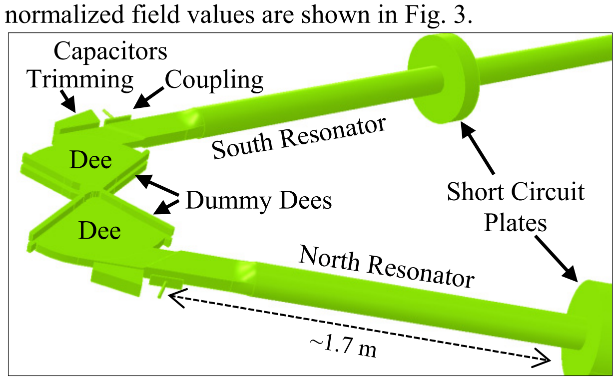

Figure 2: Model of the RF resonators without the outer conductors.

ISBN 978-3-95450-167-0

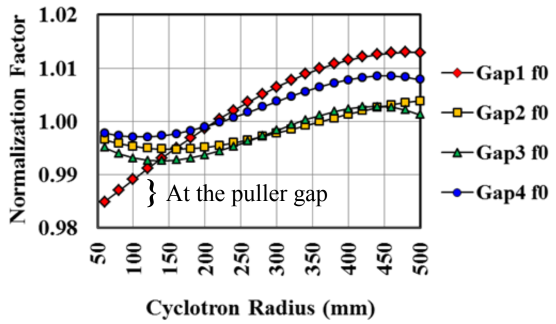

Figure 3: The calculated radial field profiles. (See Fig. 5 for the gap numbering).

Another model of the electrodes, which includes the inflector, was used to calculate the static electric field distribution with TOSCA. During particle tracking, the calculated normalized values of the RF fields are used to adjust the static electric field distribution.

The calculated effective lengths of the puller gap and subsequent 3 acceleration gaps are, respectively, 2.5 and 3.2 times larger than the respective physical lengths of 7.3 and 10 mm.

Control Program

An OPERA-3d command line program is used to combine the calculated data of the simulation models and define parameters for adjusting the conditions during the tracking of the particles through the cyclotron. The conversion of the calculated static electric field, E_s, to a time- and positional dependent field, is given by $E_t=A_R.E_s.sin(2\pi ft+\phi_0)$, where f is the RF frequency, ϕ_0 the injection phase of the particle to the dee voltage and t the time-of-flight parameter [7] that is inherently available when particle tracking is done in OPERA-3d POST [2]. The radial adjustment parameter of the RF field amplitude in an acceleration gap, A_R, is calculated in-flight from the applicable radial function shown in Fig. 3. Minor adjustments in the control program permit calculations at other harmonic numbers, implementation of alternative optimization methods and, if needed, to have flat-topping included.

RESULTS OF CALCULATIONS

A single reference particle orbit was calculated, which starts from the vertical injection axis in the centre of the cyclotron. The injection energy and inflector voltage were adjusted to deliver the particle onto the median plane after the inflector. The radial position of the particle at the entrance to the EEC and the extraction energy were optimized by adjusting its injection phase and the dee voltage, using the calculated magnetic field.

Starting on the median plane from a point between the inflector and puller, the central particle orbit was also calculated with OPAL-CYCL. Identical input parameters were used, but the radial correction factor on the dee voltage, A_R, was not implemented for OPAL-CYCL. The positions of the orbits agree well, as shown in Fig. 4.

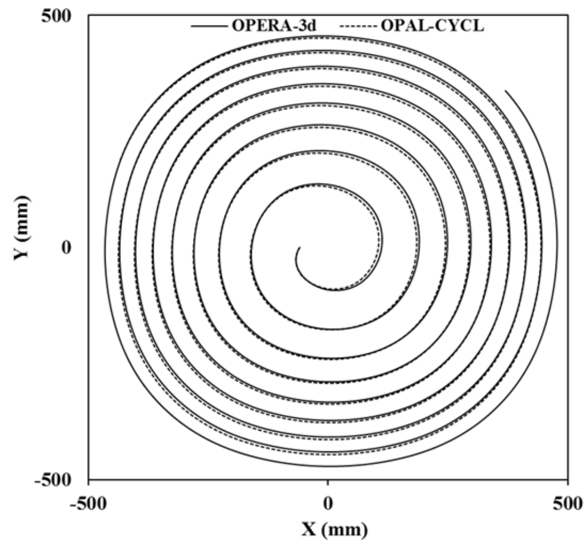

Figure 4: A comparison of the calculated orbits of the reference particle at harmonic number 6 with OPERA-3d (solid line) and OPAL-CYCL (dashed line) shows very good agreement.

A longitudinal bunch length of 14 RF degrees was simulated by using two more particles, one leading and the other lagging by 7 RF degrees from the injection phase of the central reference particle. The injection phase and dee voltage were adjusted to minimize energy spread at extraction, further referred to as optimization method 1 (OM1). The three particles were tracked from a starting position after the inflector and optimized to pass through the EEC with a radial beam width of 5 mm and energy spread of 1.3% at an extraction energy of 4.01 MeV.

For multi-particle tracking horizontal and vertical phase ellipses of 10 π mm.mrad were tracked through the machine for each of the three reference particles that define the longitudinal bunch length of 14 RF degrees.

Using OM1, the energy spread in the beam after one turn is a high 30.7% at beam energy 0.417 MeV, which implies that beam losses for high intensity beams should be expected up to extraction. The transit-time factors are 0.932 and 0.868 for the puller gap and subsequent gaps, respectively. At extraction the energy spread is 2.99% at 4.02 MeV. The calculated orbits are shown in Fig. 5.

The same beam was tracked by using another beam optimization method (OM2). It comprises an iterative process of improving the beam centring, field isochronization and injection phase corrections, and finally by changing of the injection angles of the leading and lagging particles in the beam bunch, respectively, by +1° and -1° from that of the central particles. The last step of differentiated injection angles cannot be implemented in SPC2 at this stage. The energy spread after one turn is 6% at beam energy 0.401 MeV and 1.5% at extraction energy 4.04 MeV. The optimized orbits are shown in Fig. 6. The calculated phase history of the central particle, with the 9 crossings of the centre of the first acceleration gap, is shown in Fig. 7.

ISBN 978-3-95450-167-0

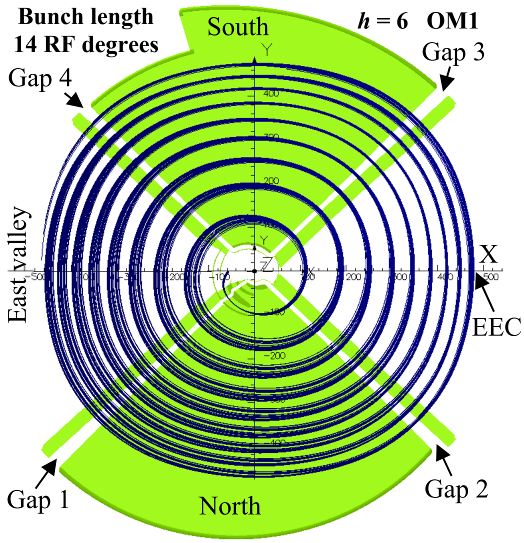

Figure 5: The calculated beam orbits for initial horizontal and vertical beam emittance of 10 π mm.mrad and a longitudinal bunch length of 14 RF degrees, optimized with OM1. The orbits are shown superimposed on the lower half of the model of the acceleration electrodes.

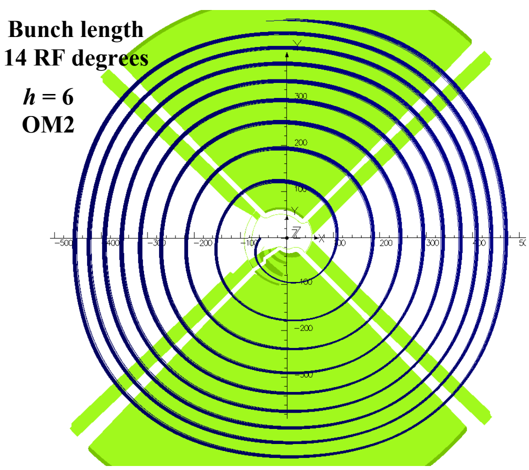

Figure 6: Using OM2, the new calculated beam orbits in SPC2 for initial horizontal and vertical beam emittance of 10 π mm.mrad and a longitudinal bunch length of 14 RF degrees, are shown superimposed on the lower half of the model of the acceleration electrodes.

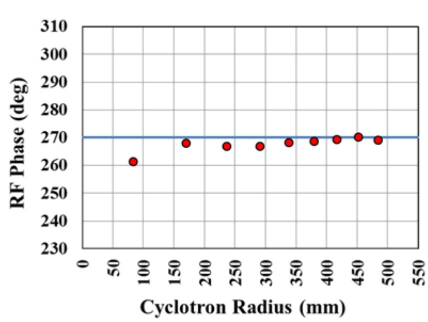

Figure 7: The calculated phase history of the central particle with its 9 crossings of the first acceleration gap, calculated with the better optimized beam (OM2) at harmonic number 6. The solid horizontal line at 270° represents the peak of the RF phase at gap 1.

Analysis of the beam transmission through the inflector showed large defocussing of the beam, especially in the vertical direction. This was later confirmed by visual inspection of the surfaces around the 10 mm high entrance window of the puller channel. Thus, with larger beam emittance beam losses can be expected at the puller window, which is located about 60 mm downstream from the inflector. Back-tracking of phase ellipses through the inflector to the injection line showed unattainable injection conditions, as is graphically illustrated in Fig. 8 with tracked orbits through the inflector.

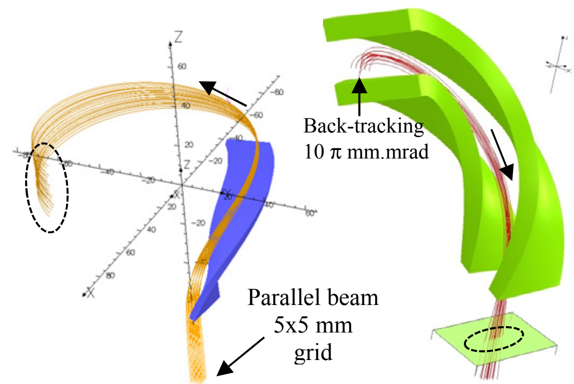

Figure 8: The strong beam defocussing effect of the inflector is illustrated in the left hand picture by the forward tracking of 25 particles, all starting parallel to the vertical injection axis (Z) from a 5x5 mm grid. One electrode plate was removed in the illustration. On the right hand side is the back-tracking calculation of a beam of particles with a horizontal and vertical phase-ellipse of 10 π mm.mrad.

The strong vertical defocussing in the inflector is quantified with the calculated transmission results, as shown in Fig. 9 for the back-tracking of horizontal and vertical emittance of 10 π mm.mrad. The vertical divergences will, with the high intensity beams, result in beam losses at the puller window.

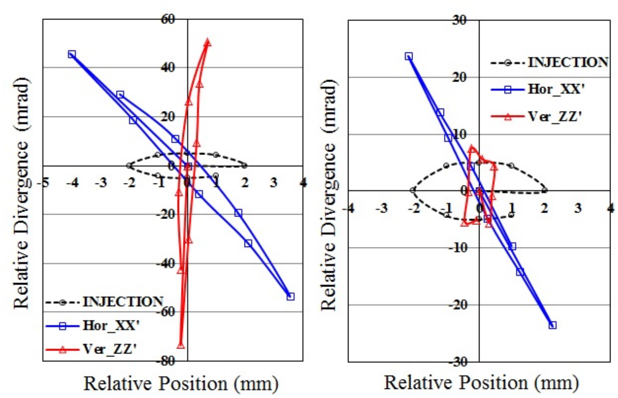

Figure 9: The calculated transmission through the inflector with an injected emittance of 10 π mm.mrad (dashed line) is shown, respectively, for the horizontal (figure on the left) and vertical (figure on the right) phase spaces. The cross-coupling to the horizontal (XX') and vertical (ZZ') phase spaces for both of the injected phase ellipses is evident.

ISBN 978-3-95450-167-0

Acceleration of $^{20}Ne^{3+}$ to 3.81 MeV at a harmonic number of 2 was also studied, even though the required frequency of 4 MHz is beyond the range of the RF system of SPC2. A horizontal and vertical emittance of 10 π mm.mrad was again tracked for each of three reference particles. The transit-time factors are 0.992 and 0.985 for the puller gap and subsequent 3 gaps, respectively.

For the two harmonic numbers, 6 and 2, and two optimization methods, OM1 and OM2, beam bunches of 14 RF degrees were compared after one turn in the cyclotron, at the EEC and at extraction. OM2 significantly improved the beam quality and consequently will improve the transmission efficiency. The calculated beam characteristics are listed in Table 1.

Table 1: Beam Quality Comparison

Harmonic number	**6**	**6**	**2**	**2**
Optimization Method	OM1	OM2	OM1	OM2
Radio-frequency (MHz)	12.16	12.16	4.053	4.053
Acceleration voltage (kV)	43.9	41.5	38.1	38.1
Bunch length (RF degrees)	14	14	14	14
Energy after 1 turn (MeV)	0.417	0.401	0.478	0.478
Energy spread after 1 turn	30.7%	6%	4.8%	1.3%
Extraction energy (MeV)	4.02	4.04	3.97	4
Extraction energy spread	3%	1.5%	2.2%	0.9%
Radial width at EEC (mm) [energy spread+emittance]	11	9	9	5
Radial width at EEC (mm) [energy spread]	7.2	3.6	5.3	2.2

The kinetic energies after one turn in the cyclotron were calculated in a vertical plane on a radial line along the centre of a valley and are shown in Fig. 10.

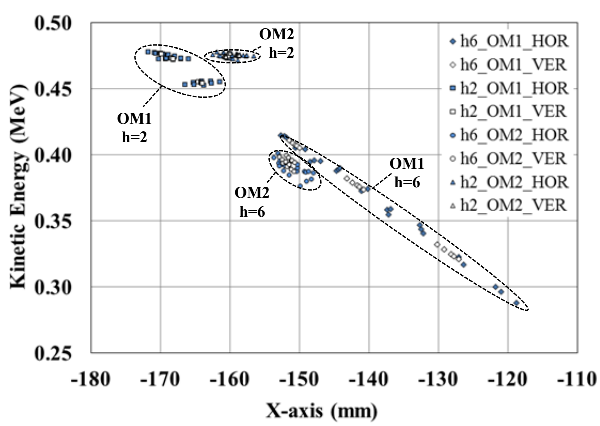

Figure 10: The beam bunch energies after 1 turn, obtained at harmonic numbers 6 and 2, for the two optimization methods.

For OM1 and harmonic number 2 a bunch length of 28 RF degrees was extracted with an energy spread of 4.2% at 4 MeV. The corresponding radial beam width due to the energy spread and emittance is 13 mm.

Using OM2 with 28 RF degree beam bunches for harmonic numbers 6 and 2, energy spreads of 4.8% and 3.2% were respectively obtained at extraction energy 4 MeV. The radial beam widths due to the energy spread and emittance are 16 mm and 10 mm, respectively.

CONCLUSIONS AND REMARKS

This study of the beam transmission through SPC2 led to the construction of several simulation models. The associated beam analysis methods and tools for 3D particle tracking can be used with any cyclotron.

The method used for minimizing the energy spread at extraction only, cannot fully compensate for the energy spread induced at the first few acceleration gaps. Large beam losses are to be expected in SPC2 with this method at harmonic number 6.

The transmission can be improved by more stringent beam optimization methods. It involves field and phase optimization, starting from the first turn in the cyclotron. The optimization methods will be studied further and implemented together with more diagnostic equipment, including a phase probe on a radial line in the cyclotron.

The spiral inflector also contributes to poor transmission through SPC2, due to its large vertical defocussing effect on the beam. An improved inflector design with significant improvement in the beam characteristics has been made.

The calculated databases will be implemented with OPAL-CYCL to calculate space-charge effects with high-intensity beams in SPC2.

The new user-friendly method of predicting isochronous magnetic fields for SPC2 from a calculated set of databases is a valuable improvement to cyclotron operation at iThemba LABS.

ACKNOWLEDGEMENTS

The study is jointly supported by the National Research Foundation of South Africa (No. 92793) and National Science Foundation of China (No. 11461141003).

REFERENCES

[1] Z. B. du Toit *et al.*, "Commissioning of the injector cyclotron for polarised and heavy ions at NAC", in *Proc. 14th Int. Conf. on Cyclotrons and their Applications*, Cape Town, South Africa, 1995, pp. 28-31.
[2] OPERA-3d, http://operafea.com
[3] A. Adelmann, C. Kraus, Y. Ineichen, S. Russel, and J. J. Yang, "The OPAL framework - User's reference manual", PSI Technical Report No. PSI-PR-08-02, 2008.
[4] J. J. Yang, A. Adelmann, M. Humbel, M. Seidel, and T. J. Zhang, "Beam dynamics in high intensity cyclotrons including neighbouring bunch effects: model, implementation and application", *Phys. Rev. ST Accel. Beams*, 064201, 2010.
[5] List of cyclotrons and booster-rings, in *Proc. 14th Int. Conf. on Cyclotrons and their Applications*, Cape Town, South Africa, 1995, entry C52, p747.
[6] J. L. Conradie *et al.*, "Status report and new developments at iThemba LABS", in *Proc. 20th Int. Conf. on Cyclotrons and their Applications*, Vancouver, Canada, 2013, MOPPT032, p95.
[7] *OPERA-3d Reference Manual*, Ver. 17R1, pp 887-888.

ISBN 978-3-95450-167-0

INJECTION LINE STUDIES FOR THE SPC2 CYCLOTRON AT ITHEMBA LABS

F. Nemulodi*, J.I. Broodryk, J.L. Conradie, J.G. de Villiers, W. Duckitt, D.T. Fourie, J. Mira, M.J. van Niekerk, R.W. Thomae, iThemba LABS, Somerset West, South Africa
J.J. Yang, T.J. Zhang, CIAE, Beijing, China

Abstract

The transmission efficiency of some ion beams through the second solid-pole injector cyclotron (SPC2) at iThemba LABS requires improvement. In order to understand the beam optics in the injection line, and match the beam to the acceptance of the cyclotron, the beam envelope behaviour from the beginning of the vertical injection-line to SPC2 was investigated with different simulation programs. The transverse effects were taken into account by the beam transport codes TRANSOPTR and TRANSPORT, while the multi-particle simulation code OPAL was used to include space-charge effects. Simulations of the effect of an additional buncher, operating at the second harmonic, on the transmission of the beam through the cyclotron were made.

INTRODUCTION

A K=8 MeV second solid-pole injector cyclotron at iThemba LABS, shown in Fig. 1, is used to pre-accelerate light and heavy ions, as well as polarized protons, before injection into the separated-sector cyclotron (SSC) for final acceleration [1]. The beams are mainly used for nuclear physics experiments. To accelerate both light and heavy ions, SPC2 was designed to utilize three constant orbit patterns. Depending on the final energy required and type of ion species to be accelerated, ions make 8, 16, or 32 turns before extraction. The transmission efficiency for the 8 turn pattern, however, requires improvement.

Figure 1: A photograph of SPC2.

The beams from the ion sources, which are situated in the SPC2 vault basement, are injected axially into the cyclotron. The DC beam is bunched using a double-gap buncher operating at the fundamental frequency before being deflected onto the median plane of the cyclotron with a spiral inflector. The beam is bunched in order to increase the number of ions that can be accelerated within the phase acceptance of the cyclotron.

In an attempt to improve the transmission efficiency of SPC2, beam dynamics simulations studies of the vertical beam line were performed using three codes. For the transverse optics of the beam along the injection line the beam transport code TRANSPORT [2] was used. The second-order beam transport code TRANSOPTR [3] was used because of its capability to include an arbitrary matrix for the spiral inflector. The Object Oriented Parallel Library (OPAL) code [4], which includes 3D space-charge effects, was utilized to investigate the bunching efficiency of an additional buncher, operating at the second harmonic, on the number of ions that can be grouped within the phase acceptance of SPC2.

TRANSVERSE OPTICS

Beams of heavy ions produced by the electron cyclotron resonance (ECR) ion sources are deflected into the vertical beam line using a 90^0 dipole magnet. The vertical beam line, shown in Fig. 2, consists of two triplets (Q1–Q6) and two solenoids magnets (SL1 and SL2). Also available are steering magnets that steer the beam in both X and Y directions [5].

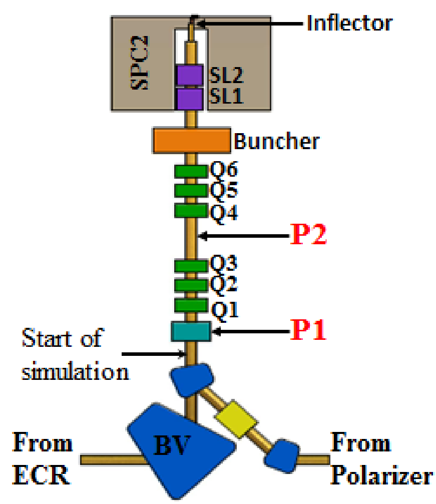

Figure 2: The axial beam line leading into the median plane of SPC2.

It is assumed that the deflection of the beam from the horizontal beam line into the vertical beam line is axisymmetric. Thus, for the present study only the beam dynamics through the vertical beam line was investigated. In the current study $^{20}Ne^{3+}$ ions with an energy of 48.50 keV were considered. The initial phase space parameters

* fnemulodi@tlabs.ac.za

ISBN 978-3-95450-167-0

are listed in Table 1. Here, x is the horizontal radius of the envelope, ɵ is the angle in the x-z plane, y is the vertical radius of the envelope, ϕ is the angle in the y-z plane, l is the bunch length, and δ relates to energy spread in the bunch. The bunch length (l) was chosen to correspond to one bunch spacing βλ = 56 mm.

Table1: Initial phase space parameters of the 48.50 keV neon beam in the vertical beam line

x (mm)	ɵ (mrad)	y (mm)	ϕ (mrad)	l (mm)	δ (%)
2	20	2	20	56	0.075

The beam envelopes were calculated using TRANSPORT and TRANSOPTR. For benchmarking purpose, the envelopes were also calculated by multi-particle simulation, using OPAL, with no space-charge effects. Figure 3 shows the calculated beam envelopes in the transverse direction for $^{20}Ne^{3+}$ ions. Also shown in the figure are the calculated beam envelopes using OPAL, taking space-charge effects into account for a 100 eμA beam current. It should be noted that for simulations with space-charge forces, the currents in the beam line elements were increased. These results show that the injection beam line is capable of handling high intensity beams.

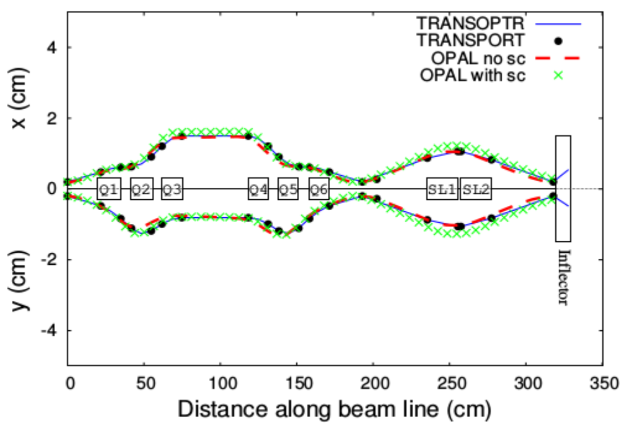

Figure 3: The calculated beam envelopes for the vertical beam line obtained from three different codes, namely, TRANSPORT, TRANSOPTR, and OPAL.

It is understood that the process of deflecting the beam onto the median plane through the spiral inflector leads to coupling in the transverse phase space. This affects the matching of the beam to the cyclotron acceptance. TRANSOPTR was used to investigate the emittances at the exit of the spiral inflector. To do this, emittances at the entrance and the exit of the inflector were compared. The emittances were optimized for lowest emittance growth by varying the settings of the solenoids SL1 and SL2. The emittances obtained for the final settings are ε_x = 40 π mm.mrad, ε_y = 40 π mm.mrad at the entrance of the inflector and ε_x = 70.2 π mm.mrad, ε_y = 40.7 π mm.mrad at the exit of the inflector. These values are considered acceptable for SPC2.

LONGITUDINAL OPTICS

The longitudinal beam dynamics were simulated using the OPAL code. The code tracks the charged particles including 3D space-charge effects. This code computes space-charge forces by solving the 3D Poisson equation with the open boundary conditions using a standard or integrated Green function method [4]. The external electromagnetic fields are obtained by means of field maps or by analytical models.

DC beams from the polarized and ECR ion sources require bunching in order to increase the number of particles within the cyclotron's phase acceptance. Currently the beam to the SPC2 is bunched using a double-gap buncher operating at the fundamental frequency. The buncher is installed in the vertical beam line between the second triplet and the solenoids as indicated in Fig. 2. The phase acceptance of SPC2 is 40^0 and 55% bunching efficiency can be achieved with this buncher as shown in Fig. 4. It is expected that by using bunchers operating at the 1^{st} and 2^{nd} harmonic frequency the bunching efficiency of particles can be increased.

Therefore, it is planned to install a second buncher, operating at the 2^{nd} harmonic, in the injection beam line. In order to find the optimal position of the buncher, two available positions, labelled P1 and P2 in Fig. 2, were investigated and compared. To use position P2 the settings on the quadrupoles Q1-Q3 were changed such that the focal point would be at P2. Because of the limited space in the vertical beam line only these two positions are realistic options that can be considered.

In OPAL a buncher is modelled by a double-gap RF cavity. Geometrical parameters of the buncher cavities are listed in Table 2. The user can vary the voltage and the phase of the sinusoidal voltage produced by the cavity. Currently the effect of the buncher in the vertical beam line is measured by observing the beam intensity on the probe situated just after the 1^{st} acceleration gap in SPC2. This technique was utilized in our simulation. By calculating the number of particles that can be bunched to within the phase acceptance of the cyclotron the buncher efficiency can be obtained. Figure 4 shows the bunching efficiency of the 1^{st} harmonic buncher obtained by varying the voltage of the buncher while the phase is kept constant. The simulations were performed with and without space-charge effects.

Table 2: Geometrical parameters of the buncher drift tubes

Buncher	Length of Centre Electrode (mm)	Gap (mm)	Aperture Radius (mm)
1^{st} Harmonic	26	2	12.5
2^{nd} Harmonic	39	2	12.5

For simulations with space-charge effects, a beam current of 10 eμA was used. The results show that 50%

ISBN 978-3-95450-167-0

bunching efficiency can be achieved with this buncher for both cases.

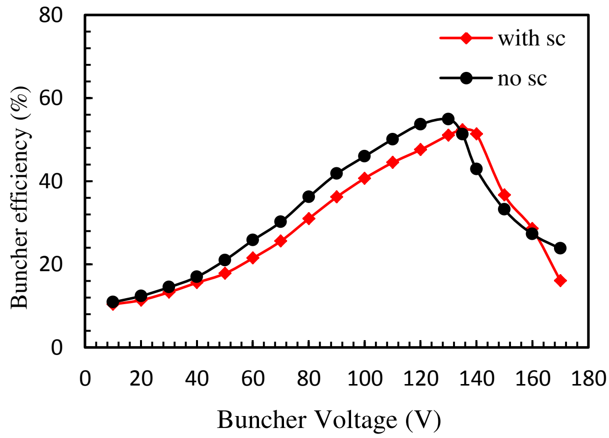

Figure 4: The bunching efficiency of the 1st harmonic buncher as a function of buncher voltage, with and without space-charge effects.

For the inclusion of the 2nd harmonic buncher the two positions P1 and P2 were investigated separately. Figure 5 shows the bunching efficiency for the two bunchers operating at the 1st and 2nd harmonic. The 2nd harmonic buncher was placed at position P1 for Fig. 5(a) while in Fig. 5(b) it was placed at P2. The 1st harmonic buncher was set to its optimal parameters and the voltage of the 2nd harmonic buncher was varied while the phase was kept constant.

For the buncher placed at P1, bunching efficiencies of 76% and 62% could be achieved, respectively for simulations without and with space-charge effects included. Whereas 77% and 73% were obtained with the buncher placed at P2 with and without space-charge effects, respectively. When space-charge is taken into account the shorter drift space between the 1st and the 2nd harmonic buncher contribute to better bunching efficiency with the 2nd harmonic buncher at position P2 compared to position P1. Due to these results, a 2nd harmonic buncher will be installed at position P2 in the near future.

INFLUENCE OF RADIAL ELECTRIC FIELD ON BUNCHING EFFECTS

The electric field experienced by the particles when passing through the buncher gaps is not homogeneously distributed radially. As a result, if one is dealing with beams with large emittances, the inhomogeneity of the electric field deteriorates the bunching effect, as is demonstrated in Fig. 6. Here, the OPERA-3d [6] code was used to investigate the bunch length at the position of the 1st harmonic buncher by tracking the particles through the 2nd harmonic buncher situated at P1. Three particles with phase of -20^0, 0^0 and +20^0, representing a bunch with length of 40 RF degrees, were tracked through the electric field at different radial positions between 0 and 10 mm from the axis. Figure 6 shows that when the particles are situated at radii larger than 8 mm, a phase deviation between 55^0 and 100^0 was obtained. As a result, the bunching effect of the 2nd harmonic buncher is destroyed before the particles arrive at the 1st harmonic buncher position.

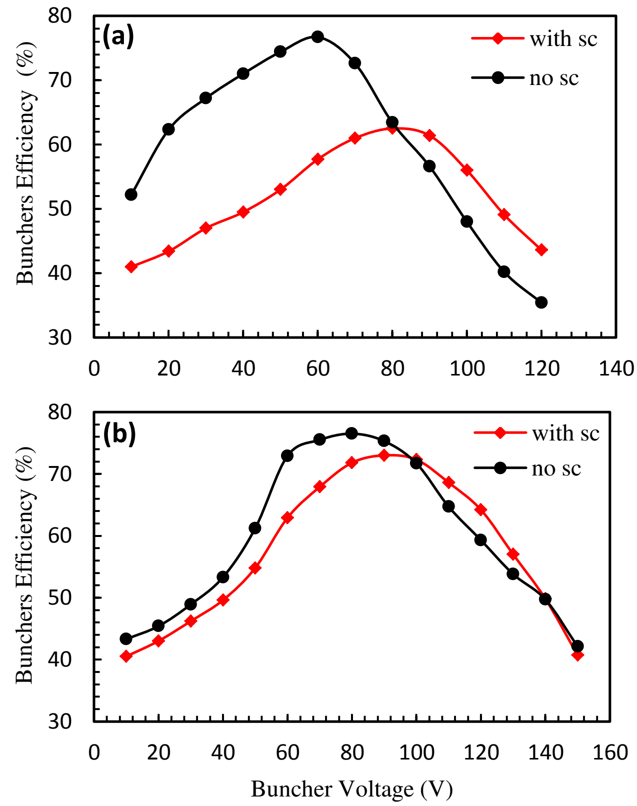

Figure 5: The bunching efficiency as a function of buncher voltage of the 2nd harmonic buncher, (a) with the buncher P1 and (b) with the buncher at P2.

To reduce this effect, grids of two by two crossed conducting wires were placed at each end of the gaps of the 2nd harmonic buncher. By using the grid, the electric field experienced by particles is more homogenous radially, hence the phase deviation is drastically reduced from 100^0 to 30^0 at a radius of 10 mm, as shown in Fig. 6.

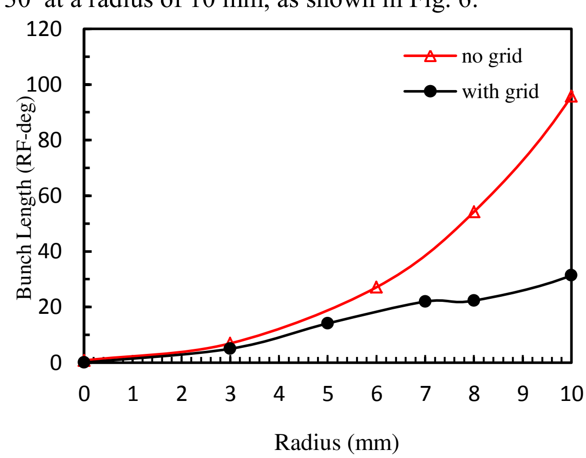

Figure 6: Bunch length of particles at the position of the 1st harmonic buncher as a function of off-axis radial position at the entrance of the 2nd harmonic buncher.

ISBN 978-3-95450-167-0

SUMMARY

The beam optics of the vertical beam line for beam injection into SPC2 were investigated. The transverse optics were studied using TRANSPORT, TRANSOPTR as well as OPAL. The inclusion of space-charge effects showed that the injection beam line is capable of handling high-intensity beams. The inclusion of the inflector transfer matrix made it possible to calculate the transverse emittances at the entrance and exit of spiral inflector. The multi-particle simulation code OPAL was used to study the longitudinal behaviour of the beam. Calculations of the buncher efficiency with two bunchers operating at 1st and 2nd harmonics show that the distance between the two bunchers is an important parameter. When the distance between the bunchers is 1.83 metres a buncher efficiency of 62% could be obtained. This increased to 73% when the distance is reduced to 1.01 metres. The OPERA-3d code were used to investigate the bunching effects on the radial dependence of the electric field.

FUTURE PLANS

Since the beam emittance considered in the present study is small, one-dimensional electric field maps were utilized to model the RF bunchers. For large emittances, three-dimensional field maps need to be considered. The next step of the simulation study will utilize the 3D electric field maps.

In order to improve the accuracy of the beam matching process in the central region of SPC2, the deflection of ions as well as the acceleration along the first few turns will be included in future simulations. The simulations will be accompanied by measurements.

ACKNOWLEDGEMENTS

The authors would like to thank their colleagues for their contribution to this work. This study is jointly supported by the National Research Foundation of South Africa (No. 92793) and National Science Foundation of China (No. 11461141003).

REFERENCES

[1] J.L. Conradie et al., "Improvements to the iThemba LABS cyclotron facilities" in *Proc. 18th Int. Conf. on Cyclotrons and their Applications*, Catania, Italy, 2007, pp. 140.

[2] PSI Graphic Transport Framework by U. Rohrer based on a CERN-SLAC-FERMILAB version by K.L. Brown et al.

[3] E.A. Heighway et al., "TRANSOPTR, a second-order beam transport design with optimization and constraints", *Nucl. Inst. Meth.* 187, p. 89 (1981).

[4] A. Adelmann, C. Kraus, Y. Ineichen, S. Russel, and J.J Yang, "The OPAL framework – User's reference manual", PSI Technical Report No. PSI-PR-08-02, (2008).

[5] J.L. Conradie et al., "Transfer Beam lines for ECR and Polarized-Ion Sources for a New Injector Cyclotron at NAC" in *Proc. 12th Int. Conf. on Cyclotrons and their Applications*, Berlin, Germany, 1989, pp. 376.

[6] OPERA-3d, http://operafea.com.

FAST SCANNING BEAMLINE DESIGN APPLIED TO PROTON THERAPY SYSTEM BASED ON SUPERCONDUCTING CYCLOTRONS*

B. Qin†, K.F. Liu, Z.K. Liang, X. Liu, W. Chen, Q.S. Chen, P. Tan, K.J. Fan, T.Q. Yu, M.W. Fan,
Institute of Applied Electromagnetic Engineering,
Huazhong University of Science and Technology (HUST), Wuhan 430074, China

Abstract

Proton therapy is recognized as one of the most effective radiation therapy method for cancers. The superconducting cyclotron becomes an optimum choice for delivering high quality CW proton beam with features including compactness, low power consuming and higher extraction efficiency. This paper introduces design considerations of the beamline with fast scanning features for proton therapy system based on superconducting cyclotrons. The beam optics, the energy selection system (ESS) and the gantry beamline will be described.

INTRODUCTION

HUST Proton Therapy Facility is a 5 years (2016-2020) Major State Research & Development Program supported by MOST (Ministry of Science and Technology, China). This is a collaborative project with teams from HUST, CIAE (China Institute of Atomic Energy), Tongji Hospital and Xiehe hospital affiliated to HUST. The main purposes of this project includes 1) R&D of a proton therapy facility based on isochronous superconducting cyclotron, with two 360 degrees gantry rooms and one fixed beam line treatment room; 2) Installation and commissioning in the International Medical Center of HUST; 3) Clinical experiments for CFDA. The main specifications are listed in Table.1.

Table 1: Main Specifications of HUST PT Facility

Parameter	Specification
Beam energy from the cyclotron	250 MeV
ESS energy range	70-250 MeV
Energy modulation time per step	⩽ 150ms
Gantry rotation range	±180 degree
Positioning precision at Iso-center	⩽0.5mm
Max. dose rate	3Gy/L/min
Field size	30cm×30cm

This paper mainly introduces design and considerations of the beamline. Since the cyclotron is designed to provide 250MeV fixed energy proton beam, ESS must be used to modulate beam energy in range of 70-250 MeV. Pencil beam scanning will be employed for fast and accurate treatment, with the main mode of spot scanning.

* Work supported by The National Key Research and Development Program of China, with grant No. 2016YFC0105305
† bin.qin@mail.hust.edu.cn

OVERALL CONSIDERATIONS OF BEAMLINE

Figure 1 shows the layout of the beamline. The degrader is placed at the downstream of the cyclotron, for better radiation control of neutrons. A DBA (double bend achromatic section) is followed with the degrader, with an energy select slit. For the gantry beamline, a downstream scanning scheme is chosen to avoid construction of large aperture 90 degrees dipole which is required in upstream scanning. Another cons is the linear dependency between the beam position and the scanning magnet current relieves difficulty of the therapy planning. To avoid the dose accumulation on skins due to un-parallel beam, the SAD (source-axis distance) is designed to around 2.8 m.

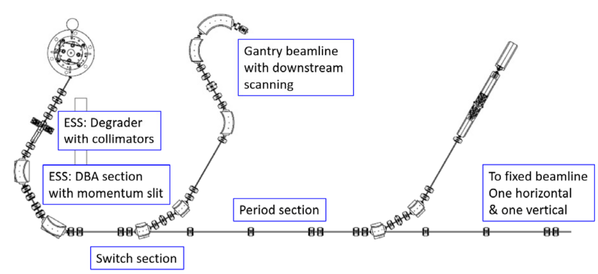

Figure 1: Layout of the beamline (correction magnets and beam diagnostics are hidden).

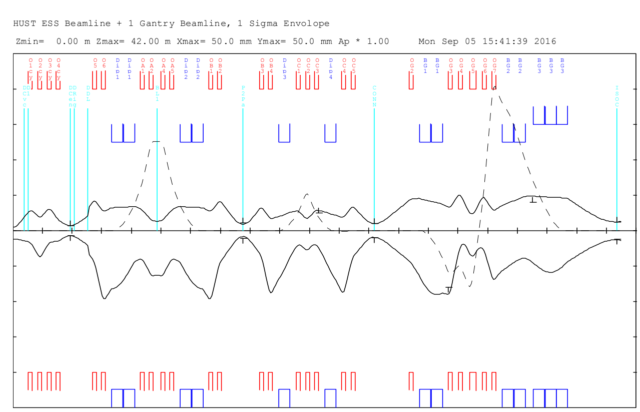

Figure 2: 1 sigma beam envelope for the main beamline including ESS and gantry beamline.

Figure 2 shows the 1 sigma beam envelope of the beamline using Transport code [1]. Main optics consideration about the beamline are:

ISBN 978-3-95450-167-0

- A multi-wedge style degrader is positioned just after a four quadrupole set from the exit of the superconducting cyclotron, to limit the neutron radiation far from the treatment room. Beam waist at the degrader center for both planes is designed to minimum the scattering effect in the degrader.
- A DBA section is followed after the degrader, with an size-changeable energy slit for limiting energy spread from 0.3% to 0.5%.
- At the connection point (CP) between the fixed beamline and the rotation gantry beamline, mirror beam x=y, x'=y' is designed to make the gantry optics identical for different rotation angle. Beam waist is necessary condition, however it will maintain a better transmission at CP.
- For effective spot scanning, at the iso-center, the double beam waist is designed, with $\sigma_x = \sigma_y =$ 2.5 mm at 250 MeV and rms emittance $\epsilon_x = \epsilon_y = 7\pi \cdot \mathrm{mm} \cdot \mathrm{mrad}$.

At first stage, spot scanning method with pencil beam will be used. When repainting is required, the energy modulation time T_e corresponding to one depth step (5 mm water equivalent) becomes important for overall treatment time. For example, for 1 Litre water radiation with 5 mm depth step, one painting for energy modulation time is 2s for $T_e = 100\ \mathrm{m}s$ and 20s for $T_e = 1s$. For HUST PT facility, $T_e = 150\ \mathrm{m}s$ is expected to control the treatment within 5 minutes for 1 Litre volume with multi-repainting. Although as reported by PSI [2], $T_e = 80$ ms has been achieved, this value is still challenging, not from the beamline magnet hardware, but from the possible disturbance of the beam quality during fast magnetic field transition.

ENERGY SELECTION SYSTEM

ESS is an essential part for proton therapy facility based on fixed energy cyclotrons. Main considerations of HUST ESS are: 1) ability for fast energy modulation in range of 70 MeV to 250 MeV, for a normalized step corresponding to 5mm water equivalent depth, the change time should be controlled within 100 ms, with a repeatable accuracy of 0.1mm water equivalent; 2) careful design of collimators and energy slit after the degrader, to shape the beam after significant growth of emittance and energy spread during energy degrading process; 3) adequate local radiation protection around the degrader; 4) redundancy for control system and beam diagnostic for treatment safety..

Figure 3 shows the schematic configuration of the degrader. A double multi-wedge scheme was chosen, due to its structure simplicity for easy maintenance and possibility for fast movement. During energy degrading in the material, the beam emittance growth is mainly caused by multiple Coulomb scattering and angle scattering is a dominated factor [3]:

$$\Delta\epsilon \approx \beta \cdot < \theta_{x/y}^2 > \quad (1)$$

Since the rms multiple scattering angle $< \theta_{x/y}^2 >$ is mainly related to the material property and thickness, in order to minimize the emittance growth $\Delta\epsilon$, double beam waist should be designed at the centre of the degrader for a minimum β function.

High density graphite will be used for degrader material. Low Z element such as Beryllium has a longer radiation length that will supress the scattering angle, however, the material processing is more difficult.

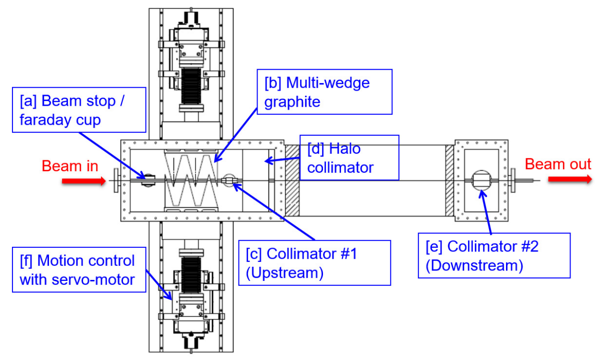

Figure 3: Schematic view of the multi-wedge degrader.

Geant4 code [4] based on Monte-Carlo algorithm was used for multi-particle simulation in the degrader [5]. For energy degrading to 70 MeV, the emittance is increased from initial $5\pi \cdot \mathrm{mm} \cdot \mathrm{mrad}$ to about $140\pi \cdot \mathrm{mm} \cdot \mathrm{mrad}$, and the spread in increased to higher than 3 MeV. By using a collimator set (Collimator #1 & Collimator #2) and an energy slit in DBA, the beam can be shaped to $5\sim10\pi \cdot \mathrm{mm} \cdot \mathrm{mrad}$ and $\pm0.5\%$ spread. However, for this energy, even after optimization of the optics and drift space between the wedges, the transmission is quite small (about 0.2%) as shown in Fig. 4.

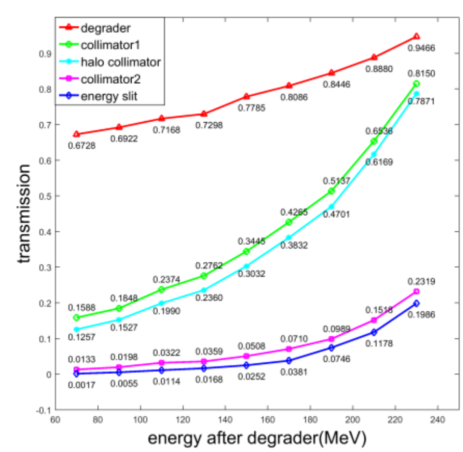

Figure 4: Transmission varies with the energy after degrader, simulated by Geant4 code.

From present study, the beam transmission in ESS varies significantly for lowest energy 70 MeV, is just 0.2%. Even for energy range 70 to 230 MeV, the transmission ratio is about 100, which leads to high intensity difference during treatment. To relieve this difference, we plan to perform intensity compensation in the beamline, to fur-

ISBN 978-3-95450-167-0

ther supress beam intensity at higher energy and limit the intensity ration within 20, for example, 1-20 nA for treatment.

GANTRY BEAMLINE

Figure 5 shows the layout of the gantry beamline, which is design for a 360 degree gantry. B1 and B2 are two 60 degree dipoles, and B3 is a 90 degree dipole with a 20 degree exit angle for better control of vertical beam envelope. Two sets of BPMs and X/Y steering magnets are configured for beam alignment.

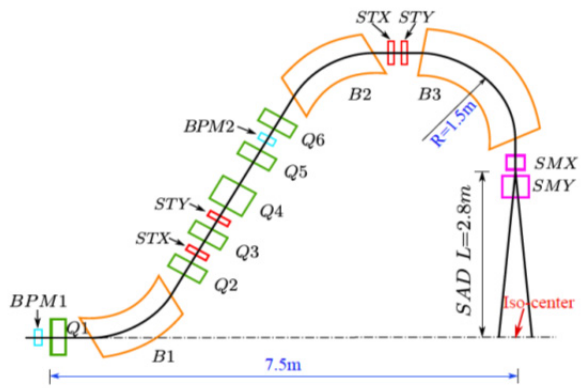

Figure 5: Schematic view of the downstream scanning gantry beamline.

Downstream Scanning and SAD

Compared to upstream scanning scheme, downstream scanning was chosen, with considerations: (1) to achieve a larger field size at the iso-center: 30 cm × 30 cm. When using upstream scanning, pitching has to be used for this size. (2) the dependency between the excitation current and the beam position is linear, which relieve the PBS (pencil beam scanning) system design. (3) to avoid the use of large aperture last 90 deg. dipole, as well as this type of dipole will further limit the energy modulation time.

The main disadvantage of downstream scanning comes from the un-parallel beam, which will bring higher dose on patient skin. To compensate this effect, a longer SAD *L*=2.8 m is adopted. A side-effect of long SAD is that the requirement for fast scanning magnet (SMX) is mitigated.

Scanning Magnet and Eddy Losses

Performance of scanning magnets is critical for pencil beam scanning. Careful design and optimization on two orthogonal scanning magnets SMX & SMY has been performed to find a compact solution with reasonable eddy losses [6]. For fast scanning magnet SMX, the upper limit of operating frequency is 100 Hz, corresponding to a scanning speed of 60 m/s. The magnetic field is 0.52 T for 250 MeV energy, which produce 55 mrad deflection angle. 0.1mm lamination steel will be used to reduce eddy current in poles.

Main eddy losses comes from the pole end due to fringe field. The cooling plate attached to the pole end is one solution, however this method will increase the magnet length. Slit cuts on the pole end is another method to cut off the eddy current efficiently, but dimensions and position of the slits are sensitive. To study these factors and optimize the eddy losses, OPERA3D with ELEKTRA / TEMPO modules is used to simulate the eddy current and temperature increase. Figure 6 shows an optimized configuration with 8 2 mm width slits. The maximum temperature is below 65 °C, while the temperature without slits will beyond 175°C. Figure 7 is the assemble view of SMX.

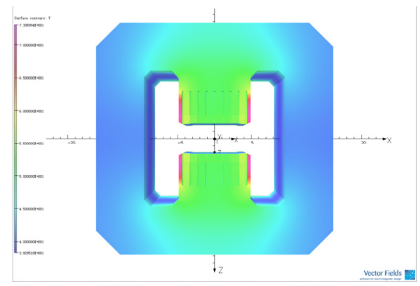

Figure 6: Eddy current and temperture analysis using ELEKTRA/TEMPO.

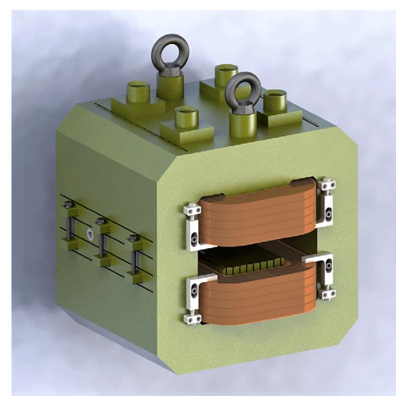

Figure 7: SMX magnet model.

CONCLUSION

Main considerations, optics design and scanning magnet design for HUST proton therapy beamline are introduced in this paper. Physical design of the ESS with help of Geant4 code has been performed, however, optimization of beam transmission and beam intensity compensation are required to achieve more stable beam delivery during treatment.

REFERENCES

[1] U. Rohrer, “PSI Graphic Transport Framework,” based on a CERN-SLAC-FERMILAB version by K.L. Brown *et al.*, 2007, `http://aea.web.psi.ch/Urs_Rohrer/MyWeb/trans.htm`

[2] E. Pedroni *et al.*, “Pencil beam characteristics of the next-generation proton scanning gantry of PSI: design issues and initial commissioning results”, *Eur. Phys. J. Plus*, vol. 126, p. 66, 2011.

ISBN 978-3-95450-167-0

[3] V. Anferov, “Energy degrader optimization for medical beam lines”, *Nucl. Instr. and Meth.* A 496, pp. 222–227, 2003.

[4] S. Agostinelli *et al*., *Nucl. Instr.Meth. Phys. Res.* A 506, p. 250, 2003.

[5] Zhikai Liang *et al.*, “Design of the Energy Selection System for Proton Therapy based on Geant4”, presented at CYCLOTRONS’16, Zurich, Switzerland, Sep. 2016, paper MOD01, this conference.

[6] Xu Liu *et* al., “Design of the Fast Scanning magnets for HUST Proton Therapy Facility”, presented at CYCLOTRONS’16, Zurich, Switzerland, Sep. 2016, paper MOD04, this conference.

ISBN 978-3-95450-167-0

PRODUCTION OF F-18 AND TC-99M RADIONUCLIDES USING AN 11-MEV PROTON-ACCELERATING CYCLOTRON*

I. Kambali †, H. Suryanto, P. Parwanto, R. Rajiman, M. Marlina,
Center for Radioisotope and Radiopharmaceutical Technology, National Nuclear Energy Agency (BATAN), Puspiptek Area, Serpong, South Tangerang, Indonesia
K. Kardinah, N. Huda, F. D. Listiawadi, H. Astarina, R. R. Ismuha,
National Cancer Center, Dharmais Cancer Hospital, Jakarta, Indonesia

Abstract

An 11-MeV proton-accelerating cyclotron has been employed to produce F-18 and Tc-99m radionuclides. In this report, F-18 radionuclide was produced from enriched-water ($H_2{}^{18}O$) target whereas Tc-99m was generated from natural molybdenum trioxide (MoO_3) target. Two recoiled radioactive impurities such as Co-56 and Ag-110m are identified in the F-18 solution whereas N-13 was recognized as an impurity in the Tc-99m production. The Co-56 radionuclidic impurity is presumably sputtered off the havar window in the target system whereas Ag-110m is originally from a silver body housing the enriched water target which is generated by secondary neutron irradiated Ag-109. In addition, N-13 impurity found in the post-irradiated MoO_3 target occurs presumably via (p,α) nuclear reaction.

INTRODUCTION

Positron and gamma ray emitting radionuclides such as F-18 and Tc-99m have been used for medical imaging of tumors, cancers and other metabolism-related diseases via the-so-called Positron Emission Tomography (PET) and Single Photon Emission Computed Tomography (SPECT) [1-4]. In Indonesia, F-18 radionuclide has been routinely produced using an 11-MeV cyclotron at Dharmais Cancer Hospital [5], whereas cyclotron-produced Tc-99m is still under investigation. Previous research suggested that radionuclidic impurities such as Co-56 and Ag-110m radionuclides were identified in the post-irradiated enriched water target, though it did not quantify the radioactivities. Further studies are, therefore, required to better understand the amount of impurities and their dependence on the proton beam doses.

In terms of technetium-99m, it has been reported that the most widely used radionuclide in nuclear medicine has experienced shortages lately [6-7] since production of the gamma emitting radioisotope has been mostly carried out using nuclear reactors while the rate of new nuclear reactor establishments is slowing down and the number of aging reactors is increasing. An alternative method of producing Tc-99m using cyclotrons has been proposed elsewhere [8] to tackle the shortage issues. Medium energy protons in the range of 8 – 18 MeV have been suggested to irradiate molybdenum (Mo) targets [9], either natural or enriched Mo to obtain high specific activity of Tc-99m, though enriched Mo-100 is preferred for better yields [10].

In this paper, production of F-18 radionuclide at different integrated proton beam currents or doses is discussed and dependence of impurity intensities on proton beam current is also presented. Moreover, preliminary result of Tc-99m production using an 11-MeV cyclotron is also highlighted in this report.

EXPERIMENTAL METHOD

The 11 MeV Cyclotron

The cyclotron employed in this investigation is a typical Eclipse Radioisotope Delivery System (RDS) 111 cyclotron located at the National Cancer Center (NCC), Dharmais Cancer Hospital in Jakarta, Indonesia, which has been described elsewhere [5]. The cyclotron accelerates 11-MeV protons at a beam current of up to 60 μA, though in this investigation the maximum proton beam employed in the target irradiation is between 20 and 30 μA, depending on the targets of interest, while the irradiation time varied between 15 and 60 minutes.

The Target Systems

The target vessel/body for F-18 production comprises of a silver body/tube and is separated from the beam window by another 50 μm thick Havar foil, which has been described elsewhere [5]. During proton bombardment, havar foil is expected to be activated via (p,n) nuclear reaction, thus the proton-generated radionuclides could potentially contaminate the enriched water target should they recoil off the havar window.

In Tc-99m production, the target system consists of an aluminum tube housing a target holder where the target is placed in, as can be seen in Figure 1. During the target irradiation, the target system was cooled by Helium and water coolant to avoid excessive heat while the temperature was monitored throughout the irradiation procedure.

Production and Analysis of F-18

Fixed energy proton beams of 11 MeV was bombarded into 1.8 mL enriched-water target ($H_2{}^{18}O$). The experiment was conducted at variable proton beam currents between 10 and 30 μA.hr. At the end of the bombardment, F-18 yields and radionuclide impurities were analyzed shortly following an hour cooling period using a portable gamma ray spectrometer. The spectrometer consists of a NaI(Tl) detector coupled to a portable pocket Multi Channel Analyzer (MCA).

* Work supported by TWAS, BATAN and NCC
† imamkey@batan.go.id

ISBN 978-3-95450-167-0

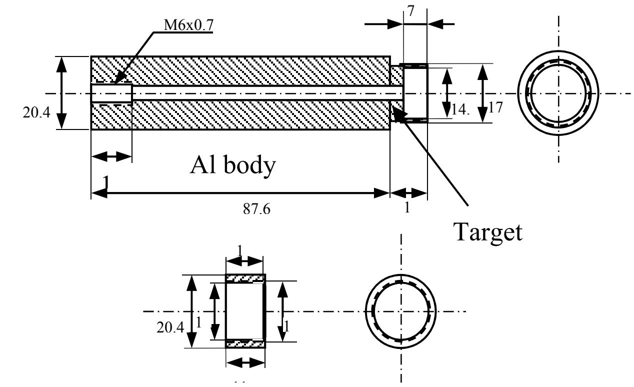

Figure 1: Target system for Tc-99m production at the National Cancer Center, Dharmais Cancer Hospital, Jakarta.

Production and Analysis of Tc-99m

Natural molybdenum trioxide (MoO_3) in the form of pellet was irradiated with the 11-MeV proton beam at an integrated beam current of 5 µA.hr. Following an hour cooling period, the post-irradiated MoO_3 target was dissolved in a NaOH 6M solution and then being analyzed using the portable gamma ray spectrometer. Observations were conducted periodically to understand the evolution of produced Tc-99m as well as impurities found in the post-irradiated target.

RESULTS AND DISCUSSION

Spectrum of F-18 and Target System

Fluorine-18 radionuclide is produced following irradiation of enriched-water ($H_2{}^{18}O$) target, which can be identified from the strong annihilation peak at 0.511 MeV as can be seen in Figure 2.

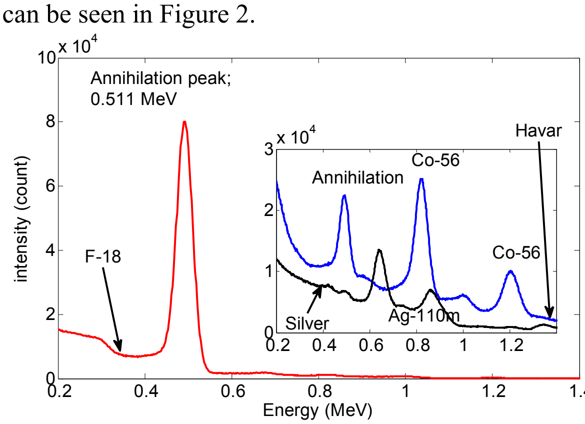

Figure 2: Gamma ray spectrum of F-18 and the target system (Havar foil and silver body).

In the target system, Havar foil which separates the proton beam and $H_2{}^{18}O$ target is also activated by the incoming proton beam resulting in Co-56 radionuclide generated from $^{56}Fe(p,n)^{56}Co$ nuclear reaction, whereas secondary neutrons are expected to cause nuclear reaction when they hit the silver body as discussed elsewhere [5]. As a result Ag-110m radionuclide is generated via $^{109}Ag(n,\gamma)^{110m}Ag$ nuclear reaction. Both Co-56 and Ag-110m are experimentally observed at significant levels as shown in Figure 2 (inset). Evidence suggests that Co-56 observed in the post-irradiated water target is originally from the Havar foil. The Co-56 impurity is presumably recoiled off the Havar window and then fall into the water target. Similarly, Ag-110m is most likely as a result of recoiling/sputtering process.

A total of nearly 588 mCi of F-18 radionuclide is produced at the end of bombardment when 30 µA.hr proton beam dose is directed to the enriched water target, whereas the yield drops to at lower proton beam of 10 µA.hr.

Radionuclidic Impurities

Previous experiment suggested that radionuclidic impurities such as Co-56 and Ag-110m were recorded in the post-irradiated $H_2{}^{18}O$ target [5], and in this investigation their presence is, again, confirmed as can be seen in Figure 4. The strong annihilation peak at 0.511 MeV is presumably as a result of over 1.022-MeV gamma ray interaction with the detector material.

In order to study the dependence of the proton beam dose on the number of Co-56 and Ag-110m impurities, $H_2{}^{18}O$ target was irradiated with proton beam doses between 10 and 30 µA.hr. It is clear from Figure 3 that the amount of the impurities is directly proportional to the proton beam dose.

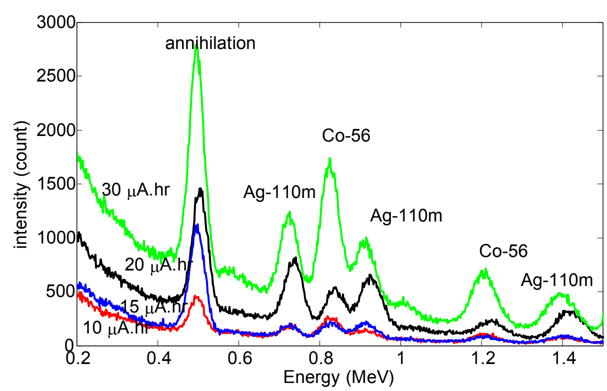

Figure 3: Gamma ray spectrum of radionuclidic impurities observed in F-18 production at variable proton beam intensities ranging from 10 to 30 µA.hr.

Details of the recorded radionuclidic impurities at different proton beam dose are given in Table 1, which indicates that no other impurities than Co-56 and Ag-110m are found in the post-irradiated enriched water target. The measured radioactivity of Co-56 impurities ranges from 0.077 µCi at proton dose of 10 µA.hr to 0.670 µCi at proton dose of 30 µA.hr, whereas Ag-110m exhibits lower radioactivity as shown in Table 1.

ISBN 978-3-95450-167-0

Table 1: Radionuclidic Impurities Observed during F-18 Production

Proton dose (μA.hr)	γ Energy (MeV)	Identified Radionuclide	Activity (μCi)
10	0.511, 0.847, 1.238	Co-56	0.077
	0.511,0.658, 0.885, 1.384	Ag-110m	0.083
15	0.511, 0.847, 1.238	Co-56	0.110
	0.511,0.658, 0.885, 1.384	Ag-110m	0.083
20	0.511, 0.847, 1.238	Co-56	0.202
	0.511,0.658, 0.885, 1.384	Ag-110m	0.330
30	0.511, 0.847, 1.238	Co-56	0.670
	0.511,0.658, 0.885, 1.384	Ag-110m	0.508

Spectrum of Tc-99m

Spectrum of post-irradiated MoO_3 following 30 minutes is given in Figure 4, which exhibits a very strong peak at 0.511 MeV belonging to N-13 radionuclide produced via $^{16}O(p,\alpha)^{13}N$ nuclear reaction, though the N-13 intensity completely disappears following a 24-hours cooling period (Note that N-13 half life is nearly 10 minutes. Apart from the N-13 peak, other peaks are also recorded by the portable spectroscopy system, which correspond to Tc-99m peak at 0.142 MeV, Mo-99 peak at 0.748 MeV, and Tc-96 peak at 0.848 MeV. Production of Tc-99m in this investigation is mostly due to $^{100}Mo(p,2n)^{99m}Tc$ nuclear reaction as well as the decay of Mo-99 which is generated from $^{98}Mo(p,\gamma)^{99}Mo$ nuclear reaction. In addition, the observed Tc-96 impurity is presumably resulted from $^{96}Mo(p,n)^{96}Tc$ nuclear reaction.

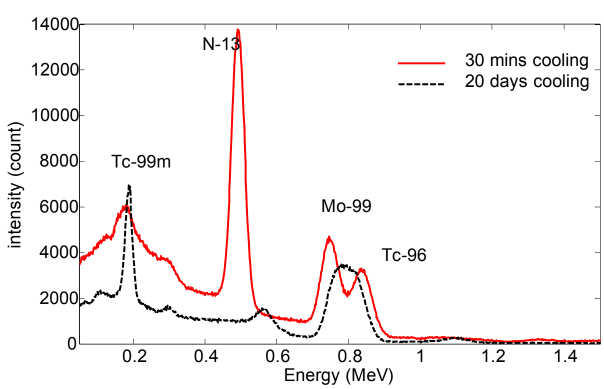

Figure 4: Gamma ray spectrum of post-irradiated MoO_3 following 30 minutes and 20 days cooling respectively.

Following 20 days of cooling period, strong Tc-99m peak dominates while the intensity of Tc-96 impurity is no longer significant (see Figure 4). At the end of bombardment, nearly 13.4 μCi of Tc-99m is produced in this investigation for proton dose of 5 μA.hr. Radionuclides produced from an 11-MeV proton irradiated natural MoO_3 target is listed in Table 2.

Table 2: Radionuclides Produced from Proton-irradiated Natural MoO_3 Target

Radio-nuclide	γ Energy (MeV)	Half-life	Nuclear Reaction
Tc-99m	0.142	6 h	$^{100}Mo(p,2n)^{99m}Tc$
N-13	0.511	10 min	$^{16}O(p,\alpha)^{13}N$
Mo-99	0.748	66 h	$^{98}Mo(p,\gamma)^{99}Mo$
Tc-96	0.848	4.3 d	$^{96}Mo(p,n)^{96}Tc$

CONCLUSION

Using an 11-MeV proton accelerating cyclotron, F-18 and Tc-99m radionuclides have been produced from enriched-water ($H_2{}^{18}O$) target and natural MoO_3 target respectively. In F-18 production, radionuclidic impurities such as Co-56 and Ag-110m are apparent. While Co-56 is presumably generated from $^{56}Fe(p,n)^{56}Co$ nuclear reaction, Ag-110m is most likely due to $^{109}Ag(n,\gamma)^{110m}Ag$ nuclear reaction. Both Co-56 and Ag-110m are expected to recoil off the havar window and silver body respectively and then fall into the enriched-water target. Experimental results also indicate that the impurity intensities increase with increasing proton beam dose.

In Tc-99m production, following an hour of cooling period, N-13 radionuclide is found to dominate the impurities present in the post-irradiated natural MoO_3, which is presumably produced via $^{16}O(p,\alpha)^{13}N$ nuclear reaction. Apart from Tc-99m peak, Mo-99 energy spectrum is also observed in the Tc-99m production route. To get higher Tc-99m yield and less impurities, enriched molybdenum (Mo-100) target is suggested for future investigation.

ACKNOWLEDGEMENT

This research was fully funded by the World Academy of Sciences (TWAS) under the Principal Investigator's Research Grant Number: 15-020 RG/PHYS/AS_I – FR3240287075. Financial support by the Indonesian National Nuclear Energy Agency (BATAN) and National Cancer Center (NCC), Dharmais Cancer Hospital – Jakarta, Indonesia is also greatly acknowledged.

REFERENCES

[1] F. Bertagna, G. Treglia, A. Piccardo, and R. Giubbini, "Diagnostic and clinical significance of F-18-FDG-PET/CT thyroid incidentalomas," *J. Clin. Endocrinol. Metab.*, vol. 97, no. 11, pp. 3866–3875, 2012.

[2] J. W. Engle, H. Hong, Y. Zhang, H. F. Valdovinos, V. Duane, T. E. Barnhart, C. P. Theuer, R. J. Nickles, and W. Cai, "Positron emission tomography

ISBN 978-3-95450-167-0

imaging of tumor angiogenesis with a 66Ga-labeled monoclonal antibody," *Mol. Pharm.*, vol. 9, no. 5, pp. 1441–1448, 2013.

[3] S. S. Gambhir, "Molecular imaging of cancer with positron emission tomography.," *Nat. Rev. Cancer*, vol. 2, no. 9, pp. 683–693, 2002.

[4] M.-C. Tu, C.-P. Lo, C.-Y. Chen, and C.-F. Huang, "Correlation of Tc-99 m ethyl cysteinate dimer single-photon emission computed tomography and clinical presentations in patients with low cobalamin status," *BMC Neurol.*, vol. 15, no. 1, p. 251, 2015.

[5] I. Kambali, H. Suryanto, and Parwanto, "Radioactive by-products of a self-shielded cyclotron and the liquid target system for F-18 routine production," *Australas. Phys. Eng. Sci. Med.*, vol. 39, no. 2, pp. 1–10, 2016.

[6] J. R. Ballinger, "99Mo shortage in nuclear medicine: Crisis or challenge?," *J. Label. Compd. Radiopharm.*, vol. 53, no. 4, pp. 167–168, 2010.

[7] J. a Osso Jr, M. F. Catanoso, G. Barrio, T. P. Brambilla, R. Teodoro, C. R. B. R. Dias, and K. N. Suzuki, "Technetium-99m - new production and processing strategies to provide adequate levels for SPECT imaging," *Curr. Radiopharm.*, vol. 5, no. 3, pp. 178–186, 2012.

[8] F. Bénard, K. R. Buckley, T. J. Ruth, S. K. Zeisler, J. Klug, V. Hanemaayer, M. Vuckovic, X. Hou, A. Celler, J.-P. Appiah, J. Valliant, M. S. Kovacs, and P. Schaffer, "Implementation of Multi-Curie Production of 99mTc by Conventional Medical Cyclotrons.," *J. Nucl. Med.*, vol. 55, pp. 1017–1022, 2014.

[9] K. Gagnon, F. Bénard, M. Kovacs, T. J. Ruth, P. Schaffer, J. S. Wilson, and S. a. McQuarrie, "Cyclotron production of 99mTc: Experimental measurement of the 100Mo(p,x) 99Mo, 99mTc and 99gTc excitation functions from 8 to 18 MeV," *Nucl. Med. Biol.*, vol. 38, no. 6, pp. 907–916, 2011.

[10] P. Schaffer, F. Bénard, A. Bernstein, K. Buckley, A. Celler, N. Cockburn, J. Corsaut, M. Dodd, C. Economou, T. Eriksson, M. Frontera, V. Hanemaayer, B. Hook, J. Klug, M. Kovacs, F. S. Prato, S. McDiarmid, T. J. Ruth, C. Shanks, J. F. Valliant, S. Zeisler, U. Zetterberg, and P. A. Zavodszky, "Direct Production of 99mTc via 100Mo(p,2n) on Small Medical Cyclotrons," *Phys. Procedia*, vol. 66, pp. 383–395, 2015.

ISBN 978-3-95450-167-0

STUDY OF THE BEAM EXTRACTION FROM SUPERCONDUCTING CYCLOTRON SC200

K.Z.Ding†, Y.F.Bi, G.Chen, Y.H.Chen, S.S.Du, H.S. Feng, J.Ge, J.J. Li,Y.T.Song,Y.H. Xie, J.X.Zheng, ASIPP, Hefei, China
G.Karamysheva, O.Karamyshev, N.Morozov, E.Samsonov, G.Shirkov, JINR, Dubna, Russia

Abstract

According to the agreement between the Institute of Plasma Physics of the Chinese Academy of Sciences (ASIPP) in Hefei, China, and the Joint Institute for Nuclear Research (JINR), in Dubna, Russia, the project of superconducting isochronous cyclotron for proton therapy SC200 is under development at both sites. The cyclotron will provide acceleration of protons up to 200 MeV with maximum beam current of ~1 µA.

Extraction system of the beam consists of electrostatic deflector and two passive magnetic channels. Electric field strength in deflector does not exceed 170 kV/cm, gradients of magnetic field in channels are in a range of 2-4 kG/cm. Both channels focus the beam in horizontal plane. Axial focusing of the beam is provided by edge magnetic field of the cyclotron.

Results of the beam tracking inside extraction system are presented. Efficiency of the beam extraction was estimated for different amplitudes of the betatron oscillations in the accelerated beam.

WORKING DIAGRAM OF CYCLOTRON

Different 3D codes have been used [1] in order to find acceptable geometry of the cyclotron magnetic system. Main purpose was to provide the working diagram without crossing of the most dangerous resonances such as $2Q_z$=1 and Q_r-Q_z=1. Many of the magnetic field maps computed by the different codes had large nonlinearities especially at edge region where a sector gap was rather small (<2 cm). These nonlinearities led to a waving of the betatron tunes and multiple crossing of the resonances. The most linear field map was obtained by the CST code [2].Figure 1 shows the working diagram of the cyclotron calculated on the base of this map. To get this diagram, the average magnetic field of the map was substituted by isochronous one. Resulting field map that correspond to presented diagram was applied for simulation of the beam acceleration up to deflector entrance.

One can see that the working point crosses the resonance Q_r-Q_z=1 at the very end of acceleration. This condition forced us to locate the deflector before full crossing of the resonance and implement extraction of the beam. The results are discussed below. The possibility that avoids crossing of this resonance is expected by means of special correctors during real shaping of the magnetic field.

* Work supported by the funding of CN-RU cooperation cyclotron design
† email address:kzding@ipp.ac.cn

Simulation of the beam acceleration shows that crossing of the $3Q_r$=4structural resonance is not dangerous. Increase in the radial amplitudes is acceptable.

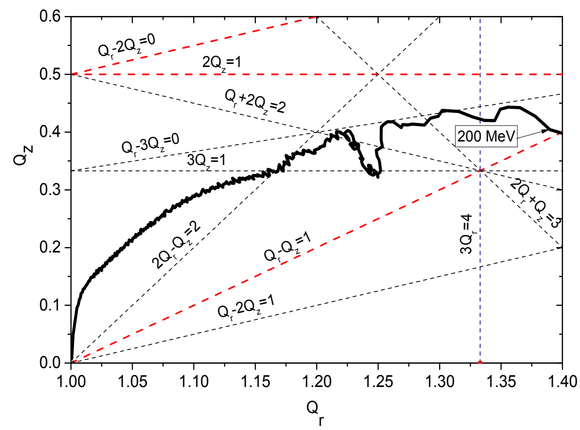

Figure 1: Working diagram of the SC200 cyclotron.

BEAM PARAMETERS AT DEFLECTOR ENTRANCE

There are two different ways to enlarge radial gain enhancement at deflector entrance, resonance and not resonance. The 1-st one was used in VARIAN C250 cyclotron [3], the 2-nd one in IBA C235 [4]. And the 2-nd will be applied in our cyclotron. In this scheme of extraction, the radial gain enhancement is mainly provided by radial betatron motion at Q_r~1.2-1.3. If amplitude of incoherent radial oscillations in accelerated beam comprises 3-5 mm then the radial width of the beam at deflector entrance is of about 2-3 mm. Not more than 10% of this value is provided by energy gain per turn, and the main part is connected with betatron motion.

In order to get the beam parameters at deflector, a bunch of 1000 protons was accelerated from the energy of 80 MeV. Initial parameters of protons were matched with the cyclotron acceptance at this energy for different amplitudes of radial oscillations in the range of 2-5 mm. Amplitude of axial oscillations was equal to 2.5 mm.

Different types of proton losses were estimated:

- axial, due to impact of the Q_r-Q_z=1coupling resonance;
- on a tip of septum, assuming 0.1 mm its thickness;
- on external side of the septum looking on the accelerated beam.

Different septum thickness along its length has been studied, constant 0.1 mm or linear increased up to 1-2 mm.

ISBN 978-3-95450-167-0

Axial profile of the beam in energy range of 80-200 MeV is presented in Fig. 2. Sum losses of the beam before its tracking inside the extraction system are shown in Fig. 3.

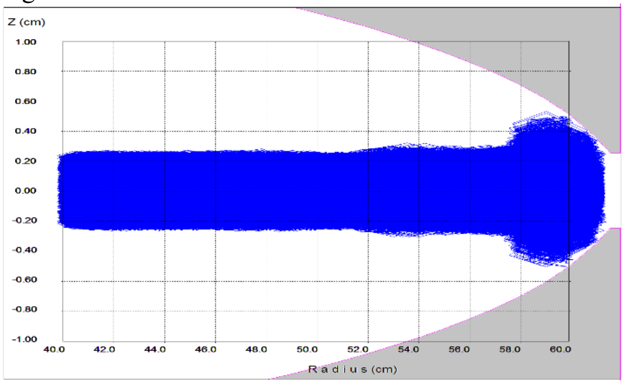

Figure 2: Axial profile of the beam in energy range 80-200 MeV. Spiral sectors are marked by grey color.

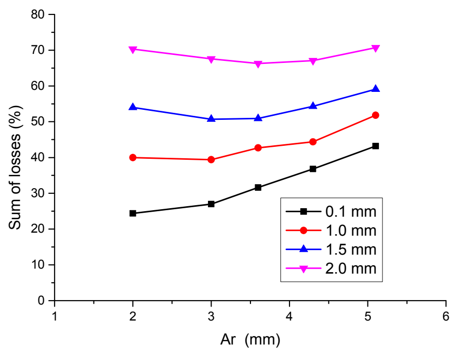

Figure 3: Sum of proton losses (axial+tip of septum+external side of septum) for different final septum thickness versus amplitude of radial oscillations.

Sum of losses does not exceed 40% even for the beam with 5 mm radial oscillations if septum has constant thickness 0.1 mm. Linear increase of septum thickness leads to essential increase of the losses on external septum side.

Parameters of protons at entrance of deflector are shown in Fig. 4 for the beam with 3 mm radial oscillations. Average energy of the beam comprises 203.6 MeV, energy spread ±0.8 MeV.

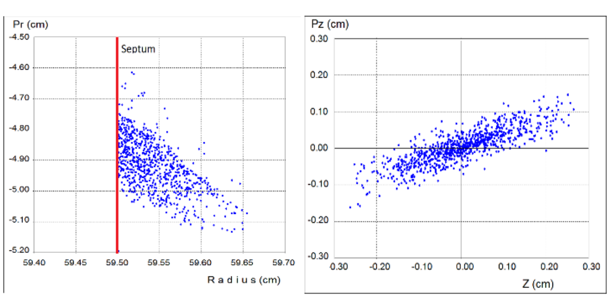

Figure 4: Position of protons on planes (r, P_r) and (z, P_z)at deflector entrance.

TRACKING IN EXTRACTION SYSTEM

The beam is extracted by means of electrostatic deflector and two passive magnetic channels. First part of extraction system is shown in Fig. 5. It consists of electrostatic deflector and passive magnetic channel 1 (MC1). The channel MC1 is subdivided into 4 parts with different cross-sections and field gradients. Channel MC1 is followed by second channel MC2 located inside the magnet yoke. Both channels focus the beam in horizontal plane, axial focusing is provided by edge magnetic field of the cyclotron.

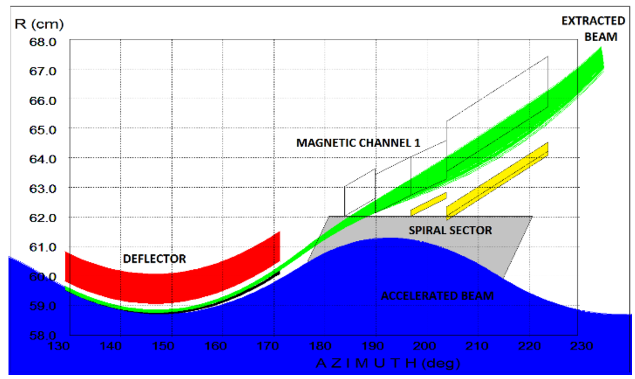

Figure 5: First part of the extraction system. Final thickness of the septum is 1 mm. Electric field in deflector is 160 kV/cm.

Proton losses were estimated during tracking of the beam inside the deflector with aperture 3 mm. Main part of these losses was detected on septum surface, losses on high voltage electrode appeared if amplitude of radial oscillations was greater than 4 mm. Sum of losses inside the deflector is presented in Fig. 6.

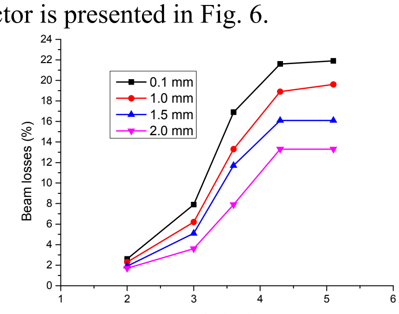

Figure 6: Sum of proton losses inside deflector (septum+high voltage electrode) for different final septum thickness versus amplitude of radial oscillations.

To estimate overall efficiency of extraction, the losses of accelerated beam (Fig. 3) were added to the losses inside deflector (Fig. 6). Resulting efficiency of extraction is shown in Fig. 7. No losses were detected inside both magnetic channels.

ISBN 978-3-95450-167-0

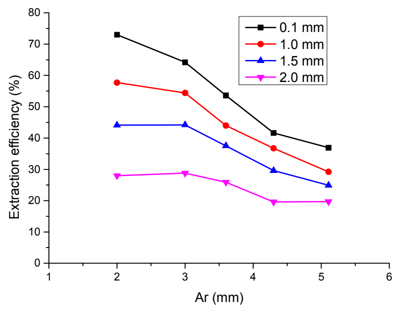

Figure 7: Resulting efficiency of the beam extraction for different final septum thickness (0.1-2.0) mm versus amplitude of radial oscillations.

Plan view of the extraction system together with trajectories of protons is presented in Fig. 8. RMS envelopes of the beam are shown in Fig. 9. Reference point for the beam extraction was defined at radius of 160 cm. Phase portraits of the beam in reference point are shown in Fig. 10. Estimated emittance of the beam is a range of about 5-10 π mm·mrad

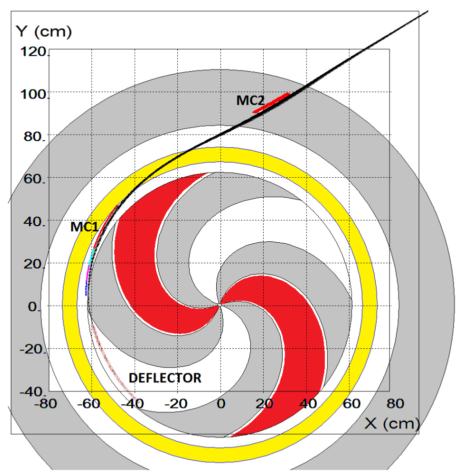

Figure 8: Schematic plan view of extraction system with proton trajectories.

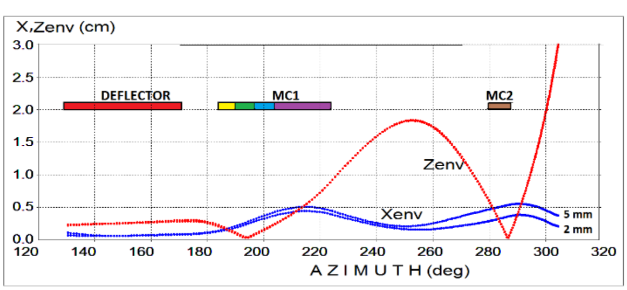

Figure 9: RMS envelopes (2σ) in extraction system. Horizontal envelopes plotted for two amplitudes of radial oscillations 2 and 5 mm.

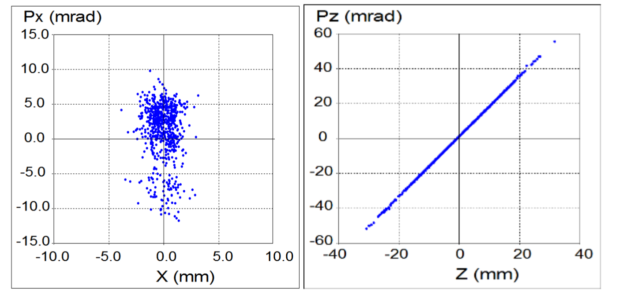

Figure 10: Phase portraits of the beam in reference point (r=160 cm).

PASSIVE MAGNETIC CHANNELS

The SC200 extraction system uses 2 magnetic channels. The first magnetic channel (MC1) is in strong magnetic field within 2.2~3.4 T. The second one (MC2) is in cyclotron yoke hole where is the magnetic field of ~1 T. These fields are much enough to magnetize the channels iron bars. So, for both channels the passive design is used. The MC1 is placed rather close to the sectors edge. Due to this fact the two initial parts of the channel have the 2 bars design, and two output ones have 3 bars system. The MC2 design has 3 iron bars. 3D design view of the MC1 is shown in Fig.11.

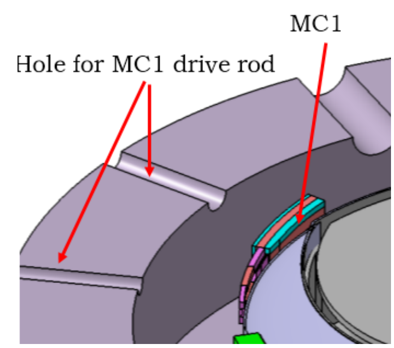

Figure 11: 3D design sketch of the MC1.

The channels magnetic field simulation was performed by 2D POISSON code. As an example, the design of MC1' 4-th part and its magnetic field parameters are shown in Fig. 12. Channel MC2 has similar geometry.

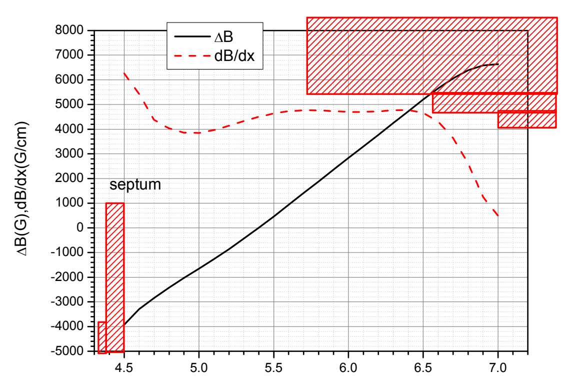

Figure 12: Cross section of 4-th part of MC1 and its field response and gradient.

ISBN 978-3-95450-167-0

CONCLUSIONS

Acceptable extraction efficiency ~50-60% is attained for the SC200 cyclotron if septum has the increasing thickness from 0.1 mm up to not more than 1 mm and the accelerated beam has the amplitude of radial oscillations up to 3.5 mm. Enlarged final septum thickness up to 2 mm leads to essential decrease of the extraction efficiency. The static voltage of 50 kV is applied on the deflector with the 3 mm aperture.

Two passive magnetic channels are used only to focus the beam in horizontal plane, and the axial focusing is provided by edge magnetic field of the cyclotron.

SC200 physical design will be ended within this year. And the magnetic field tuning plans to be kicked off next year.

REFERENCES

[1] G. Karamysheva *et al.,* "Magnetic system for SC200 superconducting cyclotron for proton therapy", presented at Cyclotrons'16, Zurich, Switzerland, September 2016, paper THP20, this conference.

[2] CST code, www.cst.com

[3] A.E.Geisler *et al.,* "Commissioning of the ACCEL 250 MeV proton cyclotron", in Proc. Cyclotrons'07, Giardini, Naxos, Italy, October 2007, pp. 9-14

[4] D.Vanderplassche *et al.,* "Extracted beams from IBA's C235", in Proc. PAC'97, Vancouver, Canada, May 1997, pp. 1045-1047.

ISBN 978-3-95450-167-0

THE ISOLPHARM PROJECT FOR THE PRODUCTION OF HIGH SPECIFIC ACTIVITY RADIONUCLIDES FOR MEDICAL APPLICATIONS*

M. Ballan[1,†], F. Borgna[2], S. Corradetti, A. Andrighetto, Istituto Nazionale di Fisica Nucleare – Laboratori Nazionali di Legnaro (INFN – LNL), Legnaro, Italy
N. Realdon, Università di Padova – Dipartimento di Scienze del Farmaco, Padova, Italy
A. Duatti, Università di Ferrara – Dipartimento di Scienze Chimiche e Farmaceutiche, Ferrara, Italy
[1]also at Università di Ferrara – Dipartimento di Fisica e Scienze della Terra, Ferrara, Italy
[2]also at Università di Padova – Dipartimento di Scienze del Farmaco, Padova, Italy

Abstract

ISOLPHARM is a branch of the INFN-LNL SPES project, aimed at the production of radioisotopes for medical applications according to the ISOL technique. Such an innovative method will allow to produce carrier-free radionuclides, useful to obtain radiopharmaceuticals with very high specific activities. In this context a primary proton beam, extracted from a cyclotron will directly impinge a target, where the produced isotopes are extracted and accelerated, and finally, after mass separation, only the desired nuclei are deposed on a secondary target.

This work is focused in the design and study of the aforementioned production targets for a selected set of isotopes, in particular for ^{64}Cu, ^{89}Sr, ^{90}Y, ^{125}I and ^{131}I. ^{64}Cu will be produced impinging Ni targets, otherwise the SPES UC_x target is planned to be used. Different target configurations are being studied by means of the Monte Carlo based code FLUKA for the isotope production calculation and the Finite Element Method based software ANSYS ® for the temperature level evaluation.

An appropriate secondary target substrate for implanting the produced isotopes is under study.

INTRODUCTION

SPES (Selective Production of Exotic Species) is a project aiming at the construction of an ISOL facility (Isotope Separation On-Line) at INFN-LNL (Istituto Nazionale di Fisica Nucleare – Laboratori Nazionali di Legnaro) for the production of radioactive ion beams of neutron rich nuclei with high purity, with mass ranging between 80 and 160 amu [1].

In this framework the ISOLPHARM project is devoted to the application of the SPES technologies for the production of innovative radiopharmaceuticals.

Radiopharmaceuticals are drugs capable of delivering a predefined dose of radiation to a biological target tissue for diagnostic or therapeutic purpose. They are usually composed by a "radioactive core" and a "carrier system" that allows to deposit radiation selectively onto the malignant tissue avoiding the compromising of healthy cells.

Since the ISOL technique allows the on-line production of high intensity and high quality radioactive ion beams [2], it might be an efficient way to produce radionuclides for radiopharmaceuticals with specific activity close to its theoretical value. The higher is the specific activity, the more effective is the radionuclide for the radiolabeling of compounds.

ISOLPHARM project will mainly deal with two aspects: the isotope production according to the ISOL technique and the radioPHARMaceuticals labelling with the produced nuclei, after the radionuclide purification.

Radionuclides will be produced by impinging a dedicated target with a primary proton beam extracted from SPES cyclotron (up to 70 MeV 350 μA). The production target will be held at high temperature (up to 2200-2300°C), thus allowing the migration of the produced nuclei towards the ion source thanks to the diffusion and effusion processes [1]. After ionization a radioactive ion beam will be extracted with a potential difference up to 40kV. Mass separation will provide the desired single-mass nuclide beam which will be deposed in an appropriate collection target. Since the collected isotopes are characterized by a single mass number, the subsequent chemical separation will provide the desired single isotope for the radiopharmaceuticals labelling. After pharmaceutical processes high specific activity drugs will be available for diagnosis and therapy (Fig. 1).

The radioisotopes interesting from a radiopharmaceutical point of view are: ^{89}Sr, ^{90}Y, ^{125}I, ^{131}I, ^{133}Xe [3, 4, 5, 6, 7], which can be produced through fission using the SPES uranium carbide target, and ^{64}Cu [8] produced through spallation on a dedicated nickel target. Different production target configurations are described in this work.

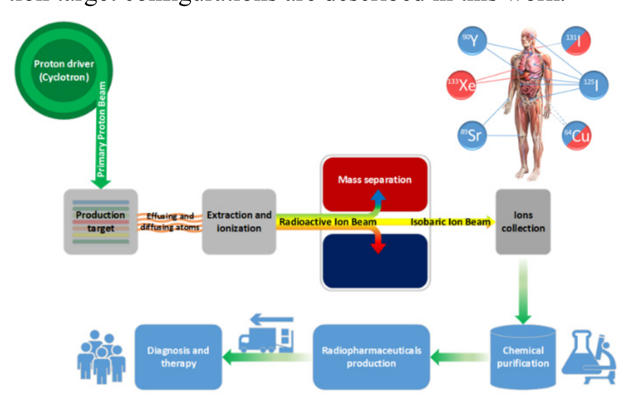

Figure 1: Overview of the ISOLPHARM project, grey balloons concern the isotope production aspects, blue balloons deal with the chemical and pharmaceutical aspects. On the top right are indicated the first planned isotopes for radiopharmaceutical labelling.

* Work supported by INFN - LNL
† michele.ballan@lnl.infn.it

ISBN 978-3-95450-167-0

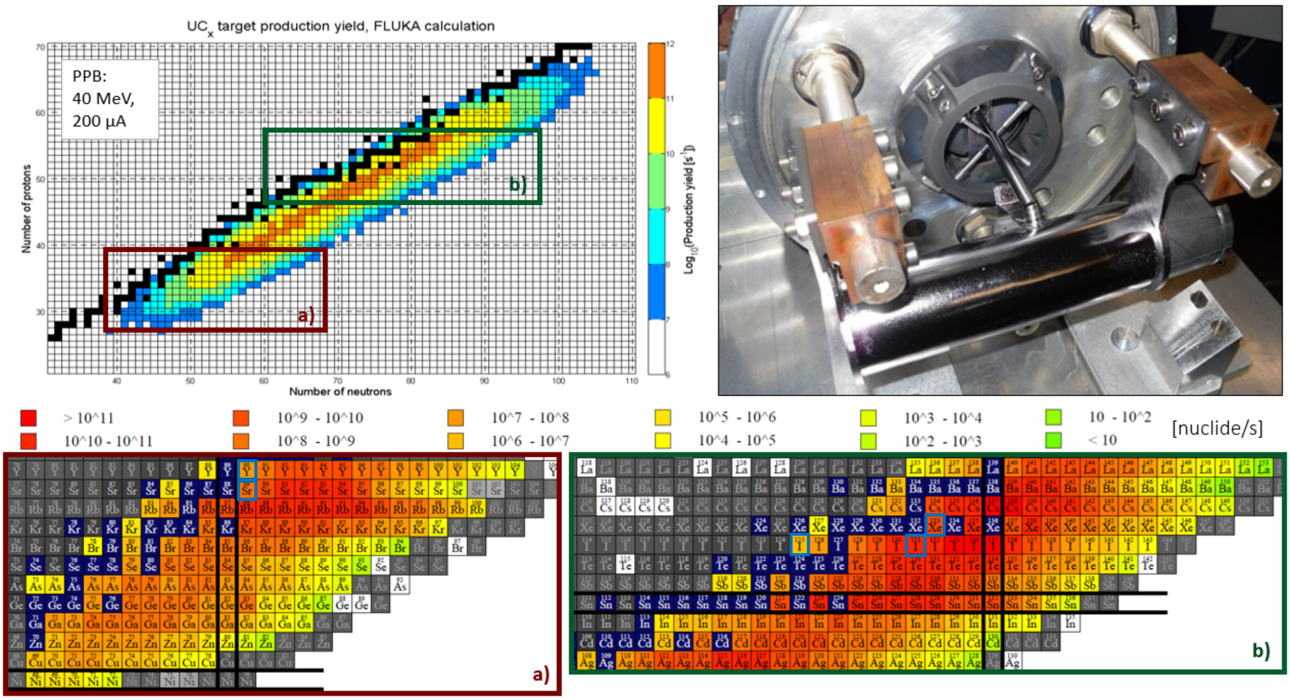

Figure 2: the production spectrum of SPES target according to FLUKA simulations, with focus on ^{89}Sr, ^{90}Y (a) and ^{125}I, ^{131}I, ^{133}Xe (b). On the top right a picture of the existing SPES target prototype, used for off-line tests.

THE UC$_X$ TARGET

In the framework of the SPES project a multi-foil uranium carbide target has been designed with the capability of generating approximately 10^{13} fissions when impinged by a 40 MeV 200 µA proton beam [9, 10].

The SPES production target is composed by 7 uranium carbide disks, characterized by a diameter and a thickness of 40 and 0.8mm, inserted opportunely spaced in a tubular graphite box. One of its extremities is closed with a thin graphite windows (0.2 mm thickness), which hinders the migration of the produced nuclei outside from the target, being alongside transparent to the proton beam. At the other side three dumping disks characterized by a thickness of respectively 0.8, 0.8 ,1 mm are capable to stop all the residual proton beam. (Fig. 3a)

The target complex is inserted into a tubular tantalum heater which provides both heat by Joule effect (heating current up to 1300 A) for target conditioning and the proper alignment to beam during irradiation. A tubular transfer line provides allows the migration of the produced isotopes towards the ion sources.

The design of such a target was developed making use of massive amount of numerical simulations, used for the estimation of both the production yields and the proton beam power deposition in the desired energy range, alongside with calculations for radioprotection purposes.

MCNPX and FLUKA are fully integrated Monte Carlo packages for the simulation of the transport and interaction of particles and nuclei with matter, which were used for these purposes. According to this numerical models SPES target production ranges between 80 and 160 amu (Fig. 2). The aforementioned models were also experimentally validated with appropriate tests at ORNL.

Table 1 summarizes the numerical results for the nuclides of medical interests (^{89}Sr, ^{90}Y, ^{125}I, ^{131}I, ^{133}Xe), which are produced by ^{238}U fission in SPES target, and have a validated medical application.

Table 1: SPES Target Production Yields - for nuclide of medical interest according to the two different codes, with a 200 µA 40 MeV proton beam

Isotope	FLUKA Calculated Yield
^{89}Sr	$2.191*10^{9}$ nuclei/s
^{90}Y	$3.458*10^{8}$ nuclei/s
^{125}I	$2.47*10^{7}$ nuclei/s
^{131}I	$1.027*10^{11}$ nuclei/s
^{133}Xe	$6.143*10^{10}$ nuclei/s

According to the ISOL technique the migration of the produced nuclei towards the ion source is due to effusion and diffusion processes (Fig. 1), as a consequence high target temperatures are required in order to gain a sufficient release rate. In particular, SPES target was designed to work at temperatures above 2000°C, allowing the extraction of the majority of the produced nuclei (the extraction of highly refractory elements is not possible).

Thermal simulations of the target behavior were performed using the Finite Element Method software ANSYS®, considering as input the proton beam power deposition calculated with FLUKA.

The mechanical design of the target was consequently optimized in order to be capable to maintain the desired temperature level (2200-2300 °C), with the sole heating power coming from the proton beam. Figure 3b shows the calculated temperature field of the target when impinged by the proton beam.

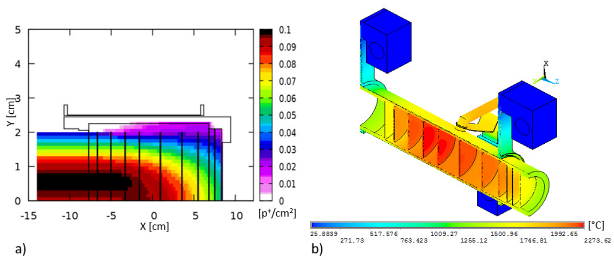

Figure 3: on the left (a) the plot of a FLUKA simulation, showing that the proton beam is entirely stopped in the target; on the right (b) the temperature field calculated with ANSYS® when the target is impinged by the proton beam.

A model for the description of the diffusion and effusion processes is being defined, taking into account the ANSYS® calculated temperatures, using Geant4, a Monte Carlo toolkit. It may lead to further optimization of the target design and to better knowledge of the overall isotope production efficiency.

THE NICKEL TARGET

^{64}Cu is a promising radioisotope currently under preclinical studies for theragnostic applications. It is commonly produced with medical cyclotrons impinging a proton beam on a nickel target via the ^{64}Ni(p,n)^{64}Cu reaction.

The production of high specific activity ^{64}Cu using the innovative ISOL technique may contribute significantly to this research activity, however, since SPES target will not produce copper isotopes, a new target concept is required.

An ISOL nickel target is currently under preliminary studies. Three different target layouts are being considered:

- a graphite foam target coated by thin layers of ^{64}Ni;
- a metallic foam nickel target, using natural nickel, which includes less than 1% of ^{64}Ni;
- a metallic foam nickel target, using enriched ^{64}Ni (around 99% of the total Ni mass used).

Foam targets were preferred because of the lower density, which may lead to a more spread proton beam power deposition, preventing the unwanted target local melting; and to shorter diffusion mean free paths, increasing the release efficiency.

The graphite foam target was soon discharged because of expected manufacturing complexity and lower calculated production.

Table 2 summarize the FLUKA calculated ^{64}Cuproduction for the three concepts, considering a 40 MeV 100μA proton beam entirely dumped in the production target.

As expected, the higher is the ^{64}Ni amount in the target, the higher is the ^{64}Cu production, however such an enriched ^{64}Ni production target is prohibitively costly.

Considering that the peak of the cross section for the ^{64}Ni(p,n) ^{64}Cu reaction is around 10 ÷ 12 MeV [11], a new target concept is being developed. It will combine a first section of natural nickel metallic foam for the degradation of the beam energy up to the preferable range, followed by a thin layer of ^{64}Ni where the beam energy is around 10 MeV, with another subsequent natural nickel section for beam stopping, thus exploiting the whole beam energy available.

Table 2: FLUKA Production Yields for ^{64}Cu - with a 100 μA, 40 MeV proton beam on different target concepts, considering 0.5 days of irradiation

Target Concept	FLUKA Calculated Yield
Natural Ni metallic foam	$2.85*10^{14}$ nuclei/s
^{64}Ni enriched metallic foam	$3.26*10^{16}$ nuclei/s

In addition, some tests are currently being performed for the evaluation of the optimal copper release temperature, with the aim to determine the target working temperature range.

THE SECONDARY TARGETS

A subsequent important issue is the definition of appropriate substrates for the development of the secondary target, where the extracted nuclei are implanted. The aforementioned substrates have to be capable of collecting the largest amount of the impinging radioactive ions and to release them with appropriate chemical dissolution processes.

In the framework of the preliminary tests for the ISOLPHARM project, beams of stable isotope of strontium, yttrium and iodine were extracted for evaluating the efficiency of the secondary target. For strontium and yttrium sodium chloride substrates were used, whereas iodine was deposed on activated carbon targets (Fig. 4). Since the deposition efficiency is dependent only from the chemical properties of both the extracted element and the target substrate, the obtained results are valid also in case of radioactive isotopes.

Table 3 summarizes the deposition efficiencies obtained during the aforementioned tests. Other tests are being performed with the aim to increase the deposition efficiency.

ISBN 978-3-95450-167-0

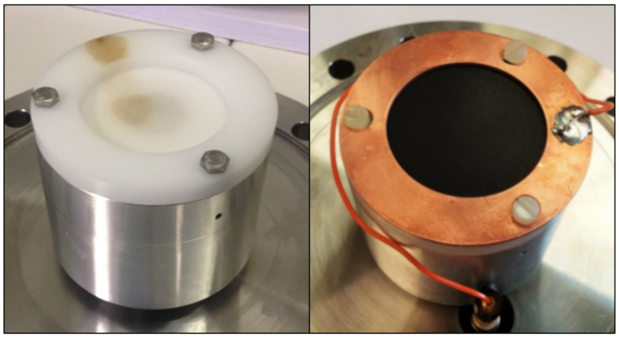

Figure 4: on the left a sodium chloride substrate for the deposition of strontium and yttrium, on the right (b) the activated carbon secondary target designed for iodine beams.

Table 3: Deposition Efficiencies Obtained in the Off-line Test Bench using Stable Isotopes Beams

Extracted Element	Secondary Target Substrate	Deposition Efficiency
Strontium	NaCl	41%
Yttrium	NaCl	55%
Iodine	Activated carbon	23%

CONCLUSIONS

It hasn't been possible yet to perform tests with RIBs since SPES facility is currently under construction.

Numerical simulations and first tests showed preliminary promising results. A large amount of the extracted ions was collected on the secondary target substrate, and chemical purification techniques are currently under investigation.

As first step this project will be focused on radionuclides which are already used or planned to be implemented in nuclear medicine. However, the ISOLPHARM method will afterwards explore the possibility of the application in nuclear medicine of further radionuclides, which were not possible to produce with the traditional techniques.

REFERENCES

[1] Monetti, A., Andrighetto, A., Petrovich, C., Manzolaro M., Corradetti, S., Scarpa, D., Rossetto, F., Martinez Dominguez, F., Vasquez, J., Rossignoli, M., Calderolla, M., Silingardi, R., Mozzi, A., Borgna, F., Vivian, G., Boratto, E., Ballan, M., Prete, G., Meneghetti, G., "The RIB production target for the SPES project", *Eur. Phys. J.* A., vol. 51, p. 128, 2015.

[2] Nilsson, T., "European RIB facilities – Status and future", *Nucl. Instr. Meth*. B, vol. 317, p. 194, 2013.

[3] Kuroda, I., "Effective use of strontium-89 in osseous metastases", *Ann. Nucl. Med.*, vol. 26, pp. 197-206, 2012.

[4] Goffredo, V., Paradiso, A., Ranieri, G., Gadaleta, C. D., "Yttrium-90 (90Y) in the principal radionuclide therapies: An efficacy correlation between peptide receptor radionuclide therapy, radioimmunotherapy and transarterial radioembolization therapy. Ten years of experience (1999–2009)", *Crit. Rev. Oncol Hematol*, vol. 80, pp. 393-410, 2011.

[5] Wyszomirska, A., "Iodine-131 for therapy of thyroid diseases. Physical and biological basis", *Nucl. Med. Rev.*, vol. 15, no. 2, pp. 120–123, 2012.

[6] Shi, F., Zhang, X., Wu, K., Gao, F., Ding, Y., Maharjan, R., Zhang, R., Zhang, F., Li, C., "Metastatic malignant melanoma: computed tomography-guided 125I seed implantation treatment", *Melanoma Res.*, vol. 24, pp. 137-143, 2014.

[7] Al-Busafi, S., Ghali, P., Wong, P., Novales-Diaz, J.A., Deschênes, M., "The utility of Xenon-133 liver scan in the diagnosis and management of nonalcoholic fatty liver disease", *Can. J. Gastroenterol*, vol. 26, pp. 155-159, 2012.

[8] Asabella, A. N., Cascini, G. L., Altini, C., Paparella, D.; Notaristefano, A., Rubini, G., "The Copper Radioisotopes: A Systematic Review with Special Interest to ^{64}Cu", *BioMed Res. Int.*, vol. 2014, May 2014, doi:10.1155/2014/786463

[9] Manzolaro, M., Andrighetto, A., Meneghetti, G., Rossignoli, M., Corradetti, S., Biasetto, L., Scarpa, D., Monetti A., Carturan, S., Maggioni, G., "Ionization efficiency estimations for the SPES surface ion source", *Nucl. Instr. Meth. Phys. Res.*, vol. 317, pp. 446-449, 2013.

[10] Manzolaro, M., Andrighetto, A., Meneghetti, G., Monetti, A., Scarpa, D., Rossignoli, M., Vasquez, J., Corradetti, S., Calderolla, M., Prete, G., "Ongoing characterization of the forced electron beam induced arc discharge ion source for the selective production of exotic species facility", *Rev. Sci. Instrum.*, vol. 85, p. 02B918, 2014. doi:10.1063/1.4857175

[11] S. Takács, F. Tárkányi, M. Sonck, A. Hermanne, "New cross sections and intercomparison of proton monitor reactions on Ti, Ni and Cu", *Nucl. Instr. Meth.* B, vol. 188, p. 106, 2002.

ISBN 978-3-95450-167-0

BEAM OPTICS CONSIDERATIONS FOR ISOTOPE PRODUCTION AT THE PSI CYCLOTRON FACILITY

H. Zhang†, J. Grillenberger, M. Seidel, Paul Scherrer Institut, 5232 Villigen PSI, Switzerland

Abstract

The isotope production beam line starts at the electrostatic beam splitter, which peels off a beam of a few tens of μA from a main beam of high intensity up to 2.4 mA. The beam optics has to ensure that the beam on target will be in right size. Due to the parasitic nature of the beam line, the beam optics also has to get along with the tuning of the main beam, especially in the sections upstream of the beam splitter. Aiming at a reliable and efficient isotope production, the beam optics is monitored for each irradiation session. The operational experience together with further development is presented.

BEAM LINE

The isotope production beam line starts at the electrostatic beam splitter EXT and ends at the target station as illustrated in Figure 1, where the important beam optics elements, namely the bending magnets, the steering magnets and the quadrupoles, are marked blue, orange and red, respectively. The length of the beam line is approximately 22 m.

The splitter EXT peels off a beam of a few tens of μA from the main beam coming from the 72 MeV Injector II cyclotron. The intensity of the peeled beam is regulated through adjusting the position of the splitter with respect to the main beam by a control loop [1].

The beam for the isotope production is deflected around 0.6° by the electrostatic field, whereas the main beam passes through a field-free region. A separation more than 40 mm may be created at the entrance of the septum magnet AYA, about 4 m downstream of the splitter EXT. The magnet AYA bends the peeled beam 17.5° further away from the main beam.

The beam energy may be reduced from 72 MeV to 40 MeV by inserting the graphite degrader DYD into the beam line. The degrader DYD locates in front of the quadrupole QYA6.

The beam position is controlled by the beam centering program through adjusting the strength of steering magnets according to the actual beam positions measured by the beam position monitors named as MYS*N* in Figure 1. Here *N* is an integer number with odd and even representing horizontal and vertical position, respectively. The measured beam positions are stored automatically into the database.

The beam profiles are measured by the beam profile monitors named MYP*N* in Figure 1. Here *N* is also an integer number with odd and even representing horizontal and vertical profile, respectively. The profile scan may be carried out with a single monitor or a group of preselected monitors. The profile measurement and the database registration are performed not automatically, but on demand.

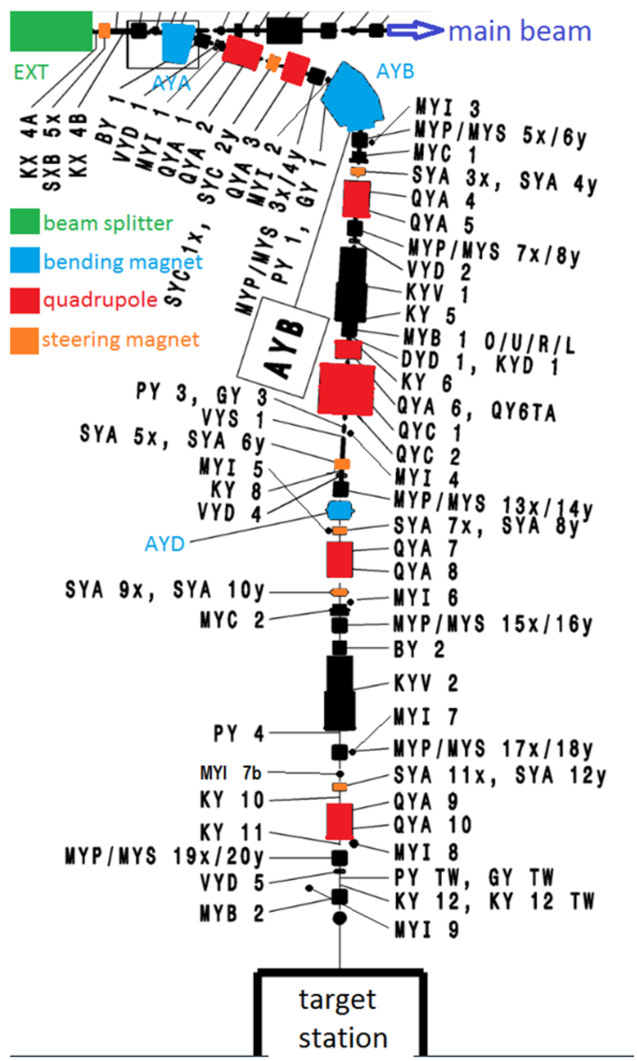

Figure 1: Isotope production beam line.

BEAM OPTICS

The beam line has to guide the beam of desired size onto the target. The challenge to the beam optics comes firstly from the fact that the required beam size differs significantly from one isotope production to another. For example, the diameter of $^{44}CaCO_3$(graphite) target for ^{44}Sc production is around 6 mm which requires a beam of 2σ less than 5 mm, while ^{64}Ni(Au) target for ^{64}Cu production requires a beam of 2σ greater than 7 mm. The difficulty arises also from the fact that the beam size on target cannot be measured in situ in real-time. The profile monitor next to the target is one meter away. The other difficulty arises from the parasitic nature of the beam line. As a

† hui.zhang@psi.ch

ISBN 978-3-95450-167-0

matter of fact, the emittance of the peeled-off beam might be significantly reduced when the main beam intensity is dropped, for instance when the intensity of the main beam has to be reduced from 2.2 mA to 1.7 mA in case that the neutron target is not in operation. In extreme case, the main beam of a few tens of µA has to be guided directly onto the isotope target. In Table 1 the measured emittance of a 50 µA beam is listed along with the intensity of the main beam. In spite of all these difficulties, the beam size can still be well controlled to meet the requirement. The setup procedure is described as following.

Table 1: Horizontal and Vertical Beam Emittance, ε_x, ε_y

Main Beam Intensity mA	ε_x **π·mm·mrad**	ε_y **π·mm·mrad**
2.4	1.18±0.06	4.6±0.3
2.25	1.12±0.05	4.0±0.5
2.05	1.07±0.05	3.8±0.4
1.85	1.02±0.05	3.6±0.5
1.65	1.02±0.04	3.3±0.4
0.05	0.86±0.06	0.64±0.04

An irradiation is often started with setting up the beam line according to a setup recently recorded during the production of the same isotope and under identical conditions. Over the years a comprehensive database has been established for the production of a variety of isotopes and under different conditions. Soon after the irradiation is started, the beam profiles are scanned, and the beam envelope is calculated with the program TRANSPORT [2]. Figure 2 shows the beam envelopes measured during ^{44}Sc and ^{64}Cu irradiations, depicted by the black and orange curves, respectively. The lower and upper halves represent the horizontal and vertical directions, while the $\top$ and $\perp$ symbols represent the 2σ beam sizes from beam profile measurement. On the figure the blue and red blocks symbolize the position, dimension and aperture of the dipole and quadrupole, respectively, while the aperture is scaled by a factor of 0.25.

From the envelope fit, the beam size on target can be indirectly derived. The beam size on target is repeatedly measured during an irradiation session. For example, ten envelope-fits are performed in a ^{44}Sc irradiation session in 90 minute, which gives typically a 2σ beam radius on target around 4.5±0.1 mm. The fluctuation of the beam size on target is thus around 2%. Figure 3 shows ten beam profiles in horizontal and vertical direction measured with the monitors one meter in front of the target, namely MYP19 and MYP20, which indicates that not only the beam size but also the beam position are stable.

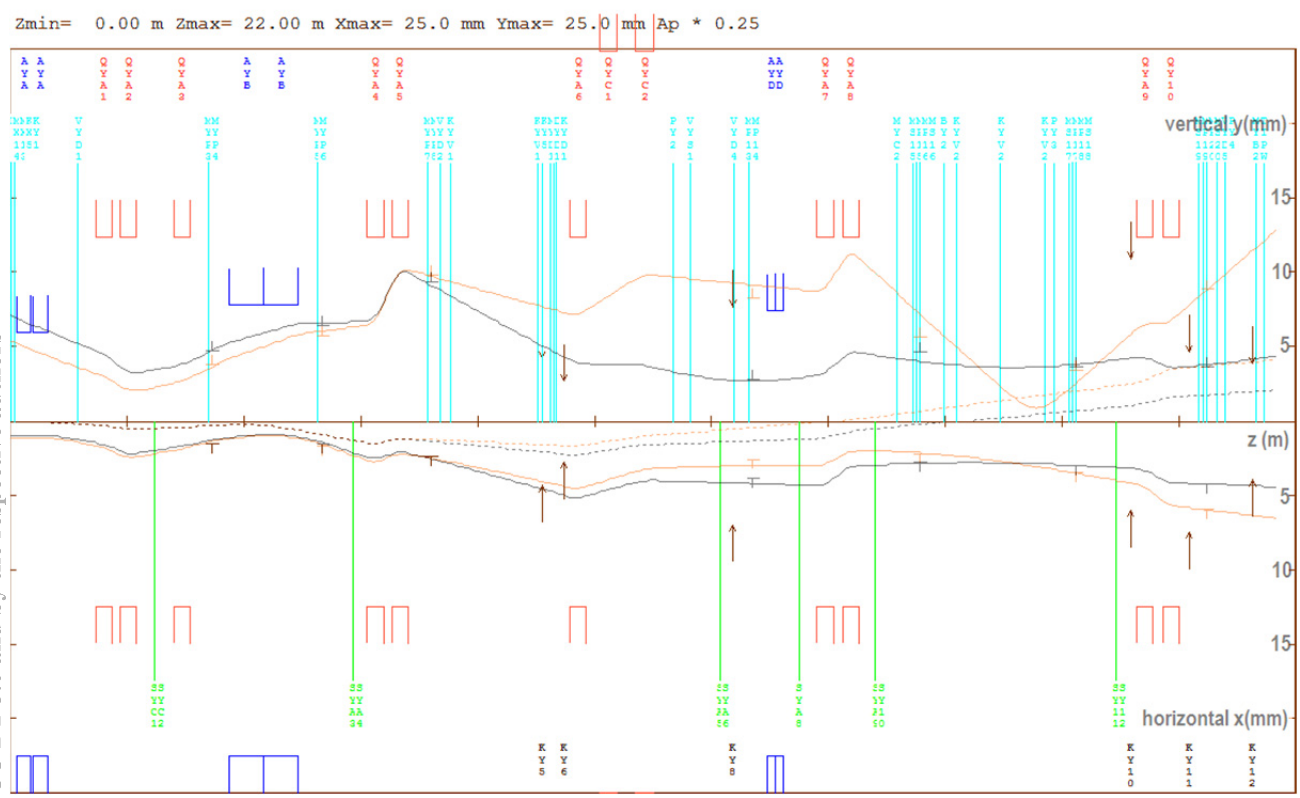

Figure 2: Beam envelopes for ^{44}Sc and ^{64}Cu productions in black and orange.

ISBN 978-3-95450-167-0

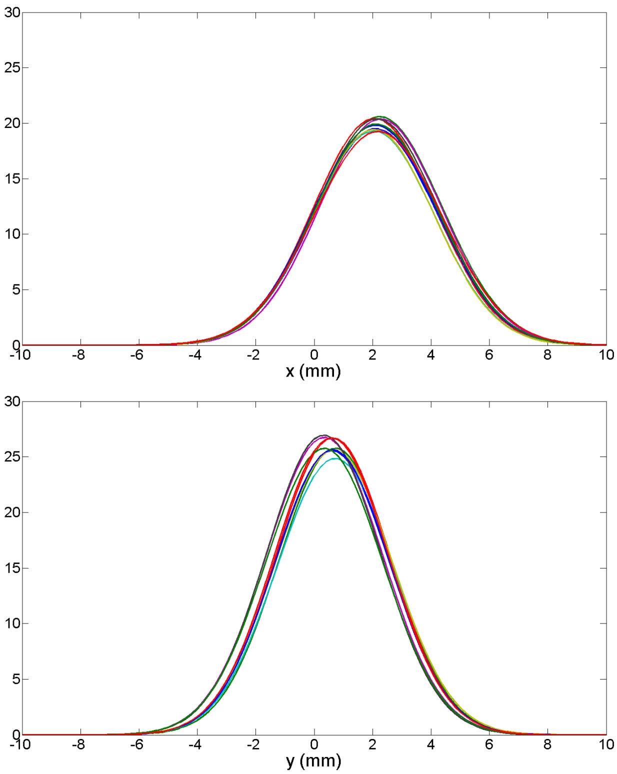

Figure 3: Ten beam profiles measured in one session. Top: horizontal; Bottom: vertical.

Provided that the target could be sufficiently cooled, the efficiency of the isotope production could be optimized by matching the beam with the target. In practice, a divergent beam is guided onto the target and the beam diameter is larger than the effective diameter of the target. For example, the 2σ beam diameter is around 9 mm, while $^{44}CaCO_3$(graphite) powder is pressed to form a thin disc 6mm in diameter. The irradiation might not be highly efficient, but can still deliver high yield. Nevertheless the target, especially the $^{44}CaCO_3$(graphite) target, may occasionally be overheated. The exact cause of target overheating can be identified only on rare occasion. There are several uncertainties, for example, the peeled-off beam might be different after tuning the main beam, or the target might be prepared in a different way, or the cooling water might be running extraordinarily. Anyway, in case that the target is overheated and that the yield is much lower than expected, the beam size has to be increased for the next irradiation by adjusting the strengths of certain quadrupoles. The adjustment is often started with a test target to avoid wasting the expensive target material. The quadrupole setting may be optimized step by step until the yield is back to high level. The setting is then stored in database for future application.

Theoretically it is possible to increase the beam size to such an extent that the target can be freed from overheating. However, the irradiation would then be inefficient and the yield would be too low for the following radiopharmacy applications. At present the yield from a reduced beam size is more than tripled so that the risk of occasional target overheating can still be tolerated.

FUTHER DEVELOPMENT

The Injector II cyclotron can deliver a beam up to 2.7 mA, while the proton facilities are licenced for the operation with a beam up to 2.4 mA. Furthermore, the Injector II cyclotron is back in operation one month before the official end of annual shutdown. Therefore it is possible to deliver a beam over 2 mA exclusively for the isotope production for four weeks every year, which is an attractive option.

On the existing isotope beam line, the so-called direct shot is actually a routine practice. A beam of 50 µA from Injector II cyclotron is deflected without splitting by the beam splitter and guided on to the target for the isotope production, in case that the 590 MeV Ring cyclotron is out of operation. However, the beam current seldom exceeds 50 µA in the past, and the limiting factors are the cooling and the shielding of the target. As the modification to the target station is rather difficult and expensive, the beam optics, specifically the maximizing of the beam-on-target size has been explored at first. Preliminary experiments have been performed applying a direct shot of 70 µA beam. The beam-on-target size can be increased up to a 2σ diameter of 30 mm. Nevertheless, the beam optics has to be significantly modified and certain quadrupoles have to be pushed near to their limits.

For the existing target station, the optimization of the cooling scheme has been high on the agenda. A more ambitious project aiming at the full use of the high power proton beam, including a new target station and a beam line connecting the Injector II and the target station, has been under discussion. The bunker for the decommissioned Injector I cyclotron could be used for the target station, while the beam line connecting Injector I and the 590 MeV Ring cyclotron could be partially reused [3].

ACKNOWLEDGEMENT

The authors would like to thank Mr. A. Sommerhalder, Mr. W. Hirzel, Mr. C. Vermeulen, and Mr. N. P. van der Meulen for communicating the details about the targets and the outcomes of the irradiations. The authors also would like to express their sincere thanks to the whole operation group.

REFERENCES

[1] M. Olivo and H. W. Reist, “A beam splitter for the parasitic use of the 72 MeV proton beam line to produce isotopes”, in *Proc. EPAC'88*, Rome, Italy, June 1988, pp. 1300-1302.
[2] U. Rohrer, “PSI Graphic Transport Framework”, based on CERN-SLAC-FERMILAB version by K.L. Brown *et al.*
[3] U. Schryber, “Status report on the PSI-accelerator facility”, in *Proc. Cyclotrons'89*, Berlin, Germany, May 1989, pp. 93-96.

ISBN 978-3-95450-167-0

ACTIVITIES FOR ISOTOPE SAMPLE PRODUCTION AND RADIATION EFFECT TESTS AT JULIC/COSY JÜLICH

O. Felden, M. Bai, R. Gebel, R.Hecker
Forschungszentrum Jülich, IKP-4, Germany

Abstract

At the Forschungszentrum Jülich (FZJ) the intermediate energy cyclotron JULIC, used as injector of the Cooler Synchrotron (COSY), and at the COSY itself, over the last years, have been enabled to perform low to medium current irradiations. Main task is to support the FZJ radionuclide research programme of INM-5, by developing, adapting and optimizing the irradiation facilities. The INM-5 target holders were implemented via an adapter section to the external target station of JULIC to obtain reliable irradiations with 45 MeV protons and 76 MeV deuterons, both for nuclear reaction cross section measurements and medical radionuclide production. For testing of radiation effects, displacement damage (DD) and single event effects (SEE), with energetic protons for electronics used in space and accelerators the beam can be extracted to a dedicated test stand, e.g. used by Fraunhofer INT. To provide these possibilities at higher energies up to 2.5 GeV as well one external beamline of the cooler synchrotron COSY is going to be equipped with a new irradiation vacuum chamber to separate the irradiation zone from the COSY-vacuum system and adaption for the dosimetry systems are done. Different dosimetry systems (PTW® Farmer ionization chambers, PTW® Bragg Peak chambers, Gafchromic® Dose sensitive foils) are available to monitor and control the ongoing irradiation. This report briefly summarizes the relevant technical activities.

INTRODUCTION

The Institute for Nuclear Physics (IKP) [1] is focusing on the tasks given by the Helmholtz Association (HGF). This comprises the design and preparations for the High Energy Storage Ring (HESR) of FAIR [2] with the PANDA experiment. The on-going hadron physics program at the Cooler Synchrotron COSY exploits the internal experimental set-up PAX. The extracted beam is used for the PANDA experiment, detector tests and also for high energy irradiation in the area of the finished TOF experiment. IKP is part of the section “Forces And Matter Experiments” (FAME) at the Jülich-Aachen Research Alliance (JARA). This joins scientists and engineers from RWTH Aachen and Forschungszentrum Jülich for experiments, theory and technical developments for anti-matter (AMS) and electric dipole moment experiments (EDM). The institute is member of the HGF project Accelerator Research Development (ARD) and pursues research on various accelerator components. The future project Jülich Electric Dipole Moment Investigation (JEDI) [3] will profit from the availability of polarized beams from the injector cyclotron and the unique capabilities and experiences at the COSY facility.

CYCLOTRON OPERATION

The COSY accelerator facility [4, 5], operated by the Institute for Nuclear Physics (IKP) at the Forschungszentrum Jülich GmbH, consists of the injector cyclotron JULIC and the Cooler Synchrotron COSY. Both accelerators are originally dedicated to fundamental research in the field of hadron, particle, and nuclear physics, to study the properties and behavior of hadrons in an energy range that resides between the nuclear and the high energy regime.

The cyclotron JULIC provides 45 MeV H^- respectively 76 MeV D^- with max. beam currents of ~10 µA. Operation of the cyclotron started 1968 and beside the Nuclear Physics experiments a small amount of the available beam time was used for irradiation. In the beginning the irradiations were performed with internal targets inside the cyclotron. But since the implementation of the target holders of the INM-5 at the external target station of JULIC via an adapter section [6], reliable irradiations can be done both for nuclear reaction cross section measurements and medical radionuclide production. In the case of the deuterons, the emphasis is on cross section measurements because the data base for many of the deuteron-induced reactions is weak. The proton beam, on the other hand, is mainly used for the production of the important β^+ emitter ^{73}Se via the ^{75}As(p,3n)-reaction over the energy range of $E_P = 40 \rightarrow 30$ MeV at beam currents of a few micro amps. A view of the adapter at the end of the beam line is given in Fig. 1.

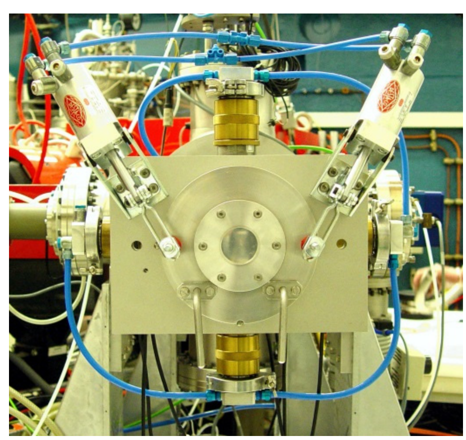

Figure 1: Head of adapter section at the external JULIC beam line.

For the last 15 years Fraunhofer INT with IKP have been operating a dedicated radiation effects test facility at an external beam line of the JULIC cyclotron [7], which can be seen in Fig. 2. Since the tests are performed in air,

ISBN 978-3-95450-167-0

the beam has to pass a 1 mm Al foil and about 1.8 m of air, which reduces the energy of the protons to 35 MeV at the surface of the target [8].

Figure 2: Beamline for Radiation Tests at JULIC.

IRRADIATION FACILITY AT COSY

The Cooler Synchrotron COSY, commissioned in 1993, provides protons and deuterons in the broad energy range from 20 MeV up to 2.5 GeV [9] by de- or accelerating the beam. The number of particles is up to 10^{11}/spill. COSY has three external beam lines (see Fig. 3) useable for testing of detector systems, accelerator components, investigations on radio-isotope-production properties or for radiation effects tests.

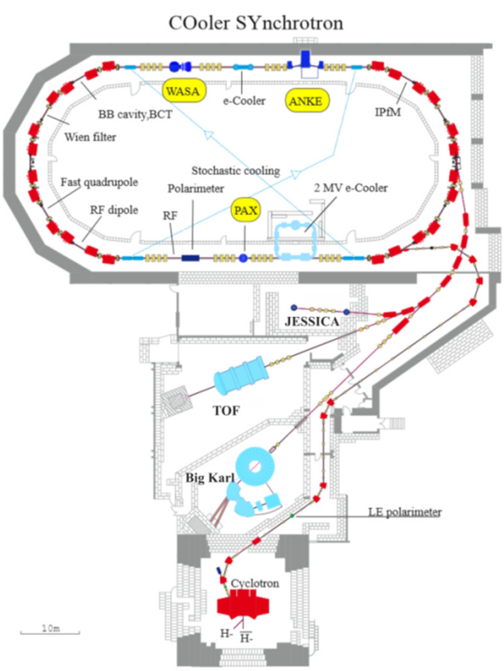

Figure 3: Layout of the COSY facility (with TOF- and Big Karl-Detector).

COSY operation has been very reproducible and reliable with ~7000 h/year. Two different extraction schemes have been used; Fast Kicker Extraction with 10^9p within 200 ns [10] and in contrasts the Slow Extraction with variable beam currents of 10^{10} p/s down to 10^4 p/s, depending on the extraction times (Fig. 4).

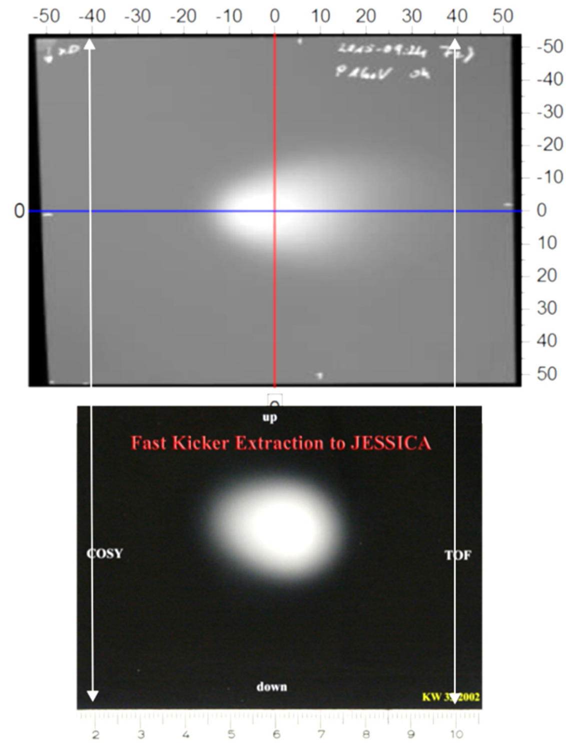

Figure 4: Beam spots at JESSICA target place with Slow Extraction (2015,up) and Fast Kicker Extraction (2002, down). The Beam spots are of similar size.

Twice a year the COSY Beam Advisory Committee (CBAC) examines applications for experiments to be carried out at COSY. Within the beam time request energies, particle numbers, safety aspects, additional things and at least the necessity of the experiment is asked for. This will be described in a short beam time proposal.

EXTERNAL EXPERIMENTAL AREAS

Since the research programs with JESSICA, TOF and Big Karl-Detector Systems ended in 2015, the detectors were dismounted and the areas cleared for new tests. While the TOF-area is intended for tests of PANDA-related detector and data-acquisition systems the other two areas are foreseen for changing installations like irradiations, detector- or radiation effects tests.

Therefore the Big Karl area as well as the JESSICA area is equipped with adjusted 3m long tables whereon different experimental setups can be mounted easily. The distance between table and beam is about 50 cm.

In addition there are remotely operable X-Y-tables to change between different probes, e.g. Fig. 5. The X-Y-tables are operated via Labview® but can be accessed via serial connection directly as well.

A vacuum chamber for irradiation has been constructed by INM-5, which is shown in Fig. 5. It will allow irradiation, separated from COSY vacuum of thin foils in a stack geometry and collection of charge in a Faraday cup. Activation studies of several potentially useful radionuclides e. g. ^{52}Fe, ^{67}Cu, ^{72}Se, etc. [11, 12], for which the database is weak and the production methods need improvement. They could be advantageously produced only if proton

ISBN 978-3-95450-167-0

beams of intermediate energy (between 50 and 150 MeV) would be available. First results using beam intensity in the nA scale are expected to commence soon.

Radiochemical separations and yield measurements will follow and be performed at the INM-5. In the first phase clinical scale production is not envisaged. It may follow if a higher current beam could be made available in due course of time.

The Big Karl area is rather big. The available length for installations behind the beam exit is about 10 m. The JESSICA area with available length of 3 m only is much more compact. The heights of the beamlines differ (TOF 2.19 m, in JESSICA 1.75 m and in Big Karl it is 1.42 m). Transverse beam spots are variable. In TOF and Big Karl it is minimal 2-3 mm while in JESSICA it is 20 mm (Fig. 4) due to absence of focusing elements. This is going to be improved; beam tracking calculations are in progress. The beam spots can be widened up to 20cm diameter.

The proton beam extraction at the chosen irradiation position is being optimized with respect to energy, shape and intensity. All beam lines are equipped with ionization chambers to measure beam current and multi wire proportional chambers (MWPC) for beam position measurements. In terms of low energy particles these measurements are destructive to the beam and are done before the irradiation or afterwards only.

Figure 5: View into the "new" Big Karl area with test setup for Radiation effects tests and the “irradiation chamber”.

To monitor and control fluence and homogeneity during the ongoing irradiation up to 12 PTW® Farmer Ionization Chambers Type 30010 and 2 PTW® Bragg Peak Chambers Type 34080 are available and can be connected via a connector-box 12xM T16007 to a PTW MULTIDOS T10004 Multichannel dose meter.

The data-visualization and acquisition is done with Labview®-Programs taking all Dosimetry-data as well as other important measures like humidity, temperature, pressure e.g. all data are stored and can be processed later. Figure 6 is showing a dose measurement at JESSICA and gives an impression on the stability and reproducibility in terms of short (shot to shot) as well as of long term operation of COSY.

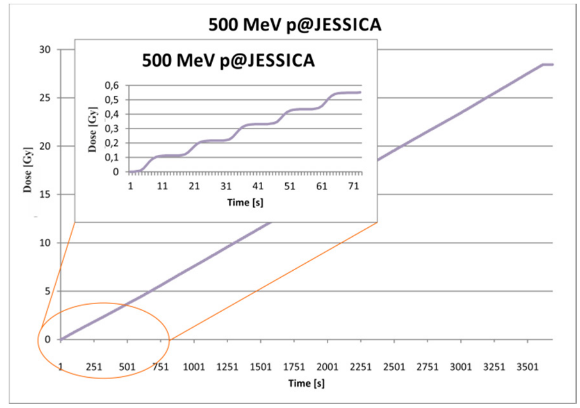

Figure 6: Irradiation at JESSICA, 500 MeV Protons over 1h to the target. The small picture shows the time structure with filling COSY, accelerating the beam and extraction to the target while the big one gives the stability.

In addition Gafchromic® self-developing foils Type EBT3 and EBT XD can be used for checking homogeneity of the irradiation as well (Fig. 7). The readout is done with an Epson® 11000 scanner. For analyzing the foils FilmQA Pro from Ashland® is available.

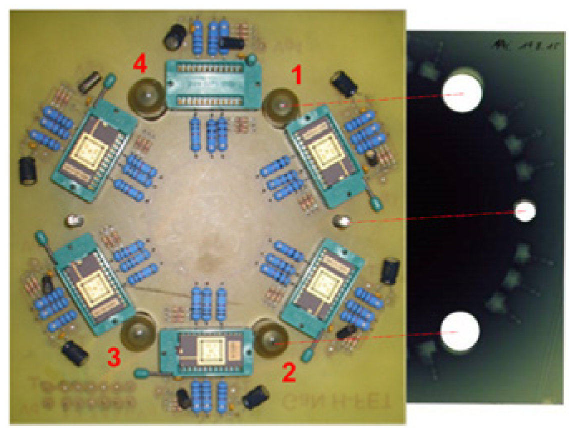

Figure 7: Test of electronic devices; Dosimetry is done with 4 Farmer chambers and a EBT3-background foil.

CONCLUSION

At the COSY accelerator facility irradiation and radiation tests with protons as well as with deuterons can be performed in the broad energy range from 20 MeV to 2.5 GeV. Three external beam lines at COSY as well as one beam line at JULIC are useable for these tests or irradiations. Available intensities can be varied from 10^{10} p/s down to 10^{4} p/s by slow extraction over long times.

REFERENCES

[1] http://www.fz-juelich.de/ikp/en

[2] http://www.gsi.de/fair

[3] http://www.collaborations.fz-juelich.de/ikp/Jedi

[4] R.Maier, “Cooler Synchrotron COSY – performance and perspectives”, *NIM* A 390 (1997), pp. 1-8.

ISBN 978-3-95450-167-0

[5] H. Stockhorst *et al.*, "Progress and Developments at the Cooler Synchrotron COSY", in *Proc. of the 8th European Particle Accelerator Conference (EPAC 03).*

[6] B. Scholten, S. Spellerberg, W. Bolten, H. H. Coenen, in *Proc. 13th Int. Workshop on Targetry and Target Chemistry*, Roskilde, Denmark, pp. 14-18, 2010.

[7] S. Metzger *et al.*, "Low Energy Proton Testing of space Electronics at JULIC", RADECS´99, p. 163 (1999).

[8] S. Hoeffgen *et al.*, "Past, Present and Future Activities for Radiation Effects Testing at JULIC/COSY", in *Proc. Cyclotrons'13*, Vancouver, Canada (2013).

[9] R. Gebel et al.,"20 Years of JULIC Operation as COSY´s Injector Cyclotron", in *Proc. Cyclotrons'13*, Vancouver, Canada (2013).

[10] D. Prasuhn, "Status of the Cooler Synchrotron COSY Juelich", in *Proc. PAC'01*, Chicago, IL, USA (2001).

[11] S. M. Qaim: *J. Radioanalyt. Nucl. Chem.* **305**, pp. 233-245, 2015.

[12] Nuclear Data Needs Whitepaper based on Workshop held at Berkeley, California, USA, May 2015, USA. Available at: http://bang.berkeley.edu/wp-content/uploads/nd_needs_whitepaper_102615-merged.pdf

ISBN 978-3-95450-167-0

A DIAMOND DETECTOR TEST BENCH TO ASSESS THE S2C2 BEAM CHARACTERISTICS

J. Van de Walle*, S. Henrotin, Y. Paradis and I.C. tKint
Ion Beam Applications, Louvain-la-Neuve, Belgium

Abstract

During the assembly and initial start-up of the superconducting synchro-cyclotron (S2C2) in the manufacturing hall at Ion Beam Applications (IBA), some key properties of the extracted beam have to be validated. A new setup was developed to assess the beam direction out of the S2C2, the beam energy variation as a function of main coil current and main coil position, and the time structure of the beam. In the future, the setup will be extended with an emittance slit. The beam detector in this setup is a sensitive "poly-crystalline diamond detector" (pCVD), which requires small amounts of beam from which a maximum amount of information can be extracted. The high sensitivity and versatility of the detector are important aspects in order to limit the activation of the S2C2 during in-factory beam tests.

INTRODUCTION

The activation of the S2C2 during in-factory beam tests has to be limited to an absolute minimum to facilitate the transport of the accelerator to the installation site. Therefore, a sensitive and versatile detector is needed to extract as much information as possible at a minimum beam intensity. Therefore, a new setup was developed which measures the beam direction, size and divergence and the beam energy variation with main coil current and horizontal main coil position.

THE EXPERIMENTAL SETUP

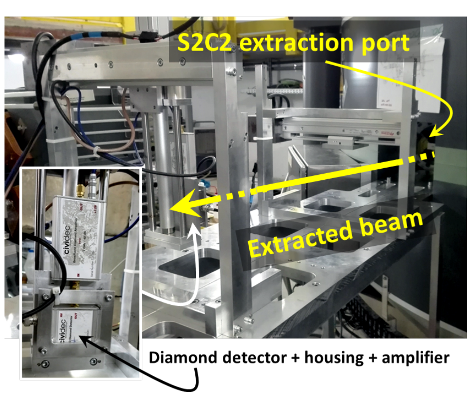

Figure 1: The diamond detector setup installed on a table directly connected on the exit port of the S2C2. The support of the diamond detector can be moved to fixed distances from the exit port and the detector itself can move continuously both horizontally and vertically in the beam. An additional support is foreseen to install an emittance slit.

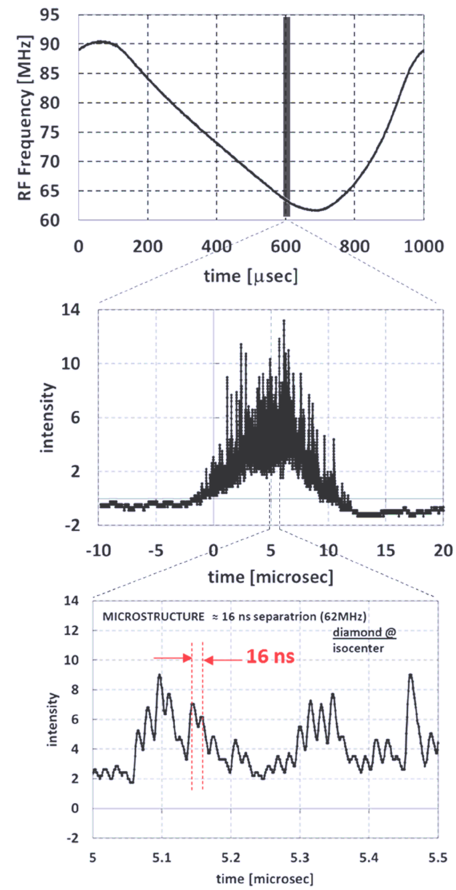

Figure 2: (top) 1 period of the RF frequency sweep in the S2C2. Extraction of the beam happens around 63 MHz. (middle) The diamond detector signal. (bottom) A zoom on the diamond detector signal. Individual proton bunches on the RF wave are visible. The bunches come out at a frequency of 63 MHz, or with a periodicity of 16 ns.

The beam detector is a "poly-crystalline diamond detector" (pCVD, see [1]) with an active surface of $10\,\mathrm{mm}^2 \times 10\,\mathrm{mm}^2$ and a thickness of 500 mm. Protons of 230 MeV loose about 400 keV in the detector. This detector is typically used as beam loss monitor or for time-of-flight measurements. In our case, the good timing properties (sharp rising time and fast fall-time) and its high sensitivity make it an excellent detector to measure small intensity pulses from the S2C2. Figure 1 shows the full setup, installed on the exit port of the S2C2. A support structure, carrying the diamond detector, can be installed at fixed distances from the exit port. The detector itself is scanned continuously both horizontally as vertically in the beam path. A second support structure is foreseen to install an emittance slit.

* jarno.vandewalle@iba-group.com

ISBN 978-3-95450-167-0

TIMING AND DETECTOR SIGNAL

Figure 2 shows the timing of the S2C2 beam. For a full explanation of the operational principles of the S2C2, see [2]. The top figure shows 1 period of the RF frequency sweep as a function of time. The beam capture in the central region happens around 87.5 MHz, whereas the extraction happens around 63.0 MHz, depending on the magnetic field configuration. The latter depends essentially on the horizontal position of the superconducting main coil. The middle part of Fig. 2 shows the diamond detector signal. The beam pulse lasts for about 10 µs and appears around the frequency of 63 MHz. The bottom figure shows a zoom in the diamond detector signal, showing the individual proton bunches on the RF wave. Since the RF frequency is around 63 MHz, the periodicity of the micro-bunches is around 16 ns.

EXTRACTION FREQUENCY

A Fourier transform of the diamond detector signal is shown in Fig. 3. The extraction frequency of the proton bunches is clearly visible around 63 MHz. When the superconducting main coil is shifted horizontally, the extracted beam energy will change, as was shown in [2]. The extracted beam energy will also change when the main coil current is changed. Measured maps were used to assess this change in energy and revolution frequency of the protons on their last stable closed orbit as a function of the main coil current and position. The energy change is 450 keV per additional Ampere in the coil and the frequency change of the last stable closed orbit is 43 kHz per additional Ampere. The revolution frequency of the last stable closed proton orbit changes with about 100 kHz per mm of coil shift. Both frequency changes have been measured and correspond very well with the calculations, as is shown in Fig. 4.

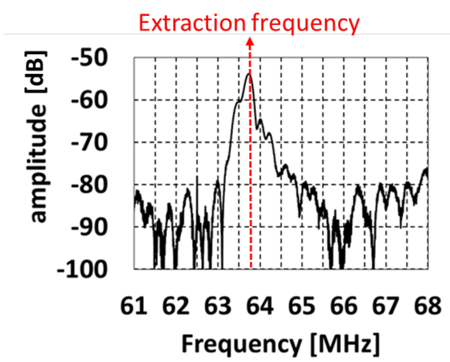

Figure 3: Zoom in the Fourier transform of the diamond signal. A peak is observed at the extraction frequency of the S2C2.

BEAM SIZE AND DIRECTION

The measured horizontal intensity profiles of the extracted beam are shown in Fig. 5 as a function of distance from the extraction port of the S2C2. As can be seen, the unfocused beam out of the S2C2 is around 50 mm wide. From the increase in beam width as a function of distance, the horizontal divergence can be derived and is measured to be around 10 mrad. From the shifted center of the beam, the exact beam direction can be determined. Figure 6 shows a comparison of the measured and calculated beam widths.

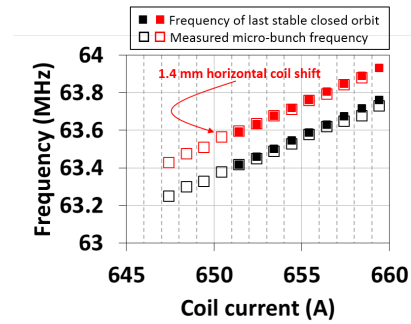

Figure 4: The measured and calculated frequency of the extracted proton microbunches, as a function of main coil current and position.

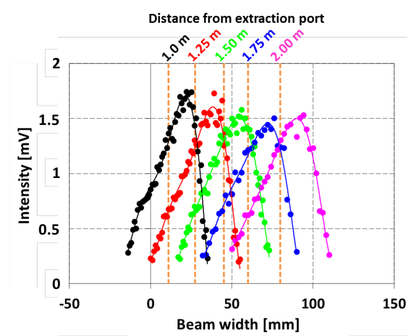

Figure 5: The measured horizontal intensity profiles of the extracted beam as a function of distance from the exit port.

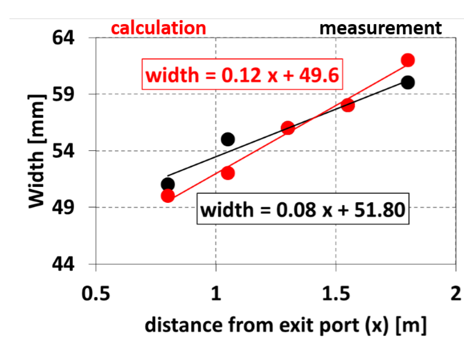

Figure 6: Comparison of the calculated and measured horizontal width of the extracted beam from the S2C2.

CONCLUSION

A new setup, based on a high sensitivity and fast diamond detector, to assess the beam characteristics (beam energy as a function of main coil current, beam direction and size and temporal profile) of the S2C2 has been developed and commissioned successfully at IBA.

ISBN 978-3-95450-167-0

REFERENCES

[1] Cividec, https://cividec.at

[2] J. Van de Walle *et al.*, "The S2C2 from source to extraction", presented at Cyclotrons'16, Zurich, Switzerland, Sep. 2016, paper THB01, this conference.

ISBN 978-3-95450-167-0

STUDY OF GEANT4 SIMULATION FOR CYCLOTRON RADIOISOTOPE PRODUCTION IN VARIOUS TARGET SIZE

Sangchul Mun, Donghyup Ha, Ho Namgoong, Mitra Ghergherehchi, J.S. Chai,
Department of Electrical and Computer Engineering, Sungkyunkwan University, 2066 Seobu-ro, Jangan-gu, Suwon, Gyeonggi-do, Korea

HuiSu Kim, Jongchul Lee, Department of Energy Science, Sungkyunkwan University, Suwon, Korea

Abstract

The application of radioisotopes in medical radiology is essential for diagnosis and treatment of cancer. The fabrication of radioisotopes has main factors that maximize the fabrication yield and minimize the costs. An effective method to solve this problem is that the usage of Monte Carlo simulations before experimental procedure [1]. This paper studies the simulation and presents cyclotron models for the energy 13 MeV with moderate beam intensity are used for production of 11C, 13N, 15O, and 18F isotopes widely applied in positron emission tomography [1]. TR-13 cyclotrons with high beam intensity are available on the market for production of most medical and industrial isotopes. In this work, the physical and technical parameters of different models are compared. Overall, this confirms the applicability of Monte-Carlo to simulate radionuclide production at 13 MeV proton beam energy.

INTRODUCTION

Compact cyclotron is normally used to produce for short-term lived radioisotopes, especially using applications for positron emission tomography (PET) [1, 2]. These kind of machines accelerate protons and also produce four positron emitters that are carbon-11, nitrogen-13, oxygen-15 and fluorine-18. The four positron emitters are easily produced by the low-energy and nuclear reactions. Normally, the methods of productions about these emitters use gas and liquid targets for employing. In addition, many medical cyclotrons are adopted both two target systems, which are generally attached directly to cyclotron. It is suitable to produce radioisotopes by using targets systems, however it didn't be optimized sufficiently about thickness with materials [2].

In this study, the Monte-Carlo simulation code Geant4 is used for optimization of target thickness as well as target materials that role as a critical assessing the yield for isotope production of system. It is a typically calculation tool that suggests particle tracking and interaction with mass. And also, it can provide wide range of applications, which is target design, calorimetry, activation and dose rate measurement. To get results harmoniously, we set out to use Geant4 to calculate following hadronic reactions for nuclear and particle physics for carbon-11, nitrogen-13, oxygen-15 and fluorine-18.

DESIGN AND SYSTEM DESCRIPTION

Geant4 is open source code, which is Monte Carlo toolkit for the tracking particles through matter. It is often used that applicate physics and medical field with various area. This simulation tool is suitable for evaluation of irradiation of target system with a large data driven physics models [1].

The simulation model is the target system of the SKKUCY-13 cyclotron. The geometry is based on a simple drawing of the system. The target system is made of cylindrical shape target chamber and target body that can modulate the energy of the beam and a target at the end of the fixed chamber. Fig.1 shows the geometry for simulation to calculate radioisotopes production. The target is made for optimization of target shapes which allows the selection of the thickness. The proton beam line passes through the tube with foil before hitting the target. This schematic drawing geometry model is generated to calculate for target configurations with adopted various thickness system.

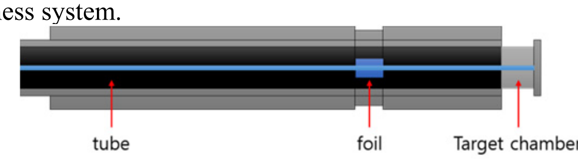

Figure 1: Geometry for radioisotope production target system.

In this paper, a further investigation has been performed via the low-energy (p, n) and (p, α) nuclear reactions cross section values for energies at 13 MeV using the TENDL library [1, 3].

To calculate the cross section values, several simulations were run using different chamber thickness and a thin 11C, 13N, 15O and 18F target in target chamber, so the energy would remain approximately constant while the proton would travel through the target. To achieve reasonable computing time, sensitive volume (the target chamber) was defined to track particles in the regions of interest. On average, around 10000 events were necessary to achieve good precision. This represents around one hour of simulation on a general purpose processor.

RESULTS AND DISCUSSIONS

The isotope number of reactions relative to ^{11}C, ^{13}N, ^{15}O and ^{18}F production were also compared to theoretical results of P. W. Schmor et al [4]. The relative simulated

ISBN 978-3-95450-167-0

result shows the comparison of number of reaction and mean energy at 13 MeV. It shows an overestimated trend in Fig. 2.

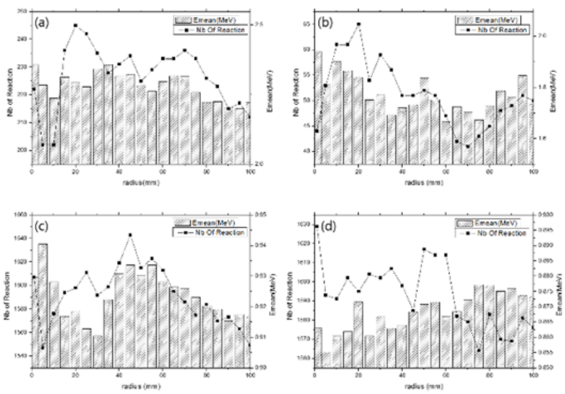

Figure 2: Number of Reactions and mean Energy for (a) ^{11}C, (b) ^{13}N, (c) ^{15}O and (d) ^{18}F at thickness range from 1 mm to 100 mm.

As the target is thick, the protons have an energy of 13 MeV when they leave it, which explains why over a large thickness range the results show an overall underestimation. However, the target radius varies between 1 to 100 mm within the target and as Fig. 2 shown. Also the expected conclusion can be explained by some inaccuracy from cross section.

For simulations with thick targets with energy 13 MeV, there is a systematic overestimation of the yield compared to theoretical results at various thicknesses. The overestimation of the cross section at thin thickness is more dominant than the underestimation at high energies, resulting in an overestimated yield when integrating over a large thickness range.

The cross section of the reaction was calculated through the simulation using the QGSP_BIC_AllHP physics model and the TENDL library, with energies 13 MeV. The first step was to verify that the cross section outcome from the simulation was the same as the TENDL cross section that is used. As shown in Fig. 3, they were in reduced value with some error due to the uncertainty of the simulation.

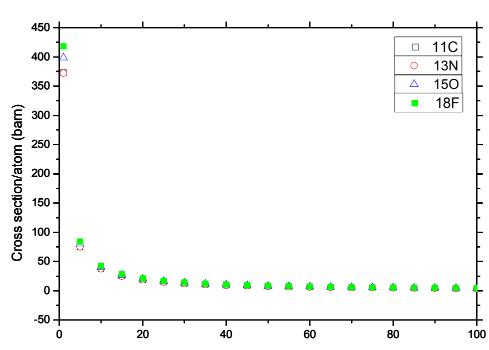

Figure 3: Production yield calculation result for (a) 11C, (b) 13N, (c) 15O and (d) 18F at various thicknesses.

The results from the simulation are shown in Fig. 4 and compared each isotopes results. The graph shows good agreement each isotopes cross section simulation results. However the simulation cross section values tend to be decline at energy 13 MeV. Figure 4 shows production yields for different radius ranges for Geant4 simulation. Overall, the simulation tends to overestimate the saturation yield with 103 ± 10 mCi/μA for 11C a thickness range from 1 to 100 mm, with protons reaching the target with an energy of 13 MeV. The theoretical yield is 100mCi/μA and the simulated yield is 103 ± 10mCi/μA, giving an overestimation of 10% compared to theory. When comparing theoretical yield and simulated yield, it is interesting to note that for a thickness range from 1 to 13 mm the simulation overestimates the yield.

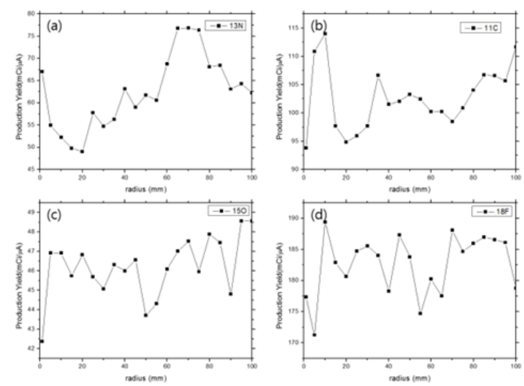

Figure 4: Cross section for each isotopes at various thickness range.

For a whole range of thickness, the theoretical yield and the simulation yield are in good agreement. This difference can be attributed to particle transport, which plays a larger role when working with a thick target. The asymmetry observe in various thickness can be explained by the fact, which leading to the results can compared between theoretical and simulated for each isotopes.

CONCLUSION

A GEANT4 toolkit for simulation of a medical cyclotron solid beamline has been developed and described in details. An example study with 11C, 13N, 15O and 18F was performed and results presented [5, 6]. Agreement between simulated yields and theoretical yields varied with reaction types. The accuracy of the simulation is subject to the quality of nuclear data files and libraries employed. A major advantage of the Monte Carlo toolkit described in the current work is the ability to study contamination isotope species for the purpose of radiation safety [7, 8]. The physics model used has just been included in the Geant4 version 10.1 and is not yet matured. Further refinement of the QGSP_BIC_AllHP physics models and nuclear database files may result in closer agreement with experimental studies.

While initial results are promising, the test cases are limited and more extensive results must be obtained to validate other target material irradiations. With further validation, the toolkit promises to be a powerful tool for studying the performance of medical cyclotron isotope

ISBN 978-3-95450-167-0

production for both contamination and radiation safety monitoring. Furthermore, this is a cost efficient approach to studying new isotope production mechanisms before investing in costly experimental studies [9]. We expect to include in GEANT4 in the near future the described software as an example where further development will be possible. All the features exposed in the paper such as the GUI will be available in open source access. A user guide will be provided, allowing users unfamiliar with the Geant4 C++.

ACKNOWLEDGMENT

This research was supported by the Basic Science Research Program through the National Research Foundation of Korea (NRF) funded by the Ministry of Science, ICT & Future Planning (NRF-2015M2B2A8A10058096, Development of education program for raising basic cyclotron human resources and publication of education contents).

REFERENCES

[1] S. Agostinelli *et al*., "GEANT4 - A Simulation Toolkit", *Nuclear Instruments and Methods in Physics Research Section A: Accelerators, Spectrometers, Detectors and Associated Equipment,* 506(3): 250-303, 2003.

[2] S. Spellerberg *et al*., "Target Development for Diversified Irradiations at a Medical Cyclotron", *Applied Radiation and Isotopes,* 104: 106-112, 2015.

[3] J. Siikanen *et al*., "A Solid Target System with Remote Handling of Irradiated Targets for PET Cyclotrons", *Applied Radiation and Isotopes,* 94: 294-301, 2014.

[4] P. W. Schmor, "Review of Cyclotrons Used in the Production of Radioisotopes for Biomedical Applications", in *Proc. Cyclotrons'10*, Lanzhou, China, September 2010.

[5] B. S. Moon *et al*., "Development of Additive [11C] CO2 Target System in the KOTRON-13 Cyclotron and Its Application for [11C] Radiopharmaceutical Production", *Nuclear Instruments and Methods in Physics Research Section B: Beam Interactions with Materials and Atoms,* 356–357: 1-7, 2015.

[6] C. Hoehr *et al*., "44gSc Production Using a Water Target on a 13 MeV Cyclotron", *Nuclear Medicine and Biology*, 41(5): 401-406, 2014.

[7] O. L. da Costa, "Testing Which is the Fitter Position Sensor for a Cyclotron Liquid Target", *Applied Radiation and Isotopes,* 83, Part A: 37-40. 2014.

[8] X. Zhang *et al*., "High Intensity Proton Beam Transportation Through Fringe Field of 70 MeV Compact Cyclotron to Beam Line Targets", *Nuclear Instruments and Methods in Physics Research Section B: Beam Interactions with Materials and Atoms*.

[9] P. Jahangiri *et al*., "An Analytical Approach of Thermodynamic Behavior in a Gas Target System on a Medical Cyclotron", *Applied Radiation and Isotopes,* 107: 252-258, 2016.

TEST PRODUCTION OF Ti-44 USING RFT-30 CYCLOTRON

E. J. Lee, Y. B. Kong, M. G. Hur, Advanced Radiation Technology Institute,
Korea Atomic Energy Research Institute, Jeongeup, Republic of Korea

Abstract

RFT-30 30 MeV cyclotron has been developed for the production of radioisotopes and their applications. Fluorine-18, which is a widely-used positron emitter, has been produced regularly since 2015. In addition, research on the production of generator radioisotopes has been performed using this cyclotron. A generator means a device used to extract the positron-emitting daughter radioisotope from a source of the decaying parent radioisotope such as ^{44}Ti and ^{68}Ge.

In this research, Sc targets were proton-irradiated in order to produce ^{44}Ti. Gamma spectra of irradiated targets were measured to confirm the production of Ti-44.

INTRODUCTION

Cyclotron-based production of generator radioisotopes has been researched for several tens of years [1,2]. A generator concept is a device that contains a parent radioisotope (RI) with relatively long half-life. A positron-emitting daughter RI can be extracted from it and used for its application. The generator can enable continuous research of positron emitter applications for a sufficiently long time without daily-production of RI using a cyclotron.

In Korea Atomic Energy Research Institute (KAERI), the production of RIs such as ^{44}Ti for Ti/Sc generator and ^{68}Ge for Ge/Ga generator has been researched recently using RFT-30 30 MeV cyclotron. Here, we present a test and actual production of ^{44}Ti via proton irradiation of Scandium (Sc) targets. Sc targets were proton-irradiated, and then, characterized using gamma spectroscopy to confirm the production of ^{44}Ti.

EXPERIMENTAL

Sc disks with a diameter of 50 mm and a thickness of 0.5 mm (Sc 99.5%, Goodfellow, England) were used as irradiation targets. Sc disks were installed at the end of the beam-line (Fig. 1), and then irradiated with a proton beam generated form a RFT-30 cyclotron at Advanced Radiation Technology Institute of KAERI. The irradiation process was carried out with water cooling in a vacuum chamber. The energy of the proton beam was ~30 MeV, and total doses were 12 and 1750 μAh. The average beam current was 10 and 30 μA, respectively.

Gamma spectrum of proton-irradiated Sc disks was measured with multi-channel analyzer (MCA).

RESULTS AND DISCUSSION

Main nuclear reaction which can be induced by the proton irradiation of Sc is ^{45}Sc(p, 2n)^{44}Ti. ^{44}Ti nuclei are created by the direct (p, 2n) reaction and ^{44}Sc nuclei are produced by following β^+ decay with a half-life of 59.1 year.

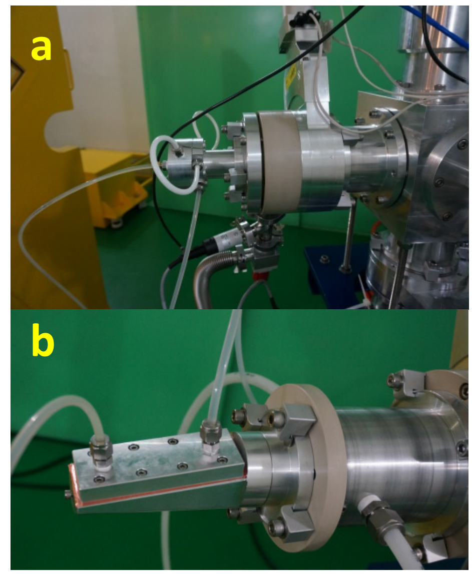

Figure 1: Installation of targets at the end of a beam-line: test target (a) and inclined target for actual production (b).

For the test production, Au-coated Sc disk was proton-irradiated. Au coating was introduced to prevent the corrosion of Sc by the cooling water. Gamma spectrum of an irradiated Sc target is shown in Figure 2. Irradiated Sc with Au coating showed several peaks centered at 67.87, 78.32, 1237 keV, emitted from ^{44}Ti. This result indicated that ^{44}Ti was successfully produced. The appearance of a peak centered at 511.0 keV, corresponding to the annihilation of β+, also proves the production of positron-emitting radioisotopes.

Some other peaks corresponding to ^{44}Sc (1157 keV) which is a daughter radioisotope of ^{44}Ti, and ^{197}Hg (268.7 keV) which is produced from Au coating are also appeared.

However, it was found that Sc target was severely damaged by the proton beam because of high beam current density. In order to resolve this problem, we fabricated and installed inclined target system (Fig. 1b). If we used inclined target, the irradiated area is greatly increased so that we can lower the beam current density. In addition, the penetration length is also increased so that much more nuclear reactions can be induced. The inclined target was proton-irradiated with a dose of 1750 μAh and separation of ^{44}Ti is under processing.

ISBN 978-3-95450-167-0

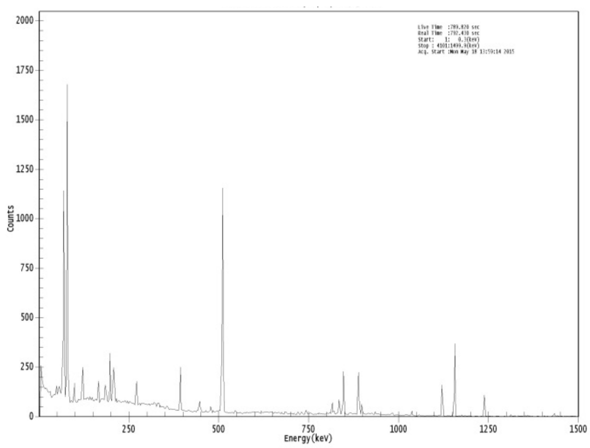

Figure 2: Gamma spectrum of proton-irradiated Sc.

CONCLUSION

^{44}Ti was successfully produced by the proton irradiation of a Sc target. If we increase the dose, sufficient amount of ^{44}Ti can be produced for the research on radiopharmaceuticals using ^{44}Ti. ^{44}Ti/Sc can be used as a generator, which enables the research on β+ emitter application without everyday-production using a cyclotron.

REFERENCES

[1] M. C. Lagunas-Solar, P. M. Kiefer, O. F. Carvacho, C. A. Lagunas, Y. P. Cha, *Appl. Radiat. Isot*. 42, 643, 1991.

[2] D. V. Filosofov, N. S. Loktionova, F. Rösch, *Radiochim. Acta* 98, 149, 2010.

ISBN 978-3-95450-167-0

SIMULATION OF OPTIMUM THICKNESS AND CONFIGURATION OF 10 MeV CYCLOTRON SHIELD

S. Azizpourian*, H. Afarideh, M.M. Afkhami Karaei, M. Mousavinia,
Amirkabir University of Technology (AUT), Department of Physics, Tehran, Iran
F. Abbasi davani, Shahid Beheshti University, Radiation Application, Tehran, Iran

Abstract

Baby Cyclotrons that made in Self-shield type have been employed for use in Medical centers for the diagnosis of cancer diseases by positron emission tomography (PET) system. Conceptual design studies and construction of a 10 MeV cyclotron have been done at the Amirkabir University of Technology. Here in we have done a discussion on simulation of gamma and neutron dose rates at a distance of one meter outside of the cyclotron shielding. This shield consist of Lead, polyethylene (10% B) layers from inside to outside respectively. With increasing the thickness of lead and polyethylene we will see a decrease in the gamma and neutron dose which received by the water phantom at a distance of one meter outside from the surface of the shield of the cyclotron. Note that the gamma and neutron dose at the beginning (without any shielding) was on the order of several thousand μSv per hour that by achieve to a certain amount of thickness of the shield, the dose was reduced to below of the limited level. In this study, the MCNPX Code has been used. In MCNPX Code that used the variance reduction techniques for decreasing relative errors of calculation which was a good method for this case study.

INTRODUCTION

With the development of cyclotron in the 1930s, radioisotopes have been produced for medicine, industry, agriculture and research significantly [1]. Cyclotron accelerators have many applications in the industrial and medical fields.

Today, fluorine is used in radiopharmaceuticals and plays an essential part in the oncology. The cyclotron accelerator is applied in medicine to produce radioisotopes for PET device using for the detection of cancerous diseases. PET is one of the ways to determine the physiological and chemical processes in the body by a quantitative method. Some radioisotopes produced by Cyclotron are ^{11}C, ^{15}O, ^{14}N, and ^{18}F which their half-lives are 20, 2, 10, and 110 minutes respectively. Operation of accelerators will produce gamma and neutron radiation. These radiations can have damaging effects to accelerator operator and those referring to accelerators department. In order to reduce the effects of this radiation, there are different ways that must comply with the principle of ALARA. One of these ways is using of a radiation shield. Depending on the kind of application, the type of radiation shielding will be important. In determining the type of radiation shield, the location and atmosphere dedicated to the cyclotron room is effective.

If the large space will be available, the cyclotron vault model can be used. Because cyclotrons have medical applications and are often used in medical centers and hospitals, there is space limitation for it. On the other hand, since short half-life radioisotopes are produced (approximately 2 hours), it is required to use them in a cyclotron nearby. These items create a situation that a self-Shield is used for radiation shielding.

WORK METHOD

In this study, we simulate a self-shield type for protection. In fact, instead of cyclotron room, a shield that attached to the cyclotron is used. It can be used anywhere. Because of producing gamma and neutron radiation in the cyclotron accelerator, each of them require their appropriate shielding. In this situation, combined shield is needed. For gamma-ray, high atomic number materials such as lead shielding are used. And for neutron radiation, low atomic number materials such as concrete, polyethylene and boron that is neutron capture also, lithium and cadmium are used.

Neutron absorption cross section of these materials are several thousands Barn [2]. This order of number is good for absorbing neutrons.

Although cadmium has a higher neutron absorption cross section than the other two materials, but it leads to strong secondary gamma-ray production and therefore, that is required to utilize thicker layer of lead for attenuation of gamma rays which is not appropriate. So it is better to use boron and lithium [3]. In this study that is based on a 10MeV cyclotron accelerator, Negative hydrogen ion beam has a current of 150 Aμ and is accelerated to 10MeV. In this model, particles are accelerated horizontally. The outer dimensions of the accelerator, which includes its height and diameter, are 1767 mm and 1760 mm respectively. Conceptual design studies and construction of a 10 MeV cyclotron have been done at the Amirkabir University of Technology [4].

Target of cyclotron is usually considered as the main source of radiation. In fact, more than 90% of radiation comes from the target, although there are reactions with other components of the cyclotron, such as the collision of proton beams and secondary radiation with the accelerator body.

A cylindrical target of 1.5 mm height, 1.2 mm inner diameter, and 3 mm outer diameter has been studied. The thickness of cylinder base, which calculated with SRIM code is 1μm and it is bombarded by proton beams. Target foil is regarded neodymium. To produce FDG, target

* Email address: samanazizpourian@aut.ac.ir

ISBN 978-3-95450-167-0

material is enriched water with oxygen-18 (95% enrichment).

As the result of reaction between Target and proton beams, Fluorine is produced. Fluorine emits beta radiation which is used in PET systems. In this reaction, neutrons and gamma rays are produced. To simulate the shielding, Lead and Polyethylene Borated is used. In this study, the optimal thickness of each material is calculated by MCNPX. In simulate shielding we need to have a high penetration in material. However the outputs must have an acceptable accuracy, it is needed to apply variance reduction techniques. For this simulation, weight window method has been used. Weight window method can be implemented in several ways in MCNP code. Here, the implemented is reducing density technique. We reduce the density of the materials to an untrue amount that can be obtained an output for Tally. So at each stage material density has increased toward its real value. At the end we should arrive to the actual appropriate output values with permissible error.

Simulations

We have used polyethylene borated (10% boron) for neutron shielding and lead for gamma shielding. Shielding geometry is cylindrical. First polyethylene and then lead stayed back of it. We wanted out of the shield the dose rate of neutron and gamma reach to a limit level. In MCNPX code, neutron and gamma dose are calculated by a water phantom out of shielding.

In this section the dose attenuated for neutron and gamma are illustrated.

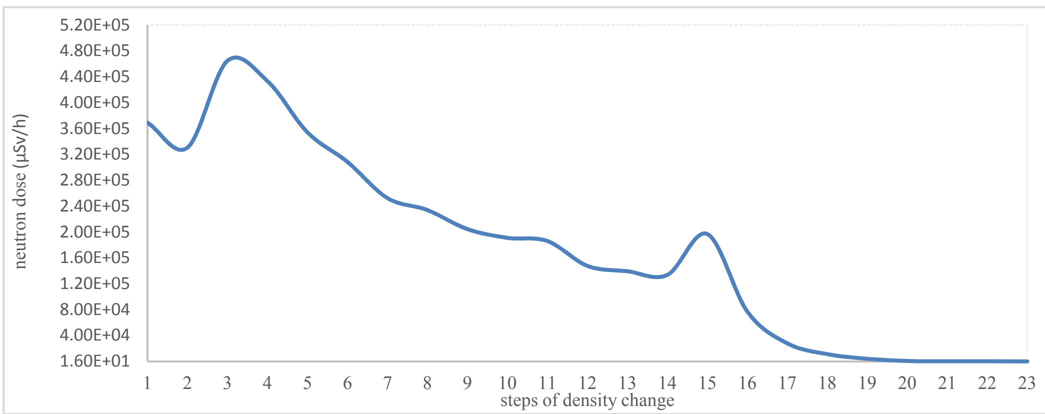

Figure 1: Neutron dose with density change technique of variance reduction.

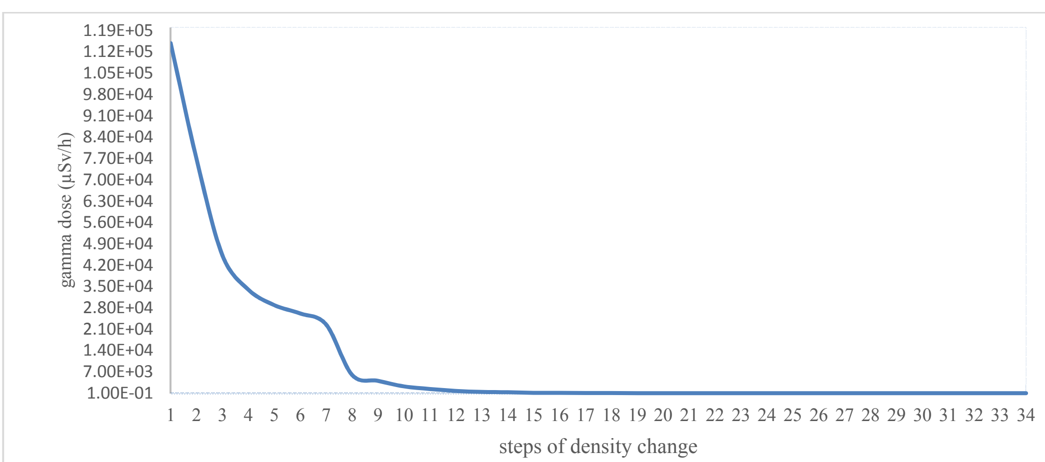

Figure 2: Neutron dose with density change technique of variance reduction.

According to Figs. 1 and 2 neutron and gamma dose rate is less than the permissible limit and was obtained 16 µsv/hr and 0.1 µsv/hr respectively. Table1 and Table2 show density values of materials at each stage of simulation. It should be noted that the density of the material during the simulation are shown in the tables.

ISBN 978-3-95450-167-0

Table 1: Material Density of Shielding for Calculating Neutron Dose in Each Stage of Simulation (Unit of Density is g/cm3)

Steps of Density Change	Lead	Poly with Boron
1	0.35	0.05
2	0.95	0.05
3	1.65	0.05
4	2.65	0.05
5	3.65	0.05
6	4.65	0.05
7	5.65	0.05
8	6.35	0.05
9	7.05	0.05
10	7.75	0.05
11	8.5	0.05
12	9.25	0.05
13	10.5	0.05
14	10.7	0.05
15	11.35	0.05
16	11.35	0.15
17	11.35	0.25
18	11.35	0.35
19	11.35	0.45
20	11.35	0.65
21	11.35	0.8
22	11.35	0.9
23	11.35	1

Table 2: Material Density of Shielding for Calculating Gamma Dose in Each Stage of Simulation (Unit of Density is g/cm3)

Steps of Density Change	Lead	Poly with Boron	Steps of Density Change	Lead	Poly with Boron
1	0/05	0/1	18	4/6	1
2	0/05	0/2	19	5/1	1
3	0/05	0/35	20	5/5	1
4	0/05	0/5	21	5/8	1
5	0/05	0/6	22	6/2	1
6	0/05	0/75	23	6/5	1
7	0/05	0/85	24	7	1
8	0/75	1	25	7/3	1
9	0/95	1	26	7/7	1
10	1/45	1	27	8/2	1
11	1/95	1	28	8/5	1
12	2/45	1	29	8/9	1
13	2/85	1	30	9/3	1
14	3/05	1	31	9/9	1
15	3/65	1	32	10/7	1
16	4	1	33	11	1
17	4/3	1	34	11/35	1

To ensure that the neutron dose does not leak out of the shield, neutron dose Map has been calculated by mesh tally. You can see neutron dose map in the Fig. 3. Dose map of neutron calculated than 20 cm inside of shield to 25 cm outside of shield. The point R=165cm is on outside surface of the shield. As seen in Fig. 3 in this point neutron dose is below than 16 µsv/hr.

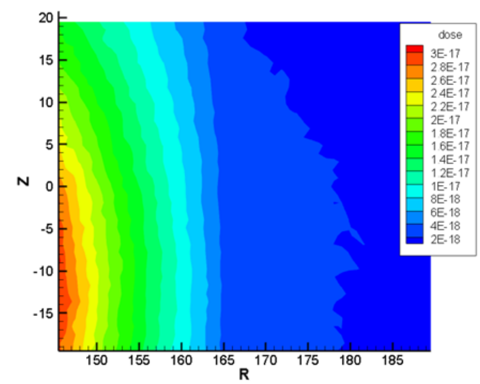

Figure 3: Dose map of neutron.

Note that the dose rate unit in the Fig. 3 is ((rem/hr)/(n/cm^2.s)). These instructions are a typical implementation of the requirements. As are visible in Figs. 4 and 5, cyclotron shield is designed in Solidworks. Also, according to simulations to calculate the dose in MCNP, designed geometry is achieved in the visual editor. Visual editor is a Sub-Program of MCNPX.

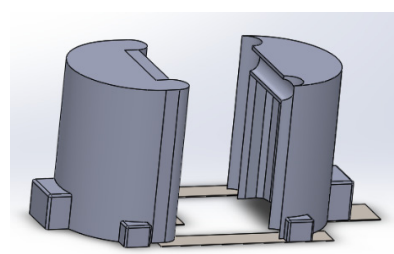

Figure 4: Geometry is designed in solidworks.

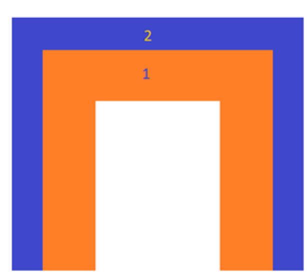

Figure 5: Geometry designed in MCNP also shows (side view) that the shielding materials. 1 is polyethylene borated and 2 is Lead.

ISBN 978-3-95450-167-0

CONCLUSION

At the end of simulation concluded that 60 cm and 35 cm are the best thicknesses for polyethylene and lead respectively. Because according to our data in these thicknesses dose rate of neutron and gamma are 16 µsv/hr and 0.1 µsv/hr on the outside surface of shield that are lower than the limitation level for radiations in determine distance. While without shielding, neutron and gamma dose rates are a few thousand microsievert per hour.

REFERENCES

[1] International Atomic Energy Agency, "Cyclotron Produced Radionuclides," Principles and Practice, Technical Reports Series, IAEA, Vienna, No. 465, 2008.

[2] B. Abdullahi and M.T. Tsepav, "The utilization of Cadmium as thermal neutron filter in the characterization of Gold matrix in NIRR-1", *International Journal of Science and Technology,* 2012.

[3] P. Rinard, "Neutron interactions with matter", *Passive Nondestructive Assay of Nuclear Materials,* pp. 357-377, 1991.

[4] R. Solhju *et al.,* "Magnet design for the 10 MeV AVF cyclotron accelerator'', Journal of the Korean Physical Society 63.7, pp. 1347-1350, 2013.

ISBN 978-3-95450-167-0

COUPLING OF CYCLOTRONS TO LINACS FOR MEDICAL APPLICATIONS

A. Garonna†, U. Amaldi, V. Bencini, D. Bergesio, C. Cuccagna, E. Felcini, M. Varasteh Anvar, M. R. Vazirisereshk, TERA Foundation, Novara, Italy

Abstract

Cyclotron and Linac technologies cover the vast majority of accelerator solutions applied to medicine. Cyclotrons with beams of H^+/H^- around 20 MeV are found for radioisotope production and cyclotrons with beams up to 250 MeV are widely used for protontherapy. Linacs are present in every medium-sized hospital with electron beams up to 20 MeV for radiotherapy and radioimaging. They have also recently become available as commercial products for protontherapy. The coupling of these two strong technologies enables to expand the capabilities of cyclotrons by using linacs as boosters. This opens the way to innovative accelerator systems allowing both radioisotope production and ion beam therapy (cyclinacs), new treatment techniques (high energy protontherapy) and new imaging techniques (proton radiography). This paper provides an overview of the technical challenges linked to coupling cyclotrons to linacs and the various solutions at hand.

INTRODUCTION

Cyclotrons

A list of all existing research and commercial cyclotrons is regularly compiled [1]. The vast majority of cyclotrons have a medical purpose as producers of radioisotopes for medical imaging and therapy. The typical primary beams of H^+/H^- ions are accelerated by normal conducting isochronous cyclotrons with kinetic energies up to 30 MeV. Compared to other accelerator technologies, cyclotrons benefit from their compactness, reliability and efficiency. Nowadays, normal conducting cyclotrons also represent the workhorse in protontherapy [2] with H^+ beams in the 235-250 MeV range. Recently, also superconducting isochronous and synchro-cyclotrons enter the protontherapy world as commercial solutions and their numbers are rapidly increasing.

Linacs

The vast majority of modern radiotherapy apparata is based on 3 GHz electron linacs, which are normal conducting copper standing-wave structures providing electron beams up to 20 MeV. They are so compact (1-2 m length) and light that they are mounted on rotating systems to irradiate the tumors from all possible angles.

† Adriano.garonna@cern.ch

TERA Foundation

For more than 20 years, the TERA foundation has played an active role in the development of accelerator and detector technologies employed in the field of hadrontherapy. Its outputs and staff are, among others, at the core of the Proton Ion Medical Machine Study [3], the CNAO Foundation [4], which has built and operates the Italian hadrontherapy center in Pavia and the company ADAM S.A. (Switzerland), which commercializes protontherapy centers based on linacs. In the field of detectors, TERA developed the Proton Range Telescope [5] installed at CNAO and the BISE (Beam Imaging with Secondary Electrons) [6] detector installed at the 18 MeV cyclotron of Swan Isotopen AG.

TERA's present activities focus on designing novel gantries that make full use of the special properties of the beams produced by hadron linacs, and also research and development in the technologies of linacs for carbon (and helium) ion acceleration [7]. In collaboration with CERN, two lines of development are pursued: a system made of an RFQ followed by three linac structures (called "*all-linac solution*") and the combination of a cyclotron and a linac, a so-called "cyclinac". This combination allows enhancing the advantages of both accelerator types and opens new possibilities in therapy and imaging for radiotherapy centers (ex-novo or based on existing cyclotrons). The main innovations of all the proposed linac systems are the rapid energy variation (at rates in the range 100-400 Hz), the small transverse emittances of the beams and the cost-effectiveness. The related research activities concern pulsed ion sources, high-gradient high-frequency linacs, new concepts for beamlines and gantries, beam tracking tools and full-scale Monte Carlo simulations from the source to the patient.

CYCLINACS

General

The use of linacs for therapy has the advantage of allowing a fast (within a few ms) modulation of the beam output energy. This is a unique feature of a cyclinac, since protontherapy cyclotron systems use degraders for energy variation in the timescale of 100-1000 ms and the synchrotron systems vary the beam energy from cycle to cycle in timescales of 1-2 s. Additionally, the linac beam has a very small transverse emittance (around 0.3 µm rms, normalized) which allows to reduce the aperture (and cost) of the high energy beam transfer line magnets.

On the other hand, there are some technical challenges linked to the design of cyclinacs and corresponding beam-

ISBN 978-3-95450-167-0

lines. Firstly, the transverse and longitudinal characteristics of the beam coming from the cyclotron do not match the small acceptance of the linac. Indeed, the transmission between the cyclotron and the linac is estimated to be less than 10 %. However, hadrontherapy treatments require low particle numbers and this is therefore not a limitation. Secondly, to make advantage of the fast energy modulation of the linac, the downstream beamlines have to minimize the dispersion and fast regulation systems have to be used for the magnets.

Proton Multi-Room Facility

The first cyclinac was proposed in 1994. It is based on a 30 MeV cyclotron, such that by night and weekends, medical radioisotopes not accessible to typical hospital cyclotrons can be produced (see Fig. 1).

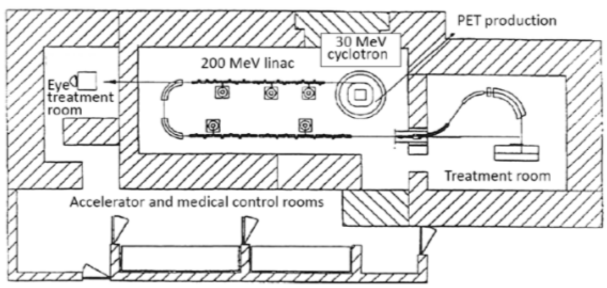

Figure 1: Layout of the first cyclinac [8].

At the end of the 90's, in collaboration with the European Laboratory for Particle Physics (CERN) and the Italian Institute for Nuclear Physics (INFN), TERA built the LI(nac)BO(oster), a 3 GHz Cell Coupled Linac which successfully accelerated a beam coming from a cyclotron from 62 to 74 MeV [9-10]. Various designs for cyclinac-based protontherapy centers have since been proposed [11]. One strong argument for this cyclinac solution is the possibility to combine the production of radioisotopes to the treatment of tumors by using a commercial proton cyclotron.

Dual Proton-Carbon Facility

At the time of writing all dual hadrontherapy centers (for proton and carbon ion treatment) are based on synchrotrons. Given the large beam rigidity required for carbon ion treatments (6.4 Tm), there is still a large margin of improvement in the footprint, cost and complexity of these accelerators. As shown in Fig. 2, in this respect, the cyclinac is a competitive solution.

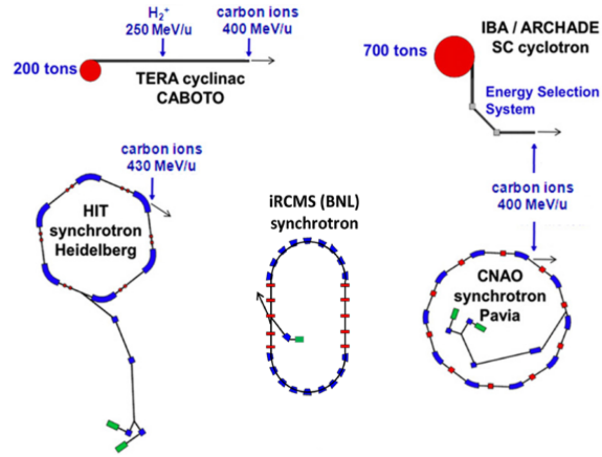

Figure 2: Dimensional Comparison of different accelerator technologies for hadrontherapy.

The linac solution for dual proton and carbon ion centers is called CABOTO [12-13]. The proposed cyclinac is composed of commercial electron beam ion sources producing C^{6+} and H_2^+, a superconducting isochronous cyclotron [14] accelerating them up to 150 MeV/u and a high-gradient 3 GHz linac boosting the energy up to 410 MeV/u. The corresponding produced beam has a 300 Hz repetition rate with pulse lengths of a few µs, as schematized in Fig. 3.

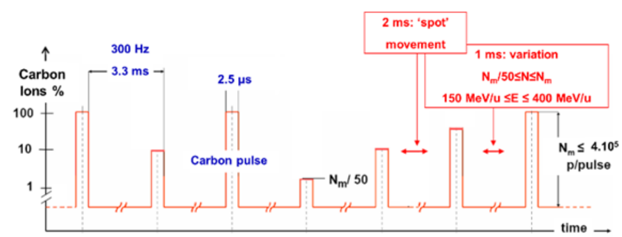

Figure 3: CABOTO Pulsed time structure (for C^{6+}).

The choice of the output energy of the cyclotron (and input energy for the linac) is strongly linked to the clinical aims of the therapy center. Indeed, an energy of 70 MeV/u would allow to use the cyclotron for proton eye tumor treatments and the linac for all deep-seated tumor treatments with both proton and carbon ion beams but would result in a larger and more energy-consuming accelerator. An energy of 230 MeV/u would allow to use the cyclotron as a stand-alone accelerator of H_2^+ molecules for 'standard' protontherapy using degrader systems and only use the linac for carbon ion treatments. This opens the possibility of a staged-approach in the treatment center's investment and treatments. The intermediate energy of 150 MeV/u (corresponding to 5 cm range in water for carbon ions) allows:

- covering the whole spectrum of tumor indications, with a linac-based active beam energy modulation system for carbon ions
- limiting the power consumption and accelerator building surface of the cyclinac

ISBN 978-3-95450-167-0

- reducing the iron weight of the cyclotron to values similar to IBA's C235 cyclotron, the protontherapy workhorse

Proton Single-Room Facility

With the progress of the accelerator technology towards compact and light machines, more and more centers are based on single-room accelerators. This allows reducing the investment cost and multiplying the number of centers in order to cover more uniformly the territory. The equivalent cyclinac solution proposed by TERA is called TULIP (Turning LInac for Protontherapy). It involves mounting the whole linac structure on a rotating gantry [15]. An example is shown in Fig. 4. The RF power transmission is made possible by high power rotating joints developed in collaboration with the CLIC [16] group at CERN.

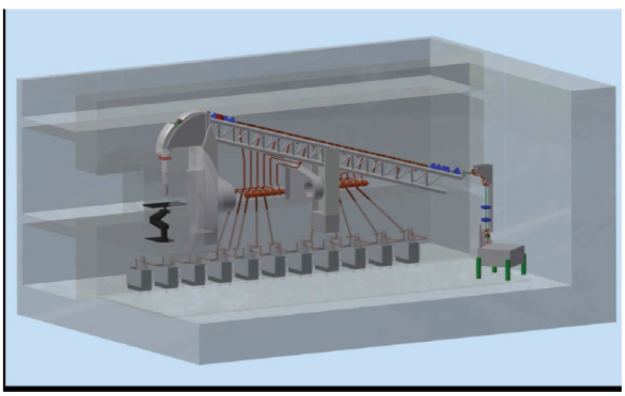

Figure 4: Artistic view of TULIP, based on a commercial 24 MeV cyclotron and 11 m Cell Coupled Linac similar to LIBO.

Proton Linac Booster

To overcome the limitations of modern protontherapy, some novel approaches are under study in the medical physics community. These include MRI-guided protontherapy, proton imaging, proton tomography and high energy protontherapy [17]. These last two applications require boosting the energy of the clinical proton beams from the currently available 230-250 MeV up to 350 MeV and more. This upgrade would allow the use of passing proton beams both for proton radiography and for the treatment of small tumors that are surrounded by multiple, relatively small critical organs [18-19]. The Paul Scherrer Institut and TERA have designed a booster based on a linac similar to the one of Fig. 4 [20].

CONCLUSION

In conclusion, cyclotrons and linacs constitute the workhorse accelerators in the medical world. Their combination was introduced by the TERA Foundation under the name 'cyclinac'. Despite the technical challenges and limitations coming from this association, cyclinacs open incredible possibilities in the fields of medical imaging and medical therapy as they can vary the beam energy in a few ms without any beam intercepting devices and can in a modular fashion expand the capabilities of existing cyclotron-based centers.

REFERENCES

[1] List of Cyclotrons, http://accelconf.web.cern.ch/AccelConf/c07/OTHERS/Cyclotron%20List%202007%20-Full.pdf
[2] Particle Therapy Cooperative Group, http://www.ptcog.ch
[3] P.J. Bryant *et al.*, "The Proton Ion Medical Machine Study", CERN, Geneva, Switzerland, Rep. CERN/PS99-010 (DI), January 1999.
[4] Fondazione CNAO, http://www.fondazionecnao.it
[5] U. Amaldi *et al*., "Construction, test and operation of a Proton Range Radiography System", *Nucl. Instr. Meth A.*, vol. 629-1, pp. 337-344, 2011.
[6] S. Braccini *et al*., "The new Bern cyclotron laboratory for radioisotope production and research", in *Proc. Int. Particle Accelerator Conf.* (IPAC2011), San Sebastian, Spain, 2011, paper THPS080, pp. 3618-3620.
[7] U. Amaldi and A. Degiovanni, "Proton and Carbon Linacs for Hadrontherapy", in *Proc. Linear Accelerator Conf. (LINAC'14)*, Geneva, Switzerland, 2014, paper FRIOB02, pp. 1207-1212.
[8] U. Amaldi, *The Italian hadrontherapy project, in Hadron Therapy in Oncology*, eds. U. Amaldi and B. Larsson, Elsevier, 1994, pp.45.
[9] U. Amaldi *et al*., "LIBO a linac-booster for protontherapy: construction and test of a prototype", *Nucl. Instr. Meth A.*, vol. 521, pp. 512-529, 2004.
[10] C. De Martinis *et al.*, "Acceleration tests of a 3 GHz proton linear accelerator (LIBO) for hadrontherapy", *Nucl. Instr. Meth A.*, vol. 681, pp. 10-15, 2012.
[11] U. Amaldi, S. Braccini and P. Puggioni, "High Frequency Linacs for Hadrontherapy", *Review of Accelerator. Science and Technology*, vol. 2, pp. 111-131, 2009.
[12] A. Garonna, "Cyclotron Designs for Ion Beam Therapy with Cyclincas", Ph.D. thesis, Phys. Dept., Ecole Polytechnique Federale de Lausanne, Switzerland, 2012.
[13] S.V. Andres *et al*., "CABOTO, a high-gradient linac for hadrontherapy", *Journal of Radiation Research*, vol. 54 (Suppl 1), i155-i161, 2013.
[14] A. Garonna *et al*., "Comparison of Superconducting 230 MeV/u Synchro- and Isochronous Cyclotron Designs for Therapy with Cyclinacs", in *Proc. Cyclotrons2013*, Vancouver, Canada, 2013, paper MO3PB04, pp. 108-110, 2013.
[15] A. Degiovanni *et al*., "Design of a fast-cycling high-gradient rotating linac for protontherapy", in *Proc. Int. Particle Accelerator Conf. (IPAC'13)*, Shanghai, May 2013, paper THPWA008, pp.3642-3644.
[16] CLIC Collaboration, "A Multi-TeV Linear Collider based on CLIC Technology", CERN, Geneva, Switzerland, Rep. CERN-2012-007, October 2012.
[17] N. K. Abrosimov *et al.*,"1000 MeV proton beam therapy facility at Petersburg Nuclear Physics Institute Synchrocyclotron", *J. Phys. Conf. Ser.*, vol. 41, pp.424-32, 2006.
[18] J. M. Schippers and A. J. Lomax, "Emerging technologies in proton therapy", *Acta Oncol*, vol. 50, pp.838-50, 2011.

ISBN 978-3-95450-167-0

[19] J. Bilbao de Mendizabal, "3 GHz linac booster design from 250 MeV to 350 MeV for medical application at PSI", MSc thesis, Phys. Dept., Université de Genève, Switzerland, 2012.

[20] A. Degiovanni, "High gradient proton linacs for medical applications", Ph.D. thesis, Phys. Dept., Ecole Polytechnique Federale de Lausanne, Switzerland, 2014.

ISBN 978-3-95450-167-0

A MULTI-LEAF FARADAY CUP ESPECIALLY FOR PROTON THERAPY OF OCULAR TUMORS

S. Seidel*, C. Kunert[1], J. Bundesmann, T. Damerow, A. Denker, Helmholtz-Zentrum Berlin, Germany
A. Weber, Charité Universitätsmedizin Berlin, Germany
[1]former Helmholtz-Zentrum Berlin, Germany

Abstract

For radiation therapy with protons knowing the beam range with high accuracy is crucial. The Multi-leaf Faraday Cup (MLFC) allows a quick and precise range measurement of the full radiation field in air. In the field of eye tumor therapy an accuracy in the submillimeter regime is required. We present an MLFC with 47 channels which can be read out simultaniuosly. Each channel consists of a 10 µm copper foil, connected to an ammeter, next to a 25 µm kapton foil. An automated preabsorber system allows range measurements in different energy regions. The achievable relative resolution of 50 µm in water meets the desired accuracy for eye tumor therapy. Furthermore is is possible to gain information about the dose distribution in water for quality assurance measurements.

MOTIVATION

Over the past years radiation therapy with protons has become a very important tool in cancer treatment. Since 1998 a collaboration of the Charité Universitätsmedizin and the Helmholtz-Zentrum Berlin (HZB) provides a treatment facility for eye cancer. Ocular tumors especially benefit from the superior dose distribution of protons. This distribution known as the Bragg-Peak provides the highest dose just before the end of the finite range in tissue (see Fig. 1).

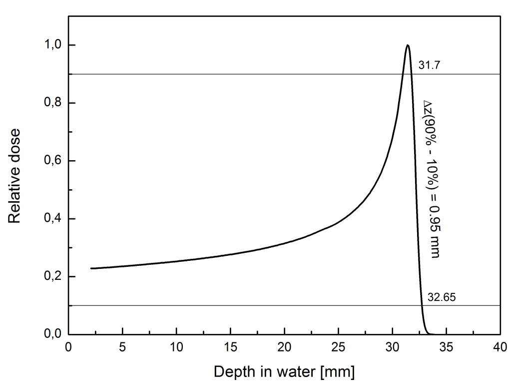

Figure 1: Typical single Bragg Peak (SBP) of the HZB cyclotron with 0.95 mm distal dose fall off (90 - 10 %).

That way it is possible to deliver the maximum dose only to the target volume and spare critical tissues highly sensitive to radiation. At our facility this leads to a local tumor control of 96 % after 5 years. The human eye is a very small organ (with a volume of 6 – 7 cm^3) and contains of several critical structures crucial for the sight, e.g. the optical nerve or the macula. When treating melanomas located close to those structures a very precise positioning of the target volume and a precise knowledge of the proton range is required.

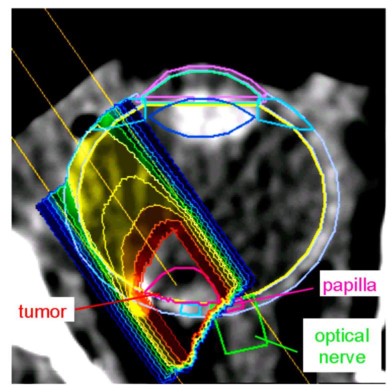

Figure 2: Planned radiation field with marked critical structures and the tumor.

At our facility we achieve a distal dose fall off (the distance between 90 and 10 percent of the maximum dose) of less than 1 mm (Fig. 1). This is also a reason why the range measurement needs to be accomplished with a resolution of 0.1 mm. During quality assurance this is usually done by measuring the dose distribution in a water phantom. The measurements are very time consuming and therefore it would be a great advantage to use a device which enables quick and precise range measurements.

METHODS AND MATERIAL

MLFC

A Multi-Leaf Faraday Cup (MLFC) is a well-suited device for a quick and precise range measurement. It is a stack of alternating conductor and insulator plates. Each conducting plate is connected to ground potential via an ammeter. Incoming protons stop in a certain plate and add positive charges which create a current by pulling electrons from the ground. Thus the differential fluence (and therefore the range) of a proton beam can be measured.

By determining the needed plate thickness and number a MLFC can be set to meet the eye tumor therapy requirements. It furthermore enables measurements of the full radiation field in air.

Our device consists of 47 copper foils with a thickness of 10 µm, which equals approx. 50 µm water equivalent. As insulator we use Kapton foils of 25 µm thickness corresponding to approx. 32 µm water.

* sophie.seidel@helmholtz-berlin.de

ISBN 978-3-95450-167-0

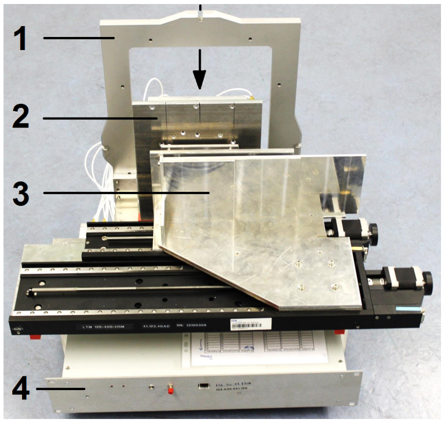

Figure 3: Final setup of our MLFC. The holder (1), the MLFC itself (2), the preabsorbing system (3) and the electronics (4). The beam direction is is shown by the arrow.

Electronics

To cover the whole radiation field we use a board with a 10 cm whole in the middle and 50 spots in a circle of 12 cm diameter, where the copper foils are soldered onto (Fig. 4). Each spot has a 50 Ω impedance connection to the "Rabbit Box" from iThemba Labs, South Africa, we use. This "Rabbit Box" consists of 48 channels which can measure electrical currents simultaneously. Therefore our final device constists of 47 copper foils and one channel for the current in the beam dump. The expected signal is in the range of pA which makes the use of special low noise cables necessary.

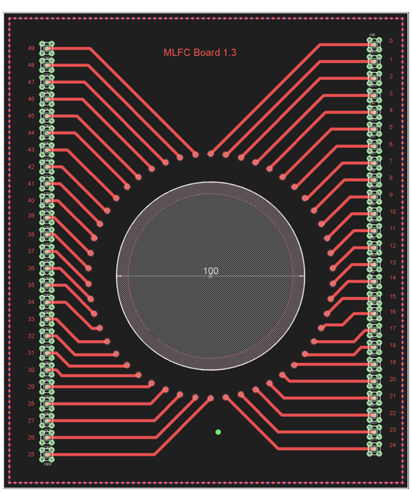

Figure 4: Schematical representation of our board with 50 spots for soldering the copper foils onto.

Preabsorber System

The whole setup is mounted onto a special holder to attach it to the treatment chair in front of the beam line in the treatment room. To measure the proton range in different energy regions (e.g. for radiation hardness testing) we use a special preabsorbing system which can vary the absorber thickness automatically. It consists of a stair with 4 steps from 0 mm to 12 mm aluminium and a double wedge for fine adjustment from 3 mm to 6 mm aluminium. This enables continuous measurements in an energy range between 30 MeV and 70 MeV. An especially for this purpose developed program varies the preabsorber automatically until the whole beam is stopped between the first and the last foil.

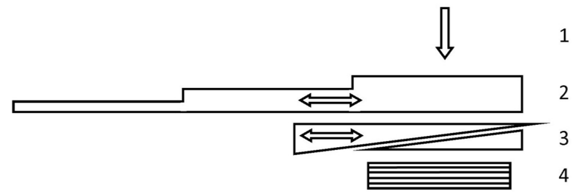

Figure 5: Schematical representation of the preabsorbing system with the beam direction (1), the stairs with 4 steps (2), the double wedge (3) and the MLFC (4).

RESULTS AND APPLICATIONS

The typical result of a measurement with our MLFC is shown in Figure 6. The preabsorber was set to 16.68 mm aluminium and the measurement was done with a beam current of 500 pA. The value of the maximum signal is within the expected range of approx. 5 % of the incoming current. The curve has an almost Gaussian shape. Therefore a Gaussian fit has been performed to determine the expected value and the variance of the differential fluence of the beam. In this particular case the expected value corresponds to an energy of 67.6 MeV. This agrees very well with the calculated value [3] of 67.3 MeV taking into account the extraction energy of the cyclotron (68 MeV) and the energy loss due to the scatter foil, the nozzle and air.

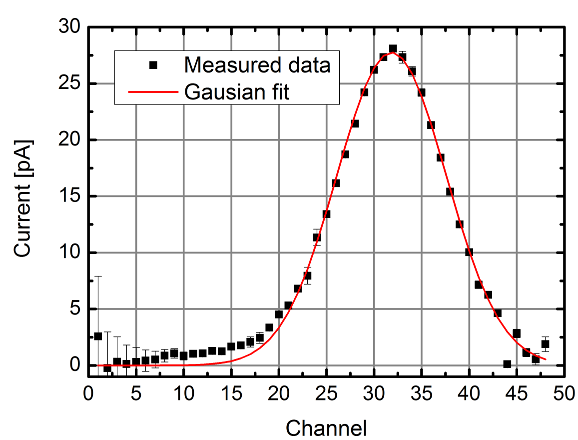

Figure 6: Typical measurement of the 68 MeV therapy beam at 500 pA with 16.68 mm aluminium as preabsorber. A Gaussian fit reveals the center being at foil 32 which corresponds to an energy of 67.6 MeV.

The relative resolution of our device is found to be 50 µm proton range in water [1] which is even more precise than the required 100 µm for eye tumor therapy.

ISBN 978-3-95450-167-0

Apart from measuring the proton range and energy of the beam, knowing the actual dose distribution in water is crucial for the quality assurance in medical physics. Since the measured signal only corresponds to the differential fluence of the protons, some calculations have to be made. It is possible to find an analytical model of the Bragg curves for therapy beams with energies up to 200 MeV [2]. The required expected value of the proton range and its variance can be obtained using our MLFC. Therefore we are able to gain information about the shape of the Bragg Peak in water. Figure 7 shows the expected result of measuring a Spread out Bragg Peak with an MLFC. The received signal is a superposition of the signals for each single energy peak.

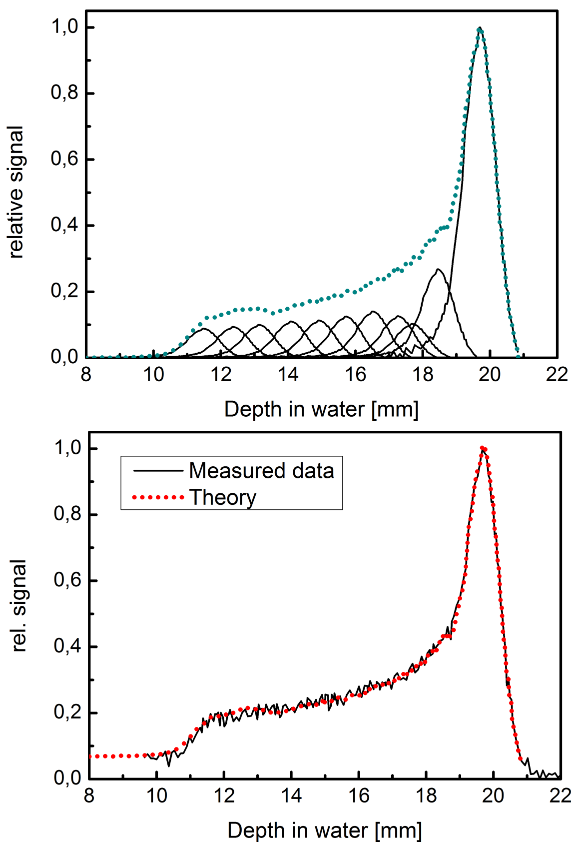

Figure 7: Measurement of a SOBP with the MLFC as a supperposition of different monoenergetic beams (upper figure). Comparison between the expected curve and the measured data (lower figure).

Using an ionization chamber has the disadvantage of being very time consuming since every value has to be aquired seperatly. Depending on the range and modulation this could take up to 10 minutes while the MLFC allows a fast measurement of several data points simultaniously in less than 3 minutes.

Figure 7 also shows the good agreement between the expected shape of the curve and the actual measurement. Figure 8 shows the results of two measurements performed with

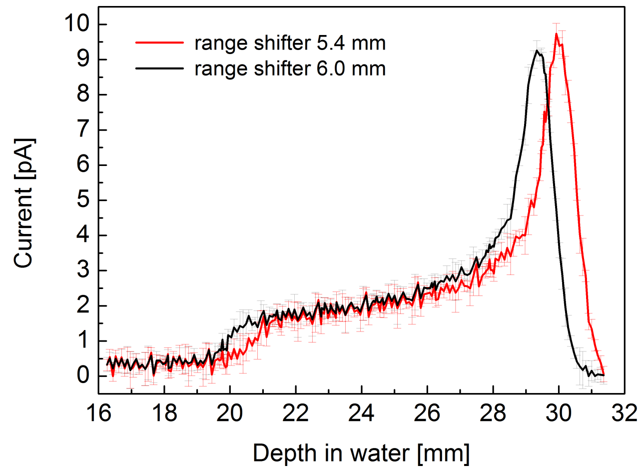

Figure 8: Comparison between the correct preabsorber of 6.0 mm (black curve) and the wrong preabsorber of 5.4 mm (red curve)

our MLFC which could be typically done for quality assurance before each patient treatment. One curve was aquired using the correct preabsorder of 6.0 mm acrylic glass for that particular patient and the other one was measured using the wrong range shifter position of 5.4 mm. The differences are clearly visible and confirm the achievable submillimeter precision of our device.

CONCLUSION

Our MLFC allows aquick and precise proton range and energy measurement in different energy regions. With a resolution of 100 µm and a relative resolution of 50 µm in water it not only meets the requirements for eye tumor therapy but it exceeds them. Furthermore in the context of quality assurance for radiation therapy, measurements of SOBP in water are possible to verify the accuracy of the range shifter position and modulation with high precision.

ACKNOWLEDGMENT

Our sincere thanks go to iThemba Labs, South Africa, for the possibility to use their Rabbit Box and their support.

REFERENCES

[1] C. Kunert, "A Multi-Leaf Faraday Cup especially for proton therapy of ocular tumors", in *Proc. 5th International Particle Accelerator Conference (IPAC'14)*, Dresden, Germany, June 2014, paper WEPRO082, pp. 2149-2152.

[2] T. Bortfeld, "An analytical approximation of the Bragg curve for therapeutic proton beams", *Med. Phys.*, vol. 24, pp. 2024-2033, 1997.

[3] "SRIM-the Stopping and Range of ions in Matter", software packages for calculation stopping power and range of ions in matter, `http://www.srim.org`

ISBN 978-3-95450-167-0

OFFLINE TESTS WITH THE NSCL CYCLOTRON GAS STOPPER*

S. Schwarz†, K. Lund, D.J. Morrissey, J. Ottarson, C. Sumithrarachchi,
NSCL, Michigan State University (MSU), East Lansing MI, USA
G. Bollen[1], S. Chouhan, J. DeKamp, M. Green, C. Magsig, A.C.C. Villari, A. Zeller
Facility for Rare Iostope Beams, MSU, East Lansing MI, USA,
[1]also at Dep. of Physics and Astronomy, MSU, East Lansing, USA

Abstract

Rare isotopes are produced at the National Superconducting Cyclotron Laboratory NSCL by projectile fragmentation at energies of ≈100 MeV/u. The NSCL has successfully used linear gas stopping cells for more than a decade to decelerate projectile fragments to the keV range; first for experiments at low-energy and more recently for reacceleration.

A novel reverse-cyclotron has been constructed by the NSCL based on a superconducting sectored-cyclotron magnet and LN_2-cooled He gas to confine and slow down the fragments. Efficient stopping is predicted even for light ions that are difficult to thermalize in linear gas cells. The thermalized ions are transported to the center by a radial RF-carpet system, extracted through the yoke with an ion conveyor and accelerated to <60 keV for delivery to users.

Measured field profiles have confirmed field calculations. The cryogenic beam-stopping chamber has been installed inside the magnet. The RF ion-guiding components have been tested successfully offline and are being prepared for low-energy ion-transport tests inside the magnet.

INTRODUCTION

The NSCL facility uses fast projectile fragmentation to provide rare-isotope beams (RIB) for a broad range of research. The production method is chemically unselective and allows the production of isotopes far from the valley of stability as evidenced by the more than 900 RIBs delivered to users at NSCL so far. While most of the beams have been provided at the production energies on the order of 100 MeV/u, beams are increasingly requested at rest or at energies of a few MeV/u.

Linear gas stopping cells have been used for more than a decade at NSCL to slow down the beam to the keV-energy range. These 'stopped beams' are delivered to NSCL's low-energy experimental area, i.e. the Penning-trap mass spectrometer LEBIT [1] and the laser spectroscopy setup BECOLA [2] as well as the re-accelerator ReA [3].

The linear gas stopping cells use solid degraders to slow down the incoming beam to an energy that can be dissipated in helium gas at a pressure of ≈100 mbar to a bar and over a typical length of a meter. While a higher pressure allows for efficient stopping in more compact cells, recent installations favor larger sizes to reduce ionization per volume and use lower pressure to benefit from efficient RF ion guiding techniques for fast ion extraction [4], [5].

Extreme purity of the stopping gas is required to prevent charge-exchange of stopped ions with contaminants and other reactions, which can lead to loss of ions and/or unwanted molecular ions. In order to provide cleaner beams, the latest generation of gas stopping cells, including a new cell currently under development at NSCL, use cryogenic cooling to freeze out contaminants.

Most of the fragments provided as stopped beams at NSCL so far had masses of ≈40 u and higher, which allowed for efficient stopping in NSCL's currently operational 1.2 m long ≈80 mbar stopping cell [6].

Slowing down energetic *light* ions with solid degraders and low-pressure gas can induce several meters of range straggling and prevent efficient stopping in gas cells of practicable size or with extraction times comparable to nuclear lifetimes. Demand for stopped light-ion beams at NSCL has been on the rise, in particular since reaction studies with RIBs at the reaccelerator ReA have become possible. Even more interest has been voiced as significantly higher beam rates are expected with the primary beam upgrade in the FRIB (Facility for Rare Iostope Beams) era. The cyclotron gas stopper will be one of several complementary stopping options, built to specifically address the demand for light ions: It provides extreme stopping length as the beam is injected into stable orbits of a cyclotron magnet. Following energy degradation to an appropriate magnetic rigidity, the beam continues in an inward-spiraling motion as it slows down in the presence of buffer gas.

The concept of a gas-filled cyclotron-type magnet has been used to slow down and trap exotic light particles at LEAR/CERN [7], it was considered for the slowing-down of light ions such as Be^+ [8] and developed for a wider application by our group [9]–[11].

CYCLOTRON GAS STOPPER CONCEPT

Figure 1 illustrates the concept of the cyclotron stopper. The high-energy beam delivered from NSCL's A1900 fragment separator enters the gas-filled stopping chamber through a penetration in the return yoke of a three-sectored cyclotron-type magnet. After ≈ 1/4 turn and at a radius of about 0.9 m, the beam passes through a solid degrader, which reduces the beam rigidity to 1.6 Tm and puts the beam on a stable orbit. At this point, the beam is nearly fully stripped. The presence of the helium gas causes the beam to lose energy and pick up electrons. In average, the rigidity of the

* Work supported by the National Science Foundation under grants PHY-09-58726 and PHY-11-02511
† schwarz@nscl.msu.edu

ISBN 978-3-95450-167-0

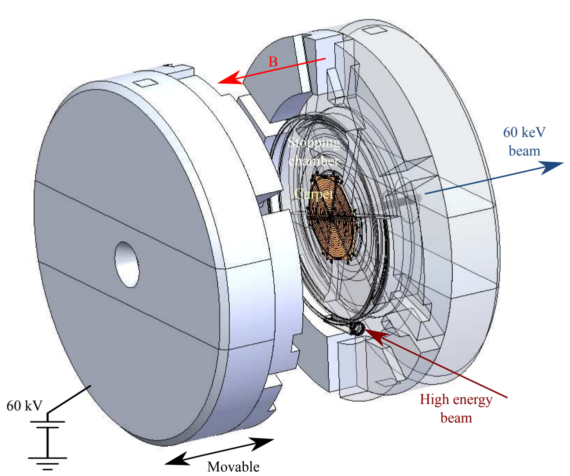

Figure 1: Sketch of the cyclotron stopper.

beam is kept smaller than needed for circular orbits and the beam slows down on an inward spiral to come to rest in a stopping volume with radius of < 0.5 m. The sectoring of the magnet is essential to provide axial focusing in the slowing-down process.

Inside the central stopping volume the thermalized ions, now singly or at most doubly-charged, are exposed to an axial electric field that pushes them towards radiofrequency (RF) ion carpets [12], installed vertically on the exit side of the magnet. The ion carpets use electric fields to transport the ions to the axis in a 'surfing'-type ion motion [13]. At this point, aided by gas flow, they enter an extraction region with a pressure of several mbar. Here a 1 m long ion conveyor [14] takes the ions through the axial bore in the return yoke. Outside the bore of the magnet, the ions pass through more pumping stages, before they are electrostatically accelerated to 60 keV energy. For this purpose, most of the cyclotron stopper infrastructure is placed at high voltage (HV).

THE MAGNET

The cyclotron gas-stopper magnet is a vertical superconducting split solenoid generating a focusing dipole field with maximum field of 2.6 T at a nominal excitation of 180 A. The design is a result of numerous Monte-Carlo type beam stopping simulations using successively refined 3D-magnetic TOSCA field maps [10], [15]. The magnet poles are divided into three hill and three valley regions. Their profiles required special care in order to provide sufficient axial focusing during deceleration and not to lose beam to an excitation of motion in the so-called Walkinshaw resonance. The clearance between the pole pieces was maximized to accept the large-emittance beam from the fragment separator and provide the necessary space for the cryogenic stopping chamber with its RF carpet structure and push-field electrodes. The minimum gap between the hills is 18 cm, leaving an effective stopping volume, 10 cm wide and ≈ 2 m in diameter.

The 4-meter diameter, 2-meter wide, 165-ton return yoke is split in two at the median plane for access to the interior of the magnet: the half housing the extraction electrode system is fixed to the floor, while the other one rests on a movable support structure that provides 1.5 m clearance when opened; see Fig. 2 for a photograph of the device. For ease of assembly and transport the yokes are made of three major parts: a lower and an upper crescent with a horizontal slab between. Base plates holding the hill-and-valley pole pieces screw into the assembly of the outer three parts. A total of 12 return-yoke inserts near the median plane complete the yoke and provide radial openings for degraders, diagnostics, electric feedthroughs, the three support links for the central stopping chamber and the injection channel. More details about magnet design and construction can be found in [11], [16].

The Cryostat

The two superconducting coils are cooled by a pair of cryostats, which are mounted into the two halves of the yoke. The cryostats use three CryoMech PT415-RM pulse-tube cryorefrigerators each and liquid-nitrogen cooled thermal shields to cool the coils to liquid-helium temperature. With a nominal cooling power of ≈ 1.35 W per cold head, the system generates and maintains its liquid inventory, a total of ≈ 15 liters, from gaseous helium. This concept avoids the problematic transfer of liquid helium to the cryostats when operated on HV. HV insulators in the He connections of the cold heads allow the compressors to remain on earth ground.

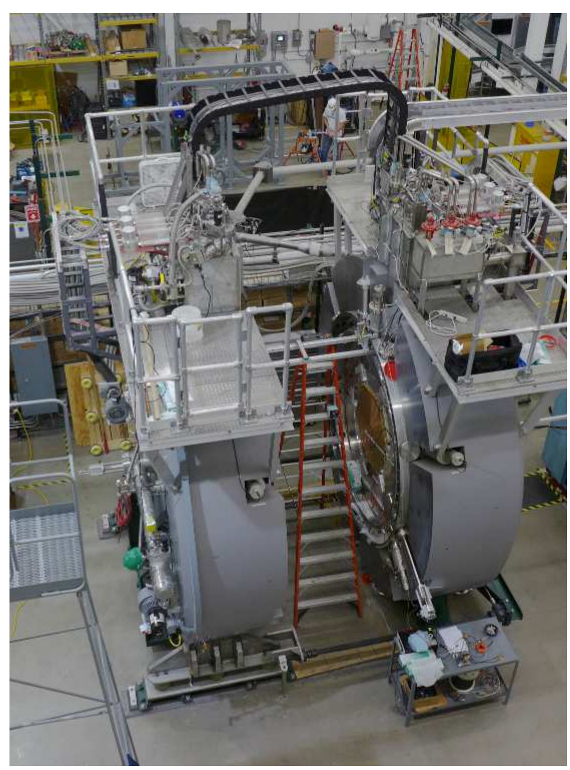

Figure 2: Photo of the cyclotron stopper, opened for installation of the ion carpets.

A complete cool-down from room temperature requires about two weeks; the liquid He inventory builds up in the last two days. More details on the cryogenic system of the cyclotron stopper can be found in [15], for reports on the performance of the cooling system see [17], [18].

Magnet Tests

After a number of tests and support link adjustments at lower currents, the magnet was brought up to the nominal field at full current in 2015. Field profiles were taken with a movable Hall probe that could slide either radially across a hill or a valley or inside the magnet's axial bore. In all cases, the measurements confirmed the calculated profiles, peaking at 2.6 T [18]. Consequently, the magnetic field index derived from the measured data agrees well with expectations [11], which has been identified as critical for efficient stopping of the injected beam.

As part of the magnet tests, the magnet's quench protection system has been tested as well, leading to valuable information on how quickly the stored energy is removed at various field levels. As an example, when a quench was triggered at the nominal current, the field decayed within 130 s to one percent, in reasonable agreement with thermal calculations [19].

The Stopping Chamber

The central aluminum vacuum chamber, which houses the RF ion carpets described below, is suspended inside the magnet by three radial tension links. Thermal isolation of the liquid-nitrogen cooled stopping chamber is facilitated by a guard vacuum. Because of limited space inside the magnet, the pole pieces of the magnet are part of the axial walls of the guard vacuum, while an extension of the fixed-side cryostat completes the vacuum chamber radially. Due to its large 2.35 m diameter, the lids of the chamber do not tolerate significant pressure differences between the inside and the guard vacuum. A pressure bypass system has been installed to protect the chamber during pumping cycles and operation at 100 mbar room-temperature equivalent pressure.

EXTRACTION ION GUIDES

While the damping force of the helium gas allows for the stopping of injected ions, it also slows down the process of extracting ions. Currently the most effective technique to transport ions quickly in high-pressure gas, e.g. in linear gas stopping cells or analytical chemistry applications, is a combination of static and inhomogeneous RF electric fields.

RF Ion Carpets

In the cyclotron stopper, a static electric field pushes the stopped ions towards a 'surfing'-type RF ion carpet, see Fig. 3 for a sketch of the arrangement and Fig. 4 for a photograph. The ion carpet is comprised of a large number of concentric electrodes. An RF voltage is applied so every electrode is 180° out of phase with its neighbor. This results in a net force that counteracts the static field generated with the push plate and positions the ions at a small distance above the carpet. In order to move the ions across the carpet, a high-frequency (HF) voltage is added with phase shifts of 90° between neighbor electrodes. Depending on conditions such as pressure, push field and RF/HF parameters, the ions can 'surf' in the troughs of the electric HF wave with transport speeds approaching the wave velocity. For a more detailed description of the concept, see e.g. [13], [14].

Several prototype carpets with different geometries, areas, electrode spacings had been built and tested [12], [20],

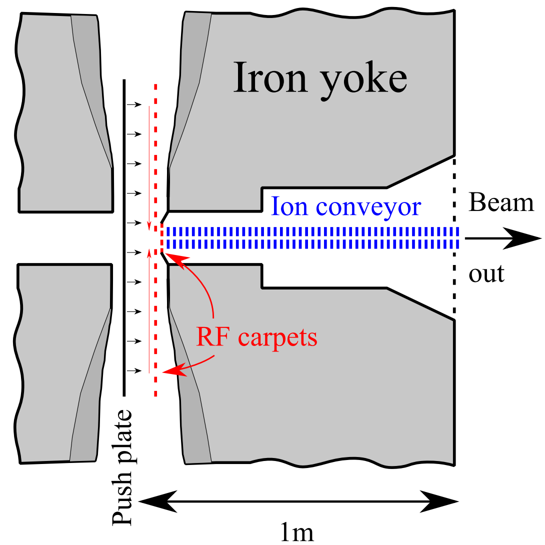

Figure 3: Sketch of the extraction system.

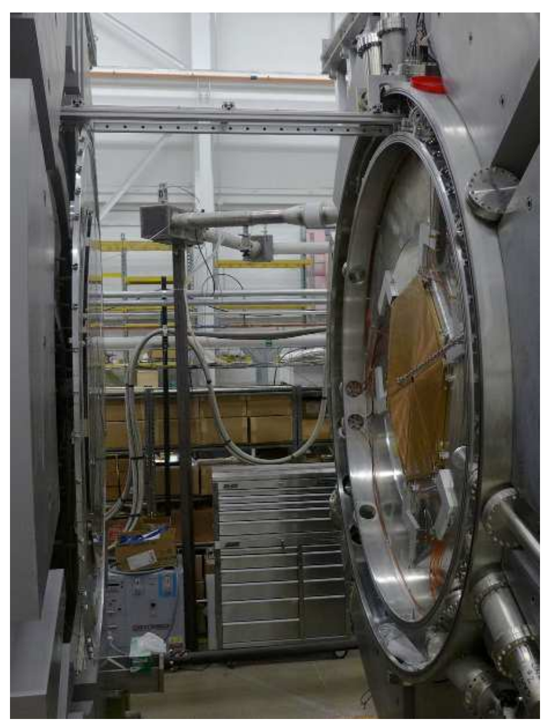

Figure 4: Closeup showing the stopping chamber with the RF ion carpets installed inside the opened cyclotron stopper.

ISBN 978-3-95450-167-0

demonstrating that ions with a wide range of masses can efficiently be transported over the required distance of a few tens of cm. The currently installed ion carpet, printed circuit boards with Kapton backing, cover a diameter of 0.89 m. With an active area of $\approx 0.6\,\mathrm{m}^2$ the 896 electrodes present a capacitive load of several nF to the RF system. Because of this load and for practical reasons, the carpet has been built as six 60-degree sectors with separate resonant RF driver circuits, capable of delivering the required RF amplitudes. To minimize RF losses, the resonant circuits have been placed at the perimeter of the carpets, in pockets added to the vacuum chamber, which use space in the pole valleys.

Ion Conveyor

Once within a radius of ≈25 mm from the axis of the cyclotron stopper, the ions continue on and through a miniature RF ion carpet, installed for differential pumping purposes and enter an ion 'conveyor' for transport through the bore of the magnet. An RF ion conveyor uses a traveling RF wave in a similar fashion as the surfing ion carpets, however it is shaped as a stack of ring-shaped electrodes to move ions along the inside [21]. In the cyclotron stopper, 536 electrodes are set up in groups of eight for 45-degree RF phase shifts; see Fig. 5 for a photograph. Despite its complexity,

Figure 5: The 1 m RF ion conveyor with a 1-1/4" wrench for scale.

this type of ion guide was chosen as it is expected to transport ions rapidly and efficiently even in the presence of the magnetic field, which drops from 2.4 T to a few 100 G along the structure.

The ion conveyor system with its entrance and exit mini-carpets have been tested in NSCL's stopping vault to benefit from existing pumping and diagnostics infrastructure. The expected pressure drops across the mini-carpet pumping barriers have been confirmed. A variable-frequency digital driver circuit has been developed to provide the required eight 45-degree phase-shifted RF signals for the conveyor. Ion transport tests through the 1 m long ion conveyor with Na, K and Rb ions, produced by surface ionization sources, have demonstrated efficiencies exceeding 80 %.

Transit times have been measured by using an electrode upstream the conveyor as a beam gate and recording the time when the resulting ion pulse appeared downstream. As an example, Figure 6 shows measured transit times of K-ions as a function of the RF wave frequency at a conveyor pressure of ≈ 4 mbar. Subtracting the expected flight time from the beam gate to the conveyor, the transit time through the conveyor can be estimated to be below 5 ms for frequencies up to 800 kHz.

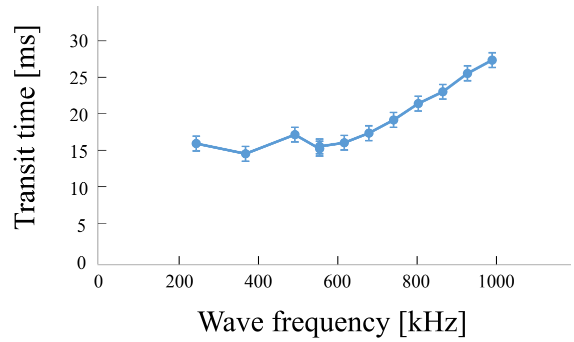

Figure 6: Measured transit times of K^+ ions through the conveyor as a function of wave frequency.

CONCLUSION, STATUS

The cyclotron stopper is currently installed in an assembly area, separated from NSCL's beam lines, in order to allow low-energy beam operation during commissioning activities. Following the recent installation of the large-scale carpets and the ion conveyor in the cyclotron stopper, ion transport tests along the entire extraction system at room temperature are about to start. A test ion source has been installed on a rotatable arm reaching across the main RF carpets. This setup will allow systematic transport tests along these RF carpets in the presence of magnetic field and helium gas. Another test with the source placed at the entrance of the conveyor and reduced gas pressure will test the ion conveyor's performance with a magnetic field gradient. A repeat of these tests with the central chamber cooled by liquid nitrogen and demonstrated operation at high-voltage are important steps before moving the cyclotron stopper from its offline location to a production area.

REFERENCES

[1] R. Ringle, S. Schwarz, and G. Bollen, "Penning trap mass spectrometry of rare isotopes produced via projectile fragmentation at the lebit facility," *International Journal of Mass Spectrometry*, vol. 349-350, p. 87, 2013.

[2] D. Rossi *et al.*, "A field programmable gate array-based time-resolved scaler for collinear laser spectroscopy with bunched radioactive potassium beams," *Review of Scientific Instruments*, vol. 85, p. 093 503, 2014.

[3] A. Villari *et al.*, "Commissioning and first accelerated beams in the reaccelerator (Rea3) of the national superconducting cyclotron laboratory, MSU," in *Proc. 7th International Particle Accelerator Conference (IPAC'16), Busan, Korea, Mar. 2016*, 2016, TUPMR024.

[4] D. Dickel *et al.*, "Conceptional design of a novel next-generation cryogenic stopping cell for the low-energy branch of the super-frs," *Nucl. Instr. Methods*, vol. B376, p. 216, 2016.

[5] G. Savard, "Large radio-frequency gas catchers and the production of radioactive nuclear beams," *Journal of Physics: Conference Series*, vol. 312, p. 052 004, 2011.

[6] K. Cooper *et al.*, "Extraction of thermalized projectile fragments from a large volume gas cell," *Nucl. Instr. Methods*, vol. A763, p. 543, 2014.

ISBN 978-3-95450-167-0

[7] L. Simons, "Recent results on antiprotonic atoms using a cyclotron trap at lear," *Physica Scripta*, vol. T22, pp. 90–95, 1988.

[8] I. Katayama, M. Wada, H. Kawakami, J. Tanaka, and K. Noda, "Cyclotron ion guide for energetic radioactive nuclear ions," *Hyperfine Interactions*, vol. 115, pp. 165–170, 1998.

[9] G. Bollen, D. Morrissey, and S. Schwarz, "A study of gas-stopping of intense energetic rare isotope beams," *Nucl. Instr. and Meth*, vol. A550, p. 27, 2005.

[10] N. Joshi, G. Bollen, M. Brodeur, D. Morrissey, and S. Schwarz, "Status of the NSCL cyclotron gas stopper," in *Proceedings of IPAC2012, New Orleans, USA*, jacow.org, TUPPR087.

[11] S. Chouhan *et al.*, "The superferric cyclotron gas stopper magnet, design and fabrication," *IEEE Transactions On Applied Superconductivity*, vol. 23, p. 4 101 805, 2013.

[12] A. Gehring, M. Brodeur, G. Bollen, D. Morrissey, and S. Schwarz, "Research and development of ion surfing rf carpets for the cyclotron gas stopper at the NSCL," *Nucl. Instr. Methods*, vol. B376, pp. 221–224, 2016.

[13] G. Bollen, "Ion surfing with radiofrequency carpets," *Int. Journal of Mass Spectrometry*, vol. 299, p. 131, 2011.

[14] M. Brodeur, N. Joshi, A. Gehring, G. Bollen, D. Morrissey, and S. Schwarz, "Traveling wave ion transport for the cyclotron gas stopper," *Nucl. Instr. Methods B*, vol. 317, pp. 468–472, 2013.

[15] M. Green *et al.*, "Progress on the MSU superferric cyclotron gas stopper magnet quench protection and cooling system," in *Proc. North-American Particle Accelerator Conference, Pasadena, CA, NA-PAC'13, 9/29 — 10/4, 2013*, jacow.org, THPBA12.

[16] S. Chouhan *et al.*, "Fabrication of the superferric cyclotron gas-stopper magnet at NSCL at michigan state university," in *Proc. European Conference on Applied Superconductivity Genoa, Italy, EUCAS2013, 9/15 — 9/19, 2013*, IOP Publishing, 2014, p. 032 010.

[17] M. Green *et al.*, "Lessons learned from the cool-down of a superconducting magnet using a thermal-siphon cooling loop," in *Proc. Cryogenic Engineering Conference and International Cryogenic Materials Conference CEC/ICMC 2015, Tucson, AZ, 6/28 — 7/2, 2015*, IOP Conference Series, 2015, p. 012 150.

[18] S. Schwarz *et al.*, "The NSCL cyclotron gas stopper – entering commissioning," *Nucl. Instr. Methods*, vol. B376, pp. 256–259, 2016.

[19] M. Green *et al.*, "Slow current discharges and quenching of the MSU superconducting cyclotron gas-stopper magnet," in *Proc. Applied Superconductivity Conference Denver, CO, Sep 4-9 2016*, 2016, 2LPo2C–03.

[20] M. Brodeur, A. Gehring, G. Bollen, S. Schwarz, and D. Morrissey, "Experimental investigation of the ion surfing transport method," *International Journal of Mass Spectrometry*, vol. 336, p. 53, 2013.

[21] A. Colburn, M. Barrow, M. Gill, A. Giannakopulos, and P. J. Derrick, "Electrospray ionisation source incorporating electrodynamic ion focusing and conveying," in Proc. CPO-7, *Cambridge, UK, July 2006*, 2008, pp. 51–60.

ISBN 978-3-95450-167-0

CHALLENGES IN FAST BEAM CURRENT CONTROL INSIDE THE CYCLOTRON FOR FAST BEAM DELIVERY IN PROTON THERAPY*

S. Psoroulas†, P. Fernandez Carmona, G. Klimpki, C. Bula, D. Meer, D. C. Weber[1]
Paul Scherrer Institut, 5232 Villigen PSI, Switzerland
[1]also at University of Zurich, Zurich, Switzerland

Abstract

The COMET cyclotron at PSI has been successfully used to treat patients with static tumours using the spot scanning technique, i.e. sequentially irradiating different positions inside the tumour volume. Irradiation time for each position ranges from micro- to milliseconds, with total treatment duration of about a minute. For some tumours (e.g. lung) physiological motion (e.g. respiration) interferes with the scanning motion of the beam, lowering treatment quality. For such mobile tumours, we are developing a new technique called continuous line scanning (CLS), aiming at reducing treatment time by more than 50%. In CLS, dose rate should stabilize (within few percent) within tenths of a millisecond. We thus implemented a first prototype for fast, real-time beam control: a PID controller sets the internal electrostatic vertical deflector of the accelerator, regulating the beam current output based on the instantaneous current measured just before the patient and the knowledge of the transmission from the accelerator to the patient. In pre-clinical experiments, we achieved good control of the global dose delivered; open issues will be tackled in the next version of the controller.

INTRODUCTION

Proton therapy step-and-shoot scanning techniques, like spot scanning [1] or raster scanning [2], have been remarkably successful in treating static tumours such as those located in the brain or in the spine [3]. The intrinsic dynamic of the scanned pencil beam, moving sequentially through the tumour volume in all three dimensions, is however a disadvantage when treating tumours moving periodically (due to respiration, like lung or liver): the interference between scanning beam motion and tumour motion [4–6] can deform the dose distribution up to a clinically unacceptable level (so-called 'interplay effect'). To reduce this effect, motion mitigation techniques have been proposed. One example is rescanning [7, 8], a technique which foresees delivering the same plan several times, each time with a reduced dose, to a moving target, in this way averaging out the interference pattern between the scanning beam motion and the target motion. Though promising, motion mitigation techniques are not widely used, since they lengthen irradiation time, lowering patient comfort and throughput. Only a handful of centres worldwide offer such treatments.

Moving away from the step-and-shoot approach could potentially provide the fast, efficient irradiation suitable for motion mitigation. In this context, at PSI Gantry 2 we are developing a new irradiation technique called continuous line scanning (CLS) [9]. CLS paints an arbitrary dose distribution in the tumour volume by continuously changing the beam current and position within an energy (=depth) layer. We have shown [10, 11] that this technique can achieve dose distributions comparable to spot scanning, but reduce the treatment time by more than 50%, depending on the irradiation conditions and the motion mitigation strategy used [12].

One of the main differences between the standard pencil beam scanning delivery techniques and CLS is the way the beam moves from one position to the next during irradiation. In dose-driven techniques like spot and raster scanning the beam moves to the next position after the full dose prescribed for the current position has been delivered. This makes them robust with respect to beam instabilities, as they can compensate such effects by shortening or lengthening the time spent at a certain position; for this reason, such techniques are standard in clinical centres. Our proposed CLS implementation is instead time-driven, meaning the treatment control system (TCS) changes the values of the actuators controlling beam position and current according to a time table; this potentially makes the irradiation faster than dose-driven systems, as CLS does not rely on integrated signals to move from one position to the next. However, this poses stronger requirements on the precision of beam delivery and on the reaction time to beam instabilities, in order to avoid deformation of the resulting dose distribution.

In this document, we report about the challenges of such a system concerning beam current control, and the solution we designed for future clinical application.

FAST CURRENT CONTROL AT THE PROSCAN FACILITY

Beam Current Control in the COMET Cyclotron

The COMET [13] (ACCEL/Varian) cyclotron accelerates the proton beam used for patient treatment at Gantry 2 to an energy of 250 MeV. The beam is extracted from the proton source using a negatively charged puller, and is then accelerated passing through 4 dees. The proton source is kept at stable extraction conditions; the beam current is modulated as required by the treatments by stopping part of the protons inside the cyclotron using collimators.

Fast current changes are achieved using an internal electrostatic deflector (so-called vertical deflector, VD), which deflects the beam towards collimators built in one

* G. Klimpki's work is supported by the 'Giuliana and Giorgio Stefanini Foundation'
† serena.psoroulas@psi.ch

ISBN 978-3-95450-167-0

of the accelerator's dees [14]. To avoid high activation of the material, the deflector is placed close to the accelerator centre so that the protons are stopped very early, during the first acceleration turns, when they still have a very low energy. Additionally, phase slits are used to limit the maximum beam current and improve stability of operation [15].

During standard (spot scanning) patient treatments at Gantry 2, the TCS requests a certain extracted current, and the accelerator control system sets the vertical deflector accordingly; in such a mode, beam current changes can be achieved in few tens of milliseconds. For CLS, though, we aim at much faster current modulation. We have thus implemented an alternative link, which directly connects the TCS with the VD power supply, achieving beam current changes within 50 µs.

Beam Transmission

After extraction, the beam passes through a degrader, followed by an energy selection system (consisting of magnets and energy selection slits), and is then transported to Gantry 2, finally reaching the patient. The degrader causes a strong energy dependence in the transmission from the accelerator to the patient [14], compensated to a certain extent by the optics of the beam transport system.

Vertical Deflector Fast Regulation Loop

To achieve precise dose delivery in time driven mode, we need to achieve good control on the beam current reaching the patient. This means compensating for both possible transmission losses and beam current instabilities, potentially occurring during irradiation.

To this aim, we have implemented a new control algorithm for the VD power supply in the TCS. The architecture is a PID controller with a lookup table for feed forward and a dual input for feedback (Fig. 2). The goal of the controller is to regulate the beam current to the set value (fed to the controller by the TCS) within 150 µs since the start of a line.

The lookup table input to the feedforward is built from measurements of the beam current at the patient as function of the VD voltage (as those in Fig. 1). The feed forward provides a first estimation of the VD voltage set value needed for the irradiation; such value can be used to compensate for transmission variation as function of energy.

An ionization chamber, placed at the end of the gantry beam line, just before the patient ('Monitor 1' in Fig. 2), provides the input to the integral controller; such a monitor accurately measures the beam current, but due to its slow rise time (about 100 µs) cannot react quickly enough to beam current instabilities. To partially improve the latency, a secondary ionization chamber ('Monitor 2' in Fig. 2, with faster rise time than Monitor 1) feeds a proportional and derivative controller to reduce settling time after fast beam current changes.

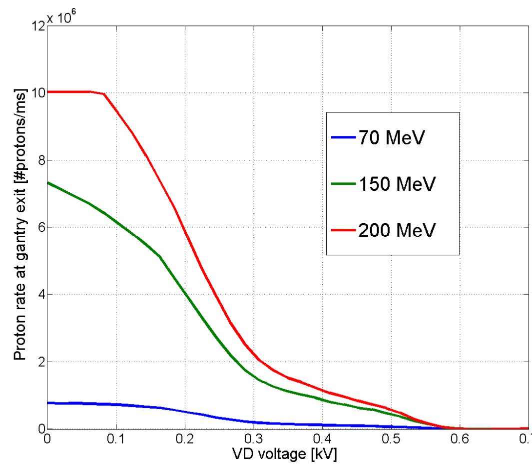

Figure 1: VD curves for different energies, measured at Monitor 1 during experiments; they show the typical shape of a lookup table used in the feedforward part of the regulation loop. The saturation effect shown at 200 MeV is due to the particular settings of the phase slits on the day of the measurement.

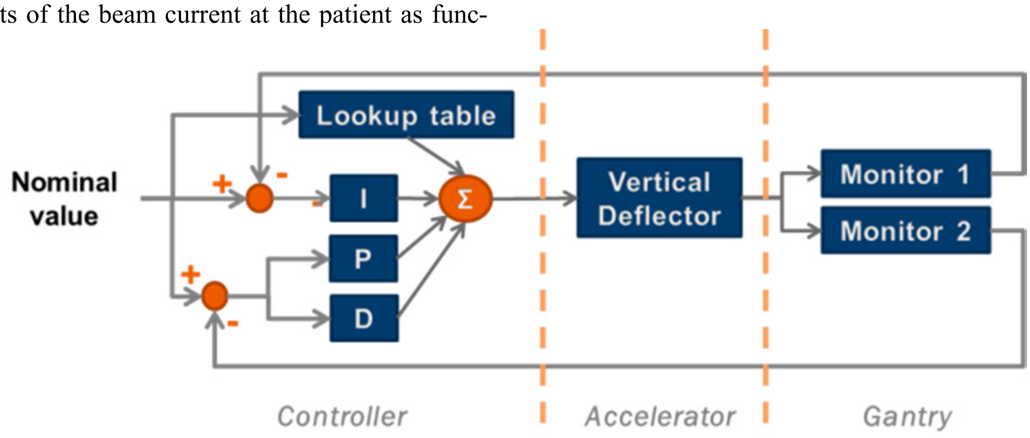

Figure 2: Schema of the feed-back regulation loop.

ISBN 978-3-95450-167-0

RESULTS AND DISCUSSION

Lookup Table Definition and Transmission

As expected due to the energy-dependent transmission, the relationship between the measured beam current at the patient and the VD voltage exhibits strong energy dependence, as shown in Fig. 1. We also observed a rather high variability in the performance of the vertical deflector, in particular from day to day, likely due to sensitivity to changing proton source conditions.

To account for both effects, we defined an initialisation procedure that measures both the VD curve of the day for a single energy, and the transmission for a certain set point, i.e. the current output at the dose monitor as function of energy for a given VD value. The two measurements are combined by the TCS in the feedforward lookup table: the TCS scales the VD curve of the day to the energy required by the treatment plan according to the transmission function.

In experiments, we have measured an uncertainty of the order of 7% on the value estimated from the lookup table; this residual uncertainty could be easily corrected by the feedback loop, and therefore we consider this method sufficiently precise.

We are still estimating the impact of the machine conditions on the beam current output. Such effects are also compensated by the feedback loop; in case of strong variations (as could occur after a cyclotron emergency switch off, for example), the VD lookup table might not provide an appropriate initial set value and hinder the performance of the loop. We plan to implement a fast online update procedure for such cases, which will provide a new lookup table without interrupting clinical operations.

VD Power Supply Overshoot

When setting the VD in open loop, we have often observed strong beam current overshoots, lasting for more than 100 µs, thus non-negligible for fast scanning proton therapy. One example is shown in Fig. 3. The overshoot shows large variations from day to day and it is difficult to parameterise across the range of set points, but exhibits relative stability over one day. Cable capacitance and a likely impedance mismatch between the power supply and the VD are (some of) the causes behind this behaviour, and we are investigating possible hardware improvements together with the manufacturer of the power supply.

To overcome this problem, we are currently testing an improved feedforward, which accounts for the delay and the overshoot of the VD power supply in the initial set point estimation.

Regulation Loop Performance

We investigated how the performance of the regulation loop is affected by both the VD power supply overshoot and the rise time of the slowest dose monitor. The latter causes a delay in the reaction time of the loop to beam current fluctuations, which limits the usable gain of the I controller to prevent instabilities. In our new design, the integration of a faster dose monitor in the P and D controller part of the loop, together with the improved feedforward, reduces the reaction time and helps regulating for the overshoot. The result is a faster settling time in comparison to simpler designs, as shown in Fig. 4.

Because of the characteristic shape of the VD curve shown in Fig. 1, i.e. the almost inverse proportionality between the beam current and the corresponding VD voltage, the loop performs better when regulating high beam currents. At low currents, the cyclotron output is less sensitive to variations of the VD voltage. This is particularly important when using CLS with rescanning, as rescanning plans might require lower currents than standard clinical plans. We have observed that, for moderately high number of rescans (above 5), regulation issues can result in clinically visible local under- and overdosage to the target. We plan to solve this current limitation by implementing a mechanism to adapt the gain of the feedback depending on the requested beam current.

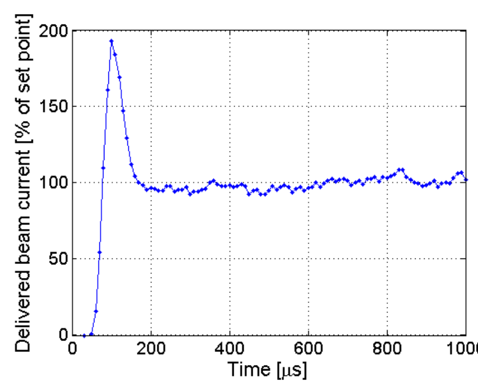

Figure 3: Example of an overshoot at the beginning of a line. Depending on different conditions, the overshoot can reach up to 200% of the set point.

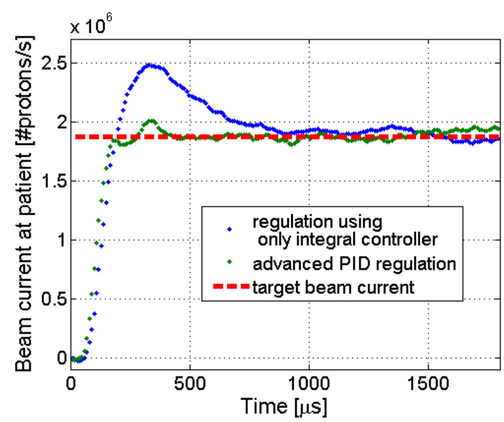

Figure 4: CLS beam current control: comparison between two options for the regulation. The advanced design presented in this work achieved the set point in about 120 µs, and does not show any overshoot, with respect to previous controller designs. A line element in a treatment can last up to several hundred milliseconds.

ISBN 978-3-95450-167-0

CONCLUSIONS

CLS is a beam scanning technique designed to administer moving targets treatments without substantial compromises in irradiation efficiency and patient throughput. Because it is a time-driven delivery technique, it strongly relies on fast and precise beam current control. We have developed a new regulation loop for the modulation of the current extracted from the COMET cyclotron, tackling issues related to energy-dependence and stability of the beam current delivered to the patient. We achieved good precision on the delivered dose within few hundreds of µs (on a total line time of several hundred milliseconds), fitting the requirements for fast irradiation. We are currently investigating the possibility to further improve the time performance and precision by having an automatic adaptation of the regulation loop parameters, to improve beam delivery precision in low current conditions.

ACKNOWLEDGEMENTS

We would like to thank our colleagues at the Centre for Proton Therapy at PSI; in particular, we would like to thank M. Eichin for his help in setting up the DAQ system used for the measurements with the beam current monitors.

REFERENCES

[1] E. Pedroni, R. Bacher, H. Blattmann, T. Böhringer, A. Coray, A. Lomax, S. Lin, G. Munkel, S. Scheib, and U. Schneider, "The 200-MeV proton therapy project at the Paul Scherrer Institute: conceptual design and practical realization.," *Med. Phys.*, vol. 22, no. 1, pp. 37–53, Jan. 1995.

[2] T. Haberer, W. Becher, D. Schardt, and G. Kraft, "Magnetic scanning system for heavy ion therapy," *Nucl. Instruments Methods Phys. Res. Sect. A Accel. Spectrometers, Detect. Assoc. Equip.*, vol. A330, no. 1–2, pp. 296–305, 1993.

[3] A. Bolsi, D. C. Weber, C. Ares, R. Schneider, J. H. Geismar, A. Schertler, E. B. Hug, T. Koch, and G. Goitein, "Spot Scanning–based Proton Therapy for Intracranial Meningioma: Long-term Results from the Paul Scherrer Institute," *International Journal of Radiation Oncology*Biology*Physics*. 2011.

[4] M. H. Phillips, E. Pedroni, H. Blattmann, T. Boehringer, A. Coray, and S. Scheib, "Effects of respiratory motion on dose uniformity with a charged particle scanning method," *Phys. Med. Biol.*, vol. 37, no. 1, pp. 223–233, Jan. 1992.

[5] C. Bert, S. O. Grözinger, and E. Rietzel, "Quantification of interplay effects of scanned particle beams and moving targets.," *Phys. Med. Biol.*, vol. 53, pp. 2253–2265, 2008.

[6] J. Seco, D. Robertson, A. Trofimov, and H. Paganetti, "Breathing interplay effects during proton beam scanning: simulation and statistical analysis.," *Phys. Med. Biol.*, vol. 54, pp. N283–N294, 2009.

[7] S. M. Zenklusen, E. Pedroni, and D. Meer, "A study on repainting strategies for treating moderately moving targets with proton pencil beam scanning at the new Gantry 2 at PSI.," *Phys. Med. Biol.*, vol. 55, pp. 5103–5121, 2010.

[8] A. Schätti, M. Zakova, D. Meer, and A. J. Lomax, "Experimental verification of motion mitigation of discrete proton spot scanning by re-scanning.," *Phys. Med. Biol.*, vol. 58, no. 23, pp. 8555–72, Dec. 2013.

[9] A. Schätti, D. Meer, and A. J. Lomax, "First experimental results of motion mitigation by continuous line scanning of protons", *Phys. Med. Biol.*, vol. 59, no. 19, pp. 5707-5723, Oct. 2014.

[10] G. Klimpki, S. Psoroulas, P. Fernandez, C. Bula, D. C. Weber, D. Meer, and A. Lomax, "Fast dose modulation in proton therapy with continuous line scanning," *Radiother. Oncol.*, vol. 118, pp. S56–S57, Feb. 2016.

[11] S. Psoroulas, G. Klimpki, P. Fernandez Carmona, C. Bula, D. C. Weber, and D. Meer, "Feasibility study of IMPT-like delivery with continuous line scanning of protons," in *PTCOG55, Prague, 2016*, 2016.

[12] G. Fattori, G. Klimpki, S. Safai, D. Weber, A. Lomax, and S. Psoroulas, "TH-CD-209-07: Preliminary Experimental Comparison of Spot- and Continuous Line Scanning with Or Without Rescanning for Gated Proton Therapy," *Med. Phys.*, vol. 43, no. 6, pp. 3887–3887, Jun. 2016.

[13] H.-U. Klein, C. Baumgarten, A. Geisler, J. Heese, A. Hobl, D. Krischel, M. Schillo, S. Schmidt, and J. Timmer, "New superconducting cyclotron driven scanning proton therapy systems," *Nucl. Instruments Methods Phys. Res. Sect. B Beam Interact. with Mater. Atoms*, vol. 241, no. 1–4, pp. 721–726, Dec. 2005.

[14] J. M. Schippers, D. Meer, and E. Pedroni, "Fast scanning techniques for cancer therapy with hadrons – a domain of cyclotrons," in *Proceedings of Cyclotrons 2010*, 2010, pp. 410–415.

[15] M. Schippers, D. Anicic, R. Dölling, A. Mezger, E. Pedroni, L. Stamsnijder, A. Geisler, H. Röcken, and J. Timmer, "Beam intensity stability of a 250 MeV SC cyclotron equipped with an internal cold-cathode ion source," in *Proceedings of Cyclotrons 2007*, 2007, pp. 300–302.

ISBN 978-3-95450-167-0

NEW TIME STRUCTURES AVAILABLE AT THE HZB CYCLOTRON

A. Denker*, J. Bundesmann, T. Damerow, T. Fanselow, D. Hildebrand, U. Hiller, C. Rethfeldt, J. Röhrich, Helmholtz-Zentrum Berlin für Materialien und Energie, Berlin, Germany

Abstract

While most of the beam time of the cyclotron is used for proton therapy of ocular melanomas, an increasing amount of beam time is used for experiments. In response to a growing demand on time structures a new pulse suppressor was developed.

The set-up of the pulse suppressor, measurements on the time structures for various beams and examples of their experimental use will be presented.

INTRODUCTION

About 90% of the beam time of the cyclotron is used for proton therapy of ocular melanomas. However, there is an increasing amount of beam time for experiments. While most of these experiments can be performed with the quasi DC-time structure of the beam from the cyclotron, there is a demand for pulsed beams with a huge variety of time structures.

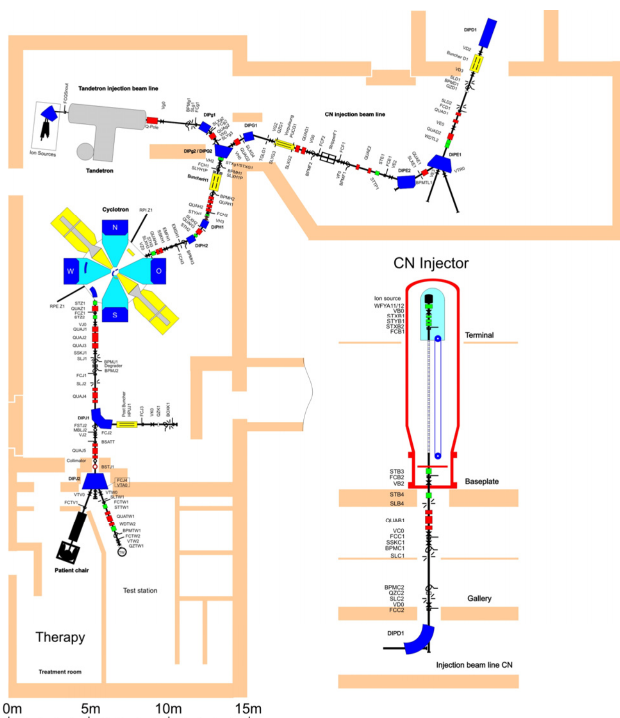

Figure 1: Layout of the accelerator. The yellow marked items influence the time structure of the beam.

Originally the accelerator complex was developed for heavy ions, as it is reflected in its first name VICKSI (*Van-de-Graaff Isochron-Zyklotron Kombination für schwere Ionen* – Van-de-Graaff Isochronous-Cyclotron combination for heavy ions) [1]. This reflects on the design of the pick-ups and the phase probes as well as the design of the bunchers and pulse suppressors. In order to analyse the time structure, we have developed a special pick-up, now permanently installed in the extraction line [2].

Figure 1 shows the actual layout of the facility with the devices influencing the time structure marked in yellow. While the Tandetron-cyclotron combination provides an extremely stable quasi DC beam, there exists no possibility to influence the time structure of the beam, as the last buncher in front of the cyclotron was designed for heavier ions with a charge to mass ratio between 1/2 and 1/8. Time structures can be achieved only using the 6 MV Van-de-Graaff as injector. A first buncher is situated in its terminal. Two bunchers and a pulse suppressor are located in the injection beam line. A second pulse suppressor on the extraction line after the 90° analysing magnet was used to get rid of parasitic pulses.

As mentioned above, for light ions we can use only the buncher in the high-voltage terminal and the first one in the beam line. Due to the lower time-focussing, the transmission through the cyclotron is only 50% compared to 100% achievable with heavy ions and the use of all bunchers. The pulse width of the beam is 1 ns for 68 MeV protons compared to 0.3 ns for heavy ions.

The limited transmission through the cyclotron is not a problem, as the requested beam intensities are far below 1 µA (DC equivalent). However, the limitations in the existing pulse suppressor yielded maximum repetition rates of 75 kHz for protons due to the necessary high voltages.

SINGLE TURN EXTRACTION

For proton therapy it is not relevant if single turn extraction is achieved. Figure 2 shows the pick-up signal of the extracted 68 MeV proton beam with a DC injection. The distances of the pulses are 50 ns, corresponding to the 20 MHz cyclotron RF and the pulse width is about 5 ns. Reflections on the cables are the reason for the multiple peaks about 5 ns after the first signal.

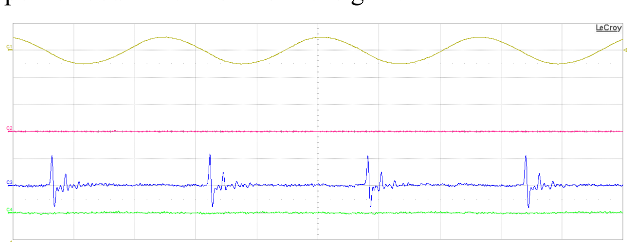

Figure 2: Pick-up signal of 68 MeV extracted proton beam (blue) with DC injection and cyclotron RF (yellow).

* denker@helmholtz-berlin.de

ISBN 978-3-95450-167-0

However, for single pulses, single turn extraction is mandatory. Figure 3 shows the pick-up signal from the extracted 68 MeV proton beam in the beginning of a tuning process. A bunched beam with a repetition rate of 75 kHz was injected. The inflection time on the suppressor was chosen to be less than 50 ns. Nevertheless, five peaks with a distance of 100 ns, corresponding to the 2nd harmonic, are observed. This is a clear indication that adjustments in the tuning of the accelerator are necessary.

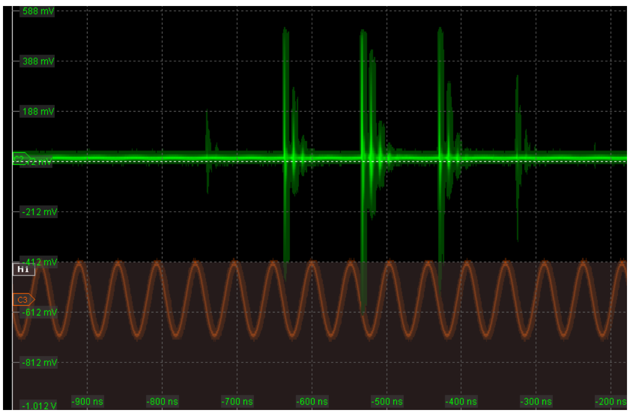

Figure 3: Pick-up signal of extracted 68 MeV proton beam (green) and cyclotron RF (red). In the beginning of the tuning process there is no single turn extraction.

For protons this pick-up provides the only mean to verify if single turn extraction is present. In contrast to our phase probes used for heavy ions, the pick-up provides just one single information in the extraction channel. Thus, tuning may be ambiguous, as both the phases of the two bunchers and the cyclotron RF as well as the magnetic field influence the signal and have to be adjusted. As can be seen in Figure 4, single turn extraction is achieved.

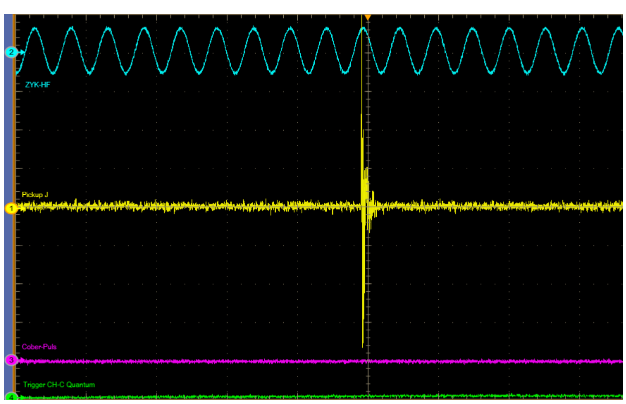

Figure 4: Pick-up signal (yellow) of extracted 68 MeV proton beam and cyclotron RF (light blue). Single turn extraction is achieved after phase adjustment and fine tuning of the magnetic field.

NEW PULSE SUPRRESSOR

The pulse suppressor consists of two adjustable parallel plates: the deflecting plate with a permanent high-voltage switched on and the injection plate with a high-frequency voltage which kicks the beam back on its flight path.

The request of the experimental side was a repetition rate of 1 MHz for single pulses. This is challenging, as for proton with 68 MeV the RF frequency of the cyclotron is close to its upper limit of 20 MHz giving a time window for injection of less than 50 ns. In addition, albeit the pulse suppressor is located at the low energy side of the cyclotron, the required voltages for the suppressor are about 1 kV for protons. For these reasons, a semiconductor HV MOS-FET switch from Behlke, Kronberg, Germany, was selected for the RF voltage of the suppressor. The parameters are given in table 1 in comparison to the old tube-based suppressor. The high frequency was chosen in order to guarantee stable operation at 1 MHz.

The electric part of the suppressor consists of:

- the electronic module for the pulsing, comprising the control unit, pulse processing, MOS-FET switch, and the HV power supply for the injection voltage
- the HV power supply for the deflection
- a heat exchanger.

The heat exchanger became necessary, as the dissipated loss is around 1500 W.

Table 1: Comparison of the parameters of the old tube-based suppressor to the semi-conductor based suppressor

Parameters	Old	New
max. repetition rate	150 kHz	2.4 MHz
max. amplitude	1.2 kV	2 kV
I_{max}	12.5 A	30 A
min. rise time	20 ns	11 ns
min. fall time	35 ns	11 ns

At the same time, the electronics for selecting the ratio and length of suppressed/unsuppressed pulses was replaced. It consisted of one 19” rack 5U and two 19” racks 2U for phase shifting and measuring. Built in the early eighties with wire-wrap cards, maintenance became difficult. In addition, the division of the pulses was only feasible in terms of 2^n of the cyclotron frequency. The new divider, from Quantum, Bozeman MT, USA, provides 8 different output-channels which may be set freely to different delays and pulse/pause ratios. The base for the division is, as with the old one, the cyclotron frequency. Figure 5 depicts the signal plan.

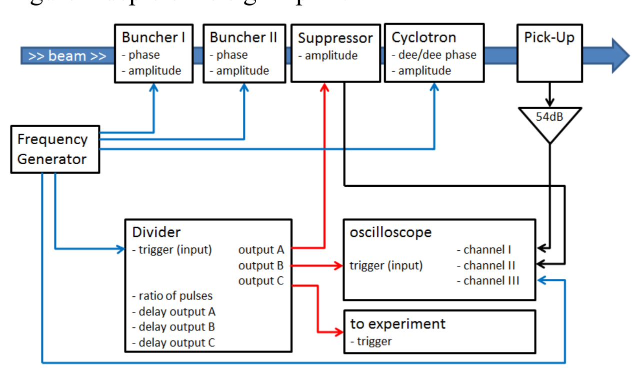

Figure 5: Signal plan of the RF elements comprising bunchers, cyclotron, pulse suppressor, pick-up, oscilloscope, and trigger signal for the experiment.

ISBN 978-3-95450-167-0

The divider is controlled by a LabVIEW programme (Figure 6) for selecting the suppression rate in whole numbers of the cyclotron frequency and selecting the pulse length. Furthermore, the delay between cyclotron frequency and suppressor is adjusted as well as the delays needed for the display in the oscilloscope and for the trigger signal to the experiment.

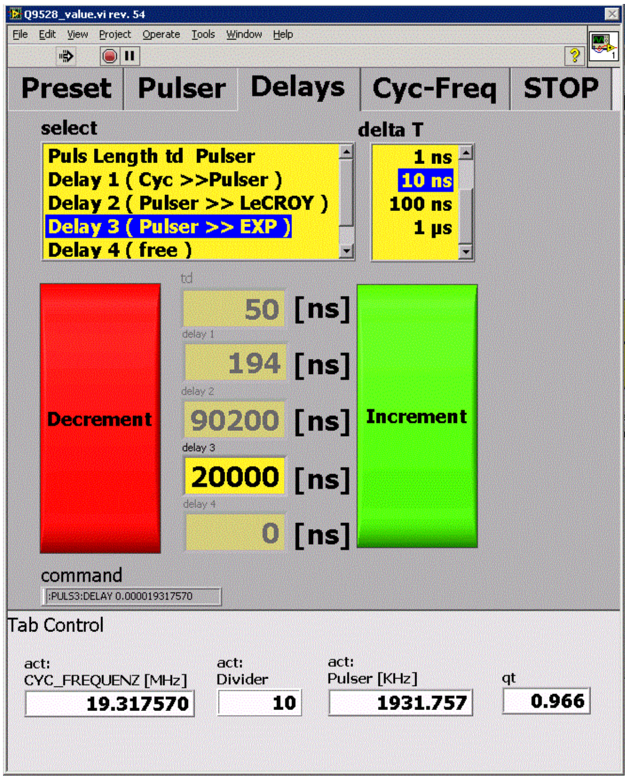

Figure 6: Screenshot of the LabVIEW programme for the control of the divider and the selection of pulse length and suppression rate.

RESULTS

For the first time, single turn extraction was achieved on our cyclotron for protons. Three different light ion beams with single pulses have been delivered to the experiment: protons with 68 MeV and helium with 50 MeV and 75 MeV respectively.

The reason for the increase of the repetition rate came from an experiment measuring the γ-ray emission from proton and α-particle irradiation of different thin targets [3]. The average beam intensity for good count rates was calculated to be in the order of 1 nA which leads to a pulse current of about 250 nA when using 75 kHz repetition rate. The request of a repetition rate of 1 MHz is based on avoiding dead-time effects in the detectors yet maintaining the average beam intensity, as well as taking the time structure of the induced background in the beam dump of a few 100 ns into account.

As shown in Figure 7, the new pulse suppressor allows us to provide pulsed beams with repetition rates greater than the requested 1 MHz. Even at the maximum repetition rate of the MOS-FET HV switch of 2.4 MHz, the suppressor was tested to be very stable without any HV dips for more than 10 hours. Thus it is far more stable at the high voltages required for protons than the old, tube-based suppressor.

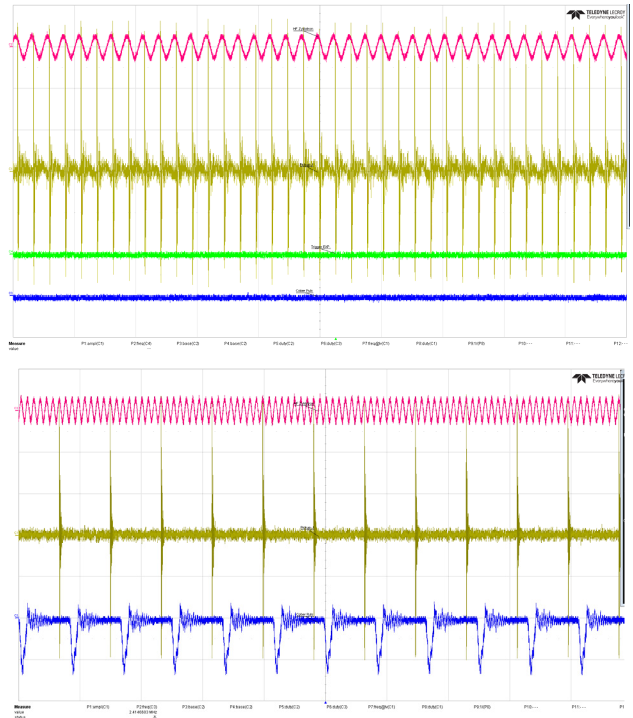

Figure 7: Time Structure of the 68 MeV proton beam. In red: cyclotron RF; blue: suppressor; yellow: pick-up signal. Upper image: suppressor switched off. Lower image: suppressor operating at a repetition rate of 2.4 MHz.

CONCLUSION

With this new pulse suppressor the repetition rate of the pulse may be varied from 2.4 MHz down to 1 Hz or less with a very stable operation. The pulse length can be freely chosen from a quasi-continuous beam to single pulses with a pulse width less than 1 ns for light ions. This was already used to simulate different time structures of synchrotrons and synchro-cyclotrons to investigate possible influences on the dosimetry.

The pulses are measured either with a specially developed Faraday cup or non-destructively with a pick-up in the extraction beam line. The measurement of single pulses with the pick-up surveys very precisely if single turn extraction is achieved.

REFERENCES

[1] K. Ziegler, "Running in of VICKSI and first operation experience", in *Proc. Cyclotrons'78*, *IEEE Trans. Nucl. Sci.* NS-26 (2), 1872 (1979)

[2] A. Denker *et al.*, "Status of the HZB cyclotron", in *Proc. Cyclotrons'13*, Vancouver, Canada, Sep. 2013, paper MOPPT002, pp. 31-33.

[3] J. Kiener, private communication, Nov. 2013.

ISBN 978-3-95450-167-0

RECENT IMPROVEMENTS IN BEAM DELIVERY WITH THE TRIUMF'S 500 MeV CYCLOTRON.*

I. Bylinskii[†], R. Baartman, K. Jayamanna, T. Planche, Y.-N. Rao, TRIUMF, Vancouver, Canada

Abstract

TRIUMF's 500 MeV H- Cyclotron, despite its 44 years age is under continuous development. Many aspects of beam delivery have been improved over the last few years. Regular 3-week cusp source filament exchange cycle has advanced to multi-months due to greatly improved filament life time. Fine source tuning allowed beam intensity rise in support of routine extraction of 300 μA of protons. The injection line model has been fully correlated with online measurements that enabled its tuning and matching to the emittance defining slits and the cyclotron entrance. Cyclotron routinely produces 3 simultaneous high intensity beams (~100 μA each). Multiple techniques have been developed to maintain extracted beams intensity stability within +/- 1%. Record extraction foil life times in excess of 500 mA-hours have been demonstrated with highly-oriented pyrolytic graphite foil material and improvements in foil holder. Beam rastering on ISOL target allowed higher yields. A single user extraction at 100 MeV was achieved by applying phase slip and deceleration inside the cyclotron.

ION SOURCE AND INJECTION LINE

A powerful test stand for H- ion source development has been built in 2012. An intense cusp source filament study carried on over a couple of years. Resulting choice of filament material and shape allowed a breakthrough in the filament life time. Regular filament change was based on a 3 weeks cycle. Recently deployed filament survived 9 weeks, when it failed prematurely for a reason unrelated to its deterioration. Presently projected filament life expectancy is about 4 months. Figure 1 shows filament current drop in time; each peak corresponds to a filament replacement.

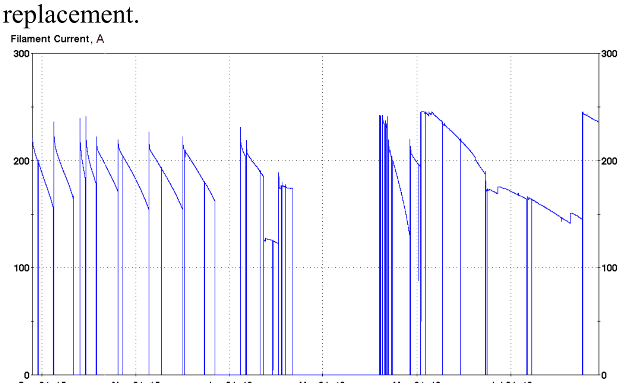

Figure 1: H- source filament current evolution.

In 2014 the ion source showed a very peculiar instability. It manifested itself as a strong dependence of beam steering at the output of the optics box on beam pulser setting (see Fig. 2). An assessment revealed an insulating coating layer on the electrostatic steering plate that was previously a grounded counterpart of the pulser deflecting plate. Electrical charge accumulated on the insulating layer was responsible for changing electrical field within steerer/deflector that caused uncontrollable beam steerinig. The problem was resolved by replacing aluminum plates with stainless steel ones.

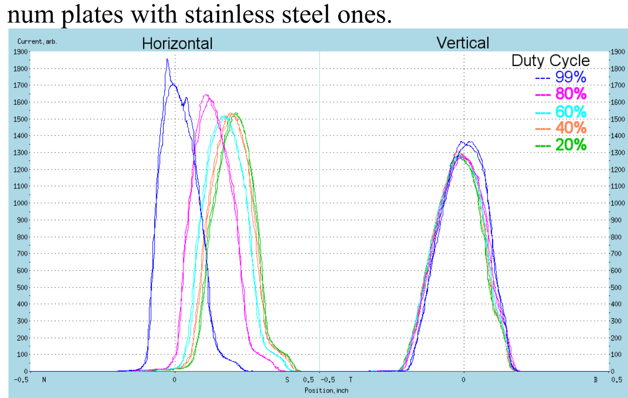

Figure 2: Beam horizontal steering vs duty cycle.

For a long time there was no clear understanding of the beam asymmetry at the exit of the source acceleration column. An OPERA model of an electrostatic steerer [1] offered an explanation to this issue: when circular apertures are used in conjunction with parallel plates and the plates have a net bias, the assembly acts partially as a quadrupole. There are two ways to avoid this effect: balancing the opposite polarity bias on the plates so the median plane becomes at ground potential or making a rectangular slot apertures of same orientation as the plates.

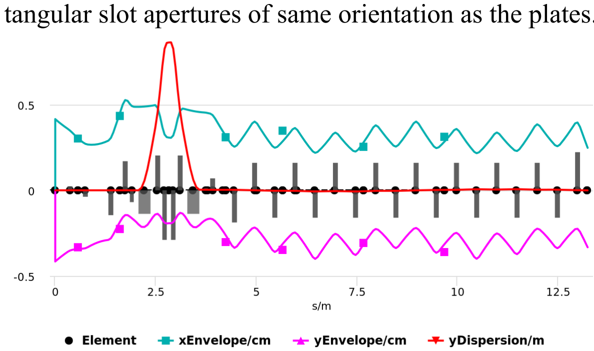

Figure 3: Beam envelope trough 1/3 of injection line; squares represent beam size at profile monitors.

Removing the quadrupole effect from the otherwise symmetrical section of beam optics allowed development of the accurate model of beam optics from the source down to the cyclotron entrance. This effort culminated by introduction of a High Level Application (HLA) that models the whole injection line. It uses online data from 5 profile monitors and live settings of the optics to reconstruct beam parameters and produces a new optics setting

* TRIUMF receives federal funding via a contribution agreement through the National Research Council of Canada
† bylinsky@triumf.ca

ISBN 978-3-95450-167-0

aiming at beam matching into emittance defining slits which are situated at the start of the first long periodic section. A typical plot of beam envelopes after matching is shown in Fig. 3. Straightforward beam tuning validated the high accuracy of the optics model. Also, a user-friendly interface has allowed smooth implementation of this first live HLA into operations.

INTENSITY STABILIZATION

Three high intensity beams are routinely extracted from the cyclotron: 100-130 μA at 480 MeV to the Meson Hall users (BL1A), up to 100 μA at 480 MeV to the ISAC facility (BL2A), and 100 μA at 100 MeV for the medical isotopes (Sr-82) production (BL2C4). Stable beams delivery is an important requirement for the operations. It is the most critical for the ISOL target where rare isotope yields are highly non-linear with respect to primary beam. This was recognized at inception of ISAC beam delivery and a palliative solution has been applied by regulating extracted beam down 2A beam line with a total intensity variation at injection using pulser which varies the duty cycle at 1 kHz at the source [2]. But, while solving the BL2A instability issue, this approach introduced magnified intensity changes in the remaining beamlines. The origin of the beam split ratio instability between BL1A and BL2A is the radial beam density oscillation induced by the ν_r = 3/2 resonance at the energy 428 MeV [3, 4] due to residual third harmonic of the cyclotron magnetic field. We were able to compensate this component with available harmonic coils 12 and 13 [3, 4]; and then compensate remaining slow drifts in extracted beam split ratio by active feedback that adjusts radial beam position by regulating first harmonic component of the harmonic coil 12 [5, 6]. Since 2013 BL2C4 has been the only high current beamline facing intensity instability and its source is not fully understood yet. We could only see that with a beam vertical mis-steering at injection it generates vertical size/position fluctuation and thus affects the fraction of the circulating beam being extracted with partially dipped 2C wide foil.

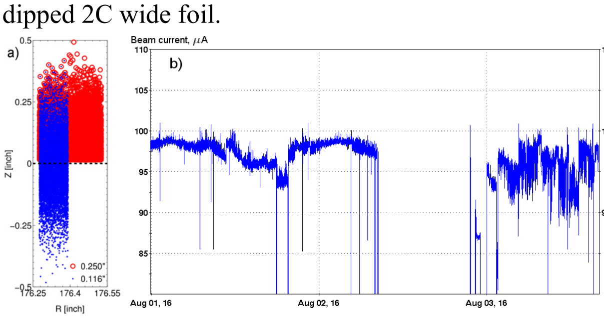

Figure 4: a) Particle distribution on fully (blue) and partially (red) dipped foils with the same split ratio 0.4.
b) BL2C4 extracted current: left part - extraction with fully dipped foil; right part - with partially dipped foil.

An ad hoc fix of this problem was suggested with employing an extraction by a narrower foil fully dipped through the beam (see Fig. 4a). In this configuration a small vertical oscillation has negligible effect on the split ratio in question. Figure 4b depicts BL2C4 intensity instability throughout the extraction foil change: from a 0.116” wide foil fully dipped in the beam to a 0.250” wide foil partially immersed in the beam. Fast instability rise is clearly visible. As a side effect, a fully dipped foil generates a vertically symmetric beam compared to a one side truncated beam produced by partial dipping. That allows better control of beam centering at the isotope production target. Also, a narrow foil generates smaller horizontal beam size that leads to lower collimator temperature at the target entrance. Beam studies aiming at identifying the source of this instability will continue.

SR-82 PRODUCTION

Since about 2 decades TRIUMF has been producing Sr-82 isotopes for medical imaging at its Solid Target Facility (STF). In 2007 the STF was upgraded to 80 μA and in 2013 with beefed-up shielding it reached its maximum capacity at 100 μA of protons. Production target is surrounded by cooling water. With 10 kW of beam power we observe water dissociation with release of O-15 isotopes into nuclear ventilation. The mitigation measure is to run radioactive exhaust through a delay line to allow substantial decay of radioactive species before releasing it to the atmosphere.

TRIUMF cyclotron is equipped with 56 pairs of co-axial trim coils, covering the entire energy range of the machine. With a proper combination of 3 of these coils, one can always create a localized field bump in B_z with tails zeroed off at both inner and outer radii, while remaining the B_r component unchanged. This allows to make a phase slip to the beam over certain radial range while minimizing any unwanted perturbations outside. We chose to create such a field bump after ~190" i.e. after BL2C4 100 MeV extraction radius, with an amplitude of ~1.0 G. This amplitude was large enough to make a 180 degree phase slip to the beam, so that the whole beam of ~50 degree phase band turns round and gets decelerated back (see Fig. 5) and passes through the 2C4 extraction foil again. This scheme is useful for the BL2C single user operation mode with a <0.4" foil taking large fraction (~100μA) of the circulating beam while still leaving small amount running to high energy where it was dumped on the diagnostic probe at ~500 MeV. The new configuration helps reducing cyclotron activation. Figure 6 shows a signal from BL2C4 capacitive probe for the beam injected at ~10% duty factor. Small decelerated fraction of the beam pulse (in red) is delayed at extraction.

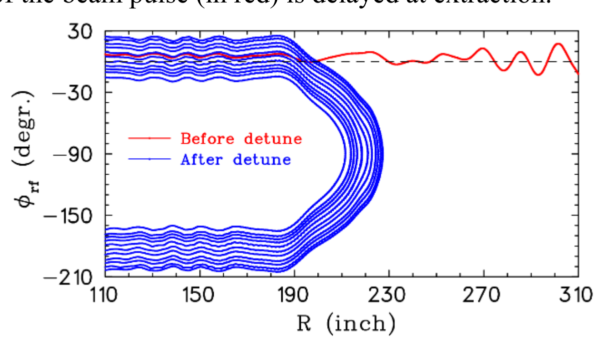

Figure 5: Phase space diagram of beam deceleration.

ISBN 978-3-95450-167-0

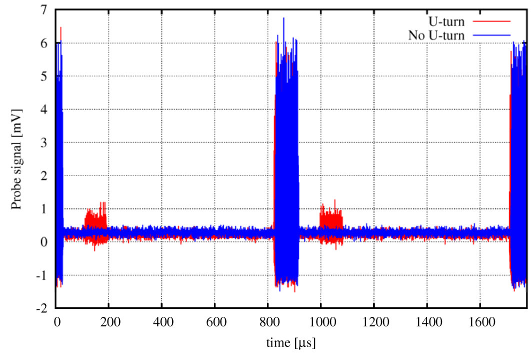

Figure 6: BL2C4 extracted beam: blue – no deceleration, red – with deceleration.

TRIUMF has further plans of Sr-82 isotope production increase. It can be achieved with elongated Rb target. Simulations suggest that with a doubled target thickness (63 mm) one can yield 50% more Sr-82. The validation test will take place this fall. In the longer term we want to redesign the whole beam transport to the STF (~5 m) and introduce beam rastering capability that will allow target temperature reduction and higher yields.

EXTRACTION FOILS

Over the last decade there was an effort to improve extraction foils [7]. Since last modification in 2011 we have collected an impressive statistic on foil life time. There was not a single foil failure in the beam. The highest charge accumulated over 4 years on 100 MeV extraction foil is 560 mA-hours, and on 480 MeV foil, 420 mA-hours. Also, earlier observed loose contamination from Be-7 released from the foils is no longer an issue. All these achievements can be attributed mostly to the choice of highly-oriented pyrolytic graphite foil material and tantalum material of the foil holder.

BEAM LOSSES

Recent achievements in ramping of machine intensity to 300 µA motivated intensive effort aiming at beam loss reduction. There are three mechanisms leading to beam losses: 1) vertical effective emittance growth; 2) electromagnetic (Lorentz) stripping; 3) stripping on residual gas.

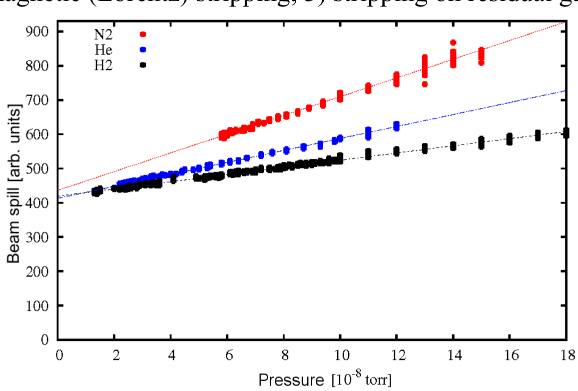

Figure 7: Beam spill vs partial pressure of some gases

The most significant high energy loss reduction from 5% to 3% was achieved by reducing extraction energy from 500 MeV to 480 MeV due to a drop in Lorentz stripping [8]. Then, after the cryo-pumping system upgrade the pressure in the tank dropped from $8\cdot10^{-8}$ to $2\cdot10^{-8}$ Torr. We evaluated the impact of partial pressure of basic gases on the beam losses and concluded that this factor adds negligible contribution to the effect and no more vacuum improvements are warranted. Figure 7 shows beam loss dependence on residual pressure of different gases. Studies of beam vertical halo will continue.

RASTERING

With beam rastering, it's expected to reduce the radial temperature gradient across the ISAC target and thus allow higher beam intensities to be accepted for the same maximum temperature. The raster magnets are located midway between the E-W splitter dipole and the final dipole. From there to the target there is a drift, a doublet quadrupole, and a drift. Theoretically, it's best to make the section from raster magnets to target point-to-parallel as needed for steering, and at the same time parallel-to-point, as needed for focusing. But in practice, it is more important to know the beam size, position and angle at the target. Given that we do not have diagnostics on board the target but upstream of the target (~1.1 m), it's critical that we have a tune where the spot size at the target better reflects the beam sampled at the upstream monitor. We developed such a tune by having polarities of the last doublet reversed from the previous. This tune is plotted in Fig. 8 (solid line), as opposed to the previous tune (dashed line) where the beam envelope gets sharply focused on the target in the vertical plane. This tune has been demonstrated to be working properly in terms of rastering with a beam spot of ~4mm, though it has little flexibility to change the spot size. Also, with a new Beam Position Monitor added into the final section of the beamline, the beam centering corrections in both position and angle is considerably facilitated.

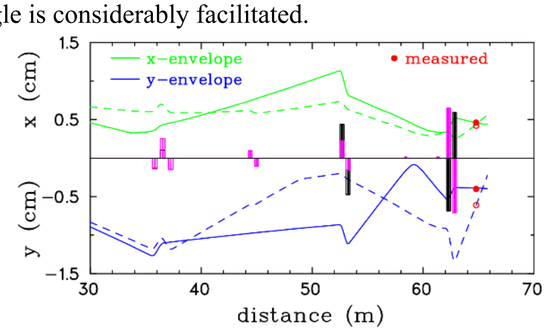

Figure 8: BL2A beam envelope: dashed lines – old tune; solid lines – new tune.

REFERENCES

[1] J.A. Maloney et al., "Electrostatic Potential Map Modelling with COSY Infinity", Nucl. Instrum. Meth. B376 (2016), pp. 171-174.

[2] G. Dutto et al., "Simultaneous Extraction of Two Stable Beams for ISAC", Proc. of EPAC'08, Genoa, Italy, 2008, pp. 3503-3505.

ISBN 978-3-95450-167-0

[3] Y.-N. Rao, R. Baartman, G. Dutto, L. Root, “Studies of the ν_r = 3/2 Resonance in the TRIUMF Cyclotron”, Proc. of *PAC’09*, Vancouver, Canada, May 2009, pp. 3940-3941.
[4] T. Planche, Y.-N. Rao, R. Baartman, “Correction of ν_r=3/2 Resonance in TRIUMF Cyclotron”, Proc. of *IPAC’12*, New Orleans, USA, 20-25 May 2012, pp. 415-417.
[5] T. Planche, Y.-N. Rao, R. Baartman, “Improvement of the Current Stability from the TRIUMF Cyclotron”, Proc. of *CYC’13*, Vancouver, Canada, Sep. 2013, pp. 414-416.
[6] J.J. Pon et al., “Stabilizing the Beam Current Split Ratio in TRIUMF’s 500 MeV Cyclotron with High-Level, Closed-Loop Feedback Software”, Proc. of *ICALEPCS’13*, San Francisco, USA, Oct. 2013, pp. 1370-1372.
[7] Y.-N. Rao et al., “TRIUMF Extraction Foil Developments and Contamination Reduction”, Proc. of *CYC’13*, Vancouver, Canada, Sep. 2013, pp. 269-271.
[8] I. Bylinskii et al., “TRIUMF Cyclotron Beam Quality Improvement”, Proc. of *PAC’11*, New York, USA, October 2011, pp. 1921-1923.

ISBN 978-3-95450-167-0

UPDATED PHYSICS DESIGN OF THE DAEδALUS AND IsoDAR COUPLED CYCLOTRONS FOR HIGH INTENSITY H_2^+ BEAM PRODUCTION*

D. Winklehner†, Massachusetts Institute of Technology, Cambridge, USA
on behalf of the DAEδALUS Collaboration.

Abstract

The Decay-At-rest Experiment for δ_{CP} violation At a Laboratory for Underground Science (DAEδALUS) and the Isotope Decay-At-Rest experiment (IsoDAR) are proposed experiments to search for CP violation in the neutrino sector, and "sterile" neutrinos, respectively. In order to be decisive within 5 years, the neutrino flux and, consequently, the driver beam current (produced by chained cyclotrons) must be high. H_2^+ was chosen as primary beam ion in order to reduce the electrical current and thus space charge. This has the added advantage of allowing for stripping extraction at the exit of the DAEδALUS Superconducting Ring Cyclotron (DSRC). The primary beam current is higher than current cyclotrons have demonstrated which has led to a substantial R&D effort of our collaboration in the last years. We present the results of this research, including tests of prototypes and highly realistic beam simulations, which led to the latest physics-based design. The presented results suggest that it is feasible, albeit challenging, to accelerate 5 mA of H_2^+ to 60 MeV/amu in a compact cyclotron and boost it to 800 MeV/amu in the DSRC with clean extraction in both cases.

INTRODUCTION

Physics Motivation

The standard model of particle physics includes three so-called "flavors" of neutrinos: ν_e, ν_μ, and ν_τ, and their respective anti-particles. These particles can change flavor (neutrino oscillations), a process that can be described using a mixing matrix. This necessarily means that neutrinos must have a small mass [1]. In addition, some experiments aimed at measuring these oscillations in more detail have shown anomalies that led to the postulation of so-called "sterile" neutrinos which would take part in the oscillation, but, contrary to the three known flavors, do not interact through the weak force [2]. Another important question is whether the three neutrino model can give rise to a CP-violating phase δ_{CP} [3], which might explain the matter-antimatter asymmetry in the universe today. DAEδALUS [4, 5] and IsoDAR [6] are proposed experiments to search for CP violation in the neutrino sector, and sterile neutrinos, respectively. In the following, we will give a brief overview of the facilities and identify and discuss the most critical aspects.

* Work supported by NSF under award #1505858.
† winklehn@mit.edu

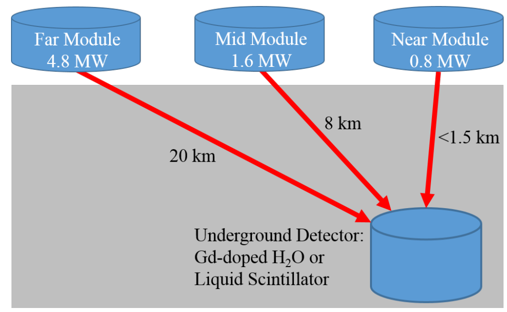

Figure 1: Schematic of the layout of DAEδALUS accelerator modules. The powers at the respective modules, are average values based on a 20% duty cycle.

Facilities Overview

In the DAEδALUS concept (described in detail in [4, 5]), three accelerator modules are placed at distances 1.5, 8, and 20 km from a large detector (see Figure 1). As the neutrino oscillation probability depends on L/E, the ratio of neutrino energy to the distance traveled [1], this scheme can work as follows: The near module constrains the flux, the mid module constrains the rise of the probability wave and the far module measures the oscillation maximum. Each of these modules consist of one or more chains of cyclotrons, as depicted in Figure 2. The neutrino distribution from the production target is more or less isotropic, which means the number of produced neutrinos needs to increase with distance if one wants to keep statistics up. Hence the higher power of the far site which will be reached by using several modules. In this way, DAEδALUS can be used to measure a δ_{CP} dependent maximum of the oscillation curve. Figure 2 shows schematically the main parts of DAEδALUS:

1. Ion source
2. Low Energy Beam Transport (LEBT)
3. DAEδALUS Injector Cyclotron (DIC)
4. Medium Energy Beam Transport (MEBT)
5. DAEδALUS Superconducting Ring Cyclotron (DSRC)
6. High Energy Beam Transport (HEBT)
7. Neutrino production target

As DAEδALUS is a big project, it makes sense to look for a staged approach and physics that can be done with only part of it. In this case using only the DIC and replacing the DSRC with a different production target comes to mind. This is IsoDAR, a search for sterile neutrinos. Here the primary H_2^+ beam at 60 MeV/amu is used to produce $\bar{\nu}_e$ through isotope-decay-at-rest. In both experiments, the primary ion beam

ISBN 978-3-95450-167-0

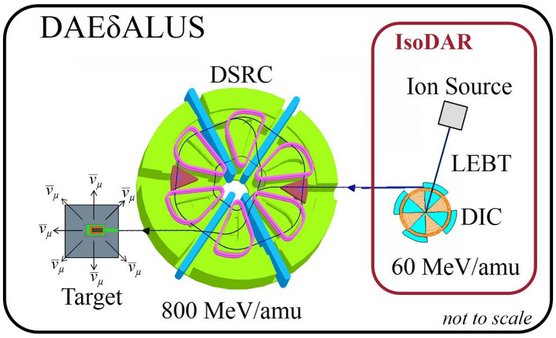

Figure 2: Cartoon picture of one single DAEδALUS module with the injector part that can be used for IsoDAR highlighted on the right.

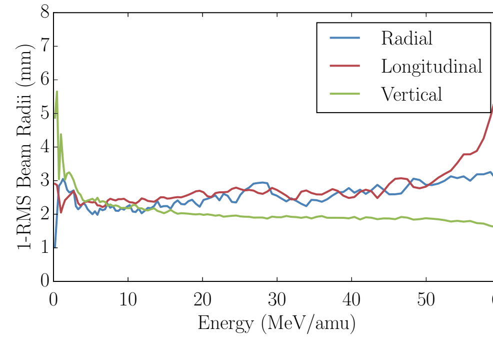

Figure 3: 1-RMS beam radii for a matched beam in IsoDAR, starting at 193 keV/amu. Collimators are placed in turn 10 (≈3 MeV/amu) which clean up beam halo, and only reduce the beam current from 6.5 mA to 5.0 mA. Data from [11].

current needs to be very high in order for the measurements to be conclusive within a certain time span. The nominal current is 5 mA. IsoDAR will operate with a 90% duty cycle, DAEδALUS with 20%. Clearly the target design is a major challenge for beam powers of 600 kW and 1.6 MW, respectively. However, for the sake of brevity and to keep with the topic of the conference, we will abstain from a discussion of the targets and instead point to the references given throughout this text. Similarly, we will not consider the MEBT and HEBT here as they are not considered high-risk. Instead, in the following section, we will discuss the ion source, LEBT, DIC and DSRC in more detail (henceforth called the "driver").

MOTIVATION OF DESIGN PARAMETERS

As the isodar front-end and cyclotron are, for all intents and purposes, identical to the DAEδALUS front-end and DIC, we will discuss IsoDAR first and consider only the DSRC in the subsequent DAEδALUS section.

IsoDAR

Recently, the DAEδALUS Collaboration published a Conceptual Design Report (CDR) for the technical aspects of the IsoDAR project [7], in which the project is discussed in much detail. The important parameters of the front end and cyclotron are summarized in Table 1. From beginning to end, the driver consists of 1.) an ion source, 2.) a LEBT with buncher, and 3.) a compact isochronous cyclotron. H_2^+ was chosen as primary beam ion because of the reduction in electrical beam current vs. particle current (after stripping),

Table 1: Important parameters for the IsoDAR driver.

Parameter	**Value**	**Parameter**	**Value**
Ion	H_2^+	Ion Source	Multicusp
$I_{\text{source, nom.}}$	35 mA DC	Injection	Spiral Infl.
Cycl. Freq.	42.1 MHz	Harmonic	6
Cycl. Type	Compact	E_{max}	60 MeV/amu
Extraction	Septum	$I_{\text{cycl., extr.}}$	5 mA avg.

which reduces space charge effects. At the same time the magnetic rigidity of the beam increases, which has to be taken into account during injection. The main challenges were identified as

1. Production of necessary initial current in the ion source.
2. Beam injection into the cyclotron through a spiral inflector of appropriate size to accommodate high rigidity.
3. Focusing and matching in the first 10 turns.
4. Ultra-low-loss extraction from the cyclotron.

About items 1. and 2. In the summers of 2013 and 2014 we tested H_2^+ ion production, LEBT and cyclotron injection in collaboration with Best Cyclotron Systems, Inc. (BCS) . The results were published in [8] and can be summarized as such: An off-resonance ion source like the one we tested (Versatile Ion Source - VIS) can provide the necessary H_2^+ ion flux, but only marginally and through pushing the source to its limits. Consequently, we are now investigating alternatives to the VIS and conventional LEBT system. We are pursuing two avenues:

- We are currently building a new multicusp ion source at MIT called MIST-1 [9], which is optimized for H_2^+.
- We are investigating the use of an RFQ to directly inject a highly bunched beam into the spiral inflector [10]. Funding for a first RFQ injector was obtained and the first phase (design study) will commence this fall.

Furthermore, during the BCS tests, we could show that a large (1.6 cm gap) spiral inflector could be built and operated at up to ±12 kV. 6 mA of a DC H_2^+ beam were injected through the spiral inflector and results compared well with simulations.

About items 3. and 4. In a previous publication, it was shown through particle-in-cell (PIC) simulations using OPAL [12] that, starting at 1.5 MeV/amu, a stationary distribution in the horizontal plane could be achieved through vortex-motion [13]. Through collimation at low energy and tuning of the RF phase, it was possible to keep the predicted

ISBN 978-3-95450-167-0

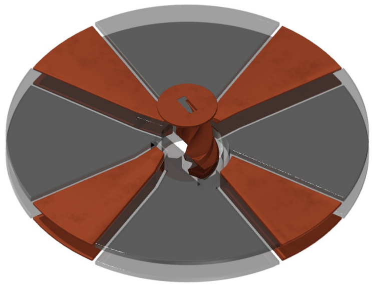

Figure 4: Preliminary CAD model of the IsoDAR central region.

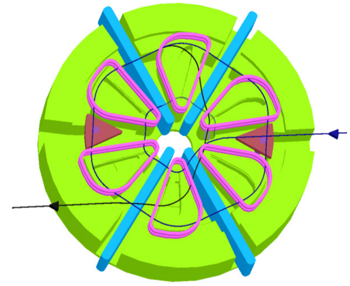

Figure 5: Preliminary CAD model of the DSRC with injection and extraction trajectories.

beam loss on the septum below 200 W. In the past few months, these simulations were extended to lower energies and matched distributions were found down to energies of 193 keV/amu. An example is shown in Figure 3. Note that the steep increase in longitudinal direction at the end stems from a resonance, which is expected to be suppressed in future design iterations of the magnetic field. The vertical beam size is fairly large in the first few four turns and then decreases rapidly. We are currently in process of designing a central region that can accommodate this large beam. The present state of the design is depicted in Figure 4.

DAEδALUS

The DAEδALUS design was reviewed in detail in [4] and the most important parameters of the DSRC are listed in Table 2. The superconducting ring cyclotron will take the 60 MeV/amu beam from the IsoDAR-like front-end and boost it to 800 MeV/amu. Detailed simulations were performed and the results published in [13]. These simulations showed that a stationary distribution forms in the DSRC which can then be extracted very cleanly through stripping extraction. A model of the current design of the DSRC can be seen in Figure 5.

CONCLUSION

DAEδALUS and IsoDAR are ambitious experiments aiming at discovering CP violation in the neutrino sector and the existence of sterile neutrinos, respectively. The requirement of 5 mA of H_2^+ has led to a substantial R&D effort on which was reported here. We have identified the injection of the necessary current into the compact DIC (almost identical to the IsoDAR main cyclotron) as the main challenge and have shown preliminary experimental studies and simulations that will soon lead into a full start-to-end simulation treatment of the system. The experimental high intensity injection studies showed that a spiral inflector with the required large size for the higher magnetic rigidity of the H_2^+ beam can be built and operated. Simulations using OPAL with the new spiral inflector option compared well to these studies and systematic injection simulations using beam currents up to the required injection currents are on the way. Parallel to the conventional LEBT front end, we have just begun a full investigation of using an RFQ for direct axial injection of a bunched beam into the spiral inflector.

Table 2: Important parameters for the DAEδALUS driver. Note that the DIC parameters are identical to the IsoDAR parameters listed in Table 1.

Parameter	Value	Parameter	Value
Ion	H_2^+	Injection	Radial
Cycl. Freq.	42.1 MHz	Harmonic	6
Cycl. Type	Ring	E_{max}	800 MeV/amu
Extraction	Stripping	$I_{cycl., extr.}$	5 mA avg.

REFERENCES

[1] KA Olive, Particle Data Group, et al. "Review of particle physics." In: *Chinese Physics C* 38.9 (2014), p. 090001.

[2] GH Collin et al. "Sterile neutrino fits to short baseline data." In: *Nuclear Physics B* 908 (2016), pp. 354–365.

[3] O Mena and S Parke. "Untangling C P violation and the mass hierarchy in long baseline experiments." In: *Physical Review D* 70.9 (2004), p. 093011.

[4] M Abs et al. "Multimegawatt DAEδALUS Cyclotrons for Neutrino Physics." In: *arXiv:1207.4895* (2012).

[5] C Aberle et al. "Whitepaper on the DAEdALUS program." In: *arXiv preprint arXiv:1307.2949* (2013).

[6] A. Bungau et al. "Proposal for an Electron Antineutrino Disappearance Search Using High-Rate ^{8}Li Production and Decay." In: *Phys. Rev. Lett.* 109 (14 Oct. 2012), p. 141802.

[7] M Abs et al. "IsoDAR@KamLAND: A Conceptual Design Report for the Technical Facility." In: *arXiv:1511.05130* (2015).

[8] D Winklehner et al. "The IsoDAR High Intensity H_2^+ Transport and Injection Tests." In: *Journal of Instrumentation* 10.10 (2015), T10003.

[9] Spencer Axani et al. "A High Intensity H_2^+ Multicusp Ion Source for an Isotope Decay-at-Rest Experiment, IsoDAR." In: *Review of Scientific Instruments* (2015). Submitted.

[10] D Winklehner et al. "An RFQ direct injection scheme for the IsoDAR high intensity H_2^+ cyclotron." In: *6th International Particle Accelerator Conference (IPAC2015)*. 2015.

[11] J Jonnerby. MA thesis. Switzerland: ETH Zürich, 2016.

[12] Andreas Adelmann et al. *The OPAL (Object Oriented Parallel Accelerator Library) Framework*. Tech. rep. PSI-PR-08-02. Paul Scherrer Institut, (2008-2015).

[13] JJ Yang et al. "Beam dynamics simulation for the high intensity DAEδALUS cyclotrons." In: *NIMA* 704 (2013).

ISBN 978-3-95450-167-0

A NOVEL USE OF FFAGS IN ERLS - IN COLLIDERS: ERHIC, LHEC AND A PROTOTYPE AT CORNELL UNIVERSITY*

Dejan Trbojevic†, Ilan Ben-Zvi, J. Scott Berg, Michael Blaskiewicz, Stephen Brooks, Kevin A. Brown, Wolfram Fischer, Yue Hao, George Mahler, Wuzheng Meng‡, Francois Meot, Michiko Minty, Steve Peggs, Vadim Ptitsyn, Thomas Roser, Peter Thieberger, Nicholaos Tsoupas, Joseph Tuozzolo, Holger Witte, Vladimir N. Litvinenko, Joseph Tuozzolo, Robert J Michnoff, Brookhaven National Laboratory, Upton, New York, USA
Ivan Vasilyevich Bazarov, James Arthur Crittenden, John Dobbins, Bruce Dunham‡, Ralf Georg Eichhorn‡, Georg H. Hoffstaetter, Yulin Li, William Lou, Christopher Mayes, J. Ritchie Patterson, Karl William Smolenski, Richard Talman, Adam Christopher Bartnik, Fumio Furata, John Barley, Daniel Sabol, Rich Gallagher, David Sagan, Cornell University, Ithaca, New York, USA
Todd Satogata, Alex Bogacz, David Douglas, Thomas Jefferson National Accelerator Facility, Newport, Virginia, USA

Abstract

We propose a novel use of Non Scaling Fixed Field Alternating Gradient beam line (NS-FFAG) to replace multiple beam lines in existing Energy Recovery Linacs (ERLs) (4-pass at Novosibirsk, ERL of CEBAF, ERL at KEK, etc.) with NS-FFAG beam lines connected with spreaders and combiners to the linac. We present two designs for the Electron Ion Colliders one at CERN-LHeC and one at Brookhaven National Laboratory-eRHIC to be placed in the tunnel of the existing Relativistic Heavy Ion Collider (RHIC) called eRHIC. The proof of principle electron accelerator with the NS-FFAG arcs is to be built at Cornell University Wilson Hall where there are already available injector, superconducting linac accelerator and the dump. There are very new developments in the NS-FFAG design never accomplished before: arc-to straight adiabatic matching with merged multiple orbits into one, permanent magnet design for the arc and straights with ability of four times in energy, etc.

INTRODUCTION

There are many ways for accelerating particles in the non-relativistic region: the neutron generators or for Accelerator Driven Subcritical System (ADS) and they could be the superconducting linacs, fast cycling synchrotrons, superconducting cyclotrons, FFAG's etc. The isochronous circular accelerator, where the beam arrives for all energies at the same time to the RF and operates in the CW mode is very advantageous. A preferred solution is a straight superconducting linac but it requires large power, long length and it is very expensive. Cyclotrons might be the preferred solution. This presentation shows examples of savings in the linac lengths in relativistic electrons acceleration for the LHeC, eRHIC, and an ERL at Cornell University (eRHIC prototype) with isochronous condition. It is not suggested that this solution could be applied for non-relativistic particles but it provides an input for new possibilities in this case. The energy recovery in all three examples is possible as the electron time of flight during acceleration is properly adjusted on the top of the RF sinusoidal wave, while during the deceleration or energy recovery it is shifted close to the minimum of the RF wave. There are multiple advantages in using ERL's in the electron ion colliders: electrons are colliding only once with hadrons, due to energy recovery the enormous power of the electron beam is brought down to the dump with initial very low energy and with the overall linac efficiency very close to 100%.

* Work performed under Contract Number DE-AC02-98CH10886 under the auspices of the US Department of Energy.
† dejan@bnl.gov
‡ On leave

Electron Energy Colliders LHeC and eRHIC

The electron ion collider LHeC goal is to study of deep inelastic scattering (DIS) into unknown areas of physics and kinematics. "The physics program also includes electron-deuteron and electron-ion scattering in a (Q^2, 1/x) range extended by four orders of magnitude as compared to previous lepton-nucleus DIS experiments for novel investigations of neutron's and nuclear structure, the initial conditions of Quark-Gluon Plasma formation and further quantum chromo-dynamic phenomena"[1].

LHeC:

The LHeC collider will collide 60 GeV maximum energy electrons with 7 TeV protons or heavy ions. The LHeC collider main parameters are shown in Table 1.

Table 1: Beam Parameters LHeC

	Protons	Electrons
Energy (GeV)	7000	60
γ	7460	11740
$\varepsilon_{x,y}$ (nm)	0.4	0.43
Beam	>430 mA	6.4 mA

ISBN 978-3-95450-167-0

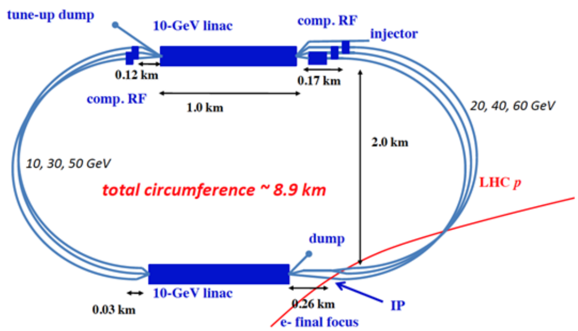

Figure 1: LHeC ERL layout including dimensions.

The LHeC ERL design layout is shown in Fig. 1. The radius of the curvature, a parameter important for the synchrotron oscillations energy loss, is R=1000 m. The limit on the total amount of synchrotron radiation loss is set to be 15 MW.

LHeC NS-FFAG ERL Proposal

The electron beam from the 17 MeV injector is transferred to the two 5.435 superconducting linacs connected with a five spreaders lines and one separate line to the collision point with the protons/ions marked as IP in Fig. 2. After passing through the two linacs the 10.87 GeV electron beam arrives to the low energy NS-FFAG arc continues from the adiabatic arc-to-straight section transition reaching to the opposite NS-FFAG arc through the same kind of adiabatic transition. The lower energy NS-FFAG arcs, arc-to-straight, straight section, straight-to-arc and opposite arc transfers three energies: 10.906, 21.829 and 32.735 GeV. The higher NS-FFAG line transfers two energies 43.644 and 54.547 GeV.

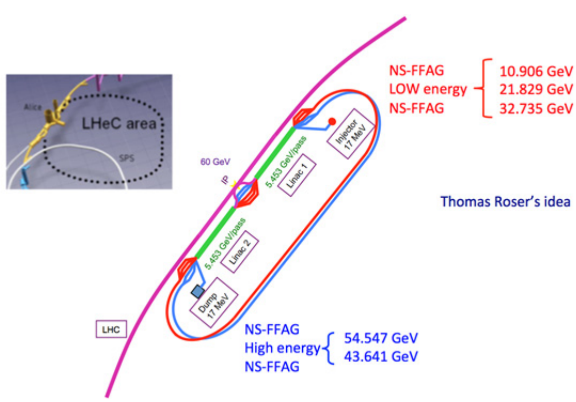

Figure 2: NS-FFAG proposal for the LHeC.

There are few significant advantages of the NS-FFAG proposal, shown in Fig. 2:

- A smaller value of the 54.547 GeV highest electron beam energy going to through the arc, not 60 GeV as in the official design reduces significantly the synchrotron radiation loss, as the dependence on energy is γ^4. Enhancement of the luminosity is equal to 1.34 as the electron current could become 8.87 mA instead of 6.6 mA to correspond to total synchrotron radiation power loss of 15 MW.
- The three separate beam lines shown in Fig. 1 are replaced with the two NS-FFAG lines.
- Not only that the number of beam lines is reduced but the size of the linacs as well: from the previous 2x10 GeV linacs to 2x5.455 GeV or 54.547% of the previous 10 GeV. This would represent a significant saving of total linac size.

The betatron functions for the central momentum energy basic NS-FFAG arcs cell of the higher energy range are shown in Fig. 3, while the orbit offsets in the same arcs cell are shown in Fig. 4. The combined function focusing and defocusing magnets are shown in both figures with detail characteristics: gradients and bending angles. The synchrotron radiation losses for the whole energy range in the NS-FFAG ERL design, with 6.6 mA (electron current of the LHeC design) and with 8.87 mA, are shown in Table 2.

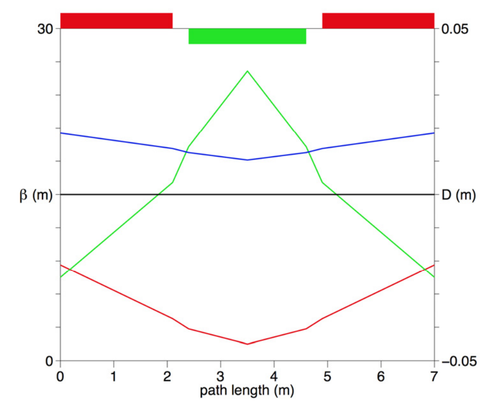

Figure 3: Betatron functions for the central energy of the higher NS-FFAG ERL design, with the combined function magnets.

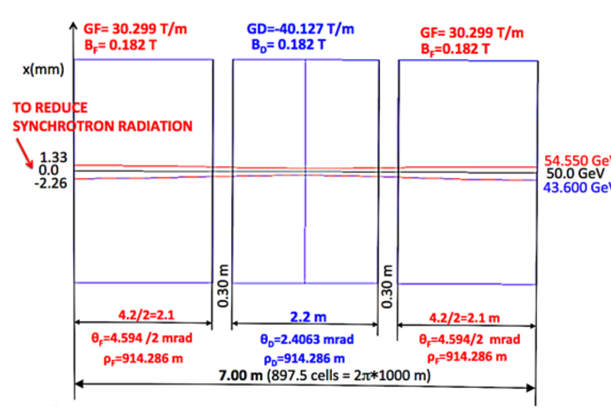

Figure 4: Orbit offsets in the higher energy range LHeC NS-FFAG ERL proposal with magnet properties: gradients and bending angles.

ISBN 978-3-95450-167-0

Table 2: Synchrotron Radiation Losses in LHeC NS-FFAG Design (electron currents of 6.6 mA and 8.87 mA)

Energy (GeV)	**8.87 mA**	**6.6 mA**
55.547	7.578	5.638
43.644	4.208	3.131
32.735	1.390	1.034
21.829	1.288	0.959
10.923	0.536	0.399
Total loss	15.000	11.161

eRHIC:

The high energy, high luminosity, polarized EIC eRHIC should: determine quark and gluon contributions to the proton spin at last, should determine what is the spatial distribution of quarks and gluons in nucleons /nuclei and understand in detail the transition to the non-linear regime of strong gluon fields and the physics of saturation in the electron ion collisions [2]. This should be a microscope for gluons and will the study the high-density gluon fields. The basic parameters of the eRHIC collider are shown in Table 3, while the layout is shown in Fig. 5. There are two NS-FFAG beam lines connected to the linac with combiners and spreaders: former at the entrance and latter at the linac exit, accordingly.

Table 3: eRHIC Beam Parameters

	e	p	$^2He^3$	$^{79}Au^{197}$
Energy, GeV/u	15.9	250	167	100
CM energy		126	103	80
Bunch f, (MHz)	9.4	9.4	9.4	9.4
Intensity, 10^{11}	0.07	3.0	3.0	3.0
B. Charge (nC)	1.1	48	32	19.6
Beam (mA)	10	415	275	165
$\varepsilon_{x,yN}$ (µm) hadron		0.2	0.2	0.2
$\varepsilon_{x,yN}$ (µm) e	23		35	58
β^* (cm)	5	5	5	5
Beam-beam		0.004	0.003	0.008
rms bunch (cm)	0.4	5	5	5
Polarization	80	70	70	none
Luminosity, 10^{33}		4.1	2.8	1.7

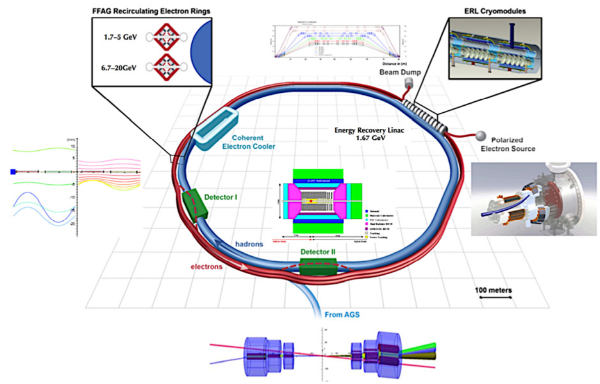

Figure 5: eRHIC layout with major components.

Two NS-FFAG beam lines are designed with the displaced focusing and defocusing quadrupoles as shown in Fig. 6 for the higher NS-FFAG beam line.

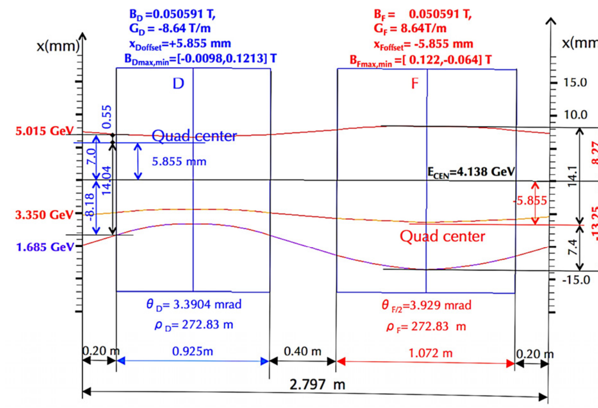

Figure 6: Orbit offsets in the basic cell for the NS-FFAG design for the larger energy range 6.68-20 GeV.

The two combined function magnets of the lower energy ring (energy range 1.6-5 GeV) are made of ±5.3 mm displaced quadrupoles in opposite radial direction, with equal but opposite sign gradients of ±8.6 T/m, with maximum orbit offsets of ±10.8 mm from the central momentum. The NS-FFAG basic cell of the larger energy range (6.68-20 GeV) is shown in Fig. 6. The values of the gradients are shown at the upper side of the figure: $G_{F,D}$ = ±8.5 T/m with the same orbit offsets from the central momentum of ±5.855 mm. One of the novelties in the proposed NS-FFAG design is the adiabatic matching from the arc-to-straight section as shown in Fig. 7.

ISBN 978-3-95450-167-0

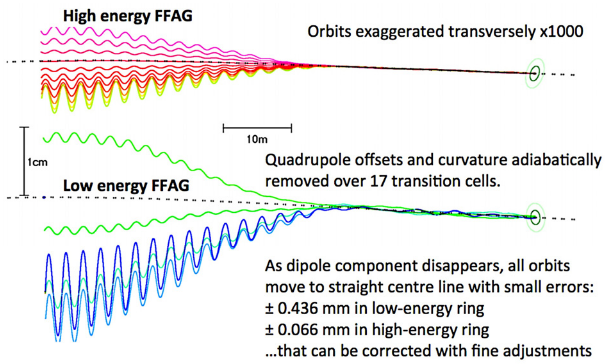

Figure 7: New property of the NS-FFAG lattice: Adiabatic removal of the quadrupole offsets and matching to the straight section.

As the arc-to-straight matching is resolved the by pass of the NS-FFAG detectors around detectors solution obtained by the same method as shown with 1000 times enlarged orbit offsets in Fig. 8:

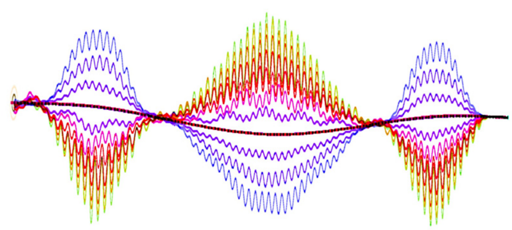

Figure 8: The by-pass of the NS-FFAG around detectors.

The basic cell design as well as selection of the central momentum is always connected towards reduction of the synchrotron radiation losses, as the synchrotron radiation loss power is proportional to $\sim B^2E^2$. It is desirable to have the smallest magnetic field for the highest energies in the focusing element as the magnetic field could be presented as $B_F=B_{Fo}+G_F{*}x_{max}$. This indicates that it is preferable to have longer focusing than the defocusing magnet as the maximum if the magnetic field of the defocusing magnet is at the radially inward part of the orbits as: $B_D=B_{Do}+G_D{*}x_{max}$ as the G_D has a negative sign.

The time of flight dependence in the NS-FFAG is a parabolic function. The maximum value of the time of flight difference at the higher energy NS-FFAG for six arcs is ~7 cm. This needs to be corrected in the spreaders and combiners, as well as ability to adjust the M_{56}. Numerous tracking studies of the electron beam emittance growth effect due to misalignment have been performed. It is very clear that the transverse misalignment and gradient magnet errors induce the emittance growth especially due a large number of cells required in NS-FFAG (as the strong focusing requires small cell length bringing large number of cells). The misalignment errors have to be corrected with the horizontal and vertical dipole correctors as well as with the gradient correctors.

The eRHIC NS-FFAG magnets will use permanent magnet material. There was previous experience with permanent magnets used for the anti-proton storage ring placed in the Main Injector at Fermi National Laboratory. They had used passive temperature compensation of the permanent magnet with a material with opposite temperature dependence [3].

NS-FFAG ERL CBETA

As there are no either present ERL's with superconducting RF with larger number of passes or a NS-FFAG ERL combination so far it is very important to test the eRHIC prototype. The Cornell University Physics Department represents an ideal place for such a combination, as there are already available:

- The 6 MeV injector has already been built and commissioned producing world record good quality electron beam.
- The superconducting RF cavities able to produce 60-70 MeV.
- The beam dump for 6 MeV electrons
- Available space in the Wilson interaction Hall.

The layout of the future NS-FFAG beam with a spreader and collider is shown in Fig. 9.

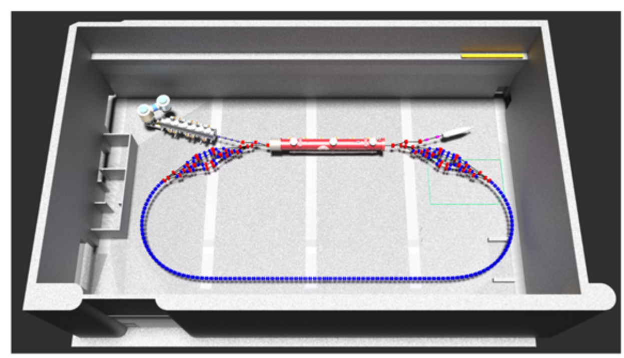

Figure 9: Layout of the eRHIC prototype at Cornell University (CBETA). The upper left corner shows the injector, followed by the Linac (red colour), following with a dump. On both sides of the linac there are a combiner (on the left side) and spreader on the right side. The NS-FFAG arc and straight section is shown by blue color.

During the last three years an excellent collaboration between the BNL and Cornell University have been established and numerous designs and studies have been performed: two type of permanent magnet have not only been designed but the prototypes have been built and measured, the vacuum chamber with the beam position monitors, spreaders-combiner, correction magnets for both types of permanents magnets, layout, Conceptual Design Report-CDR, the White paper report [3], Detail layout, studies of tolerances in misalignment using the correction magnet design, effect of the coherent synchrotron radiation on the beam longitudinal emittance, etc.

The picture of the commissioned CBETA injector is shown in Fig. 10. The simulations are shown in Fig. 11.

ISBN 978-3-95450-167-0

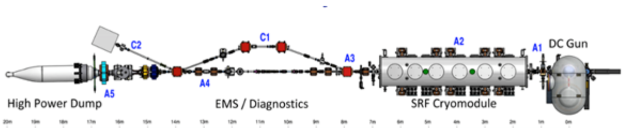

Figure 10: The fully commissioned 6 MeV injector at Cornell University.

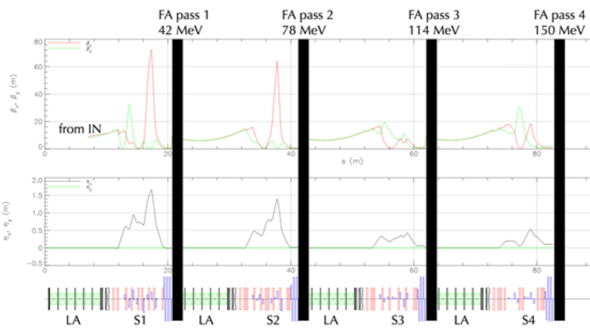

Figure 11: Simulation of the 8 passes trough the CBETA linac, spreader and combiner, NS-FFAG with the energy recovery.

CONCLUSION

A cost effective LHeC (almost twice reduction of the proposed linac size with enhanced luminosity) and eRHIC designs with 1.6 GeV linac and maximum energy of 20 GeV, as well as the 150 MeV ERL with NS-FFAG at Cornell University, are shown. At LHeC a proposal for replacement of the 2x10 GeV linacs and three arcs, with 2x5.453 GeV linacs and two NS-FFAG arcs, respectively. This would be a cost-effective solution with lower synchrotron radiation, hence with 34% larger luminosity for the same limit on the value of 15 MW for the total loss from synchrotron radiation. The ERL with NS-FFAG arcs at Cornell University will be a first ERL of that type. Advantages at Cornell University are already existing the 6 MeV injector, superconducting linac 45-70 MeV making possible to obtain with the NS-FFAG maximum energies of 150-250 or higher MeV. This will be a proof of principle for the new concept: merging FFAG beam lines with the Energy Recovery Principle.

REFERENCES

[1] J L A. Fernandez *et al.*, "A Large Hadron Electron Collider at CERN", `arXiv:1206.291`, `doi:10.1088/0954-3899/39/7/075001`

[2] E.C. Aschenauer *et al.*, "eRHIC Design Study-An Electron Ion Collider at RHIC", `https://arxiv.org/abs/1409.1633`

[3] I. Bazarov *et al.*, "The Cornell-BNL FFAG-ERL Test Accelerator: White Paper", `https://arxiv.org/abs/1504.005`

ACCELERATION OF POLARIZED DEUTERON BEAMS WITH RIBF CYCLOTRONS

N. Sakamoto, N. Fukunishi, M. Kase, K. Suda, RIKEN Nishina Center, Wako, Japan
K. Sekiguchi, Tohoku University, Sendai, Japan

Abstract

We have recently performed experiments with polarized deuteron beams at the Radioactive Isotope Beam Factory (RIBF). Tensor- and vector-polarized deuterons were produced using the RIKEN polarized ion source (PIS) [1], which is an atomic-beam-type ion source equipped with an electron cyclotron resonance (ECR) ionizer, and were accelerated to 190 MeV/u, 250 MeV/u, and 300 MeV/u with a cyclotron cascade. To measure the various spin observables, the spin orientation of the deuteron beams was freely directed by using a Wien filter. The advantage of this method is that since the velocity of the deuteron is low the size of a magnet required for the spin rotation is very compact. On the other hand it is crucial to realize strict single-turn extraction for each cyclotron because the cyclotron magnetic field causes precession of the deuteron spin resulting in a deviation between its spin orientation and the beam propagation direction. This paper describes the acceleration of the polarized deuteron beams by the RIBF accelerators and the method to confirm single-turn extraction.

INTRODUCTION

The mission of the Radioactive Isotope Beam Factory (RIBF) accelerator complex is to expand the availability of rare isotope beams. The RIBF accelerator complex was designed to provide various heavy ions with energies of up to 400 MeV/u. The versatility of the primary beams is one of the key advantages of RIBF. The acceleration mode is chosen according to the species, energies, and required intensities. Until now, 345 MeV/u beams of ^{48}Ca and ^{70}Zn, 320 MeV/u beam of α and 345 MeV/u beams of ^{78}Kr, ^{124}Xe, and ^{238}U, have been produced at RIBF using the RIKEN heavy-ion linac (RILAC) injector [2] in variable-energy mode and the RILAC2 injector [3] in fixed-energy mode, respectively. In addition, light ions d (190, 250, 300 MeV/u), ^{12}C, ^{14}N,^{16}O (250 MeV/u), and ^{18}O (230, 250, 294, 345 MeV/u) have been accelerated using the light-ion mode of the azimuthal varying field (AVF) cyclotron as an injector to the RIKEN ring cyclotron (RRC) and superconducting ring cyclotron (SRC), as shown in Fig. 1. While RIBF can provide intense heavy-ion beams for the production of radioactive isotope beams, light-ion beams are also available for physics experiments requiring high precision. Among them, a polarized deuteron beam with an intermediate energy of 100–300 MeV/u is one of the most powerful probes to study spin-dependent interactions, such as three-body-force of nucleon interactions [4]. Required turn purity was more than 99% for these experiments.

POLARIZED DEUTERON BEAMS

Production of Polarized Deuteron Beams

The RIKEN polarized ion source (PIS) is an atomic-beam-type ion source. It is a copy of one developed at Triangle University Nuclear Laboratory (TUNL) [5], and was modified at the Indiana University Cyclotron Facility (IUCF) [6].

A schematic illustration of RIKEN PIS is shown in Fig. 2. First, D_2 gas produced from heavy water in a water electrolyzer is dissociated and formed into atomic beams in a dis-

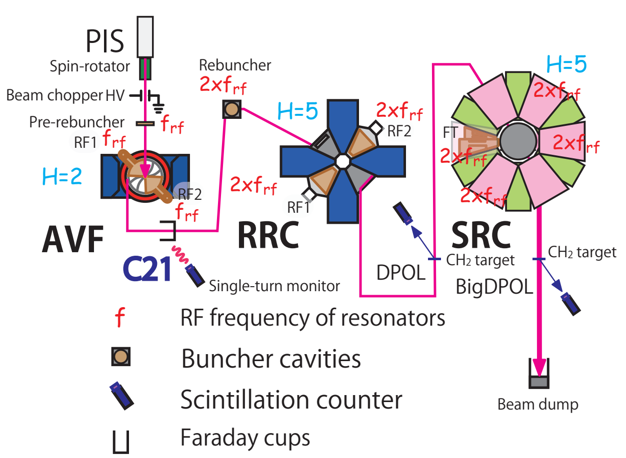

Figure 1: Setup of accelerators and monitors for polarized deuteron acceleration utilizing azimuthally varying field (AVF) cyclotron, RIKEN ring cyclotron (RRC) and superconducting ring cyclotron (SRC).

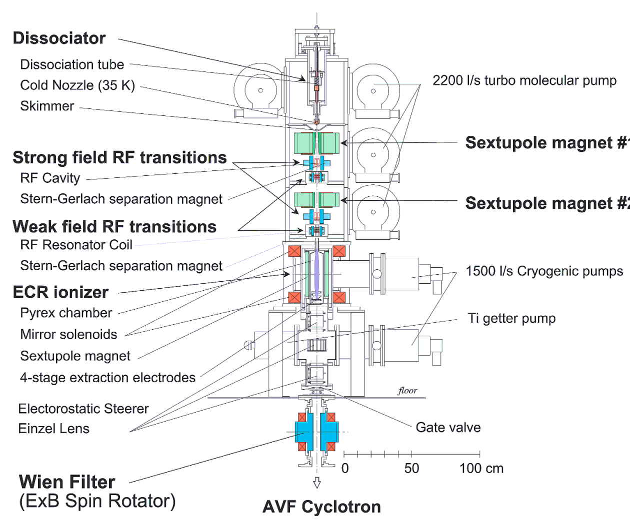

Figure 2: Schematic illustration of RIKEN polarized ion source.

ISBN 978-3-95450-167-0

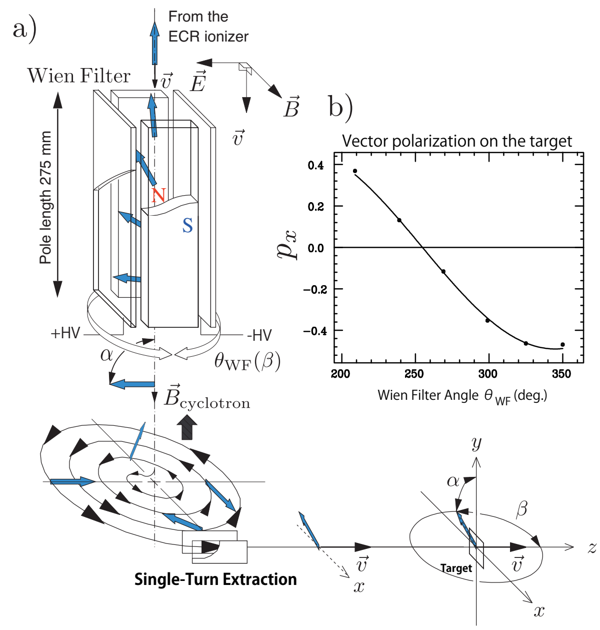

Figure 3: Method of spin-orientation control using a Wien Filter.

sociator. Next, the electron spin of the deuterium atoms is selected by passing the beam through sextupole magnets. The subsequent RF transition apparatus flips the deuteron spins using Stern-Gerlach separation magnets. RIKEN PIS is equipped with a two-stage spin selector so that any deuteron spin state represented by vector and tensor polarizations can be obtained. Spin-selected deuterium atoms are then ionized by the ECR ionizer, and the intensity of the resulting ion beam is < 100 μA. The polarization of the deuteron beam is typically 80% of the theoretical value. The orientation of the polarization of the deuteron beams, which is in the vertical direction after the ionizer, can be controlled using a so-called Wien filter installed downstream of the ECR ionizer before injection to the AVF cyclotron [7] (see Fig. 2). Using a magnetic field, the deuteron spins are tilted without changing their direction of the motion by the $\vec{E}\times\vec{B}$ field, and are rotated azimuthally by rotating the Wien Filter. The tilt and rotation angles were calibrated by observing the vector polarization, as shown in Fig. 3b.

Why Single-turn Extraction?

During acceleration by the cyclotrons, the cyclotron magnetic field causes the deuteron magnetic moment $\vec{\mu}_d = g\vec{S}_d$ (g is g-factor defined as a ratio of magnetic moment to spin) to precess according to the following equation.

$$\frac{d\vec{\mu}_d}{dt} = \gamma\vec{\mu}_d \times \vec{B}_{\text{cyclotron}}$$

Here γ is a Lorentz factor.

Controlling the spin orientation by tilting the spin prior to injection to the cyclotrons was considered unsuitable, since when the deuteron spin was tilted into the horizontal plane, the spin orientation with respect to the beam propagation direction differs turn-by-turn by an angle of $\Delta\beta = 360\times\gamma(g-1)$ degrees (g=0.8477 for a deuteron). If the deuterons have different turn numbers, i.e., if different spin orientations are simultaneously extracted, from the deuteron polarization amplitude will be reduced. To overcome the problem, single-turn extraction and maintaining the same turn number for the extracted beam was required for all these cyclotrons. Therefore, a real-time monitoring system for single-turn extraction that measures the purity of the turn is indispensable.

Table 1: Characteristics of AVF, RRC, and SRC

Cyclotron	AVF	RRC	SRC
K [MeV]	70	540	2600
R_{inj} [m]	inflector	0.89	3.56
R_{ext} [m]	0.712	3.56	5.36
Number of Sectors	4	4	6
Sector Angle [deg.]	50	50	25
RF Resonators	2	2	4+FT
Number of gaps [/res]	2	2	1
Dee Angle [deg.]	85	23.5	-
Harmonic Number	2	5	5
Frequency [MHz]	12–24	18–38.2	18–38.2
V_{acc} [MV/turn]	<0.2	0.4–0.5	1.5–2

Table 2: Accelerated Beam Energy $E_d(\equiv E_{\text{total}}/\text{A})$, RF frequency ($f_{\text{rf}}$), RF voltage ($V_{\text{rf}}$), Turn Separation ($\Delta\bar{R}_{\text{ext}}$) for Acceleration of Deuterons with an Energy of 190, 250, and 300 MeV/u.

Energy [MeV/u]		190	250	300
AVF	E_d [MeV]	4.0	4.9	5.5
H=2	f_{rf} [MHz]	12.3	13.7	14.5
	V_{acc} [kV/turn]	89	92	107
	$\Delta\bar{R}_{\text{ext}}$ [mm]	4.0	3.3	3.4
RRC	E_d [MeV]	70.4	89.9	102.5
H=5	f_{rf} [MHz]	24.6	27.4	29.0
	V_{acc} [kV/turn]	581	655	795
	$\Delta\bar{R}_{\text{ext}}$ [mm]	6.6	5.7	5.9
SRC	E_d [MeV]	187.5	252.3	298.5
H=5	f_{rf} [MHz]	24.6	27.4	29.0
	V_{acc} [kV/turn]	1403	1482	1461
	$\Delta\bar{R}_{\text{ext}}$ [mm]	7.6	5.5	4.3

Acceleration by a Cyclotron Cascade

As mentioned above, the deuterons were accelerated by the cyclotron cascade shown in Fig. 1 utilizing the AVF [7], RRC [8], and SRC [9]. The main specifications of these three cyclotrons are listed in Table 1. Table 2 lists the acceleration parameters for the deuterons with energies of 190, 250, and 300 MeV/u. The AVF cyclotron, which consists of an H-type magnet with four spiral sectors and two frequency-tunable RF resonators, was designed as a light-heavy ion injector to the RRC. The vector- and tensor-polarized deuteron beams provided by the polarized ion source were injected to the

ISBN 978-3-95450-167-0

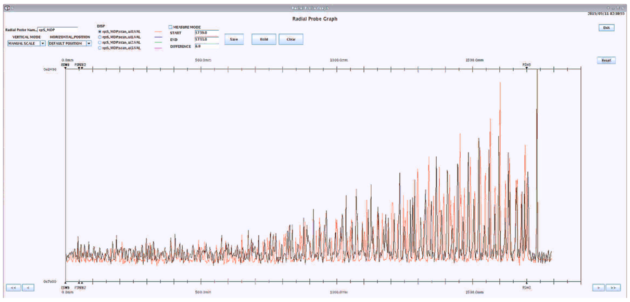

Figure 4: Beam turn patterns of the SRC with (red line) and without (black line) flat-topping, as measured by a radial probe.

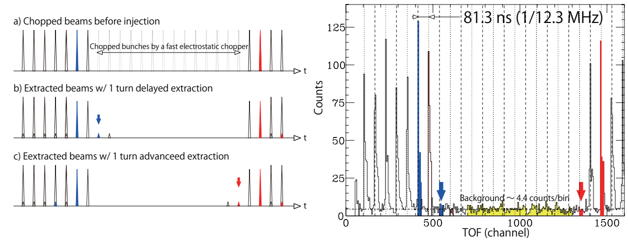

Figure 5: Left: Schematic illustration of the time structures of bunched beams before injection and after extraction. Right: Measured time structure of the extracted beams.

AVF cyclotron after passing through an electrostatic inflector, which only changes the direction of the beams. To obtain a sufficient turn separation at the extraction region, a so-called phase slit was used to reduce the longitudinal emittance at the beam injection. The RRC is a separate-sector cyclotron with four sector magnets and two double-gap RF resonators. Since the injection radius of the SRC was designed to have an identical radius to the extraction radius of the RRC (see Table 1), light-ion beams, which have a fairly large charge-to-mass ratio can be directly injected to the SRC with the same harmonic number. The SRC, which has a K-number of 2600 MeV, is capable of providing 345 MeV/u $^{238}U^{86+}$ ions with an average magnetic field of $\bar{B}$ = 1.5 T. The six-sector magnet, which utilizes superconducting technology [10], produces magnetic fields of up to 3.8 T. A deuteron energy (E_d) of 190 MeV/u requires a magnetic field of $\bar{B}$ = 0.77 T, which is below the lower limit originally intended for the SRC. Owing to the fairly high acceleration voltage produced by the four acceleration resonators (see Table 1), a sufficient turn separation was obtained at the extraction region. Furthermore, flat-top acceleration by imposing the third-harmonic RF during the deceleration phase on fundamental acceleration RF field was crucial for accepting the beams from the RRC without using a re-buncher. Figure 4 shows the beam density distributions in the case of E_d = 190 MeV/u when the third-harmonic resonator was on and off, as measured using a radial probe. The turn pattern indicated by a red line obtained with flat-topping acceleration exhibits sharp peaks and a larger separation between the tail parts of consecutive two turns compared to the black one which was taken by turning off the flat-top resonator.

SINGLE-TURN MONITORS

In the case of single-turn extraction, beam bunches are extracted through an electrostatic-deflection-channel (EDC) after N times circulation. If some portion of the bunch was not extracted at the right time, it slipped into other bunches. Therefore, single-turn extraction can be confirmed by observing the time structure of the extracted beams.

For the AVF, the time structure of beam bunches chopped using a fast electrostatic chopper system [11] was useful for measuring the turn mixing rate [12]. Since the harmonic number of the AVF was even (two), the portion extracted with 1-turn delayed ($N+1$) or 1-turn advanced ($N-1$) extraction appeared at the timing indicated by the arrows in Fig. 5b and Fig. 5c, respectively. An example of the time structure of the beam bunches is shown in the right panel of Fig. 5. The single-turn monitor shown in Fig. 1, which is a plastic scintillation counter, measured the timing of the detected gamma-rays from beam stopper C21 (Faraday Cup) inserted into the transport line. In this case, no turn mixing was found, as indicated by the blue and red arrows in Fig. 5.

For the RRC and the SRC, whose RF resonators operate at the second harmonic of that of the AVF resonators (i.e., $f_{\rm rf}^{\rm RRC,SRC} = 2 \times f_{\rm rf}^{\rm AVF}$) with an odd harmonic number of 5, a degree of turn mixing can be obtained by observing a bunch frequency of the extracted beams. An example of the measured time structure of the beams extracted from the SRC is shown in Fig. 6a. The figure shows the timing of the recoiled protons with a CH_2 target in reference to an RF signal with a frequency of $f^{\rm beam}/2$, as measured using the BigDPOL deuteron polarimeter (see Fig. 1). While the beam frequency ($f^{\rm beam}$) is the same as the RF frequency of the AVF resonators, beams extracted at the wrong timing appear among the timings of $f^{\rm beam}$, as indicated by the red arrows in Fig. 6a. In this case, the observed mixing rate was 0.07%. Figure 6b is a histogram of the time difference between scattered and recoiled particles detected in coincidence. The overall time resolution of the monitor, as estimated by the width of the peak, was 0.75 ns. The length of the beam bunches at the target position was roughly estimated from the width shown in Fig. 6a to be as short as 0.58 ns by subtracting the time resolution of the monitor estimated

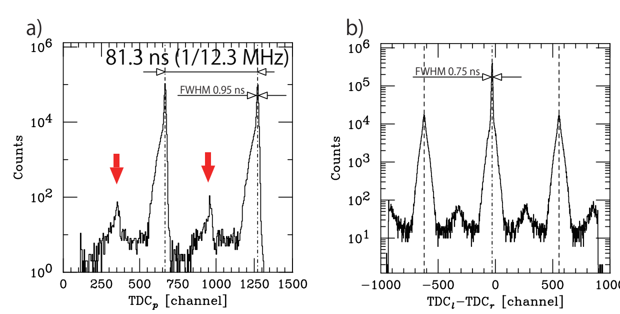

Figure 6: Measured time-of-flight and time difference between a deuteron counter and a proton counter.

ISBN 978-3-95450-167-0

from Fig. 6b, which corresponds to ± 2.6 deg. in phase of $f_{\mathrm{rf}}^{\mathrm{SRC}}$. The single-turn operation was stable and extracted turn was successfully maintained during the measurements for 2–3 days and the obtained turn purity was much more than 99%.

SUMMARY

Polarized deuteron beams with energies of 190, 250, and 300 MeV/u were used in deuteron-proton elastic scattering experiments [4]. Single-turn operation was feasible for this series of experiments, even in the case of 190 MeV/u and $\bar{B}$ = 0.77 T, which was below the lower limit originally intended for the SRC. The purity of the single-turn was satisfactory, and the accelerators were stable enough to perform the experiments.

REFERENCES

[1] H. Okamura *et al.*, *AIP Conf. Proc.*, vol. 343, p.123, 1995.

[2] M. Odera *et al.*, *Nucl. Instr. Meth. A*, vol. 227 p. 187, 1984.

[3] K. Suda *et al.*, *Nucl. Instr. Meth. A*, vol. 277, p. 55, 2013.

[4] K. Sekiguchi *et al.*, *Phys. Rev. C*, vol. 89, p. 064007, 2014; K. Sekiguchi *et al.*, *Phys. Rev. C*, vol. 83, p. 061001, 2011.

[5] T. B. Clegg, *AIP Conf. Proc.*, vol. 187, p. 1227, 1989.

[6] V .P. Derenchuk *et al.*, *AIP Conf. Proc.* vol. 343, p. 73, 1995.

[7] A. Goto *et al.*, in *Proc. Cyclotrons'89*, Caen, France, 1998, p. 51.

[8] Y. Yano *et al.*, in *Proc. Cyclotrons'92*, Vancouver, Canada, 1992, p. 102.

[9] H. Okuno *et al.*, in *Proc. Cyclotrons'04*, Tokyo, Japan, 2004, p. 373.

[10] H. Okuno *et al.*, in *IEE Trans. Appl. Supercond.*, vol. 18, p. 226, 2008.

[11] N. Inabe *et al.*, *RIKEN Accel. Prog. Rep.*, vol. 28 p. 160, 1995.

[12] M. Kase *et al.*, *RIKEN Accel. Prog. Rep.*, vol. 28 p. 156, 1995.

ISBN 978-3-95450-167-0

100 MeV H$^-$ CYCLOTRON DEVELOPMENT AND 800 MeV PROTON CYCLOTRON PROPOSAL*

Tianjue Zhang† and Jianjun Yang, China Institute of Atomic Energy, Beijing, 102413, China
on behalf of the BRIF Project Team

Abstract

Since the last cyclotron conference in Vancouver, significant milestones have been achieved on the BRIF (Beijing Radioactive-Ion Beam Facility) project. On July 4, 2014 the first 100MeV proton beam was extracted from the H- compact cyclotron. The cyclotron passed beam stability test with beam current of 25 µA for about 9 hours operation. In the year of 2015, the first radioactive ion beam of K-38 was produced by the ISOL system, and the beam current on the internal target of the 100 MeV cyclotron was increased to 720 µA. In the year of 2016, the cyclotron was scheduled to provide 1000 hours beam time for proton irradiation experiment, single-particle effects study and proof-of-principle trial on the proton radiography technology. It is also planned to build a specific beam line for proton therapy demonstration on the 100 MeV machine. In this talk, I will also introduce our new proposal of an 800 MeV, room temperature separate-sector proton cyclotron, which is proposed to provide 3~4 MW proton beam for versatile applications, such as neutron and neutrino physics, proton radiography and nuclear waste treatment.

INTRODUCTION

The Cyclotron Laboratory at China Institute of Atomic Energy (CIAE) has been devoting to cyclotron development and related applications since it was established in 1956 [1]. An 100 MeV high intensity H- cyclotron, CYCIAE-100, is being built at CIAE. The machine is selected as the driving accelerator for the Beijing Radioactive Ion-beam Facility (BRIF). Figure 1 shows the layout of this project. The energy range of extracted proton beam for CYCIAE-100 can be adjusted continuously from 75 MeV to 100 MeV and 200 - 500 µA CW beam will be provided at the initial stage [2]. The first beam of CYCIAE-100 was extracted on July 4, 2014 [3], the operation stability have been improved and beam current have been increased gradually. On May 4, 2015, the first radioactive ion beam of $^{38}K^+$ was produced by bombarding CaO target by the 100 MeV proton beam. The effort for mA beam is continuing and 1135 µA beam was got on the internal target in June of this year.

In this paper, the beam commissoning progress and subsystem improvment of the 100 MeV H$^-$ cyclotron since last cyclotron conference in Vancouver will be presented, including the multi-cusp source, buncher, matching from the energy of the injected beam, vertical beam line and central region, beam loading of the RF system and instrumentation for beam diagnostics etc. In addition, this paper also introduces the recent conceptual design progress of the pre-study of an 800 MeV, 3-4 MW separate-sector proton cyclotron, referred to as CYCIAE-800 [4], which is aimed to provide high power proton beam for various applications, such as neutron and neutrino physics, proton radiography and nuclear data measurement and ADS system.

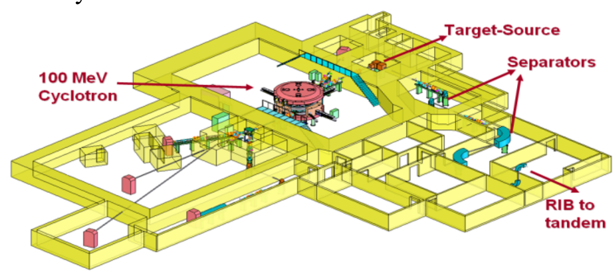

Figure 1: The layout of the BRIF project.

BEAM COMMISSIONING

By the end of 2013, all the sub-systems of CYCIAE-100, including the main magnet, the main coil, the rf system, the vacuum system, the injection system, the ion source, the diagnosis and extraction units, the lifting system and the power supply systems, were installed and assembled on site. Figure 2 shows the photograph of the cyclotron, which was taken at the time all the subsystems were installed on site. The construction of CYCIAE-100 takes the advantages of both high precision typically seen in AVF cyclotrons and strong focusing in separated sector cyclotrons. The main parameters for CYCIAE-100 are presented in Ref. [5].

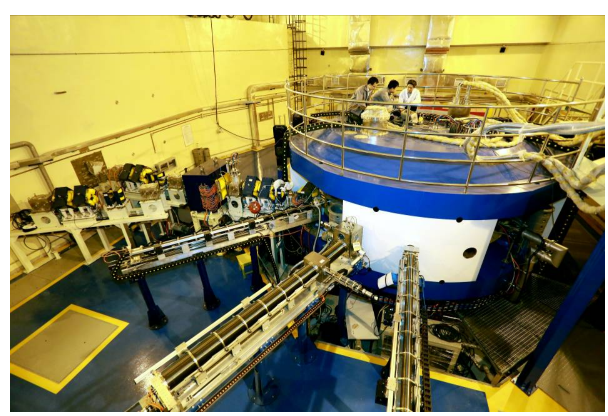

Figure 2: The 100 MeV compact cyclotron.

* Work supported by NSFC (Grant No. 11375273 and 11461141003)
† tjzhang@ciae.ac.cn

ISBN 978-3-95450-167-0

By the end of July 2013, the field mapping and shimming were finished and the required isochronous field was obtained under vacuum condition. The trim-coils system, which is usually used in this type of compact cyclotron as a supplementary method to adjust local magnetic field, is unnecessary in the CYCIAE-100 cyclotron since a small integral phase slip of less than ±10° can be reached simply by properly trimming the 16 shimming-bars. After that, the resonator conditioning was started and the multi-pacting effects at low RF power region were eliminated successfully.

The beam commissioning was launched in November, 2013. The ion source was tuned up and could provide 5mA, 35 keV H^- beam. After that, the functionality of injection line and the electrostatic inflector were tested and verified. On December 18 of 2013, we got a 320 μA DC beam on an internal target, which was positioned at the first accelerating gap. The transmission efficiency from the ion source to the exit of inflector is higher than 60%. On June 16 of 2014, the internal target was moved to 1 MeV region and a 109 μA beam current is measured under the condition of 20% rf duty cycle, corresponding to an injection efficiency of more than 10%. After that, we gradually increased the duty cycle and eventually reached CW mode operation. It is usually repeatable to get beam at 500 to 600 μA level at 1 MeV. Finally on July 4, we saw the first 100MeV beam on the extraction beam line of the cyclotron, which is a milestone of this project. Figure 3 shows the beam intensity signal on a radial probe.

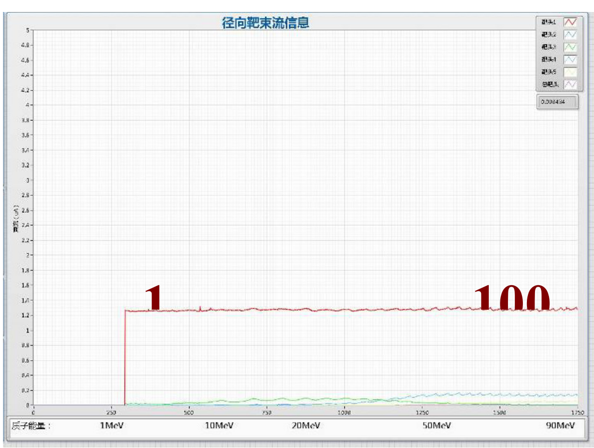

Figure 3: The beam intensity signal from a radial probe head when it slowly moved from the center to the extraction.

The beam stability was test for 12 hours on July 24. In the beginning, several beam trips happened, caused by the sparking between the two electrodes of the spiral inflector, then the major failure of a power supply device of the ion source caused beam off twice. After that the beam current was stably maintained at above 25 μA for 8 hours and 50 minutes, despite several fast beam trips caused by rf failures. This result met the requirement of acceptance for the first phase of this project.

On May 4, 2015, the first radioactive ion beam of $^{38}K^+$ was produced when the 100 MeV proton bombarded the CaO target station of ISOL system. The production of $^{38}K^+$ was 10^6 pps when the proton beam current was 1 μA. This is another milestone of the BRIF project.

BEAM INTENSITY UPGRADE

For CYCIAE-100, the ion source and injection line are installed underneath the main magnet, as is shown in Figure 4. The injection line adopts S-B-QQQ-S (S-solenoid, Q-quadrupole, B-buncher) focusing structure. The total length is about 250cm.

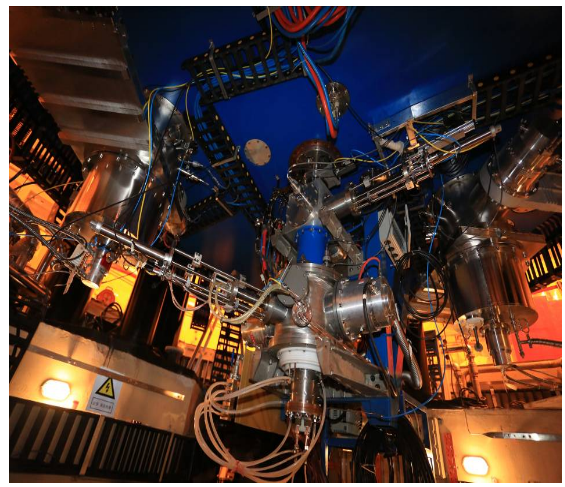

Figure 4: Ion source and the injection line.

In order to further increase beam intensity, several aspects were improved on the ion source, buncher, beam loading of the RF system, beam matching from ion source to the central region, etc.

Improvements of the Ion Source

A multi-cusp H^- ion source was adopted for the CYCIAE-100, which could supply about 10 mA DC H^- beam [6]. In order to improve the beam quality and decrease sparking events and improve the beam stability, some optimization were done on the extraction system of the ion source. The geometry of the extraction system is shown by the cross section in Fig. 5(left). It is an axially symmetric three-electrode structure including plasma, lens and ground electrodes. Sparking events were found at between the lens electrode and the x-y steering magnet, which was installed around the ground electrode. So a protection cover was placed on the steering magnet to prevent the electrons from bombarding the steering magnet. Twenty holes with diameter of 10 mm on the protection cover are drilled to ensure the gas flow and sufficient vacuum pressure.

On the other hand, in order to decrease the distance between the lens and the x-y steering magnet, a new x-y steering magnet with the shorter length was installed , for which the coil turn number is increase accordingly to maintain its deflection capability. This resulted in a smaller size of the ground electrode. So a new ground

ISBN 978-3-95450-167-0

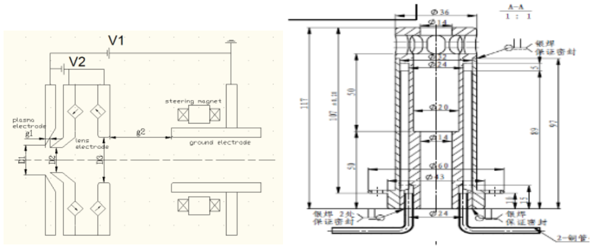

Figure 5: The geometry of the ion source extraction system and the cross-section drawn of ground electrode.

electrode was also designed. The cross-section drawn of ground electrode is shown in Fig. 5 (right).The distance between the beam limit hole and the ground electrode extraction hole is 67 mm. In order to reduce gas stripping in the ground electrode extraction region and to run the sources at optimum gas pressure in the ground electrode, 6 holes with every the size of 12 mm ×5 mm were bored on the head of the ground electrode. During the ground electrode design, the distance between the two lens was increased from 11 mm to 12 mm to improve the beam quality. By taking these measures, the extraction energy from the ion source was increased from 35 keV to 40 keV and the extracted beam current was increased from 5 mA to 10 mA DC, without sparking events during the beam stability test of one week long.

Improvements of the Buncher System

The DC beam generated by H^- cusp source is bunched by a first-harmonic non-intercepting two-gap buncher, which locates between the first solenoid and the triplet, approximately 1.1 m away from the inflector. The gap length is 5 mm and the required distance between two gaps is determined by 1/2βλ, which is 31 mm for 40 keV energy. The beam radius is limited by a collimator installed in front of the buncher and the effective buncher radius is 10 mm formed by gold plated tungsten wires, which is similar to TRIUMF design [7]. The RF-feeding system of the buncher consists of a LC matching circuit, a 600W RF solid state amplifier and an amplitude/phase control unit. The mechanical structure of the buncher is shown in Figure 6.

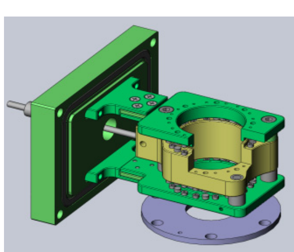

Figure 6: The mechanical structure of the buncher.

Before the beam commissioning with buncher, three major improvements were made, including the modification of the power supervising system, the measurement of the shunt impedance of the buncher and the fine tuning of the LC matching circuit.

(1) An EPICS based power monitor system was developed to monitor the RF power flow to the buncher. The system consists of a digital control board and a RF analog board. The digital control board is based on ARM Cortex-A7 CPU and run Linux OS. The RF analog board demodulates the forward power and the reflected power through two RF power detectors. A 16 bits four-channel ADC is used to digitalize the output of the power detector.

The digital control board accesses the ADC through the SPI bus and fills the sampled value of the related EPCIS process variables. The interlock is also included in the power monitor system to avoid damage.

(2) The shunt impedance of the buncher was measured by the Agilent E5070B vector network analyzer. The vector network analyzer measured the S21, using a 50 Ω loaded probe connected with the grid of the buncher as port 2, meanwhile port 1 was the conversional coupling port of the buncher. Afterward, the shunt impedance for the buncher structure was calculated as 3.5 KΩ. By knowing this value, one may calculate the beam bunching voltage by using the forward power readings.

(3) The capacitor of the LC matching circuit is coarse, which has a big temperature drift. This drift has significant adverse impact on the bunch RF matching when the RF power is switched on. The LC matching circuit has to be adjusted online, manually. To protect the 600 W RF power amplifier, a pulse signal with a duty factor is 1/10 was used to drive the buncher system. The capacitor was fixed when the amplitude of the pickup signal reached its maximum. Then the system was changed to automatic mode.

Improvements of the RF System

The RF system [8] of the 100MeV cyclotron consists of two sets of identical RF cavities [9] power transmission systems and two 100kW tetrode RF amplifiers [10] LLRF systems [11,12]. The high power level RF parts of the system are fully independent from each other, while the Low Level RF parts share one common reference clock. Thus, the LLRF systems can align the two cavities to the same phase for proton beam acceleration. The RF system has been improved for two aspects before the mA level beam commissioning, including LLRFs and cavities.

(1) The P.I. controller in amplitude control loop is an analog regulator. When the beam current is increased, the beam loading may cause an open-loop condition for the Dee voltage regulation. After the amplitude loop is closed, the RF driven signal amplitude is determined by the DSP and DDS of the LLRF system. In another word, to achieve an accurate amplitude control, the LLRF adopts a self-adaptation strategy to ensure the amplitude control loop is always closed, unless the power requirement exceeds 120% of nominal value.

(2) The tuner of the cavity consists of two DC motors, which drive a fine capacitor and a coarse capacitor, respectively. The coarse capacitor is controlled manu-

ISBN 978-3-95450-167-0

ally, while the fine capacitor is controlled by the tuning loop and works online. The fine tuner was changed to a smaller disk before the beam commissioning to achieve a better tuning performance of the RF cavity. This effort was observable in the commissioning, e.g. the residual tuning errors were reduced to less than 3 degrees for both cavities of the CYCIAE-100 cyclotron.

Installation of the Removable Internal Target

The removable target locates at the center of the magnet valley area. Driven by the cylinder and travel switch, the target could move onto the median plane and stop the arriving particles. The head of removable target is a cube made by copper and cooled by water. In order to eliminate the influence of secondary electron emission, a wing with two thin copper pieces are added on the side face of the target head. Figure 7 shows the removable internal target and the beam spot.

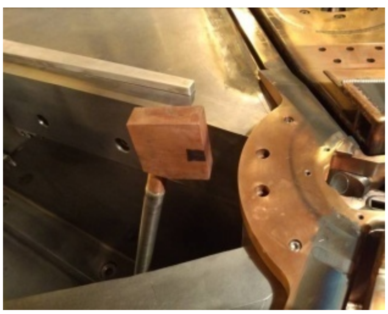

Figure 7: The removable internal target.

Beam Intensity Upgrade

The Beam Commissioning at higher intensity has been carried out after above mentioned improvements. Figure 8 shows the beam current history measured by the internal target at 1MeV, which shows the beam current on the internal target reaches 1.1 mA. Table 1 shows the bunching efficiency and acceleration efficiency for different DC beam current of H^- ion source. It shows the bunching factor can go up to factor of 2 at 3 mA beam current. It clearly shows that the bunching efficiency is in decrease with the ion beam current. However, the bunching factor can still reach 1.66 at around 9 mA beam curren. Table 1 also shows the influence of the wing on the internal target. The measured beam current will increase about 6.3% when the secondary electron emission is suppressed by the wing.

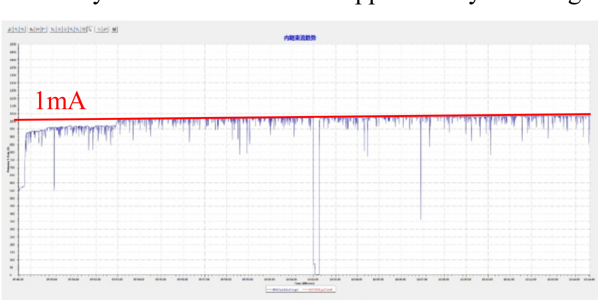

Figure 8: The beam current history measured by the internal target at 1 MeV.

Table 1: The Bunching Efficiency and Transmission Efficiency from the Ion Source to the Internal Target

Ion Source (mA)	No Buncher (μA)	With Buncher (μA)	Bunching Factor	Transmission Efficiency (%)
1.33	100	201	2.01	15.1
1.91	145	310	2.14	16.2
3.25	201	399	1.99	12.3
4.27	258	490	1.90	11.5
8.69	610	950	1.56	10.9
8.67	608	1010	1.66	11.6**

**Measured data when a wing with two thin copper pieces is added to eliminate the secondary electron emission.

A 800 MeV PROTON CYCLOTRON PROPOSAL

High power proton beam has wide applications in radiation physics, neutron science, neutrino physics, radioactive beam production and ADS system. The cyclotron is an intrinsic CW mode particle accelerator, which has the following distinguishing features: (a) low construction costs; (b) high effective power conversion rate; (c) compact structure; (d) no needs for superconducting resonators, etc. Therefore, the cyclotron can be a competitive candidate for MW-level proton beam driver. CIAE proposed a multi-functional research facility based on cascaded cyclotrons [13].

Layout of the Facility

In the latest proposal, this project will be split into three stages. In the first stage, it is proposed to construct the 800 MeV ring cyclotron and to utilize the 100 MeV, 200 μA compact H^- cyclotron CYCIAE-100 of the BRIF project as its injector; The experimental instruments for nuclear data measurement, single event effects, radiation physics and isotope production facility will be constructed as well. Then in the second stage, in order to achieve more than one MW beam power on target, the CYCIAE-100 will be superseded by a dedicated 100 MeV separated-sector injector cyclotron [14]. The spallation neutron source, proton radiography device and spent fuel post-process platform will be constructed in this phase as well. In the final stage, when the beam power reach the design of 3 MW, the beam can be deliver to the China Fast Neutron Reactor (CEFR) to compose a ADS facility.

Conceptual Design Progress

Since the year of 2009, the pre-study of this cyclotron complex was carried out, including general design [13] space charge limit [15] and the main magnet design and optimization of the main cyclotron design [16]. The main accelerator is a PSI-like ring cyclotron [17] with the beam power of 3 to 4 MW and kinet-

ISBN 978-3-95450-167-0

ic energy of 800 MeV, referred to as CYCIAE-800.

In the conceptual design, two solutions are considered. one is the proton cyclotron with conventional coils and another is the H_2^+ (two protons plus one electron) cyclotron with superconducting coils. Table 2 briefly summaries the advantages and disadvantages of the two solutions. Considering the maturity of the existing technologies and construction risk, we chose the proton cyclotron with warm magnet.

Table 2: Comparison of the Proton and H2+ Solutions

	H2+	Proton
pro	a) Multi-turn stripping extraction; b) low RF voltage is OK; c) Smaller space charge effects	a) Mature technology at MW level (PSI, TRIUMF); b) Require low B field, warm magnet is OK; c) Good extraction beam quality; d) Low Vacuum is OK
con	a) Long-lived vibrational states →dissociate b) Require SC magnet c) Need high vacuum d) No construction experience at MW level	a) Require single-turn extraction; b) Require high RF voltage; c) Larger space charge effects; d) Need flat-top cavities and/or buncher

The latest layout of the main magnet is shown in Fig. 9. The diameter and height of the magnet system is 16 m and 5.8 m, respectively. The total weight of the magnet is 3420 t and the total stored energy is 3.96 MJ.

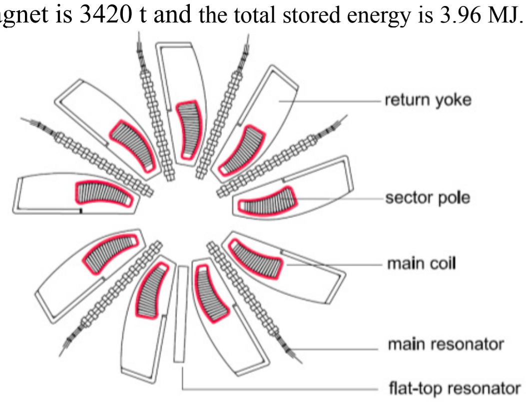

Figure 9: Schematic plot of the main magnet system of the 800 MeV cyclotron together with the rf resonators.

In this cyclotron, the rf system is a very challenging subsystem, which requires sophisticated monitoring and protection systems and components. The parameter analysis shows that, in order to extract the MW level proton beam, a single amplifier is incapable to transfer adequate power to a cavity of the design mentioned above, even if the most powerful tetrodes and state-of-the-art components are used. A possible alternative is that a cavity is fed with two complete power chains, namely two separate amplifiers, transmission lines and coupling loops. The rf resonator is modelled in 3D and the result is shown in Fig. 10. Thanks to the adequate free space between magnet sectors, the Q factor of the main resonator can reach 20,000.

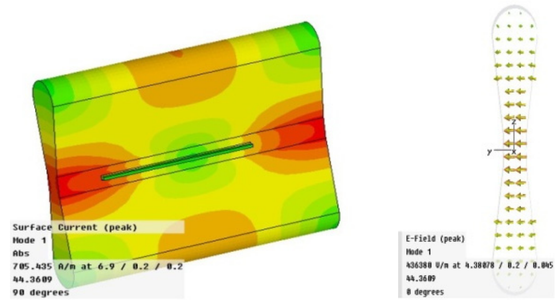

Figure 10: Surface current and E-field distribution of the rf resonators.

In this high beam power cyclotron, space charge force can play a import role in the beam dynamics. Large scale parallel particle simulation shows that the beam can be cleanly extracted from the ring cyclotron when the beam current is 3 mA (2.4 MW). Further optimization will be carried out to further increase the beam current limits.

CONCLUSION AND OUTLOOK

The beam commissioning of the 100 MeV cyclotron proceeds smoothly to high beam current. More than 1 mA beam current is already reached in the interval target. It is expected this cyclotron is capable to provide 200 to 500 μA proton beam in the coming years. More radioactive beam production experiment will be carried out on the ISOL system to optimize the charge exchange efficiency and to improve the positive surface ion source. Meanwhile, the cyclotron team has already launched the pre-study of the future high power proton cyclotron. From the pre-study, it is confirmed that a 3 MW level CW proton cyclotron with conventional coils should be feasible based on our existing technologies.

ACKNOWLEDGMENTS

The authors would like to extend their deep appreciation to a number of senior scientists and researchers from TRIUMF, PSI, INFN-LNS, etc. for their generous support and significant contribution to the cyclotron development activities at CIAE.

REFERENCES

[1] T.J. Zhang, et al., "Research progress in high intensity cyclotron technology", *Chinese Science Bulletin*, Vol. 54, Issue 21, Nov. 2009.

[2] T.J. Zhang et al., "Physics problem study for a 100 MeV, 500 microAmp H- beam compact cyclotron", in *Proc. ICAP'09*, San Francisco, USA.

[3] T.J. Zhang et al., "The beam commissioning of BRIF and future cyclotron development at CIAE", in *HB'14 talk*.

[4] T.J. Zhang, et al., "Conceptual design of an 800MeV high power proton cyclotron", *NIM B* 269 (2011) 2964–2967.

ISBN 978-3-95450-167-0

[5] T.J. Zhang, et al., "Progress on construction of CYCIAE-100", in *Proceedings of 19th International Conference on Cyclotrons and their Applications*, Sept. 6 - 10, 2010, Lanzhou, China.

[6] T.J. Zhang et al., "Experimental study for 15–20 mA dc H− multicusp source", *Review of Scientific Instruments,* 81, 02A705.

[7] T. KUO, et al., "On the Development of 2 rnA RF H- Beams for Compact Cyclotrons", in *Proceedings of the 14th International Conference on Cyclotrons and their Applications*, Cape Town, South Africa.

[8] X.L. Wang, et al. "The alternative of RF system design for the 100 MeV cyclotron at CIAE", *NIM B*, 2007, 261: 70–74.

[9] B. Ji, et al., "Design and primary test of full scale cavity fo CYCIAE-100", in *Proceedings of 19th International Conference on Cyclotrons and their Applications*, Sept. 6 - 10, 2010, Lanzhou, China.

[10] Z.G. Yin, et al., "Design, construction and commissioning of the 100 kW RF amplifier for CYCIAE-100", in *Proceedings of 19th International Conference on Cyclotrons and their Applications*, Sept. 6 - 10, 2010, Lanzhou, China.

[11] Z.G. Yin, et al., "RF control hardware design for CYCIAE-100 cyclotron". *NIM A*, 2015, 801: 104–107.

[12] Z.G. Yin, et al., "Digital control in LLRF system for CYCIAE-100 cyclotron". *NIM A*, 2016, 819: 33–36.

[13] T.J. Zhang, et al., "Conceptual Design of an 800 MeV High Power Proton Driver", *NIM B*, 2011, 269 (24): 2964-2967.

[14] M. Li et al., "Conceptual Design of a 100 MeV Injector Cyclotron". in *Proc. ICC'13*, Vancouver, 2013, pp. 224-226.

[15] J.J. Yang, et al., "Physical Design progress of an 800 MeV High Power Proton driver", in *Proc. IPAC'13*, Shanghai, 2013, pp. 342-344.

[16] J.J. Yang, et al., "Magnet Design of an 800 MeV High Power Proton Cyclotron", *IEEE Transactions on Applied Superconductivity*, 2016, 26(4):1-4.

[17] M. Seidel, et al., "Production of A 1.3 MW Proton Beam at PSI", in *Proc. IPAC'10*, Kyoto, 2010, pp. 1309-1313.

ISBN 978-3-95450-167-0

CHARGE STRIPPER RING FOR CYCLOTRON CASCADE

H. Imao, O. Kamigaito, H. Okuno, N. Fukunishi, K. Suda, N. Sakamoto, K. Yamada, Y. Yano, RIKEN Nishina Center, Wako, Japan

Abstract

In the multi-stage acceleration of heavy ions such as the acceleration at the RIKEN RI beam factory (RIBF), the electron stripping process with charge strippers is an inevitable process for the efficient acceleration. The efficiencies, however, for the charge-state conversion of very heavy ions are not so high with common charge strippers in the acceleration up to the energy around hundreds MeV/u. The total efficiency of two charge strippers for 238U acceleration at the RIBF is only 6%. It is a bottleneck for the intensity upgrade. In the present study, we designed high-efficient charge stripper rings which have applicability to the RIBF.

INTRODUCTION

In a multi-stage acceleration of heavy ions, the electron stripping of the ions with charge strippers is an essential process for efficient acceleration. When one accelerates the very heavy ion beams, such as uranium ions, up to several hundred MeV/u, it is not possible to provide full strip beams with conventional strippers. Charge state of the beams after the stripper has a distribution following the physical law. The intensity of ions should be reduced significantly in exchange for the efficient acceleration.

In the uranium acceleration at the RIKEN RI beam factory (RIBF) [1], the charge state is converted twice and the total conversion efficiency is only 6%. The low conversion efficiency is an important bottleneck to generate a high-intensity uranium beam. Such beams are strongly desired in the world because they can provide a huge breakthrough for exploring the new domain of the nuclear chart.

The FRIB project, one of the next generation heavy ion facilities in the USA [2], is planning to use the multi-charge acceleration technique. In this scheme, the beams with five charge states are accelerated and transported at the same time in the superconducting linear accelerator. Unfortunately, this technique is not applicable for the acceleration with ring-type accelerators, such as a cyclotron.

In this paper, we propose and discuss charge stripper rings which can be available as an efficient stripper in a multi-stage accelerator complex involves circular rings such as the RIBF.

URANIUM ACCELERATION AT RIBF

The acceleration scheme of ^{238}U beams at the RIBF is shown in Fig. 1. ^{238}U^{35+} beams extracted from the 28-GHz superconducting ECR ion source [3] is accelerated with an injector RILAC2 [4] and four ring cyclotrons (RRC, fRC, IRC, SRC) up to the energy of 345 MeV/u.

The charge state is converted twice at the energies of 10.8MeV/u and 51 MeV/u, respectively. The first stripper based on the He gas [5,6] converts the charge state from 35+ to 64+ with the conversion efficiency of about 20%. The second stripper of rotating carbon disk stripper [7] converts from 64+ to 86+ with the efficiency about 30%.

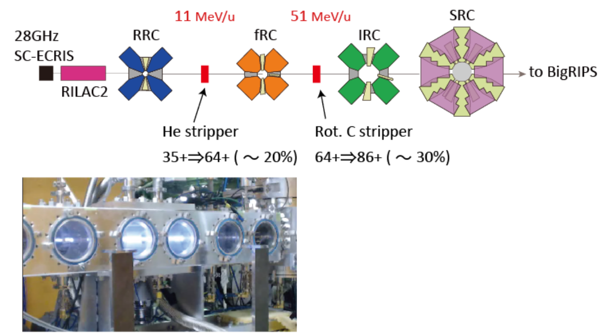

Figure 1: Acceleration scheme of ^{238}U ion beams at the RIBF.

A simple way to increase the low total conversion efficiency is to remove the first stripper and to improve the fRC to accept U^{35+} beams (K value is approximately 2200). In a design of a conventional normal conducting ring cyclotron, the new fRC should be a very huge and heavy cyclotron comparable with the SRC, the largest cyclotron in the world [8]. Although it is a sure way to improve the present intensity of uranium beams, we require further optimization of the design for the new fRC.

CONCEPT OF STRIPPER RING

We propose here the new concept of an efficient stripper ring as shown in Fig. 2. As a conventional scheme at the RIBF, ^{238}U^{35+} beams coming at the frequency 18.25 MHz are injected to the first stripper and only ^{238}U^{64+} beams (20% of the injected beams) are passed through the subsequent selection dipole magnet. The others are dumped inside the magnet.

On the other hand, in the new scheme, the beams other than the selected charge state are circulated recovering the energies and re-entered to the stripper. The beams with the selected charge state are extracted continuously, repeating this circulation process.

Assuming the conversion efficiency ε_0 = 0.2 is unchanged, the total conversion efficiency after the n-times circulation is given by $\epsilon_n = 1 - (1-\epsilon_0)^n$. Ideally, the conversion efficiency becomes 3 times higher than the initial efficiency ε_0 after the 3 times circulation. The bunch structure of the extracted beams must be preserved to match to the acceleration condition of the subsequent cyclotrons.

ISBN 978-3-95450-167-0

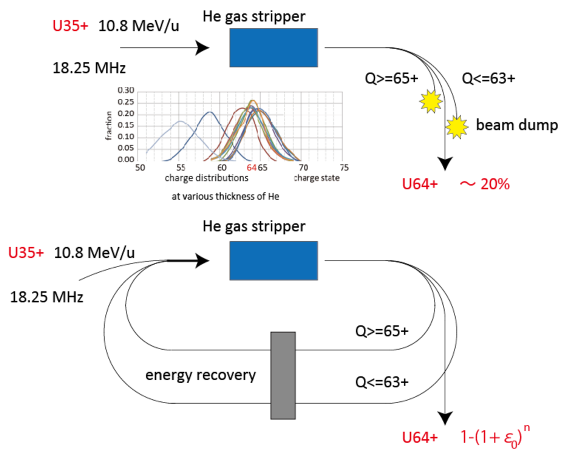

Figure 2: Concept of the charge-stripper ring.

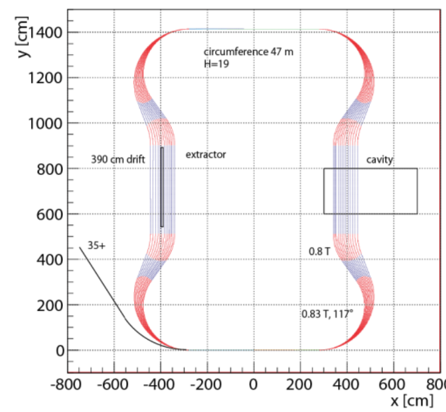

Figure 3: Schematic layout of an isometric charge-stripper ring.

ISOMETRIC CHARGE STRIPPER RING

Isometric ring to any magnetic rigidities of beams (momentum compaction factor α=0) is a possible ring preserving the bunch structure. Such isometric rings can be realized by using the combination of the bending and anti-bending magnets. The harmonics number of the circulating beams should be integer.

Figure 3 shows an example of the calculated orbit of such isometric ring. The initial U^{35+} beams coming from the RRC are injected with the charge-exchange injection method. The deposit energies in the stripper are recovered depending on the charge states q by the RF cavity located at the dispersive region. The beams with selected charge state (q_0=65+) are kicked out and extracted with the electrostatic septum similar to the EDC of cyclotrons.

The rings considered in this paper have the twofold symmetry. The more highly symmetric rings are also possible. Such rings would accept beams coming from many injectors at the same time,

Conditions to be satisfied by the half-cell of the isometric ring are followings.

1. The deflection angles are constant with Bρ.
2. The orbit lengths are constant with Bρ.
3. The endpoints of the orbit are collinear for all Bρ.

The trajectories for all q we want to circulate can be calculated under the three conditions above and the edge angles of the dipole magnets are automatically determined. The transfer matrix M(q) of the half-cell can be derived from the input parameters, drift lengths and field strengths of the dipole magnets for a selected charge state q_0. We also added quadrupole magnets at the first drift region for the tuning of the matrix M. We varied all input parameters to satisfy the stable circulating condition, $|\mathrm{TrM}(q)| < 2$. Because the circulating beams change the charge state at the stripper, the eigen ellipses for all q should be as uniform as possible.

Calculated orbits optimized for the first stripper at the RIBF are shown in Fig. 4. The ring with the magnetic field of 0.4 T is in about 20 m square. The orbit separation at the dispersive region for neighboring q is about 15 cm.

The calculated eigen ellipses are shown in Fig. 5. We note that vertically long ellipses are desirable to reduce the emittance growth due to the angular straggling in the stripper.

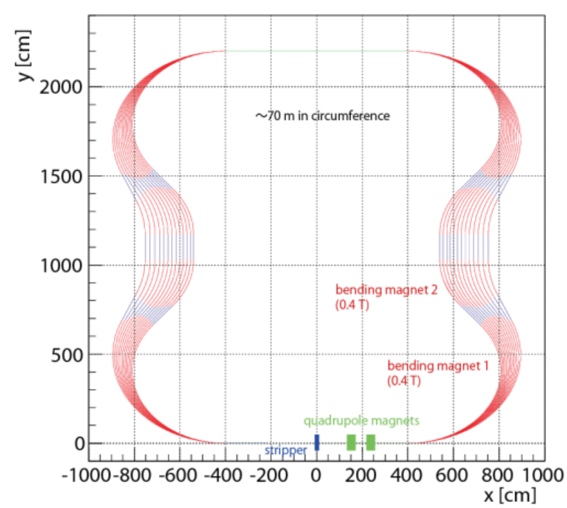

Figure 4: Equilibrium orbit for uranium beams with the charge states from 59+ to 71+.

Figure 6 is the calculated beam envelopes of x and y directions for all q. Although the tunes also depend on the charge states, the resonance would not be problematic because the charge state is not always constant in the circulation and the mean turn number is not high.

We further calculated the beam dynamics for the transverse directions in the ring by implementing the Monte-Carlo code for the charge exchange reactions. The calculation procedures are as followings:

ISBN 978-3-95450-167-0

1. Give a particle randomly on the initial ellipses matching to the intersection of the eigen ellipses.
2. Perform the Monte Carlo calculation in the stripper involving charged exchange reactions, energy loss and scattering.
3. Energy of the particle is recovered depending on q.
4. Calculate the transport matrix for the particle with the calculated q and the energy in 2 and 3 and transport the particle.
5. Repeat the calculation process between 2 and 4 until the charge state reaches at 65+.
6. Transport the particle to the extraction position and get information of extracted particle.
7. Return to 1 for the next particle.

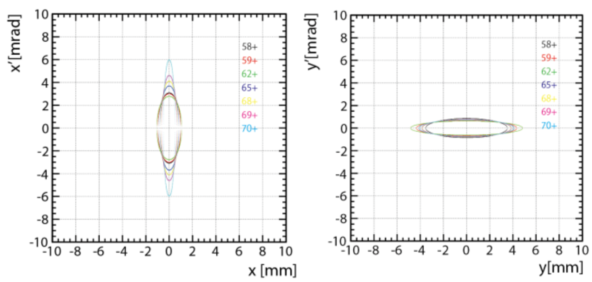

Figure 5: Eigen ellipses.

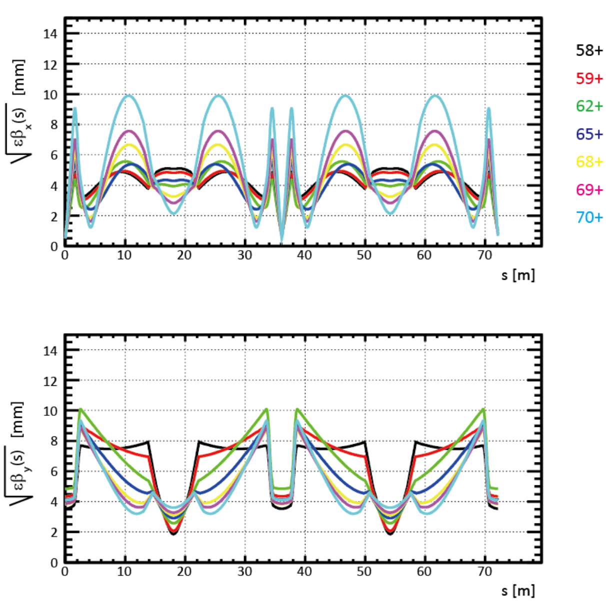

Figure 6: Horizontal and vertical betatron functions.

The He gas stripper with the thickness of 0.4 mg/cm^2 is assumed in the calculation. Figure 7 shows the calculated charge evolution and the energy degradation in the He stripper. The cross sections for the electron capture and ionization are calculated following Ref. [6].

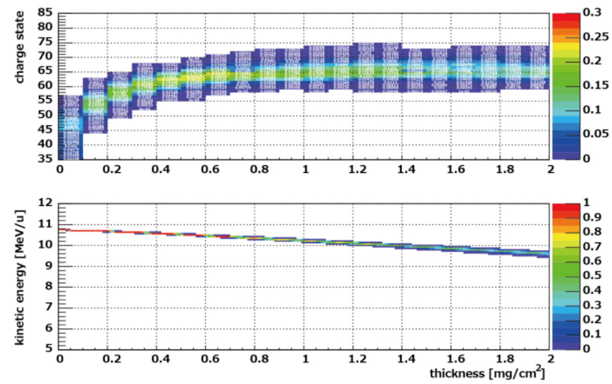

Figure 7: Charge and energy evolution in He gas.

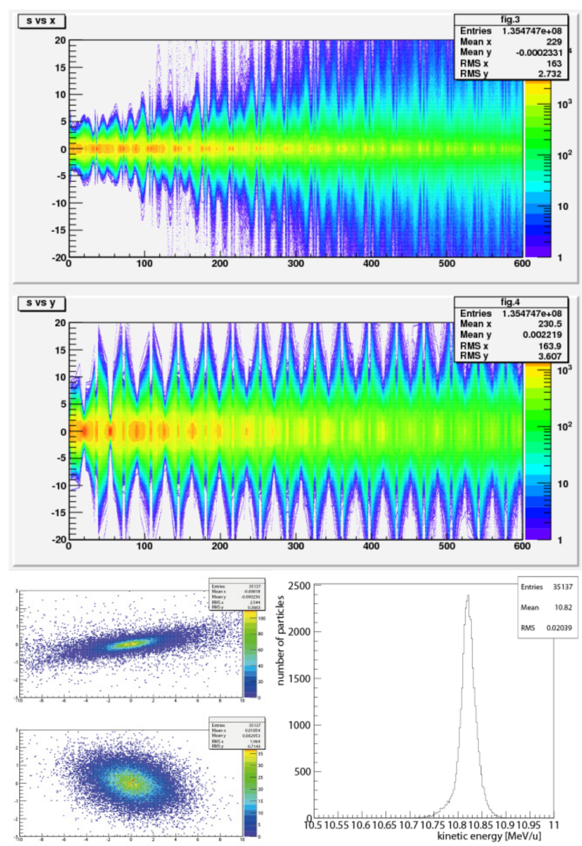

Figure 8: Figures of calculated result.

Figure 8 shows the calculated beam plots in the transverse directions. The plots in x-x' and y-y' space, and energy distribution at the ring exit are also shown. The beam with the desired charge state 65+ was extracted with the efficiency of 72% in this calculation. 9% of the beams went outside the assumed physical aperture of 10 cm square inside the ring. 14% of the beams changed the charge state outside the acceptable charge states (58-70+). The remaining 5% of beams did not reach to 65+ within the simulated 20 turns. The energy width at the exit is

ISBN 978-3-95450-167-0

comparable to that after the He stripper with the thickness of 1.4 mg/cm2, which is twice of the present thickness of the first stripper at the RIBF. The calculations for further optimized lattice are continued.

ORBIT-DIFFERENCE ADJUSTING CHARGE-STRIPPER RING

As another possible ring to keep the bunch structure, a ring can be considered, in which the orbit difference by q is adjusted to match to the bunch spacing. In this scheme, the orbit separation among neighboring charge states become large so that some components can be placed in each orbit independently. Thus the beam extraction has no problem. The orbits for respective charge states can be treated in almost independent rings.

Figure 9 shows a schematic layout of such orbit-difference adjusting ring designed for the first stripper at the RIBF. The ring designed for circulating the beams with the charge states between 62+ and 66+ and for extracting the beams with 64+. The second and third bending magnets and quadrupole triplet are placed in each orbit, independently.

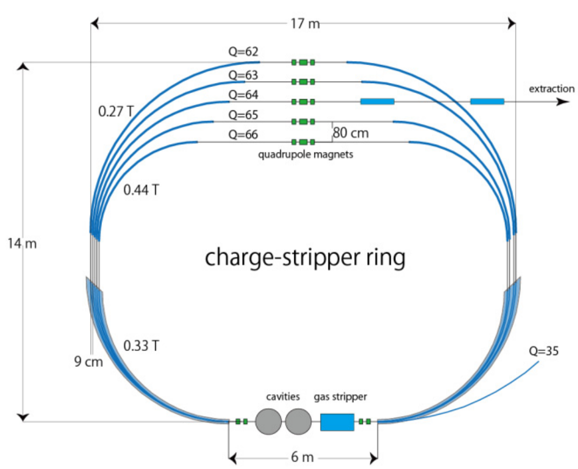

Figure 9: Orbit-difference adjusting charge-stripper ring.

As the lattice design for the isometric rings, vertically long eigen ellipses at the stripper are desirable to reduce the emittance growth due to the angular straggling. Amplitude of betatron functions and dispersion in the ring should be tolerable within realistic apertures. The achromat conditions at the position of the stripper are also desirable. In this ring, it is possible to satisfy the condition that the eigen ellipses for all q are nearly uniform. This is an advantage of this type of ring because some input parameters, edge angle and n values of magnetic channels and field values of quadrupole triplet, can be set for all q, respectively.

For the optimizations of the parameters, MINUIT [9] of CERN library was used. The optimized eigen ellipses for all q could be almost uniform with six fitting parameters for each q as shown in Fig. 10. Figure 11 shows the beta functions and dispersion in the ring. We also calculated the beam envelopes for transverse directions when the charge state is changed as 65+->63+->64+ with TRANSPORT [10] (Fig. 12). The result shows that the emittance growths for the transverse directions are strongly suppressed when the initial ellipse of the U^{35+} beam matches to the eigen ellipse of the ring.

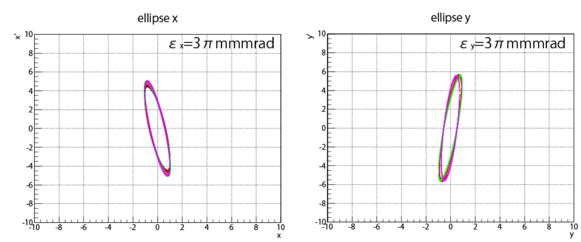

Figure 10: Optimized eigen ellipses for the beams with the charge states between 62+ and 66+.

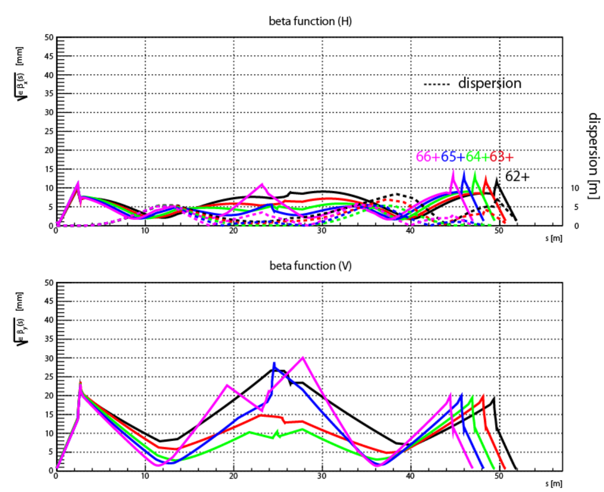

Figure 11: Beam envelopes and dispersion for horizontal and vertical directions.

ISBN 978-3-95450-167-0

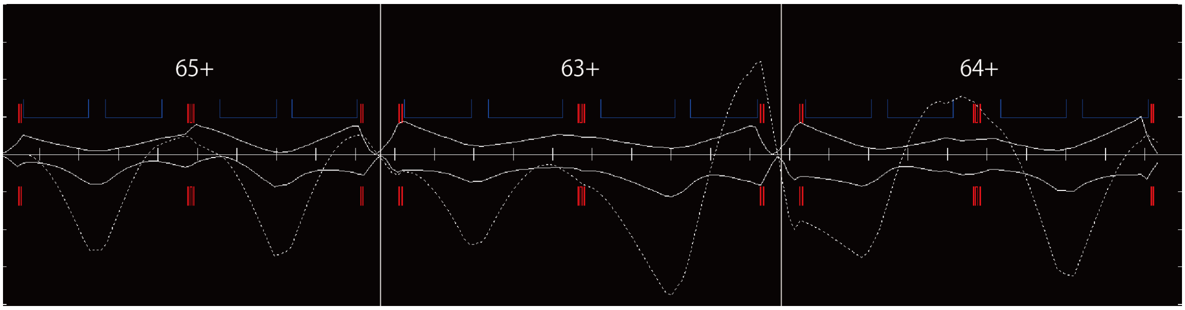

Figure 12: Beam transport calculated with TRANSPORT.

SUMMARY

Two types of high-efficient charge stripper rings which have applicability to the RIBF are proposed. Calculation methods for the lattice design are developed and demonstrated. Further optimization of lattice design and also engineering design are undergoing. Other applications, e.g., the storage ring or cooler ring, are also under consideration.

REFERENCES

[1] Y. Yano, *Nucl. Instrum. Methods Phys. Res.* B261, 1009 (2007).
[2] FRIB project; `http://www.frib.msu.edu/`
[3] Y. Higurashi et al., *Rev. Sci. Instrum*. 83, 02A308 (2012). Y. Higurashi et al., *Rev. Sci. Instrum.* 83, 02A333 (2012).
[4] K. Yamada et al.,in *Proc. IPAC'12*, TUOBA02 (2012).
[5] H. Okuno et al., *Phys. Rev. ST-AB* 14, 033503 (2011).
[6] H. Imao et al., *Phys. Rev. ST-AB* 15, 123501 (2012).
[7] H. Hasebe, et al., *in Proc. INTDS'16*, Cape town (2016).
[8] H. Okuno et al., this conference.
[9] F. James and M. Ross, MINUIT Users Guide, Program Library D506, CERN (1981).
[10] L. Brown et al., "Transport, a Computer Program for Designing Charged Particle Beam Transport System"; CERN 73-16 (1973) and CERN 80-04 (1980).

ISBN 978-3-95450-167-0

EXTRACTION BY STRIPPING IN THE INFN-LNS SUPERCONDUCTING CYCLOTRON: STUDY OF THE EXTRACTION TRAJECTORIES

G. D'Agostino, INFN-LNS, Catania, Italy and Università degli Studi di Catania, Dip.to di Fisica e Astronomia, Catania, Italy
L. Calabretta, A. Calanna, D. Rifuggiato, INFN-LNS, Catania, Italy

Abstract

The INFN-LNS Superconducting Cyclotron will be upgraded to allow for the extraction by stripping for ion beams with masses below 40 amu. By choosing properly the position of the stripper, it is possible to convoy the trajectories of the selected representative ion beams across a new extraction channel (E.C.).

Here we report the design study for the new E.C. and the simulations of the beam envelopes for a set of ions to find out the parameters of the magnetic channels necessary to focus and to steer the beams through the new extraction line. Two new compensation bars have been designed to compensate the first harmonic contribution of the new magnetic channels. The results of these simulations will be also presented.

INTRODUCTION

The INFN-LNS Superconducting Cyclotron (CS), designed over thirty years ago, is an isochronous three-sector compact accelerator with a wide operating diagram: ion species from H to Pb are accelerated with energy in the range 10-80 AMeV.

The beam extraction system, composed of two electrostatic deflectors followed by a set of magnetic channels, does not allow to achieve a beam power exceeding 100 W, due to the power dissipation on the electrostatic deflectors.

The stripping extraction is a valid alternative to increase the extracted beam power up to 2-10 kW for the ion species with mass less than 40 amu. A preliminary study demonstrated its feasibility [1] if a new extraction channel (E.C.) is drilled. Indeed, the extraction by stripping through the existing extraction channel for the ions of interest is less convenient because a wider clearance is required to allow intense ion beams pass through. Furthermore, the quadrupole component for the magnetic channels varies in a range of values wider than those necessary for the new extraction channel.

In Fig. 1 the median plane of the CS with the existing and the new extraction channels is shown together with the trajectories of two selected ions.

Thanks to high beam power, the INFN-LNS users will be also able to make researches on low cross section processes in nuclear physics. In particular, a high beam power is required by the NUMEN experiment, which proposes to measure the element of the nuclear matrix in the neutrino-less double beta decay using double charge exchange reactions [2,3], and the production of radioactive ion beams by in-flight fragmentation technique will also be enhanced [4].

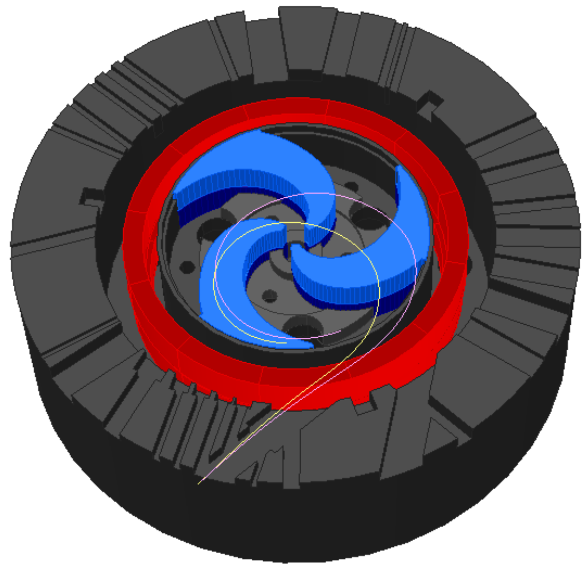

Figure 1: Extraction trajectories of some studied ions through the new extraction channel.

To accomplish the stripping extraction, a significant upgrade of the CS will be necessary, mainly because a new cryostat with new superconducting coils [5] is mandatory to have a larger vertical gap in the extraction line and additional penetrations are necessary to host new magnetic channels and new compensation bars. A general description of the CS upgrade operations is presented in ref. [6]. In addition, the existing extraction mode will be maintained to satisfy the demand of ion beams in a wide mass and energy range by the INFN-LNS community.

STUDY OF THE STRIPPING EXTRACTION

The ion species considered in the present study of the stripping extraction are ^{12}C, ^{18}O, ^{20}Ne accelerated with charge state q=Z-1 or Z-2 or Z-3 at energies in the range 15÷70 AMeV.

We assumed that all these ions of interest, at energies higher than 15 AMeV, are fully stripped of their electrons after crossing the stripper foil [7].

After the change of the charge state, the trajectory of each ion has a strong first harmonic precession and this could bring the beams to come out from the cyclotron field.

The study of the stripping extraction has been performed mainly through two codes, GENSPE and

ISBN 978-3-95450-167-0

ESTRAZ, initially developed at MSU by Gordon [8] and updated accordingly to our needs.

For each ion we used the corresponding isochronous field map to accelerate it with mass A and q=Z-1 or Z-2 or Z-3 at the required energy. The code GENSPE, with this isochronous field map as input, has been used to determine the parameters (energy, radial position and beam size) at the stripper position. For our simulations, we assumed a normalised emittance of 1 π mm.mrad. This value is quite conservative since it is more than twice the normalized emittance value of the beam delivered by our ion source.

We used the code ESTRAZ to simulate the trajectories of fully stripped ion beams for different azimuthal positions of the stripper, from the stripper foil to outside the cyclotron yoke. ESTRAZ allows also to compute the radial and axial envelopes of the beam along the extraction trajectories starting with the initial conditions found out by GENSPE code. Unfortunately, the EXTRAZ code performs the trajectory integration with step of 2°. So, we can simulate the starting point of the extraction trajectories only at discrete azimuthal positions. We plan for the near future to perform finer simulations using Spiralgap code or Cobham OPERA 3D [9].

All the present results have been validated and visualised through the FEM software by Cobham OPERA 3D. Details on the technical approach are reported in Ref. [1].

The first aim of our study was to define the cross-section and direction of the new E.C. in the CS: we fixed an exit point from the CS, which has to be crossed by all extracted trajectories in order to have an easier connection between the new extraction channel and a new extraction beam line.

For each ion, we found out the best azimuthal position of the stripper in order to have an extraction trajectory as close as possible to the exit point.

Other constraints must be satisfied by our extraction trajectories, too. They have to pass at least 70 mm away from the CS centre, to avoid any interference with the central region components; and, due to mechanical constraint, axial beam envelopes have to be lower than ±15 mm inside the pole and ±25 mm along the new E.C., which starts from the pole radius and ends after the yoke.

We were able to size down the region where to place the strippers foils in two main areas for all ions of interest, one is on the hill, [$106° < \theta_{stripper} < 122°$], just where the electrostatic deflector 1 (ED1) is placed and one on the valley, [$60° < \theta_{stripper} < 88°$], just before the ED1.

Table 1 contains some details on the ions studied and stripper positions.

This means that the cyclotron will be operated roughly 6 months per year to deliver ions using the existing ED1 and the other 50% of the year to deliver high power beams using stripping extraction through the new E.C.

Differently from the actual 30 mm of vertical gap along the EC, we fixed the vertical gap of the new E.C. equal to 60 mm to allow for the insertion of focusing magnetic channels so as to let intense ion beams pass through.

Table 1**:** List of ions to be extracted by stripping and stripper position specifications

Ion	Q_{acc}/ Q_{ext}	Energy (AMeV)	θ strip. (degrees)	R strip. (cm)
^{12}C	4/6	45.8	112	88.17
^{12}C	4/6	60.8	106	87.89
^{18}O	6/8	29.2	60	84.17
			118	87.73
^{18}O	6/8	45.5	68	84.65
			110	87.13
^{18}O	6/8	60	80	84.55
		60.9	106	88.04
^{18}O	6/8	65	88	84.86
^{20}Ne	7/10	29	122	87.64
^{20}Ne	7/10	45.6	114	87.90
^{20}Ne	7/10	60.3	108	87.04
^{20}Ne	7/10	71	108	87.81

Since the stripping extraction is a multi-turn extraction, the extracted beam will have a significant energy spread that we assume to be ≈ 0.3 % for all the considered cases. This energy spread value was initially evaluated using analytical formulas [10], but was also confirmed by some simulations using the SPIRALGAP code to evaluate the radial and energy distributions of a 20.000 accelerated particles from 1 AMeV up to the stripper position. The initial particle distributions were uniform in the range ±10° RF and inside the radial and axial eigenellipse at 1 AMeV.

One of the most relevant results of this study is that only two passive magnetic channels (MCs), named MC1S e MC2S, along the new E.C., are sufficient to permit the extraction of the beams of all ions of interest with different charge states and energies. Although MC1S and MC2S dimensions are quite far from standard as it will be illustrated below, this result reduces considerably the complexity of the stripping extraction system.

The magnetic channels will be inserted out of the radius pole to compensate the radial defocusing effect of the fringing field of the CS and to slightly steer the beam direction along the new E.C. They are iron correctors characterized by a deflecting magnetic field and a constant focusing gradient dBz/dR within the beam aperture.

For each ion, we determined with ESTRAZ the best values of the dipole and quadrupole component for the magnetic channels able to maintain the beam dimensions within the fixed values and able to direct the beam as near as possible to the exit point.

We fixed the gradient for both magnetic channels at 1.8 kG/cm, which is the highest value found for this study (it is relative to ^{18}O at energy 65 AMeV). Simulations demonstrated that this gradient permits the extraction of all ions. As an example, Fig. 2 illustrates the radial and

ISBN 978-3-95450-167-0

axial beam envelopes of ^{18}O at energy 65 AMeV computed with ESTRAZ. On the other hand, simulations show that the steering action of each magnetic channel must be different for each ion. That means that the reference trajectory has to enter the MC in a different point. Then, it is necessary to move the channels opportunely. The maximum horizontal displacement for both MC1S and MC2S is 60 mm. This value is the same for B1S and B2S, which are two compensating bars to restore the three-fold symmetry of the main field.

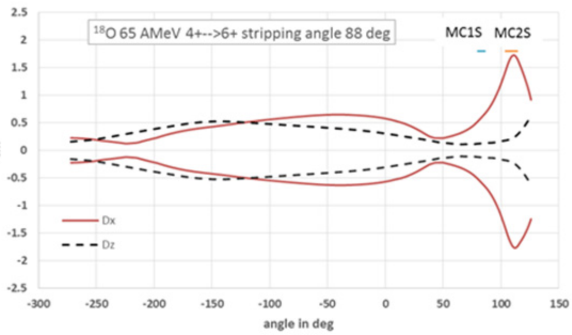

Figure 2: Radial and axial beam envelope of ^{18}O at 65 AMeV along the extraction trajectory. The energy spread is 0.3 %.

The first harmonic component of the field is mainly created by the first block of MC1S, which is the closest to the centre of the machine. The two iron bars have size 120x30x35 mm and have to be installed at ±120° respect to the position of the first block of MC1S and at R=950÷990 mm. Figure 3 shows a picture of the new compensation bars B1S and B2S and of the new magnetic channels MC1S and MC2S within the CS.

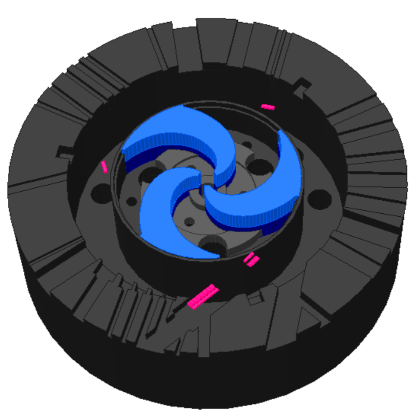

Figure 3: Picture of half CS showing the new magnetic channels and the new compensation bars relative to the new stripping extraction.

DESIGN OF THE MAGNETIC CHANNELS

The design of the magnetic channels is a key point in the present study, due to the request of a large clearance necessary to accommodate the new, larger, beam envelopes.

The magnetic channels used in the existing E.C. of our cyclotron were computed using the three bars technique [11], and the current sheet approximation, CSA, [12], which is valid in the case of uniform magnetization of the iron in an external magnetic field higher than 0.5 T.

Although MC1S, MC2S, B1S and B2S lay in the region of magnetic field higher than 0.5 T and this approach could imply a faster computation time, it cannot be used in our case. Indeed, to use the CSA, the new magnetic channels should be placed in a region of the CS where the main magnetic field is fully perpendicular to the median plane. This is not our case, therefore even if the value of the magnetic field is high enough to magnetize the iron, the magnetization vectors are not perpendicular to the median plane, then the field produced by iron MCs is different from the one produced using only coils as CSA does.

Moreover, the new MCs have more than three bars, since the gradient of the field produced by three bars, as it is in the existing MCs, is constant on a length of only few mm, much lower than the present requirements of 4 cm.

However, as a starting point to define the profiles of the MCs, we simulated the channels in CSA. Once we got the profiles to produced the needed field, we evaluated the field differences with the case of the MCs made by iron volumes and placed where they really will be. Then, we compensated them slightly changing the iron profiles in few interactions of field computation with OPERA 3D. As an example, in Fig. 4 the half of the final geometrical configuration found for the magnetic channel MC1S are shown, as well as the deflecting magnetic field and gradient really seen by the particles.

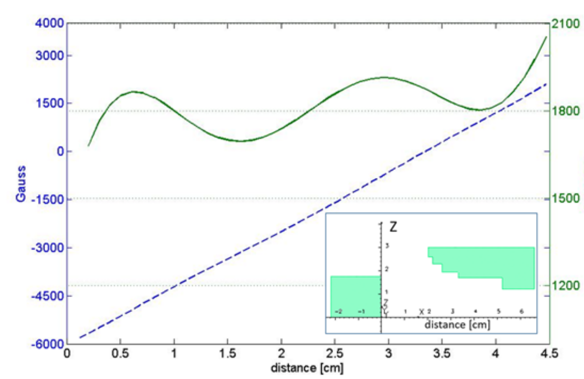

Figure 4: Geometry, dipole and quadrupole component of the magnetic channel MC1S (z=0 is the plane of symmetry).

ISBN 978-3-95450-167-0

FORCES

For the new magnetic channels and compensation bars, we evaluated the forces acting on them. Defining the z-axis perpendicular to the acceleration plane, Table 2 contains the components of the forces along the x and y directions for the magnetic channels and compensation bars in the two extreme configurations.

We evaluated also the vertical forces between the two pieces of iron, which are above and below the median plane, for each magnetic channel at each MC position.

This value does not change too much and stays always below 1.4 kN. In contrast with what happens when two iron pieces are in a vertical uniform magnetic field, the two symmetric pieces of the MCs repel each other. Indeed, they are between the upper and lower coils where the lines of the magnetic flux bend themselves around the coils attracting the iron pieces.

Table 2: Forces Acting on MCs and Compensation Bars

	At The Inner Position		At The Outer Position	
	Fx (N)	**Fy (N)**	**Fx (N)**	**Fy (N)**
MCS1	-588	6759	-936	8216
MCS2	-1330	-2490	-1060	-2330
B1S	2693	-1282	3864	-1729
B2S	2474	-1710	-3429	-2490

CONCLUSIONS

With this study we achieved the goal to fix the features of the new extraction channel necessary for the stripping extraction. We decided the cross-section and best azimuthal position for the new channel. We identified two main areas for positions of the stripper foils, and we accomplished the beam dynamics study to extract all ions of interest with the help of only two movable magnetic channels, whose iron profiles are able to generate the needed dipole and quadrupole components for each case. We also fixed angular and radial positions and dimensions of two iron bars, whose task is to compensate the first harmonic component produced by the two magnetic channels.

Furthermore, we performed the study of the forces on all these new elements.

REFERENCES

[1] A. Calanna *et al.*, in *Proc. IPAC'15*, pp. 3779-3781.

[2] C. Agodi *et al.*, *Nuclear and Particle Physics Proceedings* 265–266 (2015) 28–30.

[3] F. Cappuzzello *et al.*, *Eur. Phys. J.* A (2015) 51: 145.

[4] G. Raciti *et al.*, Nucl. Phys.; Sec A; Vol. 834; Issue: 1-4; March 1; 2010; pp. 780c-783c

[5] A. Radovinsky *et al.*, "Design of a superconducting magnet for the LNScCyclotron", *IEEE Transactions on Applied Superconductivity*, Volume:26 , Issue: 4, June 2016

[6] L. Calabretta *et al.*, "Upgrade of the LNS supeconducting cyclotron for beam power higher than 5 kW", presented at Ccyclotrons'16, Zurich, Switzerland, September 2016, paper MOA02, this conference

[7] Atomic Data and Nuclear Data Tables, Vol. 51, No. 2, July 1992, Table 2 pag.187

[8] M. M. Gordon, *Particle Accelerators* 1984, Vol.16, pp 39-62.

[9] Opera-3D Reference Manual version 18R1, Cobham, Vector Fields Ltd., UK

[10] S.S. Tomic, E. V. Samsonov, *Phys. Rev.* E, Vol. 65, 036504, 2002.

[11] E. Fabrici and A. Salomone, INFN report INFN/TC- 87/4, 1987.

[12] M. M. Gordon and D. A. Johnson, "Calculation of fields in a superconducting cyclotron, assuming uniform magnetization of the pole tips", *Particle Accelerators*, 10:217, 1980.

ISBN 978-3-95450-167-0

COLD CATHODE ION SOURCE FOR IBA CYCLONE®230

Ph. Cailliau*, J. Brison, E. Forton, J-C Amelia, Ion Beam Applications, B-1348 Louvain-la-Neuve, Belgium
J. Mandrillon, M. Conjat, P. Mandrillon, AIMA, F-06200 Nice, France

Abstract

At IBA, we use a P.I.G. floating cathode ion source for injection in the CYCLONE®230 cyclotron. The purpose of the project is to investigate how the present ion source could be replaced by a P.I.G. cold cathodes one with a longer lifetime. Experiments described in this article were done on a dedicated test setup to benchmark the different modes. A new chimney design has been developed to test cold cathode mode in CYCLONE®230 without any other mechanical modifications.

INTRODUCTION

The floating cathode source uses a tantalum filament which needs to be replaced typically every 5 to 7 days. Cold cathodes ion sources are already used in other IBA cyclotrons and allow a much longer period between two maintenance operations. H^+ cold cathode ion source has been developed with AIMA for the new synchro-cyclotron. Pulses are very short (few µs) during capture process in the synchrocyclotron, but much longer pulses (few ms) are produced in the isochronous CYCLONE®230 cyclotron.

TEST CAMPAIGN

The test bench developed with AIMA for the synchro-cyclotron source five years ago was modified to allow vertical insertion of the CYCLONE®230 source shaft in the same setup. The 1.7 Tesla large aperture magnet (see Fig. 1) and all the equipment were installed on an elevated platform, so the ion source can be vertically inserted in the vacuum box (see Fig. 2).

Figure 1: 1.7T test magnet and the vacuum system at AIMA.

Figure 2: CYCLONE® 230 source arm mounted on a dedicated insertion system underneath test magnet.

The three measurement plates collecting the different ion species and the puller electrode are at DC high voltage (15kV). The ion source is at ground potential. All these elements are located in a vacuum chamber as shown in Fig. 3.

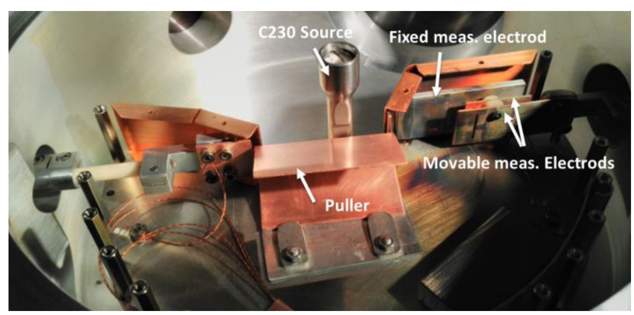

Figure 3: Test bench vacuum chamber, high voltage top plate removed. One can observe the chimney, the puller and measurement electrodes.

Arc and filament power supplies are standard CYCLONE®230 equipment. In floating cathode mode, we operate at arc voltage (Varc) below 200V. Since the cold cathode mode requires at least 800V to light up a plasma, the arc power supply was modified to generate pulses up to 500V and an additional 1 kV commercial DC power supply was connected in series.

FLOATING CATHODE SOURCE BASELINE

The first experiment consisted in recording a baseline of the actual floating cathode ion source on the test bench. The aim is characterising the source performances as function of parameters of its own design, i.e. independently of the isochronous machine central region environment. The extraction gap has been minimized for 15 kV extraction voltage and fixed on the setup.

*philippe.cailliau@iba-group.com

ISBN 978-3-95450-167-0

During a treatment scanning sequence the arc current (Iarc) is fast scanned over a large band: Iarc ramps are suitable to observe the complete band of operating points, for a given set of parameters.

To obtain the pulse illustrated in Fig. 4, gas flow is 2SCCM (optimized value), chimney slit dimensions are nominal, filament current is set in order to maximize arc power, i.e. Varc is saturated (220 V) at maximum Iarc setpoint (330 mA). Up to 2.8 mA instantaneous H+ current (IH+) can be produce on this condition.

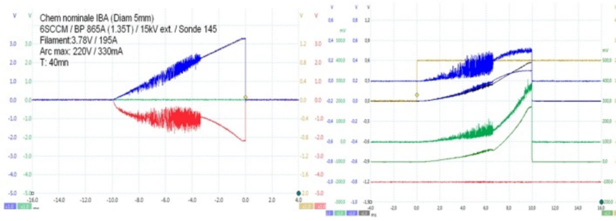

Figure 4: Left: Arc parameters, Iarc setpoint in blue, from 0 to 300mA in 10ms, Varc in red (min=-200 V); Right: H+ current (IH+) measurement in green (max=2.8 mA), other species (H_2^+ and H_3^+) total current measurement in blue (max=5 mA).

For higher filament current, Varc and IH+ are smaller for a given Iarc set point. Since we have modified the power supply to study the behaviour at higher Varc (up to 500 V) new working points have been investigated during this 'baseline' campaign with the filament source. Moreover, hot cathode modes with various types of polarisation have been tested as well. The main observation could be similar in all these potential improvements: bringing more power in the arc can either increase the H+ production, or reduce the filament current, which should impact its lifetime.

COLD CATHODE EXPERIMENT

We first removed the filament and mount a Tantalum cathode on its support to brought it to arc potential. To power the anti-cathode, we created a new isolated connection in the vacuum box.

Iarc and Varc of one hundred pulses (1ms length) are shown in Fig. 5. Gas flow is optimized at 5SCCM for nominal chimney slit size. A DC constant polarization of 740 V is superposed with pulsed Varc. Iarc setpoint is 70 mA. In that configuration the pulsed Varc reaches -220 V at the end of pulses (see Fig. 5), which is the saturation value of arc power supply of CYCLONE®230.

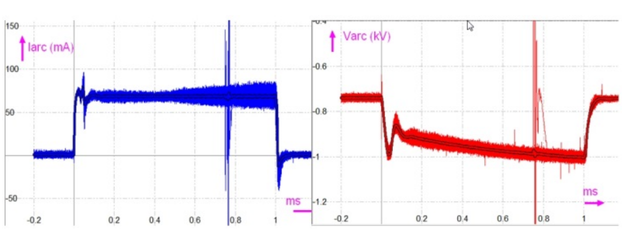

Figure 5: 100 Arc pulses of 1 ms produced at 50 Hz. Iarc (blue) and Varc (red).

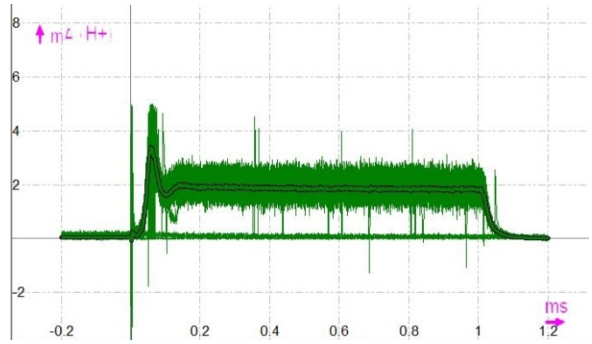

Figure 6: 100 H+ current pulses of 1ms produced at 50Hz repetition rate.

In Fig. 6 we observe the one hundred IH+ pulses obtained with these settings. 2000 νC mean charge per pulse is measured, pulse to pulse charge stability is 2.7% of mean value (1σ). Ignition overshoot last around 50 µs and reaches 3.5 mA maximum value. For a given Iarc set point and a given slit size, we observed higher protons production in cold cathodes mode than in floating cathode mode. Ignition overshoot amplitude and length decrease with dVarc/dt which is an increasing function of Iarc (with our power supply). We decided to reduce the size of the chimney slit by a factor 3 in order to work at higher Iarc set points, which strongly reduces the overshoot for a given IH+ production. This modification also leads to higher stability of the charge per pulse. Beam transmission in CYCLONE®230 central region will be increased, and it reduces optimal gas flow from 5SCCM to 1SCCM.

Another option to get rid of the overshoot applying enough DC arc voltage is to avoid ignition, i.e. maintaining a (very) small DC extracted beam. In that case CYCLONE®230 control system would have to eliminate this 'dark current' between pulses.

We have investigated production of longer pulses at high repetition rate in order to demonstrate that cold cathode mode can be suitable for uniform scanning/ double scattering US/DS treatment modes. Pulses of 9 ms at repetition rates up to 100 Hz are generated.

For a given Iarc set point, we observe that Varc is an increasing function of the repetition rate. 100 arc pulses of 9 ms at 100 Hz are illustrated in Fig. 7. Only pulsed Varc is plotted (in red), 600VDC Varc is applied in series. Stable pulses were obtained with 1050 V total arc voltage for 30 mA Iarc, when 850 V are required at 10 Hz repetition rate. In order to work with long pulses in cold cathodes mode power supply will have to deliver more voltage, and arc current is limited to 30 mA for 1000 V total arc voltage. Nevertheless, H+ production is sufficient with the nominal slit size in that case.

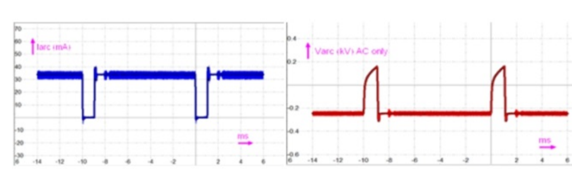

Figure 7: Arc current (blue) and arc voltage (red) for longer pulses.

ISBN 978-3-95450-167-0

COLD CATHODE, USING LAB6

Setup was modified to test Lanthanum Hexaboride (LaB6) cathodes, see Fig. 8.

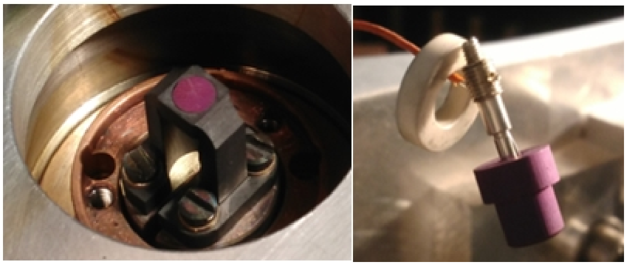

Figure 8: Left: LaB6 cathode chip and support, installed on CYCLONE®230 filament support. Right: LaB6 a-cathode with polarization pin.

As shown in Fig. 9, Ignition potential is 400 V, which can we obtained with the CYCLONE®230 arc power supply with small modifications. Improvements are mandatory to increase dVarc/dt in order to avoid overshoots and oscillations at ignition.

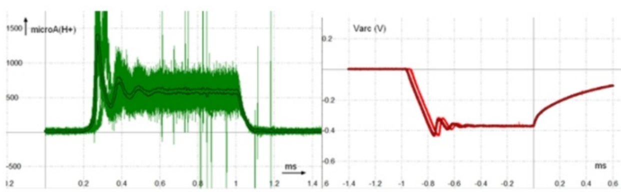

Figure 9: 100 IH^+ pulses (left) and Varc with Lab6 cathodes (right).

NEW CHIMNEY DESIGN

A new chimney design needed to be developed in order to validate some of these concepts in the CYCLONE®230 IBA cyclotron. It is mechanically compatible with the present cyclotron central region design.

In the new design a polarization is brought to the anti-cathode through a small vertical pipe in the chimney body connecting the cathode and the anti-cathode electrically, see Fig. 10.

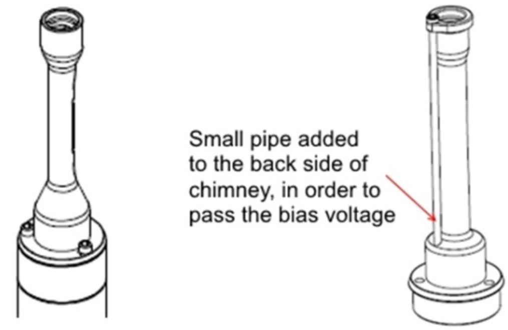

Figure 10: Regular floating cathode chimney vs modified cold cathode chimney.

Cold cathode source is currently being produced and should be tested on site in Q4 2016.

CONCLUSION

The results obtained on test bench confirm that cold cathodes mode is an alternative to filament solutions with a potentially longer life time. Possible improvements on filament source have also been identified and tested. It has been verified that cold cathodes mode is suitable for long pulses at high duty cycle rate. A new chimney design is being built. Full integration in CYCLONE®230 systems requires a new power supply with a faster regulation in order to avoid prohibitive overshoot at arc ignition.

ISBN 978-3-95450-167-0

EXTRACTION SYSTEM DESIGN FOR THE NEW IBA CYCLOTRON FOR PET RADIOISOTOPE PRODUCTION

W. Kleeven*, E. Forton, E. Kral, B. Nactergal, V. Nuttens, J. Van de Walle, S. Zaremba
Ion Beam Applications (IBA), Louvain-la-Neuve, Belgium

Abstract

At IBA, we have designed, constructed, tested and industrialized an innovative isochronous cyclotron for PET isotope production. The design has been optimized for cost-effectiveness, compactness, ease of maintenance and high performances, with a particular emphasis on its application and market. Multiple target stations can be placed around the vacuum chamber. An innovative extraction method (patent applications pending) has been designed which allows to obtain the same extracted beam sizes and properties on the target window independent of the target number. This is achieved by proper design and shaping of the magnet poles. This magnetic design is discussed together with beam dynamics simulations and beam extraction tests on the first machine.

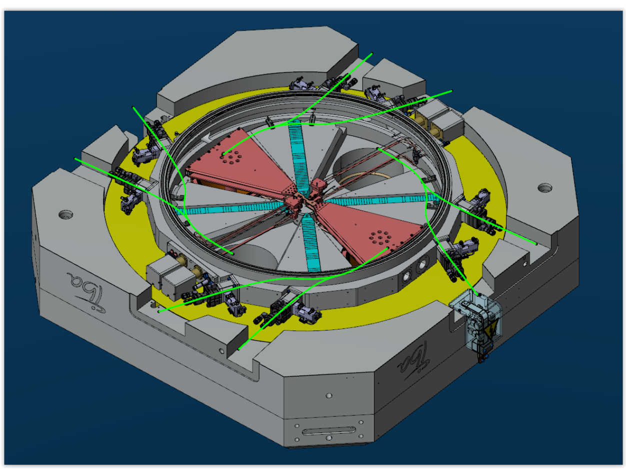

Figure 1: View on the upper half of the CYCLONE® KIUBE. In grey is shown the magnetic iron including the return yoke and the four poles. The pole-inserts (in blue) are used to shim the isochronous field. Further shown is the main coil (yellow), the accelerating structure (red) and the 8 target stations mounted on the vacuum chamber. The extracted orbits are shown in green.

INTRODUCTION

Modern medical radioisotope production cyclotrons often accelerate negatively charged ions such as H^- and/or D^-, because this allows for an easy way of extraction: the beam passes a thin stripper foil which removes the two electrons attached to the ion, resulting in an instantaneous change of sign of the orbit local radius of curvature such that the particles are directed towards the exit of the pole region. The method has several advantages: i) the very simple extraction device, ii) 100% extraction efficiency, iii) the possibility for simultaneous dual beam extraction, iv) the possibility to place several targets around the machine and and v) good beam optics. This technique is also used in the well-known IBA CYCLONE® 18/9 [1]. This cyclotron accelerates H^- to 18 MeV and D^- to 9 MeV. In recent years, the need for D^- has gradually decreased and therefore IBA decided to design the CYCLONE® KIUBE [2,3] as a new PET cyclotron accelerating only H^-. In this new machine we re-visited the extraction design to implement possible improvements. Figure 1 shows a view on the upper half of this new cyclotron.

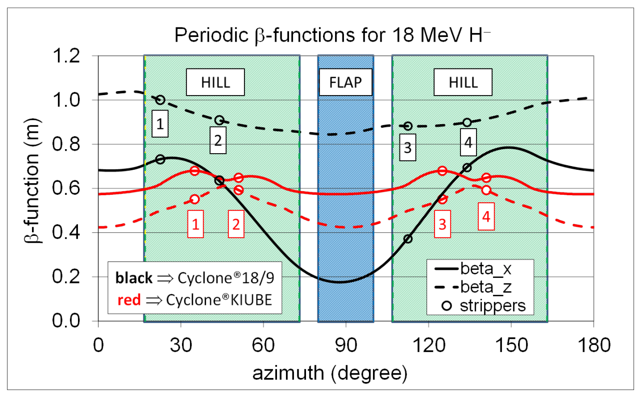

Figure 2: Periodic horizontal (solid) and vertical (dashed) β-functions along the 18 MeV closed orbit. The red curves correspond with the CYCLONE® KIUBE. For comparison, the same curves are given for the CYCLONE® 18/9 [1]

EXTRACTION DESIGN

A maximum of 8 targets can be placed around the cyclotron vacuum chamber for isotope production. For the new extraction design we looked for an optical solution such that the beam sizes on these targets i) are more or less independent of the target position and ii) have a more or less circular shape. In the CYCLONE® 18/9 the switch of the isochronous magnetic field shape from D^- to H^-, is done by two movable iron inserts (the flaps), placed in two opposite valleys. In the H^- mode, these flaps are moved close to the median plane and there introduce a considerable 2nd harmonic magnetic field component. This makes that the extracted beam optics towards the targets is quite different for extraction on the pole upstream or the pole downstream of the flap-valley.

The linear beam optics can be conveniently represented with the beta-function Twiss-parameter. The beam size X

* willem.kleeven@iba-group.com

ISBN 978-3-95450-167-0

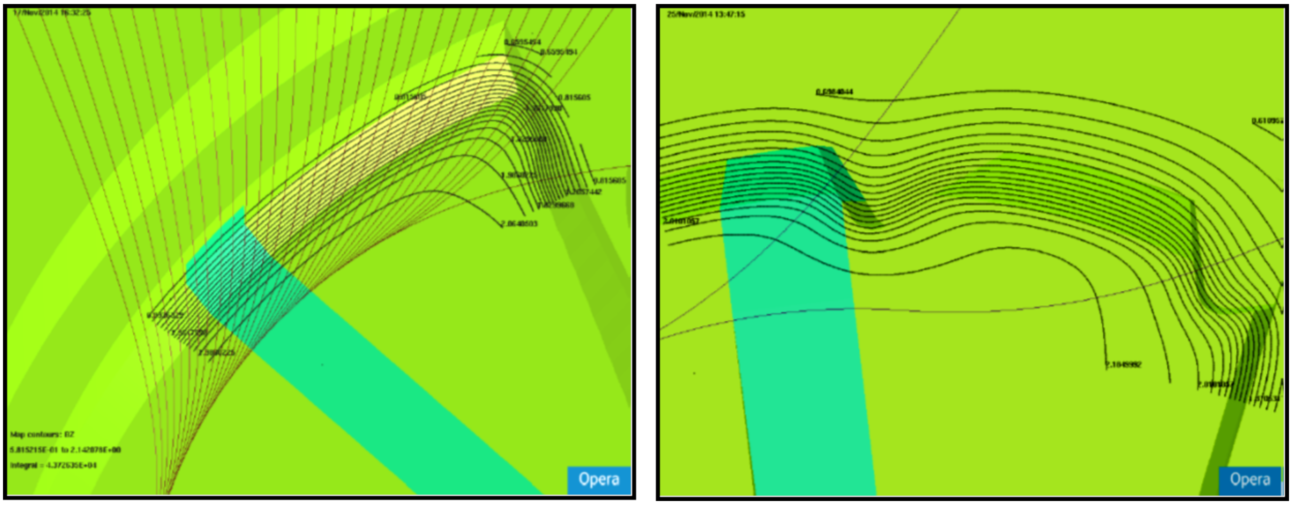

Figure 3: Iso-field lines are shown on top of the OPEAR3D model in the region of the pole radial boundary. Also shown are trajectories of a series of particles extracted at various angular positions of the stripping foil. The left figure shows that there is a rather large angle between the particle direction and the normal vector of the field-lines. This condition leads to a rather large vertical defocusing. The figure on the right shows the modification of the magnetic field pattern due to the iron cuts placed at the pole exit azimuth of the particles. Here the vertical defocusing is much weaker.

(or Z) and the beta-function β_x (or β_z) are related via the beam emittance ϵ_x (or ϵ_z) as $X = \sqrt{\epsilon_x \beta_x}$.

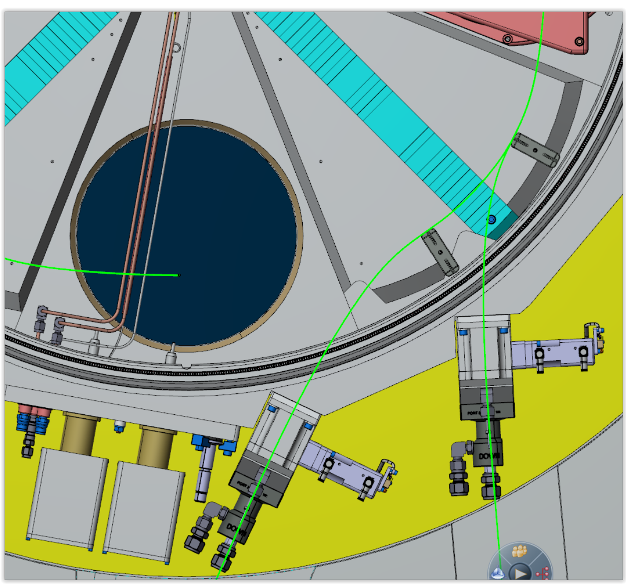

Figure 4: The radial pole contour is (a part of) an off-centred circle which closely follows the shape of the closed orbits near extraction. The pole cuts are shown and also the stripper-carousels and the extracted orbits (in green) hitting the isotope production targets.

The periodic β-function is calculated along the closed orbit and has the same n-fold symmetry. Figure 2 shows the horizontal and vertical periodic β-functions on the 18 MeV closed orbit in both the CYCLONE®18/9 (symmetry n=2) and the CYCLONE®KIUBE (symmetry n=4), as calculated with the IBA in-house tracking code AOC [4]. Also the position of the stripper foils is shown. For the CYCLONE®18/9 the horizontal β-function shows a strong variation (with about a factor 4) along the azimuth making that the optical conditions at the four stripping foil positions are substantially different. This results in substantial different beam sizes on the targets. For the CYCLONE®KIUBE this variation is much weaker. Furthermore (due to the 4-fold symmetry) the conditions from one pole to the next remain the same. It is also seen that the vertical focusing in the CYCLONE®KIUBE is substantially stronger.

In the CYCLONE®KIUBE the radial contour of the pole is a circle which is off-centred from the cyclotron geometrical centre. This circular contour very closely follows the shape of the 18 MeV equilibrium orbit. This can be seen more clearly in Figure 4. In this way, the distances from the stripper to the radial pole edge and from the stripper to the target become almost independent of the angular position of the stripper and thus also guarantees close to equal beam-spots on the target.

When the particles cross the radial pole edge, they may experience a strong vertical defocusing due to the rather large angle between the beam direction and the normal vector on the pole-contour. This then results in a largely asymmetric beam spot on the target window and thus corresponding larger losses on the circular target collimator. In order to reduce this asymmetry, a local cut has been made in the iron of the pole at the crossing angle with the beam. This can be seen in Figure 4. The modification of the iso-magnetic field lines is illustrated in Figure 3. It is seen that the extracted orbits are more perpendicular to the iso-field lines.

OPTIMIZATION AND SIMULATIONS

The geometry of the pole-cuts have been optimized in Opera3D and by particle tracking with AOC. Figure 5 shows the horizontal and vertical beta-functions along the path of

ISBN 978-3-95450-167-0

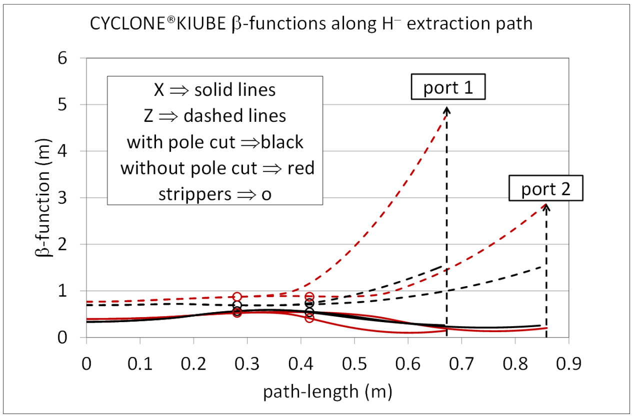

Figure 5: Horizontal (solid) and vertical (dashed) β-functions along the path of the extracted orbits. A comparison is made to show the effect of the pole cuts. Stripper positions are also shown.

the extracted orbits from the middle of the upstream valley up to the target window. Results are shown for both targets. The final pole-cut configuration is compared with a configuration without pole cut. The effect of the pole cut is clearly seen by the substantial decrease of β_z on the target window for both extraction ports.

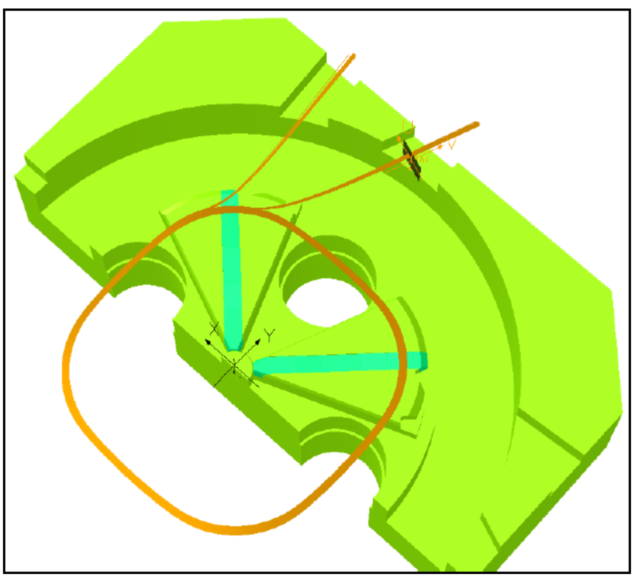

Figure 6: Trajectories are numerically integrated with the IBA in-house tracking code AOC [4] and imported into the finite element model of the CYCLONE®KIUBE magnet as developed in OPERA3D [5]. Two stripper foils placed on one pole extract the beam towards the corresponding targets. The beam spot and phase space is analysed on a patch, placed at the target entrance window.

In order to validate these results also in the non-linear condition, we tracked in AOC a beam of 1000 particles with an RF phase width of 40° and initial transverse emittances of 50 π mm-mrad from 1 MeV in the cyclotron center through the stripper foils and up to the target windows. Figure 6 shows an import of the last few turns of the computed beam into the Opera model. Then an intersecting patch is placed at the target window in order to see the beam cross-section. The result is shown in Figure 7. Here the configuration with and without pole-cuts are compared for both exit ports. It confirms that indeed a substantially better (more symmetric) beam spot is obtained on the targets.

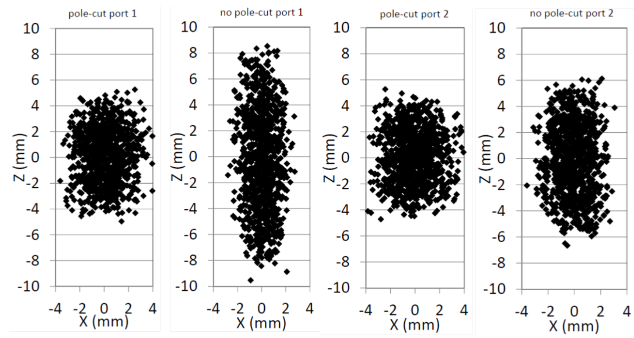

Figure 7: The beam spot on the target windows as simulated with AOC. It is seen that a more symmetric (round) shape is obtained due to the pole cuts and also that both extraction ports are almost of same shape.

CONCLUSION

The prototype of the CYCLONE®KIUBE has been successfully commissioned at the IBA-sites in Louvain-La-Neuve and is currently being installed on the customer site. The performance of the machine well exceeds the CYCLONE®18/9 in terms of beam transmission between the ion source and the stripper foils, the extraction efficiency between the strippers and the targets and also in terms of the 18-F production yields. The extraction efficiency (defined as the ratio between target current and target + collimator current) is for all 8 target positions, between 90 and 95% for a collimator diameter of 9 mm.

REFERENCES

[1] `http://www.iba-cyclotron-solutions.com/sites/default/files/ressources/C18-9_R05.pdf`

[2] E. Kral *et al.*, "Development of a new IBA cyclotron for PET production", presented at the 21th Int. Conf. Cycl. Appl., Zurich, Switzerland, Sep. 2016, paper TUD03, this conference.

[3] S. Zaremba, W. Kleeven, J. Van de Walle, V. Nuttens, S. Deneuter, and M. Abs, "Magnet design of the new IBA cyclotron for PET radioisotope production", presented at the 21th Int. Conf. Cycl. Appl., Zurich, Switzerland, Sep. 2016, paper TUP04, this conference.

[4] W. Kleeven *et al.*, "AOC, a beam dynamics design code for medical and industrial accelerators at IBA", in *Proc. 7th Int. Part. Acc. Conf.*, Busan, Korea, May 2016, paper TUOOY002, pp. 1902-1904.

[5] Cobham, `http://operafea.com`

ISBN 978-3-95450-167-0

MAGNET DESIGN OF THE NEW IBA CYCLOTRON FOR PET RADIO-ISOTOPE PRODUCTION

S. Zaremba*, W. Kleeven, J. Van de Walle, V. Nuttens, S. De Neuter, and M. Abs
Ion Beam Applications, Louvain-la-Neuve, Belgium

Abstract

An innovative isochronous cyclotron for PET isotope production has been designed, constructed, tested and industrialized at Ion Beam Applications (IBA) [1]. The design has been optimized for cost-effectiveness, compactness, ease of maintenance and high performance,which are key elements considering its application in the dedicated market. This cyclotron (patent application pending) produces 18 MeV protons and the cyclotron is called the **Cyclone® KIUBE**. Compared to the previous 18 MeV proton and 9 MeV deuteron machine from IBA, the Cyclone®18/9, the gap between the poles has been reduced from 30 mm to 24 mm and the method of pole shimming to obtain an isochronous magnetic field has been reviewed thoroughly. In early 2016, the first prototype Cyclone® KIUBE was successfully commissioned at the IBA factory and the measured proton beam intensity outperformed the Cyclone® 18/9.

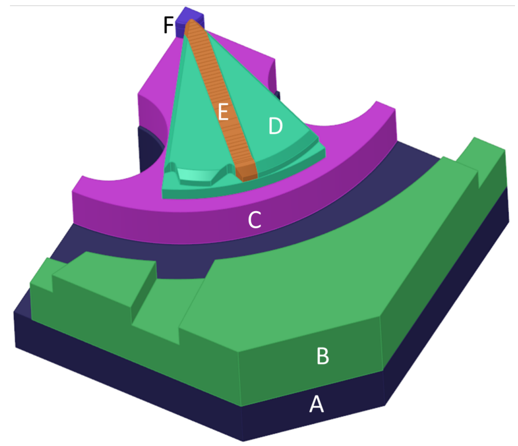

Figure 1: The magnetic circuit, including (A) the return yoke, (B) lateral return yoke, (C) sector, (D) the pole, (E) the pole insert and (F) the central plug.

MAGNET DESIGN

The magnetic design of the Cyclone® KIUBE was performed with the OPERA-3D code in combination with IBA's in-house beam dynamic codes. One symmetry period of the 4-fold symmetric Cyclone® KIUBE is shown in Fig. 1, where the (lateral) return yoke, the pole, the pole inserts (patent application pending) and sectors are indicated. The Cyclone® KIUBE fits a rectangular cuboid of 1740x1740x860 mm^3. The vertical gap between the pole faces has been reduced by 6 mm in the Cyclone® KIUBE, compared to the Cyclone® 18/9. This minor reduction allows to reduce the total current and power consumption and the overall size and weight of the cyclotron. The pole azimuthal length has been reduced from 55 degrees to 45 degrees. In this way, the valleys become wider and the pumping hole in the valley can be made bigger. It increases the pumping efficiency and improves the vacuum level. As such, beam losses of the H$^-$ ions can be reduced and the transmission efficiency can be increased. The position of the pumping holes is shown in Fig. 2. The vacuum chamber is located between the coil and the outer radius of the pole. The cut corners of the square cyclotron are filled at two opposite locations by the yoke lifting system, whereas the remaining two opposing corners are left free for auxiliary equipment. Two small openings in the lateral return yoke are present for the coil cooling and electrical connections. These holes break the four-fold symmetry of the complete cyclotron, but do not introduce large second harmonic imperfections, as will be shown in Fig. 6. The larger iron volume of the lateral return yoke next to the poles promotes the magnetic flux passage, thereby creating a sufficiently large flutter in the median plane.

A view on the pole is shown in Fig. 3. A "groove" is present in the center of the pole to accomodate the pole insert (see next paragraph). Two stripping extraction systems per pole give the possibility to install 8 targets in the different extraction ports (4) in the lateral return yoke.

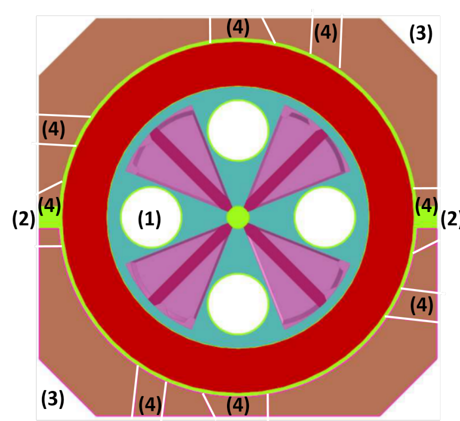

Figure 2: A top view on the Cyclone® KIUBE. 1/ the four pumping holes in the valleys, 2/ the coil electrical and cooling ports, 3/ the yoke lifting system and 4/ the extraction ports.

POLE INSERTS

The pole inserts in the Cyclone® KIUBE are the novel approach to the traditional pole edge milling (used in the Cyclone®18/9) during the magnetic mapping of the

* simon.zaremba@iba-group.com

ISBN 978-3-95450-167-0

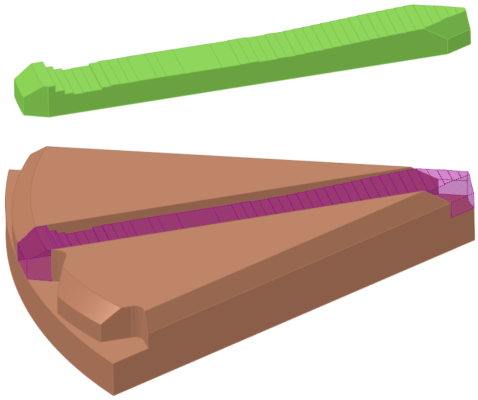

Figure 3: A view on the Cyclone® KIUBE pole. A groove is present in the middle of the pole to accomodate the pole insert. The pole insert is shown as well, where the milling profile on the face closest to the median plane is visible. The azimuthal length of the pole is 45 degrees and gradient corrector cuts on the pole outer border are present to facilitate the extraction from the cyclotron (see [2]).

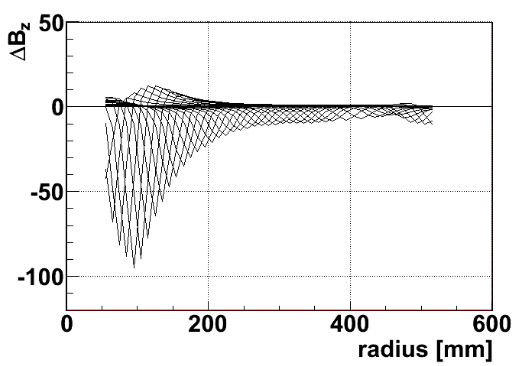

Figure 4: The effect on the average field of iron milling on the pole insert. These curves correspond to 24 identical cuts of 10 mm radial width and 5 mm depth on different radial positions.

cyclotron to obtain an isochronous magnetic field. As can be seen in Fig. 3, a large "groove" is present in the pole, which extents from the center tip of the pole to the outer edge. Inside these grooves, the pole inserts are mounted. This new design and milling method was optimized in collaboration with the machining subcontractor in order to achieve the optimum cost and time effectiveness. At the same time, the new milling method reduces possible harmonic errors due to small machining errors on the four identical pole inserts. The final shape of the pole insert is presented in Fig. 3 without the necessary holes to fix it to the pole. As seen in Fig. 3, each pole has a large, deep groove for the pole insert and two gradient corrector cuts (patent application pending) on the outer pole edge to improve the beam extraction optics [2]. The outer pole edge (patent application pending) is made of two steps to optimize the magnetic flux flow close to the extraction radius. The first step, touching the sector, has its outer edge that follows the sector geometry. The second chamfered step, close to the median plane, has its outer edge similar to the last turn trajectory.

In the prototype, the initial pole insert filled the groove

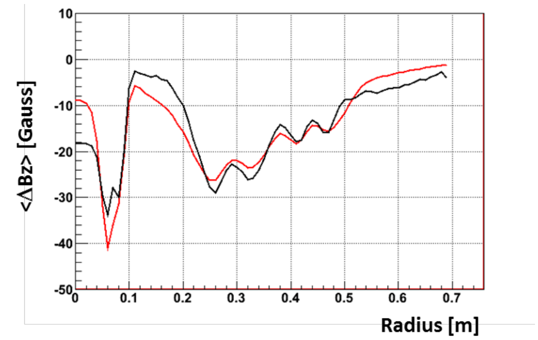

Figure 5: Comparison of a calculated and measured magnetic effect after milling of the pole insert.

up to the pole surface. Detailed OPERA3D calculations were made to assess the magnetic effect of the pole insert milling. The effect of removing a 10 mm long and a 5 mm deep triangular piece of iron was evaluated at several radial positions on the pole insert. The change in average field on each radius was evaluated and a so-called "shimming matrix" was constructed. Typical profiles are shown in Fig. 4. Figure 5 shows a comparison of a simulated milling effect (on the average field) and the measured magnetic effect (the difference of the average magnetic field in a magnetic map before and after the milling). The shimming matrix changes with the cutting depth and has been recomputed for the final profile of the pole insert. For the next cyclotrons, the initial profile of the pole insert is close to the prototype final profile and the shimming matrix corresponding to the final profile is used to reduce milling iterations.

MAPPING RESULTS

Figure 6 compares the first and second harmonics in the Cyclone® KIUBE and the Cyclone® 18/9. The first harmonic is much lower than in the Cyclone® 18/9, most probably due to the more symmetric milling of the pole inserts, compared to the shimming of the pole edges in the Cyclone® 18/9. The high harmonic 2 in the Cyclone® 18/9 is due to the presence of movable pole inserts in the two opposing free valleys for the acceleration of 9 MeV deuterons, which are not present in the Cyclone® KIUBE.

The tune diagram of the Cyclone® KIUBE is shown in Fig. 7. The potentially destructive resonances near $2\nu_z$=1 and ν_r=$2\nu_z$ are rapidly crossed near 4 MeV due to the large energy gain per turn. From tracking calculations in the in-house particle tracking code AOC [3] and from experimental measurements on the Cyclone® KIUBE prototype, no important beam losses have been observed near 4 MeV.

Figure 8 shows the integrated phase slip as a function of the average equilibrium orbit radius in the prototype Cyclone® KIUBE and confirms the quality of the isochronous magnetic field after the final pole insert milling.

ISBN 978-3-95450-167-0

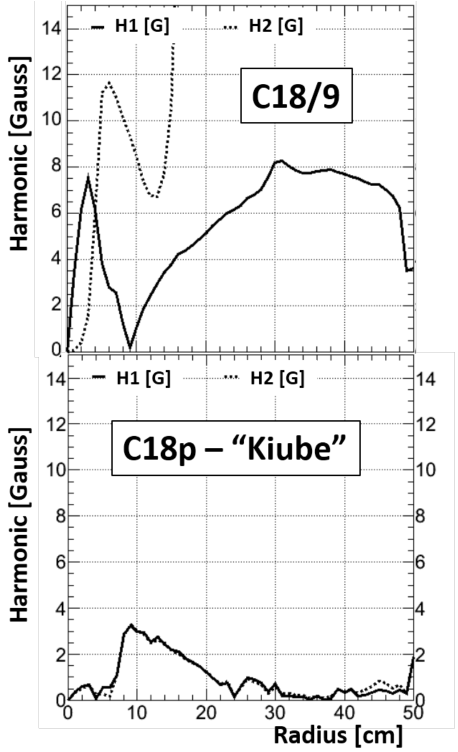

Figure 6: The 1st and 2nd harmonics in the measured magnetic map: (top) in the Cyclone® 18/9 and (bottom) in the Cyclone® KIUBE. The large harmonic 2 in the Cyclone® 18/9 is due to the presence of movable iron inserts in the valleys.

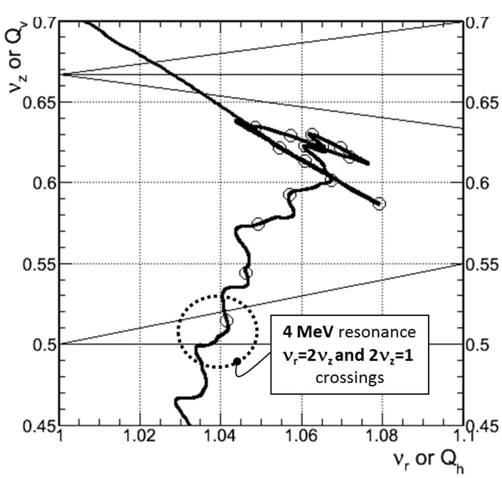

Figure 7: Tune diagram of the Cyclone® KIUBE.

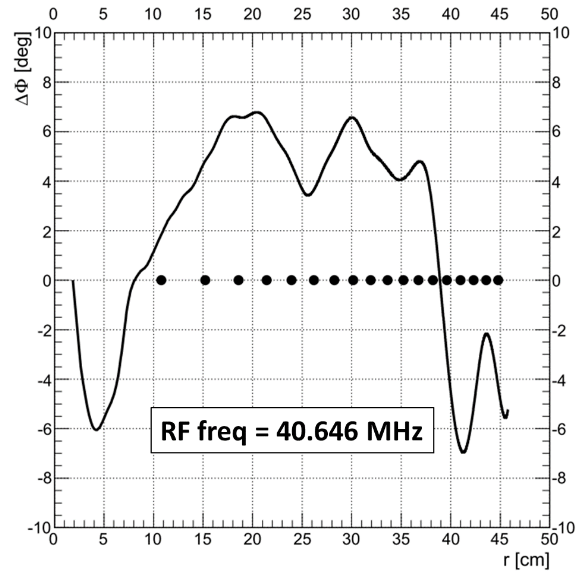

Figure 8: The integrated phase slip as a function of the average equilibrium orbit radius in the prototype Cyclone® KIUBE

CONCLUSION

The prototype of the Cyclone® KIUBE has been successfully commissioned at the IBA factory. The new IBA Cyclone® KIUBE outperforms the classical IBA Cyclone® 18/9 in terms of all important parameters (beam intensity, size, weight, pumping speed, beam transmission, extraction efficiency, power consumption) confirming the correct design of the cyclotron magnet and other cyclotron subsystems.

REFERENCES

[1] B. Nactergal *et al.*, "Development of a New IBA Cyclotron for PET production", presented at Cyclotrons'16, Zurich, Switzerland, Sep. 2016, paper TUD03, this conference.

[2] W. Kleeven *et al.*, "Extraction System Design for the New IBA Cyclotron for PET Radioisotope Production", presented at Cyclotrons'16, Zurich, Switzerland, Sep. 2016, paper TUP03, this conference.

[3] W. Kleeven *et al.*, "AOC, A Beam Dynamics Design Code for Medical and Industrial Accelerators at IBA", in *Proc. IPAC'16*, paper TUPOY002.

ISBN 978-3-95450-167-0

INSTALLATION AND COMMISSIONING OF THE Cyclone®70P: Zevacor PROJECT

B. Nactergal*, J-M. Geets, R. Vigneron, T. Vanderlinden, J-L. Delvaux, W. Kleeven, S.Zaremba, Ion Beam Applications (IBA), B-1348 Louvain-la-Neuve, Belgium

Abstract

In October 2013, IBA sold its first Cyclone®70p, extracted 70 MeV proton machine to Zevacor Pharma, Indianapolis, IN, USA.

This brand new machine combine the advantages of the design of the Cyclone®30 HC (1,5mA extracted beam) and the Cyclone®70 XP (multi-particle). Moreover, this high energy cyclotron has been optimized for H^- ions acceleration, activation reduction and long term beam production.

The installation will be used for high power and long term irradiations of rubidium Rb targets to produce strontium ^{82}Sr generator applied in the field of cardiac imaging.

From cyclotron to beam lines and up to the target station, all subsystems have been reviewed to reach highest level of quality, reduce the activation (by the use of low activation material and reduction of beam losses) and finally optimized the maintenance.

For that delivery, the machine will be equipped with 6 beam transport lines and 2 solid target station units.

In June 2015, about 21 months after contract signature, the IBA Factory Acceptance Tests have been successfully performed in Belgium and the machine was shipped to Indianapolis, IN, USA to be installed in Customer factory cyclotron vault.

RIGGING AND INSTALLATION

In September 2015, the Cyclone® 70P and auxiliary equipment have been successfully rigged (inserted) into the various vaults (see Figs. 1-3).

This 140 tons cyclotron and its surrounding equipment reached their final position in a few days allowing the installation start up.

The installation has been started according to ambitious schedule (3 months in advance of the contractual planning) thanks to a very good collaboration with the Customer during the whole building construction.

COMMISIONING

The Cyclone® 70P for Zevacor Pharma (Figs. 4-6)is delivering 70 MeV proton beam to up to 6 target vaults.

All those vaults (cyclotron and targets) have typically 4m concrete walls to shield it.

The beam is extracted thanks to stripper shaft (variable energy from 30 to 70 MeV) through 2 switching magnets located on each side of the cyclotron to the beam lines.

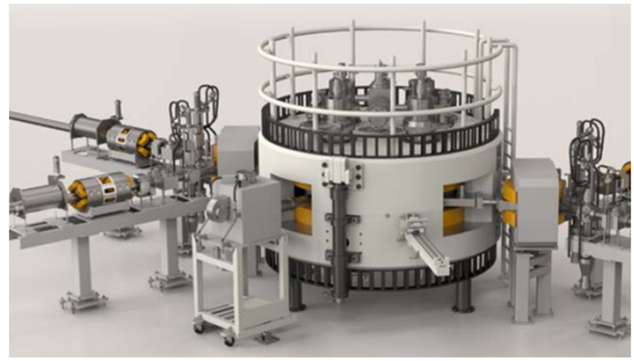

Figure 1: Cyclone® 70P general overview.

Figure 2: Cyclone® 70P rigging in Indianapolis.

Figure 3: Cyclone® 70P in vault in Indianapolis.

* benoit.nactergal@iba-group.com

ISBN 978-3-95450-167-0

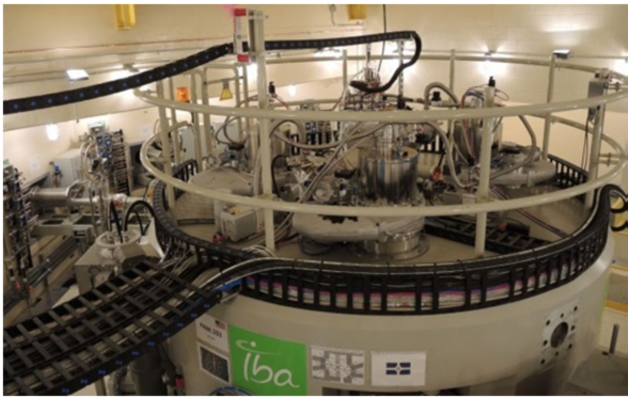

Figure 4: Cyclone® 70P : ion source.

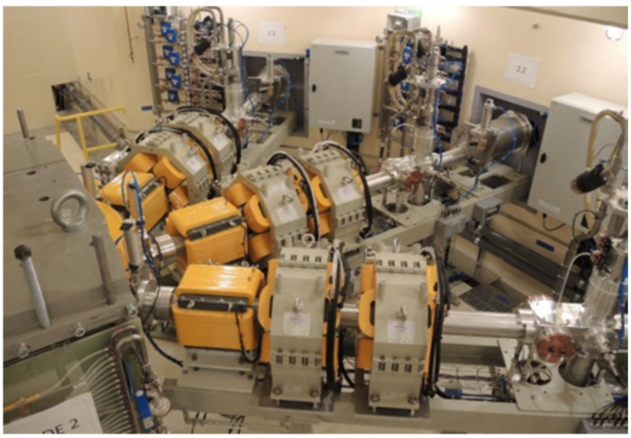

Figure 5: Cyclone® 70P: 3 beam lines on one side.

Figure 6: Cyclone® 70P: cyclotron beam transport line and the solid target station

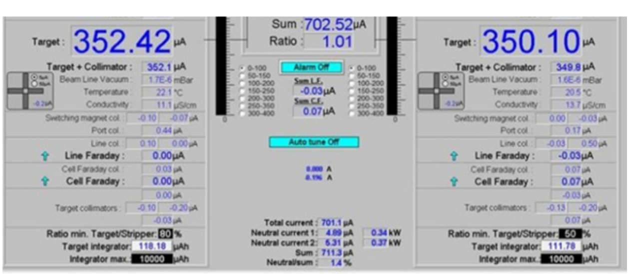

Figure 7: Cyclone® 70P: first full beam extraction (dual beam mode).

In March 2015, the beam was optimized and then was extracted at 70 MeV out of the cyclotron and injected into several beam transport lines.

The beam was transported during the first week in the single beam and then in the dual beam mode.

About 8 weeks later, full beam (700 µA in dual beam mode) was successfully extracted on specific beam stops (beam dumps). See Figure 7.

The machine commissioning started with the RF system in November 2015 up to the internal beam production in December 2015.

By end of January 2015, the whole equipment installation (i.e., cyclotron, beam lines, targets and ancillaries) have been done, piped, wired, etc. The whole system was ready for beam extraction.

The internal beam losses (i.e., magnetic and vacuum stripping losses) at full beam current represent only about 1% of total beam current thanks to the choice of the RF mode (harmonic 4) and the optimization of vacuum pumping system.

From June to end of July, site acceptance tests and training have been performed on the machine. By the end of July 2016, the full system was accepted by Customer and the hand-over has been done.

CONCLUSIONS

IBA successfully designed a 70 MeV proton-only accelerator. This brand new machine has been designed, assembled, installed and validated in less than 32 months (i.e. about 5 months ahead of contractual schedule).

This world record planning was reached thanks to the close collaboration with Customer on building construction and commissioning.

“The collaboration with IBA on this project has been great from the start, said Zevacor Molecular Executive Vice President and Chief Operating Officer, John Zehner.

IBA worked closely with our management team to provide the timely information needed to complete this complicated project ahead of schedule by several months.

Our expectations have been exceeded in both the technical support and equipment specifications. We definitely recommend IBA for the supply of high energy cyclotrons.”

ISBN 978-3-95450-167-0

DESIGN OF THE Cyclone® 70 P

S. Zaremba*, M. Abs, J-L. Delvaux, B. Nactergal, W. Kleeven, J. Van de Walle, and V. Nuttens
Ion Beam Applications (IBA), B-1348 Louvain-la-Neuve, Belgium

Abstract

The IBA Cyclone® 70 P is a high intensity 70 MeV proton-only cyclotron dedicated to the production of radioisotopes for PET generators and SPECT. The nominal power of the extracted beam goes above 50kW (750µA@70MeV). The proton-only cyclotron was developed based on the previous experience of the multi-particle Cyclone® 70 XP running in Nantes, France.

Numerical tools have been extensively used to optimize the magnetic field, to avoid potentially harmful resonances during acceleration and improve the acceleration efficiency of the cyclotron. In addition, electromagnetic and mechanical calculations permitted to obtain a low dissipated power and electromechanically robust design of the RF system. The vacuum computations have permitted to optimize the beam transmission, the placement and type of cryopumps.

This new development of Cyclone® 70 P was the initial part of the successfully finished IBA project also presented during this conference [1].

MAGNET DESIGN

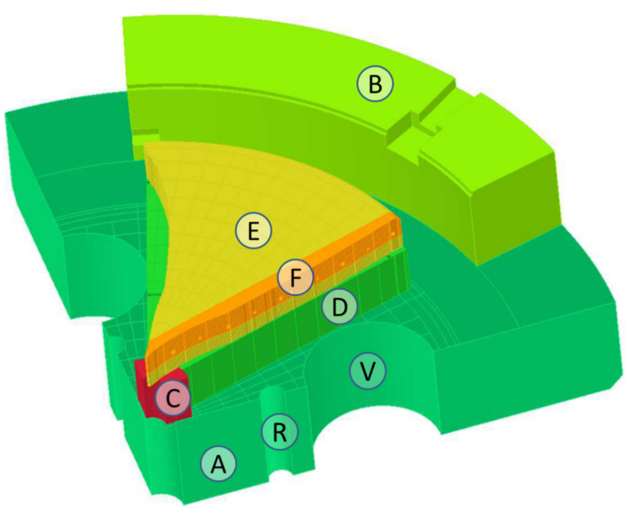

Figure 1: Cyclone® 70 P – lower (or upper) one period of the four-fold rotational symmetry.

The Cyclone® 70 P magnet, Figure 1, consists of: top (bottom) return yoke (A) having diameter of 3820 mm. The lateral return yoke (B) closes the magnet of 1700 mm high. The central plug (C) and the sector (D) create the base for the pole (E) with the outer radius of 1240 mm.

The removable pole edge (F) attached to the, stair-like, lateral pole edge is iteratively milled during mapping process to obtain the isochronous magnetic field for accelerated H^- ions.

The total iron weight is about 108 tons and the resistive coils add next 4 tons.

The cyclotron vacuum chamber and the coil fill the space between the outer radii of the pole and sector and the inner radius of the lateral return yoke.

The vertical gap between poles and between removable pole edges is constant 40 mm and more than 40k Ampere-turns are necessary to reach the required field level in the median plane.

Two ports are located in each valley. The vacuum pumping port (V) diameter is large (520 mm). The dee stem, the dee cooling tubes pass through the small diameter (100 mm) port (R).

The shape of the second lateral pole edge is fixed and its small spiralization helps to obtain higher vertical tune ν_z and to avoid dangerous resonances.

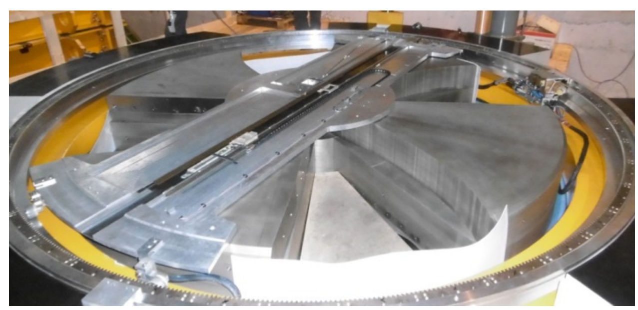

Figure 2: The lower half of the Cyclone® 70 P and the mapping system.

The new mapping system, Figure 2, measuring the magnetic field axial component in the cyclotron median plane on any chosen radial and azimuthal grid was also developed in this project.

The mapping system is supported by the cyclotron lateral return yoke and allows magnetic field measurements practically to the radius where magnetic field values are close to zero between resistive coils.

The magnetic field of the cyclotron model was used to determine the central region geometry. The measured field was used for the crosscheck and the optimization of the spiral inflector of the axial injection system.

The same fields have been used to find positions of the strippers to extract 30-70 MeV protons and to determine the position of the port in the lateral return yoke where the extraction system shaft passes and pivots.

Magnetic field values for radii beyond the outer coil radius, necessary for extraction calculations, have been taken from the calculated models.

* simon.zaremba@iba-group.com

ISBN 978-3-95450-167-0

VACUUM SYSTEM DESIGN

Models for vacuum computation, residual gas stripping and magnetic stripping have been developed, based on accurate orbit length using the closed orbit analysis, the dee voltage and different vacuum levels on poles, RF valleys and non-RF valleys.

The residual gas stripping model, including the outgassing effect of various pole surface finishing, has been used to optimize the number of pumps, their positions, their pumping speed and the pole finish material.

Various resonator configurations have been studied for a single-stem design and an optimal solution was selected with excellent electromagnetic properties, electrical and mechanical stability and minimized mechanical construction and operation costs.

The final configuration of the system is based on the 100 kW tetrode amplifier with a direct capacitive coupling to the cavity.

The RF system frequency is 60.83 MHz ±1 MHz.

The nominal dee voltage in the cyclotron center is 50 kV. The dee voltage increases about 40% at large radii to produce larger turn separation. Larger turn separation reduces energy spread, facilitates beam extraction and beam transport downstream.

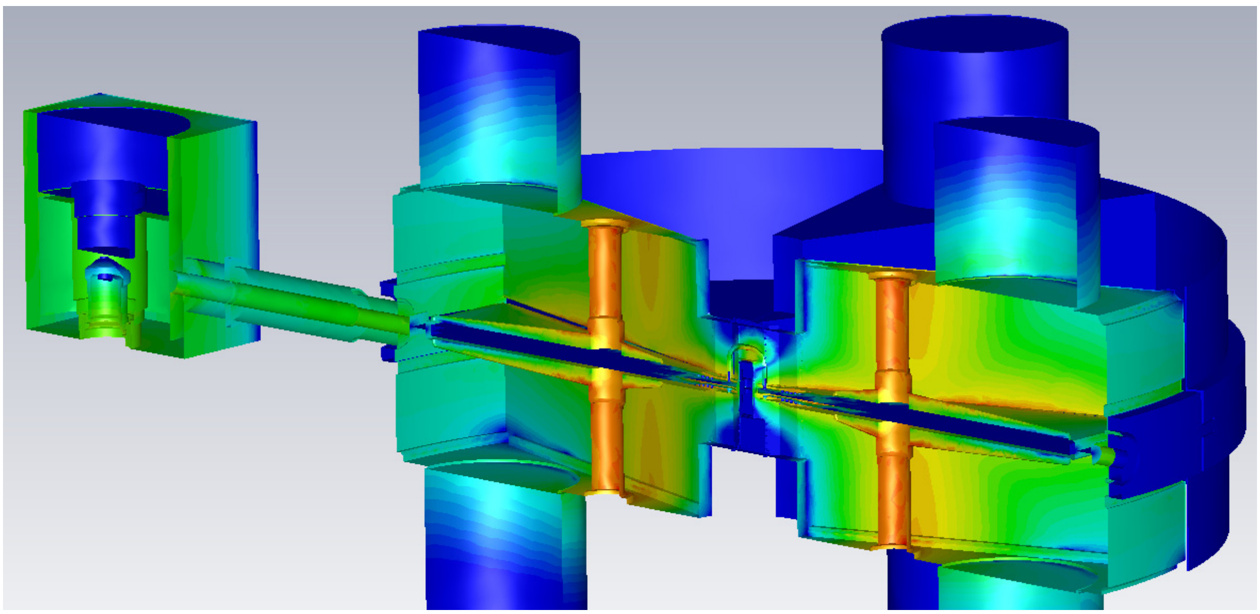

Figure 3: Cyclone® 70 P – the distribution of RF currents in the cavity and final amplifier.

The results of calculations of the magnetic stripping were used to confirm the choice of cyclotron magnetic field.

The models of the residual gas and magnetic stripping losses are dependent on experimental data. The calculated combined effects have been firstly crosschecked with measurements in cyclotrons already produced by IBA. A good agreement between calculation results and experimentally measured data added confidence to apply the same method in the new Cyclone®70p. The results indicated the benefit of the nickel plating of the poles, defined the minimum requirements concerning the vacuum pumps and showed that the total beam losses will not exceed 3% in total.

RF SYSTEM DESIGN

The electromagnetic and the mechanical design of the resonant cavity for the Cyclone® 70 P has been done using CST Microwave Studio to define the shape of the cavity geometry and deduce the accelerating voltage profile, surface current distribution, Figure 3, and total power loss.

Water-cooled dees are connected in the cyclotron center to simplify the configuration using one amplifier, one cavity tuning, one single LLRF control system, one 5 kW solid state driver. The connection of the dees in the center is shielded to avoid the penetration of the RF electric field between electrodes of the spiral inflector.

To be cost-effective, the RF design reused the maximum high-reliability IBA standard components to ensure long life and spare parts service.

The RF system has been assembled. The resonance frequency was adjusted to specifications by machining the dee pillars and then the all system was tested to nominal voltage and power.

The RF system frequency given by CST results is very close to the reality. The dee voltage was measured using a collimated X-ray detector at various positions along the acceleration gap. The quality factor was 20% better than expected and about 32 kW were needed to drive the cavity to a nominal dee voltage of 50 kV.

ISBN 978-3-95450-167-0

CONCLUSIONS

Cyclone® 70 P cyclotron was designed in a short time thanks to extended IBA know-how and experience. Then the cyclotron was produced rapidly. IBA factory acceptance tests and acceptance tests during commissioning at the customer site confirmed that all cyclotron subsystems works as requested. Today (Sept 2016) the cyclotron and the rest of the system is already used by the customer [1].

REFERENCES

[1] B. Nactergal *et al.*, “Installation and Commissioning of the Cyclone® 70 P”, presented at Cyclotron'16, Zurich, Switzerland, paper TUP05, this conference.

ISBN 978-3-95450-167-0

COMMISSIONING AND TESTING OF THE FIRST IBA S2C2

S. Henrotin*, M. Abs, E. Forton, Y. Jongen, W. Kleeven, J. Van de Walle and P. Verbruggen
Ion Beam Applications, Louvain-la-Neuve, Belgium

Abstract

The first unit of the IBA superconducting synchrocyclotron (S2C2), used in the Proteus®ONE compact proton therapy solution, has been installed and commissioned in Nice. In this communication, we will present some selected results of the commissioning with the main focus on the accelerator aspects, showing the influence of machine parameters on beam properties like stability, energy and intensity, which are key elements in proton therapy applications.

THE PROTEUS®ONE LAYOUT

Figure 1 shows the S2C2, installed at the testing facilities in Louvain-la-Neuve (Belgium), and the layout of the compact gantry, which is attached to the S2C2. Together, they constitute the main components of the Proteus®ONE proton therapy system. More information on the S2C2 characteristics can be found in [1]. The compact gantry is described in [2]. A main feature of the compact gantry is the integration of the energy selectrion system (ESS) in the gantry itself (see Fig. 1). At the end of the ESS, the dispersion is maximized and a slit is present to select the needed proton energy.

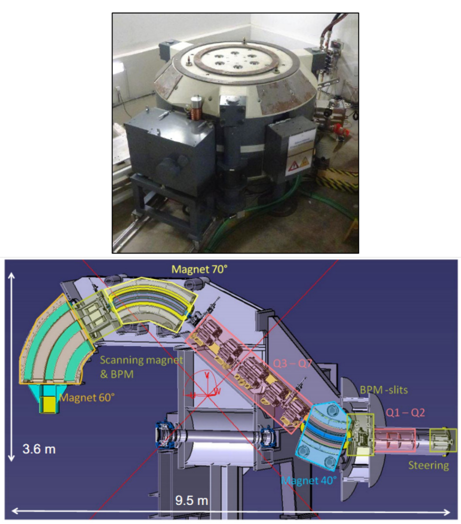

Figure 1: (Top) The S2C2 installed at the testing facilities. (Bottom) the compact gantry layout. The S2C2 and the compact gantry constitute the Proteus®ONE system.

THE S2C2 TIMING

Figure 2 shows the timing properties of the S2C2. The green line shows the source arc current feedback (pulsed cold cathode source), the red line shows the RF frequency sweep (periodicity of 1 ms) and the black line shows the dee voltage profile during acceleration. The blue line is the measured beam signal induced on a senstive diamond probe [3]. These timings are repeated at a frequency of 1 kHz, which is the periodicity of the RF frequency sweeps.

Table 1: S2C2/Proteus®ONE Main Properties and Key Figures

Nominal beam energy	230 MeV
Max. clinical charge at isocenter	4.5 pC
Energy spread at nominal energy	≈400 keV
Pulse repetition rate	1 kHz
Pulse duration	10 μs
RF frequency range	60-90 MHz

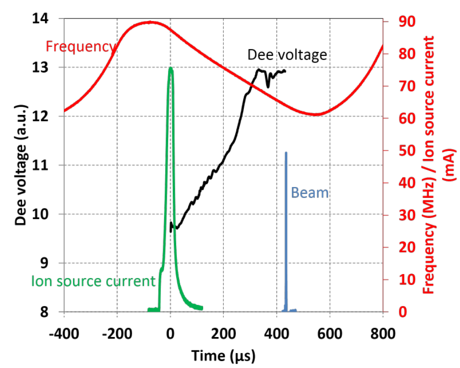

Figure 2: Timing properties of the S2C2 in the Proteus®ONE system: the source timing, dee voltage regulation, RF frequency sweep and the beam signal.

EMITTANCE

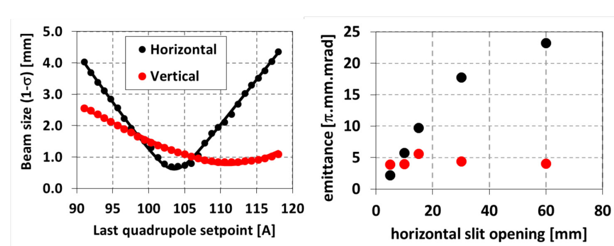

Figure 3: (Left) the horizontal and vertical beam spot size on the degrader position (≈2.0 m after the S2C2 exit port) (Right) the evolution of the horizontal and vertical emittance as a function of a horizontal slit, installed prior to the degrader.

Figure 3 shows the measured beam size on the position of the energy degrader, 2 m downstream from the S2C2 exit port. Two quadrupoles and a horizontal slit are positioned

* sebastien.henrotin@iba-group.com

ISBN 978-3-95450-167-0

between the S2C2 exit port and the Beam Profile Monitor (BPM), which is part of the degrader system. A small and symmetric beam spot of 1 mm can be obtained at this position. From a variable quadrupole measurement, the horizontal and vertical emittance of the S2C2 has been measured. The horizontal emittance is much larger than the vertical emittance, but can be reduced by closing the horizontal slit. For the high energies this is necessary to have the optics in the compact gantry independent from the orientation of the gantry. Figure 4 shows the calculated horizontal and vertical emittances with a fitted RMS-emittance. The measured and calculated emittances agree very well.

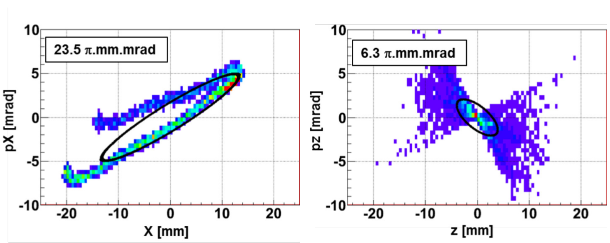

Figure 4: Simulated horizontal and vertical emittance at the exit port of the S2C2.

PULSE INTENSITY MODULATION

Figure 5 shows the total pulse charge as a function of the applied dee voltage. The dee voltage is expressed in percentage of the maximum dee voltage, which is clinically allowed in the current configuration of the treatment mode in the Proteus®ONE. The latter is imposed by the maximum allowed dose deposition in one pulse at the isocenter, taking into account the transmission efficiency from the S2C2 to the isocenter. The pulse-to-pulse charge variability has a Gaussian distribution and the standard deviation, measured over 1000 pulses (1 s), is shown in Fig. 5 as percentage of the mean charge.

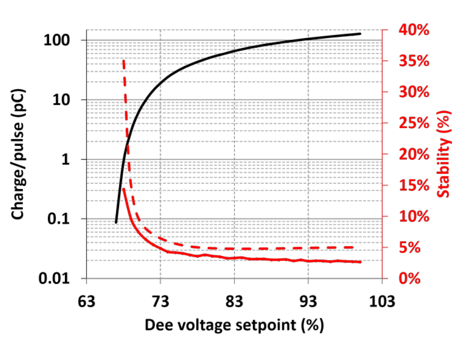

Figure 5: (Black) Pulse charge as a function of the dee voltage setpoint, expressed as % of the maximum allowed setpoint. (Red) Stability of the pulse charge, observed over 1000 pulses. The dashed line indicates the specification on the stability of the pulse charge in Pencil Beam Scanning.

BEAM ENERGY

As was shown in [1], the orbit centering in the S2C2 depends crucially on the source position in the central region. It was found that the orbit centering can be different for different dee voltages, in case the source is not well centered. Tests were performed to assess the sensitivity of the extracted beam energy on the source position. Figure 6 shows the measured beam profile on the BPM at the end of the ESS as a function of dee voltage, for a shifted source and for a well centered source. As expected, the distribution on this BPM changes (the mean position shifts) as a function of dee voltage for a shifted source position. This

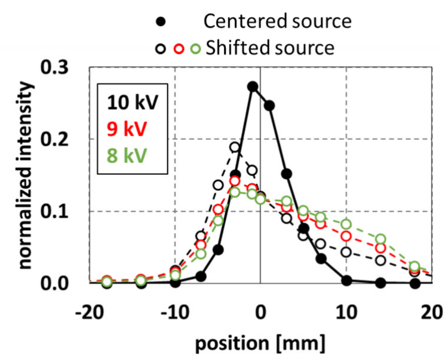

Figure 6: Beam profile observed at the end of the Energy Selection Systems (ESS, see Fig. 1) as a function of dee voltage for a centered (filled symbols) and a shifted source (open symbols) in the S2C2.

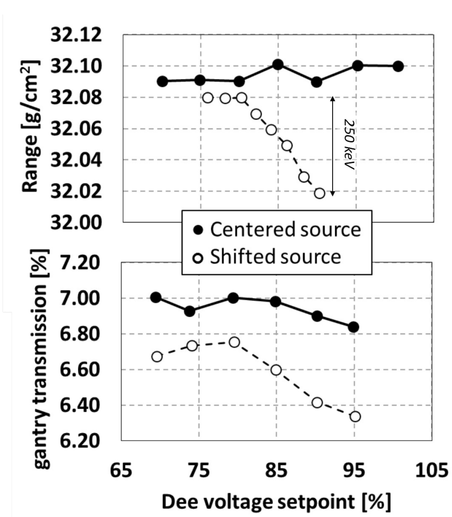

Figure 7: Measured range at isocenter -without energy degrader- (top) and measured gantry transmission (bottom) as a function of dee voltage for a shifted and a centered source.

indirect observation of small extracted beam energy shifts is confirmed by a range measurement in a water phantom at isocenter. Figure 7 shows the range for the shifted and centered source positions. Clearly, the beam energy is stable

ISBN 978-3-95450-167-0

and maximized for a well centered source. The bottom part of Fig. 7 shows the gantry transmission efficiency for the different source positions. The influence of the changing energy (open symbols) is clearly seen as well. A precise and reproducible source positioning system has been developed to ensure the correct positioning of the source in the S2C2.

DEE VOLTAGE REGULATION

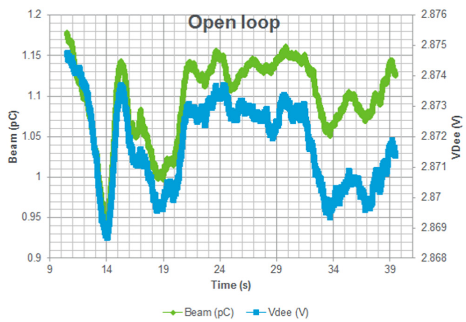

Figure 8: Slow fluctuations of the dee voltage amplitude influences the beam intensity over longer period (without regulation).

The dee voltage is regulated precisely to ensure a good stability of the dee voltage during the capture in the central region (which determines the pulse-to-pulse charge stability) and to prevent beam losses during acceleration. Figure 8 shows the measured pulse charge and the measured dee voltage at capture over a long period of 30 s, illustrating the sensitivity of the total pulse charge to the exact dee voltage amplitude at capture. The drift, observed in Fig. 8 over longer periods can be minimized by a closed regulation loop of the dee voltage, which is currently implemented in the S2C2 control system. The dee voltage regulation during the acceleration is based on the measurement of the bucket area of the separatrix, where the idea is to keep the bucket area either constant or growing during the acceleration. A dee voltage profile before and after optimization of the regulation is shown in Fig. 9 together with the measured bucket area.

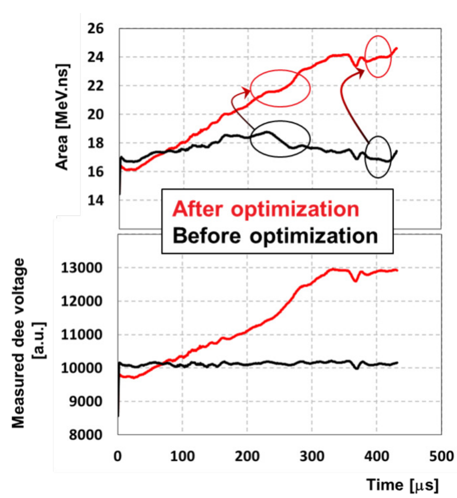

Figure 9: Measured dee voltage and calculated bucket area of the separatrix before and after optimization of the dee voltage profile during acceleration, to prevent beam losses.

CONCLUSION

During the clinical commissioning of the S2C2 with the Proteus®ONE system, challenges encountered have been investigated in depth. Solutions presented in this contribution have been successfully implemented.

REFERENCES

[1] J. Van de Walle *et al.*, "The S2C2 from source to extraction", presented at Cyclotrons'16, Zurich, Switzerland, Sep. 2016, paper THB01, this conference.

[2] E. Pearson *et al.*, IEEE Transactions on Applied Superconductivity, **24**, 3 (2014)

[3] J. Van de Walle *et al.*, "A Diamond Detector Test Bench to Assess the S2C2 Beam Characteristics", presented at Cyclotrons'16, Zurich, Switzerland, Sep. 2016, paper MOP19, this conference.

THE USE OF GRAPHENE AS STRIPPER FOILS IN SIEMENS ECLIPSE CYCLOTRONS

S. Korenev, R. Dishman, Siemens Healthineers, Knoxville, TN 37932, USA
A.M. Yerba, Siemens PETNET Solutions, Denver, CO 80210, USA
N. Mesheriakov, Siemens LLC, Moscow, Russia
I. Smirnov, Siemens LLC, Ekaterinburg, Russia
I. Pavlovsky, R.L. Fink, Applied Nanotech Inc., Austin, TX 78758, USA

Abstract

This paper presents the results of an experimental study for the use of graphene foils as an extractor (stripper) foil in the 11-MeV Siemens Eclipse Cyclotron. The main advantage of graphene foils compared with carbon is very high thermal conductivity. The graphene also has significant mechanical strength for atomically thin carbon layers. The life time of these foils is more than 16,000 μA*H. The graphene foils showed a significant increase in the transmission factor (the ratio of the beam current on the stripper foil to the current on the target), which was approximately more 90%. The technology in fabricating these graphene foils is shown. The pros and cons of using the graphene material as a stripper foil in cyclotrons are analysed.

INTRODUCTION

The use of stripper foils in the cyclotrons with negative hydrogen ions allows for easy output of the proton beam from the cyclotron into the target [1]. The 11-MeV Eclipse Cyclotron [2] uses this approach for the production of medical isotopes. The standard stripper foils based on carbon materials are widely used for these goals. The discovery of graphene [3] and the unique properties of graphene have created a large interest in this material as a stripper foil compared to the standard graphite and carbon foils. The main difference is the thermal conductivity of graphene which is up to 20 times higher than that of polycrystalline graphite. This gave interest for the application of graphene as a stripper foil in accelerators of charged particles and especially in commercial cyclotrons, such as the Eclipse cyclotron. The preliminary application of graphene foils from Applied Nanotech [4] as a stripper foil shows the main advantages of this material in comparison with the standard carbon and graphite foils. The main focus of this study was to determine the lifetime of stripper foils and to understand any cyclotron operating performance improvements. One the main questions was to characterize the radiation damage of graphene under irradiation by negative hydrogen ions with a kinetic energy of 11 MeV and current up to 100μA.

THE TECHNOLOGY OF FABRICATION FOR GRAPHENE FOILS

The technology for the fabrication of graphene foils is described in more detail in [5]. The foil fabrication method is based on the controlled reduction of graphene oxide by hydrazine with addition of ammonia in an aqueous dispersion. The dispersion of graphene oxide with loading of 0.5% wt. in water was obtained from Angstron Materials. The dispersion was reduced for 4 hours at 95°C and then cooled down to room temperature. The thickness of graphene foils was controlled by using a calculated volume of graphene dispersion knowing the loading of graphene. A commercially available stainless steel filter holder was used to make graphene foils by pressure filtration. The diameter of the fabricated foils was 13 cm. The filter holder allowed increasing the differential pressure across the filter. A compressed air line with a pressure regulator was connected to the filter holder to pressurize the air space above the graphene dispersion. Pressure up to 300 kPa was used to filter the dispersion. Commercially available polymer filter membranes with a diameter of 142 mm were used for the filtration. After filtration, graphene foils still on the filter membrane were removed from the filter holder and peeled off the filter membrane to obtain free-standing graphene foils. The described process can be adapted to fabricate foils with a wide range of foil thickness and using different isotopes of carbon.

EXPERIMENT

The experiments with graphene foils with a thickness of about 3μm (0.5mg/cm^2) were conducted on four Siemens Eclipse cyclotrons. The graphene foils were installed on the carousels of the Eclipse cyclotron. The general picture of the graphene material is shown in Figure 1.

a) b)

Figure 1: General view of graphene foils: a) fabricated foil; b) graphene cross section.

ISBN 978-3-95450-167-0

The dimension of graphene stripper on the carousel of Eclipse cyclotrons is 10mm x 10mm.

Experiments were conducted on the Siemens Eclipse Cyclotron [2], an example of is shown in Figure 2.

Figure 2: View of the Eclipse cyclotron.

The main experiments were conducted with main parameters of Eclipse cyclotrons:

1 Energy of negative hydrogen ions is 11 MeV.
2. Beam current on the foils ranged from 30 to 100 µA.
3. Beam current on the Faraday Cups (target) ranged from 25 to 80 µA.
4. Beam diameter of negative hydrogen ions is about 10 mm.

EXPERIMENTAL DATA

The experimental data was collected from four Eclipse cyclotrons. The summary of data for the transmission factor measurements is given in Table 1. The experimental study of high current mode of Eclipse cyclotrons with dual proton beam 80 µA on each target showed a decreasing level of the ion source current (arc current); see the plot in Figure 3. The bias current level was also observed to decrease during the experiments. The main experimental result of testing of cyclotron with graphene stripper foils is high transmission factor allowing the decreasing of ion source current. The good experimental correlation is decreasing of thickness with high thermal conductivity and ion source current permits us to work with a relative low current ion source. This in turn increases the life time of ion source.

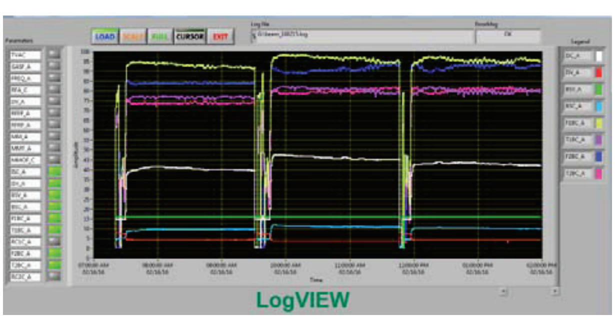

Figure 3: The log file display.

Table 1: Experimental Data

Cyclo-tron	Proton Beam Current (µA)	Transmission Factor (*) (%) Reg/Gr		Ion Source Current (*) (mA) Reg/Gr
1	2 x 55	86/75	92/78	230/192
2	2 x 25	80/81	88/89	120/90
3	2 x 60	75/88	89/90	340/250
	2 x 75	70/72	87/92	500/300
4	2 x 60	73/82	82/90	320/220
	2 x 80	70/85	82/93	600/450

(*) for Regular/Graphene stripper foils

LIFE TIME OF GRAPHENE FOILS

The lifetime of stripper foils is determined by 2 main mechanisms: radiation defects and sublimation [6, 7]. The experiments with graphene foils on the Eclipse cyclotron showed the radiation defects and sublimation have place. The lifetime of graphene foils determined by beam losses of the transmission factor and the mechanical destruction of graphene foil. The main contribution to lifetime is temperature from dissipation of beam energy. Typically considering dissipated power of the beam in the stripper is 1%, we have total dissipated power for beam in the Eclipse cyclotron of about 10 W for a 90 µA beam into the foil (for production of dual beam 2x80 µA). The distribution of temperature in graphene foil using Comsol Multiphysics package is shown in Table 2.

The lifetime test of the graphene foils on one of the Eclipse Cyclotrons was tested and resulted in a lifetime of 16,000 µA*Hours, which is 60% higher than the existing specification.

Table 2: Temperature Distribution in Stripper Soil

Dissipation Beam Power (W)	T_{min} Graphene (°C)	T_{max} Graphene (°C)	T_{min} Graphite (°C)	T_{max} Graphite (°C)
10	355	552	251	706

Figure 4 shows a picture of damaged graphene foil as observed at the end of this lifetime test.

Figure 4: A damaged graphene foil.

ISBN 978-3-95450-167-0

DISCUSSION ABOUT USING OF GRAPHENE AS A STRIPPER FOILS

The use of Graphene as a stripper foil shows benefits in comparison to the regular polycrystalline graphite foils. The main pros and cons of graphene compared with the standard stripper foils are provided in Table 3.

Table 3: Comparison of Strippers

Stripper Foil Type	Pros	Cons
Carbon	Low cost	Lifetime Thermal conductivity Foil ablation
DLC	Lifetime Small thickness	High cost Fabrication technology
Polycrystalline graphite	Low cost	Lifetime Thermal conductivity Foil ablation
Graphene	High thermal conductivity Small thickness Lifetime	Fabrication technology Limited suppliers

RECOMMENDATIONS

The graphene foils can be competitors to other carbon foils that are used as stripper foils, such as a DLC or polycrystalline graphite. Our investigations showed the benefits of using the graphene stipper foils. The question remains as to whether the technology to fabricate the graphene foils will continue to develop as well as the resulting cost.

CONCLUSIONS

In conclusion we can say that graphene stripper foils have a future that will require additional testing on diffrenet types of accelerators with stripper foils. The main advantuge of the graphene stripper foils is their unique properties, such as a high thermal conductivity and high mechanical strength compared to the standard carbon and graphite type foils.

ACKNOWLEDGMENT

Authors want to say thanks to James Hinderer, J. Bret Miller from Siemens Healthineers and Leif Thuesen from Applied Nanotech for their support and help with this work.

REFERENCES

[1] A.I. Papash, Yu.G. Alenitcki, "Commercial Cyclotrons Part 1. Commercial cyclotrons in energy range 10-30 MeV for isotope production", *Physics of Elementary Particles and Atomic Nuclei,* vol. 39, pp. 1150-1214, 2008.

[2] Siemens, `http://www.siemens.com/mi`

[3] Wikipedia, `https://en.wikipedia.org/wiki/Graphene`

[4] Applied Nanotech, `http://www.appliednanotech.net`

[5] I. Pavlovsky and R.L. Fink, "Graphene stripper foils", *J. Vac. Sci. Technol.,* B 30, 03D106 , 2012.

[6] E.A. Koptelov, S.G. Lebedev, and V.N. Panchenko, "A model of carbon stripper target failure under ion beam bombardment", *Nucl. Instr. Meth.*, vol.256, pp.247-250, 1987

[7] B. Gikal *et al.*, "Calculation of lifetime of charge-exchanging carbon target in intense heavy ion beams", *Communication of JINR*, No: P9-2005-110, 2005.

ISBN 978-3-95450-167-0

DIAGNOSTIC TOOL AND INSTRUMENTATION FOR HANDLING 50 KW BEAM POWER

P. Antonini†, E. Boratto, A. Calore, D. Campo, D. Conventi, J. Esposito, A. Lombardi, M. Maggiore, M. Poggi, L. Pranovi, LNL-INFN, Legnaro (Pd), Italy

Abstract

The SPES facility entered the commissioning phase and the 70 MeV cyclotron is delivering the proton beams at the maximum power permitted. The INFN team has developed additional beam instrumentation in order to stop the particles at different power allowing the tuning of the beamline and to check the particles losses during the transport. In particular, a beam dumper able to stop up to 55 kW beam power has been constructed and tested as well as the beam loss monitor system by INFN team. Here we present the status of the beam instrumentations supplied by INFN and the results achieved during the test with the beam.

INTRODUCTION

For the SPES facility at Laboratori Nazionali Legnaro of INFN in Italy a 70 MeV proton cyclotron has been installed and is being commissioned. To safely verify the capability of the machine, and correctly tune both cyclotron and beam line, several diagnostic have been developed and installed. Among them most relevant are Faraday cups (FC) for low power (up to 1 kW) beam, a more powerful beam dumper (BD) to stop the full power (700 µA, 70 MeV, i. e. 49 kW) beam and ionization chambers beam loss monitors, divided into four sectors to be able to highlight misalignment of the beam on the beam line. The general layout of the cyclotron vault is shown in Fig. 1.

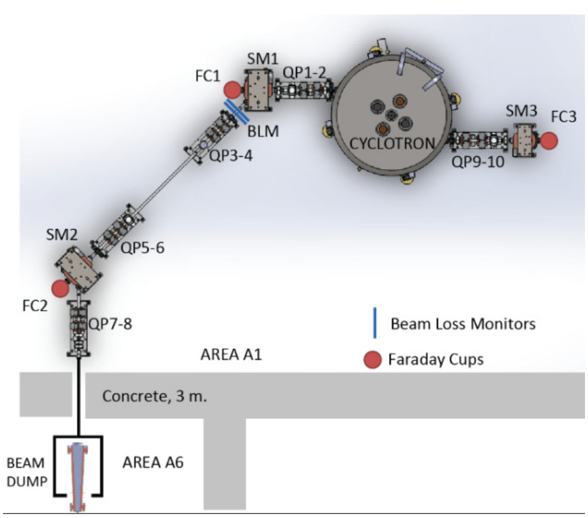

Figure 1: General layout of the cyclotron vault, showing the cyclotron, the main diagnostics and the focusing quadrupoles (QP).

LOW POWER FARADAY CUPS

Two low power water-cooled (closed-circuit) Faraday cups (FC) have been installed. They are able to withstand and measure up to 1kW:

- 14 µA, 70 MeV
- 28 µA, 35 MeV

The temperature of the FCs are measured with Pt1K sensors, current is measured directly through a current amplifier, and 50 mm Pb shielding wrap the FCs to allow access to the cyclotron vault. The FCs are made of oxygen-free high conductivity (OFHC) copper. The thickness of the copper at the impact walls span from a minimum of 8 mm, were the cooling water flows, to a maximum of 24 mm. The FCs were simulated using Comsol software, using as a cooling medium water, 3 litres/min, at 20 °C inlet temperature. The thermal power simulated is a cylinder with depth of 7.09 mm, with Gaussian power distribution (with $\sigma = 5$mm) with cylindrical symmetry, as shown in Fig. 2.

The simulated temperature profile on the symmetry axis at 500 W incident power is shown in Fig. 3. The beam is arriving from the right side. The curves refer to different elapsed times since start of the beam.

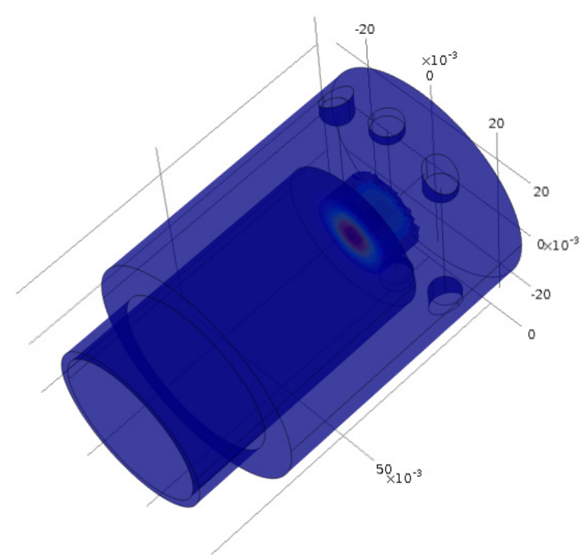

Figure 2: In blue the simulated FC volume, in red at its centre the thermal load of gaussian profile.

ISBN 978-3-95450-167-0

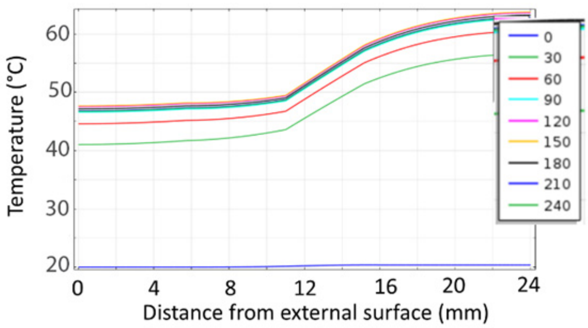

Figure 3: Results from the numberical simulations of the temperature along the symmetry axis, with 500 W input power (70 MeV; 6 µA).

The graph shows that after 240 the regime temperature of the hottest point of the Faraday Cup is at less than 70 °C.

During operations the FCs were not operated up to regime temperature. The measured temperatures on the external side of the FCs (see Fig. 4 to locate the temperature sensors, Pt1k) never exceeded 35 °C. The FCs were insulated from the cyclotron using viton o-rings and plastic clamping rings.

The two FCs were eventually shielded with 50 mm of lead to allow maintenance in the cyclotron vault.

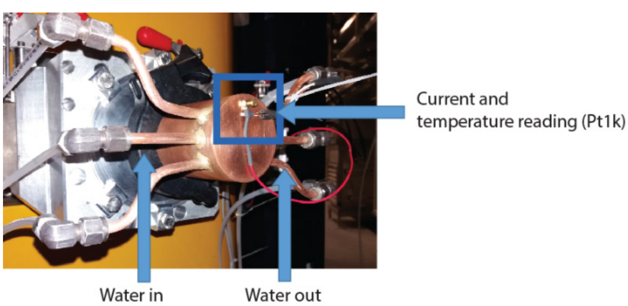

Figure 4: The blue square indicates the positions of the temperature sensor and of the current pick-up of the low-power Faraday Cup.

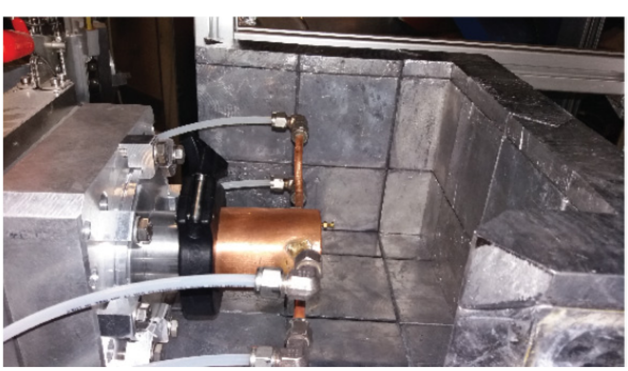

Figure 5: The FCs are shielded with 50 mm Pb bricks, to allow maintenance. Here only partial shielding is shown.

HIGH POWER BEAM DUMPER

To demonstrate the full power (700 µA, 70 MeV) capability of the cyclotron, a beam dumper (BD) has been developed. It is cooled by a separate circuit, to avoid mixing of activated water with the water used for other purposes. Pressure level near the BD, and 12 thermocouple temperature sensors serve as diagnostics to monitor the condition of the BD. The positions of the temperature sensors relative to the BD are shown in Fig. 6.

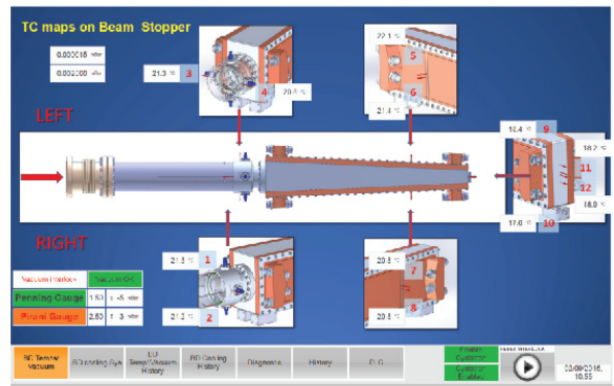

Figure 6: Screen shot of the diagnostic system of the BD.

Monitoring of the power dissipated by the cooling system provides a rough but reliable indication of the total power of the beam.

BEAM LOSS MONITORS

Two beam loss monitors, based on ionization chambers are used to verify both losses on the beam lines and misalignment between beam and line. They are made of two faces, separated by 20 mm air gap, biased by 500 V. The current of each sector is read by a current/voltage amplifier and acquired through a multiplexer. The currents can be read directly on an oscilloscope and through a LabView code the alignment of the beam is directly seen.

The monitors proved useful to set beam line parameters.

ACKNOWLEDGEMENT

The authors would like to acknowledge the prompt and valuable help of all the staff at LNL-INFN. Best Theratronics team also has been very helpful during the installation of the diagnostics.

ISBN 978-3-95450-167-0

A NEW CONCEPT OF HIGH CURRENT POWER SUPPLY FOR THE MAIN CYCLOTRON MAGNET AT TRIUMF*

S. Carrozza, F. Burini, E. Ferrari, M. Pretelli, G. Taddia,
OCEM Power Electronics, Bologna, Italy
Q. King, G. Le Godec, G. Hudson, M. Bastos, CERN, Geneva, Switzerland
D. Louie, Y. Bylinski, R. Nussbaumer, TRIUMF, Vancouver, Canada

Abstract

A sophisticated power supply was studied and designed to supply a high current to the main magnet of the TRIUMF cyclotron. The power supply will be operated with a current up to 20000 A in DC mode. It has been designed using a modular approach, with a 12-pulse input rectifier and two DC link which feeds sixteen DC/DC chopper modules in parallel connection.

The conceived power supply integrates a sophisticated control and a precise current measurement chain developed at CERN for the Large Hadron Collider (LHC).

This paper presents the solution described in the design report, the choice of the main purchased components which will lead to a final assembly and test before the end of 2016.

CONVERTER TOPOLOGY

The main components are:

- Input Circuit Breakers and Pre-charge Circuit.
- Two Rectifier Transformers.
- Two Main Rectifier stages (with fuses).
- Two passive RLC Filters downstream from each Main Rectifier stage.
- Output stage composed of 16 switching IGBT modules operating in parallel.
- Freewheeling diodes across the output bars.

The main input contactor/breaker (MCB) is realized by a motorized circuit breaker, which provides manual and remote ON/OFF functionality to the power supply.

The ground breaker is located at the input of the power supply: it is a manual switch with a keyed lock-out feature which allows the output of the breaker to be connected to ground only when the main input contactor/breaker is open.

To limit the inrush current during the start-up of the power supply a pre-charge resistive branch is used, remotely enabled via an auxiliary contactor.

The input stage realizes a 12-pulse topology through two three-phase transformers, phase-shifted by 30 degrees.

The two rectifier stages, each composed of a rectifier bridge plus a damped LC filter, realize two separated DC-links for the downstream chopper modules. Each DC-link provides the input for the following switching stage, each composed of eight chopper modules operating in parallel.

All the switching modules have an output filter inductor, and converge on a damped capacitive filter, placed at the output of the power supply.

*TRIUMF receives federal funding via contribution agreement through the National Research Council of Canada.

A free-wheeling diode (realized with 3 devices in parallel) is located across the output bus bars to correctly discharge the energy stored in the magnet when the power supply turns off.

Technical Specifications

A list of main technical specifications for the power supply is presented in Table 1.

Table 1: Main ratings of the power supply

PARAMETER	VALUE
Output Current/Voltage	20000 A / 80 V
Output Power	1600 kW
Mode of operation	DC
Regulation Mode	Constant Current
Topology	IGBT based buck converter
Equivalent Output Switching Frequency	16 x 10 kHz = 160 kHz (10 kHz for each module and 8 PWM carriers phase-shifted)
Absolute Accuracy	±1 part in 10^4
Current Ripple	±2 ppm of 20 kA for the range 17 kA to 20 kA
Short Term Stability (5 min) @ max I_{OUT}	≤ 2 ppm of 20 kA
Long Term Stability (8 hour) @ max I_{OUT}	≤ 5 ppm of 20 kA
Power Factor	≥ 0.96
THDin	Typical of a 12-pulse rectifier stage
AC Input	3ϕ, 3-wire, 800 VAC
Cooling	Air and Water cooling
Footprint	20.7 x 8.4 feet

Chopper Modules

The output stage is a chopper converter that consists of 16 modules in parallel. Each module has three IGBTs in parallel with the same PWM and every IGBT has its own inductor (see Fig. 1). The switching frequency is exactly 10 kHz and the power of each module is up to 100 kW.

The 16 modules are controlled with a phase-shift to increase the effective switching frequency to 160 kHz and thus reduce the ripple in the output current.

Layout

The power supply is composed of five cubicles (max dimensions per cubicle 2500x1500 mm) plus an air-conditioned control cabinet (see Fig. 2).

ISBN 978-3-95450-167-0

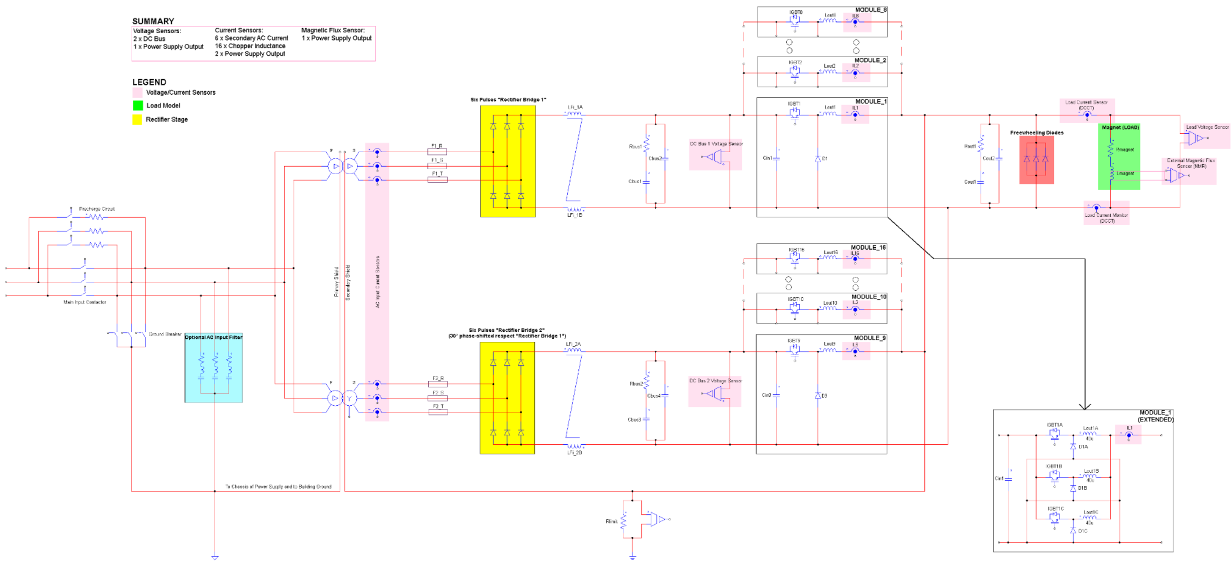

Figure 1: Power supply schematic.

In the first cubicle there is the input circuit breaker and pre-charge circuit, the second and third cubicles house the rectifier stages, each composed of a transformer, diode stack and DC filter. In the fourth cabinet there are the sixteen switching modules. In the fifth cubicle are located the two high-precision Direct-Current Current Transducer (DCCT) heads. Four symmetric vertical return bus-bars surround the DCCT heads, which are themselves around a single central vertical conductor. This symmetry is important as it avoids local saturation of the DCCT cores and maximises their performance.

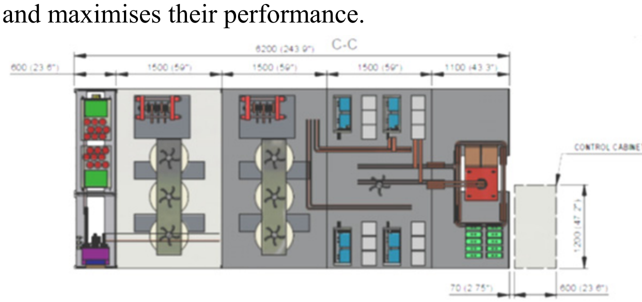

Figure 2: Top view of the power supply cubicles.

CONTROL ELECTRONICS

In order to guarantee the stability, accuracy and precision requirements in the output current are met, the power supply will use a reliable control system developed at CERN.

The CERN Type-10 RegFGC3 crate is an evolution of the controls originally created for the power supplies used in the Large Hadron Collider (LHC) [1, 2]. It is based on a CERN-designed embedded control computer called a Function Generator/Controller (FGC). The RegFGC3 platform uses a third generation FGC (see Fig. 3) in combination with other specialised cards to provide all the regulation, control and interlocking services needed by a switch-mode power supply.

The FGC3 has a USB interface and an Ethernet interface. Normally the Ethernet interface is used to connect the FGC3 to an FGC_Ether fieldbus [3], however, at least initially at TRIUMF, the new power supply will be controlled through the USB interface. This is simpler but significantly slower than the Ethernet interface, but for short commands and responses, it is fast enough. It is also possible to monitor the performance of the regulation through the USB interface as it has two channels, one for commands and responses and the other used to stream six signals at 1 ksps. The six signals transmitted can be selected from a long list of signals in the FGC3.

Figure 3: FGC3 controller and Type-10 RegFGC3 Crate.

Current Regulation

The FGC3 contains a TI TMS320C6727 DSP running the CERN Converter Control Libraries [4, 5]. The regulation library implements a 15^{th}-order RST algorithm and can synthesize the RST coefficients to support a dead-beat PII regulator, as used in the LHC. It is also possible to calculate the RST coefficient externally using Matlab or equivalent.

The existing power supply uses a flux-loop to stabilise the field to better than 1 ppm of nominal, using a fully analogue regulation circuit [6]. The FGC3 will implement the same functionality digitally by using the fourth ADC input to digitize the flux-loop signal and modulating the current reference based on this measurement.

The TRIUMF cyclotron magnet has an inductance of 120 mH and a resistance of 3.9 mOhms. The time constant is thus about 30 seconds and the stored energy will be 24 MJ at 20 kA.

ISBN 978-3-95450-167-0

Voltage Regulation

The Type-10 RegFGC3 crate was developed for the control of modular switch-mode power supplies in the range from 50 kW to several MW. It includes an FGC3 and a CERN-designed DSP board dedicated to implementing the voltage regulation and the generation of the PWM firing signals (see Fig. 4).

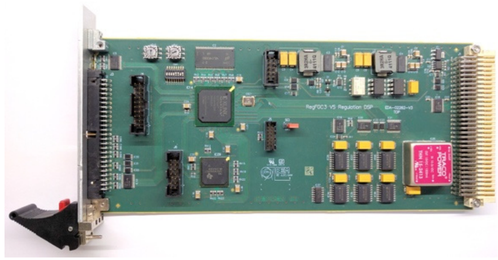

Figure 4: RegFGC3 DSP board for voltage regulation and generation of PWM firing signals.

This board uses a TI TMS320C28346 DSP, which includes nine high- and nine low-resolution PWM generators. The DSP software is flexible and is configured to drive eight high-resolution PWM signals, phase shifted, at 10 kHz. Adaptation logic in the power supply uses these PWM signals to create the IGBT control signals for the 16 modules.

Current Acquisition

The TRIUMF application requires short term stability for the current in the order of two part per million (ppm) of nominal (20 kA), after the first five minutes following a current change (see Table 1). Repeatability must be of the same order and current ripple must be within ±2 ppm of 20 kA for the range from 17 kA to 20 kA.

The performance of the current regulation, in particular stability and repeatability, greatly depends on the current measurement system. The current measurement chain for the new power supply is composed of a DCCT head, DCCT electronics and an Analog-to-Digital Converter (ADC).

Two independent measurement chains are used for redundancy purposes. The DCCTs are 20 kA TOPACC-HC (LHC type) from PM Special Measuring Systems. This is the same model as the LHC 13 kA DCCTs [7], proven to deliver ppm level stability over many years of operation of the LHC. As for the ADCs, four channels based on the LTC2378-20 are available on the FGC3 analogue board. An on-board temperature stabilized reference voltage is included for automatic ADC calibration.

The DCCTs and the ADCs have sub ppm level short term stability after warm up and under stable temperature conditions. The DCCT Temperature Coefficient (TC) is in the order of 1 ppm/ºC and the ADC TC is about 2 ppm/ºC. To guarantee stable conditions and therefore meet the stability requirements, the DCCTs and the Type-10 RegFGC3 crate will be permanently powered and will be housed in an air-conditioned cabinet (see Fig. 5). The temperature inside the cabinet is kept stable to ±1ºC by the air conditioning unit.

In addition, to further reduce temperature dependent errors, the TC of the ADCs will be measured and used with an online correction algorithm in the FGC3 to correct for temperature dependency.

Figure 5: Air-conditioned cabinet for the DCCT and controls electronics.

SUMMARY

The upgrade of the TRIUMF cyclotron main magnet power supply is a key part of the global consolidation project for the cyclotron. The new power supply must fit within the same floor space as the existing supply, and deliver the same high-level of performance, while assuring high reliability and maintainability for at least the next twenty years.

REFERENCES

[1] F. Bordry, H. Thiesen, “RST Digital Algorithm for controlling the LHC magnet current”, CERN, Geneva, Switzerland, LHC Project Report 258, Dec. 1998.

[2] Q. King *et al*, “The All-Digital approach to LHC power converter current control”, *Proc. 8th Int. Conf. on Accelerator and Large Experimental Physics Control Systems (ICALEPCS'01)*, San Jose, USA, Nov. 2001, paper THBT004, pp. 453-455.

[3] S. Page *et al.*, “Migration from WorldFIP to a low-cost Ethernet fieldbus for power converter control at CERN”, *Proc. 14th Int. Conf. on Accelerator and Large Experimental Physics Control Systems (ICALEPCS'13)*, San Francisco, USA, Oct. 2015, paper TUPPC096, pp. 805-808.

[4] Q. King *et al.*, “Function generation and regulation libraries and their application to the control of the new main power converter (POPS) at the CERN CPS”, *Proc. 13th Int. Conf. on Accelerator and Large Experimental Physics Control Systems (ICALEPCS'11)*, Grenoble, France, Oct. 2011, paper WEPMN008, pp. 886-889.

[5] Q. King *et al.*, “CCLIBS: The CERN Power Converter Control Libraries”, *Proc. 15th Int. Conf. on Accelerator and Large Experimental Physics Control Systems (ICALEPCS'15)*, Melbourne, Australia, Oct. 2015, paper WEPGF106, pp. 950-953.

ISBN 978-3-95450-167-0

[6] K. Reiniger *et al.*, "Stability Improvements in the TRIUMF Cyclotron magnetic field to ± 0.7ppm". *Journal de Physique Colloques*, 1984, 45 (C1), pp.C1-225-C1-228.

[7] G. Hudson, K. Bouwknegt, "4-13kA DC current transducers enabling accurate in-situ calibration for a new particle accelerator project, LHC", *11th European Conf. on Power Electronics (EPE),* Dresden, Germany, Sept. 2005

ISBN 978-3-95450-167-0

DEVELOPMENTS OF ION SOURCES, LEBT AND INJECTION SYSTEMS FOR CYCLOTRONS AT RCNP

#T. Yorita, M. Fukuda, K. Hatanaka, K. Kamakura, Y. Yasuda, S. Morinobu, T. Saito, T. Kume , S. Hara , H.W. Koay, R. Yamanoshita,
RCNP, Osaka University, Osaka, Japan

Abstract

Several developments for cyclotrons at Research Center for Nuclear Physics (RCNP) Osaka University have been carried recently in order to improve the high intense ions in MeV region.

The additional glazer lens on axial injection of AVF cyclotron has been installed to improve the beam transmission to inflector of AVF cyclotron. Additional buncher for the heavy ion injection like Xe beam which requires high voltage bunching in comparison with the proton case also has been installed. Extension of baffle slits on injection line of Ring Cyclotron also has been done to extend the flexibility of injection orbit. Modification of low energy beam transport (LEBT) from ion sources to AVF injection axis including the development of real time emittance monitors also has been carried. This new fast emittance monitor realizes the more efficient tuning of ion source beam which should be matched to acceptance of cyclotron.

INJECTION AXIS OF AVF CYCLOTRON

To improve the beam current accelerated by AVF cyclotron, two components have been installed on the injection axis of AVF cyclotron. Those are additional buncher and glaser lens.

Buncher

To improve the beam current of heavy ion, especially of Xe, additional buncher has been installed on injection axis. In Fig. 1, existing buncher is shown by “b” and located 2550mm above median plane (MP) of AVF. This existing one makes saw wave by RF combining with 1x, 2x and 3x harmonics and maximum saw voltage is +-600V. This buncher can bunch lighter ion which has small m/q and is accelerated with higher frequency, but the voltage or distance from median plane are not enough for heavy ion like Xe. So additional new buncher is installed to help to improve beam current in combination with existing one. This new buncher makes saw wave by charge-discharge circuit with maxmum voltage of 0~+1200 V at 2 MHz operation, 0~+600 V at 6 MHz and 0~+200 V at 20 MHz. The installation position is 4600 mm above the median plane as shown in Fig. 3 by “a”.

The beam test has been done for several ions. For the proton with acceleration frequency of 9.32 MHz, the optimized beam current at extraction of AVF cyclotron is 4.1μA with existing buncher only, 0.57μA without any buncher, 3.5μA with new one only, and 5.0μA with both bunchers. For the 12C5+ case with 10.2 MHz RF, the optimized beam current at extraction of AVF cyclotron is 400 nA with existing buncher only, 175 nA without any buncher, 550 nA with new one only, and 760 nA with both bunchers. These show that new buncher works well especially for heavier ion with combination with existing one.

Glaser Lens

To improve the efficiency of AVF injection, additional glaser lens has also been installed. Previously the injection axis has only 3 glasers shown as d, e and f in Fig. 1, it was hard to deliver the beam through the region of 0~2000 mm above the median plane where the beam pipe size is narrow of 57 mm in diameter and only the beam with the size up to 5 mm at the iris slit shown by “g” in Fig. 3 can be delivered. So new additional glaser is installed at the position of “c” shown in Fig. 1. With this new additional glaser, now the beam with the size of 10 mm at the iris slit can be delivered.

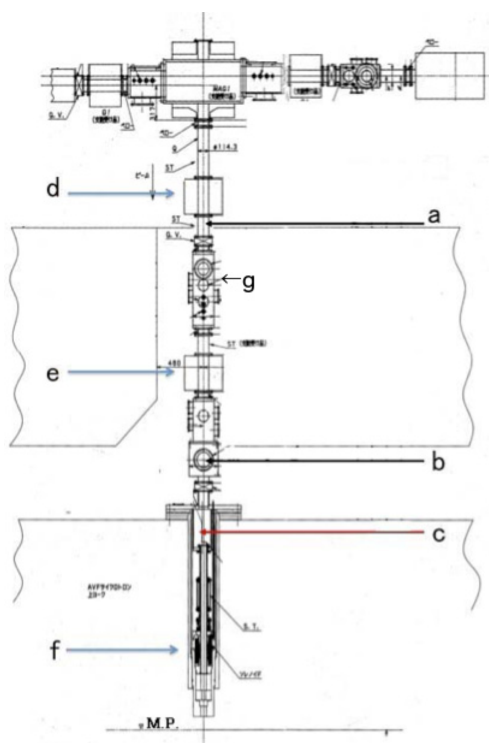

Figure 1: Schematic side view of injection axis of AVF Cyclotron. a: new buncher, b: existing buncher, c: new glaser, d~f: existing glaser, g: iris slit.

#yorita@rcnp.osaka-u.ac.jp

ISBN 978-3-95450-167-0

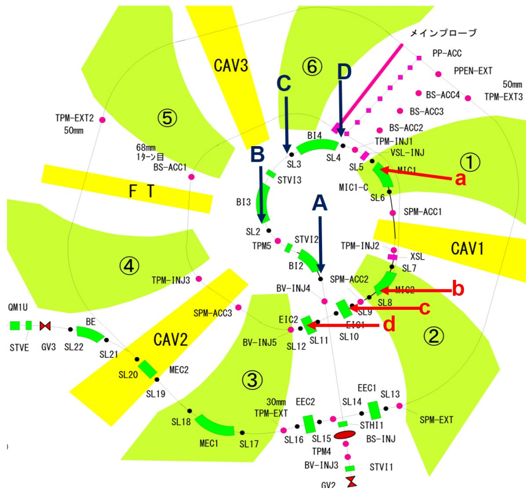

Figure 2: Schematic view of Ring cyclotron: A~D are baffle slits on injection line, a and b are slits of magnetic channel and c and d are electrostatic channel.

INJECTION TO RING CYCLOTRON

To improve the injection efficiency of Ring cyclotron, extensions of baffle slits on beam injection line have been done to expand the flexibility of beam injection orbit. In Fig. 2, A~D show the baffle slits of injection line, a and b are the slit of magnetic channel, and c and d are electrostatic channel. These slits have been extended as far as protection of components works. Figure 3 shows the examples of the extension. After these slit extension, optimum current of MIC2 shown in Fig. 2 has drastically decreased, the current ratio of this MIC2 and analyzing magnet downstream of AVF extraction takes smaller value of 1.3~1.9 than the previous of 2.0~2.5. This means that the optimum trajectory has been changed due to slit extensions.

Figure 3: Examples of baffle slit extension: left figure shows magnetic channel slit extended from 15 mm X 15 mm to 33 mm X 30 mm and right figure shows slit of B in figure 4 which extended from 30 mm X 24 mm to 36 mm X 30 mm.

The injection efficiency represented by the ratio of beam current at BS_ACC1 and BS_INJ shown in Fig. 2 also seems to be improved from 25~65% to 67~97%. To clarify that this efficiency improvement is due to slit extension and to improve the efficiency more, further study should also be done for transport line between AVF cyclotron and Ring cyclotron.

FAST EMITTANCE MONITOR ON LEBT

For higher efficient tuning of ion beam, development of new Pepper Pot Emittance Monitor (PPEM), which can do real time measurement, has been done referring to several another works [1,2]. Existing emittance monitor [3] is fast but it takes 70seconds to get emittance εx, εy, that is far from real time measurement. This new PPEM consists of pepper-pot mask, multichannel plate (MCP), mirror, and CCD camera as shown in left figure of Fig. 4. The material of pepper-pot mask is phosphor bronze of 50 μm in thickness. The hole size of the mask is 70 μm in diameter and hole pitch is 3mm at a regular pattern as shown in right figure of Fig. 4. MCP is HAMAMATSU F2226 and its effective diameter is 77 mm. The fluorescence screen of MCP is P46 (Y3Al4O12:cerium). The wavelength of the fluorescence is 530 nm, and decay time of afterglow to 10% of the peak brightness is 0.2~0.4 μs. The pepper-pot mask and MCP are install on beam axis at right angle. The distance between pepper-pot mask and MCP is 50 mm. Surface reflex mirror is also installed on beam axis at 45 degrees to reflect the MCP screen image to CCD camera via view port with quartz window. Those pepper-pot mask, MCP and mirror are mounted on a plate, and can move away from beam axis by air cylinder when the PPEM doesn't measure the emittance. CCD camera is SONY XCD-U100 for the fast measurement and the image data is transferred to PC via IEEE1394b. Its bit rate is 800Mbps. The CCD size is 7x5.3 mm2 with 1600x1200 pixels. The grey scale depth of the image is 8 bit, that is, 256. The focal length of C mount lens used here is 25mm, and the

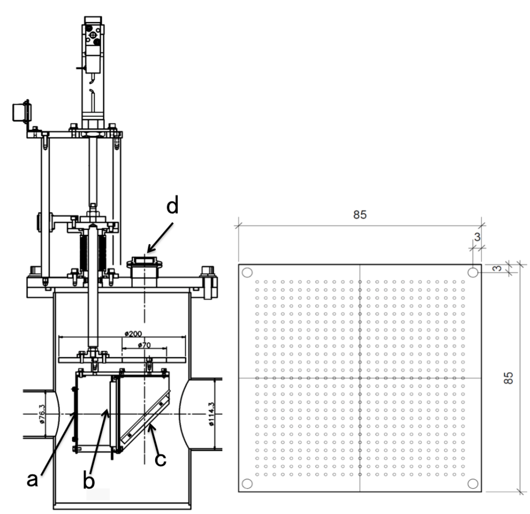

Figure 4: Right figure shows pepper-pot mask and left figure shows the schematic view of PPEM. 'a' is pepper-pot mask, 'b' is MCP, 'c' is mirror and 'd' is view port for CCD camera. 'a'~'c' components are placed on the beam axis.

ISBN 978-3-95450-167-0

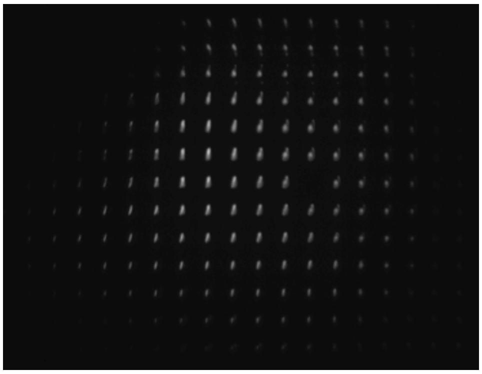

Figure 5: Typical image data. 4 D-distribution is clearly seen.

between the lens and MCP screen is about 400 mm on optical axis, then the image size of 3 mm on MCP screen is corresponding to 45 pixels. The F value of this lens is 1.4 in order to get the bright image as much as possible.

MCP is operated with high voltage (MCP HV) of 600~700V. The voltage between MCP and screen is set to 2kV. Typical image of the PPEM is shown in Fig. 5 and a regular pattern can be seen. Intensities of each elements of the pattern show the beam distribution in (x, y), and every element shows the (x', y') distribution at corresponding each (x, y). So 4-dimensional (4D) distribution G(x, y, x', y') of the beam is directly obtained from this CCD image. And then the phase space distribution g(x, x') can be obtained by integrations of this G(x, y, x', y') over y and y'.

Beam test for PPEM has been done with 2C5+ beam and the measures value of emittance is 70% consistent with existing one. Measurement time of PPEM is now 0.5 second that is fast enough for efficient ion source tuning.

CONCLUSION

Several developments have been done for the purpose of improve the current of the beam accelerated by cyclotrons: additional buncher and glaser have been install on injection axis of AVF cyclotron, the baffle slits on injection of Ring cyclotron have been extended and PPEM monitor on LEBT has been developed. Those components work well. For further improvement of beam current, more detail development with those components and existing components combination would be done.

REFERENCES

[1] A. Pikin, A. Kponou, J. Ritter, V. Zajic, BNL-note C-A/AP/#244 July 2006.

[2] H. R. Kremers, J. P. M. Beijers, and S. Brandenburg, *Rev Sci Instrum.* 2013 Feb;84(2):025117 .

[3] K. Kamakura *et al.*, *IEEE Transactions on Nuclear Science*, vol. 63, no. 3, p. 1710, 2016.

ISBN 978-3-95450-167-0

HIGH ACCURACY CYCLOTRON BEAM ENERGY MEASUREMENT USING CROSS-CORRELATION METHOD

A. Hendy, F. Alrumayan,
King Faisal Specialist Hospital and Research Centre, Riyadh, Saudi Arabia
K. Kezzar, H. Kassim, King Saud University, Riyadh, Saudi Arabia

Abstract

This paper propose a method to measure the proton beam energy of the CS-30 cyclotron by using two fast current transformer (FCT) and accurately estimate THE TIME OF FLIGHT (TOF) using windowed cross-correlation method. Currently available techniques use pulse width or edge delay measurement to get the TOF. However, the accuracy of these methods are limited by sampling rate, signal level, noise, and distortion. By using Cross-Correlation and interpolation, we can get a fractional delay measurement, and the system works with low level signals (low beam current) and it is robust in the presence of noise and distortion.

INTRODUCTION

The CS-30 cyclotron is 30-inch AVF cyclotron requires a high energy gain per turn and a fixed frequency RF system. It was assembled and tested at TCC in USA before being shipped to Saudi Arabia [1-3]. The CS-30 can accelerate four different particles with different energy levels. Table 1 gives more details about the CS30 specifications and Figure 1 is a photo of the accelerator and its vault.

Beam energy is very important parameters in beam diagnostic process either for radioisotope production or proton therapy. Cyclotrons is known to produce bunches of protons with nanosecond duration and repetition frequency the same as the RF of the Dee voltage. Beam energy can be estimated using Time of Flight (TOF) method while using either single pickup or dual pickups and the pickup can be capacitive or inductive [4, 5]. In single pickup, ToF is estimated by measuring the pulse width of the pickup output and in dual pickups ToF is estimated by measuring the delay between the two waveforms output from the pickups. The two pickups of inductive type is the method of choice in this paper; in this case ToF is obtained by measuring the delay between the two waveforms output from two fast current transformer (FCT) separated by a suitable distance. The FCT converts the beam current bunches into voltage pulses waveform that can be acquired using Analog to Digital Converter (ADC) and send to the PC for digital signal processing.

Delay measurement usually done using edge to edge delay measurement [4, 5], in this case the accuracy is limited by the ADC sampling rate, signal level, noise, and distortion. However, the proposed method calculates the cross-correlation of the two FCT outputs and interpolates the result to get the time of the peak value, which represents the delay between the two waveforms. In this case the delay accuracy is a fraction of the sampling rate which means very high accuracy and the system works with low level signals (low beam current) and high noise levels. Further accuracy improvement is obtained by measuring the temperature and compensate for dimensions change of the FCT fixture due to thermal expansion.

Table 1: Main Specifications of CS-30 [2]

Parameter	Value
Proton Energy	26.2 MeV
Deuteron Energy	15.0 MeV
Helium-3 Energy	38.0 MeV
Helium-4 Energy	30.0 MeV
External Beam Power	2000 Watts
Pole Diameter	38 inch
Number of Sectors	3
Weight	22 T
Number of Dees	2
Acceleration Mode	Fundamental
Voltage Gain per Turn	100 kV

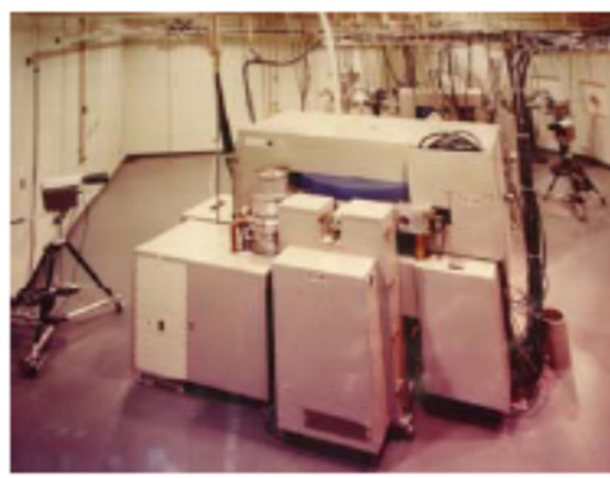

Figure 1: A Photo of the CS30 Cyclotron.

TIME OF FLIGHT (TOF) BASED ENERGY MEASUREMENT

For fast proton, the relativistic kinetic energy E_k can be calculated from [6]:

$$E_k = mc^2(\gamma - 1) \tag{1}$$

where:

$$\gamma = \frac{1}{\sqrt{1-\left(\frac{v}{c}\right)^2}} \tag{2}$$

ISBN 978-3-95450-167-0

and v can be estimated using the flight path l (distance between the two pickups) and the time of flight (TOF) t.

$$v = \frac{l}{t} \tag{3}$$

Worst case error of v due to measurement errors of l and t is given by

$$\Delta v = \left|\frac{dv}{dt}\,\Delta t\right| + \left|\frac{dv}{dl}\,\Delta l\right| \tag{4}$$

Hence

$$\frac{\Delta v}{v} = \left|\frac{\Delta t}{t}\right| + \left|\frac{\Delta l}{l}\right| \tag{5}$$

and worst case error of E_k resulting from the error of v

$$\Delta E_k = \left|\frac{dE_k}{dv}\,\Delta v\right| \tag{6}$$

$$\frac{\Delta E_k}{E_k} = \left|(\gamma+1)\gamma\,\frac{\Delta v}{v}\right| \tag{7}$$

The above equation gives a clear idea about how the energy estimation affected by the measurement errors of either l or t. If assumed that the γ is near 1 then 1 percent error of l measurement will result in 2 percent error of E_k estimation, also 1 percent error of t measurement results in 2 percent error of E_k estimation. This explains the importance of accurately measuring the TOF and the distance between the two pickups.

To keep the error of energy measurement, due to the error of t, below 1% then the error of time measurement should be less than 0.5% or 0.047 ns. And also for l the error should be less than 0.5% or 3.25 mm.

CROSS-CORRELATION METHOD

Cross-correlation method is commonly used to measure the delay between two signals. In this case, delay can be estimated by finding the peak of the cross-correlation between the two signals. It is required to interpolate the points at the peak in order to improve the delay estimation accuracy. We used two simulated signals with arbitrary delay to find the best interpolation method. We try linear interpolation, and cubic spline in which the later gives more accurate results. Also Hanning window is used before the cross-correlation to force the ends to zero to prevent the error due to phase rotation. By using such a method, it's not required to acquire the signal starting from a certain point (trigger point) and this make the acquisition easier.

A LabVIEW program was developed to determine accurately the time difference between two collected signals as shown in the schematic diagram in Figure 2. To ensure highly accurate results, the software was tested using two simulated signals with a known time delay. It was able to determine the delay value accurately. An example of simulated signal is shown in Figure 3:

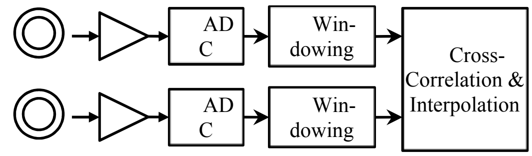

Figure 2: Cross-Correlation method either hardware of software.

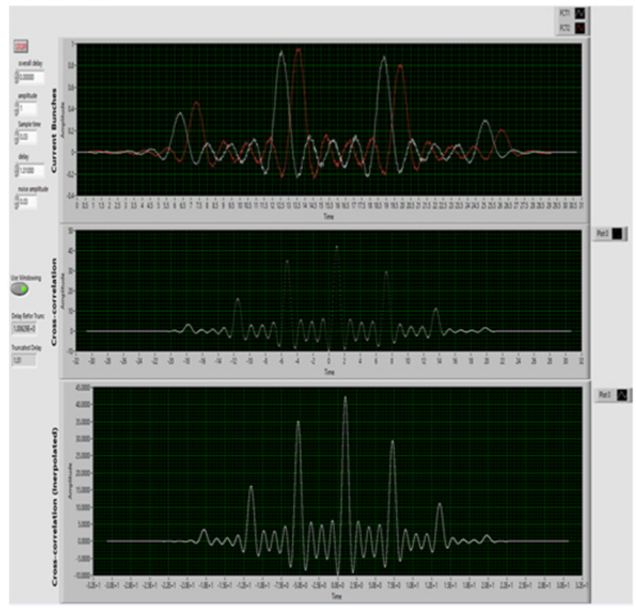

Figure 3: A simulated signal was created using Labview.

EXPERIMENTS AND TOF MEASUREMENT

Figure 4 shows the setup made inside one of cyclotron beamlines, to measure the delay between two bunches. The main detectors in our experiment were two FCT detectors made by Bergoz. These were passive devices with a rise time of 1 ns. They contained no electronics, making them suitable for use in a radiation area. They were installed around an acrylic-made cylinder attached to the beamline. The cylinder's other end was capped by 50 µm of Havar foil. The distance between the two FCTs is 65 cm.

The calibration of the hardware was performed as shown in Figure 5. A signal generator was used to produce an arbitrary signal at a frequency of 26.8 MHz (cyclotron frequency), which was allowed to pass through the two FCTs along identical BNC cables of the same length. Initially, the delay between the two values was 2 ns due to mismatch between the cables and amplifier. Therefore, a delay line was added to one side of the circuitry, reducing the delay to 50 ps. During experiments, the cyclotron was operated to produce 1 µA. The output from the FCT was amplified Equivalent output voltage was approximately 5 mV measured we used a Digital Storage Oscilloscope (DSO) for data acquisition, and data processed offline on the PC using LabVIEW software.

ISBN 978-3-95450-167-0

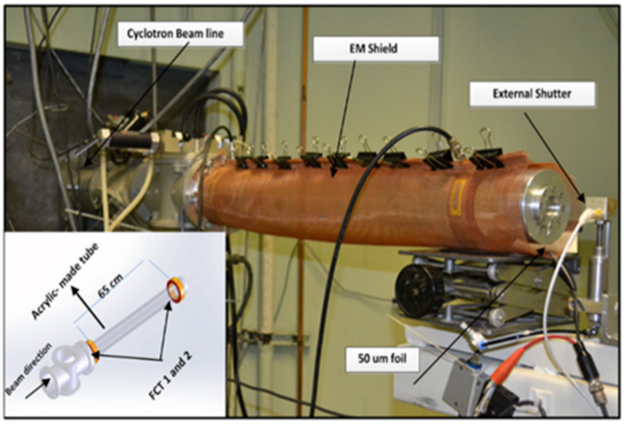

Figure 4: Experimental setup for energy measurement. The two FCT can be seen under the copper mesh. The distance between them is 65 cm. the purpose of the EM shield is to reduce electromagnetic noise.

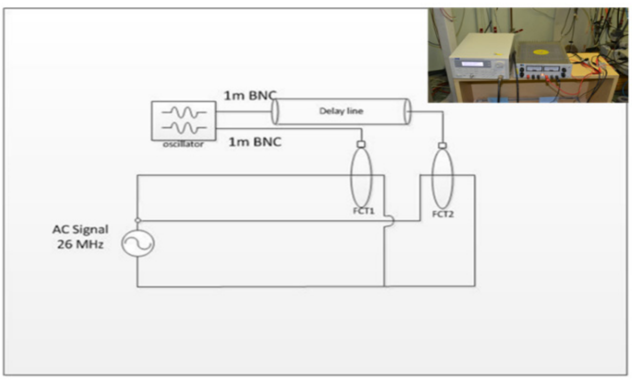

Figure 5: Arrangement of capacitive pickup to perform calibration of the experiment setup.

Measurement of the time delay takes place between one edge of the 1st pickup (FCT) output and the next edge, of same polarity (rising of falling), of the 2nd pickup (FCT) output [3]. In this case the error of time measurement is equals to the sampling interval of the ADC. Sampling can be Real Time Sampling (RTS) or Equivalent Time Sampling (ETS) [7]. Using of RTS cannot be used without interpolation because it will give large error. For example if the sampling rate is 1GSPS (Giga Sample per Second), the sampling interval is 1ns and time measurement error will be ±1 ns this gives error of measured TOF about 35%. Using ETS, on the other hand, will increase the sampling rate by acquire more cycles but the signal should be stable and has limit noise.

RESULTS AND DISCUSION

Figure 6 shows the waveforms measured from FCT 1 and FCT 2. In our experiment, the distance between the two pickups is 2065 cm. considering speed of protons as:

$$\frac{v}{c} = \sqrt{1 - \left(\frac{1}{1+\frac{E_k}{m_0 c^2}}\right)^2} \qquad (8)$$

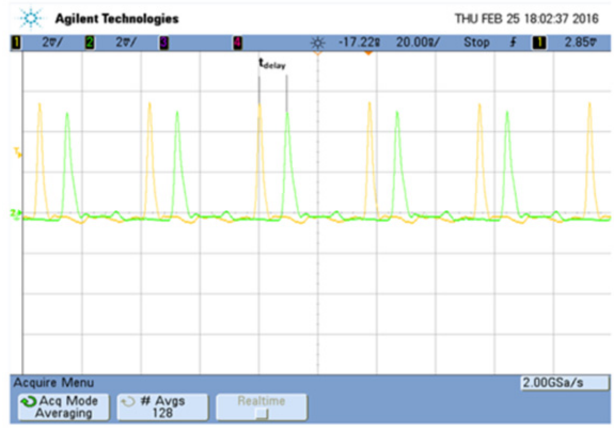

Figure 6: TOF measurement from FCT1 and FCT 2.

Hence, for 26.2 MeV proton energy, v is 6.915x10 m/s. With length of 65 cm, the measured time delay between the two signals was 9.4023 ns. Cyclotron energy was calculated to be 25.99 MeV. As the value of cyclotron energy given in the CS-30 manual is 26.2 MeV for protons, the difference between actual and calculated energy was <2.0%.

CONCLUSION

In this paper, beam energy of the CS30 cyclotron has been determined using cross correlation technique. Time of flight is a method of choice in this experiment due to its high accuracy and less exposure to radiations. Energy measured with TOF and Cross correlation showed that its 25.9 MeV.

ACKNOWLEDGEMENT

This project was supported by the NSTIP strategic technologies program in the kingdom. Award No. (14-MAT-1233-20).

REFERENCES

[1] J. W. Stetson, R. M. Lambrecht, M. Sajjad, and F. W. Zielinski, "A status report of the cyclotron facility at King Faisal Specialist Hospital and Research Centre" in *Proc. 11th Int. Conf. on Cyclotron and their Applications*, Tokyo, Oct. 1986, pp. 678-681.

[2] G. O. Hendry "Compact cyclotron engineering for application", *AIP Conference Proceedings*, 1972.

[3] F. Alrumayan *et al.*, "Status report of the cyclotrons C-30, CS-30 and RDS-111 at KFSHRC, Saudi Arabia".

[4] C. S. Lee *et al.*, "The Time-Structure Measurement of the 50-MeV Pulsed Proton Beam using a Single Toroidal Coil," *Journal- Korean Physical Society*, Feb. 1997, vol. 32 no. 1, pp. 20-24.

[5] S. Varnasseri *et al.*, "Test bench experiments for energy measurement and beam loss of ESS-BILBAO", in *Proc. IBIC'13*, Oxford, UK, 2013

[6] Stanley Humphries, Jr., "Principles of Charged Particle Acceleration".

[7] Tektronix Application Note, "Real-Time Versus Equivalent-TimeSampling", `http://www.tek.com/document/application-note/real-time-versus-equivalent-time-sampling`

ISBN 978-3-95450-167-0

MAGNETIC FIELD MEASUREMENT SYSTEM OF CS-30 CYCLOTRON

F. M. Alrumayan, A. Algaith, J. Schneider, A. Hendy,
King Faisal Specialist Hospital and Research Center (KFSHRC), Riyadh, Saudi Arabia
S. Al-Ghamdi, H. Kassim, King Saud University, Riyadh, Saudi Arabia

Abstract

The magnetic field of the CS-30 Cyclotron at King Faisal Specialist Hospital and Research Centre (KFSHRC) has been measured using Hall probe-based mapping system. Although the CS-30 Cyclotron was under full operation for 3 decades, yet, it was crucial to evaluate the stability of beam orbits and also to study the low extraction efficiency, particularly after stripping the cyclotron coils and its three sectors. The rational for stripping magnetic component was to replace the pole tip seal underneath the frame.

The Hall probe was mounted on a high precision X - Y stage, which was driven by three stepping motors, two motors for Y - axis and a motor for X - axis. The 3MH5 digital Tesla-meter is a high performance magnetic field measuring instrument, based on the Hall Effect magnetic field to voltage transducer. It has digital data correction to provide 0.01% accuracy and it provides the possibility of automatic data acquisition via USB port of our computer.

In this paper, a Hall probe mapping system and the results of the magnetic measurement of the CS-30 magnet are described.

INTRODUCTION

The CS-30 cyclotron at King Faisal Specialist Hospital and Research Center (KFSHRC) has been operating since 1982 for production of radioisotopes, such as ^{18}F and ^{15}O for positron emission tomography applications [1].

Some cyclotrons, including the CS-30 at KFSHRC, contain sets of harmonic coils, also called trim coils, arranged to supply a weak field that acts as a magnetic pump and enhances the main magnetic field in the central region and in the extraction region. Depending on the polarity of the electric current applied to those coils, they can generate a positive field, enhancing the main magnetic field, or a negative one (in the opposite direction) which weakens the main field slightly.

Additionally, cyclotrons have an extraction system, comprising the equipment that extracts the beam from the accelerated region to the main beamline of the cyclotron. In negative ion cyclotrons (whose accelerated particles are negative ions), this is done by stripping electrons from the negative ions using carbon foils [2]. In positive ion machines, the mechanism is more complicated, consisting of an electrostatic deflector (which has two parts: a septum made of tungsten, held at zero potential, and a high voltage electrode) and a magnetic channel to eliminate the magnetic field effect of the extracted beam. On the last rotation, particles experience a strong electric field capable of modifying slightly the trajectory of their orbit.

The magnetic field of CS-30 magnet was measured using the Hall mapping method described in [2-6]. For measurement of cyclotron magnets, the Hall probe mapping system at many laboratories use the polar coordinate system [2-4]. It is mounted on a high precision x–y stage, which is driven by a stepping motor at end of the Hall probe carrier, and maps the magnetic field in the polar coordinates. The system used the **'flying mode'** field-mapping method in which the data acquisition is made while the Hall probe moves [4]. The requirements of the field measurement system for CS-30 are listed in Table 1.

Table 1: Specifications of the Mapping System

System specifications &Unit	Value
X scan capability (mm)	1000
Y scan capability (mm)	1000
Mechanical resolution (μm)	1
Range of magnetic field (T)	2
Relative error for $\langle B(r)\rangle$-measurement (%)	0.01

HALL MAPPING SYSTEM

The teslameter and Hall probe have been used widely to measure the magnetic fields of cyclotrons. The 3MH5 digital teslameter is a high performance magnetic field measuring instrument, based on the Hall effect magnetic field-to-voltage transducer (Hall probe). It has digital data correction to provide 0.01% accuracy and it provides the possibility of automatic data acquisition via a USB port. The Hall probe is mounted on a high precision X-Y stage driven by three stepping motors, one for the x-axis and two for the y-axis. The stepping motors are run by a 3-axis stepper controller/driver (TMCM-3110). Time resolution of the x-axis and y-axis can reach up to 25 and 34 μm respectively. The time resolution of the Hall probe is 100 ms; however, measurements were taken every 200 ms. The Hall probe has a built-in temperature sensor to compensate for variation in temperature.

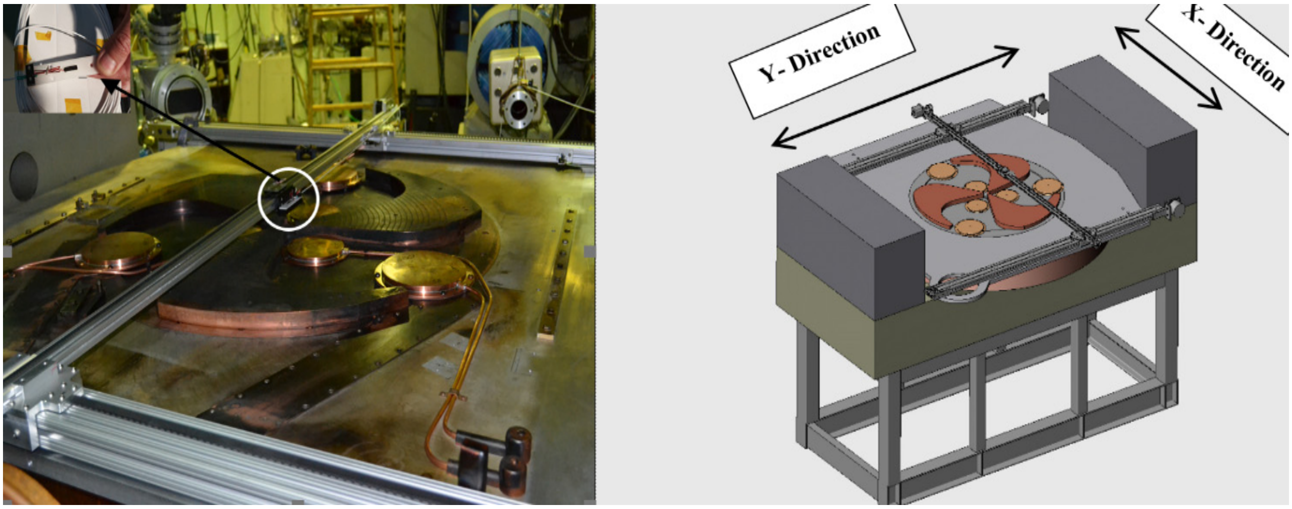

Figure 1: The setup of the magnetic mapper inside the region of interest (A 3D model of the CS-30 is shown to the right). The accelerated area in the CS-30 cyclotron is 96 cm.

A graphical user interface (GUI) was developed to control the measurement of the magnetic field using LabVIEW software, a graphical environment for the development of sophisticated measurement and control systems using intuitive graphical icons and wires that resemble a flowchart. Figure 2 shows a snapshot of the GUI; its motor controller is to the right. The software itself has many advantages, including the continuous saving of the acquired data in external memory. Additionally, it draws 3D graphs of the magnetic field while acquiring the data. The mapping system has the further advantage of measuring the magnetic field in both polar (r, Ø) and x-y coordinates. In polar form, it collects the values radially in steps of 0.5 cm (the total radius is 51 cm) every 1° for a total of 360°. Thus, the total number of points collected was 36,720. In x-y coordinates, the motion step was 0.5 cm in the x and y-directions.

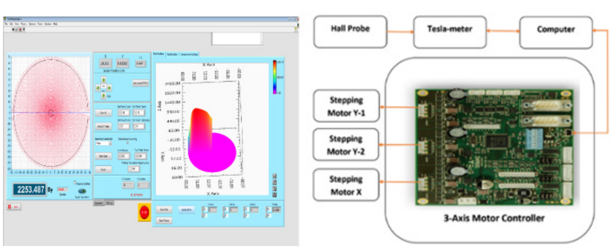

Figure 2: LabVIEW-based software to collect magnetic field values and its axis controller.

FIELD MEASUREMENT RESULTS

The result of Hall probe mapping for the CS-30 cyclotron magnet at an excitation current of 326 A is shown in Fig. 3. This figure shows a typical profile of a magnetic field for a cyclotron magnet. The measured magnetic field at the hills and valleys are ~2.2 and 1.4 T respectively. This measured field data in Cartesian coordinates have been converted into the field data in the polar coordinates for the equilibrium orbit calculation. For the data calculation the following mesh points in cylindrical coordinates were chosen as:

$$r_k = 5k\ \text{mm}\ ; k = 0, 1, 2, 3, \ldots, 51$$

$$\theta_l = l^0\ , l = 0, 1, 2, \ldots, 359$$

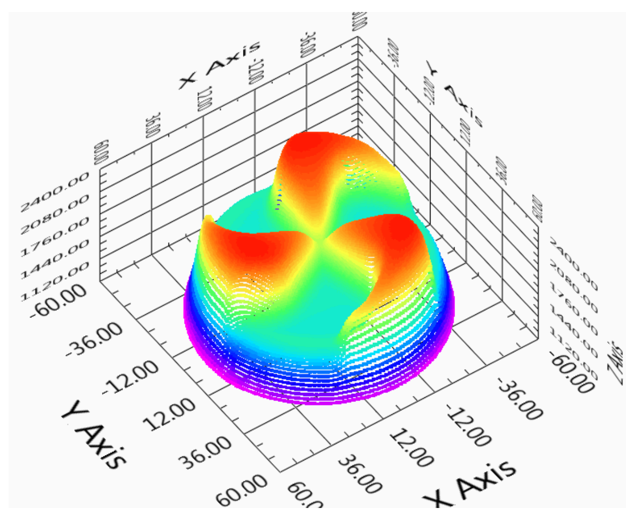

Figure 3: A profile of measured magnetic field of the CS-30 cyclotron.

Figure 4 shows the average magnetic fields along the equilibrium orbits. it also shows that the average magnetic field increases slowly along the radius in accordance with the isochronous equation:

$$w = \frac{q<B(r)>}{\gamma(r) m_0} \tag{1}$$

where w is the cyclotron frequency, q is the particle charge, $< B(r >$ is the average magnetic field, the relativistic factor $\gamma(r)$ increases with the radius, and m_0 is the rest mass of the particle.

ISBN 978-3-95450-167-0

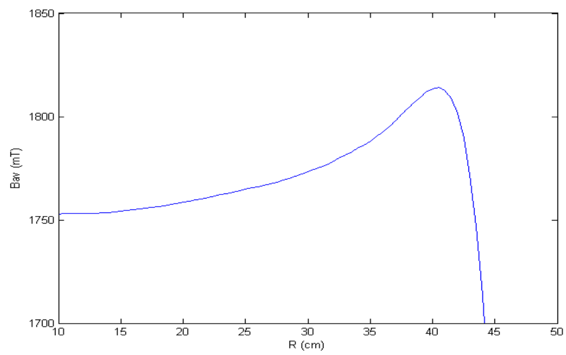

Figure 4: The average magnetic field along the equilibrium orbit as a function of the radius.

Figure 5 shows the computed radial focusing frequency based on the measured magnetic field. And this figure shows that between R =10 cm and around 40 cm, ν_r is above the $\nu_r = 1$ resonance. However, around $R = 10$ cm, the beam passes through the $\nu_r = 1$ resonance. This is due to the small field bump applied near the center, as mentioned above. However, it is not so harmful to the beam because the beam passes through this resonance quickly. Near the extraction region, there is also $\nu_r = 1$. Figure 6 Shows that the average ν_z is about 0.48, but particle crosses the $\nu_z = 0.2$ resonance near $R = 10$ cm.

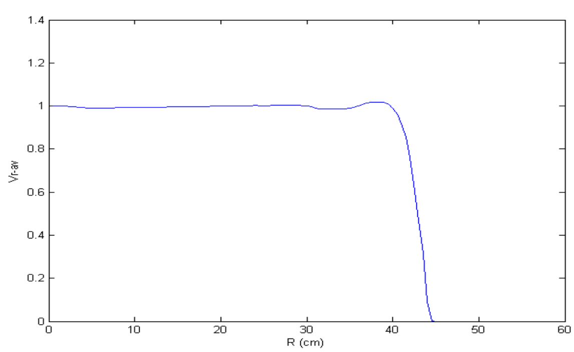

Figure 5: Radial focusing frequency as a function of the radius.

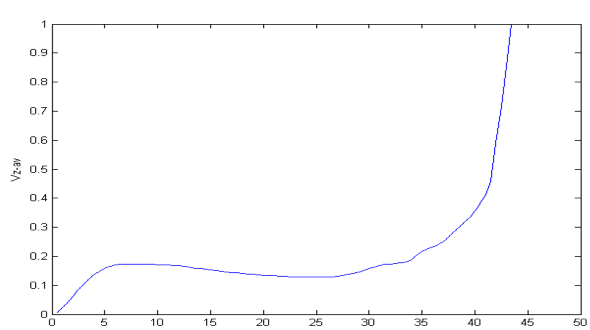

Figure 6: Vertical focusing frequency as a function of the radius.

CONCLUSION

The Hall probe mapping system provides accurate measurement. The maximum field obtained is 2.2 T and the average is 1.8 T. The average magnetic field error along the beam orbit is less than 0.015%.

ACKNOWLEDGEMENT

This project was supported by the NSTIP strategic technologies program in the kingdom. Award No. (14-MAT-1233-20).

REFERENCES

[1] F. Alrumayan *et al.*, "Status report of the Cyclotrons C-30, CS-30 and RDS-111 at KFSHRC", Saudi, Arabia.

[2] K. H. Park *et al.*, "Field mapping system for cyclotron magnet", *Nucl. Inst. Meth. in Phy. Res.*, A 545 pp. 533-541, 2005.

[3] B. Berkes, O. Brombach, O. Szavits. "Fast field mapping device for cyclotron magnets", *IEEE Transaction on Magnetics*, vol. MAG-17, no. 5, Sep. 1981.

[4] I. Bolshakova *et al.,* "High precision mapper for cyclotron magnet", *IEEE Transactions on Applied Superconductivity*, vol. 14, no. 2, Jun. 2004.

[5] J. Zhong *et al.*, "The design of magnetic field measurements system for CYCIAE-100", *IEEE Transactions on Applied Superconductivity*, vol. 20, no. 3, Jun. 2010.

[6] K. H. Park *et al.*, "Field Mapping System for the KIRAMS-30 cyclotron magnet", *Journal of the Korean Physical Society*, vol. 54, no. 4, Apr. 2009, pp. 1475-1480.

THE ASSEMBLY AND ADJUSTMENT OF THE SECOND STRIPPING PROBE SYSTEM FOR CYCIAE-100

Shizhong An[1], Lipeng Wen, Jiansheng Xing, Genshou Liu, Lei Cao, Yang Wang, Xiaoliang Fu, Yinlong Lv, Xiaotong Lu, Yiwang Zhang, Zhenguo Li, Gaofeng Pan, Tianjue Zhang,
China Institute of Atomic Energy, Beijing, 102413, P.R. China

Abstract

A 100 MeV H- compact cyclotron is under construction at China Institute of Atomic Energy (CYCIAE-100). The proton beams ranging from 75 MeV - 100 MeV with 200 µA beam intensity will be extracted in dual opposite direction by charge exchange stripping devices. The stripping probe system is the key part of extraction system for CYCIAE-100. The first stripping extraction system was installed in 2014 and it has satisfied all kinds of requirements for the proton beam extraction. The first 100MeV proton beam was got on July 4, 2014 and the beam current was stably maintained at above 25 µA for about 9 hours on July 25, 2014. The first RIB with ISOL system driven by 100 MeV proton beam was generated in 2015. The second stripping system was installed in 2015 after the assembly and adjustment. The beam commissioning based on the second stripping system will be finished and the extracted proton beam parameters will be measured in detail in this year.

INTRODUCTION

A 100 MeV H- compact cyclotron is under constructed in China Institute of Atomic Energy (CYCIAE-100) [1-3]. The machine is selected as the driving accelerator for the Beijing Radioactive Ion-beam Facility (BRIF). 75 MeV - 100 MeV proton beams with 200 µA - 500 µA beam intensity will be extracted in dual opposite direction by charge exchange stripping devices [3]. In total 7 target stations will be built based on CYCIAE-100 for the fundamental and applied researches. For CYCIAE-100, the diameter of main magnet is 6160mm, corresponding to 4000mm for the magnet pole. The magnet is 2820mm high with a total weight of 435 tons. The quality factor of the two rf resonators reach 9500, which is highest value among the existing compact cyclotrons in the world. Two identical 100 kW RF amplifiers have been adopted to drive two cavities independently. In order to reduce the beam losses caused by residual gas stripping process, a high-speed cryo-panel system is utilized to raise the vacuum to $5*10^{-8}$ torr level. By the end of 2013, all the sub-systems of the cyclotron are installed and assembled on site. The first stripping extraction system was installed in 2014 and it has satisfied all kinds of requirements for the proton beam extraction. The first 100MeV proton beam was got on July 4, 2014 [4] and the beam current was stably maintained at above 25 µA for about 9 hours on July 25, 2014. The first RIB with ISOL system driven by 100 MeV proton beam was generated in 2015. The operation stability have been improved and beam current have been increased gradually. 720 µA beam was got on the internal target at the beginning of this year. The effort for mA beam is continuing and 1135 µA beam was got on the internal target in June of this year [5]. Figure1 is the fresh photo of the cyclotron and its beam line.

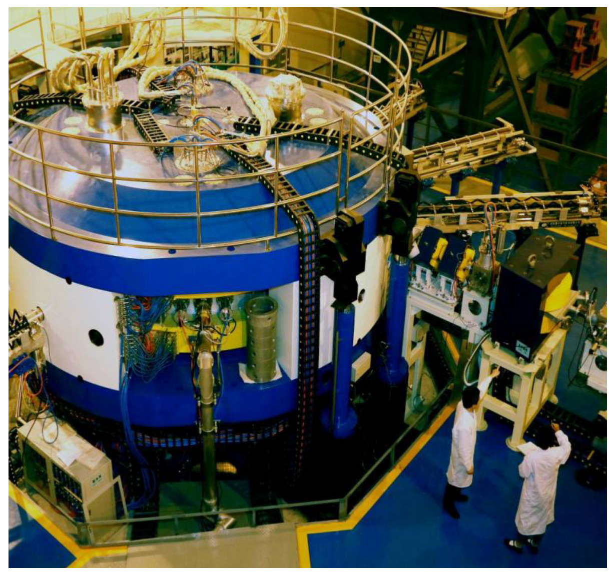

Figure 1: The 100 MeV compact cyclotron.

The second stripping system was installed in 2015 after the assembly and adjustment. After the debugging, the stripping probe system can work very well. The movement precision is better than 0.1mm and the precision of azimuthal movement is better than 0.01 degree, which satisfies the design requirement. The beam commissioning based on the second stripping system will be finished and the extracted proton beam parameters will be measured in detail in this year.

THE DESIGN AND CONSTRUCTION OF STRIPPING PROBE SYSTEM

The stripping probe system is the key part of extraction system for CYCIAE-100. Two stripping probes with carbon foil are inserted radially in the opposite direction from the main magnet pole and the obtained two proton beams by charge exchange after stripping foil are

[1] szan@ciae.ac.cn

ISBN 978-3-95450-167-0

transported into the crossing point in a combination magnet center separately under the fixed main magnetic field [6]. The combination magnet is fixed between the adjacent yokes of main magnet in the direction of valley region. The stripping probe system is the most complex device among the individual devices and it includes the following parts: foil exchanger, rotation driving, rotation support, rod motion, bellows the base, and corresponding vacuum and control systems. The auto controlled precision is very high for different movements. In order to save the foil changing time, the structure of the foil changing system in the vacuum is adopted. The foil automatic changing machine is outside the magnetism yoke and 12 pieces foil can be changed in one time. The stripping foil thickness of 150 - 180 μg/cm^2 is adopted for CYCIAE-100.

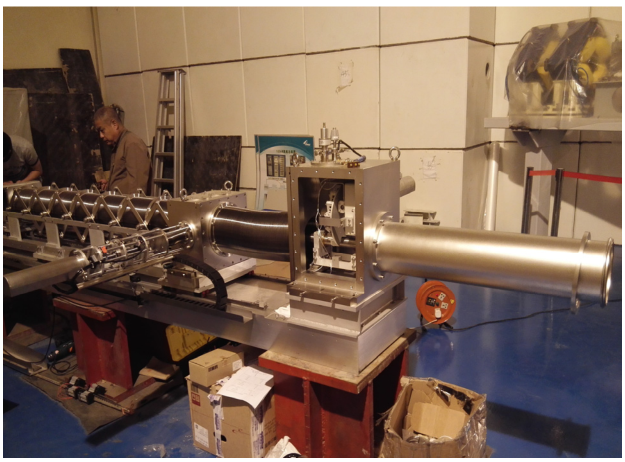

Figure 2: Main structural model of stripping probe.

According to the extraction design, the stripping probe can be moved in the radius direction and rotated in the azimuth direction and swing around the fix point. The minimal inserted position of the stripping probes is at R=160cm and the swaying angle is ±5 degree. The radial movement range of stripping probe is about 110 Cm. The precision requirement of the movement orientation for the stripping system is very high. In total 12 carbon foils are installed and can be replaced in the operation. The stripping probe is mainly consisting of 6 parts, i.e., foil exchanger, rotation driving, rotation support, rod motion, bellows and the base. In the process of designing, several schemes have been gradually determined, including the point selection under the vacuum condition, driving mode of the rod rotation and structural design of the foil exchange in the vacuum. The length of stripping probe is 4752mm and the total weight is about 600 kg. Figure 2 shows the whole second stripping probe system and Figure 3 shows the stripping foil exchanger device.

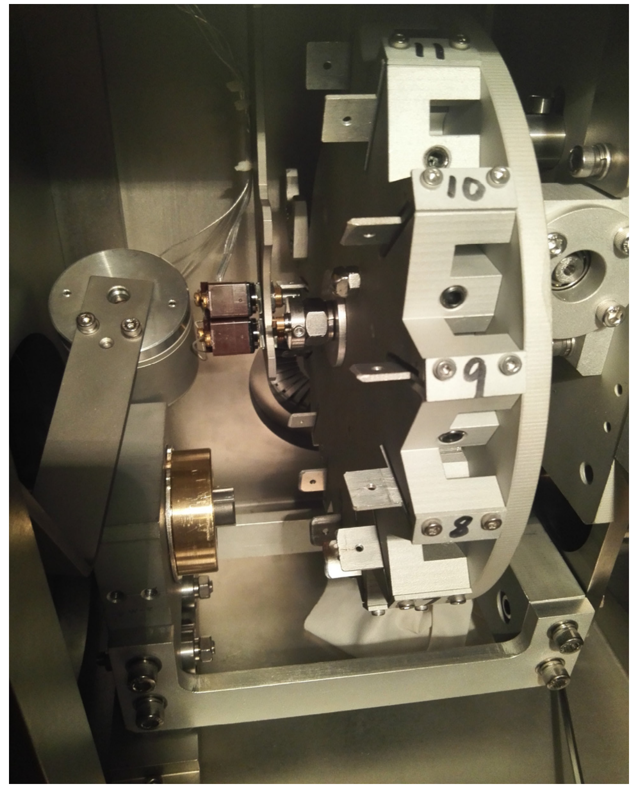

Figure 3: Stripping foil exchanger with 12 pieces foils.

To achieve the required accuracy, the closed control loop is used in the design, as shown in Figure 4. The microprocessor MSP430F149 communicates with control computer through serial port, getting the position setting information from the control interface, and this information is then sent to the control circuit. Position feedback signal, read by a high precision potentiometer, is sent to the control circuit to control the servo motor driver MSE421 together with the position setting information, thus forming the closed control loop. The output signal from microprocessor is a digital signal, and an ADC is needed to change the digital signal to a voltage signal for the amplifiers. The DAC7631, 16-bit, serial input, voltage output, guaranteed 15-bit monotonic performance is used in the design and ±2.5V reference voltages are got from the servo motor driver MSE421. The influence of mechanical errors can be eliminated through the closed loop in the design. High precision components are chosen, such as the servo motor with a small inertia, together with a 250:1 gear head. Servo motor driver MSE421 from Mclennan, the driving current, feedback factor can be adjusted easily by switch. Taking the fine regulating for example, the total length is 340mm with accuracy better than 0.1mm, error less than 0.03%. The LWH400 position potentiometer from Novotechnik, the linearity is better than ±0.05%, repeatability is better than 0.01mm. In the design, high precision low noise amplifier OPA2227 is chosen, with an offset voltage of 100 μV and temperature drift of 0.6 μV/oC. In the design of PCB, weak signal should be well protected.

ISBN 978-3-95450-167-0

Siemens PLC STEP7 development environment is used in the second stripping probe system to control the main accurate positioning, interlock in the riot shaft closed motor and stripping of movement target four road safety chain effect. Compared with the analog comparator control, PLC with the digital signal control can reduce the errors of the control volume and has a more precise input and feedback. Motor swing caused by using analog circuit can be controlled effectively with PLC control system and connection circuit becomes simple. Logic control is more intuitive and the movement of stripping probes is easier to debug. After the adjustment for the second stripping probe system, the first one will be used PLC control too.

Figure 4: Layout of the stripping foil control system.

THE ASSEMBLY AND ADJUSTMENT OF THE SECOND STRIPPING PROBE SYSTEM

The machining process of the second stripping probe system was finished in 2015 and the assembly and adjustment was finished in 2015 and was installed afterwards. After the adjustment, the stripping probe system can work very well. The movement precision is better than 0.1mm, which satisfies the design requirement. Figure 5 shows the installed second stripping probe system. Figure 6 shows the control interface of the second stripping probe.

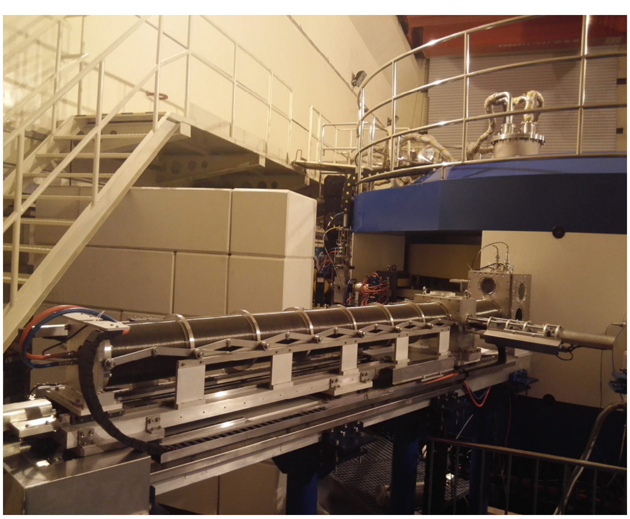

Figure 5: The installed second stripping probe system.

Figure 6: The control interface of the stripping probe.

SUMMARY

For CYCIAE-100, the second stripping system was installed in 2015. More design details for the second system are improved due to the experiment of the first one. The PLC digital control is used for the second system and it is much easier to debug and control the whole system. After the debugging, the stripping probe system can work very well. The movement precision is better than 0.1mm and the precision of azimuthal movement is better than 0.01 degree, which satisfies the design requirement. The beam commissioning based on the second stripping system will be finished and the extracted proton beam parameters will be measured in detail in this year.

ACKNOWLEDGEMENTS

The authors are grateful to Dr. Yi-Nong Rao from TRIUM, who give us considerable help and providing materials concerning the cyclotron under design. Also the authors would like to give the grateful acknowledge to Dr. Wernor. Joho from PSI, about the extraction discussion and lots of useful suggestions from him.

REFERENCES

[1] Tianjue Zhang, et al., A New Project of Cyclotron Based Radioactive Ion-beam Facility, APAC 2004.
[2] Tianjue Zhang, et al., 100 MeV H- Cyclotron as an RIB Driving Accelerator, CYC 2004.
[3] Tianjue Zhang, et al., CYCIAE-100, a 100 MeV H- cyclotron for RIB production, N.I.M B 261 (2007) 1027-1031.
[4] Tianjue Zhang and Jianjun Yang, The Beam Commissioning of BRIF and Future Cyclotron Development at CIAE, HB2014 (Invited talk).
[5] Tianjue Zhang, Shizhong An, et al., mA Beam Acceleration Efforts on 100 MeV H- Cyclotron at CIAE, ECAART-2016, Jyväskylä, Finland.
[6] Shizhong An, et al., Stripping extraction system for CYCIAE-100, CYCIAE Design note in Chinese, 2006.

ISBN 978-3-95450-167-0

THE CONTROL SYSTEM DEDICATED FOR BEAM LINE OF PROTON RADIOGRAPHY TEST-STAND ON A 100 MeV CYCLOTRON CYCIAE-100*

Y.W. Zhang†, L. Cao, J.J. Yang, H.R. Cai, X.T. Lu, Y. Wang, L.P. Wen, T.J. Zhang,
China Institute of Atomic Energy, Beijing, 102413, China

Abstract

This paper outlines the design of the control system for beam line ofproton radiography on 100 MeV cyclotron CYCIAE-100. The project proposed by the China Institute of Atomic Energy (CIAE). For high intensity operation, a dedicated controls system and stabilized operation environment are preferable. In order to satisfy the requirements of this proton radiography control system, we have built a complex control system which contains PLC controller, MOXA controller, IOC and EPICS system. In this paper, the designing, constructing and commissioning of the proton radiography control system will be described.

INTRODUCTION

CYCIAE-100 100MeV H- compact cyclotron is the main component of HI-13 tandem upgrade project. It can provide the proton beam of 70-100 MeV with beam current of 200-500 μA. CYCIAE-100 consists of some subsystem such as main magnet system, RF system, main vacuum system, beam detection system, control system and so on. The control system is an important subsystem which main function is to carry out the devices of CYCIAE-100 automation control.The first beam of CYCIAE-100 was extracted on July 4, 2015 [1]. In previous work, we have completed the main magnet system and vacuum system. With the improve of system stability, in June of 2016, 1135 μAbeam was got on the internal target.

Nowadays, proton radiography is a main tool for providing a development direction for advanced hydrotesting research. For x-ray radiography, its advantages are simplicity and relatively low cost of the facilities, the main element of which is an electron accelerator. But x-ray with high penetrating power passing through an object engender photon showers which result in background noise in the recorded image. In thick objects, the photon noise can completely conceal the useful image. Proton radiography does not have these problems. In terms of penetrating power, protons significantly surpass x-rays. In 2014, the low energy proton radiography system utilizes a 11MeV proton beam to radiograph thin static objects, which developed at CAEP [2].

* Work supported by by NSFC (Grand Nos.11375273 and 1146114103) and the CNNC Youth Innovation Team Founding.
† dteach@yeah.net

OVERALL DESIGN

Proton radiography requires a particular magnetic lens system to provide a point-to-point imaging from the object to the image. The design detail is described in Ref. [3]. For the above reason, the beam precise control must to take into account at the beginning of the control system design. In the beam line of proton radiography there are many subsystems, such as magnet power system, vacuum system, water cooling system, beam detection system and stripping probe system. Considering for a lot of signals to be control, we use the SIMEMENS S7 series Programmable Logic Controller (PLC) controller which CPU model are S7-400, S7-300 and ET-200. Because of the SIMEMENS S7 series have exceptional stability. The MOXA controller is used to receive analog feedback signals. The Experimental Physics and Industrial Control System (EPICS) [4] is the like a bridge connects the Input/Output Controller (IOC) and the Operator Interface (IOC) which stored in the INSPUR server. The structure of proton radiography control system is shown in Figure 1.

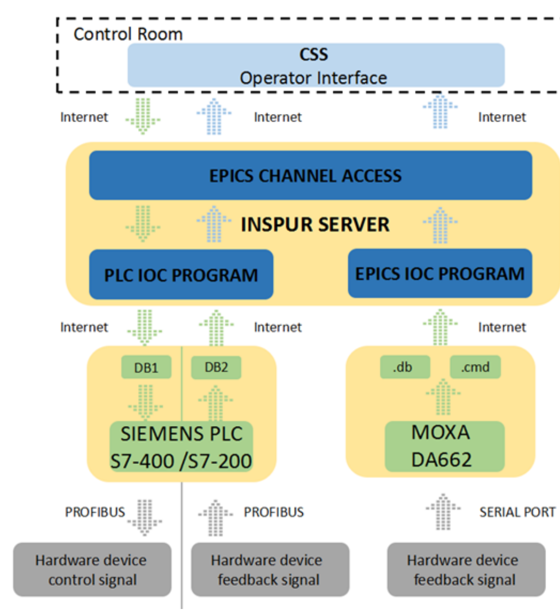

Figure 1: The structure of proton radiography control system.

ISBN 978-3-95450-167-0

INPUT/OUTPUT CONTROLLER DESIGN

We use SIMEMENS S7 series, CPU model for S7-400/S7-300 and ET-200. Communication between PLC and ET-200 adopts PROFIBUS. In this Beam Control System, there are three main categories of PLC program function block. They respectively are interlock system for control devices power, special blocks for communication between devices and general function block for complete logic control. DB is the communication module of PLC. It is evident from Figure 1 that DB1 gives the control commands to the devices and DB2 accept the feedback signal form the devices. For chose the PLC, there are two reasons. Firstly, it is known that stability is the fundamental requirement in the control system. SIEMENS PLC S7-400 can provide a stable platform. Because of the CPU can work interchangeably. Secondly, S7-400 uses a modular design. It contains a variety of modules, for example SM modules、CP modules、FM modules. All these modules can be directly connected to the beam diagnostics devices. It can collect a lot of feedback signals of the device. During the control process, PLC can provide a rich programming models. This allows us to perform complex logic control.

We also use MOXA controller. MOXA is a kind of multi-serial port embedded computer. Communication protocol is used RS232/RS485. This device is connected to a power device and vacuum gauges. It has the advantage of multi-channel feedback signals can be collected on a single device. Figure 2 and Figure 3 show the connection of these devices.

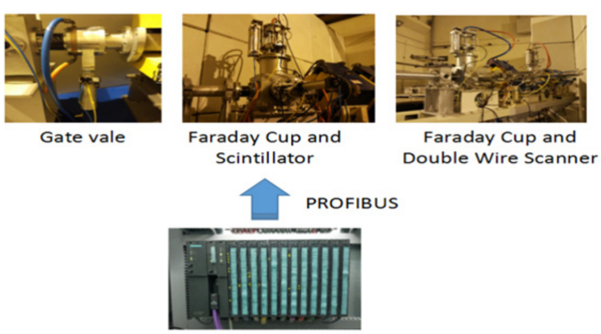

Figure 2: The connection of the PLC.

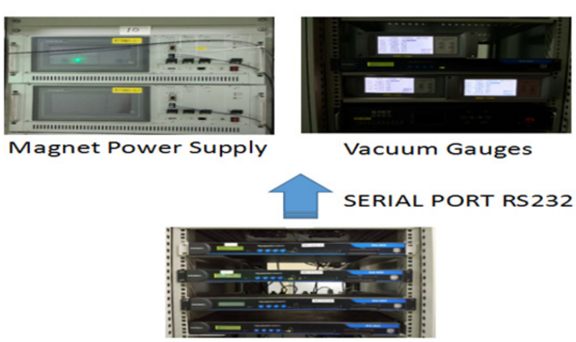

Figure 3: The connection of the MOXA.

Unlike other beam line of CYCIAE-100. In order to maintain the accuracy of the beam, there are more beam diagnostics devices and vacuum gauges in the beam line of proton radiography. In particular, those analog signals from vacuum gauges will complicate the control logic. To keep the code of PLC simple, we use the Visual EPICS Database Configuration Tool (Visual DTC). Visual DCT is an EPICS configuration tool completely written in Java and therefore supported is various systems. The Visual DCT program is shown in the Figure 4. The 'ai' block is a feedback signal which type is word from the MOXA controller. The 'bo' block is a control signal which type is bite from the PLC. The function of Visual DCT is not only to communicate the MOXA controller and the PLC but also can change the type of the signal. Therefore, we can save saved a lot of work to writing the program in PLC.

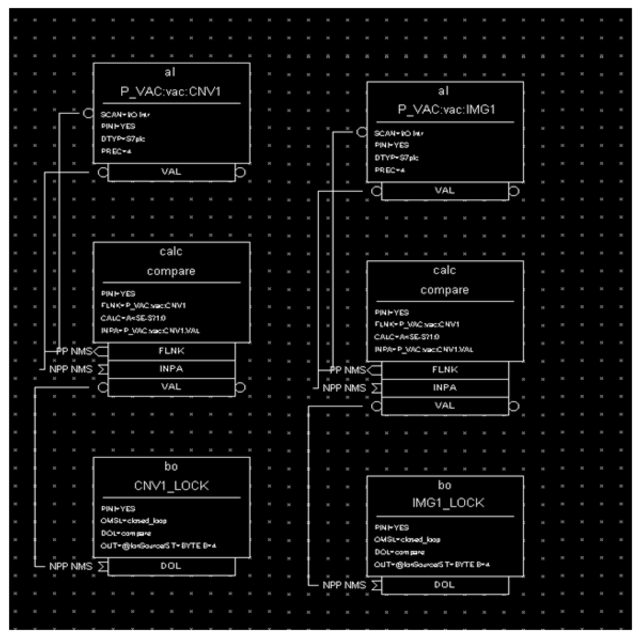

Figure 4: The program of the Visual DCT.

EPICS is a set of Open Source softwaretools, libraries and applications developed collaboratively and used worldwide to create distributed soft real-time control systems for scientific instruments such as a particle accelerators, telescopes and other large scientific experiments. In EPICS, the control algorithms are stored in independent databases which are not combined until the system is loaded onto the IOC. All the databases and the IOC program is stored on the INSPUR server. EPICS runs on processors which use a real-time kernel, therefore the rate at which EPICS database records are processed is deterministic. All these characteristics are important for the beam line control system delivers.

ISBN 978-3-95450-167-0

Channel access (CA), the ‘backbone’ of EPICS, hides all details of TCP/IP network from both devices and servers. It connects all devices with all servers. CA also creates a very solid ‘firewall’ of independence between all devices and server code, so they can run on different processors, and even be from different versions of EPICS. Using a host tool, the database is described in terms of function-block objects called ‘records’. About 50 record types exist for performing such chores as analog input and output; binary input and output and other tasks. For supports not only Windows OS, but also other operating system like Linux OS or MAC OS. The Linux OS was installed on the INSPUR server because of its stability. The IOC program of PLC and MOXA controller are stored separately in the database of server. It consists of two parts, one is the file of records which describes the properties of the signals, the other is the file of initiator program. During control process, operator can login the server remotely and loading the initiator program files. When the IOC program is running, the signals will be send to the OPI from the devices of beam line.

OPERATOR INTERFACE DESIGN

Control System Studio (CSS) [5] is an Eclipse-based collection of tools to monitor and operate large scale control systems. It is dedicated to supplying tools for control system, data integration and data visualization to enable users to achieve their objectives. BOY is an Operator Interface (OPI) development and runtime environment. PV Manager is the library that talks to the control system. Simple PV Layer is a layer that provides a simpler and abstract interface to talk to PV Manager. BOY only needs to talk the Simple PV interface. At OPI is a graphical user interface that displays live control system data to operators and allow them to input data to the control system. The OPI of our Beam Line of Proton Radiography control system (Figure 5) clearly shows all the devices running status. All digital signals and analogue signals through the EPICS to OPI. All the operations are completed in OPI. We use the vividly image instead of the simple switch button. This makes the interface more attractive.

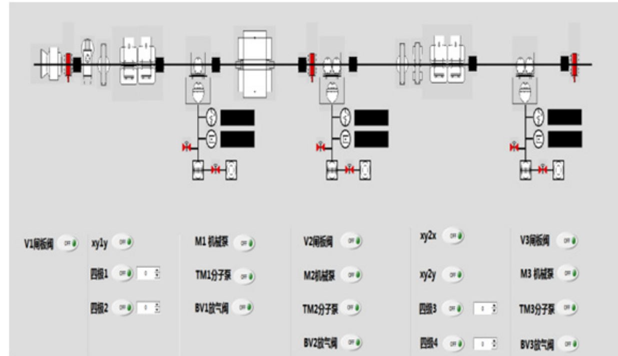

Figure 5: The OPI of the beam line control system.

CSS/BOY supports not only EPICS, but also other frameworks like DOOCS or TINE. Moreover, it can run on all the most common operating systems such as Windows, Unix and Mac X OS. This makes the whole control system has strong portability.

CONCLUSION

The design work for Control System Dedicated for Beam Line of Proton Radiography on 100 MeV Cyclotron CYCIAE-100 has shown in this paper. Results indicate that the designed parameters and the control system are reasonable and could meet the requirements for basic beam line of proton radiography. In the next step, the Alarm System and Data Base system will be built by using CSS.

REFERENCES

[1] J.J. Yang, et al., “New Development of the High Power Proton Cyclotrons at CIAE”, in *Proc. of 12th Symposium on Accelerator Physics*, Lanzhou, China, pp.16-19, (2014).

[2] T. Wei, et al., “First experimental research in low energy proton radiography”,*Chinese Physics C* Vol. 38, No. 8 (2014) 087003.

[3] J.J. Yang, et al., “Proton Radiography Experiment Based on a 100 MeV Proton Cyclotron” , in this proceedings.

[4] Experimental Physics and Industrial Control System. `http://www.aps.anl.gov/epics`

[5] Control System Studio `http://controlsystemstudio.org`

THE HIGH QUALITY WATER COOLING SYSTEM FOR A 100 MeV CYCLOTRON*

Zhenguo Li†, Hongru Cai, Tao Ge, Longcheng Wu, Gengguo Liu
Lei Cao, Junyi Wei, Jianjun Yang
China Institute of Atomic Energy, Beijing

Abstract

A high quality water cooling system with total heat power dissipation of 500 kW has been built and successfully used for a 100 MeV high intensity Cyclotron. The main features of this system are high water quality with specific conductivity bellow 0.5 μS/cm, high cooling water temperature stability better than ±0.1 ℃ for long time operation，and much electric power-saving in comparing with classical design. For some special usages, such as high beam power target and vacuum helium compressor, they all are well treated and reasonably separated from the main cooling system. There are totally 108 distributed water branches corresponding to different sub-equipments of the cyclotron. The water cooling system is under automatic control with PLC, the operation status and all parameters can be remotely monitored from the control room. All of the involved equipments can be switched on/off by one key, no on-duty staff is needed at normal conditions. This system has been put into commissioning for two years and proved successful and reliable.

INTRODUCTION

Beijing Radioactive Ion-beam Facility (BRIF) has been built at China Institute of Atomic Energy (CIAE). As a key component of BRIF project, CYCIAE-100 provides a 75 MeV – 100 MeV, 200 μA– 500 μA proton beam [1,2]. The main part of heat power dissipation coming from different equipments of the cyclotron should be taken away by water cooling system, which is totalling about 500 kW. There are some special requirements, such as high beam power target with strong radioactivity and vacuum helium compressor requiring ultra-low temperature cooling water. Besides, the main magnet power supply and RF system require cooling water have higher temperature stability to maintain their high specifications, external ion source locating at 40 kV high level require the cooling water of low conductivity. All of the special requirements should be considered in the general design of the water cooling system.

Unique climate of Beijing is another factor of considerations for the water cooling system design. The four-seasons are clear and there is a much difference in temperature between summer and winter, usually above 50 . Fully take the advantage of the natural environments of Beijing could save much electric power and decrease the operation cost during the continuous run terms.

GENERAL DESIGN

Based on the requirements of the 100 MeV cyclotron, the cooling water system was generally designed with one main system and two sub-systems. The main system is used for the most part of equipments of the cyclotron, and the two sub-systems are used for hot targets and vacuum helium compressor respectively.

The key parts of the main system are located in the recycling water supply room and the cooling devices including a large scale of heat dissipation tower and 10 cryo-generators are located outside nearby. A specially designed water storage tank with a separator inside is used for internal and external recycling water simultaneously. The de-ionized water production and water quality improving devices are built online to keep the cooling water always in good conditions. The cooling water delivered to the RF power generators, RF cavities, main magnet coils, ion-source, beam lines and so on through different water tubes and distributed branches.

There are totally 108 distributed water branches corresponding to different sub-equipments of the cyclotron. At each branch, there are one water flow switch for safe inter-lock, one flow meter for monitoring, one temperature sensor for remote diagnostics.

The cooling water used for the high power targets is supplied by a dependant water loop located in the radioactive-protective room, which has heat exchange with the main cooling system but physically separated from it to avoid any pollute of the main cooling water.

The cooling water of 15 ℃ required by vacuum helium compressor is provided with another separated water cooling system, because it is much different in temperature from the main cooling water of about 25 ℃.

The general diagram of water cooling system is shown in Fig. 1.

† lizgciae@hotmail.com

ISBN 978-3-95450-167-0

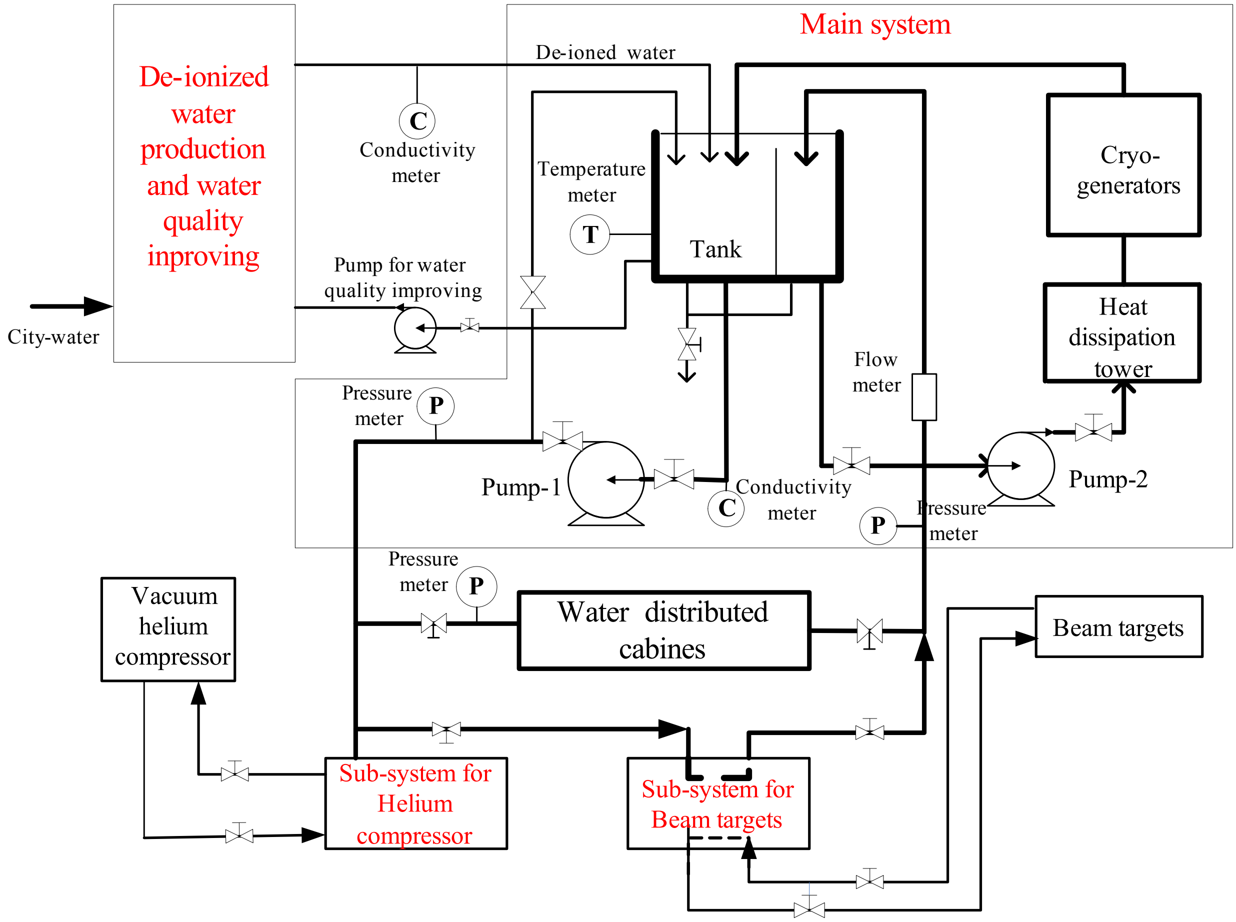

Figure 1: The overall diagram of water cooling system.

MAIN FEATURES OF THE SYSTEM

High stability of water temperature, high water quality, much electricity and water saving, operation reliability are the main features of the system.

Stability of cooling water temperature is better than ±0.1 ℃ for long time operation, see Fig. 2. Water temperature is controlled through two loops or two steps: firstly, the showering pump with changeable rotation rate is used in the heat dissipation tower and controlled with water temperature at tower exit; secondly, the 10 cryo-generators on/off sequence are well programmed based on water temperature in the tank.

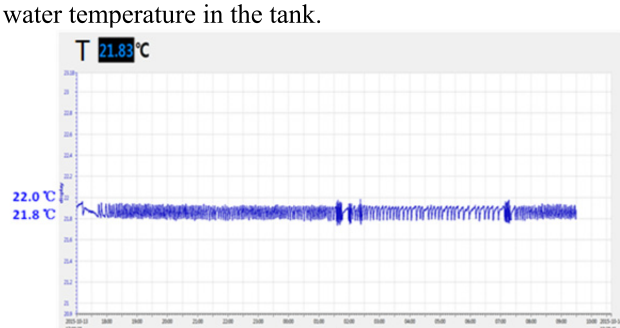

Figure 2: The cooling water temperature display.

The conductivity of cooling water maintains bellow 0.5 μS/cm, see Fig. 3. It is realized with an online water quality improving loop including a conductivity sensor, a recycling water pump and an EDI device, which can automatically put on /off according to cooling water conductivity.

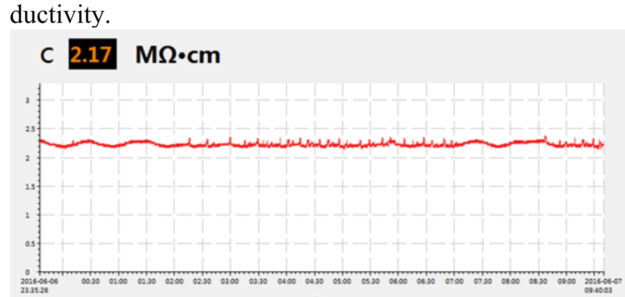

Figure 3: The cooling water quality display.

Water cooling system has adopted a combination of tower and cryo-generators (see Fig. 4), and kept tower dissipation in advance with cryo-generators as a complement. It takes the advantages of the climate in Beijing and fully uses the natural resources. The practice is shown that power consumed by cooling tower is only about one fourth comparing with cryo-generators for same amount of heat dissipation. There is much electricity saved in this

ISBN 978-3-95450-167-0

way for a continuous operation. The online water quality improving loop usually delivers about 10% waste water, but it is much better than the city water in quality. All the waste water produced by EDI is fully reused, only its small part is drain away. The electricity and water saving could cut off much operation cost.

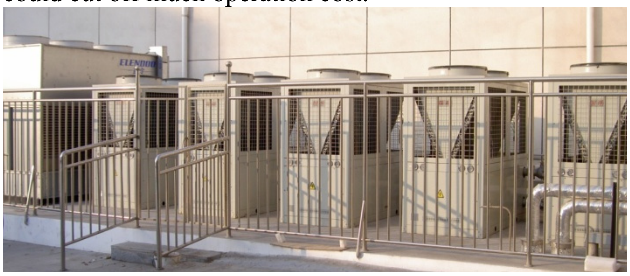

Figure 4: The picture of cooling tower and cryogenerators.

All equipments of this water cooling system have proved reliable since its commissioning. The whole system is under automatic control and can be switched on/off by one key, no on-duty staff needed at normal conditions.

OPERATION STATES

The cooling water system for 100 MeV cyclotron was put into commissioning at end of 2013, supporting the 100 MeV proton beam extracted from the machine in July of 2014. Its main specifications are satisfactory, especially well meet the high stability required by the main magnetic field, RF generators and RF cavities, reducing their temperature drift and providing stable conditions for their long-term operation.

Safety Interlocks with other individual equipments through different branch water flow switches, water temperature monitors and PLC net programming.

System controls, operation status and all parameter monitoring could be done remotely in the control room. Some dynamic displays are given bellow in Fig. 5:

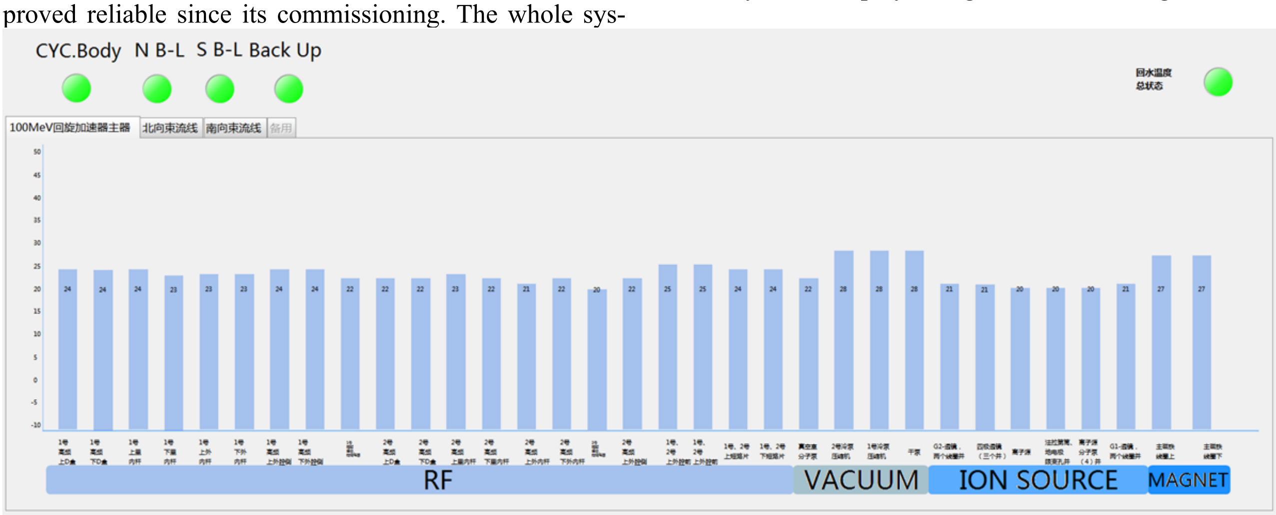

Figure 5: One of the display pages for distributed water branches.

CONCLUSION

This cooling water system is oriented to the 100 MeV cyclotron. It involves a main system and two sub-systems to meet the different needs of the cyclotron. The combination of cooling tower and cryo-generators was adopted from a consideration of Beijing climate and power saving. Two control loop regulations made its high stability possible. Online water quality improving device installed has kept the conductivity of cooling water always at good conditions. More than two years operation has proved its high qualities and reliability.

REFERENCES

[1] Z.G. Li, *et al.*, “General Engineering Considerations for the 100 MeV Cyclotron”, in *Proceedings of the 19th International Conference on Cyclotrons and their Applications*, Tokyo, Japan, Oct. 2004.

[2] T.J. Zhang, Z.G. Li, Y.L. Lv, “Progress on Construction of CYCIAE-100”, in *Proceedings of the 19th International Conference on Cyclotrons and their Applications*, Lanzhou, China, Sep. 2010, pp. 308-313.

ISBN 978-3-95450-167-0

PRELIMINARY DESIGN OF RF SYSTEM FOR SC200 SUPERCONDUCTING CYCLOTRON

Gen Chen†, Yanfang Bi, Chujie Chao, Yonghua Chen, Kaizhong Ding, Hansheng Feng, Yuntao Song, Yongsheng Wang, Manman Xu, Qingxi Yang, Xin Zhang, Jinxing Zheng, Jian Zhou, ASIPP, Hefei, China
Oleg Karamyshev, Galina Karamysheva, Nikolay Morozov, Evgeny Vasilievich Samsonov, Grigori Shirkov, JINR, Dubna, Russia

Abstract

The SC200 is a compact superconducting cyclotron, which is designed under the collaboration of ASIPP (Hefei, China)-JINR (Dubna, Russia), for proton therapy. The protons are accelerated to 200 MeV with maximum beam current of ~500 nA. The very high mean magnetic field of 2.9 T-3.5 T (center-extraction) challenges the design of radio frequency (RF) system because of the restricted space. The orbital frequency of the protons is ~45 MHz according to the magnetic field and beam dynamics. The RF system is supposed to operate at 2rd harmonic of ~90 MHz. Two RF cavities located at the valley of the magnet have been adopted. The preliminary design of RF system, which consists of active tuning, coupling and so on, is presented. The computation and simulation showed good results to ensure the RF cavities operating at the 2rd harmonic and the proper variation of acceleration voltage versus radius.

INTRODUCTION

The SC200 superconducting proton cyclotron is designed under the collaboration of ASIPP and JINR for proton therapy. The RF cavity is the critical and complex component of SC200. The RF cavity works as a resonator to generate necessary voltage between Dee gaps to accelerate protons continuously. The half-wavelength coaxial resonant cavity has been adopted in SC200. It is mainly composed of stem, Dee, coupling loop, tunable shorted terminal, cavity, as shown in Fig. 1.

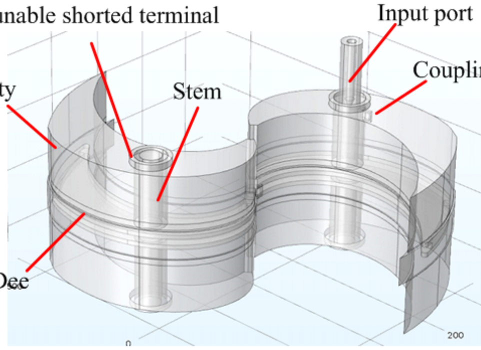

Figure 1: RF cavity structure.

According to the physical design requirements of SC200 Superconducting Proton Cyclotron [1-3] the main technical parameters of RF cavity are described in Table 1.

Table 1: Technical Parameters of SC200 RF Cavity

Parameter	Value
Frequency	90 MHz(2 harmonic)
Cavity number	2
Source power	~100 kW
Cavity type	λ/2 coaxial
Accelerate voltage	60 kV(Center)~ 120 kV(Extraction)
Dee azimuthal extension	40°
Dee Cavity azimuthal extension	50°

Due to the high magnetic field of cyclotron， the compact structure has challenged the requirements of RF design. First, the resonance frequency and correct voltage distribution have to fit the requirements of acceleration, especially in the central region and extraction region. What's more, the proper coupling and tuning method should be found to cover possible working frequency. Finally, the operation stability and thermal consideration need to be taken into account.

ACCELERATION

Resonance frequency (f) and quality factor (Q value) are the important characteristic parameters to describe the performance of the resonant cavity (RF cavity). Table 2 shows the simulation results from different codes, respectively. The simulation results show good agreement.

The eigen-frequency of ~90 MHz has been found with correct voltage distribution along the radius of Dee, as shown in Fig. 2. The Q value has been estimated with and without the surface loss of cavity. The typical value of Q is ~7000 which is reasonable and acceptable. The Q value (~4500) has decreased as the surface of cavity was set up to loss material (copper).

Table 2: Eigen Mode Analysis Results

Software	f (MHz)	Q (without loss of cavity)	Q (with loss of cavity)
CST	90.6	7230	4590
HFSS	89.6	6880	\
COMSOL	89.46	\	4067

† chengen@ipp.ac.cn

ISBN 978-3-95450-167-0

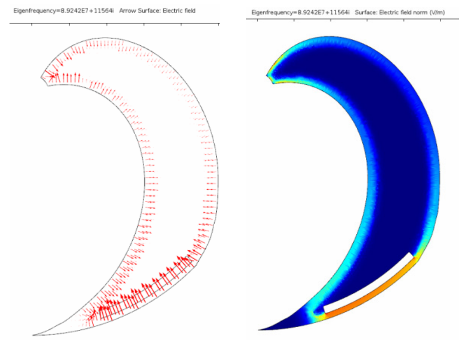

Figure 2: The electric field vector diagram at f=89.24 MHz.

Voltage Analysis

The function of the RF cavity is to generate the high-frequency electric field in the gap between the electrode and the ground. Each turn the proton cross the gap, it will be accelerated by the electric field. Therefore, it is extremely essential to analyze the distribution of the Dee voltage.

Accelerating voltage was obtained according to the integral of azimuthal component of the electric field in the accelerating gap on a fixed radius. Comparing with the simulating results from various codes: HFSS, CST, COMSOL, the bilateral voltage distribution along the radius was shown in Fig. 3.

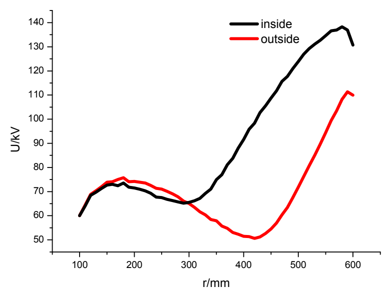

Figure 3: The analysis results of COMSOL.

Based on the good consistency of above simulation results, the 60 kV at central region and 120 kV at extraction region have been achieved.

Power Loss

Due to the lossless of energy in vacuum, the power loss of the RF cavity just involves the surface loss of the conductors. Thus, the power loss can be written as:

$$P_W = \frac{1}{2}\sqrt{\frac{\pi\mu f}{\sigma}}\int |H|^2 \partial S \qquad (1)$$

Where μ is the copper permeability, $\mu = 4\pi\times10^{-7}$ H/m, f is the working frequency, $f = 9.07\times10^{7}$ Hz, σ is the conductivity of the cavity materials, $\sigma = 5.8\times10^{7}$ S/m(copper); H is the magnetic intensity vector, which is calculated by MICROWAVE STUDIO [4].

In order to design the water cooling system, the cavity is divided into several parts to consider the loss of each part. According to the above formula of the cavity power loss, the magnetic intensity vector H of the corresponding position has been integrated on the surface of each part. Then the total power loss of the cavity is 84.2 kW. The proportion and the distribution of power loss of each part have been calculated, as shown in Table 3.

Table 3: The Power Loss of Each Part

Part	Power Loss(kW)	Proportion(%)
Stem	21.06	25.01
Dee	34.33	40.77
Cavity	28.59	33.96
Coupling loop	0.1516	0.18
ALL	84.2	\

TUNING

Because of the RF power loss, the increasing temperature must influence the resonance frequency of Dee cavity. To cope with such frequency shift, the inductance tuning (tunable shorted terminal) has been adopted， as shown in Fig. 4. The tuning system is designed to cover the resonant frequency of 90 MHz with bandwidth of ±1 MHz.

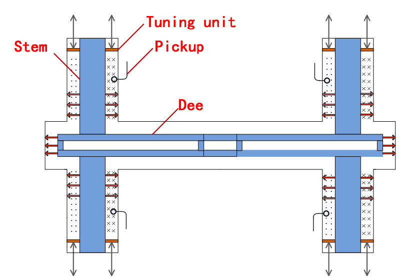

Figure 4: Double cavity structure.

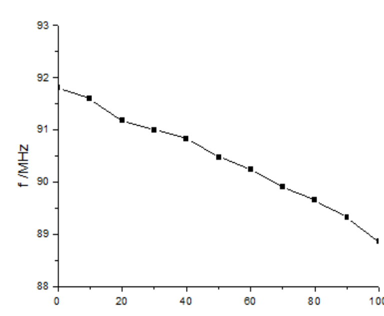

Figure 5: Resonance frequency as a function of mobile distance.

Figure 5 shows the simulation result, the x-coordinate represents the tunable distance of the shorted terminal, the y-coordinate represents the resonance frequency of the cavity. The minimum and maximum frequency can be found: Fmin=88.8 MHz and Fmax=91.8 MHz.

ISBN 978-3-95450-167-0

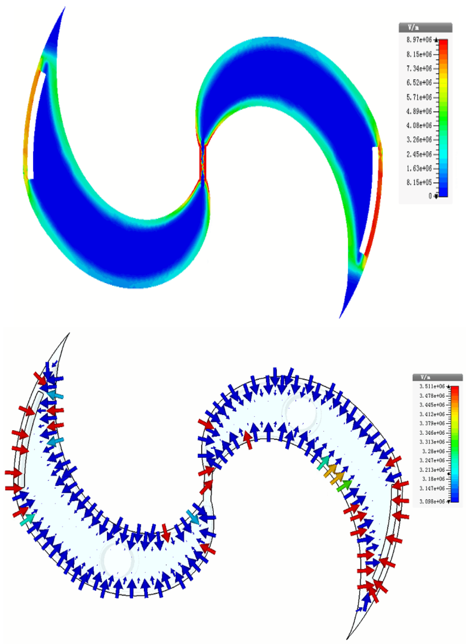

Figure 6: Electric field distribution.

What’s more, In the case of double cavity, there are four tuning units, as shown in Fig. 4. The electric field of the left and right cavities will be unbalanced if the positions of the tuning units are not symmetrical. Figure 6 shows the simulation results of such unbalanced electric field with the asymmetrical position of tuning units. It can be easily found that the electric field of the right cavity is significantly larger than the left one. Therefore, the pick-up signals of each tuning unit need to be calibrated to achieve the feedback control in the low level radio frequency (LLRF) system to keep the balance of electric field.

COUPLING

The role of the coupling device is to transmit the RF power into the RF cavity [5]. In SC200, the cavity is a high impedance device, which should be matched to the characteristic impedance (50 ohm) of the transmission line through coupling loop, as shown in Fig. 7. The stem has been used as the outer conductor of coaxial transmission line, meanwhile the inner conductor of transmission line goes through the stem and forms a coupling loop in the RF cavity. Due to the compact and integral design of stem and coaxial line, there are no additional holes on the magnet yoke for coupling design.

In order to achieve the matching at the working frequency of 90 MHz, the shorted terminal is turned to ensure that the resonant frequency of the RF cavity is 90 MHz. And then, the coupling loop area has been changed to achieve the minimum of the scattering parameter S11. The matching point can always be found by changing the area of coupling loop, and the reflection coefficient is significantly related to the resonant frequency of the RF cavity and the position of the shorted terminal, see Figs. 8 and 9.

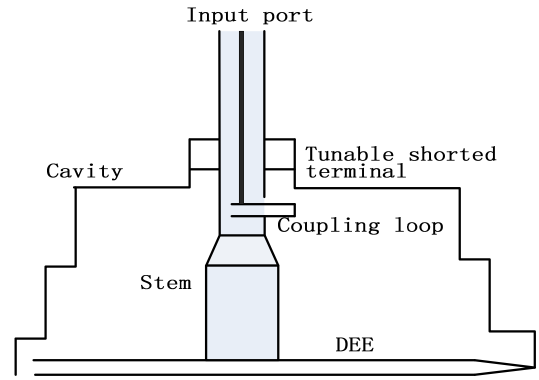

Figure 7: Coupling loop within the stem.

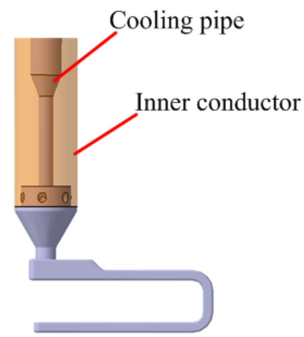

Figure 8: Inductive coupling loop.

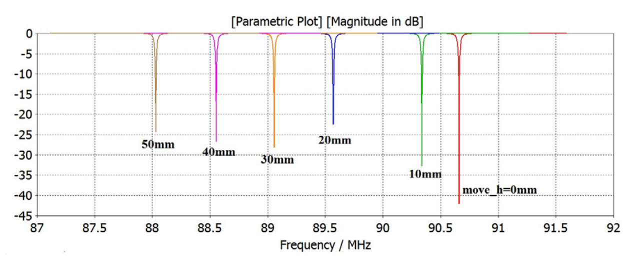

Figure 9: Reflection coefficient at various positions

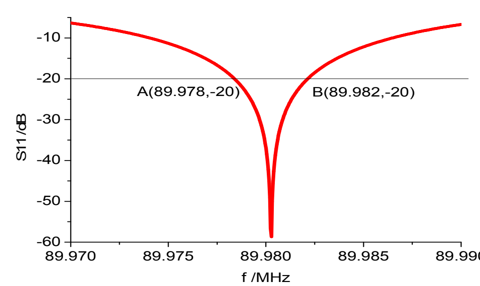

Figure 10: Reflection coefficient.

The bandwidth approximates 4 kHz, as shown in Fig. 10. The reflection coefficient S11 can be optimized to -40 dB by adjusting the area of coupling loop carefully.

THERMAL ANALYSIS

As we know, the thermal deformation of RF cavity caused by the power loss significantly affects the resonance frequency. What is worse, the deformation of Dee will impact on the balance of acceleration electrical field and the proton orbit.

Due to the complexity of RF cavity, each component of the RF cavity has been simulated respectively. The simulation results of power loss (Table 3) are used as the boundary condition of these components in ANSYS codes.

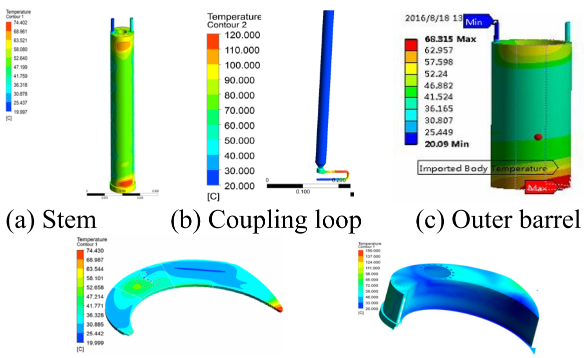

(a) Stem (b) Coupling loop (c) Outer barrel

(d) Dee (e) Cavity

Figure 11: Temperature distribution.

Thermal analysis has been done, but the results are not very good and satisfactory. The temperature distribution is extremely nonuniform, and the local temperature is too high to operate stably, as shown in Fig. 11. Therefore, the water cooling system needs to be further optimized to achieve acceptable and stable operation temperature of each part.

DISCUSSION AND CONCLUSION

The characteristic parameters of RF cavity have been accomplished based on the simulation. The accurate eigen mode at the working frequency of 90 MHz has been found. The Q value is about 7000 that can meet with the design requirement. The tuning system is designed to cover the resonant frequency of 90MHz with bandwidth of ±1 MHz, and the adjusting range of frequency is 88.8 MHz ~ 91.8 MHz. The coupling design has been completed through inductive coupling.

The 60 kV at central region and 120 kV at extraction region have been achieved, which can prove the needed acceleration voltage at the central and extraction region. The total power loss of the cavity is 84.2 kW, and then the RF source with maximum power of ~100 kW was designed to meet the requirement.

For future work, the mockup design and measurement have been put on the agenda, besides the cooling system.

REFERENCES

[1] G. Karamysheva *et al.,* "Design studies of the compact superconducting cyclotron for proton therapy", in *Proc. ICAP'15*, Shanghai, China, 2015, pp. 109-111.

[2] Y. Jongen *et al.,* Compact superconducting cyclotron C400 for hadron therapy, *Nuclear Instruments and Methods in Physics Research*, section A, vol. 624, issue 1, pp. 47–53, 2010.

[3] Y. Jongen *et al.* "RF cavity design for superconducting C400 cyclotron", *Physics of Particles and Nuclei Letters*. pp. 386−390, 2011.

[4] M. P. David, *Microwave Engineering*, Publishing House of Electronics Industry, Beijing, 2008.

[5] P. K. Sigg, "RF for cyclotrons", CERN, Geneva, Switzerland, Rep. CERN-2006-012, 2006, pp. 231-251.

ISBN 978-3-95450-167-0

NEURAL NETWORK BASED GENERALIZED PREDICTIVE CONTROL FOR RFT-30 CYCLOTRON SYSTEM

Young Bae Kong, Eun Je Lee, Min Goo Hur†, Jeong Hoon Park, Yong Dae Park, Seung Dae Yang
Radiation Instrument Research Division, Korea Atomic Energy Research Institute,
Jeollabuk-do, Republic of Korea 580-185

Abstract

Beamline tuning is time consuming and difficult work in accelerator system. In this work, we propose a neural generalized predictive control (NGPC) approach for the RFT-30 cyclotron beamline. The proposed approach performs system identification with the NN model and finds the control parameters for the beamline. Performance results show that the proposed approach helps to predict optimal parameters without real experiments with the accelerator.

INTRODUCTION

Beamline tuning is an important and critical issue in the accelerator control. The control is to manipulate the devices of the system in order to make the accelerator be the desired state. The operators should control the accelerator system to obtain the desired output. Especially, beam tuning is a difficult task for the accelerator. Beamline tuning is to manipulate the control parameters of beamline to obtain the desired beam shape. For the beam tuning, the operators should manipulate the parameters based on the measured information during the operation. Beamline tuning requires human resources and is time consuming works since the accelerator is very non-linear and highly complex.

Researches using the neural network have been proposed for the beam tuning. In SLAC, artificial intelligence (AI) technique has been proposed for accelerator control [1]. The approach utilizes the feedback control approach based on the neural network. The approach trains the neural network with the beamline emulator and then controls the steering magnets of the beamline. Another approach has been proposed for the control of the ion source of the RFT-30 cyclotron [2]. The approach trains the ion source model using the neural network and then finds the optimal parameters to obtain the desired ion source current.

In this work, we propose a neural network based generalized predictive control (NGPC) approach for the RFT-30 cyclotron beamline. First, the proposed approach constructs the beamline model by using the NN based system identification procedure. Next, the model predictive control (MPC) approach is used for finding the optimal parameters for the beamline tuning. The proposed approach can reduce the beam tuning time and enables effective beamline tuing. Moreover, combined with other control approach, it enables beam auto-tuning and control automation.

† hur09@kaeri.re.kr

CONTROL PROBLEM OF RFT-30 CYCLOTRON BEAMLINE

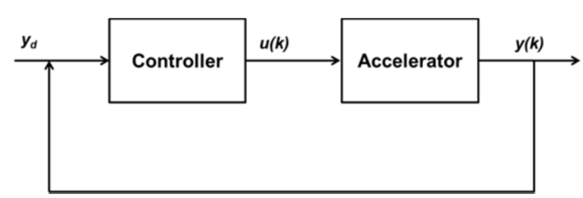

Figure 1: Overview of the accelerator feedback control.

Control means to manipulate the input signals to obtain the desired output signals. Figure 1 shows the accelerator feedback control system. Assume that $y(k) \in R^m$ is m-dimensional plant (i.e., accelerator) output and $u(k) \in R^n$ is n-dimensional control input, and reference target y_d is a control objective. The controller receives the error $e(k) = y_d - y(k)$ and then decides the control input $u(k)$. Control problem is defined as minimizing the error $e(k)$ between the reference target y_d and the plant output $y(k)$.

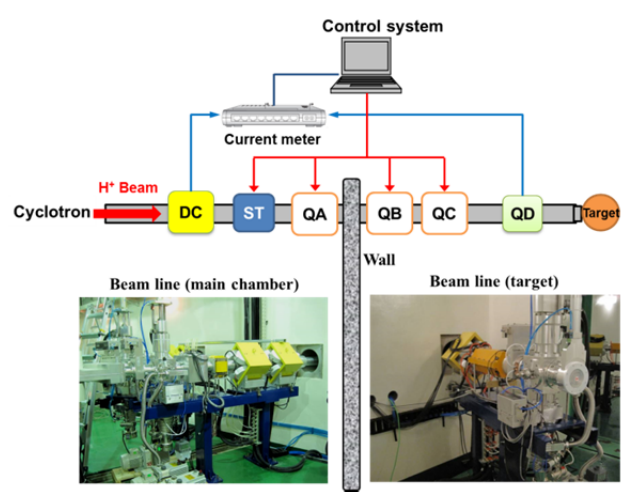

Figure 2: Overview of the RFT-30 cyclotron beamline.

Figure 2 shows the beamline system of the RFT-30 cyclotron. The RFT-30 cyclotron is a 30 MeV proton accelerator for radioisotope (RI) production and research. The RFT-30 is composed of four beamlines which are used for transmitting the proton beam to a target system. As shown in Fig.2, each beamline is composed of drum collimator (DC), steering magnet (ST), quadrupole magnet (QA, QB, QC), quadrant (QD), and vault/target faradaycup (FC). Steering magnet controls the center position of the proton

ISBN 978-3-95450-167-0

beam and quadrupole magnet changes the shape of the proton beam. Beamline quadrant is used for measuring the current and the distribution of the beam, and it is composed of top, bottom, left, right parts. The cyclotron operator measures the current data from the beamline and then performs beamline tuning by adjusting the steering magnet and the quadrupole magnet to modify the beam.

NEURAL NETWORK BASED PREDICTIVE CONTROL FOR RFT-30 BEAMLINE

In this work, we propose a neural network based predictive control approach for RFT-30 cyclotron beamline system. The proposed approach is composed of NN training procedure and model predictive control (MPC) procedure. Figure 3 shows the block diagram of the proposed approach for RFT-30 cyclotron beamline.

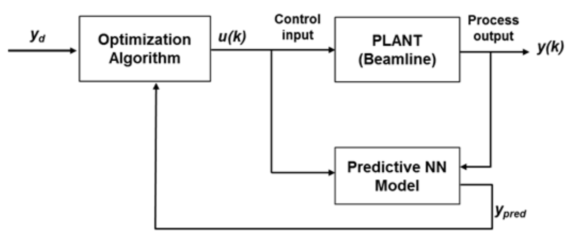

Figure 3: Block diagram of NN predictive control approach for RFT-30 cyclotron.

In the NN training procedure, the approach constructs the beamline prediction model based on the neural network. Based on the NN prediction model, the controller finds optimal control input by using the model predictive control approach.

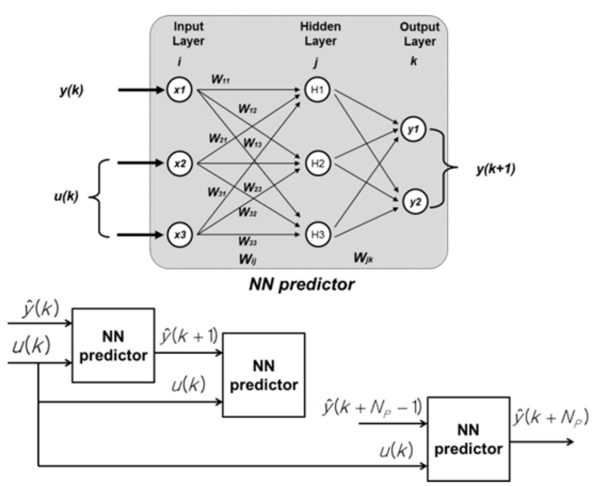

Figure 4: N-step ahead prediction model using neural network.

The NN prediction model is constructed through *N-step* ahead prediction approach. Figure 4 shows the *N-step* ahead NN prediction procedure using the neural network. The process output $y(k+1)$ at next time step is obtained by predicting the output with the NN predictor, and the prediction procedure is iterated to the future time step $k+N_p$.

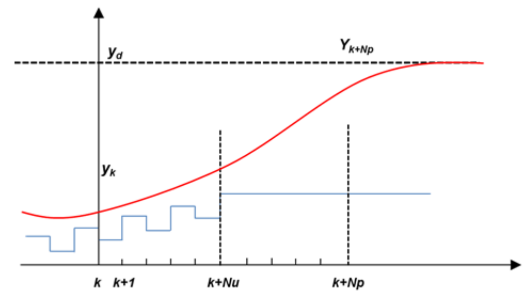

Figure 5: Generalized predictive control approach for RFT-30 cyclotron.

After the NN training procedure, the approach finds the optimal control input by using the model predictive control scheme [3]. Model predictive control approach is defined as minimizing cost function:

$$\text{Minimize} \quad \sum_{i=1}^{Np}\left[y_d - \hat{y}(k+i-1)\right]^2 + \lambda \sum_{i=1}^{Nu}\left[u(k) - u(k+i-1)\right]^2 , \quad (1)$$

where N_p is the prediction horizon, y_d is the reference trajectory, N_u is the control horizon, u is the control input, and λ is the weighting factor. As shown in Fig. 5, the basic principle of MPC is to maintain the reference trajectory y_d by predicting the value $y(k+1)$, $y(k+2)$, …, $y(k+N_p)$. Equation (1) is to find optimal $u(k)$ and it is nonlinear unconstrained minimization problem. We apply the quasi-newton algorithm to solve the optimization problem.

PERFORMANCE RESULTS

To analyze the performance of the NGPC approach, we evaluated simulations based on the RFT-30 cyclotron beamline. First, we performed NN training by using the accelerator simulation code SAMM [4]. Figure 6 shows the structure of the beamline simulation. The initial beam conditions of the beamline are set in the simulation. The input parameters of the steering magnet and the quadrupole magnet are randomly generated and then calculate the process output by using the beamline emulator. Based on the input and the output parameters, the beamline model is constructed using the neural network. Next, the reference trajectory is established and the optimal control inputs are calculated using the predictive controller. Control input is performed through one-step ahead prediction and Nu is set to 1. We calculate the second term of cost function by using $\Delta u(k)=u(k)-u(k-1)$. This procedure is iterated to the maximum time step. Simulation parameters are shown in Table 1.

ISBN 978-3-95450-167-0

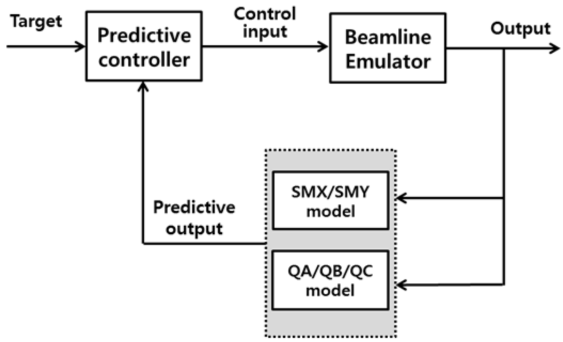

Figure 6: Generalized predictive control approach for RFT-30 cyclotron.

Table 1: Simulation Parameters

Parameter	Description	Value
Target	Reference target of proton beam	-
Yout	Output from beamline emulator	-
SMX/SMY	Steering magnet input	Max 0.02 T
QA/QB/QC	Quadrupole magnet input	Max (T/m) 3.54/3.15/1.89
Tmax	Maximum time step	100
Np	# of prediction horizon	2
Nu	# of control horizon	1
λ	Weighting factor	0.3

Figure 7 shows the performance results for the beamline simulation. We randomly change the center position and shape of the proton beam at every 10 step. As shown in Fig. 7, the process output of the beamline is close to the reference trajectory. Although the reference target is suddenly changed, the error between the target and the process output is small. The simulation results show that the proposed NGPC approach enables beamline tuning when the initial beam is constructed and the reference target is set up.

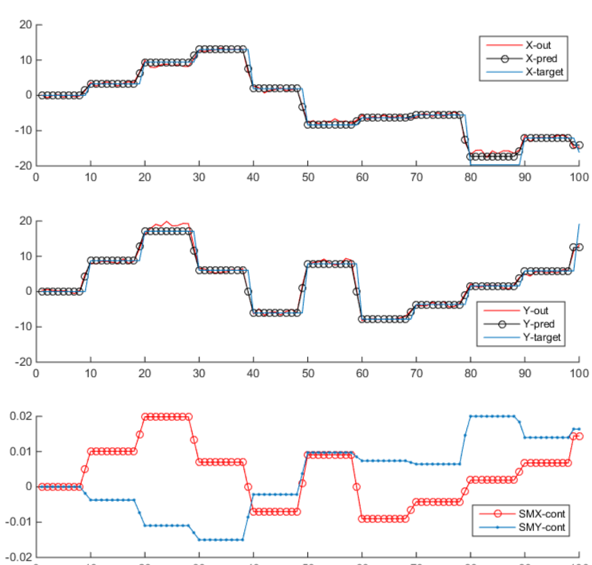

(a)

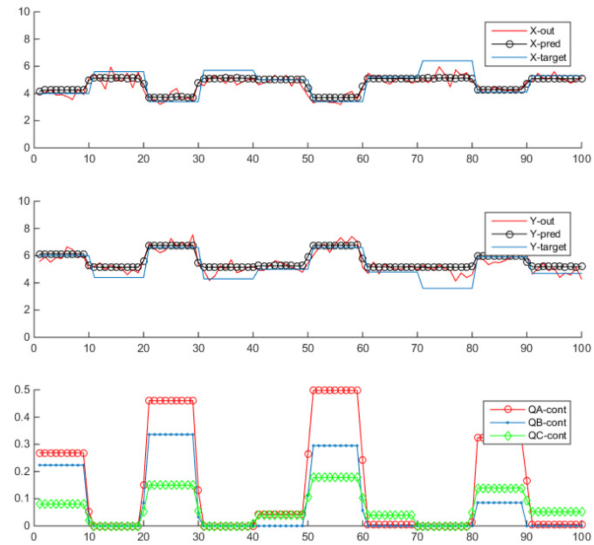

(b)

Figure 7: Performance results of the GNPC (a) Steering magnet control (b) Quadrupole magnet control.

CONCLUSIONS

In this work, we proposed a neural network based predictive control approach for the RFT-30 cyclotron beamline system. The beamline tuning is a difficult task and time consuming work for the human operators. The proposed approach enables the human operators to be easy beam tuning and provides the operators with reducing the time and cost required for the accelerator operation. We plan to implement the proposed approach into the RFT-30 cyclotron control system and conduct the real experiments using the real time beamline control system.

REFERENCES

[1] D. Nguyen *et al.*, "Accelerator and Feedback Control Simulation Using Neural Networks", in *Proc. PAC'91*, IEEE Particle Accelerator Conference, San Francisco, California, USA, May 1991, pp. 1437-1439.

[2] Y. B. Kong *et al.*, "Predictive Ion Source Control Using Artificial Neural Network for RFT-30 Cyclotron", *Nuclear Instruments and Methods in Physics Research A*, 806, 2016: 55-60.

[3] D. Soloway and P. J. Haley, "Neural Generalized Predictive Control," *IEEE International Symposium on Intelligent Control*, (1996): 277-282.

[4] `http://pcwww.liv.ac.uk/~awolski/main_links_computercodes.htm`

PLC CONTROL SYSTEM FOR VACUUM AND 20 kW RF AMPLIFER

Huisu Kim†, Jongchul Lee
Department of Energy Science, Sungkyunkwan University, Suwon, Korea
Mitra Ghergherehchi, Sangchul Mun, Ho Namgoong, Donghyub Ha, Jong- Seo Chai*
College of Information & Communication Engineering, Sungkyunkwan University, Suwon, Korea

Abstract

Since 2015, the Sungkyunkwan University has been upgrade 10 MeV cyclotron (SKKUCY-10) prototype for producing radio isotopes. For stable and robust cyclotron operation, local controller is main issue. Especially, RF and Vacuum is main part for control system and each sub system fault result in damage to the other sub systems. To solve those problem, we integrate RF amplifier and vacuum local controller by LS PLC (Programmable Logic Controllers). Integrated Interlock event is also processed at one controller. This paper describe system requirement for RF amplifier and vacuum and discuss the detailed design and software development by PLC programming at SKKUCY -10.

INTRODUCTION

Robust and reliable SKKUCY-10 control system is required to operate stably cyclotron for produce radioisotopes. During several year, Sungkyunkwan University has been develop and test SKKUCY-10 prototype control system. SKKUCY-10 controller has one Compact-RIO main controller and several local controllers that include magnet, RF and Ion source hardware [1]. SKKUCY-10 main control system was implemented to realize supervisory Control and Data Acquisition (SCADA). At operating by main controller, RF AMP and vacuum subsystem faults and sequence error sometime result in critical damage to other subsystem such as RF power generation at low vacuum level. To solve those problem, we replace RF and vacuum local controller to one integrated PLC. Developed PLC controller was implemented based on RF, vacuum system requirement and operation sequence.

SYSTEM REQUIREMENT

Figure 1 show the scheme of RF and vacuum system. Integrated vacuum and RF control system require to operate and monitor all hardware. It also require interlock function to protect each machines from damage during operating cyclotron. To fulfil requirement of controller each SKKUCY-10 RF and vacuum system analysis was implemented and based on analysis, interlock mechanism was developed.

RF AMP Requirement

SKKUCY-10 three-stage RF amplifier consist of pre-amplifier, intermediate power amp (IPA) and Power amp (PA). Through tree-stage RF amplifier, RF power is amplified to 20 KW. In SKKUCY-10 RF amplifier, 350V IPA and 7500V PA Vacuum tube anode power supply were required [2]. Heating for Electron emission from cathode was considerable for warming-up procedures. At least 120 second filament warming-up time was set for stable vacuum tube performance. RF amplifier interlock is also considerable parameter for protection from high voltage. Overload parameter from each cathode current and VSWR value is used for major Interlock parameter for amplifier.

VACUUM Requirement

Dual vacuum pump architecture is main properties of SKKUCY-10 vacuum system. Dual vacuum make it possible to decrease time to reach high vacuum level (10^{-6} Torr) and also machine fault probability. Two diffusion pump and two rotary pump are connected through magnet valley holes. At initial step to make vacuum state, rotary pump are used. Using Rotary pump, 10^{-2} Torr Vacuum level can be reached. After reached those low vacuum level, diffusion pump are operated. Vacuum level mainly determine state of vacuum system. According to vacuum level and pump states, roughing, foreline and gate valve are operated.

Interlock

In order to machine protection and personal safety, each system interlock conditions and system interaction during high power RF test were considered. Table 1 show RF and vacuum signal and condition for interlock.

Table 1: Signal and Condition for Interlock

Value	condition	Event
VSWR OVELOAD	PA over Voltage	RF oscillator off
IPA&PA OVERLOAD	IPA & PA Cathode over current	RF oscillator, &PA off
PA Water flow status	Flow rate	RF oscillator , HV off
PA air cooling status	Contact switch off	RF oscillator , HV off
Pump status 1&2	False	RF oscillator off
Vacuum status	Vacuum level	RF oscillator off
EMERGENCY STOP	Ture	HV off

*jschai@skku.edu

ISBN 978-3-95450-167-0

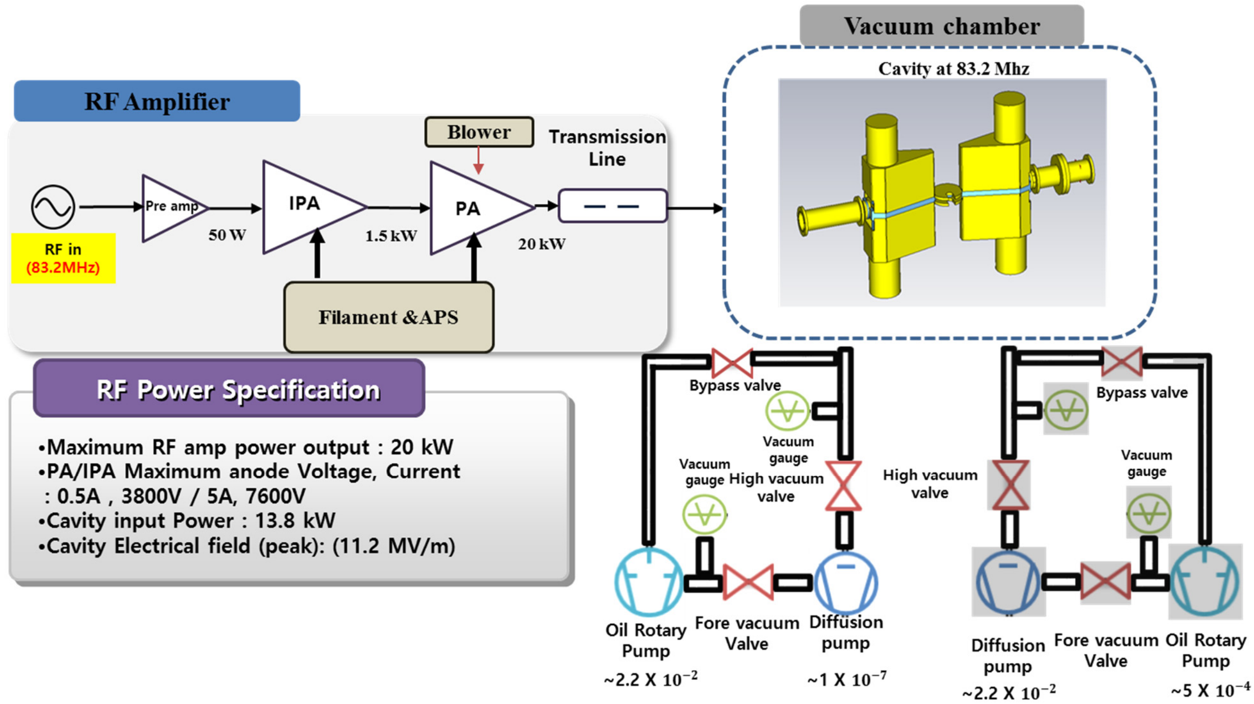

Figure 1: Architecture of RF AMP and vacuum system.

To conduct high power RF test, there are two type of event for Interlock exist. One object of interlock event is to protect from vacuum status fault to damage AMP and cavity and it is possible by switching off oscillator. VSWR overload protection was implemented by VSWR board in Figure 2. To detect VSWR overload its op amp circuit compare Voltage from direction coupler with reference voltage. VSWR board output consist of digital output to indicate VSWR interlock and RF detector voltage that is adjusted to PLC voltage input module range. Other object is protection from amp itself fault. Amp fault include high voltage overload and cooling status of AMP and it is prevented by shutting off power amplifier high voltage.

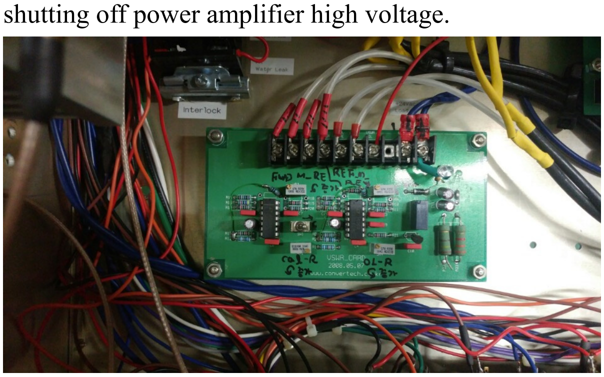

Figure 2:VSWR board for VSWR overload.

Operating Procedure

Vacuum and RF AMP operation sequence start from making low vacuum state in SKKUCY-10 chamber. Oil Rotary pump can reach 2.2×10^{-2} torr. Transition condition to operate diffusion pump is determined by chamber vacuum degree (5×10^{-2} Torr). In our system, we set 5×10^{-6} Torr in SKKUCY-10 vacuum chamber as RF amp operation start-up condtions. RF amp operation is start from air cooling of AMP rack. air cooling, filament and anode power supply is turned on according to sequence of amp operation steps. To Intergrated operating procedure realization. Periodic check for interlcok condition and machine states are required

CONTROL SYSTEM IMPLEMENT

Due to the cost efficiency, stability and reliability, PLC is employed for platform. In our controller, The XGB series PLC was used and its main unit is XBC-DN64H. It has 32 DC 24 input point and 32 transistor output point. Input units default response time is 3 ms and on/off voltage is DC 19V/6V. Output unit response time is within 1 ms. PLC Main unit is used to realize sequence and interlock function of controller. The other used modules are 4 channel XBF-AD04A and XBL-EMTA. XBF-AD04A is analogue voltage and current input module that can be select by switch [3]. Its voltage input range is from 0 V to 10 V and current input range is 0 ~ 20 mA. This unit is used for measuring pressures and RF power. Figure 3 show ladder diagram of Vacuum pleasure calibration from Analog input module.it convert from voltage to digitalized vacuum value.

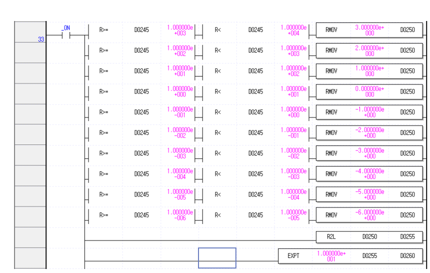

Figure 3: Ladder diagram of Vacuum pressure calibration from XBF-AD04A module.

ISBN 978-3-95450-167-0

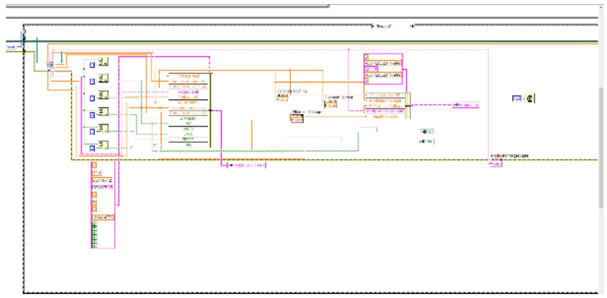

Figure 4: Ladder diagram of auto operation mode.

XBL-EMTA is 100 Mbps Ethernet communication module for remote control. LS PLC Modbus TCP/IP protocol was used for communication between LS PLC as shown in Figure 4 and main control platform (NI – Compact RIO). Realization of Human Machine Interface (HMI) is based on producer/consumer design pattern and it is also made for main control program of SKKUCY-10 cyclotron. HMI for AMP & Vacuum control is shown in Figure 5.

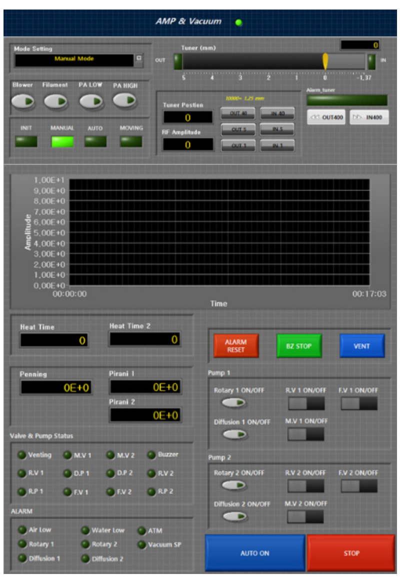

Figure 5: HMI for AMP & Vacuum control.

In HMI, manual & auto sequence is selected by “AUTO ON” button Automation process is implemented in XBC-DN64H PLC. Digital input and output variables is mainly used for auto scan code. Timer and comparison operator is used for timing delay for each step and condition for next step as show in Figure 6.

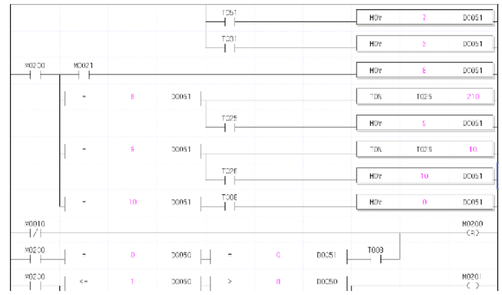

Figure 6: Ladder diagram of auto operation mode.

DISCUSSION

In this paper, integrated Vacuum and RF amp local controller has been presented. Integrated Controller provide automated process for amp and vacuum machine by PLC. Interlock function also realized by using plc module and HMI for integrated controller is also developed. Its HMI and integrated controller will be replaced from original two independent controller for machine stability and management of interlock. Development of integrated controller will be continuously expand to Low level RF controller.

ACKNOWLEDGMENT

This work was supported by the National Research Foundation of Korea (NRF) grant funded by the Korean government (MSIP:Ministry of Science, ICT and Future Planning) (NRF-2015M2B2A8A10058096.)

REFERENCES

[1] Y. S. Lee *et al.,* "The Development of Control System for 9 MeV Cyclotron," *Science and Technology* 2012: 0925001.

[2] H. S. Song *et al.,* "Development of an 83.2 MHz, Three-Stage RF Amplifier for the SKKUCY-9 Cyclotron," *IEEE Transactions on Nuclear Science* 61.6 (2014): 3579-3583.

[3] LS Industrial System co. ltd. http://eng.lsis.biz

DEVELOPMENT OF MAGNETIC FIELD INSTRUMENTATION FOR 10 MeV CYCLOTRON

Ho Namgoong†, Donghyup Ha, Hyojeong Choi, Sangchul Mun, Woojung Jun, Mitra Ghergherehchi, J.S. Chai*,Department of Electrical and Computer Engineering, Sungkyunkwan University, 2066, Seobu-ro, Jangan-gu, Suwon, Gyeonggi-do, Korea
HuiSu Kim, Jongchul Lee, Department of Energy Science, Sungkyunkwan University, Suwon, Korea

Abstract

To produce a radio isotope for Positron Emission Tomography (PET), 10 MeV compact Cyclotron was installed at Sungkyunkwan University. This cyclotron had been produced 10 MeV proton beam. For this cyclotron magnet, the magnetic field measurement instrumentation was being developed. The hall probe sensor was used for field measurement. This hall probe sensor moves radial direction and angular direction by mechanically. The Magnetic field measurement instrumentation measures the field in the range of 5 mm for radial direction and 1 degree for angular direction. Magnetic field was measured with and without cooling. Magnetic field was carried with 4 Gauss without cooling and 0.1 Gauss with cooling. Our developed magnetic field measurement instrumentation has 0.1 Gauss of an error and 0.01 Gauss of resolution over 9 hours.

INTRODUCTION

The SKKUCY-10 Cyclotron at the Sungkyunkwan University was been developed since 2015 for production of proton beam. 10 MeV proton beam can produce radioisotopes for positron emission tomography (PET) imaging. To produce 10 MeV proton beam, magnetic field was modified by calculated magnetic field error. The magnetic field error between isochronous field and designed field should be less than 15 Gauss to get high quality of proton beam [1, 3].

This paper presents a development of magnetic field measurement instrumentation for compact cyclotron. The Hall probe sensor can measure ~3 T range, 0.01 Gauss resolution [2]. Specification of hall probe sensor was shown as Table 1.

The coil of the electromagnet creates heat and it interrupt the magnetic field while cyclotron operating. Also the unexpected vibrations of magnetic field measurement instrumentation cause measurement errors. These kinds of errors had been fixed by taking data processing and the operation methods of the measurement system.

Magnetic field measurement instrumentation measures the field in the range of 5 mm for radial direction, and 1 degree for angular direction. Field measurement program is based on LABVIEW. It can monitor the field intensity synchronously, and it is utilized for full field mapping of 10 MeV cyclotron.

DESIGN AND SYSTEM DESCRIPTION

The specification of hall probe sensor was shown as Table 1. The magnetic field range of SKKUCY-10 cyclotron was 0.33 T to 2.17 T and operating temperature was around 50°C. This hall probe sensor was expected high accuracy of measurement.

Table 1: Specification table of hall sensor probe [2]

Parameters	Values
Field measurement range	~ 3 T
Field measurement resolution	0.001 ~ 0.01 Gauss
Temperature Range	-20 °C ~ 60°C
Temperature stability	± 10ppm of reading/°C
Accuracy at 25°C	± 0.01%

3D model of magnetic field measurement instrumentation for 10 MeV cyclotron are given in Fig. 1. The hall sensor probe was on the bracket ①. It will rotate mid-plane of magnet. The step motor ② was installed at valley, which is connected with rotation jig using by tension belt. The Rotation plate ③ prevent the rotation jig form tilting when magnetic field measurement instrumentation operates. The hall probe sensor had been moved by spur gear ④ and ratchet gear ⑤ along the radial direction. The Linear guide ⑥ supports hall probe sensor.

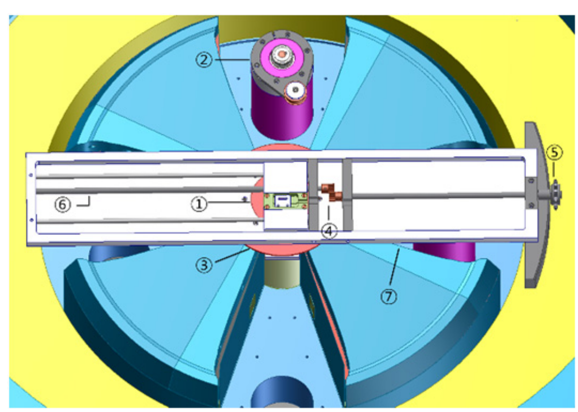

Figure 1: 3D Model of Magnetic Field Measurement Instrumentation. ① : Step motor, ② : Hall Probe Sensor bracket, ③ : Rotation Plate, ④ : Spur Gear, ⑤ : Ratchet Gear, ⑥ : Linear Guide, ⑦ : Rotation jig.

ISBN 978-3-95450-167-0

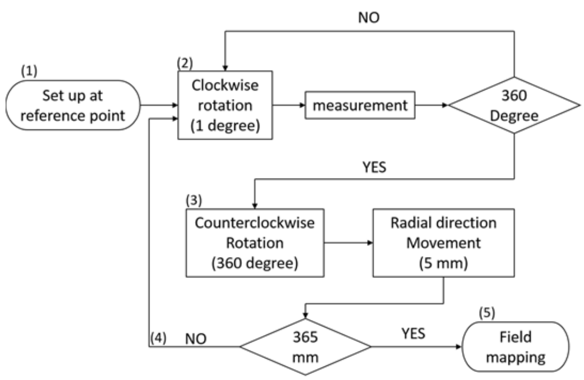

Figure 2: Flow chart of magnetic field measurement.

The flow chart of magnetic field measurement was shown as Fig. 2. This program is based on LABVIEW program [4]. Measurement process was described in the following steps.

(1) The hall probe sensor set up as reference point.
(2) Magnetic field measure with same step size of θ (1 Degree) while rotating in clockwise direction at same radius.
(3) The hall probe sensor was rotate in the counter-clockwise direction, and then it was move 5 mm along the radial direction.
(4) Measure the radial region of R=365 mm of the electromagnet repeating the procedure (2) and (3).
(5) Map the measured data in 2D field mapping.

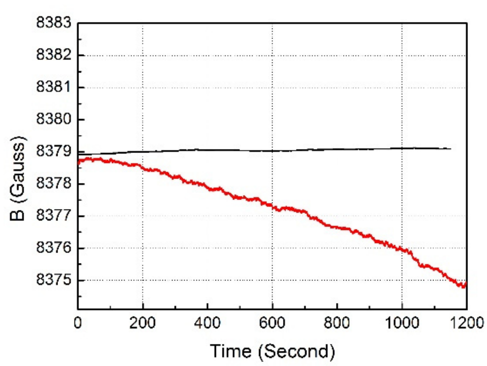

Figure 3: Magnetic field variation.

The magnetic field variation is shown in Fig. 3. Red line shows that the magnetic field had been reduced about 4 Gauss in 20 minutes and temperature had risen when the field was measured in a fixed point. Black line shows that the magnetic field is constant with the value of 8379 Gauss when the field was measured in a same position during 20 minutes. The electromagnet coil creates heat and it interrupts the magnetic field while cyclotron operating. When the temperature of the electromagnet increase, the magnetic field had been reduced. The magnetic field of the electromagnet is formed by the flowing current in the coil which causes the particles of the iron to be arranged along the constant direction that generates the polarity. When the heat is applied to the electromagnet, the kinetic energy of the uniformly polarized particles increases, to that the polarity falls away and finally the magnetic field decreases. Whenever the temperature of the electromagnet maintain constantly, the magnetic field is approximately 0.1 gauss. The range of the magnetic field tuning is -15 to +15. Magnetic field measurement result was constant at a stable condition.

RESULTS AND DISCUSSIONS

There are some errors caused by the load generated from step motor or measurement instrument while operating the magnetic field measurement instrumentation. The magnetic field had been compensated by getting rid of data with large amount of error or receiving more data in the same position with increasing the sampling number of the Hall probe sensor to 5. Figure 4 represents the result for the magnetic field in R=30 cm while operating the measurement instrument. The measurement had been conducted with 10 A for the current of the coil. and the magnetic field on the hill and valley were 2500 Gauss, 700 Gauss respectively.

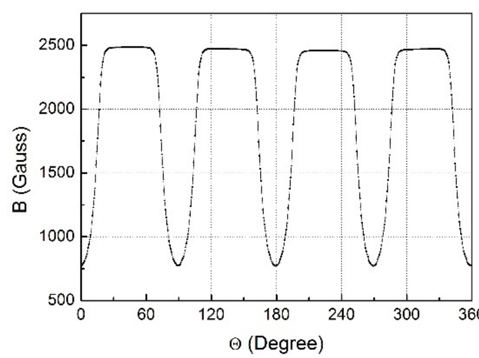

Figure 4: Magnetic field measurement.

Figure 5 shows error bar of measurement. The error of magnetic field was around 0.1 Gauss and it was guarantee high accuracy of measurement.

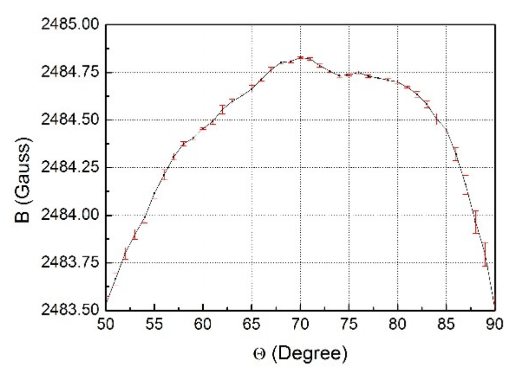

Figure 5: Error bar of magnetic field measurement.

ISBN 978-3-95450-167-0

Table 2: Parameters of Magnetic Field Measurement

Parameters	Values
Radial step range	1 ~ 15 mm
Radial measurement resolution	5 mm
Angular step range	0.07 ~ 360 Degree
Angular measurement resolution	1 Degree
Sampling number	5
Field measurement range	0 T ~ 3 T
Field measurement Resolution	0.01 Gauss
Measurement Time	9 hour
Magnetic field error	0.1 Gauss

Magnetic field measurement instrumentation specification is shown as Table 2. This instrument designed for measuring the magnetic field of 10 MeV Cyclotron. Magnetic field measurement instrumentation measures the field in the range of 5 mm for radial direction, and 1 degree for angular direction. The range is adjustable in the program code. The hall probe sensor takes 5 data each measurement step for increase accuracy of measurement.

CONCLUSION

In this study, Magnetic field measurement instrumentation for compact cyclotron has been developed. Magnetic field measurement instrument measures the field in the range of 5 mm for radial direction and 1 degree for angular direction. The range is adjustable in the program code. Magnetic field measurement instrumentation can monitor the field intensity synchronously. It was adopted simple structure and magnetic field measurement error was less than 0.1 Gauss. It is utilized for full field mapping of electromagnet with high accuracy.

ACKNOWLEDGMENT

This research was supported by the Basic Science Research Program through the National Research Foundation of Korea (NRF) funded by the Ministry of Science, ICT & Future Planning (NRF-2015M2B2A8A10058096, Development of education program for raising basic cyclotron human resources and publication of education contents]

REFERENCES

[1] B.-N. Lee, *et al.* "Design study of a 9 MeV compact cyclotron system for PET." Journal of the Korean Physical Society 62(11): 1595-1599, (2013).

[2] Group3technology, http://www.group3technology.com/vdb/document/10

[3] P.L. Rossiter, The Electrical Resistivity of Metals and Alloys, Cambridge University Press , (1987).

[4] National instruments, http://www.ni.com/en-us.html

METHODS OF COMPENSATION OF THE BEAM VERTICAL DIVERGENCE AT THE EXIT OF SPIRAL INFLECTOR IN CYCLOTRONS

I.A.Ivanenko, JINR, Dubna, 141980, Russia

Abstract

While the axial injection into the cyclotron, the beam is turned from axial direction into median plane by means of inflector. Commonly used type of inflector is an electrostatic spiral inflector. The spiral inflector is easy to handle and has a good beam transmission factor. On the other hand, the negative feature of spiral inflector is the beam vertical divergence at its exit. It leads to increasing of beam vertical dimension and aperture losses at the first orbits. The methods of compensation of the beam vertical divergence at the inflector exit are considered at present report. These methods are used at FLNR JINR cyclotrons and give good results in transmission factor, beam quality and operation modes.

INTRODUCTION

The axial injection systems of FLNR cyclotrons (U400, U400M, IC100, DC280) are equipped by spiral inflectors. The calculations and exploitation experience show the aperture losses in the cyclotron centre because of the beam vertical divergence at the inflector exit. It not only worsens the beam intensity and quality, but decreases the inflector operation time.

The beam vertical divergence at the inflector exit appears because the ions, shifted from the central ion trajectory, have the different length of the paths inside the inflector and so spend a different time in the inflector electric field. It leads to the difference in the rotation angles of the ions. The ions with initial shifting towards the cyclotron centre, -h start position at the Figure 1, have a smallest length of the path and receive incomplete rotation angles, less then 90°. And vice versa, the ions with +h shifting at the start position receive rotation angle more then 90°. The farther ion is shifted from the central trajectory, the more this angular difference.

The calculations have shown that this effect is stronger for the ions, shifted along the transverse, median axis h at the inflector entrance and not so actual for shifting in vertical, u axis direction.

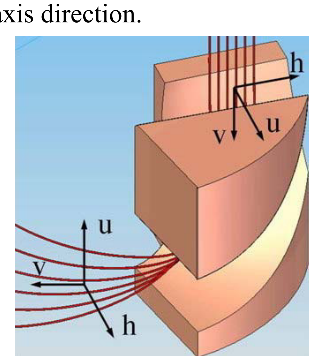

Figure 1: The computer model of spiral inflector and trajectories of ions with initial shifting along axis h.

The beam behaviour at the inflector exit was investigated by calculations and experiments for U400 cyclotron. It was found that the beam after inflection has a strong vertical divergence, that leads to aperture losses at the inflector box and dees noses, Figure 2. The experimental beam track was received on thermo-sensitive film at the first accelerating gap window. This situation is typical for cyclotrons, equipped with spiral inflector.

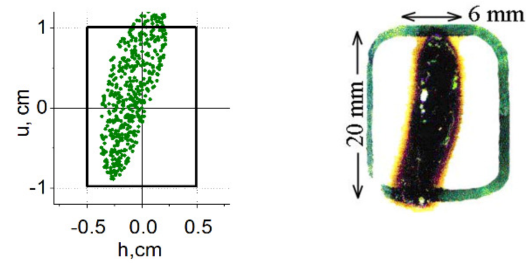

Figure 2: The calculation and experimental results - beam track at U400 first accelerating gap window.

There are some methods of decreasing of the beam vertical divergence after spiral inflector. Usually to produce vertical focusing of the beam, the additional correcting element is placed between the inflector exit and the first accelerating gap. Such element could be either the passive magnetic channel [1] or the electrostatic quadrupole lens [2]. Unfortunately, the additional correcting elements need special place for installation at the cyclotron centre and it could be a problem especially for compact cyclotrons. Another method, used at FLNR cyclotrons, is a special form of the inflector electrodes, which produces the electric field with focusing effect [3].

PASSIVE MAGNETIC CHANNEL

First efforts to solve the problem of beam vertical divergence after inflector were undertaken for U400 cyclotron. Because the very intensive physical program, about 7000h/year and a short cyclotron maintains time, the installation of passive magnetic channel was chosen [4]. It took not much time and reconstruction efforts. The iron pieces of channel were installed inside inflector box, which could be easily extracted from vacuum chamber.

Passive magnetic channel provides the local gradient of the magnetic field about 4kGs/cm along 25mm of the beam path between the inflector exit and the first accelerating gap. At this distance, the beam is focused vertically and is defocused horizontally. The horizontal divergence is not strong because, as a rule, the beam at the spiral inflector exit has a constriction point in horizontal, h axis direction. Because a very intensive energy growth, provided by 4 dees with 130kV of RF, the accelerated beam don't "feel" magnetic field perturbation beyond the magnetic channel.

ISBN 978-3-95450-167-0

The installation of passive magnetic channel provides the reduction of beam vertical dimension before first accelerating gap, compare Figures 2 and 3. The experimental results shown the increasing of transition factor at the cyclotron output from 7÷9% up to 10÷12%. The time between the maintenance of spiral inflector was increased from 3 month up to 9 month.

The stationary placing of the passive magnetic channel inside the inflector box is a disadvantage of this method. When the inflector azimuthal position is changed, the radial positions of the beam and magnetic channel could mismatch. Probably, this situation we see at the Figure 3.

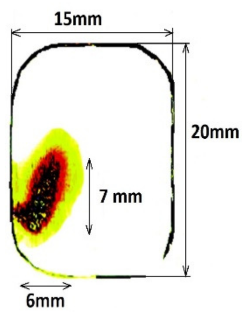

Figure 3: The beam track at U400 first accelerating gap window after passive magnetic channel installation.

ELECTROSTATIC QUADRUPOLE LENS

Now the activities on creation of the new heavy-ion isochronous cyclotron DC280 are carried out at FLNR. The isochronous cyclotron DC-280 will produce accelerated beam of ions with A/Z= 4 - 7 to energy W= 4 – 8 MeV/n and intensity up to 10 pμA (for 48Ca).

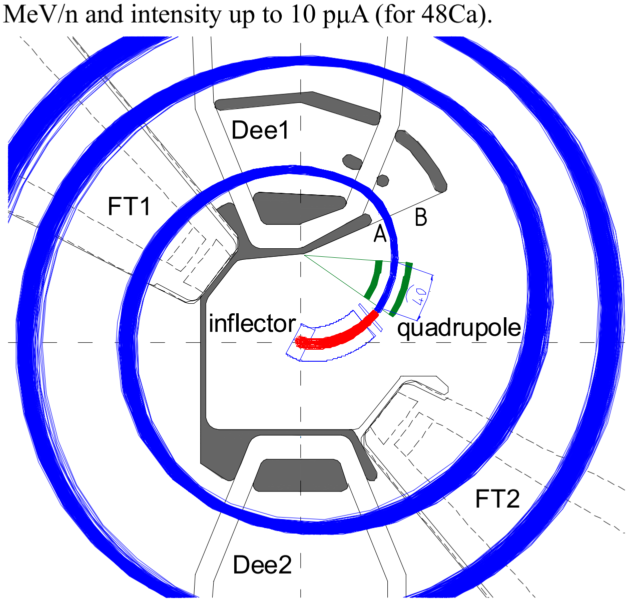

Figure 4: The central region of DC280 cyclotron. Inflector of 7.5 cm magnetic radius is placed.

Because of a wide range of operation modes, the electrostatic quadrupole lens was chosen as a focusing element. Quadrupole lens places between the inflector exit and first accelerating gap and provides the operative smooth correction of the injected beam. It could be uses not only for beam focusing, but also as a steering to adjust the beam position at the first accelerating gap.

DC280 quadrupole lens has aperture 22mm and length 40mm along the central ion trajectory. The quadrupol electrodes repeat the form of the beam trajectory, Figures 4 and 5, and have a potential up to ±3 kV. Four power sources provide the potential for each electrode separately to use the lens as a steering.

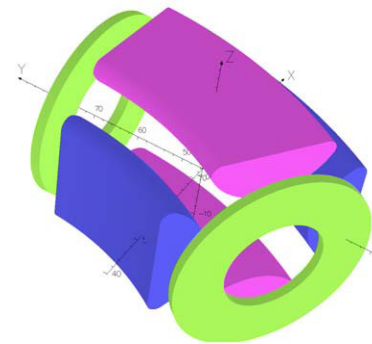

Figure 5: Computer model of quadrupole lens.

The quadrupole lens is a part of the inflector block and is rigidly attached to inflector. The inflector block could be placed into the cyclotron centre operatively by the radial directed rod through the vacuum gateway. The mechanism of the inflector block provides smooth azimuthal and radial tuning of inflector and quadrupol position. To cover the wide range of operation modes of DC280 cyclotron, two inflector blocks with magnetic radiuses 75mm, position A, and 92mm, position B, will be used, see Figure 4.

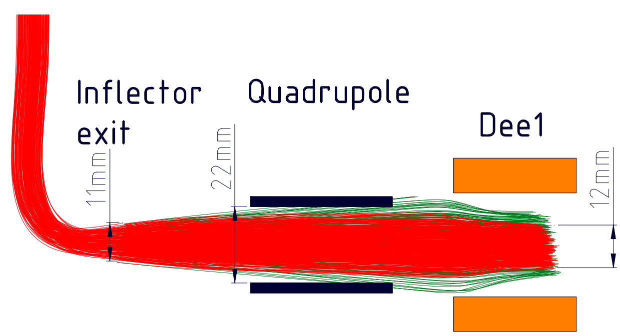

Figure 6: Beam trajectory through inflector, quadrupol and first dee puller when quadrupol is turned on or off.

The calculations show what the beam transition factor from inflector exit to the cyclotron extraction radius is about 75%, when the quadrupole lens is uninstalled. The main losses take place at the first orbits in the cyclotron center because the high amplitude of the beam vertical oscillations. The installation of electrostatic quadrupolelens decrease the beam vertical divergence after the inflector exit, Figure 6. As a result, the amplitude of beam vertical oscillations along acceleration is deceased too. On the over hand, the beam gets a small growth of amplitude of radial oscillations. Nevertheless, the summary result shows the increasing of transition factor along acceleration up to about 98 %.

ISBN 978-3-95450-167-0

INFLECTOR WITH SPECIAL FORM OF ELECTRODES

As it mentioned before, the installation of the passive magnetic channel at U400 cyclotron has some disadvantage – its stationary placing inside the inflector box. Unfortunately, the exchanging of magnetic channel on quadrupole lens at the operated cyclotron has technological problems. Another way to solve this problem is finding the method to affect to the beam when it passes through the inflector.

The numerical studies of the beam transition through spiral inflector show the possibility of compensation of the beam vertical divergence by means of special form of the inflector electric field. Such electric field not only bends the beam from the axial direction into the cyclotron median plane, but provides the focusing of the beam inside the inflector. To achieve it the additional, transverse component of the electric field is used.

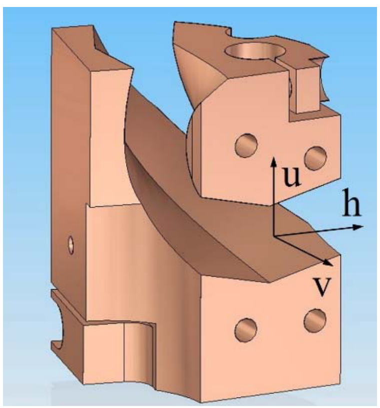

Figure 7: The new form of electrodes of U400 inflector.

This component is directed along transverse h-axis to the central ion trajectory and focuses the beam in haxis direction inside the inflector. At this case, the beam ions move closer to the central ion trajectory. It leads to decreasing of dispersion of the ions path length in the inflector electric field and, accordingly, to decreasing of dispersion of ions rotation angle in the vertical direction. Summary, the vertical beam dimension at inflector exit is decreased and the problem of aperture beam losses at the first accelerating gap is eliminated. The efficiency of this method depends on the depth of the electrodes profiling. It was found that the optimal depth of electrodes profiling for U400 inflector is 2.5mm. Of course, the beam after inflection gets a small radial defocusing, but calculations showed that this negative effect not so relevant for the beam motion, and latest experiments confirm it, Figure 8.

The spiral inflector with profiled form of electrodes were manufactured and placed into U400 cyclotron centre. The electric and magnetic radiuses of the new inflector are the same as for "classic" inflector and the old electrodes just were replaced with the new one.

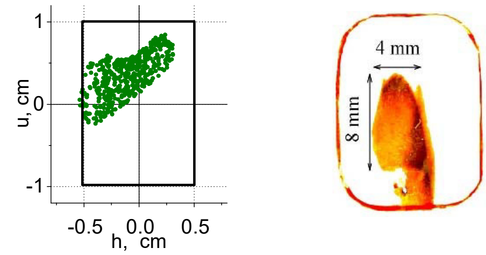

Figure 8: The calculation and experimental results - beam track at U400 first accelerating gap window. Inflector with special form electrodes is installed.

Figures 2 and 8 present the comparison of calculated and experimental beam tracks at U400 first accelerating gap window before and after installation of the new inflector. The experimental results with new inflector shown the increasing of the beam intensity at about 30%. It could be mentioned what the operation with new inflector makes the operative tuning of U400 cyclotron much easier and quicker.

SUMMARY

Different methods of compensation of the beam vertical divergence at the spiral inflector exit were used at FLNR new and operated cyclotrons. The calculations and experimental results showed a high efficiency of this compensation in increasing of the beam intensity. The choice of the method is dependent on constructive and operational features of cyclotrons.

ACKNOWLEDGEMENT

Special thanks to Frederic Chautard and Alain Savalle, GANIL, for useful recommendations and help in design of quadrupole lens for DC280 cyclotron.

REFERENCES

[1] G. Gulbekian, I. Ivanenko, I. Kalagin, A. Morduev, "The compensation of beam vertical defocusing after the spiral inflector by using the passive magnetic channel", in *Proceedings of the 7th European Particle Accelerator Conference (EPAC'00)*, 24 – 28 June 2000, Vienna, p.p. 1504 – 1506.

[2] M. Lieuvin *et al.*, "Commissioning of Spiral, the GANIL radioactive beam facility", in *Proceedings of the 16th Conference on Cyclotrons and Their Applications,* 13 – 17 May 2001, Michigan, USA, p.p. 59 – 63.

[3] B. N. Gikal, G. G. Gulbekian, I. A. Ivanenko, "U400 Cyclotron Spiral Inflector with Beam Vertical Focusing Effect", in *Proceedings of the 1th International Particle Accelerator Conference (IPAC'10),* 23 – 28 May 2010, Kyoto, Japan.

[4] G. Bellomo, "Design of passive magnetic channels", in *Proceedings of the 13th Conference on Cyclotrons and Their Applications,* pp. 592 – 595.

ISBN 978-3-95450-167-0

AXIAL INJECTION CHANNEL OF IPHC CYCLOTRON TR24 AND POSSIBILITY OF ION BEAM BUNCHING

N.Kazarinov#, I.Ivanenko, JINR, Dubna, Russia
F.Osswald, IPHC, Strasbourg, France

Abstract

The CYRCé cyclotron (CYclotron pour la ReCherche et l'Enseignement) is used at IPHC (Institut Pluridisciplinaire Hubert Curien) for the production of radio-isotopes for diagnostics and medical treatments. The TR24 cyclotron produced and commercialized by ACSI (Canada) delivers a 16-25 MeV proton beam with intensity from few nA up to 500 microA. The axial injection and bunching of the H- ion beam by means of multi harmonic buncher is considered in this report. The buncher may be installed in the axial injection beam line of the cyclotron. The use of a grid-less multi-harmonic buncher increases the accelerated beam current and gives an opportunity for new proton beam applications. The main parameters of the sinusoidal (one-harmonic) and multi-harmonic bunchers are evaluated.

INTRODUCTION

The beam transport and bunching of the **H⁻** ion beam by means of multi-harmonic buncher which may be installed in the axial injection beam line of the TR24 [1] cyclotron is considered. Using a buncher will give an opportunity to increase the accelerated beam current. The results of the simulation in the first order of the beam optics are given in this report. The simulation of beam transport was carried out by means of 3D version of MCIB04 program code based on momentum method [2].

BEAM LINE LAYOUT

The scheme of the beam line and the approximate length of the optical elements are shown in Fig.1. This scheme was the basis for simulation of the dynamics of the ion beam.

H⁻ ION BEAM PARAMETERS

H⁻ ion beam is produced in the CUSP ion source [3] with kinetic energy of 30 keV. The beam emittance is strongly dependent on beam current. For H- ion beam currents varying from 1 mA to 5 mA the initial beam diameter is equal to 10 mm and the normalized beam emittance is changing within range 0.1÷0.4 π mm×mrad. The main parameters of the **H⁻** ion beam used in the simulation are contained in Table 1.

Table 1: **H⁻** Beam Parameters

Parameter/notation	Value	Unit
Charge/ Z	1	
Mass number/ A	1	
Kinetic energy/ W	30	keV
Beam diameter/ d	10	mm
Beam geometric emittance / ε	50 π	mm×mrad
Ion beam current/ I	5	mA
Neutralization factor/ f	0.95	

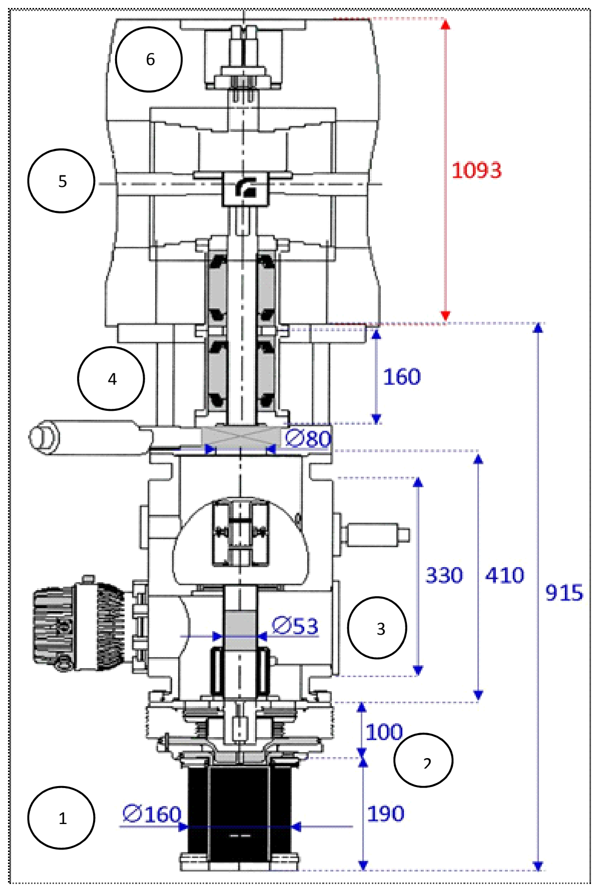

Figure 1: Axial injection beam line of TR24 cyclotron. 1 - CUSP ion source; 2 - extraction electrodes; 3 - EM steering (H/V); 4 - EM quad doublet; 5 - ES deflection; 6 - cyclotron.

#nyk@jinr.ru

SIMPLIFIED BEAM LINE SCHEME

The simplified scheme of the beam line is shown in Fig. 2.

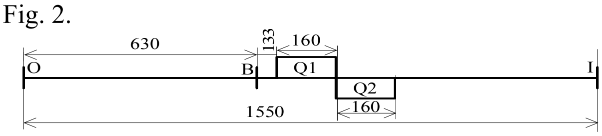

Figure 2: Beam line scheme. O – object point; I – spiral inflector; B – buncher; Q1,2 – quadrupole lenses.

The object point O is placed at the edge of the CUSP source (see Fig. 1).

LONGITUDINAL MAGNETIC FIELD

The distribution of the longitudinal magnetic field B in the injection channel has been defined by scaling of the field of the cyclotron IC-100 (pole diameter 1 m) [4]. The scaling factor is equal to ratio of the pole diameters of the cyclotron magnets. The plot of this distribution is shown in Fig. 3.

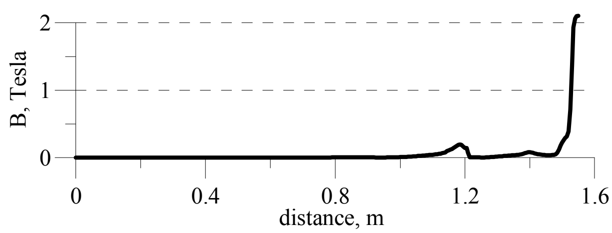

Figure 3: Longitudinal magnetic field.

BEAM NEUTRALIZATION

The beam current from CUSP ion source may achieve up to 5 mA. The transport of the beam with a big current is impossible without reasonable assumption about beam space charge neutralization. In the simulation the neutralization factor was equal (fixed) to 95% and assumed to no change along the beam line.

BEAM TRANSPORT

The gradients of quadrupoles lenses were fitted to minimize the amplitude of the beam envelopes oscillation at the entrance of the spiral inflector for both degrees of freedom. The fitted values of the quadrupoles coefficients are equal to K1[Q1]=31.1 m^{-2} and K1[Q2]=29.9 m^{-2}.

The results of simulation of beam transport through the axial injection beam line are shown in Figs. 4-5.

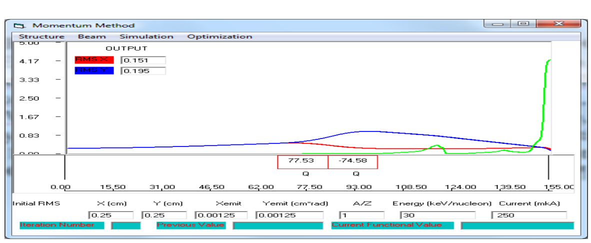

Figure 4: User interface of MCIB04 program (3D momentum method version) with beam envelopes and longitudinal B-field distribution.

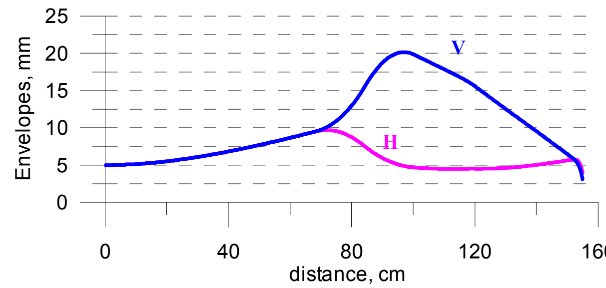

Figure 5: Horizontal (H) and vertical(V) $\mathbf{H}^-$ ion beam envelopes.

As may be seen from Fig. 5 the beam matching is not very good. The beam dimensions are sufficiently greater than matched beam radius which is approximately equal to 1 mm. This is explained by the use of the quadrupole lenses for beam focusing. The solenoid focusing is more convenient for the axial injection channel.

BEAM BUNCHING

The beam bunching may be realized by sinusoidal (one-harmonic) or multi-harmonic buncher B installed before quadrupole Q1 (see Fig. 2) at the distance of 92 cm from median plane of cyclotron. The electric field in the buncher produces the modulation of the longitudinal momentum of the ions. After the drift space this modulation gives the longitudinal modulation of the ion beam density. The modulation of momentum $\delta = \Delta p / p$ in the general case is defined as follows:

$$\delta = -\frac{eU_1}{2W}\sum_{n=1}^{N}\frac{U_n}{U_1} Sin\frac{2\pi n}{\lambda}z \qquad (1)$$

Here z – is the deviation of longitudinal coordinate of ions from the beam center of mass; n – harmonic number of the buncher; N – full number of the harmonic; λ – spatial period of modulation of the longitudinal density of the beam; U_n – effective voltage of the n-th harmonic of the spatial distribution $E(z)$ of the electric field of the buncher. In the symmetric case the voltage U_n is expressed by formula:

$$U_n = \int_{-\infty}^{\infty} E(z) Cos\frac{2\pi n}{\lambda} z dz \qquad (2)$$

The plot of function $E(z)$ for the one-gap buncher (symmetric case) is shown in Fig. 6.

ISBN 978-3-95450-167-0

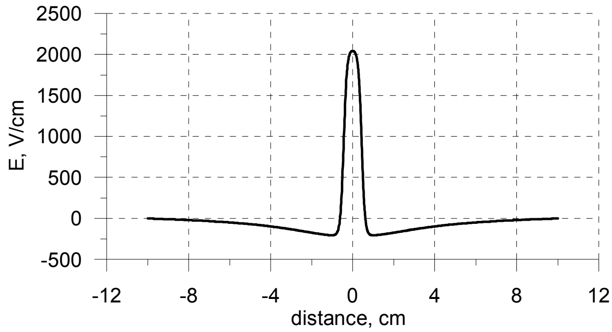

Figure 6: The distribution $E(z)$ for one-gap buncher.

The optimum value of ratio U_n/U_1 defined by achievement of the maximum of the bunching efficiency is equal to:

$$U_n/U_1 = (-1)^n/n \quad (3)$$

The optimum value of the effective amplitude of first harmonic U_1 is inverse proportional to the distance between buncher and median plane of the cyclotron. The grid-less four-harmonic buncher has been successfully used at ATLAS facility [5].

The bunching efficiency – the ratio of the number of ions within phase interval 20 degrees of RF field of the cyclotron for bunched beam and non bunched beam, for various types of multi-harmonic buncher are shown in Fig. 9. The numbers at the curves correspond to full number of harmonic N in formula (1).

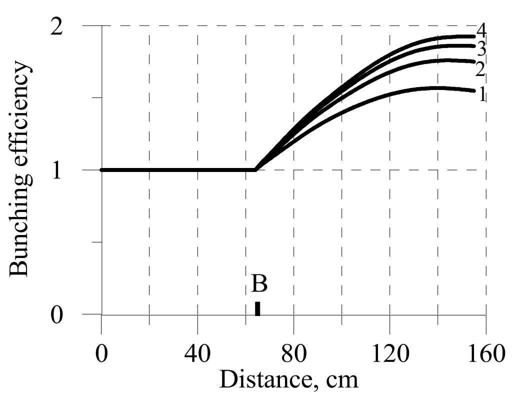

Figure 7: The bunching efficiency for various type of multi-harmonic buncher along the axial injection line. N = 1-4.

The optimum voltage amplitude of the first harmonic U_1 = 0.17 kV in the considering case.

As may be seen from Fig. 7 the bunching efficiency is increased with increasing of the full number of harmonics N. In the case of N = 4 the bunching efficiency is maximal and equal to 1.9. Therefore the accelerated beam current may be approximately in two times greater as compared with the case of absence of the bunching.

REFERENCES

[1] Advanced Cyclotron Systems Inc., `http://www.advancedcyclotron.com/cyclotron-solutions/tr24`

[2] V. Aleksandrov, N. Kazarinov, and V.Shevtsov, “3D Intense Beam Dynamics Simulation Using the Moments Method”, *PEPAN Letters*, vol. 5, N7 (149), Dubna, 2008, pp.625-628K.

[3] M. Jayamanna, M. McDonald, P. W. Schmor, D. H. Yuan, “The TRIUMF Compact DC H$^-$/D$^-$ Ion Source”, in *Proc. EPAC’90*, 12-16 June 1990, Nice, France, pp. 647-649.

[4] B. Gikal, S. Dmitriev, G. Gulbekian, P. Apel’, V. Bashevoi, S. Bogomolov, O. Borisov, V. Buzmakov, A. Cherevatenko, A. Efremov, I. Ivanenko, O. Ivanov, N. Kazarinov, M. Khabarov, I. Kolesov, V. Mironov, A. Papash, S. Patschenko, V. Skuratov, A. Tikhomirov, N. Jazvitsky. “Cyclotron based complex IC-100 for scientific and applied research”, in *Proc. 18th Int. Conf. on Cyclotrons and their Applications*, Giardini Naxos, Italy, 30 September – 5 October 2007, p.27.

[5] P.N. Ostroumov, V.N. Aseev, A. Barcikowski, B. Clifft, R. Pardo, S. I. Sharamentov, M. Sengupta, “Beam Test of a grid-less multi-harmonic buncher”, in *Proc. PAC’07*, Albuquerque, New Mexico, USA, May 2007, p. 2242.

ISBN 978-3-95450-167-0

THE DESIGN OF THE MEDICAL CYCLOTRON RF CAVITY*

X.W Wang†, F.Yong, R.F Zhang, Institute of Modern Physics, Lanzhou, China

Abstract

In the cyclotron, RF system as an essential component provides energy for the ions is accelerated. However, the RF cavity is the most important equipment which produced the accelerating field. According to the physical requirements, RF cavity, the resonant frequency of that is 31.02 MHz, was designed in the paper.

THE RF CAVITY DESIGN AND SIMULATION WITH CST

On the basis of the physical design requirements, the relevant physical parameters of the RF cavity have been given, as shown in Table. 1.

Table 1: Basic Parameter of the Cavity

Name	Results
Resonant Frequency	31.02
Dee Voltage	60-70KV
Dee Angle	33°
Extraction Radius	750mm
Injection Radius	35mm
Phase Stability	≤±1o
Amplitude Stability	≤5×10-4
Frequency Stability	≤1×10-6

The Structural Design of the Cavity

The cyclotron RF cavity adopts half-wave resonant structure, which of the accelerate gap is 8mm. Its structure diagram is shown in Fig. 1.

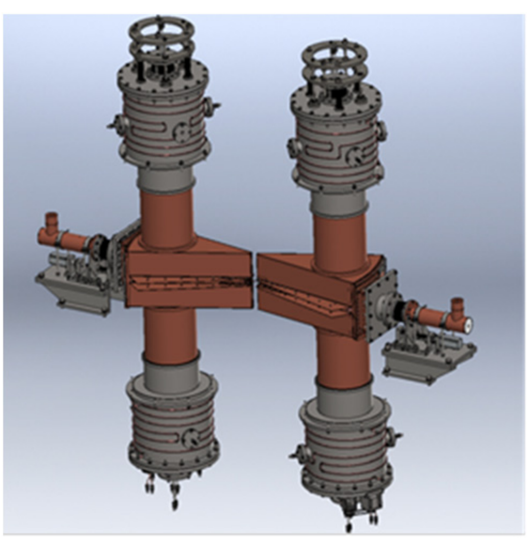

Figure 1: The cavity structure.

Simulation with CST

According to the structure parameter, the three-dimensional model is founded with CST. The simulation results show that the resonant frequency is 30.95 MHz, Q value is 7400 and power loss is 20 kW. The field distribution is shown in Fig. 2.

According to the structure parameter, the three-dimensional model is founded with CST. The simulation results show that the resonant frequency is 30.95 MHz, Q value is 7400 and power loss is 20 kW. The Field distribution is shown in Fig. 2.

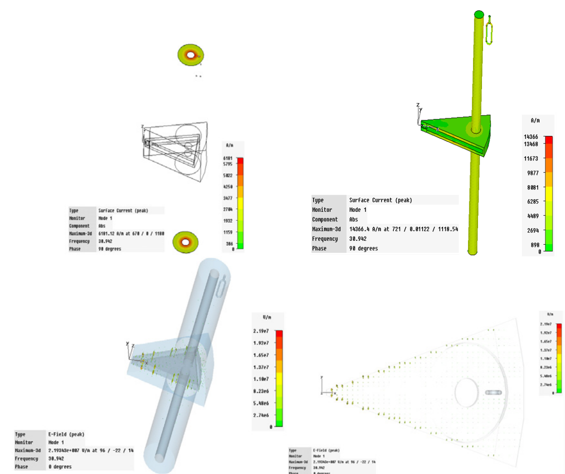

Figure 2: Electric-magnetic field and surface current distribution.

The tuning mode of the resonant cavity includes coarse-tune with short-plate and fine-tuning. The height of the short plate influences the frequency and Q value of the cavity. The curve is shown in the Fig. 3.

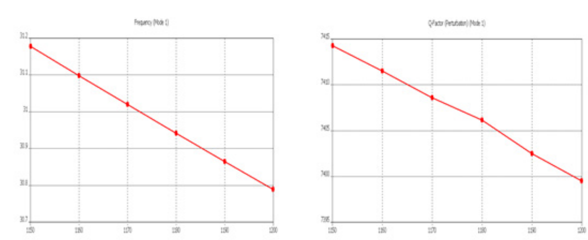

Figure 3: The change curve of the Q value and frequency.

MEASUREMENT RESULT OF THE CAVITY

Finally, the measured and commissioning results are shown in Table 1. The system has been operational for about 2 years. The system is stable and reliable.

* Work supported by IMP
† wangxw@impcas.ac.cn

ISBN 978-3-95450-167-0

Table 1 The Measured and Commissioning Results

Parameter	Calculated Value	Measure Value Cavity1	Cavity2
Frequency, MHz	31.02	31.054	31.036
Q value	7400	6200	6020
S11	0.055	0.023	0.010
Fine tuner range, kHz	40	38	40
The cavity loss power/kW	70	70	70.5
Temperature rise, ℃	8	6	6.5
Shun Imped., kΩ	245	232	220

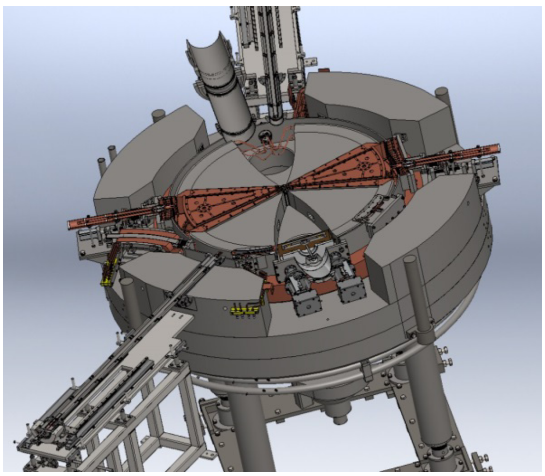

Figure 4: Cyclotron internal structure.

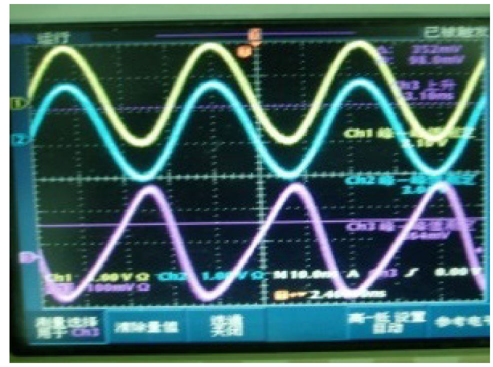

Figure 5: The cavity sampling signal.

CONCLUSION

The paper introduces the RF design of the 31.02MHz cyclotron cavity, including RF cavity simulation. At the same time, when the cavity machining had been completed in May 2013.the cyclotron RF system include 2 sets 50 kW power amplifier and LLRF as well as cavity, the RF system has finished commissioning. The cyclotron has also finished commissioning, the extraction beam has reached 10uA, to satisfy the physics demands.at present the cyclotron has been detecting for EMC and electrical safety.

REFERENCES

[1] Xianwu Wang *et al.*, "Calculation and measurement of Q-factor for RF D-circuit of cyclotron", *High Power Laser and Particle Beams*, vol. 17, no. 12, China, Dec. 2005, pp. 1885-1887.

ISBN 978-3-95450-167-0

COMPACT MEDICAL CYCLOTRONS AND THEIR USE FOR RADIOISOTOPE PRODUCTION AND MULTI-DISCIPLINARY RESEARCH

Saverio Braccini*, Albert Einstein Center for Fundamental Physics (AEC),
Laboratory for High Energy Physics (LHEP), University of Bern,
Sidlerstrasse 5, CH-3012 Bern, Switzerland

Abstract

Compact medical cyclotrons are conceived for radioisotope production in a hospital-based environment. Their design in terms of field shape, stability and radio-frequency (RF) is aimed at obtaining high intensity (>150 μA) beams at kinetic energies of the order of 20 MeV. To guarantee high performances, an optimization procedure during the commissioning phase is crucial as well as a regular preventive maintenance. Beyond radioisotope production, these accelerators can be the heart of a multi-disciplinary research facility once access to the beam area and beams down to the pA range are possible. The first requirement can be achieved by means of an external beam transport line, which leads the beam to a second bunker with independent access. Currents down to the pA range can be obtained by specific ion source, RF and magnetic field tuning procedures, opening the way to nuclear and detector physics, radiation protection, radiation bio-physics and ion beam analysis developments. On the basis of the experience gained with the cyclotron at the Bern University Hospital, the accelerator physics aspects of compact medical cyclotrons are discussed together with their scientific potential.

INTRODUCTION

Cyclotrons are fundamental tools in modern medicine. They are employed to treat cancer by particle teletherapy [1, 2] and to produce radiolabelled compounds for diagnostic imaging and metabolic therapy [3, 4].

In the last years, a remarkable scientific and technological progress led to the development of several commercial medical cyclotrons. They presently represent reliable and affordable solutions to fulfill the needs of research laboratories, radio-pharmaceutical companies and healthcare institutions. In this process, the interplay among academia and industry has been crucial and the majority of the cyclotrons and of the related equipment on the market is the result of spin-off endeavors.

Medical cyclotrons can be schematically classified in five categories on the basis of their main characteristics: the energy and the intensity of the accelerated beams. As reported in Table 1, proton therapy cyclotrons feature the largest energy and the lowest intensity. They can be based on conventional or on superconducting technology. Their problematics are different with respect to the machines designed for radioisotope production [2] and will not be discussed here.

* saverio.braccini@lhep.unibe.ch

Some research laboratories have recently installed 70 MeV cyclotrons which can be used for the production of specific radioisotopes (ex. ^{82}Sr for ^{82}Rb generators) and for research activities. These accelerators can provide beams of different energy and accelerate also alphas or deuterons. Along this line, 30 MeV cyclotrons are installed in research laboratories or in radiopharmaceutical companies producing Single Photon Emission Tomography (SPECT) radioisotopes (^{131}I in particular). Both 70 and 30 MeV cyclotrons require a large infrastructure and are therefore quite rare. The most common medical cyclotrons feature a beam energy in the range 15-25 MeV and are excellent tools to produce ^{18}F ($T_{1/2}$=110 minutes), the most common and requested radioisotope for Positron Emission Tomography (PET). These accelerators are compact, cost effective and can be installed in a hospital-based facility. There are more than 300 cyclotrons of this kind in operation and their number is continuously increasing [3]. For simplicity, I will refer to them as compact medical cyclotrons and they will be discussed in detail throughout this paper. Other commercial medical cyclotrons feature smaller beam energies and are often devoted to the production of only one PET radioisotope in limited quantities. They will not be further discussed.

Compact medical cyclotrons usually run during the night or early in the morning to produce short-lived radioisotopes for PET imaging. They are available during daytime and their beams could in principle be used for multi-disciplinary research. To exploit their valuable science potential, specific conditions must be fulfilled. Since daily radioisotope production induces high residual radioactivity, the cyclotron bunker is accessible only for very short periods which are

Figure 1: The compact medical PET cyclotron and its research beam line installed at the Bern University Hospital.

ISBN 978-3-95450-167-0

Table 1: Schematic Classification of Commercial Cyclotrons*

	Main Use	Typical User	Max. Proton Energy (MeV)	Max. Beam Current (µA)
A	Proton therapy	Hospital	200-250	10^{-3}
B	Radioisotope production / research	Research laboratory	70	500-700
C	SPECT radioisotope production	Research lab. / industry	30	500-1000
D	**PET radioisotope production**	**Hospital / industry**	**15-25**	**100-400**
E	PET radioisotope production	Hospital	10-12	50

* Compact medical cyclotrons are highlighted in bold.

not suitable for research activities. A beam transfer line is therefore needed not only to shape the beams but also to lead the accelerated particles to a separate research area with independent access. Furthermore, beams in the picoampere and nanoampere range are mandatory for developments in nuclear and detector physics, material science, radiation biophysics, and radiation-protection. These intensities are 5 to 8 orders of magnitude lower with respect to the design ones and specific studies and optimizations of the accelerator are mandatory to obtain stable research beams.

One compact medical cyclotron is installed at the Bern University Hospital (Inselspital) [5, 6]. It is shown in Figure 1 and serves daily for the production of ^{18}F used for the synthesis of PET radio tracers with full Good Manufacturing Practice (GMP) industrial standards. Thanks to its beam transfer line, a rich multi-disciplinary scientific program is ongoing in complete synergy with industrial radioisotope production. On the basis of the experience gained with this facility, the accelerator physics aspects of compact medical cyclotrons are discussed and their scientific potential highlighted.

COMPACT MEDICAL CYCLOTRONS

Compact medical cyclotrons are commercial accelerators designed and optimized for the production of PET radioisotopes. Their main characteristics are determined by the physics of the concerned nuclear reactions. In particular, the process ^{18}O(p,n)^{18}F has a cross section of 100-700 mb in the range 4-16 MeV with the maximum around 6 MeV. This sets the value of the extracted beam energy. The beam current is determined by the amount of activity to be produced, which in turn depends on the cross section. As an example, about 500 GBq of ^{18}F can be produced in 120 minutes by bombarding two targets simultaneously with a total current of about 150 µA. After the synthesis, this corresponds to about 200-250 GBq of FDG, the most common PET radiotracer. Being the typical injected dose for one examination 400-500 MBq, a single cyclotron can serve several PET centers.

The main compact medical cyclotrons presently available on the market are reported in Table 2. Their typical weight is 22-24 tons and their dimensions less than 2×2×2 m^3. Being so compact, they well match the needs of a hospital-based facility. They are usually shielded by a bunker with about 2 m thick concrete walls. Local target shielding is sometimes used to match specific space needs. Compactness, high-performance, reliability and cost effectiveness are crucial and research is moving in this direction, as shown by the evolution of the cyclotrons produced by the Belgian company IBA (Figure 2). Due to the large currents, the considerable neutron fluxes and the high produced and induced activities, radiation protection is a critical issue to be taken into account in the design either of the accelerator or of the whole facility.

Some selected features of these accelerators are discussed in the next subsections, ideally following the trajectory of the accelerated ions from their source to the target.

Ion Source

All compact medical cyclotrons in Table 2 accelerate H$^-$ ions and, often as an option, D$^-$. These ions are produced in a plasma generated by an ion source fed by a gas bottle. Hydrogen purity is a key feature and maximum care has to be payed in the design and construction of the gas transfer lines. In particular, the presence of oxygen has a strong influence in the amount of produced ions and on the long term performance of the source. Cyclotrons are equipped with one or two sources. The main design choice is between external or internal ion sources. Cusp type external sources have the advantage of providing larger currents and to be accessible for maintenance without venting and opening the cyclotron. On the other hand, the design of the central region is more complex since a specific low energy (~25 keV) injection line (ex. one quadrupole doublet and a tilted spiral inflector) is needed. As a consequence, this solution is more expensive.

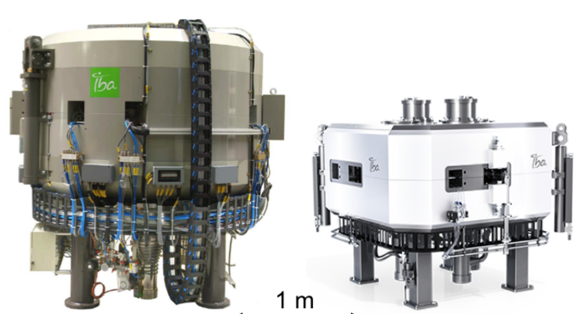

Figure 2: Comparison between the Cyclone 18/9 (total weight 24 tons, first design 1986) and the new KIUBE (17 tons, launched in 2016). (Courtesy IBA)

ISBN 978-3-95450-167-0

Table 2: Main Compact Medical Cyclotrons*

Manufacturer	Model	Particles	Energy (MeV)	Max. Beam Current (μA)	Source	Extracted Beams
ACSI	TR19	H^- (D^-)	14-19 (9)	>300 (100)	Ext. Cusp	2
ACSI	TR24	H^-	15-24	>300	Ext. Cusp	2
Best	15p	H^-	15	400	Ext. Cusp	2
Best	25p	H^-	25	400	Ext. Cusp	2
GE	PETtrace	H^- / D^-	16.5 / 8.4	>80 / 60	Int. PIG	6
IBA	Cyclone 18/9	H^- (D^-)	18 (9)	>100 (65)	Int. PIG	8
IBA	KIUBE	H^-	18	200	Int. PIG adjustable	8
Sumitomo	HM-18	H^- / D^-	18 (10)	>90 / 50	Int. PIG	2

* Presently available on the market, and as indicated by row D in Table 1.

Internal Penning ion gauge (PIG) sources allow for an easier design and are cost effective. The ions are extracted by a puller directly connected to the RF of the cyclotron. The distance between the chimney and the puller is critical and has to be carefully adjusted during maintenance. To perform this operation, the accelerator has to be vented and opened. To be able to optimize the source at any time, a remotely controlled motorized system has been realized for the IBA KIUBE cyclotron. Two H^- sources can be installed in the same machine, as in the case of the Bern cyclotron. Since the sources can be swapped in about one minute, this is an important feature to enhance production reliability. Internal sources emit positive ions into the vacuum chamber with a negative impact on the vacuum. A much stronger pumping system is therefore needed. Furthermore, the worse vacuum conditions translate into an enhancement of H^- ions undergoing stripping before extraction. Up to about 50% of the H^- ions extracted from the source are transformed into the so called neutral beam (H^0) which produces activation of the vacuum chamber. A regular check and maintenance (typically 3 or 4 times a year) of the ion source(s) is very important to keep high performances (Figure 3).

Central Region

The central region is one of the most critical issues in cyclotron design since even tiny variations of the magnetic field have a large influence on the beam due to its low energy (below ~1 MeV, corresponding to a radius of less than ~10 cm). To minimize beam losses, the extracted current and the stability of the beams have to be optimized during commissioning by fine-tuning the magnetic filed. This is done by means of a shimming procedure that needs high currents and cannot be performed at the factory due to induced activation. In the case of the Bern cyclotron, 10 cm diameter 100 μm thick discs were inserted in the central region to locally tune the magnetic field. Although time consuming, this procedure is important not only to allow high performance for radioisotope production but also to obtain stable low currents beams for research activities.

Magnet, Vacuum and RF System

Compact medical cyclotrons are room-temperature sector-focused machines, usually featuring two dees and four sectors. Superconducting cyclotrons for radioisotope production are under study although this technology brings complications in a hospital-based environment.

The main coil is used to generate the magnetic field that shapes the trajectory of the particles. Vertical focusing is realized via the hill-valley structure of the poles. High accuracy of the magnetic field is of paramount importance and is assured by an iterative construction process performed by the manufacturer in which the field is mapped and, on the basis of trajectory calculations, the poles are mechanically modified. This procedure is repeated till when the required precision is reached. To optimize the beam in case of dual beam extraction, secondary re-centering coils are used to locally modify the magnetic field. This feature is machine dependent and its optimization needs care. In Bern, stable dual asymmetric beams have been also obtained (ex. 100 μA on one target and 50 μA on the other), opening the possibility of the production of two different radioisotopes at the same time. Most of the cyclotrons accelerate particles in the horizontal plane. The vertical acceleration plane (as in the case of the the GE PETtrace) has the advantage of a more comfortable opening and an easier access to the internal parts during maintenance.

The vacuum system must be powerful, especially for cyclotrons equipped with internal ion sources. A vacuum level of better than 10^{-5} mbar is needed during irradiations. This is realized using oil diffusion pumps (ODP) always kept in operation and connected in correspondence of the valleys.

A fixed frequency RF system is chosen mostly to limit the costs. This implies a careful tuning during the commissioning phase aimed at minimizing the reflected power. In the case of the IBA 18/9 cyclotron, the frequency of 42 MHz is used which corresponds to the second harmonic for protons and to the fourth for deuterons. To correct for the effects due to the mass defect of the deuterons, the magnetic field is slightly modified by moving the so called flaps inside the valleys of the magnet. The RF peak voltage typically ranges

ISBN 978-3-95450-167-0

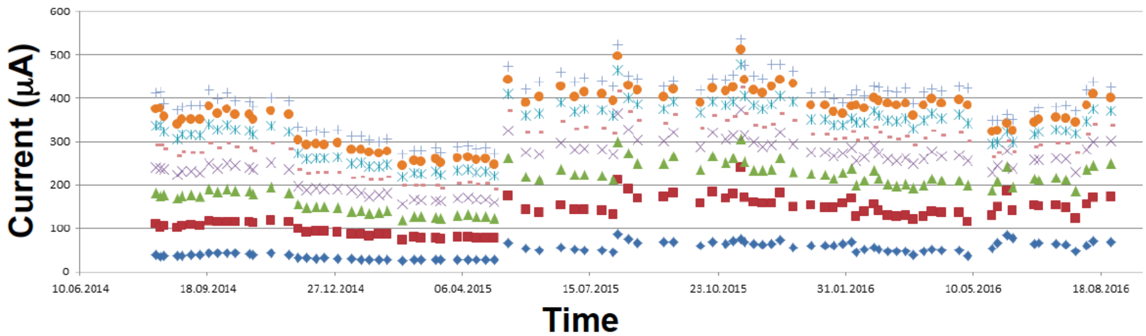

Figure 3: The beam current measured with a probe located in the central region is checked weekly to monitor the performance of the ion sources. The effects of maintenance are clearly visible. Different colors correspond to different settings of the arc current of the PIG ion source of the Bern cyclotron.

between 25 and 50 kV. It determines the number of turns and influences the transverse beam emittance.

Extraction

Extraction is obtained by stripping the negative ions. This method is simpler and more cost effective with respect to magnetic septa used in positive ion cyclotrons. About ~5 µm thick pyrolytic carbon foils are used as strippers. Their efficiency is about 100%. When inserted in the beam, they have to stand temperatures of about 1500° C or more due to the power released by the protons and, mainly, by the stripped electrons. For this reason, they may get damaged during operation and they have to be carefully inspected and possibly changed during maintenance. It is important to remark that the development of efficient and reliable strippers significantly contributed to the success of negative ion medical cyclotrons. The radial position of the stripper determines the extraction energy. Several foils (usually 2 or 3) are mounted on a rotating carrousel to allow for a quick substitution without opening the cyclotron. The angle of the stripper with respect to the beam can be adjusted to optimize extraction. In some machines, the extraction energy can be varied by moving the stripper radially inside the vacuum chamber. All the cyclotrons of Table 2 allow bombarding two targets at the same time. This is the so called dual beam mode. It is realized by inserting two strippers located approximately at an angular distance of about 180°. On the other hand, the number of the extracted beams may vary. Some manufacturers opted for the extraction in only 2 points where the beam dimensions are optimized for target bombardment. This solution has the drawback of the need of a multiple target holder if, as it is usual, more than two targets are used. Other manufacturers chose a different design in which the beam is extracted in 6 or 8 out-ports where targets can be mounted. Since the beam envelope varies all along the turns, the beam characteristics are not the same on all the ports.

RADIOISOTOPE PRODUCTION

Besides ^{18}F, other relevant PET isotopes are: ^{11}C (20 min.), ^{13}N (10 min.) and ^{15}O (122 sec.). Being characterized by much shorter half-lives, they have necessarily to be used within the centre where they are produced. For this reason, they are interesting more for scientific than for industrial purposes. In the last years, research concentrated on the development of methods for the production of standard as well as novel radioisotopes for PET imaging. A short summary follows with emphasis on the accelerator physics aspects. More details can be found in References [7, 8].

Targets

Targets can be classified in three categories according to the state of the bombarded material: gas, liquid and solid. They are mounted directly on the out-port of the cyclotron. Gas and liquid targets consist of a water cooled irradiation chamber of a few cubic centimeters volume which is filled with a specific material (ex. $H_2{}^{18}O$ water for ^{18}F production). The beam enters the chamber through a thin window which faces a second window in contact with the vacuum chamber of the accelerator. The few millimeter gap between the two windows is used to flow helium for cooling. Aluminum or havar alloy is used for the windows while the target body is usually made of aluminum or niobium. The choice of the materials depends on the produced radioisotope and its chemistry since even tiny impurities may have severe negative implications on the yield of the synthesis and on the purity of the final product. During bombardment, the beam should be as stable as possible either in shape or in intensity. Beam hot spots have to be avoided. Since no focusing elements are usually present between the stripper and the target, the operator has to optimize the beam by means of the stripper angle, the main and the re-centering coils as well as the RF peak voltage. Solid target stations are the main tool to produce novel PET radioisotopes. The target material is usually electroplated on an aluminum or platinum disk. The use of compressed powder target materials is presently under study. After irradiation, the disk is released and brought out of the cyclotron bunker via a manual or a remotely controlled (mechanic or pneumatic) system.

ISBN 978-3-95450-167-0

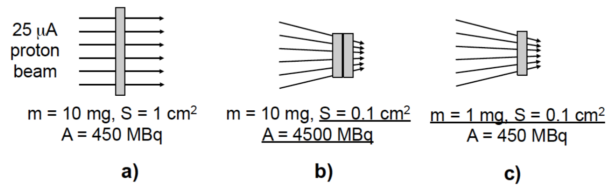

Figure 4: Different scenarios for the production of ^{43}Sc using a solid target station. Standard beam (a); highly focused beams (b and c).

Non-standard Radioisotopes

Non-standard radioisotopes (ex. ^{64}Cu, ^{66}Ga, ^{76}Br, ^{86}Y, ^{89}Zr, ^{124}I for PET; ^{67}Ga, ^{123}I, ^{111}In for SPECT; ^{165}Er for therapy) can be produced by irradiation of very rare and expensive highly enriched materials by means of solid target stations. Their production in quantity and quality suitable for clinical applications presents several challenges, including crucial accelerator physics issues. As a sound example, let's consider the production of scandium, a novel isotope for theranostics (^{44}Sc and ^{43}Sc for PET and ^{47}Sc for metabolic therapy) under study in Bern. In particular, ^{43}Sc can be produced with compact proton cyclotrons via the reactions ^{43}Ca(p,n)^{43}Sc and ^{46}Ti(p,α)^{43}Sc. As shown in Figure 4, only a few mg of enriched material can be used and the beam current is limited to about 25 µA in commercial solid target stations. Furthermore, the beam extracted from the cyclotron has a cross section S of about 1 cm^2 or more. These constraints severely limit the amount of produced activity (case a). If the beam could be focussed on a surface of 0.1 cm^2, a factor 10 could be gained (case b) or, alternatively, the same activity could be obtained with one tenth of the material (case c). To reach this goal, a focussing system is needed together with beam monitoring detectors able to control on-line the position and the shape during irradiation. The beam energy is also a crucial parameter. In particular, ^{43}Sc and ^{44}Sc are produced at the same time and their ratio is strongly energy dependent.

MULTI-DISCIPLINARY RESEARCH

The science potential of compact medical cyclotrons extends far beyond novel radioisotopes for medical applications. With an infrastructure encompassing a beam transfer line, a second bunker and an optimized cyclotron able to provide currents down to the pA range, considerable beam time can be devoted to multi-disciplinary research without any interference with industrial routine production. This is the case of the Bern cyclotron laboratory, where nuclear physics (ex. scandium production cross sections), novel particle detector and radiation protection (ex. radioactivity induced in air by proton and neutron beams [9]) studies are on-going. Furthermore, radiation hardness of materials and electronic components is investigated for the ATLAS experiment at CERN and for the JUICE mission of ESA. Ion beam analysis and radiation biophysics studies are also possible. All these activities are based on specific accelerator and detector physics developments.

Low Currents

Compact medical cyclotrons are designed to produce beams larger than 100 µA. To obtain stable beams down to the pA range, specific procedures have to be developed based on ion source, main coil and RF tuning [10]. Collimators can also be employed. The arc current of the ion source has to be set at the minimum allowing a stable plasma. This is usually enough to reduce the extracted current to about 1 µA. The main coil and the RF peak voltage can then be tuned to vary the intensity outside the isochronous condition. Stable beams down to 1 pA have been obtained for several hours with the Bern cyclotron. This procedure requires care and a continuous adjusting is necessary to compensate effects mostly due to the warm-up of the main coil.

Beam Monitoring Detectors

Good knowledge of the beam is essential to set-up and monitor its characteristics according to specific needs. Compact medical cyclotrons are usually equipped with general purpose beam monitoring devices sensitive only above ~1 µA and with a limited spatial resolution. The beam position if often controlled only by reading the current on collimators. Specific beam monitoring devices (such as Faraday cups or secondary emission detectors (SEM)) have to be developed for low current research applications. Along this line, a novel compact profile monitor detector (named UniBEaM [11]) was designed and constructed by the AEC-LHEP group to measure, control and use low- (pA, nA) as well as high-intensity (µA) beams. Its spatial resolution is below 100 µm. It is based on specific Ce and Sb doped scintillating fibres moved through the beam. The produced light is collected to measure the beam profile. The industrialization of this instrument is licensed to the Canadian company D-Pace.

Beam Transfer Lines

The optimization of the injection of the beam extracted from a medical cyclotron into a long (~6 m) transfer line requires care. In particular, the beam must be centered in position and angle with an accuracy better than 1 mm and 1 mrad, respectively. This could require the adjustment of the radial position of the strippers [12]. For this reason, the measurement of the exit position and angle of the beam with

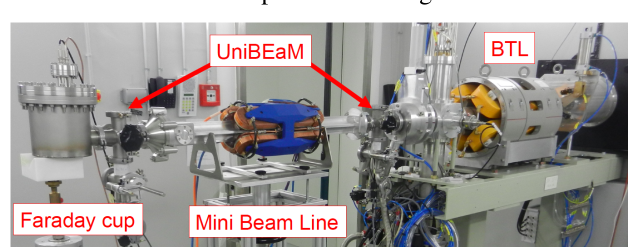

Figure 5: The mini beam line under test at the end of the beam transfer line (BTL) at the Bern cyclotron laboratory.

ISBN 978-3-95450-167-0

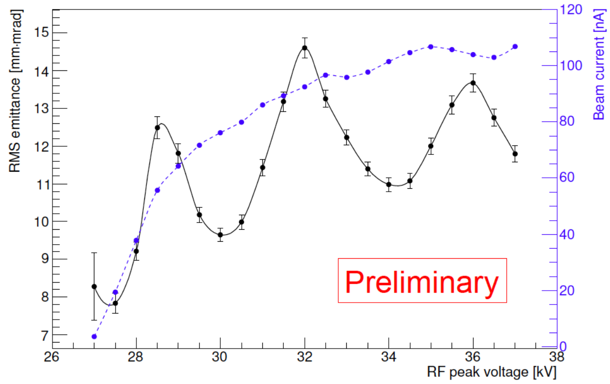

Figure 6: The horizontal transverse beam emittance and the beam current versus the RF peak voltage.

respect to the vacuum chamber is recommended as the first step of the commissioning.

Aiming at enhancing radioisotope production capabilities, compact focusing and steering elements to be installed between the exit port of the cyclotron and the target would be highly beneficial, especially in the case of solid target stations. For this purpose, D-Pace developed a 40 cm long compact mini beam line [13]. It consists of a quadruple doublet and a horizontal-vertical steering system embedded in a single light magnet. Its full characterization is in progress in Bern by means of UniBEaM detectors located before and after this novel device (Figure 5).

Transverse Beam Emittance and Simulation

A predictive simulation is a fundamental tool to study the set-up of a beam transfer line according to specific needs. The main input is represented by the transverse beam emittance and by the Twiss parameters, which are poorly known for compact medical cyclotrons. Furthermore, these parameters are machine dependent and vary according to conditions such as the status of the ion source or the type of strippers. Their measurement is usually performed by means of the quadrupole variation method, which requires a precise knowledge of the field gradient in the quadrupoles and is time consuming. To obtain an on line measurement of both the Twiss parameters and the transverse beam emittance, a method was developed based on four UniBEaM detectors [14]. This procedure does not require any knowledge of the focusing elements of the beam line. Based on the measurements of four profiles and a best fit procedure, the transverse beam emittance can be studied as a function of the main parameters of the cyclotron. The horizontal beam emittance as a function of the RF peak voltage is shown in Figure 6, where the influence of RF on the betatron motion is visible.

CONCLUSIONS AND OUTLOOK

Compact medical cyclotrons are the tool of choice for the production of radioisotopes for PET imaging. Designed to fulfill the needs of hospital-based facilities, they are characterized by a high science potential that started to be exploited only in the last years. A growing multi-disciplinary scientific community [15] is clustering around these particle accelerators for the benefit of science and society.

REFERENCES

[1] U. Amaldi *et al.*, “Accelerators for hadrontherapy: from Lawrence cyclotrons to linacs”, *Nucl. Instr. Meth.* A vol. 620, p. 563, 2010.

[2] D. L. Friesel and T. A. Antaya, “Medical cyclotrons”, *Reviews of Accelerator Science and Technology (RAST)*, vol. 2, p. 133, 2009, 133.

[3] P. Schmor, “Review of cyclotrons for the production of radioactive isotopes for medical and industrial applications”, *Reviews of Accelerator Science and Technology (RAST)*, vol. 4, p. 103, 2011.

[4] T. J. Ruth, “The production of radionuclides for radiotracers in nuclear medicine”, *Reviews of Accelerator Science and Technology (RAST)*, vol. 2, p. 17, 2009.

[5] S. Braccini *et al.*, “The new Bern cyclotron laboratory for radioisotope production and research”, in *Proc. IPAC’11*, San Sebastian, Spain, Sep. 2011, p. 3618.

[6] S. Braccini, “Particle accelerators and detectors for medical diagnostics and therapy”, Habilitationsschrift, University of Bern, 2013; `http://arxiv.org/abs/1601.06820`

[7] “Cyclotron produced radionuclides: principles and practice”, IAEA technical report 465, Vienna, Austria, 2008.

[8] “Cyclotron produced radionuclides: physical characteristics and production methods”, IAEA technical report 468, Vienna, Austria, 2009.

[9] S. Braccini *et al.*, “Study of the radioactivity induced in air by a 15 MeV proton beam”, *Radiation Protection Dosimetry* vol. 163, p. 269, 2015.

[10] M. Auger *et al.*, “Low current performance of the Bern medical cyclotron down to the pA range”, *Meas. Sci. Technol.* vol. 26, p. 094006, 2015.

[11] M. Auger *et al.*, A detector based on silica fibers for ion beam monitoring in a wide current range, 2016 JINST 11 P03027.

[12] S. Braccini, “The new bern PET cyclotron, its research beam line, and the development of an innovative beam monitor detector”, *American Institute of Physics (AIP) Conf. Proc.* vol. 1525, p. 144, 2013.

[13] D. P. Dehnel *et al.*,“ An integrated self-supporting mini-beamline for PET cyclotrons”, in *Proc. CYCLOTRONS’13*, Vancouver, Canada, Sep. 2013, p. 251.

[14] K. P. Nesteruk *et al.*, “Study of the transverse beam emittance of the Bern medical cyclotron”, in *Proc. IBIC’15*, Sep. 2015, Melbourne, Australia, p. 134.

[15] See for example the European Cyclotron Network (CYCLEUR); `http://www.lhep.unibe.ch/cycleurnetwork`

ISBN 978-3-95450-167-0

STUDIES AND UPGRADES ON THE C70 CYCLOTRON ARRONAX

F. Poirier, S. Girault, Arronax, Saint-Herblain, and CNRS – DR17, Rennes France
F.Bulteau Harel, J.B. Etienne, X.Goiziou, F. Gomez, A.Herbert, L.Lamouric, D. Poyac, H.Trichet, Arronax, Saint-Herblain, France
C. Huet, Arronax, Saint-Herblain, and EMN, Nantes, France
E. Mace, Arronax, Saint-Herblain, and INSERM, Nantes, France

Abstract

The multi-particle cyclotron C70 Arronax is fully running since 2010 and its RF run time has increased up to 4400 hours in 2015. The accelerator is used for a wide variety of experiments (physics cross-sections, radiolysis, radiobiology) and radio-isotope productions. This requires runs with 7 orders of intensity range from a few pA up to 350 µA and a large range of particles energy.

Machine and beamline studies are continuously needed. For example magnet intensity scan inside the cyclotron and in the beamlines, respectively with compensation coils and the quadrupoles have been done. These scans caracterise performances of the machine and help both operations and mitigation of particle losses. Additionally beam loss monitors and control systems are being devised to support further the high intensity and precision requirements on the runs. Also a pulsed train alpha beam system located in the injection has been designed. The proof of principle with a dedicated run has been performed.

The results of the machine studies and status of these developments are presented in this paper.

INTRODUCTION

The cyclotron Arronax [1] (Accelerator for Research in Radiochemistry and Oncology at Nantes Atlantique), running since 2010, the year of its commissioning, has started in 2011 its hands-on phase [2]. Arronax has gradually increased the number of hours it uses the cyclotron.

The cyclotron delivers beams separately in six vaults surrounding the main cyclotron vault [3]. Five of the vaults are used for high intensity beams and the sixth one, beamline for experiments, is dedicated to low and ultra-low intensity (<100 electric pA).

The priority list for production of radio-isotopes covers both isotopes for imaging and therapy. It includes, but not exclusively, ^{82}Sr, ^{64}Cu, ^{211}At and ^{166}Ho. ^{211}At requires an energy degrader that has been installed in one of the beamline and as for ^{166}Ho, a neutronic activator is in use, all at intensities above 10µA.

RANGE OF OPERATION

The cyclotron provides four types of positively charged particles (proton, alpha, deuterons, HH+) which intensity and energy can be modified according to the experimental needs. Figure 1 shows a map of the operation range for each particle at intensity from a few nA up to 100s of µA on the target with energies from 32 MeV up to 70.3 MeV for protons. Protons and deuterons have the widest energy range mainly due to cross-section measurements being performed at Arronax on numerous physics production channels [4]. Several runs with protons for ^{82}SR production have started in 2016 at 150µA on target, extending the production capacities at Arronax.

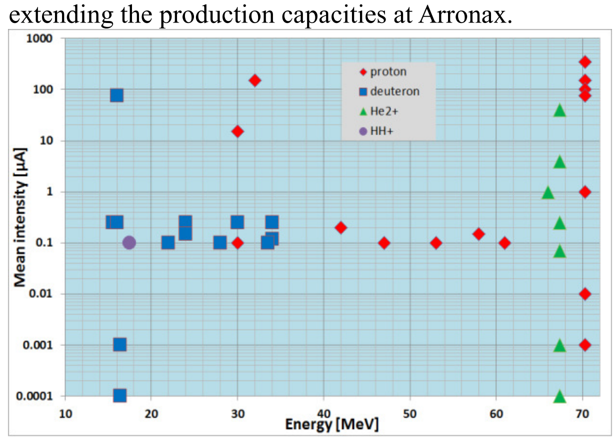

Figure 1: The operation range for the C70 Arronax with the 4 particles in use.

THE MACHINE OPERATION

The use of the cyclotron, here expressed in term of number of RF hours, has increased over the years up to 4400h in 2015 as shown in Fig.2, being limited mostly by manpower. Each year includes 4 main preventive maintenances that are performed over a week. Also, a Computerized Maintenance Management System (CMMS) – MaintiMedia from Tribofilm, is in place since 2015, to support the general maintenance follow-ups.

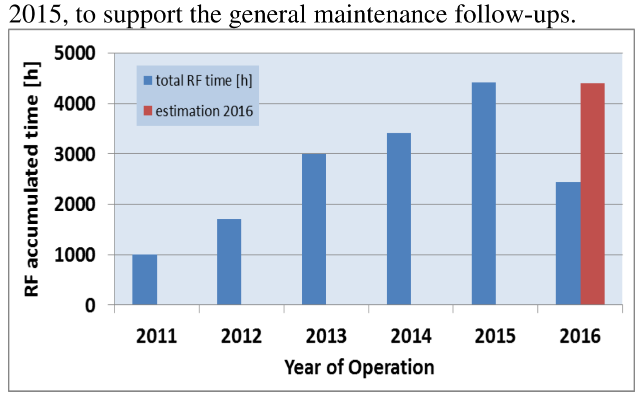

Figure 2: RF accumulated time per year since 2011 and as of august for 2016 and estimation for this year.

The settings on the machine parameters at the beginning of a run are systematically adjusted to increase

ISBN 978-3-95450-167-0

the transmission rate and as the operation last and magnets elements temperature increase, parameters such as main coils are optimised. In the case of new beam parameters e.g. new particle energy and/or intensity, being developed, systematic studies are planned.

The studies include transmission rate and also scans with various settings on the machine as shown later.

Table 1: Transmission Rate for the 3 Main Particles

Particles	Estimated Intensity in cyclotron [μA]	Transmission rate (End-of_line/injection)
H+	252	43%
D+	64	37%
He2+	26.6	10%

The transmission rate from the faraday in the injection to the end-of-line is indicated in the table 1. The particles losses are mainly in the injection and below 2 MeV. Additional losses are along the trajectory in the cyclotron (neutral particles at the level of 4.4% for protons) and along the beamlines (a few percentage).

MACHINE OPERATION STUDIES

The cyclotron is constituted of several internal magnets beside the main coil which provide the average magnetic field for the valley and hills. These are 3 compensation coils at 3 different radius (internal, medium and external) and paired harmonic coils. While in a dual-beamline run, the compensation ones are adjusted such that maximum current is obtained at both exit and the harmonic ones are set such that symmetry in intensity is observed. A scan of the intensity on faraday cups at the extraction exit was performed as a function of the compensation coils. The result is plotted in Fig. 3 for the intensity as a function of the external and medium coil and shows a region of maximum transmission with a large stability area (red). It also indicates some region to be avoided as a discontinuity on the magnet elements is present when passing 0A. This type of scan did show the need to perform regular check with newly constructed sets of magnet taking into account several multi-scan results. This type of scan with the help of dedicated beamline diagnostics can be used to track the status of the beam (eg resonances in the machine leading to beam blow-up, and modification of the beam shape) and stabilises overall runs. Taking into account these scans will have to be mitigated with the modification of the particles final kinetic energy.

BEAMLINE OPERATION STUDIES

Emittance measurements are important for check of the stability of the machine, determining focusing spots on the target and losses in the beamlines. This is addressed first though quadrupole scans in the beamlines.

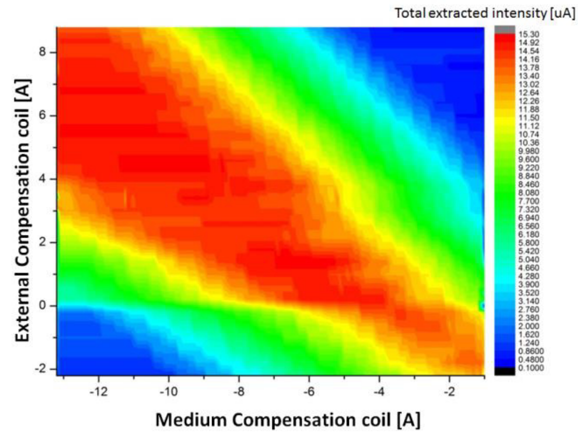

Figure 3: Total extracted intensity [uA] on both-side faraday cup as a function of compensation coils medium and external settings.

Quadrupole scan have been performed at intensities between 10 up to 30 μA. These scans have the goal to find the best setting for transmission rate in the beamline, for adequate beam size at the target location, emittance measurements studies and potential use in ballistic beam-based alignment to optimise the trajectory of the beam inside the beamline.

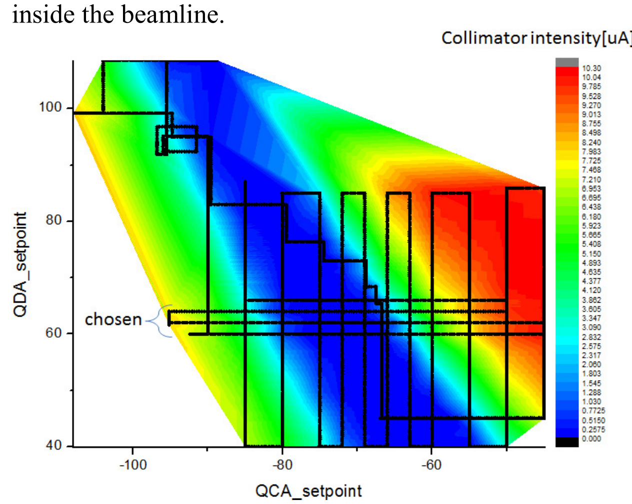

Figure 4: Quadrupole scan result with the 2 last consecutive magnets in the beamline. The coloring represents the interpreted intensity level on the collimators in the horizontal plane and the black dots the actual data points.

The scan of Fig. 4, was first obtained to select data that could be used to perform first preliminary emittance measurements. The criteria being two-fold: centered position of the beam and a full shape containing a deep in the scan. The chosen scan are indicated in Fig. 4. The technique uses first a transformation of the signal on the 10 mm aperture radius collimator into beam dimension. The fitted beam size is plotted as a function of strength in the quadrupole setting. The parabola obtained is then fitted to acquire the emittance according to:

$$\varepsilon_x = \sqrt{AC}/d^2$$

ISBN 978-3-95450-167-0

Where A and C are parameters of the fitting parabola [5] similar to single-wire scan and d is, a distance, here a fixed conversion factor from the simulation model in use.

The technique is at the present time being tested for robustness. It relies on simulations model with G4Beamline [6] for the transformation of the signal on the collimator to a beam size. The first measurements indicated variation in the emittance by a factor of 4 for runs separated by a few weeks.

MACHINE AND BEAMLINES ADAPTATION

End-of-beamline users require inter-bunch time which can modified from the initial 30.45 MHz. Using a technology composed of a 3.3 kV chopper in the injection and a 60kV sinusoidal deflector in the experimental beamlines, that is already in place, a new control system on the chopper was devised. This system allows a “start-stop” mode with a fixed number of bunches and various settings for the inter-bunch time. Figure 5 shows the results with 1282000 bunches on the end-of-beamline intensity. Implementations include an EPICS (Experimental physics and industrial control system) software and PIC18 microcontrolers.

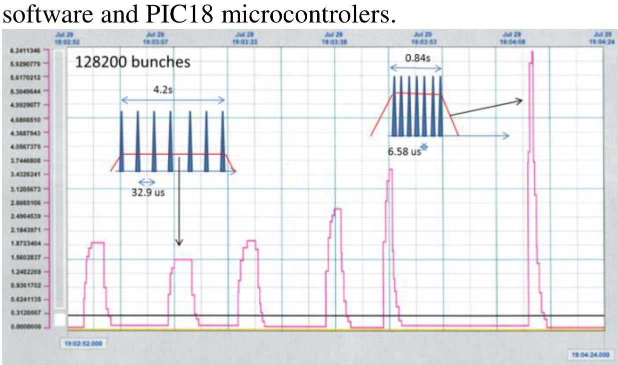

Figure 5: Intensity at the end of the beamline for the “start-stop” pulsation system.

The cyclotron computing environment has as well evolved. An EPICS system has been installed, initially developed with Cosylab, first as a core to retrieve data coming from the simantec S7 Siemens PLC of the accelerator and second as the possible foundation for the extension of the local network. Using a parallel CP-443 Ethernet card, it allows to access the accelerator data without impacting the main control system provided by IBA.

This network (Fig. 6) is foreseen to be the base for several beam diagnostics and technical environment measurements (eg water, gaz). An EPICS software, developed by Ithemba, for Beam Loss monitors is also being tested to later help the extension of beam diagnostics on beamlines and the cyclotron vault. Additionally, various upgrades are being performed on the beamlines, the irradiation stations, and the cyclotron environments (eg collimators, water cooling).

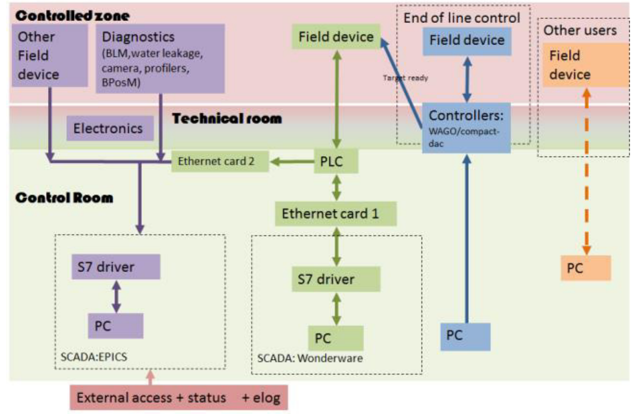

Figure 6: The intermediary planned phase for the computing environment of the cyclotron.

CONCLUSION

The use of the C70 arronax has increased over the years and several operational investigations are being carried out through magnet settings studies. Also a first emittance measurement with collimators at high intensity is being addressed with a model dependant methodology. Operation requirements have lead the need to develop a pulsation system that will extend to a pulsed train system in the injection and also, being part of a long term plan, the computing environment of Arronax is broadening through installation of new EPICS control systems.

ACKNOWLEDGMENT

This work has been, in part, supported by a grant from the French National Agency for Research called "Investissements d'Avenir", Equipex Arronax-Plus noANR-11-EQPX-0004 and Labex IRON noANR-11-LABX-18-01.

One of the authors, F.Poirier, acknowledges the work of the students A.Letaeron and A.Sengar respectively on the particle pulsation and first emittance measurements.

REFERENCES

[1] F. Haddad *et al.*, “Arronax, a high-energy and high-intensity cyclotron for nuclear medicine”, Eur J Nucl Med Mol Imaging. 2008, 35, 1377-1387.

[2] F. Poirier *et al.*, “The C70 ARRONAX in the hands-on phase”, IPAC12, May 2012, MOPPD024.

[3] F. Poirier *et al.*, “The C70 ARRONAX and Beamline Status”, IPAC11, Sept. 2011, WEPS069.

[4] C. Duchemin, “Étude de voies alternatives pour la production de radionucléides innovants pour les applications médicales”, Ph.D. thesis, Subatech, 2015.

[5] M.G. Minty, F.Zimmermann, “Measurement and control of Charged Particle Beams”, p.103, Springer, 2003.

[6] T.J. Roberts *et al.*, “G4beamline Simulation Program for Matter dominated Beamlines”, EPAC08, June 2008, WEPP120.

ISBN 978-3-95450-167-0

DEVELOPMENT OF THE CYCLONE® KIUBE: A COMPACT, HIGH PERFORMANCE AND SELF-SHIELDED CYCLOTRON FOR RADIOISOTOPE PRODUCTION

B. Nactergal*, M. Abs, S. De Neuter, W. Kleeven, E. Kral, V. Nuttens, J. Van de Walle and S. Zaremba, Ion Beam Applications (IBA), B-1348 Louvain-la-Neuve, Belgium

Abstract

About 15 months ago, at IBA, we have launched the design, construction, tests and industrialization of an innovative isochronous cyclotron for PET isotope production (patent applications pending). The design has been optimized for cost effectiveness, compactness, ease of maintenance, activation reduction and high performances, with a particular emphasis on its application on market. Multiple target stations can be placed around the vacuum chamber. An innovative extraction method (patent applications pending) has been designed which allows to obtain the same extracted beam sizes and properties on the target window independent of the target position.

INTRODUCTION

This isochronous cyclotron for PET radioisotope production produces fixed energy 18MeV proton beam and is called the **Cyclone® KIUBE**, Figure 1.

Today, three versions are available producing 100µA, 150µA and 180µA on target and the option with self-shielding is also available.

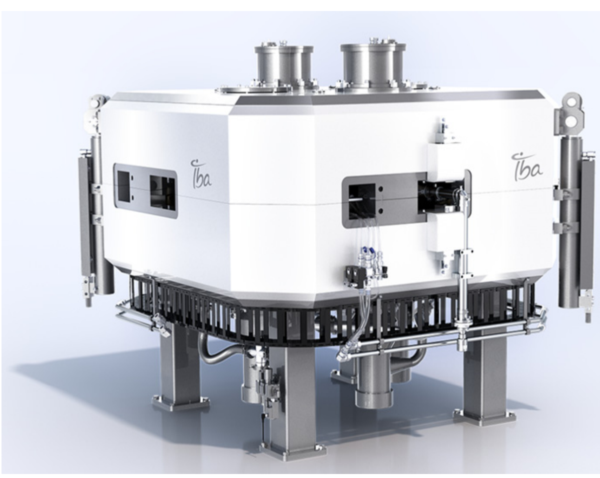

Figure 1: CYCLONE® KIUBE.

DESIGN

General Layout

The Cyclone® KIUBE, Figure 2, is a new concept starting from scratch. All the subsystems have been redesigned and optimized for high power beam production and reduced maintenance. During the study phase, all the teams have been largely challenged to meet requirements and systematic tools as TRIZ methods have been used.

First of all, the magnet system [1] has been designed to reduce the machine footprint, to make the access to all the sub-components easier and simplify the self-shielding concept. The median plan height has been modified to ensure an easy access to all the cyclotron components for maintenance.

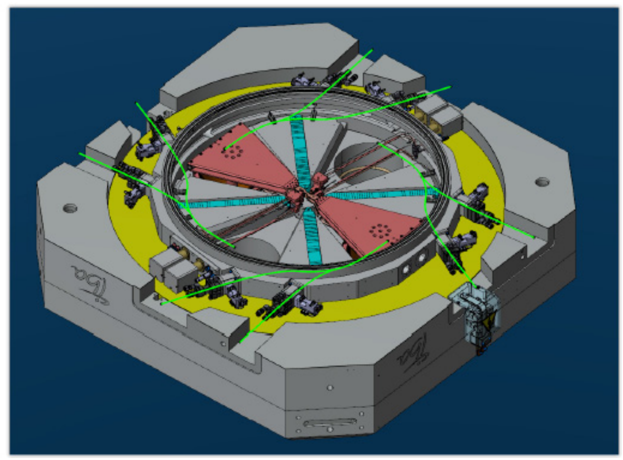

Figure 2: Magnet and extraction general overview.

The pole shape has been optimized [2] to ensure the same beam quality (shape and intensity) on the 8 targets surrounding the machine. The Figure 3 presents the top view of the pole with two gradient corrector cuts.

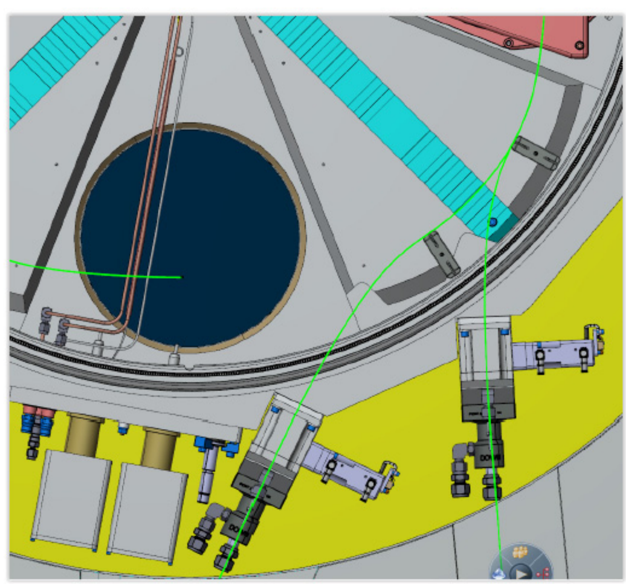

Figure 3: Two extraction systems per pole.

* benoit.nactergal@iba-group.com

ISBN 978-3-95450-167-0

Vacuum System

The vacuum system has been optimized for beam transmission and quick production restart after maintenance. The base vacuum is typically around 3.0E-7 mbar with RF on (40 kV dee voltage at 40.65 MHz). The evolution of the vacuum chamber pressure, from atmospheric pressure without cyclotron venting, is presented in Figure 4.

To	15 min	30 min	45 min
Full open	1.9 E-5 mbar	3.6 E-6	< 2.4 E-6

Figure 4: Pumping speed with 4 pumps after 2h opening without N_2 venting.

Beam Production

The machine has been redesigned around the "twin proton" concept allowing a redundancy during beam production.

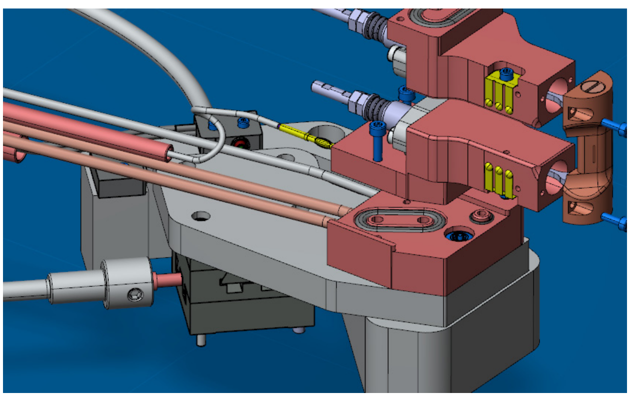

Figure 5: Ion source positioning system.

The two ions sources have been also equipped with a remote positioning system, Figure 5, ensuring the azimuthal and longitudinal automatic positioning. This positioning system allows the ion source to move remotely and be positioned without any machine opening. Continuously the ion source position could be optimized to maximize beam production.

The way to perform maintenance has been also optimized allowing the extraction of the source head easily (to maintain the ion source cathodes and chimney) out of the cyclotron. The Figure 6 presents the way to dismount the ion source.

Beam Transmission

Thanks to the several improvements, beam transmission, presented in Figure 7, and beam performance have been drastically improved comparing to the classical Cyclone® 18/9. This reduces beam losses and cyclotron activation during operation allowing easier and safer cyclotron maintenance.

For maintenance purpose, as well, the gate valves and the target have been designed to reduce the maintenance and to allow a quick disconnection of the target from the support. The special tools for handling and positioning have been developed to limit the personal exposure.

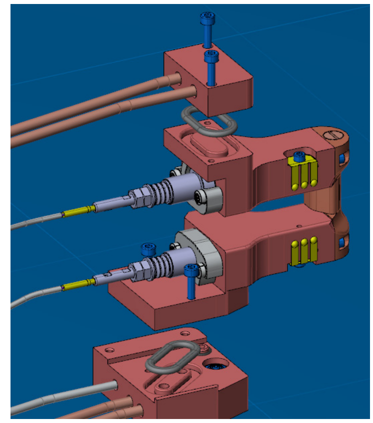

Figure 6: Ion source maintenance.

Porter valve H2 flow	Transmission 4 ODP	2 ODP
4 T – 150µA	81 %	
6 T – 180 µA	> 77 %	63 %

Figure 7: Beam transmission performance as a function of the number of ODP oil diffusion pumps.

Vault

Finally, thanks to the size reduction with respect to the classical Cyclone® 18/9, the vault height could be reduced from 3m to 2.5m. The top of the yoke is for Cyclone® KIUBE at the distance 1.6m vs 2.2m from the vault floor for Cyclone® 18/9.

For existing site or site with local constraints, IBA developed as well a self-shielding for the machine. The artistic view of the Cyclone® KIUBE self-shielding is presented in Figure 8.

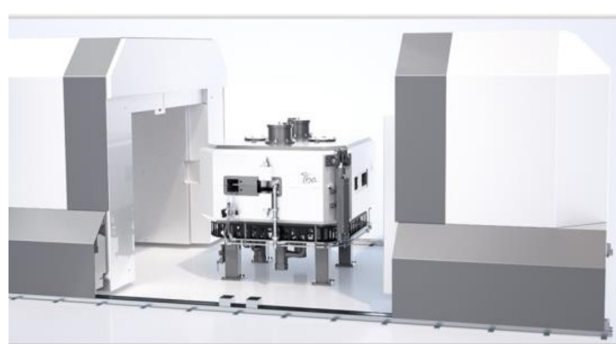

Figure 8: Cyclone® KIUBE and self-shielding.

Thanks to this option and the job performed by our Integralab team (integration of the quality control, hot cells, radio-chemistry,…), IBA can propose now the full radiopharmacy installation on a footprint smaller than 100m².

ISBN 978-3-95450-167-0

CONCLUSIONS

The new Cyclone® KIUBE has been successfully designed, commissioned at the IBA factory and installed on our partner side. Cyclone® KIUBE outperforms the classical IBA Cyclone®18/9 in terms of beam intensity, size, weight, pumping speed, beam transmission, extraction efficiency and power consumption. The self-shielding option has been as well designed for 100µA and 150µA configurations.

REFERENCES

[1] S. Zaremba *et al.*, “Magnet Design of the New IBA Cyclotron for PET Radioisotope Production”, presented at Cyclotrons’16, Zurich, Switzerland, paper TUP04, this conference.

[2] W. Kleeven *et al.*, “Extraction System Design for the New IBA Cyclotron for PET Radioisotope Production”, presented at Cyclotrons’16, Zurich, Switzerland, paper TUP03, this conference.

ISBN 978-3-95450-167-0

BEST 70P CYCLOTRON COMMISSIONING AT INFN LN LEGNARO

V. Sabaiduc, T. Boiesan, M. Carlson, D. Du, L. A.C. Piazza,
V. Ryjkov, M. Stazyk, S. Talmor, J. Zhu, R. Johnson, K. Suthanthiran,
Best Cyclotron Systems Inc., Vancouver, BC, Canada
T. Evans, I. Tarnopolski, P. Zanetti, Best Theratronics Ltd., Ottawa, ON, Canada

Abstract

Best Cyclotron Systems Inc (BCSI) has designed and manufactured a 70 MeV compact cyclotron for radioisotope production and research applications. The cyclotron has been built at the Best Theratronics facility in Ottawa, Canada for the INFN-LNL laboratory in Legnaro, Italy. The cyclotron has an external negative hydrogen ion source, four radial sectors with two separated dees in opposite valleys, cryogenic vacuum system and simultaneous beam extraction on opposite lines. The beam intensity is 700 microamperes with variable extraction energy between 35 and 70 MeV. The beam commissioning performances at the customer site are reported.

BEAM COMISSIONING

The cyclotron and beam line equipment has been installed and commissioned at INFN LN Legnaro and the *Factory Acceptance Test* (FAT) has been successfully repeated before proceeding with high energy beam acceleration.

1 MeV Acceleration

The cyclotron is equipped with a low energy beam intercepting probe located at the 1 MeV radius. The probe is used to optimise the beam transport through the *Low Energy Beam Transport (*LEBT) line and characterise the beam injection efficiency and acceleration to 1 MeV. A complete characterisation up to 1 MeV has been done and reported [1] as part of the FAT.

Beam intensity and stability parameters have been confirmed to better values as shown in Table 1.

Table 1: Beam at 1 MeV Probe

Parameter	Value
Beam current	900 µA
Ion source current	8.5 mA (max. 15 mA)
Injection efficiency	10.3%.
Beam ripple	±1% of the average value stability better than 5 µA

High Energy Acceleration

Beam acceleration to high energy was scheduled in several steps to ensure that beam tuning on target was optimum while maintaining the beam losses to a minimum. The beam line layout as shown in Fig. 1 allowed us to install multiple low power Faraday cups at the exit of each beam line switching magnet in addition to the high power beam dump of 50 kW (INFN supply) installed in target vault A6. Tests on Faraday cups were conducted at low beam currents of 3 to 20 µA single and double beam extraction. Beam delivery operation and tunes were verified and optimised at 100 µA beam current on the beam dump.

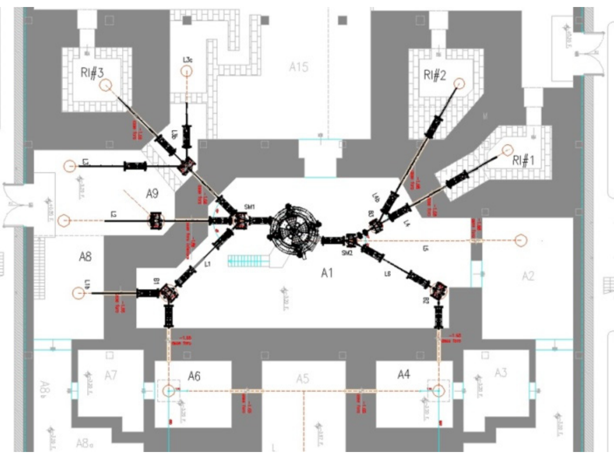

Figure 1: Beam line layout.

Beam Profile Measurement

Two helical wire beam scanners per beam line were installed to characterise the beam profile during the tuning process. Scans have been done up to maximum beam current by closely monitoring the power dissipation on the wire (increased rotation speed at higher beam powers). Figure 2 shows the beam profile (peak voltage) for wobbler off and on status versus *x* axis position.

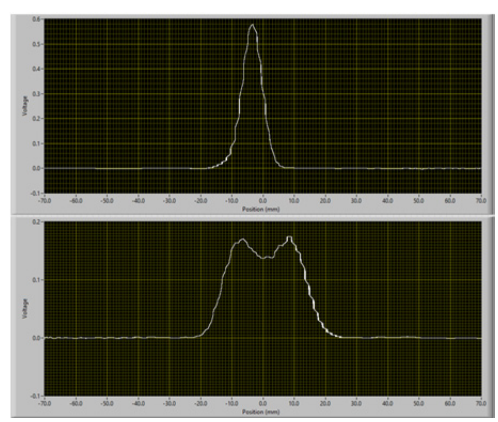

Figure 2: Beam profile (V), wobbler off/on versus *x* axis position.

Pulsed Beam

Two methods of pulsing the beam intensity were considered: amplitude and phase modulation. In either case the modulated parameter was switched between values:

ISBN 978-3-95450-167-0

one that completely eliminates the beam and the other corresponding to the optimum operational setting.

Amplitude and Phase Modulation The separated resonator design and digital Low Level Radio Frequency (LLRF) [2, 3] controller allows for the amplitude and phase of the accelerating voltage to operate in pulsed mode of various configurations (in phase or phase modulation). Both features allow for the beam current intensity to be controlled in pulse peak power and/or ramp-up mode as may be required by the target power management. Features can also be used to compensate for beam loading effects in addition to the movable coupler design. Figure 3 shows the in phase amplitude modulation of the dee voltage between 40 to 60 kV (100 ms period 50% duty factor, 70 MeV, 100 µA average, 200 µA peak beam).

When using amplitude modulation at higher beam currents, we investigated and confirmed spills on beam line during the transient time of the accelerating voltage by monitoring one of the four slits in first beam line section.

The spills increased with the peak current as illustrated in Fig. 4, at the same time showing the induced RF amplitude instability due to the strain of a sudden increase in beam loading (400 µA peak current, 100 ms period 50% duty factor). The trace in the middle (magenta) corresponds to the current on one of the slits, showing a burst during this transition.

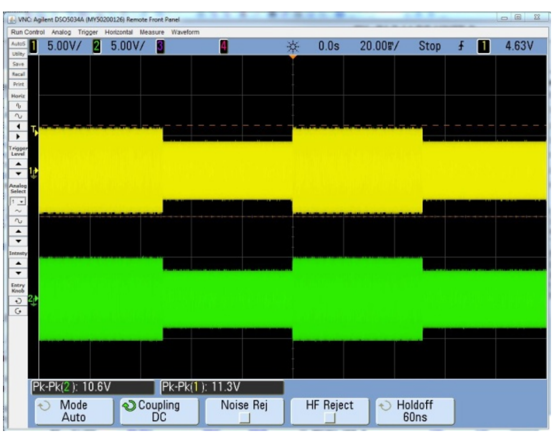

Figure 3: Amplitude modulation (sample) versus time.

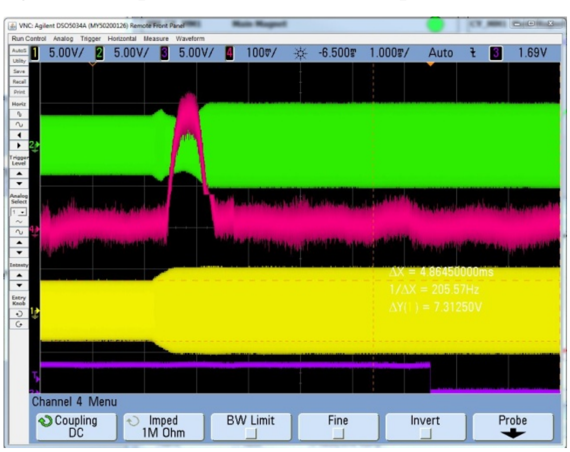

Figure 4: Amplitude modulation, peak current (400 µA) versus time.

Amplitude versus Phase Modulation In order to determine if any beam losses occur during the acceleration when either the accelerating voltage or phase between resonators is changed, a comparative measurement was done between the 1 MeV and extraction probe currents.

The characteristic of beam transmission versus the accelerating voltage shows both currents being identical. Therefore, no losses in the cyclotron occur when using an amplitude ramp-up procedure. Results are shown in Fig. 5 where it can also be noted that when the acceleration voltage was decreased to 40kV, the beam reduced to zero.

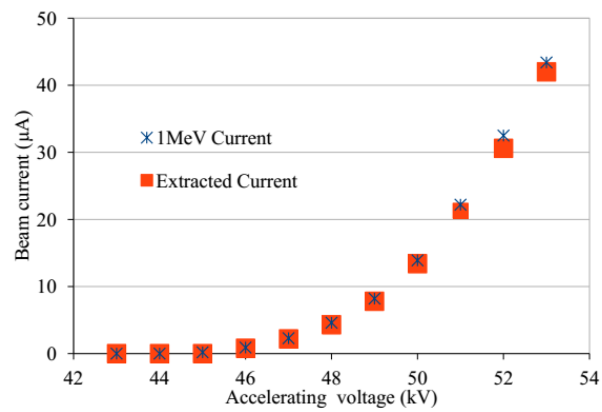

Figure 5: Beam transmission with amplitude.

The experiment was repeated by incrementally changing the delay between resonators while the accelerating voltage was fixed at an optimum value. The measurement started from the 120 degree (out-of-phase) condition where it has been established that the beam is completely off; zero beam on the 1 MeV probe. Results were immediately observed when reducing the phase difference between resonators as shown in Fig. 6. There was a significant difference between the 1 MeV and extraction probe currents indicating losses in the acceleration, 16.6 versus 3.1 µA. The immediate conclusion was to not use the phase modulation for beam control at high intensity currents.

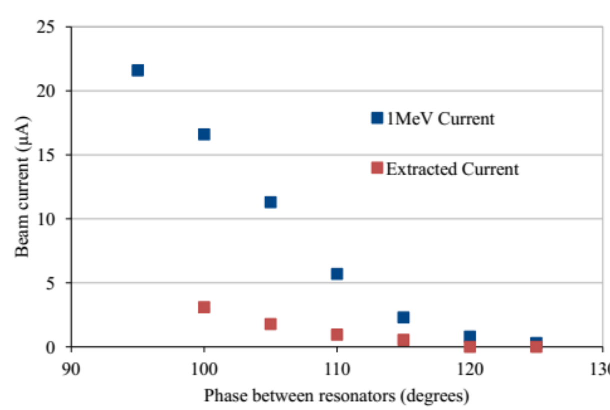

Figure 6: Beam transmission versus phase difference.

ISBN 978-3-95450-167-0

500 µA Beam on Target

After exploring beamline operation at 100 µA, the current on the beam dump was gradually increased and sustained at every 100 µA increment to confirm stable, problem-free operation at each level before the next increase.

Figure 7 illustrates this ramp up to 400 µA of beam on target, followed by a ramp up to 500 µA on the next day (see Fig. 8). At that time the INFN beam dump developed a vacuum leak and the operation was stopped.

BEAM LINE LOSSES

Beam losses along beam line have been measured at various current levels with the tune optimised to minimise the losses. The value is measured as a percentage of unaccounted currents versus the extractor probe current. Unaccounted currents have been measured as the difference between extractor probe current and sum of all beam line currents (slits, baffles and target currents). Values are given in Table 2 for several beam current levels.

Vacuum at high beam power The vacuum level has been consistently stable at values near 5x10^{-8} Torr with all systems operating and no beam acceleration. Accelerating and extracting 500 µA of beam caused the vacuum level to increase to approximately 6.5x10^{-8} Torr as shown in Fig. 8.

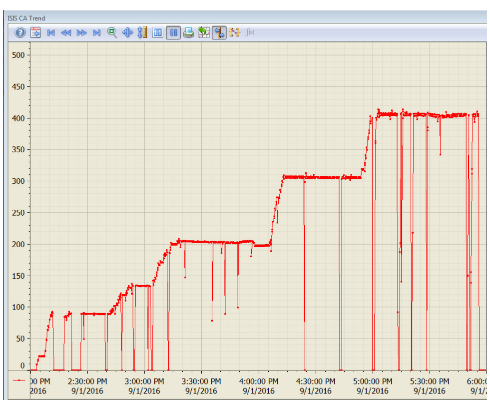

Figure 7: Beam current on target ramp-up (µA), versus time.

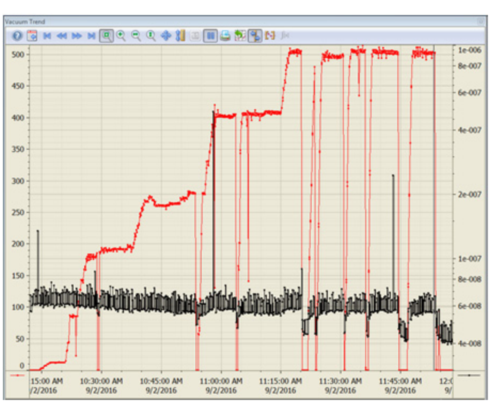

Figure 8: Vacuum and beam current (µA) versus time.

Table 2: Beam Line Losses

Beam Current on Target	Value
300 µA	0.2%
400 µA	0.5%
500 µA	0.5%

RADIATION LEVELS

Radiation surveys were periodically done after most significant runs. Activity levels have been noted at the typical locations at and around the Faraday cups and first set of beam line slits. No significant active spots have been detected along the beam line pipe. Some small activation spots have been found after pulsed beam operation. Those are most likely associated with increased slit spills observed during pulsed operation

The facility radiation survey system monitors in real time the level of radiation in vaults, air exhaust chimney and cooling water for the cyclotron. It was noted that all activity levels sensitively decreased when tuning was optimised and beamline slits current were reduced. Detail results are presented in [4].

ACKNOWLEDGMENT

The BCSI team and management would like to acknowledge the continuous support that INFN LN Legnaro scientists, engineers and directors provided during the entire duration of the contract, from earlier stages of design through the installation and commissioning of the cyclotron. We also would like to acknowledge Dr. Bruce Milton's contribution and Dr. Tianjue Zhang's continuous advice to the design and construction of the 70 MeV cyclotron.

REFERENCES

[1] V. Sabaiduc *et al.*, "BEST 70P cyclotron factory test", in *Proc. IPAC'15*, Richmond, VA, USA, 2015, paper THPF003, pp. 3680-3682.

[2] V. Sabaiduc *et al.*, "Resonator system for the BEST 70 MeV cyclotron", in *Proc. Cyclotrons'13*, Vancouver, Canada, 2013, paper TU2PB04, pp. 153-155.

[3] G. Gold and V. Sabaiduc, "Design of a digital low-level RF system for BEST medical cyclotrons", in *Proc. Cyclotrons'13*, Vancouver, Canada, paper TUPPT024, pp. 203-205.

[4] M. Maggiore *et al.*, "Status of the high intensity proton beam facility at INFN", presented at the 21 Int. Conf. on Cyclotrons and their Applications (Cyclotrons'16), Zurich, Switzerland, Sep. 2016, paper FRA03, this conference.

ISBN 978-3-95450-167-0

SOME EXAMPLES OF RECENT PROGRESS OF BEAM-DYNAMICS STUDIES FOR CYCLOTRONS

W. Kleeven*
Ion Beam Applications (IBA), Louvain-la-Neuve, Belgium

Abstract

Two subjects are highlighted. The first is the problem of high space charge effects in cyclotrons. The second is the the progress in development of tools and simulations for industrial and medical cyclotrons at IBA.

INTRODUCTION

This paper reviews examples of recent progress in beam dynamics studies for cyclotrons. The paper is not extensive, but rather follows developments of two subjects during the past years and tries to add an educational accent. The first is the problem of high space charge. This subject is at this moment very important, in view of possible applications of (compact) cyclotrons for ADS, or for generating high fluxes of neutrinos for experiments such as IsoDAR or Daeδalus (see this conference [1]). Examples are given of the increased understanding based on (semi-)analytical models and of the latest developments and achievements based on numerical simulations. The second subject is the progress in simulations for industrial and medical accelerators as has been achieved at our company during the last years.

SPACE CHARGE IN CYCLOTRONS

One can distinguish roughly three types of intensity limiting space charge effects in cyclotrons: i) the problem of beam blowup due to the weak vertical focusing in the cyclotron center, ii) the problem of loss of turn separation due to space charge induced energy spread and iii) the problem of space-charge induced halo for poorly matched beams.

Space Charge Effects in the Cyclotron Center

This paragraph refers to papers of Rick Baartman, Thomas Planche and Yi-Nong Rao [2–5]. In the central region of a (compact) cyclotron, the azimuthal magnetic field variation falls quickly to zero and Tterefore the magnetic vertical focusing becomes very weak. The beam current is limited by the space charge vertical defocusing and the resulting vertical losses on the central region.

The incoherent vertical tune shift inversely depends on the kinetic energy of the particle. Thus increasing the injection energy helps to increase the current limit. This is done for example at PSI (870 keV) and at Triumf (300 keV). A drawback is that losses at these higher injection energies can already be harmful. Furthermore such high injection energies can not be done in smaller machine. For compact cyclotrons, one has to rely on the weak electric focusing of the RF gaps.

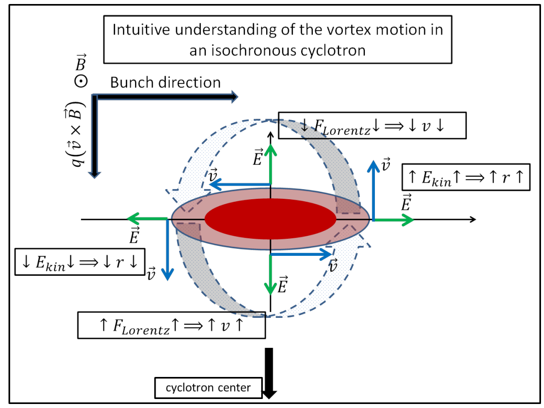

Figure 1: Intuitive understanding of the vortex motion

This focusing is RF-phase dependent. The bunch-center must cross the gap on the falling RF slope . This means that the head of the bunch experiences weaker focusing than the tail. By this, space charge causes progressive loss of the bunch head [2]. When using a (spiral) inflector, the beam needs to be strongly compressed in three dimensions (by bunching and transverse focusing). The beam at the inflector exit is therefore strongly mismatched with respect to the weak vertical focusing. The complicated spiral inflector optics strongly correlates the 6D phase space. Both effects result in strong emittance growth [5].

Loss of Turn-Separation Due to Space Charge

This paragraph refers for some part to a nice overview paper of Rick Baartman [6] in the 2013 Vancouver cyclotron conference. In an isochronous cyclotron, the space charge effect induces a vortex motion and an increase of energy spread in the bunch. An intuitive understanding of the this is obtained from Fig. 1. Here the bunch is moving clockwise from left to right. Due to the outward directed space charge force, the leading particles gain energy. In an isochronous cyclotron they can only move to higher radius. Trailing particles loose energy and move to lower radius. The radially exterior particles experience a reduction of centripetal force and fall behind in phase. The opposite happens for the interior particles.

The bunch density shows an effect of macroscopic rotation (vortex). If the the space charge equipotential curves would be similar to that of the ellipse and the space charge force would remain perfectly linear, then the elliptical bunch-shape would be conserved. Generally this is not the case and the bunch starts to deform (spiralize) such that the outer part of the bunch will rotate slower than the core.

* willem.kleeven@iba-group.com

ISBN 978-3-95450-167-0

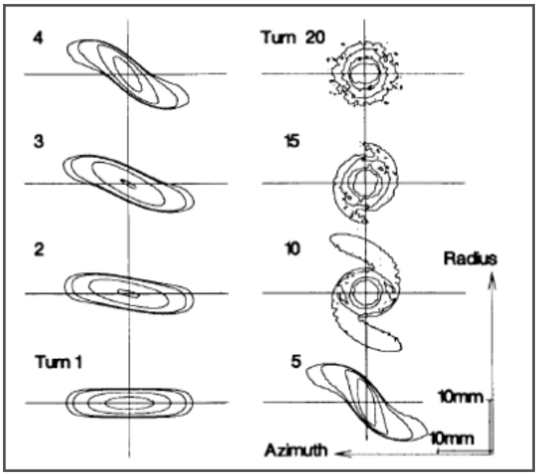

Figure 2: Simulation by Stefan Adam [7] of a 1 mA bunch accelerated in the PSI injector II

Stefan Adam from PSI first started with efforts to simulate the longitudinal space charge effects in their injector and ring cyclotron [8]. Figure 2 shows a later (1995) simulation [7] of a 1 mA bunch accelerated in the PSI injector II, with an initial phase width of 15°, during 20 turns. It is seen that the core of the bunch rotates faster than the envelope, resulting in an initial deformation of the bunch. After 10 to 15 turns a round beam emerges with an intense core, surrounded by halo. Halo reduces with better initial matching

The vortex effect was first recognized in 1969 by Mort Gordon [9] who explained that, due to the Coriolis forces in a rotating frame, the particles in the bunch execute a steady state velocity pattern which is directed along the equipotential curves of the space charge potential. However, at the same time he found that this effect could be neglected in the then known practical case where the bunches were much longer than wide. In 1981 Werner Joho [10] elaborted furher on Gordon's idea, using a model of multiple turns with constant azimuthal length (sector- or pie-model) to calculate the space charge induced energy-spread and its effect on the turn-separation. This resulted in a formula showing an intensity limit proportional to the cube of the energy gain per turn (or RF-voltage; so a $1/n^3$ dependence; n is turn number). This formula is still found to be correct although the sector model has been invalidated later with the numerical confirmation of the vortex motion at PSI.

In 1988 the author of this paper [11] applied the 3D beam-envelope approach of Sacherer [12] to derive differential equations for the full set of second moments of a space charge phase space in an Azimuthally Varying Field (AVF) cyclotron. One of the outcomes was a proof of existence of stationary round bunches. Another was that such bunches follow envelope equations that are similar to the Kapchinsky-Vladimirsky (KV) equations.

In 2001 Bertrand and Ricaud [13] used an elegant and simple model of a spherical non-relativistic bunch in a homogeneous magnetic field. The solution of the particle linear equations of motion show the existence of two modes of oscillation. The motion is found to be stable if the total charge Q in the bunch is smaller than a threshold $Q_{max} = \pi\epsilon_0(m/q)\omega_c^2 r^3$ (where ω_c is the cyclotron frequency and r the bunch radius). It is interesting to see that this can be also formulated as follows:

$$\omega_p < \frac{1}{2}\sqrt{3}\omega_c \,, \tag{1}$$

where ω_p is the plasma-frequency ($\omega_p = \sqrt{nq^2/m\epsilon_0}$ and n is particle density). This suggest that the plasma-frequency ω_c is a critical parameter.

In his 2013 paper [6] Baartman explores further the models of Kleeven and Bertrand/Ricaud and provides a deeper insight into the vortex physics. The two modes are interpreted as coupled betatron (r, P_r) and dispersion (E, Φ) motion. For $Q \ll Q_{max}$ the betatron oscillations are fast and the energy oscillations slow. For $Q = Q_{max}$ the acceptance approaches zero and both frequencies are equal to 1/2. This is a beam with zero emittance and laminar flow. Figure 3 shows the tunes of both modes.

Baartman also derives a formula for the intensity limit of separated turn cyclotrons which applies if the injected bunch is sufficiently short such that the vortex motion causes the bunch to curl up into a single droplet.

$$I_{max} = \frac{h}{2g_r\xi^3\beta^3\gamma\nu_x^4}\frac{V_{rf}^3}{V_m^2 Z_0} \,. \tag{2}$$

This formula shows a depence with a third power of the RF-voltage V_{rf}, but also the scaling with respect to the particle type (mass $V_m = mc^2/q$), the RF harmonic mode h, the tune ν_x, and the relativistic parameters β and γ.

Acceleration effects are considered and a qualitative threshold is found for the vortex motion to take place: below the threshold the bunches maintain their phase length (thus bunch length increasing like $R\delta\theta$), but above it the bunch length remains constant and thus decreases in phase length. This threshold is $2\pi\Delta\nu_r \ll \delta\beta/\beta$, stating that the space charge induced tune shift must be (considerably) larger than the relative velocity increase due to acceleration.

The vortex effect makes that bunches with a high length to width ratio break up into small approximately circular

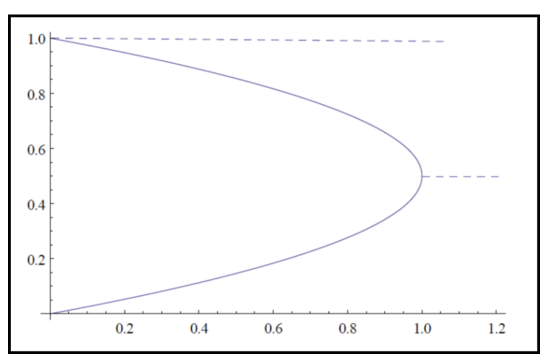

Figure 3: Tunes $\nu_{r\pm} = \frac{1}{2}(1 \pm \sqrt{1 - Q/Q_{max}})$ of the two modes as a function of Q/Q_{max}

ISBN 978-3-95450-167-0

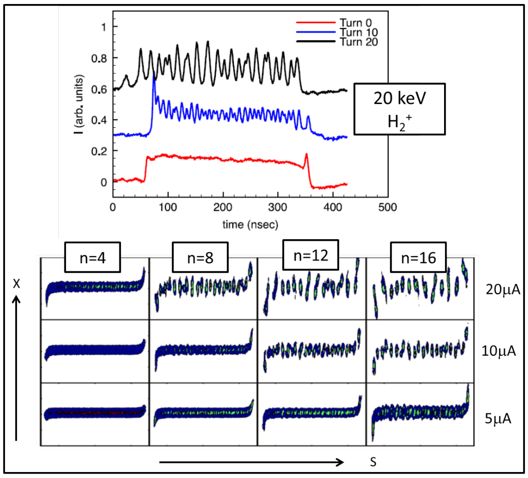

Figure 4: upper: longitudinal bunch profiles measured on a fast Faraday cup in the SIR at MSU for a bunch peak current of 9.3 μA. lower: beam simulations in the SIR with the PIC tracking code CYCO. Each frame contains a median plane projection of the bunch and has a size of 5 cm × 45 cm (x × s). Droplets start to appear quickly, depending on the peak current (from Pozdeyev [14]).

droplets. This was shown both experimentally and by simulations in the 2003 thesis study of Pozdeyev [15] on the Small Isochronous Ring (SIR) at MSU (see Fig. 4).

Recently Antoine Cerfon *et al.* have introduced a new fluid dynamics approach in which they directly obtain an approximate solution of the collisionless Vlasow equation [16–18]. The main simplifications and assumptions made are the following: i) the space charge is not too strong such that $\omega_p/\omega_c < 1$ (equivalent to saying that the incoherent tune shift is small). ii) the beam size is mainly determined by dispersion and little by emittance (close to laminar phase space), iii) a non-relativistic, 2-dimensional coasting beam in homogeneous B-field is considered. The first assumption makes that the time-scale associated with betatron oscillations is much smaller (faster) than the time scale associated with space charge. This allows to apply an averaging procedure to the Vlasow equation that results in a simple fluid-like equation for the particle density n. Together with the Poisson equation this gives two simple coupled 2D partial differential equations that describe the radial-longitudinal space-charge induced vortex motion in the isochronous cyclotron:

$$\frac{\partial n}{\partial t} + \delta^2(\nabla\phi \times \mathbf{e}_z) \cdot \nabla n = 0\,, \tag{3}$$

$$\Delta\phi = -n\,, \tag{4}$$

where $\delta = \omega_p/\omega_c$. Since the vector $\nabla\phi \times \mathbf{e}_z$ in Eq. (3) is proportional to $\vec{E} \times \vec{B}$, the vortex motion can be intuitively understood as the nonlinear advection of the bunch by the $\vec{E} \times \vec{B}$ velocity field (similar to Gordon's idea). Note that the δ^2-term in the above equation can just be eliminated by a proper time scaling. This implies that (within the assumed approximations) the beam intensity does not affect the nature but only the time scale of the vortex motion.

The strength of the model is that it provides an interpretation of complicated PIC simulation results and identifies the basic contributing mechanisms without the need of large supercomputers and long computing times. Figure 5 shows two examples of simulations. Of course the approach does not give the quantative precision as PIC codes such as for example OPAL. Such precision is needed for actual designs. Both approaches are complementary. Another observation made by Cerfon is that the fluid equations are isomorphic to the two dimensional Euler equations for a fluid of uniform density. This means that results known from fluid dynamics theory on the behaviour of isolated vortices can be directly interpreted in the language of beam dynamics in cyclotrons. Based on this, predictive statements can be made such as for example: *i) round beams with monotonically decreasing density profiles are stable to finite perturbations ii) elliptic beams with smooth, monotonically decreasing density profiles are subject to spiraling and axisymmetrization iii) elliptic bunches with too high aspect ratios break up into smaller bunches due to Rayleigh's inviscid shear instability.*

For high-intensity cyclotrons with an ESD, turn-separation at extraction is crucial (avoid septum losses) and a good matching is needed at injection such that the vortex-effect occurs quickly, resulting in circular bunches. For too long bunches their sizes increase and a large halo devel-

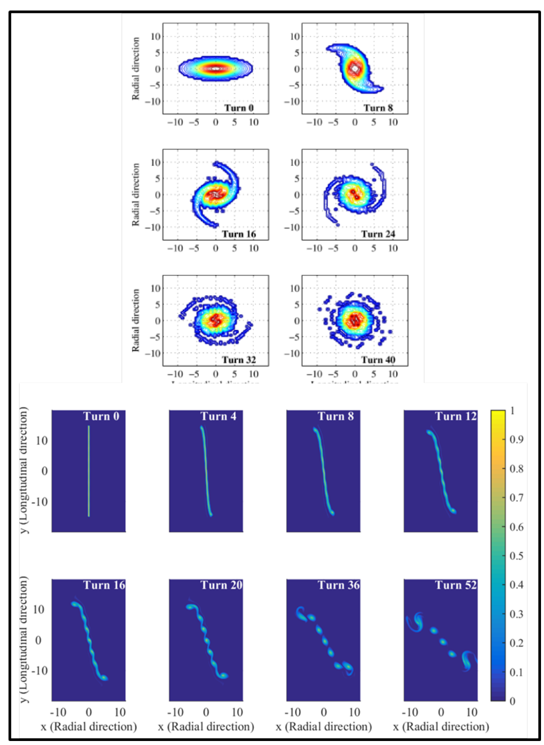

Figure 5: Upper: formation of a round beam core surrounded by a low density halo as simulated with the fluid-dynamic approach by Cerfon [17] for $\delta^2 = 0.2$. Lower: simulation of the beam break-up [18].

ops, resulting in high extraction losses. For the PSI injector II cyclotron the vortex motion is so strong that very short bunches are obtained such that the flattop system is no longer needed [19] (and is actually used for acceleration). In the PSI ring cyclotron the space charge effect is not strong enough to produce the circular bunches. Here the relative phase of the flattop cavities is detuned such that the energy gain in the tail of the bunch is larger than in the head, thereby counteracting the linear part of the longidutinal space charge force and the related energy spread [20].

A reference in the numerical simulation of space charge effect is the code OPAL (Object oriented Parallel Accelerator Library). It is a PIC space charge tracking code, for large accelerator structures and is developed mainly at PSI [21]. It extensively relies on parallel processing and is able to simulate large numbers of accelerated particles (order 10^6) in cyclotrons resulting in very precise beam density and profile predictions. It has been (and still is) used extensively in simulations of the PSI injector II cyclotron as reported in this conference by of Anna Kolano [22]. It also has been applied for other cyclotrons such as for example the PSI ring cyclotron [20,23], the CIEA 100 MeV H- cyclotron [24], the proposed IsoDAR injector cyclotron and the Daedalus superconducting ring cyclotron [25], but also for other machines such as FFAG's [26] The code remains under further development. It can simulate the space charge effect of neighboring bunches [23]. Besides space charge it has various other simulation applications such as wake-fields, multipacting and particle-matter interaction. An update on OPAL is given also in this conference by Andreas Adelmann [27]. Figure 6 shows some results of a OPAL simulation of the IsoDAR cyclotron.

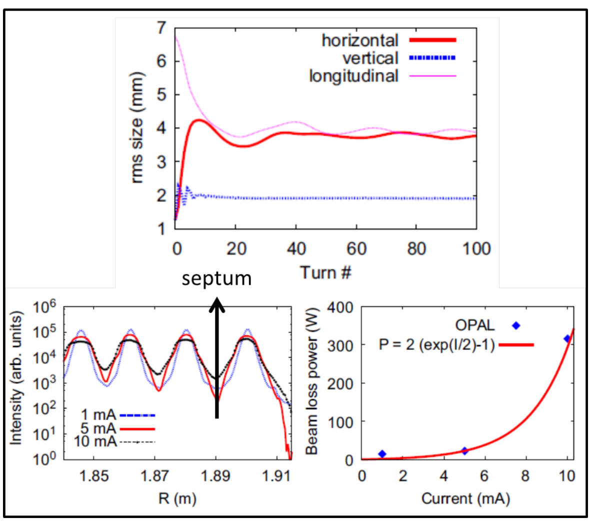

Figure 6: OPAL simulation of IsoDAR. Upper: a long Gaussian bunch (aspect ratio 5/1, $\Delta\Phi$=40°) of I_{ave} =5 mA H_2^+ is coasting at 3 MeV. After 10 to 15 turns, the bunch obtains the circular match due to the vortex effect. This suggest that, as in the PSI injector II, flattop cavities are not needed and 4 accelerating cavities can be placed in the valleys. Lower: the use of a large number of macroparticles (10^6) allows to predict with high dynamic range (10^4) the density profile in between the last two turns and to estimate the losses on the septum (0.5 mm) of the ESD as function of the beam current and also to optimize collimators placed closer to the center to reduce beam-halo. Based on such simulations it is claimed that IsoDAR can extract the 5 mA of H_2^+

.

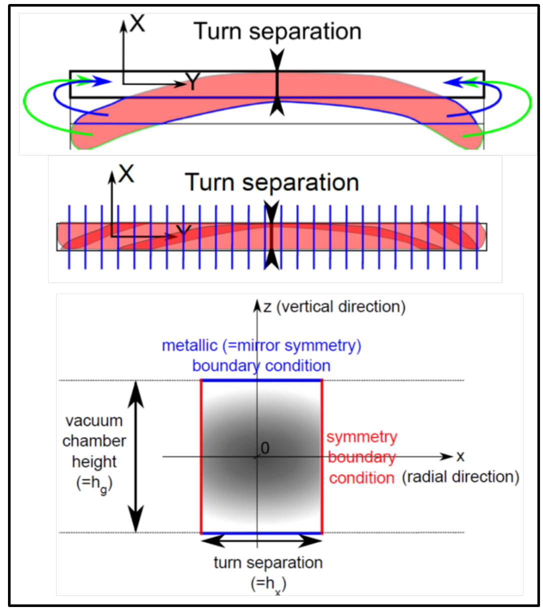

Figure 7: Illustration of the use of radial periodicity in the space charge code TRICYCLE [4,28].

For cyclotrons using stripping extraction (such as H^- at Triumf or H_2^+ in the proposed Daedalus ring-cyclotron [25]) a large turn-separation ΔR at extraction is not needed and the space charge induced energy spread is not harmfull for extraction. The relation between energy and radius remains unique (except for the small contribution of emittance) and the quality of extracted beam is not really affected. These machines can accept a large phase width at injection (up to 60°). Bunches are long and also may have a large radial extend due to energy spread. At large radii, turns overlap and the effects of neighboring turns become essential. The neighboring bunch feature is available in OPAL and has been used succesfully in simulations of the PSI ring cyclotron [23] and the CIAE 100 MeV H^- cyclotron [24]. For the Triumf case, with extreme long bunches, OPAL would require a very large number of particles and a large grid. Thomas Planche *et al.* [4,28] made a code (TRICYCLE) which uses periodic boundary conditions in the radial direction to solve the Poisson equation (see Fig. 7). This is allowed assuming that bunch shape evolves slowly turn by turn. This considerably reduces computation time, because only one bunch needs to be followed during the simulation.

Bunches are sliced radially by a box with a width of the turn separation ΔR. Parts of the bunch that are outside of the box, are returned into it by a radial shift of ΔR. The box is sliced longitudinally to create a number of 2D surface-charge density distribution (in X-Z plane) For each slice the

ISBN 978-3-95450-167-0

3D Poisson equation is solved by FFT with proper boundary condition (x ⇒ periodic, y ⇒ open, z ⇒ metallic). A simulation result is shown in Fig. 8.

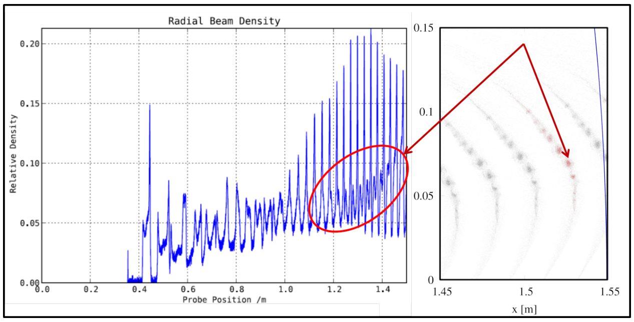

Figure 8: Observation of the beam break-up in a measured radial probe track (left) and TRICYCLE simulation (right) of a high space charge bunched beam (410 µA) during the first 30 turns in the Triumf cyclotron central region [28].

For the DAEδALUS/IsoDAR studies, extensive injection line space charge simulations have been done. This paragraph refers to a paper made by Daniel Winklehner *et al.* [29]. The project calls for 50 mA of H_2^+ injected from the ion source into the LEBT. Simulations need to also take into account space charge compensation: the effect that slow electrons from the beam-residual gas interaction are trapped in the beam potential well, thereby reducing space charge. The Particle-In-Cell (PIC) code WARP [30,31] as developed at LBNL/LLNL was used. The space charge compensation depends on the beam line vacuum. The pressure distribution along the line was simulated with the Monte Carlo program MOLFLOW [32]. The space charge compensation is estimated at each time-step, based on an analytical/empirical modeling of the physical processes. Initial particle distributions were obtained from self-consistent 3D ion source extraction simulations, done by the Catania group with the code KOBRA-INP [33]. The dual-particle (p and H_2^+) DC ion beam in the LEBT is transported through a series of transversal slices along the z-axis. From the different possible field-solvers in WARP, the XY-slice solver was used (longitudinal fields are small and ignored) The simulations were bench-marked against measurements done on a LEBT test-stand provided by Best Cyclotron Systems (BCS) in Vancouver (see Fig. 9).

As is shown in Fig. 9, even with the long chain of simulations needed (i) ion source extraction, ii) beam line vacuum, iii) space charge neutralization and iv) dual particle beam transport with space charge), a good fit with measurements was obtained. For IsoDAR, this is not the end of the journey because the beam transport, transmission, optics and matching through the inflector and cyclotron central region (CR) is a crucial and very complex 3D space charge problem. This question needs to be answered, in order to be able to estimate the highest intensity achievable with such a cyclotron. Efforts are ongoing to include the spiral inflector and the CR into OPAL. Alternatively, RFQ injection has been explored [34]. The strong mismatch between the RFQ

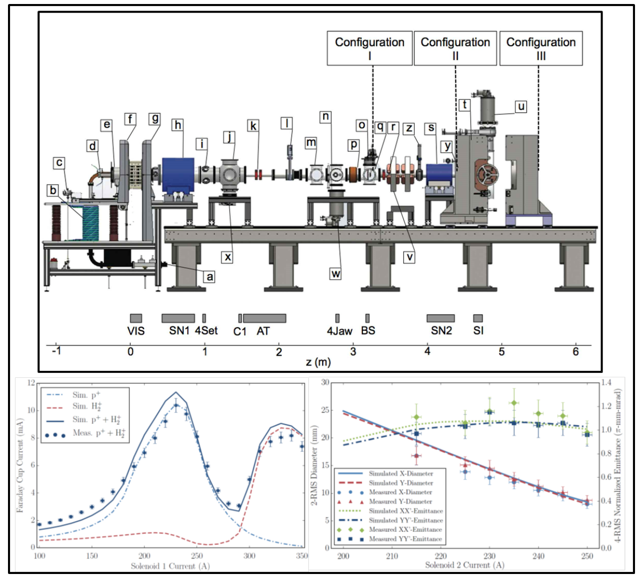

Figure 9: Upper: layout of the test stand of BCS as used for benchmarking the IsoDAR LEBT simulations. Lower left: comparisson of measured and simulated beam current at the Faraday cup (placed at z=3.2 m from the Catania Versatile Ion Source (VIS) extraction aperture.) versus solenoid SN1 excitation. Lower right: a similar comparisson of beam emittance and diameter (at z=4.8 m) as function of the second solenoid SN2.

extracted beam and the inflector acceptance seems problematic however.

SOME RECENT PROGRESS AT IBA

During the last few years IBA made quite some efforts in order to precisely simulate orbits and beams in all their different types of accelerators. The program phase-motion integrates the coupled motion of orbit-center and longitudinal phase space over multiple pulses (several 10^5 RF periods) in the proton-therapy superconducting synchro-cyclotron S2C2. This is reported in this conference by Jarno Van de Walle *et al.* [35]. The Advanced Orbit Code (AOC) [36] facilitates design studies of critical systems and processes in medical and industrial accelerators. Examples are : i) injection into and extraction from cyclotrons, ii) central region, beam capture and longitudinal dynamics studies in synchro-cyclotrons, iii) studies of resonance crossings, iv) stripping extraction, v) beam simulation from the ion source to the extraction, vi) beam transmission studies in gantries, vii) calculation of Twiss- functions, viii) space charge effects.

For the space charge option, a particle-to-particle solution was chosen. Here the self-field acting on one particle is obtained as the sum of contributions of all other particles. Of course this slows down the calculation for large number of particles N (computing time scales as N^2). But the cyclotron injection and central region problem (and also the Rhodotron [37]) does not require very high precision (a few percent is already good) and therefore it is not required to use a very

ISBN 978-3-95450-167-0

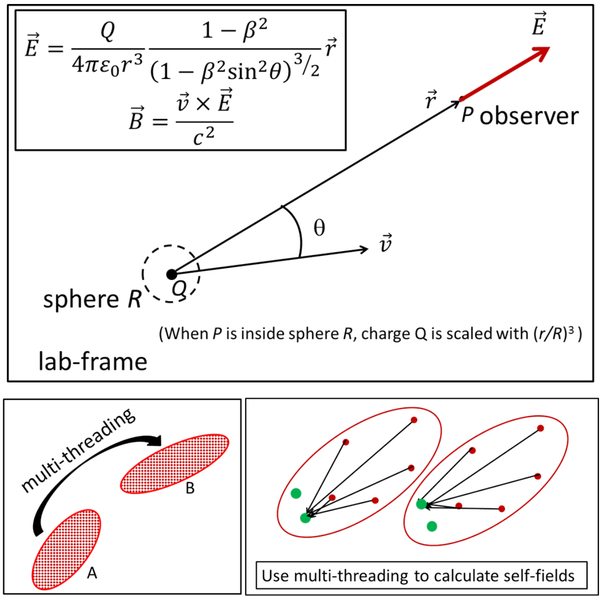

Figure 10: Illustration of calculation of self-fields in AOC (upper) and the use of multi-threading in both the particle integration (lower left) and SF-calculation (lower-right)

.

large number of particles (10000 can be enough). A big advantage of the chosen method is that one can immediately include the space charge option together with the existing fully 3D features of the $(\vec{E}, \vec{B})$-fields and with a complex 3D shape of a reference orbit (such as for the spiral inflector) already available in AOC.

At IBA one wants to also simulate the industrial CW electron accelerator Rhodotron. This machine (in the range from 5 to 10 MeV) has high average beam power in the range of 20 kW to 700 kW. There is some similarity to cyclotrons in the sense that i) the beam is re-circulating several (order 10) times into the same coaxial accelerating-cavity (see Fig. 11), ii) the machine runs with an RF similar to cyclotrons (100-200 MHz) and iii) one orbit period is equal to an RF period. In this machine i) electrons are accelerated from low energy (30 keV) to fully relativistic (10 MeV); ii) one bunch may be very far from mono-energetic, and iii) the direction of particle velocities in the bunch may differ over 180° in the re-circulating dipole magnets. Therefore, a fully relativistic approach was chosen (a Lorentz frame moving with the bunch as commonly used in PIC codes, can not be well defined due to ii) and iii) above).

The relativistic $\vec{E}$-field from a moving point charge is radially directed but not isotropic and the magnetic field is perpendicular to $\vec{E}$ and $\vec{v}$ (see Fig. 10). In order to avoid singularities in the calculations of self-fileds, a virtual sphere R is placed around the charge Q. For an observer inside this sphere, Q is scaled with $(r/R)^3$. Here R is estimated from the rms volume of the bunch and the number of particles in the bunch. The evolution of the self-fields (SF) is iteratively determined as follows: i) calculation of self-fields at A: SF(A), ii) integration of particles from A to B assuming constant SF along the path, iii) calculation of SF(B), iv) re-integration from A to B applying linear interpolation between SF(A) and SF(B), v) repeating of iii) and iv) until the error is considered small enough. This method is not necessarily slower (may even be faster) then a single evaluation approach, because the step from A to B may be taken larger. In most practical cases 2 iterations are sufficient. Both particle integration and SF calculation is done using multi-threading. Two examples of a AOC space charge calculation are shown in Fig. 11 and Fig. 12.

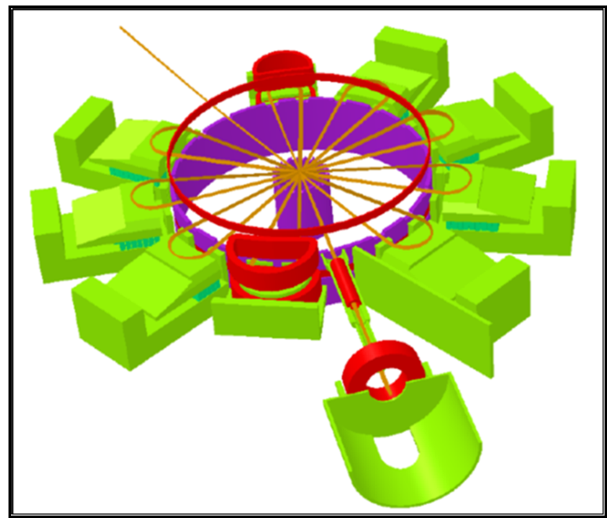

Figure 11: AOC space charge simulation of a I_{ave}=10 mA electron beam in the TT50 Rhodotron, starting at 35 keV from the egun and accelerated upto 10 MeV during 10 passes through the cavity and the re-circulating magnets.

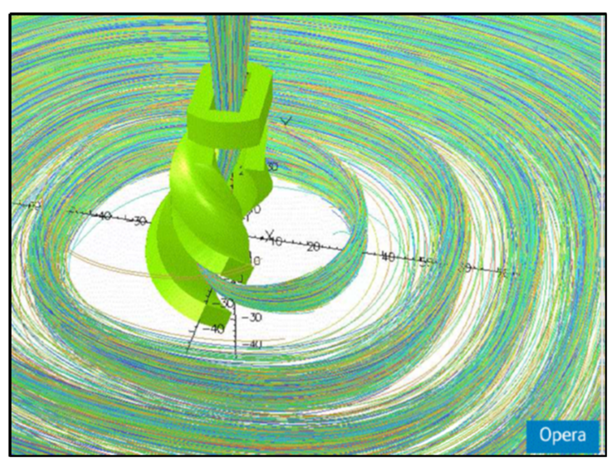

Figure 12: AOC space charge simulation of a bunched I_{ave}=2 mA H^- beam (5000 particles), injected in the axial bore of the CYCLONE®70, going through the cyclotron spiral inflector and accelerated during 5 turns in the central region. For clarity, the dee-structure and magnet structure are not shown. The structure of the program is such that an RF buncher and injection line focusing elements could be included in a rather straightfort manner.

ISBN 978-3-95450-167-0

REFERENCES

[1] D. Winklehner, "Updated Physics Design of the DAEdALUS and IsoDAR Coupled Cyclotron for High Intensity H_2^+ Beam Production", presented at Cyclotron'16, Zurich, Switzerland, paper TUB02, this conference.

[2] R. Baartman, "Intensity limitations in compact H^- cyclotrons", in *Proc. 14th Int. Conf. Cycl. Appl.*, Capetown, 1995 p. 440.

[3] R. Baartman, "Cyclotron matching injection optics optimization", in *Proceedings PAC'09*, Vancouver, Canada, pp. 4372-4374.

[4] T. Planche, Y.-N Rao, and R. Baartman, "Space charge effects in isochronous FFAGS and cyclotrons", Workshop on High-Intensity and High-Brightness beams, *Proc. HB2012*, pp. 231-234.

[5] R. Baartman, "Cyclotron Matching injection optics optimization", in *Proc. PAC'09*, Vancouver, Canada, pp. 4372-4374.

[6] R. Baartman, "Space charge limit in seperated turn cyclotrons", in *Proc. Cyclotrons'13*, Vancouver, Canada, p.305.

[7] S. Adam, "Space charge effects in cyclotrons - from simulations to insights", in *Proc. 14th Int. Conf. Cycl. Appl.* (1995), pp. 446-449.

[8] S. Adam, W. Joho, and C. J. Kost, "Longitudinal space-charge-effects in the SIN Injector II and in the SIN ring cyclotron", in *Proc. 9th Int. Conf. Cycl. Appl.* Caen 1981, pp. 529-531.

[9] M. M. Gordon, "The longitudinal space charge effect and energy resolution", in *Proc. 5th Int. Cycl. Conf.* (1969), p. 305.

[10] W. Joho, "High intensity problems in cyclotrons", in *Proc. 9th Int. Cyclo. Conf.* (1981), p. 337.

[11] W. Kleeven, "Theory of accelerated orbits and space charge effects in an AVF cyclotron", thesis Einhoven University, 1988.

[12] F. J. Sacherer, "RMS Envelopes Equations with Space Charge", in *Proc. PAC'71*, p. 1105.

[13] P. Bertrand and Ch. Ricaud, "Specific cyclotron correlations under space charge effects in the case of a spherical beam", in *Proc. 16th Int. Cyclo. Conf.* (2001), p. 379.

[14] E. Pozdeyev, J. A. Rodriguez, F. Marti, and R. C. York, "Longitudinal beam dynamics studies with space charge in small isochronous ring", *Phys. Rev. ST Accel. Beams* 12, 054202 (2009).

[15] E. Pozdeyev, "CYCO and SIR: New tools for the numerical and experimental studies of space charge effects in the isochronous regime", Ph.D. thesis, MSU, (2003).

[16] A. J. Cerfon, J. P. Freidberg, F. I. Parra, and T. A. Antaya, "Analytic fluid theory of beam spiraling in high intensity cyclotrons", *Phys. Rev. ST Accel. Beams* 16, 2013, 024202.

[17] A. J. Cerfon, O. Bühler, J. Guadagni, F. I. Parra, and J. P. Freidberg, "Vlasow equation approach to space charge effects in isochronous machines", in *Proc. Cyclotrons2013*, pp. 310-314.

[18] A. J. Cerfon, "Vortex Dynamics and Shear-Layer Instability in High-Intensity Cyclotrons", *Physical Review Letters* 116, 174801 (2016).

[19] J. Grillenberger, M. Humbel, A. Mezger, M. Seidel, and W. Tron, "Status and further development of the PSI high intensity proton facility", in *Proc. Cyclotrons2013*, Vancouver, Canada, pp. 37-39.

[20] Y. J. Bi, A. Adelmann, *et al.*, "Towards quantative simulations of high power proton cyclotrons", emphPhys. Rev. ST Accel. Beams 14 (2011) 054402, pp. 1-8.

[21] A. Adelmann *et al.*, "The OPAL Framework - User's Reference Manual", PSI internal report PSI-PR-08-02 (2016).

[22] A. Kolano, "A Precise 3D Beam Dynamics Model of the PSI Injector II", presented at Cyclotron'16, Zurich, Switzerland, paper MOD03, this conference.

[23] J. J. Yang, A. Adelmann, M. Humbel, M. Seidel, and T. J. Zhang, "Beam Dynamics in High Intensity Cyclotrons Including Neighboring Bunch Effects: Model, Implementation and Application", *Phys. Rev. ST Accel. Beams* 13, 064201, 2010.

[24] T. Zhang, H. Yao, J. J. Yang, J. Zhong, and S. An, "The beam dynamics study for the CYCIAE-100 cyclotron", *Nucl. Instr Meth. Phys. Res.* A676 (2012) pp. 90-95.

[25] J. J. Yang, A. Adelmann, *et al.*, "Beam dynamics simulation for the high intensity DEAδALUS cyclotrons", *Nucl. Instr. Meth. Phys. Res.* A704, (2013) 84-91.

[26] S. L. Sheehy *et al.*, "Progress on simulation of fixed field alternating gradient accelerators", in *Proc. IPAC2015*, Richmond, VA, USA, pp. 495-498.

[27] A. Adelmann, "Update on OPAL", presented at Cyclotron'16, Zurich, Switzerland, paper WEA04, this conference.

[28] T. Planche and Y.-N. Rao, "Simulations of TRIUMF Cyclotron Central Region using tricycle", Triumf internal note, 2016.

[29] J. Alonso, S. Axani, L. Calabretta, D. Campo, L. Celona, J. M. Conrad, A. Day, G. Castro, F. Labrecque, and D. Winklehner, "The IsoDAR High Intensity H2+ Transport and Injection Tests", JINST, `http://iopscience.iop.org/1748-0221/10/10/T10003`.

[30] D. P. Grote, A. Friedman, J.-L. Vay and I. Haber, "The WARP code: Modeling high intensity ion beams", in *Proc. 16th Intern. Workshop on ECR Ion Sources*, (M. Leitner, ed.), vol. 749, AIP, 2004.

[31] D. P. Grote, "WARP manual", 2000.

[32] R. Kersevan, "Moflow user's guide", available from the author, 1991.

[33] P. Spädtke, "Kobra3-inp user manual", version 3.39, 2000.

[34] D. Winklehner, R. Hamm, J. Alonso, and J. Conrad, "An RFQ direct injection scheme for the IsoDAR high intensity H_2^+ cyclotron", in *Proc. IPAC2015*, pp. 3384-3386.

[35] J. Van de Walle *et al.*, "The S2C2: From Source to Extraction", presented at Cyclotron'16, Zurich, Switzerland, paper THB01, this conference.

[36] W. Kleeven *et al.*, "AOC, a beam dynamics design code for medical and industrial accelerators at IBA", in *Proc. 7th Int. Part. Acc. Conf.*, Busan, Korea, May 2016, paper TUOOY002, pp. 1902-1904.

[37] Y. Jongen *et al.*, "Rhodotron Accelerators for Industrial Electron-Beam Processing: a Progress Report", in *Proc. 5th Eurean Part. Acc. Conf.*, Sitges-Barcelona (1996) pp. 2687-2689.

ISBN 978-3-95450-167-0

SIMULATION OF THE BEAM DYNAMICS IN THE AXIAL INJECTION BEAM LINE OF FLNR JINR DC280 CYCLOTRON

N. Kazarinov#, I. Ivanenko, JINR, Dubna, Russia

Abstract

DC280 is novel cyclotron which is created i the FLNR JINR. This cyclotron allows accelerating the ions of elements from Helium to Uranium with the mass to charge ratio in the range of 4 – 7.5 providing ion currents up to 10 pμA. The simulation of ion beam dynamics in the high voltage axial injection beam line of DC280 cyclotron is presented. One part of the injection system is placed at the High Voltage Platform and other part is in the grounded yoke of the DC-280 magnet. The 3D electromagnetic field maps of the focusing solenoids, analyzing magnet, accelerating tube and spherical electrostatic deflector are used during this simulation. The calculated efficiency of ion beam transportation is equal to 100%.

INTRODUCTION

The DC-280 [1] injection system has to provide ion beam transport from the ECR-ion source to the cyclotron centre and capturing into acceleration more than 70 % of ions with the mass to charge ratio of A/Z=4÷7.5 [2].

The experience of operation of FLNR cyclotrons demonstrates the substantial dependence of the efficiency of injection on the beam current for ions with energies of about 15 keV per unit charge. At the ion beam currents of 10 μA the efficiency of capture into acceleration reaches 50÷60 % while for the ion currents of 80÷150 μA it decreases down to 30÷35%. This effect may be explained by increasing of the beam emittance at high level of the microwave power in the ECR ion source and influence of the space charge on bunching of the ion beam. To improve the injection efficiency due to decreasing of both the emittance and the influence of space charge the injection energy has to be increased.

The axial injection system of the DC-280 cyclotron has two pieces of High Voltage Platforms (HVP). The maximal voltage on the HVP is 75 kV. Every HVP is equipped by an ECR ion source with injection voltage of 25 kV, the focusing elements (solenoids) and the magnets for ion separation. The high voltage accelerating tube is installed at the edge of the HVP to increase the ion energy (up to 100×Z keV in maximum). The acceleration in high voltage accelerating tube allows decreasing the ion beam emittance in about 1.5 times. The beam is matched at the entrance of the acceleration tube by means of the electrostatic lens.

For rotation of the ion beam onto vertical axis the spherical electrostatic deflector is used. To increase the efficiency of acceleration the multi-harmonic buncher is used. It is placed in the vertical part of the channel just after the electrostatic deflector. The buncher is working at 1, 2 and 3 harmonics of the RF system of the cyclotron. The ion beam emittance is matched with the acceptance of the spiral inflector by two solenoids installed at the vertical part of the beam line.

The numerical simulation of the ion beam dynamics in the axial injection channel has been performed by using the 3D electromagnetic field maps of the ECR ion source, solenoidal lenses, analyzing magnet [3], electrostatic lenses, accelerating tube and spherical electrostatic deflector [4]. All calculations have been done with the help of MCIB04 program code [5].

BEAM LINE ELEMENTS

Scheme of the axial injection channel is shown in Fig. 1

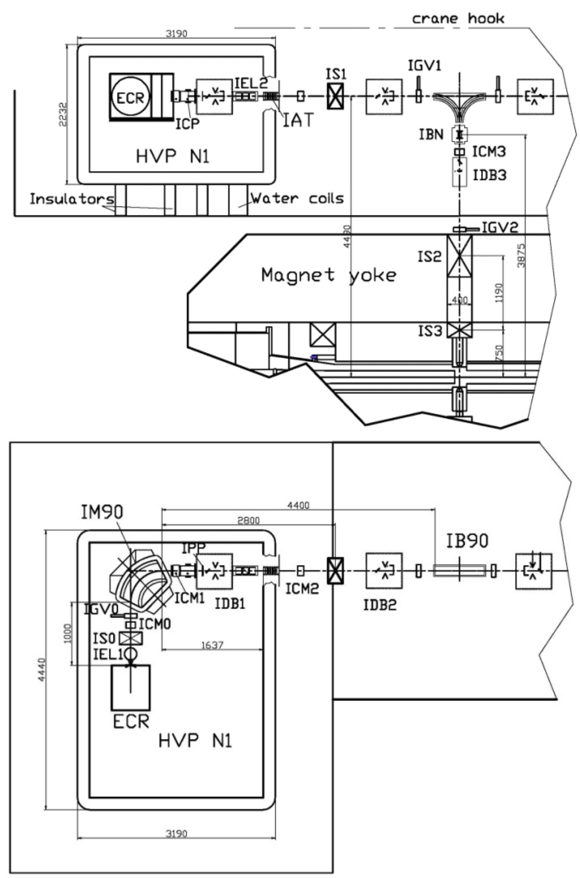

Figure 1: Scheme of axial injection channel. HVP – High Voltage Platform; ECR – ECR ion source; IS0-3 – solenoids; IM90 – analyzing magnet; IEL1,2 – electrostatic lenses; IAT – acceleration tube; IB90 – spherical electrostatic deflector; IBN – multi-harmonic buncher; IDB1-3 – diagnostic box.

#nyk@jinr.ru

ISBN 978-3-95450-167-0

ECR Ion Source

Two types of ECR ion sources are installed at HVP: The permanent magnets ion source DECRIS-PM [6] and the superconducting ion source DECRIS-SC [7]. The first one has to produce high intensities (15÷20 pμA) of ions with medium masses (for example, $^{48}Ca^{7+,8+}$), the second one has to produce high charged heavy ions, such as $^{238}U^{39+,40+}$. The accelerating voltage U and magnetic field B on-axis distributions in DECRIS-PM ion source are shown in Figs. 2,3, correspondingly.

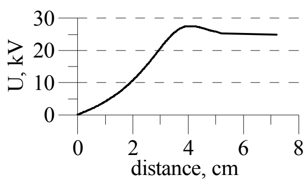

Figure 2: Accel. voltage

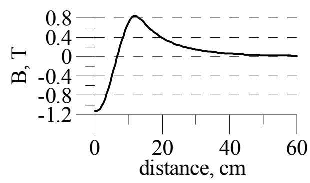

Figure 3: Magnetic field

Analyzing Magnet IM90

The 3D computational model of the magnet is shown in Fig. 4. The bending magnetic field distribution at reference orbit is shown in Fig. 5.

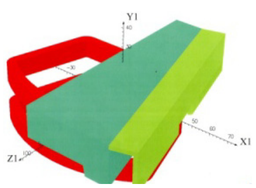

Figure 4: 3D magnet model.

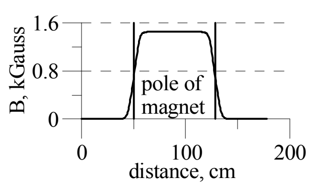

Figure 5: Bending field.

Lens IEL2 and Acceleration Tube IAT

The on-axis field strength E and voltage U of the lens IEL2 and the acceleration tube IAT are shown in Figs. 6,7.

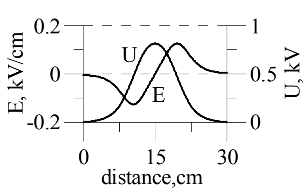

Figure 6: Lens IEL2.

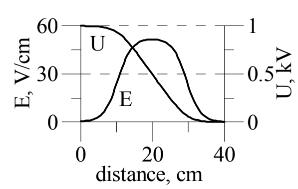

Figure 7: Accel. tube IAT.

Spherical Electrostatic Deflector IB90

The 3D model of the deflector is shown in Fig. 8. The bending electric field E is shown in Fig. 9.

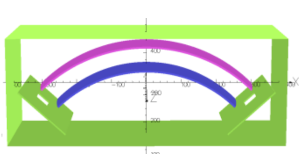

Figure 8: 3D deflector model.

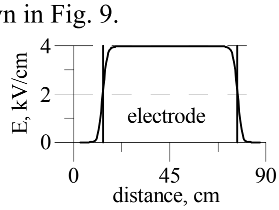

Figure 9: Bending electric field at reference orbit.

Focusing Solenoids IS0-3

The induction of the magnetic field B at the axis of the solenoids IS0-3 is shown in Figs. 10,11.

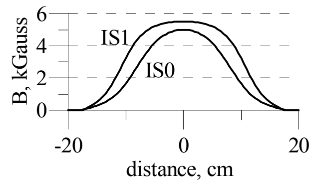

Figure 10: Solenoids IS0,1.

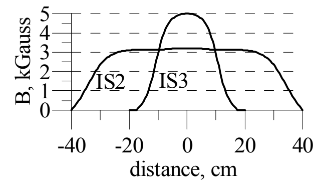

Figure 11: Solenoids IS2,3.

Multi-harmonic Buncher

In the presence of beam space charge the effect of bunching on transverse ion motion may be described by means of replacement of the beam current I by its effective value $k_b I$ [8]. The dependence of bunching coefficient k_b on distance from the buncher is shown in Fig. 12.

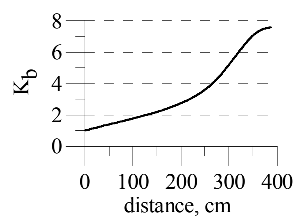

Figure 12: Bunching coefficient k_b.

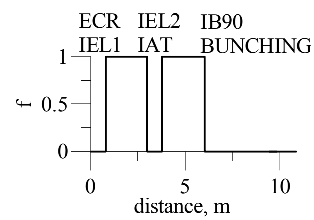

Figure 13: Neutralization factor f.

The efficiency of the beam bunching in the 20-degree phase interval of the accelerating RF field is equal to 80%.

BEAM NEUTRALIZATION

In the numerical simulations the full compensation of the beam space charge (by slow electrons accumulated in a beam) in all magnetic elements and drift spaces was supposed. The compensation was absent in the electrostatic elements, such as: the ECR ion source; the Einzel lenses IEL1,2; the deflector IB90; the accelerating tube IAT and also at the vertical part of the channel after the buncher IBN. The dependence of neutralization factor f on distance along the beam line is shown in Fig. 13.

CYCLOTRON MAGNETIC FIELD

The magnetic field of the cyclotron in the vertical part of the beam line B for various level of the magnetic field in the center B_0 is shown in Fig. 14.

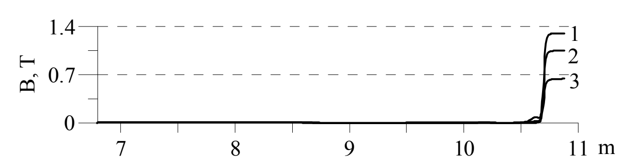

Figure 14: Cyclotron magnetic field. Curve 1 – B_0=1.3 T; curve 2 – B_0=1 T; curve 3 – B_0= 0.64 T.

ISBN 978-3-95450-167-0

SIMULATION REZULTS

The transport of $^{48}Ca^{8+}$ ion beam with kinetic energy of 75 keV×Z is presented as example. The calculated efficiency of the beam transport is equal to 100%. The dependence of the horizontal and vertical beam envelopes on length along the channel are shown in Fig. 15.

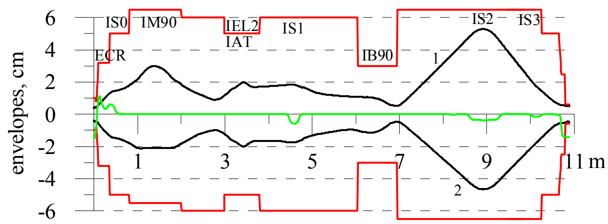

Figure 15: Horizontal (curve 1) and vertical (curve 2) $^{48}Ca^{8+}$ beam envelopes; aperture (red line) and longitudinal magnetic field (green line).

The beam envelopes near the magnetic plug and inflector are shown in Fig. 16. The designations are the same as in Fig. 15.

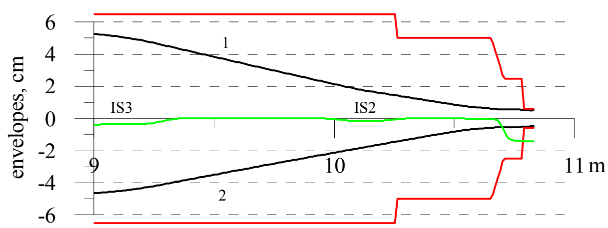

Figure 16: Beam envelopes near magnetic plug and inflector.

The kinetic energy W of the beam is shown in Fig. 17.

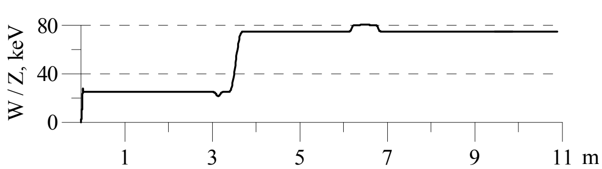

Figure 17: Kinetic energy per unit charge.

The horizontal (red curve) and vertical (blue curve) beam emittances are shown in Fig. 18. The decreasing of the beam emittance is explained by increasing of kinetic energy in the acceleration tube IAT.

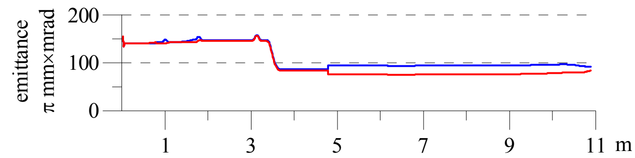

Figure 18: Beam emittances

The simulation results show that the system of the axial injection of the cyclotron complex DC-280 is able to provide the high efficiency of capture and subsequent acceleration of the beam up to the final energy.

REFERENCES

[1] G.G. Gulbekyan, S.L. Bogomolov, O.N. Borisov, S.N. Dmitriev, J. Franko, B. Gikal, I.A. Ivanenko, I.V. Kalagin, V.I. Kazacha, N.Yu. Kazarinov, N.F. Osipov, and A. Tikhomirov, “Development of FLNR JINR Heavy Ion Accelerator Complex in the Next Seven Years: New DC-280 Cyclotron Project”, in *Proc. IPAC’11*, San-Sebastian, Spain, Sep. 2011, p. 2700.

[2] G.G. Gulbekyan, V. Bekhterev, S.L. Bogomolov, A.A. Efremov, B. Gikal, I.A. Ivanenko, I.V. Kalagin, N.Yu. Kazarinov, M.V. Khabarov, V.N. Melnikov, N.F. Osipov, S.V. Prokhorov, and A. Tikhomirov, “The project of HV axial injection for DC280 cyclotron at FLNR JINR”, in *Proc. RuPAC’14*, Obninsk, Russia, Oct. 2014, p. 333.

[3] N.Yu. Kazarinov and I.A. Ivanenko, “Magnets of injection and extraction systems of cyclotron DC280”, in *Proc. RuPAC’14*, Obninsk, Russia, Oct. 2014, p. 339.

[4] N. Kazarinov and I. Ivanenko, “Electrostatic deflector of the cyclotron DC-280 axial injection channel”, in *Proc. HIAT’15*, Yokohama, Japan, Sep. 2015, p. 71.

[5] V. Alexandrov, N. Kazarinov, and V. Shevtsov, “Multi-Component Ion Beam”. in *Proc. RuPAC’04*, Dubna, Russia, Oct. 2004, p. 201.

[6] V. Bekhterev, S. Bogomolov, A. Efremov, and N. Konev “Development of the magnetic system for new DECRIS-PM ion source”, in *Proc. ECRIS’14*, Nijniy Novgorod, Russia, Aug. 2014, p. 111.

[7] V. Alexandrov, N. Kazarinov, and V. Shevtsov, “Multi-component ion beam code”. in *Proc. RuPAC’04*, Oct. 2004, Dubna, Russia, p. 201.

[8] N. Kazarinov and I. Kalagin, “The computation of the bunching system of intense ion beam by moments method”, in *Proc. Cyclotrons’07*, Oct. 2007, Giardini Naxos, Italy, p. 201.

ISBN 978-3-95450-167-0

SPACE-CHARGE SIMULATION OF TRIUMF 500 MeV CYCLOTRON*

T. Planche†, R. Baartman, Y. Bylinsky, Y.-N. Rao, TRIUMF, Vancouver, Canada

Abstract

We present a method to improve computation efficiency of space charge simulations in cyclotrons. This method is particularly efficient for simulating long bunches where length is large compared to both transverse size and turn separation. We show results of application to space charge effects in the TRIUMF 500 MeV cyclotron.

INTRODUCTION

The TRIUMF 500 MeV cyclotron accelerates H^- ions, and uses charge exchange extraction. No turn separation is required for extraction, which allows a very large phase acceptance of this machine (about 60°) [1]. Bunches are very long, and have a very large energy spread between the head and the tail (see for instance Fig. 8). Each bunch therefore occupies a large and slim volume in real space. Solving Poisson equation in a PIC code over such a large volume would require a significant computation time.

In addition, at high energy the turn separation is several times smaller than the radial beam size even for an infinitesimal phase slice. It is therefore essential to take into account the effect of many overlapping neighbouring turns. The multibunch calculation used in `OPAL` [2], is most appropriate when bunch length and width are comparable, but in the TRIUMF case, the bunch length can be 400 times its width.

To overcome these difficulties, we use periodic boundary conditions in the radial direction. This trick, originally proposed by Pozdeyev as a possible way to improve his code `CYCO` [3, 4], is presented in Ref. [5]. The radial dimension of the box inside which Poisson's equation is solved is equal to the turn separation. Particles of the bunch that fall out of this box are returned to the box assuming radial periodicity (see Fig. 1). In fact, these particles appear to belong to the neighbouring turns. The charge density in this 3D box is divided onto slices cut along the y direction (see Fig. 1). To take into account the image charge, we use "metallic" boundary conditions in the vertical direction; to simulate the effect of neighbouring turns, we use periodic boundary conditions in the radial direction.

We have implemented such a 3-D Poisson's equation solver into a piece of code that we call `tricycle`

Poisson Solver Test

To test our Poisson's equation solver we compute the electric potential from a static sphere of charge constituted of 10^6 randomly distributed macro-particles; results are shown in Fig. 2.

* This work has been supported by the Natural Sciences and Engineering Research Council of Canada. TRIUMF also receives federal funding via a contribution agreement through the National Research Council of Canada.

† tplanche@triumf.ca

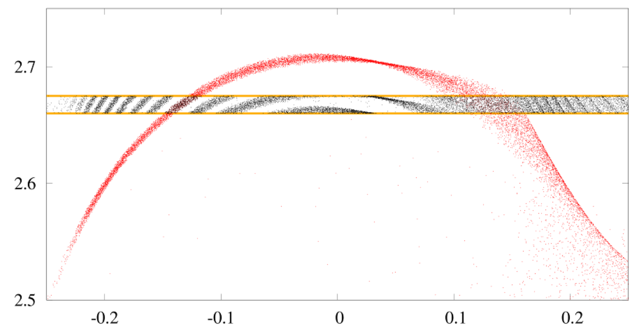

Figure 1: Beam folding applied to accelerated turn #100 of TRIUMF. The original particle distribution is shown in red (in top view). The folded beam in show in black. The yellow line materializes the edge of the box inside which Poisson's equation is solved; perodic boundary condition is applied along those two sides. Coordinates are in metres.

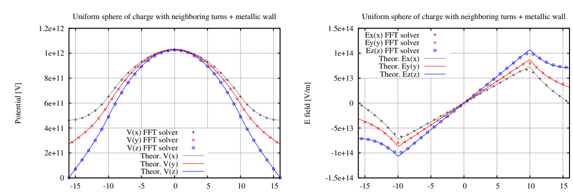

Figure 2: Electrostatic potential (left) and electric field (right) from a uniform sphere of charge; the dots presents results from `tricycle` with a $32 \times 32 \times 32$ size PIC grid; solid lines are from theory. Note the three different boundary conditions in x, y, and z: periodic (neighbouring turns), open, and metallic (potential=0), respectively.

The theoretical electrostatic potential from a uniform sphere of charge with such boundary conditions writes:

$$V(x,y,z) = \sum_{i_x=-\infty}^{+\infty} \sum_{i_z=-\infty}^{+\infty} (-1)^{i_z} f(x - i_x \Delta x, y, z - i_z \Delta z) \quad (1)$$

where Δz is the vertical gap of the vacuum chamber, Δx the turn separation (x here is along the radial direction), and $f(x,y,z)$ is derived from Gauss's law:

$$f(x,y,z) = \begin{cases} \dfrac{Q}{\epsilon_0 4\pi r} & r \geq R\,, \\[2ex] \dfrac{Q}{\epsilon_0 8\pi R}\left(3 - \dfrac{r^2}{R^2}\right) & r < R\,, \end{cases} \quad (2)$$

where $r = \sqrt{x^2 + y^2 + z^2}$, R is the radius of the sphere, and ϵ_0 is the vacuum permitivity.

ISBN 978-3-95450-167-0

SINGLE PARTICLE TRACKING

Closed Orbits and Tune

An equilibrium orbit search algorithm similar to the one proposed by Gordon [6] was implemented; linear optics parameters were calculated based on Ref. [6]; results agree well with CYCLOPS (see Fig. 3).

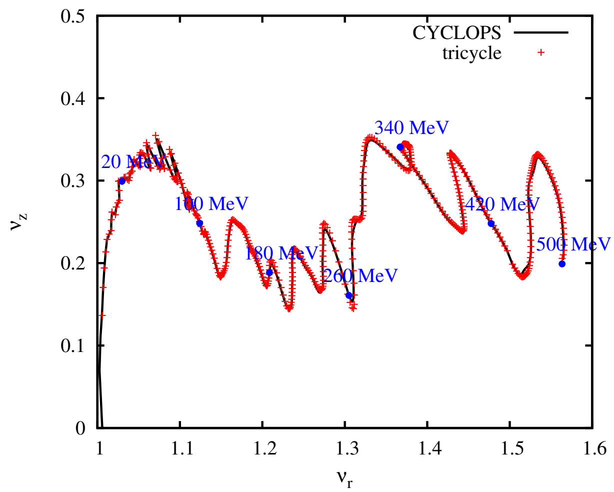

Figure 3: Tune diagram obtained by CYCLOPS and tricycle using TRIUMF cyclotron standard field map "policyinita6.dat".

RF Acceleration

Next step was to implement acceleration. To simplify the tracking through the rf gap, and to save on computation time, we chose to model the gap crossing as a thin rf kick using:

$$\begin{aligned} \delta E_k &= qV_{\text{rf}} \sin \phi \\ \delta z' &= K \frac{1-a}{2} z \\ \delta r' &= K \frac{1+a}{2} (r - r_0) \end{aligned} \tag{3}$$

where δE_k is the energy kick; q the charge of the particle; V_{rf} the rf field amplitude; ϕ the rf phase; $\delta z'$ and $\delta r'$ are the vertical and radial focusing kicks; a is a geometrical factor describing the geometry of the rf gap: $a = -1$ is for an horizontal rf gap (focusing only vertically), $a = 0$ is for a round (or square) gap, etc; r_0 is the radial position of the gap center; the focal power K is given by Reiser's formula [7]:

$$K = \frac{V_{\text{rf}}}{V_c} \frac{\pi}{\beta \lambda_{\text{rf}}} \cos(\phi) + \frac{F}{2b\pi} \left(\frac{V_{\text{rf}}}{V_c} \right)^2 \sin^2(\phi) \tag{4}$$

with β the ratio of the particle to the speed of light; λ_{rf} the rf wave length; V_c the average of the particle 'kinetic' energy across the rf gap; F a form factor that we took equal to 1. b is of the order of (half) the extend of the electric field: it changes with R from 0.5 to 2 inches following the geometry of our rf gap.

Single particle tracking with acceleration was compared with results from our reference code CYCLONE for the first few turns in the cyclotron where vertical focusing is mostly electric. CYCLONE uses a 3D electric field map to model rf acceleration. As shown in Figs. 4,5 our thin kick model agrees resonably well with CYCLONE.

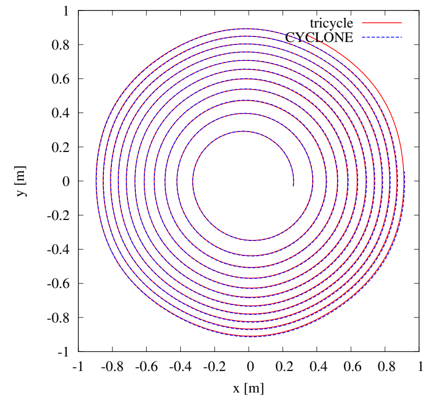

Figure 4: Acceleated orbit obtained from CYCLONE and tricycle

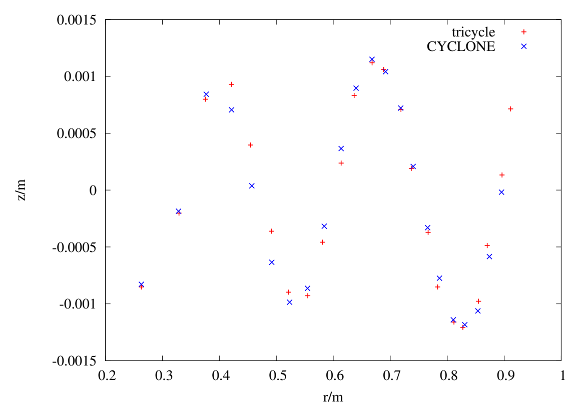

Figure 5: Vertical motion of a single particle (seen at each rf gap crossing) obtained from CYCLONE and tricycle

MULTIPARTICLE TRACKING

Without Space Charge

The 6×6 beam σ-matrix calculated by TRANSOPTR at the exit of the spiral inflector/deflector (see [8]) was used to generate a 6D fully correlated initial particle distribution, including the coupling effects of the axial cyclotron field, longitudinal motion, and the coupling in all 3 planes due to the spiral inflector. A Gaussian distribution is used in every direction. Simulation results are compared to actual measurements in Fig. 6 and Fig. 7.

With Space Charge

We use here the initial particle distribution as in the previous section, with space charge of 22 pC per bunch (*i.e.* $\sim 500\mu$A at 100% duty cycle). The beam breakup is clearly

ISBN 978-3-95450-167-0

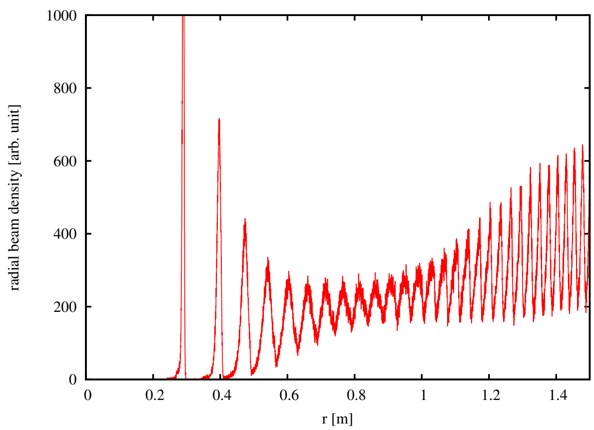

Figure 6: Simulation result from tracking a bunched beam without space charge, plotted as one of our radially-scanning low energy probes would see it.

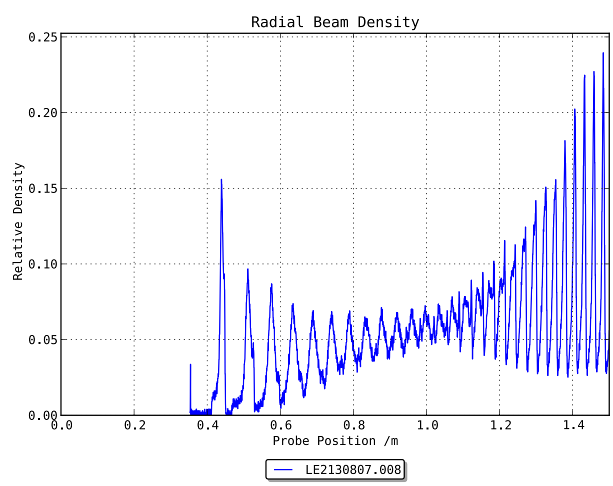

Figure 7: Measurement results from a radial low energy probe scan, when injected a low space-charge beam (using a 'pepper-pot' to reduce intensity by a factor 100) bunched with only the first harmonic buncher, and injected ~ 20° off crest (on the falling side of the rf wave). Note that our low energy probe cannot quite reach the first turn.

visible at turn#30 (see Fig. 11), and becomes very convoluted by turn #300 (see Fig. 12). The beam breakup causes fine structure to appear on the radial density plot from about turn#20.

The fine structure measured experimentally (see Fig. 10) from the very first turns is not due to vortex motion in the cyclotron but rather comes from the complex on-linear space-charge effects during the bunching process (see Fig. 13). Only the smoothed Gaussian 6D hyperellipsoid from TRANSOPTR is used to start our multi-particle simulation. We plan to expand `tricycle` to include the injection line.

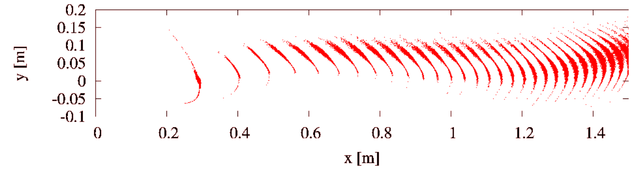

Figure 8: Simulation result from tracking bunched beam without space charge for 35 turns; this top view shows "snapshots" taken every 5 (=harmonic number) rf periods.

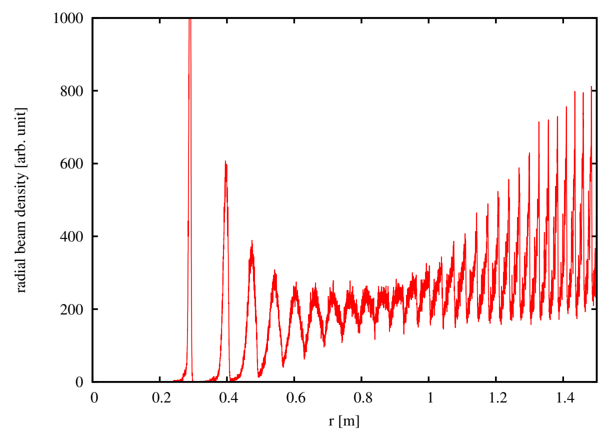

Figure 9: Simulation result from tracking a 500 μA bunched beam with space charge, plotted as one of our radially-scanning low energy probes would see it.

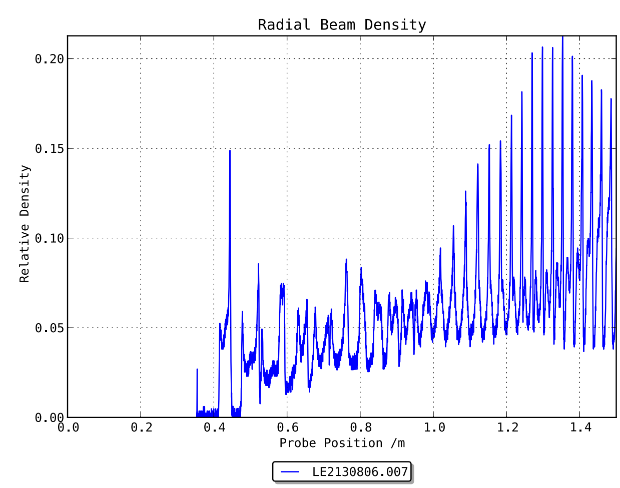

Figure 10: Measurement results from a radial low energy probe scan, when injected a high space charge beam when injecting ~ 410 μA equivalent (100% duty cycle) beam.

REFERENCES

[1] J. Richardson, E. Blackmore, G. Dutto, C. Kost, G. Mackenzie, and M. K. Craddock, "Production of simultaneous, variable energy beams from the TRIUMF cyclotron," *IEEE Transactions on Nuclear Science*, vol. 22, no. 3, pp. 1402–1407, 1975.

ISBN 978-3-95450-167-0

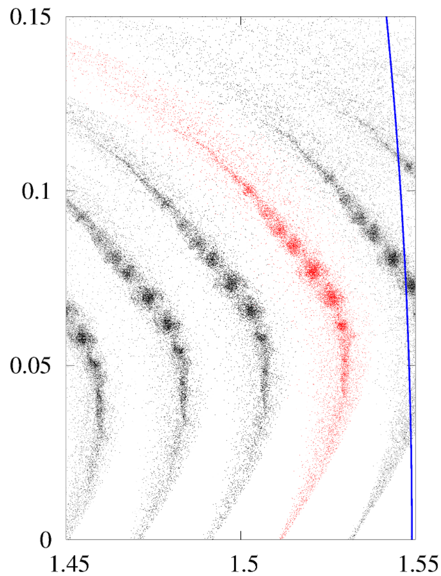

Figure 11: Turn #30 shown together with neighbouring turns. The Blue lines is an arc of circle centered on the machine center. Plot is Cartesian; the x-axis is mainly radial and y is azimuthal; both in metres.

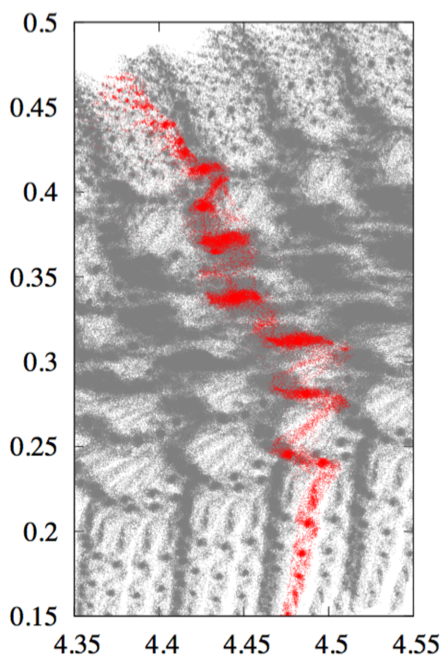

Figure 12: Simulated TRIUMF turn #300 (red) shown together with neighbouring turns. Plot is Cartesian; the x-axis is mainly radial and y is azimuthal; both in metres. Colour has been darkened to make fine structure more visible.

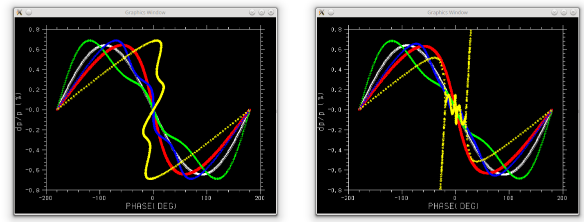

Figure 13: Longitudinal phase space simulation of bunching with (right) and without (left) space charge through our injection line using SPUNCH [9]; each colour corresponds to different locations along the beamline. Our bunching system is constituted of two separate bunchers, operating respectively on the first and second harmonics of the main rf frequency.

[2] A. Adelmann, C. Kraus, Y. Ineichen, and J. Yang, "The opal (object oriented parallel accelerator library) framework," *Paul Scherrer Institut, Tech. Rep. PSI-PR-08-02*, vol. 2010, 2008.

[3] E. Pozdeyev, "CYCO and SIR: New tools for numerical and experimental studies of space charge effects in the isochronous regime," Ph.D. dissertation, Michigan State University, 2003.

[4] E. Pozdeyev, private communication, 2012.

[5] T. Planche, Y. Rao, and R. Baartman, "Space charge effects in isochronous ffags and cyclotrons," *Proceedings of HB*, pp. 231–234, 2012.

[6] M. M. Gordon, "Computation of closed orbits and basic focusing properties for sector-focused cyclotrons and the design of 'cyclops'," *Part. Accel.*, vol. 16, pp. 39–62, 1984.

[7] M. Reiser, "First-order theory of electrical focusing in cyclotron-type two-dimensional lenses with static and time-varying potentials," *Journal of Applied Physics*, vol. 42, no. 11, pp. 4128–4138, 1971.

[8] R. Baartman, "Optics design of the ISIS vertical section replacement," TRIUMF, Tech. Rep. TRI-DN-09-11, 2009.

[9] R. Baartman, "SPUNCH: a space charge bunching computer code," in *Cyclotrons and their applications: Proceedings, 11th International Conference, Tokyo, Japan, October 13-17*, 1986, pp. 238–239.

ISBN 978-3-95450-167-0

A NEW DIGITAL LOW-LEVEL RF CONTROL SYSTEM FOR CYCLOTRONS

W. D. Duckitt†, J. L. Conradie, M. J. van Niekerk, J. Abraham,
iThemba LABS, Somerset West, South Africa
T. R. Niesler, Stellenbosch University, Stellenbosch, South Africa

Abstract

Stable control of amplitude and phase of the radio frequency (RF) system is critical to the operation of cyclotrons. It directly influences system performance, operability, reliability and beam quality. iThemba LABS operates 13 RF systems between 8 and 81 MHz and at power levels of 50 W to 150 kW. A critical drive has been to replace the 30 year old analog RF control system with modern technology. To this effect a new generic digital low-level RF control system has been designed. The system is field programmable gate array (FPGA) based and is capable of synthesizing RF signals between 5 and 100 MHz in steps of 1 µHz. It can achieve a closed-loop amplitude stability of greater than 1/10000 and a closed-loop phase stability of less than 0.01º. Furthermore, the system is fully integrated with the Experimental Physics and Industrial Control System (EPICS) and all system and diagnostic parameters are available to the Control System Studio clients. Three prototypes of the system have been in operation since November 2014. A general analysis of RF control systems as well as the methodology of design, implementation, operational performance and future plans for the system is presented.

INTRODUCTION

iThemba LABS is a multi-disciplinary cyclotron research facility situated in South Africa. It operates 13 RF systems between 8 and 81 MHz and at power levels of 50 W to 150 kW to deliver particle beams for nuclear physics experiments, radiotherapy and the production of radioisotopes.

A critical drive has been to replace the 30 year old legacy analog RF control system with modern technology. To this effect a new generic digital low-level RF control system has been designed.

CURRENT STATE OF TECHNOLOGY

Continuing rapid advances in Field Programmable Gate Arrays (FPGA), digital signal processing (DSP), high speed digital to analog converters (DAC) and high speed analog to digital converters (ADC) have made it feasible to develop state of the art digital RF control systems [1,2].

For example, PEFP have developed a digital low level RF (DLLRF) system for a linac accelerator [2]. They achieved 1% amplitude and 1˚ phase stability using a mixture of analog and digital hardware.

INFN LNS developed a DLLRF system for their cyclotrons utilizing direct digital synthesis ICs from Analog Devices [3]. This approach achieved a phase stability of 0.1˚.

In a joint project, JAERI and KEK achieved a 0.2% amplitude stability utilizing a mixture of analog and digital hardware for a linac accelerator [4].

A similar study demonstrated that it is possible to measure an RF signal with a phase accuracy of 0.05˚ and an amplitude accuracy of 0.02% using high-speed ADCs and FPGAs [5].

Finally, LEPP achieved 0.02˚ phase and 0.01% amplitude stability when applying their DLLRF to their linac system [6].

These advances demonstrate that DLLRF control systems can produce an RF signal with an amplitude stability that can rival or exceed that of analog systems.

METHODOLOGY OF DESIGN

In our DLLRF control system design particular attention was paid to direct digital synthesis (DDS) techniques, the performance and capabilities of high speed DACs, ADCs and DSP techniques used for demodulation of RF signals.

We set out to achieve 0.01% amplitude and 0.01˚ phase resolution over an operating frequency of 5 to 100 MHz. A market analysis revealed suitable DACs to achieve this, but it also highlighted that there were no ADCs available that could achieve true 16 bit amplitude resolution between 5 and 100 MHz.

Our solution was to use a heterodyning approach and mix the RF signal down to an intermediate frequency (IF) that is sampled with an appropriate ADC [7].

State of the art digital designs utilize in-phase and quadrature (I/Q) demodulation to extract phase and amplitude information [1, 2, 4, 7]. Integrated circuit devices have been developed for telecommunications applications to determine I/Q components [8]. These devices, however, do not operate over our full frequency range and cannot detect phase deviations below 0.2˚. Hence these devices are not suitable for our purposes.

The solution was to develop hardware utilizing FPGAs. The FPGA-based solution offered a highly customizable development platform which was an excellent base for experimenting with hardware design and the optimization of techniques and algorithms. A Xilinx Spartan 6 FPGA was chosen in our final implementation. The design and performance of the production version of the new DLLRF control system is discussed in the following sections.

ISBN 978-3-95450-167-0

PRODUCTION SYSTEM OVERVIEW

A photograph of the new DLLRF control system is shown in Fig. 1. Each module performs a certain function, i.e., RF Control, RF Synthesis, IF Sampling, RF Amplification and Mixing, an Interlock Interface, and can be easily removed and replaced for maintainability.

Figure 1: A photograph of the new digital low-level RF control system.

All RF signals are also easily accessible through the sub-miniature version A (SMA) links on the front panels. The rear of the system, shown in Fig. 2, provides connections to the RF amplifier signal, pickup signal, reference, and input and output interlocks. The rear centre panel can also be quickly removed to service the internal power supplies.

Figure 2: A photograph of the rear side of the new digital low-level RF control system.

The operation of the system is best explained using the high-level block diagram in Fig. 3. The system modules correspond to the red regions of the block diagram and the sections below describe how the system works.

Time Synchronisation

The control systems are synchronised by supplying the same 10 MHz reference signal to each one. This is connected to the N-type connector at the top right corner of the rear side of the enclosure and fed through to the front. The SMA linkage connects the reference to the phase locked loop (PLL) on the RF synthesis module.

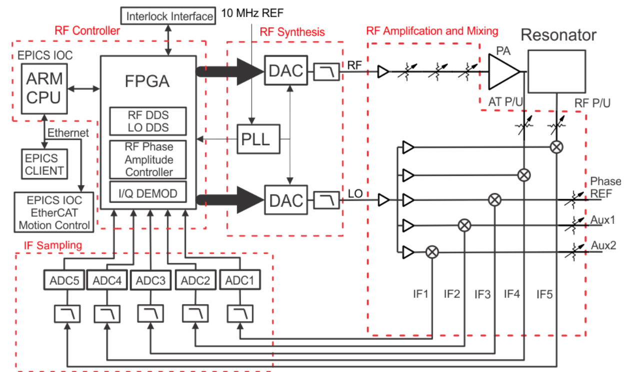

Figure 3: A block diagram of the new digital low-level RF control system.

The PLL, as illustrated in Fig. 3, locks a 2.4 GHz voltage controlled oscillator (VCO) to the 10 MHz reference signal. All the high speed and system clocks are divided down internally in the PLL and distributed to the high speed DACs and FPGA.

RF Synthesis

The RF and local oscillator (LO) signals are digitally synthesized within the FPGA using direct digital synthesis. The RF frequency is programmable in steps of 1 μHz between 5 and 100 MHz and the phase in steps of 0.0001° in the current configuration. The digital 16 bit data of the RF and LO signals are synchronously streamed from the FPGA via the back plane to the high speed DACs on the RF synthesis module. The reconstructed signals are low pass filtered by a 100 MHz low pass filter. The LO and RF signals are then connected via SMA linkage to the RF amplification and mixing module.

RF Amplification and Mixing

A high dynamic range is maintained in the transmit RF signal chain by using a 25 dB amplifier cascaded with three 32 dB attenuators that are digitally programmable in 0.5 dB steps as indicated in Fig. 3.

A high dynamic range is maintained in the input channels by a 32 dB, 0.5 dB digitally programmable step attenuator on each input.

The LO signal is amplified and distributed to each of the RF mixers and the IF signal for each channel is connected to a corresponding input on the IF sampler card via the SMA linkage.

The RF output, RF pick-up, RF phase reference, auto-tune and two auxiliary input signals are connected via SMA linkage to the SMA feed-throughs on the far right-hand side of the front of the enclosure and then internally connected to the N-type connectors on the rear left side of the enclosure.

IF Sampling

The system uses a 1 MHz IF. The five IF channels are first low-pass filtered to remove the image frequency and then sampled by 16-bit 10 MHz successive approximation

ISBN 978-3-95450-167-0

register (SAR) ADCs. The digital data is streamed via the back plane to the FPGA for demodulation.

IF Demodulation

In-phase and quadrature (I/Q) demodulation is performed on each of the IF streams within the FPGA and amplitude and phase information is calculated from the I/Q signals. A 10 MHz demodulator decodes the amplitude and phase information which is then fed into the amplitude and phase closed-loop controllers. Another demodulator decodes all five channels' amplitude and phase information at a data rate of 2.5 kHz. These channels are fed into a slower control loop for the auto-tune control and are also sent to the client to display the information in real time.

RF Control

Closed-loop control is performed in the FPGA at 10 MHz using two separate amplitude and phase proportional-integral-derivative (PID) controllers that modulate the amplitude and phase of the RF DDS. The performance of the system under closed-loop control is discussed later on.

CPU, FPGA and EPICS Interface

All registers within the FPGA are presented to the central processing unit (CPU) through a memory mapped interface. The CPU runs Debian 8.4 Linux and an EPICS input-output controller (IOC).

An EPICS Asyn driver provides a connection between the EPICS records and the memory mapped registers and FIFO buffers of the FPGA. All registers and settings are then available to the Control System Studio (CSS) clients.

EtherCAT Motion Control

In 2015 iThemba LABS adopted EtherCAT as its new industrial communication standard. The EPICS EtherCAT interface [9], as developed by the Diamond Light Source, has been fully integrated to work with stepper motor, DC motor, analog input and output and digital input and output terminals as provided by Beckhoff [10]. This means that all tuneable RF elements in the power amplifiers, such as the grid and anode circuits, and the tuneable elements within the resonators, such as the coupling capacitors, short-circuit plates, and auto-tune trimmer capacitors, are under EPICS EtherCAT based motion control. The set points for the tuneable elements are determined by load curves and set in the CSS user interface.

Automation and Sequencing

A State Notation Language based EPICS sequencer has been used to fully automate the operation of the system. The sequencer program was designed to allow manual as well as automatic configuration. Manual configuration mode allows the user to manually find resonance and adjust the system parameters. When automatic configuration is selected and the system is powered up for the first time, a power on reset initialisation is performed. The power on reset initialisation adjusts system parameters for the operating frequency. It will then move into a cold-start mode and find the resonance peak by applying a small amount of RF power to the resonator and sweeping the trimmer capacitor across its full range. This is illustrated in Fig. 4 where two sweeps of the trimmer have been made, one with a low RF power and one with a higher RF power where the effects of multipactoring can be seen on the top trace. If the multipactoring effect is noticed the user should adjust the resonance search mode power to a level where a sharp peak is seen as is illustrated in the lower trace in Fig. 4.

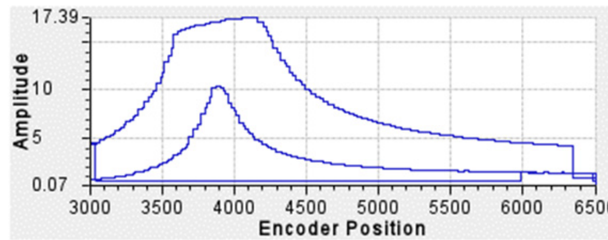

Figure 4: Amplitude vs trimmer capacitor encoder position during automatic resonance search mode for a low as well as a higher RF power level that results in multipactoring.

Once the resonance peak is found, the sequencer will switch on the RF at the predetermined kick level and then reduce it to a hold level after 200 ms. If the feedback signal is stable then the trimmer capacitor auto-tune control followed by the phase and amplitude PID controllers are enabled. The sequencer then increases output power to the desired set point. Once the set point is reached normal operation can occur. The system then enters a warm-start mode. Should any interlock or trip occur and clear within the predetermined time, the sequencer will switch on and restore operation at the current trimmer capacitor position. Should this be unsuccessful or should the maximum time elapse, the system will attempt to switch on from the cold-start state. Should this be unsuccessful, the system will attempt to find resonance by sweeping the trimmer capacitor and subsequently switch on and restore the system. Should this final attempt also fail the system will stop in an error state and the engineer responsible will need to investigate the problem.

User Interface

A CSS operator interface has been developed for the control system and allows the operator to set the amplitude and phase set points. Real-time display of 10 ms and up to 100 seconds of the amplitude and phase of the RF pickup signal is available to the operator allowing intuitive feedback and diagnostic ability.

A separate, multi-tabbed CSS engineering user interface provides all system-level parameters to the user. This allows the user to control the parameters for the resonance search modes, kick and ramp profile, trip levels, sequencer modes, auto-tune control, and amplitude and phase PID control modes. It also displays the transmit

ISBN 978-3-95450-167-0

and receive signal chains schematically. This allows the user to intuitively interact with any of the parameters and optimize the system.

OPERATIONAL HISTORY

Since the commissioning of the prototypes on the injector cyclotron SPC2 in November 2014, a total of 52 particle beams have been produced. The lowest and highest frequencies of operation have been 11.379999 MHz to produce a 120 MeV $^{4}He^{2+}$ beam using 4.2 kW forward power and 26.000645 MHz to produce a 51.4 MeV $^{3}He^{1+}$ beam using 8.8 kW forward power.

The lowest and highest forward power used during operation have been 2.1 kW to produce a 134 MeV $^{36}Ar^{7+}$ beam and 21.3 kW to produce a 200 MeV proton beam at 26 MHz.

The system performed without error for all 52 particle beams.

PRODUCTION STATUS

iThemba LABS is in the process of manufacturing 35 production versions to ensure a sufficient supply of spare components for the foreseeable future and to meet international collaboration commitments. To date, 10 systems have been fully assembled and tested and will be installed at the facility in the coming months.

COMPARISON OF OLD AND NEW SYSTEMS

A comparison of the performance of the old and new control systems was performed at 12.228267 MHz. This frequency was chosen because SPC2 was scheduled to operate at this frequency for 3 consecutive weekends. This made it easier to change between control systems.

The comparison was performed with 2.6 kW forward power delivered to the south side resonator. The normalized magnitude spectrum of the RF pickup signals under closed-loop control was used to compare the two systems. The spectrum measurements are shown in Fig. 5.

The normalized magnitude spectrum of the old control system is illustrated in black and the new control system in red. The plot of each system also includes the envelope of the normalized magnitude spectrum, which indicates the spurious free dynamic range (SFDR) and a filtered noise floor which gives an indication of each system's noise floor.

The old control system has a SFDR of 30 dB which is a result of the 50 Hz side lobes injected into the system by the synthesizer. The signal to noise ratio (SNR) close to the carrier is 60 dB. This corresponds to the previously reported amplitude stability of 0.1% [11].

The SNR away from the carrier decreases to 50 dB and only reaches 60 dB again at approximately 150 Hz.

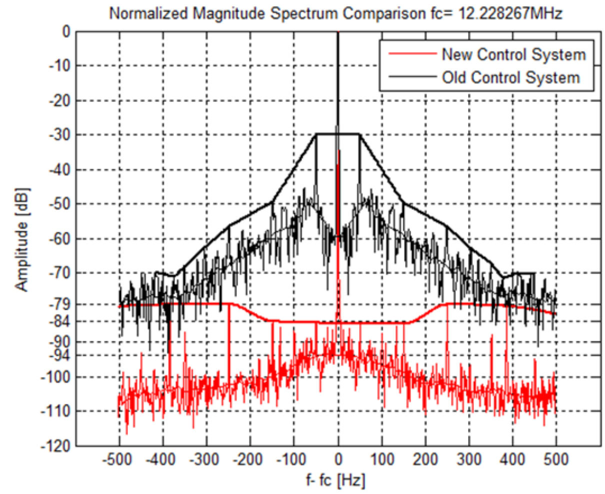

Figure 5: The normalized magnitude spectrum of SPC2 south resonator under closed-loop control at 12.228267 MHz using the old and new control system.

With the new control system, SPC2 south resonator operates with a SFDR of 79 dB, 250 Hz away from the carrier and 84 dB below 150 Hz. The mean noise floor close to the carrier is approximately -94 dB. However, there are various spurs close to the carrier and one would therefore prefer to use the SFDR figure of 84 dB as the SNR.

The SNR improvement of the new over the old system close to the carrier is therefore 54 dB and the wideband improvement of the SFDR is 49 dB.

The new control system communicates the amplitude and phase measurements to the CSS client at a data rate of 2.5 kHz. Figure 6 shows 41 seconds of amplitude and phase information captured during the magnitude spectrum measurement in Fig. 5. From Fig. 6 the amplitude stability is 1.6/14406 or -79.08 dB which corresponds to the SFDR of the new control systems.

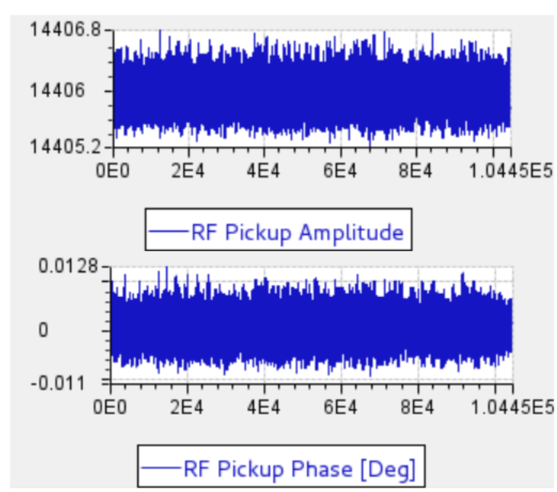

Figure 6: The RF pickup signal's measured amplitude and phase for the new control system during the test at 12.228267 MHz.

ISBN 978-3-95450-167-0

BEST SYSTEM PERFORMANCE

The ultimate performance of the control system is dependent on the mechanical stability of the load resonator. For SPC2, the mechanical stability is greatest at its highest operating frequency of 26 MHz. The best closed-loop amplitude and phase stability can be achieved at this frequency.

Fig. 7 shows an amplitude and phase stability of greater than 0.01% and 0.01° respectively for 100 seconds.

The normalized magnitude spectrum for closed-loop and open-loop operation with 12.6 kW on load at 26 MHz is shown in Fig. 8. The SNR under closed-loop control close to the carrier is greater than 80 dB and the SFDR has improved from 58 dB in open-loop to greater than 80 dB in closed-loop mode which corresponds to the amplitude stability in Fig. 7.

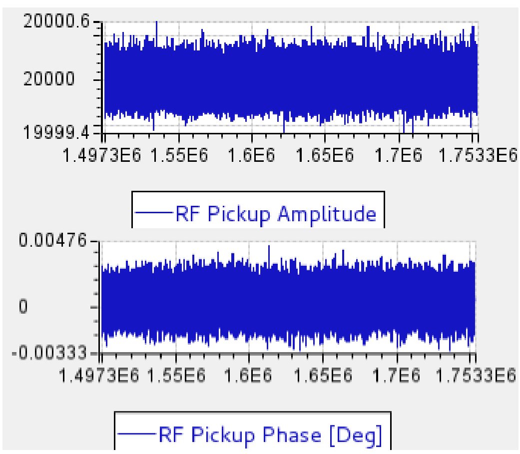

Figure 7: The RF amplitude and phase measurements of SPC2 south resonator under closed-loop control at 26 MHz with 12.6 kW power delivered to the resonator.

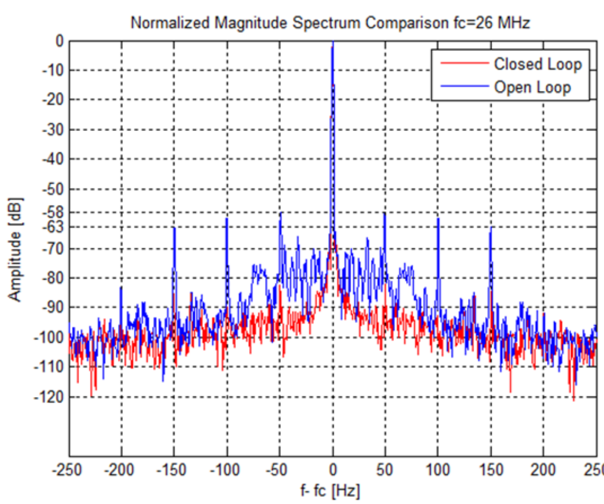

Figure 8: The closed-loop and open-loop magnitude spectrum of SPC2 south resonator at 26MHz with 12.6 kW power delivered to the resonator.

CONCLUSION

iThemba LABS has successfully designed a generic DLLRF control system for cyclotrons and other RF devices in the frequency range 5 to 100 MHz. These systems can achieve an amplitude and phase stability of greater than 0.01% and 0.01°, respectively. Performance and operational reliability have been successfully demonstrated by the three prototype versions on SPC2 since November 2014.

The manufacturability and reproducibility of the system has been demonstrated by the assembly of production versions. The incorporation of EPICS EtherCAT-based motion control enables the system to be easily deployed at other facilities.

REFERENCES

[1] M. E. Angoletta, "Digital low level RF", in *Proc. EPAC'06*, Edinburgh, Scotland, UK, Jun. 2006 pp. 1847-1851.

[2] I. H. Yu *et al.*, "Digital RF feedback control system for 100 MeV proton linac of PEFP", in *Proc. APAC'04*, Gyeongju, Korea, Mar. 2004, pp. 309-311.

[3] A. Caruso, A. Spartà, Z.Yin, and A. Longhitano, "Steps forward in the digital RF control system at LNS", in *Proc. 18th Int. Conf. on Cyclotrons and Their Application (Cyclotrons'07)s*, Catania, Italy, Oct. 2007, pp. 476-478.

[4] S. Michizono, S. Anami, M. Kawamura, S. Yamaguchi, and T. Kobayashi, "Digital RF control system for 400-MeV proton linac of JAERI/KEK joint project", in *Proc. LINAC'02*, Gyeongju, Korea, Aug. 2002, pp. 184-186.

[5] R. Liu *et al.*, "FPGA-based amplitude and phase detection in DLLRF", *Chinese physics C 33*, no. 7, Jul. 2009, pp. 594-598.

[6] M. Liepe *et al.*, "Pushing the limits: RF field control at high loaded Q" in *Proc. PAC*'05, Knoxville, USA, May 2005, pp. 2642-2644.

[7] T. Shilder, "RF applications in digital signal processing", *CERN Accelerator School: Course on Digital Signal Processing*, Sigtuna, Sweden, May 2007, pp. 249-283.

[8] *DC to 50 MHz, Dual I/Q Demodulator and Phase Shifter,* Analog Devices, 2005, `http://www.analog.com/en/products/rf-microwave/iq-modulators-demodulators/iq-demodulators/ad8333.html`

[9] R. Mercado, I. Gillingham, J. Rowland, and K. Wilkinson, "Integrating ethercat based IO into EPICs at Diamond", in *Proc. ICALEPCS'11,* Grenoble, France, Oct. 2011, pp. 662- 665.

[10] Beckhoff, `https://www.beckhoff.com/`

[11] Cyclotrons, Individual Designs: Entry C38, in *Proc. 17th Int. Conf. Cyclotrons and Their Applications*, Tokyo, Japan, Oct. 2004, p586.

ISBN 978-3-95450-167-0

HYBRID CONFIGURATION, SOLID STATE–TUBE, REVAMPS AN OBSOLETE TUBE AMPLIFIER FOR THE INFN K-800 SUPERCONDUCTING CYCLOTRON*

A. Caruso†, F. G. Caruso, A. Longhitano, A. Spartà, INFN-LNS, Catania, Italy
J. Sura[1], Warsaw University, Warsaw, Poland
G. Primadei, CERN, Geneva, Switzerland

Abstract

An insertion of a solid state amplifier is substituting the obsolete first stage of a full tube RF power amplifier. The amplifier is based on two tube stages. The first, equipped by a tetrode, the RS1054, was being manufactured by Thales until some years ago. Some spare parts have been ordered but not enough to guarantee smooth cyclotron operation for the next few years. It was necessary to come up with a new solution. We were basically at a crossroad: replace the first stage with another tube still in production or change the technology from tube to solid state. A study, from market research to the technology point of view was carried out and the final decision was to use a solid state stage as an innovative solution for this kind of power vs frequency range of operation. The prototype of this hybrid amplifier has been in operation with our cyclotron since January 2015. The details of these decisions, the description of the modified amplifier (solid state – tube) and the successful results of this hybrid configuration will be shown in this presentation.

RF AMPLIFIERS STORICAL OVERVIEW

The RF power amplifiers are made by two tetrode stages driven by solid state commercial amplifiers. The drivers are class A, wideband, 50 dB gain and a maximum out power of 200 W. The RF power amplifier can deliver a maximum power of 75 kW, the total gain between 1st and 2nd stage is about 30 dB. The first stage is wideband, based on the tetrode RS1054L by Thales, in ground-cathode configuration, air-forced cooling. The second stage is a narrow band stage, common grid configured, based on 4CW100000E by CPI, water cooled.

Figure 1: RF amplifiers and the 1st – 2nd stages view.

The three RF power amplifier cabinets with the internal view of the final stage are shown in Fig. 1. The tuning system for all the frequency range (15-50 MHz) is automatic. This amplification system was made, under technical specification by our Institute, at the end of 1980s. Since the commissioning of the Superconducting Cyclotron, 1994, the amplifiers have been operating, related to the RF power stages, without significant changes or upgrade. The robust and classical electrical design of the amplifiers has ensured, more or less, an uninterruptable operation, for the last 30 years. Figure 2 shows a simple block diagram of the RF system, with drivers and final amplifiers [1].

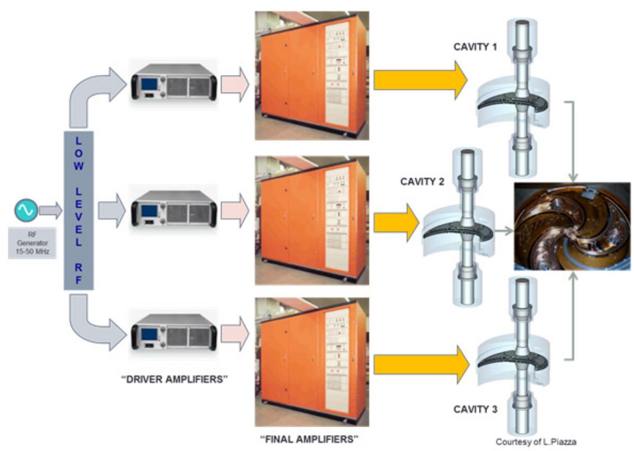

Figure 2: Block diagram of the RF system.

The total gain between drivers and final amplifiers is approximately around 80 dB. The distribution is about 50 dB for the driver and 30 dB for the final amplifier. The final is divided between 14 and 16 dB respectively for the 1st and 2nd stages. Despite the cost of the two tetrodes, in terms of spare parts, has greatly increased in the last decade, we decided to continue operating with this configuration. But some expedients was adopted. For example, we optimized the main parameters of the amplifiers, to reduce the maximum output power from 75 kW to 30 kW, enough for our cyclotron performance and as result, the average life span of the tetrodes was increased. We decided to refurbish the exhausted tetrodes, instead of buying new ones, reducing the cost by a third, and the reconstructed tetrode, can be considered like new. Unfortunately, this refurbished technique can be done only for the second stage, the 4CW100000E by CPI, while for the first stage, the RS1054L by Thales, it was not available. Apparently, the type, hardware and geometry of the tetrode itself made the rebuilding of the Thales tetrode almost impossible [2, 3].

* INFN-LNS
† caruso@lns.infn.it

ISBN 978-3-95450-167-0

TETRODE VS SOLID STATE

In any case, the main reason for modifying the amplifiers and consequently changing the first stage, was the end of production of the tetrode, RS1054E, in a few months. The strong decrease in demand on the worldwide market for this specific tetrode, was the reason Thales stopped production altogether. We were only given the opportunity to buy the last three tetrodes at the very unreasonable price of about 60 k€! In the meanwhile the cyclotron was in operation, the total RS1054L spare parts were not many, no specific planning was scheduled, in terms of funding/timing, because Thales sent us notification a very short time before ending production. Figure 3 shows the schematic of the RF amplifier and, in the dotted line, the obsolete 1st stage to be removed and replaced.

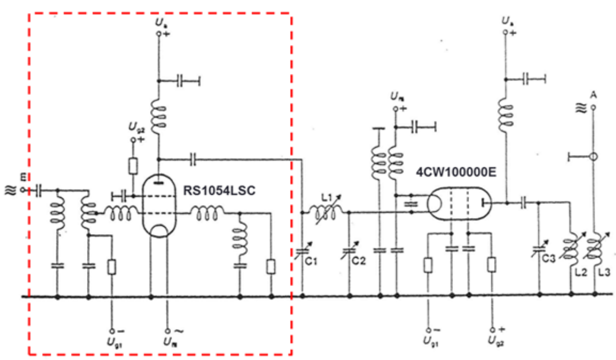

Figure 3: RF schematic, part to be removed in dotted line.

Obliged to change this tetrode, we had two options: use another tetrode or a new solid state technology. The first approach was more conservative, we considered more than one possible tetrode. Commercial partners such as Eimac and Thales offered very few valid alternatives and, it is not a plug and play job, some hardware modifications have to be made, like new sockets, some changes in the polarization network, redesign of the matching board between the 1st and 2nd stages, and recalibration of the RF response. As a possible alternative to the originally used RS1054L the CPI tube 4CX3500A was selected. This tube is less powerful than the original one but was selected because we thought that the final power of 30kW was enough for normal cyclotron activity. The obsolete and new tetrodes are shown in Fig. 4.

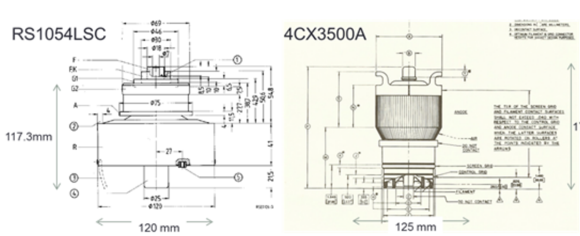

Figure 4: Mechanical difference between the two tetrodes.

The most critical parameter is the input capacitance of the 4CX3500A as it influences the input circuit negatively. The existing input wide band circuit has to be redesigned in order to cope with the higher tube capacitance. An insertion of new crowbar circuit in the anode power supply plus retuning of anode matching circuit.

The positive points of this "conservative" choice are:

- 4CX3500 cost is relatively low, high efficiency, high reliability, robustness;
- apparently no end of production in the near future, according to the manufacture;
- CPI, ensured total assistance to rebuild the tube in case of failure (not necessary to buy a bright new tube every the time).

The risk and negative points of this operation are:

- The tetrode manufacturer can notify the end of the production of this new tetrode at any moment. With a very short margin in terms of time, according to our experience;
- It is not possible to store a lot of spare parts, economic and vacuum tube technology;
- Cost/timing of the total operation is quite high.

But, the most important point, to investigate other solutions, for example the new emerging solid state technology, was the increased number of dismissed tetrodes and absence of new products in our frequency/power range.

Figure 5 shows the trend of the power tube market. The area of our interest inside the dotted line is empty.

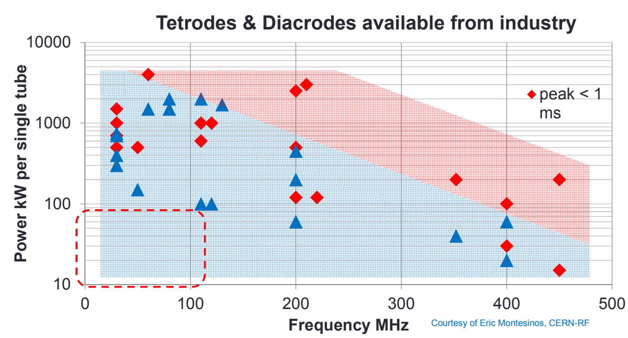

Figure 5: Frequency and power range of tetrodes.

The interest of the market in our frequency/power range is moving from vacuum tube to solid state devices. The miniaturization of the RF power components and the maximization of power per single device is only one reason for this new trend. The new solid state technology is going to cover the slice of market under a power of 100 kW and up to few hundred MHz of bandwidth [4].

SOLID STATE AMPLIFIER FIRST STAGE

Removing the first stage based on the tetrode and installing a solid state amplifier means to adapting and matching this new device mainly in terms of impedance and amplification factor. In the original configuration of the amplification section, according to Fig. 2, the driver, a commercial amplifier, was connected to the main amplifier, through a 50Ω wide band input circuit of the first stage, based on the tetrode RS1054. The output of this stage, through a further matching section, a variable π-filter tuning system, is connected with the input of the second stage, cathode of the 4CW100000E tetrode. For

ISBN 978-3-95450-167-0

each frequency, the variable components of the matching networks, tune the amplifier parameters and maximize the transmission. Our goal, once the first tetrode is removed, is to minimize the hardware modification of the remaining amplifier, adapt the new solid state first stage, reproduce the previous performance and contain the cost. The block diagram of the new amplification sections, in Fig. 6, includes a solid state amplifier, as the new first stage, a matching box, the second stage of the main amplifier.

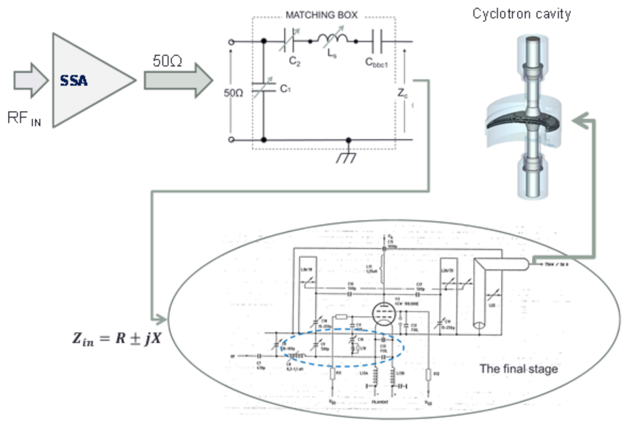

Figure 6: Block diagram of the new amplification section.

The core of the system is the matching box. This wide band tuneable circuit adapts, in terms of impedance, the standard 50 Ω first stage solid state amplifier output, with the input section of the second stage, tetrode based. The matching is between the real part of the tetrode 4CW100000E cathode impedance, Z_c and Z_0 (50Ω). We may use the simple Γ-matching network, because $Z_c \ll Z_0$. The SSA plus the matching box includes the driver and the first stage, based on the obsolete RS1054L. Figure 7 shows the matching box in details, with the matching formulas, in terms of impedance transformer, to adapt the cathode equivalent load with the standard SSA 50Ω [5].

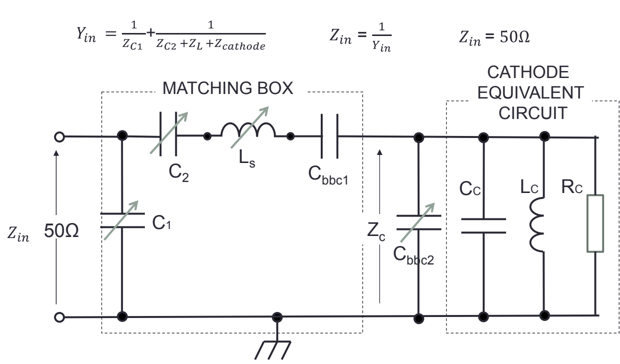

Figure 7: Matching box connected with the cathode load.

Through the matching box we can easily connect all the commercial or custom solid state amplifiers. The second stage of the main amplifier, with this impedance transformer, shows always 50Ω, after the tuning of the variable vacuum capacitors, C_1 and C_2, basically the 2 new elements of this circuit. The remaining components of the matching box were parts of the original amplifier. Figure 8 shows the main steps of the amplifier revamps of the first stage, from tetrode into solid state based. We have removed the tetrode RS1054L, the space available is occupied by two new elements of the matching network, C_1 and C_2, variable vacuum capacitors 10-1000pF, the amplifier cabinet is closed and the manual tuning has been done.

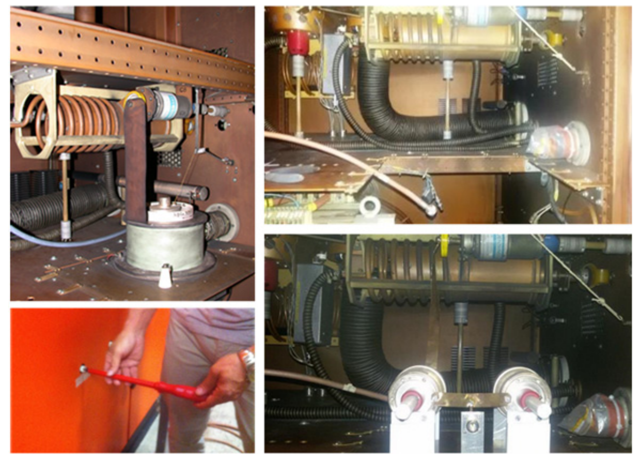

Figure 8: Step by step, from tetrode to SSA as first stage.

All the frequency range is perfect matched at 50Ω, an example of this result, at 43,61 MHz is shown in Fig. 9.

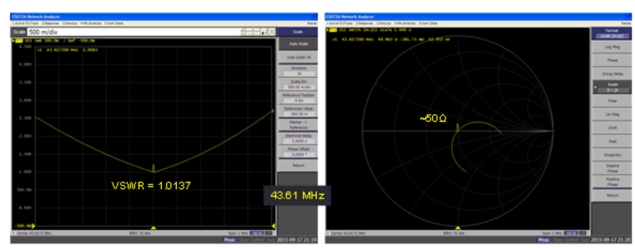

Figure 9: Matching between SSA and 2nd final stage.

CONCLUSION

In conclusion, we obtained very successful results:

- The frequency range 15-50 MHz was achieved;
- Mismatch up to 2.0:1 was tested too (30%);
- The system works very well with a lot of final 1st stage configuration (tetrode, mosfet, bjt, new LDMOS etc) of the SSA drivers, we used amplifier research, Kalmus, ENI, dB, in-house custom amplifier based on BLF188XR;
- Enough power, 20-30 kW, at the output of the final tetrode, was achieved in the cyclotron cavity;
- Automatic tuning of the matching network, in the near future.

In the end, the solid state solution greatly reduces the cost of the revamp and the maintenance operations. Only one amplifier is equipped with this new solution, the other 2 are still working with the tetrode 1st stage, until the last spare parts, related to the RS1054L, are used up.

ISBN 978-3-95450-167-0

REFERENCES

[1] A. Caruso,"The RF system of the k-800 superconducting cyclotron at INFN-LNS", in *Proc. InPAC'13*, Calcutta, India, paper IT-15.

[2] THALES, `https://www.thalesgroup.com`

[3] CPI, CPI Power Grid Devices - Eimac Products `http://www.cpii.com`

[4] NXP, http://www.nxp.com/

[5] A. Caruso *et al.*, "The new axial buncher at INFN-LNS", in *Proc. ICCA'13*, Vancouver, Canada, paper TU2B02.

ISBN 978-3-95450-167-0

DESIGN AND SIMULATION OF CAVITY FOR 18 MeV CYCLOTRONS

S. M. Mousavinia†, H. Afarideh, M. Mohamadian,
Amirkabir University of Technology, Tehran, Iran
M. Ghergherechi, Sungkyunkwan University, Suwon, Korea

Abstract

RF system is the key part of the cyclotron and cavity is the key part of RF systems. The basic parameters of cavity design are the resonant frequency, Dee voltage, RF phase and RF power. Proper operation of the cavity depends on the suitable voltage distribution in accelerating gap, phase stability in the cavity and as well as optimal scattering parameters. In this simulation using CST MWS, different parts of the cavity such as Stem and Dee are optimized to achieve optimum dimensions for the desired resonant frequency, Dee voltage and RF power. Main properties of the designed cavity are resonant frequency at 64.3 MHz, Dee voltage of 45 kV and RF power of 11 kW.

INTRODUCTION

IRANCYC-18 is an 18 MeV compact low energy cyclotron for short life medical isotope production. The RF system is designed to accelerate 150 μA of H− ions to 18 MeV. The RF specifications are shown in Table 1.

Table 1: Main RF Specifications

Parameter	Value
Resonant Frequency	64.3 MHz
Harmonic Number	4
Dee Voltage	45 kV
Resonant Mode	λ/4
Matching Impedance	50 Ω
Material	OFHC copper
Number of Dee	2
Dee angle	44

The RF system is composed of λ/4 delta cavities housed inside the valleys of the magnet, power amplifiers, power switch, directional coupler, transmission lines, coupling and tuning capacitors and low level control circuits. Block diagram of RF system is shown in Fig. 1. RF power has been capacitively coupled into the cavity by rigid coaxial line, also a tuning capacitor is used to adjust the cavity frequency.

DESIGN ITEMS

The Operating frequency of resonant cavity is 64.3 MHz. This cavity works at fourth harmonic [1]. In the design of the cavity, the main parts are Dee, Stem and central region. Angle and width of the Dee and the gap between the Dee and Liner as accelerating region are the points that in the design should be considered. The suitable angle and width of Dee is calculated on the basis of Eq. (1) [2]. Also the distance of the accelerating gap can be calculated on the basis of electric field and required voltage as well as considering the Kilpatrick's criterion.

$$\Delta E_k = V_{dee}.N.q.\sin\left(\frac{h.\alpha}{2}\right) \quad (1)$$

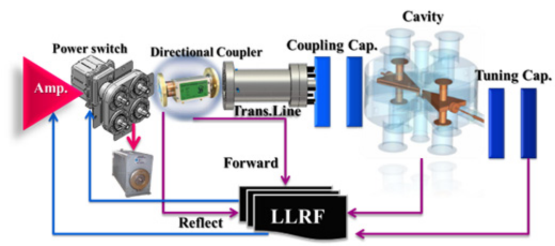

Figure 1: Block diagram of RF system.

Another important part of the cavity is Stem that with regard to the capacitive role of Dee, Stem have an inductive role of cavity circuit. The structure of Stem is like a coaxial line that can play three roles in the design:

1. Inductive's role of Stem can change the resonant frequency [3]
2. Shunt impedance of the cavity structure has direct relation to Stem dimensions and therefore with cavity losses.
3. Displacement of Stem along the accelerating gap can change the voltage distribution along the accelerating gap [4].

CST MWS software has been chosen for design and simulation. CST STUDIO SUITE is a general-purpose electromagnetic simulator based on the Finite Integration Technique (FIT), unlike most numerical methods, FIT discretizes the following integral form of Maxwell's equations rather than the differential one [5]. Geometry designed in this software which has been shown in Fig. 2.

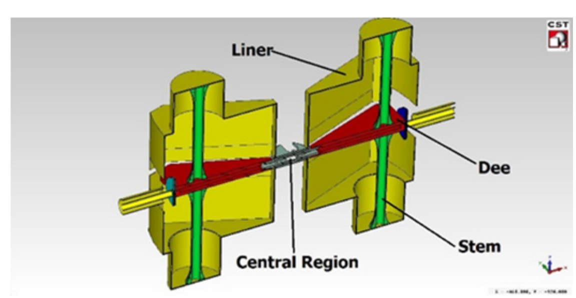

Figure 2: Designed geometry in CST MWS.

ISBN 978-3-95450-167-0

Coupling and Tuning

Power couplers can generally be defined as networks designed to transfer power from an RF power source to a cavity [6]. Possible problems during operation of the cyclotron that may be occur due mismatch, including:

1. The transmitter may not be able to supply enough power to maintain the desired accelerating voltage if the cavity's resonant frequency drifts too far from the driving frequency;
2. The power supply could be damaged by dissipation of excessive power reflected back from the load;
3. Break-down and sparking could occur;
4. The phase and amplitude response of the transmitter may be severely affected by the change in the load

Coupling in RF systems of accelerators will be done in two ways, electric coupling (capacitive) or magnetic coupling (inductive), that in this study, the capacitive one has been chosen.

According to the complicated operating conditions, the resonant frequency of the cavity may be shift with deformation resulting from the unexpected variability of such factors as temperature, gravity, instability of the voltage source, multipacting and so on. Therefore, it is necessary to design a frequency tuning device.

SIMULATION RESULTS

With regard to the capacitive rule of Dee and also equation $C = A/d$ and $f = 1/(2\pi\sqrt{LC})$, Optimum dimensions have been obtained for Dee height and the gap between Dee and Liner that has been shown in Fig. 3.

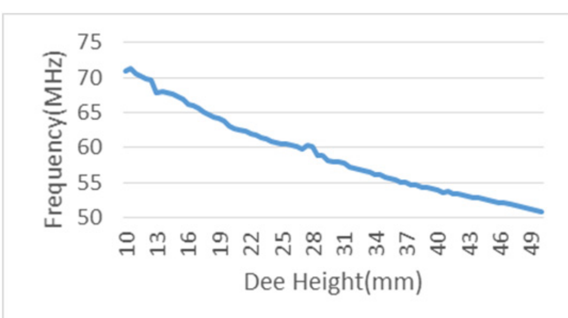

Figure 3: Frequency vs Dee height.

After simulation of different gaps size, finally, with regard to beam dynamic requirements and also Kilpatrick's criterion that at a frequency of 64.3 MHz is 5.22 mm, size of the gap has been chosen to 10 mm. Figure 4 shows the Dee voltage along the accelerating gap.

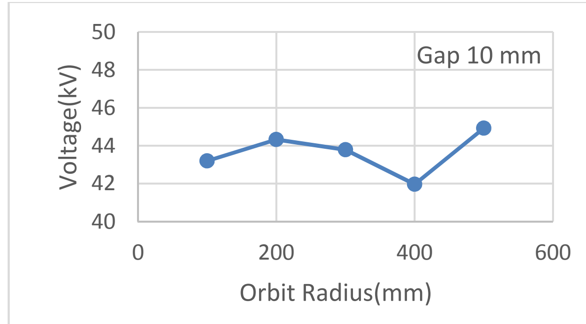

Figure 4: Dee voltage along the accelerating gap.

Process passed in above repeated also for length and radius of Stem and eventually, according to the obtained results, radius of 55 mm and a length of 530 mm were chosen for Stem.

And also, in coupling and tuning section, they have been chosen capacitively too. In the both sections, the purpose was the selection of optimum radius for capacitors. In Fig. 5a, S_{11} has been shown for different radius of coupling capacitors and Fig. 5b has been illustrated the final optimum coupling.

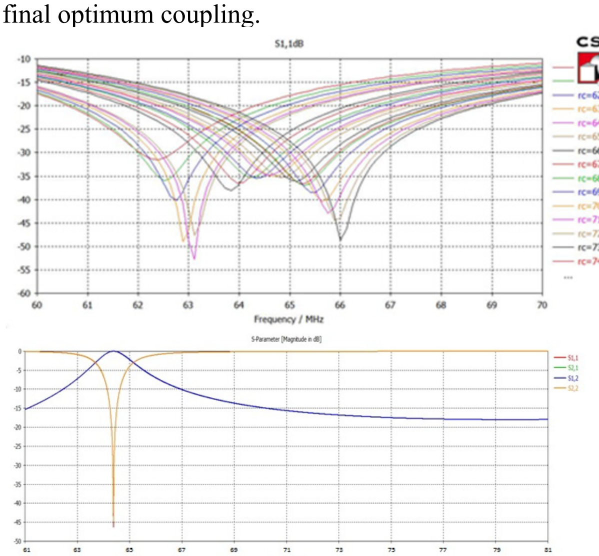

Figure 5: a) Determination of the optimum radius for coupling capacitor, b) Final optimum coupling.

In Fig. 6, plot of frequency vs distance between two plates of capacitors has been given. Accuracy of tuning that will be done with servo motor is $\frac{0.12\ MHz}{0.03\ mm}$.

In Figs. 7a and 7b, the electric and magnetic field has been shown respectively. As it has been indicated, concentration of the electric field is on the accelerating gap and concentrate of magnetic field is on Stem.

ISBN 978-3-95450-167-0

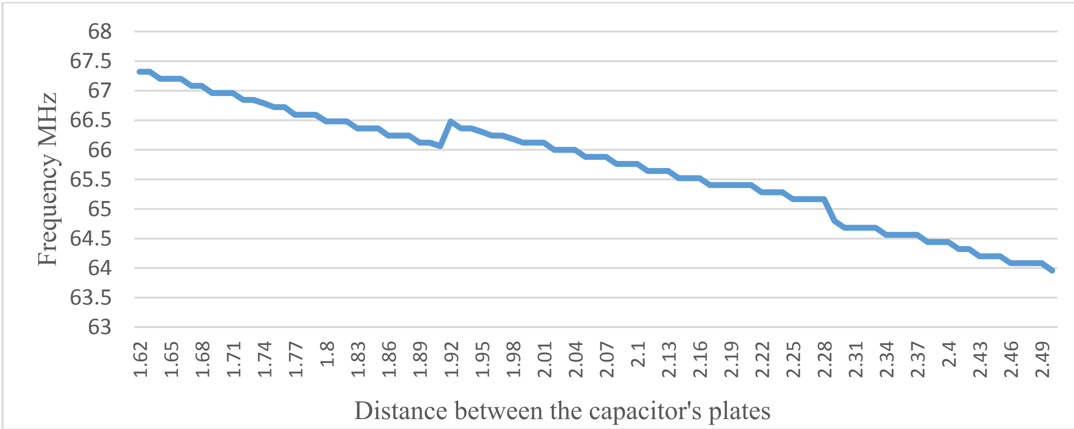

Figure 6: Frequency vs. distance between two plates of capacitors.

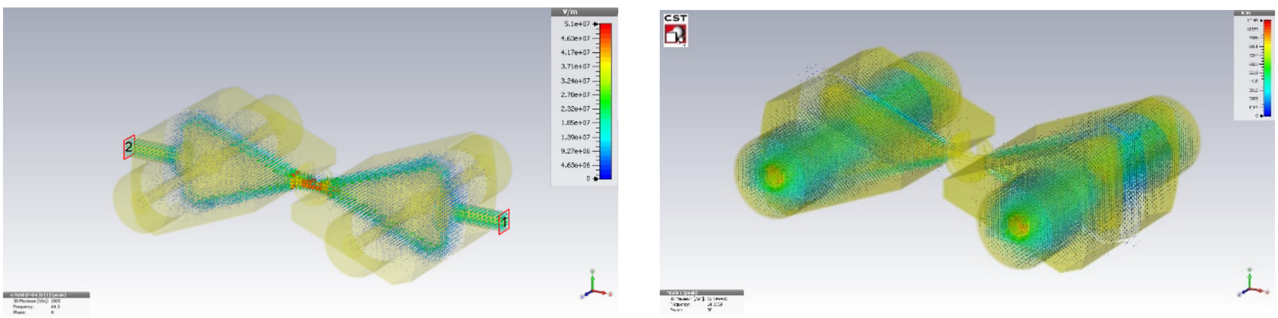

a b

Figure 7: a) Electric field, b) Magnetic field.

CONCLUSION

Design and simulation of cavity for 18 MeV cyclotron in CST MWS has been presented. This design is based on results of magnet calculations and design experience of IRANCYC-10, a 10 MeV compact cyclotron. The simulation results accords to our expected design goals.

REFERENCES

[1] N.R. Kalkhoran *et al.*, "Improvement of 18 MeV cyclotron magnet design by TOSCA Code", in *Proc. 7th Int. Particle Accelerator Conf. (IPAC'16)*, Busan, Korea, May 2016, pp. 1397-1399, doi:10.18429/JACoW-IPAC2016-TUPMR060

[2] M.J. Jakobson and F.H. Schmidt, "Characteristics of a Proposed Double-Mode Cyclotron", *Phys. Rev.*, vol. 93, issue 2, p. 303, 1954.

[3] C. Bieth, "Critical features of RF systems for large cyclotrons", in *Proc. 10th Int. Conf. on Cyclotrons and their Applications*, Michigan, USA, May 1984, pp. 294-298.

[4] N. Schmid, "Design of a fixed frequency delta resonator with positive gradient radial voltage distribution", *IEEE Transactions on Nuclear Science,* vol. 26, issue 2, pp. 2194-2197, 1979

[5] CST Microwave Studio Manual, 2014

[6] D. Alesini, "Power coupling", CERN Accelerator School: Specialised Course on RF for Accelerators; 8-17 Jun. 2010, Ebeltoft, Denmark, CERN Yellow Report, CERN-2011-007, 2011, pp. 125-147, arXiv:1112.3201.

ISBN 978-3-95450-167-0

A COUPLED CYCLOTRON SOLUTION FOR CARBON IONS ACCELERATION

V. Smirnov*, S. Vorozhtsov, Joint Institute for Nuclear Research, Dubna, Russia

Abstract

A concept of coupled cyclotrons for acceleration of carbon ions (charge 6+) to 400 MeV/nucleon by a separated sector cyclotron consisting of six sector magnets with superconducting coils is proposed. Injection to the machine will be provided by a compact 70 MeV/nucleon cyclotron. The accelerator complex is intended for setting up a radiation therapy facility employing carbon ions. The advantages of the dual cyclotron design are typical of cyclotron-based solutions. The first design studies of the sector magnet of the main cyclotron (magnetic field increases from 4.2 T to 6.5 T, RF frequency 73.56 MHz, RF mode 6) show that it is feasible with acceptable beam dynamics. The accelerator has a relatively compact size (outer diameter of 8 m) and can be an alternative to synchrotrons.

INTRODUCTION

Development of accelerators for producing carbon beams with the energy of 400–450 MeV/nucleon for hadron therapy appears to be an increasingly important issue today. The existing facilities for producing these beams are mainly based on synchrotrons. It seems interesting to use isochronous cyclotrons instead, as is the case in proton therapy. However, the developed designs of compact superconducting cyclotrons have some disadvantages in addition to their advantages [1]. An alternative solution can be a facility based on a superconducting sector cyclotron justified in detail in [2]. The design of this facility should comply with a number of conditions. First, the size and weight of the accelerator must be as small as possible, which makes it expedient to use the maximum high magnetic field. Second, the injection energy should be low enough for the injector to be of tolerable size. Third, the magnetic system design should be feasible, that is, the parameters of the superconducting coil (engineering current density, acting forces) should be adequate and the space between the sectors should be large enough to accommodate accelerating elements, inject a beam, etc. [3]. A separate task is to develop a system such that both maintains isochronism of the magnetic field and allows beam acceleration with a minimum number of resonance crossings.

INJECTION SYSTEM

The injection energy is chosen to be 70 MeV/nucleon because the accelerator with this final energy can be also used to accelerate H_2^+ ions. Their subsequent stripping allows obtaining protons of the appropriate energy suitable for medical applications. This cyclotron can be used for treating eye melanomas and also for producing radioisotopes.

A compact superconducting cyclotron seems to be the most optimal option. The magnetic rigidity of 70-MeV/nucleon C^{6+} ions is about that of 250-MeV protons in the Varian cyclotron [4]. So, some technical solutions of the Varian machine can be applicable to the injector. The use of an external carbon ion source limits the central magnetic field to a maximum of 3.0 T because of performing injection through a spiral inflector. Another constraint comes from the necessity to have the same RF frequency in the injector and in the booster machines, which also governs the central magnetic field in the injector. The optimum solution is a cyclotron with a central field of 2.4 T operating at the fourth harmonic of the accelerating field. The magnetic field is formed by four spiral sector shims. With an acceptable spiral angle of 50°, the external diameter of the accelerator will be no larger than 3 m and the weight will be about 90 t.

The system for injection in the main cyclotron consists of four magnetic channels and an electrostatic deflector (Fig. 1).

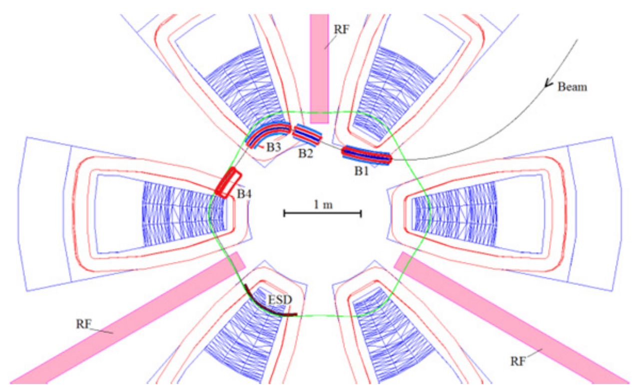

Figure 1: Injection system

The central fields in the channels are 1.2, 1.4, 1.4, and 0.8 T. The fourth magnetic channel comprises a septum. The strength of the electric field on the electrostatic deflector (ESD) is 80–90 kV/cm and can be slightly varied to ensure good beam centering.

As far as possible, the channels are arranged in the region of the magnetic field with a large gradient. The channel structure made such as to provide increasing or decreasing magnetic fields allows compensating for the negative effect of the main field on the transverse emittance of the beam. The axial distance between the coils with their cryostats in the beam injection region is

*vsmirnov@jinr.ru

ISBN 978-3-95450-167-0

~400 mm, which is enough to house the magnetic channels. In addition, the distance between the pole tips of the sector magnet in the area intended for the third magnetic channel is large enough to install this channel. No problem arises with the formation of the required isochronous field since the major contribution to the cyclotron magnetic field can be from the superconducting coils. The negative magnetic induction in the valley is the highest at medium radii, amounting to 1.4 T. At the center of the accelerator it is also high, being 1.2 T. The beam path in the valley is not linear. Passing through the valley, the beam moves alternately in the increasing and decreasing magnetic field, which leads to the alternating ion focusing.

For injection, the beam should be shaped at the entrance to the valley so as to have the smallest spread in angles. The following parameters of the beam at the entrance to the valley near the final radius were chosen for the dynamics analysis: transverse emittances 2 π mm mrad, transverse size 5 mm, and the Twiss parameter $\alpha = 0$. The spread in angles is below ±1 mrad. The orbit separation at the location of the electrostatic deflector is ~4 mm. The beam losses on the ESD septum are only ~15% with the septum thickness increasing along its length from 0.2 to 0.5 mm. During the beam tracing, the transverse size of the injected beam is no larger than ±6 mm. The size of the beam passing through the ESD is acceptable (±4 mm). With the deflector aperture of 10 mm, there should be no beam guiding problems.

MAIN CYCLOTRON

The magnetic rigidity of the carbon ions extracted from the main cyclotron with energy 400 MeV/nucleon is about 2.4 times that at injection. Therefore, the accelerator cascade could have an external size of about 12 m (Fig. 2), noticeably smaller than that of the synchrotron-based facilities currently used for hadron therapy.

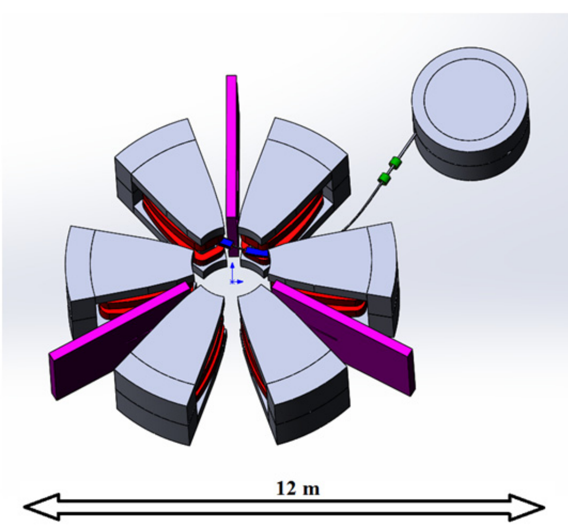

Figure 2: Acceleration complex including injector.

Injection at a relatively low energy leads to a considerable decrease in the magnetic field flutter from the initial to the final radius, which makes the working point to cross dangerous resonances. To increase the flutter near the final radius, the axial distance between the upper and lower coils in this region should be decreased. This coil arrangement causes a decrease in the mean field at small radii. An increase in the azimuthal size of the sectors can compensate for the missing magnetic field. The space between the neighboring sectors should be large enough to accommodate cryostats with coils and accelerating systems. According to some data, the critical engineering current density can be brought up to 150 A/mm^2. However, the operational value is considered to be 50–70 A/mm^2.

The following requirements were imposed on the magnet design: a) space for the installation of the coil cryostat 50–70 mm; b) axial distance between the coils no smaller than 120 mm; c) avoiding concave parts of the coil wherever possible.

All the magnetic field calculations were performed on a three-dimensional basis using the Opera3D code. It was found out from a series of calculations that for the above requirements to be fulfilled, the central magnetic field that governs the particle circulation frequency should be no higher than 1.6 T. With this field, the extraction radius of ions with the energy of 400 MeV/nucleon is 278 cm, and the external diameter of the cyclotron is as large as 8 m. Desired minimization of the variation in the frequency of axial free oscillations entails a necessary increase in the magnetic field flutter at medium radii, where the superconducting coil must thus be convex. This shape allows avoiding additional problems with forces acting on the coil. The magnetic induction in the region of the coil is as high as 7.2 T. The maximum field is 7 T in the hills, 2.7 T in the yoke, and 8 T in the pole tips. The main parameters of the accelerator are presented in Table 1.

Table 1: Basic Cyclotron Parameters

Parameter	Value
Ion type	$^{12}C^{6+}$
Number of sectors	6
RF system	3 × 200 kV
RF frequency	73.56 MHz
RF mode	6
Average magnetic field: injection/extraction	1.64/2.11 T
Maximal magnetic field: injection/extraction	4.22/6.40 T
Energy: injection/extraction	70/400 MeV/u
Radius: injection/extraction	143/278 cm
Air gap between sectors	88-135 mm
Dimensions: diameter × height	8 m × 2.2 m
Total weight (sectors + coils)	310 t

ISBN 978-3-95450-167-0

The yoke of a sector externally measures 3.2 × 2.0 × 2.2 m^3. The sector weighs 50 t. The operational engineering current density in the superconducting coil is 62 A/mm^2, and its cross section is 170 × 330 mm^2. The coils are tilted with respect to the median plane at angles of ±4°. Axial profiling of both the pole tip and the pole itself is used to shape the isochronous field (Fig. 3).

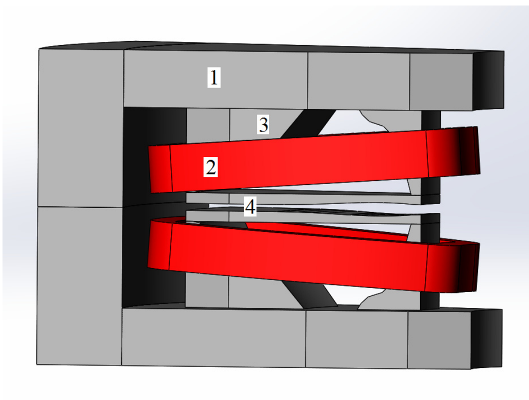

Figure 3: Magnet sector: 1 – yoke, 2 – superconducting coil, 3 – pole, 4 – pole tip.

Additional space between the neighboring sectors allows the azimuthal size of the sector to be varied, which combined with variation of the position of the coil permits producing the required field shape. Thus, it is possible to select a structure in which flutter increases with the radius and the variation range of the frequency Qz is the smallest (Fig. 4). A change in the azimuthal size of the coil leads to a shift of the frequency in the entire range of radii, and it becomes possible to prevent the working point from crossing dangerous resonances associated with the axial frequency of betatron oscillations (Qz = 1, 2Qz = 3, Qr − Qz = 0). Unfortunately, the crossing of the 2Qz − Qr = 1 and 2Qr − Qz = 2 resonances cannot be avoided. Their danger is to be investigated later.

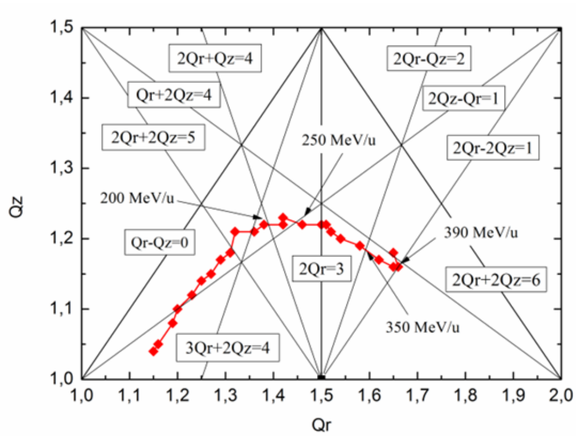

Figure 4: Tune diagram.

Isochronization of the calculated field was performed as follows. First, dependence of the mean magnetic field on the radius is calculated by the analytical formula:

$$B(r) = b \cdot \left[1 - \left(\frac{r}{a}\right)^2\right]^{-1/2}, \quad (1)$$

$$a = c / \omega_0,\ b = m \cdot \omega_0 / q.$$

Here m is the ion mass, q is the ion charge, and ω_0 is the particle circulation frequency.

Next, when the initial configuration of the magnet is obtained and the data on the magnetic field parameters (flutter, maximal spiral angle) are available, the dependence of the mean field on the radius is calculated using the Gordon algorithm [5]. Then the closed orbit is calculated for the given ion energy using one of the particle tracing codes. The magnetic field is multiplied by the scaling factor so that the particle circulation frequency in this orbit coincides with the isochronous frequency. The calculated correction is then registered at the crossing of the orbit with the sector central line for subsequent shimming. The above procedure is repeated for all ion energies. The ultimate result is the correction to the available magnetic field calculated along the central line of the sector. Calculations show that two or three iterations are enough to obtain the ultimate result.

Using the above magnetic field isochronization algorithm, we managed to keep the deviation of the beam phase from the optimum value within ±30°. The deviation of the magnetic induction from the required one along the central line of the sector varies within ±20 Gs. The 3D calculations of the field revealed that in order to keep the beam phase within the given limits, the axial profiles of the pole shim and the pole must be manufactured with the respective accuracy of ±0.2 mm and ±1 mm. In the beam phase calculations, the energy gain was given analytically in accordance with the accelerating voltage and the particle phase during the crossing of the accelerating gap. The acceleration is supposed to be performed by the RF field of three cavities located in the valleys with the accelerating voltage amplitude of 200 kV. In this case, the central particle makes 1240 revolutions to reach the final energy.

CONCLUSION

This design study has been carried out to show that a coupled superconducting cyclotron complex is a serious candidate for a light-ion medical facility. The cyclotron is more compact than the synchrotron and simpler to operate. The cyclotron elements specified in the current design are realistically achievable. The short-term activity on the project development includes:

- Concept of beam extraction from the cyclotron.
- Configuration of the accelerating system.
- Calculation of forces acting on the superconducting coil.
- Injector design and beam transport to the injection point of the separated sector cyclotron.

ISBN 978-3-95450-167-0

REFERENCES

[1] V. L. Smirnov and S.B. Vorozhtsov, "Modern compact accelerators of cyclotron type for medical applications", *Physics of Particles and Nuclei*, vol. 47, no. 5, pp. 863–883, 2016.
[2] J. M. Schippers *et al.*, "A novel design of a cyclotron based accelerator system for multi-ions therapy", in *Proc. Heavy Ion Accelerator Technology (HIAT'09)*, Venice, Italy, Jun. 2009. pp.74-78
[3] S. Sanfilippo *et al,* "Design study of a 3.5 T Superconducting Sector Magnet in a 450 MeV/nucl Booster Cyclotron for Carbon Ion Therapy", *IEEE Transactions on Applied Superconductivity*, vol. 21, no 3, pp. 1838-1843, 2011.
[4] A. E. Geisler *et al*., "Commissioning of the ACCEL 250 MeV proton cyclotron", in *Proc. 18th Int. Conf. on Cyclotrons and their Applications (CYCLOTRONS'07)*, Giardini Naxos, Italy, Oct. 2007, pp. 9–14.
[5] M. M. Gordon, "Computation of closed orbits and basic focusing properties for sector focused cyclotrons and the design of 'Cyclops'*", Particle Accelerators*, vol. 16, pp. 39–62, 1984.

ISBN 978-3-95450-167-0

NEW DEVELOPMENTS AT iTHEMBA LABS

J. L. Conradie, L. S. Anthony, S. Baard, R. A. Bark, A. H. Barnard, J. I. Broodryk, J. C. Cornell, J. G. de Villiers, H. du Plessis, W. Duckitt, D. T. Fourie, P. Gardiner, M. E. Hogan, I. H. Kohler, C. Lussi, R. H. McAlister, J. Mira, H. W. Mostert, F. Nemulodi, M. Sakildien, G. F. Steyn, N. Stodart, R. W. Thomae, M. J. van Niekerk, P. A. Van Schalkwyk,
iThemba LABS, Somerset West, South Africa

A. Andrighetto, A. Monetti, G. Prete, M. Rossignoli,
INFN, Laboratori Nazionali di Legnaro, Viale dell'Università 2, 35030 Legnaro, Padova, Italy

Abstract

iThemba LABS has been in operation for more than 30 years and is now at a stage at which refurbishment and – in some cases – replacement of the infrastructure and critical components is required. The replacement and refurbishment of the cooling system, which include the cooling towers and chillers, the 4.4-MVA uninterruptable power supply batteries and other critical components, are discussed. Progress with a facility for low-energy radioactive ion beams will be reported on. A proposal to remove radioisotope production from the separated sector cyclotron (SSC) and the production of the future radioisotopes with a commercial 70-MeV cyclotron to make more beam time available for nuclear physics research with the SSC will also be discussed. Developments on our electron cyclotron resonance ion sources, the PIG ion source and low-level digital RF control system have also been carried out. Good progress with integration of the existing control system to an EPICS control system has been made. The adoption of EtherCAT as our new industrial communication standard has enabled integration with much off-the-shelf motion, actuator and general interface hardware.

BEAM STATISTICS

The SSC's performance over the past six years is shown in Table 1. The increase in the number of interruptions can be expected as the facility has now been in operation for 30 years. The time lost due to interruptions has increased to more than 10% for some years. This is at the upper limit of what can be tolerated for medical applications. There was an increase in the beam time lost due to power failures. The facility has run without the Uninterruptable Power Supply (UPS) for more than two years, i.e. since early 2013. The average number of power interruptions without the UPS was about 3 per month. This meant that the various subsystems of the accelerators were prone to power failures, which resulted in increased downtime. Another factor which accounts for the increased downtime is interruptions relating to various radio-frequency (RF) systems of the accelerators. Many of these interruptions were due to power amplifiers. A project was initiated to build spare RF amplifiers for the injector cyclotrons and bunchers and refurbish the power amplifiers of the SSC. All the low-level RF control systems will be replaced during the next 2 years. To reduce the unscheduled interruptions to about 5% of scheduled beam time, the rate of refurbishment and replacement of the infrastructure has been increased.

Table 1: Operational Statistics of the SSC for the past 6 Years

Year	Beam supplied as		% of scheduled beam time for	
	% of total time	% of sched-uled time	Energy changes	Inter-ruptions
2010	67.6	82.18	5.2	7.3
2011	68.9	85.91	5.4	4.8
2012	69.9	82.04	6.1	7.9
2013	63.0	81.17	6.2	10.7
2014	67.3	80.81	5.4	8.1
2015	64.1	77.69	5.6	10.8

INFRASTRUCTURE REFURBISHMENT

A number of infrastructure refurbishment projects have been initiated recently. Two of the larger projects are the replacement of the batteries of the 4-MVA uninterruptable power supply and the chillers of the central cooling plant. Both these projects will make a valuable contribution to sustainable stable operation of the facility.

Cooling Towers and Chiller Upgrade

The accelerator complex utilizes a central cooling plant for all the cooling requirements. The heart of the system comprises four water-cooled chillers, seven cooling towers and associated pumps supplying chilled water at 6°C with a capacity of 4.4 MW. The chillers are operated in parallel and switched in on demand as the heat load increases. Since installation in 1982 the system has performed well, but has become inefficient and troublesome to maintain. During 2011 the cooling towers have been replaced and subsequently funds have been approved to replace the chillers and pumps during 2016. An extended mid-year maintenance period of 2 months has been scheduled to allow the work to be completed. As part of the upgrade a new programmable logic controller (PLC) and building management system (BMS) will also be installed. The new equipment will not only be more reliable, but will also offer a sustainable energy saving due to the high Coefficient of Performance (COP) of the modern technology chiller units.

ISBN 978-3-95450-167-0

Replacement of 4.4-MVA UPS Batteries

The batteries that supply backup power to the 4.4-MVA UPS have recently been replaced. The previous gel-technology batteries lasted only 3 years. The new installation of low-antimony alloy, vented lead-acid batteries from BAE has a lifetime of 20 years. A total of 4 banks of 264 *BAE 25 OGI 2000* [1] batteries were installed. The installation is dimensioned to keep the facilities operational for 20 minutes at full load. A photograph of the new installation is shown in Fig. 1.

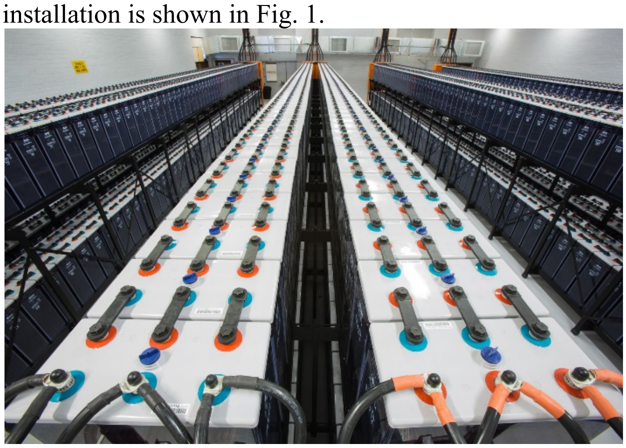

Figure 1: The new 4.4-MVA battery installation.

LOW-ENERGY RARE-ISOTOPE BEAM FACILITY

To stay abreast and explore new frontiers in the field of nuclear physics, iThemba LABS has embarked on a flagship project to establish a Rare-Isotope Beam (RIB) facility, to augment the existing research facilities. Of special interest is the study of neutron-rich nuclei, which is only possible with the production and analysis of RIBs.

As a precursor, iThemba LABS has received a Strategic Infrastructure Grant from the National Research Foundation (NRF) for a pilot project to construct a Low-Energy RIB (LERIB) test facility to develop the techniques for RIB production. Knowledge, experience and equipment gained with this endeavour will be carried over into a full-fledged RIB facility that will include charge breeding, beam cooling and post-acceleration.

A Memorandum of Agreement (MOA) was drawn up and signed during February 2015 to formalize collaboration between the NRF and the Istituto Nazionale di Fisica Nucleare (INFN) in Legnaro, Italy. The MOA involves the procurement of a replica of the Target/Ion Source (TIS), shown in Fig. 2 that has been developed by Laboratori Nazionali di Legnaro (LNL) in Legnaro, Italy for their SPES project. The TIS produces radioactive ions via the Isotope Separation On-line (ISOL) method and will form the basis of the proposed LERIB test facility at iThemba LABS. Neutron-rich atoms can be produced by proton-induced fission of uranium. The SSC will be used as the driver for the LERIB facility.

As part of the collaboration an online test of the power dissipation of the multi-slice target assembly has been performed at iThemba LABS [2]. A 60-µA, 66-MeV proton beam from the SSC was stopped on the target assembly, comprised of 13 thin silicon carbide discs housed in a graphite container. The test results validated the thermal finite-element simulations and confirmed that the multi-foil target system is suitable for ISOL-RIB production.

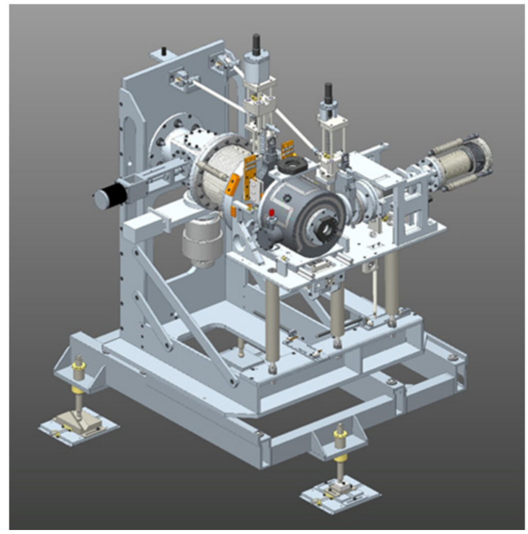

Figure 2: 3D illustration of the complete LNL front-end housing of the Target/Ion Source (TIS).

A new building will be constructed to house the vaults, the LERIB test facility and infrastructure, as illustrated in Fig. 3. The atomic species of interest will be selectively ionized, using either surface or resonant laser ionization, and the isotope will be selected with a high resolution mass separator. Thereafter the ions will be transported to a number of end stations for low-energy (<60 keV) experiments.

RADIOISOTOPE PRODUCTION FACILITY

Previously iThemba LABS reported on a proposal for the acquisition of a 70-MeV H^- cyclotron with two extraction ports for simultaneous production of radio-active ion beams (RIBs) and medical and industrial radioisotopes [3]. The existing cyclotron complex would be available for post acceleration of the radioactive ion beams.

Since then a comprehensive feasibility study to investigate all aspects of the proposal has been completed. Part of the feasibility study included a detailed preliminary design of the new facility, including the buildings and infrastructure. The outcome of the feasibility study revealed a number of reasons to reconsider the viability of the proposal:

a) Due to beam intensity instabilities resulting from dual beam extraction, simultaneous production of RIBs and isotopes will be problematic and is not recommended.
b) The injector cyclotron, which is intended for use as part of the post-acceleration scheme for RIBs uses axial injection and has poor transmission of 5 to

ISBN 978-3-95450-167-0

15% for heavy ions. It is therefore not ideally suited for the intended application.

c) The post-acceleration chain from source to the end-station is very long (>150m). It will be challenging to achieve stable beam transport over long periods.
d) The complete beam acceleration and transport system will need a vacuum system upgrade of at least one order of magnitude to limit beam losses.
e) The new buildings and infrastructure that are required will be expensive.

The outcome of the feasibility study made it clear that simultaneous production of RIBs and radioisotopes will be problematic and very costly. Therefore alternative solutions had to be considered. For these reasons it was decided to separate RIBs and radioisotope production by utilising a commercial 70-MeV H-minus cyclotron as a driver for a dedicated radioisotope production facility. Removing isotope production from the SSC will increase the beam time for nuclear physics research by at least a factor of 2.

This idea prompted the initiation of a Technical Design Study to investigate the feasibility of a dedicated radioisotope facility utilising as much as possible of the existing infrastructure to limit the cost of the project. Existing infrastructure will become available when iThemba LABS stops proton therapy treatment in 2017. A dedicated proton therapy facility for South Africa will be pursued. A number of options for a dedicated radioisotope production facility have been investigated. The most feasible layout is illustrated in Fig. 3. There are two vaults with two bombardment stations in each for the production of radioisotopes. Each bombardment vault [4] will host a high-intensity (350 µA), and a low intensity (100 µA) target station. The target stations will be shielded to reduce activation of the equipment and the vault itself. The 70-MeV H-minus cyclotron will be in a separate vault between the two bombardment vaults. This is an economic configuration since existing vaults will be used.

ION SOURCE DEVELOPMENT

iThemba LABS operates two electron-cyclotron-resonance ion sources. ECRIS4, which was originally built by GANIL for the Hahn Meitner Institute [5, 6], delivers ion beams from gases and fluids. In recent years this source has been equipped with an injection system for the so-called Metal Ions from Volatile Compound (MIVOC) method [7]. The production of nickel and ruthenium beams was studied. A second ECRIS, GTS2, which is based on the design of the Grenoble Test Source [8], is used to supply beams for nuclear physics experiments, which require elements like ^{1,2}H, ^{3,4}He, ^{14}N, ^{16,18}O, ^{20}Ne, ^{36,40}Ar and ^{86}Kr. In addition, under our collaboration with the ion source group at CERN, experiments for the production of intense xenon beams were performed. The source was optimized for different charge states ranging from 18+ to 25+. Beam currents of the order of 50 eµA were obtained with CW operation. For injection into the RF linear accelerator at CERN short pulses are required, which can be produced from the source in the so-called after-glow regime. In this mode, intensities of the order of 100 eµA with oxygen supporting gas were achieved [9].

Since 1994 the atomic beam source has delivered nuclear spin polarized protons for physics experiments. The source consists of a dissociater, a polarizer, and an ionizer. In 2013 the Paul Scherrer Institute donated their ECR ionizer unit, that was used in their polarized ion source, to iThemba LABS. Because the ECR principle is known to be more efficient than an electron bombardment ionizer of the CERN-AMAC design and will deliver a better beam quality with a lower energy spread, the unit was integrated into the source. First beam experiments to determine the polarization degree and beam performance will be carried out in the near future.

During the past few years, a source of concern was the instability of the proton beam extracted from the internal PIG source of solid-pole injector cyclotron SPC1. The influence of the composition and density of the lanthanum hexaboride (LaB_6) pellets, used as cathodes and anti-cathodes, in the source was investigated. This led to a recommendation to decrease the density of the LaB_6 pellets by 5%. This results in quicker degradation of the cathode (lifetime about 1 week) and reduces coating of the cathode surface exposed to the plasma by sputter material from the anode. With the new LaB_6 pellets the source stabilizes much faster and a more stable extracted proton beam is obtained.

IMPLEMENTATION OF AN EPICS CONTROL SYSTEM

In 2008 we made the decision to convert our OS/2-based distributed control system to EPICS. Currently 60% of the control hardware is under EPICS control. In order to aid the migration of the control system to EPICS we adopted EtherCAT as our new industrial communication standard in 2015. We built on the work done by the Diamond Light Source [10] and have successfully integrated stepper motors, dc motors, analog and digital input and output terminals as provided by Beckhoff and Weidmuller. This has given iThemba LABS the advantage that we are now able to easily deploy modern off-the-shelf hardware under EPICS control.

NEW DIGITAL LOW-LEVEL RF CONTROL SYSTEM

A new digital low-level RF (DLLRF) control system to replace the 30-year-old analog RF control systems has successfully been developed. The system [11] is based on field-programmable gate arrays (FPGAs) and is capable of synthesizing RF signals between 5 MHz and 100 MHz in steps of 1 µHz. It can achieve a closed-loop amplitude stability of better than 1/10000 and a closed-loop phase stability of less than 0.01º. A total of 35 new RF controllers have been manufactured, of which 10 systems have been fully assembled and tested. Three of these systems are in operation. The remaining systems will be installed during the coming months.

ISBN 978-3-95450-167-0

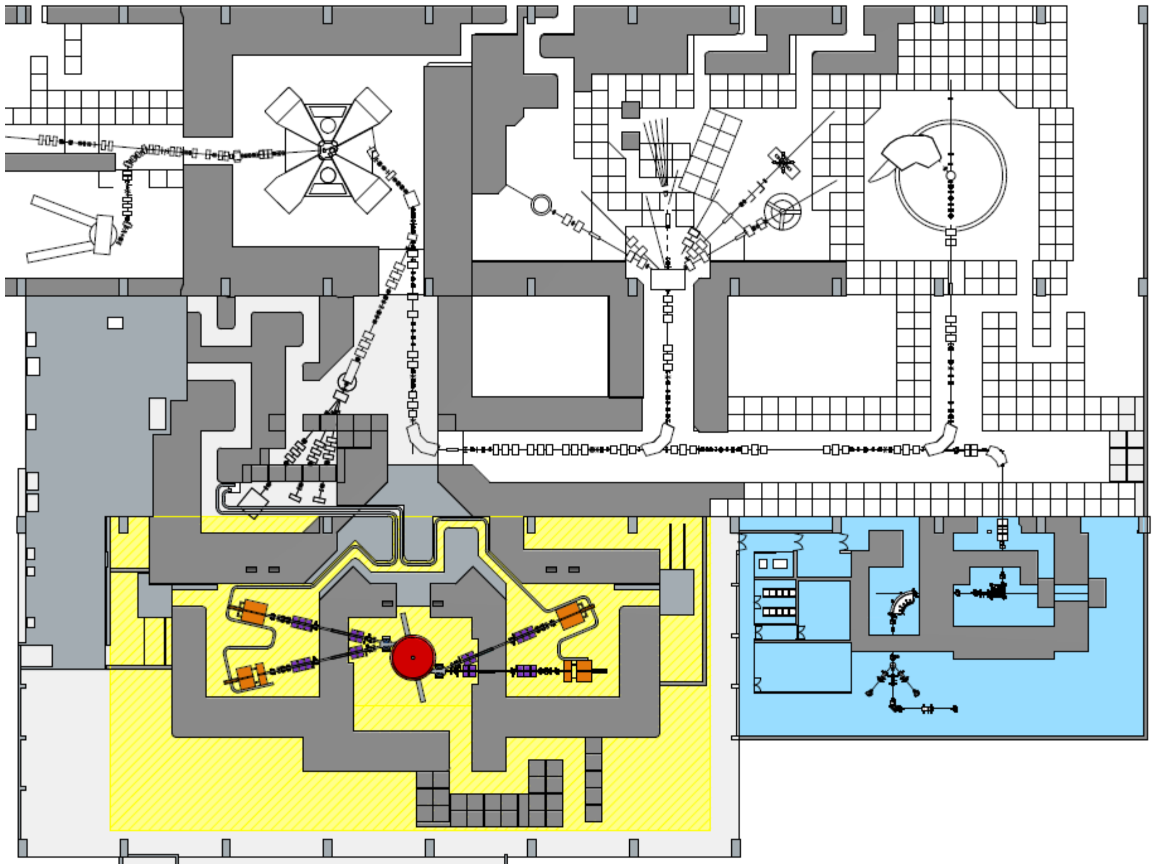

Figure 3: Layout of the proposed 70-MeV H-minus radioisotope production facility (yellow) and the low-energy rare isotope facility (blue).

CONCLUSIONS

A great effort, in manpower and finance, to refurbish and replace old infrastructure components to reduce the unscheduled interruptions back to about 5% of scheduled time has been started.

The LERIB project will be the first isotope separation on line (ISOL) facility at iThemba LABS and will open up a new field of research. The first beam from the LERIB is planned for 2019. The proposed dedicated radioisotope production facility with a commercial 70-MeV cyclotron will also have benefits for nuclear physics research, since it will at least double the beam time available from the existing SSC because radioisotope production with the SSC will be stopped. This proposal is financially attractive because existing buildings and infrastructure will be used.

REFERENCES

[1] 25 OGI 2000, BAE, `http://www.baebatteriesusa.com/products/docs/OGi%202V%20400-2400AhTechnical%20Specification-2011.pdf`

[2] A. Monetti *et al.*, "On-line test using multi-foil SiC target at iThemba LABS", Eur. Phys. J. A (2016) 52: 168.

[3] J. L. Conradie *et al.*, "Status Report and New Developments at iThemba LABS", in *Proc. Cyclotrons'13*, Vancouver, Canada, Sep. 2013, p 94.

[4] G.F. Steyn *et al.*, Nucl. Instr. and Meth. in Phys. Research A 727 (2013) 131– 144.

[5] P. Sortais, Nucl. Instr. and Meth. B98, 1995, p. 508.

[6] H. Waldmann and B. Martin, Nucl. Instr. and Meth. B98, 1995, p. 532.

[7] J. Arje, H. Koivisto, M. Nurmia, in *Proc. 11th International Workshop on ECR Ion Sources*, Groningen, 1993, p. 27.

[8] D. Hitz, D. Cormier, J. M. Mathonnet, in *Proc. EPAC'02*, Paris, June 2002, p. 1718.

[9] R. Thomae, *et al.*, in *Proc. of the 16th Int. Conf. on Ion Sources*, New York, USA, August, 2015, Rev. Sci. Instr. 87, 02A731 (2016).

[10] R. Mercado *et al.*, "Integrating EtherCAT Based IO into EPICs at Diamond", in Proc. *ICALEPCS'11*, Grenoble, France, Oct. 2011, pp. 662- 665.

[11] W. D. Duckitt *et al.*, "A new Digital Low-Level RF Control System for Cyclotrons", presented at Cyclotrons'16, Zurich, Switzerland, September 2016, paper WEB01, this conference.

ISBN 978-3-95450-167-0

DEVELOPMENT OF FLNR JINR HEAVY IONS ACCELERATOR COMPLEX (DRIBs III)

G.G. Gulbekian, S.N. Dmitriev, Yu.Ts. Oganessian, B.N. Gikal†, I.V. Kalagin, S.L. Bogomolov, I.A. Ivanenko, N.Yu. Kazarinov, N.F. Osipov, S.V. Pashchenko,
Joint Institute for Nuclear Research, FLNR, Dubna, Moscow Region, Russia

Abstract

The status of the FLNR JINR cyclotrons and plans of their modernization are presented. At present time, three isochronous cyclotrons: U400, U400M and IC100 are under operation at the JINR FLNR. The new isochronous DC-280 cyclotron is being created at the FLNR JINR for the new Super Heavy Element Factory.

INTRODUCTION

The Flerov Laboratory of Nuclear Reactions of Joint Institute for Nuclear Research (FLNR JINR) scientific program on heavy ion physics consists of experiments on synthesis of heavy and exotic nuclei using ion beams of stable and radioactive isotopes and studies of nuclear reactions, acceleration technology and applied research.

Presently, the FLNR JINR has four cyclotrons of heavy ions: U400, U400M, IC100, that provide performance of the basic and applied researches. Total annual operating time of the U400 and U400M cyclotrons is more than 10000 for many years (Fig. 1). The old U200 cyclotron is out of operation now.

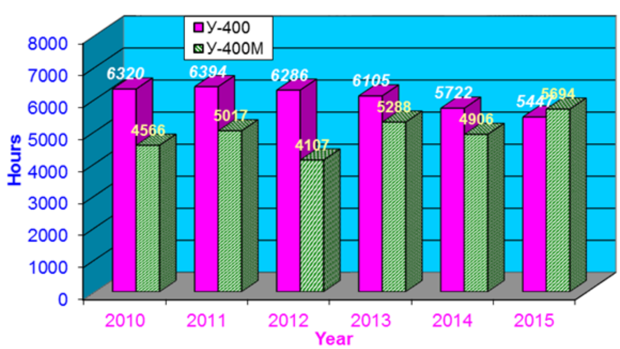

Figure 1: U400 and U400M operation in 2010-2015.

At present time the project of Super Heavy Element Factory is being performed at the FLNR JINR [1]. The project implies design and creation of the new DC280 cyclotron which has to provide intensities of ion beams with middle atomic masses (A~50) up to 10 pμA. The FLNR JINR facilities are shown in Fig. 2.

U400 CYCLOTRON

The isochronous U400 cyclotron has been in operation since 1978 [2]. The cyclotron produces ion beams of atomic masses 4-209 with energies of 3-29 MeV/nucleon. The main parameters of the U-400 are presented in Table 1. About 66% of the total time has been used for acceleration of $^{48}Ca^{5+}$ ions on the U400 cyclotron for synthesis of superheavy elements. New prospects for the synthesis of superheavy elements may appear to be connected with the usage of the intense beam of neutron-rich ^{50}Ti. The beam of ^{50}Ti ions has been accelerated into the U400 cyclotron. The extracted beam intensity of the of ^{50}Ti ions was about 0.5 pμA [3].

In 2014 the cyclotron was equipped by a dedicated channel for SEE testing of electronic components for ROSCOSMOS [4].

The U400 modernization is planned. The aims of the modernization are increasing the total acceleration efficiency and possibility to vary ion energy fluently at factor 5 for every mass to charge ratio (A/Z). The width of ion energy region will be 0.8-27 MeV/nucleon. The project of U400 modernization intends decreasing the magnetic field level at the cyclotron center from 1.93-2.1T to 0.8-1.8T, see Tab.1 (U400R). The axial injection and ion extraction systems will be changed. For the ion extraction both the stripping foil and the deflector methods are considered. Moreover, the project intends changing the U400 vacuum, RF and power supply systems. The expected ion beam intensities will be at least 2.5 times more than U400 ones [5].

Table 1: Comparative Parameters of U400 and U400R

Parameters	U400	U400R
	Value/Name	
Magnet weight	2100 t.	2100 t.
Magnet power	850 kW	200 kW
RF system power	100 kW	100 kW
Magnetic field level	1.93-2.1 T	0.8-1.8 T
The A/Z range	5-12	4-12
The frequency range	5.42-12.2 MHz	6.5-12.5 MHz
Harmonic modes	2	2-6
The max extraction radius	1.72 m	1.8 m
Vacuum level	$(1\text{-}5)\cdot 10^{-7}$ Torr	$(1\text{-}2)\cdot 10^{-7}$ Torr
Ion extraction method	Stripping foil	Stripping foil Deflector
Number of ion extraction directions	2	2

† gikal@jinr.ru

ISBN 978-3-95450-167-0

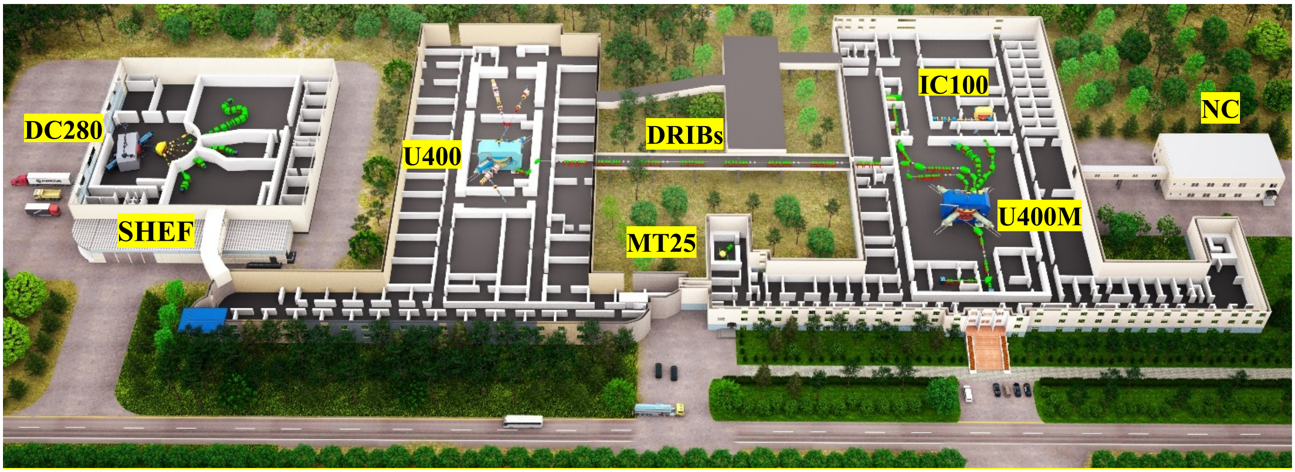

Figure 2: Layout of the Flerov Laboratory buildings, where: U400, U400M, IC100, DC280 are heavy ion cyclotrons, MT25 is the microtron, SHEF is the Super Heavy Element Factory, NC is the Nanotechnology Centre.

The cyclotron ion beam extraction system will be equipped with an electrostatic deflector and a passive focusing magnetic channel (Table 1).

The U400 experimental hall will be essentially modernized. The total experimental building will be extended to about 2000 m^2. New halls will be attached to the old building from sides (Fig. 3). The new experimental area will consists of six separated halls located on two floors. Every hall will be radiation shielded.

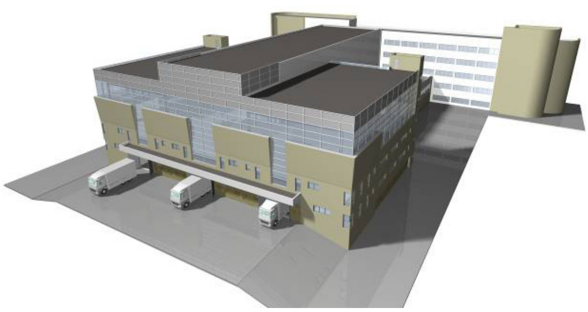

Figure 3: A sketch of the new U400 experimental hall.

U400M CYCLOTRON

The isochronous U400M cyclotron has been in operation since 1991. The cyclotron was originally intended for acceleration ion beams with A/Z=3-3.6 (A- atomic weight of the accelerated ion; Z - ion charge when accelerated) at energies of 34-60 MeV/nucleon. The beam extraction method is performed by ion stripping method. In 2008 the U400M possibilities have been extended by addition of the ion beams with A/Z=8-10 at energies of 4.5-9 MeV/nucleon. The additional ion beams intended to carry out physical experiments on synthesis the new super heavy elements and applied researches. The new axial injection system of the U400M was put into operation in 2006.

Two types of spiral inflectors are used to inject ions into the cyclotron centre for low and high energy regimes. At present, the U400M has two opposite directions of ion extraction with corresponding ion beam transport lines. To produce required ions the 14 GHz ECR ion source DECRIS-2 and the superconducting 18 GHz ECR ion source DECRIS-SC2 are being used [6]. Switching from one ion source to another is carried out by rotating the analysing magnet (Fig. 4).

In the period from 2010 to 2015 the cyclotron was equipped by two dedicated channels (low and high energy) for SEE testing of electronic components for ROSCOSMOS [4]. Acceleration of $^{84}Kr^{20+}$ to energies of 27 MeV/nucleon, $^{132}Xe^{30+}$ to 24 MeV/nucleon and $^{209}Bi^{37+}$ to 15 MeV/nucleon has been realized for SEE testing.

In 2016 the new channel for the ACCULINA 2 experimental setup has been created.

In the nearest future we plan to increase the energies of light ions to 60-80 MeV/nucleon by using ion extraction by an electrostatic deflector from ultimate cyclotron radiuses.

IC100 CYCLOTRON

The isochronous IC100 implanting cyclotron was put into operation the in 1985 with PIG internal ion source.

Due to the upgrade in 2003 IC100 was equipped with external axial beam injection system and the superconducting ECR ion source (DECRIS-SC [6]) which allowed to produce intensive beams of highly charged ions of Xenon, Iodine, Krypton, Argon and other heavy elements of the Periodic Table with A/Z=5,545,95 at energies of 0.9-1.1 MeV/nucleon. The focusing system of injection line consists of a solenoidal lens and a quadrupole lens situated between the ECR and the 90°magnet, also three solenoids placed in the vertical part of the injection channel. Spiral inflector is installed into the center of the accelerator. The accelerated beam extraction system consist of electrostatic deflector and two focusing magnetic channels. In routine operation IC100 provides intensities of the $^{86}Kr^{+15}$ and $^{132}Xe^{+23}$ ion beams up to 3 μA.

Special-purpose beam transportation line with polymer film irradiation unit and beam scanning system has been created as well as a box for heavy ion beam research.

ISBN 978-3-95450-167-0

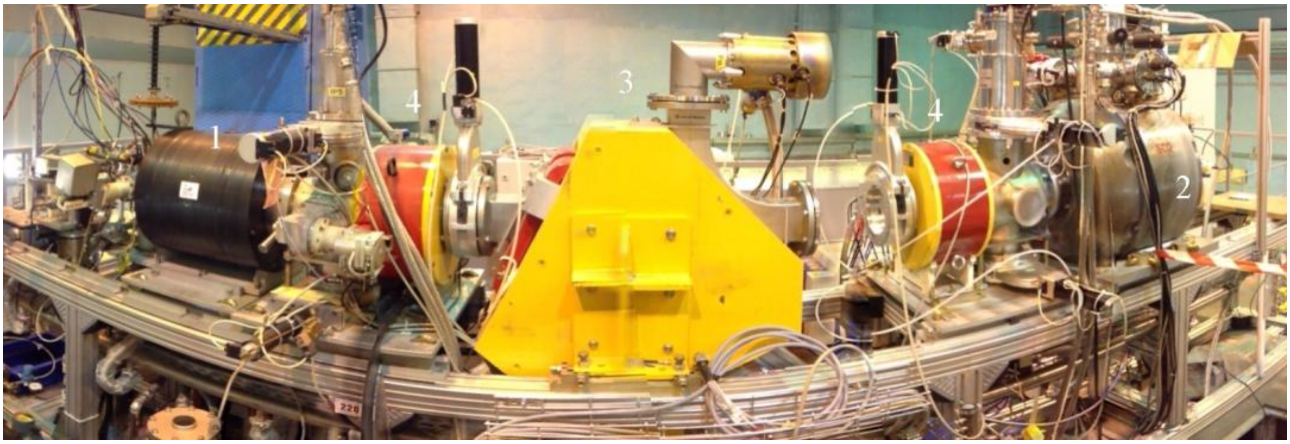

Figure 4: DECRIS-2 (1) and DECRIS-SC2 (2) ion sources at the U400M injection, where (3) is the analysing magnet, (4) is the focusing solenoids.

DC280 CYCLOTRON

The new accelerator will significantly increase the potential of the existing accelerator complex of the FLNR. The DC280 cyclotron designed at the Flerov Laboratory of Nuclear Reaction of the Joint Institute for Nuclear Research in Dubna (FLNR, JINR, Dubna) is intended for carrying out fundamental and applied investigations with ions from He to U (masses from A = 2 up to 238) produced by ECR sources (Fig. 5).

The DC280 will be the basic facility of the Super Heavy Element Factory (SHEF) that is being created at the FLNR. The energy of the ions extracted from the cyclotron may vary from 4 up to 8 MeV/amu. The expected intensity of extracted beam at DC280 is 10 pμA for ions with masses up to 50 [5]. In according to FLNR plans the cyclotron has to be assembled in the period from 2016 to 2017. The cyclotron commissioning will be in the end of 2017 [7].

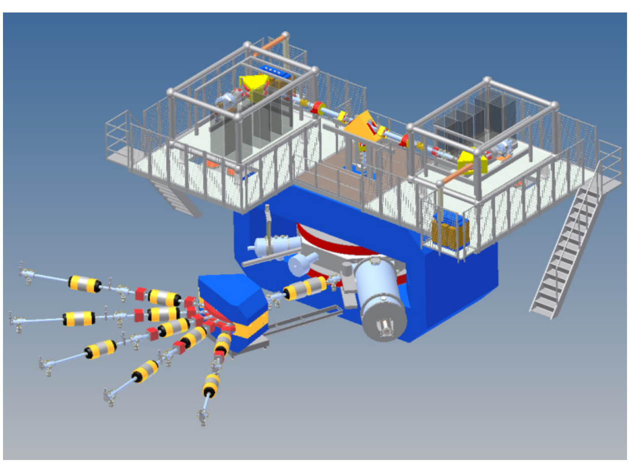

Figure 5. Layout of the DC-280 assembling.

CONCLUSION

The Flerov Laboratory plans implies essential development of the cyclotron complex to 2023.

ACKNOWLEDGMENT

The authors would like to thank the excellent technical support from the FLNR JINR cyclotrons staff.

REFERENCES

[1] G. Gulbekyan, B. Gikal, S. N. Dmitriev, S. L. Bogomolov, O. N. Borisov, I. A. Ivanenko, N. Yu.Kazarinov, V. I. Kazacha, I. V. Kalagin, N.F. Osipov, A. V Tikhomirov, and J. Franko, “Development of FLNR JINR heavy ion accelerator complex in the next 7 years. Project of new DC-280 cyclotron”, in *Proc. PAC’11*, San Sebastian, Spain, 2011, pp. 2700-2702.

[2] G. Gulbekian and CYCLOTRONS Group, “Status of the FLNR JINR Heavy Ion Cyclotrons” in *Proc. 14 Int. Conf. on Cyclotrons and their Applications*, Cape Town, South Africa, 1995, pp. 95-98.

[3] S. Bogomolov, A. Bondarchenko, A. Efremov, K. Kuzmenkov, A. Lebedev, K. Lebedev,V. Lebedev, V. Loginov, N. Yazvitsky, Z. Asfari, and B.JP. Gall, “Production of ion beams from ECR ion sources by MIVOC method”, in *Proc. RuPAC’14*, Obninsk, Russia, 2014, pp. 432-434.

[4] I. V. Kalagin, G. G. Gulbekyan, B. N. Gikal, S.V. Mitrofanov, V.A. Skuratov, Yu.G. Teterev, and V.S. Anashin, “Using the FLNR accelerator complex for SEE testing. State of art and future development”, in *Proc. RADECS’15*, Moscow, Russia, 2015, pp. 278-283.

[5] G. Gulbekyan, B. Gikal, S. N. Dmitriev, S. L. Bogomolov, O. N. Borisov, I. A. Ivanenko, N. Yu.Kazarinov, V. I. Kazacha, I. V. Kalagin, N. F. Osipov, A. V. Tikhomirov, and J. Franko, “Development of FLNR JINR Heavy Ion Accelerator Complex in the Next 7 Years. Project of New DC-280 Cyclotron”, in *Proc. PAC’11*, San-Sebastian, Spain, 2011, pp. 2700-2702.

[6] S.Bogomolov *et al.*, “Resent development in ECR ion sources at FLNR JINR”, in *Proc. RuPAC’12*, Saint-Petersburg, Russia, 2012, pp. 203-207.

[7] G. G. Gulbekian, S. N. Dmitriev, Yu. Ts. Oganessian, B. N. Gikal, I. V. Kalagin, S. L. Bogomolov, I. A. Ivanenko, N. Yu. Kazarinov, G. N. Ivanov, N. F. Osipov, “Status of the DC-280 cyclotron project”, presented at the 21st Int. Conf. on Accelerators and their Applications, Zurich, Switzerland, Sep. 2016, paper THP25, this conference.

STATUS OF THE TEXAS A&M UNIVERSITY CYCLOTRON INSTITUTE*

D.P. May, J.E. Ärje, L.N. Gathings, B.T. Roeder, F.P. Abegglen, G. Chubaryan, H.L. Clark, G.J. Kim, G. Tabacaru, A. Saastamoinen, Texas A&M University, College Station, Texas, USA

Abstract

Both the K500 superconducting cyclotron and the older K150 (88”) conventional cyclotron at the Texas A&M University Cyclotron Institute are in constant use for both experimental physics and chemistry as well as for customer-based, radiation-effects testing. In addition, an upgrade program using the K150 as a driver for the production of radioactive beams to then be accelerated to intermediate energies by the K500 Cyclotron is ongoing. Both a light-ion guide and a heavy-ion guide are being developed for this purpose. The status of the cyclotrons and of the associated electron-cyclotron-resonance ion sources (ECRIS) and the H-minus ion source used on the K150 as well as the status of the upgrade are presented.

INTRODUCTION

The Texas A&M K500 superconducting cyclotron was commissioned in 1988, while the Texas A&M K150 cyclotron (formerly the 88”) was recommissioned in 2007. Beams are injected into each cyclotron by dedicated ECR ion sources, while a negative hydrogen/deuterium source injects into the K150, as well. Figures 1 and 2 are representations of the beams run by the K500 and K150, respectively. Figure 3 demonstrates the division of K500 time in the last three years devoted to nuclear physics and nuclear chemistry (8684 hrs.) and to outside use (9567 hrs.), mainly consisting of computer-chip single-event-effects (SEE) testing by a variety of satellite and avionic concerns. In addition, there is an ongoing effort to develop a K500+K150 radioactive-beam capability which will supplement the radioactive beams provided by the momentum-achromat-recoil spectrometer (MARS) [1].

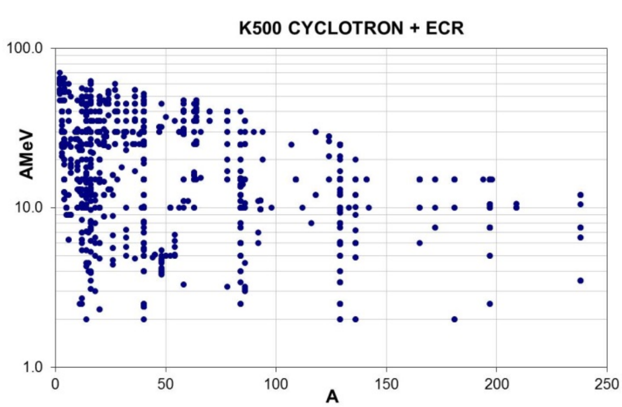

Figure 1: Beams run to date by the K500.

*Work supported by U. S. Dept of Energy Grant DE-FG02-93ER40773

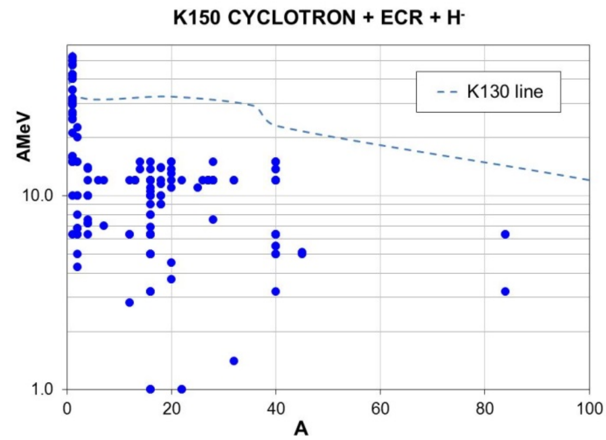

Figure 2: Beams run to date by the K150.

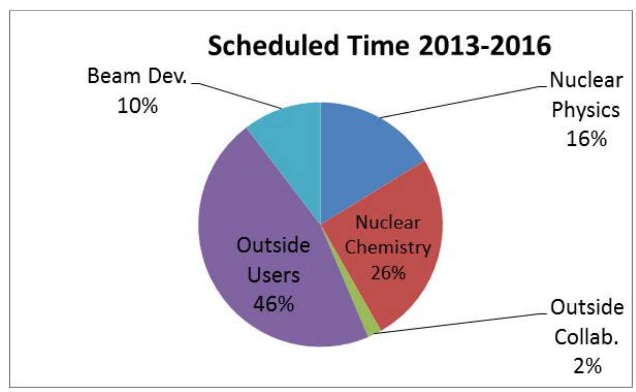

Figure 3: Division of K500 scheduled time.

CYCLOTRONS

The K500 and its injector 6.4 GHz ECRIS (ECR1) continue to operate well, averaging 6212 hours per year of beam-on-target over the last three years. The central inflector was replaced recently with a new one with electrodes fabricated from aluminum. The older tantalum electrodes showed considerable wear from heavy-ion sputtering.

The K150 has just recently come into extensive use although it still suffers from poor vacuum (3 X 10^{-6} torr) since the installed cryopanel remains unconnected to a coolant supply. As previously reported [2] K150 beams are tuned using the trim-coil program CYDE with field maps generated by TOSCA. An analysis of the field by TOSCA with the rectangular yoke included does not yield an appreciable first harmonic in the acceleration region, but both the middle-radius harmonic coils, valley coils 3 and 4, are extensively used for tuning in addition to the central and extraction harmonic coils, valley coils 1 and 5.

ISBN 978-3-95450-167-0

The injector H-minus source for the K150 has operated well with occasional filament replacements and also with the replacement of the filter region permanent magnets which had eroded in their cooling water. The operation of the 14.5 GHz injector ECRIS (ECR2) for the K150 was considerably stabilized with the replacement of the stainless-steel, injection-end flange with one fabricated from copper. A high-temperature oven, similar to one constructed for the LBL VENUS ECRIS [3], has been constructed for this source (see Fig. 4). A crucible fabricated with a tantalum tube is clamped between two water-cooled current leads with current supplied by a 150 Ampere, low-voltage power supply. The oven is mounted axially on a dedicated injection flange. The temperature capability has allowed a beam of titanium to be developed for the source.

Figure 4: The copper clamps and the detached, tantalum crucible for the high-temperature oven.

THE SEE PROGRAM

At present both cyclotrons provide beam for the SEE program, the K500 since 1995 and the K150 only recently. A test station has been installed in the K150 vault for SEE mainly with protons, while a dedicated cave has been outfitted with a test station for K500 beams. Users are interested in the effects of ion beams on individual electronic components, and for this purpose they need a broad variety of beams that can be uniformly spread across the area of a device. Suites of beams at various energies have been developed to provide an array of linear-energy-tranfer (LET) capabilities on-target at low fluxes (10^3 pps/cm^2 or less). To this end three suites of beams have been developed for the K500. The first suite at 15 AMeV consists of alphas, nitrogen, neon, argon, copper, krypton, silver, xenon, holmium, tantalum and gold. The second at 25 AMeV consists of alphas, nitrogen, neon, argon, krypton, silver and xenon. The third at 40 AMeV consists of nitrogen, neon, argon and krypton-78. The energy of these beams allows for a uniform LET across the depth of the device with in-air testing.

Figure 5 shows the test station. Beams can be delivered with a high degree of uniformity over a 1.8" x 1.8" cross sectional area for measurements inside the vacuum chamber and 1" diameter circular cross sectional area for the in-air station. Uniformity is achieved by using a scintillator-detector array. A degrader-foil system makes it possible to set the desired beam LET value at a particular depth inside the target without changing the beam or rotating the target. The beam energy is reduced by means of a degrader system with foils having a suitable thickness and orientation with respect to the incident beam.

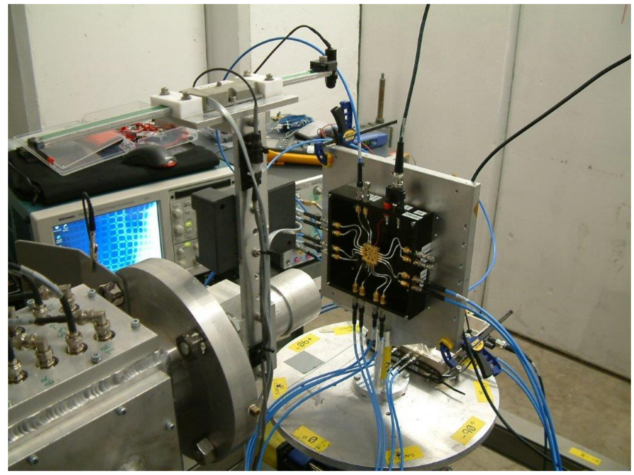

Figure 5: SEE Test station with in-air set-up.

Charge-states for ions in each suite are chosen so that the charge-to-mass ratios (Q/M) are closely grouped so that only small changes in the cyclotron trim-coils and main coil need to be made between the various beams while the cyclotron frequency is left fixed. To save time between beam changes within each suite the injection line which uses only magnetic components is left fixed, and the extraction-voltage of ECRIS is varied to match those components. As a consequence the injected beam energy does not exactly match the inflector/central-region geometry. The time-savings for beam changes is more important to the users than the consequent reduction in flux on target. In fact low flux is usually required, and this is controlled by via attenuators in the injection line.

All the beams from solid materials in these suites are provided by sputtering into the ECRIS. An eight-lead high-voltage feed-through is positioned through a radial port. To switch between solids requires just changing leads and applying the sputtering voltage.

ACCELERATED RIB PROGRAM

Light-Ion Guide

Progress has been made toward a better understanding of the parameters that go into successful operation of the light-ion-guide/charge-breeding ECRIS system (LIG/CB-ECRIS). The flux of radioactive ions from the LIG has continued to improve, and the charge-breeding of radioactive ions has been detected. Recently a short, two-stage sextupole (see Fig. 6) following the design of the University of Jyväskylä Cyclotron Laboratory was installed [4]. An 8mm diameter aperture between the stages blocks a majority of the helium flow from the target cell, and two apertures in the acceleration region further reduce this flow. Figure 7 shows the LIG/CB-ECRIS up through the 90° analysing magnet. The charge-bred ions are directed

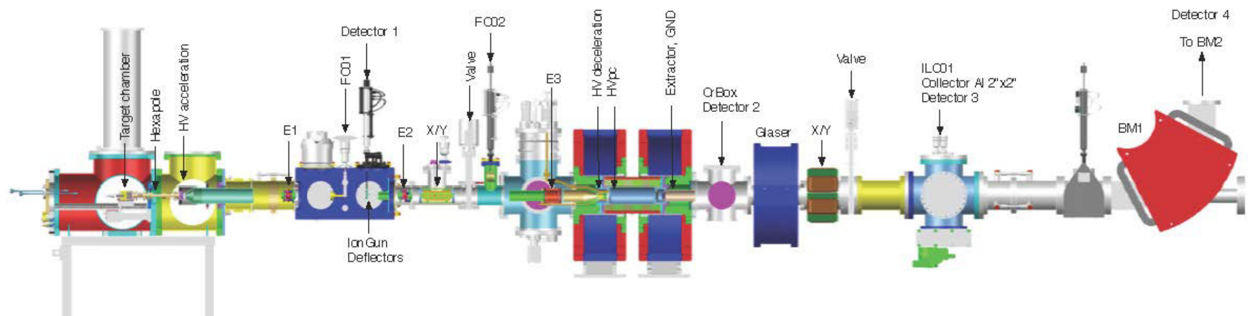

Figure 7: The LIG/CB-ECRIS line from the target-cell chamber to the 90-degree analyzing magnet.

vertically above the shielding for eventual injection into the K500 cyclotron. The target chamber and sextupole are held at high voltage so that exiting ions are accelerated by a grounded puller.

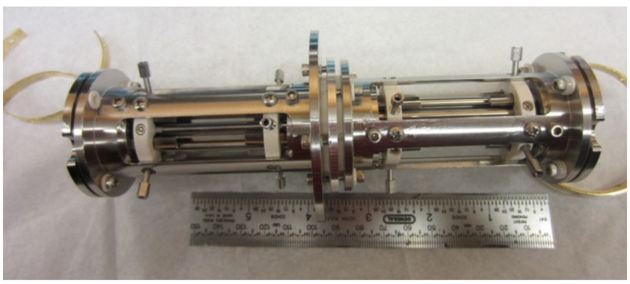

Figure 6: The sextupole.

Two detection stations for betas, each consisting of a rotatable aluminum foil and a shielded silicon detector, were placed in the beam-line, one at a point approximately half-way between the acceleration region and the entrance of the CB-ECRIS and another at a point immediately down-stream of the CB-ECRIS puller. Measurements using a 4.0 μA proton beam and a ^{64}Zn target producing ^{64}Ga via (p,n) gave a calculated flux of 2 x 10^4 pps at the first detection station, although if the beam is not tightly focused on the foil the geometric detection efficiency may be lower, and the actual flux may be higher. For the purpose of determining conditions for charge-breeding of ions coming from the LIG, the one-plus alkali ion source was mounted perpendicular to the beam line in the chamber midway between the LIG and the CB-ECRIS. An electrostatic 90° deflector was mounted in the chamber to steer the ions in the direction of the CB-ECRIS. An aperture was machined into the positive plate to allow passage of the LIG beam. Rubidium from this source could be successfully charge-bred with this system.

Tests with the charge-breeding of the 64Ga beam from the LIG have produced high charge-states, the peak of the distribution being a measured flux of 64Ga12+ at 23 pps with a much lower intensity proton beam. LIG tests with a radioactive thorium source also have yielded a charge-bred beam of 220Rn with a maximum charge of 29+. The fluxes are low at present. One indication of a problem is a measured wide range (~100 volts) of voltage difference between the LIG and the CB-ECRIS in addition to a measured peak of this ΔV at a much higher voltage than for the charge-bred rubidium. This energy degradation and spread of the LIG beam could be due to excess helium gas from the target cell in the accelerated-beam region.

Heavy-Ion Guide

Significant progress has been made in the design and construction of the beam transport system for the heavy-ion guide. To capture radioactive species after the heavy-ion-guide gas catcher and direct them to the different devices, a complex RFQ system has been designed and constructed. The RFQ system consists of a 30 cm long DC-drag cooling RFQ located immediately after the gas catcher's exit hole at a relatively high helium gas pressure zone and a micro-RFQ mounted at the end of the DC-drag cooling RFQ. The micro-RFQ is 2 cm long and has a 4.5 mm exit hole, which is necessary to ensure efficient differential pumping. The micro-RFQ can be coupled individually with three other DC-drag RFQs which are mounted inside a large vacuum chamber on a remotely controlled position system. Two curved RFQs deliver radioactive ions either horizontally to the CB-ECRIS injection line or vertically above the shielding to a superconducting solenoidal Penning trap. Additionally there is a third straight section RFQ that leads to an ortho-time-of-flight (Ortho-TOF) mass spectrometer and a fourth 90° port that points directly to the CB-ECRIS ion source for tuning the injection line with 1+ alkali ion sources.

Logistical problems up to now have prevented the installation of the superconducting solenoidal spectrometer BIGSOL in line with the heavy-ion target cell. For initial testing purposes it has been proposed to use the products from a radioactive ^{252}Cf source.

Pilot-Beam Technique for Acceleration and Transport

Pilot-beams techniques for the acceleration of low flux beams from the CB-ECRIS by the K500 have been explored using the K500 main field to distinguish between species [2]. To prepare for the acceleration and transport to target of extremely low flux radioactive beams, a test was performed using the rf frequency to distinguish between a high and a low-flux beam. A 14 AMeV $^{16}O^{3+}$ (Q/M =.1876, f =12.237 MHz) beam from the CB-ECRIS was tuned in the K500 and transported to a focus at the entrance of MARS. A charge-bred beam of $^{85}Rb^{16+}$

ISBN 978-3-95450-167-0

(Q/M=.1885) mixed with the beam of $^{16}O^{3+}$ was then accelerated in the K500 by raising the rf frequency by 56 kHz. Since all the magnetic components up to the target remained the same, the $^{85}Rb^{16+}$ beam appeared as a focused spot on target. The spectrometer with a silicon-detector telescope in the focal plane, which had been calibrated previously with a 14 AMeV $^{84}Kr^{16+}$ beam, was used to identify the beam as rubidium.

While observing the $^{16}O^{3+}$ beam with a PMT-Scint detector at the MARS focal plane, a 12 kHz shift in the rf was needed to eliminate the beam. So it appears that ions with Q/M differences of less than about one part in 10^{-3} cannot be cleanly separated by the cyclotron. In these cases stripping of the accelerated beam can possibly allow different species to be separated in the beam-line.

FUTURE PROGRESS

The programs at the Cyclotron Institute remain healthy, and with performance improvements in the operation of the K150 the SEE program will expand and the radioactive beam program will be fully supported with driver beams.

REFERENCES

[1] R.E. Tribble, R.H. Burch and C.A. Gagliardi, Nucl. Instrum. and Meth. A 285 (1989) 441.

[2] D.P. May, B.T. Roeder, R.E. Tribble, F.P. Abegglen, G. Chubaryan, H.L. Clark, G.J. Kim, G. Tabacaru, and J. Ärje, "Progress toward the facility upgrade for accelerated radioactive beams at Texas A&M" in *Proc. 20th Int. Conf. on Cyclotrons and their Applications (CYC'13),* Vancouver, Canada, Sept. 2013, p. 22.

[3] T.J. Loew, S.R. Abbott, M.L. Galloway, D. Leitner, C. M. Lyneis, "Design of a high temperature oven for an ECR source for the production of uranium ion beams", in *Proc. of the 22nd Particle Accelerator Conference (PAC'07)*, Albuquerque, NM, USA, June 2007, p.1742.

[4] P. Karvonen, I. D. Moore, T Sonoda, T Kessler, H. Penttila, K. Peräjä, P Ronkanen and J. Äystö, https://arxiv.org/pdf/0806.1135.pdf

THE S2C2: FROM SOURCE TO EXTRACTION

J. Van de Walle*[1], M. Abs[1], M. Conjat[2], E. Forton[1], S. Henrotin[1], Y. Jongen[1], W. Kleeven[1], J. Mandrillon[1,2], P. Mandrillon[1], P. Verbruggen[1]
[1] Ion Beam Applications, Louvain-la-Neuve, Belgium
[2] AIMA, Nice, France

Abstract

The superconducting synchro-cyclotron (S2C2) is the new compact 230 MeV proton cyclotron which will be used in the ProteusONE® proton therapy solution by Ion Beam Applications (IBA). Apart from being the first constructed superconducting cyclotron at IBA, the S2C2 is also the first synchro-cyclotron at IBA. In order to study the beam dynamics in this type of accelerator, new computational tools had to be developed which deal with the much larger number of turns compared to IBA's isochronous cyclotrons, the characteristic longitudinal capture in the central region and the regenerative extraction mechanism. This contribution is structured in four parts. In a first part, the general properties of the S2C2 are discussed (magnetic field, RF frequency, tune, ...). The three following parts discuss in detail the injection, acceleration and extraction.

GENERAL PROPERTIES

The S2C2 is a weak focusing cyclotron with a central field of 5.75 T. The average field as a function of radius is shown in Fig. 1(top). The bottom panel of Fig. 1 shows the

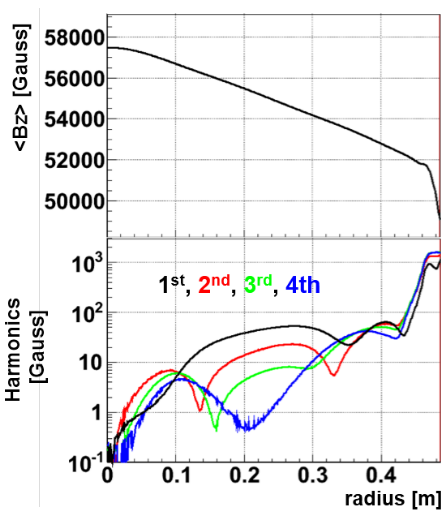

Figure 1: Average magnetic field (top) and first four harmonic components of the magnetic field (bottom) as a function of radius.

first four harmonic components. The first harmonic dominates between the center and 40 cm, whereas all harmonics rise drastically beyond 45 cm due to the presence of the extraction elements, which induce a localized field bump of 1 Tesla. The horizontal and vertical tunes (ν_r and $2\nu_z$) of

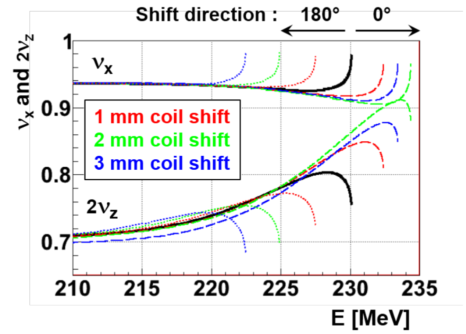

Figure 2: The horizontal tune (ν_r) and twice the vertical tune ($2\nu_z$) as a function of energy for different main coil positions. Black = nominal position, dashed colored = shift away from the regenerator, dotted colored = shift towards the regenrator.

the S2C2 are shown in Fig. 2 as a function of energy and for different horizontal positions of the superconducting main coil. As can be seen, the Walkinshaw resonance (ν_r=$2\nu_z$) is crossed when the coil is shifted by >2mm away from the regenerator. The precise horizontal main coil positioning is crucial to avoid the Walkinshaw resonance and determines the extracted beam energy (when ν_r=1).

The RF frequency varies from around 90 to 60 MHz, covering the injection and extraction frequencies at 87.6 and 63.2 MHz, resp. One full RF frequency cycle (1 ms) is shown Fig. 3.

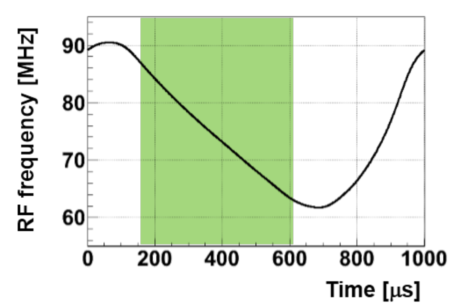

Figure 3: One period (1 ms) in the RF frequency cycle. The acceleration period is indicated in green and lasts about 450 µs.

Figure 4 shows a magnetic field map in the median plane and the position of the regenerator, the septum, the extraction channel and the yoke penetrations for the three horizontal tie rods.

* jarno.vandewalle@iba-group.com

ISBN 978-3-95450-167-0

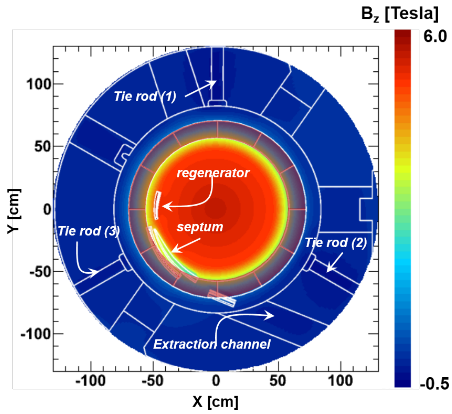

Figure 4: Complete magnetic field map (measured + simulated). Positions of the regenerator, the tie rod yoke penetrations, the septum and the extraction channels are shown.

INJECTION

Due to the small injection energy and the high central magnetic field, the first turn in the S2C2 has a radius of only 3 mm. Figure 5 shows the off-centering of protons after 30 turns in the S2C2 as a function of their initial RF phase at injection. The RF phase convention is shown in the inset. During injection, the phase acceptance ranges from 20 to 90 degrees. During acceleration, the stable phase range is 20 to 260 degrees, as determined by the separatrix. When the source is perfectly centered, the orbit centering is not dependent on the initial RF phase, nor on the applied dee voltage. When the source is shifted by 1 mm, the orbit centering depends strongly on the initial RF phase and on the applied dee voltage (see Fig. 5 - open symbols). The bottom panels of Fig. 5 shows the beam profile at the end of the "energy selection system" in the gantry of the ProteusONE® system. At this position, the dispersion is maximized and we have a good image of the energy distribution in the beam (≈130 keV/mm). The open and filled symbols refer to an off-centered and centered source, resp. The mean energy shifts by about 160 keV and the energy spread is higher for an off-centered source. The top panel of Fig. 6 shows the distribution of the protons in the stable separatrix at 3 MeV, or, equivalently 8 µs after the reference time, defined as the time when the RF frequency equals the cyclotron frequency in the center of the S2C2. The lower panel shows the relative time (with respect to the reference time) at which the proton was captured at the source. The total capture time is ≈6 µs and protons which are captured "late", reside near the borders of the separatrix and risk to fall out of the stable separatrix, if the total "bucket area" reduces during acceleration.

ACCELERATION

A synchronous proton will make ≈40000 turns in the S2C2 from the source up to extraction. With the "Advanced Orbit Code" (see [1] and [2]), the equations of motion are integrated precisely as a function of time. The precision of the integration process comes at the cost of high computation

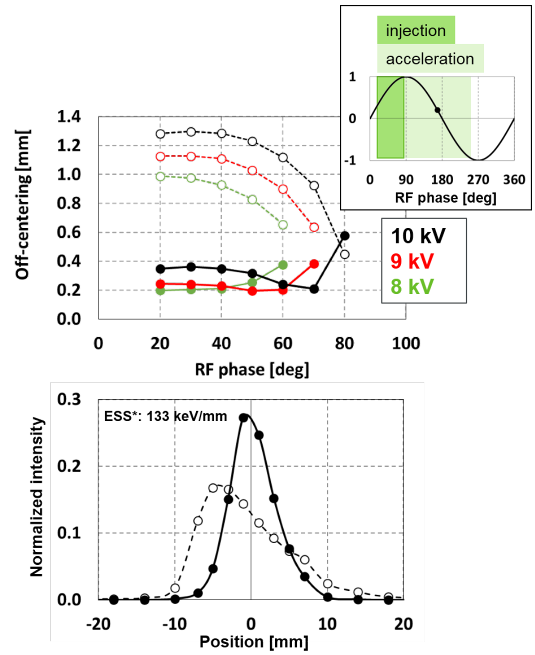

Figure 5: (Top) Orbit off-centering as a function of dee voltage and source position : (filled symbols) centered source (open symbols) 1 mm shifted source. The inset shows the accepted RF phase range at injection and during acceleration. (Bottom) energy distribution at the end of the Energy Selection System (*ESS) in the gantry.

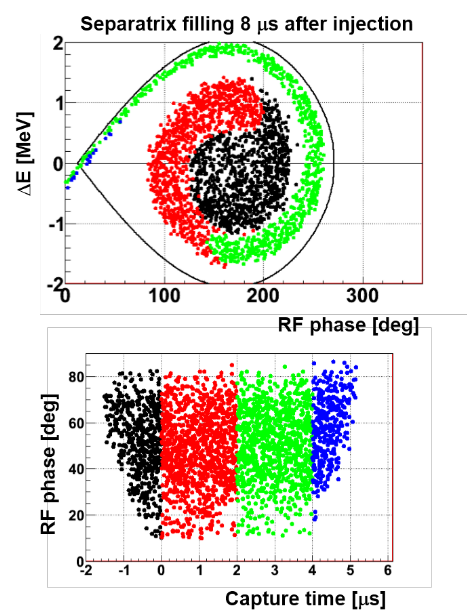

Figure 6: (Top) Filling of the longitudinal separatrix at 3 MeV. (Bottom) the accepted RF phases at injection as a function of the relative injection time. The color codes indicate the link between capture time and position inside the separatrix.

time. Simulating a statistically relevant amount of protons in order to deduce beam properties or to study the impact of

ISBN 978-3-95450-167-0

perturbations in the S2C2 (radial fields, magnetic harmonics, source shifts, etc ...) would require too much time. Therefore, a new code was developed which tracks only the relevant parameters during acceleration: the RF phase, the energy and the orbit center coordinates. This code is referred to as the "phase motion code". The equations of motion for the energy and RF phase are :

$$\frac{dE}{dt} = eF_{RF}V_{RF}sin(\phi) \quad (1)$$

$$\frac{d\phi}{dt} = 2\pi(F_{RF} - F_p) \quad (2)$$

where E and e are the kinetic energy and charge of the proton, F_{RF} is the RF frequency, F_p the revolution frequency of the proton, V_{RF} the RF voltage and ϕ the RF phase of the proton. One proton was simulated in AOC from the source up to extraction (calculation time ≈30 min). The properties of the proton, 10 µs after initial capture were input as initial conditions to the "phase motion" code. The energy as a function of time, calculated with "AOC" and "phase motion" is shown in Fig. 7 in black and red (resp.) and the similarity is good. The equations of motion for the orbit

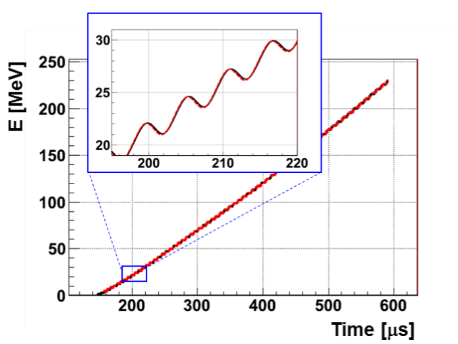

Figure 7: Calculated evolution of the proton energy versus time : (black) "AOC" (red) "phase motion". See text for details.

center coordinates (x_c and y_c) in "phase motion" are derived from the following Hamiltonian (see [3])

$$\begin{aligned} H(x_c, y_c) &= \frac{1}{2}(\nu_r - 1)(x_c^2 + y_c^2) \\ &+ \frac{r}{2}(A_1x_c + B_1y_c) + [D_3x_c + D_4y_c][x_c^2 + y_c^2] \\ &+ \frac{1}{4}(A_2 + \frac{1}{2}A_2')(x_c^2 - y_c^2) + \frac{1}{2}(B_2 + \frac{1}{2}B_2')x_cy_c \\ &+ \frac{1}{48r}(D_1[4x_c^3 - 3x_c(x_c^2 + y_c^2)] + D_2[3y_c(x_c^2 + y_c^2) - 4y_c^3]) \\ &+ O(4) \end{aligned}$$

where the first line includes parameters related to the average field, the second, third and fourth line include parameters related to the first, second and third harmonics (and their derivatives, see [3]). The result of the integration of the equations of motion derived from the above Hamiltonian is shown in Fig. 8. The figure compares the orbit center coordinates of all stable closed orbits (green line), the orbit center evolution of an accelerated proton calculated in AOC (black line) and the orbit center coordinates integrated in the "phase motion" code (red line). In the top figure, the average field and the first harmonic are taken into account, in the bottom figure also the second and third harmonics are taken into account in the "phase motion" code. This illustrates that the evolution of the orbit centers in the S2C2 is fully determined by the first harmonic and the average field up to around 225 MeV. Beyond this energy, more harmonics need to be taken into account to accurately describe the evolution of the orbit center, illustrating the effect of the regenerator (see also Fig. 1) and the instability of the orbit center when approaching the $2\nu_r$=2 resonance. The phase motion code

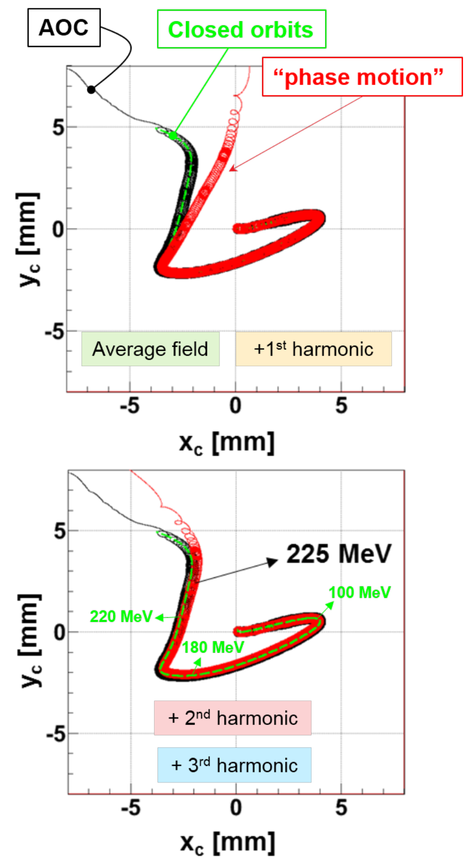

Figure 8: (Green) closed orbit centers for all energies. (Black) evolution of the orbit center for a proton simulated in AOC from source to extraction. (Red) evolution of the orbit center, calculated in "phase motion", with initital conditions at 3 MeV taken from AOC : (top) average field and first harmonic (bottom) second and third harmonic also included.

allows to study what happens to a proton which falls out of the stable separatrix, since the beam properties can be tracked over several RF frequency sweeps (ms range). Figure 9 shows how the energy of such a lost proton fluctuates over two RF frequency sweeps. Clearly, when the RF frequency equals the revolution frequency of the proton, the energy changes resonantly, but the proton is not recaptured

ISBN 978-3-95450-167-0

in the stable separatrix. The bottom part of Fig. 9 shows a statistical distribution of the energy gained or lost by a proton when the RF frequency equals its revolution frequency. The blue and red curves correspond to energy changes on the falling and rising edge of the frequency curve, resp. On average, energy is lost on the falling edge and energy is gained on the rising edge. Since the dee voltage is set to a lower value when the frequency is rising, the effect of energy gain is minimized and on average there is no energy gain.

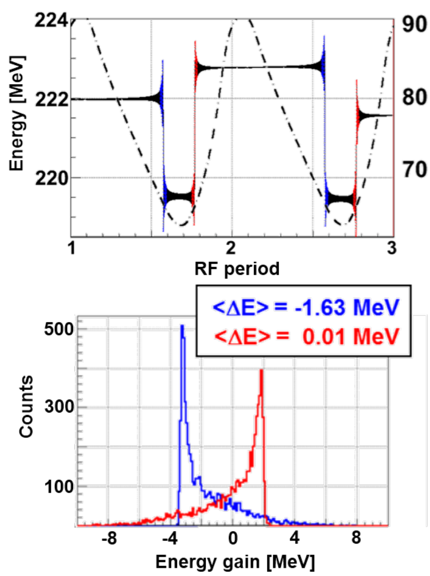

Figure 9: (Top) evolution of the energy of a lost proton during 2 RF frequency cycles. (Bottom) statistical energy change of the proton over 20 RF frequency cycles on the falling and rising frequency flank (blue and red, resp.).

EXTRACTION

Before the beam can be extracted from the S2C2, the main coil has to be aligned vertically in order to eliminate radial fields in the median plane. From AOC simulations, we deduced a position inside the S2C2 where the radial orbit displacement near extraction is maximized and the effect of a vertically misaligned coil is seen in the last turn of the proton. Figure 10 shows a comparison of two irradiated gafchromic films inside the S2C2 where the coil was 0.5 mm too low (middle) and well aligned (top). The bottom figure shows the simulated (AOC) effect of a 0.5 mm vertically misaligned coil on the vertical displacement of the last turn. The observation of the linearity between vertical displacement of the last turn at this position in the S2C2 and the vertical coil displacement facilitates the vertical alignment of the coil.

From Fig. 9 it is clear that "lost protons" can gain enough energy to be extracted on the rising edge of the frequency curve, on the condition that they are lost close to the extraction energy. The latter condition was achieved experimentally by dropping the dee voltage very close to extraction. Figure 11(top) shows a "standard" dee voltage profile where the dee voltage is lowered at the minimum RF frequency

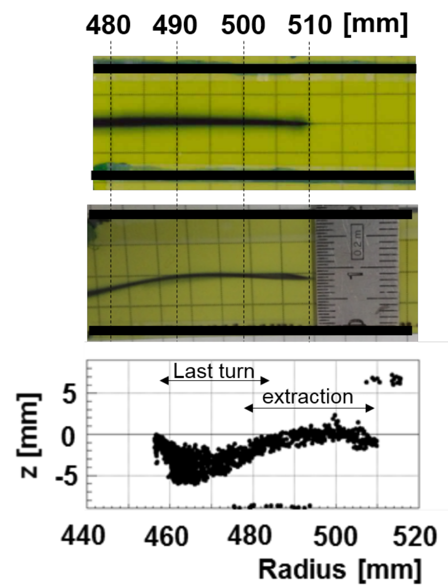

Figure 10: Measured (top) and simulated (bottom) vertical displacement of the beam in the last turn due to a 0.5 mm vertical misalignment of the main coil.

(green) and one profile, where the dee voltage is lowered very close to the extraction frequency (red). The signal observed on a "poly crystalline diamond probe" (pCVD, see [4] and [5]) is shown in the lower 2 panels of Fig. 11. With a "standard" dee voltage profile, beam is observed only at the extraction frequency on the falling edge (middle panel of Fig. 11). When the dee voltage is dropped close to extraction, two small peaks are observed around the "normal" extraction frequency. Consistent with the results of the phase motion code, protons are extracted at the extraction frequency on the rising edge of the frequency curve. The second peak before the extraction frequency are "lost protons" which get extracted because of a resonance in their orbit center coordinates (=emittance blow up in the S2C2). This can be understood from the equations of motion of the orbit center coordinates, which have the form

$$\frac{dx_c}{dt} = (\nu_r - 1)y_c + \alpha x_c + \beta y_c + \ldots$$
$$\frac{dy_c}{dt} = (\nu_r - 1)x_c + \alpha' x_c + \beta' y_c + \ldots$$

where the coefficients α,β,α' and β' contain harmonic components of the magnetic field, which are related to the energy via the radius on which the harmonics are evaluated and the magnetic rigidity of a proton at that radius. In first order, the orbit center oscillates with a frequency equal to $(\nu_r\text{-}1)F_p$ and the energy (and thus the coefficients α,β,α' and β') oscillates with a frequency equal to $F_{RF}\text{-}F_p$. A resonance can occur when

$$F_{RF} = F_p \pm (\nu_r - 1)F_p$$

In AOC and phase motion, such a resonance of the orbit center was indeed observed. The AOC calculation is shown

ISBN 978-3-95450-167-0

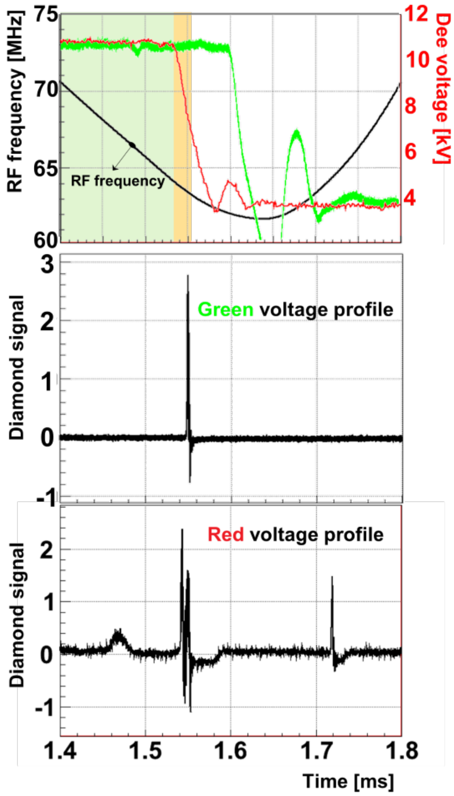

Figure 11: (Top) The frequency curve and two dee voltage profiles. (Middle) Extracted beam for the "standard" dee voltage profile. (Bottom) Extracted beam for the "red" voltage profile. See text for details.

in Fig. 12, where the proton is extracted due to instability of its orbit center exactly at the RF frequency corresponding to $F_{RF}=F_p+(\nu_r-1)F_p$.

With the knowledge of what happens to "lost protons", an effort was made to avoid at all cost that protons are lost near extraction. This is accomplished by keeping the total bucket area increasing or constant during the acceleration.The bucket area is calculated with the following input parameters: the measured dee voltage, the measured derivative of the RF frequency and a variety of derived quantities from a closed orbit analysis (relation between F_p, energy, time, etc ...). Combining results from AOC calculations in the central region, "phase motion" calculations from 3 MeV to 225 MeV and AOC calculations from 225 MeV to extraction, all extracted beam properties can be calculated. Table 1 compares measured and calculated extracted beam properties.

CONCLUSION

In order to study the extracted beam properties of the S2C2 we have developed different computational tools. These new tools have enabled us to study the orbit centering and its impact on the extraction process and have given new insights in the evolution of protons which fell out of the stable bucket area during acceleration. The acquired in-

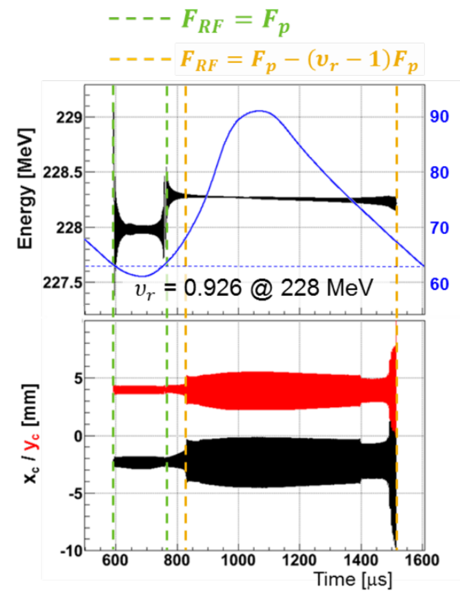

Figure 12: AOC simulation of a lost proton close to extraction : (top) energy resonances when the RF frequency equals the revolution frequency of the proton and (bottom) resonances in the orbit center coordinates, leading to extraction due to orbit center instability.

Table 1: Measured and Simulated Extracted Beam Properties

Property	simulated	measured
Energy spread	150 keV	≈400 keV
$\Delta E/\Delta I_{coil}$	440 keV/A	440 keV/A
ΔE/(mm source shift)	200 keV/mm	≈200 keV/mm
Pulse duration	8 µs	8 µs
Extraction efficiency	50 %	≈35 %
Horizontal emittance	20 π mm mrad	23.2 π mm mrad
Vertical emittance	4 π mm mrad	3.2 π mm mrad

depth understanding of beam dynamics inside the S2C2 is important to make it a reliable and controlled medical accelerator.

REFERENCES

[1] W. Kleeven *et al.*, "AOC, A Beam Dynamics Design Code for Medical and Industrial Accelerators at IBA", in *Proc. IPAC'16*, paper TUPOY002.

[2] W. Kleeven *et al.*, "Overview of Recent Progress of Simulations for Cyclotrons", presented at Cyclotrons'16, Zurich, Switzerland, Sep. 2016, paper WEA01, this conference.

[3] H.L. Hagedoorn and N.F. Verster, NIM **18,19** (1962) p.201-228

[4] J. Van de Walle *et al.*, "A Diamond Detector Test Bench to Assess the S2C2 Beam Characteristics", presented at Cyclotrons'16, Zurich, Switzerland, Sep. 2016, paper MOP19, this conference.

[5] Cividec, `https://cividec.at`

ISBN 978-3-95450-167-0

THE IONETIX ION-12SC COMPACT SUPERCONDUCTING CYCLOTRON FOR PRODUCTION OF MEDICAL ISOTOPES

J. Vincent, G. Blosser, G. Horner, K. Stevens, N. Usher, X. Wu, Ionetix Corporation, Lansing, Michigan, USA
S. Vorozhtsov, V. Smirnov, Joint Institue for Nuclear Research, Dubna, Russia

Abstract

A 12.5 MeV, 25 μA, proton compact superconducting cyclotron for medical isotope production has been produced. The machine is initially aimed at producing 13N ammonia for Positron Emission Tomography (PET) cardiology applications. With an ultra-compact size and cost-effective price point, this system offers clinicians unprecedented access to the preferred radiopharmaceutical isotope for cardiac PET imaging. A systems approach that carefully balanced the subsystem requirements coupled to precise beam dynamics calculations was followed. The system is designed to irradiate a liquid target internal to the cyclotron and to minimize the unnecessary radiation. The scientific design of the machine has been described elsewhere.[1] The overall engineering, construction, commissioning, and experience at the first customer site will be described here.

INTRODUCTION

An ultra-compact, 12.5 MeV, proton, isochronous, sector focused, superconducting cyclotron for medical isotope production has been produced and large scale manufacturing is being ramped up. The cyclotron is designed to be auto-tuned and does not require a skilled dedicated operating or maintenance staff. As shown in Figure 1, the first installation on the customer site occurred on January 30, 2016 at the University of Michigan followed by the first production of N13 on February 28, 2016. The machine features a patented cold steel yoke and pole design [2] in conjunction with warm iron logarithmically spiralled focusing sectors. Initially a batch of three machines have been manufactured and tested, and three additional machines are under construction in a production facility currently capable of producing up to 32 machines per year.

Table 1: Cyclotron Parameters

Parameter	Value
ION Source	PIG, Cold Cathode
Central Magnetic Field	4.5 T
Number of Sectors	3
RF Frequency	68 MHz
Peak Dee Voltage	≤ 20 KV
Final Energy	12.5 MeV
Maximum Beam Intensity	25 μA
Installed Weight	~ 2.3 tons

The cyclotron will be discussed in terms of five systems consisting of 1) Magnet, 2) RF, 3) Ion Source, 4) Target, and 5) Controls & Instrumentation. Since this is a commercial project, details of the engineering will be described at a conceptual level.

Figure 1: Beta Installation at the University of Michigan.

SUPERCONDUCTING MAGNET

Figure 2 shows the structure of the superconducting magnet. It is a conduction cooled, cryogen free design cooled by a single PT-415 pulse tube cryo-cooler. It requires approximately two days to evacuate the cryo-vessel to below 10 mTorr followed by approximately ten days to fully cool it to operating values. The magnet is normally left continuously charged in persistence mode and requires approximately five hours to charge or discharge. The cold steel design simplifies the magnet design while also eliminating tune drift due to steel temperature fluctuations.[2] Although the conduction cooled cold steel magnet simplifies the design and improves stability, this comes at a cost of significantly increasing design complexity and tolerances while also decreasing the available space for other systems. This design requires a systems approach to ensure that one system component (e. g. beam dynamics, median plane spacing, etc.) is not overly optimised with the unintended detriment to another (e.g. RF, target, etc.).

ISBN 978-3-95450-167-0

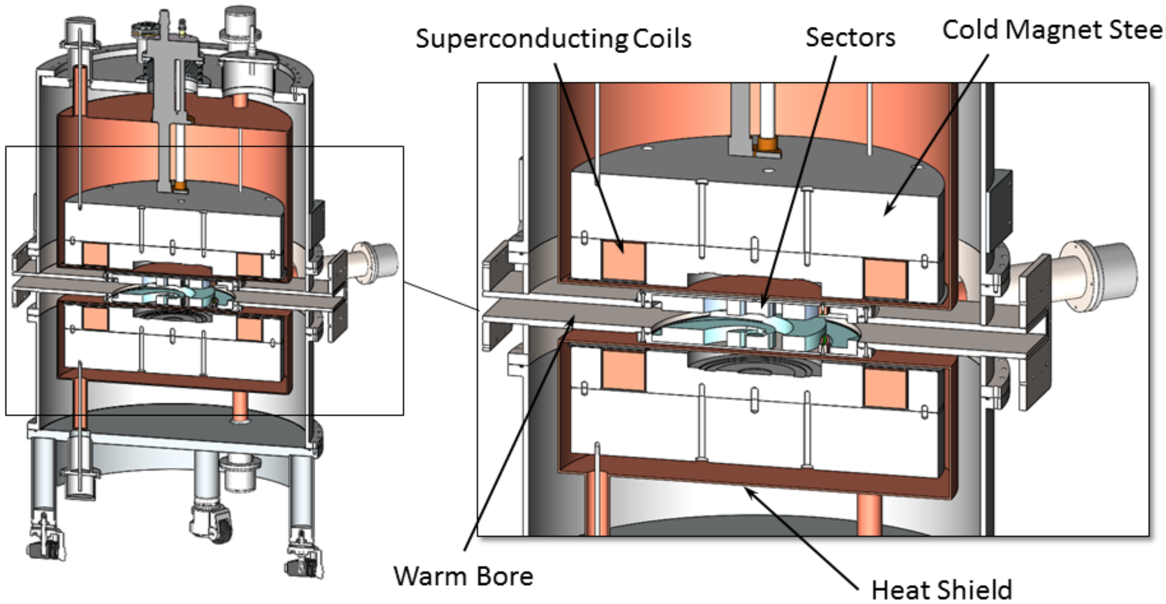

Figure 2: ION-12SC superconducting magnet structure.

RF SYSTEM

The RF system consists of 1) a resonator, 2) a solid-state amplifier, and 3) a digital RF controller.

RF Resonator

The resonator shown in Figure 3 is a vacuum insulated stripline structure using a finger contact based sliding tuner, an adjustable loop coupler, and a classic ~175 degree dee. The support structure is normally connected to the cyclotron such that the resonator may be inserted or retracted smoothly and rotated for service without discharging the magnet. The so-called dummy dee is simply a slotted bar connected to the resonator that both provides the precision accelerating gap and a mount for the ION source. Spring loaded pins couple the dummy dee bar to internal constructs in the cyclotron to ensure the ion source gap and ion source are precisely aligned with the cyclotron. The ion source gap may be precisely adjusted external to the cyclotron with the resonator fully installed and under vacuum.

Table 2: RF Parameters

Parameter	Value
Drive Power	< 6 KW
Nominal Input Impedance	50 Ohms
VSWR	< 1.5
Tuning Range	66 – 69 MHz
Water Cooling	4 GPM
Dee Angle	~175 degrees

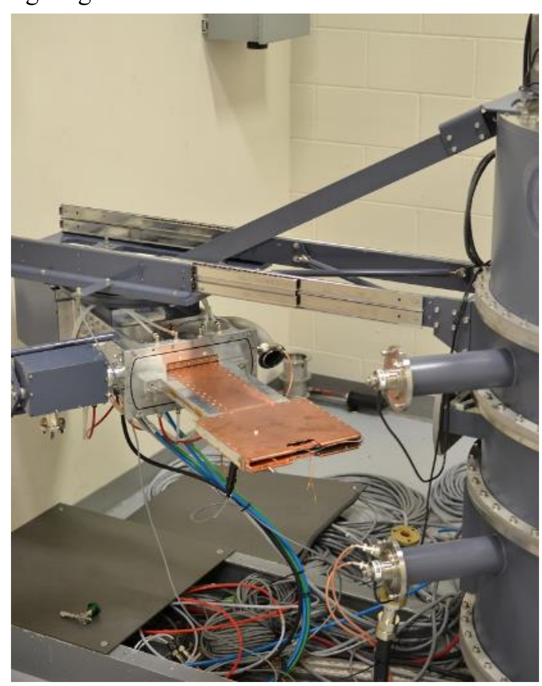

Figure 3: RF cavity shown on support structure.

RF Solid State Amplifier

The solid state amplifier is a 6 KW commercial unit built to Ionetix specifications. It consists of two rack mounted 5U water cooled 3KW amplifiers as shown in Figure 4 combined through an air cooled 4U rack mounted unit. The amplifier features a 62 dB of gain, a full power operating efficiency of 72 %, a 66.5 – 70.5 MHz bandwidth, and may be into a VSWR of up to 1.5. The amplifier is housed in the control rack.

ISBN 978-3-95450-167-0

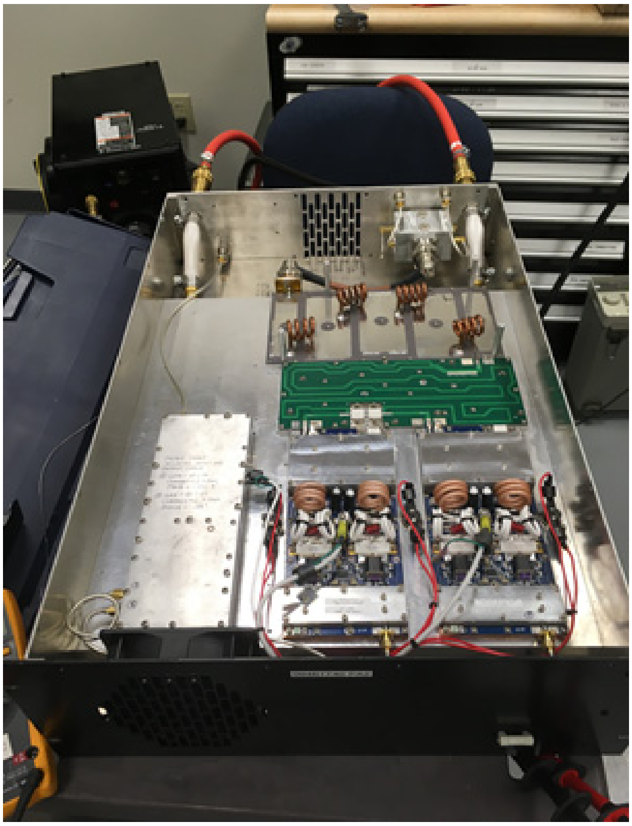

Figure 4: 3KW amplifier unit being tested.

RF Instrumentation and Control

The RF control unit is an Ionetix custom designed unit. The controller automatically tunes, regulates, and protects the resonator and amplifier. It applies direct digital sampling to read the cavity voltage from a pickup loop, and the forward and reflected power from an inline directional coupler at the cavity input port. The controller provides an output to drive the amplifier with up to 13 dBm of signal. The ADRC control algorithm [3] is applied to ramp and maintain the cavity amplitude. Additionally, the cavity tune is found and maintained by applying a PID algorithm to monitor and maintain the forward power to cavity phase to a pre-set value by actuating the stepper motor based cavity tuner.

ION SOURCE

The ion source is a cold cathode design using Tantalum cathodes and Boron nitride insulators. It has a single piece body and chimney manufactured from Beryllium Copper that measures 40mm wide by 25 mm tall as shown in Figure 5. The source opening is a 1.65 x 0.5 mm slit with a 30-degree bevel through a 0.2mm wall. It is a current controlled device that may be adjusted to operate from 0.1 to 15 mA at voltages that follow varying from 600 to 1.6 KV with gas flows from 0.3 to 0.9 sccm respectively. With the current cyclotron tune, the nominal operating point is ~5mA arc at <1KV necessary to produce ~10 uA of beam on target as shown in figure 10. The source has been tested in a test stand for up to 400 hours of continuous operation without failure and over 1100 cycles of 20 minute on and 20 minute off operation. The testing exceeds the operation expected between the nominal 3-month maintenance cycles. In operation, the ion source is fastened to the indirectly cooled so-called dummy dee that is a component of the overall rf assembly.

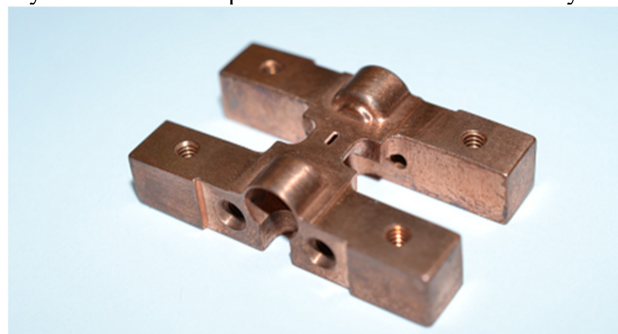

Figure 5: The Ion Source Body.

TARGET & BEAM PROBE

The port on the opposite side of the RF system is used for both the beam probe and the internal liquid target, shown in Figures 6 and 7. The beam probe covers the radial path from 4.6 cm to 15.1 cm, and can be fitted with a carbon block or stack of thin borosilicate glasses for beam current and energy measurement during the commissioning. The internal liquid target is designed to maximise transmission into the water while reducing neutron radiation. The target uses a thin graphene window and has a volume of ~3.0 ml of O^{16} water for N^{13} or O^{18} water for F^{18} isotope production. Both the beam probe and the target have a graphite shield to prevent the aluminium frame from being exposed to the beam.

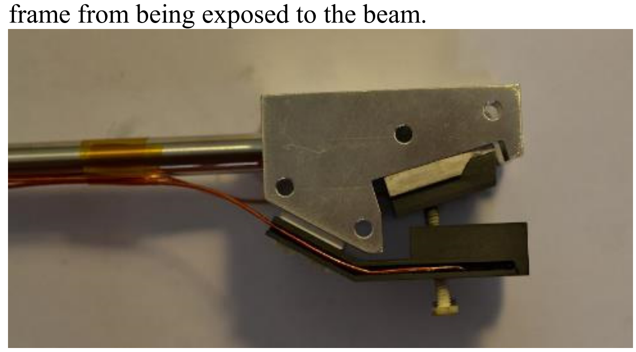

Figure 6: Beam probe.

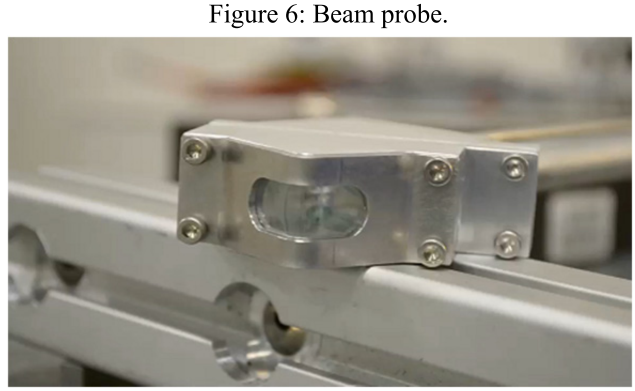

Figure 7: Internal liquid target.

CONTROLS & INSTRUMENTATION

All of the system electronics, not specifically built into a remote component, are contained in a standard 19" electronics rack as shown in Figure 8. This includes the rf amplifier and controller as shown in figure 8. The controls are based on a standard industrial Programmable Logic Controller (PLC) coupled through a custom interconnecting Printed Circuit Board (PCB). The PCB contains intervening signal conditioners as required. In this manner, point-to-point wiring is replaced by quality controlled manufactured cables thus reducing wiring errors and manufacturing time to a minimum.

Figure 8: Electronics rack installed at the University of Michigan Medical School.

OPERATION EXPERIENCE

In addition to the beta unit installed at the University of Michigan, the 2nd manufactured unit was installed at the Ionetix facility in Lansing, Michigan in June, 2016. Extensive beam commissioning was performed that included adjustments made to magnet position, RF gap and ion source position to optimize the cyclotron performance.

Figure 9 shows the Ion-12SCcyclotron beam intensity vs. radius measured with the beam probe at a RF frequency of 67.123 MHz and voltage of 17 kV. The beam intensity drops between ~80 mm to 110 mm is correlated nicely with the neutron radiation observed. This is caused by reduction in beam turn separation during beam acceleration, causing a portion of the proton beam to pass through the edge of the carbon block and hit the metal parts nearby. Adjusting the edge angle of the carbon block leads to smaller measured intensity drops and therefore less neutron radiation observed.

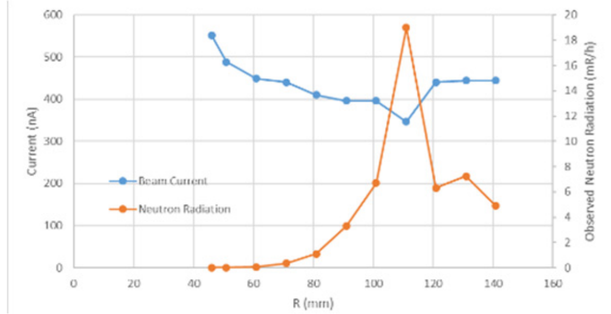

Figure 9: Measured beam current and neutron radiation vs. radius.

As one can see from Figure 9, the beam transmission from radius of 60 mm to the target position of 141 mm is about ~95%. The estimated maximum beam energy based the range of beam penetration through the borosilicate glasses is about ~12.1 MeV. Based on our beam commissioning experience both at UM site and Ionetix facility, the projected beam intensity on the target is well within reach of the design goal of 25 uA, as shown in Figure 10.

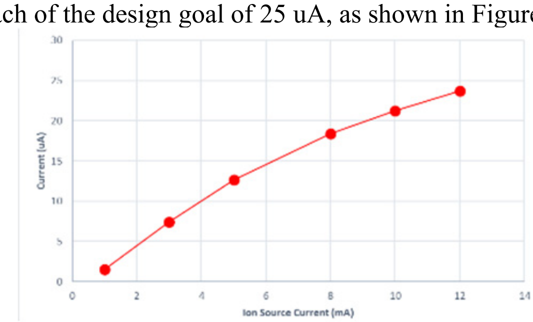

Figure 10: Projected beam intensity on target vs. ion source current.

CONCLUSION

The R&D and commissioning for the ION-12SC ultra-compact superconducting cyclotron for medical isotope production has been successfully completed at Ionetix, and large scale manufacturing is being ramped up to satisfy the expected market demand.

ACKNOWLEDGMENT

The authors wish to thank Superconducting System Inc., Tesla Engineering LTD and Technalogix Inc. for their valuable contributions in magnet and RF system engineering and manufacturing for the Ion-12SC project. In addition, we acknowledge Dr. Timothy Antaya as the company founder and for the cold steel concept.

REFERENCES

[1] V. Smirnov, S. Vorozhtsov, and J. Vincent, "Design Study of an Ultra-Compact Superconducting Cyclotron", *Nucl. Instr. Meth.* vol. 763, pp. 6–12, 2014.

[2] T. Antaya, "Compact, Cold, Superconducting Isochronous Cyclotron", US8558485 B2, Oct. 15, 2013.

[3] J. Vincent *et al*, "On Active Disturbance Rejection Based Control Design for Superconducting RF Cavities", *Nucl. Instr. Meth.* vol. 643, pp. 11–16, 2011.

ISBN 978-3-95450-167-0

DEVELOPMENT OF HTS MAGNETS FOR ACCELERATORS

K. Hatanaka*, M. Fukuda, S. Hara, K. Kamakura, K. Shimada, Y. Yasuda, T. Yorita, Research Center for Nuclear Physics, Osaka University, Ibaraki, 567-0047 Osaka, Japan
H. Ueda, Graduate School of Natural Science and Technology, Okayama University, 700-8530 Okayama, Japan

Abstract

At RCNP, we have been developing magnets utilizing first generation HTS wires for this decade. HTS materials have advantages over LTS materials. Magnets can be operated at 20 K or higher temperature and cooled by cryo-coolers. The cooling structure becomes simpler and the cooling power of a cooler is higher. Owing to a large margin in operating temperature, it is possible to excite HTS magnets by AC or pulsed currents without quenching. After successful tests of proto type models, two magnets have been fabricated for practical use. Their design and operational performance of two models and the switching dipole magnet are discussed.

INTRODUCTION

High critical temperature superconductor (HTS) materials were discovered in 1986 for the first time [1]. Since then, new HTS materials have been developed to achieve higher critical temperature. At present, two kinds of wires are commercially available having length over several hundred meters. They are based on Bi-2223 (the first generation wire) and REBCO (the second generation wire). Although HTS wires have several advantages over low critical temperature superconducting (LTS) wires, application studies of HTS wires have been limited so far. We have been developing magnets by applying the first generation wires for more than 10 years at the Research Center for Nuclear Physics (RCNP) of Osaka University.

Three model magnets were fabricated; a mirror coil for an ECR ion source [2], two sets of race track coils for a scanning magnet [3], and a 3T super-ferric dipole magnet having a negative curvature [4]. They were excited with AC and pulse currents as well as DC currents and their performance was investigated. After successful performance tests of proto type models, two magnets have been fabricated for practical use. A cylindrical magnet generates a magnetic field higher than 3.5 T at the center to polarized 210 neV ultra cold neutrons [5]. A switching dipole magnet is excited by pulse currents in order to deliver accelerated beams to two target stations by time sharing.

MODEL MAGNETS

Air core magnets were fabricated and measured AC losses were compared to simulations. A two-dimensional scanning magnet was designed to model a compact system for the cancer treatment [3]. The magnet was designed to deflect 230 MeV protons by 80 mrd in both the horizontal(x) and vertical (y) directions as shown in Fig. 1. The iso center is at 1.25 m from the magnet and the irradiation field is 200 mm by 200 mm.

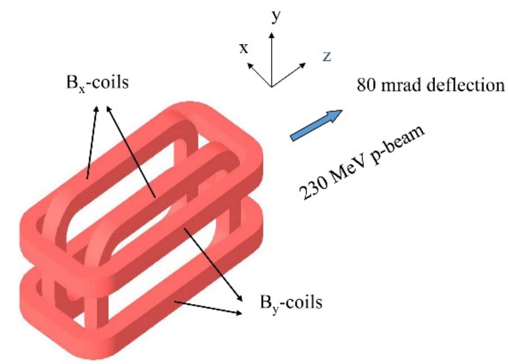

Figure 1. A schematic layout of the scanning magnet. They generate the horizontal (B_x) and vertical (B_y) field.

The magnet consists of two sets of two racetrack shaped coils. Specifications of coils are summarized in Table 1. Three double pancakes are stacked to form one coil. 9 mm thick brass cooling plates are inserted between pancakes. Figure 4 shows an assembled B_x coil which is vacum impregrated by epoxy resin. Detailed structure of coil is described in ref. [3]. The HTS tape was supplied by American Superconductor Corporation. The Ic of the tape was measured at 77 K in a 10 m pitch before winding and was between 125 and 140 A corresponding to an electric field amplitude of 1 μV/cm.. The Ic of the each pancake and stacked coil were measured in a liquid N_2 bath and were 56-62 and 40-43 A, respectively. Two single-stage GM refrigerators are used to cool coils and thermal shields separately. An AL330 of CRYOMECH, Inc. is used to cool coils and it has a cooling capacity of 45 W at the desined operating temperature 20 K. From the temperature dependence of the Ic ($B_\perp$) characteristics of the tape, Ic is estimated to be 260 A.

Table 1: Specifications of Coils of the Scanning Magnet.

Inner size	B_x: 150 mm x 300 mm B_y: 150 mm x 380 mm
Cross-section	30 mm x 30 mm
Separation	70 mm
Maximum field at the center	0.6 T
HTS tape length/coil	B_x: 420 m, B_y: 460 m
Number of turns/coil	420 turns
Stacking/coil	3 Double pancakes
Inductance/coil	B_x: 75 mH, B_y: 92 mH

* hatanaka@rcnp.osaka-u.ac.jp

ISBN 978-3-95450-167-0

A pair of coils are electrically connected in series and used as a scanning magnet excited by AC or pulsed currents. AC loss was measured by electrical method at 77 and 20 K [3]. There are several AC loss components observe in both LTS and HTS magnet [6, 7]. They are (1) hysteretic magnetization losses in the superconducting material, (2) dynamic resistance losses generated by a flux motion in the conductor, (3) coupling losses through the matrix and (4) eddy current losses in the matrix and metallic structures including cooling plates. In addition, there are (5) Ohmic losses at exciting currents above the critical current for HTS magnets. Each component shows a specific dependence on the frequency (*f*), the amplitude of the external magnetic field (*B*), and the transport current (*I*). In the critical state medel (CSM), the hysteresis loss per cycle is analytically formulated by Brant st al. [7] as follows,

$$Q_{hys} \propto 2\ln[\cosh(x)] - x\tanh(x) \quad (1)$$

where $x=B/B_{c0}$ and $B_{c0}=\mu_0 J_c d/\pi$. J_c is the critical current density and d thickness of the conductor tape. Figure 2 shows AC losses of the two B_x coils in series measured at 20 K. Upper points are total losses scaled (left axis) and lower ones are losses per cycle (the right axis). The observed dissipated power per cycle is almost independent of the frequency of the transport current and the current dependence is well described by the formula (1).

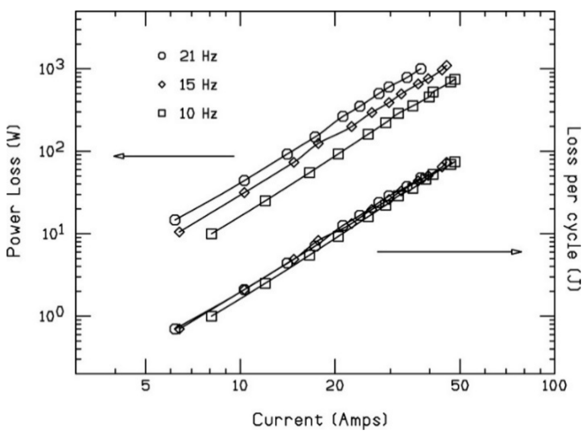

Figure 2. Measured AC losses at 20 K of the B_x coils in series. Data points at the same frequency are connected by line. Details are described in the text.

A dipole magnet was fabricated to investigate a potential application of HTS coils to synchrotron magnets [4]. It is a super-ferric magnet with race-track coils which have a negative curvature inside. The specification of the magnet is summarized in Table 2. The HTS tape is from Sumitomo Electric Industries, Ltd. Ic values of tape, double pancakes and stacked coils were measured at 77 K to be 160-189, 60-70 and 47-51 A, respectively. There were no damages observed during tape winding process. Figure 3 shows the assembled cold mass consisting of poles and coils. Coils are fixed to poles to withstand the radial electro-magnetic expansion force. Poles are laminated with 2.3 mm thick carbon steel plates to excite the magnet by pulse currents. Plates were bent before stacking, welded to form a pole and finally annealed to remove the stress. The weight of the total cold mass is 250 kg. The magnet was successfully excited with the DC current of 300 A to generate 3 T at the center. Coil was also excited with pulsed current with the ramping speed of 100 A/s corresponding to 1 T/s.

Table 2: Specifications of the Model Dipole Magnet.

Magnet	Central bending radius	400 mm
	Bending angle	60 degrees
	Pole gap	30 mm
	Maximum field at the center	3 T
	Cold mass	250 kg
Coil	Number of turns/coil	300 turns

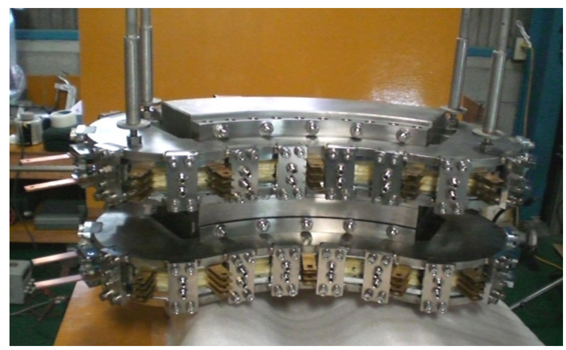

Figure 3. Photograph of the poles and coils of the model dipole magnet.

SWITCHING DIPOLE MAGNET

We have more beam time requests than available at our cyclotron facility. To provide more beam to users, beam sharing between two target rooms are planned, for example at the UCN and muon production targets. To put it into practice, a conventional normal conducting magnet will be replaced by a pulsed magnet which is shown in Fig. 4. The magnet consists of a laminated yoke and two cryostats. B-2223 wire with reinforcing copper alloy (DI-BSCCO type HT-CA from Sumitomo Electric Industries, Ltd.) and insulation tape are wound into double pancake coil and are conduction cooled by 10 K GM cryocoolers (SRDK-408S2 from Sumitomo Heavy Industries, Ltd.). The typical cooling power of the 2nd stage is 16 W at 20 K and 2 W at 7.5 K. Figure 5 shows the structure of a cryostat. Each cryostat contains a radiation shield thermally connected to the 1st

Table 3: Design Parameters of the HTS Dipole Magnet

Coil	Inner size	1,142 mm x 580 mm
	Number of DP	2
	Numbers of turns	256 x 2
	Inductance	2.5 H
Magnet	Temperature	< 20 K
	Rated current	200 A
	Field at center	1.6 T

ISBN 978-3-95450-167-0

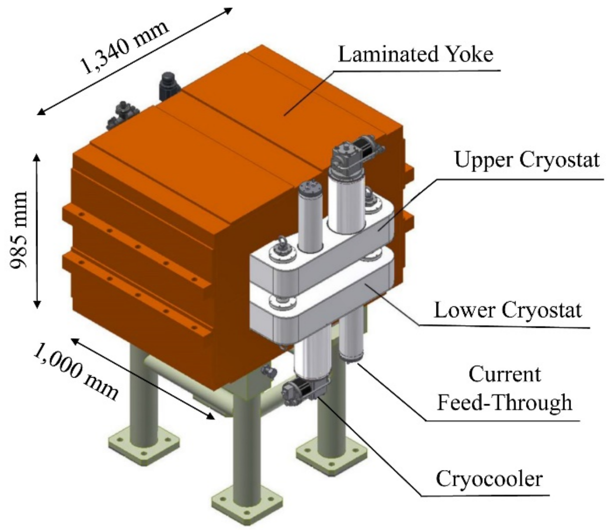

Figure 4: HTS switching dipole magnet..

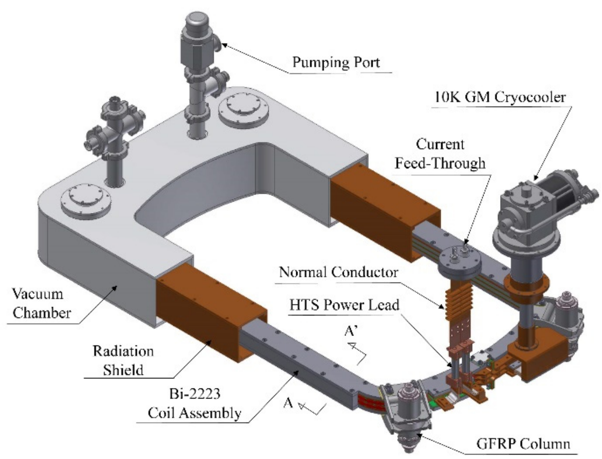

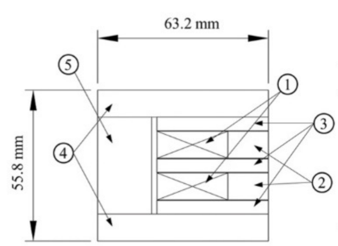

No.	Description	Material
1	Bi-2223 DPC	
2	Winding Frame	Stainless Steel
3	Cooling Plate	Copper
4	Reinforcing Plate	Stainless Steel
5	Reinforcing Bar	Stainless Steel

Figure 5: Structure of a cryostat (upper panel) and A-A' cross sectional view of and major component list of the coil assembly (lower panel).

Figure 6 shows the initial cooling performance of the-magnet. It takes 50 hours to cool the whole magnet down to operational temperature. Thermometer B is measured near the connecting point to a cryocooler and A at the far end of the coil assembly. For time sharing of a beam, rapid excitation is required. The magnet's iron core is laminated and the power supply is designed to perform 20 A/s ramping with 2.5 H of the coil's inductance. A temperature history during a pattern operation is shown in Fig. 7. Coil temperature stays in the operating temperature with a large margin during 30-second exiting and 60-second degaussing pattern. The saturated temperature after two hours of operation is lower than 8.5 K. The result confirmed the thermal design. To provide precise beam switching, the highly stable field strength is required. We are performing systematic measurements of the magnetic fields to find the optimum conditions.

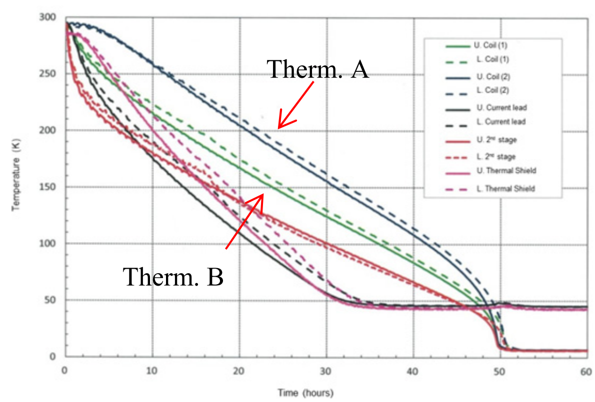

Figure 6: Initial cooling performance of the HTS magnet.

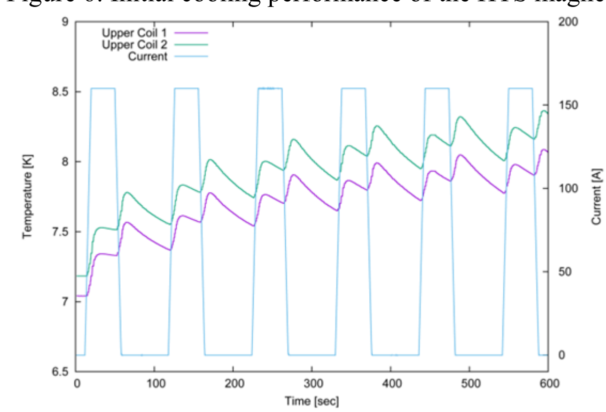

Figure 7: Temperature of upper coil during pattern operation.

REFERENCES

[1] J. G. Bednorz and K. A. Müler, Physical B 64 (1986) 189.
[2] K. Hatanaka, S. Ninomiya, Y. Sakemi, T. Wakasa, T. Kawaguchi, N. Takahashi, Nucl. Instr. Meth. in Phys. Res. A 571 (2007) 583-587.
[3] K. Hatanaka, J. Nakagawa, M. Fukuda, T. Yorita T..Saito, Y. Sakemi, T. Kawaguchi, K. Noda, Nucl. Instr. Meth. in Phys. Res. A 616 (2010) 16-20.
[4] K. Hatanaka, et al., in *Proc. of IPAC'12*, New Orleans, Louisiana, May 2012, paper TUOAC02, p. 1095.
[5] K. Hatanaka, et al., in *Proc. of IPAC'13*, Shanghai, China, May 2013, paper THPME007, p. 3522.
[6] C. M. Friend, "AC Losses of HTS Tapes and Wires", Studies of High Temperature Superconductors, A. V. Narlikar, Ed. New York: Nova Science Publishers, 2000, vol. 32, pp. 1-61.
[7] E. H. Brandt and M. Indenbom, Phys. Rev. B 48 (1993) 12893-12906.

STATUS OF HYDROGEN ION SOURCES AT PKU*

Yuan Xu, Shixiang Peng#, Haitao Ren, Tao Zhang, Jingfeng Zhang, Jiamei Wen, Wenbin Wu, Zhiyu Guo and Jiaer Chen, SKLNPT & IHIP, School of Physics, Peking University, Beijing 100871, China
Ailin Zhang, School of Physics, UCAS, Beijing 100049, China

Abstract

Cyclotrons are quite often to be used to accelerate different hydrogen ion beams with high intensity for different purposes around the world. At Peking University (PKU), special efforts were paid on developing compact 2.45 GHz microwave driven ion sources with permanent magnets to generate high intensity H^+, H_2^+, H_3^+ and H^- ion beams as well as other ion beams. For the positive ion beam, we can easily produce a 130 mA hydrogen ion beam with H^+ fraction higher than 92% with a PKU standard ϕ100 mm × 100 mm 2.45 GHz ECR ion source. Also we have got 42 mA H_2^+ beam and 20 mA H_3^+ beam with a specifically designed 2.45 GHz ECR ion source under different operation condition. The fractions of H_2^+ and H_3^+ are higher than 50% within the mixed hydrogen ion beams for each case. Recently, a Cs-free volume H^- source based on 2.45 GHz microwave was developed successfully in our lab. It can generate 45 mA H^- beam with duty factor of 10% and a 29 mA beam at CW mode at 35 keV. Its operation duty factor can vary from 1% to 100%. The power efficiency is about 29 mA/kW in CW mode and 21 mA/kW in 10% (100 Hz/1 ms) pulsed mode. A 300 hours 50 keV/50 mA CW proton beam continuous operation with no beam trip demonstrated that PKU 2.45 GHz ECR ion source has high stability and reliability. Details of these sources will be presented in the paper.

INTRODUCTION

Cyclotrons are wildly used in fundamental physics research, medical therapy, radioisotopes production etc. In principle, cyclotrons can accelerate various ions from hydrogen to uranium. Among numerous ions, hydrogen ions (H^+, H^-) are most commonly to be accelerated by cyclotrons. For example, about 10 mA CW H^+ ion beam was injected into the Cockcroft-Walton pre-accelerator of the 590 MeV cyclotron at PSI, which was one of the most powerful cyclotron around the world. [1] Moreover, negative hydrogen ion (H^-) was also very popular as it could be stripped as H^+ at the extraction area of cyclotron so that very high extraction efficiency could be achieved by using charge-exchange extraction method. [2] At TRIUMF, about 15 mA CW H^- ions were needed to inject into a TR30 cyclotron. [3] Otherwise, for some medical cyclotrons, several mA H^- ions extracted from ion source were required for isotope production. [4]

Nowadays, high current high power facility is an important trend for cyclotrons. But accompanying with the increasing of beam current, the space charge effect caused by repulsive force between particles leads to strong beam loss in cyclotron. To solve this problem, it is proposed to accelerate H_2^+ or H_3^+ ions, which have much lower generalized perveance, and then strip them at the export of cyclotron to get H^+. [5] The DAEδALUS project is an example on this idea. [6, 7] DAEδALUS accelerator will produce 800 MeV H^+ with a beam current of 10 mA. This current already exceeds the limitation of present cyclotrons and is unacceptable for the machine. To reduce the space charge effect and achieve the extracted current from the cyclotron, H_2^+ ion beam will be used to take place of H^+.

2.45 GHz microwave driven ion source has the reputation for its high current, low emmitance, long lifetime and high stability. [8] It can operate in pulsed and CW mode. At PKU, high current ion sources driven by 2.45 GHz microwave has been developed for several decades. [9] Single charged ions such as H^+, O^+, N^+, Ar^+, D^+ etc. can already be generated by the ion source. In addition, H_2^+, H_3^+ and H^- ions were also extracted from this kind of ion source by modifying the structure and adjusting operation parameters. [10, 11] Up to now, the 2.45 GHz microwave ion source at PKU has been utilized by the Separated Function Radio Frequency Quadrupole (SFRFQ) project, [12] the Peking University Neutron Imaging FaciliTY (PKUNIFTY) project, [13] Coupled RFQ & SFRFQ, [14] Dialectical Wall Accelerator(DWA) [15] and the Xi'an Proton Application Facility (XiPAF) [16]. During the operation of these facilities, the ion sources developed at PKU have already shown very good performance and stability. More details of hydrogen ion sources at PKU will be reported in this paper.

PROTON ION SOURCE

The standard structure of the microwave ion source at PKU is shown Fig. 1. [13] It is a very compact ion source with an outer diameter of 10 cm and a length of 10 cm, and its weight is lower than 5 kg. The magnetic field is generated by three NdFeB permanent magnetic rings. Microwave generated by magnetron is injected into the ion source through a circulator, a three-stub tuner, a directional coupler, a dc-break waveguide and a standard BJ26 rectangular waveguide. A three-layer Al_2O_3 microwave window is used here to couple the microwave with plasma chamber, and a protective BN disc is mounted to prevent the bombardments of electrons. The extraction system is composed of three electrodes: plasma electrode, screening electrode and ground electrode. The diameter of the beam emission aperture is ϕ6 mm.

Many efforts were carried out to improve the beam current, beam quality, proton fraction as well as source stability and reliability. Up to now, a 130 mA H^+ beam with proton fraction of 92% was extracted at 50 kV from

*Work supported by National Basic Research Program of China NO. 2014CB845502 and NSFC NO. 91126004, 11175009 and 11305004.
#sxpeng@pku.edu.cn

ISBN 978-3-95450-167-0

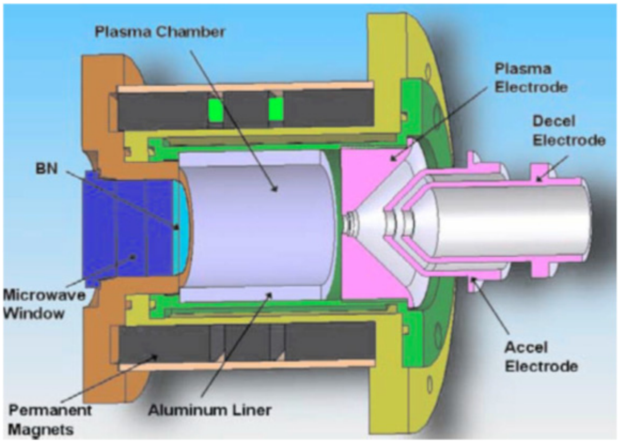

Figure 1: The schematic diagram of ECR ion source at PKU [13].

the ion source in pulsed mode with duty factor of 10% (100 Hz/1 ms). The peak RF power was about 2 kW and H_2 gas consumption was 2 sccm. The rms emmitance of the beam is 0.16 π.mm.mrad. The waveform of the total current is shown in Fig.2. In CW mode, the source could also work very well. Around 100 mA ion beam was extracted after improving the water-cooling and operation parameters. [17] To characterize the lifetime and stability of the ion source at PKU, a long time experiment was done in June 2016. [18] A 50 mA CW H^+ beam was continuous extracted with energy of 50 keV for 300 hours, and the input power was around 500 W. A screenshot of the monitor computer at the end of longevity test is shown in Fig.3. During 300 hours' test, no beam-off or beam drop happened during the 294 hours' duration, and the ion beam availability was 100%.

H_2^+ & H_3^+ ION SOURCE

H_2^+ and H_3^+ exist inevitably in the mixed ion beam from hydrogen ion source. Generally, H_2^+ ion is generated by direct ionization of molecular hydrogen H_2 which is a pilot process for proton generation, and H_3^+ is created by

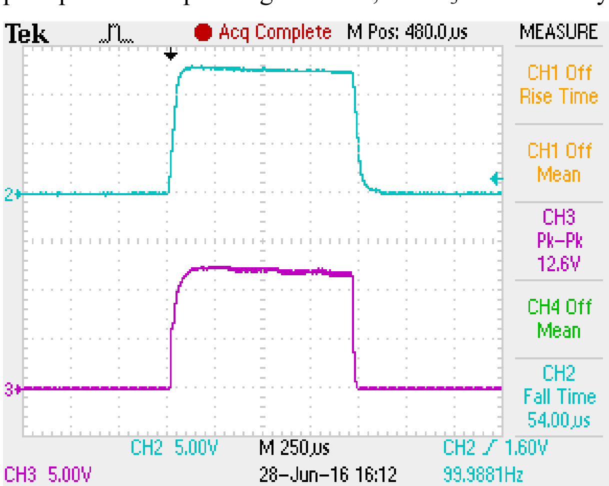

Figure 2: The waveform of 130 mA proton beam in pulsed mode.

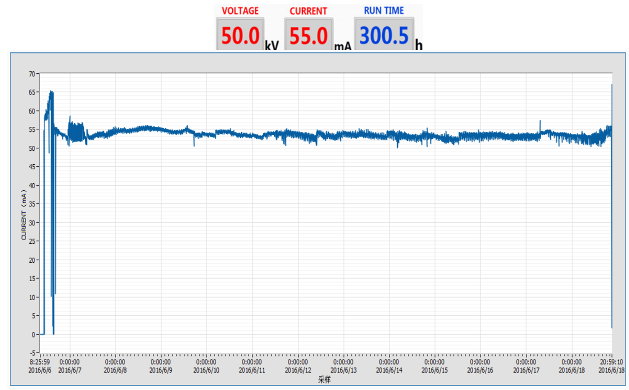

Figure 3: Screenshot of the monitor computer at the end of longevity test. (Top: extraction voltage, instantaneous current, and counting hours. Bottom: beam current versus elapsed time) [18].

dissociative attachment process. The structure of ion source for hydrogen molecular ions was similar to that of proton source. The most differences were the diameter and the material of the plasma chamber. [19] For H_2^+ generation, a 64 mm diameter chamber, which was larger than normal proton source, was preferred. Moreover, materials with high recombination coefficient such as stainless steel should be used to enhance the yield of H_2^+.

After modifying the ion source and optimizing the operation parameters, high current H_2^+ and H_3^+ beam were extracted with identical ion source. With operation pressure 6.5×10^{-4} Pa (the pressure was measured in the vacuum chamber after the extraction system) and rf power 1400 W, pure 42 mA H_2^+ ion beam with ion fraction of 54% was extracted at 45 kV in pulsed mode. It is shown in Fig.4 that the fraction of H_2^+ is obviously higher than H^+. By increasing the pressure to 2×10^{-3} Pa and decreasing the rf power to 1000 W, 20 mA H_3^+ with fraction of 55% was got also in pulsed mode (Fig.5). Actually, if sacrificing the current, the fraction of H_3^+ could reach nearly 70% by further reducing the input power.

In general, the operation parameters should be adjusted thoroughly as molecular ions are easily destructed. For H_2^+ ion generation, a lower operation pressure and moderate rf power are needed. However, for H_3^+ ions, the pressure should be increased and the rf power should be decreased to some extent.

NEGATIVE HYDROGEN ION SOURCE

PKU ion source group has developed the 2.45 GHz microwave driven Cesium-free volume negative ion source for several years, and formal upgraded sources named as No. 1, No. 2, No. 3 and No. 4 H^- source were manufactured. [10] After theoretical and experimental study, tens of mA H^- beam both in pulsed mode and CW mode were obtained. [20] The duty factor of these four sources was variable from 1% to 100% by adjusting the rf power supply.

The principle of the H^- ion source is shown in Fig. 6. The source body of the PKU 2.45 GHz microwave-driven

ISBN 978-3-95450-167-0

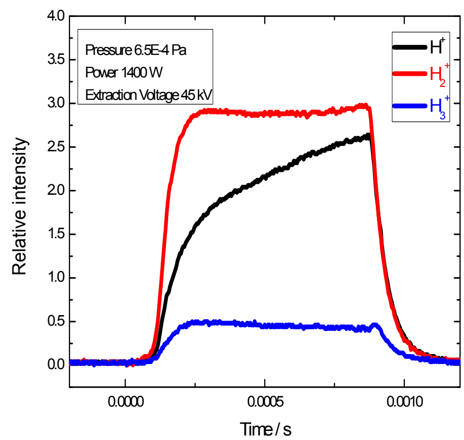

Figure 4: Profiles of H^+, H_2^+ and H_3^+ beam pulse. (6.5×10^{-4} Pa, 1400 W).

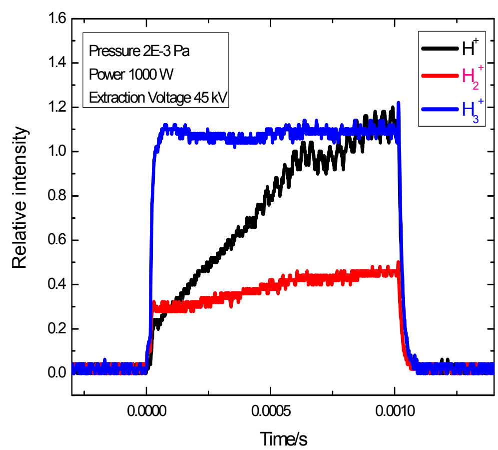

Figure 5: Profiles of H^+, H_2^+ and H_3^+ beam pulse. (2×10^{-3} Pa, 1000 W).

H^- source is consisted of a microwave matching part (microwave window), a plasma chamber, and a connection flange for the source body installation. Just like the 2.45 GHz positive ion source, the ECR filed, the filter magnetic field and e-dump filed are all generated by permanent magnets. The discharge chamber is physically

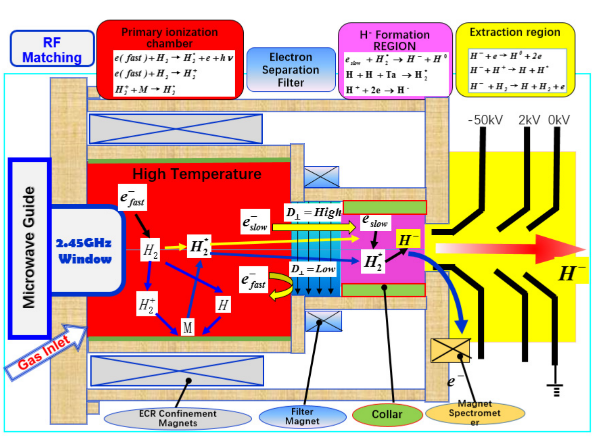

Figure 6: The principle of PKU No.4 H^- ion source [10].

separated into three sections: the primary ionization chamber (ECR-zone) where high temperature electrons interact with hydrogen molecules to generate excited H_2^*, the filter region acting as electron energy filter which only has a high diffusion coefficient for lower energy electron (<1 eV), and the H^- formation region where H_2^* interacts with low energy electrons. Most of electrons near the outlet could be dumped inside the plasma chamber by transverse magnetic field so that they will not be co-extracted with H^- ions. Tantalum liners are placed in both primary ionization chamber and H^- formation region to increase the population of excited hydrogen molecule the population of excited hydrogen molecule by surface effect. In the design of this H^- ion source, no Cesium (Cs) is used which makes the operation of the source more easily and safely.

A 45 mA pure H^- current in pulsed mode with 100 Hz/1 ms was extracted in 35 keV with 2100 W RF power from No. 4 H^- Source, and a 29 mA H^- current was extracted in CW mode with RF power of 1000 W, the detailed parameters of the conditions could be found in Table 1. [21] As shown in Table 1, the power efficiency of this kind of ion source can be as high as 29 mA/kW in CW mode and 21 mA/kW in pulsed mode which is much higher than that of typical RF-driven H^- ion source with or without Cs.

Table 1: Optimal Operation Parameters with PKU Cs-Free 2.45 GHz Microwave-Driven H^- Ion Source.

Operation mode	Pulse	CW
Gas pressure (Pa)	4.0×10^{-3}	4.5×10^{-3}
RF Power (W)	2100	1000
Duty factor	10%	100%
Extraction voltage (kV)	35	35
Current (mA)	45	29
Power efficiency (mA/kW)	21.4	29

CONCLUSION

2.45 GHz microwave driven ion sources have been developed at PKU for several decades. After improvements, the ion sources can already produce high current H^+, H_2^+, H_3^+ and H^- ions to fulfil the requirements of cyclotrons. For positive hydrogen ions, 130 mA H^+, 42 mA H_2^+, and 20 mA H_3^+ ion beam could be extracted in pulsed mode. Moreover, result of the long-time continuous test with 50 mA CW H^+ beam demonstrates that the stability and reliability of the ion source are very promising. For negative hydrogen ion source, 29 mA CW H^- beam and 45 mA pulsed beam can be generated with very high power efficiency. In conclusion, it is promising to use 2.45 GHz microwave driven ion source in cyclotrons as it has very high reliability to generate both CW and pulsed beam.

ISBN 978-3-95450-167-0

ACKNOWLEDGMENTS

This work is supported by the National Basic Research Program of China No. 2014CB845502 and the National Science Foundation of China No. 91126004, 11175009 and 11305004.

REFERENCES

[1] P. A. Schmelzbach *et al.*, in *Proc. Cyclotrons'07*, Giardini, Italy, 2007, pp. 292.
[2] H. Etoh *et al., Rev. Sci. Instrum*. **87**, 02B135, 2016.
[3] T. Kuo *et al.*, *Rev. Sci. Instrum*. **67**, 1314, 1996.
[4] P. W. Schmor, *in Proc. Cyclotrons'10,* Lanzhou, China, 2010, paper FRM2CIO01, pp. 419.
[5] L. Calabretta *et al.*, in *Proc. Cyclotrons'10,* Lanzhou, China, 2010, paper TUA1CIO0, pp. 298.
[6] Jose R. Alonso *et al., Rev. Sci. Instrum*. **85**, 02A742, 2014.
[7] S. Axani *et al., Rev. Sci. Instrum*. **87**, 02B704 (2016).
[8] R. Gobin *et al., Rev. Sci. Instrum.* **83**, 02A345 (2012).
[9] S. X. Peng *et al., in Proc. ECRIS'10*, Grenoble, France, 2010, paper TUCOCK02, pp. 102.
[10] S. X. Peng *et al., AIP Conf. Proc*., **1655**, 070005, (2015).
[11] Y. Xu *et al.*, in *Proc. IPAC'13*, Shanghai, China, paper MOPFI035, 2013, pp. 363–365.
[12] S. X. Peng *et al., Rev. Sci. Instrum.*, vol. **79**, 02B706, 2008.
[13] H. T. Ren *et al., Rev. Sci. Instrum.,* vol. **81**, 02B714, 2010.
[14] S. X. Peng *et al.*, *Rev. Sci. Instrum.*, vol **85**, 02A712, 2014.
[15] S. X. Peng *et al., Nucl. Instr. and Meth. A*, **763,** 120, 2014.
[16] S. X. Zheng *et al.,* in *Proc. HB'16,* Malmö, Sweden, 2016, paper MOPR006, pp. 56.
[17] H. T. Ren, S. X. Peng *et al., Rev. Sci. Instrum.,* **83,** 02B905, 2012.
[18] Shi-Xiang Peng *et al.*, "Significant breakthrough on stability and reliability of PKU high intensity CW 2.45 GHz ECR proton source", *Chinese Physics B,* Summited (2016/8).
[19] Yuan Xu *et al.*, *Rev. Sci. Instrum.*, **85**, 02A943, 2014.
[20] S. X. Peng, *et al*., *Rev. Sci. Instrum.,* **87**, 02B125, 2016.
[21] T. Zhang, S. X. Peng *et al., in Proc. NIBS2016,* Oxford, UK, 2016, paperTueO7.

ISBN 978-3-95450-167-0

DEVELOPMENT AND VALIDATION OF A FAST CRYOCOOLER MAINTENANCE SYSTEM

V. Nuttens†, E. Forton, T. Lamon, Y. Paradis, Ion Beam Applications, Louvain-la-Neuve, Belgium
A. Zhukovsky, MIT/PSFC, Cambridge, Massachusetts, USA

Abstract

At IBA, we have been developing and testing new systems to simplify cryocooler maintenance at a minimal cost (material, interruption of service). A local heating system has been designed to heat-up both stages of a cryocooler to room temperature while keeping the cold mass at a low temperature. The heating system has to fulfill severe requirements such as high power density, compatibility with vacuum and low temperature, and easy operation. The whole system has been designed and tested in a dedicated test bench and then duplicated onto a full-size superconducting coil. It has been extensively tested under different conditions to prove that the heating system is robust and reliable and has no impact on the superconducting coil performances.

INTRODUCTION

The basic principle of the developed system for maintenance relies on a patent that dates back to the 90's [1]. It consists in performing a quick local heating of the cryocoolers to room temperature while keeping the cold mass as cold as possible. This method, also known as cold swap, requires that the cryogenic system and the heating system can support the mechanical stress induced by the large temperature gradient that will occur during the heating operation.

A preliminary study had demonstrated that the required heating power to reach room temperature in our superconducting coil in 20 minutes was 1kW for a cryocooler second stage and 500W for a first stage [2]. Given the available space in the cryostat, high power density resistors are required. They also have to be vacuum and cryogenics compatible and be robust and reliable over more than 20 years. Finally, the heat load due to all the wiring must be compatible with the available cooling power.

DEDICATED TEST BENCH

A dedicated test bench has been designed and used to test the different components of the heating system (Fig. 1). The turbo pump allows to reach a good vacuum level in the chamber in 3 h. A small aluminium thermal mass has been attached to the second stage of a Sumitomo RDK415D2 cryocooler (Fig. 2) and it takes another 4 h to reach the final temperature of 6.3 K without the use of any superinsulation. Each stage cryohead was equipped with one Cernox and one Pt100 per stage to monitor the temperature. Several vacuum feedthroughs allow us to monitor each stage temperature and also to control and monitor separately each heater resistor. A LabVIEW™ program has been developed to record the temperatures, pressure and also to control the two power supplies for the first and second stage separately.

† vincent.nuttens@iba-group.com

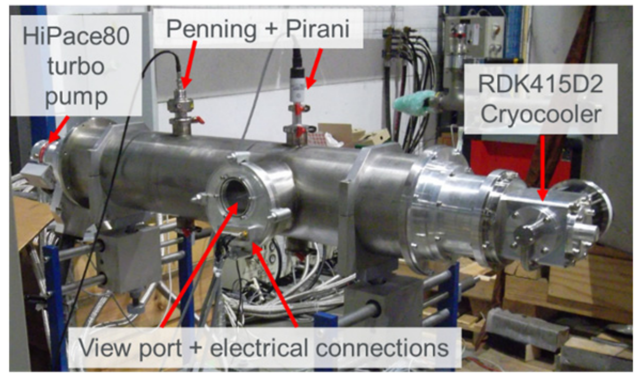

Figure 1: Dedicated test bench.

This test bench allows us to iterate rapidly on the design of the heaters and their wiring to make them robust, safe and reliable. The heating resistors have been tested extensively for vacuum and cryogenic compatibility, reliability after several tens of cycles between 4 K and room temperature. Destructive tests were also performed to check the robustness of the resistors and their safe operation condition. Thermal anchoring of all the wiring was also very important to avoid local hot spot and reduce the heat load to the second stage where only a few watts are available at 4 K. The full heating system (for 1st and 2nd stage) for a single cryocooler head has been designed, tested and validated on this test bench.

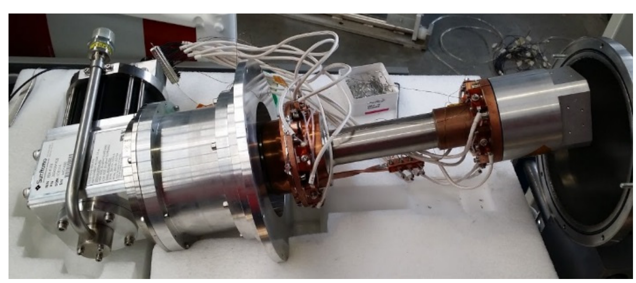

Figure 2: 1st and 2nd stage heating system.

INTEGRATION IN A SUPERCONDUCTING COIL

Proof of Concept of the Cold Swap Maintenance

As soon as the heating system was validated, it was reproduced for the four cryoheads of a R&D superconducting coil. The objective was to validate the required heating power and to evaluate the maximum temperature reached by the cold mass and hence the subsequent cooling time.

ISBN 978-3-95450-167-0

For redundancy reason, a total heating power of 2 kW was installed on each of the four second stages and 1.5 kW on the first ones. A Cernox and a Pt100 on each of the first and second stages assure the redundancy for the temperature measurement.

After the integration of the heating system in the superconducting coil, the magnet was cooled down. All the temperatures within the coil were carefully monitored to assess the impact of the heat load of the heating system. It has been observed that neither the cool down time nor the final temperature were impacted by the heating system.

The heating system was then used to warm-up locally each of the four cryocoolers successively. The upper cryoheads were maintained at room temperature during 30 minutes and the lower ones during 40 minutes, corresponding to the time to perform the cryohead servicing. Only one cryohead was really maintained, the other three were only heated to simulate maintenance but the cryoheads were not serviced. The maximal temperature at the end of this process was 65 K. On this coil, the cooldown time to recover 4 K was 35 h. It is then possible to perform the maintenance of the four cryohead of a superconducting coil using the cold swap method over a weekend.

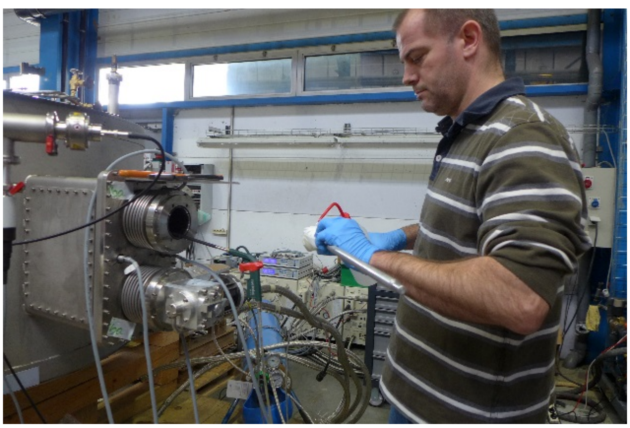

Figure 3: Cryohead maintenance with the cold swap method.

Impact on the Magnet Performances and Structure

The full system was then integrated in a production coil whose mechanical design is slightly different from the R&D one. The objective was to evaluate the impact of any mechanical stress introduced by the heating process on the magnet performance and magnet structure integrity. Indeed, the cold swap method imposes to have large temperature gradient inside the superconducting coil during the maintenance operation.

Again, neither the superconducting coil cool down time nor final temperature were impacted by the added heating system. The superconducting coil acceptance tests (nominal field, test quench, fast ramp-up) were rerun successfully without any impact on the coil performances.

After that, the following cycling sequence was executed:

1. For each of the four cryohead, heat-up the 1st and the 2nd stage to room temperature and maintain 300 K for 30 minutes to simulate the maintenance operation (4.5 h in total);
2. Cool down the magnet to 4 K (~30 h);
3. Check the heater resistances value and electrical insulation.
4. Ramp-up the magnetic field to nominal current (4 h);
5. Ramp-down the magnetic field.
6. Check the heater resistances value and electrical insulation.

All the superconducting coil properties (coil temperature, pressure, tie-rods forces, voltage taps, …) were recorded by the magnet control system. A separate LabVIEW™ program was developed to regulate and record the heating system power and monitor the thermometers used for the cryohead maintenance.

In total, eight cycles were performed. All the cycles were highly reproducible in term of maximal temperature after heat-up, cooldown time, nominal temperature after cooldown, maximum temperature during magnet ramp-up. The heaters resistance and insulation tests were also highly reproducible indicating a high stability, reliability and robustness of the heating system. The analysis of the forces on the tie-rods also shows that the heating process tends to release the forces in the superconducting coil.

CONCLUSIONS

The cold swap method has proven to allow for a maintenance while keeping the cold mass of the superconducting coil at a maximum of 65 K. The time to recover the magnet nominal temperature allows for a maintenance over a weekend. The coil performances (nominal temperature, ramp-up time) are not impacted by the heating system. Also, the heat-up tends to release the forces in the coil without impacting the structure of the superconducting coil. This system is now implemented in every superconducting coil.

ACKNOWLEDGEMENT

We acknowledge the ASG Superconductors company for providing support to this project.

REFERENCES

[1] W. Strasser, "Method for carrying out maintenance work on a refrigerator, device and refrigerator for carrying out the method", US 4,995,237, Feb. 26, 1991.

[2] A.L. Radovinsky *et al*, "Cold head maintenance with minimal service interruption", *IOP Conf. Series: Materials Science and Engineering,* vol 101, p. 12181, Dec. 2015

ISBN 978-3-95450-167-0

PLANNING CONSIDERATIONS FOR RADIOISOTOPE PRODUCTION CYCLOTRON PROJECTS - REGULATORY FEEDBACK

A. N. Alwani, Canadian Nuclear Safety Commission, Ottawa, Canada

Abstract

Over the last ten years, there has been a significant increase in projects to build, operate or upgrade cyclotrons in Canada. This is largely driven by their increased use for the production of radioisotopes.

The Canadian Nuclear Safety Commission regulates the use of nuclear energy and materials to protect health, safety, security and the environment in Canada. Its mandate includes the oversight of particle accelerators. The CNSC regulates the full life cycle of such facilities, with regulatory oversight though construction, commissioning, operation, and decommissioning activities.

This paper outlines common practices for such projects, highlighting the particular aspects that should be considered in the early stages of project planning and providing examples of best practices and challenges that, if properly addressed, help ensure continued safe operation of the facility through its entire life cycle.

The paper discusses the necessary elements of effective planning for such projects, touching on layout and space considerations; workload projection and maximum research capacity; shielding penetrations; cooling water circuit activity; storage of active components; management of radioactive waste from cyclotron and processing labs; construction and commissioning project management; integration of equipment safety systems and building safety systems; nuclear ventilation and filtration options; and strategies for staffing and training.

INTRODUCTION

The Canadian Nuclear Safety Commission (CNSC) regulates the use of nuclear energy and materials to protect health, safety, security and the environment in Canada. Construction, commissioning, operating or decommissioning a radioisotope production cyclotron facility requires a licence from the CNSC [1]. The applicant provides to the CNSC, at each licensing phase, information to demonstrate that safety aspects have been covered in the project and to convince the regulator that no undue risk is introduced by conducting the proposed activity [2, 3].

Experience has shown that prudent design with careful consideration of safety at the very early stage of the project as well as along with the evolution of the project is vital to the overall safe operation of the facility. Deficiencies in the design are often difficult to fix or costly. The following are examples of safety considerations which could be easy to miss by the proponents especially at the early stages of the project.

LAYOUT AND SPACE

A radioisotope production cyclotron facility is more than merely a vault to host the machine and a control room. The footprint needed for the processing and servicing areas is large. For medical institutions which are often located in dense urban areas, the available space is an issue. The layout should allow to host all the required equipment and to permit the implementation of all contamination controls. Also, it should allow easy and safe movement of the workers and materials within the facility and to and from the facility.

WORKLOAD PROJECTION AND MAXIMUM PRODUCTION CAPACITY

Nowadays, there are many cyclotron designs available commercially with increasing beam currents and energy. For conventional isotope supply such as PET isotopes, the machine beam current doesn't need to be very high. A single target machine with 150 µA beam current on target would probably be sufficient to supply a reasonably large demographic area. The research programs associated with new projects are often less defined in the beginning and the needs for beam current, the number of beamlines, and hours of operation, are hard to predict.

The safety implications are two folds; first, the proponent should establish a safety envelop for the maximum parameters they want to design the facility against. This safety envelope will be used to design the shielding required for the target areas and/or the cyclotron bunker. It will also, define the maximum radioactivity that will be present in the target which must be confined at all time. This is used to assess the consequences of target failures and any release to the facility or the environment in case of an accident.

Second; since in practice, the urgency and needs is what drives the progress of the project, it often happens that the proponent is keen on proceeding with a partial operation of the facility such as the clinical isotope part but is not ready for the more advanced research on other parts of the facility. The CNSC may permit approval of the project in phases, i.e., allowing limited operation of the facility. However, this requires a rigorous quality assurance program and change control to clearly define the various phases of the project and what is allowed and what is not allowed at any given time.

SHIELDING PENETRATIONS

Cyclotron bunkers are normally built with thick concrete walls. Penetrations are needed for various purposes such as product transfer, electrical, control, cooling water circuits and ventilation. Also, the facility may have under the floor service channels passing through walls. Penetra-

ISBN 978-3-95450-167-0

tions present weak points in the shielding. Normally, they are positioned so as to avoid direct eye sight from the radiation source to the area outside being protected and to minimize leakage of radiation especially neutrons. Efforts are made to minimize the diameter or the cross section of the penetrations as much as practically possible.

Shielding calculations may be performed using empirical formulae or Monte Carlo simulations. The latter provides better estimates for the radiation fields outside the shielded bunker. Details about the penetrations should be used for the shielding estimates. This is to avoid having to potentially have to add more shielding after the fact and the space has been allocated or the walls already built. Add-on shielding, to reduce the leakage from penetrations, could take valuable space in the work area; it would make access to certain areas impractical and might constitute tripping hazard.

The same issue above applies to any gaps under the bunker door. The tolerance for the door design, in the case of mazeless doors, and the possible leakage underneath should be analyzed at the time of shielding design.

COOLING WATER CIRCUIT ACTIVITY

Cooling water is used to cool components mainly targets and collimators. The heat load is depending on the target design, beam intensity and collimation efficiency. Along with the heat, water will be radioactive especially with short-lived activity. The design should look into the potential of activation of the water volume and devise a solution to prevent from exposing the workers to high radiation fields during the cyclotron running.

Predicting the level of water activation during operation under maximum operating parameters has some uncertainty. Proponents should apply conservative estimates for these components and either install or have provisions for implementing particular measures to reduce the radiation from cooling circuits outside the shielded bunker. This may include delay loops in the circuit in the exclusion area or special shielding for the heat exchanger area. In either case, space is needed to potentially accommodate such measures.

STORAGE OF ACTIVE COMPONENTS

The amount and the need for storage of active components vary between one machine and another. This is not only related to the workload and use of the machine but also to its design and the performance of the machine. So far, the number of machines installed and operating is not large enough to predict standard maintenance and servicing needs. Many components, especially targetry components, are prototypes or under testing and development.

It is possible that a storage location for activated components is rarely used. However, in the case to the contrary, when no shielded space is available in the original design, this becomes a safety concern. A location for storage far from bunker is not practical and might discourage the operators from safely storing the active components in the designated locations, leading to components being temporarily stored in an inappropriate area.

The cyclotron bunker and/or a target room might be attractive options for storing active components due to their proximity to the cyclotron and to the fact that the areas are shielded and rarely occupied. However, the potential high residual radiation fields in the target areas might be a negative factor due to the dose to the workers accessing the area.

Having sufficient space to store the components underground or inside a shielded box is acceptable. Adding a storage container after the fact might reduce the work area or access around the target stations or the cyclotron, both of which are required for the safe use of the facility and traffic of workers.

MANAGEMENT OF RADIOACTIVE WASTE FROM CYCLOTRON AND PROCESSING LABS

The procedural aspect of waste management is not necessarily finalized with hammering out all the details at the design phase. It is somehow dependent on the volume, nature and the activity of the potentially radioactive waste and the decay rate of the radioactivity processed. However, having sufficient space to store the waste safely in the proximity of the work area is important. An inappropriate waste storage location, whether for interim, i.e., during the processing, or for longer-term waste storage, is practically useless, since workers might use makeshifts instead. A storage location outside the work area is not recommended as it introduces unnecessary movements crossing the contamination zone barriers.

CONTAMINATION CONTROL ZONES AND HAND AND FOOT MONITORS

For an isotope production and processing cyclotron facility, the design of the zoning of the facility with regard to the susceptibility of contamination is a challenge. There are various considerations which are not all compatible. "Clean" rooms, or areas to meet the medical requirements, are normally inserted in the facility and present the heart of conventional medical radio tracer production such as FDG. Also, depending on the recent operation of the cyclotron and the isotopes produced including their half-lives, the needs for contamination control check at the exits vary.

It is expected that at the exit of a contamination control area that hand, foot and goods are checked clear of contamination. Also, all gloves, overshoes and lab coats removed must be kept at the check point of the contamination control area. If contamination is found on an item, there must be at provision to store the contaminated items safely and appropriately at the exit/check point.

Whether it is a handheld contamination detector, a full body or a hand and foot monitor, a minimum space is required to accommodate the setup and the "contamination control" station. When this is not fully taken into account at the design stage, the introduction of a contamination control check point is done on the expense of other operational requirements, such as corridors and access

ISBN 978-3-95450-167-0

entrances. This could make the access and exit point to a contamination control zone crowded or narrow.

Finally, if the operator of the facility intends to operate the facility under various schemes where contamination hazards may be different, the design should allow for different access protocols for contamination control purposes with distinct and clear procedures for what is required at each case. More specifically, it is possible to define different exit paths or verification requirements depending on the mode of operation.

CONSTRUCTION AND COMMISSIONING PROJECT MANAGEMENT

Most of the new projects for radioisotope production cyclotrons in Canada belong to medical or academic institutions. They often have little or no previous experience with this type of facility. The institutions should build the project team with enhanced knowledge and experience with or training on this special type of facility.

The radiation safety and regulatory resources required for such projects is much more than what is needed for other conventional facilities and licensing such as medical linacs or nuclear medicine applications. While in a case of a medical electron accelerator for instance, a medical physicist and radiation safety officer might be able to oversee the project from the regulatory and safety side, in the case of a cyclotron, it is usually different individuals or groups performing these two tasks. Coordination of the communications with the regulator and satisfying the regulatory requirements is an important task that should not be postponed until it might be too late for the project where design decisions have already been made.

INTEGRATION OF EQUIPMENT SAFETY SYSTEMS WITH BUILDING SAFETY SYSTEMS

A radioisotope production cyclotron facility comprises several systems performing various monitoring and control functions. The cyclotron machine safety interlock proper is only a part of many other safety systems ensuring the safe operation of the facility. For instance, a plug type door for a cyclotron bunker is often controlled by its own operating, movement and interlock system. The nuclear ventilation system normally has its own back up, monitoring and control features which are part of the building monitoring. There are many other examples such as electrical safety, fire protection system, drainage or sump monitoring, target transfer systems, hot cell monitoring, as well as radiation monitoring systems. Each of these systems has one or more safety functions meaning that it monitors certain parameters and either alerts the operator or triggers an action like shutdown or diversion or switching to render the process safe.

Usually, these systems are designed and installed by different specialized companies or groups with varying degrees of familiarity with the other components of the overall facility. It is critical that these systems work together and communicate properly to achieve the desired functions. Designing, building and commissioning the interface between these systems requires particular attention from the part of the project management to ensure common understanding of each system input and output requirements.

As every system needs to be maintained and tested periodically, it is a good practice to design a periodic verification program covering all the involved systems and features of the facility and its auxiliary systems. Designing the facility with the notion of integration of safety is useful also for compliance verification purposes as the regulator requires the licensee assurance and verification that all work as intended without safety degradation.

NUCLEAR VENTILATION AND FILTRATION OPTIONS

In general, two streams of ventilation are required for a cyclotron facility for isotope production; one for the cyclotron and its targets and one for the processing hot cells and fume hoods. Routine operation generates airborne activity from air activation in the vault and target area near high intensity neutron fields. This represents a continuous, but often of limited concern, stream of small radioactive release to the facility stack. More of a concern is activity escaped during processing in the hot cells or from the targets during or after irradiation.

Some older designs have used delay tanks to slow releases until decay. Nowadays, more efficient filtration with charcoal filters is considered the norm. The filters could be close to the source or at the stack depending on the design choices and space limitations. New hot cell designs come with ventilation interlocks where ventilation stops when a detector at the exhaust of the hot cell detects a high level of airborne activity. In such situations, the hot cell air volume is open to an emergency system of storage tanks under negative pressure to suck the contaminated air volume.

If the processing side and the cyclotron side of the facility are to use the same stack, protection against backflow should be devised and analyzed during the original design and an upgrade to any leg of the nuclear ventilation system.

An analysis, at the design stage, of the consequences of releases from failed targets or processing should define the source term releases that should be filtered or confined by the ventilation protection systems.

STRATEGY FOR STAFFING AND TRAINING

The design and commissioning of the project as well as building the various components of the facility constitute an excellent opportunity to train staff for operation and safety functions to run the facility in the future. It is expected that the applicants document all design basis arguments and decisions during the progress of the project. This is usually mandated by their quality assurance programs. It is also required that all the facility defining safety parameters are documented as part of the licence

ISBN 978-3-95450-167-0

application and will eventually be part of the licence requirements when a licence is issued.

It is strongly recommended that the applicant build the facility operation team right from the start of the project. This team will be involved in the regulatory interactions as well with the commissioning tests of the facility. Ideally, contracts with specialized companies to deliver and or install certain components of the facility should include training provisions. A long initial training period is often needed for new staff to get familiar with the operation and safety of the facility and to understand the logic behind the chosen design options. By introducing the new staff to the project prior to the operation and during the progress of the project, the above mentioned safety vulnerability can be eliminated.

CONCLUSION

Designing and building a cyclotron facility for isotope production requires careful planning and taking into account all safety considerations related to the various components and aspects of the facility. The Canadian Nuclear Safety Commission promotes safe design and early consideration of safety factors right from the start of the project. A number of recommendations are brought to the attention to the proponents during the planning phase to ensure the highest level of safety during the operation phase.

REFERENCES

[1] *Nuclear Safety and Control Act,* `http://laws-lois.justice.gc.ca/eng/acts/N-28.3/`

[2] *Class II Nuclear Facilities and Prescribed Equipment Regulations,* `http://laws.justice.gc.ca/eng/regulations/sor-2000-205/FullText.html`

[3] *Radiation Protection Regulations,* `http://laws.justice.gc.ca/eng/regulations/sor-2000-203/page-1.html`

ISBN 978-3-95450-167-0

OPERATION AND MAINTENANCE OF RF SYSTEM OF 520 MeV TRIUMF CYCLOTRON*

N.V. Avreline, V.L. Zvyagintsev, I.V. Bylinskii, C. Bartlett, B. Jakovljevic, T. Au
TRIUMF, Vancouver, B.C., Canada

Abstract

1 MW CW 23 MHz RF system of the TRIUMF 520 MeV Cyclotron has been in operation for over 40 years. Continuous development of the RF power amplifiers, the waveguide system and of the measurement and protection devices provides reliable operation and improves the performance of the RF System. In this article, operation and maintenance procedure of this RF system are analyzed and recent as well as future upgrades are being analyzed and discussed. In particular, we discuss the improvements of the transmission line's VSWR monitor and their effect on the protection of the RF system against RF breakdowns and sparks. We discuss the new version of input circuit that was installed, tested and is currently used in the final stage of RF power amplifier. We analyze various schematics and configurations of the Intermediate Power Amplifier (IPA) to be used in the future. The thermo-condition improvements of the Dee voltage probe's rectifiers are described.

INTRODUCTION

TRIUMF 520 MeV Cyclotron's high power RF system consists of three main parts – the 1.8 MW CW RF amplifier, the transmission line (TL) and the resonator [1]. The TL itself is composed of two coaxial lines with wave impedances of 50 and 30 ohm. The second part of the TL has three capacitor stations that match 50 ohm impedance of the TL's first part with the coupling loop port of the resonator that is at TL's terminus.

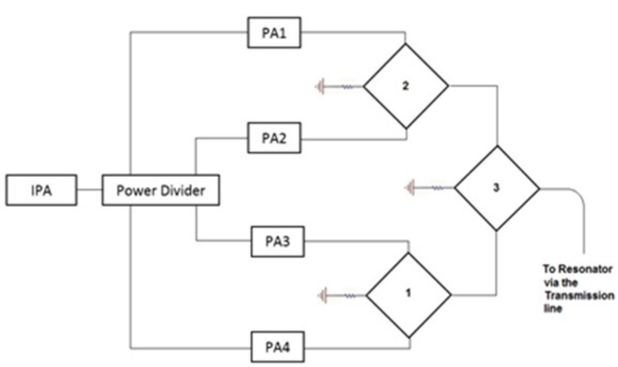

Figure 1: RF System of the 520 MeV cyclotron.

*TRIUMF receives federal funding via a contribution agreement through the National Research Council of Canada.

TRANSMISSION LINE RESONATOR OPERATION AND SPARK PROTECTION

Instability in the RF system's operation appears when there are sparks, electrical breakdowns and multipactor discharge in the resonator. The VSWR monitor is used to protect the RF system. This monitor turns off the RF system, if the reflected power in one of the 12 channels exceeds a specified threshold value. The RF control system analyses the rate of Dee voltage drop, classifies the events and then tries to recover the system. The follow up analysis of where sparks and electrical breakdowns took place is done using an oscilloscope. The oscilloscope operates in stand-by mode otherwise. An example of a typical signal pattern that illustrates a spark inside the resonator is presented in Fig. 2.

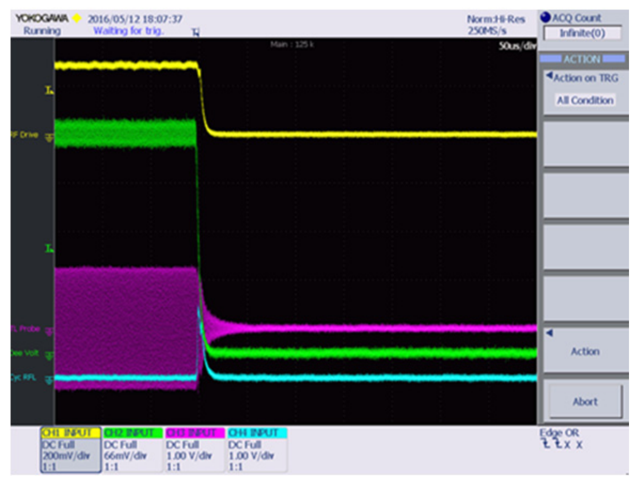

Figure 2: Resonator RF signals following a spark, when drive is OFF (yellow – drive amplitude, green – Dee voltage, pink – RF signal, blue – rectified voltage of the reflected signal).

The rate of Dee voltage drop allows to determine, whether this spark happened inside the resonator or inside the TL and how large the spark was. The RF control system has sensors to determine the Dee voltage drop and if zero Dee voltage is detected. If either case is detected the RF control system generates the signal to turn OFF the RF drive and to determine the time when RF system's recovery should be attempted.

However, if these sensors didn't respond properly or responded with some delay, the standing beat wave in the TL could reach double amplitude of the original signal (see Fig. 3). As a result, some parts of the TL such as matching capacitors, the water feedthrough or the TL conductors and insulators could be damaged.

ISBN 978-3-95450-167-0

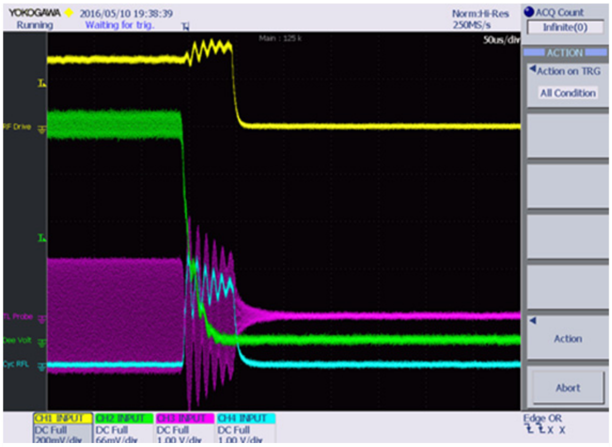

Figure 3: RF beat signals following a spark in the oscilloscope, when the drive is ON (yellow – drive amplitude, green – Dee voltage, pink – RF signal, blue – rectified voltage of the reflected signal).

To prevent the case demonstrated in Fig. 3 and to protect cyclotron equipment, the RF switch was built into the VSWR monitor to disconnect the RF drive from the RF amplifiers.

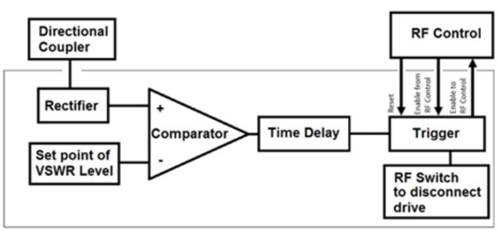

Figure 4: The block diagram for one channel of the high VSWR detector in the VSWR monitor.

Some of the weakest parts of the TL to damage following a spark are the water hoses between the outer and the center conductors of the TL. The water entrances into the center conductor are simulated in HFSS v15.0 (see Fig. 5).

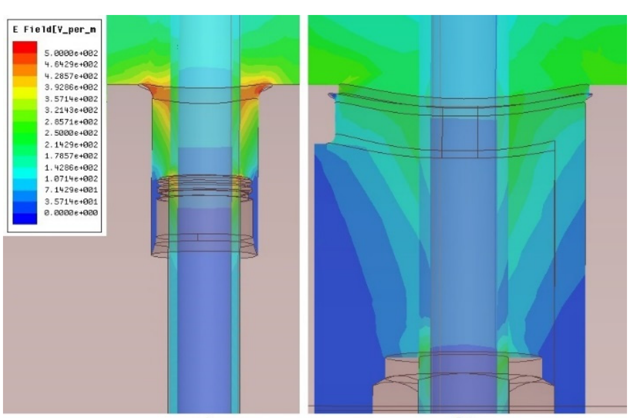

a) b)

Figure 5: Simulation of the RF field near the water feedthrough in the TL for the original (a) and the new design (b).

In order to improve TL's reliability, the configuration of the conductors in the area with the highest RF field was modified. A simulation in HFSS determined that the RF field is three times higher near the water feed (ε=81) into the central conductor. As a solution, the compression fitting was moved deeper into the central conductor.

HIGH POWER RF AMPLIFIER

The high power RF amplifier is composed of the intermediate power amplifier (IPA), the splitter, four high power amplifiers (PA) and three combiners (see Fig.1). The performance and the stability of the RF system is dependent on the quality of vacuum tubes, the ability of the high power RF capacitors to operate in high RF voltage and on the condition of the DC power supplies.

PA Tuning, Operation and Development

Each of the four PAs are composed of two 4CW250,000E tetrodes that operate in push-pull mode. Those amplifiers are designed to operate up to 450 kW CW. In order to increase the life time of these tubes they are operated at a 50% lower power and 10% lower filament current (with respect to the nominal values). As a result the tetrodes' lifetime is now beyond 135,000 hours.

During the last maintenance period, the PA4 amplifier was upgraded. A new input circuit was installed in order to improve its accessibility and to reduce the downtime involved in troubleshooting as well as during input capacitor replacement.

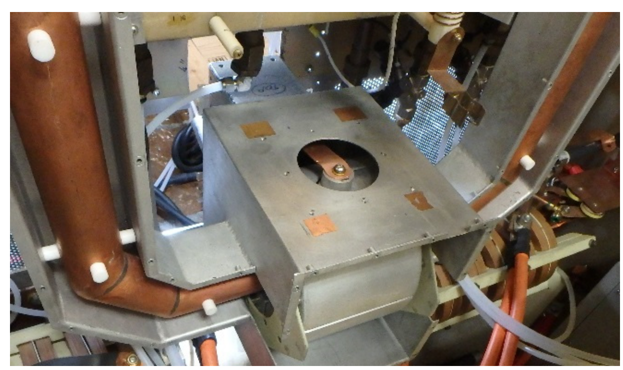

Figure 6: Installation of a new PA4 input circuit.

IPA Operation, Tuning and Development

The IPA consists of two stages: a pre-amplifier pentode and a final tetrode. The maximum power that could be reached under the current design is 100 kW. However, in order to increase the life time of the IPA tubes, a 4CW100,000E tetrode is used at the output stage to reach only 50 kW and is operated at 10% lower filament current.

The tetrode stage is loaded with the Pi-network which is connected to the 4-way splitter. This splitter distributes the output power between PAs inputs. To determine the impedance of this load, the method of variations of capacitances [2] was applied to the Pi-network. Independent variations of C37, C40 (see Fig. 7) from the

ISBN 978-3-95450-167-0

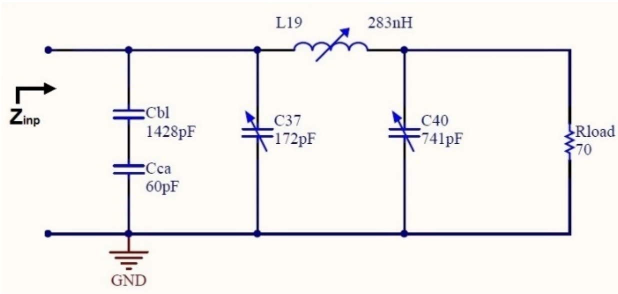

Figure 7: The load schematics setup for the variable capacitance method.

original values allow to derive five equations for resonance conditions with C37, C40 and L19 being the unknown variables.

$$Im\big(Z_{inp}(\omega_1, R_{load}, C_{bl}, C_{ca}, C_{37}, C_{40}, L_{19})\big) = 0$$

$$Im\big(Z_{inp}(\omega_2, R_{load}, C_{bl}, C_{ca}, C_{37}', C_{40}, L_{19})\big) = 0$$

$$Im\big(Z_{inp}(\omega_3, R_{load}, C_{bl}, C_{ca}, C_{37}, C_{40}', L_{19})\big) = 0$$

$$C_{37}' = C_{37} + \Delta C_{37}$$

$$C_{40}' = C_{40} + \Delta C_{40}\ ,$$

where $\omega_1, \omega_2, \omega_3, R_{load}, C_{bl}, C_{ca}$ are the measured values, values of C_{37}, C_{40}, L_{19} are the unknowns. MathCAD Prime 3.1 has been used to solve this system of equations.

This more precise measurement of load impedance allowed to determine the regime of tubes. As a result, the screen current was reduced, which allowed more stable tube operation.

Currently the IPA is being redesigned. The new IPA configuration will have four independent 12 kW solid state amplifiers directly connected to the inputs of PA amplifiers. The amplitude and the phase will be fixed before each IPA input. The development of a new IPA design will be carried out in several stages. Currently the IPA is based on pentode and tetrode vacuum tubes, where the tetrode has the neutralization circuit via the pentode load. The goal of the first stage of the new design is to make these tubes independent. In the second stage of the new design, the pentode will be replaced by a 2 kW solid state amplifier. In order to achieve independence of the pentode and the tetrode, a different neutralization circuit is proposed for the tetrode (Fig. 8). This circuit has been developed using the prototype that currently is used as a part of TRIUMF's ISAC-1 particle accelerator. The mechanical design and the series of simulations in Micro-Cap and Altium Designer 10 are currently completed. The equivalent circuit for neutralization and the results of simulation in Micro-Cap presented on Fig. 9. The current timeline is to rebuild and test IPA in the winter shutdown of 2017.

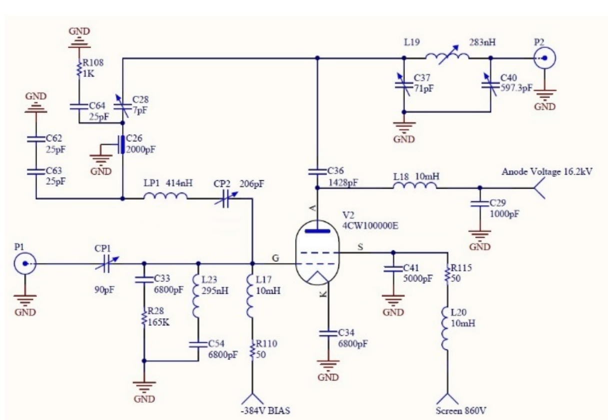

Figure 8: The tetrode stage with a new neutralization.

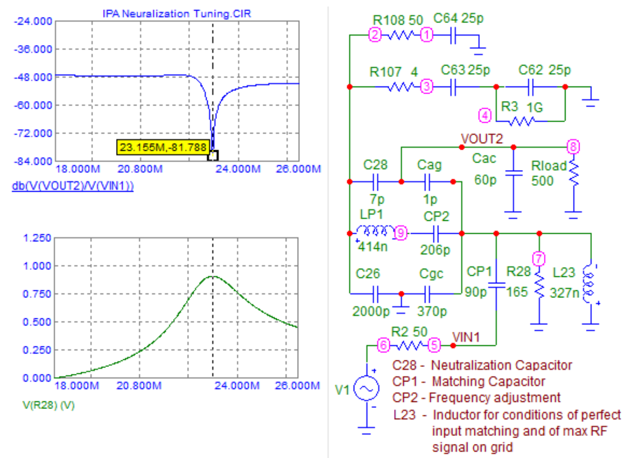

Figure 9: Simulation of neutralization tuning.

MAINTENANCE OF RF SYSTEM

All high power RF components such as vacuum capacitors of the amplifier, combiners and the TL have an annual maintenance service carried out during the 4-month winter shutdown or during the 10 days of the autumn mini shutdown. A hi-pot test for the capacitors and the vacuum tubes, inspection and cleanup of RF components, a low and high power level tuning are carried out during those maintenance periods. An inspection of the TL, the vacuum capacitors of the matching stations, the booster resonator, the water cooling pipes and hoses in the vault are also performed during every winter shutdown.

CONCLUSION

Fine tuning of PAs and the IPA, installation of the RF switch in the VSWR monitor, thermo-stabilization of the Dee voltage rectifiers resulted in stable operation of the high power RF system for a period of few months without any major interruptions.

REFERENCES

[1] Y. Bylinski, S. Calic, K. Fong, R. Poirier, "TRIUMF Cyclotron RF System Refurbishing", in *Proc. 17th International Conference on Cyclotrons and their Applications*, Tokyo, Japan, Oct. 2004, pp. 326-329.

[2] E.L. Ginzton, "Resonant-cavity characteristics: Measurements of R_o/Q_o", in Microwave Measurements, Leonard I. Schiff, Consulting Editor, Mcgraw-Hill Book Company, Inc., New York, Toronto, London, 1957, pp. 435-438.

ISBN 978-3-95450-167-0

STATUS OF THE COSY/JÜLICH INJECTOR CYCLOTRON JULIC

M. Bai, O. Felden, R. Gebel, H.-P. May[†], Forschungszentrum Jülich, IKP-4, Germany

Abstract

The accelerator facility COSY/Jülich is based upon availability and performance of the isochronous Jülich Light Ion Cyclotron (JULIC) as pre-accelerator of the 3.7 GeV/c COoler SYnchrotron (COSY). From 1993 to 2014 JULIC provides in 24/7 operation for more than 6500 hours/year polarized or unpolarized negatively charged light ions for COSY experiments in the field of fundamental research in hadron, particle and nuclear physics. The cyclotron has reached in spring 2016 in total about 285000 hours of operation since commissioning in 1968. The on-going program at the facility foresees increasing usage as a test facility for accelerator research and detector development for realization of the Facility for Antiproton an Ion Research (FAIR), and other novel experiments on the road map of the Helmholtz Association and international collaborations. In parallel the COSY beam and the cyclotron beam are also used for irradiation and nuclide production for fundamental research purposes. For that purpose the irradiation capabilities and diagnostic tools have been upgraded in the last years. Experience with special rf devices and pulsed ion sources for JULIC enables the development of dedicated tools for experiments and other accelerators, e. g. a pulsed 100 keV source for protons and negative ions for the ELENA project at CERN.

INTRODUCTION

The Institute for Nuclear Physics (IKP) [1] is focusing on the tasks given by the Helmholtz Association (HGF). This comprises the design and preparations for the High Energy Storage Ring (HESR) of FAIR [2] with the PANDA experiment. The on-going hadron physics program at the Cooler Synchrotron COSY exploits the internal experimental set-up PAX. The extracted beam is used for the PANDA experiment and also for high energy irradiation in the area of the finished TOF experiment. IKP is part of the new section "Forces And Matter Experiments" (FAME) at the Jülich-Aachen Research Alliance (JARA). This joins scientists and engineers from RWTH Aachen and Forschungszentrum Jülich for experiments, theory and technical developments for anti-matter (AMS) and electric dipole moment experiments (EDM). The institute is member of the new HGF project Accelerator Research Development (ARD) and pursues research on various accelerator components. The future project Jülich Electric Dipole Moment Investigation (JEDI) [3] will profit from the availability of polarized beams from the injector cyclotron and the unique capabilities and experiences at the COSY facility.

CYCLOTRON OPERATION

Since 1968 the Cyclotron JULIC (see Fig. 1) has been operational and provided overall more than 285000 hours availability for experiments and beam development [4-6]. The fraction of the run time since start of commissioning as COSY's injector in 1992 is shown in Fig. 2. In the first 4 years on H_2^+-beams were used for the stripping injection into the synchrotron ring. Two negative ion sources provide beam for routine unpolarized operation [7]. A source of the charge exchange type provides polarized particles beam.

Figure 1: The isochronous cyclotron JULIC.

About 98% of the scheduled beam time could be provided for experiments. Excluded were short events, like sparks, which are recovered automatically by rf control computer or by operator's reaction. The most common reasons for these events were power drops, shortage in water cooling and failures in the rf subsystem. The time for septum exchanges has substantially decreased after essential improvements have been done.

Cyclotron Maintenance

The Cyclotron is in use since end of 1968. Most of the systems for injection and acceleration were improved and refurbished between 1980 and 1992. A new rf generator has been installed in 1992. Wear-out symptoms have been observed, analysed and fixed during the last decade. The vacuum system and its control system have been upgraded with respect to oil-free operation. The central adjustable air-line tuner has been replaced in 2007.

[†]h.may@fz-juelich.de

ISBN 978-3-95450-167-0

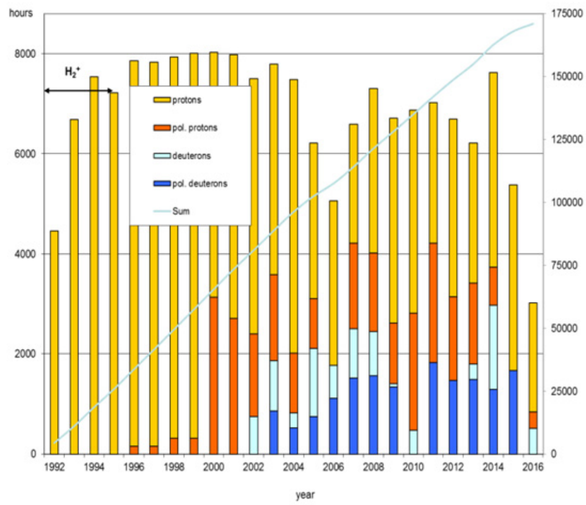

Figure 2: Provided beam hours from the cyclotron since start-up for COSY operation.

A laser station for cleaning of surfaces was bought in 2012. This equipment enables an excellent and smooth cleaning of surfaces, which have been contaminated during the beam operation, without mechanical damages and chemical remains. For this reason the reliable function of high loaded components like tungsten buttons of the pol. ion source, the hyperboloid inflector of the injection and high voltage insulators could be improved.

Septum Deflector Progress

Like other systems of the cyclotron the septum was optimized for Q/A = ½ and the transmission for H- does not reach the quality of D^- extraction, where 70 % can be reached. Sparking and high dark current, due to depositions on the isolator, limit the usability of the septum for operation at voltages above 30 kV. The current septum is a significantly improved version. It is formed by a tungsten wire fence in a titanium support and. The high voltage electrode is supported by ceramic insulators. A method has been developed to make a vacuum tight join between the ceramic and titanium end caps without any additional material. The ceramic supports are also used for the cooling fluid Flourinert FC770. These and many detail modification increased the standing time. The current septum was mounted in 2011 and it functions without serious mistakes till present.

ION SOURCE DEVELOPMENT

Unpolarized Ions

For commissioning of COSY, and for the first three years of the experimental program, an in-house developed 2.45 GHz microwave source delivered $H2^+$ beam without any significant downtime. After 1996, two independent sources for unpolarized beams have been installed. Both sources are of the multi cusp type and have been delivered by IBA, Louvain-La-Neuve (Belgium), and AEA, Culham (England). Both provide at least 300 µA in pulsed operation. With 150 µA at the injection of the cyclotron, 10 µA extracted beam current can be achieved.

Polarized Ions

The polarized ion source has been built and set in operation by a collaboration of groups from Bonn, Erlangen and Cologne. The source is designed to deliver polarized H^- or D^- within the acceptance of the cyclotron during 10…20 ms injection period of COSY. High polarization and brilliance is provided by the colliding beams source. In a charge exchange reaction between a ground-state nuclear polarized hydrogen, or deuterium beam and a fast neutral caesium beam, a negatively charged beam is produced with high selectivity. Brilliance and polarization can be adjusted. The original design value of 30 µA at the exit of the source has been surpassed in routine operation in 2005 and peak values around 50 µA have been achieved [8]. The peak intensities of polarized beams extracted from the cyclotron have exceeded 2 µA for H^- and D^-.

Improvements of the Ion Source Control

Actual activities are the replacement of the partially DOS based control systems for the ion sources and their vacuum equipment to a STEP7-PLC. A graphical user interface (GUI) based on WinCC enables easy and reproducible operation and monitoring (see Figs. 3 and 4).

New Ion Sources

Within the framework of the Helmholtz Association's ARD program, new ion sources for future projects like ELENA at CERN and for FAIR are under development. ELENA is a compact ring for cooling further deceleration of 5.3 MeV antiprotons delivered by the CERN Antiproton Decelerator down to 100 keV [9]. A new source for commissioning of the small synchrotron was developed and installed at CERN in 2015. It is shown in Fig. 5. It is designed to provide µs pulses of 100 keV p and H^- beams with high brilliance.

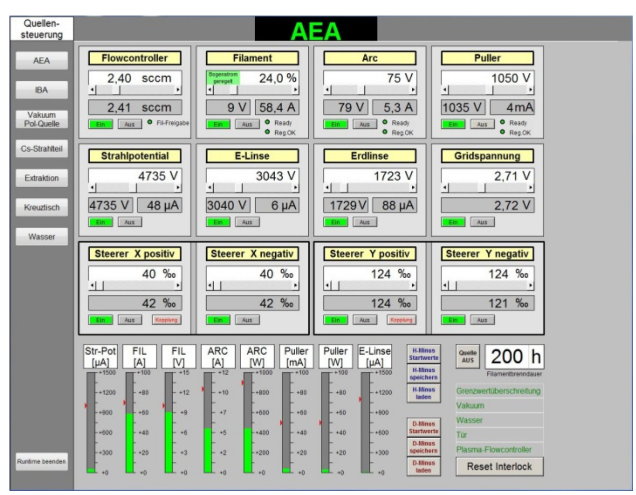

Figure 3: GUI for ion source operation parameter.

ISBN 978-3-95450-167-0

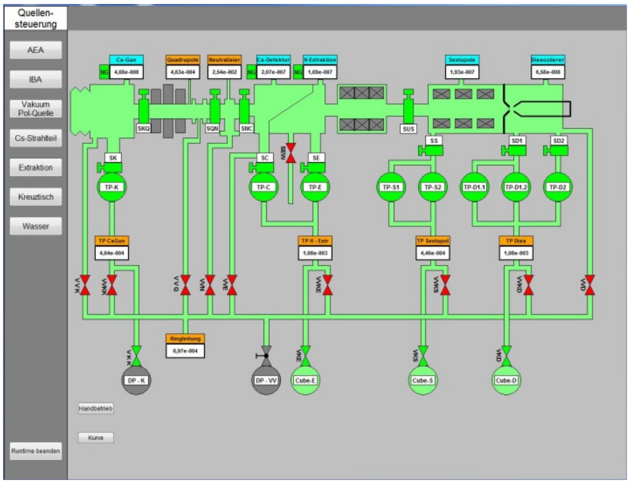

Figure 4: GUI for vacuum operation of polarized source.

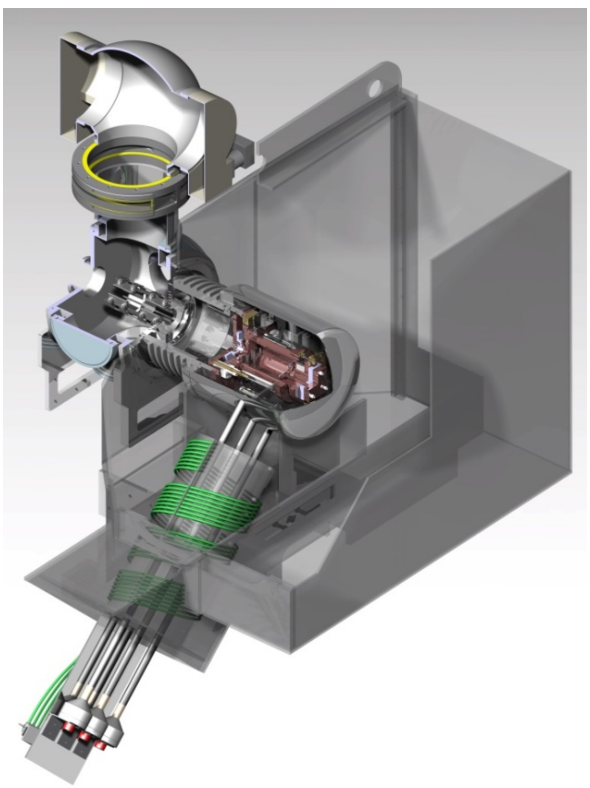

Figure 5: 100keV ion source for CERN's ELENA project.

FURTHER ACTIVITIES

Irradiations

The cyclotron is equipped with a target behind the septum, which provides special support for fast exchange of irradiated target constructions. An overview of the actual activities for irradiation and nuclide production are described in [10].

Monitoring and Diagnosis

To get a better understanding of the correlation of beam behaviour and external influences on the cyclotron a new, more comfortable monitoring system based on LabView shall be installed. In the first step a system for monitoring and fine control of the main magnetic field was installed. It controls the B-field in between a range of 0.4 µT and shows deviations e. g. caused by internal magnetic steerers for beam displacement (see Fig. 6).

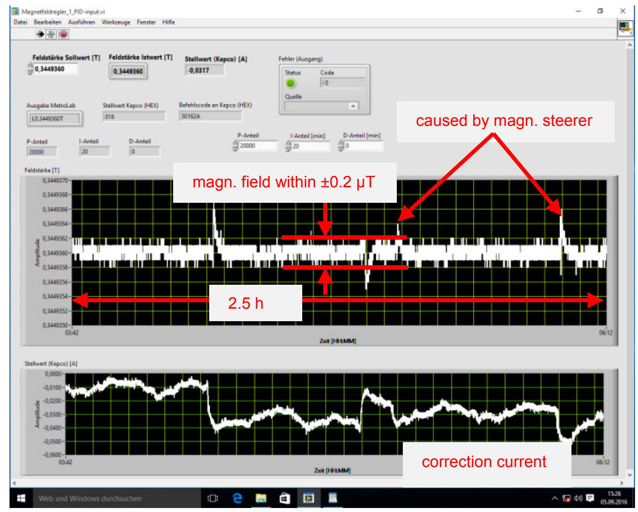

Figure 6: Magnetic field fine regulation by LabView controller during extraction optimization with internal steering magnets.

REFERENCES

[1] http://www.fz-juelich.de/ikp/en
[2] http://www.gsi.de/fair
[3] http://www.collaborations.fz-juelich.de/ikp/Jedi
[4] R. Maier, Cooler Synchrotron "COSY – performance and perspective", NIM A 390, (1997) p. 1.
[5] W. Bräutigam *et al.*, "H- operation of the cyclotron JULIC as injector for the cooler synchrotron COSY-Jülich", in *Proc. Cyclotrons'98*, Caen, France, June 1998, IOP (1999) p, 654.
[6] W. Bräutigam *et al.*, "Extraction of D- beams from the cyclotron JULIC for injection into the cooler synchrotron COSY", in *Proc. Cyclotrons'01*, East Lansing, USA, May 2001, AIP (2001), p, 123.
[7] R. Gebel *et al.*, "Negative ion sources at the injector cyclotron JULIC for the cooler synchrotron COSY", in *Proc. Cyclotrons'04*, Tokyo, Japan, October 2004, Particle accelerator Society of Japan, (2005) p. 287.
[8] O. Felden *et al.*, "Tripling the total charge per pulse of the polarized light ion source at COSY/Jülich", AIP Conference Proceedings 925, (2007) p. 105.
[9] W. Oelert *et al.*, "AD performance and its extension towards ELENA", Hyperfine Interact 213, p. 227, (2012) https://espace.cern.ch/elena-project.
[10] O. Felden *et al.*, "Activities for isotope sample production and radiation effect tests at JULIC/COSY Jülich", presented at Cyclotrons'16, Zurich, Sept. 2016, paper MOP18, this conference.

ISBN 978-3-95450-167-0

BEAM INTENSITY MODULATION CAPABILITIES OF VARIAN'S PROBEAM® ISOCHRONOUS CYCLOTRON

S. Busold*, H. Röcken, Varian Medical Systems Particle Therapy GmbH, Troisdorf, Germany

Abstract

Varian's ProBeam® 250 MeV superconducting proton cyclotron is an isochronous cyclotron for radiological applications using pencil beam scanning mode and provides continuous beam (at its fundamental frequency of 72 MHz). In its clinical operation mode, up to 800 nA of proton beam are specified and routinely extracted. Even more can be extracted in technical mode. The cold cathode Penning ion source provides enough protons to reach this current, and a layer-to-layer intensity modulation of the scanned beam is realized with an internal electrostatic deflector, which is used to vary the extracted beam current between maximum and zero. However, for research applications there is sometimes the request for higher flexibility, in particular for higher possible beam intensities and faster beam intensity modulation. In order to explore capabilities of the machine for such research modes, experimental investigations have been performed: Pulsed beams with repetition rates of up to 2 kHz and variable pulse lengths down to 4 µs as well as peak currents during pulse of up to 30 µA are in the accessible range with only changes at power supply level.

STANDARD OPERATION MODE

The ProBeam cyclotron delivers up to 800 nA proton beam in clinical operation. Protons are generated in the internal cold cathode Penning ion source, which is running continuously and allows varying the beam current via setting of the internal discharge current. The relation between both is found to be linear in the typically used internal discharge range (80 to 280 mA). The source parameters typically need adjustment only once at the start of each treatment day, and in general need little tuning along cathode life time to compensate for the normal wear of these parts.

Fast beam intensity modulations during treatment are possible via an internal electrostatic deflector. This deflector is designed for switching frequencies up to 2 kHz and switching times from one stable deflection level to another within less than 100 µs. This time scale for precise switching is determined by ringing, which is caused by the electrical properties of the voltage supply line from power supply to cyclotron. Beam blocking voltage level, however, can be exceeded permanently within only 3 µs.

*contact: simon.busold@varian.com

MODIFICATIONS

Generation of high intensity proton beams for experimental operation is possible via modifications on power supply level and considering the general constraint that the average extracted proton current should not exceed approx. 1 µA for machine safety reasons.

From this follows directly: A pulsed beam operation is necessary to limit the average current. In particular, a pulsed operation of the ion source supports this operation mode by allowing much higher short term internal discharge currents (thus extracted beam currents), that would not be stable in continuous operation mode of the source. In the following section, such a pulsed mode of the ProBeam's ion source is characterized.

Change to Pulsed Ion Source Mode

An additional electrical module (one standard 19" rack slot) was installed at the ion source power supply. It basically consists of a capacitor which is constantly charged by the power supply, and a wave form generator controlled high voltage switch, as well as means for current and voltage diagnostics. An extensive parameter scan has been performed at a dedicated ion source test stand [1] at *Paul Scherrer Institut* (PSI) and the dependencies on pulse rate, duty, applied discharge voltage, and hydrogen gas pressure within the source have been evaluated. Although absolute numbers for the extracted beam at this test stand and extracted beam at the cyclotron may not be compared directly, the general scaling behaviour might well be. Results are shown in Figure 1 and Figure 2. Due to the source operation at the test stand at lower magnetic field (approx. 1 T) higher internal source pressures and lower internal discharge currents are used compared to the ProBeam cyclotron.

Several general characteristics could be observed and are in accordance to the expectations in this operation mode:

- Stable operation at much higher peak discharge currents during pulses compared to continuous mode is possible.
- Towards high duty factors the behaviour approaches the continuous mode.
- Shortest pulse lengths result in highest average currents during pulse.
- Higher voltage leads to higher currents.
- Lower H_2 gas pressure is also beneficial for higher currents.

ISBN 978-3-95450-167-0

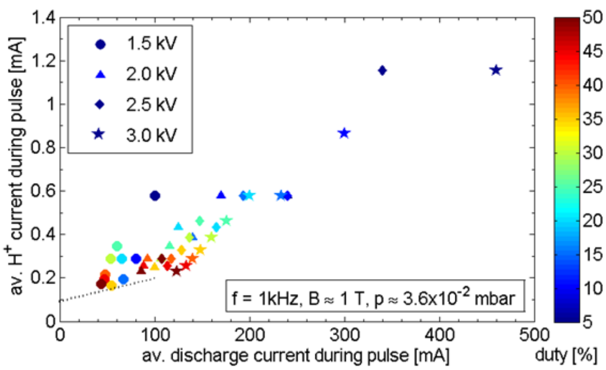

Figure 1: Average extracted proton current during pulses at $3.6x10^{-2}$ mbar hydrogen gas pressure within source. Dashed line indicates standard continuous source operation (duty = 100%).

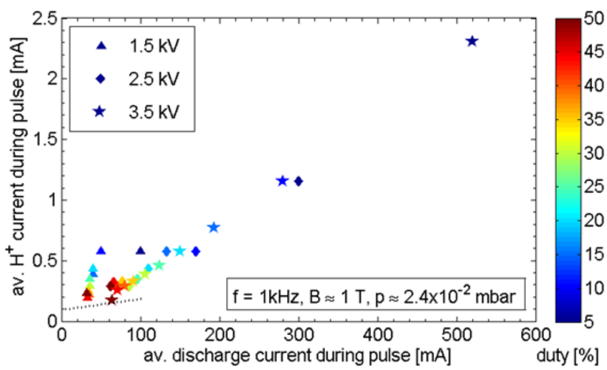

Figure 2: Average extracted proton current during pulses at $2.4x10^{-2}$ mbar hydrogen gas pressure within source. Dashed line indicates standard continuous source operation (duty = 100%).

Compared to continuous mode, the average proton current during pulse could be increased by a factor x10 to x20 at 1 kHz pulse repetition rate, 5% duty, 3.5 kV applied high voltage, $2.4x10^{-2}$ mbar hydrogen gas pressure and a magnetic field of 1 T in the test stand. Peak currents of the extracted protons could not be measured directly in the experimental setup, but can be estimated by analyzing the discharge current characteristic and making the reasonable assumption that the extracted current is proportional to the discharge current.

At switching, the discharge current rises quickly (approx. 4 µs) from zero to a maximum value (depending on applied voltage) and then exponentially decreases (half life approx. 10 µs) towards a constant value, see Figure 3. In the case of 3.5 kV applied voltage a peak discharge current of approx. 2 A was measured. The observed behaviour is independent from repetition rate and duty, and the increased average current towards lowest pulse lengths can completely be attributed to this initial effect of quick discharge current rise after switching and consecutive exponential decay to a DC equivalent level. Considering only the 10 µs around the maximum discharge current, a current increase of at least a factor x30 as compared to continuous operation can be calculated. Additionally, a clear scaling with applied discharge high voltage was observed, giving potential for easy further increase of peak currents.

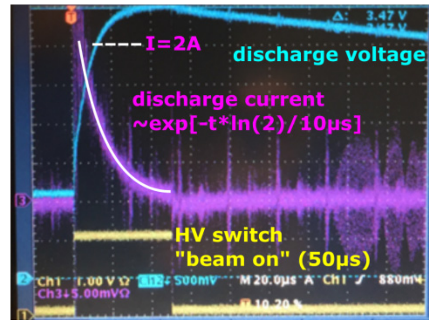

Figure 3: Discharge characteristic (current and voltage) for pulsed operation with 1 kHz repetition rate and 5% duty at 3.5 kV applied voltage.

In order to produce clean short and high intensity proton bunches, the cyclotron's internal deflector might be used to cut out part of the pulsed beam from the ion source. A brief overview is given in the following section.

Modification of the Electrostatic Deflector System

The cyclotron's internal electrostatic deflector can be used to modulate the beam intensity even on µs time scale if the voltage supply cable is matched to suppress ringing.

Calculations show that the system can produce proton pulses down to 4 µs pulse length. Experimentally this has been demonstrated at PSI on an appropriately modified system. Figure 4 shows the picture of such a 4 µs short proton bunch, measured with a fast scintillator and photo diode system connected to an oscilloscope.

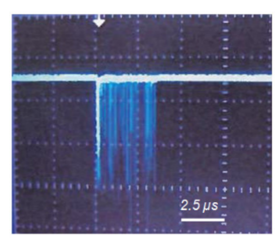

Figure 4: Approx. 4 µs short proton pulse, detected at PSI via a fast scintillator and photo diode (courtesy of J. M. Schippers *et al.*).

CONCLUSION AND DISCUSSION

For research and experimental modes we have introduced a pulsed proton beam delivery mode for the ProBeam cyclotron via moderate modifications at power supply level. Pulsing the ion source and optimizing the internal electrostatic deflector system gives access to pulsed beams (≤2 kHz) with short pulse lengths (≥4 µs) and high peak intensities.

The pulsed mode operation of the ion source was successfully demonstrated at a dedicated test stand at PSI and

ISBN 978-3-95450-167-0

a peak current increase of at least a factor x30 was achieved. Thus, scaling from 1 µA extracted current in continuous mode at the ProBeam cyclotron, an increase to ≥30 µA average current during several µs short beam pulses is possible.

Space charge influences are not to be expected for these currents yet. Furthermore, beam loading is also not expected to be an issue, as the maximum beam power at 30 µA proton current would be 7.5 kW and thus only 6.5% of the total radiofrequency power input into the resonator. Regulation of this influence is possible with the machine's control system.

ACKNOWLEDGEMENT

Many thanks to the PSI staff for their kind support and contributions, especially to P. Frey and J. M. Schippers.

REFERENCES

[1] S. Busold *et al.*, "Recent ion source developments for Varian's ProBeam cyclotron", presented at Cyclotrons'16, Zurich, Switzerland, September 2016, paper THP06, this conference.

RECENT ION SOURCE DEVELOPMENTS FOR VARIAN'S PROBEAM® CYCLOTRON

S. Busold*, H. Röcken, Varian Medical Systems Particle Therapy GmbH, Troisdorf, Germany
J. M. Schippers, A. S. Partowidjojo, Paul Scherrer Institut, Villigen, Switzerland

Abstract
The cold cathode Penning ionization gauge (PIG) type proton source of the Varian's ProBeam® 250 MeV superconducting isochronous cyclotron suffers from the usual cathode/chimney erosion during operation. Furthermore, a relatively high hydrogen gas flow is needed to generate a proton beam in the µA range, which induces conditions for RF operation below optimum. In the quest to increase cathode/chimney life time and thereby directly extend service intervals, thus reducing the total cost of ownership, several experimental investigations have been performed at a dedicated test bench at Paul Scherrer Institut (PSI), Switzerland, including material studies, a detailed operation analysis and switching to a hot cathode design.

THE ION SOURCE TEST STAND

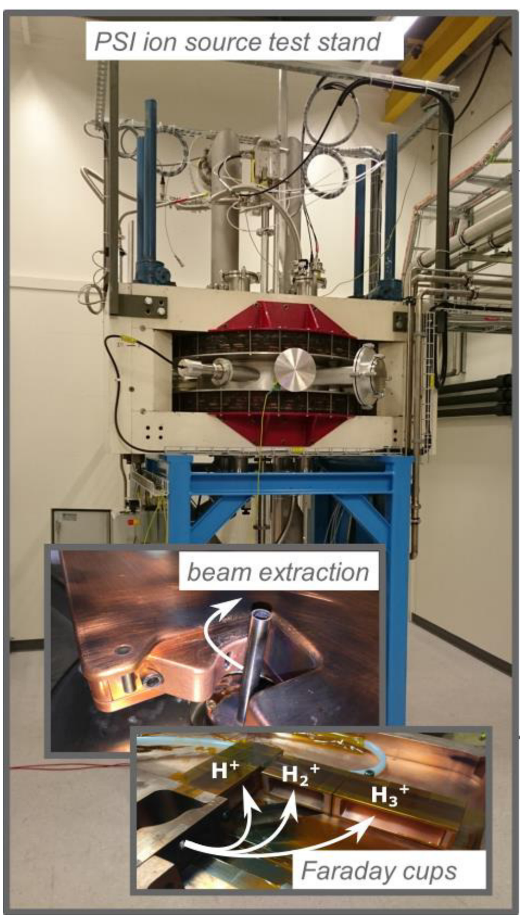

Figure 1: Picture of the test stand. Inserts show beam extraction from source and diagnostic setup.

The dedicated ion source test stand used for this work is located at PSI, Switzerland. A picture of the setup shown in Figure 1. It provides up to 1.4 T central magnetic field, extraction from ion source with typically -30 kV voltage, and ion species separating diagnostics (Faraday cups).

The ProBeam ion source can be operated and its performance experimentally investigated. The main difference to the situation in the ProBeam cyclotron is the lower magnetic field as provided by the test stand's normal conducting magnet. This reduces the confinement of the charged particles in the source plasma and results in higher necessary internal gas pressures, which are achieved by higher hydrogen gas flow rates into the source. While the source in the ProBeam cyclotron is typically run with 1 to 2 sccm hydrogen gas flow, the test stand is operated in the range of 8 to 16 sccm. This difference has to be considered when comparing the results presented here to the situation in the ProBeam cyclotron.

The second difference to the ProBeam cyclotron is the DC extraction at typically -30 kV at the test stand. This does not affect the internal source operation, and has only an influence on the absolute values of the extracted current.

THE COLD CATHODE ION SOURCE

To sustain the internal source plasma, the cold cathode Penning ion source relies on secondary electron emission induced by ions hitting the cathodes. The (only slightly ionized) hydrogen plasma contains mainly H^+ and H_2^+ ions, which have only low secondary electron emission yields (range: 0.2 to 0.5) at the typically used cathode potentials in the range of -1 to -1.8 kV. A stable discharge between few and up to about 300 mA is possible. A schematic of such a source is shown in Figure 2.

*contact: simon.busold@varian.com

ISBN 978-3-95450-167-0

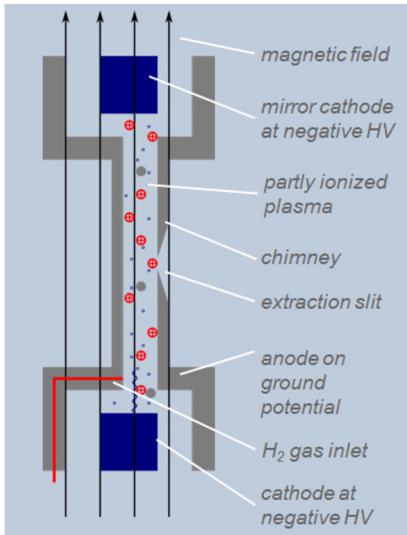

Figure 2: Schematic of the cold cathode Penning ion source. For a typically fixed geometry and constant magnetic field, the discharge characteristics are only depending on internal gas pressure and cathode high voltage.

The cathode material is tantalum (Ta), which is commonly used in such sources due to its low sputter rates and thus potentially high life time. However, it is like other refractory materials prone to hydrogen embrittlement, possibly causing mechanical issues within the material. As the relevant processes are temperature dependent, a thermal analysis of the source design has been performed, resulting in expected cathode surface temperatures in the range of 400 °C due to ion bombardment during operation. This value could also be experimentally verified via IR temperature measurements during source operation. The results of these measurements are shown in Figure 3. The discharge power is for the ProBeam cyclotron typically around 300 W.

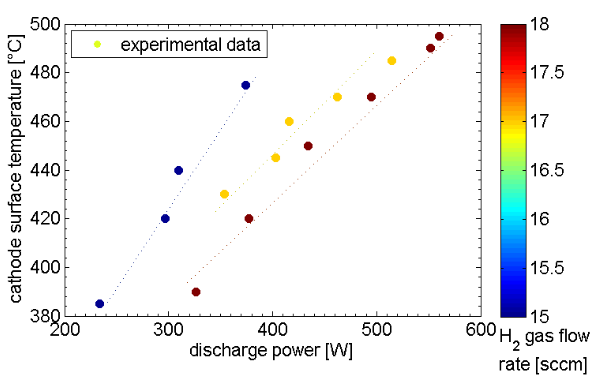

Figure 3: Experimental cathode surface temperature measurements for different flow rates.

First tests of alternative materials have been performed: While titanium suffered from massive sputtering, tungsten showed a similar but still worse behaviour than tantalum, and with niobium massive cracking and material break-up was observed.

Extracted Beam Characterization

Ions are extracted from the source plasma through a small slit in the chimney. Particle trajectories can be determined by extraction potential, geometry, magnetic field strength and charge over mass ratio. With this information three isolated Faraday cups were placed in the setup to independently measure the extracted currents of H^+, H_2^+ and heavier particles (e.g. H_3^+).

Measurements have been performed for different discharge currents and hydrogen gas pressures within the source. Results are shown in Figure 4.

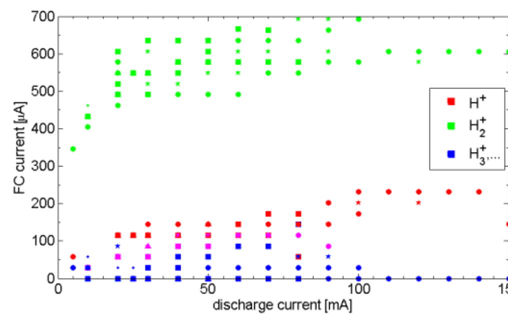

Figure 4: Extracted hydrogen ions from the cold cathode Penning source in dependency of discharge current (x axis) and hydrogen gas pressure (symbol shape).

The dominating ion species is H_2^+. As in general expected from literature, the proton fraction increases with increasing discharge current. In the here performed investigation a slight increase from less than 20% to more than 30% is observed. Furthermore, the ion species ratio is found to be independent from the hydrogen gas pressure within the tested regime of $2x10^{-2}$ to $4x10^{-2}$ mbar. However, scanning a wider pressure range in the ProBeam cyclotron showed a pressure dependency in favour of lower pressures for the proton fraction efficiency.

An estimate on the degree of ionization of the source plasma is possible: Gas flow rates in the range of 12 sccm correspond to equivalent particle currents of 800 mA at full ionization. Measured are instead about 800 µA total electrical current, thus a degree of ionization in the order of 0.1% is assumed, which is in the expected range for such plasmas.

A HOT CATHODE ION SOURCE DESIGN

A hot cathode source design yields several advantages: The necessary electron emission to sustain the source plasma is now a direct process via thermionic electron emission, thus decoupling the electron emission from background gas pressure. This enables the use of lower gas flow rates, which improves the overall vacuum conditions in the cyclotron and is beneficial, e.g., for RF stability; additionally, lower possible cathode potentials might reduce cathode sputtering. Commonly used designs with hot filaments, however, do not seem to be the ideal choice for highest life time of operation. Thus, an approach is

ISBN 978-3-95450-167-0

tested using boride crystals (LaB_6 and CeB_6). These cathodes are commercially available in many types.

Some special thought has to be given to the typically demanding vacuum constrains with these cathodes. However, these general values can be relaxed to some extent when considering the specific partial pressures: While already low partial pressures of O_2 or water vapor lead to significant cathode poisoning and evaporation, the material is basically immune to larger hydrogen partial pressures as the ones to be expected in a proton source design [1].

One cathode of the Penning arrangement was replaced by the hot cathode while the other one was kept in place as mirror cathode at the same potential. Furthermore a power supply for active electrical heating of the hot cathode to working temperatures (around 1500 °C) and a new gas flow controller to access lowest flow rates for hydrogen down to 0.05 sccm was added.

As expected, the hot cathode shows a different operation behavior. Significant current could be extracted already around a drastically reduced hydrogen flow rate of 0.3 sccm (compared to 8 to 16 sccm necessary flow for the cold cathode in the test stand). Furthermore, the expected reduction in necessary cathode potential is observed.

Extracted Beam Characterization

Figure 5 shows first operation results for the hot cathode in the ion source test stand. The worse proton production efficiency is obvious, but still absolute proton numbers seem to be sufficient. The optimum cathode voltage of 300 V is very promising for reduced sputtering effects.

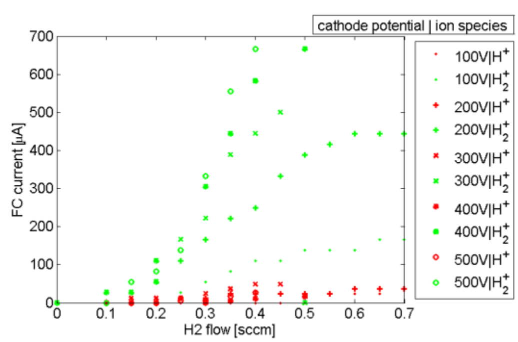

Figure 5: Extracted hydrogen ions from the hot cathode Penning source in dependence of gas flow rate and cathode potential (symbol shape).

CONCLUSION AND OUTLOOK

A test stand for ion source studies is operational at PSI, Switzerland, and first investigations have been carried out to optimize the performance of the ProBeam cold cathode Penning ion source. Additionally, the development of a potentially extended life time hot cathode design is ongoing.

ACKNOWLEDGEMENT

Many thanks to P. Frey and the technical staff of PSI for their kind support and contributions. We also want to acknowledge Dreebit GmbH for the layout of the hot cathode source.

REFERENCES

[1] H.E. Gallagher, J App Phys 40, 44 (1969).

DEVELOPMENT OF CONTROL SYSTEM FOR 10 MeV CYCLOTRON*

M. Hassani†, S.Y. Ghorashinejad, H. Afarideh
Faculty of Energy Engineering & Physics / AmirKabir University of Technology, Tehran, IRAN

Abstract

AmirKabir University of Technology is developing a 10 MeV cyclotron to produce radio isotopes. In order to operate the cyclotron stably, all sub-systems in the cyclotron are controlled and monitored consistently. The control system has been developed based on PLC and the operation is monitored by HMI permanently. Also, the control console located in the control room, provides data logging and controlling different steps of operation by the operator. In addition, the system can be remotely accessed over the network to monitor the status of cyclotron easily. The configuration of the control system for 10 MeV cyclotron will be presented in this paper.

OVERVIEW OF 10 MeV CYCLOTRON

The cyclotron accelerates the negative hydrogen particle to produce radioisotopes, and a couple of sub-systems make the particle acceleration possible. The cyclotron consists of cooling system, vacuum system, magnet system, ion source system, and RF system.

In order to accelerate the particle stably, it is necessary to fix the temperature and humidity of the environment. In addition, the order of vacuum inside cyclotron should be under 1×10^{-6} mbar. A double-stage high-vacuum system has been installed to improve the vacuum state. The cyclotron includes a panning ion gauge (PIG) type ion source for generating negative hydrogen from plasma by the use of arc power supply outside of cyclotron. The electromagnet field made by both RF system and magnet system accelerates the negative hydrogen for the desired energy level. The RF system is composed of two parts which are RF resonator and RF amplifier. The RF amplifier provides the high power RF signals to RF cavity to increase the dee voltage up to 50kV for electric field inside the cyclotron. The electric field is regulated by RF tuner. The average magnetic field is 1.71 T generated by about 143A coil current from magnet power supply (MPS) [1].

CONTROL SYSTEM DESIGN

The control system has access to each sub-system, and monitors the status of each device. In addition, the control system should set the proper parameters depending on the monitoring data from sub-systems, and prevent from the emergency situation occurred during the operation sequence of cyclotron. Therefore, we have carried out a requirement analysis starting from the system specification, and then designed the control system considering capability, expandability and accessibility to achieve high reliability and safety for the system [2].

* Work supported by the Ministry of Science, Research and Technology of Iran.
† mojtaba.hassani@aut.ac.ir

The architecture of the control system consists of two parts; a host computer and a main control system (PLC). The main control system gathers the status signals of all sub-systems and supervises the whole cyclotron, comprehensively. Many parameters used in main control system, are shared with the host computer, so an operator can control the cyclotron through the host computer [3]. Each of sub-systems have a sub-program and interlock functions in PLC to protect them from unexpected damages. The primary specifications of 10 MeV cyclotron are shown in Table 1.

Table 1: Specifications of 10 MeV Cyclotron

System	Parameter	Specification
Magnet	Max/Min magnetic field	0.26/1.83 T
Ion source	Type	PIG
	H2 gas flow rate	0 ~ 10 SCCM
	Beam current	100 μA
RF	Frequency	71 MHz
	Dee voltage	50 kV
	Power	15 kV
Vacuum	Level of vacuum	1×10^{-6} mbar
Cooling	Water Temp.	20 ºC
	Water Resistivity	> 10 MΩ

Cooling System Control

The cooling system is a basis system with vacuum system for beam acceleration of cyclotron. The important parameters of cooling system are water temperature, resistivity, pressure, and flow. Therefore, the parameters are controlled in real time and consistently by different controllers which are installed in the chiller. PLC controls and monitors the status of cooling system by output analogue signals (4~20 mA) of chiller's controllers.

Vacuum System Control

The developing cyclotron has initial vacuum state (about 1×10^{-2} mbar) by using rotary pump, and then makes the high vacuum state (about 1×10^{-6} mbar) by using turbo-molecular pump. There are many valves such like roughing valve, fore-line valve, and main valve, between each vacuum pump and chamber. The vacuum level is measured by pirani and penning gauges. PLC receives the monitoring signals of vacuum status from gauges and controls the vacuum pumps and valves, simultaneously.

ISBN 978-3-95450-167-0

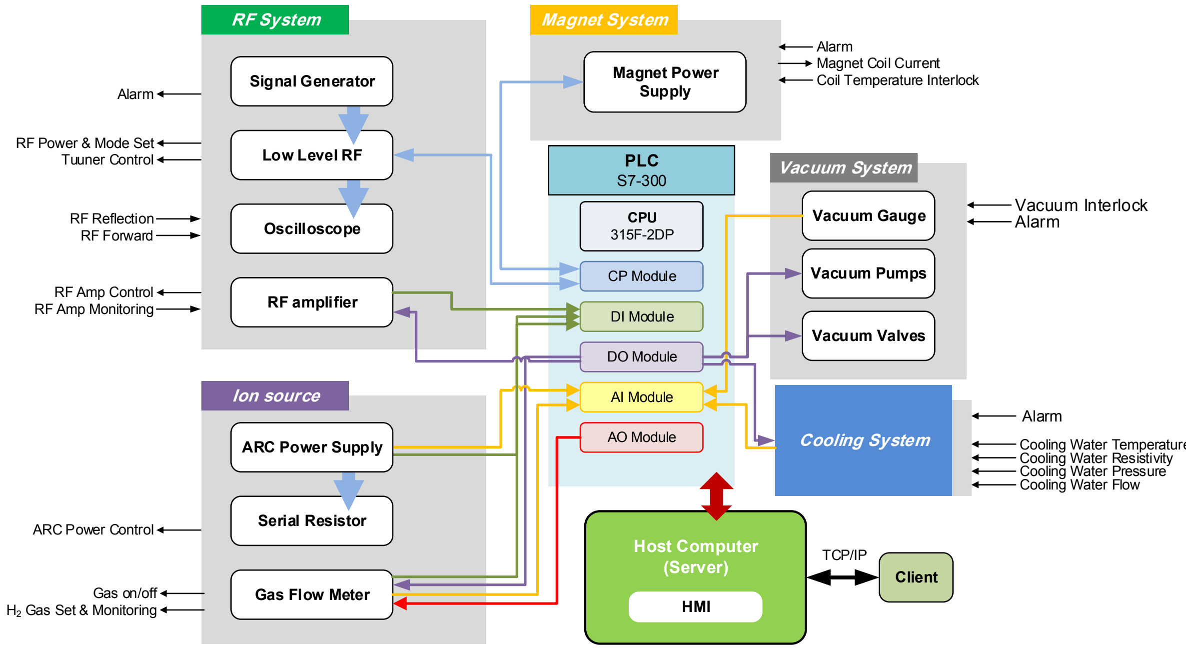

Figure 1: Architecture of 10 MeV cyclotron control system.

Magnet System Control

Magnet system is in charge of beam focusing and acceleration, and the magnet power supply (MPS) provides the current to electromagnet of cyclotron. The MPS includes control module based on FPGA, so that it can make the stability of provided coil current below 10ppm. Also, the magnet power supply can interface with main control system (PLC) through Modbus protocol. Therefore, PLC can access the magnet power supply and share the information about operation such like current value and interlock signals (over current, over heat, etc.).

RF System Control

The RF amplifier consists of pre-amplifier, intermediate power amplifier (IPA) and power amplifier (PA). The PLC can fulfil the sequence control with input and output signals for operation of RF amplifier. So, it can monitor the status of RF amplifier related to overload or interlock, and control the operation of RF amplifier.

The RF system also includes a Low Level RF (LLRF) to generate RF signal which is delivered to RF pre amp. The LLRF has internal oscillator, so that it can generate 71MHz RF signal by itself. It is also possible to receive the RF reference signal from external RF oscillator [4]. The PLC controls the RF power, RF mode (CW/Pulse), and RF duty (when the RF mode is pulse type). In addition, the LLRF can control the motor of RF tuner to regulate the resonant frequency of RF cavity. The main control system can access the LLRF by serial communication (RS485) and share the data.

Ion Source System Control

For the stable generation of negative hydrogen plasma, the ion source system needs hydrogen gas and high voltage at least 2 kV. Therefore, we adopted the gas flow meter for control the gas quantity constantly, and ARC power supply to provide high voltage/current to ion source. The gas quantity, passed from gas flow meter is 0~5V analogue signal which is monitored by PLC and monitoring system. This quantity can be set by PLC too. In addition, a 24 V digital signal (DIO) has been used for ON/OFF control of gas flow meter. The PLC can perform the control task and status monitoring of ARC power supply through a port on it.

IMPLEMENTATION

We implemented the control system by SIEMENS PLC as hardware platform and Totally Integrated Automation Portal (TIA Portal) as software to take into account the performance and convenience in use.

Hardware Platform Implementation

We have used SIEMENS PLC (CPU 315F-2DP) which has high performance as main control system. In addition, the platform is a modular type, so it is flexible.

Software Design

The control system software is classified into two programs; One is the program for main control system (real-time target), and the other is the program for host PC. The program for main control system performs control and data acquisition about operation of sub-systems. The data gathered by real-time target is exchanged with host computer program via TCP/IP protocol. The program for host computer includes the human machine interface (HMI) and the operator can control the cyclotron by this program. This HMI has been designed by WinCC in TIA Portal software.

Logging process data and alarms with WinCC Logging supports the acquisition and processing of process data from the cyclotron. An evaluation of the logged process

ISBN 978-3-95450-167-0

data then provides information on the operating status during the in process (production, processing, process etc.).

Process sequences can be documented, the capacity utilization or the production quality can be monitored or recurring fault conditions can be logged. Benefits of data logging are:

- Early detection of danger and fault conditions.
- Avoidance of downtimes by means of predictive diagnostics.
- Increase in product quality and productivity due to regular evaluation of log.

The values from external and internal tags can be saved in process data logs. In addition, data logging can also be triggered by events, e.g. when a value changes. WinCC Logging also lets us log alarms and document operational states and error states of the system.

Remote Control

The control system can be accessed remotely by the network clients via TCP/IP protocol. Using the web browsing program, one of the clients fully use the main control user interface provided by the host machine at a time.

Many tasks require special qualifications or are restricted by the process to special user groups. Carrying them out requires rights that are assigned to special user groups and users. WinCC (TIA Portal) supports the user in creating and managing user groups and users and in assigning the required rights in engineering and during runtime. The actual user can then be accepted in the user administration with a user name or user ID and password even during operation and then be assigned to a user group without any further changes to the configuration.

CONCLUSION

The 10 MeV cyclotron has a number of sub-systems. These sub-systems exchange the data of status with main control system. The main control system is implemented based on SIEMENS PLC (CPU 315F-2DP) which has high performance, so that the control system can perform the tasks for control and monitor the cyclotron with high reliability. The main control system communicates with host computer, and it is possible to control remotely via TCP/IP protocol.

REFERENCES

[1] R. Solhju *et al.*, "Design of 10 MeV Cyclotron Accelerator", *Iranian Journal of Physics Research*, vol. 15, pp. 225-234, 2015.

[2] J. Jacky *et al.*, "Control System Specification for a Cyclotron and Neutron Therapy Facility", in *Proc. PAC'91*, San Francisco, California, USA, May 1991, pp. 1359-1361.

[3] Y. S. Lee *et al.*, "The Development of Control System for 9 MeV Cyclotron", in *Proc. Cyclotrons'13*, Vancouver, BC, Canada, September 2013, paper TUPPT004.

[4] M. S. Sharifi Asadi Malafeh *et al.*, "New Approach in Design of Efficient Low Level RF Circuit for 10 MeV Cyclotron", *Iranian Journal of Physics Research*, vol. 15, pp. 235-242, 2015.

ISBN 978-3-95450-167-0

MECHANICAL ASPECTS OF THE LNS SUPERCONDUCTING CYCLOTRON UPGRADE

G. Gallo†, G.Costa, L.Allegra, G.Messina, E.Zappalà,
INFN - Laboratori Nazionali del Sud, Via S. Sofia 62, 95125 Catania, Italy

Abstract

The Superconducting Cyclotron (CS) is a three sectors compact accelerator with a wide operating diagram, capable of accelerating heavy ions with q/A from 0.1 to 0.5 up to energies from 2 to 100 MeV/u. The proposed upgrade to increase the light ion beam intensity by means of extraction by stripping implies many modifications of the median plane. The main activities of the mechanical upgrade are: the actuation of the new magnetic channels for the extraction by stripping and the realization of the two extraction modes, by stripping and by electrostatic deflection. For the magnetic channels and compensating iron bars, we are studying the problems of mechanical handling. To obtain the two extraction modes, we are trying to design a new set that allows for the exchange of two devices: electrostatic deflectors and stripper with its magnetic channels for stripping extraction.

INTRODUCTION

The Superconducting Cyclotron (CS) is an accelerator which was designed for low intensity beams, whose main limitations to extract high beam power are the two electrostatic deflectors. The goal of the upgrade is to make extraction by stripping possible, interchanging the stripper with one of the two electrostatic deflectors, to achieve high power beams for the set of beams of interest and, at the same time, to maintain the versatility of the CS [1]. The detailed study of the beam dynamics along the stripping trajectory, for various ions at different energies, has led to the need for a new extraction channel. The interference of this channel with the electrostatic deflector handling, is the start of our study of the technical implications on the CS median plane.

RESULTS ON THE STRIPPING EXTRACTION

A study about beam dynamics of the stripping extraction, was necessary to compute stripping extraction for every ion and energy whatever the charge state of the accelerating particle is [2]. The results of this study are reported in another paper presented at this conference and are summarized in (Fig. 1).

The optimization of the different particles and energy trajectories allow us to have a common extraction point, for the purpose of making easier the design of the new extraction channel.

†gallo@lns.infn.it, giuseppe.costa@lns.infn.it

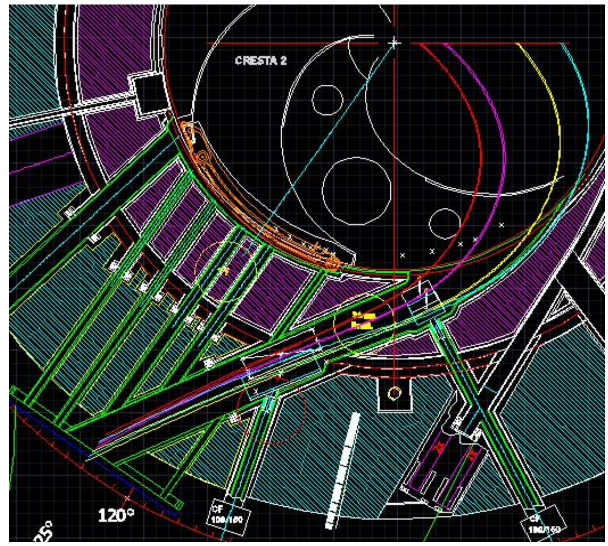

Figure 1: The different particle trajectories after the stripper crossing.

MECHANICAL ASPECTS

The fundamental mechanical aspects of the extraction by stripping, concern the modifications of the median plane of the CS (Fig. 2). Due to the design of the new extraction channel, there is the necessity of moving one of the lifting points of the vacuum chamber (from 107° to 90°). This forced us to rotate the position of the three horizontal suspensions (from 96°, 216°, 336° to 41°, 161°, 281°) because in the 90°-110° area, there is not enough space to allocate both the lifting point and the horizontal suspension. The new lifting points positions are 90°, 210°, 330°. The 41° and 281° horizontal suspensions caused respectively the suppression of the M7 and M2 magnetic channels, which were designed as part of the electrostatic extraction equipment but have never been used in the real life. Moreover the radial penetration for the beam injection was removed. Furthermore for the new extraction by stripping, a study has been done for the design of the magnetic channels. Able to reduce locally the magnetic field and to focus the beam in the radial direction, as a result of this study, two magnetic channels, M1S and M2S, are necessary: they are made up of three iron bars that we have to block inside a steel housing to avoid their movements. Through the simulations, we obtained the force values in the three directions and their range on the median plane for every ions. About the channel M1S, the resultant force is of about 9 KN, towards the CS centre. There is no need to remove it except in emergency case from the inner side of the CS. Its mechanical handling, for the necessary movement, had an interference with the old extraction channel (Fig. 3).

ISBN 978-3-95450-167-0

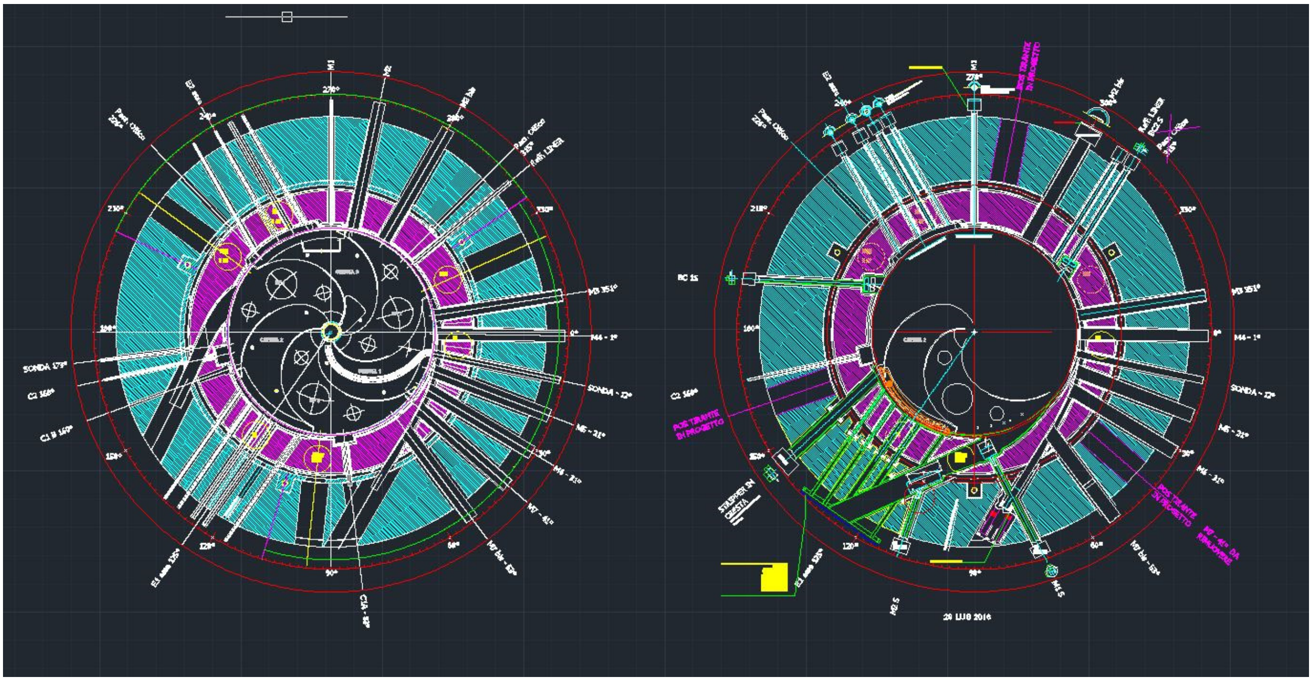

Figure 2: The current median plane (left) and the new median plane (right).

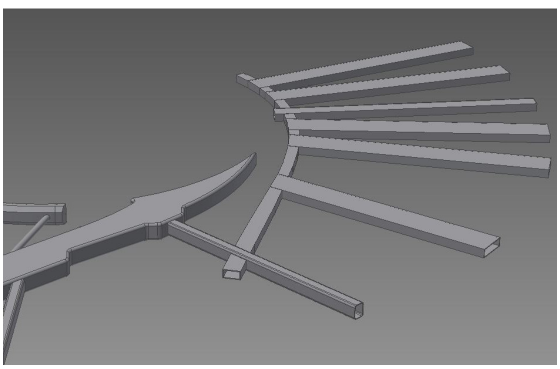

Figure 3: Interference between M1S mechanical handling and the old extraction channel.

Therefore we will design a fork system in that critical zone, that allows for the beam clearance, in the electrostatic extraction mode. We will simulate mechanical stresses on the link between the fork and the handling shaft, because the load is very high. About the channel M2S, the resultant force is of 3 KN, towards the direction opposite to the CS centre and it must be possible to remove it through the new extraction channel which is necessary for beams to be extracted by electrostatic deflection, because M2S interferes with one of the electrostatic deflector shaft. To compensate the imperfection field generated by M1S and M2S, we designed two iron bars, B1S and B2S; through the simulations, we obtained the force values in the two directions and their ranges on the median plane. In both cases, the resultant force is of about 4 KN, towards the CS centre and we are studying their mechanical issues. The mechanical handling, near to the B2S, is for the Liner cooling. To implement the two extraction modes, by stripping and by electrostatic deflection, we had to solve the critical interference between the new extraction channel and the electrostatic deflector handling. Our project is to weld the extraction channel with the three deflector penetrations and with a flange: this would not have critical consequences because all the components are of steel (Fig. 4).

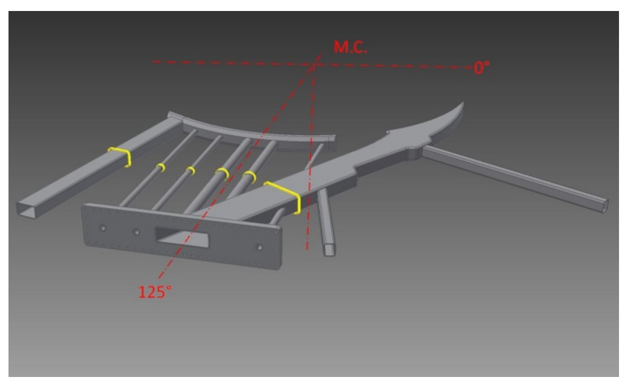

Figure 4: Assembly of the extraction channel with deflector penetrations.

We are studying two interchangeable chambers, to be coupled with the terminal flange of the assembly, to take into account the two extraction modes. Every chamber has the necessary features: for the extraction by stripping, the extraction channel continuation, for the extraction by deflector, the holes for the mechanical handling. We are considering the use of bellows for the penetration, useful during the cryostat construction. We are studying how to compensate the possible misalignments of the two tubes of each penetration: they are necessary to conjugate the requirement of the acceleration chamber (internal tube) with the cryostat (external tube). The bellow should allow us the last butt fusion between the two tubes.

ISBN 978-3-95450-167-0

STRIPPING SYSTEM

To extract the beam we need to use a moveable stripper foils (Fig. 5). The positions of the stripper foil stay in the area of the electrostatic deflector. To adjust the radial and azimuthal position of the stripper foil, a preliminary solution consist of an arm rotating around a fixed point and a belt, placed inside the arm, moved by a endless screw system, through two pulley. On the arm a minimum of 8 stripper foils will be mounted; they roll along the belt and only one of them will be hitted by the beam.

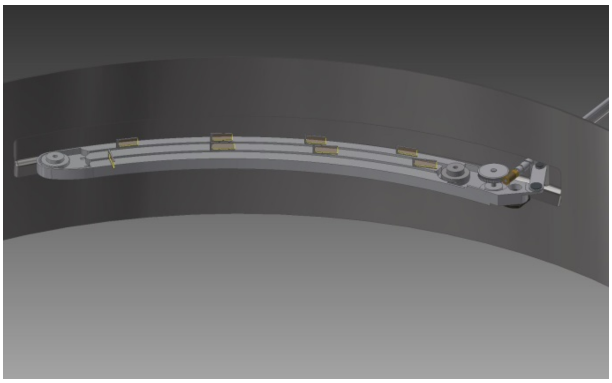

Figure 5: Stripping system.

CONCLUSION

The CS upgrade, required a starting phase, whose objective was to verify the feasibility of the extraction by stripping by a wide number of simulations that proved the design of a new extraction channel. Then we modified the median plane: the change of lifting points and horizontal suspensions position and the suppression of magnetic channels. For the new magnetic channels, we are studying the interferences of their mechanical handling and to obtain the two extraction modes, by stripping and by electrostatic deflection, we are designing two interchangeable chambers outside the CS yoke, to allow us the alternation between the new extraction channel and the electrostatic deflector handling.

REFERENCES

[1] A. Calanna *et al.*, "Proposal to upgrade the LNS Superconducting Cyclotron", INFN LNS Internal Report.

[2] A. Calanna *et al.*, "Proposal to increase the extracted beam power from the LNS-INFN Superconducting Cyclotron", in *Proc. HIAT'15*, Yokohama, Japan, Sep. 2015, paper MOA1C03, pp. 23-26, ISBN 978-3-95450-131-123.

STATUS AND UPGRADE OF THE CRYOGENIC PLANT OF THE LNS SUPERCONDUCTING CYCLOTRON AFTER 25 YEARS OF OPERATION*

F. Noto, M. Cafici, A. Carbonaro, A. Pagano, A. Di Stefano, F. Speziale,
INFN - Laboratori Nazionali del Sud, Via S. Sofia 62, 95125 Catania, Italy

Abstract

The Superconducting Cyclotron (CS) is a compact accelerator with three sectors with a wide operating diagram, capable of accelerating heavy ions with values q/A from 0.1 to 0.5 up to energies from 10 to 80 MeV/u. An upgrade of the CS superconducting magnet is in progress to extend the capability of the machine to high intensity beam facilities.

In this paper we describe the status of CS Cryostat and its Cryogenic Plant after 25 years of continuous operations at 4.2 K with the exception of the stop of about one year for the tenth test and the stop for restoring of the liquefier and the main issues happened during that long time. We describe the last complex and demanding procedure for the revamping of the He liquefier, its ancillary parts, other cryogenic parts of the CS, with special attention about the Piping and Instrumentation, gas analysis, Heat Exchangers, LN_2 transfer lines, Human-Machine Interface, vacuum system for thermal isolation, GHe recovery system and the optimization for the consumption of electrical power.

In conclusion we describe some hypothesis about the future upgrade of the Cryogenic system and the new Cryostat of the CS, in special way we analyse an approach to redefine the interconnection, piping boundary line and cryogenic diagnostic.

INTRODUCTION

The solution for the actual cryostat has been evaluated and the final decision was to include the superconducting coils in the helium bath. This solution, in principle, has then determined a macroscopic structural of practically forced cryostat.

DESCRIPTION

Below we will illustrate in detail the structure of the Superconducting Cyclotron and the relative plant. A detailed description of the cryogenic system can be found elsewhere [1].

Cryostat

The total of the actual cryostat is shown in Fig. 1. The entire complex is made of AISI 316L. It has an internal diameter of 1980 mm and an outer diameter a 2720 mm, with a height of 1740 mm for a total weight of approximately 4000 kg. The coils are realized with the system of the "double pancakes", stacked and subsequently and preloaded when in position. The coils inside the helium vessel are fixed to the annular structure (Median Plane).

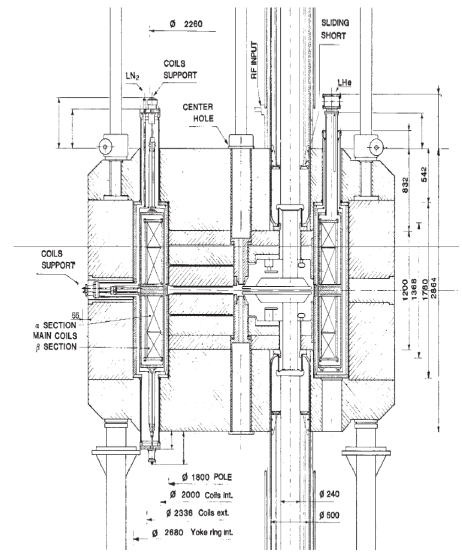

Figure 1: CS scheme.

Under the action of the weight, it is discharged on the inner wall in the case of the lower coil, and the maximum force of repulsion between the coils of 60 tons, the specific voltage stress applied to the tie rods is less than 20 kg/mm^2, and this force of container of helium, the latter with a thickness of 10 mm reduces the tensile stress at only 0.7 kg/mm^2.

The Median Plane has a thickness of 300 mm, corresponding to the separation between the coils. In it, three radial openings with an axial dimension of 200 mm are formed, which allow the passage of the beams and the housing of electrostatic and magnetic deflectors channels. The helium container is suspended from the vacuum chamber by means of vertical tie rods which therefore must withstand the total weight of the container and of the coils and the magnetic forces resulting from any asymmetry of the magnetic field.

An assessment of these forces in the event of a possible inaccuracy of mounting tolerable, up to about 0.5 mm, provides negligible values with respect to the weight of the complex coil-container of helium. The helium vessel has a weight of about 18,000 kg. There are 3 “upper” vertical tie rods made in titanium alloy (6% Al and 4% V) with a diameter of 18 mm immersed in the cold mass. Each of them in theory could support the total force applied to the structure (Fig. 1). Moreover there are 3 lower tie rods with a diameter of 6 mm to block the structure.

As you can see from Fig. 1, the tie rods have the task of supporting the entire structure, while the three lower links keep the coils in a fixed position.

ISBN 978-3-95450-167-0

Plants

The cryogenic circuit is based on a Helial refrigerator delivering 180 W or 53 l/h of LHe at 4.3 K without LN_2 precooling and about 100 l/h with precooling.

PROBLEMS ALONG 25 YEARS

During these years of continuous operations, the plant was stopped by small failures, generally half a day long. The main causes of stop were: power line and water cooling plant failure (about 80%) and failure of the cryogenic plant. Only in June 1994, just during the first acceleration test, there was a serious stop due to a valve failure and consequent entrance of air inside cold box, causing the rupture of the bearings that support the turbines of the liquefier. The problem has been attributed to the plastic cap damage of a pressure reducer. Thanks to the plant supplier that was able to ship two new turbines in a short time, the liquefier was restarted after a 5 days stop, and after 7 day from accident we could supply LHe to the magnet.

In 2006, a warm up was made approximately from June 2006 to February 2007 for the ten years checks required by the law regulation (PED). In the first next cool down one of the insulation vacuum leak was manifested itself almost immediately. This leak had very particular characteristics: the reached stationary vacuum was two orders of size larger than what we had previously (from 10^{-7} bar to 10^{-5} bar). The leak singularity was the fact that over the next 6 months, peaks of 10^{-3} bar occurred for a period of a few hours, and then of course returned to the normal pressure value. These pressure peaks, at intervals approximately weekly, produced obviously the interruption of the CS activities.

To overcome this problem, a campaign of study was done and one of N_2 shields was isolated, because our system provides three independent shields N_2. This leak in the circuit of the insulating vacuum, was create a N_2 accumulation on the 4.2 K wall. When this N_2 accumulation became significantly large, it detached from its seat and it stop, at the 80 K wall, or at room temperature wall, vaporizing and creating the pressure peak.

The solution was found by isolating one at a time every shield and pumping on it with a rotary in the circuit to eliminate all the N_2 current.

These test results indicate a leak in the external shield and the inner shield, but the biggest leak in the second one. Because the independence of each of the N_2 shield circuits, it was possible to isolate the inner shield. This solution is still working and the circuit is currently under vacuum with a rotary pump and so the gap was reported to 10^{-6} bar.

Currently, to overcome these current pressure peaks, a warm-up to 80 K is necessary to clean the 4 K wall from condensed N_2. This 80 K warm up has made two times years.

LIQUEFIER REVAMPING

During these 20 years of operations, the entire liquefier system needed a general maintenance.

The main reasons necessary to the maintenance were:

1. PLC Obsolescence (MECI SYCLOP 1987)
2. Wear of the whole field instruments (valves, solenoid valves, temperature control, etc.)
3. Gas He leaks in the fittings of the refrigeration plant

About the PLC obsolescence, agreed with the liquefier manufacturer, it proceeded with the replacement and installation of a new PLC upgraded model used in those years (SIEMENS S7), in this way the manufacturer guaranteed the technical support.

Regarding the field instrumentation, we decided the total replacement of all components suppliers.

About the gas He leak, we proceeded to the piping complete replacement using the stainless steel fittings only for the two ferrule tube fittings (Fig. 2).

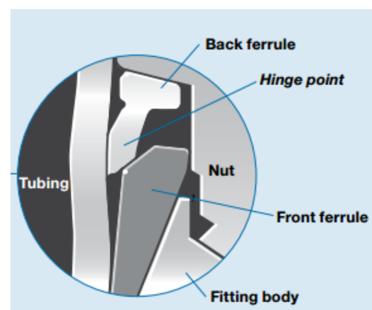

Figure 2: Two ferrule tube fitting system.

CS UPGRADE

The project to upgrade the Superconducting Cyclotron, whose objective is the increase of the intensity of light ions, is based on the application of a method of extraction from the one currently in place. Until now, the limitation on the intensity, of 1012 pps, is due to the current mode of the beam extraction with the aid of two electrostatic deflectors. This limitation can be overcome through the use of extraction by stripping that in the case of ions with mass <40 and for the energies of our interest has a efficiency close to 100%. A feasibility study on the beam dynamics along the extraction trajectories for stripping, confirms that a new extraction channel is needed. The new channel will be in addition to the existing extraction channel used for the extracted beams by means of electrostatic deflection and which will be maintained to allow the extraction of all the ion beams which may continue to be extracted with the current intensity.

The extraction by stripping implementation therefore involves the construction and installation of a new superconducting magnet to replace the current. The feasibility of the superconducting magnet has been established through a conceptual study that included magnetic, structural, thermal analysis and the estimated consumption of helium and liquid nitrogen.

ISBN 978-3-95450-167-0

Requirements to the cryogenic system were specified in terms of maximum consumption of the coolants, 20 l/h of helium at 4 K and 18 l/h of LN_2 at 77 K, which (by the enthalpy of vaporization) translates into 14.4 W and 805 W of heat loads at respective stages. The cooling scheme of the magnet is shown in Fig. 3. The upper and lower sets of alpha and beta coils are placed respectively in closed, annular vessels located symmetrically around the median plane of the cyclotron [2].

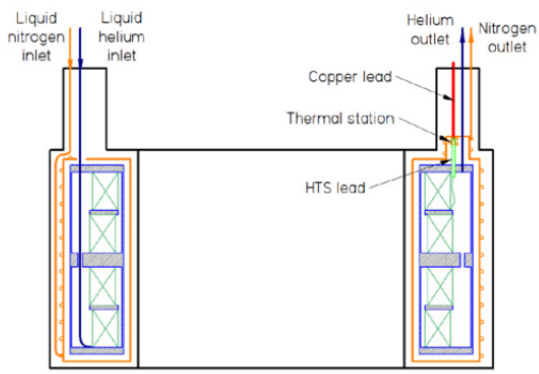

Figure 3: Cooling scheme.

Both sets of alpha and beta coils are cooled by immersion in boiling liquid helium bath at atmospheric pressure. The liquid is introduced by a transfer line directly connected to the magnet vessel, the one below the cyclotron median plane. The cryogen fill and vent lines are directed to a cryogenic plant through one of the three service chimneys at the top of the cryostat. Current leads protruding from the ends of the coils are directed to a set of hermetic feedthroughs mounted to the top plate of the upper magnet vessel, where they connect to high temperature superconductor current leads, which span the gap between the upper magnet vessel and a liquid nitrogen cooled thermal station, where they connect to conduction cooled copper leads which complete the link to room temperature. The instrumentation lead wires similarly exit the magnet vessel through hermetic connectors mounted to the top plate of the upper magnet vessel. The instrumentation wires are similarly heat sink to a LN_2 cooled thermal anchor before continuing out of the cryostat through one of the service chimneys. The cold mass is surrounded by an aluminium radiation shield, which is cooled by a forced flow of boiling liquid nitrogen in the tracers located at both the inner and outer surfaces of the radiation shield. All cold surfaces are covered with Al foil to reduce radiation heat loads. The radiation shield is covered with multilayer insulation (MLI) to reduce a heat flux from the room temperature walls of the solenoid vacuum vessel. Two pairs of 2 kA current leads are considered for both alpha and beta coils circuits bringing the total number of the current leads to four. Each of the leads is comprised of a room temperature (300 K) to intermediate (77 K) temperature optimized copper wire and a high temperature superconductor (HTS) lead between the intermediate temperature intercept and the 4 K end.

Tables 1 and 2 show itemized heat loads at both stages.

Table 1: Heat Load to Liquid Helium

Heat Load Source	Heat Load, W
Radiation from shield, 100% margin	1.0
Convection of residual helium gas	0.3
Conduction along support rods	0.3
Conduction along instrumentation wires	0.25
Heat leak through 4 HTS current leads	1.92
Heat dissipation in 8 x 2 joints	0.32
Nuclear heating	2.0
Total heat load to liquid helium	6.09

Table 2: Heat Load to Liquid Nitrogen

Heat Load Source	Heat Load, W
Radiation through MLI, 100% margin	40
Thermal conduction along support rods	6
Heat load through 4 current leads	340
Total heat load to liquid nitrogen	386

They comprise less than half of the respective liquid helium and liquid nitrogen specs. The remaining margin will be partially used to compensate losses in the transmission lines and in the helium liquefier [3].

The main difference with the current coils is the design of the cold mass. The existing coils consist of a set of wound double pancakes with pretension [1]. This solution is cryostable and it has worked very well. In the new coils design the maximum overall current density is 54 A/mm^2 instead of 35 A/mm^2 in the old design.

To simplify the construction process and to reduce the costs we choose to build the new coils epoxy impregnated (potted) using helium pooled cooling scheme. This choice is supported by the worldwide experience, for the construction of this kind of coil.

CONCLUSION

The current cryogenic plant as reported has shown a remarkable efficiency and reliability in the course of these 25 years, this results in addition to the excellent design are also due to maintenance work carried out by the LNS technical staff. CS Upgrade with a new cryostat and coils will change very little the actual configuration of cryogenic plant.

REFERENCES

[1] E. Acerbi *et al.*, "The Milan superconducting cyclotron project", in *Proc. Cyclotrons'81,* Caen, France, Sep. 1981, pp. 169-176.

[2] A. Radovinsky *et al.*, "Conceptual design of a auperconducting magnet for the LNS cyclotron", Design Report.

[3] A. Radovinsky, L. Calabretta, J. Minervini, P. Zhukovsky, P. Michael, and A. Calanna, *IEEE Transactions on Applied Superconductivity*, volume 26, issue 4, June 2016.

ISBN 978-3-95450-167-0

IMPROVEMENT OF THE NIRS-930 CYCLOTRON FOR TARGETED RADIONUCLIDE THERAPY

Satoru Hojo†, Takashi Wakui, Ken Katagiri, Masao Nakao‡, Akinori Sugiura, Akira Noda, and Koji Noda, NIRS, QST, Chiba-shi, Japan

Abstract

In recent years, the production of radionuclides for Targeted Radionuclide Therapy (TRT) with the NIRS-930 cyclotron has been one of the most important activities in National Institutes for Quantum and Radiological Science and Technology (QST, NIRS).

In the production of ^{211}At, for example, a target material with low melting point is irradiated with a high intensity helium ion beam. A vertical beam line has the advantage in irradiation with low-melting-point target. Therefore, a vertical beam line has been modified for the production of radionuclides. This line was used for neutron source with beryllium target.

The beam intensity and beam energy are important parameters for the effective production of radionuclides for TRT. In order to increase beam intensity, the acceleration phase and injection energy have been optimized by measuring beam phase. The beam energy has been measured by TOF and adjusted by tuning the acceleration frequency. Those studies and improvement are reported.

INTRODUCTION

The NIRS-930 cyclotron was installed in 1974 for a fast neutron therapy and production of radionuclide [1]. The fast neutron therapy was terminated in 1994. At present, the NIRS-930 cyclotron is mainly used for production of radionuclides. Other purposes of the NIRS-930 cyclotron are research of physics, developments of particle detectors in space, research of biology, and so on.

Recently, the TRT has been one of the most important activities in NIRS, QST. Therefore, production of alpha emitter radionuclides for TRT is increased. The operation time for production of radionuclide at the NIRS-930 cyclotron is shown in Fig. 1. In recent five years, the operation time of helium ion beam is increasing. In 2015, the operation time of helium ion beam was increased to 479 hours, which was higher than that of proton beam and was more than 50% of that for production of radionuclides.

VERTICAL BEAM PORT

A layout of NIRS cyclotron facility is shown in Fig. 2. The HM-18 cyclotron is only used for production of PET-radiopharmaceuticals. The NIRS-930 cyclotron has 10 beam ports, and 5 beam ports of them are exclusively used for radionuclide production. The C-1 and C-2 beam ports are used for production of PET-radiopharmaceuticals. The C-4 beam port is used for production of metal radionuclides such as ^{62}Zn/^{62}Cu for SPECT. The C-9 and C-3 are vertical irradiation ports. The C-9 beam port is used for production of radionuclides with a low-melting-point solid target such as 124I and 76Br [2]. The C-3 beam port was used for fast neutron therapy, and this beam port has been modified for radionuclides production recently. This beam line has wobbler magnets for avoiding heat concentration on a target [3].

In order to produce radionuclides for TRT, the target material with low melting point is irradiated with a high intensity beam. Because an irradiation face doesn't change even if the target melts, the vertical beam port has the advantage in irradiation with low-melting-point target. Therefore, the radionuclides for TRT is produced using these two vertical irradiation ports. ^{211}At has been produced for TRT using the C-9 beam port [4].

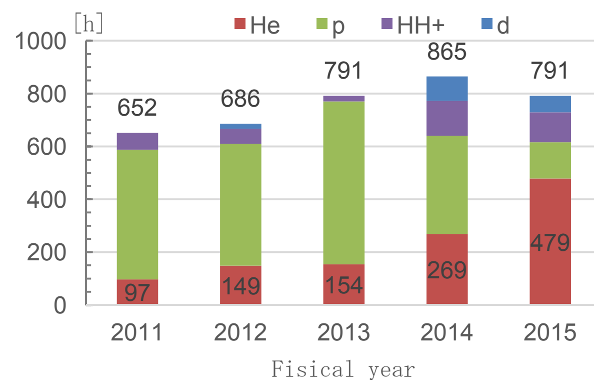

Figure 1: The operation time for production of radionuclide.

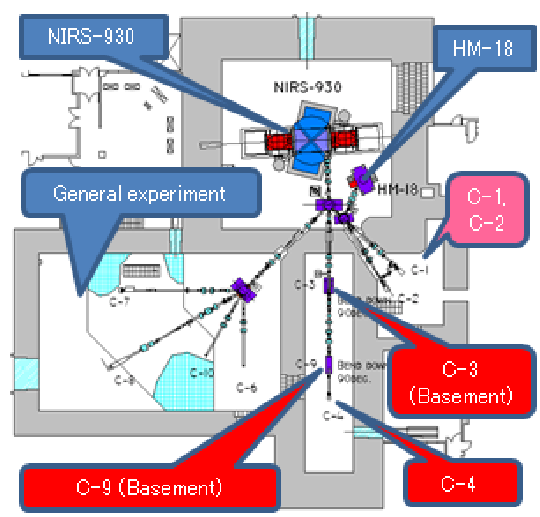

Figure 2: Layout of the NIRS-930 cyclotron. C-3: Radionuclides production using heat damageable targets; C-9: Radionuclides production ^{124}I, ^{76}Br, etc; C-4: Radionuclides production for SPECT; C-1, C-2: Production of PET-radiopharmaceuticals.

† hojo.satoru@qst.go.jp
‡ Present Address: RCNP, Osaka University

ISBN 978-3-95450-167-0

REQUEST FOR BEAM IN PRODUCTION OF RADIONUCLIDE FOR TRT

The beam energy is an important parameter for producing radionuclides for TRT. A certain beam energy is required to keep contamination level low. A high beam intensity is also required, because the beam irradiation time can be shortened by the increase of production rate. Therefore, a higher injection efficiency and a higher extraction efficiency are needed for the NIRS-930 cyclotron.

Accuracy of Beam Energy

In recent years, production techniques of radionuclides such as ^{211}At have been developed and applied for studies of TRT at NIRS. In the production of ^{211}At, the beam energy is an important factor for the quality of ^{211}At. Cross sections of ^{209}Bi(alpha, 2n)^{211}At and ^{209}Bi(alpha, 3n)^{210}At are shown in Fig. 3. The incident beam energy which has a high production rate of ^{211}At is around 30 MeV. However, when the incident beam energy exceeds 28 MeV, ^{210}At is also produced. The decay product from ^{210}At is ^{210}Po, which is very high radiotoxic. In order to keep ^{210}At level low, the control of incident beam energy is indispensable. Therefore, the beam energy was measured and adjusted at the NIRS-930 cyclotron.

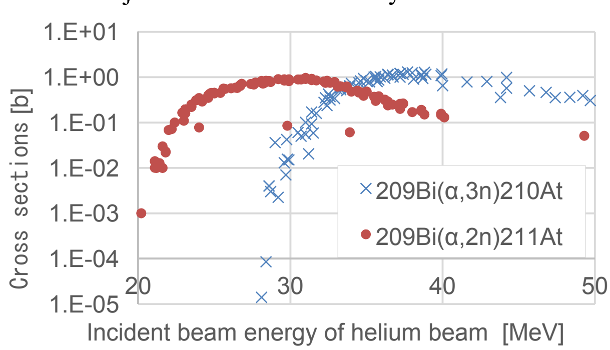

Figure 3: Cross sections of ^{209}Bi target with helium beams. Dates are taken from EXFOR [5].

The Beam Energy Measurement and Adjustment

The most preferable beam energy from the cyclotron is 34 MeV with an estimation of energy loss by the structure of the target system. The beam energy on target is then 28 MeV.

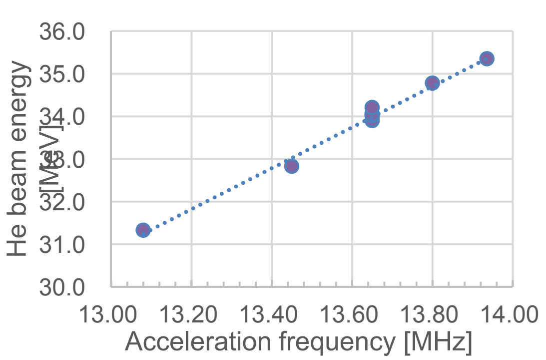

Figure 4: Measured beam energy as a function of acceleration frequency with He beam.

The beam energy was measured by the time-of-flight (TOF) system [6] and was adjusted by changing acceleration frequency. The TOF system uses two electrostatic pickup monitors. The result of the beam energy measurement by changing acceleration frequency is shown in Fig. 4. The acceleration frequency for production of ^{211}At has been determined to 13.65 MHz from the results of this measurement.

The extraction beam energy was measured at daily operation. The difference between nominal and actual energies at daily operation of 34 MeV helium beam is shown in Fig. 5. The difference between nominal and actual energies were roughly within 0.3%.

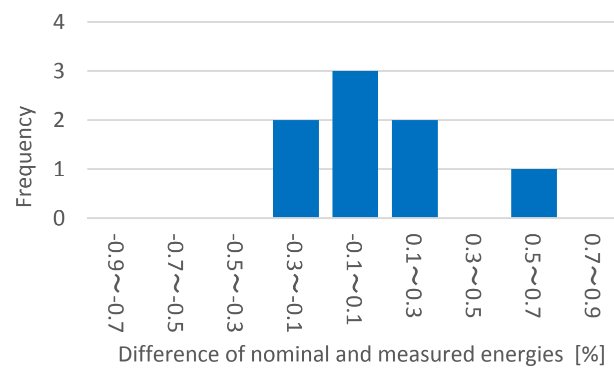

Figure 5: The difference between nominal and actual energies at daily operation of 34 MeV helium beam.

Extraction Efficiency

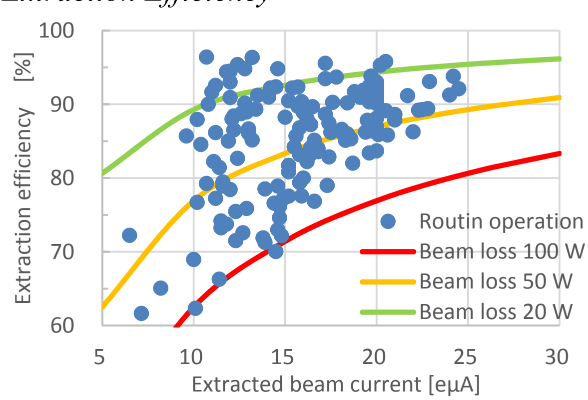

Figure 6: The extracted beam intensity as a function of extraction efficiency in routine operation.

A demand on higher beam intensity for 34 MeV He^{2+} is growing in radionuclide production for TRT. Therefore beam intensity has been increased to 24.5 μA by adjusting operation parameter [7]. A higher extraction efficiency is needed for high intensity beam. Here, the extraction efficiency is the ratio of beam current at a deflector entrance and at an exit of the cyclotron. If the extraction efficiency is low, the extraction system such as a deflector are damaged and activated. The extracted beam intensity as a function of extraction efficiency in the routine operation and the lines of beam loss (100, 50, 20 W) are shown in Fig. 6. The beam loss at extraction beam intensity over 20 μA in the routine operation was below 100 W.

ISBN 978-3-95450-167-0

Injection Efficiency

The injection beam current is defined as the beam current at inflector electrode when the inflector voltarge is zero volt. The injection efficiency is percentage ratio of the injection beam current and the beam current at cyclotron radius 100 mm. The injection efficiency with and without buncher as a function of injection beam current are shown in Fig. 7. The injection efficiency with buncher is declined with increasing the injection beam current.

The average injection efficiency without buncher is 22%. The beam phase width can be estimated from this injection efficiency. The average beam phase width without buncher is estimated to be 79.2 degree from the average injection efficiency.

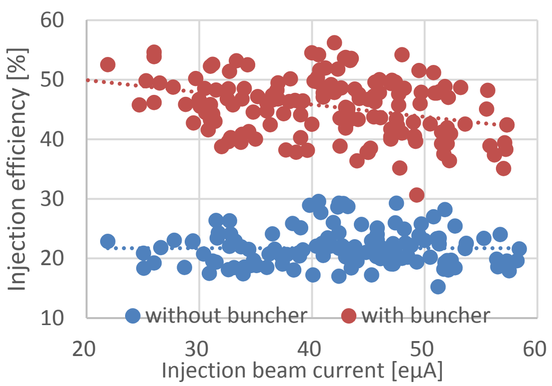

Figure 7: Dependence of injection efficiency with buncher and without buncher on injection beam current.

The dependence of a beam bunch length on the beam intensity was simulated by SPUNCH [8] to confirm the buncher gain and one-dimensional longitudinal space charge effects. In this calculation, the injection beam current at inflector ranges from 30 to 60 eμA. The results are shown in Fig. 8. The beam bunch length becomes wider by increasing the injection beam current.

The buncher gain is defined as the ratio of the beam current with and without buncher at cyclotron radius of 100 mm. The buncher gain in routine operation is shown in Fig. 9. The buncher gain tends to decline with increasing the beam current. We also calculated the buncher gain by SPUNCH using the beam phase width of 79.2 degree. The results of the calculation for the injection energy of 10.8, 12.8, and 14.8 keV are also shown in Fig. 9. The buncher gain is declined with increasing the injection beam current as with the injection efficiency. It was confirmed the decline in the buncher gain by space charge effects of injection beam was the cause of the decline in the injection efficiency. From Fig. 9, the calculated buncher gain becomes larger with increasing energy. Thus, the buncher gain can be increased with the higher injection energy. It is suggested that a modification of the central region such as an inflector electrode is needed to increase the beam current of 34 MeV He^{2+}.

CONCLUSION

The NIRS-930 has been used for production of radionuclide for TRT. The energy of extracted beam was measured and adjusted. The difference between nominal and actual energies were to be roughly within 0.3% in the routine operation. In the beam extraction, the beam loss was less than 100 W. For the beam injection, a modification of the central region to increase the injection energy is needed to suppress the space charge effect.

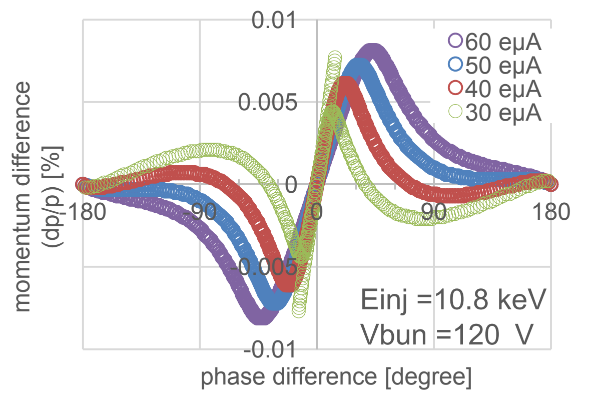

Figure 8: The calculation of the bunch length at the inflector by SPUNCH. The dependence the injection beam current of 30 to 60 eμA. Einj: Injection energy to the cyclotron, Vbun: buncher voltage.

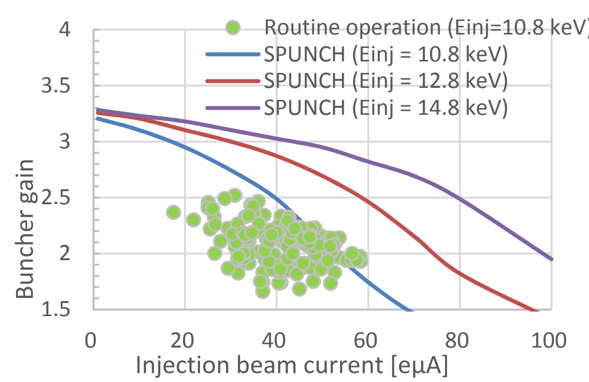

Figure 9: The buncher gain at cyclotron radius 100 mm.

REFERENCES

[1] H. Ogawa, *et al*, IEEE Trans. Nucl. Sci. NS-26, No.2 (1978) p. 1988.

[2] K. Nagatsu *et al*., "Fully automated production of iodine-124 using a vertical beam", Applied Radiation and Isotopes 69 (2011) 146–157.

[3] K. Katagiri, *et al*., "Design of beam transport lines for radioisotope production systems in NIRS cyclotron facility"in *Proc. IPAC'2014*, Dresden, Germany, June 2014, paper WEPRO088, pp 2162-2164.

[4] K. Nagatsu, *et al*., "Production of ^{211}At by a vertical beam irradiation method" Applied Radiation and Isotopes 94 (2014) 363–371.

[5] EXFOR `http://www.jcprg.org/exfor/` Hokkaido University Nuclear Reaction Data Centre (JCPRG).

[6] S. Hojo, *et al*., "A beam energy measurement system at NIRS-930 cyclotron" in *Proc. Cyclotrons'04*, Tokyo, Japan, October 2004 p. 407.

[7] S. Hojo, *et al*, “Progress on the upgrade for TRT at NIRS Cyclotron Facility” in *Proc. HIAT2015*, Sept. 2015, paper MOPA07, p. 48.

[8] R. Baartman, “SPUNCH - A space charge bunching computer code”, in *Proc. Cyclotrons’86*, Tokyo, Japan, Oct. 1986, p. 238.

ISBN 978-3-95450-167-0

STUDY ON ENERGY UPGRADE AND BEAM TRANSMISSION EFFICIENCIES FOR RIKEN K-70 AVF CYCLOTRON

J. Ohnishi, A. Goto, M. Kase, RIKEN Nishina Center, Wako, Japan
Y. Kotaka, Center for Nuclear Study, the University of Tokyo, Wako, Japan

Abstract

The central region of the RIKEN AVF cyclotron was modified in order to increase the beam energy of protons and M/Q = 2 ions, and acceleration tests were performed. Before the modification, we investigated the injection acceptance in the modified structure of the central region. In the acceleration tests, the energy of protons was successfully increased from 14 MeV to 30 MeV in the acceleration harmonics 1 (H = 1) operation. On the other hand, in the conventional acceleration harmonics 2 (H = 2) operation, the transmission efficiencies were lower than those before the modification.

INTRODUCTION

The RIKEN AVF cyclotron [1] was commissioned in 1989 and is used as a stand-alone machine and an injector for the RIKEN ring cyclotron. Its K-value is 70 MeV, and the maximum extraction energies to date are 14 MeV for protons and 12.5 MeV/u for M/Q= 2 ions. This cyclotron has been operated jointly by RIKEN and the Center for Nuclear Study, the University of Tokyo. The operation time was 2900 h in 2014, and the information regarding its operation is described in Ref. 2.

Figure 1 shows the acceleration performance of the AVF cyclotron. The maximum magnetic field is 1.76 T. The RF frequency ranges 12–24 MHz and the nominal dee voltage is 50 kV. Until 2009, the operational region had been limited to the yellow area, but in order to increase the beam energies to meet the demands from users for nuclear physics and radioisotope production, the modification of the central region of the cyclotron was designed by Vorozhtsov et al. [3] and was executed in the summer of 2009. As a result, the operational region has been expanded to the blue area in Fig. 1, while the extraction energies have increased to 12 MeV/u from 9 MeV/u for M/Q = 2 ions. After this modification, in order to further increase the extraction energy (to 30 MeV for protons), they also designed another structure with a smaller RF shield by changing the support structure of the inflector. Figure 2 shows the superimposed plan views of the central region. One is for the existing structure (S1) modified in 2009, and the other is for the tested structure (S2), in which the RF shield was made smaller. The region accelerated in the structure S2 is expanded to the green area in Fig. 2. Using the structure S1 or S2, light ions such as protons can be accelerated in the acceleration harmonics 1 (H = 1). The displacement between H = 1 and 2 in the blue and green areas is caused by an acceleration phase-shift from the peak of the dee voltage for H = 1 acceleration. In the H = 1 operation, protons can be

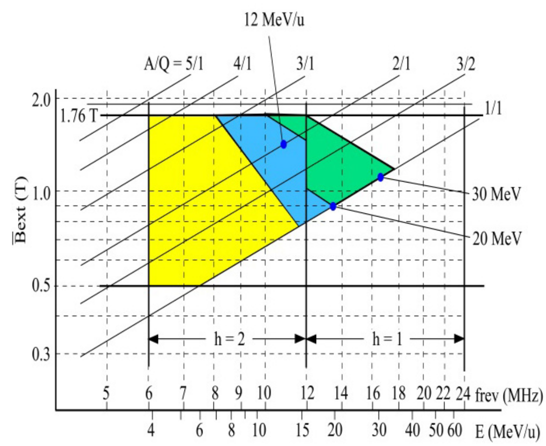

Figure 1: Acceleration performance of the AVF cyclotron. The yellow, blue, and green areas correspond to the original (before 2009), existing, and currently-tested geometries, respectively.

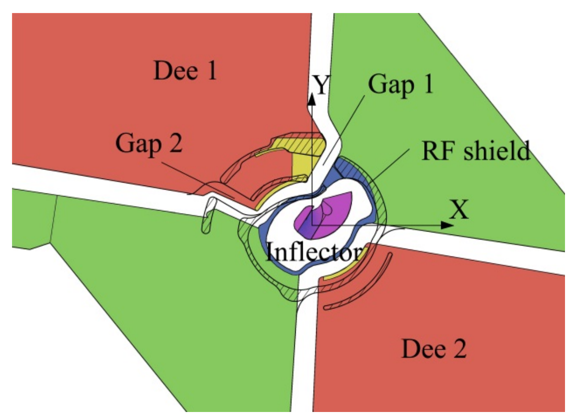

Figure 2: Existing and tested geometries of the central region. The shaded area indicates the existing geometry.

accelerated up to 20 MeV for S1 and 30 MeV for S2. An acceleration test of 20 MeV protons was executed in the existing S1 structure in July 2016. Moreover, in August, we changed the central region from the existing structure S1 to the structure S2, and performed the acceleration tests. In the tests, in addition to the acceleration of 20 and 30 MeV protons, the H = 2 acceleration test was also performed to check whether the transmission efficiencies through the cyclotron deteriorated.

TRACKING SIMULATION

Before modifying the central region with the structure S2 and performing tests, we re-studied the influence on shows a computer model used for the calculation of the the injection acceptance by tracking calculations. Figure 3

ISBN 978-3-95450-167-0

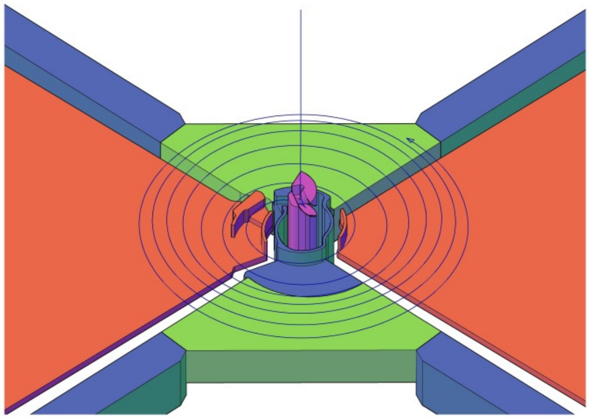

Figure 3: Computer model for electric field calculations. The model shows the lower side from the median plane, except for the inflector.

shows a computer model used for the calculation of the electric fields. The electric and magnetic fields were calculated by using Opera-3d [4]. The RF fields were treated statically and also calculated with Opera-3d. The enhancement of the magnetic field in the central region (bump) was set to be approximately 1.5% inside the radius of 150 mm. The starting point of the particles in the tracking calculation was defined at 200 mm above the median plane, and the acceptances were evaluated at this point. The space charge effect was not considered in our calculations.

Acceptance for Lateral Direction

Figure 4 shows the acceptance of 12 MeV/u deuterons calculated for S1 and S2. The x and y axes lie along the magnetic yoke of the cyclotron, as shown in Fig. 2. The acceptance is defined as a distribution in the phase space of the particles accelerated beyond a radius of 150 mm. The dee voltage is 45 kV in these calculations. The phase angles to the RF fields of all particles are set to be constant at the starting point. However, those at the first acceleration gap spread to widths of approximately 25° and 57° in the x and y directions because of the difference in the orbit lengths in the inflector.

Figure 5 shows the acceptance sizes calculated for 12 MeV/u deuterons as a function of phase angle for the dee voltage of 45 kV. The phase angle is defined as the RF phase when the particle injected along the central axis passes the center of the first acceleration gap. In the case of Fig. 4, the phase angle of the central particle was 4°. As the acceptance of the inflector was 550π mmmrad, the rest of the particles were lost before accelerating to a radius of 150 mm: more than 90% of them are lost on the upper and lower surfaces of the dee electrodes with an inner height of 24 mm. It was found that the acceptance for S1 is almost the same or slightly larger than that for S2.

Figure 6 shows the dee-voltage dependence of the acceptance sizes calculated for 30 MeV protons and 12 MeV/u deuterons. In this case, protons are accelerated in S2 in H = 1 operation, and deuterons in S1 in H = 2. The phase angles of the central particle in the center of the

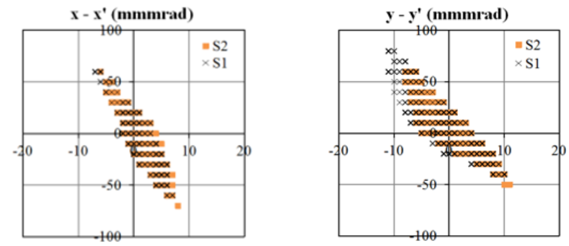

Figure 4: Acceptance shapes for 12 MeV/u deuterons calculated for S1 and S2. See text for the calculation conditions

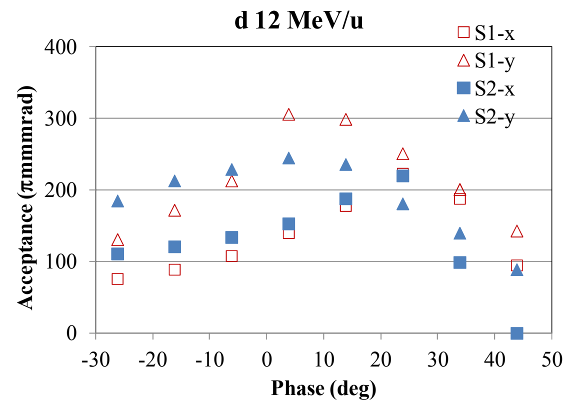

Figure 5: Acceptance sizes of 12 MeV/u deuterons calculated for both S1 and S2 as a function of the phase at the tracking starting point. (See text).

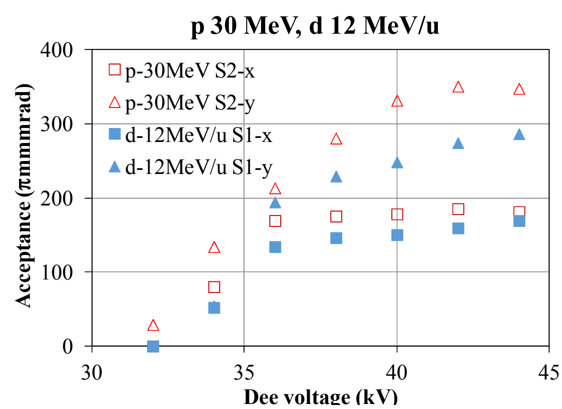

Figure 6: Acceptance sizes for 30 MeV protons and 12 MeV/u deuterons as a function of dee voltage. The acceptances of the protons and deuterons were calculated for S1 and S2, respectively.

first acceleration gap were approximately 4° for all cases. This figure indicates that it is possible to accelerate protons at 30 MeV with the same dee voltage as, and a larger acceptance size than, that for 12 MeV/u deuterons.

Acceptance for Longitudinal Direction

Figure 7 shows the phase distributions of particles at the center of the acceleration gaps, which are injected along the central axis and are accelerated to more than seven turns. Figure 7(a) shows a comparison between S1

ISBN 978-3-95450-167-0

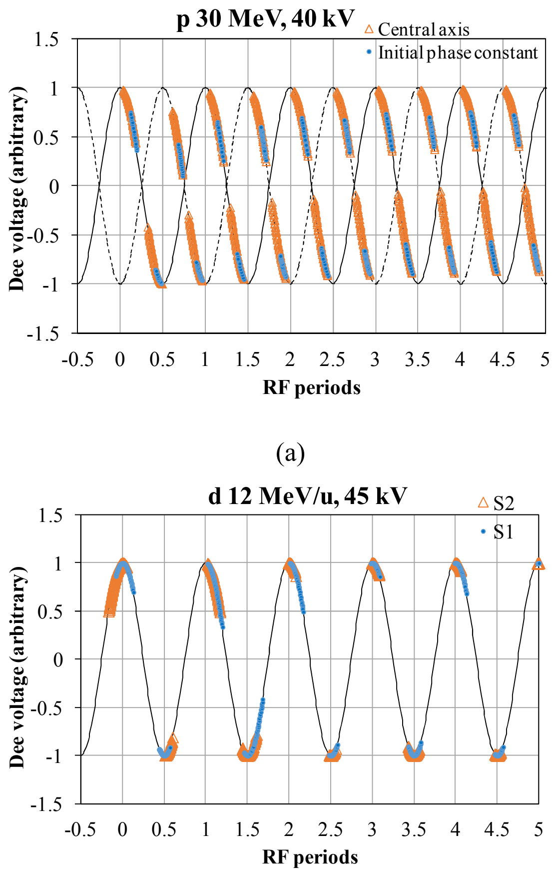

(b)

Figure 7: Phase distributions at the center of the acceleration gaps of the particles accelerated to more than seven turns. See text for details.

and S2 calculated for 12 MeV/u deuterons at a dee voltage of 45 kV. In case of S1, the particles pass the center of the first and second gaps at the phase of voltage peaks, and the phases are delayed at the third and subsequent gaps. The beams passing acceleration gaps are subjected to focusing and divergence forces in the vertical direction at the entrance and exit of the acceleration gaps, respectively. Therefore, the particles passing the gap at the delayed phase from the peak are subjected to a net focusing force. On the other hand, in case of S2, as the position of the second gap is located further downstream than that in case of S1, the phase at the first gap advances, and the particles are subjected to a net divergence force at the first gap. This is considered to be a cause for the smaller acceptance for S2 than that for S1 at the delayed phase region, as seen in Fig. 5. Figure 7(b) shows the phase distributions for H = 1 acceleration of 30 MeV protons at a dee voltage of 40 kV. The orange triangles correspond to the particles injected along the central axis with all phases, and the blue circles to the particles with a constant phase at the starting point, but with different initial positions and angles in the x-direction. The spreads in phase for the blue circles are due to the differences of orbit length in the inflector.

ACCELERATION TESTS

We modified the central region from S1 to S2 and performed acceleration tests in August 2016. In these tests, we not only tried increasing the energy of proton beams by the H = 1 operation, but also investigated the influence on the transmission efficiencies through the cyclotron in the H = 2 operation. Table 1 gives a summary of the acceleration tests. A total of seven beams were accelerated. As the machine time was restricted to within 36 h, the mean adjustment time for acceleration of one beam was approximately 4 h. In the table, I36 and C01 indicate the positions of Faraday cups located just above the yoke of the cyclotron and 2 m downstream from the exit of the cyclotron. In the H = 1 operation, 20 MeV protons could be accelerated without difficulty, but the beam current for 30 MeV protons was as small as 1.1 μA. This was because the dee voltage was insufficient owing to the deterioration of the RF cavities. On the other hand, the transmission efficiencies (beam current ratio of I36 and C01) in the H = 2 operation were worse than those before the current modification. It was confirmed that the beam currents for 14 MeV protons and 12 MeV/u deuterons can reach 20 μA, which is the limit due to radiation safety. The beam current of $^{22}Ne^{7+}$ was almost the same as before. However, the transmission efficiency for $^{22}Ne^{5+}$, which simulates $^{84}Kr^{20+}$, was approximately 60% of the peak performance to date. The transmission efficiency for Fe beams was only 10%, while its efficiency so far had been larger than 20% or occasionally 30%. In general, the transmission efficiencies in the H = 2 operations in S2 were rather poor compared with those in S1, although the time for machine study was not sufficient. Therefore, we have decided to revert the tested structure to the existing one because the use of this new structure could be at risk of affecting the operations for users' experiments.

Table 1: Summary of Acceleration Test.

Ion	Energy	RF frequency (MHz)	Harmonics	I36 (μA)	C01 (μA)
p	14 MeV	23	2	90	14.3
H_2^+	12 MeV/u	21.25	2	57	9.6
$^{22}Ne^{7+}$	6.0 MeV/u	15.05	2	42	7.5
$^{22}Ne^{5+}$	4.0 MeV/u	12.3	2	12	2
p	20 MeV	13.6	1	76	10
p	30 MeV	16.5	1	116	1.1
$^{56}Fe^{15+}$	5 MeV/u	13.8	2	1.2	0.12

CONCLUSION

We modified the central region of the RIKEN AVF cyclotron in order to increase the beam energy, and performed acceleration tests. In the tracking simulations, the injection acceptance in the modified central region was not very different from that for the existing structure. In the acceleration tests, we successfully increased the beam energy of protons from 14 MeV to 30 MeV. On the other hand, the transmission efficiencies in the H = 2 operations were lower than those before the modification. Hereafter,

ISBN 978-3-95450-167-0

we will analyze the results of the acceleration tests and review the structure of the central region.

REFERENCES

[1] A. Goto et al., "Injector AVF cyclotron at RIKEN," in *Proc. Cyclotrons'89*, May 1989, pp. 51–53.

[2] N. Tsukiori et al., "AVF operations in 2014," RIKEN Accel. Prog. Rep., vol. 48, p. 327, 2015.

[3] S. B. Vorozhtsov et al., "Modification of the central region in the RIKEN AVF cyclotron for acceleration at the H=1 RF harmonic," in *Proc. Cyclotrons'10*, Sept. 2010, pp. 138–140.

[4] `http://operafea.com`

ISBN 978-3-95450-167-0

DESIGN OF RF PICK-UP FOR THE CYCLOTRON

Dong-Hyup Ha, SangChul Mun, Ho Namgoong, Mitra Ghergherechi, Jong-Seo Chai,
College of Information & Communication Engineering, Sungkyunkwan University,
Suwon, Korea
Jongchul Lee, SeungWook Shin, HuiSu Kim , Department of Energy Science, Sungkyunkwan
University, Suwon, Korea

Abstract

The radio-frequency (RF) pick-up for RFT-30 cyclotron which was located in the Korea Atomic Energy Research Institute (KAERI) was designed by Sungkyunkwan University in Korea. This paper covers proper position of RF pick-up and things to consider when designing. Our RF pick-up antenna is designed for RFT-30, but approach to design process can be used any RF pick-up antenna design. This paper provide some tendency graph according to position of RF pick-up.

INTRODUCTION

Recently cyclotron is used many research field such as nuclear reactions, nuclear physics, radioisotope applications, life science and so on. Various field needs variable performance of beam. Reliable output beam is necessary to get good results [1].

Cyclotron is a kind of particle accelerator. RF cavity is a component of cyclotron, which accept electromagnetic field from RF source and serves accelerating field to particles.

There are some problems when RF power input to RF cavity, such as inputting power variation or mismatched impedance. Sometimes device should be stopped operating because of these problems. It is possible to solve these problem that using RF pick-up. Because RF pick-up accept electromagnetic signal in real time. The signal of RF pick-up is applied to cyclotron control system, it is possible to safe driving. Our RF pick-up design is going to use RFT-30 and RF pick-up used in RF system, so Table.1 is contained. Simulation results were performed by CST microwave studio [2].

Table 1: Specification of RFT - 30 Cyclotron RF System [3]

Parameter	Value
RF frequency	64.05 MHz
Number of Dees	2
Dee angular width	39 deg
RF amplifier power	50 kW
Number of Harmonics	4

SIMULATION PROCEDURE

RF pick-up is measuring resonance signals in RF cavity, such as resonance frequency. In this work, we can find RF cavity quality factor, impedance matching status and so on by using these signals.

RF pick-up is same principle to RF power coupler. However role of two things are different. Purpose of RF coupler is transportation of RF power from RF generator to RF cavity, whereas purpose of RF pick-up antenna is measuring electric field in excited RF cavity by RF power. RF pick-up is connected with a measuring instrument directly. So, in design of RF pick-up, we must consider status of measuring instrument such as maximum acceptance power.

It would be significant to take the appropriate location of the RF pick-up and not to affect the performance of the RF cavity when designing the RF pick-up. The appropriate position represents to get RF power supplement that should not exceed the measurement limitation of the network analyser.

Prior to starting the design, coupling type must be determined.

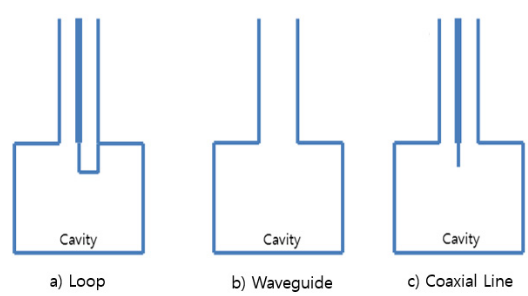

Figure 1: Different types of RF power coupler.

There are 3 types of RF power coupler are shown in Fig. 1. If magnetic field passing through the loop, induced current is generated. This current becomes pick-up signal at loop type coupler. Waveguide type is directly connected to RF cavity and waveguide performs a RF pick-up, coaxial line type usually is used in electric field.

ISBN 978-3-95450-167-0

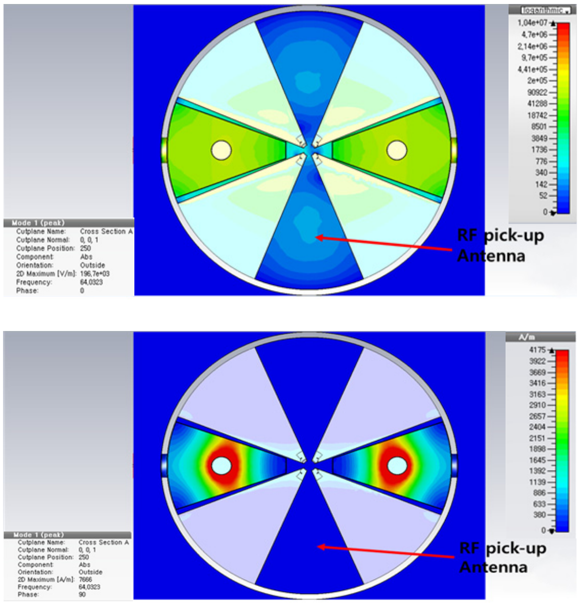

Figure 2: The electric field (upper) and magnetic field (lower) at RF pick-up position.

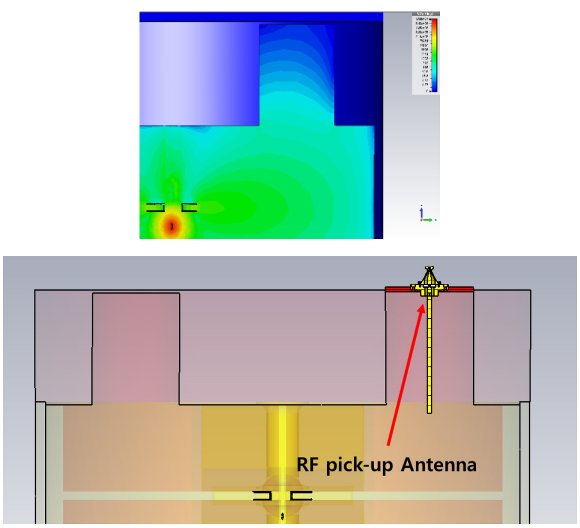

Figure 3: Electric field in cavity (upper) and position of RF pick-up (lower).

Because RFT-30 cyclotron was already development, so the position of RF pick-up is limited. We can use only two regions of valley. Figure 2 shows electric field and magnetic field in valley region. The electric field exists in this region whereas magnetic field rarely exists. This is the reason we are using coaxial type probe.

Figure 3 is Electric field in cavity and position of RF pick-up. The closer to the beam acceleration plane, the closer to the beam acceleration plane, the stronger intensity of electric field is generated. And the closer to the electromagnet yoke, the weaker electric field is generated. This means that it is possible to get high intensity signals at RF pick-up, which is closer to the beam acceleration plane.

For proper positioning of RF pick-up, simulation is progressed according to penetration depth. The result of simulation is checked by S-parameter S21.

$$\mathrm{S21[Magnitude, dB]} = 10 \times \log_{10}\frac{P2}{P1} \qquad (1)$$

P2 means power coming into port 2. In other words, it means pick-up signals intensity at RF pick-up antenna. P1 means power coming into RF cavity from RF coupler. Therefore S21 means ratio of delivered power in RF cavity to pick-up power at RF pick-up. We can calculate real electric power at RF pick-up by using S21 data.

Figure 4 shows relation between antenna penetration depth and S21 magnitude (dB). Range of RF pick-up penetration depth is determined from 200 mm to 400 mm because there are rarely magnitude signals below 200 mm and it is possible to cause structurally unstable above 400 mm. In this graph, the more deeply penetration depth of the antenna is able to get more magnitude at RF pick-up.

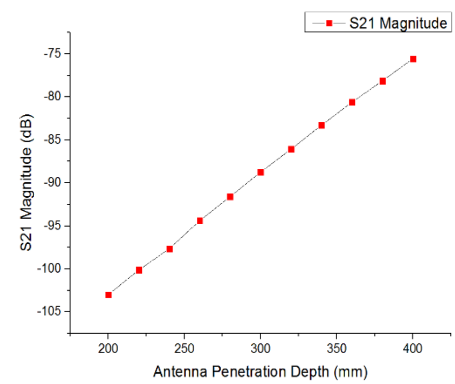

Figure 4: RF pick-up penetration depth versus S21 magnitude (dB).

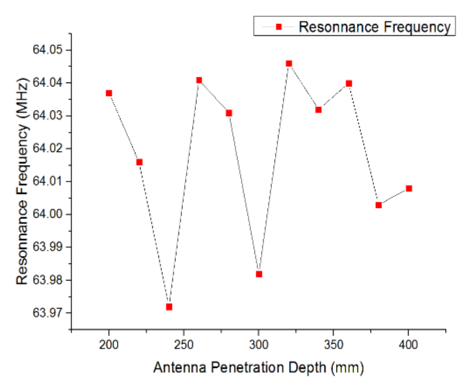

Figure 5: RF pick-up penetration depth and resonance frequency (MHz).

ISBN 978-3-95450-167-0

As mentioned earlier, RF pick-up should minimize effect on RF cavity systems. So, simulation was done for resonance frequency, and impedance matching according to RF pick-up penetration depth. Figure 5 shows Relation between Antenna penetration depth and resonance frequency (MHz)

There are some changes in frequency (±0.03 MHz). Resonance frequency of RFT-30 is 64.05 MHz, 0.03 MHz is just 0.05%, so this value is negligible.

Figure 6 shows impedance matching state. This means that it is often called coupling state. Through smith chart, it is possible to know RF coupling state. Smith chart is usually expressed circle. If the circle passing through exactly smith chart center (50Ω), this state is called critical-coupled state. When the circle is drawn larger than critical-coupled state, this state called over-coupled state. And the circle is drawn smaller than critical-coupled stated, this stated called under-coupled state. When RF cavity is critical-coupled state, RF cavity is accept all power from RF power coupler. In other words, there is no power reflection.

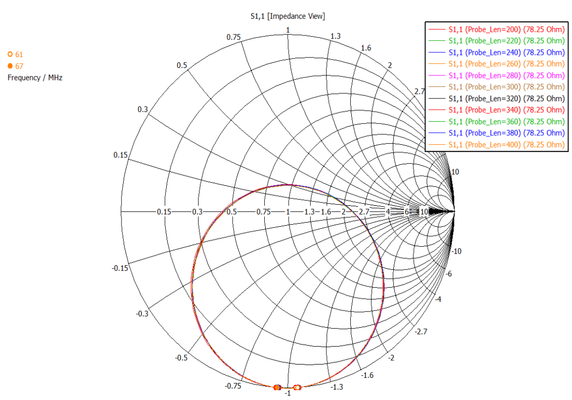

Figure 6: Smith chart according to RF pick-up penetration depth.

Also particle accelerators are designed critical-coupled state during operation. When particle beam enter into RF cavity, this beam act as impedance section (beam loading). In General, RF cavity for particle accelerators is designed over-coupled state, and when beam enter into RF cavity, over-coupled state moved critical-coupled state [4].

CONCLUSION AND DISCUSSION

Although the RF pick-up penetrate deeply, RF cavity has little effect as shown Fig. 6. However antenna length becomes longer, it can cause structurally unstable. Signals from RF pick-up is used measuring instrument and control systems. If high power enter into measuring instrument and control systems, it can cause equipment failure. So, we must know exactly pick-up power. When length of the antenna is 400 mm, S21 magnitude is -75 dB. It means that if inputting power is 50 kW, pick-up power is 1.58 mW. This power is proper to control systems and is not dangerous to the measuring instruments and control systems.

This RF pick-up is very useful to withdraw reliable beam at RFT-30 cyclotron. In addition, approaching method to the RF pick-up design and production will be useful in the design of all the cyclotrons RF pick-up.

ACKNOWLEDGEMENT

This work was supported by the National Research Foundation of Korea (NRF) grant funded by the Korean government (MSIP:Ministry of Science, ICT and Future Planning) (NRF-2015M2B2A8A10058096)

REFERENCES

[1] K. P. Nesteruk *et al.*, "Study of the transverse beam emittance of the Bern medical cyclotron", *4th Int. Beam Instrumentation Conf. (IBIC'15)*, Melbourne, Australia, Sep. 2015, pp. 134-138.

[2] CST Microwave studio, `www.cst.com`

[3] J.-S. Chai *et al.*, "Commissioning of KIRAMS-30 cyclotron for nuclear science research", *18th Int. Conf. on Cyclotrons and their Applications*, Giardini Naxos, Italy, Oct. 2007, pp. 45-50.

[4] S. Shin *et al.*, "Development of the RF cavity for the SKKUCY-9 compact cyclotron", *Nuclear Instruments and Methods in Physics Research, Section A: Accelerators, Spectrometers, Detectors and Associated Equipment,* vol. 795, pp. 276-283, 2015.

ANALYSIS OF THE PLASMA CHARACTERISTICS FOR BEAM CURRENT OPTIMIZATION FOR TR-13 CYCLOTRON ION SOURCE

W. J. Jun†, S.C. Mun, H. Namgoong, D.H. Ha, M. Ghergherehchi, J.S. Chai,
Department of Electrical and Computer Engineering, Sungkyunkwan University, 2066, Seobu-ro, Jangan-gu. Suwon, Gyeonggi-do, Korea

Y. H. Yeon, J. C. Lee, H .S. Kim,
Department of Energy Science, Sungkyunkwan University, 2066, Seobu-ro, Jangan-gu, Suwon, Gyeonggi-do, Korea

Abstract

There is a TR-13 cyclotron that extracts energy of 13 MeV protons which is located in Sungkyunkwan University. The researchers in this laboratory were eager to improve the technical problems of the components and finally optimize the beam profile. The finally extracted beam current is critically depends on the initially extracted beam from the Ion Source Injection System (ISIS). The ISIS is composed of several electrical instruments. The voltage or current which is applied to these components can affect the finally extracted beam profile. However, the original values for the input voltage or current is almost fixed to special values that had been written in the operation manual. It means that the bad condition of this cyclotron cannot be matched for these values which had been conducted in the best condition of the operation. So, by using the programmable logic controller (PLC), it is possible to use varying inputs in various conditions, and the beam current is able to be stabilized much better than applying the constant input values. Finally, this paper would show the tendency of the plasma generation in terms of modulating the applying input values which occurs inside the ion source chamber. It represents the plasma characteristics that critically influence the beam current.

INTRODUCTION

TR-13 cyclotron is originally manufactured from TRIUMF company in Canada. IT accelerator engineering centre in Sungkyunkwan University tried to manage this cyclotron's for engineering research.

One of the most significant factors for the performance of the accelerator is the extracted beam current. The beam current depends on lots of background environments such as the vacuum level, stability of the input/output power, or gas injection and so on. And also the firstly extracted beam from the ion source chamber can be the primary points for intensifying the finally extracted beam current. Since the last beam profile is strongly affected by the initially extracted beam from the ion source, the beam flows in the ion source injection system should be considered weightily. The ion source injection system consists of ion source, steering magnets, quadruple magnets, inflector, etc. Though, the plasma generation can be the systemic function for the whole structure of the ion source injection system [1, 2].

In the ion source chamber, negative hydrogen ion generating reaction is performed under several conditions. The simple procedures follows: hydrogen gas injection, electron emission form the high current filament, arc discharge between hydrogen gas and the electrons, plasma region displacement, ion beam extraction. Within these procedures, the operator can manipulate many conditions in the ion source chamber. Briefly, the negative hydrogen ion beam generation is dependent to vacuum level, arc discharge, electron emission, plasma potential, and extraction voltage which is able to be controlled by PLC system. Thus, this paper will represents the feature inside the ion source chamber on the part of plasma characteristics [4].

EXPERIMENTS

Experiments with variety of conditions had been conducted, and it shows many specific tendencies. Every electronical devices are remotely controlled by PLC unit.

Mass flow controller (MFC) in this system is a device that control the flowing amount of the neutral hydrogen gas that coming from the gas source to the ion source chamber. It can decide the vacuum level in the ion source chamber and thus the amount of the hydrogen particles to be reacted with electrons can be controlled [3].

The controlling range of the hydrogen has injection is 0~10 SCCM and the whole range is covered for the experiments.

Figure 1 features the operation of the power supplies (Arc P/S, Filament P/S, Plasma P/S) within the condition of arc voltage : 100V, arc current : 2A, plasma potential : 3.1V), without injecting the hydrogen gas. In the experiments, only the arc current ,the plasma potential, steering magnet and the extraction lens voltage had been changed. The arc current is decided by the amount of the generated plasma, and plasma potential corresponds to the displacement of the plasma region in the ion source chamber. And they determine the total amount of the extracted beam. The plasma current and the extractor lens current of each situations had been observed in this experiment. Conclusively, the graphs show that in order to increase the beam current extracted from the ion source, the extractor lens current should not reach to saturation level earlier.

†suwj@skku.edu

ISBN 978-3-95450-167-0

Figure 1: Ion source power supplying unit (Xantrex).

RESULTS

MFC & Power Supply Control

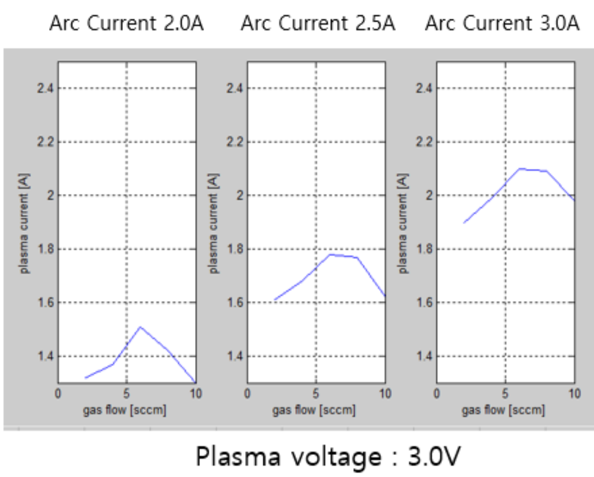

Figure 2: Plasma current with MFC control and various arc current in plasma potential 3.0V.

Figure 2 shows several suggestions. The gas injection level is optimized around 6~8 SCCM that makes the quantity of the plasma maximized. And also the arc current works same as the function of the gas injection level. The vacuum level of the ion source chamber had been increased linearly from 1.3E^{-6} mbar to 2.8E^{-6} mbar in step size of 5E^{-7} when the hydrogen injection had been completed.

There can be several assumption with Figure 3 and 4. From Figure 3 the extraction current and bias current show keep going down since the bunch of the beam in the plasma get closer to the lens electrodes that makes the power supply output flows into the plasma region. And that is the reason why the extraction power supply shows constant current mode. Also, the ionized subject, plasma, makes the common ground of the whole power supply to be connected with short circuit. Whenever the flowing current exceeds the limitation of the power supply output current, then the beam cannot be extracted anymore as like shown in the right side graph of Figure 4 (saturated beam current).

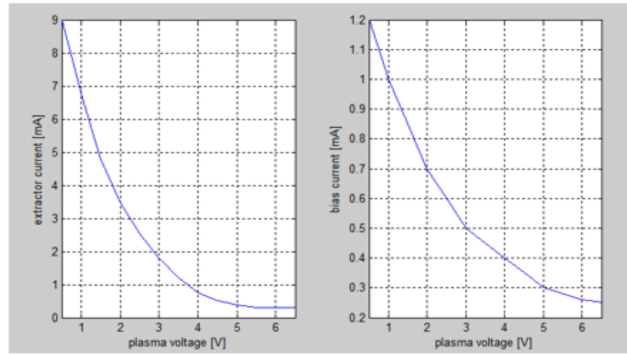

Figure 3: Extractor lens current and bias power supply current with plasma voltage control.

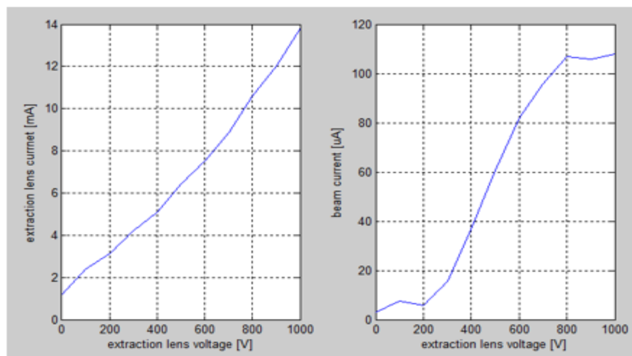

Figure 4: Extractor lens current and beam current with extractor lens voltage control.

Ion Source Lens Modelling

Table 1 shows the extraction voltages for constant current mode of the extractor lens power supply and the extraction current for the voltage value of extractor lens power supply is zero with increasing plasma potential values. The maximum output of the extractor lens power supply is 5kV, 15mA. Constant current mode of the power supply means that the beam current cannot be extracted more than the maximum power supply output. So as to increase the beam current, the extraction power supply must not reach to maximum output level as mentioned above.

Table 1: Extractor Lens CC Mode Experiment Result

Plasma voltage [V]	**Plasma current [A]**	**Extraction voltage when CC mode starts [V]**	**Extraction current when extraction voltage is 0V [mA]**
0.0	0.43	0	15, CC mode
0.4	0.43	0	15, CC mode
0.8	0.43	0	15, CC mode
1.2	0.43	0	15, CC mode
1.6	0.43	0	15, CC mode
2.0	0.43	0	15, CC mode
2.4	0.43	0	15, CC mode

ISBN 978-3-95450-167-0

2.8	0.53	35	13.35
3.2	0.77	40	9.75
3.6	1.03	45	7.5
4.0	1.27	60	5.7
4.4	1.43	75	4.35
4.8	1.58	105	2.85
5.2	1.78	185	1.35
5.6	1.92	255	0.585
6.0	2.05	295	0.405
6.4	2.12	300	0.315
6.8	2.14	300	0.255
7.2	2.18	295	0.225
7.6	2.19	305	0.180
8.0	2.23	305	0.150

Moreover, CST studio simulation result shows the electric potential tendency nearby the plasma lens and the extractor lens [5]. This analysis would represents that the extracted beam can be distorted in unexpected way whenever the plasma region is not well created in the ion source chamber which can cause to large amount of bema loss in front of the faraday cup. In Figure 5 the electric field shows like shape of an arc. It means the direction of the negative hydrogen ion beam would be curved in diverging way. Then the beam will bump into the electrode to make CC mode. Whenever the starting point of the beam is adjusted to another point, the beam will not collide into the unexpected location. That means the plasma displacement, the plasma potential, is the important parameter to be considered.

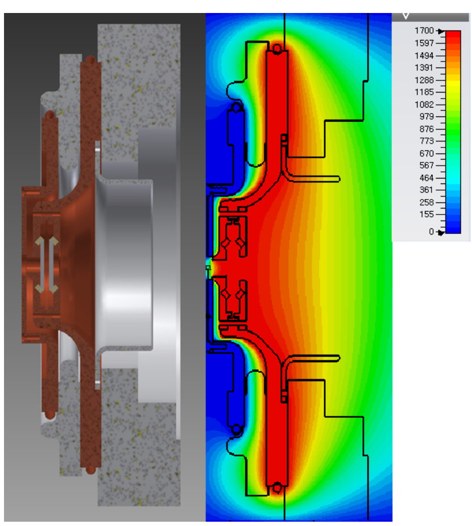

Figure 5: Electric potential analysis of the plasma & extractor lens CST studio E-solver.

DISCUSSION & CONCLUSION

The ion source operation for the TR-13 cyclotron requires many sophisticated experimental environments. Many factors such as vacuum level, power supply output, or perhaps humidity should be regarded as the main causes for good beam profiles. The importance of the applying voltages on the extractor and plasma lens are written in this paper. It was shown that large amount of plasma have nothing to do with the beam current, but the exact position of the plasma region might influence the extracted beam profile. And the tool for finding the optimized distance between the plasma region and the plasma lens can be determined by the extractor lens current. Additionally, there are subsidiary effects of the arc current or any other reasons such as SCCM level can also be the significant keys to make the beam current better.

After putting together the overall results in Table1, Figure 2, Figure 3, and Figure 4, finally there shows some obvious disposition of the beam profile with respect to applying inputs.

1. Adjust the plasma voltage to modulate the displacement of the plasma region where the beam initially start.
2. Increase the arc current considering with the injection of gas flow.
3. Take account for the load resistance of the extractor lens power supply to make the extraction current weakly.

Each sentences are dominant for increasing the beam current. After improving the electrical instruments to brand-new ones or find the optimized values for ion source operation, the whole performance will be upgraded.

ACKNOWLEDGEMENTS

This work was supported by the ICT R&D program of MSIP/IITP. [R0101-16-0126(10043897), Development of 500 cGy level radiation therapy system based on automatic detection and tracing technology with dual-head gantry for 30% reducing treatment time for cancer tumour]

REFERENCES

[1] John. J. Livingood, "Principles of Cyclic Particle Accelerator", *D. Van Nostrand Company*, 1961.
[2] B. Wolf, *Handbook of Ion Sources*, Chapter 2, CRC Press, Tokyo, 1995.
[3] I. G. Brown, *The Physics and Technology of Ion Sources*, John Wiley & Sons, Singapore, 1988.
[4] Y. H. Yeon *et al.*, "Development and Discharge Characteristics of Negative Hydrogen Ion Source for the SKKUCY-9 Cyclotron", *Nuclear Instruments and Methods in Physics Research A: Accelerators, Spectrometers, Detectors and Associated Equipment*, vol. 763, p. 510-516, 0168-9002, Nov. 2014.
[5] CST-Particle studio, `http://www.cst.com/`.

ISBN 978-3-95450-167-0

BEAM BASED CALIBRATION MEASUREMENTS AT THE PSI CYCLOTRON FACILITY

C. Baumgarten, Paul Scherrer Institute, Villigen, Switzerland

Abstract

The PSI high intensity proton accelerator (HIPA) facility consists of a Cockcroft-Walton accelerator and two cyclotrons, INJECTOR 2 and the Ring machine (see Fig. 1). It is in operation since four decades [1]. Though the design details of the original machine are well documented, a considerable number of changes have been made to various components in the course of time. Moreover some measurements like magnetic field mappings or the survey of central region collimators can only be done in the construction and/or assembly phase, either for mechanical reasons, due to restrictions of time schedule or due to the activation of components. Further development of the facility requires precise beam dynamics models (for instance with OPAL [2]) which in turn requires an accurate machine description.

INTRODUCTION

An effective method to test the consistency of the data used to model the machine is based on the combination of beam tracking simulations and beam based measurements. We present some results of such beam based alignment and calibration measurements that have been made during beam development shifts with INJECTOR 2. They allows to cross-check collimator positions, Dee voltage distribution, turn patterns, beam energy and trim coil field profiles using measurements of radial probes, phase pickups and profile monitors. A sensible reconstruction of cyclotron parameters starts

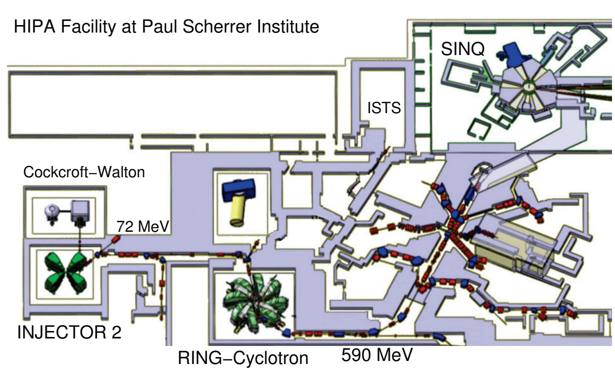

Figure 1: High Intensity Proton Accelerator (HIPA) Facility at PSI. The Cockcroft Walton delivers typically 10 – 12 mA protons DC. After the formation of bunches by two bunchers in the injection line of INJECTOR 2, the beam is accelerated to 72 MeV and transported to the RING cyclotron. The 590 MeV proton beam of maximal 2.4 mA is used to produce pions, muons using carbon targets and neutrons by spallation in the swiss neutron source SINQ.

with the RF-frequency ω_{rf}, the parameter which is usually well-known or easy to measure. Based on the frequency it is possible to determine the average magnetic field as seen by the beam, provided that some kind of phase measurement is available. The PSI INJECTOR II for instance is equipped with 8 phase probes (MIF1-MIF8) required for the adjustment of the isochronism. The long radial probe (RIL1) can be used to localize the turns at the azimuth of the probe. The radius gains allow to reconstruct the energy gain as a function of radius. The energy gain per radius gain of the cyclotron is given by

$$\frac{dE}{dR}(R) = \frac{E\,\gamma\,(\gamma+1)}{R}\,, \tag{1}$$

which can be crosschecked also with computed equilibrium orbit data. Then the energy gain per turn is

$$\frac{dE}{dn}(R) = \frac{dE}{dR}(R)\,\frac{\Delta R}{\Delta n}(R)\,. \tag{2}$$

Measurements with the long radial probe (RIL1) have been performed during a beam development shift in 2015. For this calibration measurement, the buncher located in front of INJECTOR II in the 870 kV injection line was switched off in order to ensure a beam of well-known and sharp energy. We picked the peak positions of RIL1-0005Y15.SDDS, shown together with RIL1-0002Y15.SDDS in Fig. 2. The PSI INJECTOR 2 is specifically well-suited for such measurements, as the phase curve of the beam is almost flat such that the radius gain can be directly used to compute the Dee voltage. Once frequency, dee voltage and field are resonably well known, it is possible to use the beam position measurements of the long probe RIL1 to match the starting conditions of tracking computation to the position data.

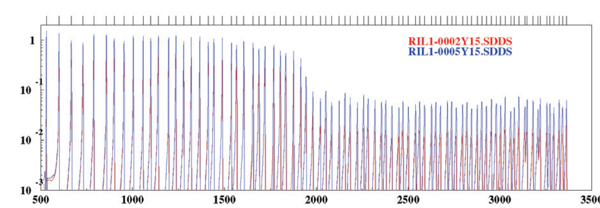

Figure 2: Measured raw data of the long radial probe RIL1 (INJECTOR II) and the beam positions. From turn number and extraction energy, one can directly compute the *average* energy gain per turn.

Figure 3 shows the resulting energy gain as derived from the RIL1 beam position measurements. The energy gain matches well to historical data of the resonator voltage profiles. The turn-by-turn analysis of the radius gain is shown in Fig. 4. Though we find a wide range between injection and extraction where the turn pattern is in excellent agreement with the simulated orbit, the agreement is less convincing in the more critical areas of injection and extraction, respectively. We hope that we can achieve further improvements

ISBN 978-3-95450-167-0

by the incorporation of the trim coil fields into the magnetic field model.

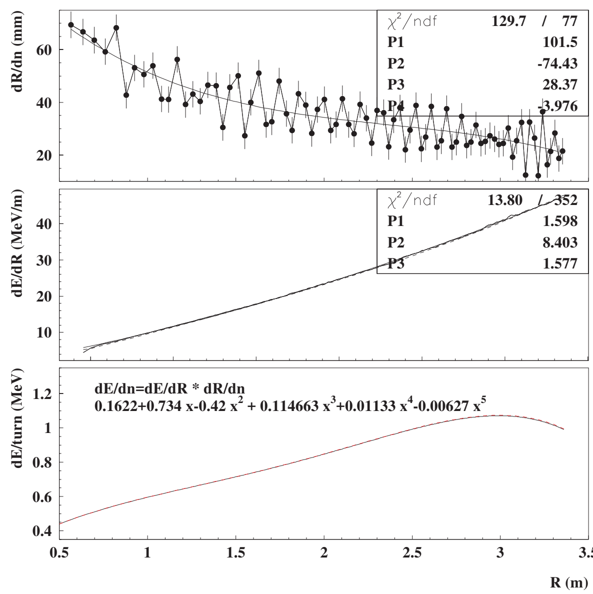

Figure 3: Upper: Radius gain of the turns as measured by radial probe, fitted by a polynomial. Center: Energy over radius gain according to Eq. (1) compared with E.O. computation. Bottom: Computed energy gain for INJECTOR II with polynomial fit.

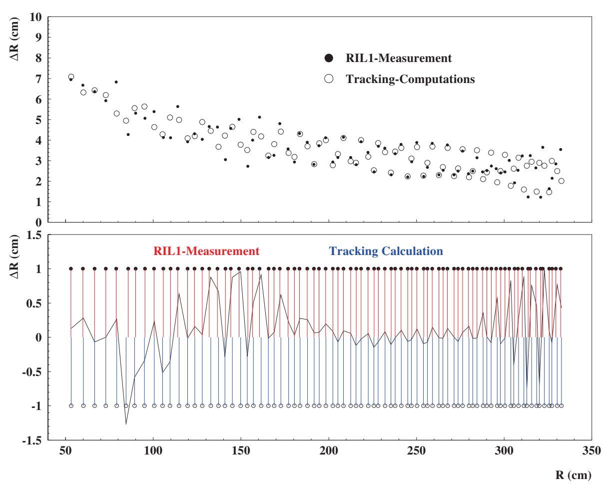

Figure 4: Top: Comparison of beam orbit tracking computation (open circles) with RIL1 peak positions (filled circles). Bottom: Comparison of radius gains, the red lines are indicating measured peak positions while the blue lines indicate the tracking results. The black curve shows the difference between both. In the range from 180-300 cm, the agreement is excellent, but at small and high radius, significant deviations are observed. However, the purpose, namely to determine the beam positions in the center, could be achieved.

COLLIMATOR POSITIONS IN THE CENTRAL REGION

The last possibility to shape the beam without activating components is the central region of INJECTOR II. For this purpose INJECTOR II is equipped with a considerable number of moveable collimators that allow to cut the beam in the first turns. Several of these collimators have two jaws that can be moved independently in order to provide maximal flexibility of beam collimation. Only two resonators accelerate the beam in this area, which allows to obtain an individual voltage calibration of all accelerating dees. A precise mechanical survey of the collimator positions is challenging due strong limitations for a direct access. Though the absolute calibration of the positions is not essential for machine operation, it is important for a precise beam dynamics model [3].

Due to the strong space charge the beam developes a vortex-motion about its own center, which is responsible for the formation of a compact core but also for the formation of the beam halo. This process of beam and halo formation is strongly influenced by the various collimators in the central region of INJECTOR II. Therefore reliable position informations are of vital importance for a realistic beam model with space charge. The 3D-PIC code OPAL [2], developed at PSI, allows to model high intensity beams including space charge and first steps towards a precise beam dynamics model have been done [3].

As the collimators are equipped with beam current readouts, they might also be helpful to survey the intensity distribution of the beam in the central region. Figure 5 shows examples of the position measurements and Fig. 6 how these positions were connected with beam tracking and RIL1 measurements to a complete model. We hope that this model will help us in the future to better understand the space charge induced vortex motion and halo formation in the center of INJECTOR II and to further reduce beam losses at extraction. Low extraction losses are also the precondition for a further increase of beam current.

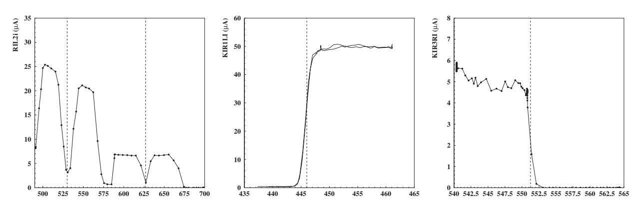

Figure 5: Examples of scans of current readings as a function of the collimator positions. Left: Collimator mounted on RIL2-drive. Center: KIR1L (left jaw of KIR1). Right: KIR3R (right jaw of collimator KIR3).

The replacement of the 3rd harmonic resonators, formerly used as flattop resonators, by normal accelerating resonators with higher voltage is planned for 2017/2018. This upgrade will further increase the turn separation and is thus expected to allow for an even higher beam intensity [4]. Specifically for a precise beam dynamics model of the INJECTOR II is expected to be helpful.

As shown in Fig. 6, the results of the beam based survey confirmed most but not all position readings.

ISBN 978-3-95450-167-0

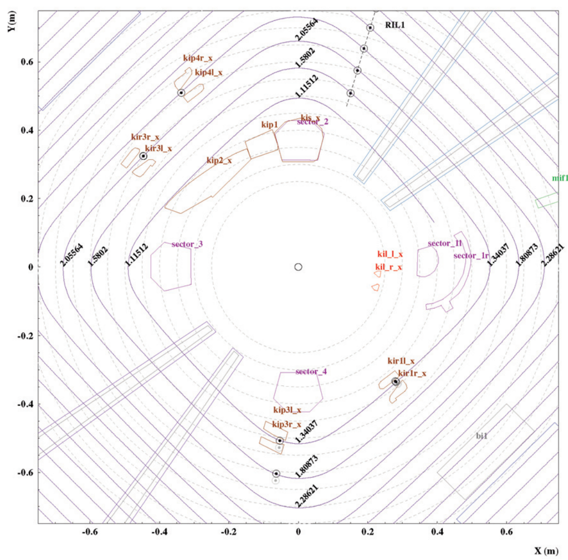

Figure 6: Top view of the central region of INJECTOR II. With the beam positions fixed at RIL1 (at $\theta \approx 80°$) the tracking and the voltages of resonator 1 (gaps in cyan) and resonator 3 (gaps in magenta), the beam position at the various collimator angles are computed (open black circles at the collimators) and compared to the position reading of the collimators. We found two devices, namely the RIL2-collimator and KIR1 where the computed beam positions deviated from the position readings of the device (grey open circles). For the KIP3-collimator mounted on the drive of RIL2, the deviation was found to be about 20 mm and for KIR1 about 5 mm, while all other positions agreed well with the computed beam positions.

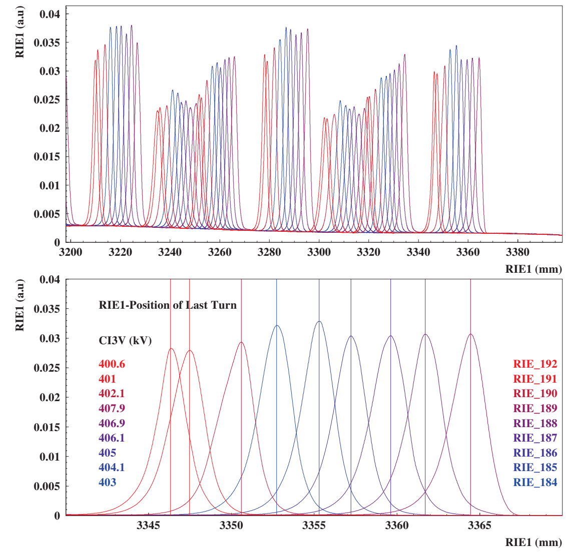

Figure 7: Top: Raw data of beam profiles as measured with the first radial extraction probe RIE1 for different voltages CI3V of resonator 3. Both, the absolute positions as well as the shift of the positions by the change of the resonator voltage can be compared with the tracking calculations. Bottom: A zoom of the last turn, the precise radial positions of highest intensity are indicated by vertical lines.

INJECTOR II is equipped with additional short range radial probes RIE1 and RIE2 that allow to study the beam positions of the last turns prior to extraction with high accuracy (see Fig. 7). Analogue to the central region we plan to survey the exact positions of the septum of the electrostatic extraction element (EID) and the first septum magnet of the 72 MeV beamline (AXA). Both elements can be remotely controlled with respect to radius and angle. A direct mechanical verification of old calibrations of these elements is practically excluded due to the relatively high dose rate in the extraction area.

SUMMARY

In preparation of future machine upgrades and replacement of components we launched a program of beam based survey and alignment measurements. The purpose of this program is to achieve a self-consistent set of cross-checked calibration and alignment data of RF voltages, collimator positions, phase probe calibrations [5], trim coil and sector magnetic field strength that provides realistic boundary conditions for machine beam dynamics simulations. Furthermore the program provides the beam profiles and beam position data that are required for the validation of precise beam dynamics models and simulations with OPAL and other tracking tools. The long-term plan is to achieve detailed information for a better understanding of beam core and halo formation and that allows to reduce halo formation and to reduce beam losses.

ACKNOWLEDGMENT

We thank the crew of the PSI machine operators for their kind support.

REFERENCES

[1] W. Joho, Contrib. to PAC 1975, *IEEE Trans. on Nucl. Sci.*, Vol. NS-22, No. 3 (1975), pp. 1397-1401.

[2] Y. J. Bi, A. Adelmann, R. Dölling, M. Humbel, W. Joho, M. Seidel, and T. J. Zhang, *Phys. Rev. ST Accel. Beams* 14, 054402 (2011).

[3] A. M. Kolano, R. J. Barlow, A. Adelmann, C. Baumgarten, "A Precise Beam Dynamics Model of the PSI Injector 2 to Estimate the Intensity Limit", in *Proc. of IPAC'14*, Dresden, Germany, paper TUPRI031 (2014)

[4] M. Seidel *et al*, "Production of a 1.3 MW Proton Beam at PSI", in *Proc. IPAC'10*, Kyoto, Japan, paper TUYRA03, pp. 1309-1313 (2010).

[5] A. S. Parfenova, C. Baumgarten, J. M. Humbel, A. C. Mezger, A. V. Petrenko, "Measurements of the Beam Phase Response to Correcting Magnetic Fields in PSI Cyclotrons", in *Proc. IPAC2016*, Busan, Korea, Mar. 2016, paper TUPMR019, pp. 1271–1273, doi:10.18429/JACoW-IPAC2016-TUPMR019, 2016.

ISBN 978-3-95450-167-0

AUTOMATED DOCUMENTATION OF TUNES IN THE BEAM LINES OF THE COMET CYCLOTRON

R. Dölling†, Paul Scherrer Institut, 5232 Villigen PSI, Switzerland

Abstract

The proton beam from the COMET cyclotron can be transported to three gantries and two horizontal lines [1]. The beam energy is adjusted by a variable degrader. For each branch several "tunes" are defined, each listing the previously evaluated magnet, degrader and collimator settings for a certain beam energy [2]. The beam quality at the end stations is routinely checked meticulously in the frame of treatment quality assurance [3]. Independently of this, software has been developed (in the frame of the machine control system) to collect, for series of tunes, all available information on the beam and on the machine settings in the active beam line. Routinely used, this allows a close observation of the stability and reproducibility of the machine and keeps ready consistent data sets for detailed studies. This tool can also be used to collect, in a short space of time, extensive data for beam dynamics simulations with OPAL [4] or optimisation procedures based thereon [5], to verify the beam line performance after changes to hardware or software, or to check the functionality of the beam diagnostics. The data set characterising a single tune is organised systematically, allowing to share data viewers with standard beam diagnostics.

ENVIRONMENT

In the PROSCAN beam lines, beam profiles are measured by multi-strip ionisation chambers (MSIC) and the beam energy by multi-leaf Faraday cups (MLFC) [6]. The channels of a single monitor can be read out simultaneously to reduce the effect of beam noise. The signals of current, halo and loss monitors and from slits, stoppers and collimators can also be read out. Monitors and stoppers are inserted into the beam by compressed air actuators. All these parameters as well as all actual machine parameters and settings in the database [7] can be accessed or, if possible, set via EPICS. Information on the tune settings can be read from tune files or interpolated from tune tables [8]. MATLAB is permanently running on a 64-bit Linux-PC in order to get short start-up times [7]. A MATLAB-EPICS interface is available [9].

MEASUREMENT SOFTWARE

A MATLAB program allows to set a tune and the beam current (in the right order and adapted to transmission, in order to prevent overcurrent at the end station), to change predefined machine settings (to modify the tune), to measure statically (i.e. after settling of the tune) predefined monitors, to log predefined machine parameters, to store the tune settings and changes (Fig. 1). For each measured tune, a tune data file with a MATLAB structure (Fig. 2) is stored, containing all the information well organized and accessible. Predefined script files can be loaded to do this for sequences of tunes. In addition, for each sequence a protocol file is generated, listing the measured tunes with modifications.

Within a tune measurement, drive movements and measurements are sequenced effectively and controlled (to e.g. make sure that the monitor movements are finished before a measurement starts or to stop the sequence in case of unexpected behaviour). This allows to perform the sequences reliably and much faster than it would be possible 'by hand'. E.g. the measurement of a tune from COMET to Gantry 3 entrance takes a minute (38 profiles, 1 MLFC, 162 signals from diagnostics or machine parameters, transients).

The program can run compiled or not compiled. For test purposes, options can be chosen to not move drives or set tunes or set beam current or open first stopper. This allows testing without mastership of the facility (when these actions are reserved for other users) or a dry run without feeding beam into the lines.

Measurement of Transients

The electronics reading out the monitors can measure waveforms of profiles or of individual signals. Up to 4095 samples with a minimum time step of 0.2 ms can be taken. (For larger time steps, the signal is integrated.) This allows to observe profiles or other signals also during the transition from one tune to the next (Fig. 3, Fig. 2 lower part). Of course with the limitation that only one beam-destroying monitor can be used at a time. At least the beam current after the cyclotron is measured in this way for each tune data file, in order to document the beam current fluctuations caused by the ion source [10].

AUXILIARY SOFTWARE

The measurement software already roughly depicts profiles in the GUI to allow the user to see if the sequence is running correctly.

A post-processing routine evaluates for a batch of tune data files the transient profiles, adds the results to the data structure and stores it in new files. Due to the large number of profiles, this step is too time-consuming to do it already during the measurement sequence.

A simple viewer allows to load a tune data file and to depict the information on the static measurement (evaluated profiles, MLFC, tune details, logged parameters, comments, error messages). Another viewer depicts the transient measurements (Fig. 3).

These routines again are written in MATLAB, allowing a simple reading of tune data files. To make the data available to OPAL, a simple batch routine is used to export text files.

† rudolf.doelling@psi.ch

ISBN 978-3-95450-167-0

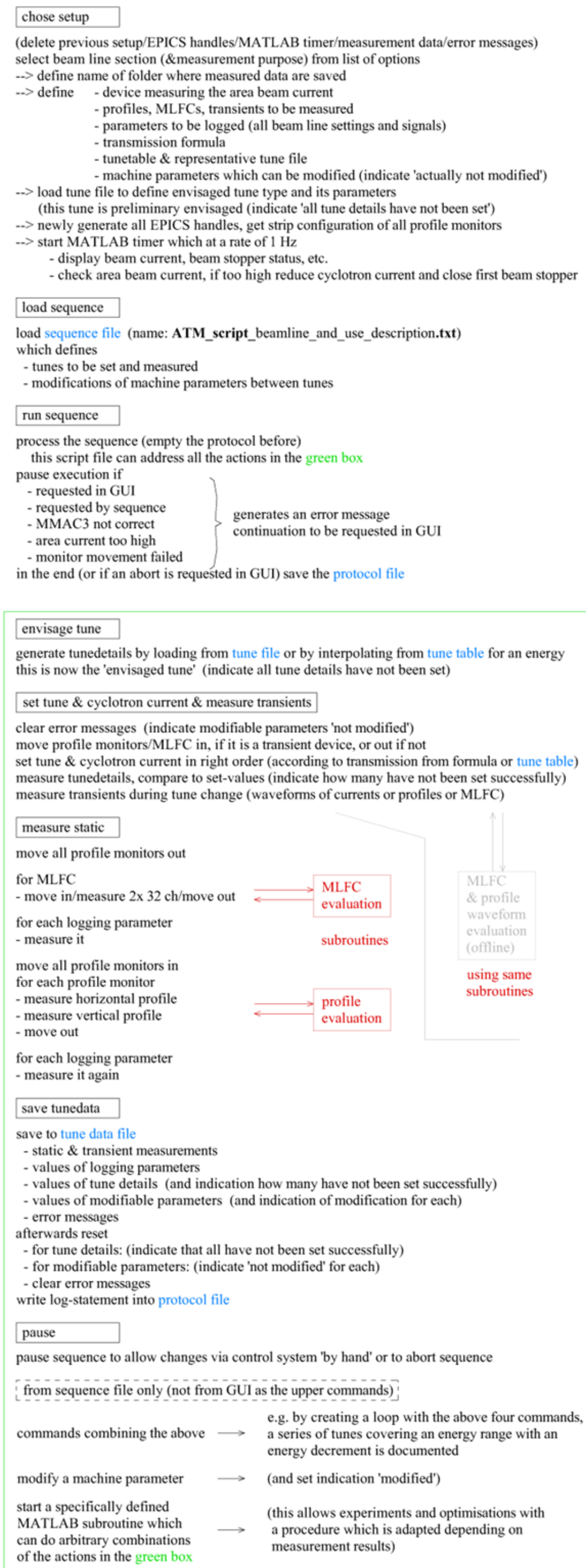

Figure 1: The full framed headings indicate the processes which can be started from the GUI.

Figure 2: Structure of data stored in a tune data file. Grey: Data added by an offline-evaluation.

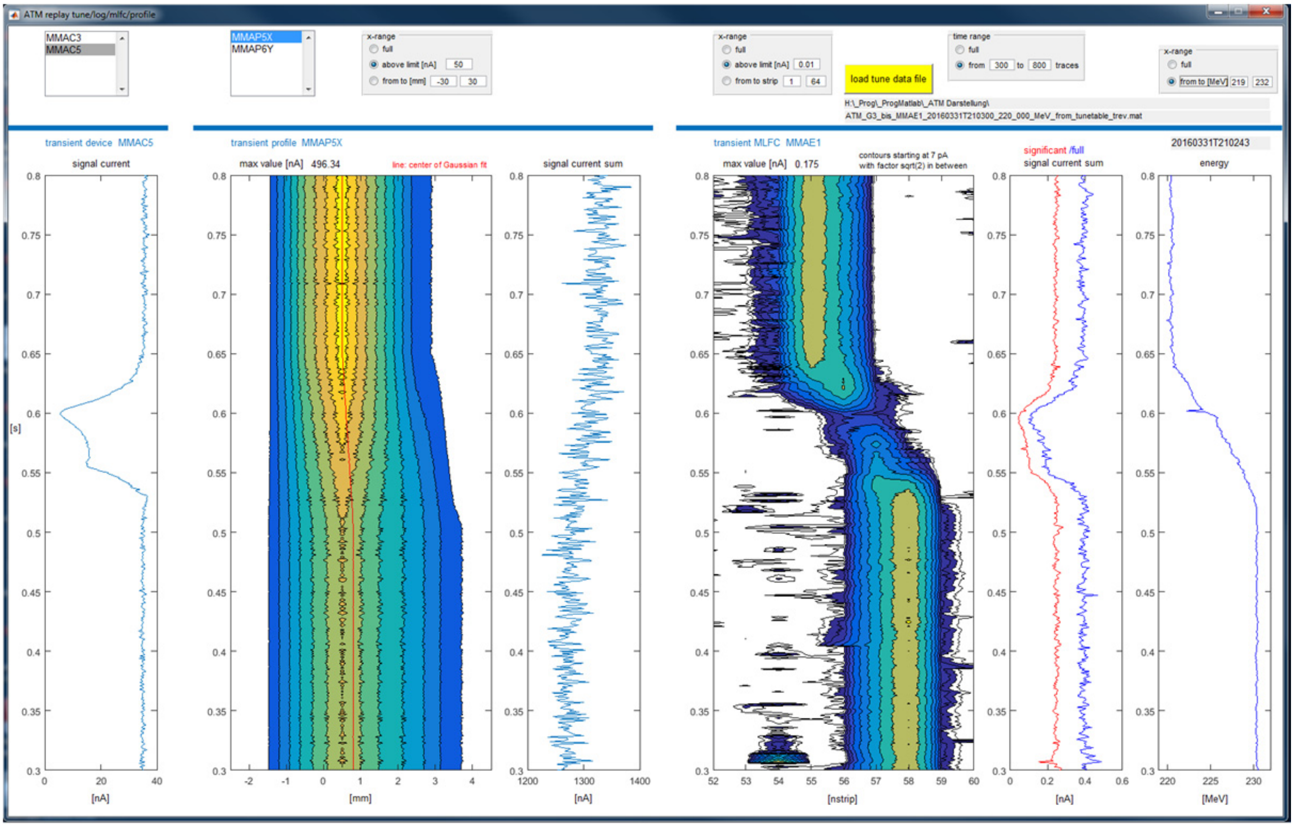

Figure 3: Transient measurement (time step 1 ms). Left: Current monitor in front of MLFC. Middle: Profile in front of degrader. Right: Beam energy from MLFC. During the tune change from 230 MeV to 220 MeV, the current from the cyclotron (3rd plot from left) changed only marginally to compensate for the changing transmission to the end of the beam line. Farther downstream (1st plot from left), the beam current drops significantly, because the beam optics is not correct while the magnets are ramping not perfectly synchronized. Despite the very low beam current during the transition, the energy change is given quite well by the MLFC (6th plot from left). At lower energies this is not the case because the beam completely vanishes during the transition. The horizontal beam centre in front of the degrader shifted, probably due to a misalignment of the beam line.

CONCLUSION

The software allows to predefine extensive measurement tasks quite flexible and to repeatedly perform them very fast, reliably and documented. The used MATLAB data structure facilitates post-processing and visualisation. As mentioned in the abstract, this can be used for several purposes. It extends the concept of taking "complete" consistent data sets [11], which proved already useful at PSI's high power proton machine.

ACKNOWLEDGEMENT

I like to thank H. Lutz for hardware and software support in the machine control system environment.

REFERENCES

[1] J. M. Schippers *et al.*, "The SC cyclotron and beam lines of PSI's new proton therapy facility PROSCAN", Nucl. Instr. Meth. B, vol. 261, pp. 773–776, 2007.
[2] E. Pedroni *et al.*, "Pencil beam characteristics of the next-generation proton scanning gantry of PSI: design issues and initial commissioning results", *The European Physical Journal Plus*, vol. 126, no. 7, p. 66, 2011.
[3] S. Lin *et al.*, "More than 10 years experience of beam monitoring with the Gantry 1 spot scanning proton therapy facility at PSI", *Medical Physics*, vol. 36, no. 11, p. 5331, 2009.
[4] A. Adelmann *et al.*, "OPAL User Manual", PSI-PR-08-02, 2008-2016, `http://amas.web.psi.ch`
[5] V. Rizzoglio, PSI, private communication, June 2016.
[6] R. Dölling *et al.*, "Beam diagnostics for the proton therapy facility PROSCAN", in *Proc. AccApp'07*, Pocatello, USA, July 2007, pp. 152-159.
[7] H. Lutz, PSI, private communication, June 2016.
[8] S. Psoroulas, PSI, private communication, June 2016.
[9] S. Ebner, "Matlab Channel Access", presented at EPICS User Meeting, 18 October 2015, Melbourne, Australia, `https://events.synchrotron.org.au/event/15/contribution/6`.
See also:
`https://github.com/channelaccess/ca_matlab`.
[10] R. Dölling, PROSCAN Reports P24/DR84-516.2, December 2005; P24/DR84-703.2, March 2007.
[11] R. Dölling, "Bunch-shape measurements at PSI's high-power cyclotrons and proton beam lines", in *Proc. Cyclotrons2013*, Vancouver, Canada, September 2013, paper TU3PB01, pp. 257-261.

ISBN 978-3-95450-167-0

SUPPRESSION OF RF RADIATION ORIGINATING FROM THE FLATTOP CAVITY IN THE PSI RING CYCLOTRON

Markus Schneider†, Andreas Adelmann, Nathaniel Pogue, Lukas Stingelin,
Paul Scherrer Institut, 5232 Villigen PSI, Switzerland

Abstract

In the PSI Ring cyclotron, protons are accelerated from 72 MeV to 590 MeV. In several upgrade programs, the beam current was increased from the initial design value of 100 µA up to 2.4 mA. The rf-system of this separated sector cyclotron consists of 4 copper cavities running at 50 MHz for the main acceleration. For the purpose of increasing the phase acceptance of the Ring, an aluminum flattop cavity is operated at a gap voltage of 555 kVp at the 3rd harmonic frequency.

As a result of the progressively increased flattop voltage, this cavity was pushed toward its mechanical and electrical limits. As a consequence, rf-power is leaking into the cyclotron's vacuum space and is causing several problems. A visible effect was the formation of plasma in the vacuum chamber [1].

In the last shutdown, an attempt was made to reduce the radiated rf-power. On the vacuum sealing between the flattop cavity and sector magnet 6, a shim was installed which reduces the gap for the beam from 60 mm to 25 mm in height. Results of this intervention will be presented and compared with finite element model simulations.

INTRODUCTION

The flattop cavity in the Ring cyclotron is located between Sector Magnet 6 (SM6) and Sector Magnet 7 (SM7) as shown in Fig. 1. AS2 and AS3 are rf-radiation probes.

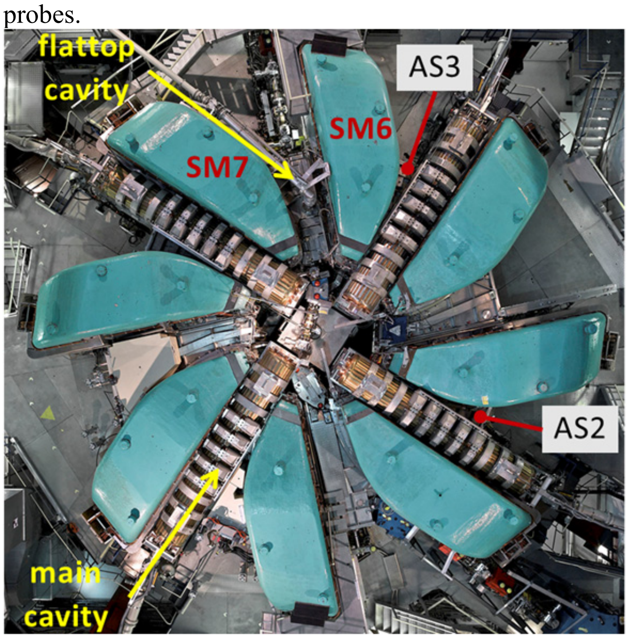

Figure 1: The PSI Ring cyclotron.

The FT cavity is directly attached to the vacuum chamber on the SM7 side by an O-ring. However, an expandable sealing (see Fig. 4) is installed between the cavity and SM6. This expandable sealing is an O-shaped bellow made of aluminum, holding an O-ring on both sides. For a vacuum tight connection it is pressurized by air to 0.7 Bar. For installation in the machine, the expandable sealing is shrunk by applying vacuum. This sealing has a vertical gap size of 60 mm.

Simulations showed that the radiated power of the flattop cavity could be reduced, by adding a metal shim (25 mm vertical gap size, 102 mm length) outside the cavity into the beam aperture from 11.9 kW to 3.3 kW. This is a reduction of 8.6 kW or 75% [2].

It turned out to be difficult to add such a shim on the flattop cavity towards SM7 because a mechanical support holding the shim is needed. Additionally, for the installation of such a shim the cavity would have to be taken out of the ring cyclotron.

A much easier way to install a shim was to reduce the gap in the expandable vacuum sealing on the SM6 side of the flattop cavity. Figure 2 shows a cross section of flattop cavity, expandable vacuum sealing with shim, and vacuum chamber of sector magnet.

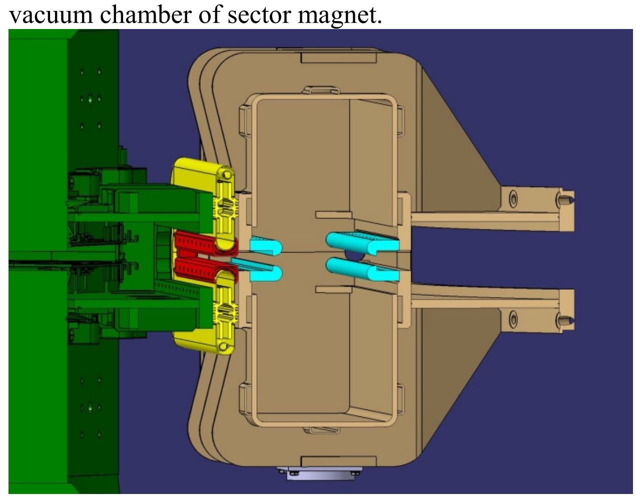

Figure 2: Cross section of flattop cavity (beige) with electrodes (cyan), expandable vacuum sealing (yellow) with shim (red) and vacuum chamber of sector magnet 6 (green).

SHIM

The design of the new shim was straight forward. The gap size should be lowered to 25 mm and the maximum length is given by the space between SM6 and flattop cavity such that the sealing could still be installed. We decided to use an aluminum sheet of 4 mm thickness which is formed into a U-shape (see Fig. 3). The expand-

† markus.schneider@psi.ch

ISBN 978-3-95450-167-0

able sealing's top and bottom inside radius have this U-profile. For a good rf-contact to the sealing the U-shape was changed to a C-shape with a sharp corner pressing into the sealing. On both sides we added a block of aluminum to get the 25 mm distance between the upper and lower profile. As fixation for the shim on the sealing over a distance of 180 mm, clamps were added. We could tighten the C-profile with screw to get a smooth contact to the vacuum sealing. The clamps on the ends of the profile were used to center the shim vertically in the gap.

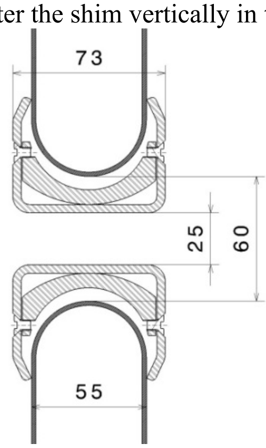

Figure 3: Cross section of expandable sealing with shim. Dimensions of vertical gap and length in mm.

It was difficult to find a manufacturer who was able to bend the aluminum sheet into the C-profile with the expected tolerances over a length of 2.72 m.

TESTS

In January 2016 we received a window of 2 weeks for tests during the shutdown. Two different setups were tested. The first one was to collect data without shim, so as to have measurements during normal operation with the standard expandable sealing. After 1 month shutdown of the cyclotron is was important to have actual reference data.

Then the cyclotron was vented and the vacuum sealing was taken out to install the shim on it. The shim could not be mounted on the expandable sealing on the first attempt because some welded joints were thicker than expected. After some mechanical fine tuning on the shim, which did not affect the principal geometry, we managed to finish the installation. Figure 4 shows a photo of the vacuum sealing with the installed shim.

To avoid multipactoring in our shim we decided to paint the surfaces with “Aquadag 18 %” [3]. This gives a thin layer of graphite on the aluminum surface and lowers the secondary emissions coefficient of electrons.

Then we reinstalled the sealing in the cyclotron and after applying vacuum and conditioning we made our second measurements. Each of those two iteration lasted for about one week.

We expected to see a difference in the power fed into the cavity at the same gap voltage, because less power should be radiated into the machine. On the other hand we used some pickups installed in the vacuum chambers to measure the rf-signal. Such as AS2 is an inductive pickup near the main cavity 2 and AS3 is a capacitive pickup near cavity 3 (see Fig. 1).

MEASUREMENTS

Parameters were measured as a function of the gap voltage. We started on the highest gap voltage and then lowered it in steps of 50 kVp. From point to point it took about 15 minutes to have stable thermal conditions of the flattop cavity. During measurements the main magnets were on and the main cavities were off.

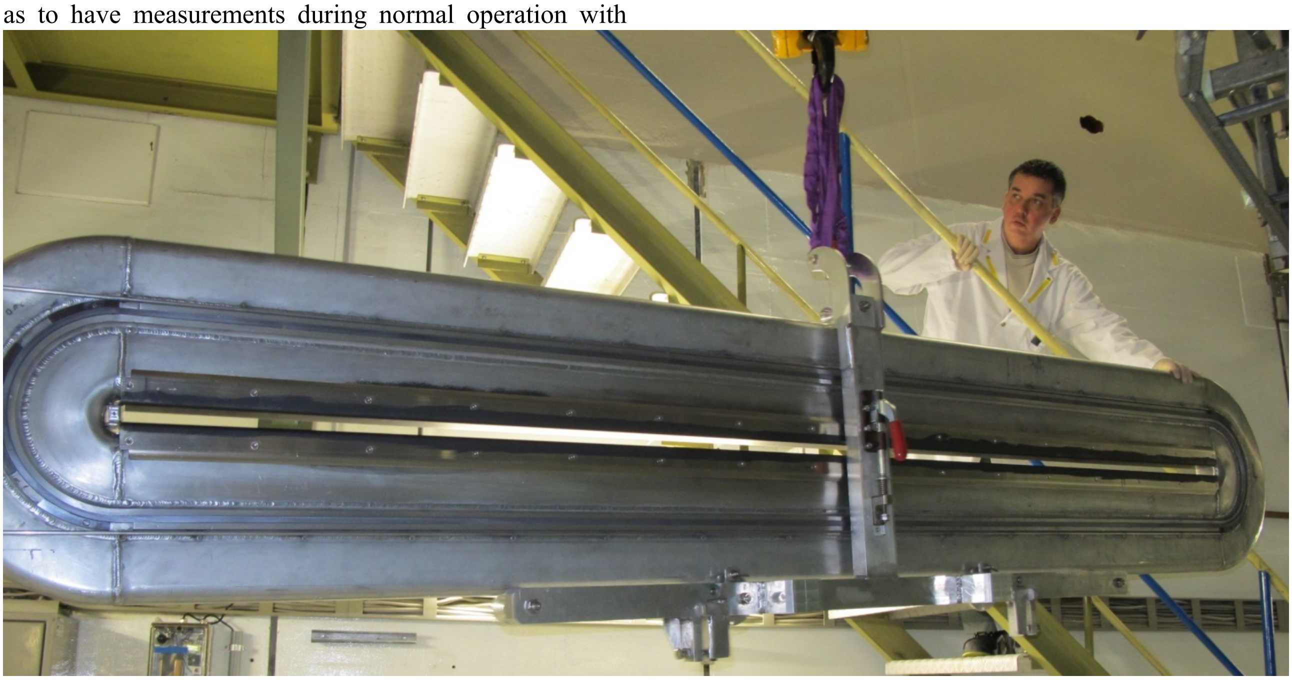

Figure 4: Transport of expandable sealing with shim for installation into the Ring cyclotron.

ISBN 978-3-95450-167-0

Power Versus Gap Voltage

Figure 5 shows the power fed into the cavity versus the gap voltage. Contrary to the simulations, which showed a difference of 8.6 kW at 500 kVp gap voltage, with and without shim the same power was needed during both tests.

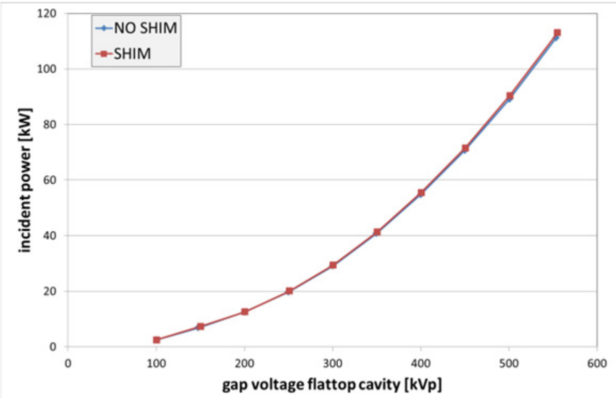

Figure 5: Incident power versus gap voltage of flattop cavity.

Normally the flattop cavity is fed with 102 kW to achieve the 555 kVp. During the two tests, the power was 112 kW for the nominal gap voltage. The additional 10 kW must be fed into multipactoring around the flattop cavity. Higher levels on the ionization chambers are another indicator for this. The same effect was observed after the shutdown 2015 and could be solved by painting several surfaces around the flattop with Aquadag. Such an intervention would have needed at least another week, which was not possible during the assigned test time.

Pickup Signals

The pickup signals were measured by using a spectrum analyzer. In Fig. 6 the signal of the pickup at 151.9 MHz versus the gap voltage is presented. At the probe AS2 the signal was about 4.5 dB lower with the shim. At AS3 a reduction of about 6 dB was measured.

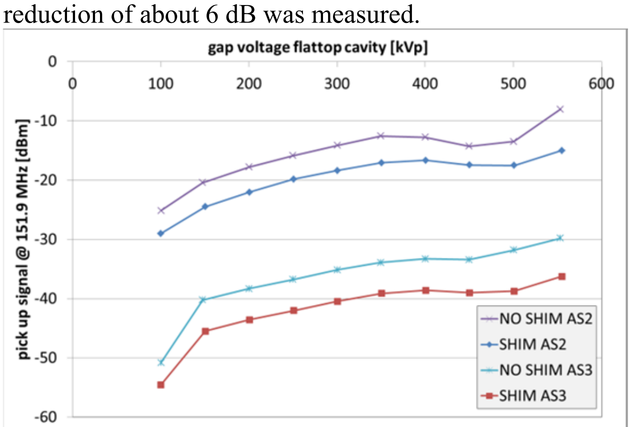

Figure 6: Pickup signals versus gap voltage.

Measurements with Main Cavities

At the end of each test, data was taken with all cavities on normal operation voltage. Table 1 compares those values.

Table 1: Pickup Signals with all Cavities on Nominal Voltage

	NO SHIM	SHIM	difference
AS2 @ 50.6 MHz	1.03 dBm	1.03 dBm	-
AS2 @ 151.9 MHz	-17.90 dBm	-23.86 dBm	-5.96 dB
AS3 @ 50.6 MHz	-44.81 dBm	-44.87 dBm	-
AS3 @ 151.9 MHz	-27.84 dBm	-32.88 dBm	-5.04 dB

CONCLUSION

A metal shim was successfully installed on the expandable sealing for the tests during the shutdown 2016. The pickup signals measured during power tests were 5 to 6 dB lower compared to the setup without shim. This is in the range of the estimated results from the simulations. Nevertheless the expected reduction of the power fed into the cavity was not observed during the tests.

The shim is an improvement to reduce the radiated power from the flattop cavity, but does not solve all the plasma problems observed in the PSI Ring cyclotron. Unfortunately there was no pickup on the SM7 side of the flattop cavity, to see if the power leakage increased at the SM7 side as a result of the reduction on the SM6 side. Further investigation will be needed. A measurable reduction in power might be seen, if the shims are located on each side of the cavity.

The installed shim reduces the vertical gap to 25 mm. Because there is no protecting device to avoid that the beam hits the shim, it was taken out of the machine after the tests.

During both runs more power was needed for the nominal cavity voltage. This could be temporary solved by excessive painting in and around the flattop cavity with Aquadag in the shutdown after the test.

ACKNOWLEDGEMENT

The author would like to acknowledge Urs Heidelberger for support with the expandable vacuum sealing, Harald Siebold for assistance with CAD drawings, and the PSI rf group for support during the tests.

REFERENCES

[1] N.J. Pogue, A. Adelmann, M. Schneider and L. Stingelin, “Examination of the plasma located in PSI Ring Cyclotron”, in *Nucl. Instr. Meth. A,* vol. 821, pp. 87-92, 2016

[2] N.J. Pogue, L. Stingelin and A. Adelmann, “Analysis and suppression of RF radiation from the PSI 590 MeV cyclotron Flat Top Cavity”, in *Nucl. Instr. Meth. A,* vol. 828, pp. 156-162, 2016

[3] Emerson & Cuming, “AQUADAG 18% Colloidal Graphite in Water”, `http://www.lindberg-lund.com/files/Tekniske%20datablad/EC-AQUADAG-18-TD.pdf`

ISBN 978-3-95450-167-0

OPERATIONAL STATUS OF THE UNIVERSITY OF WASHINGTON MEDICAL CYCLOTRON FACILITY

R. Emery, E. Dorman, University of Washington Medical Center, Seattle, Washington, USA

Abstract

The University of Washington Medical Cyclotron Facility (UWMCF) is built around a Scanditronix MC50 compact cyclotron that was commissioned in 1984 and has been in continual use since. Its primary use is in the production of 50.5 MeV protons for fast neutron therapy. While this proton energy is too low for clinical proton therapy, it is ideal for proton therapy research in small animal models. In addition to the protons used for fast neutron therapy and proton therapy research, the MC50 is able to accelerate other particles at variable energies. This makes it useful for medical isotope research, including isotopes such as ^{211}At, ^{186}Re, and ^{117m}Sn that are being developed to target and treat metastatic disease at the cellular level.

The original accelerator and therapy control systems were run on a DEC PDP-11 with a custom centralized I/O system built around the Z80 processor and chipset. Over the last 10 years we have continually been upgrading the controls while remaining operational, moving to a distributed system developed with the open source Experimental Physics and Industrial Control System (EPICS) toolkit.

INTRODUCTION

In '78-'79 the National Cancer Institute (NCI) awarded contracts to 4 institutions to construct, develop, and operate state-of-the-art fast neutron therapy facilities: University of Washington (UW), Fox-Chase Cancer Center (FCCC), M.D. Anderson (MDA), and University of California, Los Angeles (UCLA). Of these four facilities, the UW fast neutron therapy program is the only one still in existence. The longevity of the UW facility can be ascribed to a commitment from physician and faculty leadership, an exceptional maintenance and upgrade program, and the fact that the facility was designed with the flexibility to support a variety of research programs. The UWMCF was built around a Scanditronix MC50 cyclotron that can produce 28-50.5 MeV protons, 13.6-23.8 MeV deuterons, and 27-47.3 MeV alphas and in addition to producing beam for fast neutron therapy, it also produces beam for medical isotope production, proton therapy research, and radiation effects testing.

OPERATIONS AND MAINTENANCE

The cyclotron facility was built inside the UW Medical Center (UWMC). At the end of construction and commissioning, ownership, operation, and all documentation was turned over to the UW. This model is quite different than most of the modern proton therapy facilities where operation and maintenance are done under service contracts by the accelerator manufacturers. This model has allowed the UW to develop in-house expertise and provided the freedom to modify and upgrade the facility to support changing research needs. The facility is maintained by an in-house engineering/physics group of 5.5 full time employees. The facility operates Tuesday-Friday 7:30 am - 4:30 pm, and is shut down for maintenance on Mondays. There are no planned maintenance shutdowns beyond the Mondays and facility downtime has averaged less than 1.5% over the last 20 years.

The Medical Cyclotron Facility is operated as a cost center within the UW and the service it sells is beam time. The facility is entirely reliant on the business it generates for income and is not allowed to operate with a surplus or deficit. If it does it must adjust its reimbursement rate based on projected usage and operating cost estimates. The primary customer is the UWMC. They pay for beam time required for patient treatments and account for roughly 90% of the income. The remaining income comes from grant based research (isotope and proton therapy research) and commercial users (isotope production and radiation effects testing).

RECENT UPGRADES

The original accelerator and therapy control systems were based on a centralized PDP11/23 control computer and Z80 based I/O devices. For the last 10 years there has been a concerted effort to upgrade the control system to a distributed PC system using the Experimental Physics and Industrial Control Systems (EPICS) toolkit. At this point the new therapy control system has been developed and commissioned, and the accelerator control system has been upgraded with the exception of the RF subsystem, which will be completed soon. One major change to the new therapy control system is the inclusion of a Digital Imaging and Communications in Medicine (DICOM) server to allow for the standardized transfer of treatment plans.

FAST NEUTRON THERAPY

The fast neutron therapy beam is generated by focusing protons (65-75 μA) on a 10.5 mm thick beryllium target housed in a rotating gantry. The neutron beam is flattened with a tungsten flattening filter downstream of the beryllium target, and can then be modified with one of three onboard tungsten wedge filters (30deg.-45deg.-60deg.) to create a wedged profile. The neutron beam is finally collimated with a 40-leaf steel/polyethylene multi-leaf collimator. The standard therapy dose rate is 60 cGy/min at d-max (1.7 cm) for a 10.3x10.0 cm field.

We have recently developed a Monte Carlo model of our neutron therapy beam using MCNPX. The model developed allows us to simulate percent depth dose, lateral dose profiles, and neutron fluence. Preliminary results are in good accordance with measured values. [1]

ISBN 978-3-95450-167-0

The next steps are to use the model for treatment plan verification and to investigate microdosimetry and relative biological effectiveness (RBE). As our beam model evolves into a new treatment planning system we will investigate Neutron Intensity Modulated Radiation Therapy.

ISOTOPE RESEARCH

The multi-particle/variable energy capability of the Scanditronix MC50 cyclotron provides for unique research opportunities beyond radiation therapy. This functionality has helped sustain the facility in the face of declining neutron patient volumes. The UWMCF is now routinely producing 211-At for research in pretargeted radioimmunotherapy at the UWMC and the Fred Hutchinson Cancer Research Center, and 117m-Sn for clinical studies in treating arterial vulnerable plaque. [2-4].

PROTON THERAPY RESEARCH

The UWMCF was originally equipped with two fast neutron treatment vaults: one with a rotating gantry and multi-leaf collimator, and the other with a fixed horizontal port and square insert collimators. The fixed beam vault had only been used for physics and radiation biology research, never for routine patient treatment. Because of an increased interest in proton therapy we have removed the beryllium target station and neutron collimator from the fixed beam treatment head, extended the vacuum chamber, and installed a mechanical mounting system to allow for image guided proton therapy research. Current research includes proton activated PET scanning [5] and image guided proton beam research for preclinical in vivo studies.

RADIATION EFFECTS TESTING

The UWMCF has seen recent increase in requests for radiation effects from US aerospace companies. The ability to deliver proton, neutron, alpha, and deuteron beams at various energies along with in-house Monte Carlo modelling and high availability make the UW facility attractive for radiation effects testing.

CONCLUSION

After 32 years the UW Medical Cyclotron Facility is running well and is one of the few remaining centers worldwide treating with fast neutrons. The biggest threat to continued operations is declining patient treatments, which provide the bulk of funding for the facility. Beyond neutron therapy, the facility has an established isotope production and research program and is developing a proton therapy research program as well as a Monte Carlo based radiation effects testing program.

REFERENCES

[1] G. Moffitt, R. Stewart, G. Sandison, R. Emery, T. Jevremovic, "MCNPX modeling of the fast neutron beam at the University of Washington", in *Proc. American Nuclear Society 2013 Student Conference*, Massachusetts Institute of Technology, April 2013.

[2] K. Gagnon, R. Risler, S. Pal, D. Hamlin, J. Orzechowski, R. Pavan, S. Zeisler, D.S. Wilbur, "211 at production using an external target system", presented at *Proc. 14th International Workshop on Targetry and Target Chemistry (WTTC),* Playa del Carmen, Mexico, Aug. 2012, AIP Conf. Proc.

[3] Y. Chen, B.T. Kornblit, D.S. Wilbur, D. Hamlin, G. Sale, E. Santos, R. Storb, B. Sandmaier, "Durable donor engraftment after radioimmunotherapy using alpha-emitter astatine-211-labeled anti-CD45 antibody for conditioning in canine dog leukocyte antigen (DLA)-identical marrow transplant", *Blood* vol. 119, p. 1130-1138, (2012).

[4] N.R. Stevenson, "The Production and Applications of High Specific Activity Sn-117m", in *Proc. CAARI 2010*, Fort Worth, Texas, August 2010.

[5] M. Nyflot, E. Ford, S. Bowen, G. Battistoni, R. Nicolini, M. Narayanan, E. Dorman, R. Emery, P. Kinahan, G. Sandison, A. Del Guerra, R. Miyaoka, "Proton dose verification in the murine model with positron emission tomography of activated radioisotopes", in *Proc. IEEE Nuclear Science Symposium and Medical Imaging Conference*, Seoul, Korea, October 2013.

ISBN 978-3-95450-167-0

MAGNETIC SYSTEM FOR SC200 SUPERCONDUCTING CYCLOTRON FOR PROTON THERAPY

G. Karamysheva, O. Karamyshev, N. Morozov, E. Samsonov, G. Shirkov, JINR, Dubna, Russia
Y. Song, Y. Bi, H. Feng, J. Li, S. Du, J. Zheng, K. Ding, G. Chen, Y. Chen, J. Ge, J. Zhou, ASIPP, Hefei, China

Abstract

The superconducting cyclotron SC200 for proton therapy that is under design by ASIPP (Hefei, China) and JINR (Dubna, Russia) will be able to accelerate protons to the energy 200 MeV with the maximum beam current of 1 μA. A conceptual design study with 3D codes for the superconducting cyclotron magnet has been carried out during 2015-16 at ASIPP and JINR. The main design considerations are reviewed. The results obtained by numerical field computation for a suitable choice of design parameters are presented. Results of numerical calculations are the basis for technical design of SC200 cyclotron.

CYCLOTRON OVERVIEW AND ITS PARAMETERS

In order to respond to the increasing interest in Russia and China for proton therapy, JINR and ASIPP have started the development of a dedicated proton therapy facility in frame of the China-Russia joint research center on superconducting protons accelerator. The center has been founded in Hefei, east China's Anhui province recently. The research center, co-built by the Joint Institute for Nuclear Research of Russia and Institute of Plasma Physics of Chinese Academy of Sciences, aims at developing SC200 - China's first compact superconducting cyclotron for medical application - within three years. SC200 will be used for accurate treatment of cancer. The systems and components related to SC200 is expected to be manufactured by the Institute of Plasma Physics by 2017 and both parties will jointly assemble these systems and components and complete the whole project by 2018.

The main SC200 cyclotron design characteristics:

- Compact design similar to the lot existing cyclotrons
- Fixed energy, fixed field and fixed RF frequency
- Bending limit W=200 MeV
- Accelerated particles: protons
- Superconducting coils enclosed in cryostat, all other parts are warm
- Injection by PIG ion source
- Extraction with an electrostatic deflector and passive magnetic channels

MAGNETIC SYSTEM SIMULATION

The preliminary choice of the magnetic system parameters was provided by 2D codes (POISSON [1] and OPERA-2D [2]). At this stage the basic magnet system sizes and sectors gap parameters were estimated. The optimization of the spiral sectors parameters and final choice for magnet design has been done by TOSCA, the magneto-static module of OPERA-3D, 3D code ANSOFT MAXWELL [3] and CST code [4].

At the each step of the magnet optimization the simulated magnetic field maps were analysed by the beam dynamic codes and the beam extraction procedure was studied too.

The SC200 cyclotron model view is shown in Fig. 1. The magnetic field map calculated in the median plane of the cyclotron is shown in Fig. 2.

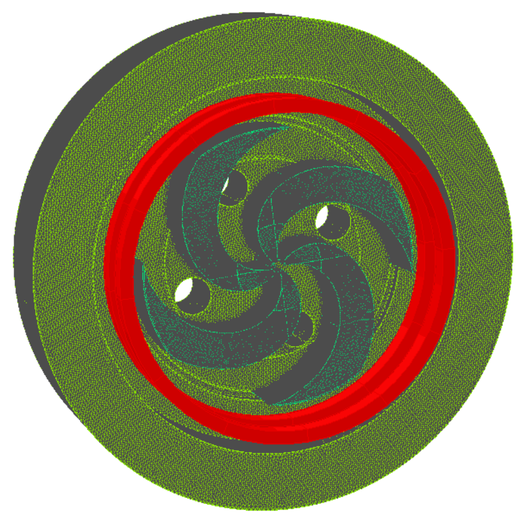

Figure 1: Layout of the TOSCA model for SC200 cyclotron.

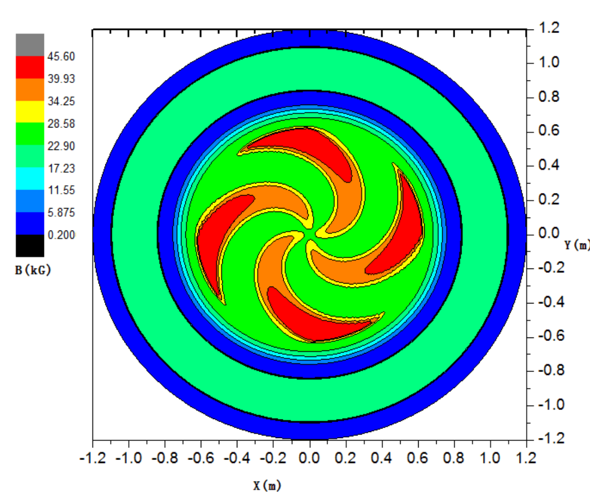

Figure 2: Contour plot of median plane magnetic field.

ISBN 978-3-95450-167-0

The average magnetic field shaping was realized by:

- Magnet pole profiling (additional valleys sectors are used),
- Sectors gap profiling at the final radii,
- Small profiling of the sectors azimuth width,
- Tuning of the vertical and radial position of the magnet main excitation coils.

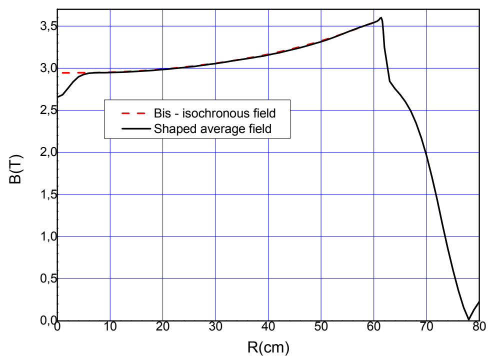

Figure 3: Average magnetic field.

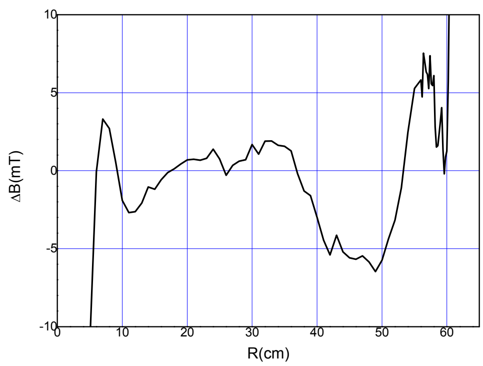

Figure 4: Accuracy of the required average magnetic field shaping.

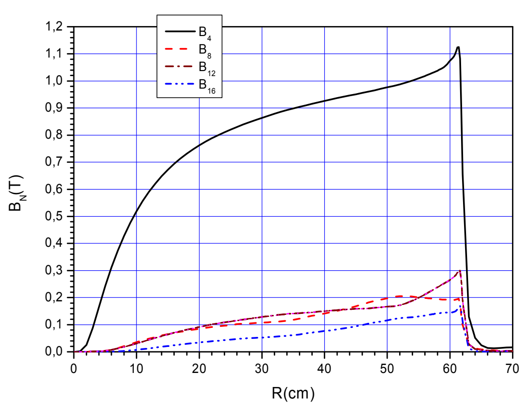

Figure 5: Multiple Fourier harmonics of cyclotron magnetic field.

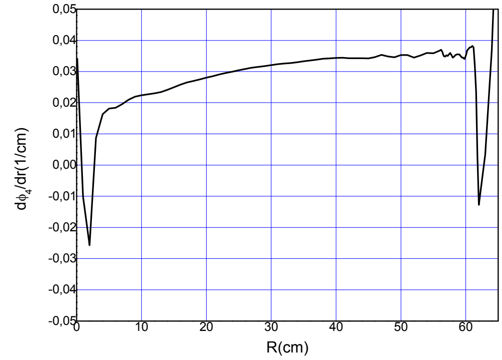

Figure 6: Derivative of the fourth harmonic phase.

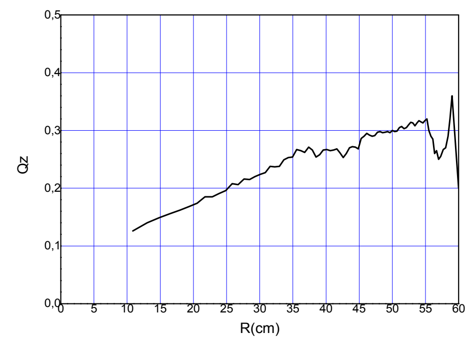

Figure 7: Vertical betatron frequency for the isochronous cyclotron magnetic field.

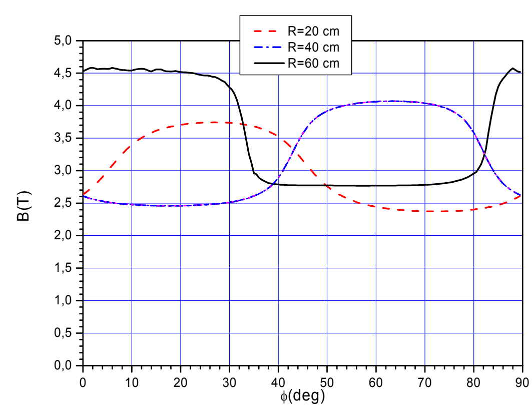

Figure 8: SC200 magnetic field for R=20, 40, 60 cm.

The shaped average magnetic field is shown in Fig. 3. The final deviation of the average magnetic field from isochronous one (Fig. 4) was achieved in range ± (5-6) mT. The basic number Fourier harmonics are shown in Fig. 5 and the fourth harmonic phase derivative in Fig. 6. The optimized sectors geometry provides vertical tune Qz~ 0.3, near the cyclotron extraction region Qz was shaped as close as possible to 0.35 (Fig. 7). Such law of Qz leads to smaller vertical beam size and to not so hard tolerance condition for the magnetic field horizontal components in the median plane of the cyclotron. The azimuth magnetic field distribution for three cyclotron

ISBN 978-3-95450-167-0

radii R=20, 40 and 60 cm is shown in Fig.8. The main parameters of the magnet are shown in Table 1.

Table 1: Main Parameters of the Magnet SC200

Parameters	Value
Average field (central/extraction)	2.9/3.6 T
Hill/valley field	2.8/4.6 T
Number of sectors	4
Sector angle	40 deg
Maximum spirality	65 deg
Sector gap (max/min)	40/5 mm
Valley gap (max/min)	600/530 mm
Pole diameter	1.24 m
Dimension (diameter/height)	2.2/1.22 m
Ampere*turns (1 coil)	750 000
Weight	30 t

MAGNET, COILS AND CRYOSTAT

The preliminary design of SC coils and cryostat is shown in Fig. 9. The magnetic field simulation has resulted in providing the preliminary cyclotron design (Fig. 10).

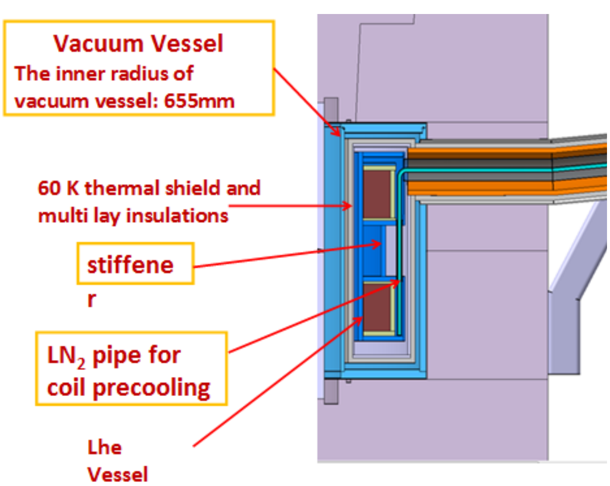

Figure 9: Preliminary design sketch of the cryostat.

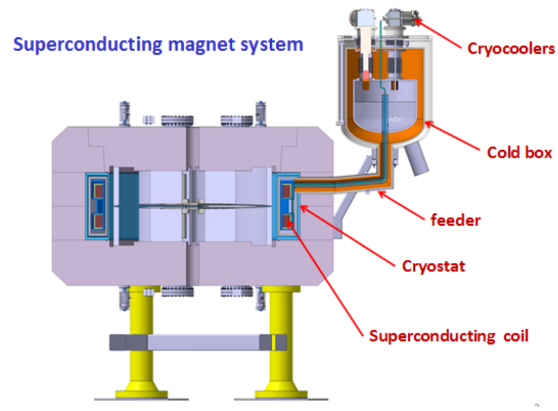

Figure 10: SC200 cyclotron magnet preliminary design.

CONCLUSION

The computer modelling by the 3D codes of the magnet system for SC200 superconducting cyclotron has been performed. The fine optimization of the magnet yoke and spiral sectors parameters has been realized in the cyclotron compact design. The computer models have provided the field maps which allowed to verify by beam dynamic simulation the feasibility of a superconducting proton cyclotron with energy 200 MeV. The technical design of the cyclotron should be realized to the end of 2016.

REFERENCES

[1] POISSON/SUPERFISH User's Guide, LA-UR-87-115, Los Alamos Accelerator Code Group.

[2] OPERA 2D and 3D, Software for Electromagnetic Design, www.cobham.com/technicalservices .

[3] MAXWELL 3D, www.ansoft-corporation.software .

[4] CST code, www.cst.com

ISBN 978-3-95450-167-0

STATUS OF THE ISOL CYCLOTRON SYSTEM IN RISP*

J. Kang†, H. M. Jang, B. Kang, J. W. Kim, J. H. Lee, Institute for Basic Science, Daejeon, Korea

Abstract

An ISOL system has been developed for providing neutron-rich RI beam to multi-disciplinary users by Rare Isotope Science Project (RISP) of the Institute for Basic Science (IBS) in Korea. The ISOL system is composed of proton driver, target/ion source station, mass separator, charge breeder, and A/q separator. A selected beam of interest is then injected into re-accelerator, which is a superconducting linac. A 70 MeV proton cyclotron was chosen as the proton driver to induce direct fission of UCx target. The final goal of beam power on target is 70 kW, which will be achieved gradually from 10 kW during post-RISP. Recently, commercial H^- compact cyclotrons and high-intensity cyclotrons have been considered for its extension of multi-purpose uses. In this paper, the specifications of the cyclotrons along with concerned issues and the status of our procurement plan will be presented.

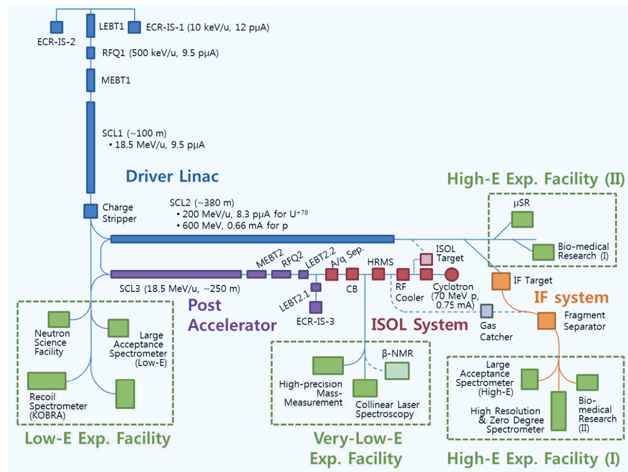

Figure 1: Conceptual diagram of the RAON.

INTRODUCTION

RISP was launched to develop RAON, the name of the heavy-ion accelerator, in 2011. The RAON can utilize both the Isotope Separation On-Line (ISOL) and In-flight Fragmentation (IF) to produce rare isotopes for multi-disciplinary uses (see Fig. 1). The RAON is composed of a driver linac, an IF system, an ISOL system, a post-accelerator, high-energy experiment facility I&II, a very-low-energy experiment facility, and a low-energy experiment facility. The driver linac has two superconducting ECR ion sources, a LEBT, a RFQ, a MEBT, a low-energy superconducting linac (SCL1), a charge stripper, and a high-energy superconducting linac (SCL2). The IF system is employed of an IF target, a pre-separator, and a main separator. The driver linac can accelerate heavy ions up to an energy of 200 MeV/u with a maximum beam power of 400 kW. The ISOL system consists of a 70 MeV proton cyclotron, a target/ion source, a mass separator, a charge breeder, and an A/q separator followed by a post-accelerator system. Not only the IF system and the ISOL system operates independently but also the beam from the ISOL system can be injected via the post-accelerator and SCL2 to IF system for more exotic rare isotopes. The conceptual design and technical design studies on RAON accelerator systems have been conducted since 2012. RISP will be accomplished by the end of 2021.

ISOL system will use a proton cyclotron system as a proton driver and UCx targets to produce neutron-rich (n-rich) isotopes. The final goal is direct fission of ^{238}U by 70 kW proton beam. A 70 MeV proton cyclotron and high-intensity deuteron cyclotrons have been considered to produce more than 70 kW proton beam. Cost, fabrication time, and feasibility aspects were taken into account to choose a suitable cyclotron for RISP.

MAIN ISSUES

The operating plan of the cyclotron is to continuously supply the 70 kW proton beam on the UCx target uniformly over 300 hours for n-rich isotopes. Carbon stripper foil's lifetime, thermal control system of the UCx target, and beam losses inside a cyclotron are critical issues to satisfy the operating plan. The lifetime of a carbon stripper foil is about 20 000 μAh for 100 μg/cm^2 [1, 2]. It is not possible to meet the beam operating time by one carbon foil when the beam current is 1 mA. Applying a multiple foil extraction system with at least 15 foils is introduced, the required operating time can be achieved. However, the beam stop during foil replacement is unavoidable. In this situation, the thermal control of the UCx target and quick foil-exchange systems are necessary to maintain specific temperature of the target. In addition, radio activation inside a cyclotron is concerned about maintenance due to the beam losses by Lorentz stripping and vacuum dissociation during acceleration and extraction [3]. Even several percentage of beam losses at 70 kW can cause high radio-activation in a cyclotron. High vacuum pressure and/or high Dee voltage are needed to minimize the beam losses.

CANDIDATES FOR AN ISOL DRIVER

A High-intensity cyclotron such as the PSI injector II cyclotron was debated at the beginning of the RISP. PSI injector II is a separated sector cyclotron and can accelerator the proton up to 72 MeV with 2.5 mA. A 70 MeV proton cyclotron was reviewed by ISOL group at the conceptual

* Work supported by Rare Isotope Science Project (RISP) through the National Research Foundation of Korea (NRF) funded by Ministry of Science, ICT and Future Planning (MSIP) (NRF-2013M7A1A1075764)
† gaenuinei@ibs.re.kr

ISBN 978-3-95450-167-0

design phase in 2012. At that time, commercial 70 MeV cyclotrons are in operation or planning by ARRONAX [4, 5] and SPES project [6–8], respectively (see Table 1). Moreover, deuteron compact or separated-sector cyclotrons have been discussed to take into account the efficiency of n-rich isotopes production rate and the diversity of research field through international review programs [9–11] (see Table 2). Even though deuteron cyclotrons are advantageous for high current, it is required additional components of a injector, a energy converter and radiation shielding blocks accompanying more budget and longer development time.

Table 1: The Specifications of Commercial Cyclotrons

Parameters	IBA (Belgium)	BCSI (USA)
Energy	35–70 MeV,	35–70 MeV
Max. current	750 µA	750 µA
Extraction ports	Dual	Dual
Magnet sectors	4	4
Magnetic field (hill, valley)	1.7 T, 0.12 T	1.6 T, 0.12 T
RF harmonics	4	4
RF frequency	62 MHz	56.2 MHz
Ion source	Multicusp	Multicusp
Operating site	ARRONAX, France (2010)	INFN, LNL, Italy (2015)

Table 2: The Specifications of Deuteron Cyclotrons

Parameters	Proton cyclotron	Deuteron cyclotron	Deuteron cyclotron
Beam characteristics	70 MeV, H^-, 0.7–1 mA	40 AMeV, D^-, H^{2+}, 1–1.5 mA	60 AMeV, D^+, H^{2+}, 1–2 mA
Beam power	70 kW	120 kW	240 kW
Pole radius	1.35 m	1.66 m	2.1 m
RF cavity	2	2	4
RF frequency	60 MHz	32.8 MHz	32.8 MHz

REQUIREMENTS FOR AN ISOL DRIVER

As a result, commercial 70 MeV H^- compact cyclotron was chosen for a RAON ISOL driver. The power of UCx target which is under development is 10 kW and will be 35 kW and 70 kW gradually in post-RISP. We will upgrade the beam current regarding the high-power target development.

As to the main issues, a carousel system with multiple foils and rapid foil exchange time is needed to continuously produce 70 MeV, 1 mA proton beam. The exhange of carousel system should be easy and done outside the cyclotron without opening the magnet to maintain the vacuum. The beam losses in a cyclotron is dominated by the vacuum dissociation. High vacuum level below 1×10^{-7} Torr is required to minimize the beam losses in the level of less than 2 % inside the cyclotron. Additionally, a carbon blocks should be installed inside an extraction vacuum chamber to prevent activation of a vacuum chamber by neutralized H ions which is not fully stripped at the carbon foil.

The number of extraciton ports will be two, east-side port and west-side port. The east-side port will be used for Online test facility and multi-purpose facility. The west-side port will be dedicated to two ISOL targets. The beamline from the west-side port will be branched into two beamlines up to two target bunkers, repectively. The main components of the beamline are dipole magnets, quadrupole magnets, steering magnets, faraday cups, collimators, beam viewers, scanning system, neutron shutters, wire grids, and vacuum system. The wobbling or a raster scanning system will be placed in downstream of the beamline in a cyclotron vault for unform beam distribution on the ISOL target surface with a diameter of 50 mm. It is important to uniformly irradiate the beam on the UCx target surface to avoid local overheat. The uniform irradiation can be realized by various types of scanning systems. The neutron shutter next to the scanning system will be used to reduce the neutron leakage from the bunker when the beam is not used. Especially, a faraday cup, wire grid, and collimator before ISOL target in the bunker is required to monitor beam current and profile.

The RAON control system is based on EPICS (Experimental Physics and Industrial Control System). The main cyclotron control system should be integrated with the RAON EPICS. All the subsystems of the cyclotron should be controlled by PLC based hardware.

The main requirements for a RAON ISOL driver are summarized in Table 3.

BUILDING LAYOUT

The design of the RAON facility is ongoing. The cyclotron system will be accommodated in ISOL building of RAON facility. The building consists of one basement and two stories. The cyclotron vault, the water cooling system, and two ISOL target bunkers are on basement (see Fig. 2). The power supply room for cyclotron system is on the 1st floor and the ISOL and cyclotron control room is on the 2nd floor.

The concrete shielding walls have been designed about 2.7 m thick to shield against 70 MeV neutrons to reduce the dose rate outside the shield wall to less than 5 µSv/h. The beam losses in a cyclotron were assumed to be 10 % of 1 mA.

CONCLUSION

The maximum beam current of commercial 70 MeV cyclotrons is 750 µA. The UCx target for 70 kW beam power is also not designed, yet. RISP has decided to adopt the commercial 70 MeV H^- compact cyclotron and to upgrade the beam current up to 1 mA as increasing the target capac-

ISBN 978-3-95450-167-0

Table 3: The Requirements for a RAON ISOL Driver

Parameters	Values
Acceleration beam	H⁻
Extraction beam	H⁺
Extraction energy & stability	35–70 MeV, <1%
Beam current & stability	≥750 µA, <5%
No. of extraction ports	2
Extraction	Multiple Carbon stripper foils by carousel system
Continuous operating time	>300 hours
Beam size & uniformity on target	50 mm, <5% with wobbling system
Horizontal beam emittance	<10π mm-mrad
Vertical beam emittance	<5π mm-mrad
Beam transport	Two beamlines up to ISOL targets
Vacuum pressure	$<1 \times 10^{-7}$ Torr
Control system	PLC based hardware integrated with RAON EPICS control system

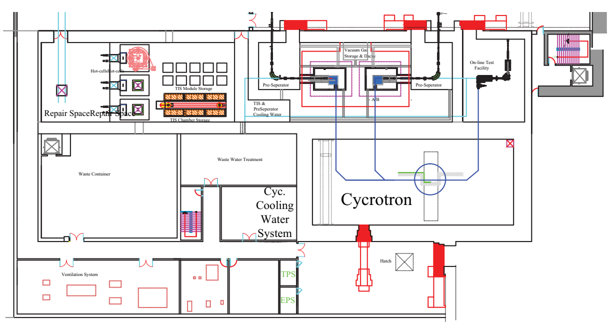

Figure 2: The basement floor plan of ISOL building. The cyclotron vault, the water cooling system room, and the ISOL bunkers are located on this level.

ity for the future work. Beamline configuration has not been fixed yet.

The project agenda is to complete the cyclotron system installation and get the first beam at the target by the end of 2019. The procurement process has just begun to meet the milestone. The bidding is expected to be held in September 2016 and the contract is expected to be made in this year-end.

REFERENCES

[1] J. H. Kim, J. W. Kim, and Y. S. Kim “Thermal Distribution of a Carbon Foil Used to Extract a 30-MeV Proton Beam”, *JKPS*, vol. 63, pp. 1296–1301, Oct. 2013.

[2] J. H. Kim *et al.*, “Investigation of Cyclotron Carbon Foil Lifetime in Relation to its Thickness”, in *Proc. CYC2013*, paper TUPSH005, pp. 227–229.

[3] T. Zhang *et al.*, “Beam Loss by Lorentz Stripping and Vacuum Dissociation in a 100 MeV Compact H⁻ Cyclotron”, in *Proc. PAC’09*, Vancouver, BC, Canada, May 2009, paper FR5REP111, pp. 5035–5037.

[4] J. Martino, “ARRONAX, A High Intensity Cyclotron in Nantes”, in *Proc. CYC2007*, Giardini-Naxos, Sicily, Italy, Oct. 2007, pp. 215–218.

[5] L. Medeiro-Romao *et al.*, “IBA C70 Cyclotron Development”, in *Proc. CYC2007*, Giardini-Naxos, Sicily, Italy, Oct. 2007, pp. 54–56.

[6] G. Prete, A. Andrighetto, J. Esposito, P. Mastinu, and J. Wyss, “The SPES project: a second generation ISOL facility”, *Physics Procedia*, vol. 26, pp. 274–283, 2012.

[7] M. Maggiore, A. Lombardi, and L. A. C. Piazza, “Status Report of the 70 MeV H⁻ Cyclotron”, INFN, LNL, Italy, Rep. 238, 2012.

[8] M. Maggiore *et al.*, “Status of SPES Facility for Acceleration of High Intensity Protons and Production of Exotic Beams”, in *Proc. IPAC2014*, Dresden, Germany, June 2014, paper MOPRI079, pp. 791–793.

[9] L. Calabretta, T. Zhang, and A. Goto, “Review of the Cyclotron Subsystem Design Features for ISOL System”, April 2014.

[10] L. Calabretta, “Review of the Comparison between Proton and Deuteron Cyclotrons”, May 2015.

[11] A. Adelmann *et al.*, “Proposal for a High Power Deuteron Cyclotron at RISP”, in *Proc. HIAT2015*, Yokohama, Japan, Sep. 2015, paper MOPA06, pp. 45–47.

ISBN 978-3-95450-167-0

DESIGN OF A BEAMLINE FROM CYRCé FOR RADIOBIOLOGICAL EXPERIMENTS

E. Bouquerel†, E. Traykov, T. Adams, G. Heitz, C. Maazouzi, C. Matthieu, F. Osswald, M. Pellicioli, M. Rousseau, C. Ruescas, J. Schuler, IPHC, UNISTRA, CNRS, 23 rue du Loess, 67200 Strasbourg, France

Abstract

The PRECy project (Platform for Radiobiological Experiments from CYRCé) foresees the use of a 16-25 MeV energy proton beam produced by the recently installed TR24 cyclotron at the Institut Pluridisciplinaire Hubert Curien (IPHC) of Strasbourg for biological tissues irradiation. One of the exit ports of the cyclotron will be used for this application along with a combination magnet. The platform will consist of up to 3 or 5 experimental stations linked to beamlines in a dedicated 15 m x 13 m area next to the cyclotron vault. One of the beamlines will receive proton beams of a few cm diameter at intensities up to 100 nA. The status of the design of the first beam line is presented. The characterization of the proton beam parameters has been performed using the quad scan method. TraceWin and COSY Infinity codes allowed simulating the beam envelopes and defining the electromagnetic equipment that will compose the beamline.

INTRODUCTION

In October 2013, the Institut Pluridisciplinaire Hubert Curien (IPHC/CNRS) of Strasbourg inaugurated its brand new circular accelerator manufactured by ACSI (CAN) [1]. This cyclotron, called CYRCé (*Cyclotron pour la Recherche et l'Enseignement*), works at energies between 16 and 25 MeV for intensities up to 500 µA (Fig. 1).

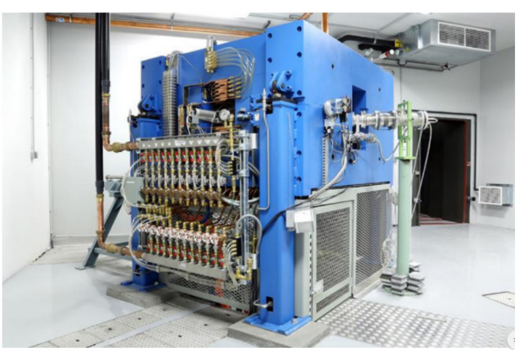

Figure 1: Picture of CYRCé in the casemate.

The accelerator mainly delivers ^{18}F and ^{64}Cu radioelement but also ^{11}C, ^{13}N, ^{15}O, ^{18}F, ^{124}I, ^{64}Cu, ^{68}Ge, ^{76}Br, ^{89}Zr for positron emission tomography (PET) and ^{123}I, ^{111}In, ^{67}Ga, ^{57}Co, ^{99}mTc for single-photon emission computed tomography (SPECT).

†elian.bouquerel@iphc.cnrs.fr

PRECy

A Multi-Phase Project

The PRECy project aims at developing a platform for radiobiological studies from CYRCé. They will be performed for a better understanding of the RBE (Relative Biological Effectiveness) *in vitro* and *in vivo* in small animals (mice) and the study of combination treatment with chemotherapy and proton therapy. The project is divided into two phases over the years 2015 - 2020:

- Phase I (2015-2017): Extraction and Transport of 25 MeV proton beams, out of the existing casemate, to the experimental low energy stations dedicated to *in vitro* studies of the interaction of protons with the cells. By slowing down the beam, it will be possible to cover a range of energy ranging from a few hundred keV to 25 MeV and allow experimental measurements of the RBE on cell cultures and more fundamentally on the molecules constituting the living. The goal is to better understand the effects of the dose deposition at low linear energy transfer (LET) where biological effects are most important.
- Phase II (2018-2020): Extraction, acceleration of protons up to 70 MeV and beam transport to the experimental halls of high energy radiation biology for the *in vivo* study (small animal). The acceleration system should allow to vary the energy of the beam and scanning a surface to enable a dose deposition in a volume (tumor) defined.

At low energy (Phase I), it will be possible to measure the biological effects *in vitro* at the Bragg peak (at the level of the tumor) and *in vivo* in subcutaneous tumors implanted in small animals. The post accelerating protons up to 70 MeV (Phase II) will allow measuring biological effects at low linear transfer, upstream of the Bragg peak (before the tumor) and thus to study the effects of radiation on healthy tissues crossed during treatments. In addition, this power increase will work *in vivo* orthotropic tumors.

rpPET Beamline

rpPET is a joined collaboration between IPHC and the Paul Strauss Centre [2] which started in 2015 for a period of 36 months. It consists in studying the relationship between the physical dose and biological effects in a proton therapy in mice by Positron Emission Tomography.

The rpPET beamline is entirely located inside the casemate and is composed of collimators, Faraday cups and of a steerer.

ISBN 978-3-95450-167-0

THE DIPOLE SWITCHER MAGNET

A dipole magnet manufactured by ACSI is located at one of the exits of CYRCé and allows 2 extraction beamlines with a deflection of +/- 22 degrees: one for rpPET and one for PRECy. It is used as a combination magnet to accept the various extracted energies (and entrance angles) and also acts as a switching magnet to bend the beam down either of the two beamlines. Typical operating values are ~0.75 T for the field and around 120 A for the current.

BEAM PARAMETERS

Beamline Requirements for PRECy

The beamline must fulfill the following conditions:

- The particle used by the system is the proton,
- The intensity available must be from 0,01 pA to 100 nA,
- The energy deposited must be constant (< 1%),
- The irradiation should be performed over a surface of 10 to 20 mm diameter, and must be homogeneous in depth,
- Passive modulated proton beams system,
- Irradiations can be done vertically.

CYRCé parameters

To design and define the optical elements mandatory to provide an efficient beam through this beamline, the proton beam delivered from the cyclotron has to be clearly characterized. Table 1 presents the physical parameters of the beam extracted from the cyclotron.

Table 1: CYRCé Beam Parameters

Parameter	Value
Particle	H^+
Intensity (μA)	10^4 pps – 400
Max energy (MeV)	24.4
Momentum (MeV/c)	218.033517
γ-1	0.026644717
β	0.226346713
Bρ (T.m)	0.727281529
Time Structure	CW (85 MHz RF)
Beam profile	Gaussian

At this point, no clear information was given concerning the emittances and their uncertainties. Therefore, measurements were necessary to estimate them.

EMITTANCE MEASUREMENTS

The determination of the beam transverse emittances can be performed by different methods [3]. A first attempt was done by Degiovanni et al. [4] using Gafchromic™ EBT3 films. Another method, the quad scan technique, uses the combination of quadrupole(s) together with profilers.

Experimental Setup

It consisted of a doublet of quadrupoles (QA-QB) and 2 profilers (DIAG 1-2) (Fig. 2). Measurements were performed for protons at kinetic energies of 18 MeV and 25 MeV and at intensity of few tens of nano amperes.

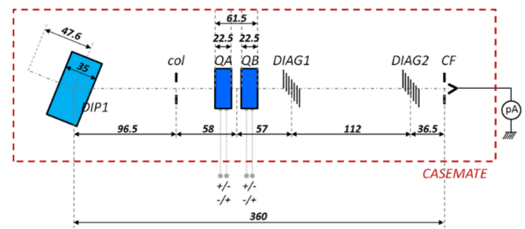

Figure 2: The quad scan setup (distances are in cm).

Results

Some of the measured beam profiles presented multiple peak structures and/or were out of axis according to the intensity applied to the quadrupoles. The fitting process of the data was done considering only the single peak curves. Corrections were applied to the ones being out of axis. An overall estimation for the emittances at a proton energy of 25 MeV gave (rms) ε_x = 1.90 ± 0.25 π mm.mrad and ε_y= 3.71 ± 1.35 π mm.mrad. Multiple peak structures were observed in a greater number at 18 MeV which made the estimation of the emittances difficult at such energy (Fig. 3). These structures were always present in the horizontal plane.

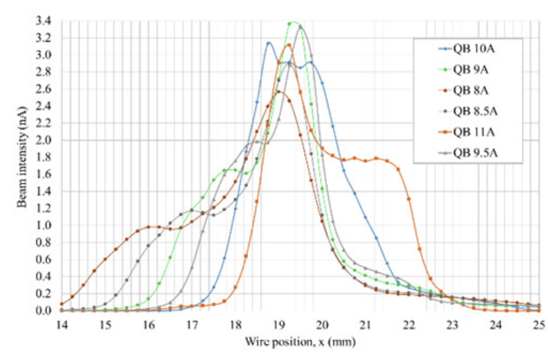

Figure 3: Beam profile at 18 MeV.

Discussions

These multiple peak structures could come from two causes: two different dipole and foil settings were used for the different DIAG positions and measurements in the horizontal plane may not be precise due to re-centering. Also, more than one proton energy could actually be extracted from the cyclotron due to foil positions and the extraction angles. To investigate further the phenomenon, simulations of the beam envelopes were performed. Three different cases were simulated and combined: a proton beam of 25 MeV (case 1), of 24.75 MeV and being horizontally off axis of – 3 mrad (case 2) and of 25.25 MeV and being horizontally off axis of + 3 mrad (case 3).

ISBN 978-3-95450-167-0

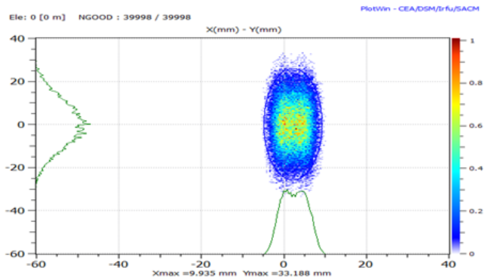

Figure 4: Multiple peak structure simulated.

The combination of the different cases confirmed the formation of a multiple peak structure and a shift of the beam profiles (Fig. 4). Other types of emittance measurements are foreseen in September 2016, using slits.

BEAMLINE DESIGN

Several configurations are possible once the beam exits the casemate: it can either be split using a switching dipole or reach the different experimental stations by a 'fishbone' layout (Fig. 5).

Figure 5: Possible layouts of the beamlines.

The use of a switching dipole after the casemate has been retained as it eases any other experimental station and beamline to be setup without adding a dipole each time. A 5-exit switching dipole is under discussion here.

Beam Optics

Preliminary simulations of the beamline were performed using the values given by [4] for the emittances (Table 2).

Table 2: Beam Parameters for Simulations

Parameter	Value
Emittances, ε_x / ε_y (4rms)	17 / 5 π mm mrad
Beam divergence, Δx / Δy	1.4 / 0.4 mrad
Beam size, σ_x / σ_y	3.03 / 3.12 mm
Dp/p (rms)	1 %

The two conditions set up on the transport codes were: beam waist at the diagnostics positions and position/angular achromaticity at the second dipole. Trace-Win [5] and COSY Infinity [6] showed similar results. According to the codes, beam sizes of less than 20 mm can be achieved at the casemate wall using either a doublet or a triplet. Field gradients of the quadrupoles do not exceed 5.13; 4.38 T/m (QP1; QP2) when using the doublet and 2.4;1.71;1.77 T/m (QP1; QP2; QP3) when using the triplet configuration. The use of a doublet seems to be sufficient to manage the beam inside the casemate.

Equipment

The main objective of the beamline is to ensure the good quality of the proton beam before it reaches the experimental room. While obtaining more accurate values concerning the transverse emittances to refine the beam transport simulations, a list of equipment that will compose the first section of the beamline was established (Fig. 6). The main constraints when designing the beamline is to leave at least one-meter gap somewhere to allow maintenance operations to take place when necessary.

Beam manipulation devices

- Quadrupoles. It is foreseen to use new magnetic quadrupoles in the casemate to ensure good quality and avoid maintenance issues near the cyclotron during operation periods. Quadrupoles to be used will have magnetic length of about 225 mm and aperture of 30 mm. These characteristics are subject to slightly change according to the emittances that still to be confirmed and/or updated.

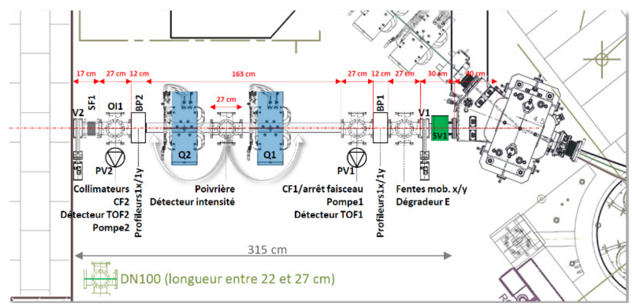

Figure 6: Elements composing the beamline. Q1/Q2: quadrupole 1/2. SV1: steerer.

- Steerer. The extraction process of the beam from the cyclotron can induce off axis beam propagations. Therefore, a steerer is necessary to ensure the good alignment of the beam before it reaches the optical devices.
- Other devices will be positioned on the beamline to impact the protons such as degraders, collimators or/and slits to shape the beam before it enters the focusing system or the wall pipe. Between four and five cross boxes will implement the beamline for these purposes.

Beam diagnostics Profilers will be positioned before and after the quadrupoles to check the good alignment of the beam. In case of misalignment the steerer will correct its position. Faraday cups will measure or stop the beam in case of emergency. TOF detectors (Pepperpot) would also be added along the beamline.

ACKNOWLEDGMENT

The PRECy project is supported by the *Contrat de Projet Etat-Région* (CPER) Alsace Champagne-Ardenne Lorraine 2015-2020.

ISBN 978-3-95450-167-0

REFERENCES

[1] D. Brasse, P. Marchand, A. Ouadi, and M. Pellicioli, Cyrcé, un cyclotron pour la recherche et l'enseignement en Alsace, *L'Actualité Chimique,* 2014, 386, pp. 9-14.

[2] Paul Strauss Centre, `http://www.centre-paul-strauss.fr`

[3] M. G. Minty and F. Zimmermann, "Measurement and Control of Charged Particle Beams", *Springer-Verlag Berlin and Heidelberg GmbH & Co. K* (21 May 2003), ISBN 978-3-662-08581-3, p. 364.

[4] A. Degiovanni *et al.*, "Emittance measurements at the Strasbourg TR24 cyclotron for the addition of a 65 MeV linac booster", in *Proc. Cyclotrons'13,* Vancouver, Canada, Sep. 2013, pp. 329-331.

[5] TraceWin, `http://irfu.cea.fr/Sacm/logiciels/index3.php`

[6] COSY Infinity, `http://www.bt.pa.msu.edu/index_cosy.htm`

ISBN 978-3-95450-167-0

STATUS OF THE DC-280 CYCLOTRON PROJECT

G.G. Gulbekian, S.N. Dmitriev, Yu.Ts. Oganessian, B.N. Gikal, I.V. Kalagin†, S.L. Bogomolov, I.A.Ivanenko, N.Yu.Kazarinov, G.N. Ivanov, N.F.Osipov,
Joint Institute for Nuclear Research, FLNR, Dubna, Moscow Region, Russia

Abstract

The current status of the project of the DC-280 cyclotron is presented. The DC-280 will be the basic facility of the Super Heavy Element Factory which is being created at the FLNR JINR. The main parts of the DC-280 are already made. In according to FLNR plans the cyclotron has to be assembled in the period from 2016 to 2017. The cyclotron commissioning will be in the end of 2017.

INTRODUCTION

The DC-280 cyclotron designed at the Flerov Laboratory of Nuclear Reaction of the Joint Institute for Nuclear Research in Dubna (FLNR, JINR, Dubna) is intended for carrying out fundamental and applied investigations with ions from He to U (masses from A = 2 up to 238) produced by ECR sources. The DC-280 will be the basic facility of the Super Heavy Element Factory (SHEF) that is being created at the FLNR. The energy of the ions extracted from the cyclotron may vary from 4 up to 8 MeV/amu. The expected ion beam intensity at DC-280 extraction is 10 pμA for ions with masses up to 50 [1]. The main parameters of the DC-280 cyclotron specified in Table 1.

Table 1: Main Parameters of the DC-280

Parameter	Value
Injecting beam potential	Up to 100 kV
Pole diameter	4 m
A/Z range of accelerated ions	4-7.5
Magnetic field	0.6-1.35 T
K factor	280
Gap between plugs	400 mm
Valley/hill gap	500/208 mm/mm
Magnet weight	1100 t
Magnet power	300 kW
Dee voltage	2x130 kV
RF power consumption	2x30 kW
Flat-top dee voltage	2x13 kV
Flat-top power consumption	2x2 kW
Beam orbit separation	10-16 mm
Radial beam bunch size	3 mm
Electrostatic deflector length	1300 mm
Electrostatic deflector voltage	80 kV
Magnetic channel length	900 mm
Magnetic channel gradient	4.6-8.4 T/m
Efficiency of beam transfer	>50%
Total accelerating potential	up to ~ 40 MV

† kalagin@jinr.ru

The DC-280 (Fig. 1) will be equipped with high voltage injection system. The system will consist of two high voltage (HV) platforms with ECR sources. The injection has to provide effective ion transportation from the ECR-ion source to the cyclotron center [2]. To produce required ions, two types of ECR ion sources will be created at the FLNR: the DECRIS-PM source with permanent magnets [3] and a superconducting ECR one.

The DC-280 will be the isochronous cyclotron with four pairs of focusing sectors. For ion acceleration, two main 40° dees and two flat-top 20°dees will be used [4]. The expected beam parameters are listed in Table 2.

Table 2: Expected Beam Parameters of the DC-280

Ion	Ion energy [MeV/amu]	Intensity [pps]
^{7}Li	4	1×10^{14}
^{18}O	8	1×10^{14}
^{40}Ar	5	1×10^{14}
^{48}Ca	5	6×10^{13}
^{54}Cr	5	2×10^{13}
^{58}Fe	5	1×10^{13}
^{84,86}Kr	5	2×10^{12}
^{136}Xe	5	1×10^{12}
^{238}U	7	5×10^{10}

Figure 1: Layout of the DC-280 in the SHEF building (see Fig. 2).

The cyclotron ion beam extraction system the will be equipped with an electrostatic deflector and a passive focusing magnetic channel (Table 1).

To transport accelerated ion beams to experimental setups five beam lines will be utilized. All the beam lines will have the common switching magnet. The experimental hall will be divided into three separated parts that have to be radiation shielded. The total experimental area will be about 1000 m^2 [5].

ISBN 978-3-95450-167-0

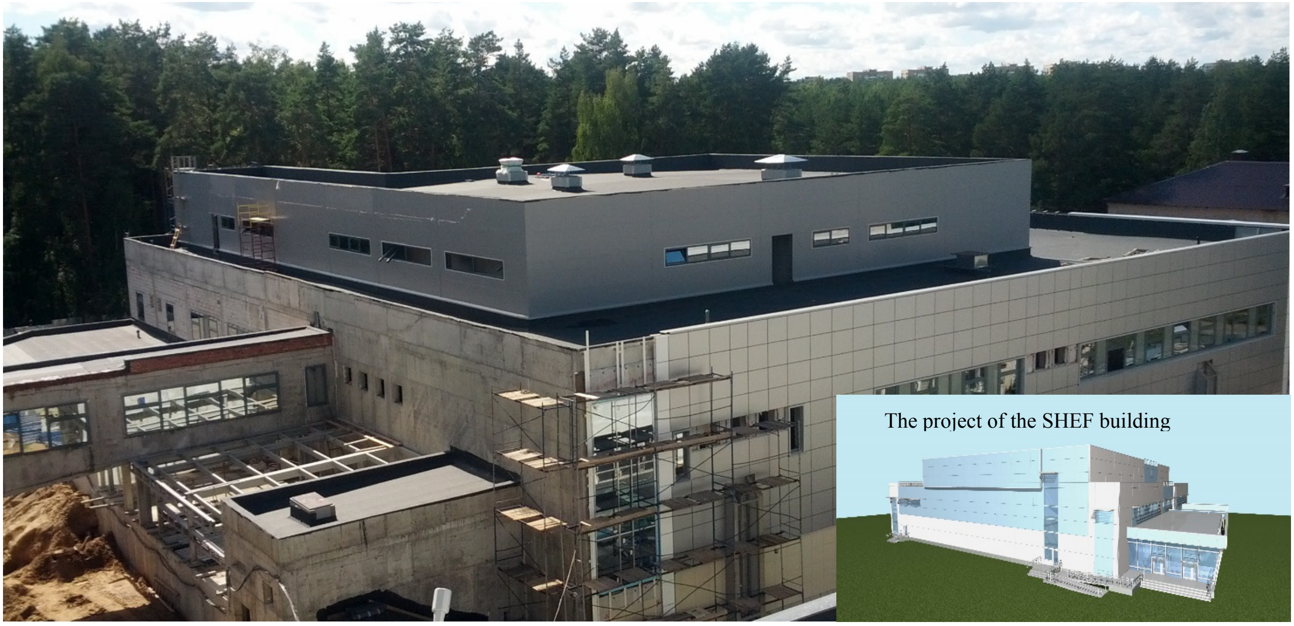

Figure 2: The SHEF building under construction at the Flerov Laboratory. August 2016.

STATUS OF DC-280 SYSTEMS

The main parts of the cyclotron, such as the main magnet with the vacuum chamber, the RF resonators, the dees and the beam transport lines have been manufactured and ready to be assembled. Other cyclotron parts are in manufacturing process and have to be supplied before the mid of 2017.

Main Magnet

The main magnet (Fig. 3) with the vacuum chamber has been manufactured at the "NKMZ" plant, Ukraine. Now we are preparing to the magnet assembling in the SHEF building. The power supply for the magnet has been made by the EVPU, Slovakia.

Figure 3: The main magnet of the DC-280 at plant.

RF Resonators, Dees and generators

The RF resonators (Fig. 4) with shafts have been manufactured at the "ZAVKOM" plant, Tambov, Russia. The main dees (Fig. 5) have been made at the EVPU, Slovakia. The flat-top dees are being manufactured at the JINR. The RF generators have been made by the QEI Corporation, NJ, USA.

Figure 4: The RF resonator.

Figure 5: Copper dees at the EVPU.

Main Coils, Trimming Coils Quadrupoles

The main magnet coils have been manufactured at the "N&V" firm, Romania. The block of radial trimming coils have been produced by the EVPU. The blocks of azimuthal trimming coils (Fig. 6) have been made at the GKMP, Bryansk, Russia.

Figure 6: The blocks of azimuthal trimming coils.

Axial Injection

At the first stage, we are creating only one HV planform with the DECRIS-PM ion source. The HV platform will be manufactured and tested at the FLNR. The DECRIS-PM magnetic system has been produced by "ITT-Group", Moscow, Russia (Fig. 7). The ion source will be assembled and tested at the FLNR. The beam focusing solenoids and the analyzing magnet (AM) of the injection channel are being manufactured at the EVPU. The 75 kV acceleraton tube was supplied by the "NEC" company, USA. All vacuum elements of the channel, such as vacuum lines, the AM vacuum chamber, diagnostic boxes, the Einzel lens, the electrostatic bender and the polyharmonic buncher have been made at the "Vacuum Praha" firm, Czech Republic.

Figure 7: The DECRIS-PM magnetic system.

Beam Transport Channels

The magnetic beam focusing elements (quadrupole lenses, steering magnets) have been manufactured by the "N&V". The switching magnet with a vacuum chamber (Fig. 8) has been manufactured at the "NKMZ".Vacuum elements of the channels have been made at the "Vacuum Praha".

Figure 8: The switching magnet.

Beam Extraction System and Diagnostics

The electrostatic deflector will be produced at the JINR. The focusing magnetic channel and beam diagnostics such as Faraday cups, profilometers, current probes have been produced at the Institute for Nuclear Research of the Academy of Science, Bulgaria.

Auxiliary Systems

Vacuum pumps and other components have been supplied by "Vacuum Praha". The vacuum pumping system will be created at the FLNR. The water cooling system is being created at the FLNR.

CONCLUSION

The main parts of the DC-280 have been manufactured. In according to FLNR plans the main magnet of the cyclotron has to be assembled in the end of 2016. Other systems will be mounted in 2017. The DC-280 commissioning will be in the end of 2017.

REFERENCES

[1] G. Gulbekyan, B. Gikal, S. N. Dmitriev, S. L. Bogomolov, O. N. Borisov, I. A. Ivanenko, N. Yu.Kazarinov, V. I. Kazacha, I. V. Kalagin, N.F. Osipov, A. V Tikhomirov, and J. Franko, "Development of FLNR JINR Heavy Ion Accelerator Complex in the Next 7 Years. Project of New DC-280 Cyclotron", in *Proc. PAC'11*, San Sebastian, Spain, 2011, pp. 2700-2702.

[2] G.G. Gulbekian, B.N. Gikal, V.V. Bekhterev, S.L. Bogomolov, A.A. Efremov, I.A. Ivanenko, N.Yu. Kazarinov, I.V. Kalagin, V.N. Melnikov, N.F. Osipov, S.V. Prokhorov, A.V. Tikhomirov, and M.V. Khabarov, "The project of the HV axial injection for the DC-280 cyclotron at the JINR FLNR", in *Proc. RuPAC'14*, Obninsk, Russia, 2014, pp. 333-335.

[3] V. Bekhterev, S. Bogomolov, A. Efremov, and N. Konev "Development of the magnetic system for new DECRIS-PM ion source", *in Proc. ECRIS'14*, Nijniy Novgorod, Russia, 2014, p. 111-113.

[4] G. Gulbekian, B. Gikal, I. Ivanenko, and N. Kazarinov, "DC-280 cyclotron central region with independent flat-top system", in *Proc. IPAC'11*, San Sebastian, Spain, 2011, pp. 2703-2705.

[5] G.G. Gulbekyan, B.N. Gikal, G.N. Ivanov, I.V. Kalagin, V.I. Kazacha, N.Yu. Kazarinov, M.V. Khabarov, V.N. Melnikov, N.F. Osipov, A.V. Tikhomirov, and Y.G. Teterev, "The project of the beam transportation lines for the DC-280 cyclotron at the JINR FLNR", in *Proc. RuPAC'14*, 2014, Obninsk, Russia, pp. 336-338.

ISBN 978-3-95450-167-0

KURRI FFAG'S FUTURE PROJECT AS ADSR PROTON DRIVER

Y. Ishi*, Y. Kuriyama, Y. Mori, M. Sakamoto, T. Uesugi
Kyoto University Research Reactor Institute, Kumatori, Osaka, Japan

Abstract

The accelerator complex using FFAG synchrotrons at KURRI has been operated for the ADSR experiments connecting the 100 MeV proton beam line with the research reactor facility so called KUCA since 2009. Fruitful results have been produced for the reactor physics using various configurations of the nuclear fuel core and variations of the neutron production target. Since higher energy beams such as 300 – 500 MeV are desired for the further study of the ADSR system, we are investigating the energy upgrade possibility of the accelerator complex. One of the candidates is to construct a new FFAG ring which adopts continuous acceleration with fixed frequency (serpentine acceleration) outside of the existing.These higher energy beams can be used for neutron or muon production experiments as well as ADSR study.

INTRODUCTION

An Accelerator Driven Sub-critical Reactor (ADSR[1]) is a hybrid system which is composed of a nuclear reactor facility and an accelerator facility.It sustains a nuclear fission chain reaction induced by a large amount of spallation neutron obtained by irradiation of a heavy metal target using high energy proton beams generated by accelerators. The nuclear reactor plays the role of neutron booster which amplifies the neutron flux from the target.

These days, especially after the severe nuclear accident in Fukushima Japan, the ADSR is paid attention not only as an energy production facility but as a device which transmutes long-lived radioactive materials such as the minor actinide (MA) to other materials whose lifetimes are much shorter than the original ones [1]. In the nuclear fuel cycle, MAs can be processed in a fast breeder. But in terms of the stability of the critical operation, the fraction of the MAs in the fuel system is limited as a few percent. On the other hand, in the ADSR, MA can be loaded up to some 30 % because the fuel system is operated as sub-critical.

At the Kyoto University Research Reactor Institute (KURRI), basic experimental studies about the ADSR have been started since 2009 using a one of research reactors Kyoto University Critical Assembly (KUCA) [2]. In these studies, the KUCA has been operated in the sub-critical mode and FFAG accelerators has been used as a proton driver. In this report, an overview of the FFAG accelerator complex, a current status of the usage of beams and discussion of possible upgrades of it will be presented.

* ishi@rri.kyoto-u.ac.jp
[1] Sometimes it is also referred as ADS which stands simply for Accelerator Driven System.

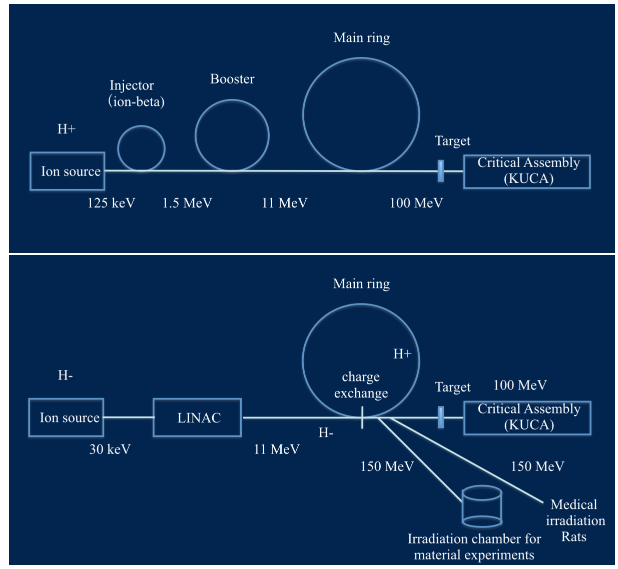

Figure 1: The schematic diagram of the FFAG Accelerator Complex. The upper is the original configuration, the lower is the upgraded one. The injector system composed of the Injector (ion-beta) and the Booster has been replaced by the H^- linac.

OVERVIEW OF THE FFAG ACCELERATOR COMPLEX AT KURRI

The schematic diagram of the KURRI-FFAG accelerator complex is shown in Fig. 1. The complex used to have 3 FFAG rings: the ion-beta, the booster and the main ring. All three rings adopt an FFAG focusing scheme [3]. However, the original injector system, which was composed of the ion-beta and the booster has been replaced by the 11 MeV H^- linac in order to increase the beam intensity. Table 1 shows the basic parameters of the complex. Figure 2 is an overview of the complex. The main ring has 2 extraction energies: 100 MeV for the ADSR experiments and 150MeV for other irradiation experiments.

The new injector system consists of 3 linacs RFQ, DTL1 and DTL2. It was adopted as an injector of the ERIT ring [4]. The injection beam line is shown in Fig. 3. The H^- beams are injected into the FFAG main ring through a charge stripping foil made of carbon. In this injection scheme, no pulse device is used. Even orbit merging magnets are not necessary because the H^- beams are merged into the circulating beam inside the main magnet of the main ring as shown in Fig. 4. The beam current extracted from the main ring has been increased by a factor of 10 because of this replacement.

ISBN 978-3-95450-167-0

Table 1: The Basic Parameters of KURRI-FFAG Accelerator Complex

Linac	
Repetition rate	<200 Hz
Peak current	<5 mA
Pulse length	< 100 µs (uniform)
Energy	11 MeV
Main ring	
Field index k	7.5
Magnetic field	1.6 T (max.)
Energy	11 - 100 or 150 MeV
Revolution frequency	1.6 - 6.2 MHz
Rf voltage	4 kV

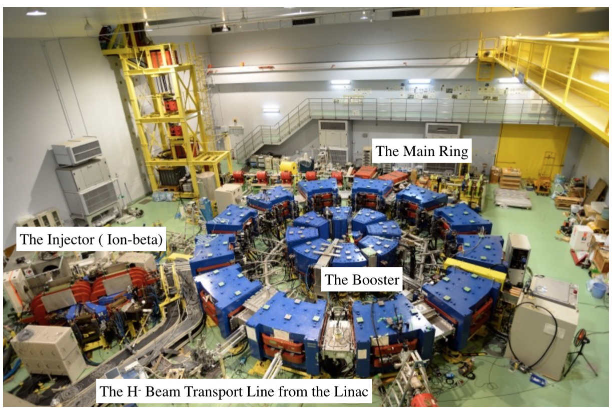

Figure 2: FFAG Accelerator Complex at KURRI.

USAGE OF BEAMS

The proton beams from the FFAG complex are delivered to users of various experiments: the ADSR experiments, the irradiation experiments for the materials and the biological experiments with irradiation to living animals (rats) for a basic study of BNCT [2]. Figure 5 shows the break down of the machine time for each user group. The machine time was measured as the integration of time when the beam was on.

[2] Stands for Boron Neutron Capture Therapy

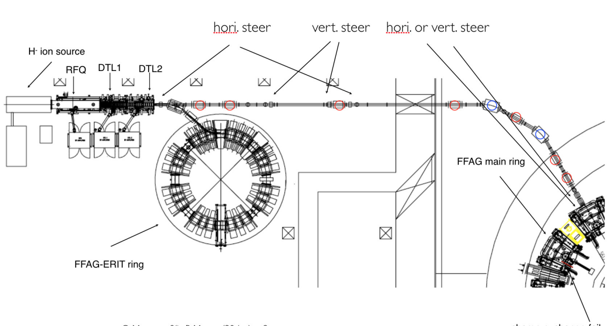

Figure 3: The H$^-$ beam transport line.

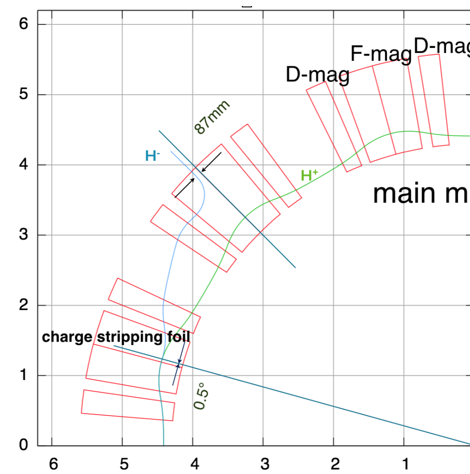

Figure 4: The H$^-$ beam injection using the charge stripping foil.

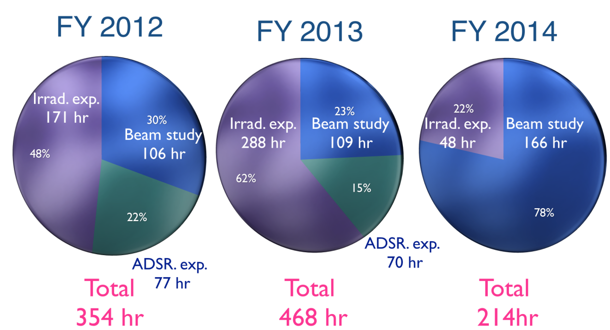

Figure 5: The machine time breakdown of KURRI-FFAG facility in recent 3 years.

For the ADSR experiments, the beam is transported from the accelerator facility to the sub-critical fuel system located at one of the core in the KUCA called “A-core” (Fig. 6). Two kinds of measurement are performed in the KUCA: dynamic characteristics measurements detecting prompt and delayed neutrons and static measurements of neutron energy spectrum or reaction rate distributions using radio-activation of the indium (In). The result of dynamic measurements from the first experiment in the world is shown in Fig. 7. There are 2 components in the neutron counting rate: the fast component decaying exponentially and the slow component caused by delayed neutrons almost constant in time. The presence of the delayed neutrons indicates that neutrons generated through nuclear fission chain reaction inside the fuel system. This series of ADSR experiments are ongoing since 2009 changing experimental conditions such as material of the neutron production target, configuration of the fuel system and beam intensity. The results from these experiments can be seen in the articles [5]- [9]

FUTURE PROJECT

In order to make the facility multi-capable, we are investigating two upgrade possibilities: (1) Increasing the beam

ISBN 978-3-95450-167-0

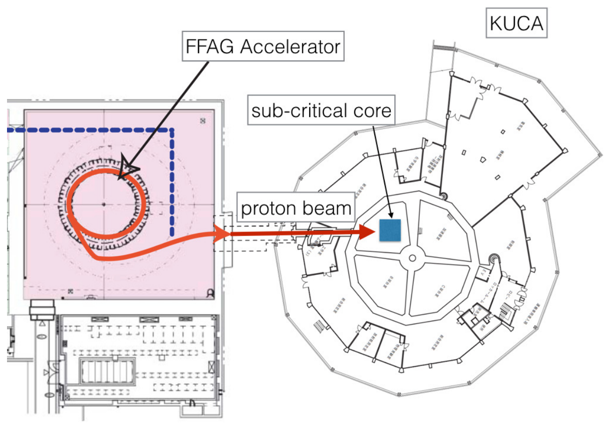

Figure 6: The connection between the FFAG accelerator complex and KUCA.

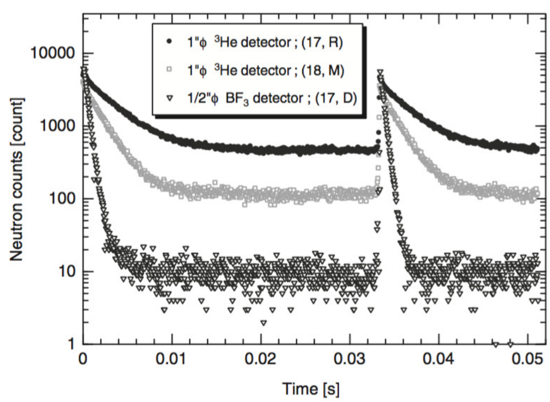

Figure 7: Measured prompt and delayed neutron behaviors obtained from different configurations of detectors.

current up to the order of μA by increasing the repetition rate at the order of 100 Hz. (2) Energy upgrade by adding a new ring outside the main ring.

Beam Stacking at High Energy Orbit

As a candidate of high intensity proton driver of spallation neutron source, potentially, an FFAG accelerator has advantage in terms of high repetition rate such as 100 - 1000 Hz. However, some users desire low spill rate (~10 Hz) for the experiments e. g. neutron radiography using TOF which needs to get rid of contamination from the pulse of different timing. FFAG rings can provide long interval pulse for users, while the machine operation itself is kept at high repetition rate by using rf stacking after acceleration [10]. This scheme reduces space charge effects at injection energy. For the machine, charge in each bunch can be reduced by high repetition rate. In the high energy region i. e. outer radius, accelerated beams are stacked and circulating around until necessary amount of charge is accumulated. For users, highly compressed beam with long time interval can be delivered.

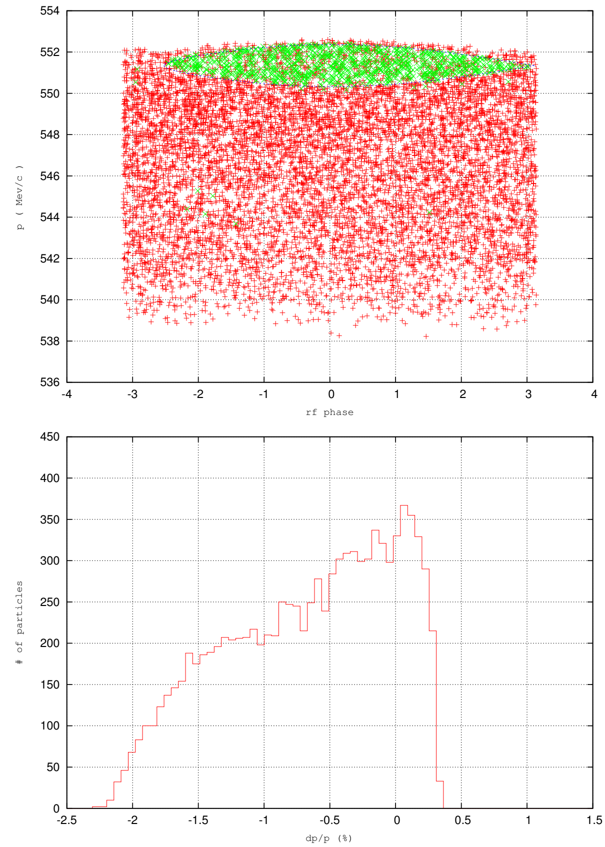

Figure 8: Results of the beam stacking simulation. The upper is the phase space plots from the stacking simulations with adiabatic landing and the lower is the momentum distribution after the beam stacking.

To confirm the feasibility of rf stacking at extraction energy, simulation studies have been carried out. Figure 8 shows the results from the stacking simulations. In the upper,a longitudinal phase space structure are shown. The vertical axis is the momentum and the horizontal one is the rf phase. The red points are stacked particle coasting around the extraction orbit, the green ones are accelerated particles landing on the extraction orbit and the blue lines are separatrices. In these simulations, the acceleration goes up to 150 MeV. While the landing process is going on, already stacked particles are slipping below the bucket in the phase space. Eventually, beams have been stacked below the extraction momentum. In the lower, momentum distribution is plotted. After first acceleration, full width of momentum spread is about 0.5%, the final momentum spread after 10 stacks is 2.5% of full width. This is much smaller then naive guess that is intrinsic momentum spread of each stacked beam multiplied by number of stacks i. e. 0.5 % ×10.

Although simulation studies showed that adiabatic landing, where the rf voltage is adiabatically reduced, is effective to suppress the momentum spread of the stacked beam, experimental study is necessary.

ISBN 978-3-95450-167-0

Table 2: Parameters of the 400 MeV FFAG Ring

Lattice	16-cell
Field index k	0.672
Energy	150 - 400 MeV
Average orbit radii	6.6 - 9.3 m
Magnetic field	1.3 T
Tune	(1.356, 2.248)

An Additional Ring

Number of neutrons produced through the nuclear spallation process strongly depends on the beam energy of the primary protons. If the beam energy is increased from 100 MeV to 400 MeV, the number of neutrons corresponding to single primary proton is increased by a factor of 20. Therefore, the energy upgrade of the accelerator facility is desired by the reactor physicists.

Fortunately, there is an enough space to build an additional higher energy ring outside the main ring. A basic design of the additional ring is being carried out. The layout of the complex with a newly designed 400 MeV FFAG ring is shown in Fig. 9. Basic parameters of the new ring are shown in Table 2. The ring consists of 16 cells. Beta functions for one cell are shown in Fig. 10.

The k is set to a rather small value of 0.672. This value of k makes a *serpentine acceleration* [11] possible. The longitudinal phase space structure in this acceleration scheme is shown in Fig. 11. Generally, the profits of this scheme are follows

- Since a fixed frequency is used, high electric field of the acceleration cavity is easily obtained.
- This makes a fast and continuous acceleration possible.
- The ERIT mechanism [12] can be applied to make secondary particles such as pions and their decay muons.

In the ordinary ERIT system as shown in Fig. 12, the ring is operated in a storage mode. However, in the extended ERIT system, the ring is in an acceleration mode. In this operation mode, since the beam hits the target at the maximum energy, the production efficiency of the secondary particles becomes high compared with the case of the storage mode.

SUMMARY

An FFAG accelerator complex for the ADSR study has been constructed at KURRI. The first ADSR experiment in the world has been done successfully in KUCA by using 100 MeV proton beam from the complex in 2009. Since then, fruitful results have been produced from these experiments. In order to increase the beam current, the original injector system composed of the ion-beta and the booster has been replaced by the H$^-$ linac. The beam current from the main ring has been increased by a factor of 10 by this replacement. Now the proton beams from the FFAG complex are used by the experiment in various fields such as the material science or the biological science as well as the reactor physics in KUCA.

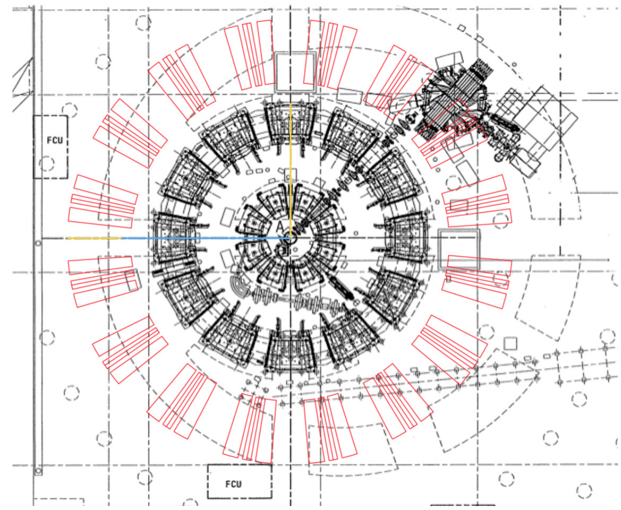

Figure 9: A layout of the complex with a newly designed 400 MeV FFAG ring, which surrounds the main ring.

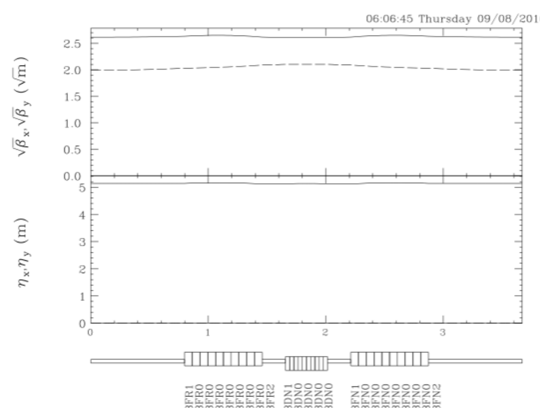

Figure 10: Beta functions for a basic cell of the 400 MeV FFAG ring.

Not only for higher performance in the ADSR experiments, but for the extension to the pulsed neutron source, a beam stacking at the high energy orbit is considered. In addition to the existing FFAG accelerators, a new 400 MeV FFAG ring is now under consideration for the energy upgrade of the complex. It adopts the serpentine acceleration to realize the extended ERIT mechanism, which can produce secondary particles such as pions and their decay muons efficiently.

ACKNOWLEDGMENTS

This work was supported by MEXT(the Ministry of Education, Culture, Sports, Science and Technology) of Japan in the framework of a task entitled "Research and Development for an Accelerator-Driven Sub-critical System Using an FFAG Accelerator".

ISBN 978-3-95450-167-0

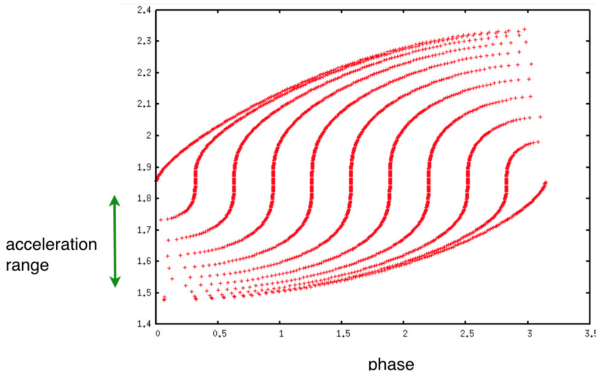

Figure 11: A phase space structure in the longitudinal direction for the serpentine acceleration.

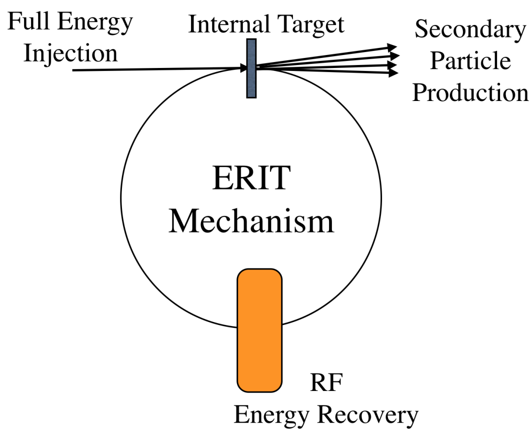

Figure 12: The ERIT mechanism to produce secondary particles.

REFERENCES

[1] K. Tsujimoto *et al.*, "Accelerator-Driven System for Transmutation of High-Level Waste" *Progress in Nuclear Energy*, vol. 37, p.339–344(2000).

[2] C. H. Pyeon *et al.*, "First Injection of Spallation Neutrons Generated by High-Energy Protons into the Kyoto University Critical Assembly" *J. Nucl. Sci. Technol.*, vol. 46, no. 12, p. 1091(2009).

[3] Y. Ishi *et al.*, "Present Status and Future of FFAGs at KURRI and the First ADSR Experiment", in *Proc. 1st International Particle Accelerator Conference (IPAC'10)*, Kyoto, Japan, May 23 2010, paper TUOCRA03, p. 1327–1329.

[4] T. Uesugi *et al.*, " FFAGs for the ERIT and ADS Project at KURRI ", in *Proc. 11th European Particle Accelerator Conference (EPAC'08)*, Genoa, Italy, June 2008, paper TUOBM04, p. 1013–1015.

[5] C. H. Pyeon *et al.*, *Ann. Nucl. Energy.*, vol. 38, p. 2298 (2011).

[6] C. H. Pyeon *et al.*, *Nucl. Sci. Eng.*, vol. 117, p. 156 (2014).

[7] C. H. Pyeon *et al.*, *Nucl. Eng. Technol.*, vol. 45, p. 81 (2013).

[8] A. Sakon *et al.*, *Nucl. Eng. Technol.*, vol. 50, p. 481 (2013).

[9] A. Sakon *et al.*, *Nucl. Eng. Technol.*, vol. 51, p. 116 (2014).

[10] Y. Ishi *et al.*, "Beam Stacking for High Intensity Pulsed Proton Beam with FFAG", in *Proc. 52th ICFA Advanced Beam Dynamics Workshop on High-Intensity and High-Brightness Hadron Beams (HB2012)*, Beijing, China, Sep. 17 2012, paper MOP210, p. 64–67.

[11] E. Yamakawa *et al.*, "Serpentine Acceleration in Zero-Chromatic FFAG Accelerators" *Nucl. Instr. Meth.*, PRA, vol. 716,p. 46–53 (2013).

[12] Y. Mori, *Nucl. Instr. Meth.*, A, vol. 536, p. 591(2006).

COMPACT SUPERCONDUCTING CYCLOTRON SC200 FOR PROTON THERAPY

Galina Karamysheva†, Semion Gurskiy, Oleg Karamyshev, Nikolay Morozov, Dmitriy Popov, Evgeny Samsonov, Grigori Shirkov, Stepan Shirkov, Grigoriy Trubnikov, JINR, Dubna, Russia
Yanfang Bi, Gen Chen, Yonghua Chen, Kaizhong Ding, Hansheng Feng, Junjun Li, Yuntao Song, Yahong Xie, Qingxi Yang, Jinxing Zheng, ASIPP, Hefei, China

Abstract

The SC200 superconducting cyclotron for hadron therapy is under development by collaboration of ASIPP (Hefei, China) and JINR (Dubna, Russia). Superconducting cyclotron SC200 will provide acceleration of protons up to 200 MeV with maximum beam current of 1 μA in 2017-2018. We plan to manufacture in China two cyclotrons: one will operate in Hefei cyclotron medical center the other will replace Phasotron in Medico-technical center JINR Dubna and will be used for cancer therapy by protons. Now we present results of simulation of magnetic, accelerating and extraction systems. The cyclotron is very compact and light, the estimate total weight is about 35 tons and extraction radius is 60 cm. We have performed simulations of all systems of the SC200 cyclotron and specified the main parameters of the accelerator. Average magnetic field of the cyclotron is up to 3.5 T and the particle revolution frequency is about 45 MHz, these parameters increases the requirements for the accuracy of all simulations.

INTRODUCTION

The Medico-technical complex (MTC) JINR annually treated at the proton beam more than 100 people. For treatment MTC uses proton beam with energy up to 200 MeV specializing mainly on treatment of head localizations.

The 200 MeV final energy has been chosen for SC200 cyclotron based on the experience of work of the MTC JINR and statistics for necessary depth of treatment provided by HIMAC (Japan) concerning the treated patients from 1995 to 2001 [1].

The proton beam with energy 200 MeV can irradiate all of the tumor localizations with a maximum depth of 25 cm. SC200 cyclotron will also be used for eye melanoma treatment at energies 60-70 MeV after degrading beam energy. Degrading the 200 MeV energy to 60-70 MeV would provide better beam quality compared to degrading from conventional energy 250 MeV.

Taking into account the fact, that the size and cost of the cyclotron are approximately determined by the maximum proton energy, it was decided to limit the maximum proton energy to 200 MeV.

SC200 is an isochronous superconducting compact cyclotron. Superconducting coils will be enclosed in cryostat, all other parts are warm. Internal ion source of PIG type will be used. It is a fixed field, fixed RF frequency and fixed 200 MeV extracted energy proton cyclotron. Extraction will be organized with an electrostatic deflector and magnetic channels. For proton acceleration we are planning to use 2 accelerating RF cavities, operating on the 2nd harmonic mode.

† gkaram@jinr.ru

MAGNET SYSTEM OF CYCLOTRON SC-200

The design of the SC200 magnetic system is described in details in [2]. Most accurate results of simulations were received in the parametrized model of the magnet (see Fig. 1) created in CST studio. Change of parameters automatically changes computer model. In addition, sector geometry can be replaced by importing from Matlab. Results of simulations are exporting to Matlab for analyzing by conventional CYCLOPS-like code or for particle acceleration in 3D fields. So we had powerful model to change quickly a number of parameters of the magnet in order to receive isochronous field with suitable betatron frequencies.

Figure 1: 3D meshed model of the magnet, central “plug” (steel cylinder connecting the sectors) is 4cm in diameter.

Isochronism of the average field was reached by decreasing of the sector width correspondently to orbital frequencies in closed orbits. Initially azimuth width of sector was equal 40 degrees. Azimuthal width of sector against radius which provide isochronous field is shown in Fig. 2. Maximal cut of the sector width will reach 18 mm. Orbital frequencies of the final average field (Fig. 3) are presented in Fig. 4. From Fig. 4 we can estimate that difference between mean field and isochronous is about 1-2 G in accelerating region. We would like to notice that all results were received with not very big number of mesh cells about 4 millions.

ISBN 978-3-95450-167-0

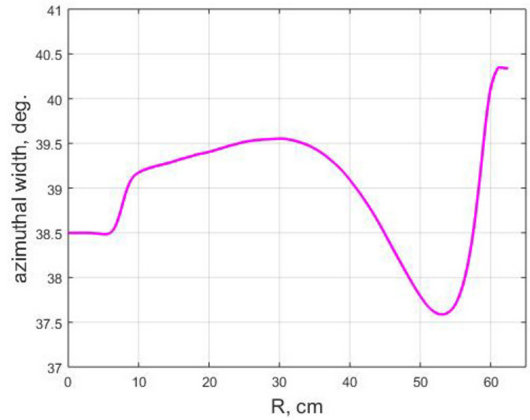

Figure 2: Azimuthal width of sector.

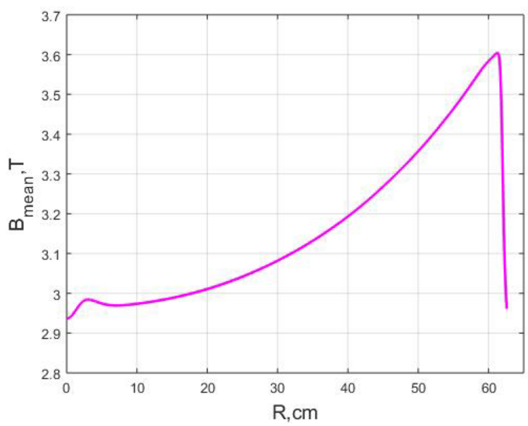

Figure 3: Average magnetic field along the radius.

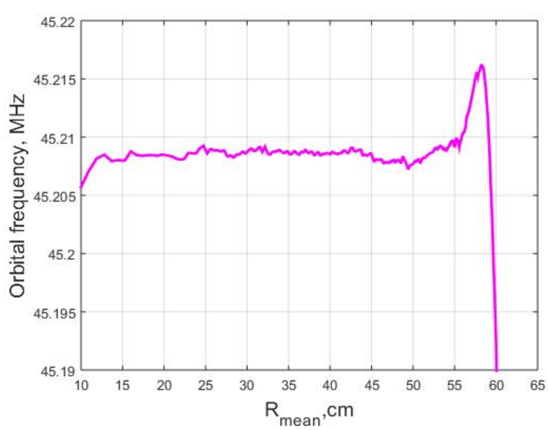

Figure 4: Orbital frequency against mean radius.

CYCLOPS-like code was used to calculate the betatron tunes. Betatron tunes are presented in Fig. 5.

As we are going to use just 2 RF cavities operating on 2nd harmonic mode, each 50 degrees in azimuthal length, the acceleration is going to be relatively week on each turn. So avoiding resonances is crucial for the design of the SC200 cyclotron.

Many efforts have been done to avoid the most dangerous resonances during acceleration 2Qz=1 and Qr-Qz=1. One can see that the first resonance is avoided completely while the second one is close at the end of acceleration. We are going to continue as well our efforts to avoid this resonance by changing magnet parameters at edge region while real shaping of the magnetic field.

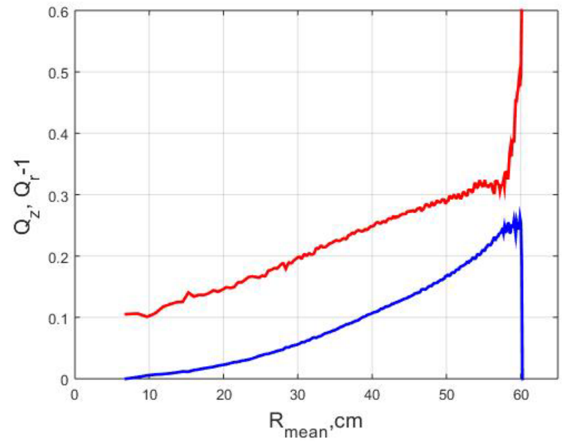

Figure 5: Vertical and radial betatron tunes in SC200.

RF SYSTEM

Two RF cavities, connected in the centre will be working on the 2nd harmonic on approximately 90MHz.

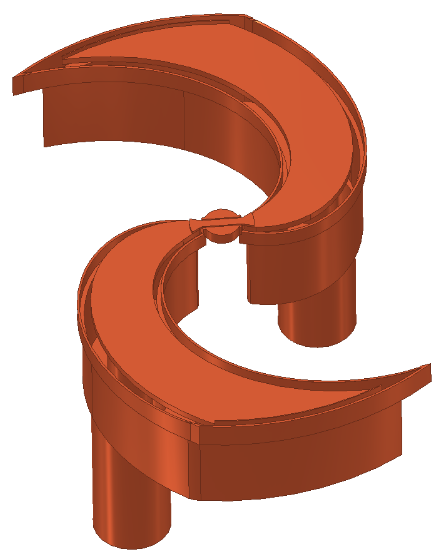

Figure 6: Overview of 3D model of RF system.

From the beam dynamics point of view the choice of 2nd harmonic is not the best solution, as the acceleration rate will be lower compared to 4th harmonic which seems like a natural choice for a cyclotron with 4 sector structure.

However, operating on 180 MHz would raise problems with the extraction of particles from the ion source and the generators on 180 MHz are not widely available as compared to 90 MHz ones. As we avoid all critical resonances and extraction scheme does not require high acceleration rate we are able to use just 2 cavities on the

ISBN 978-3-95450-167-0

2nd harmonic. Computer simulations of the cavity was performed (see model in Fig. 6) Suitable accelerating frequency and voltage along radius (Fig. 7) were achieved. Accelerating system is described more detailed in report [3] of this conference.

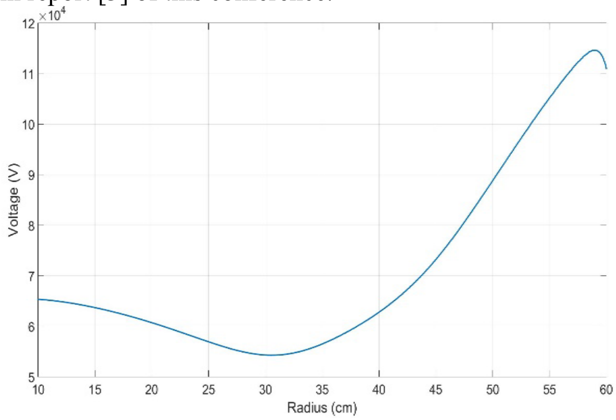

Figure 7: Mean acceleration voltage along radius.

CENTRAL REGION STUDIES

Internal PIG proton source will be used in our cyclotron, so our simulations start from the inside of the source. We have built a 3D model of the source and the central region. In order to increase the efficiency of the extraction of the protons from the source the first accelerating gap between the tip of the RF dee and the source should be kept as small as possible. However, sparking must be prevented, so we need to provide safe distance in both vertical and horizontal directions. The compact size of the accelerator is the major challenge in the design of the central region. The cylinder, connecting the sectors in the central region has to be as small as possible in diameter, so the magnetic field variation can start at the smaller radius to help with the vertical focusing, but also has to be big enough and close enough to the median plane to provide the area with the decreasing magnetic field (so-called “bump”).

We have chosen to use 60 kV in the central region, and in this case the major problem was to bypass the source on the first turn. In order to do so, we had to shape the dee tips in the centre in such way to provide optimal acceleration rate.

We have used our 3D model of the RF system and the magnet in order to simulate the particle trajectories in the central region. It is clear that focusing and the energy gain using are good enough. However, it is very important to keep in mind that the final design will be strongly affected by the changes in magnet model, when we will get the measured BH curve of the steel, that will be used in the SC200 magnet.

EXTRACTION

Simulations show that the extraction can be provided by deflector with electric field 160 kV/cm and two magnetic channels MC1 and MC2 focusing the beam in horizontal plane (see Fig. 8) [4].

No need of the channel to focus the beam in vertical plane. This is provided by drop of edge magnetic field. The collimator will be used to match the beam parameters with requirements imposed by a transport system.

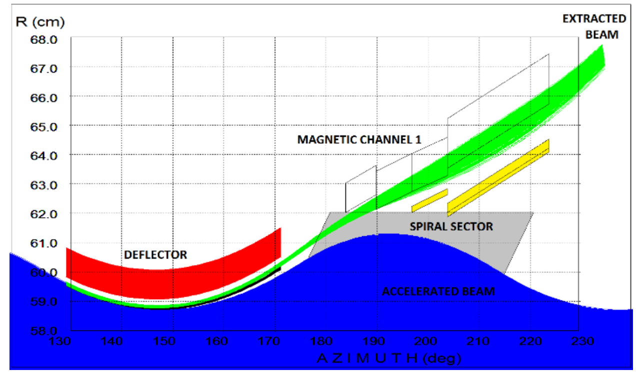

Figure 8: First part of the extraction system with deflector and MC1.

Extraction efficiency has been estimated for different changes of the septum thickness along its length and for different values of the beam radial oscillations during acceleration. Maximum attainable extraction efficiency ~75% is achieved if amplitude of radial oscillations does not exceed 2 mm and septum has constant thickness 0.1 mm.

CONCLUSION

Computer simulation of main systems of SC200 cyclotron has been performed. Simulations show that it is possible to have suitable magnetic field. Proper accelerating frequency and voltage along radius were achieved in computer simulations of the cavity. Extraction can be provided by deflector with electric field 160 kV/cm and two magnetic channels MC1 and MC2 focusing the beam in horizontal plane. The technical design of the cyclotron will be finished in 2016

REFERENCES

[1] Y. Hirao, “Results from HIMAC and other Therapy Facilities in Japan”, in *Proc. 16th Int. Conf. on Cyclotrons and their Applications*, *AIP Conference Proceedings*, 2001, vol. 600, issue 1, p. 8.

[2] G. Karamysheva *et al.*., “Magnetic System for SC200 Superconducting Cyclotron for Cyclotron Therapy”, presented at the 21st Int. Conf. on Cyclotrons and their Applications (Cyclotrons’16), Zurich, Switzerland, Sep. 2016, paper THP20, this conference.

[3] G. Chen *et al.*, “Preliminary Design of RF System for SC200 Superconducting Cyclotron”, presented at the 21st Int. Conf. on Cyclotrons and their Applications (Cyclotrons’16), Zurich, Switzerland, Sep. 2016, paper TUP17, this conference.

[4] K. Ding *et al.*., “Study of the Beam Extraction from Superconducting Cyclotron SC200”, presented at the 21st Int. Conf. on Cyclotrons and their Applications (Cyclotrons’16), Zurich, Switzerland, Sep. 2016, paper MOP14, this conference.

ISBN 978-3-95450-167-0

HIGH INTENSITY AND OTHER WORLD WIDE DEVELOPMENTS IN FFAG ACCELERATORS

S. L. Sheehy*, John Adams Institute for Accelerator Science, University of Oxford, UK

Abstract

Here I present an overview of developments in Fixed Field Alternating Gradient accelerators, focusing on high intensity hadron accelerator designs. I will detail progress in studies of space charge effects and simulation, experimental characterisation of a 150 MeV proton FFAG at KURRI in Japan, experimental optimisation of FFAGs and novel FFAG developments for future applications.

INTRODUCTION

Fixed field Alternating Gradient (FFAG) accelerators combine strong focusing optics like a synchrotron with a fixed magnetic field like a cyclotron. Unlike a synchrotron, the magnetic field experienced by the particles is designed to vary with radius, rather than time. In the original types of FFAG invented in the 1950's and '60's, the vertical component of the magnetic field B_y varies with radius R according to the 'scaling law' according to

$$B_y = B_0(\frac{R}{R_0})^k, \tag{1}$$

with field index k, reference radius R_0 and field at that radius B_0. In the radial sector FFAG the alternating gradient is achieved with opposite sign 'F' and 'D' magnets, whereas in the case of the spiral sector FFAG, the polarity does not change but a spiral angle is used to gain additional focusing.

A revival of interest since the 1990s has seen a number of FFAGs constructed, including scaling and linear non-scaling variants for protons [1, 2] and electrons [3] respectively. Since this time, the range of FFAG designs has rapidly diversified and there are now designs with non-linear field profiles and non-radial edge angles, racetrack shapes or super-periodic structures, dispersion suppression sections, vertical orbit movement and other innovations. While it would be impossible to give an exhaustive review of such developments here, I will highlight examples to direct the reader toward the general direction of travel in this constantly evolving field.

In recent years, the focus of the community has started to shift away from basic proof-of-principle designs and further toward designing FFAG accelerators for real world applications. This has led to a significant amount of novel development in the field, for example, through recent work towards recirculating FFAG arcs for the eRHIC project.

In the high intensity direction, work is underway to establish design principles for high intensity FFAG accelerators for applications including radioisotope production, neutron spallation sources and accelerator driven systems (ADS). This has highlighted the need to establish a better understanding of the limitations of these machines with high bunch charge. From 2013 an international collaboration between institutes in Japan, UK and USA has been formed to use an existing scaling proton FFAG accelerator at Kyoto University Research Reactor Institute (KURRI) in Japan to work toward exploring the high intensity regime in FFAG accelerators. Experimental campaigns have thus far been aimed at characterising this machine in detail. At the same time, a detailed simulation and code development programme is underway, highlighting the complexities of benchmarking observed FFAG dynamics to simulation models, particularly when imperfections exist in the machine.

Alongside this new direction, FFAG accelerators are considered to be a promising option for medical applications at lower intensity due to their capability of high repetition rate and variable energy extraction operation with no limitation on top energy. Detailed concepts of FFAGs for proton and ion therapy have now been developed taking into consideration the desire for proton tomography capability. As this field moves toward optimised accelerators with rapid variable energy extraction, the FFAG concept is particularly promising for beam-lines and gantries with large energy acceptance over the entire treatment range while maintaining a fixed magnetic field. This and other potential applications will be discussed in the latter section.

TOWARD HIGH INTENSITY

General Features of FFAGs for High Intensity

Fixed field accelerators which employ DC magnets lend themselves naturally to high power operation, as the repetition rate of the machine can be increased above the 50-60 Hz of rapid cycling synchrotrons up to 100 or 200 kHz, dependent only on the rf system. If the magnets are superconducting or permanent magnets, the energy efficiency may be improved over existing machines which employ rapidly ramped, resistive magnets.

In this regime, we have to differentiate between high power beams and high intensity beams. In a cycled machine such as a synchrotron, a beam with high power requires a very high intensity and very high peak current, whereas for a CW machine a very high power can be achieved with relatively low peak current. The peak current determines the space charge tune shift and the main beam dynamics issues to be addressed.

In the FFAG community ideas are being developed for CW cyclotron-like machines which maintain strong focusing to higher energies using edge angles and arbitrary field profile with radius [4–6]. Concepts which introduce additional degrees of freedom to the orbit shape or movement, such

* suzie.sheehy@physics.ox.ac.uk

ISBN 978-3-95450-167-0

a vertical orbit variation in order to achieve isochronous orbits [7], could also achieve CW operation.

Regardless of the choice of CW or high repetition rate machines for high power, there are a number of features of the FFAG which are relevant to operation in this regime. FFAG accelerators typically have a large momentum acceptance and a large dynamic aperture, with a larger horizontal aperture than vertical. This leads to some novel features such as the ability for the horizontal emittance to be made larger than the vertical to mitigate space-charge effects.

For example the vertical space charge tune shift is given by:

$$\Delta Q_v = -\frac{n_t r_p}{\pi \epsilon_v (1 + \sqrt{(\epsilon_h/\epsilon_v)}\beta^2\gamma^3} \frac{1}{B_f}. \tag{2}$$

Where n_t is the total number of particles in the accelerator and r_p is the classical proton radius, $\epsilon_{h,v}$ are the horizontal and vertical emittances and B_f is the bunching factor. If one can vary the horizontal to vertical emittance ratio and increase the repetition rate of a pulsed machine, one might conceivably increase the average power by a large factor without increasing the number of particles in the machine. For example increasing the $\sqrt{(\epsilon_h/\epsilon_v)}$ factor by 3 and changing the repetition rate from 25 Hz to 100 Hz would increase the average beam power of a 1 MW machine to 8 MW for the same bunch charge. It is then still possible to increase the injection energy to take advantage of the $\beta^2\gamma^3$ factor.

The flexibility of the FFAG is also an advantage. As the magnetic field is temporally fixed, the rf profile can be varied to manipulate the beam in a flexible way. Beam stacking at high energy may allow a flexible repetition rate for extraction of beams for neutron users, for example.

KURRI-FFAG Experimental Collaboration

With these potential capabilities in mind, an international collaboration was established in 2013 to use an existing proton FFAG at Kyoto University for beam studies, using the 'main ring' 150 MeV proton FFAG at KURRI, Japan. This has recently resulted in a comprehensive characterisation [8] including orbit matching, tune measurement, field index measurement, closed orbit distortion and correction, dispersion measurement and a measurement of energy loss due to the beam stripping foil. The main machine parameters are shown in Table 1 and the ring is shown in Figure 1.

Table 1: Parameters of the 150 MeV FFAG

Parameter	Value	
r_0	4.54	m
Cell structure	DFD	
N_{cells}	12	
k, field index	7.6	
Injection Energy	11	MeV
Extraction Energy	100 or 150	MeV
f_{rf}	1.6-5.2	MHz
B_{max}	1.6	T

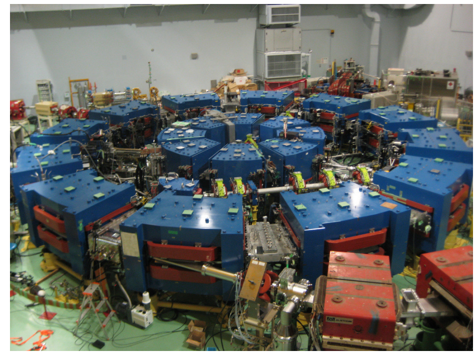

Figure 1: The KURRI 150 MeV FFAG is the larger ring shown here with the pre-2011 injector ring. H^- charge exchange injection from the linac occurs in the top left of the image.

Future goals of the collaboration are to work toward operational regimes which demonstrate high intensity capability. This includes experimental work with asymmetric emittance operation, dynamic aperture studies, proof of principle of beam stacking [9] at high energy and re-shaping of the bunch timing structure. In hardware terms, the addition of an extra rf cavity will reduce beam losses during rf capture and throughout the acceleration cycle.

Simulations and Space Charge

There are a range of simulation codes now available to model FFAG accelerators. The beam orbit in an FFAG moves radially with momentum, as in a cyclotron. Synchrotron simulation codes which assume a central orbit independent of momentum are unsuitable for studying FFAGs as they do not reproduce the correct dynamics. A few codes which remove the constraint of the existence of the central orbit were selected to perform benchmarking, including OPAL, Zgoubi, SCODE, MAUS and EARLIETIMES, although others exist [10]. The detailed benchmarking of these codes against each other for basic dynamics and with space charge effects is ongoing [11]. An example of code benchmarking for the betatron tunes in the KURRI 150 MeV FFAG are shown in Fig.2. Note that a discrepancy exists between these benchmarked simulation results and real experimental results which is due to magnetic field imperfections. This has led to new ideas of how to correct FFAG dynamics in the presence of imperfectly scaling magnetic fields [12].

Of these codes, OPAL [13] incorporates a highly sophisticated 3D space charge solver, and has recently been updated to include variable frequency acceleration capability essential for modelling non-CW FFAGs.

Frozen model space charge effects are included in SCODE and have also now been included in one of the most frequently used tracking codes for FFAGs, called 'ZGOUBI'. [14].

ISBN 978-3-95450-167-0

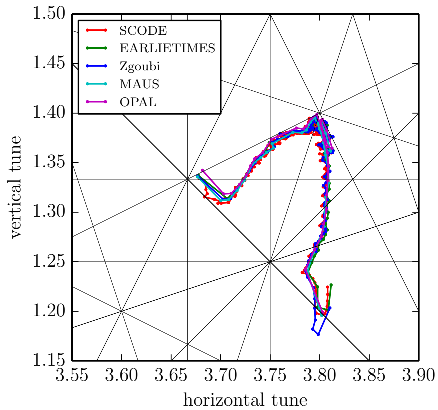

Figure 2: Benchmarking of simulation codes for betatron tunes in the KURRI-FFAG.

DESIGN STUDIES FOR HIGH POWER APPLICATIONS

Design Studies for Future Neutron Spallation Sources

In recent years, proton beam powers for neutron spallation sources have surpassed the 1 MW level. Future sources are expected to provide ever higher power beams with low losses, low energy consumption, low capital cost and with greater flexibility than current machines. In the UK, preliminary design studies are underway for a future neutron source in 15-20 years time. Two options are being considered at present; a rapid cycling synchrotron and an FFAG.

The main FFAG options being considered are the so-called 'pumplet' model [15] which uses five magnets per cell to achieve stable tunes and a new innovation called the 'DF Spiral FFAG' [16]. In this 1.2 GeV design a small negative field is introduced on one side of the main spiral magnet of a spiral FFAG. This increases the field flutter effect as in a cyclotron to overcome a limitation of regular spiral FFAGs which have relatively weak focusing in the vertical plane. It also introduces a new variable - the ratio between the F and D magnets - which can provide further control over dynamics.

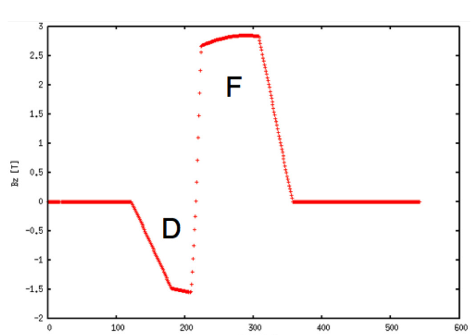

Figure 3: The vertical component of magnetic field experienced by a particle traversing a sector of the DF-Spiral FFAG.

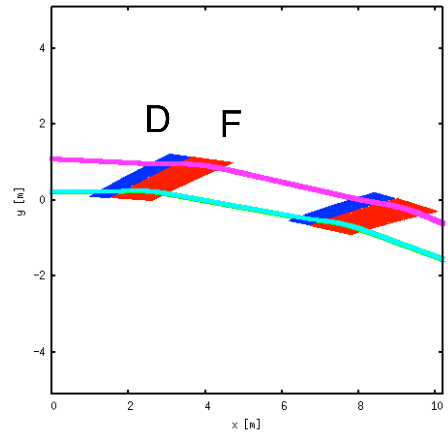

Figure 4: Layout of two cells of the DF-Spiral FFAG.

This design has the advantage of a long straight section of around 5 m for injection and extraction, however this long straight has some dispersion. The impact of dispersion in regions of injection, extraction, rf acceleration and collimation must be considered.

Perhaps the most unconventional idea for these machines is to use direct proton injection with a tilted septum to paint in 4D transverse phase space, rather than H^- charge exchange injection. This technique is currently under study, which will simplify the injection chicane and reduce issues of multiple scattering, thermal and lifetime effects associated with high power beams on stripping foils. Encouraging initial results show that a zero-loss system could be possible with up to 350 turns accumulated at injection for a spallation source type ring [17].

Design Studies for ADS

For the application to accelerator driven systems (ADS), a very high average beam power of 10 MW or higher is required in CW mode, which translates to an average beam current of around 10 mA. To achieve this, a number of proposals for fixed frequency rf FFAGs exist [18].

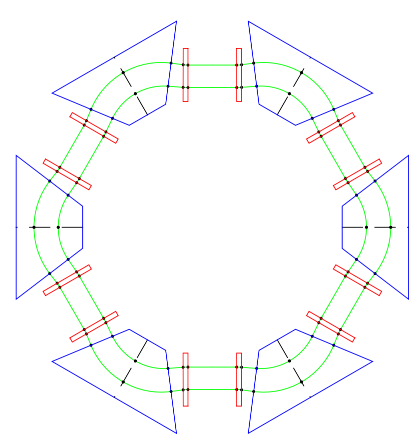

Figure 5: An example of a 6-sector 1 GeV FFAG design for ADS.

Johnstone et al., have developed designs in which the orbit at each momentum can be made proportional to velocity in order to achieve isochronicity and at the same time the betatron tune can be controlled through both edge and weak focusing [4–6]. This is in contrast to a classical cyclotron where the main field is predominately the dipole field, which has limitations in adapting the path length to velocity into the relativistic regime.

An initial simulation campaign showed promising beam stability at 10 mA. Further work remains to achieve isochronicity better than ±1%, full space charge simulation with acceleration and demonstration of sufficient turn separation at extraction. Initial engineering concepts for the main magnets and a superconducting rf solution exist.

Design Studies for Muon Transmutation

One future application of high intensity particle beams is the transmutation of long lived fission products (LLFP) through muon capture. A novel design incorporating energy recovery with an internal target is now under detailed study, which could produce 10^{16} negative muons from a 2.5 mA proton beam with fixed frequency radio-frequency system for re-acceleration [19, 20]. Muons are produced through interactions with an internal target. This idea builds on the successful demonstration machine ERIT (Energy Recovery Internal Target) [21] at KURRI, Japan, shown in Fig. 6.

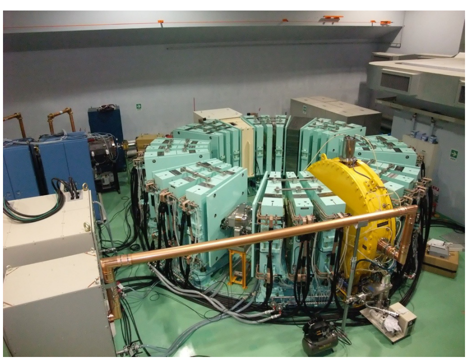

Figure 6: The ERIT accelerator at Kyoto University Research Reactor Institute, Japan.

Radioisotope production

Compact high current FFAGs may also be applied to radio-isotope production. One such design is the Proton Isotope Production (PIP) design [22] shown in Fig.7. This is a cyclotron-like FFAG being studied for proton energies up to 26 MeV for the production of radioisotopes, in particular ^{99m}Tc. The magnetic field varies from 0.99 to 1.03 T up to a 1.5 m radius and the gradient is optimised with the magnet geometry to stabilise the tunes and enhance beam focusing whilst maintaining isochronicity. The use of a thin internal target and recycled beam is being investigated as it could greatly improve production efficiency. At present, simulations with a 20 mA beam in OPAL show good transmission through the acceleration cycle of over 98%. Further studies into radial injection are ongoing.

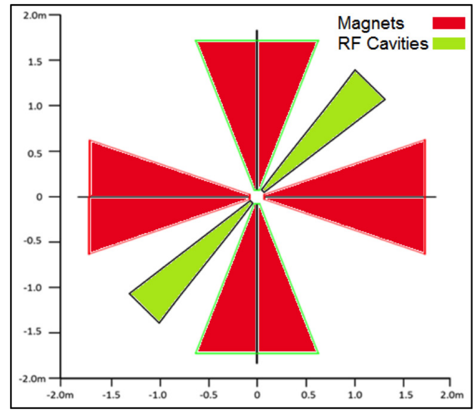

Figure 7: A view of the PIP ring. The internal target would be located in one long gap between sectors.

OTHER DESIGN STUDIES AND INNOVATIONS

Medical Applications

Developments continue for the design of medical FFAG accelerators. The PAMELA (Particle Accelerator for MEdicaL Applications) design study reduced the aperture size by implementing the second stability region of the equations of motion [23]. This was taken as the starting point for a normal-conducting proton accelerator up to 330 MeV for proton tomography as part of the NORMA design study [24]. This further study included an extension to a racetrack design, detailed parameter scans of the working point and dynamic aperture.

Continued work on non-scaling arbitrary field FFAG designs now includes a concept for ions including Helium and Carbon from 70/90 to 430 MeV/u [25, 26]. The design is based on a racetrack configuration which allows long straight sections, where an extraction system based on a bipolar field is located. While this has not yet been demonstrated in an operating machine, it would allow a fast variable energy extraction system with no degrader. The design is near to isochronous for CW operation, which leads to a large cyclotron-like radial aperture for both the magnets and rf system.

One of the most promising applications for FFAG optics in the medical field is in the treatment gantries. The FFAG concept is able to support a fast variation in beam energy to scan depth-wise during treatment without the need to adjust the field strength. Recent work in this direction includes a lightweight permanent magnet gantry for proton therapy and a compact superconducting gantry for ion therapy [27]. A novel type of asymmetric Halbach magnet has been designed and prototyped for this application.

Other Applications

It is worth noting that there has been a lot of recent development in the lepton non-scaling FFAG field as part of the eRHIC project, where one proposal is to use FFAG arcs for the energy recovery recirculating linac design. This reduces

ISBN 978-3-95450-167-0

the number of required arcs as multiple energies can travel through a single FFAG arc, but does lead to the requirement of matching and correction with multiple simultaneous orbits. This has led to innovations in adiabatic matching techniques to adjust optical parameters smoothly between FFAG arcs and straight sections [28], novel permanent magnet designs [29], modelling of synchrotron radiation in FFAG arcs as well as detailed beam dynamics calculations.

Continued developments are also seen in particle physics applications such as the NuPIL (Neutrinos from PIon beamLine) [30] design and for the generation of neutrino beams in nuSTORM [31] facility to provide a muon beam for precision neutrino physics, where long straight sections and matching sections are well developed for scaling FFAGs.

DISCUSSION

The FFAG idea is often considered a completely different class of accelerator, but in reality it is just a generalised fixed field accelerator. It should be noted that in cyclotrons, reverse magnetic fields are now being incorporated into next generation high power designs. As FFAG designs continue to evolve, some are heading toward CW mode operation like a strong focusing version of a cyclotron, while others have a flexible structure and superperiods like a synchrotron. Particularly for high intensity and high power hadron designs, there is a good opportunity for the accelerator community to work together to share experience from operational high power cyclotrons and synchrotrons particularly in terms of hardware, injection and extraction systems where these are appropriate.

REFERENCES

[1] M. Aiba et al., Development of a FFAG Proton Synchrotron, in *Proceedings of EPAC2000*, Vienna, Austria, pp. 581–583.

[2] Y. Mori, Present Status of FFAG Proton Accelerators at KURRI, in *Proc. International Particle Accelerator Conference, IPAC'11*, San Sebastian, Spain, 2011, paper WEPS077, pp. 2685–2687.

[3] S. Machida et al., Acceleration in the Linear Non-Scaling Fixed-Field Alternating-Gradient Accelerator EMMA, Nat. Phys., vol. 8, no. 3, pp. 243?247, Jan. 2012.

[4] C. Johnstone et al., 1 GeV CW Nonscaling FFAG for ADS, and Magnet Parameters, in *Proc. International Particle Accelerator Conference, IPAC'12*, New Orleans, USA, 2012, paper THPPR063, pp. 4118–4120.

[5] C. Johnstone and M. Berz, Advances in Nonlinear Non-Scaling FFAGs, Int. J. Mod. Phys. A, vol. 26, no. 10 - 11, p. 1690, 2011.

[6] S. L. Sheehy et al., The potential for a high power FFAG proton driver for ADS, in *11th International Topical Meeting on Nuclear Applications of Accelerators, AccApp 2013*, Bruges, Belgium, 2013, pp. 261–265. `http://arxiv.org/abs/arXiv:1310.3588`.

[7] S. J. Brooks, Vertical Orbit Excursion FFAG Accelerators with Edge Focussing, in *Proc. International Particle Accelerator Conference, IPAC'12*, New Orleans, USA, 2012, paper MOPPD019, pp. 406–408.

[8] S. L. Sheehy, et al., Characterization techniques for fixed-field alternating gradient accelerators and beam studies using the KURRI 150 MeV proton FFAG, Prog. Theor. Exp. Phys. 7 (2016), 073G01.

[9] Y. Ishi et al., Beam stacking for high intensity pulsed proton beam with FFAG, in *Proceedings of HB2012*, Beijing, China, paper MOP210, pp. 64–66.

[10] M. K. Craddock and Y.-N. Rao, Cyclotron and FFAG studies using cyclotron codes, in *Proceedings of Cyclotrons and their Applications*, 2010, p. THA1CCO04.

[11] S. L. Sheehy et al., Progress on Simulation of Fixed Field Alternating Gradient Accelerators, in *Proc. International Particle Accelerator Conference, IPAC'15*, Richmond, VA, USA, 2015, paper MOPJE077, pp. 495–497.

[12] M. H. Tahar, Tune compensation in Fixed Field Alternating Gradient accelerators, in *FFAG Workshop 2016*, London, Sept., 2016.

[13] A. Adelmann, et al., The OPAL (Object Oriented Parallel Accelerator Library) Framework, PSI-PR-08-02, 2008-2015, `https://amas.psi.ch/OPAL`.

[14] M. H. Tahar, Space charge developments in Zgoubi, application to KURRI FFAG lattice studies, in *FFAG Workshop 2016*, London, Sept., 2016.

[15] G. H. Rees, Non-isochronous and isochronous, non- scaling, FFAG designs, in *Proceedings of the 18th International Conference on Cyclotrons and their Applications*, Sicily, 2007, paper MOP1197, pp.189–192.

[16] S. Machida, Design of a proton driver for neutron/muon production, in *FFAG Workshop 2016*, London, Sept., 2016.

[17] C. R. Prior, Studies of High Intensity Proton FFAGs at RAL, in *Proceedings of HB2016*, Malmo, Sweden, paper WEAM6X01, pp. 379–384.

[18] L. Calabretta and F. Méot, Cyclotrons and FFAG Accelerators as Drivers for ADS, Rev. Accel. Sci. Tech. 8 (2015), 77-97.

[19] Y. Mori, Muon nuclear transmutation project for nuclear waste, in *FFAG Workshop 2016*, London, Sept., 2016.

[20] Y. Mori, Nucl. Instr. Meth., PRS, A563(2006) 591-595.

[21] K. Okabe, Y. Mori, M. Muto, An Intense Neutron Source with Emittance Recovery Internal Target (ERIT) using Ionisation Cooling, in *Proceedings of EPAC'08*, Genoa, Italy, 2008, paper THPP067, pp. 3512?3514.

[22] D. Bruton et al., A compact and high current FFAG for the production of radioisotopes for medical application, in *Proc. International Particle Accelerator Conference, IPAC'16*, Busan, Korea, 2016. paper TUPOY023, pp. 1957–1959.

[23] K. J. Peach, et al., Conceptual design of a nonscaling fixed field alternating gradient accelerator for protons and carbon ions for charged particle therapy, Phys. Rev. ST Accel. Beams, vol. 16, no. 3, p. 030101, Mar. 2013.

[24] S. Tygier, et al., The PyZgoubi framework and the simulation of dynamic aperture in fixed-field alternating-gradient accelerators, Nucl. Instrum. Meth. A, 775, pp. 15-26, 2014.

[25] J. Taylor, HEATHER ? HElium ion Accelerator for radioTHERapy, in *FFAG Workshop 2016*, London, Sept., 2016.

[26] C. Johnstone, Compact CW nonscaling FFAGs for medical applications, in *FFAG Workshop 2016*, London, Sept., 2016.

ISBN 978-3-95450-167-0

[27] D. Trbojevic, FFAG gantries, in *FFAG Workshop 2016*, London, Sept., 2016.

[28] D. Trbojevic et al., NS-FFAG for electron-ion collider in RHIC (eRHIC), in *Proceedings of PAC2013*, Pasadena, CA USA paper TUPBA13, pp. 553–555.

[29] Generalised Halbach Magnets a Non-Scaling FFAG Arc, in *FFAG Workshop, FFAG'16*, London, UK, 2016.

[30] J. B. Lagrange et al., FFAG Beam Line for NuPIL - Neutrinos from a Pion Beam Line, in *Proc. International Particle Accelerator Conference, IPAC'16*, Busan, Korea, 2016. paper THPMB054, pp. 3372–3374.

[31] J. B. Lagrange et al., NUSTORM FFAG Decay Ring, in *Proc. International Particle Accelerator Conference, IPAC'16*, Busan, Korea, 2016. paper THPMB053, pp. 3369–3371.

ISBN 978-3-95450-167-0

HEAT TRANSFER STUDIES OF THE IRANCYC-10 MAGNET AND ITS EFFECTS ON THE ISOCHRONOUS MAGNETIC FIELD

S. Sabounchi†, H. Afarideh, R. Solhju, F. Zakerhosseini,
Energy Engineering and Physics Department, Amirkabir University of Technology, Tehran, Iran
M. Ghergherehchi,
School of Information and Communication Engineering, Sungkyunkwan University, Suwon, Korea

Abstract

In magnets for cyclotron, one of the prominent problems is difference between simulation and feasible operations. By considering more factors in simulation these difference can be reduced. Thermal effect and heat transfer is one phenomenon which can change favourite features of the magnets. IRANCYC-10 is a compact AVF cyclotron which is in manufacturing phase at AmirKabir University of Technology. In IRANCYC-10 heat transfer studies have been done for RF cavity, RF transmission line and PIG ion source. In this paper, accurate simulation of heat transfer and magnetic field have been done. Also thermal effects on isochronous magnetic field for IRANCYC-10 is investigated. For heat transfer and CFD simulations, Ansys CFX and for magnetic simulation Opera 3D Tosca have been used. The initiate magnet ampere-turn in simulation is 45201 and water mass flow rate for magnet system is considered 53 lit/min.

INTRODUCTION

IRANCYC- 10 is a 10 MeV cyclotron for accelerating of H^- in FDG production which is under manufacturing phase at AmirKabir University of technology [1] IRANCYC-10 exclusively has been designed for FDG production in hospital. Heat transfer and thermal analysis has been done for RF cavity, RF transmission line and PIG ion source [2], [3] and [4] in IRANCYC-10. In this project heat transfer and temperature raise for coil of the IRANCYC-10 has been simulated. As one of the main parts of this machine, AVF magnet have been designed by opera 3D Tosca. AISI 1010 is used for this magnet [5]. In Table 1 and Figure 1 relevant parameters of the magnet and magnetic field mapping can be seen.

Table 1: Relevant Parameters

Parameter	Value
Pole radius	45 cm
Maximum Magnetic field in main plan	1.78 T
Initiate Ampere turn	45201
Number of coil pancakes	18
Material of the coil	OFHC Copper (C 10100)

This magnet had been designed by Opera 3D Tosca and it was optimized as much as possible. On the other hand there is always difference between simulation and feasible problems and this difference create time-consuming tuning of the machine. One of the major reasons for the discrepancy between the simulation and operation in magnet of the cyclotrons, is temperature raise of the coils. In operation when the coil start to heat and raise temperature in fact it can effect OFHC copper conductivity. So other parameters of the magnet can change and isochronous field will be effected. Heat transfer study and optimized cooling system is essential in order to reduce inconsistency between magnetic field and isochronous field. In these coils it is almost impossible to eliminate the heat effects on the magnets even with the cooling system so it should be diminished and compensated if it is significant. This study is useful in cyclotron tuning phase.

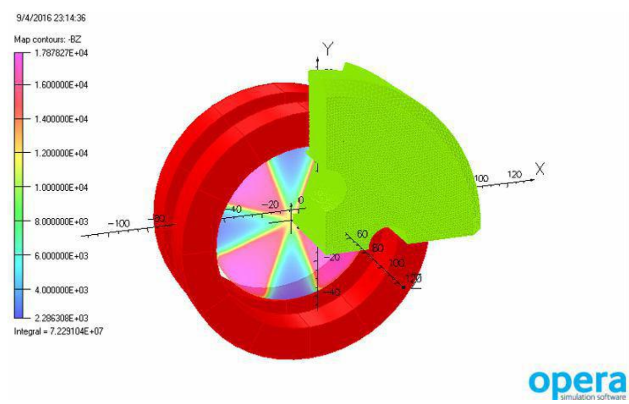

Figure 1: Magnetic field mapping.

COOLING CHARACTERISTICS

The coil of IRANCYC- 10 made of 18 pancakes in Figure 2 one pancake is shown. The main reason is less pressure drop of the cooling water. In this coil like other conventional coils in AVF cyclotrons, hollow conductors has been used. The dimension of this hollow conductor is rectangle (10*10 mm) and its hollow is circle (5.7 mm diameter). In order to avoid erosion and other mechanical problems in OFHC copper, the maximum velocity of the water should be less than 2.43 m/s [6]. So the maximum mass flow rate of each hollow conductor can be calculated by Eq. (1):

$$\dot{m} = \rho \times V \times A \ . \tag{1}$$

ISBN 978-3-95450-167-0

In Eq. (1) $\dot{m}$ is mass flow rate (Kg/s), ρ is density (Kg/m^3), V is velocity of the water (m/s) and A is the cross section area of the cooling line (m^2). In this cooling line the diameter of the hollow is 5.7 mm so the maximum mass flow rate should be less than 62 gr/s.

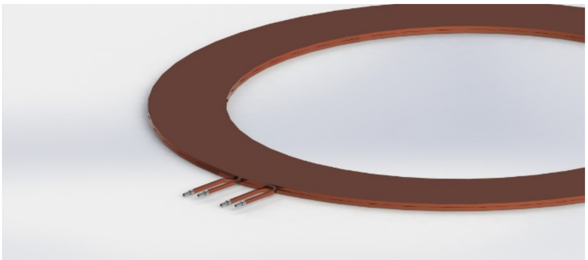

Figure 2: Pancake of coil.

For heat generation in a hollow conductor, Resistance of one hollow conductor extracted from basic equation (Eq. (2)). Total Heat generation for one hollow conductor by considering the safety factor of 1.33 is resulted 500 w. This safety factor can compensate other parameters which were not considered.

$$R = \rho \frac{L}{A} \tag{2}$$

In Eq. (2), ρ is resistivity, L length of the conductor and A is cross section area of the conductor. Also the cooling water is deionized and resistivity of the water will be checking during the operation. The resistivity of the cooling water will stay more than 3 $M\,\Omega.cm$ for all parts which need cooling water in IRANCYC-10 [7].

CFD GEOMETRY

As one of the most accurate codes for CFD simulations, Ansys CFX has been used for heat transfer simulation. For CFD simulations in coil of the IRANCYC- 10 all parts modelled by SolidWorks and all joints considered as perfect connection which does not make a difference in simulation. Also the exact geometry of the coil in too complex for CFD simulation and it is almost impossible to converge the residual during the calculations in order to extract accurate values. The geometry of the coil is Symmetric in term of heat transfer. So for Ansys CFX, an equivalent geometry in term of heat transfer has been designed for CFD simulation. In Figure 3 this geometry can be seen. This geometry contained one hollow conductor in a pancake and by reducing the volume of the calculations, the accuracy of the CFD simulation became significant. Also the number of contacts reduced to just two contacts, upper surface of circle hallow and bottom side. In these contacts, OFHC copper appointed as contact body and deionized water as a target body.

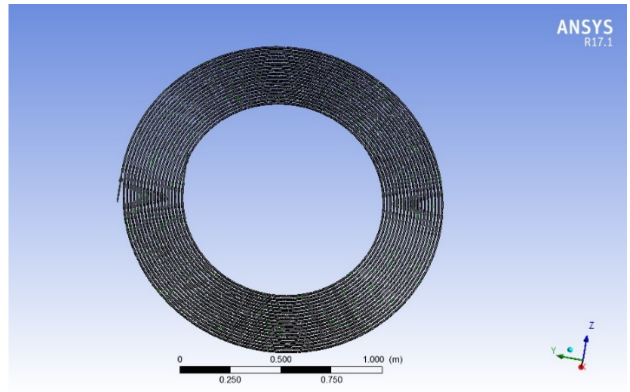

Figure 3: Geometry for CFD simulation.

CFD MESHING

In this simulation although efforts have been made to make the geometry simpler by designing the equivalent shape, it was still challenge to make meshing with high quality. Twisted shape and sharp edges are the main reason for difficulty in meshing. Tetrahedral patch conforming which is usually used for complex geometries did not resulted to high quality meshing. The method of sweep has been used for meshing in this simulation. Sweep is more effective in term of aspect ratio and skewness but some geometries are not sweep able. Meshing with significant quality has been created by optimized parameters. In Table 2 meshing statistics for fluid domain has been shown.

Table 2: Meshing Statistics

Parameter	Value
Maximum Skewness	0.6
Maximum Aspect Ratio	8.24
Total number of Elements	3966782
Total Number of Nodes	5010720
Element Size	7e-4 m

In Ansys CFX solver the aspect ratio for the fluid domain should be less than 50 in order to good convergence and accuracy of the simulation. Also parameter of skewness is crucial in mesh quality. In Figure 4, relation between skewness and mesh quality has been shown. As it can be seen from table 2, maximum aspect ratio and skewness in fluid domain is 8.24 and 0.6 which is incredibly suitable for this geometry [8].

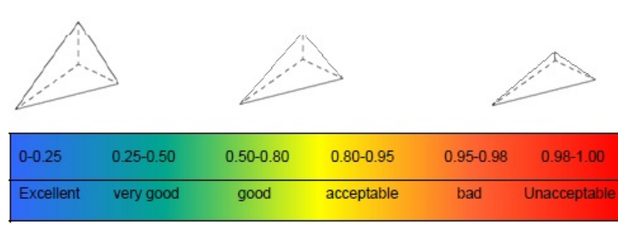

Figure 4: Skewness and mesh quality.

ISBN 978-3-95450-167-0

CFD SIMULATION

After high quality meshing, Ansys CFX has been tuned for precise simulation. In this simulation two domain has been defined OFHC copper and cooling water. Copper domain, a subdomain has been considered for heat generation. In this problem, heat generation is completely uniform in OFHC copper so it was applied as total source energy. In fluid domain water considered as continuous fluid and for turbulence model Shear Stress Transport has been applied. This model is combination of k-omega and k-epsilon in different regions. In eddy diffusivity for turbulent flux closure for heat transfer, value of 0.85 has been appointed as prandtl number. At inlet mass flow rate considered 24.5 gr/s and in outlet, average static pressure appointed with zero. Initial temperature of water and copper has been set as 293 kelvin.

By high resolution advection scheme, high resolution turbulence numeric and RMS of 10e-4 convergence has been achieved. In Figure 5, temperature distribution of the one pancake can be seen.

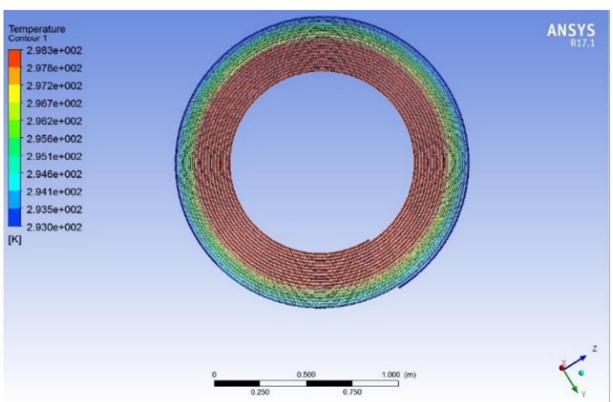

Figure 5: Temperature distribution.

MAGNETIC FIELD CHANGES

As it can be seen the maximum temperature raise in coil is 5.3 kelvin. Even this range of temperature raise can effect on the isochronous magnetic field. The main reason of this phenomenon is changing of the conductivity and ampere- turn in magnet. In this coil after consider the temperature raise the ampere- turn changed to 44622.

In Figure 6, two magnetic fields before and after the temperature raise can be seen. The red curve is field which is fitted to isochronous field without temperature effect and after considering heat transfer blue curve has been resulted. It can be seen that the maximum difference is 50 G.

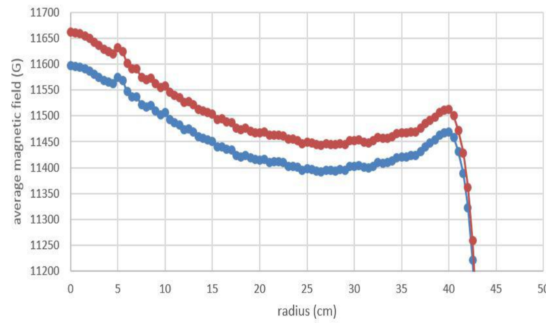

Figure 6: Temperature effect on magnetic field.

CONCLUSION

This study can be useful at tuning phase of IRANCYC-10. In fact it can provide the better simulation and diminish the inconsistency between feasible and simulation. In Table 3 final results is shown. For 22 pancakes total mass flow rate is 53 lit/ min has been considered

Table 3: Final Results

Parameter	Value
Maximum Temperature Change	5.3 °C
Ampere-turns Change	580 Ampere-turns
Difference from Isochronous Magnetic Field	50 G

REFERENCES

[1] DMCA, http://camp.aut.ac.ir/

[2] S. Saboonchi, H. Afarideh, M.R. Asadi, M. Ghergherehchi , and J.S. Chai, "Heat transfer study and cooling of 10 MeV cyclotron", in *Proc. Cyclotrons`13*, Vancouver, BC, Canada, Sep. 2013, paper TU2PB03, pp. 150-152.

[3] S.Sabounchi, M.Mohamadian, M.Salehi, H.Afarideh, M.Ghergherehchi, and J.S.Chai, "Cooling and Heat Transfer of the IRANCYC-10 Transmission Line", in *Proc. IPAC`16*, Busan, Korea, May 2016, paper TUPMR015, pp. 1259-1261.

[4] F. Zakerhosseini, S. Sabounchi, H. Afarideh, J. Chai, and M. Ghergherehchi, **"**Heat transfer study of PIG ion source for 10 MeV cyclotron", in *Proc. IPAC'16*, Busan, Korea, May 2016, paper TUPMR013, pp. 1256-1258.

[5] R.Solhju, *et al.,* "Design of a 10 MeV Cyclotron Accelerator", *Iranian Journal of Physics Research*, vol 15, no 2, May 2016. pp. 225-234

[6] The copper development association Inc. https://www.copper.org/applications/plumbing/techcorner/designing_piping_systems.html

[7] E. Swetin, M. Kirshenbaum, and C. Putnam, "Cooling Water Systems for Accelerator Components at the Advanced Photon Source", *2nd International Workshop on Mechanical Engineering Design of Synchrotron Radiation Equipment and Instrumentation (MEDSI02)*, September 2002 – Advanced Photon Source, Argonne National Laboratory, Argonne, Illinois, USA, pp. 445-453.

[8] Ansys Meshing Application Introduction, Appendix A, Mesh quality, April 2009, pp. 5-10.

ISBN 978-3-95450-167-0

RECIRCULATING ELECTRON BEAM PHOTO-CONVERTER FOR RARE ISOTOPE PRODUCTION*

A. Laxdal†, R.A. Baartman, I. Bylinskii, F.W. Jones, T. Planche‡, A. Sen,
TRIUMF, Vancouver, BC, Canada
S. Ganesh, Waterloo University, Canada

Abstract

The TRIUMF 50 MeV electron linac has the potential to drive cw beams of up to 0.5 MW to the ARIEL photo-fission facility for rare isotope science. Due to the cooling requirements, the use of a thick Bremsstrahlung target for electron to photon conversion is a difficult technical challenge in this intensity regime. Here we present a different concept in which electrons are injected into a small storage ring where they make multiple passes through a thin internal photo-conversion target, eventually depositing their remaining energy in a central core absorber which can be independently cooled. We discuss design requirements and propose a set of design parameters for the Fixed Field Alternating Gradient (FFAG) ring. Using particle simulation models, we estimate various beam properties, and electron loss control.

INTRODUCTION

In 1999 W.T. Diamond published a paper [1] stressing the possibility of producing high yields of neutron-rich radioactive ions, using a high power electron beam from an e-linac as the driver accelerator for a Radioactive Ion Beam (RIB) facility. The electron beam could be scanned over a large area of a high Z Bremsstrahlung-production target. This would significantly reduce the power density on the Bremsstrahlung-production target and on the isotope-production target. A big advantage is that, such a facility would come at low cost, compared with other beam accelerators.

As a result during the following decade a couple of laboratories around the world tried to capitalize on this idea. At Flerov Laboratory of Nuclear Reactions, Joint Institute for Nuclear Research in Dubna, Russia, a 50 MeV compact accelerator of the microtron type MT-25 [2] was built and the first experimental results were published in 2002 [3]. From IPN Orsay, in France, the results of the ALTO facility [4] based on a linear accelerator at 50 MeV were published in 2008. Both facilities chose a low power regime of operation of 500 W of electron beam power. ARIEL (the Advanced Rare IsotopE Laboratory) started at TRIUMF in 2010, first with the e-linac design, fabrication and installation. This first phase was complete in 2014, followed by the start-up of the electron target station design, and other concomitant projects and accelerator energy upgrades. The challenging aspect of ARIEL is to design and build a target station capable of dissipating up to 500 kW (50 MeV, 10 mA) of electron beam power.

In this paper we name the Bremsstrahlung production target, the converter and the isotope production target, the target.

Figure 1 shows experiment results from Dubna [3]. This graph shows that only the photons at energy around 10-20 MeV induce fission reactions by exciting the Giant Dipole Resonance (GDR) of the ^{238}U nucleus. The overlapping area on Figure 1 of the GDR and the γ-quanta spectrum contains the photons of interest. The power carried by photons with energies above 3 MeV will cause thermal loads onto the converter and target. Since this is an intrinsic property of the production of photonuclear reactions, it cannot be reduced without lowering the production of radioisotopes in the target.

The low energy photons undergo photoelectric absorption (between 1 keV and 1.5 MeV) and Rayleigh scattering (below 100 keV) depositing their energy in matter. On the high-energy side, photons contribute to Compton scattering (significant up to 10 MeV) and pair production (starting at 1.022 MeV and growing for increasing photon energies), which impacts the heating up of the converter and the target, without producing any fission reactions.

An ideal configuration would have only the intrinsic power of the produced Bremsstrahlung brought to interaction with the target, with neither charged particles (electrons and positrons) nor low energy photons reaching the target.

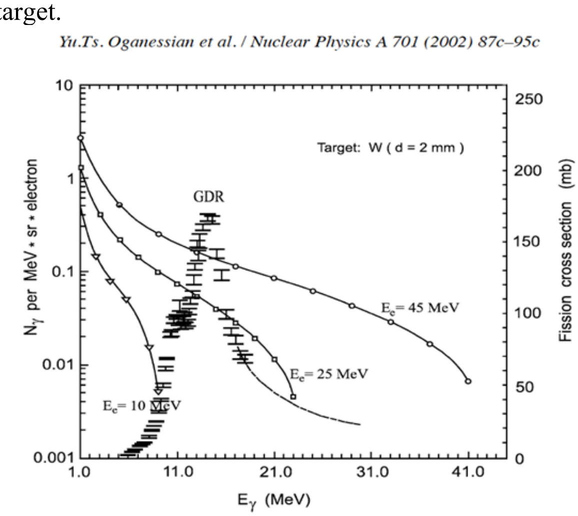

Figure 1: The γ-quanta spectrum (left scale) produced by electrons with various energies. The experimental points (right scale) correspond to the ^{238}U photo-fission cross-section [3, 5].

* TRIUMF receives federal funding via a contribution agreement through the National Research Council of Canada. ARIEL & e-linac construction are funded by BCKDF and CFI.
† aureliat@triumf.ca ‡ tplanche@triumf.ca

ISBN 978-3-95450-167-0

MOTIVATION

Since the geometry and the design of the converter and target play an important role for the optimization of the radioisotopes production, a new conceptual design is proposed in this paper.

Conceptual Design

The proposed design consists of a spiral scaling FFAG magnetic structure [6] to inject a cw electron beam. The FFAG structure is used to provide suitable horizontal and vertical focusing to the circulating electron beam.

A thin converter is placed inside the FFAG. The simulations are performed using multi-particle transport Monte Carlo FLUKA [7], and crosschecked in GEANT4 [8]. In the FLUKA and GEANT4 simulations below (see Figures 2, 3 and 4) one can see the electron fluence and respectively the photon fluence of a 5-sector spiral scaling FFAG electron beam is making multiple passes through a 0.1 mm thick tantalum foil. By using a very thin convertor secondary electrons with low energies get trapped in the magnetic flux lines and deposit their energy in a central core absorber and in the vacuum chamber walls, which can be cooled externally. The isotope production target is placed outside of the magnet. In this way most photons will reach the target and induce the photo-fission reactions. The specifications of the 5-sector spiral scaling FFAG are summarized in Table 1.

To inject a cw electron beam at 50 MeV in horizontal direction a turn separation is necessary between the first turn and all the other turns of the electron beam. In this turn separation the injection septum is placed.

To get a turn separation we first choose a phase advance between the convertor and the injection point of ~180°, so that large angles from scattering through the foil do not contribute to the beam size at the injection point. Note: in this way the beam size at the injection point is dominated by dispersion.

The desire is to have a very thin converter foil so that secondary particles produced in the foil do not deposit their energy in the foil, in order to reduce the temperature of the converter. Secondary electrons and positrons, for instance, will escape the foil, spiral along the magnetic flux lines, and eventually deposit their energy on the vacuum chamber walls. To get additional turn separation we drive the ν_r = 1 resonance using a controlled first harmonic field error. The effect of driving this resonance is illustrated in Figure 5. In this way we obtain a turn separation of about 5 mm (see Figures 2 and 4).

Table 1: Specifications of the 5-Sector Spiral Scaling FFAG

Geometrical field index	k = -0.1
Spiral angle	$\chi = 65°$
Maximum field	< 0.9 T
Radial tune	$\nu_r = 0.997$
Vertical tune	$\nu_{rz} = 1.23$

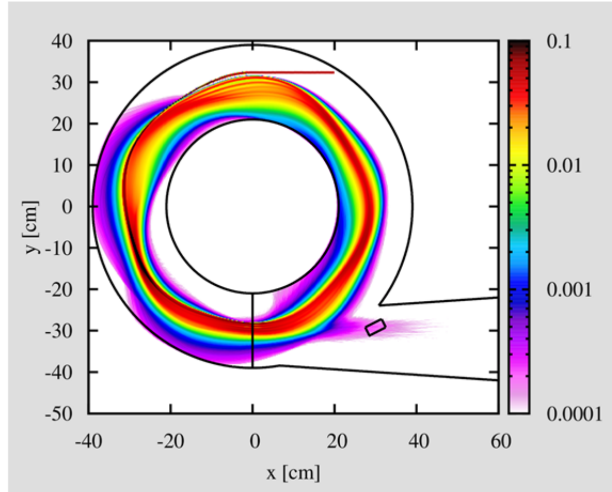

Figure 2: Electron Fluence (projected along z, arb. unit).

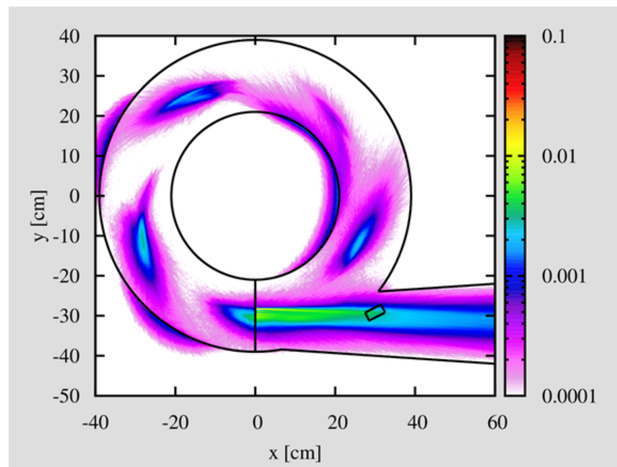

Figure 3: Photon Fluence (projected along z, arb. unit).

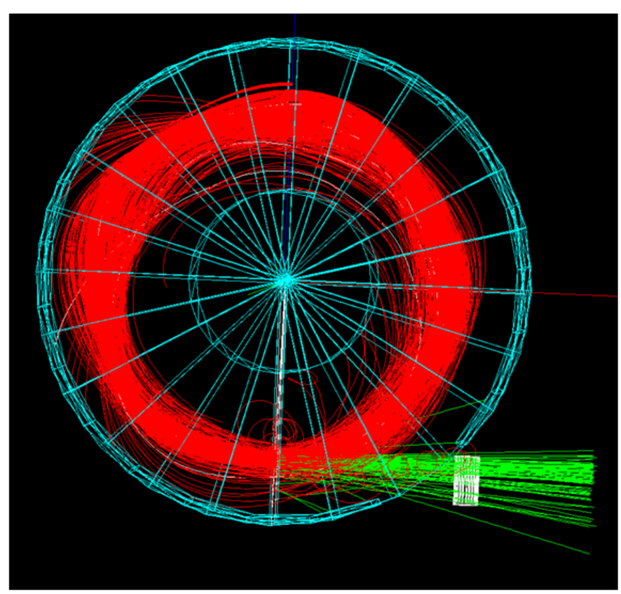

Figure 4: Visualization of electron and photon trajectories in Geant4 (top view).

ISBN 978-3-95450-167-0

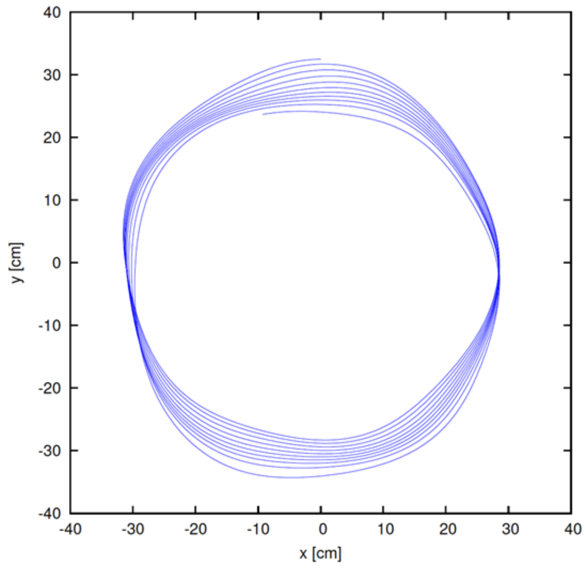

Figure 5: The orbit of a single electron (our reference particle) is shifted in the y direction using a controlled first harmonic field error that drives the $\nu_r = 1$ resonance.

THERMAL ANALYSIS

The energy deposition from FLUKA [7] is input in ANSYS [9] to perform the thermal analysis.

The thermal analysis is done for a 1 mA and 1.5 mA of electron beam at 50 MeV. The tantalum converter foil thickness is 0.1 mm and the size of the beam spot is 1 cm^2. The uranium carbide target density is $\rho = 3.5$ g/cm^3 and its volume 16 cm^3. The figure of merit is the fission rate in the uranium carbide target.

See simulation results in Table 2 and target temperature in ANSYS for 1.5 mA of primary electron beam in Figure 6.

An optimized setup would have: (1) a larger beam spot on the converter foil; (2) a reduced temperature gradient in the target and (3) a high fission rate in the target.

The temperature gradient in the target can be reduced using external ohmnic heaters, but the primary electron beam flux dictates the maximum temperature in the converter foil and the target. Using a FFAG structure, the optics can be adjusted to optimize the power density (and the beam size) on the converter and implicitly on the target. In an uranium carbide target the maximum operational temperature should be below 2100 °C [10]. The converter foil should operate at temperatures below 2500 °C although it can withstand temperatures up to 2700 °C but the foil has to be exchanged more often.

CONCLUSIONS

In this design the interaction of the charged particles with the uranium carbide target is significantly reduced. Mainly photons are interacting with the target and the energy deposition onto the target is reduced.

Since the electron beam is re-circulated, in case of a converter failure, the target is protected from a direct impact with the primary electron beam.

Table 2: Simulation results from FLUKA [7] and ANSYS [9] for fission rate, temperature and power deposition in 0.1 mm tantalum converter foil and the uranium carbide target. Convertor and target are cooled only through thermal radiation. Electron beam energy is 50 MeV.

Simulation	1 mA	1.5 mA
Fission Rate [fis/sec]	$1x10^{11}$	$1.5x10^{11}$
Max Temperature Converter [°C]	2370	2722
Power in Converter [W]	614	921
Max Temperature Target [°C]	1549	1840
Power in Target [W]	276	414
Total Power [kW]	50	75

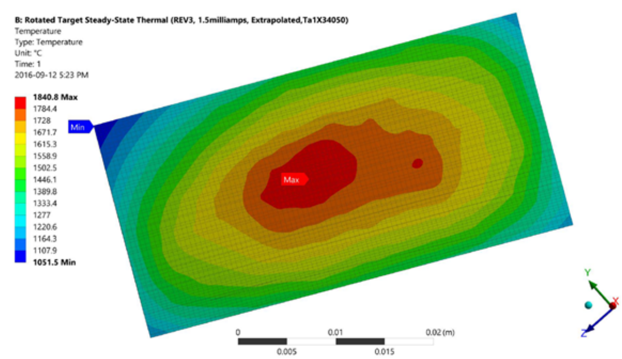

Figure 6: ANSYS thermal analysis for an uranium carbide target heated by photons generated from a primary electron beam of 1.5 mA.

The water-cooling system can be placed on outside of the vacuum chamber, so away from the electron beam, to reduce the water radiolysis.

The photon cone is transformed into a photon band, which means a more homogenous photons distribution on the target.

The proposed design should be further optimized to be compatible with the full beam power that the ARIEL electron linac can deliver.

REFERENCES

[1] William T. Diamond, “A radioactive ion beam facility using photofission”, *Nuclear Instruments and Methods in Physics Research* A, vol. 432, issue no. 2–3, pp. 471–482, 1999.

[2] A. G. Belov *et al.*, in: Yu.P. Gangrsky (Ed.), *Workshop on Application of Microtrons in Nuclear Physics*, JINR Preprint D-15-93-80, 1993, p. 20.

[3] Yu. Ts. Oganessian, S. N. Dmitriev, J. Kliman, O. A. Maslov, G. Ya. Starodub, A. G. Belov and S. P. Tretiakova, “RIB product ion with photofission of uranium”, *Nuclear Physics* A, vol. 701, issue no. 1–4, pp. 87–95, 2002.

[4] M. Cheikh Mhamed, S. Essabaa, C. Lau, M. Lebois, B. Roussiere, M. Ducourtieux, S. Franchoo, D. Guillemaud Mueller, F. Ibrahim, J. F. LeDu, J. Lesrel, A. C. Mueller, M. Raynaud, A. Said,

ISBN 978-3-95450-167-0

D. Verney, and S. Wurth, “RIB production by photofission in the framework of the ALTO project: First experimental measurements and Monte-Carlo simulations”, *Nuclear Instruments and Methods in Physics Research,* vol. B 266, pp. 4092–4096, 2008.

[5] J.T. Caldwell *et al.*, *Phys. Rev.* vol. C 21 p. 1215, 1980.

[6] K. R. Symon, D. W. Kerst, L. W. Jones, L. J. Laslett, and K. M. Terwilliger, “Fixed-Field alternating-gradient particle accelerators”, *Phys. Rev.* vol. 103, p. 1837, published 15 September 1956.

[7] A. Ferrari *et al.*, “FLUKA: a multi-particle transport code”, Internal Reports, CERN-2005-10, 2005, INFN/TC_05/11, SLAC-R-773.

[8] S. Agostinelli *et al.*, “Geant4 - A simulation toolkit", *Nuclear Instruments and Methods,* vol. A 506, pp. 250-303, 2003; J. Allison *et al.*, “Geant4 Developments and Applications”, *IEEE Transactions on Nuclear Science,* vol. 53, issue no. 1, pp. 270-278, 2006.

[9] ANSYS® Academic Research, Release 16.0.

[10] Y. Zhang and G. D. Alton, “Design of high-power ISOL targets for radioactive ion beam generation”, *Nuclear Instruments and Methods in Physics. Research, Section A: Accelerators, Spectrometers, Detectors and Associated Equipment*, vol. 521, issue no. 1, pp. 72–107, 21 March 2004.

ISBN 978-3-95450-167-0

SINGLE STAGE CYCLOTRON FOR AN ADS

P. Mandrillon, M. Conjat, AIMA Developpement, Nice, France

Abstract

In order to cope with the challenge of an ADS demonstrator, the accelerator is required to deliver a beam driving power in the range of 5 to 10 MWatt. Therefore it is mandatory to propose an accelerator design able to address highly demanding criteria which are a challenge for high power accelerator designers.

Taking into account the outstanding performances of the PSI ring cyclotrons, it is clear that cyclotrons are competitive challengers to high power linacs. The preliminary design studies of two options of a Single Stage Cyclotron Driver show that this concept could bring attractive solutions in term of reliability, cost effectiveness and power efficiency.

Some critical aspects of these designs which make use of the reverse valley magnetic field concept will be discussed in this paper.

THE PIONEERS OF HIGH POWER CYCLOTRONS

The requirements for ADS open different technical solutions for the driver accelerator. This reminds « the Meson factory race » in the 1970's where two rather different cyclotron designs were proposed in the same energy domain (500 to 600 MeV) to produce mesons.

These two large cyclotrons, the Swiss SIN [1] (today PSI) and the Canadian TRIUMF [2] were designed for 100 µA beam intensities which were very challenging in the 70's.

These two cyclotron facilities are based on rather different concepts.

THE PSI H+ TWO STAGES CYCLOTRON

The PSI has proved the soundness of large separated magnet spiral sectors (8) concept with 4 powerful large single gap RF λ/2 cavities delivering up to 600 KV peak voltage at the running-in. This design imposed a two stages cyclotron with a 72 MeV injector cyclotron (Figure 1). The cyclotrons operate with a high extraction efficiency based on the "single turn operation mode".

Since 1974 an outstanding intensity improvement program has been carried out. In 1984 the Philips compact isochronous injector has been replaced by a four separated sectors injector with an external 870 KeV injection line. In order to reduce the number of turns in the booster ring cyclotron, new copper resonators have been installed in 2008, resulting in a higher energy gain per turn. Since the very beginning the extracted beam intensity has been raised by a factor 20 and today the PSI cyclotron chain is delivering a 2.2 mA-590 MeV beam [3] with a 5.10^{-4} beam losses on the septum of the booster deflector.

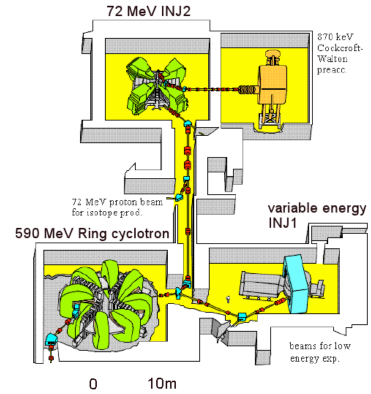

Figure 1: The layout of the two stages PSI cyclotron chain. INJ2 is the four separated sectors cyclotron superseding the old INJ1 compact cyclotron.

THE TRIUMF H- SINGLE STAGE CYCLOTRON

The TRIUMF design is the pioneer of a "single stage" acceleration up to 525 MeV exploiting the negative H- ion acceleration with two simultaneous extracted beams at 100 % extraction efficiency.

The relativistic electromagnetic stripping effect of the H- ions (the second electron is weekly bounded, 0.754 eV) requires a low magnetic field. Therefore the size of the machine is large (extraction radius 6.9 m, total iron weight of the magnet 2500 tons), the maximum B-field in the sector median plane being close to 6.1 kGauss. Besides a strong spiral is needed to achieve the vertical focusing (maximum spiral angle close to 70 deg.). As shown on the Figure 2, the acceleration is achieved by an unusual RF system made of λ/4 large resonators resulting in a single « Dee-gap » providing a 400 KeV peak energy gain per turn. The resonators are fed by a 1.8 MWatt RF Amplifier chain. The injection is external and axial from a 300 KeV injection line. The stripping extraction works in the "overlapping turns" extraction mode.

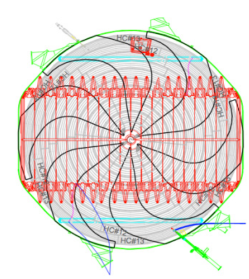

Figure 2: The TRIUMF 6 sectors single stage cyclotron with the RF resonators in red.

ISBN 978-3-95450-167-0

EXAMPLES OF HIGH POWER CYCLOTRON DESIGNS

Inspired by the successful and promising high intensities of the PSI cyclotron chain, multi-stages high power cyclotron designs have been proposed. A good review of these designs is given in the L.Calabretta and François Méot [4] paper, which is briefly summarized hereafter:

The Energy Amplifier Driver

For driving the Energy Amplifier proposed by Prof. C. Rubbia [5] in 1995, a 3 stages cyclotron (Figure 3) has been investigated in details [6]. The goal was to deliver a 12 MWatt proton beam (12 mA - 1 GeV). The extraction method which was chosen was the PSI "separated turns" mode. Hence low number of turns in each stage was mandatory resulting in high energy gain per turn in the two last stages:

Two compact injector cyclotrons able to deliver 6.25 mA-15 MeV beam in a 30 deg RF phase width. One injector extracting H- beam by a classical electromagnetic septum channel and the second injector extracting H- beam by stripping to provide H+. These two 15 MeV beams are funneled up to the injection line in an intermediate stage four Separate Sector Cyclotron (ISSC) accelerating the beam up to 120 MeV. A final stage ring cyclotron made of 12 magnet sectors and 6 RF cavities boosts the energy up to 1 GeV.

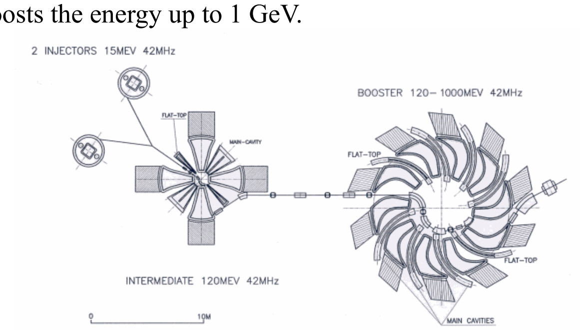

Figure 3: The 3 stages cyclotron of the Energy Amplifier.

The PSI Dream Machine

A layout of a multi-stages 10mA proton beam at 1 GeV was also investigated by T. Stammbach [7] at PSI. The final booster is shown in Figure 4.

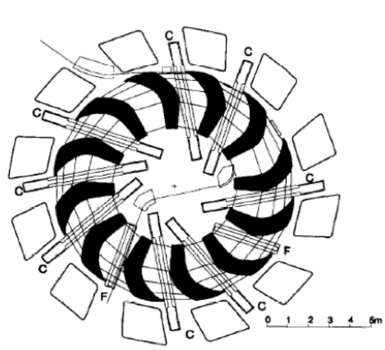

Figure 4: The 10 MWatt "Dream Machine", a 12 separated sectors – 8 RF cavities.

The 800 MeV/u DAEδALUS Cyclotron Chain

The proposed design to drive the DAEδALUS [8] experiment is a two stages cyclotron complex based on H2+ acceleration which has important advantages:

- a compact injector cyclotron which accelerates H2+ beams up to 60 MeV/amu. The extraction is made by turn separation via two usual electrostatic deflectors.
- the Superconducting Ring Cyclotron (SRC) boosts the beam energy up to 800 MeV/amu. The extraction of the beam as protons is made by stripping of the H2+. The SRC is made of 6 sectors excited by RIKEN-type [9] superconducting coils. Acceleration is given by 4 large monogap PSI-type resonators. The high magnetic rigidity of H2+ requires a maximum 4.72 T magnetic field in the sectors. As shown in Figure 5, the extracted trajectory is a long path due to the internal inwards motion of the stripped H+ beams.

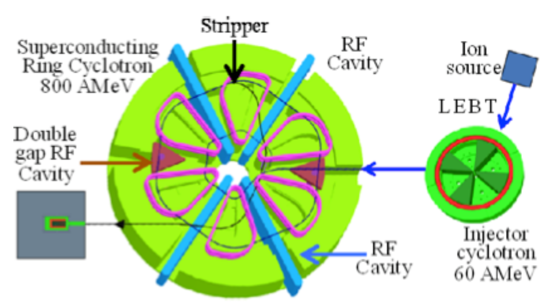

Figure 5: Layout of the two stages DAEδALUS cyclotron chain. The SRC H2+ 800 MeV/amu cyclotron is equipped with 6 RF cavities (4 large PSI type monogap cavities and 2 double gap cavities).

The TAMU 800 MeV Superconducting Strong Focusing Cyclotron

This 800 MeV-15 MW design proposed by the Texas A&M University [10] is a two stages superconducting cyclotron.

It is a stack of coupled-cyclotrons providing 3 beams of 5 MW each in parallel (cf. Figure 6). It uses superconducting RF resonators with a high quality factor, about 10^{10} at 4.2°K. It uses strong focusing by quadrupole channels to obtain high betatron tune numbers. The 100 MeV injector is a stack of three coupled-four sectors cyclotrons. The booster ring is made of :

- 12 Flux coupled stack of dipole magnet sectors with low magnetic field (0.6 T). Therefore the overall diameter of the machine is large, about 20 m.
- 10 superconducting 100 MHz RF cavities providing a 20 MeV energy gain per turn resulting in 35 turns to reach the extraction energy. A 5 cm dynamic aperture is obtained on the extraction radius.

The large energy gain per turn allows the possibility to insert Strong Focusing transport channels made of Panofsky Quadrupoles providing a strong gradient of the order of 4 T/m.

ISBN 978-3-95450-167-0

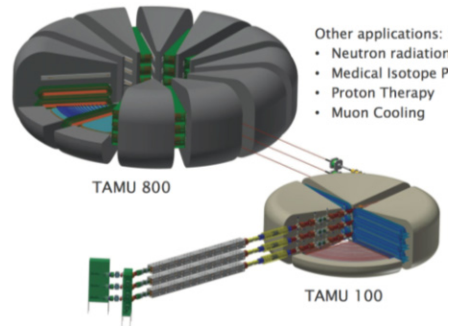

Figure 6: The two stages, strong focusing 800 MeV 3 stack cyclotron.

THE LESSONS FROM THE PIONEERS

Over the last 20 years, the regular and impressive progress toward high intensity acceleration has delivered important lessons:

Simulations

Figure 7 shows the excellent agreement between simulations, which take into account beam halo using the OPAL code, and the current measurements with the radial probe of the PSI final booster. This performance [11] demonstrates that the cyclotron community has the ability to simulate the acceleration of high power beams.

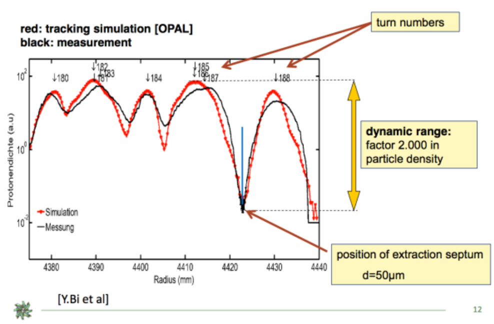

Figure 7: Comparison between simulated and measured relative beam intensity in the turn separation extraction process in the PSI Ring Cyclotron showing the losses on the extraction septum.

Showstoppers

As seen from Figure 8, the main weak point of PSI down time in 2009 was the extraction, i.e., the electrostatic devices with the septa (27%).

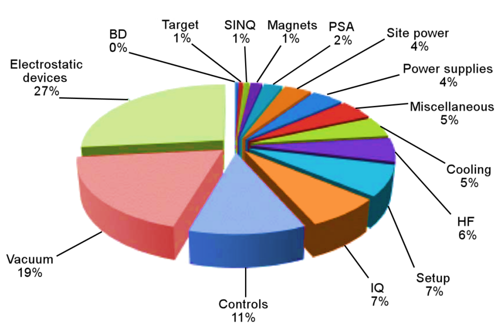

Figure 8: The main causes of PSI downtime in 2009.

To overcome this difficult extraction problem, a possible way is to avoid interactions between the circulating high power beam and the material of the extraction device by:

- either the single turn extraction which requires a multi-stage cyclotron complex
- or the overlapping turns which requires a "septum free" extraction device.

Extraction Issue

Single Turn Extraction In this process, on the extraction radius R where the radial betatron tune number is νr ,at the maximal kinetic energy T= E0(γ-1), the radial separation d between the accelerated turns resulting from the Energy gain per turn E_g is given by the following expression :

$$d = R\frac{\gamma}{\gamma+1}\frac{E_g}{T}\frac{1}{\nu_r^2}$$

In cyclotrons, longitudinal space charge forces dominate. An insight in the intensity limit was given by the W.Joho [12] practical formula:

$$I_{max} = 1.4_{mA} T_{MeV} \beta_{max} \Delta\phi/2\pi \ (100 \text{ turns}/N)^3$$

where T is the final kinetic energy, β_{max}=v/c of the particle, Δϕ the phase width of the beam which makes N turns in the cyclotron.

For the present performances of the PSI machine as shown in Figure 7 with 188 turns in the ring and Δϕ= 8°, we find 2.18 mA which is very close to the measured 2.2 mA.

The remarkable properties of the approximate I_{max} formula are that:

I_{max} does not depend on the final radius or beam shape.

I_{max} is inversely proportional to N^3, hence requiring powerful accelerating cavities to provide high peak voltages.

The drawback of this extraction is the need of an intermediate energy injector to reduce the number of turns in the booster ring. The matching of the different injection/extraction channels is highly demanding and could be a source of reduced reliability for an industrial design.

Overlapping Turns Extraction The stripping extraction which removes electrons (from H- or H2+) uses this method. The efficiency is high but there are still drawbacks. The binding energy of H- is weak (0.75 eV) and the acceleration at high energy requires a low magnetic field resulting in a large size machine (TRIUMF-type). Nevertheless the binding energy of H2+ (2.8 eV) allows acceleration in a high magnetic field which reduces the drawback of having twice the magnetic rigidity, resulting in an acceptable radius increase compare to a proton machine (cf. DAEδALUS).

Moreover, this process uses a thin stripping Carbon foil which has a limited lifetime due to heating by electrons, fatigue effects, radiation damages and production of neutral hydrogen (with a low probability).

ISBN 978-3-95450-167-0

An alternative attractive possibility is the "septum free" extraction in a reverse field valley, which requires a bump increasing the negative field of the valley, produced by iron bars outside the median plane. This method avoids any interaction with the circulating beam, and obviously, in this process, turns could overlap.

SINGLE STAGE CYCLOTRON DRIVERS (S2CD^{TM})

Two options of a single stage cyclotron were investigated [13].

- option A: acceleration of protons up to 600 MeV (10 mA) and extraction by a "septum-free" channel
- option B: based on the acceleration of H2+ ions up to 1600 MeV kinetic energy delivering 800 MeV (10 mA) protons by stripping

Common Features

Three features common to the two options are discussed.

Feature1 A 6 sectors magnet excited by a single large superconducting coil whose particular shape is producing a reverse magnetic field in the valleys in order to get a strong field flutter, hence a strong vertical focusing ν_z^2. This reverse valley field concept was explored by M.K.Craddock [14].

The symmetry of the sectors makes easy the shimming of the magnet on the axis of the sectors (Figure 9).

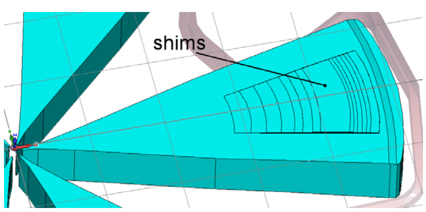

Figure 9: Sector shimming.

Figure 10 illustrates the magnetic field in the median plane. The Figure 11 shows the reverse field at large radii in the axis of the valleys. The large magnetic field flutter provided by the reverse valley field avoids spiraling the sector edges to get a strong vertical focusing. This allows to install classical double gap RF delta cavities in the valleys. The figure shows the equilibrium orbits of the option A in the first quadrant.

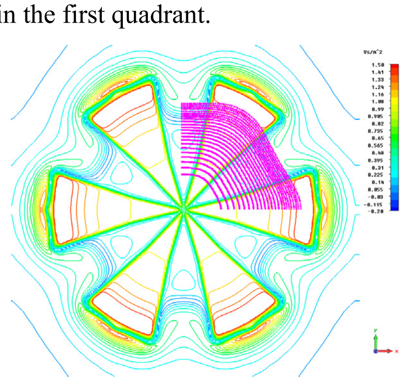

Figure 10: The 6 sectors B-field of the option A.

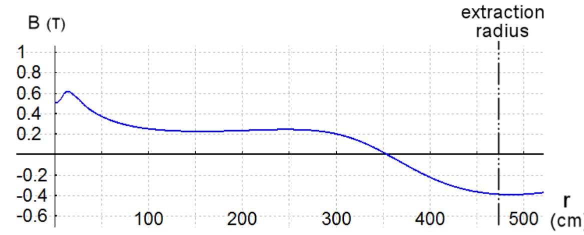

Figure 11: Radial plot of the magnetic field in the valley.

Figure 12 shows the resulting focusing betatron frequencies.

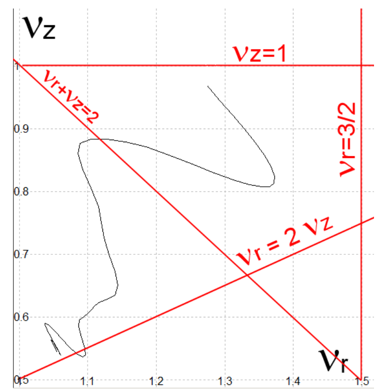

Figure 12: Focusing frequencies νr and νz.

Feature 2 Acceleration is provided by 6 delta cavities in the valleys. Double-gap RF cavities have been selected because they allow acceleration at low energy and are compatible with axial injection in a single stage cyclotron design. This cavity consists of a classical half-wave resonator with a delta-shaped resonant line (with a central dee and a stem) as shown on the Figure 13. It has been defined with the help of the electromagnetic code CST from Microwave Studio.

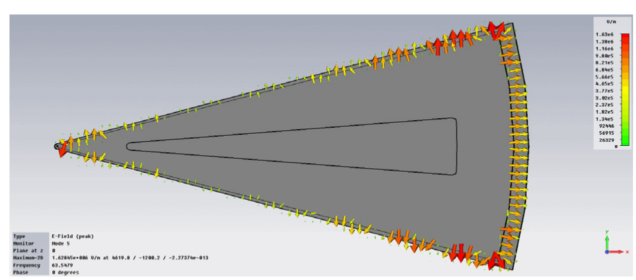

Figure 13: The delta double gap cavity.

A radial increasing peak voltage law, from 160 KVolts at injection up to 450 KVolt at extraction, is obtained. Moreover the large size of the stems allows to install the pumping system. No thorough investigation of the RF transmitters has been carried out up to now.

The following table gives the characteristics of the RF accelerating cavities.

ISBN 978-3-95450-167-0

Table 1: Main Characteristics of the Single Stage Cyclotron RF Cavities

	Option A: H+	**Option B: H2+**
Type of cavity	λ/2, double-gap, tapered walls	
Frequency	49 MHz	36.3 MHz
Peak Voltage / injection	160 kV	160 kV
Peak Voltage / extraction	450 kV	450 kV
Losses / cavity	400 kW	350 kW
Beam Power / cavity	1000 kW	1300 kW
Total power / cavity	1400 kW	1650 kW
Total Electric Power/ cavity (DC/RF η=70%)	2000 kW	2360 kW

Feature 3 The beam is injected axially in the central region. A particular feature of the magnet is the large space (low magnetic field) in the central region which allows a multi-beam acceleration, i.e., up to 3 beams, provided by 3 low energy axial injection lines fed by 3 ion source platforms (cf. Figure 14).

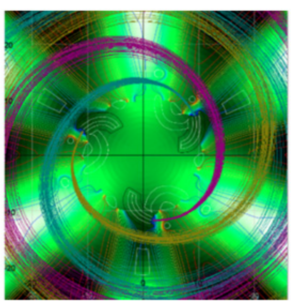

Figure 14: Central region with 3 simultaneous injected beams.

The 2 Extraction Possibilities

The particular geometry of the reverse valley field concept makes the extraction very attractive by using the overlapping turns extraction in two different ways:

Option A: The extraction of protons is “septum free”, i.e., an anti-septum channel is needed, therefore highly reducing the burden of septum losses, hence the constraints of single turn extraction (Figure 15).

Option B: The extraction of protons by stripping of H2+ in the reverse valley field is a very short outwards oriented path for two reasons: the jump of the center of curvature outside the cyclotron and the twice smaller radius of curvature of the protons (Figure 16).

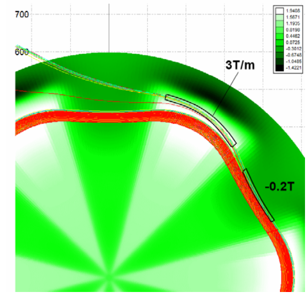

Figure 15: H+ extraction with a negative (-0.2T) field bump in the valley and a 3T/m gradient corrector in the downstream sector. Only the last 50 MeV acceleration is shown.

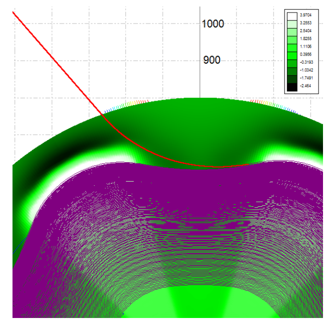

Figure 16: The short extraction path of stripping extraction of H2+ in the reversed valley field.

Critical Issues

In order to reach the high level of reliability of an industrial cyclotron-based ADS demonstrator, the following issues should be further investigated:

Superconducting Coil The complex shape for getting the reverse field in the valleys and the length (48m for the H+ option) of the coils are certainly a big technical challenge.

RF cavities Each large RF cavity will have to handle in the 1.4 to 1.65 MWatt total power. According to experts, one single RF window can handle up to 700-800 Kwatt. Obviously this means that three such windows are needed for each cavity. Because of the presence of magnetic stray fields, it is not possible to locate the power amplifier close to the cavities. Therefore the power has to be transmitted through long RF feeders to the coupling loops.

Extraction This is certainly the most important concern for minimizing the beam losses. According to the PSI experience in a multi-stages cyclotron the different extraction channels with their septa are the most frequent causes of troubles and reduce the MTBF. Therefore a single stage cyclotron concept eliminates these channels. Further detailed studies of the overlapping turns extraction are in progress for the two options.

H2+ acceleration (option B) For cyclotrons accelerating H2+, a high vacuum quality is required. For large machines the outgasing rate of the RF cavities and

ISBN 978-3-95450-167-0

of the vacuum chamber should be carefully controlled. CERN technical experience in this field on the needed passivation processes is certainly relevant.

Moreover the dissociation of the vibrational states contained in the beam could be critical. Nevertheless this issue is certainly worth being more deeply investigated (e.g. choice of the ion source type) because of the possible high energies of the removed protons.

CONCLUSIONS

To enter the 5-10 MW beam power domain while keeping the beam losses within the accelerator in the 0.01 % to 0.05 % range requires to investigate new concepts for increasing the reliability while decreasing the costs.

Parallel Concept

The studies of three various cyclotron designs reveal a common feature, the parallel concept aiming at obtaining a multiplying factor for the accelerated intensity while lowering the space charge problems and reducing the beam trips:

- Daeδalus: Acceleration of H2+ ions allows a factor 2 on the extracted proton beam intensity owing to the stripping.
- TAMU: the Superconducting Strong Focusing multi-stage cyclotron is a stack of three separate proton beams allowing a factor 3 on the final intensity.
- S2CD: the single stage concept via the injection of three beams in a common median plane of acceleration reduces by a factor 3 the requirements of a single injection stage.

Single Stage Cyclotron

Avoiding an injector cyclotron reduces the number of components and could be an asset for extraction reliability. In addition to the compactness of such a single stage based facility (Figure 17), it should also certainly result in a cost effective solution for an ADS demonstrator.

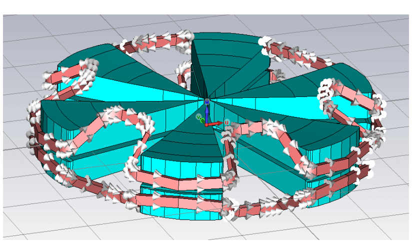

Figure 17: 3D view of the 6 sectors single stage AIMA Developpement cyclotron with reverse valley B-Field

High Global Yield of the Accelerator

The power needed to run the cyclotron driver should be optimized to reach a global yield close to 40 %. Therefore for feeding the large magnets, superconducting technology is required.

Table 2 provides a tentative rough preliminary estimates for the electric power needed to run a single stage 600 MeV-6 MWatt cyclotron.

Table 2: Total Electric Power of an H+ Single Stage Cyclotron (Option A)

Total RF Power	12 MW
Superconducting Magnet	1 MW
Injection (3 sources+3 axial lines with bunching, foc. lenses, inflectors)	1 MW
Extraction channel	1 MW
Total Electric Power	15 MW

Therefore for this 6 MW beam power the overall efficiency of the single stage H+ cyclotron is about 40%.

ACKNOWLEDGEMENT

The authors are indebted to J. Mandrillon for his important contribution to the preliminary studies. They also wish to thank T. Rogen, CERN, for his support for RF cavities calculations and our colleagues L. Calabretta and M.Seidel for providing informations for this paper.

REFERENCES

[1] H.A. Willax, "Status report on SIN", in *Proc. 7th Int. Conf. on Cyclotrons and their Applications*, Zurich, Switzerland, 19-22 August 1975.

[2] J.R. Richardson, "The status of TRIUMF", in *Proc. 7th Int. Conf. on Cyclotrons and their Applications*, Zurich, Switzerland, 19-22 August 1975.

[3] M. Seidel, "High intensity and high power aspects of cyclotrons", ECPM-2012 PSI, Villigen, Switzerland, private communication.

[4] L. Calabretta and F. Méot, "Cyclotrons and FFAG accelerators as drivers for ADS", *Rev. of Accelerator Science and Technology* , vol. 8, pp. 77-97, 2015.

[5] C .Rubbia et al., "Conceptual design of a fast neutron operated high power energy amplifier", CERN, Geneva, Switzerland, CERN/AT/95-44, 29th September 1995.

[6] N. Fiétier and P. Mandrillon, "Beam dynamics and space charge aspects in the design of the accelerators for the energy amplifier", in Proc. 14th Int. Conf. on Cyclotrons and their Applications, Cape Town, South Africa, 1995.

[7] T. Stammbach *et al.*, "The feasibility of high power cyclotrons", *Nuc. Instrum. Methods Phys. Res. B*, vol. 113, p. 1, 1996.

[8] A. Calanna *et al.*, "The cyclotron complex for the DAEδALUS experiment", in *Proc. 20th Int. Conf. on Cyclotrons and their Applications*, Vancouver, Canada, 2013.

[9] A. Goto *et al.*, "The K500 superconducting ring cyclotron of RIKEN RI beam factory-overview and status", in *Proc. 15th Int. Conf. on Cyclotrons and their Applications*, Caen France, 1998.

[10] S. Assadi *et al.,* "Strong focusing Cyclotron : FFAG for high current applications", FFAG Workshop, in *Proc. 20th Int. Conf. on Cyclotrons and their Applications*, Vancouver, Canada, 2013.

[11] Y.J. Bi, A. Adelmann, *et al.*, "Towards quantitative predictions of high power cyclotrons", *Physical Review STAB Accel. Beams*, vol. 14, issue 5, 2011.

ISBN 978-3-95450-167-0

[12] W. Joho, “High intensity beam acceleration with the SIN cyclotron facility”, in *Proc. 11th Int. Conf. on Cyclotrons and their Applications*, Tokyo, Japan, 1986.

[13] M. Conjat, J. Mandrillon, and P. Mandrillon, “Cyclotron drivers for ADS”, Thorium Energy for the World, in *Proc. ThEC13*, CERN, Geneva, Switzerland, 27-31 Oct. 2013, pp. 249-258.

[14] M.K. Craddock and Y.N. Rao, “Cyclotron and FFAG studies using cyclotron codes”, in *Proc. 19th Int. Conf. on Cyclotrons and their Applications,* Lanzhou, China, 2010.

ISBN 978-3-95450-167-0

STATUS OF THE HIGH INTENSITY BEAM FACILITY AT LNL-INFN

M. Maggiore, A. Lombardi, G. Prete, P. Antonini, A. Calore, D. Campo, L. Pranovi, J. Esposito, L. De Ruvo, D. Benini, E. Boratto, M. Calderolla, N. Ciatara, P. Favaron, D. Zafiropulos, L. Sarchiapone, G. Bisoffi, Laboratori Nazionali di Legnaro INFN, Legnaro (PD), Italy

Abstract

In 2016 the SPES (Selective Production of Exotic Species) project [1] has entered in the commissioning phase at Laboratori Nazionali di Legnaro (LNL) with the first operations of the proton driver accelerator. The project, whose main goal is the research in nuclear physics with Radioactive Beams (RIBs), has foreseen the construction of a new building hosting the accelerator able to deliver protons up the energy of 70 MeV and 50kW of beam power to be used as a primary beam for the ISOL source and for a production beam for other applications. The new facility design has been expanded and upgraded for taking advantage of the dual simultaneous extraction of beams from the Cyclotron in order to provide a multipurpose high intensity irradiation facility. Today the new facility is partially installed and the Cyclotron supplied by Best Cyclotron System Inc (BCSI) company [2] with the related beam transport lines are under commissioning. The status of the commissioning of the high power accelerator and the capabilities of the facility as multipurpose high intensity proton beam laboratory will be presented.

INTRODUCTION

SPES project aims to provide high intensity and high quality beams of neutron-rich nuclei to perform forefront research in nuclear structure, reaction dynamics and interdisciplinary fields like medical, biological and material sciences. The production of exotic nuclei is based on ISOL technique providing low energy secondary beams that will be isotopically selected by a High Resolution Mass Spectrometer, then ionized by a breeding process, and finally re-accelerated by the actual ALPI machine operating at LNL. The primary beam is provided by a cyclotron able to accelerate H^- ion up to the energy of 70 MeV and 700 μA of average current. The protons are extracted by the stripping of H^- at different energies varying from 35 to 70 MeV. The main advantage of the H^- acceleration is the possibility to extract simultaneously two proton beams by sharing the total current available. Since only 200 μA current is needed for the production of radioactive ions, the remnant current is available for other applications. For that reason an independent area of SPES facility has been built and equipped in order to deliver proton beams for multipurpose applications in parallel sessions with RIBs production. Up to 10 experimental stations are foreseen to be irradiated by proton beams and three of those are put into bunkers shielded for receiving high power beam (up to 50 kW).

FACILITY DESCRITPION

SPES building has been thought to accommodate the cyclotron, the beam transport lines and the target stations for RIBs productions. In addition, several target areas are arranged around the area A1, where the cyclotron is placed. Figure 2 shows the overall layout of the underground level of the new facility.

Two main extraction beamlines come from the cyclotron, then by means of two switching magnets (SM1 and SM2) the beam may be guided up to 6 beamlines (3 for each SM) that allow to get directly the target stations or to reach additional switching dipoles. Finally, up to 10 target stations can be supplied by the beam.

The actual configuration foresees a single complete beamline (BL1) up to A6 area where a 50 kW beam dumper was installed and the first section of the second extraction line including the switching magnet (SM2).

The 70 MeV Cyclotron

The driver of SPES project is a resistive cyclotron able to deliver two simultaneous proton beams with energy varying within 35 and 70 MeV and 700 μA total current.

The cyclotron and the beamline (see Fig. 1) have been supplied and installed by BCSI on 2015. The cyclotron is a 4 straight sectors machine, accelerating H^- ion that are extracted by the stripping process to get the proton beams. In order to minimize losses due to the Lorentz stripping during the acceleration, the cyclotron operates with a peak magnetic field of 1.6 T. The extraction radius is about 1300 mm and total weight is 160 tons.

Figure 1: Picture of actual installation at SPES building of LNL.

ISBN 978-3-95450-167-0

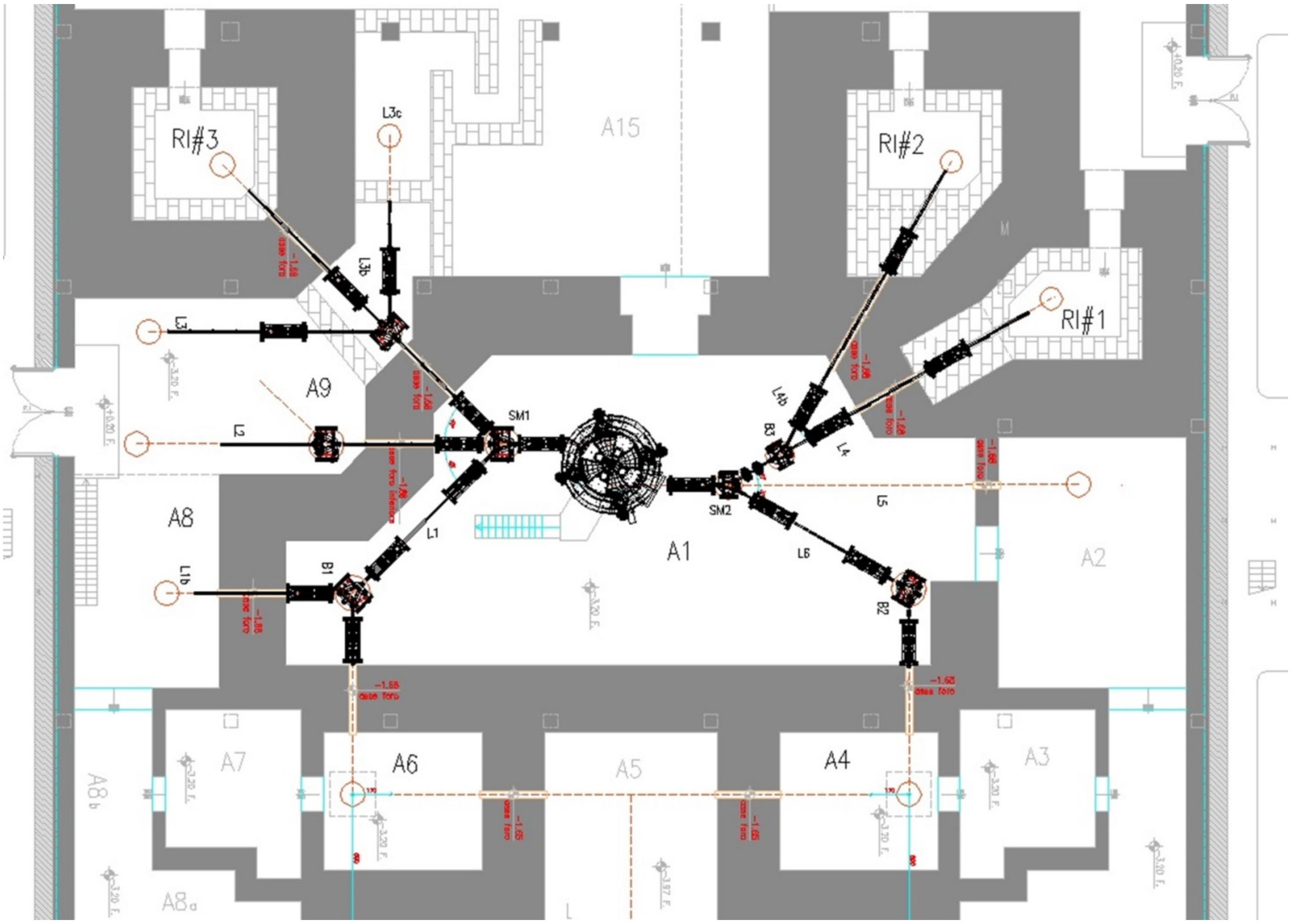

Figure 2: Overall layout of underground level of SPES building.

An external multi-cusp type ion source developed by BCSI provides the H⁻ beam to be injected into the cyclotron by the axial beamline

The RF system consists of 2 half-wave cavities placed into the valleys, providing up to 70 KV of accelerating voltage. The device operates in 4th harmonic mode at the frequency of 56 MHz. In order to maximize the performance and to optimize the control of the system, the cavities are independent and two amplifier chains, synchronized by a dedicated oscillator, feed the needed power (100 kW of total power available).

The extraction mechanism allows changing the stripper foil without breaking the vacuum in the accelerating chamber, and a novel design of a cartridge case allows to store up to 20 stripper foils permitting the machine to run for 15 day without long time beam interruptions.

The ISOL Target Stations

The cyclotron can operate at the same time two beamlines. Mainly, at least one extracted beam is dedicated to irradiate the ISOL target placed on A6 and A4 area. We expect to irradiate the ISOL target continuously for 15 days, then the same number of days are expected for cooling and maintenance. In that case, the beam is switched on the other available ISOL target station.

The main target is composed by 7 discs of Uranium Carbide compound (UCx) appropriately spacing to allow to dump 40 MeV of proton and to get up to 10^{13} fission per second for RIBs production.

To get a uniform beam distribution on the target and to avoid thermal stresses that could destroy it, a wobbler system is placed just before to enter into A6 and A4 rooms.

The Radioisotope Production Stations

Since the necessary current for RIBs production is 200 μA, the residual amount of the available accelerated current is about 500 μA. With such a current and 35-40 MeV of energy, the main purpose of the second available beam extracted from the cyclotron is the research and the production of innovative radioisotopes (LARAMED project [3]) to be used in medical diagnostics.

This activity will be held in the 3 bunkers RI1, RI2 and RI3, where 3 meter concrete shielding walls allow to irradiate the dedicated targets with 40 kW of beam power. The three bunkers are ready to be equipped with pneumatic system for the transportation of irradiated targets to the hot cells. Such a system for radiochemical treatment is still under evaluation.

ISBN 978-3-95450-167-0

The Neutron Generation Stations

The A9 and A8 areas of the facility are dedicated for irradiation of targets with proton for high flux neutrons generation and other applications (NEPIR project [4]). In particular two continuous energy neutron beamlines where the neutrons are produced in a rotating composite target made of Be and a heavy element such Pb or Ta essentially tailored for Single Event Effects (SEE) study. The second beamline is a multipurpose line based on a thick (proton stopping) W high power target: added moderators can be tailored to produce neutrons with the energy spectrum of interest for the measurements for Atmospheric Neutron Emulator (ANEM).

An additional application of high power proton beam is the generation of a quasi mono-energetic neutron (QMN) source with a controllable peak energy in the 35-70 MeV range using an assortment of thin Li and Be production target (1-4 mm thick). A multi-angle collimator will be used to correct data taken in forward direction, by subtracting data obtained at larger angles. This multidisciplinary line is of particular interest for studying threshold effects and to calibrate simulation codes.

BEAM OPERATION

BCSI started the commissioning of the cyclotron and beamlines on March 2016. Such a commissioning is being done in different phases starting from acceleration up to 1 MeV towards extraction and transport of the beam at full power. In early September 2016 the proton beam was extracted and delivered to the end of the beamline 1 (BL1 in Fig. 2) with a maximum energy of 70 MeV and 500 μA [5].

INFN provided the safety and radiological survey systems and the high power beam dumper which has been installed in A6 bunker. Moreover two low power faraday cups have been supplied by INFN and a couple of ionization chambers have been placed along the beamline in order to monitor the beam losses in critical points i.e. at the exit of the switching magnets [6].

The Safety and Radiological Survey System

The Radiological Survey System (RSS) consists of a network of gamma and neutron monitors positioned inside the different areas at underground level, including the control room, the equipment room and the services area on the upper floor. Two Exhaust Gas Analysis Systems (EGAM) monitor the activation of the air coming from A1 and A6 rooms and they are interlocked with the cyclotron in order to stop the beam in case of excess the limit of 1Bq/g.

During the beam operation the level of radiation detected by the monitors placed in the rooms adjacent to the “hot” areas A1 and A6 do not exceed the dose rate of few μS/h (mostly neutrons with beam on), while no variation from background level was measured in second floor. On the other side, the dose rate measured in A1 (cyclotron room) and A6 (beam dumper bunker) gets high values of neutrons and gamma radiation proportionally to the energy and current delivered.

High Power Beam Dumper

The LNL team has developed and built the dumper able to sustain up to 50 kW of proton beam whose energy does not exceed the 70 MeV and 700 μA of current. It consists of two copper plates tilted by an angle of 10 deg in order to increase the surface where the beam will hit by reducing the power density released. The two copper plates are bolted on an aluminium frame and an indium sealing between these allows the vacuum seal. In order to reduce the residual activation of the bunker environment and allow a fast removing operation of the device once the cyclotron commissioning is completed, a series of shields of lead (50 mm thick) and high density polyethylene layers (350 mm full width) have been assembled around the structure.

The beam dumper has successfully operated up to 500 μA and 70 MeV of proton beam and a small detectable leak actually is limiting its performance.

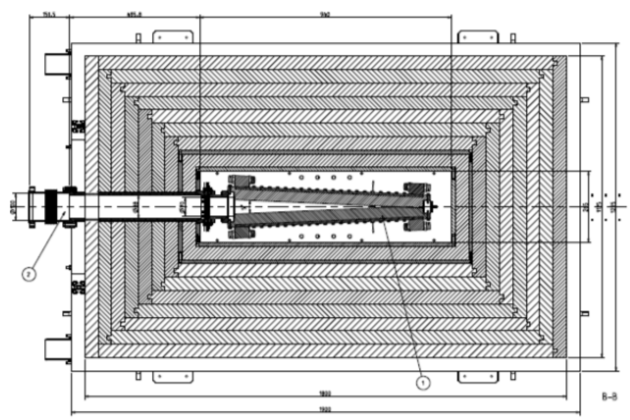

Figure 3: Top view of a section of the beam dumper and its shielding structure.

CONCLUSION

The new facility built for SPES project at LNL is now entered in the operation phase. The commissioning of the cyclotron and the beam transport lines is proceeding and very promising results have been achieved in terms of final performance of Cyclotron and beamlines. The facility is still upgrading since an additional beamline for research on radioisotope production is expected to be supplied by the end of 2017. Moreover the supply of a compound structure for radiochemical treatment of irradiated target is under evaluation.

ACKNOWLEDGEMENT

The INFN team would line to acknowledge the BCSI technical staff and management for the excellent job and fruitful collaboration during the installation and commissioning of the 70 MeV cyclotron.

ISBN 978-3-95450-167-0

REFERENCES

[1] G. Prete *et al.*, "The SPES project: a second generation ISOL facility", *Physics Procedia*, vol.52, pp. 274-283, 2012.

[2] Best Cyclotron Systems, Inc., `www.bestcyclotron.com`.

[3] J. Esposito *et al.*, "The LARAMED project at INFN-LNL", *EuChemMS Proceedings*, 2012.

[4] L. Silvestrin *et al.*, "SPES and the neutron facility at LNL", *EPJ Plus,* 131:72, 2016.

[5] V. Sabaiduc *et al.*, "Best 70P cyclotron commissioning at INFN-LNL", presented at the 21st Int. Conf. on Cyclotrons and their Applications (Cyclotrons'16), Zurich, Switzerland, Sep. 2106, paper TUD04.

[6] P. Antonini *et al.*, "Diagnostics and Instrumentation tool for high power proton beams", presented at the 21st Int. Conf. on Cyclotrons and their Applications (Cyclotrons'16), Zurich, Switzerland, Sep. 2106, paper TUP09.

ISBN 978-3-95450-167-0

STABLE AND EXOTIC BEAMS PRODUCED AT GANIL

O. Kamalou, F. Chautard, A. Savalle, GANIL, Grand Accélérateur National d'Ions Lourds, CEA-DSM/CNRS-IN2P3, Bvd H. Becquerel, BP 55027 14076 Caen Cedex 5, France

Abstract

The GANIL facility (Grand Accélérateur National d'Ions Lourds) at Caen produces and accelerates stable ion beams since 1982 for nuclear physics, atomic physics, and radiobiology and material irradiation. Nowadays, an intense exotic beam is produced by the Isotope Separation On-Line method at the SPIRAL1 facility (being upgraded to extend the range of post-accelerated radioactive ions) or by fragmentation using LISE spectrometer. The review of the operation from 2001 to 2016 will be presented, with a focus on last year achievements and difficulties.

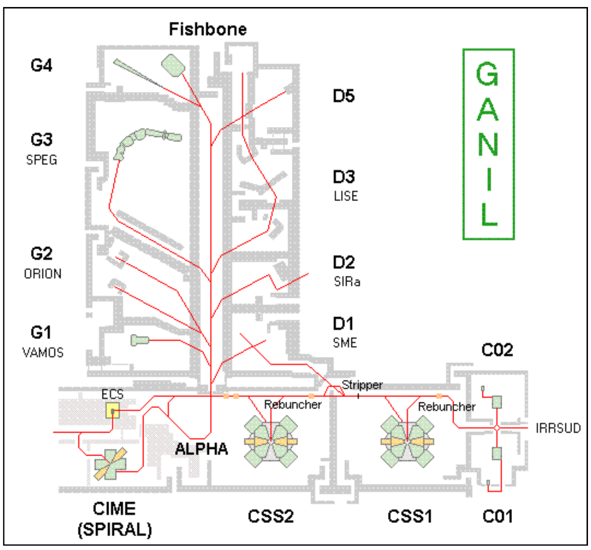

Figure 1: GANIL layout.

OPERATION REVIEW

Multi-beam delivery is routinely done at GANIL using its 5 existing cyclotrons (Fig. 1):

1. Beams from C01 or C02 are sent to an irradiation beam line IRRSUD (<1MeV/A).
2. A charge state of the ion distribution after the ion stripping foil downstream CSS1 is sent to atomic physics, biology and solid states physics line D1 (4-13MeV/A).
3. A high-energy beam out of CSS2 is transported to experimental areas (<95MeV/A), for nuclear physics and previous applications.
4. Finally, stable beams from SPIRAL1 source can be sent to LIRAT (<10keV/q) or post-accelerated by CIME and used for testing detector for example.

During radioactive beam production with SPIRAL1, the combinations are reduced to the two first (cases 1, 2), CSS2 beam is sent toward the SPIRAL1 target, and radioactive beam is sent to the experimental areas.

In addition, Ion sources are available in "hall D" building for atomic physics at very low energy.

2001-2016 GANIL OPERATION STATUS

Since 2001 (Fig. 2), more than 50172 hours of pilot beam time has been delivered by GANIL to physics, which correspond to 88.6 % of scheduled experiments.

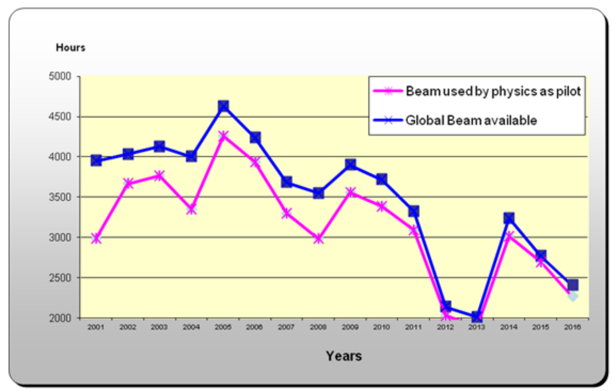

Figure 2: Beam time available for physics over 16 years.

On average, the number of beams delivered per year has increased until 2010. Owing to the construction and assembly of the new SPIRAL2 accelerator and upgrade of SPIRAL1, the running time has been shrinked to devote more human ressources to the project SPIRAL2, in particulier in 2012 and 2013 with only 2000 hours of experiments time (instead of 3500 hours per years).

Figure 3 shows the statistic running of the machine over 15 years. 67.2 % of beam time is dedicated to Physics and 12.4% for machine tuning.

In 2015 (March to July), the pilot beam time was 78%, the failure rate is only 8%. On the other hand, the SME and IRRSUD operation were decreased by several water leaks.

ISBN 978-3-95450-167-0

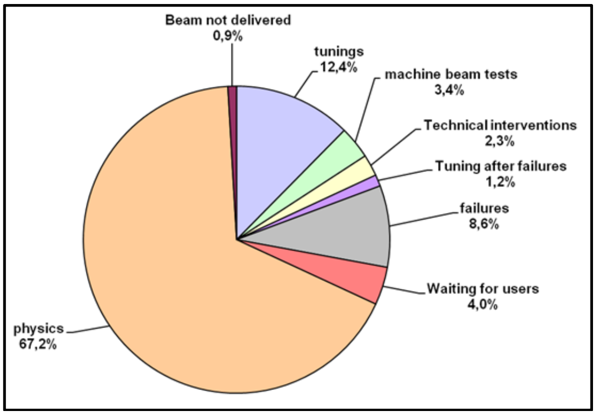

Figure 3: Statistic running of the machine between 2001 and 2016.

WATER LEAK PROBLEMS

The GANIL facility encounters water leak problems mainly on the RF cooling circuits (an example given in figure 4). The cavity of the injector C01 is out of order since March 2016 (Figure 5). A new cavity is under construction. The impact on the beam-time available for the physics is becoming visible. Therefore, in the frame of a preliminary study in 2011, several causes were identified that may induce corrosion or erosion of our circuits. An exhaustive check of the parameters of the water compared to the literature showed that some improvement can be done. Curative or preventive actions foreseen are under consideration:

Figure 4: an example of corroded pipe cooling.

1. Closing the water circuits and keep water free circuits and from any gas dissolves (Oxygen, $CO2$,…).
2. Go towards a pH above 7 and limit its reduction while being ensured to keep a high resistivity
3. Installation of new mixed beds equipped with electromagnetic sluice gates controlled by a regulation on the basis of measurement of the conductivity of water in order to maintain water with pH> 7.
4. Measure the proportion of sulphates and chlorides.
5. Decrease locally the water flow rate for cooling of power supplies and RF circuits.
6. Maintaining the temperature of the fluids as low as possible.

Figure 5: Electrode cavity of C01.

SPIRAL1 UPGRADE

The first Isotope Separator On Line System installed at GANIL, named SPIRAL1, has delivered radioactive ions for 13 years. Radioactive atoms produced by fragmentation of swift heavy ions on a carbon target are ionized in an ECR multi-charged ion source before being post-accelerated in a cyclotron. The cyclotron energy is 1.2 to 25MeV/A using harmonics 2 to 6.

Due to the design of the Target Ion Source System (TISS), mainly gaseous ions are produced. To satisfy the request of physics community for extending the choice of ions to those made from condensable elements, with masses up to Xe, an upgrade of SPIRAL1 has been undertaken [1]. Beams and technical options considered during the prospective phase have been sorted out. A schematic of the ongoing upgrade is presented in Fig. 6.

ISBN 978-3-95450-167-0

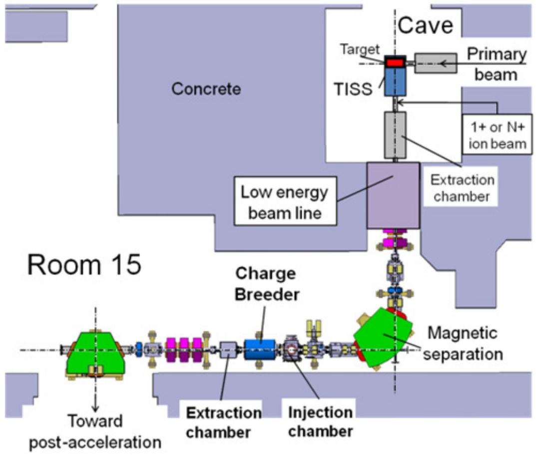

Figure 6: Schematic of the SPIRAL1 upgrade.

A new targets (Nb, SiC,..) and new type of Surface ionization, FEBIAD (Forced Electron Beam Induced Arc Discharge) or ECR (Electron Cyclotron Resonance) ion sources [2, 3] will be installed in the production cave after its modification to provide 1+ beam of condensable elements. Out of the cave and after mass separation, a Phoenix charge breeder will be installed on the present low energy beam line to increase the charge of the radioactive ions from 1+ to N+ for post-acceleration to get energy up to 25MeV/A using CIME accelerator [4].

In 2013 modifications of the production cave have been done in order to install different types of sources.

The charge breeder, based on the phoenix booster developed at LPSC Grenoble, has been used at ISOLDE to measure its performance. Several improvements have been done since. Beam optics, vacuum quality and beam purity are improved [5, 6].

The booster and its injection and ejection beam optics system have been tested at LPSC Grenoble in 2015.

Nuclear safety authorization was given on 11th of February 2015. The processes of installation and modification of the beam line will be finished soon (see Figure 7 before and after beam line modification). The commissioning with stable beam is scheduled by the end of 2016.

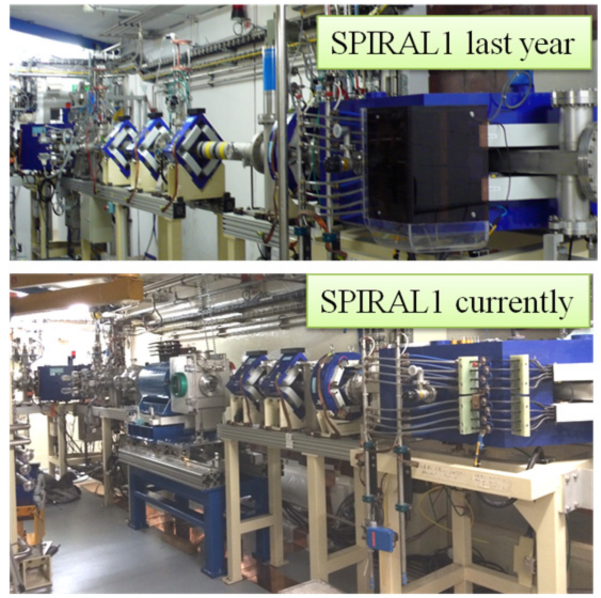

Figure7: Evolution of SPIRAL1 low energy p branch with the insertion of the charge booster.

REFERENCES

[1] P. Jardin *et al.*, *Rev. Sci. Instrum.*, vol. 83, p. 02A911, 2012.
[2] S. Sundell *et al.*, *Nucl. Instr. Meth. B*, vol. 70 pp. 160-164, 1992
[3] R. Vondrasek *et al.*, *Rev. Sci. Instrum*, vol. 83, p. 02A913, 2012.
[4] C. Tamburell, Thesis, ISN Grenoble, 1996.
[5] O. Bajeat *et al.*, *Nucl. Inst. Meth. in Phys. Res. B*, vol. 317, part B, pp. 411-416, 2013.
[6] P. Delahaye *et al.*, *Nucl. Instr. Meth. in Phys. Res. A*, vol. 693, p. 104, 2012.

ISBN 978-3-95450-167-0

PROTON RADIOGRAPHY EXPERIMENT BASED ON A 100 MeV PROTON CYCLOTRON*

J.J. Yang†, X. Zhen, S.M. Wei, Y.L. Lv, F. Wang, Y.W. Zhang, L.P. Wen, J.Y. Liu, H.R. Cai, T. Ge, S.P. Zhang, L. Cao, T.J. Zhang, Z.G. Li
China Institute of Atomic Energy, Beijing, 102413, China

Abstract

A proof-of-principle test-stand for proton radiography is under construction at China Institute of Atomic Energy (CIAE). This test-stand will utilize the 100 MeV proton beam provided by the compact cyclotron CYCIAE-100, which has been built in the year of 2014, to radiograph thin static objects. The assembling of the test-stand components is finished by now. We will carry out the first proton radiography experiment in this July and hopefully we can get the first image before the opening of this conference. In this paper, the designing, constructing and commissioning of the proton radiography system will be described.

INTRODUCTION

Proton radiography is a new scatheless diagnostic tool providing a potential development direction for advanced hydrotesting research. In comparison with flash radiography, proton radiography has higher penetrating power, higher detection efficiency, less scattered background, inherent multi-pulse capability, more exact material identification and large standoff distance between test objects and detectors. Proton radiography was firstly used for dynamic experiments on a proton energy 800 MeV linear accelerator facility at the Los Alamos National Laboratory [1]. Proton radiography on static objects with a single pulse and energy to 24 GeV was carried out at the the Brookhaven National Laboratory in the year of 2011 [2]. In 2014, a low energy proton radiography system was developed at Chinese Academy of Engineering Physics, which utilizes a 11 MeV proton beam to radiograph thin static objects [3].

As a driving accelerator for Beijing Radioactive Ion-beam Facility (BRIF), a 100 MeV H- compact cyclotron, normally referred to as CYCIAE-100, was constructed to provide the proton beam of 70-100 MeV with beam current of 200 μA [4]. The first beam of CYCIAE-100 was extracted on July 4, 2014 [5]. The operation stability have been improved and beam current have been increased gradually. 720 μA beam was got on the internal target at the beginning of 2016. The effort for mA beam is continuing and 1135 μA beam was got on the internal target in June of 2016. This cyclotron can provide two proton beams simultaneously for the ion source of the Isotope Separation On-Line system (ISOL) and experimental instrument in the experiment hall, as is shown in Figure 1. In the experiment hall, a switching magnet guides the beam to different beam lines. It is scheduled to build a low energy proof-of-principle test-stand for proton radiography based on the down-left beam line.

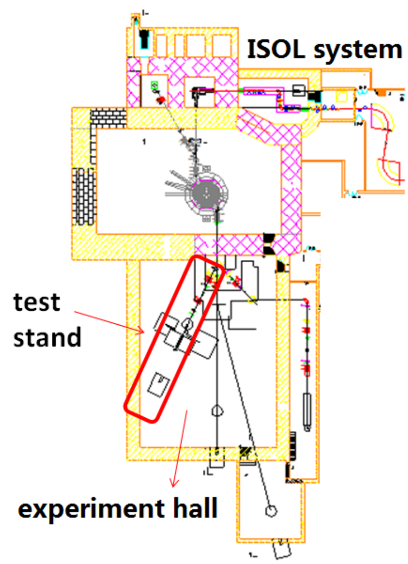

Figure 1: Layout of the BRIF facility.

BEAM LINE DESIGN

Proton radiography requires a particular magnetic lens system to provide a point-to-point imaging from the object to the image. Zumbro, Mottershead and Morris suggested a type of lens, normally referred to as Zumbro lens, whose first-order transfer matrix is the ***-I*** matrix, which means means the matrix element $R_{12} = R_{34} = 0$ [6]. The Zumbro lens has a Fourier plane at the mid-plane of the lens, where the position of a particle is determined by its initial angle only and is independent of its initial position (angle sorting), as is shown in Figure 2. The particles of large MCS angle in a matched beam can be removed through a transverse collimator at the Fourier plane. To form a Fourier plane, the incident particle's transverse displacement ⁄ and angle deviation along beam direction ⁄' must be strongly correlated and comply with the following formula:

$$\omega \equiv /'/ / = T_{116}/T_{126} \tag{1}$$

where T_{116} and T_{126} represents the second order chromatic aberrations of the Zumbro lens in TRANSPORT notation [7]. This means the matched beam emittance should equal zero, as is shown in Figure 3 (left).

* Work supported by by NSFC (Grand Nos.11375273 and 1146114103) and the CNNC Youth Innovation Team Founding.
†yangjianjun2000@tsinghua.org.cn

ISBN 978-3-95450-167-0

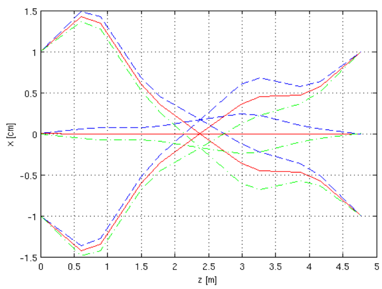

Figure 2: the point-to-point imaging in Zumbro lens. The Fourier plane is formed in the mid-plane of the lens.

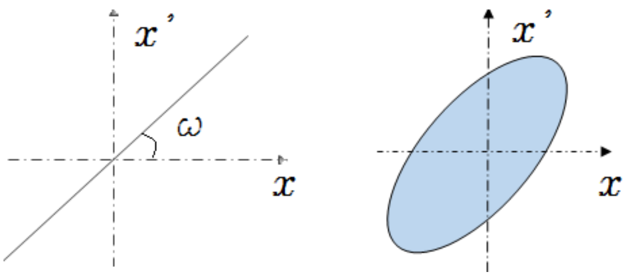

Figure 3: schematic of the ideal (left) and practical beam distribution from cyclotron (right).

But in reality, the transverse emittance of the beam from the the 100MeV cyclotron is typically nonzero, as is shown in Figure 3 (right). Therefore, it is necessary to reformulate the beam shape. In the design, the 100 MeV proton beam passes through a pinhole collimator of a inner diameter of 2 mm. The preserved central particles of the beam passes through a thin aluminium diffuser to expend the angular divergence and then passes through a sets of quadruples to reach the required correlation between particles' transverse displacement and angle deviation, as is expressed in formula (1).

Then the matched beam penetrates the thin object and the transmitted protons pass through the Zumbro magnetic lens system to form a point-to-point focusing from object to image. A radio-chromic film is positioned on the image plane. The optical density distribution of the film varies linearly with absorbed doses of the particles. The particles with large multiple Coulomb scattering angle can be removed through transverse collimation at the Fourier plane, where the proton is sorted by its angular divergence.

The design philosophy of the test-stand is fully using the existing devices and equipments and minimize the additional required ones. There are seven spare quadruples on site. So four sets of them are used in the imaging lens section and three sets of them are used in matching lens section. In addition, since the pinhole collimator will be heavily radio-activated during beam operation, this equipment must be positioned in the blockhouse and be shielded.

The beam optics design was done by using TRANSPORT code. As the first step, the imaging lens fitting determines the magnetic field strength of the four imaging quadruples and the value of ω, which was taken as the fitting conditions for the matching lens fitting process. The resultant beam envelops in the beam line in both the horizontal and vertical directions are shown in Figure 4. The length of the imaging lens and matching lens are 4.76 m and 6.28 m, respectively.

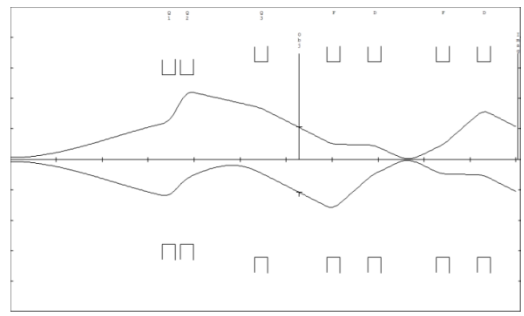

Figure 4: Beam envelops of the beam line .

MECHINCIAL DESIGN

Based on the physical design, the detailed mechanical design of the beam line elements and the radiation shielding are carried out. Figure 6 shows the mechanical assembling drawing of the beam line. Besides the seven quadruples, the beam line also includes a couple of steering magnet, two diagnostic boxes (installing two faraday cups, one double-wire scanner, one quartz plate and two turbo pumps) , one object box, one collimator box, one imaging box and a beam dump in the end.

The pinhole collimator is a critical equipment, because up to 80% of the 100 MeV, 200 μA beam will be lost on it and the power dissipation is about 16 kW. Therefore the water-cooling needs to be designed very carefully. The designed pinhole collimator consists of a inner cone and a sleeve. The cone surface was designed to increase the effective beam-heating area. A 3D FEM model was built to carry out thermal analysis. The steady temperature distribution is shown in Figure 5. The result shows the maximal temperature is 534 K under the condition of the water flow rate of 2 m/s, which is lower than melting point of copper material.

ISBN 978-3-95450-167-0

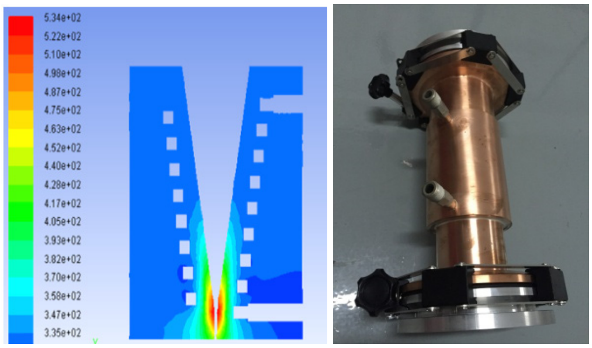

Figure 5: Steady temperature distribution in the pinhole collimator(left) and its photo of this device (right).

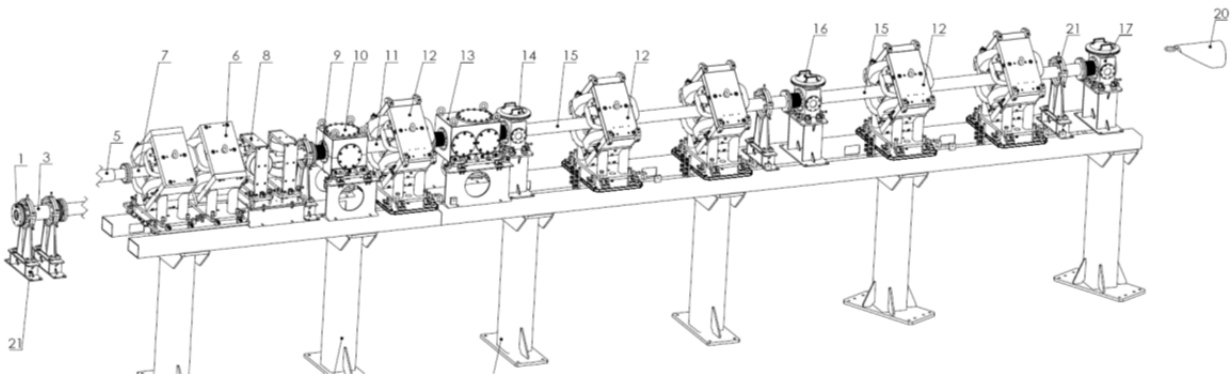

Figure 6: The mechanical assembling drawing of the test-stand.

TEST-STAND CONSTRUCTION

Manufacturing of all the test-stand components was finished and installed on site by June of 2016, as is shown in Figure 7.

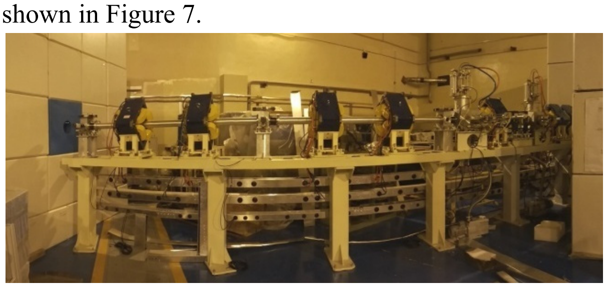

Figure 7: Photo of the assembled proton radiography test-stand.

The alignment accuracy of beam line element is better than 0.1 mm. Tow Faraday cups are installed to monitor to measure the beam current, one two-wire scanner is installed to measure the beam profile. two movable fluorescence targets are installed to monitor the beam position at low beam current. In order to maintain good vacuum conditions, two turbo pumps together with vacuometers are installed on the bottom side of the diagnostic boxes. The vacuum leak test shows no evident vacuum leakage exists on the beam line and the vacuum pressure can reach 1.0E-6 mbar within 30 minutes. In order to reduce the radiation level of the beam line, the pinhole collimator and the diffuser are positioned in the shielding blockhouse. A beam dump is positoned at the end of the beam line to collect the proton beam. The EPICS-based remote control system is already installed in the control room. The design detail of the control system is described in the reference [8]. Fig.8 show several manufactured objects of different the pattern thickness and material for proton radiography test.

Figure 8: The manufactured objects of different.

CONCLUSION AND OUTLOOK

The test-stand is now ready for beam commissioning. The proton radiography experiment is scheduled in next month. In the first step, the pinhole collimator will be replaced by a straight beam pipe and beam test will be carried out to make sure that the beam passes through the centre of pinhole collimator and quadrupoles. Once the operation parameters of the beam line elements is finalized, the pinhole collimator will be installed to its position to carry out proton radiography experiment.

ISBN 978-3-95450-167-0

REFERENCES

[1] N. King, et al., “An 800-MeV proton radiography facility for dynamic experiment,” *Nucl. Instrum. Methods in Phys. Res. A*, 424, 84–88 (1999).
[2] S. Morris, et al., “Flash radiography with 24 GeV/c proton”, *J. Appl. Phys*., 109, 104905–104909 (2011).
[3] T. Wei, et al., “First experimental research in low energy proton radiography”, *Chinese Physics C* Vol. 38, No. 8 (2014) 087003.
[4] T.J. Zhang et al., “Design and Construction Progress of CYCIAE-100, A 100 MeV H- Cyclotron At CIAE”. in *Proceedings of ICC’07*, Catania, p.33, (2007).
[5] J.J. Yang, et al., “New Development of the High Power Proton Cyclotrons at CIAE”, in *Proc. of 12th Symposium on Accelerator Physics*, Lanzhou, China, pp.16-19, (2014).
[6] C.T. Mottershead, J.D. Zumbro, “Magnetic Optics for Proton Radiography”, in *Proceedings of the Particle Accelerator Conference.* Canada Vancouvev, pp.1397-1399, (1997).
[7] PSI Graphic Transport Framework by U. Rohrer based on a CERN-SLAC-FERMILAB version by K.L. Brown et al.
[8] Y.W. Zhang, et al., “Control System Dedicated for Beam line of proton radiography on a 100 MeV cyclotron”, this conference.

ISBN 978-3-95450-167-0

List of Authors

Bold papercodes indicate primary authors

— A —

Abbasi Davani, F. MOP22
Abegglen, F.P. THA04
Abraham, J. WEB01
Abs, M. TUP06, TUP07, TUD03, THB01
Adams, T. THP24
Adelmann, A. **MOB03**, MOD03, **WEA04**, THP18, THC02
Afarideh, H. MODM02, MODM03, MOP03, MOP22, WEB03, THP07, THD02
Afkhami Karaei, M. MODM02, **MOP03**, MOP22
AL-Ghamdi, SA. TUP13
Algaith, A. TUP13
Allegra, L. THP09
Alrumayan, F.M. TUP12, **TUP13**
Alwani, A.N. **THP02**
Amaldi, U. MOE01
Amelia, J.C. TUP02
An, Shizhong. MOP05, **TUP14**
Andrighetto, A. MOP15, THA02
Anthony, L.S. THA02
Antonini, P. MOP04, **TUP09**, FRA03
Arje, J. THA04
Astarina, H. MOP13
Au, T. THP03
Avreline, N.V. **THP03**
Azizpourian, S. MOP03, **MOP22**

— B —

Baard, S. THA02
Baartman, R.A. TUA04, WEA03, THD03
Bai, M. MOP18, THP04
Ballan, M. **MOP15**
Barcikowski, S. MOD02
Bark, R.A. THA02
Barley, J. TUB03
Barlow, R.J. MOD03
Barnard, A.H. THA02
Bartlett, C.D. THP03
Bartnik, A.C. TUB03
Bastos, M.C. TUP10
Baumgarten, C. MOD03, **THP16**
Bazarov, I.V. TUB03
Böker, J. **MOC02**
Bechstedt, U. MOC02
Ben-Zvi, I. TUB03
Bencini, V. MOE01
Benini, D. FRA03
Berg, J.S. TUB03
Bergesio, D. MOE01
Bergmann, R.M. MOC01
Bi, Y.F. MOP14, TUP17, THP20, THP27, THC03
Bisoffi, G. FRA03
Blackmore, E.W. **MOBS02**
Blaskiewicz, M. TUB03
Blosser, G.F. THB02
Bogacz, S.A. TUB03
Bogomolov, S.L. THA03, THP25
Boiesan, T. TUD04
Bollen, G. TUA01
Boratto, E. TUP09, FRA03
Borgna, F. MOP15
Bouquerel, E. **THP24**
Braccini, S. **TUD01**
Brandenburg, S. **MOBS01**
Brison, J. **TUP01**, TUP02
Broodryk, J.I. MOP10, MOP11, THA02
Brooks, S.J. TUB03
Brown, K.A. TUB03
Bula, C. TUA02
Bulteau-harel, F. TUD02
Bundesmann, J. MOE02, TUA03
Burini, F. TUP10
Busold, S. **THP05**, **THP06**
Bylinskii, I.V. **TUA04**, TUP10, WEA03, THP03, THD03

— C —

Cafici, M. THP10
Cai, H.R. TUP15, TUP16, FRB03
Cailliau, P. TUP01, **TUP02**
Calabretta, L. **MOA02**, TUC03
Calanna, A. MOA02, TUC03
Calderolla, M. FRA03
Calore, A. MOP04, TUP09, FRA03
Campo, D. **MOP04**, TUP09, FRA03
Cao, L.C. TUP14, TUP15, TUP16, FRB03
Carbonaro, A. THP10
Carlson, M. TUD04
Carrozza, S. **TUP10**
Caruso, A.C. **WEB02**
Caruso, F. WEB02
Chai, J.-S. MOP03, MOP08, MOP20, TUP22, TUP23, THP14, THP15
Chao, C. TUP17
Chautard, F. FRB02
Chen, G. MOP14, **TUP17**, THP20, THP27, THC03
Chen, J.E. THB04
Chen, Q.S. MODM04, MOP12
Chen, W. MOD01, **MODM01**, MODM04, MOP12
Chen, Y. MOP14, TUP17, THP20, THP27, THC03

ISBN 978-3-95450-167-0

Choi, C.U. **MOP09**
Choi, H.J. TUP23
Chouhan, S. TUA01
Chubaryan, G. THA04
Chung, M. MOP09
Ciatara, N. FRA03
Cihak, M. MOP02
Clark, H.L. THA04
Colmant, T. FRA02
Conjat, M. TUP02, THB01, FRA01
Conradie, J.L. MOP10, MOP11, WEB01, **THA02**
Cornell, J.C. THA02
Corradetti, S. MOP15
Costa, G. THP09
Crittenden, J.A. TUB03
Cuccagna, C. MOE01
Cuttone, G. MOA02
Cvachovec, F. MOP17

— D —

D'Agostino, G. MOA02, **TUC03**
Damerow, T. MOE02, TUA03
Dantsuka, T. MOA01
Dölling, R. **THP17**
De Neuter, S. TUP04, TUD03
de Ruvo, L. FRA03
De Villiers, J.G. **MOP10**, MOP11, THA02
DeKamp, J. TUA01
Delvaux, J.L. TUP05, TUP06
Denker, A. MOE02, **TUA03**
Di Stefano, A. THP10
Ding, K.Z. **MOP14**, TUP17, THP20, THP27, THC03
Dishman, R. TUP08
Dmitriev, S.N. THA03, THP25
Dobbins, J. TUB03
Dorman, E.F. THP19
Douglas, D. TUB03
Du Plessis, H. THA02
Du, D. TUD04
Du, Sh. MOP14, THP20
Duatti, A. MOP15
Duckitt, W. MOP11, **WEB01**, THA02
Dunham, B.M. TUB03

— E —

Eichhorn, R.G. TUB03
Emery, R.C. **THP19**
Esposito, J. TUP09, FRA03
Etienne, J.B. TUD02
Evans, T. TUD04

— F —

Fan, K. MODM01, MOP12
Fan, M. MOP12
Fanselow, T. TUA03
Favaron, P. FRA03
Felcini, E. MOE01
Felden, O. **MOP18**, THP04
Feng, H. MOP14, TUP17, THP20, THP27, THC03
Feng, J. THP27
Fernandez Carmona, P. TUA02
Ferrari, E. TUP10
Fischer, W. TUB03
Forton, E. TUP01, TUP02, TUP03, TUP07, THB01, THP01, **FRA02**
Fourie, D.T. MOP11, THA02
Frey, M. **THC02**
Fu, X.L. TUP14
Fujimaki, M. MOA01
Fukuda, M. MOB01, TUP11, THB03, **THP12**
Fukunishi, N. MOA01, TUB04, TUC02
Furuta, F. TUB03

— G —

Gad, Kh.M. MOP08
Gallagher, R.E. TUB03
Gallo, G. **THP09**
Ganesh, G. THD03
Gardiner, P.G. THA02
Garonna, A. **MOE01**
Gathings, L.N. THA04
Gökce, B. MOD02
Ge, J. MOP14, THP20
Ge, T. TUP15, TUP16, FRB03
Gebel, R. MOC02, MOP18, THP04
Geets, J.-M. TUP05
Ghergherehchi, M. MODM02, MODM03, MOP03, MOP08, MOP20, TUP22, TUP23, WEB03, THP14, THP15, THD02
Ghorashinejad, Y. THP07
Gikal, B. **THA03**, THP25
Girault, S. TUD02
Goiziou, X. TUD02
Gomez, F. TUD02
Goto, A. THP13
Gotz, M. MOP02
Green, M.A. TUA01
Grillenberger, J. MOP16, **THA01**
Gsell, A. WEA04
Gulbekyan, G.G. THA03, THP25
Guo, Z.Y. THB04
Gurskiy, S. THC03

— H —

Ha, D.H. MOP08, MOP20, TUP22, TUP23, **THP14**, THP15
Hahn, G. MOP09
Hao, Y. TUB03
Hara, S. TUP11, THB03, THP12

Hasebe, H. MOA01
Hassani, M. **THP07**
Hatanaka, K. TUP11, **THB03**, THP12
Hecker, R. MOP18
Heitz, G. THP24
Hendy, A.M. **TUP12**, TUP13
Henrotin, S. MOP19, **TUP07**, THB01, FRA02
Herbert, A. TUD02
Higurashi, Y. MOA01
Hildebrand, D. TUA03
Hiller, U. TUA03
Hoffstaetter, G.H. TUB03
Hogan, M.E. THA02
Hojo, S. **THP11**
Horner, G.S. THB02
Hou, S.G. **MOP05**
Huda, N. MOP13
Hudson, G. TUP10
Huet, C. TUD02
Hur, M.G. MOP21, TUP19

— I —

Ikezawa, E. MOA01
Imao, H. MOA01, **TUC02**
Ineichen, Y. WEA04
Ishi, Y. **THC01**
Ismuha, R.R. MOP13
Ivanenko, I.A. **TUP25**, TUP26, WEA02, THA03, THP25
Ivanov, G.N. THP25

— J —

Jakovljevic, B. THP03
Jancar, A. **MOP17**
Jang, H.M. THP22
Jayamanna, K. TUA04
Jendrzej, S. **MOD02**
Johnson, R.R. TUD04
Jones, F.W. THD03
Jongen, Y. TUP07, THB01
Jun, W.J. TUP23, **THP15**

— K —

Kalagin, I.V. THA03, **THP25**
Kamakura, K. TUP11, THB03, THP12
Kamalou, O. **FRB02**
Kambali, I. **MOP13**
Kamigaito, O. MOA01, TUC02
Kang, B. THP22
Kang, J. **THP22**
Karamyshev, O. MOP14, TUP17, THP20, THP27, THC03
Karamysheva, G.A. MOP14, TUP17, THP20, THP27, **THC03**
Kardinah, K. MOP13
Kase, M. TUB04, TUC02, THP13
Kashiwagi, H. MOB01
Kassim, H.A. TUP12, TUP13
Katagiri, K. THP11
Kazarinov, N.Yu. **TUP26**, **WEA02**, THA03, THP25
Kezzar, K. TUP12
Kidera, M. MOA01
Kim, G.J. THA04
Kim, H.S. MOP08, MOP20, **TUP22**, TUP23, THP14, THP15
Kim, J.-W. THP22
King, Q. TUP10
Kirch, K. **MOAW02**
Kiselev, D.C. **MOC01**
Kleeven, W.J.G.M. **TUP03**, TUP04, TUP05, TUP06, TUP07, TUD03, **WEA01**, THB01, FRA02
Kleinrahm, A. MOD02
Klimpki, G. TUA02
Koay, H.W. TUP11, THP12
Kohler, I.H. THA02
Kolano, A.M. **MOD03**
Komiyama, M. MOA01
Kong, Y.B. MOP21, **TUP19**
Kopecky, Z. MOP17
Korenev, S. **TUP08**
Kotaka, Y. THP13
Kral, E.K. TUP03, TUD03
Kumagai, K. MOA01
Kume, T. TUP11, THP12
Kunert, C.S.G. MOE02
Kurashima, S. **MOB01**
Kuriyama, Y. THC01

— L —

Lamon, T. THP01
Lamouric, L. TUD02
Laxdal, A. **THD03**
Le Godec, G. TUP10
Lee, E.J. **MOP21**, TUP19
Lee, J. MOP09
Lee, J.C. **MOP08**, MOP20, TUP22, TUP23, THP14, THP15
Lee, J.H. THP22
Lee, T.-Y. MOP09
Li, J. MOP14, THP20, THC03
Li, M. MOP06
Li, M. THP27
Li, Y. TUB03
Li, Z.G. TUP14, **TUP16**, FRB03
Liang, Z.K. **MOD01**, MODM01, MODM04, MOP12
Listiawadi, F.D. MOP13
Litvinenko, V. TUB03
Liu, G.G. TUP16
Liu, G.S. TUP14
Liu, K.F. MOD01, MODM01, MODM04, MOP12

ISBN 978-3-95450-167-0

Liu, X. MOD01, MODM01, **MODM04**, MOP12
Liu, Z.W. MOP05
Lombardi, A. MOP04, TUP09, FRA03
Longhitano, A. WEB02
Lou, W. TUB03
Louie, W. L. TUP10
Lund, K.R. TUA01
Lussi, C. THA02
Lv, Y.L. TUP14, FRB03

— M —

Maazouzi, C. THP24
Mace, E. TUD02
Maggiore, M. MOP04, TUP09, **FRA03**
Magsig, C. TUA01
Mahler, G.J. TUB03
Maie, T. MOA01
Mandrillon, J. TUP02, THB01
Mandrillon, P. TUP02, THB01, **FRA01**
Marlina, M. MOP13
Martin Yebra, A. TUP08
Matej, Z. MOP17
Matthieu, C. THP24
May, D.P. **THA04**
May, H.P. **THP04**
Mayes, C.E. TUB03
McAlister, R.H. THA02
Meer, D. TUA02
Meng, W. TUB03
Méot, F. TUB03
Meshcheryakov, N.D. TUP08
Messina, E. THP09
Metzger-Kraus, C.J. WEA04
Minty, M.G. TUB03
Mira, J. MOP11, THA02
Miyawaki, N. MOB01
Mohamadian, M. **MODM03**
Monetti, A. THA02
Mori, Y. THC01
Morinobu, S. TUP11, THP12
Morozov, N.A. MOP14, TUP17, **THP20**, THP27, THC03
Morrissey, D.J. TUA01
Mostert, H.W. THA02
Mousavinia, M. MOP03, MOP22, **WEB03**
Mun, S.C. MOP08, **MOP20**, TUP22, TUP23, THP14, THP15

— N —

Nactergal, B. TUP03, TUP04, **TUP05**, TUP06, **TUD03**
Nagase, M. MOA01
Nagatomo, T. MOA01
Nagayama, K. THP12
Nakagawa, T. MOA01
Nakamura, M. MOA01
Nakao, M. THP11
Namgoong, H. MOP08, MOP20, TUP22, **TUP23**, THP14, THP15
Nemulodi, F. MOP10, **MOP11**, THA02
Niesler, T.R. WEB01
Noda, A. THP11
Noda, K. THP11
Noto, F. **THP10**
Nussbaumer, R.B. TUP10
Nuttens, V. TUP03, TUP04, TUP06, TUD03, **THP01**

— O —

Oberdorfer, F. MOD02
Oganessian, Y.T. THA03, THP25
Ohnishi, J. MOA01, **THP13**
Okumura, S. MOB01
Okuno, H. **MOA01**, TUC02, **FRBF01**
Osipov, N.F. THA03, THP25
Osswald, F.R. TUP26, THP24
Ottarson, J. TUA01
Ozeki, K. MOA01

— P —

Pagano, A. THP10
Pan, G.F. TUP14
Pang, X. WEA04
Paradis, Y. MOP19, THP01
Park, J.H. TUP19
Park, Y.D. TUP19
Partowidjojo, A.S. THP06
Parwanto, P. MOP13
Pashchenko, S.V. THA03
Patterson, J.R. TUB03
Pavlovsky, I. TUP08
Peggs, S. TUB03
Pellicioli, M. THP24
Peng, S.X. **THB04**
Pfeiffer, G. THA02
Piazza, L. AC. TUD04
Planche, T. TUA04, **WEA03**, THD03
Poggi, M. TUP09
Pogue, N. THP18
Poirier, F. **TUD02**
Popov, D.V. THC03
Poyac, D. TUD02
Pranovi, L. MOP04, TUP09, FRA03
Prechtl, M. MOB02
Prete, G.P. THA02, FRA03
Pretelli, M.P. TUP10
Primadei, G. WEB02
Psoroulas, S. **TUA02**
Ptitsyn, V. TUB03

ISBN 978-3-95450-167-0

— Q —

Qin, B. MOD01, MODM01, MODM04, **MOP12**
Quets, S. FRA02
Quilitzsch, S. MOC02

— R —

Rahimpour Kalkhoran, N. **MODM02**
Rajiman, R. MOP13
Rao, Y.-N. TUA04, WEA03
Röcken, H. THP05, THP06
Realdon, N. MOP15
Ren, H.T. THB04
Rethfeldt, C. TUA03
Rifuggiato, D. MOA02, TUC03
Rizzoglio, V. WEA04
Roeder, B.T. THA04
Röhrich, J. TUA03
Rogers, C.T. WEA04
Roser, T. TUB03
Rossignoli, M. THA02
Rousseau, M. THP24
Rueß, R. MOB02
Ruescas, C. THP24
Russell, S.J. WEA04
Russo, A.D. MOA02
Ryjkov, V. TUD04

— S —

Saastamoinen, A. THA04
Sabaiduc, V. **TUD04**
Sabol, D.M. TUB03
Sabounchi, S. MODM02, MODM03, **THD02**
Sagan, D. TUB03
Saito, T. TUP11, THP12
Sakamoto, M. THC01
Sakamoto, N. MOA01, **TUB04**, TUC02
Sakildien, M. THA02
Sakurai, H. **TUB01**
Salehi, M. MODM03
Samsonov, E.V. MOP14, TUP17, THP20, THP27, THC03
Sarchiapone, L. FRA03
Satogata, T. TUB03
Satoh, T. MOB01
Savalle, A. FRB02
Scarpa, D. FRA03
Schippers, J.M. THP06
Schneider, J.F. TUP13
Schneider, M. **THP18**
Schuler, J. THP24
Schwarz, S. **TUA01**
Schweickert, H. MOD02
Seidel, M. **MOAW01**, MOP16, THA01, **FRB01**
Seidel, S. **MOE02**
Sekiguchi, K. TUB04
Sen, A. THD03
Sheehy, S.L. WEA04, **THD01**
Shimada, K. THB03, THP12
Shin, S. MOP09
Shin, S. THP14
Shirkov, G. MOP14, TUP17, THP20, THP27, THC03
Shirkov, S.G. THC03
Smirnov, I.B. TUP08
Smirnov, V.L. **WEB04**, THB02
Smolenski, K.W. TUB03
Sobbia, R. MOC01
Solhju, R. MOP03, THD02
Song, G.F. MOP05
Song, Y. MOP14, TUP17, THP20, THP27, THC03
Spartà, A. WEB02
Speziale, F. THP10
Stazyk, W. TUD04
Stevens, K. THB02
Steyn, G.F. THA02
Stingelin, L. THP18
Stodart, N. THA02
Stursa, J. **MOP02**
Suda, K. MOA01, TUB04, TUC02
Sugiura, A. THP11
Sumithrarachchi, C. TUA01
Sura, J. WEB02
Suryanto, H. MOP13
Suthanthiran, K. TUD04

— T —

Tabacaru, G. THA04
Taddia, G.T. TUP10
Taft, F. MOP03
Talanov, V. MOC01
Talman, R.M. TUB03
Talmor, S. TUD04
Tamura, H. THP12
Tan, P. MOP12
Tarnopolski, I. TUD04
Thieberger, P. TUB03
Thomae, R.W. MOP10, MOP11, THA02
Thorson, S. TUP01
Tkint, I.C. MOP19
Traykov, E.K. THP24
Trbojevic, D. **TUB03**
Trichet, H. TUD02
Trubnikov, G.V. THC03
Tsoupas, N. TUB03
Tuozzolo, J.E. TUB03

— U —

Uchiyama, A. MOA01
Ueda, H. THB03, THP12
Uesugi, T. THC01

ISBN 978-3-95450-167-0

Usher, N.R. THB02

— V —

van de Walle, J. **MOP19**, TUP03, TUP04, TUP06, TUP07, TUD03, **THB01**, FRA02
Van Niekerk, M.J. MOP11, WEB01, THA02
van Schalkwyk, P.A. THA02
Vanderlinden, T. TUP05
Varasteh Anvar, M. MOE01
Vaziri Sereshk, M. R. MOE01
Verbruggen, P. TUP07, THB01, FRA02
Vigneron, R. TUP05
Villari, A.C.C. TUA01
Vincent, J.J. **THB02**
Vorozhtsov, S.B. WEB04, THB02

— W —

Wakui, T. THP11
Wang, C. MOP06, WEA04
Wang, F. MOP05, FRB03
Wang, S.Y. TUP17
Wang, X.W. **TUP27**
Wang, Y. TUP14
Watanabe, S. MOA01
Watanabe, T. MOA01
Watanabe, Y. MOA01
Weber, A. MOE02
Weber, D.C. TUA02
Wei, J.Y. TUP16
Wei, S.M. TUP15, FRB03
Wen, J.M. THB04
Wen, L.P. MOP05, TUP14, FRB03
Winklehner, D. **TUB02**, WEA04
Witte, H. TUB03
Wohlmuther, M. MOC01
Wolf, C.R. **MOB02**
Wu, L.C. TUP16
Wu, W.B. THB04
Wu, X. THB02

— X —

Xie, Y.H. MOP14, THC03
Xing, J.S. TUP14
Xu, M. TUP17
Xu, Y. THB04

— Y —

Yamada, K. MOA01, TUC02
Yamanoshita, R. TUP11, THP12
Yamasawa, H. MOA01
Yang, J.J. MOP06, MOP10, MOP11, TUC01, TUP15, TUP16, WEA04, **FRB03**
Yang, Q. TUP17, THC03
Yang, S.D. TUP19
Yano, Y. TUC02
Yasuda, Y. TUP11, THB03, THP12
Yeon, Y.H. THP15
Yin, Z.G. TUP15
Yong, F. TUP27
Yorita, T. **TUP11**, THB03, THP12
Yoshida, K. MOB01
Yu, T. MOP12
Yuyama, T. MOB01

— Z —

Zach, V. MOP02
Zafiropoulos, D. FRA03
Zakerhosseini, F. THD02
Zanetti, P. TUD04
Zappalà, E. THP09
Zaremba, S. TUP03, **TUP04**, TUP05, **TUP06**, TUD03
Zeller, A.F. TUA01
Zeng, Zeng. THP27
Zha, J. MOD01
Zhang, A.L. THB04
Zhang, D.S. **MOP06**
Zhang, H. **MOP16**
Zhang, J.F. THB04
Zhang, R. TUP27
Zhang, S.P. FRB03
Zhang, T. THB04
Zhang, T.J. MOP05, MOP06, MOP10, MOP11, **TUC01**, TUP14, TUP15, FRB03
Zhang, X. TUP17
Zhang, Y.W. TUP14, **TUP15**, FRB03
Zhen, X. FRB03
Zheng, J. MOP14, TUP17, THP20, **THP27**, THC03
Zhou, J. TUP17, THP20
Zhu, J. TUD04
Zhukovsky, A. THP01
Zvyagintsev, V. THP03

ISBN 978-3-95450-167-0

Institutes List

Advanced Radiation Technology Institute, Korea Atomic Energy Research Institute
Jeongup-si, Jeollabuk-do, Republic of Korea
- Park, Y.D.

AIMA
Nice, France
- Conjat, M.
- Mandrillon, J.
- Mandrillon, P.

ANI
Austin, USA
- Pavlovsky, I.

ASIPP
Hefei, People's Republic of China
- Bi, Y.F.
- Chao, C.
- Chen, G.
- Chen, Y.
- Ding, K.Z.
- Du, Sh.
- Feng, H.
- Feng, J.
- Ge, J.
- Li, J.
- Li, M.
- Song, Y.
- Wang, S.Y.
- Xie, Y.H.
- Xu, M.
- Yang, Q.
- Zeng, Zeng.
- Zhang, X.
- Zheng, J.
- Zhou, J.

AUT
Tehran, Iran
- Afarideh, H.
- Afkhami Karaei, M.
- Azizpourian, S.
- Ghorashinejad, Y.
- Hassani, M.
- Mohamadian, M.
- Mousavinia, M.
- Rahimpour Kalkhoran, N.
- Sabounchi, S.
- Salehi, M.
- Solhju, R.
- Taft, F.
- Zakerhosseini, F.

BATAN
South Tangerang, Indonesia
- Kambali, I.
- Marlina, M.
- Parwanto, P.
- Rajiman, R.
- Suryanto, H.

BCSI
Vancouver, Canada
- Boiesan, T.
- Johnson, R.R.
- Stazyk, W.
- Suthanthiran, K.
- Talmor, S.
- Zhu, J.

Best Theratronics Ltd.
Ottawa, Ontario, Canada
- Carlson, M.
- Du, D.
- Evans, T.
- Piazza, L. AC.
- Ryjkov, V.
- Sabaiduc, V.
- Tarnopolski, I.
- Zanetti, P.

BNL
Upton, Long Island, New York, USA
- Ben-Zvi, I.
- Berg, J.S.
- Blaskiewicz, M.
- Brooks, S.J.
- Brown, K.A.
- Fischer, W.
- Hao, Y.
- Litvinenko, V.
- Mahler, G.J.
- Meng, W.
- Méot, F.
- Minty, M.G.
- Peggs, S.
- Ptitsyn, V.
- Roser, T.
- Thieberger, P.
- Trbojevic, D.
- Tsoupas, N.
- Tuozzolo, J.E.
- Witte, H.

CERN
Geneva, Switzerland
- Bastos, M.C.
- Hudson, G.
- King, Q.
- Le Godec, G.
- Primadei, G.

ISBN 978-3-95450-167-0

Charite
Berlin, Germany
- Weber, A.

CIAE
Beijing, People's Republic of China
- An, Shizhong.
- Cai, H.R.
- Cao, L.C.
- Fu, X.L.
- Ge, T.
- Hou, S.G.
- Li, M.
- Li, Z.G.
- Liu, G.G.
- Liu, G.S.
- Liu, Z.W.
- Lv, Y.L.
- Pan, G.F.
- Song, G.F.
- Wang, C.
- Wang, F.
- Wang, Y.
- Wei, J.Y.
- Wei, S.M.
- Wen, L.P.
- Wu, L.C.
- Xing, J.S.
- Yang, J.J.
- Yin, Z.G.
- Zhang, D.S.
- Zhang, S.P.
- Zhang, T.J.
- Zhang, Y.W.
- Zhen, X.

CNRS - DR17
RENNES, France
- Girault, S.
- Poirier, F.

CNSC
Ottawa, Canada
- Alwani, A.N.

CNS
Saitama, Japan
- Kotaka, Y.

Cornell University (CLASSE), Cornell Laboratory for Accelerator-Based Sciences and Education
Ithaca, New York, USA
- Barley, J.
- Bartnik, A.C.
- Bazarov, I.V.
- Crittenden, J.A.
- Dobbins, J.
- Dunham, B.M.
- Eichhorn, R.G.
- Furuta, F.
- Gallagher, R.E.
- Hoffstaetter, G.H.
- Li, Y.
- Lou, W.
- Mayes, C.E.
- Patterson, J.R.
- Sabol, D.M.
- Sagan, D.
- Smolenski, K.W.
- Talman, R.M.

Cyclotron ARRONAX
Saint-Herblain, France
- Bulteau-harel, F.
- Etienne, J.B.
- Girault, S.
- Goiziou, X.
- Gomez, F.
- Herbert, A.
- Huet, C.
- Lamouric, L.
- Mace, E.
- Poirier, F.
- Poyac, D.
- Trichet, H.

Dharmais Cancer Hospital
Jakarta, Indonesia
- Astarina, H.
- Huda, N.
- Ismuha, R.R.
- Kardinah, K.
- Listiawadi, F.D.

EMN
Nantes, France
- Huet, C.

ETH
Zurich, Switzerland
- Kirch, K.

FRIB
East Lansing, Michigan, USA
- Bollen, G.
- Chouhan, S.
- DeKamp, J.
- Green, M.A.
- Magsig, C.
- Villari, A.C.C.
- Zeller, A.F.

FZJ
Jülich, Germany
- Bai, M.
- Bechstedt, U.

- Böker, J.
- Felden, O.
- Gebel, R.
- Hecker, R.
- May, H.P.
- Quilitzsch, S.
- Wolf, C.R.

GANIL
Caen, France
- Chautard, F.
- Kamalou, O.
- Savalle, A.

HS Coburg
Coburg, Germany
- Prechtl, M.
- Rueß, R.

Huazhong University of Science and Technology, State Key Laboratory of Advanced Electromagnetic Engineering and Technology,
Hubei, People's Republic of China
- Chen, W.
- Liang, Z.K.
- Liu, X.
- Yu, T.
- Zha, J.

HUST
Wuhan, People's Republic of China
- Chen, Q.S.
- Fan, K.
- Fan, M.
- Liu, K.F.
- Qin, B.
- Tan, P.

HZB
Berlin, Germany
- Bundesmann, J.
- Damerow, T.
- Denker, A.
- Fanselow, T.
- Hildebrand, D.
- Hiller, U.
- Kunert, C.S.G.
- Metzger-Kraus, C.J.
- Rethfeldt, C.
- Röhrich, J.
- Seidel, S.

IBA
Louvain-la-Neuve, Belgium
- Abs, M.
- Amelia, J.C.
- Brison, J.
- Cailliau, P.
- Colmant, T.
- De Neuter, S.
- Delvaux, J.L.
- Forton, E.
- Geets, J.-M.
- Henrotin, S.
- Jongen, Y.
- Kleeven, W.J.G.M.
- Kral, E.K.
- Lamon, T.
- Nactergal, B.
- Nuttens, V.
- Paradis, Y.
- Quets, S.
- Thorson, S.
- Tkint, I.C.
- van de Walle, J.
- Vanderlinden, T.
- Verbruggen, P.
- Vigneron, R.
- Zaremba, S.

IBM Research - Zurich
Rueschlikon, Switzerland
- Ineichen, Y.

IBS
Daejeon, Republic of Korea
- Jang, H.M.
- Kang, B.
- Kang, J.
- Kim, J.-W.
- Lee, J.H.

IIAA
Huddersfield, United Kingdom
- Barlow, R.J.

IMP/CAS
Lanzhou, People's Republic of China
- Wang, X.W.
- Yong, F.
- Zhang, R.

INFN/LNL
Legnaro (PD), Italy
- Andrighetto, A.
- Antonini, P.
- Ballan, M.
- Benini, D.
- Bisoffi, G.
- Boratto, E.
- Borgna, F.
- Calderolla, M.
- Calore, A.
- Campo, D.
- Ciatara, N.
- Corradetti, S.

ISBN 978-3-95450-167-0

- de Ruvo, L.
- Esposito, J.
- Favaron, P.
- Lombardi, A.
- Maggiore, M.
- Monetti, A.
- Poggi, M.
- Pranovi, L.
- Prete, G.P.
- Rossignoli, M.
- Sarchiapone, L.
- Scarpa, D.
- Zafiropoulos, D.

INFN/LNS
Catania, Italy

- Allegra, L.
- Cafici, M.
- Calabretta, L.
- Calanna, A.
- Carbonaro, A.
- Caruso, A.C.
- Caruso, F.
- Costa, G.
- Cuttone, G.
- D'Agostino, G.
- Di Stefano, A.
- Gallo, G.
- Longhitano, A.
- Messina, E.
- Noto, F.
- Pagano, A.
- Rifuggiato, D.
- Russo, A.D.
- Spartà, A.
- Speziale, F.
- Zappalà, E.

INSERM
Nantes, France

- Mace, E.

Ionetix
Lansing, Michigan, USA

- Blosser, G.F.
- Horner, G.S.
- Stevens, K.
- Usher, N.R.
- Vincent, J.J.
- Wu, X.

IPHC
Strasbourg Cedex 2, France

- Adams, T.
- Bouquerel, E.
- Heitz, G.
- Maazouzi, C.
- Matthieu, C.
- Osswald, F.R.
- Pellicioli, M.
- Rousseau, M.
- Ruescas, C.
- Schuler, J.
- Traykov, E.K.

iThemba LABS
Somerset West, South Africa

- Abraham, J.
- Anthony, L.S.
- Baard, S.
- Bark, R.A.
- Barnard, A.H.
- Broodryk, J.I.
- Conradie, J.L.
- Cornell, J.C.
- De Villiers, J.G.
- Du Plessis, H.
- Duckitt, W.
- Fourie, D.T.
- Gardiner, P.G.
- Hogan, M.E.
- Kohler, I.H.
- Lussi, C.
- McAlister, R.H.
- Mira, J.
- Mostert, H.W.
- Nemulodi, F.
- Pfeiffer, G.
- Sakildien, M.
- Steyn, G.F.
- Stodart, N.
- Thomae, R.W.
- Van Niekerk, M.J.
- van Schalkwyk, P.A.

JAI
Oxford, United Kingdom

- Sheehy, S.L.

JINR/DLNP
Dubna, Moscow region, Russia

- Popov, D.V.

JINR
Dubna, Moscow Region, Russia

- Bogomolov, S.L.
- Dmitriev, S.N.
- Gikal, B.
- Gulbekyan, G.G.
- Gurskiy, S.
- Ivanenko, I.A.
- Ivanov, G.N.
- Kalagin, I.V.
- Karamyshev, O.
- Karamysheva, G.A.
- Kazarinov, N.Yu.

ISBN 978-3-95450-167-0

- Morozov, N.A.
- Oganessian, Y.T.
- Osipov, N.F.
- Pashchenko, S.V.
- Samsonov, E.V.
- Shirkov, G.
- Shirkov, S.G.
- Smirnov, V.L.
- Trubnikov, G.V.
- Vorozhtsov, S.B.

JLab
Newport News, Virginia, USA
- Bogacz, S.A.
- Douglas, D.
- Satogata, T.

KAERI
Daejon, Republic of Korea
- Hur, M.G.
- Kong, Y.B.
- Lee, E.J.
- Park, J.H.
- Yang, S.D.

King Faisal Specialist Hospital and Research Centre
Riyadh 11211, Kingdom of Saudi Arabia
- Algaith, A.
- Alrumayan, F.M.
- Hendy, A.M.
- Schneider, J.F.

KIRAMS
Seoul, Republic of Korea
- Hahn, G.

KSU
Riyadh, Kingdom of Saudi Arabia
- AL-Ghamdi, SA.
- Kassim, H.A.
- Kezzar, K.

KVI
Groningen, The Netherlands
- Brandenburg, S.

Kyoto University, Research Reactor Institute
Osaka, Japan
- Ishi, Y.
- Kuriyama, Y.
- Mori, Y.
- Sakamoto, M.
- Uesugi, T.

LANL
Los Alamos, New Mexico, USA
- Pang, X.
- Russell, S.J.

LHEP
Bern, Switzerland
- Braccini, S.

M.I.T. Plasma Science and Fusion Center
Cambridge, USA
- Zhukovsky, A.

Masaryk University
Brno, Czech Republic
- Matej, Z.

MIT
Cambridge, Massachusetts, USA
- Winklehner, D.

MSU
East Lansing, Michigan, USA
- Bollen, G.

NIRS
Chiba-shi, Japan
- Hojo, S.
- Katagiri, K.
- Nakao, M.
- Noda, A.
- Noda, K.
- Sugiura, A.
- Wakui, T.

NPI
Řež near Prague, Czech Republic
- Cihak, M.
- Gotz, M.
- Stursa, J.
- Zach, V.

NSCL
East Lansing, Michigan, USA
- Lund, K.R.
- Morrissey, D.J.
- Ottarson, J.
- Schwarz, S.
- Sumithrarachchi, C.

OCEM
Valsamoggia, Italy
- Burini, F.
- Carrozza, S.

ISBN 978-3-95450-167-0

- Ferrari, E.
- Pretelli, M.P.
- Taddia, G.T.

Okayama University
Okayama, Japan
- Ueda, H.

PAL
Pohang, Republic of Korea
- Lee, J.
- Lee, T.-Y.
- Shin, S.

PKU
Beijing, People's Republic of China
- Chen, J.E.
- Guo, Z.Y.
- Peng, S.X.
- Ren, H.T.
- Wen, J.M.
- Wu, W.B.
- Xu, Y.
- Zhang, A.L.
- Zhang, J.F.
- Zhang, T.

PSI
Villigen PSI, Switzerland
- Adelmann, A.
- Baumgarten, C.
- Bergmann, R.M.
- Bula, C.
- Dölling, R.
- Fernandez Carmona, P.
- Frey, M.
- Grillenberger, J.
- Gsell, A.
- Kiselev, D.C.
- Klimpki, G.
- Meer, D.
- Partowidjojo, A.S.
- Pogue, N.
- Psoroulas, S.
- Rizzoglio, V.
- Schippers, J.M.
- Schneider, M.
- Seidel, M.
- Sobbia, R.
- Stingelin, L.
- Talanov, V.
- Weber, D.C.
- Wohlmuther, M.
- Zhang, H.

QST/Takasaki
Takasaki, Japan
- Kashiwagi, H.
- Kurashima, S.
- Miyawaki, N.
- Okumura, S.
- Satoh, T.
- Yoshida, K.
- Yuyama, T.

RCNP
Osaka, Japan
- Fukuda, M.
- Hara, S.
- Hatanaka, K.
- Kamakura, K.
- Koay, H.W.
- Kume, T.
- Morinobu, S.
- Nagayama, K.
- Saito, T.
- Shimada, K.
- Tamura, H.
- Yamanoshita, R.
- Yasuda, Y.
- Yorita, T.

RIKEN Nishina Center for Accelerator-Based Science
Wako, Saitama, Japan
- Imao, H.

RIKEN Nishina Center
Wako, Japan
- Dantsuka, T.
- Fujimaki, M.
- Fukunishi, N.
- Goto, A.
- Hasebe, H.
- Higurashi, Y.
- Ikezawa, E.
- Imao, H.
- Kamigaito, O.
- Kase, M.
- Kidera, M.
- Komiyama, M.
- Kumagai, K.
- Maie, T.
- Nagase, M.
- Nagatomo, T.
- Nakagawa, T.
- Nakamura, M.
- Ohnishi, J.
- Okuno, H.
- Ozeki, K.
- Sakamoto, N.
- Suda, K.
- Uchiyama, A.
- Watanabe, S.
- Watanabe, T.
- Watanabe, Y.
- Yamada, K.

- Yamasawa, H.
- Yano, Y.

RIKEN
Saitama, Japan
- Sakurai, H.

Shahid Beheshti University
Tehran, Iran
- Abbasi Davani, F.

Siemens Healthcare
Moscow, Russia
- Meshcheryakov, N.D.
- Smirnov, I.B.

Siemens Medical Solutions Molecular Imaging
Knoxville, TN, USA
- Dishman, R.
- Korenev, S.
- Martin Yebra, A.

SKKU
Suwon, Republic of Korea
- Chai, J.-S.
- Choi, H.J.
- Gad, Kh.M.
- Ghergherehchi, M.
- Ha, D.H.
- Jun, W.J.
- Kim, H.S.
- Lee, J.C.
- Mun, S.C.
- Namgoong, H.
- Shin, S.
- Yeon, Y.H.

Stellenbosch University
Matieland, South Africa
- Niesler, T.R.

STFC/RAL/ASTeC
Chilton, Didcot, Oxon, United Kingdom
- Rogers, C.T.
- Sheehy, S.L.

TERA
Novara, Italy
- Amaldi, U.
- Bencini, V.
- Bergesio, D.
- Cuccagna, C.
- Felcini, E.
- Garonna, A.
- Varasteh Anvar, M.
- Vaziri Sereshk, M. R.

Texas A&M University Cyclotron Institute
College Station, Texas, USA
- Arje, J.
- Gathings, L.N.
- May, D.P.
- Roeder, B.T.
- Saastamoinen, A.

Texas A&M University, Cyclotron Institute
College Station, Texas, USA
- Abegglen, F.P.
- Chubaryan, G.
- Clark, H.L.
- Kim, G.J.
- Tabacaru, G.

Tohoku University, Graduate School of Science
Sendai, Japan
- Sekiguchi, K.

TRIUMF, Canada's National Laboratory for Particle and Nuclear Physics
Vancouver, Canada
- Au, T.
- Avreline, N.V.
- Baartman, R.A.
- Bartlett, C.D.
- Blackmore, E.W.
- Bylinskii, I.V.
- Jakovljevic, B.
- Jayamanna, K.
- Jones, F.W.
- Laxdal, A.
- Louie, W. L.
- Nussbaumer, R.B.
- Planche, T.
- Rao, Y.-N.
- Sen, A.
- Zvyagintsev, V.

UNIFE
Ferrara, Italy
- Ballan, M.

UNIST
Ulsan, Republic of Korea
- Choi, C.U.
- Chung, M.

University of Chinese Academy of Sciences
Beijing, People's Republic of China
- Zhang, A.L.

University of Defence
Brno, Czech Republic
- Cvachovec, F.

ISBN 978-3-95450-167-0

University of Huddersfield
Huddersfield, United Kingdom
- Kolano, A.M.

University of Victoria
Victoria BC, Canada
- Bartlett, C.D.

University of Washington Medical Center
Seattle, Washington, USA
- Dorman, E.F.
- Emery, R.C.

University of Zurich, University Hospital
Zurich, Switzerland
- Weber, D.C.

Università degli Studi di Ferrara
Ferrara, Italy
- Duatti, A.

Università degli Studi di Padova
Padova, Italy
- Borgna, F.
- Realdon, N.

Universität Duisburg-Essen
Essen, Germany
- Barcikowski, S.
- Gökce, B.
- Jendrzej, S.

UW/Physics
Waterloo, Ontario, Canada
- Ganesh, G.

VF, a.s.
Cerna Hora, Czech Republic
- Jancar, A.
- Kopecky, Z.

VMS-PT
Troisdorf, Germany
- Busold, S.
- Röcken, H.

Warsaw University
Warsaw, Poland
- Sura, J.

ZAG
Eggenstein-Leopoldshafen, Germany
- Kleinrahm, A.
- Oberdorfer, F.
- Schweickert, H.

ISBN 978-3-95450-167-0

Participants List

— A —

AALTONEN, Rauno
International Electric Co. Oy
Helsinki, FINLAND

ABDEL-BARY, Mamdouh
Varian Medical Systems PT
Troisdorf, GERMANY

ADELMANN, Andreas
PSI
Villigen PSI, SWITZERLAND

AFARIDEH, Hossein
Department of Energy Engineering and Physics, Amir Kabir University of Technology
Tehran, IRAN

AJMO, Barbara
PSI
Villigen PSI, SWITZERLAND

AKCOELTEKIN, Ender
VARIAN
Troisdorf, GERMANY

ALGHAITH, Ahmed
King Faisal Specialist Hospital
Riyadh, SAUDI ARABIA

ALHO, Kimmo
International Electric Co. Oy
Helsinki, FINLAND

ALRUMAYAN, Faisal
KFSHRC
Riyadh, SAUDI ARABIA

ALWANI, Abdul
Canadian Nuclear Safety Commission
Ottawa, CANADA

AN, Shizhong
CIAE
Beijing, CHINA

ANTONINI, Piergiorgio
INFN
Legnaro, ITALY

AOKI, Takamichi
Hitachi, Ltd., Research & Development Group
Hitachi-shi, Ibaraki-ken, JAPAN

AVRELINE, Alexandre
University of British Columbia
Vancouver, CANADA

AVRELINE, Nikolai
TRIUMF
Vancouver, CANADA

— B —

BAUMGARTEN, Christian
PSI
Villigen PSI, SWITZERLAND

BEECKMAN, William
Sigmaphi
Vannes, FRANCE

BERGHMANS, Vincent
JEMA S.A.
Louvain-la-Neuve, BELGIUM

BERTRAND, Patrick
GANIL
Caen, FRANCE

BLACKMORE, Ewart
TRIUMF
Vancouver, CANADA

BOLDT, Oliver
VARIAN Medical Systems Particle Therapy GmbH
Darmstadt, GERMANY

BOUQUEREL, Elian
CNRS/IN2P3
Strasbourg, FRANCE

BOUTERFA, Mohamed
ProSense
Louvain-la-Neuve, BELGIUM

BRACCINI, Saverio
University of Bern
Bern, SWITZERLAND

BRANDENBURG, Sytze
KVI-Center for Advanced Radiation Research, University of Groningen
Groningen, NETHERLANDS

BRUDERER, Sylvain
Magentasys
Villigen PSI, SWITZERLAND

BUGMANN, Marlen
PSI
Villigen PSI, SWITZERLAND

BUSOLD, Simon
VMS-PT
Troisdorf, GERMANY

BYLINSKII, Iouri
TRIUMF
Vancouver, CANADA

BÖKER, Jürgen
Forschungszentrum Jülich
Institute for Nuclear Physics
Jülich, GERMANY

— C —

CAILLIAU, Philippe
IBA
Louvain-la-Neuve, BELGIUM

CALABRETTA, Luciano
INFN-LNS
Catania, ITALY

CALANNA, Alessandra
INFN-LNS
Catania, ITALY

CALZOLAIO, Ciro
PSI
Villigen PSI, SWITZERLAND

CAMPO, Daniela
INFN-LNL
Legnaro, ITALY

ISBN 978-3-95450-167-0

CARUSO, Antonio
INFN-LNS
Catania, ITALY

CAVELLIER, Matthieu
SIGMAPHI
Vannes, FRANCE

CHAI, Jong Seo
Sungkyunkwan University
Suwon-si,Gyeonggi-Do
REPUBLIC OF KOREA

Chatzifotiadis, Daniil
251 G.N.A
Athens, GREECE

CHEN, Gen
Institute of Plasma Physics,
Chinese Academy of Sciences
Hefei, CHINA

CHEN, Wei
Huazhong University of Science
and Technology
Wuhan, CHINA

CHOI, Chulun
UNIST
Ulsan, REPUBLIC OF KOREA

CHRIN, Jan
PSI
Villigen PSI, SWITZERLAND

COJOCARU, Gabriel
TRIUMF
Vancouver, CANADA

CONJAT, Matthieu
Aima Developpement
Nice, FRANCE

CONRADIE, Jacobus Lodewikus
iThemba LABS
Cape Town, SOUTH AFRICA

CORRADETTI, Stefano
INFN-LNL
Legnaro, ITALY

COSTA, Giuseppe
INFN-LNS
Catania, ITALY

CRAHAY, Jean
JEMA S.A.
Louvain-la-Neuve, BELGIUM

— D —

D'AGOSTINO, Grazia
LNS-INFN and
University of Catania
Catania, ITALY

DE VILLIERS, John Garrett
iThemba LABS
Cape Town, SOUTH AFRICA

DENKER, Andrea
Helmholtz-Zentrum Berlin
Berlin, GERMANY

DING, Kaizhong
Institute of Plasma Physics,
Chinese Academy of Sciences
Hefei, CHINA

DODGE, Bill
Buckley Systems International
Rowley, USA

DORMAN, Eric
University of Washington
Medical Cyclotron Facility
Seattle, USA

DUCKITT, William Dawid
iThemba LABS
Cape Town, SOUTH AFRICA

DU, David
Best Cyclotron Systems
Vancouver, CANADA

DUPERREX, Pierre-André
PSI
Villigen PSI, SWITZERLAND

DÖLLING, Rudolf
PSI
Villigen PSI, SWITZERLAND

— E —

EHRENFRIED, Markus
Siemens Healthcare
Erlangen, GERMANY

EMERY, Robert
University of Washington Medical Center
Seattle, USA

— F —

FAN, Kuanjun
Institute of Applied Electromagnetic
Engineering, Huazhong University
of Science and Technology
Wuhan, CHINA

FAN, Mingwu
Huazhong University of Science
and Technology
Wuhan, CHINA

FELDEN, Olaf
Forschungszentrum Jülich,
Institut für Kernphysik, IKP
Jülich, GERMANY

FOIERA, Silvio
PSI
Villigen PSI, SWITZERLAND

FORTON, Eric
IBA
Louvain-la-Neuve, BELGIUM

FREI, Marcel
Ampegon
Turgi, SWITZERLAND

FREY, Matthias
PSI
Villigen PSI, SWITZERLAND

FUKUDA, Mitsuhiro
Osaka University
Ibaraki, Osaka, JAPAN

ISBN 978-3-95450-167-0

— G —

GARONNA, Adriano
TERA Foundation
Geneva, SWITZERLAND

GATHINGS, Leigh N.
Texas A&M University,
Cyclotron Institute
College Station, USA

GAUBERT, Gabriel
Pantechnik
Bayeux, FRANCE

GEBEL, Ralf
Forschungszentrum Jülich
Jülich, GERMANY

GERBERSHAGEN, Alexander
PSI
Villigen PSI, SWITZERLAND

GHERGHEREHCHI, Mitra
Sungkyunkwan University
Suwon-Si, REPUBLIC OF KOREA

GIKAL, Boris
FLNR JINR
Dubna, RUSSIA

GREWE, Marc
Varian Medical Systems
Particle Therapy GmbH
Troisdorf, GERMANY

GRILLENBERGER, Joachim
PSI
Villigen PSI, SWITZERLAND

GRINHAM, Rebecca
Edwards Vacuum
Burgess Hill, UNITED KINGDOM

— H —

HATANAKA, Kichiji
RCNP, Osaka University
Ibaraki, JAPAN

HEIKKINEN, Pauli
University of Jyväskylä
Jyväskylä, FINLAND

HOJO, Satoru
QST, NIRS
Chiba, JAPAN

— I —

IMAO, Hiroshi
RIKEN
Wako, JAPAN

ISHI, Yoshihiro
Kyoto University
Research Reactor Institute
Osaka, JAPAN

IVANENKO, Ivan
JINR
Dubna, RUSSIA

— J —

JAGGI, Vinder
Micromatter Technologies Inc.
Surrey, CANADA

JANCAR, Ales
VF, a.s.
Cerna Hora, CZECH REPUBLIC

JENDRZEJ, Sandra
Uinversity of Duisburg-Essen
Essen, GERMANY

JENSEN, Holger
PET and Cyclotron unit, Rigshospitalet
Coepnhagen, DENMARK

JOHANSSON, Stefan
Turku PET Centre
Turku, FINLAND

JOHO, Werner
PSI
Villigen PSI, SWITZERLAND

JONGEN, Yves
Ion Beam Applications sa
Louvain-la-Neuve, BELGIUM

— K —

KALAGIN, Igor
JINR FLNR
Dubna, RUSSIA

KAMALOU, Omar
GANIL
Caen, FRANCE

KAMBALI, Imam
National Nuclear Energy Agency
Jakarta, INDONESIA

KANG, Joonsun
Institute for Basic Science
Daejeon, REPUBLIC OF KOREA

KAN, Richard
PSI
Villigen PSI, SWITZERLAND

KARAMYSHEV, Oleg
Joint Institute for Nuclear Research
Dubna, RUSSIA

KAZARINOV, Nikolay
Joint Institute for Nuclear Research
Dubna, RUSSIA

KEENS, Simon
Ampegon
Turgi, SWITZERLAND

KIM, George
Cyclotron Institute, Texas A&M Univ.
College Station, USA

KIM, Hui Su
Sungkyunkwan University
SUWON-SI, REPUBLIC OF KOREA

KIM, Jongwon
Institute for Basic Science
Daejeon, REPUBLIC OF KOREA

KIRCH, Klaus
ETH
Zurich, SWITZERLAND

KISELEV, Daniela
PSI
Villigen PSI, SWITZERLAND

ISBN 978-3-95450-167-0

KLARNER, Fabian
Varian Medical Systems
Troisdorf, GERMANY

KLEEVEN, Willem
IBA
Louvain-la-Neuve, BELGIUM

KOLANO, Anna
University of Huddersfield
Huddersfield, UNITED KINGDOM

KONG, Young Bae
Korea Atomic Energy Research Institute
Jeongeup, REPUBLIC OF KOREA

KOPECKY, Zdenek
VF, a.s.
Cerná Hora, CZECH REPUBLIC

KURASHIMA, Satoshi
National Institutes for Quantum and
Radiological Science and Technology
Takasaki, JAPAN

KÜNZLER, Toni
MEWASA AG
Wangs, SWITZERLAND

— L —

LAXDAL, Aurelia
TRIUMF
Vancouver, CANADA

LEE, Eunje
Korea Atomic Energy Research Institute
Jeouneup-si, REPUBLIC OF KOREA

LIANG, Zhikai
Huazhong University of Science
and Technology
Wuhan, CHINA

LIU, Kaifeng
Huazhong University of Science
and Technology
Wuhan, CHINA

LIU, Xu
Huazhong University of Science
and Technology
Wuhan, CHINA

LOISELET, Marc
UCL
Louvain-la-Neuve, BELGIUM

— M —

MACHIDA, Shinji
STFC Rutherford Appleton Laboratory
Didcot, UNITED KINGDOM

MAGGIORE, Mario
INFN-LNL
Legnaro, ITALY

MANDRILLON, Jérôme
IBA
Louvain-la-Neuve, BELGIUM

MARX, Michaela
DESY
Hamburg, GERMANY

MATEJ, Zdenek
Masaryk university
Brno, CZECH REPUBLIC

MAY, Donald
Cyclotron Institute,
Texas A&M University
College Station, USA

MAY, Hans-Peter
Forschungszentrum Jülich,
Inst. für Kernphysik, IKP-4
Jülich, GERMANY

MINE, Nicolas
IBA
Louvain-la-Neuve, BELGIUM

MINERVINI, Joseph
Massachusetts Institute of Technology
Cambridge, USA

MISZCZAK, Jan
Heavy Ion Laboratory,
University of Warsaw
Warsaw, POLAND

MIYASHITA, Yuji
Mitsubishi Electric Corporation
Advanced Technology R&D Center
Hyogo, JAPAN

MOHAMADIAN, Masoumeh
Amirkabir University of Technology
Tehran, IRAN

MORI, Yoshiharu
Kyoto University, RRI
Osaka, JAPAN

MOROZOV, Nikolay
Joint Institute for Nuclear Research
Dubna, RUSSIA

MOUSAVINIA, Seyyed Mohsen
Amirkabir University of Technology
Tehran, IRAN

MUN, SangChul
SungKyunKwan University
Suwon, REPUBLIC OF KOREA

— N —

NACTERGAL, Benoît
IBA
Louvain-la-Neuve, BELGIUM

NAKANISHI, Tetsuya
Nihon University,
College of Industrial Technology
Narashino-shi, JAPAN

NEMULODI, Fhumulani
iThemba LABS
Cape Town, SOUTH AFRICA

NOTO, Francesco
Istituto Nazionale Fisica Nucleare
Laboratori Nazionali del Sud
Catania, ITALY

— O —

OHNISHI, Jun-ichi
RIken Nishina Center
Wako, JAPAN

OKUNO, Hiroki
RIKEN Nishina Center for
Accelerator-based Science
Saitama, JAPAN

OSSWALD, Francis
CNRS/IN2P3
Strasbourg, FRANCE

— P —

PATEL, Rajendra
PiezoMotor AB
Uppsala, SWEDEN

PIAZZA, Leandro
Best Theratronics
OTTAWA, CANADA

PIERRE, Mandrillon
Aima Developpement
Nice, FRANCE

POIRIER, Freddy
Arronax / CNRS
Saint Herblain, FRANCE

POSTIAU, Nancy
Université Catholique de Louvain
Louvain-la-Neuve, BELGIUM

PRANOVI, Lorenzo
INFN-LNL
Legnaro, ITALY

PRETELLI, Miguel
OCEM Power Electronics
Valsamoggia, ITALY

PSOROULAS, Serena
Centre for Proton Therapy, PSI
Villigen PSI, SWITZERLAND

— Q —

QIN, Bin
Huazhong University of Science
and Technology
Wuhan, CHINA

— R —

RADOVINSKY, Alexey
Massachusetts Institute of Technology
Cambridge, USA

RIFUGGIATO, Danilo
INFN - LNS
Catania, ITALY

RISLER, Ruedi
University of Washington Medical Center
Seattle, USA

RUESS, René
HS Coburg
Nürnberg, GERMANY

RÖCKEN, Heinrich
Varian Medical Systems
Troisdorf, GERMANY

— S —

SABAIDUC, Vasile
Best Cyclotron Systems
Vancouver, CANADA

SABOUNCHI, Saeed
Amirkabir University of Technology
Tehran, IRAN

SAKAMOTO, Naruhiko
RIKEN NISHINA CENTER
WAKO, JAPAN

SAKURAI, Hiroyoshi
RIKEN Nishina Center
Wako, JAPAN

SAMSONOV, Evgeny
JINR
Dubna, RUSSIA

SCHAA, Volker RW
GSI
Darmstadt, GERMANY

SCHIPPERS, Marco
PSI
Villigen PSI, SWITZERLAND

SCHMIDT, André
PSI
Villigen PSI, SWITZERLAND

SCHNEIDER, Markus
PSI
Villigen PSI, SWITZERLAND

SCHWARZ, Stefan
NSCL / Michigan State University
East Lansing, USA

SCHWEICKERT, Hermann
ZAG Zyklotron AG
Eggenstein-Leopoldshafen, GERMANY

SÉBASTIEN, Henrotin
IBA
Louvain-la-Neuve, BELGIUM

SEIDEL, Mike
PSI
Villigen PSI, SWITZERLAND

SEIDEL, Sophie
Helmholtz-Zentrum Berlin
Berlin, GERMANY

SHEEHY, Suzie
John Adams Institute,
University of Oxford
Oxford, UNITED KINGDOM

SHIRKOV, Grigori
Joint Institute for Nuclear Research
Dubna, RUSSIA

SMIRNOV, Victor
JINR
Dubna, RUSSIA

SNUVERINK, Jochem
PSI
Villigen PSI, SWITZERLAND

STANDAERT, Laurent
Université catholique de Louvain
Louvain-la-neuve, BELGIUM

STURSA, Jan
Nuclear Physics Institute,
Czech Academy of Sciences
Řež near Prague, CZECH REPUBLIC

ISBN 978-3-95450-167-0

— T —

TAN, Ping
Huazhong University of Science
and Technology
Wuhan, CHINA

THOMSON, Jana
TRIUMF
Vancouver, CANADA

TIEDE, Artur
Zyklotron AG
Eggenstein-Leopoldshafen, GERMANY

TODD, Damon
Lawrence Berkeley National Laboratory
Berkeley, USA

TORTORA, Mattia
CAEN ELS D.O.O.
Sezana, SLOVENIA

TRBOJEVIC, Dejan
Brookhaven National Laboratory
Upton, USA

— V —

VAN DE WALLE, Jarno
Ion Beam Applications
Louvain-la-Neuve, BELGIUM

VAN DER KRAAIJ, Erik
Ion Beam Applications
Louvain-la-Neuve, BELGIUM

VAN DER MEULEN, Nicholas
PSI
Villigen PSI, SWITZERLAND

VOROZHTSOV, Sergey
Joint Institute for Nuclear Research
Dubna,141 980, RUSSIA

— W —

WANG, Bing
IMP
Lanzhou, CHINA

WANG, Xian wu
IMP
Lanzhou, CHINA

WINKLEHNER, Daniel
MIT
Cambridge, USA

WITTSCHEN, Jürgen
Varian Medical Systems
Troisdorf, GERMANY

WOLF, Christian
University of Applied Sciences of Coburg
Untersiemau-Scherneck, GERMANY

WU, Xiaoyu
Ionetix Corporation
Lanisng, USA

— X —

XIA, Jiawen
Institute of Modern Physics,
Chinese Academy of Sciences
Lanzhou, CHINA

XU, Dayu
Lanzhou Kejin Taiji Corporation, LTD
Lanzhou, CHINA

XU, Yuan
Institute of Heavy Ion Physics
Beijing, CHINA

— Y —

YANG, Jiancheng
Institute of Modern Physics,
Chinese Academy of Sciences
Lanzhou, CHINA

YANG, Jianjun
CIAE
Beijing, CHINA

YANG, Weiqing
Institute of Modern Physics,
Chinese Academy of Sciences
Lanzhou, CHINA

YORITA, Tetsuhiko
Osaka University
Ibarakishi, Osaka, JAPAN

YU, Tiaoqin
Huazhong University of Science
and Technology
Wuhan, CHINA

— Z —

ZAREMBA, Simon
IBA
Louvain-la-Neuve, BELGIUM

ZHANG, Hui
PSI
Villigen PSI, SWITZERLAND

ZHANG, JieXi
Antaya Science and Technology
Hampton, USA

ZHANG, Tianjue
CIAE
Beijing, CHINA

ZHANG, Xiaoqi
Lanzhou Kejin Taiji Corporation, LTD.
Lanzhou, CHINA

ZHENG, Jinxing
Institute of Plasma Physics,
Chinese Academy of Sciences
Hefei, CHINA

ISBN 978-3-95450-167-0